NASA/TP—2006-212490/VOL2/PART2

NASA Aeroelasticity Handbook
Volume 2: Design Guides
Part 2

John K. Ramsey
Glenn Research Center, Cleveland, Ohio

November 2006

NASA STI Program . . . in Profile

Since its founding, NASA has been dedicated to the advancement of aeronautics and space science. The NASA Scientific and Technical Information (STI) program plays a key part in helping NASA maintain this important role.

The NASA STI Program operates under the auspices of the Agency Chief Information Officer. It collects, organizes, provides for archiving, and disseminates NASA's STI. The NASA STI program provides access to the NASA Aeronautics and Space Database and its public interface, the NASA Technical Reports Server, thus providing one of the largest collections of aeronautical and space science STI in the world. Results are published in both non-NASA channels and by NASA in the NASA STI Report Series, which includes the following report types:

- TECHNICAL PUBLICATION. Reports of completed research or a major significant phase of research that present the results of NASA programs and include extensive data or theoretical analysis. Includes compilations of significant scientific and technical data and information deemed to be of continuing reference value. NASA counterpart of peer-reviewed formal professional papers but has less stringent limitations on manuscript length and extent of graphic presentations.

- TECHNICAL MEMORANDUM. Scientific and technical findings that are preliminary or of specialized interest, e.g., quick release reports, working papers, and bibliographies that contain minimal annotation. Does not contain extensive analysis.

- CONTRACTOR REPORT. Scientific and technical findings by NASA-sponsored contractors and grantees.

- CONFERENCE PUBLICATION. Collected papers from scientific and technical conferences, symposia, seminars, or other meetings sponsored or cosponsored by NASA.

- SPECIAL PUBLICATION. Scientific, technical, or historical information from NASA programs, projects, and missions, often concerned with subjects having substantial public interest.

- TECHNICAL TRANSLATION. English-language translations of foreign scientific and technical material pertinent to NASA's mission.

Specialized services also include creating custom thesauri, building customized databases, organizing and publishing research results.

For more information about the NASA STI program, see the following:

- Access the NASA STI program home page at *http://www.sti.nasa.gov*

- E-mail your question via the Internet to *help@sti.nasa.gov*

- Fax your question to the NASA STI Help Desk at 301–621–0134

- Telephone the NASA STI Help Desk at 301–621–0390

- Write to:
  NASA STI Help Desk
  NASA Center for AeroSpace Information
  7115 Standard Drive
  Hanover, MD 21076–1320

NASA Aeroelasticity Handbook
Volume 2: Design Guides
Part 2
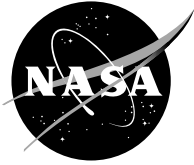
John K. Ramsey
Glenn Research Center, Cleveland, Ohio

Level of Review: This material has been technically reviewed by a committee of peers.

Available from

NASA Center for Aerospace Information   National Technical Information Service
7115 Standard Drive   5285 Port Royal Road
Hanover, MD 21076–1320   Springfield, VA 22161

Available electronically at http://gltrs.grc.nasa.gov

Acknowledgments

NASA Aeroelasticity Handbook
Volume 1: Database Users Manual

Volume 2: Design Guides[1]

Fixed-Wing Guides

Turbomachinery Guides

Propeller and Rotor Guides

---

[1]NASA Aeroelasticity Handbook, Volume 2: Design Guides, Part 2 (NASA/TM—2006-212490/VOL2/PART2, which does not include document 1 "Flutter Criteria for Preliminary Design" from the "Fixed-Wing Guides" section) is available to all requestors in printed form from the NASA Center for AeroSpace Information, 7121 Standard Drive, Hanover, MD 21076. It is also available online from http://gltrs.grc.nasa.gov.

Panel Guides

Scaling Guides

Part 1: Flutter Criteria for Preliminary Design[*]

Gilmore Harris
LTV Aeronautics and Missiles Division
Chance Vought Corporation
Dallas, Texas

This document (part 1 of vol. 2) is not available in this printed report. It is available to qualified requestors only on CD-ROM from the NASA Center for Aerospace Information 7115 Standard Drive, Hanover, Maryland 21076.

---

[*]This document was first published as Eng. Rep. 2–53450/3R467 by LTV Aeronautics and Missiles Division, Chance Vought Corporation, for the U.S. Government under the Navy, Bureau of Naval Weapons Contract NOw 61–1072c.

Flutter Prevention Handbook: A Preliminary Collection[*]

D.D. Liu, D. Sarhaddi, and F.M. Piolenc
ZONA Technology, Inc.
9489 E. Ironwood Square Drive, Suite 100
Scottsdale, Arizona 85258–4578

Part A: Flutter Model Design and Ground Vibration Testing

Lee S. Wasserman
Delta Dynamics, Inc.

Foreword

Abstract

In this article, the author presents his in-depth research/development and summarizes his lifelong experience in three major areas of flutter testing, namely, Flutter Model Design, Flight Flutter Testing and Aircraft Ground Vibration Testing.

For flutter prevention, seven essential cases of flutter are selected for discussion in which cause and cure for each case are clearly displayed.

---

[*]This document was taken from the original report: Liu, D.D.; Sarhaddi, D.; and Piolenc, F.M.: Flutter Prevention Handbook: A Preliminary Collection, WL–TR–96–3111, 1996, first published by the Flight Dynamics Directorate, Wright Laboratory, Air Force Materiel Command, Wright-Patterson Air Force Base.

1.) Bending-Torsion Flutter
>   Cause: Lift forces caused by torsional vibration equal to or greater than the damping forces caused by bending vibration.
>   Cure: Mass balance, increase in torsional stiffness.

2.) Control Surface Flutter
>   Cause: In most cases by mass unbalance about the hinge line.
>   Cure: Mass balance or mass overbalance.

3.) Tab Flutter
>   Cause: Low rotational stiffness and/or free play of the tab about the hinge line.
>   Cure: Increase the frequency of tab rotation.

4.) Propeller Whirl Flutter
>   Cause: Wing mounted engines - coupling results from the yawing and pitching motions of the engines.
>   Cure: Stiffened engine mounts.

5.) Panel Flutter
>   Cause: Aerodynamic and inertia forces acting on fabric or thin metal surfaces with inadequate supporting structure.
>   Cure: Better supporting structure or stiffened skins.

6.) Active controls in some cases have caused flutter but have also been used to prevent flutter.

7.) Shock Wave/Control Surface
>   Cause: The shock position changes with the control surface angle and the shock causes flow separation.
>   Cure: Dampers or a wedge on the wing surface at the shock location to stabilize the shock position.

Introduction

Bending - Torsion flutter occurs when the lift forces caused by torsional vibrations are equal to or greater than the damping forces caused by bending vibrations. In most cases, the bending stiffness will be too low to balance the inertia forces at the flutter frequency, so some lift due to torsion will be required. In addition, the torsional frequency will have to be reduced to the flutter frequency by a twisting moment consisting of the lift at the quarter chord and the inertia force at the center of gravity. The damping moments about the quarter chord produced by torsional vibrations will also have to be balanced. The balance will be supplied by the acceleration of the center of gravity caused by bending vibrations. Low flutter speeds will occur with low torsional stiffness and with the center of gravity location of most sections substantially behind the aerodynamic centers. Reductions in the flutter speed will also occur when a surface like an all-movable stabilizer has a low pitch stiffness. If the bending-to-torsion frequency ratio at zero airspeed is increased and the elastic axis is well ahead of the center of gravity of each section, a substantial reduction in flutter speed can occur. However, the flutter speed will reach a minimum value and then increase as the bending to torsion frequency ratio increases.

Control surface flutter occurs when the control surface vibrations about the hinge line provide the lift and/or moment required to cancel out the damping caused by bending and torsion of the supporting surface. Control surface flutter is caused in most cases by mass unbalance about the hinge line. However, when the fixed surface vibrates in torsion as well as in bending, the moment of inertia of the control surface adds to the moments caused by mass unbalance, so in such cases, mass overbalance will be required for flutter prevention. The frequency ratio effect for control surfaces is similar to the effect in bending torsion flutter in that flutter can be prevented by control surface frequencies which reduce the response of the control surface below the value required to cancel the damping of the supporting surface.

Tab flutter is similar to control surface flutter since mass unbalance and low tab frequencies cause the tab to move in the direction to balance the damping due to control surface rotation and torsion. Symmetrical control surface rotation is restrained by the stiffness of the control system. Most trim tab flutter is caused by low rotational stiffness and/or free play of the tab about its hinge line. Geared tabs are more likely to flutter if the tab rotation leads the control surface rotation since the moment acting to rotate the tab is in the same direction as the moment caused

by mass unbalance. Tabs used in the control system to rotate the control surface (spring tabs) are the most critical to flutter because the control system dynamics limits the frequency of tab rotation.

Metal structures have raised the bending-torsion flutter speeds above the limit diving speeds of most aircraft except when engine nacelles, bombs and fuel tanks are attached to the wing structure. The reduction in the torsional frequency and the possibility of critical bending-to-torsion frequency ratios have resulted in flutter in the operating range.

Propeller whirl flutter has occurred in airplanes with engines mounted on the wing. The instability is caused by both the gyroscopic and aerodynamic coupling of propellers resulting from yawing and pitching motions of the engines.

Panel flutter has occurred due to the aerodynamic and inertia forces acting on fabric and or thin metal surfaces with inadequate supporting structure.

Active controls have caused flutter in some cases, but have also been used to prevent flutter.

Shock waves have caused flutter of control surfaces because the shock position changes with the control surface angle and the shock causes flow separation which produces unstable moments about the control surface hinge line. In most cases, mass balance will not prevent this type of flutter and dampers must be used. In one case, it has been reported that the problem has been solved by a wedge located on the wing surface at the shock location.

1. Vibration Modes and Frequencies

a.) Measurement of frequencies and mode shapes

There are a number of methods that have been used to measure the frequencies and mode shapes at zero airspeed. The problems include the suspension of the aircraft, the location of the shakers, the wave form of the excitation, the instrumentation, and the method of evaluating the test data.

b.) Use of vibration data to indicate the probability of flutter

Vibration data have been used as an indication of the probability of flutter. For example, if the data showed highly coupled motions of bending and torsion of fixed surfaces, a low bending-to-torsional flutter speed is possible. In the case of control surfaces, a lagging motion of large amplitude with a large response of the fixed surface indicates the probability of a low flutter speed. A similar situation exists for control surfaces and tabs.

c.) Use of vibration data in flutter calculations

Flutter calculations can be conducted using measured coupled modes, (i.e. with no mass or elastic coupling). If uncoupled modes are used, agreement between the predicted and measured coupled modes obtained during ground vibration tests indicate that the amount of coupling is correct.

2. Flutter Prevention

a.) Mass Balance

Mass balance has been the most widely used method to prevent control surface flutter. A frequently used method is uniform mass balance with distributed weights. Overbalance can be required when the supporting structure vibrates in both bending and torsion. In this case, the increase in the moment of inertia caused by the balance weight must be limited or a reduction in the flutter speed can occur.

b.) Changes in stiffness

When mass balance is not practical, stiffness changes may be necessary. For control surfaces and tabs, raising the rotational frequency is often the most practical method of preventing flutter. Stiffness changes as well as mass balance are frequently used to prevent flutter due to the mounting of nacelles, external fuel tanks and weapons on

the wing structure. Center of gravity locations near the quarter chord have prevented flutter of tip tanks. Fins to stabilize the tanks in pitch have also been used.

c.) Dampers

Hydraulic dampers have been used to prevent shock induced flutter of control surfaces.

d.) Tailoring of composites
e.) Active controls

Active controls have been used to prevent flutter in cases where dampers as well as changes in mass and stiffness are either not effective and/or not practical.

3. Flutter Models

a.) Need for models

Flutter models are needed because of the difficulty of accurately predicting flutter with existing theory. The occurrence of flutter after the airplane has been constructed can result in very large increases in costs.

b.) Scaling rules

Geometric scaling with the same materials in the model and aircraft results in the same flutter speeds.

c.) Design and construction of low speed models

Low speed models are constructed by reductions in the scaled stiffness of the model. Since geometric scaling of the structure with reduced thickness of the materials is normally impractical, the usual construction consists of a spar which provides all of the stiffnesses and rigid sections attached to the spar which provide the aerodynamic shape and the scaled mass distribution. At least six separate sections are used with small gaps between each section. The space between these gaps can be closed with a flexible material.

d.) Design and construction of transonic models

Transonic models have been constructed in two ways. One method is to use hollow spars to keep the weight down and to cover the spars with balsa sections that add a limited amount of stiffness. Chordwise low density balsa has been found to be acceptable. The second method is to use geometric scaling with the materials having the same stiffness properties required to provide the scaled stiffness values.

e.) Structural tests of models

The use of mirrors on the model to reflect light beams projected from a slide projector has been used to measure the slopes of the model structure under loads. The slide in the projector produces vertical lines for torsion measurements and horizontal lines for bending measurements. A measuring board with vertical and horizontal scales is used to read the slopes in bending and torsion. The bending stiffness EI may be determined from the formula $M = EI(d\theta/dx)$, where M is the bending moment and $d\theta/dx$ is the resulting change in slope of the wing with x (spanwise direction). The torsional stiffness GJ may be determined from the formula $T = GJ(d\gamma/dx)$ where T is the twisting moment and $d\gamma/dx$ is the resulting change in angle of twist with x (spanwise direction). Influence coefficient measurements with electronic or mechanical dial gages have also been used.

f.) Inertia tests of models

In sectionalized models, the weight center of gravity (c.g.) and moment of inertia of each section is measured. The spar weights are calculated from the spar geometry and the combined spar and section weight and inertia are computed. For models with scaled structures, the total weight, center of gravity and moment of inertia are measured

and compared with theoretical values. Where costs will permit the destruction of a model, the model can be cut into sections and the weight center of gravity and moment of inertia of each section is measured.

Flutter Model Design

Scale Factors

One approach which will lead to an understanding of the scale factors is to become familiar with geometric scaling and the applicable scaling rules. If all of the dimensions of a structure are reduced without changing any of the materials or methods of construction, the resulting structure is said to be geometrically scaled. The frequencies of the resulting structure multiplied by the length scale factor will be equal to the frequencies of the full scale structure. For example, a geometrically scaled model with a length scale factor of 1/10 will have frequencies equal to 10 times the full scale frequencies. To prove this key point with a simple example, consider a cantilever beam with a weight attached to the end. The elastic constant is $3EI/L^3$ and the mass is proportional to L^3, so the frequency is proportional to the square root of $3EI/L^6$. For geometric scaling EI is proportional to L^4, so the frequency is proportional to $1/L$ or the frequency times L is a constant.

The structural velocity is the frequency times the scaled amplitude. For a tenth scale geometrically scaled model, the scaled amplitude is 1/10 and since the frequency is 10 times full scale, the velocity ratio is unity. The ratio between the air velocity V and the structural velocity is usually specified as $V/b\omega$, where b is the semichord of an airfoil and ω is the frequency. The scaling rules require that $V/b\omega$ be the same for the model and full scale structure. This rule implies that $V/L\omega$ is a constant.

The other key model scale factor in addition to the length ratio and the velocity ratio is the density ratio. The values of the density and velocity ratios are established by the conditions in the wind tunnel. For example, if the density of the air in the wind tunnel is twice the density of the air in the flight condition being simulated, the scaled weight of each model component must be doubled. In addition, if the air velocity in the wind tunnel is half of the velocity of the full scale flight condition, the velocity ratio of the model must be reduced to one half, which requires that the frequency ratio be halved because $V/b\omega$ is fixed. If the model weights are doubled, the velocity ratio will remain unchanged, provided that the stiffness is also doubled, since the frequency ratio will not be changed. If the stiffness is reduced to half and the weight is doubled, the frequency ratio will be halved and therefore the velocity ratio will be halved.

The ratio q equals the density ratio multiplied by the square of the velocity ratio, which is 2 x 1/4 or 1/2 for the above case. To obtain the model stiffness, the geometrically-scaled stiffness is multiplied by the ratio q.

There are a number of reasons why geometrical scaling is not used for flutter models. One major reason is that the typical aircraft structure is so complicated that scaling each element of the structure as well as the geometric tolerances would be completely impractical. In addition, the scale factors must be changed to simulate the velocity, density and (in transonic and supersonic testing) the Mach number of the full scale flight conditions in the wind tunnel.

The concept of geometric scaling is mainly useful for calculating the scale factors to be applied in designing the model. For example, the weight is proportional to L^3, the static unbalance proportional to L^4, and the moment of inertia proportional to L^5 for a density ratio of unity which is true for geometric scaling. The bending and torsional stiffnesses EI and GJ are proportional to L^4 for the density and velocity ratios of unity applicable to geometric scaling. For other density ratios, all the scale factors are multiplied by the density ratio. For other velocity ratios, EI and GJ are also multiplied by the square of the velocity ratios.

It was mentioned previously that the density ratio multiplied by the square of the velocity ratio is proportional to the ratio q so that the EI and GJ are proportional to L^4q where q is the ratio defined earlier. The angle of twist or bending due to a moment is proportional to $1/(L^3q)$ while the angle of twist due to a load is proportional to $1/(L^2q)$. The deflection due to a moment is the same as the angle of twist due to a load. The deflection due to a unit load is proportional to $1/Lq$. The scaled weight is proportional to L^3 multiplied by the density ratio so that the static deflection under gravity is proportional to $(L/V)^2$ and the static deflection divided by the scale is proportional to

L/V^2. To obtain scaled model deflections under gravity, the velocity ratio must equal the square root of the inverse of the scale. V^2/L is sometimes defined as the ratio g.

The physical significance of the scaling rules may be determined from the equations of equilibrium. The same equations of equilibrium must apply to the model and full scale aircraft, if the model test results are to be directly applied to predict the full scale results. All the forces or moments involved in the equations of equilibrium must therefore change by the same percentage as the scale is changed.

For example, the mass times the acceleration must change by the same percentage as the spring constant times the displacement or $L^3\omega^2 L$ must be proportional to L^2 or $(AE/L)L$. For this reason, L^2W^2 or $L\omega$ equals a constant as indicated above for geometric scaling. The aerodynamic forces are proportional to q multiplied by L^2 so $L^4\omega^2$ multiplied by the density ratio which is proportional to the inertia force must be proportional to L^2q or $L^2\omega^2/V^2$ or $V/(L\omega)$) must be constant. The concept of maintaining the force and/or moment ratios independent of the scale is useful in checking the scaling rules for other types of forces or moments such as damping and/or friction.

Low Speed Flutter Models

The technical difficulties and high cost of designing, building and testing models in transonic and supersonic tunnels has led to the use of flutter model tests in low speed tunnels. The test results have proven to be useful at transonic speeds because the mechanism of classical flutter is relatively independent of Mach number up through the transonic range. Mach number effects have been obtained with the concept of Mach number corrections. The shift in the center of pressure and the change in the lift curve slope have been used in the past to estimate such corrections. However, more accurate corrections can now be obtained with the use of compressible subsonic and supersonic theory.

The usual low speed flutter model component consists of a skeleton made up of metal spars which simulate the stiffness distribution of the full scale structure including the control surfaces plus a number of balsa sections fastened to the spars. The balsa sections are used to transmit the airloads and some of the inertia loads to the spars. (See fig. 1).

The design problems are as follows:

1.) Spar Design
2.) Spar Joints
3.) Attachments of Balsa Sections, Control Surfaces, Actuators and Pylons to the Spars
4.) Balsa Sections
5.) Control Surfaces
6.) Actuators
7.) Pylon Design
8.) External Stores
9.) Model Mounting Systems

Spar design.—A key requirement of spar design is to obtain the scaled stiffnesses with adequate strength within the allowable weight. The first step is to obtain the required model values of the vertical and fore and aft bending stiffnesses EI_x and EI_z, the torsional stiffness GJ and the allowable weight. Deflections perpendicular to wing, horizontal tail and vertical tail surfaces are usually defined to be in vertical bending. Deflections in the planes of these surfaces toward the leading or trailing edges are defined to be in fore and aft bending. For the fuselage, lateral bending stiffness is used instead of the fore and aft bending. If full scale data are supplied, the full scale EI and GJ are multiplied by L^4 times the ratio q to obtain the model EI and GJ values and the full scale weight per inch of span is multiplied by L^2 times the density ratio to obtain the model weight per inch. The model weights are usually converted to grams per linear inch because of the light weights of certain model components. The weight of the balsa covering can in most cases be held to 40 percent of the total section weight and the weight of the ballast weights about 10 percent, so that not over 50 percent of the model section weight can be used for the spar weight. Since the spar strength will increase as the spar height is reduced and the area and thus the weight is increased, it is
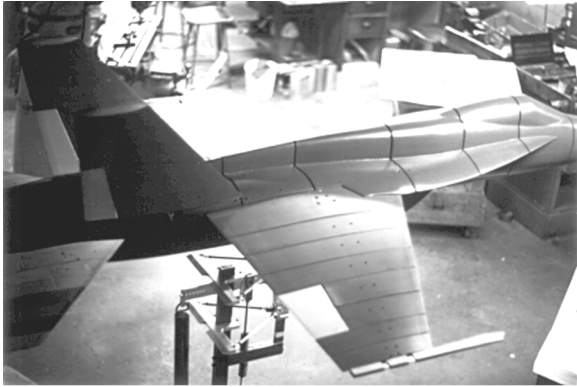
Figure 1.—Low speed flutter model.
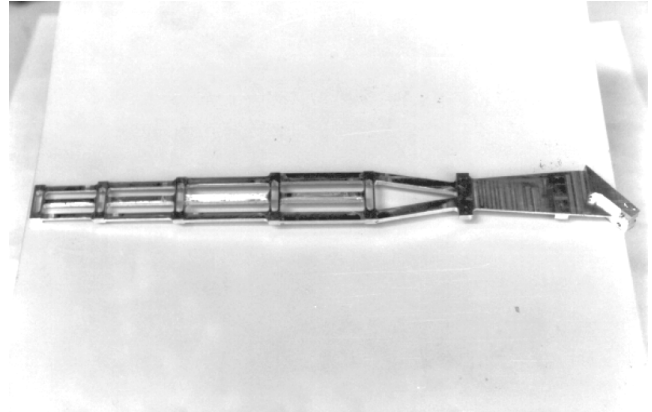
Figure 2.—Control surface spar design.

good design practice to use the maximum allowable spar weight. Nevertheless, the maximum spar weight will be less than 50 percent of the total weight in model sections having high densities.

Solid spars milled from 2024-T3 aluminum (see fig. 2) are usually used, although magnesium alloy is substituted in those cases where the aluminum spars will equal or exceed the 50 percent weight limitation. In very few cases will hollow spars be required in low speed flutter models. The wing and tail spars are normally rectangular in cross section with a fore and aft flange while the fuselage spars may be similar or may be shaped like tees, crosses or tubing to which vertical or horizontal flanges are fastened depending on the values of EI_z, EI_x and GJ. Obtaining the correct values of EI_z in the fuselage spar is usually but not always more important than obtaining the correct values of the fore and aft stiffness in the airfoil surfaces. The ratio of the width b of the spar to the height a of the spar is determined by the ratio of GJ and EI_x. (The use of b for the width and a for the height was selected arbitrarily.) Curves of J/I_x, I_z/I_x, J/A^2, and I_x/A^2 vs. b/a were computed using the formulas for J in Timoshenko's "Theory of Elasticity" or Roark's "Formulas for Stress and Strain". The values of I are the area moments of inertia according to the elementary theory of bending.

The value of b/a determined from the graphs using the required J/I_x value also determines the cross sectional area A and thus the weight per inch which is obtained by multiplying A by the density if the material. If the fore and aft EI is too low, then a thin fore and aft flange may be machined integrally at the center line which will increase the fore and aft EI with minimum changes of the other stiffnesses but with a small increase in weight. In some cases however, the fore and aft flange is moved above the center line to increase the bending EI without adding weight. The other problem which occasionally shows up is a higher required ratio of J/I_x than can be obtained with a rectangular spar. Some designers have added thin webs at plus and minus 45 degrees to the elastic axis on the top and bottom spar surfaces to obtain the increased J/I_x ratio. The other possibility is the addition of an auxiliary spar which adds more to GJ than EI_x because the chordwise connecting strips between the spars are more flexible in transmitting bending moments than in transmitting twisting moments.

The graphical solutions mentioned above were used to solve spar design problems before the availability of low cost personal computers. Simple programs for solving spar design problems on personal computers have now eliminated the need for such graphs. One approach in such programming is to input the scale factors, the full scale EI and GJ values and the elastic moduli and density of the material and use the computer to provide the spar dimensions and the weight distribution. If the spar weight distribution exceeds the allowable values, magnesium alloys may be substituted for 2024-T3, or a hollow spar may be used. The use of model values of EI, GJ and weights as computer inputs is another possibility and has some advantage because model values for different aircraft tend to be similar regardless of the full scale values.

Spar joints.—Joints in the spar skeleton (see fig. 3) must be carefully designed to provide adequate strength and rigidity without any slippage. The joints should be as strong as the spars being connected together and as rigid as practical. Joints made with machine screws which balance the applied moments by tension loads in the screws have proven to be satisfactory in most cases while bolts in shear are usually unsatisfactory because of slippage.
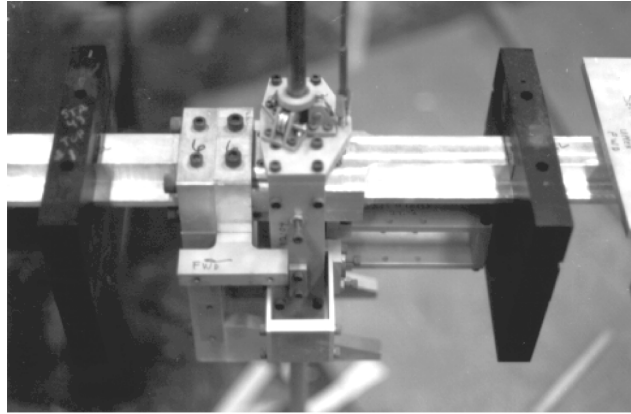
Figure 3.—Fuselage spar joints.

Blocks machined into the end of spars to be joined together is one design concept but a lot of material must be removed. Machine screws through the blocks between two spars will resist vertical and fore and aft bending moments with tension loads on the screws as long as the initial tension on each screw is high enough to prevent load reversal. The torsion moment will be resisted by friction unless the flanges are locked together over a key or a pin or an additional block is bolted perpendicular to the other blocks or machined integral with one of the blocks and bolted to the other block. Another concept involves tapering the spars at a joint and using four screws to balance out vertical bending and torsion moments. Fore and aft moments would have to be balanced by a key, additional blocks or friction.

Attachments to the spar.—The balsa covering is fastened to the spars in sections so that the balsa does not increase the spar stiffness. The attachment is usually made with machine screws and small blocks machined integrally with the spar. Other attachments to the spar including control surfaces, actuators and pylons are made in a similar manner. The blocks are perpendicular to the spar elastic axis and extend over a short length of spar so that a minimum amount of spar strain energy will be stored in the blocks. Nevertheless, it is a good design practice to include some increase in the spar stiffnesses due to the blocks, particularly for those in torsion. The spar between each block supporting a balsa section may be of constant cross section with average stiffness values or may be tapered to represent the scaled stiffness distribution.

Balsa sections.—The number of balsa sections may be as high as 10 for each wing and 12 for the fuselage. Six sections are used for tail surfaces and four to six for control surfaces. The balsa sections must be designed to transmit some of the inertia and all of the aerodynamic loads to the spars at the highest flutter frequencies expected in the wind tunnel tests. Since there will be some flexibility in the attachment between the spar and the sections, the ratio of the section motion to the spar motion will increase as the frequency and the air loads increase. This flexibility between the spar and the sections can introduce substantial errors in the results. The key section design problem is therefore to minimize such errors by making the sections and attachment as rigid as possible within the allowable weight. For this reason, the sections are usually built with most of the balsa grain running perpendicular to the spar or streamwise if the sections are built in the streamwise direction. The sections are usually built in halves, split at the spar centerline. The grain at the leading and trailing edge is usually spanwise to increase the rigidity. The balsa section halves are glued together and at the same time are glued to 2024-T3 aluminum alloy plates called bridges. Each balsa section is slid over to the spar to the correct position and the bridges are fastened to the spar blocks with machine screws and nuts. To improve the glue joints between the balsa and the bridges, holes are sometimes drilled through the bridges before assembly to the balsa.

The sections are covered with fiberglass or silk if weight permits or otherwise are covered with paper for increased strength and rigidity (see figs. 4 and 5). Each section including the bridge plates can be removed as a unit from the spar to check the weight, c.g. location and the moments of inertia.

Other types of bridges have been used in an effort to increase the rigidity of the balsa sections. One bridge design has four hardwood or metal shear webs forming a sort of "X" frame to provide stiffness in both roll and pitch. The shear webs are mechanically fastened to a block containing holes for bolting the section to the spar
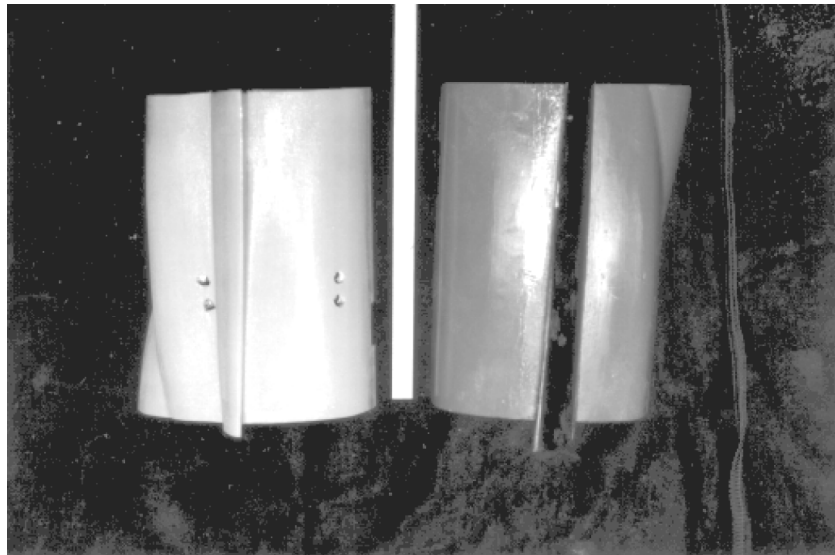
Figure 4.—Balsa sections mounted to sheet metal frame and covered with fiberglass (top view).
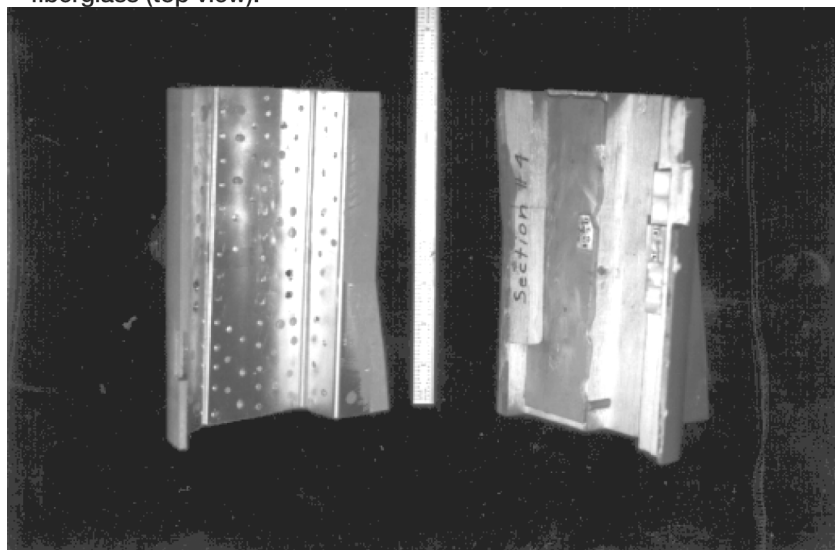
Figure 5.—Balsa sections mounted to sheet metal frame and covered with fiberglass (bottom view).

blocks or in the case of metal webs may be integral with the section block. Hollow balsa sections consisting of ribs covered with balsa planking have been used with these bridges. For thick airfoils, this type of construction may weigh less than the solid balsa sections although the weight of the glue will frequently be more than the weight saved by reducing the volume of the balsa wood. In addition, the contours of solid balsa sections may be machined eliminating the need for most of the hand work required on built up sections.

In cases where the spar weight is much less than 50 percent of the section weight, some of the extra weight should be used to increase the strength and stiffness of the balsa sections. However, heavy concentrated weights such as fuel weights should not be carried by the balsa sections but should be fastened directly to the spar.

At one time sample balsa sections were built for measuring the weight, strength and rigidity before the final section design was approved. However, the use of computer programs to compute the weight, rigidity and the strength has reduced the need for such samples. Nevertheless, strength tests on the completed model are still considered desirable to evaluate the effectiveness of the glue joints. The spar strength may be used to compute the

required strength of the balsa sections although the maximum wind tunnel dynamic pressure or some substantial percentage of the pressure may also be used.

Control surfaces.—The design of control surfaces is similar to the design of fixed surfaces except that the scaled stiffnesses may be only the torsional stiffness or in some cases the torsional and vertical bending stiffnesses. In addition, scaling the static unbalance and moment of inertia about the hinge line is usually more important than scaling the weight since excess weight may be used as part of the ballast weights of the supporting surface. However, the weight must be kept within tolerance in low density sections.

The design of the hinges for control surfaces is a key problem because the friction torques should be reduced to a minimum or at the very least should be reduced in proportion to the reduction in the scaled inertia and aerodynamic torques. If the friction torques on the model are excessive, the results will not be acceptable. Flexure hinges usually work much better than ball bearing hinges because the ball bearing hinges can not be easily aligned when there are more than two hinges unless the model design provides a definite procedure for aligning each bearing. Flexure hinges using silk or nylon threads have been tried but usually fail after a single flutter point so flexure hinges using beryllium copper or spring steel have proven to be superior. Another possibility is to use plastic strips made from nylon to obtain low hinge stiffnesses. Since flexure hinges are somewhat fragile, a single ball bearing hinge is sometimes used to prevent the loss of a control surface due to flexure hinge failure. In lieu of the bearing hinge, other safety devices should be installed to prevent loss of control surface when flexure hinges are used. The other problem with hinges is the transmission of loads or moments across the hinges due to flutter. In some cases, it is desirable that each hinge be mounted on a torsion flexure to reduce the moments transmitted across the hinge due to bending of the fixed surface and/or the control surface.

Actuators.—The simulation of actuators is another key problem. Torsion bars have proved to be the best solution in most cases since the bars do not load up the hinges and the bars fit into the space between the control surface leading edge and the fixed surface trailing edge. The bars are usually designed to withstand plus or minus five degrees of rotation without yielding. In some cases a double torsion bar will be necessary to store enough energy. For some actuators, a strip of beryllium copper is bent to form a "U" shape representing two bars connected together with actuator arms at the other ends of the "U" connected to the fixed and movable surfaces. Single or double torsion bars can be formed from spring steel before heat treating or can be machined from 2024-T3. The formula for J can be determined from the graphs mentioned above or from a computer program.

Pylon design.—Pylon design is one of the more difficult problems encountered in low speed flutter models. The pylons may be used for mounting external stores or engines. The objective is to obtain the required stiffnesses or influence coefficients with a structure consisting of beams machined from solid stock as a one piece unit or with a series of beams assembled together with machine screws. In addition to the bending and torsion deflections due to the beams, shear deflections using double cantilevers must occasionally be added.

In general, it will be helpful to follow the full scale load paths in the model but high stresses may prevent this approach. In some cases stops can be used to prevent failure of the pylon due to high stresses.

Computer programs based on beam theory have proven to be quite useful for establishing the final design. In general, there will be two three by three matrices of stiffness of influence coefficients that must be matched. One for symmetric and one for anti-symmetric motion of the pylon. To start the analysis, a system of three beams is setup that appears to simulate the real structure. The location and/or angle of the beams is along the axis that reduces the vertical and fore and aft loads to loads perpendicular to the beams and axial loads so that by ignoring the axial deflections, a two-by-two matrix is obtained. The three unknowns, are the EI values of each beam and the three conditions are the pitch angle due to a pitching moment, the vertical displacement due to a load and the pitch angle due to a load or the displacement due to a moment which are the same. On the first try, the solution may yield unacceptable results such as negative values of EI. The lengths of the beams may be changed or shear deflections may be added until an acceptable design is achieved. For the anti-symmetric case, the approach is to select an elastic axis that separates out the effects of GJ and gives values for EI_z for the three beams. The final step is to determine the values of GJ for each of the beams or the total value of the torsional stiffness. Care must be used in attaching balsa sections to pylons to avoid stiffening the pylon and interfering with pylon deflections (see fig. 6).

External stores.—Computer programs have been developed for store design. For a rigid store (the store is broken up into seven or more sections - see fig. 7) the inputs are the radius and coordinates at the ends of each section. The program calculates the volume, c.g. and radius of gyration of the assembly about the c.g. as well as
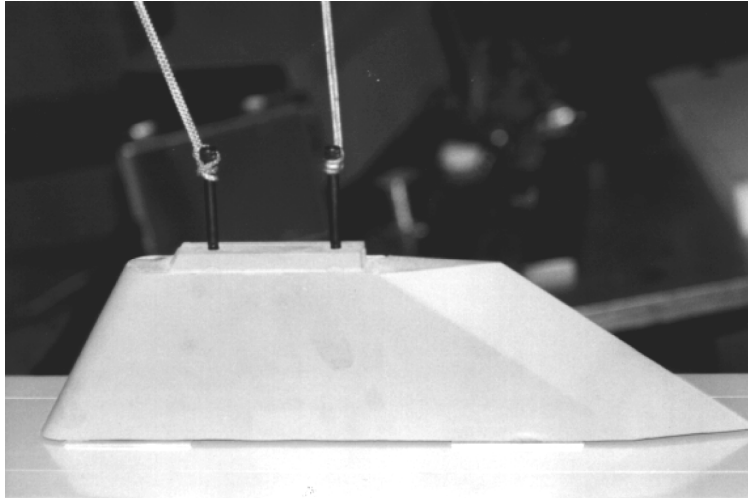
Figure 6.—Pylon design.

Figure 7.—External stores.

the density required for the total weight. If the density is much higher than the density of hard wood, the weight, moment of inertia and unbalance about the c.g. are computed for a hard wood covering. The program then computes the changes in the weight, static unbalance and moment of inertia that must be added to meet the design require- ments. The distance of the added weight from the c.g. is then computed to correct the unbalance. The moment of inertia due to the added weight is then subtracted from the total moment of inertia that must be added.

The next step is to design a metal bar that will add the correct weight and moment of inertia. The radius of gyration to provide the additional moment of inertia is used to establish the length of the rod and the area of the rod is determined from the weight that must be added and the corrected density of the material in the rod. The corrected density is the difference between the density of the rod and the density of the hard wood. The rod is usually drilled with holes for the attachment of the store to the pylon.

If the store density is about the same or lower than the density of hard wood, balsa wood may have to be used for the outside contour. In this case, 2024-T3 may be used for the rod or no rod will be used if the area is too small. It this case, a 2024-T3 plate will be cemented to the balsa for mounting the store to the pylon. In addition, the weights required to properly balance the store will be calculated using a computer program with the locations of the ballast weights as additional inputs.

The design of flexible stores is somewhat similar to the design of fuselages although the spar in many cases will be a solid or hollow aluminum alloy cylinder with a tapered or stepped wall thickness. Rings will be machined around the cylinder to support the ballast weights and balsa or hard wood sections. The external sections and

ballast weights are either clamped around the rings or held to the rings with machine screws if the thickness of the rings is sufficient.

Mounting Systems.—The mounting system (see fig. 8) should provide three symmetrical and three antisymmetrical rigid body degrees of freedom with frequencies 1/3 or less of the lowest flutter frequency. While this requirement can be satisfied with many different mechanical systems including cable systems and four bar linkages, the rod mount has been used in more low speed flutter model tests than any other type of mount. The rod mount consists of a slider, a gymbal and a vertical rod. The slider rolls up and down on the rod on ball bearings or ball bearing rollers to provide the vertical translation degree of freedom. Three bearings located at 120 degree angles are fastened to each end of a cylinder which fits with ample clearance around the rod. The front bearings at each end of the cylinder take out the drag loads. The other two bearings are spaced just to touch the surface of the rod. In most cases, one of the bearings will be adjustable to reduce the play. Two shafts machined integrally or bolted at the center of the slider cylinder fit ball bearings mounted in a rectangular gymbal to provide the pitch degree of freedom. The gymbal in turn will have bearings or shafts mounted at 90 degrees from the pitch direction to provide the roll degree of freedom. Springs are installed in the gymbal mechanism to provide stability of the model in roll and pitch in the wind tunnel. The bending of the rod provides the fore and aft and lateral translation degrees of freedom. The yaw degree of freedom is provided by the rotation of the model around the rod. The mounting system must be designed to provide the flutter model with static and dynamic stability during wind tunnel operations. Static stability will be obtained if the aerodynamic center is behind the elastic axis. While this situation is almost always the case in yaw, the pitch elastic axis is placed behind the c.g. to prevent dynamic instability in the pitch and translation degrees of freedom. If the aerodynamic center is ahead of the pitch elastic axis, sufficient pitch stiffness must be supplied to prevent static divergence of the model. The other instability that has shown up in wind tunnel tests is Dutch roll. One solution that has been satisfactory in most cases is to use a strong roll spring. In most rod mounts, the yaw frequency will be zero at zero airspeed and will increase as the tunnel q is increased. If the yaw frequency approaches the roll frequency, Dutch roll is likely to occur if the dihedral effect and the roll-yaw product of inertia are both of the same sign and are of sufficient magnitude. Positive dihedral causes the wing which is yawed to the forward position to produce upward lift and thus an up rolling moment while positive product of inertia causes a rolling moment in the opposite direction for the same yaw position. In some rod suspension systems, there are no roll bearings and the roll degree of freedom is provided entirely by the flexibility of the rod.

The model should be positioned near the center of the tunnel with the wings level during the wind tunnel tests. One method involved the use of electric motors to drive the control surfaces for trimming the model in pitch and roll. This method is satisfactory but complicates the model design. It was noticed, however, that the trim settings
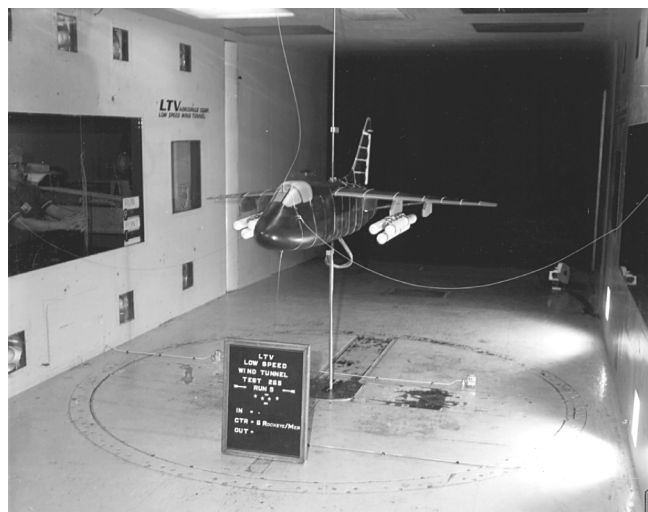
Figure 8.—Mounting systems.

changed very little during a test program so setting the trim manually was tried. In this case, the model was positioned in the center of the tunnel by supporting the model on a spring connected to a cable which in turn was connected to a winch. The latest design involves two cables connected to the fuselage forward and aft of the rod and one cable connected to the slider on the rod. The spacing of the front and rear cables is about twice the radius of gyration. The angle of attack and the position of the model can be changed by adjusting both the front or rear cables and the cable connected to the slider is used to pull the model up against the stops. At the present time, the three-cable system cannot be used for balancing large unsymmetrical loadings. It appears that a fourth cable connected to the model through a spring to apply a moment about the roll axis will have to be added if balancing large static rolling moments is desired. Otherwise, the rolling moment will be balanced by the roll spring and bending of the rod.

The mounting system should be designed to prevent destruction of the model due to violent instability or flutter. It is essential that the rod must not fail regardless of what happens to the model. This criterion requires a stress analysis of the rod with conservative loads and moments and the use of high strength material in the rod. The rod is usually installed with some initial tension to keep the stresses down. Since the rod will not be stiff enough to limit the angle of attack, external cables and/or stops in the suspension system should be used to limit the angles of yaw and pitch to safe values at the top q of the wind tunnel tests. If the model is flown with a c.g. substantially behind the rod, the initial contact should be with a stop behind the c.g. so that if the model hits a stop, the airloads caused by model pitch will tend to hold the model against the stop.

High Speed Models

High speed models (see figs. 9 to 12) are designed to be tested at the same Mach number as the full scale airplane as well as at the same density ratio. The velocity ratio is therefore the same as the ratio of the speed of sound in the wind tunnel to the speed of sound at the flight condition being simulated. For air tunnels, the speed of sound ratio is proportional to the square root of the ratio of the absolute static temperature on the wind tunnel to the absolute static temperature of the atmosphere at the altitude being simulated. Since the speed of sound ratio is about 0.85 to 0.9 for air tunnels, the velocity ratio is much higher than for low speed models and thus the model frequencies, stiffnesses (EI and GJ) and strengths must be much higher than for low speed models. The key problem is to obtain the scaled stiffness and strength without exceeding the scaled weight.
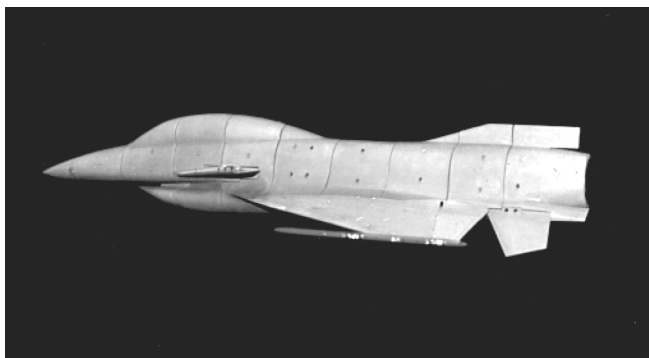
Figure 9.—High speed flutter model.
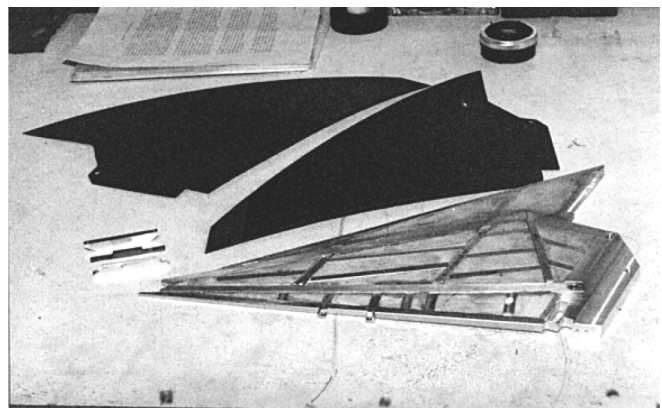
Figure 10.—Carbon graphite skin model.
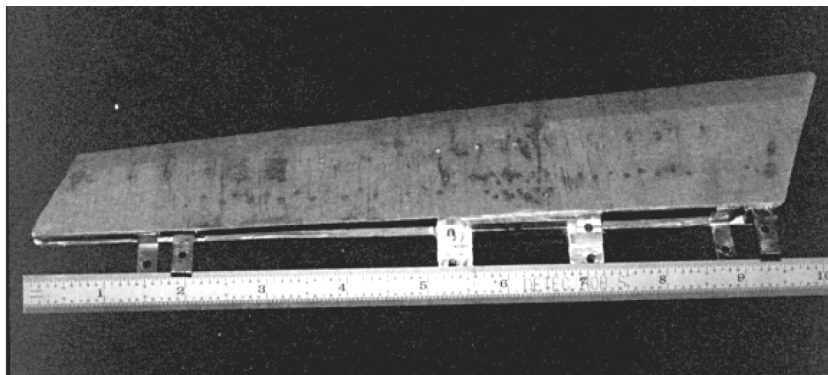
Figure 11.—Leading edge flap design showing actuator and flexure hinges.
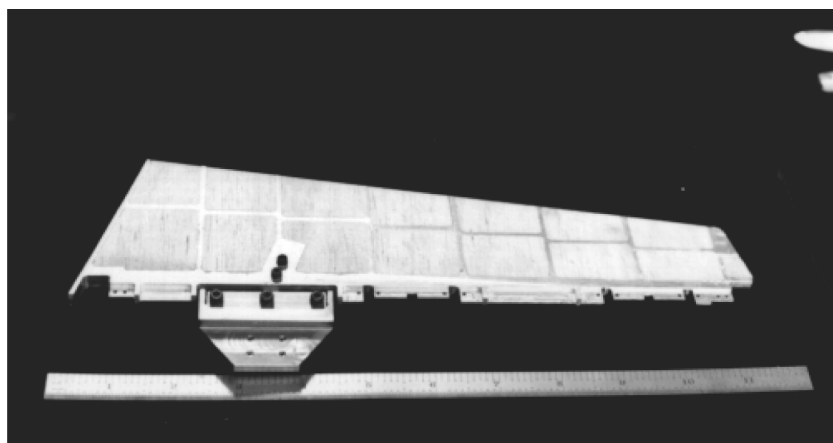
Figure 12.—Flaperon design showing actuator and hinge points.

High speed wind tunnels.—High speed flutter models have been tested in blowdown tunnels, continuous flow pressurized air tunnels and the continuous-flow pressurized Freon tunnel at Langley Field. The blowdown tunnel has the advantage of higher density ratios at transonic and supersonic speeds than either of the other types of tunnels, but the test section sizes are smaller to limit the amount of air that is used in each run (or blow) to the amount that is available at the required pressure in the compressed-air tanks. Continuous-flow high-pressure air tunnels are usually limited to sea-level density at Mach one and thus will be above sea-level at the higher Mach numbers. In Freon, the speed of sound is only about one half of the speed of sound in air, which means a stiffness ratio of about 0.25 at sea-level density. In this case, the stiffness ratio is not low enough for the normal low speed flutter model design procedure and not high enough for a high speed design based on an approximate simulation of the full scale structure.

Model design for transonic blowdown tunnels.—In the transonic blowdown tunnels which are used for flutter model testing, the usual density ratio ranges from 1.5 to 2.0 and the velocity ratio is the square root of the static temperature ratio which equals about 0.79 at a Mach No. of unity. The static temperature in the test section is related to the temperature in the high pressure tank by the quantity $1/(1+0.2\,M^2)$ which equals about 0.833 at Mach one. The high pressure tank usually starts at the ambient temperature but the temperature will drop as the air is used which gives an average ratio of about 0.79 to the ambient temperature. This ratio will change with the flight condition and also if the tank is equipped with heaters. The temperature ratio times the density ratio is the q ratio for transonic model design. However a 30 to 40 percent stiffness reduction is usually used to provide the model with a margin of safety in stiffness. The resulting q ratio for a transonic model with a density ratio of 1.5 will therefore be about 1.5 x 0.79 x 0.71 or about 0.85. To obtain the full scale flutter q at the simulated altitude, the model flutter q may be divided by 0.85 but the resulting full scale q will not include the margin of safety. However, if 1.185 which

equals 1.5 x 0.79 is used as the divisor, the resulting lower value of the full scale q will include the margin of safety. The full scale frequency is obtained for the above case by multiplying the model frequency by the scale and dividing by the square root of (0.79 x 0.71).

It has been shown above that geometric scaling will provide unity ratios of the velocity and $V/b\omega$. Multiplying the stiffness by 0.79 reduces the frequency ratio to the square root of 0.79 but $V/b\omega$ remains unchanged since the velocity ratio is reduced by the same factor. Increasing the density ratio to 1.5 does not change the $V/b\omega$ if the stiffness is also increased by 1.5. Incorporating the margin of safety reduces the frequencies and increased the $V/b\omega$ values for the model, since V is fixed by the Mach number and the tunnel static temperature. The increased $V/b\omega$ value means that the angle of attack due to the vibration velocity is reduced in comparison to the angle of attack due to the vibration amplitudes of twist and bending slope or control surface rotation. The smaller damping forces resulting from the lower frequencies will in general increase the probability of flutter for control surfaces and other flutter cases which have a limited positive damping range. Despite this violation of the scaling laws, this situation is considered acceptable when the definite flutter points which are needed for verification of the theory cannot be obtained in the wind tunnel with the correct $V/b\omega$ values or the design and/or fabrication of a model with the correct $V/b\omega$ values is not practical with available flutter model technology.

Although higher $V/b\omega$ values for the model than for full scale will lead to conservative results, it is well known that the flutter q is relatively insensitive to changes in $V/b\omega$ for classical bending-torsion flutter as long as the $V/b\omega$ values are in the range where the slope of the lift curve remains relatively constant. The unsteady aerodynamic pressures include the inertia pressures which are proportional to ω^2, the damping pressures which are functions of $V/b\omega$ and proportional to $V\omega$ and the lifting pressures which are also functions of $V/b\omega$ and proportional to V^2. In classical bending-torsion flutter, the lifting pressures must raise the bending frequency to the flutter frequency and, in combination with the inertia forces, must provide the couple that twists the structure. The flutter q therefore tends to be a function of the slope of the lift curve, the torsional stiffness and the distance between the aerodynamic center and the center of gravity, and is affected much less by changes in the $V/b\omega$ ratio. For other types of flutter, a more detailed analysis should be used to evaluate the effects of violating the $V/b\omega$ scaling rule.

In the blowdown type of transonic tunnel, the usual test procedure is to start with low density at a selected Mach number and increase the density until flutter occurs. The value of q as a function of Mach number is given by the formula $0.7M^2P$, where M is the Mach number and P is the static pressure. Using P equal to 14.7 psi at sea level, the full-scale value of q at a Mach number of unity will be about 10.29 psi or 1482 psf. In the tunnel at 1482 psf and a temperature ratio of 0.79, the density ratio will be 1/0.79 or 1.26, which means that the weight of each model component should be 1.26 times the geometrically-scaled weight to simulate the sea-level test condition. If the model density ratio is 1.5, the altitude at 1482 psf in the wind tunnel corresponds to a density ratio of 1.5/1.26, or about 6000 ft. The sea-level value of q in the tunnel for a density ratio of 1.5 is 12.26 psi or 1764 psf. It is clear that this value equals 1.5 x 0.79 times the sea level q. Higher altitudes which are critical in testing for certain cases of control surface flutter or buzz may be simulated by adding weights to the model without increasing the model stiffness. However, the effects on flutter of the increased values of $V/b\omega$ for the model should be evaluated in most cases by analysis.

The higher EI and GJ values required for transonic models can be achieved in many cases within the allowable weight by the substitution of hollow box spars in place of the solid spars used on low speed models. Initially the spars were made in two halves milled from 6061-ST or a magnesium alloy and then welded together and heat treated.

More recent models have been constructed from chemically-etched 2024-T3 sheet attached to channels formed from either 2024-T3 or 6061-ST or 6061-O. In this latter case the channels are heat treated after forming. End grain balsa with grain running normal to the top and bottom plates is cut to precise dimensions using a sanding disc on a milling machine or a grinding wheel on a surface grinder to control the heights of the box beams. The top and bottom sheets are cemented to the spars and the balsa using 3M 3813 adhesive and a clamping fixture to maintain the proper pressure on the glue joints until the adhesive sets up. In addition, aluminum 2014 alloy brads 0.035 inch in diameter and 3/16 to 1/4 inches long are added as required across joints to prevent tension failures of the adhesive. In this assembly, holes are drilled across the joints with diameters about 0.035 inches, the brads are dipped into an epoxy adhesive such as EA956 or REN and are driven into place in the holes. The brads are grooved

on the outside diameter to improve the holding power. Care must be taken not too fail the joint adhesive in the process of nailing the structure together.

The spar weight per inch is still maintained at 50 percent or less than the total weight, as is the case for low speed models. The combined weights of the top and bottom sheets per inch should not exceed about 40 percent of the total weight per inch. From this calculation the area of the skins can be determined by dividing 40 percent of the weight per inch by the density of 2024-T3 or about 45.4 grams per cubic inch. The scaled value of $I(EI/E)$ is used to determine the mean height required between the skins from the formula

$$a_m = \left(3.6\frac{I}{A}\right)^{0.5}$$

(1)

where

      A is the total skin area, and
      a_m is the mean distance between the top and bottom skins.

In the formula, 90 percent of the required I is assumed to be provided by the top and bottom skins, and the rest by the spars. The skin thickness is normally less than 0.032, but is selected to obtain the spar width necessary for GJ, or from the fore and aft stiffness, whichever is larger. The usual formula for the torsional stiffness, i.e.

$$J = \frac{4AB^2}{\int\frac{1}{t}ds}$$

(2)

is used to determine the width of the box required for J since AB is the mean area enclosed by the box and the width of the box is AB divided by the mean distance between the skins. Since this formula gives too high a value of GJ for tapered beams, and if solid balsa covering is to be used, the torsional stiffness is increased further, so the spar is usually designed to provide from 75 to 90 percent of the required GJ. The 90 percent value is used when the J/I ratio is 3.5 or more. The value for I is computed without correction as the area moment of inertia about the neutral axis including the spars. The above approach is facilitated by the use of computer programs.

Detailed flutter model design is similar to conventional mechanism design except that the weight, stiffness and strength of each component must be computed as part of the design process. In general, the structural or spar weight should not exceed 40 percent of the total allowable weight in each model section or the section cannot be properly mass balanced. Mass balancing usually means obtaining the correct weight, c.g. location and moment of inertia of each section. A computer program is used to compute the masses which must be added to satisfy these mass balancing requirements.

In addition to the spar design, the other model design problems are the hinges and actuators for the control surfaces, the pylons and external stores, and the connections between major components such as the fuselage and the wings and the fuselage and the tails. Beam theory is normally used to solve the majority of the model structural design problems. The design objective is to have each part perform its required function with the correct stiffness as well as with an acceptable static strength and weight and a minimum of friction and hysteresis. In addition the design should be as simple as possible to minimize the cost of machining and inspection.

Since many engineering man hours must be spent converting the engineering calculations described above into the drawings and instructions which a shop needs for the fabrication of the model hardware, advanced design techniques involving the use of CAD systems would appear to offer substantial savings in cost and time.

The models must be tested to determine the actual mass and stiffness distributions. Most of the stiffness tests are made by fastening mirrors to the model and reading the changes in the slope angles of the mirrors under external loads or moments applied to the model (see fig. 13). Cross wires projected from a slide projector are reflected by the mirrors and focused on a scale. The motion of the cross wires on the scale are approximately proportional to the
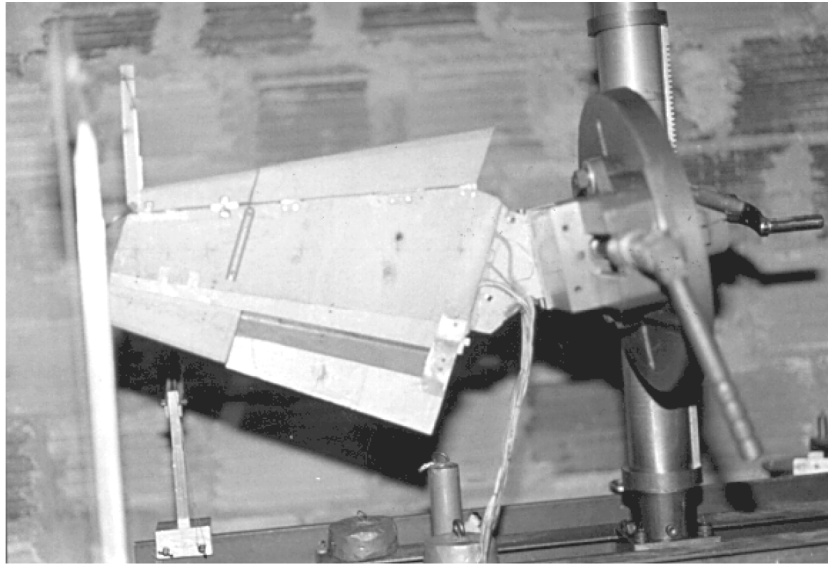
Figure 13.—Mirror deflection testing.

change in angle of the corresponding mirror. Using the rule that the angle of incidence equals the angle of reflection, it can be seen that the motion of the cross hairs equals the change in angle multiplied by twice the distance between the mirror and the scale. It the light beams are nearly perpendicular to the mirrors, the above rule can be used without applying corrections.

The mirror test technique has proven to be fast and quite accurate. The major problem is hysteresis in the model structure which causes the readings not to return to the zero positions when the loads are removed.

Computer programs are available to compare the measured readings with the required readings. The change in angle with respect to distance along a beam equals M/EI or T/GJ, where M is the bending moment and T is the twisting moment. For a given distance along the spar, the angle changes equal the integrals of the above quantities.

To locate the center of gravity of a model component, the component is balanced at two angular positions on a knife edge or the edge of a triangular scale. Lines are drawn on the model for the two positions and the intersection of these lines is the center of gravity. To obtain the moment of inertia, the model component is fastened to a bifilar pendulum with the c.g. at the center of rotation of the pendulum. The period of the oscillation is measured and the ratio of the moment of inertia to the weight is computed using the formula:

$$\frac{I}{Wt} = \left(\frac{g}{l}\right)\frac{d^2}{\omega^2} \tag{3}$$

where

        g is the acceleration due to gravity,
        d is half the distance between the strings,
        l is the length of the strings and
        ω is the frequency in radians per second.

The frequency in radians per second is equal to $6.282/T$ where T is the period in seconds. The formula for the bifilar pendulum includes the increase in the effective mass when the radius of gyration is greater than d. When I/Wt equals d^2, the formula reduces to the case of the simple pendulum for which ω equals the square root of g/l. At the present time, the period is measured with a stop watch which is somewhat slow since 10 or more cycles are counted

to improve the accuracy. It is possible that an electronic timer in combination with a optoelectronic device could be used to save test time since only a small number of cycles would have to be measured.

Flight Flutter Testing

Flight flutter testing is used to demonstrate safety from flutter for the airspeeds and altitudes at which flutter analyses, wind tunnel flutter model tests, and past experience with flutter problems indicate that the margins of safety are the lowest. A second reason for such testing is to produce flight test data that can be used to show that the margins of safety against flutter meet or exceed the values in the specifications for the aircraft. If the aircraft carries fuel in the wing, wing mounted engines, external stores on the wing including weapons and/or tip tanks, additional flight flutter testing will be required if the flutter prediction program indicates a number of loading conditions that will produce flutter within the flight envelope.

In the years of flight flutter testing before 1940, a number of such tests with vibration excitation equipment resulted in structural failures and deaths to the flight crews. Although this result slowed up this method of testing, there has been a substantial increase in the number of such tests because of requirements established by the government to obtain approval for high performance passenger and military aircraft. This increased emphasis on flight flutter testing has also led to improvements in flutter prediction methods including unsteady aerodynamics, flutter calculations using digital computers, wind tunnel tests of flutter models and ground vibration testing. Modifications of the flutter analyses are carried out if the mode shapes and frequencies measured during ground vibration testing are substantially different from the values used in predicting flutter before completion of construction of the first aircraft of each new design.

The advantages of flight flutter testing with vibration excitation equipment are as follows:

1.) If flutter occurs, the airspeed required to initiate flutter will almost always be reduced if the amplitudes of vibration of the structural components involved are increased well beyond the amplitudes encountered by random air disturbances during dives by test pilots.

2.) The decrease in airspeed at the start of the flutter will usually cause flutter to be less violent when it does occur because of the decreases in the aerodynamic forces and moments.

3.) Substantial vibration responses will tend to prevent nonlinear forces and moments from producing false indications of safety from flutter. Such non-linearities include static hinge friction, excessive boundary layer thicknesses and preloaded springs. If the skins of the structure of a wing, stabilizer or fin is close to buckling due to static loads, substantial vibration responses will result in reduced frequencies.

4.) Explosive types of flutter such as bending-torsion of fixed surfaces can often by detected before flutter occurs by the reduction in the gains of the amplifiers that is required to prevent overloading. In one case involving the excitation of bending-torsion flutter with a rotating weight vibrator, the gains of the amplifiers had to be reduced several times due to the decreases in damping and increases in the vibration responses that occurred as the flight speed approached the flutter speed.

Some warning of the approach to flutter has been obtained without the use of vibration excitation equipment. In one case of spring tab flutter with a preloaded tab spring, the neon bulbs that were used to indicate overloading of the amplifiers started flashing well before the vibrations could be detected by the members of the flight crew. Another method for detecting the approach to flutter involves the use of an oscilloscope for detecting the phase and amplitude relationships between bending and torsion. An electrical output signal proportional to the torsional vibration amplitude is connected to move the spot, produced by the electron beam, along one axis (either vertical or horizontal), and the electrical output signal proportional to bending vibration is connected to cause the spot to move along the other axis. The gains are adjusted to keep the motions of the spots within the limits of the scope. At speeds well below the flutter speed, the motion of the spot is random, indicating that the phase angles and amplitude ratios between bending and torsion are changing with time. As flutter is approached, the spot will move in an ellipse or circle for a small number of cycles. This display, which indicates a definite phase angle and amplitude ratio between bending and torsion, can be used by the flight crew as a warning not to increase the airspeed unless approval is obtained from the engineering department.

The equipment suitable for flight flutter testing is as follows:

1) Vibration excitation equipment - A single rotating weight or counter-rotating weights are driven by D.C. shunt motors. The connection between the motor and the rotating weights can be through a reduction gear or by means of a flexible shaft connected to the reduction gear. In this case, the reduction gear must be mounted on separate bearings. Two type of aerodynamic vibrators have been used; conventional oscillating vanes, and the combination of a flat plate with a variable speed rotating slotted cylinder at the trailing edge. Sketches of the various types of excitation equipment are shown in figures 14 through 16.

Counter-rotating weights

Weight

Motor

Single rotating weight
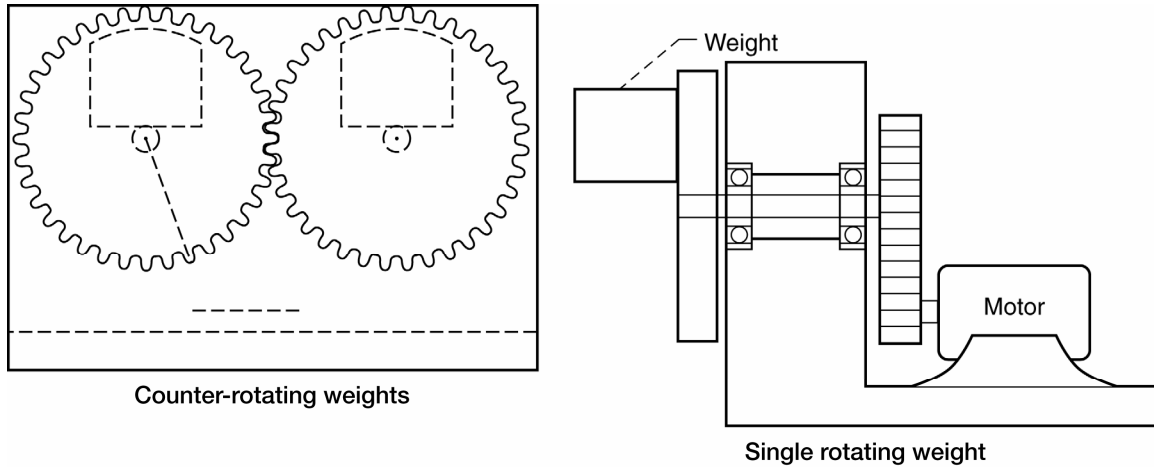
Figure 14.—Rotating weights.

Air stream

Motor
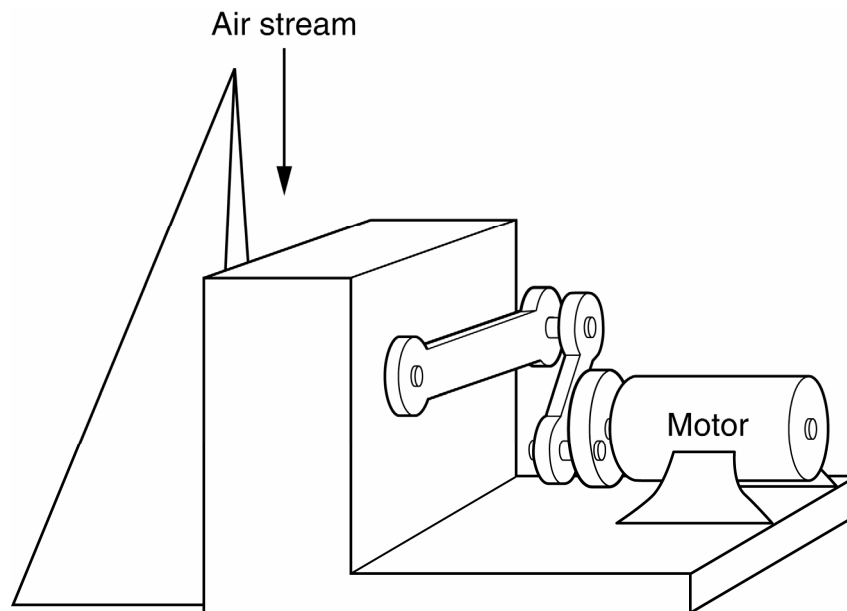
Figure 15.—Oscillating vane.
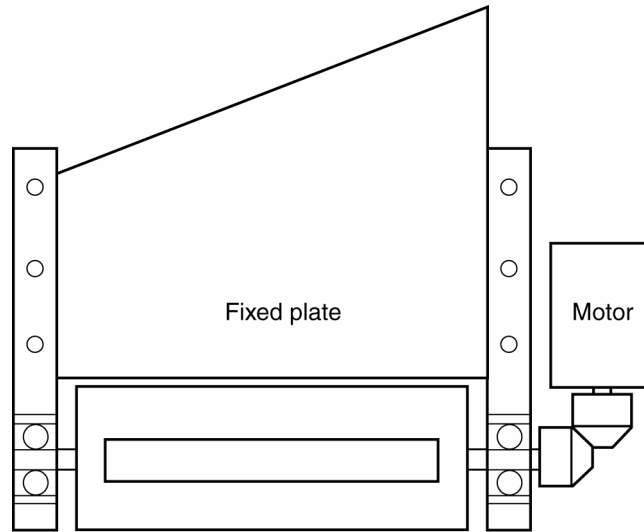
Figure 16.—Slotted cylinder.
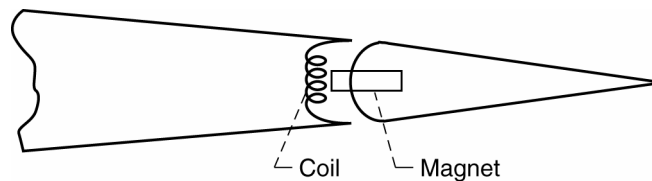
Figure 17.—Coil and magnet.
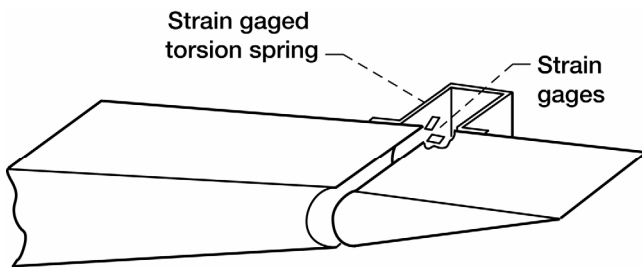
Figure 18.—Strain gaged torsion spring.
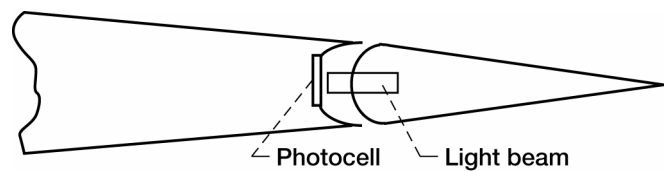
Figure 19.—Photocell light beam.

2)   Vibration measuring instruments for use during flight flutter testing include strain gages, accelerometers and velocity pickups. Vibrations of control surfaces and tabs have been measured by using a magnet attached to the control surface and a coil attached to the supporting surface with an output proportional to the rotational velocity of the control surface and/or tab relative to the supporting surface. Strain gages on a torsion beam attached between the control surface and supporting surface, and photoelectric devices, have also been used. Sketches of some of the measuring devices are shown in figures 17 through 19.

The installation of suitable vibration excitation and measuring equipment should be determined by the mode shapes indicated by the flutter analysis. For fixed surfaces including wings, stabilizers and fins, the oscillating

aerodynamic vanes are usually located at the tips of the surfaces and the airfoils with rotating cylinders are located just inboard of the tips. Mechanical shakers consisting of rotating weights are usually located near the leading edge inboard of the tip to produce a substantial torsional response. The vibration measuring equipment should be located to indicate the type of flutter that is expected. However, practical difficulties in locating the measuring equipment, such as no removable cover plates in the structure at the desired locations, must be considered. This problem can be solved by making the installation of test equipment in the test airplane during construction.

In certain cases, vibrations in flight have been caused by separated air flow. Such flow separation may be detected by pressure measurements on the external surfaces at high speeds and by means of yarn tufts attached to the surface at airspeeds low enough that the tufts will remain attached to the surface. Flow separation induced by shock waves has been encountered in a number of high performance aircraft. One method for preventing such separation has been to use vortex generators. Another method that has been used successfully in one case is to install a wedge at the location of the shock on the wing. It is believed that the wedge stabilizes the position of the shock wave. Dampers have been used on many aircraft to prevent excessive vibrations of control surfaces due to shock-induced flow separation. Typical vortex generators are shown in figure 20 and the wedge is shown in figure 21.

When flutter is encountered during high speed flights by test pilots, an extensive effort is made by the engineering department to determine the cause of the problem and to test modifications of the airplane such as mass balance and/or dampers, if the control surfaces are involved. Since extensive modifications of the structure after the airplane has been constructed can be extremely expensive, the actual modification is determined by the joint effort of the flutter, structural and manufacturing groups under the supervision of the chief engineer. Major structural modifications are often evaluated by means of wind tunnel tests of flutter models before the changes are made and additional flight flutter tests are conducted.

Although aircraft with top speeds well below the speed of sound are less likely to flutter, it is recommended that companies and individuals who design and build such aircraft consider employing an experienced flutter engineer as a consultant to prevent flutter problems that might result in the destruction of the airplane and injury or death to the pilot. Although the exact causes of deaths or injuries in home built aircraft are not known, ground vibration testing and simple flutter analyses may uncover structural and flutter problems. In some low speed aircraft, the structural frequencies involved in flutter can be low enough so that suitable excitation of the structure in flight can be made by oscillating the control pedals or control column. The control wheel can also be used for the unsymmetrical excitation of the ailerons. If flutter is approached, the forces required to move the control surfaces will be reduced because of the reduction in damping. Low frequency vibration responses can usually be observed and/or felt by the test personnel so that the installation of vibration measuring equipment may not be necessary.
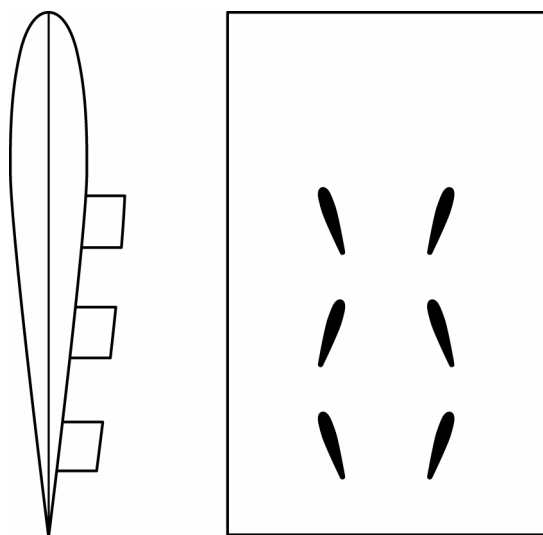
Figure 20.—Vortex generators.
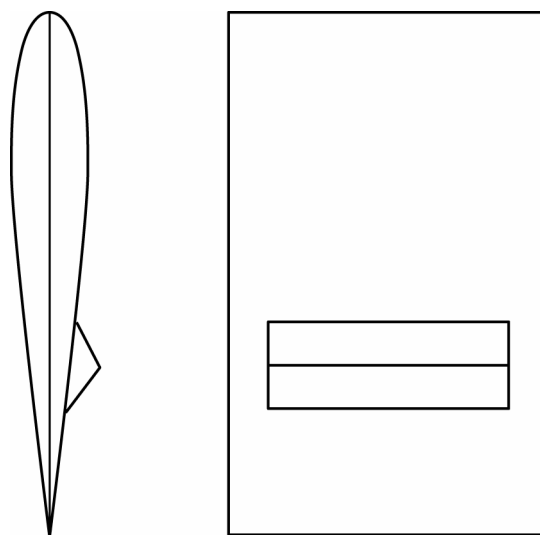
Figure 21.—Wedge.

Aircraft Ground Vibration

Test Techniques

One objective of ground vibration testing is to obtain the vibration amplitude distributions, (mode shapes) and the frequencies of the structure for use in the prediction of flutter problems. Most flutter problems involve two or more of the following types of vibration: bending and torsion of fixed surfaces, rotation and/or torsion of control surfaces and rotation of tabs. Flutter occurs when the aerodynamic damping due to motions in one vibration mode such as wing bending is balanced by the lift due to the angle of attack in another vibration mode such as wing torsion. Figure 22 illustrates two of the vibration modes of a wing-aileron combination.

The primary causes of flutter are as follows:

1.) Insufficient torsional stiffnesses with center of gravity locations of spanwise sections substantially behind the quarter chords on wings, stabilizers and fins.

2.) Control surfaces with center of gravity locations of spanwise sections behind the hinge lines and inadequate rigidities in the control systems.

3.) Trim tabs with inadequate stiffnesses in the rotational restraints and/or excessive free play.

4.) Spring tabs with inadequate stiffnesses in the rotational restraints coupled with motions of the control systems.

Wing bending

Node line
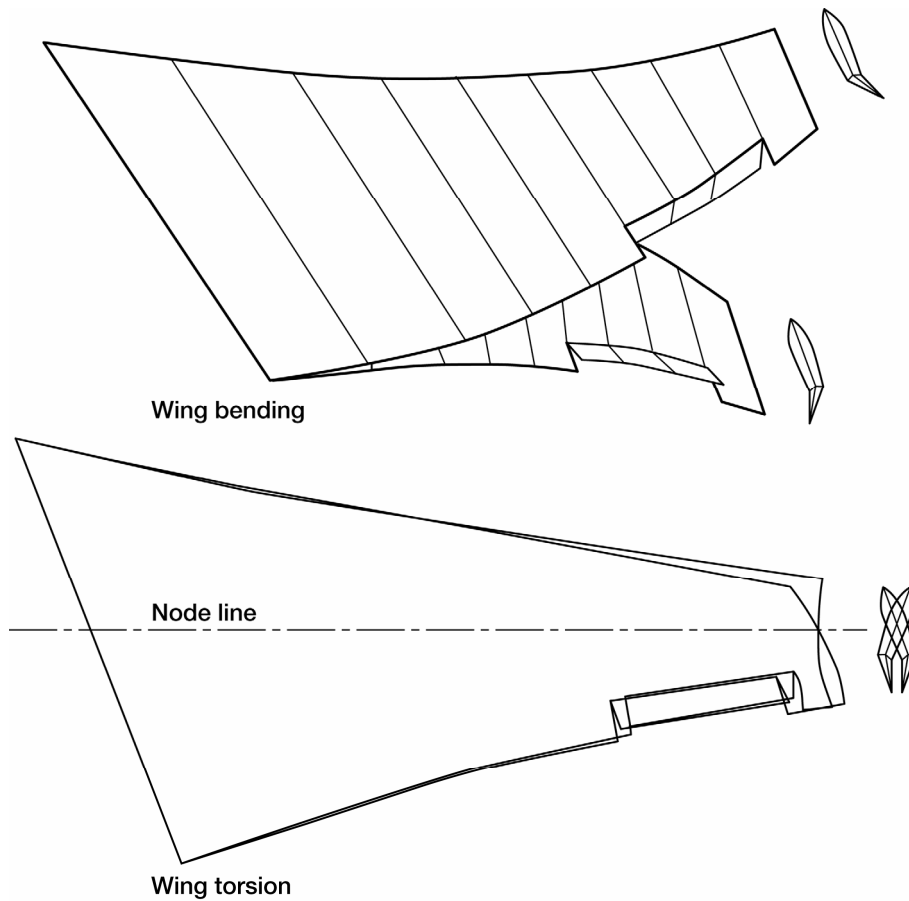
Wing torsion

Figure 22.—Wing-aileron vibration modes.

5.) External stores on the wing including engines, tip mounted fuel tanks, and heavy wing mounted weapon systems which produce unstable coupling between bending and torsion.

6.) Wing mounted engines with propellers which produce unstable gyroscopic and aerodynamic couplings between pitch and yaw.

7.) Horizontal tails mounted on the tops of vertical tails which produce unstable coupling between fin torsion and stabilizer yaw with fin bending and stabilizer roll.

8.) Rotational flexibilities at the roots of all movable horizontal tails which substantially lower the torsional frequencies.

9.) Active control systems.

Although theoretical predictions of the frequencies and mode shapes before construction of the aircraft can be subject to significant errors, such predictions are very useful in the planning of ground vibration testing as well as in flutter calculations and flutter model programs which are completed before the aircraft has been constructed.

The equilibrium conditions applicable to dynamic analysis require that the internal inertia, damping and spring forces acting on each mass must balance any external forces which are applied or the internal forces must be in balance at locations in the structure where there are no external forces. It is obvious that the equations of equilibrium apply for all vibration testing no matter how nonlinear or highly damped the structure may be or what types of force inputs are applied. However, the usual analytical procedures for dynamic analysis make use of the normal modes of vibration which can only exist in structures that are linear.

The following problems encountered in the ground vibration testing of aircraft should be considered in order to obtain the required normal mode information with sufficient accuracy and with the efficient use of the manpower available to conduct the tests.

1.) Providing rigid body frequencies which are low compared to the structural frequencies
2.) Locating the shakers
3.) Selecting the waveforms used for inputs to the shakers
4.) Measuring the responses
5.) Processing of the test results

Providing low rigid body frequencies.—Some success has been obtained in meeting this objective by supporting the aircraft on the landing gear with reduced pressures in the tires. In this case, there will be some linear damping caused by motions of the shock struts. However, such damping forces will usually be small compared to the inertia and elastic forces in the structural frequency range.

Air springs beneath the tires have been used to improve the isolation. Although, retracting the landing gear might be desirable to simulate flight conditions, the support system is likely to be too complicated to be used. If such a support system is desired, the aircraft could be supported from above using three cables to provide the yaw, lateral and fore and aft degrees of freedom and tension springs connected between the cables and the aircraft to provide the vertical, pitch and roll degrees of freedom. The cables should be eliminated if the tension springs would provide all six degrees of freedom within the allowable frequency range. Compression springs located beneath the aircraft would be another potential mounting system.

Locating the shakers.—The vibration modes involved in potential flutter problems should be considered when determining the most useful locations of the shakers. All shaker locations which produce substantial vibration amplitudes of the components of the aircraft whose motions can cause flutter would be satisfactory. For wings without stores, engines and tip tanks, as well as for stabilizers and vertical tails, the usual practice has been to locate the shakers near the tips of the structures and phase the shakers on wings and stabilizers to obtain symmetric and antisymmetric modes. To excite the torsional modes, the shakers should be installed well ahead or behind the torsional nodal lines. Such locations would be just ahead of the trailing edge control surface or near the leading edge or just behind the leading edge control surface if such a surface is used. While two shakers could be installed near each wing tip and phased to produce forces for bending excitation and torques for torsion, this installation is only required if the torsional response is not adequate with one shaker installed near each tip. If the vibration responses of control surfaces are not adequate, direct attachment of the shakers to the control surfaces should be used.

However, if dampers are attached to the control surfaces, tests should be run with and without the dampers. For spring tabs, the response of the control system as well as the response of the tab should be measured. In this case, it will be necessary to attach a shaker to the control system if the response is inadequate with a shaker attached to the control surface. The vibration amplitude of the tab should be large enough to overpower tab restraints caused by preloaded springs.

For wings with external stores, direct attachment of shakers to each of the stores which might cause flutter would be required if the response of the store is too small to overcome non-linearities as well as for accurate measurements when the shakers are attached near the wing tips.

Direct attachment of the shakers to the control surfaces should be made if the surfaces are used for active control. The active control system should be energized during such tests.

The methods of attaching shakers to the above structures include: a) attaching the shaker rods to a plate with machine screws where threads are available on the surfaces of the aircraft structure to mount the plate with a bolt, and b) holding the shaker rod against the structure using a vacuum inside a rubber vacuum cup attached to the shaker rod. Another possibility is to glue a mounting plate to end grain wood which is attached to the structure with fast drying glue which can be easily removed after the test has been completed. It is desirable that bending moments at the end of the shaker rod be reduced with a universal joint with minimum free play and low friction.

Figures 23 through 26 demonstrate different placements of shakers:

Figure 23.—Shaker location (view #1).
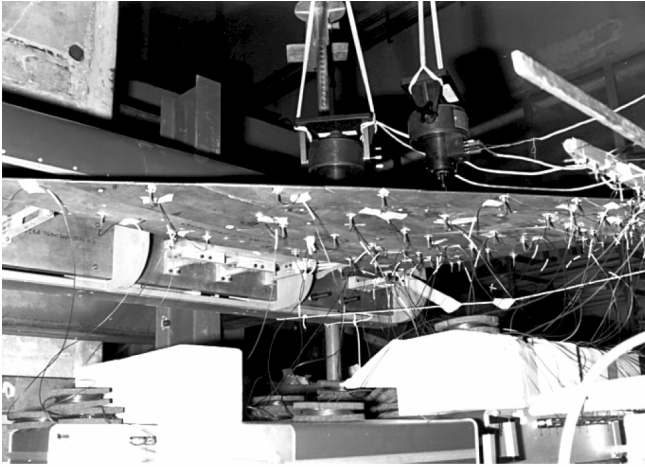
Figure 24.—Shaker location (view #2).
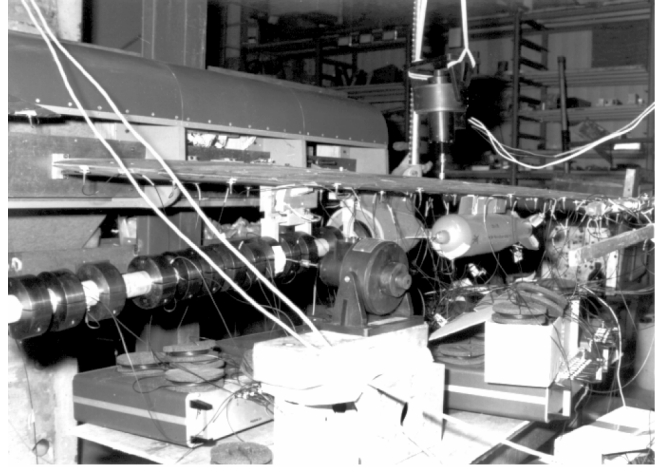
Figure 25.—Shaker location (view #3).
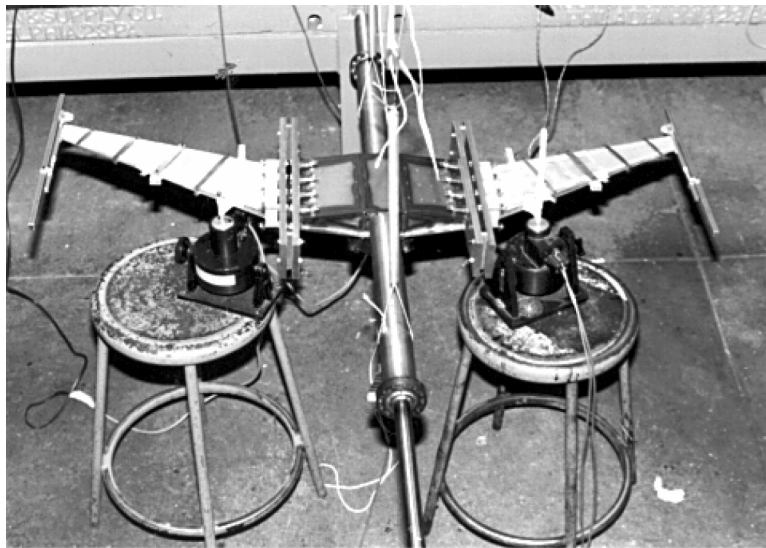
Figure 26.—Shaker location (IORN bird).

Shaker inputs.—It is recommended that sine dwell be used as the shaking force since the mode shapes and frequencies can be measured directly from the outputs of accelerometers or other vibration measuring devices. Although more complicated shaker inputs have been used to save test time, the calculations of the mode shapes and frequencies are based on the assumptions of linear theory which will not be applicable at certain locations in the actual structure. In addition, the concentration of the input forces at one frequency with sine dwell provides the high energy excitation which is often necessary to overcome friction, free play and other non-linear effects including structures using skins which buckle at high loads. Nevertheless, where accurate theoretical predictions have been made and previous experience with similar structures using complicated vibration inputs has been satisfactory, an input waveform containing all the frequencies of interest could be tried to save test time. Figure 27 demonstrates some typical shaker inputs:

Instrumentation.—Roving vibration measuring pickups (accelerometers or devices which respond to vibration amplitude or velocity) have been used by some test engineers.

In this case, one vibration pickup should be mounted on the structure to provide a reference amplitude and the roving pickup should be held against the structure with a restraint which will not affect the frequency and damping. In some cases, test personnel can use one hand to hold the pickup against the structure. In other cases, the pickup can be mounted on a spring restrained light weight four bar linkage which test personnel can use for the same purpose. A typical design for such a linkage is shown in figure 28.

Improved data processing is possible with the installation of a large number of pickups. However, the use of a good math model can be used to reduce the number. Tests should be made with a sufficient number of pickups to determine if the correlation with theory appears to be acceptable. If the agreement is satisfactory, additional pickups will not be required. Sine dwell should be used in cases where a large number of pickups have been installed, since the amount of test time that might be saved with more complex inputs will usually be small compared to the time required for calibrating and installing the pickups.

Fast drying glue can be used to install lightweight pickups directly to the structure where the external surface is flat. In other locations, the pickups should be fastened to thin metal plates glued to end grain wood pads which are contoured to fit the surface and can be glued with fast drying glue. For heavier pickups, thicker metal plates should be used so that the pickups can be mounted with machine screws.
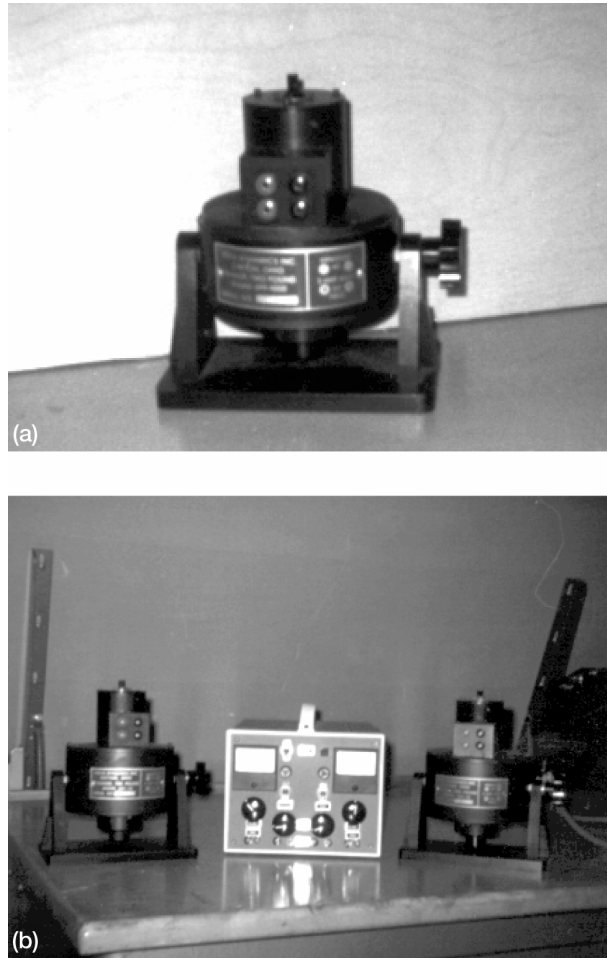
Figure 27.—Shaker input.
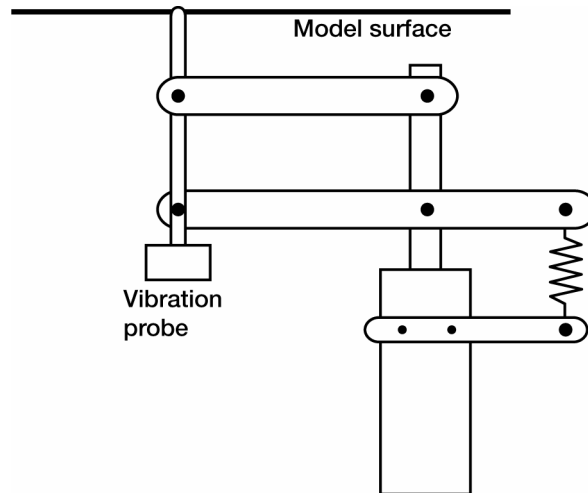
Figure 28.—Four bar linkage vibration probe support.

Data processing.—Measuring the response using a multichannel oscilloscope or recorder with an adequate frequency response has been widely used to obtain the amplitudes, frequencies and phase angles excited during ground vibration testing. However, some of the digital systems in use at the present time might be almost univer-sally used in the future to save engineering hours. In this case, the data would be digitized and stored on disks for later processing. However, enough data should be processed during a vibration test to insure that the results are sufficiently accurate so that the test will not have to be repeated.

Engineers with sufficient flutter experience can usually make this decision correctly by studying the vibration amplitudes and phase angles in the vibration modes that might result in flutter.

Additional Information Concerning Modal Analysis

Orthogonality between two natural modes is computed by multiplying each mass by the product of its displacements in the two modes and summing the results over all the masses. If the displacement of each mass in the two modes are in different directions, each product is multiplied by the cosine of the angle between the directions. A zero result from the summation indicates that the modes are orthogonal. The advantage of using orthogonal modes is that the response in each mode can be computed using the equations for a single degree of freedom system.

For each normal mode, the generalized coordinate is the displacement of the structure at a reference station. This displacement is multiplied by a function (mode shape) giving the ratio of the displacement of each point in the structure to the displacement at the reference station. The effective mass in each normal mode is computed by multiplying each mass by the square of the ratio of the amplitude of the mass to the amplitude at the reference station and summing the results for all the masses. The effective spring force is computed by multiplying the effective mass by the square of the undamped natural frequency and the effective damping can be computed from the amplitude ratio at resonance or from decay records. The effective input force is the actual force multiplied by the amplitude of the structure in the direction of the force at the point where the force is applied.

The amplitude and the phase angle of vibration in a single degree of freedom system caused by a force P is given by the formula

$$P = m\omega^2 x - kx(1 + jg) \tag{4}$$

in which m is the mass, k is the spring constant, ω is the frequency in radians per second and g is the damping coefficient. A vector plot may be drawn to determine the response. $m\omega^2 x$ is located along the positive x-axis, kx is located along the negative x-axis and $-kxjg$ is located on the negative y-axis. At low frequencies, P is located a few

degrees above the x-axis since $m\omega^2 x$ is small compared to kx and kg is usually small compared to k. At resonance, $m\omega^2 = k = m\omega_n^2$ where ω_n is the natural frequency, so the force P leads the displacement by 90 degrees.

At high frequencies, $m\omega^2$ is much greater than k, so P leads the displacement by slightly less than 180 degrees. A typical vector diagram is shown in figure 29.

If the force inputs of the shakers are known, the effective mass in each natural mode might be calculated from the value of the effective force, the amplitude of the reference station at resonance and the decay of free vibrations. The effective force must be large enough to produce a substantial response in the mode for which the effective mass is being computed. The response at resonance is P/kg and if g is determined from the damping of free vibrations, k can be computed. The effective mass is then equal to k/ω^2. One problem with this method is that the value of g obtained from the decay of the amplitude of a mode excited during a ground vibration test may vary with the amplitude. For this reason, the measured effective mass should be compared with the effective mass computed from the measured vibration amplitudes and the computed weights.
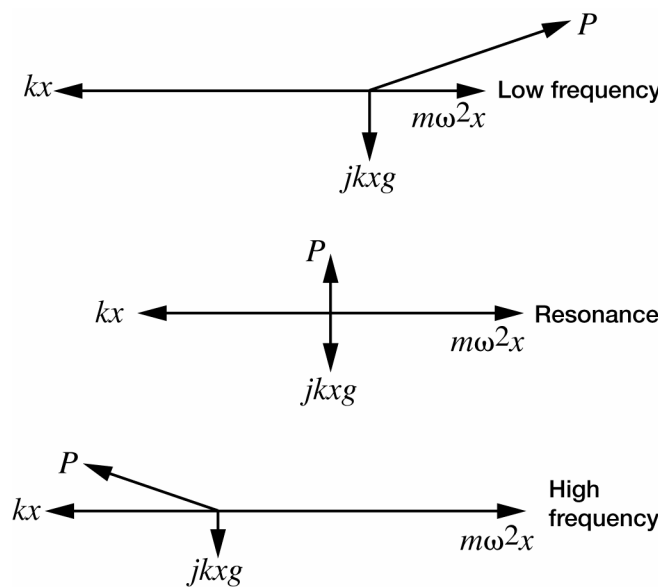
Figure 29.—Typical vector diagram.

Flutter Prevention Handbook: A Preliminary Collection[*]

D.D. Liu, D. Sarhaddi, and F.M. Piolenc
ZONA Technology, Inc.
9489 E. Ironwood Square Drive, Suite 100
Scottsdale, Arizona 85258–4578

Part B: Aerodynamic and Mass Balance Effects on Control Surface Flutter

Robert E. Donham and George A. Watts
REDINC

Foreword

Abstract

Six cases of flutter of full scale aircraft or wind tunnel models, shown in the table below, are discussed as to flutter type, cause and correction. Also included are descriptions of several control surface/tab systems and how they function. Mass and aerodynamic balance types and design rules are also discussed.

Case	Flutter	Cause	Cure
1	aileron/wing torsion	stores distribution	relocate stores or placard
2	vertical fin/rudder	excess rudder aerodynamic balance	placard
3	vertical fin/rudder	concentrated mass balance	mass balance redistribution
4	stabilator rotation/bending	rotation/bending mode coupling	mass balance redistribution
5	wing/aileron	excess control surface rotational inertia	reduced inertia+static mass overbalance
6	elevon/wing torsion	wing torsion/aileron rotation coupling	not applied

---

[*]This document was taken from the original report: Liu, D.D.; Sarhaddi, D.; and Piolenc, F.M.: Flutter Prevention Handbook: A Preliminary Collection, WL–TR–96–3111, 1996, first published by the Flight Dynamics Directorate, Wright Laboratory, Air Force Materiel Command, Wright-Patterson Air Force Base.

It is imperative that flutter not occur within the useable flight envelope of an aircraft and that a safe-speed margin beyond envelope boundaries be maintained. Furthermore, flutter margins must be attained efficiently, to forestall the accumulation of excessive structure or ballast weight that could compromise payload.

A companion consideration to flutter in flight vehicle design is the provision of sufficient structure stiffness to prevent static aeroelastic divergence, control reversal and excessively large stability derivatives. Though not the primary subject of this handbook, static aeroelasticity methodology can be useful in the analysis of certain types of flutter and this is briefly discussed.

The common features of classical flutter phenomena and means of detecting them theoretically and experimentally are explored. Standard rules for designing aerodynamic geometry, internal structural arrangements and mass balance distributions to minimize the possibility of flutter without large weight penalties are discussed.

The cases cited are of flutter encountered, during the design/development phase of actual aircraft, in flight or in dynamically scaled wind tunnel model tests. In some cases flutter occurred despite application of the rules of good design for flutter prevention.

Introduction

The term "flutter" is applied to many differing dynamically unstable mechanisms produced by fluid flowing past structures and their mass distributions. Flutter implies unexcited (or self-excited) structure vibration amplitudes that increase exponentially in time without limit, (or to a limit fixed by some nonlinearity of the system). Among these are types not currently amenable of theoretical analysis such as: smokestack and bridge flutter induced by shed bluff-body vortex streets and the closely related highly-swept-wing flutter caused by leading-edge vortex shedding at high angle-of-attack at subsonic speed. At transonic speed, single degree-of-freedom aileron buzz induced shock boundary-layer interaction is another form of flutter. These nonanalytic forms and panel flutter (of aircraft skin panels) are not discussed here.

This contribution discusses types of aircraft flutter predictable through the use of linear attached-flow unsteady aerodynamic theories. These instabilities result from the interaction of two or more fundamental vibration modes. Such modes may include the overall vehicle "rigid" body and other mechanical modes as produced, for example, by hinged control surfaces and rotating propellers. In some cases, largely non-aerodynamic, natural modes of vibration such as: wing fore and aft motions coupled with fuselage yaw (wing scissors motion); vertical fin pitch coupled with fuselage vertical bending; and horizontal yaw coupled with fuselage lateral modes (horizontal stabilizer scissors) must be included.

Some Types of Flutter

Despite this limited view, the list of mechanisms that lead to "catastrophic" flutter continues to grow. A few are as follows:

Wing/aileron flutter.—An interaction of wing bending, wing torsion and aileron rotation. Found in both swept and unswept wings. Can be symmetric or antisymmetric. Is similar to fin-rudder and horizontal tail-elevator flutter. Full distributed static mass balance prevents bending/control surface flutter but may not prevent torsion/control surface flutter. This is discussed in Case 5.

Fixed surface/control surface/tab flutter.—Tab rotation induces a control surface rotation that in turn creates a fixed surface aerodynamic force. Freeplay or lack of adequate tab actuator stiffness can lead to flutter when the tab is not mass balanced.

Wing/body flutter.—Low-frequency interaction of wing bending and "rigid-body" plunge and pitch modes. Low body pitch inertia, as found in flying wings, for example, can lead to this form of flutter. Short period mode can couple with wing bending and in some cases with wing torsion, especially when large tip tanks are in use.

Hump-mode flutter.—One of several flutter mechanisms produced by the interaction of podded engines and wing vibration modes. Found in transport aircraft. Similar effects can be seen when control surfaces couple with fixed surface modes.

External stores flutter.—Induced by added mass, can be affected beneficially by a lack of symmetry of the spanwise mass distribution. In fighter aircraft, use of wing pylon MER (Multiple Ejection Racks) and TER (Triple

Ejection Racks) external store configurations might still become critical for unsymmetric intermediate combinations of stores. An example involving a twin turbofan aircraft is presented in Case 1.

Propeller whirl-flutter.—A precessive oscillation of the propeller and engine relative to the airframe. Affected by low structural stiffness of the engine-propeller system mounting. Involves cross coupled yaw and pitch degrees of freedom driven by propeller aerodynamic and gyroscopic moments.

Objectives

This contribution addresses the following aspects of the classical forms of flutter found in aircraft:

- Aircraft design to minimize the possibility of catastrophic flutter.
- The definition, mathematical description and theoretical analysis of aeromechanical systems employed in flutter analysis.
- Ground vibration testing to verify the mathematical model of the aircraft inertia-elastic system.
- Wind tunnel flutter testing.
- Flight testing procedures that lead to minimum risk during flutter exploration.

The diversity of the flutter situations encountered in actual aircraft is illustrated by six examples. Each flutter mechanism and how it was found are discussed. The corrective actions taken and success or lack of success of steps on the way to a safe configuration are noted.

Aircraft Design for Flutter Safety, Structural and Ballasting Efficiency

Flutter Mechanisms—General Discussion

All mechanizations of flutter depend on the interaction of aerodynamic, inertia, and elastic forces. Structural elastic (or spring) forces react with inertia (or accelerated mass) forces to create the oscillatory character of flutter seen in the orthogonal (or independent) natural vibration modes of the system. Aerodynamic forces modify the elastic forces to change the frequencies of the fundamental natural modes. They also act to couple certain of the modes together. This creates timewise phase lags between them and results in positive or negative damping of the new combined modes of the total system. Aerodynamics may thus lead to strong damping, of the otherwise conservative (or nondissipative) system, or to the divergent oscillation, known as flutter.

Configuration Effects on Flutter

An aircraft typically consists of a slender body of small lift effectiveness but large forward-located mass and pitch and yaw moments of inertia. To this body are attached surfaces of great lift effectiveness and relatively little weight, such as the wings and tail surfaces. Engine, fuel and external pylon mounted store weights, however, may be distributed spanwise across the wing.

Wing mass distribution effects.—The chordwise location of the wing spanwise mass distribution plays a major role in the flutter stability of the wing-body system. Two dimensional unsteady aerodynamic theory shows that motions with node lines aft of the leading edge to about fifty percent of chord are stable. Location of the mass centroid distribution aft of the elastic axis tends to be destabilizing. (The elastic axis is the spanwise locus of chordwise points along which concentrated normal forces may be applied without inducing wing elastic twist, usually near forty percent of chord).

Control surface effects.—Trailing-edge control surfaces, unless irreversibly actuated, complicate the behavior of wing-body systems. This is due to the large aerodynamic forces delivered to the wing modes by such surfaces. At subsonic speeds, for example, a one degree rotation of a control surface of 30 percent chord produces lift equivalent to a 2/3 degree rotation of the whole wing section, across the span of the control surface. The centroid of the section lift added to the wing will be located 15 percent of the chord length aft of that produced on the wing by an equivalent angle-of-attack (AOA) change.

Any oscillation of a manually controlled (or essentially free floating) control surface therefore causes very large lift and twisting moments on the supporting surface with attendant vertical and rotational accelerations.

A control surface displacement producing a force or moment in phase with (or in the direction of) an elastic rate of change of deflection of the main surface promotes flutter. A flutter occurrence, however, requires a coupling between the control and the main surface degrees of freedom.

An example of such coupling is provided when the first moment of the mass of a control surface is located aft of its hinge line. If a wing tip, oscillating in plunge is at the top of its stroke and accelerating downward, an aileron with its mass center aft of the hinge line will rotate trailing-edge upward. This produces a downward aerodynamic force, in the direction of the wing tip velocity. Any lag in the control surface displacement or its aerodynamic force buildup, relative to the wing tip displacement can result in flutter.

Mass balancing.—The above problem is usually solved by shifting the mass centroid of the control surface to the hinge line by the addition of counterweights forward of the hinge line. This is called mass balancing. It is very effective in suppressing bending mode coupling but overbalance is required for torsion mode decoupling. This is discussed in Case 5.

Federal airworthiness requirements impose arbitrarily large design loads on mass balance support structure to make sure weights do not fall off. The supporting structure and attachment of concentrated mass balance weights used on control surfaces on small aircraft must withstand inertia limit loads normal to the control surface imposed by accelerations up to 24g.

Effects of control surface tabs.—A further complication to the flutter dynamics of an airplane with a free-floating (or manually operated) control surface occurs with the addition of a tab (a small hinged surface) to the control surface trailing-edge. This results in three surfaces in tandem with two intermediate hinges connecting them.

The purpose of a tab is to reduce the control surface hinge moment to make manual control easier. It does this by rotating in the opposite direction to that desired of the control surface. Its position at the trailing-edge of the control surface allows its small force, in the wrong direction, to produce a large control surface hinge moment in the direction desired. Thus the system of three surfaces can provide the desired net lift force with a zero net hinge moment.

A trim tab is usually rotated to a fixed displacement relative to its elevator, for example, to produce a required steady tail lift force with zero hinge moment and stick force. It does not affect the rate of change of hinge moment application per unit deflection of the elevator. In some aircraft, tab rotation is, in addition, geared to elevator deflection for the purpose of reducing "stick force per g". It is then referred to as a geared tab. Another variation consists of allowing the control surface to float free about its hinge axis while the stick force is applied directly to the tab. The tab then supplies the required hinge moment to the control surface with little force feedback to the stick. Tabs are usually not mass balanced unless free, as are spring tabs. All tabs must be irreversible, frequency criteria and free play requirements must be met, unless the tab is properly balanced and has no unsafe flutter characteristics.

Effects of control-surface aerodynamic balance.—A more common way of reducing the stick force per g is through the use of aerodynamic balance. This is accomplished by tailoring the control surface planform geometry so that some lifting area lies ahead of the hinge line. This area provides hinge moment in a direction opposite to that provided by regions aft of the hinge line. Two methods are in common use: the aerodynamic horn—an area projection well forward of the hinge line near the surface tip and the set-back hinge—that distributes the forward projected area uniformly along the control surface span by placing the control surface hinge line well aft of the leading-edge.

Aerodynamic balance partially balances the hinge moment produced by normal pressure aft of the hinge-line. The designer must be careful not to overbalance the control surface or it will statically diverge to full throw (to the mechanical stop).

Aerodynamic balance reduces the hinge moment per unit control surface rotation at a given dynamic pressure. This reduces the aerodynamic spring constant and frequency of the control surface rotational degree of freedom. Flutter of a wing and aerodynamically unbalanced aileron, for example, may take place when the rigid rotational frequency of the aileron approaches that of a higher frequency bending or torsion mode of the wing. The effect of aerodynamic balance is to raise the airspeed at which the frequency coalesces and flutter will occur.

In addition, movement of the hinge-line to a position aft of the control surface leading-edge progressively reduces damping of the surface rotation mode.

These two effects can convert a mild low-speed flutter into a severe flutter problem at high speed.

Control surface dampers.—Control rotation-mode dampers may be employed when surfaces are too thin to house mass balances. They are also useful in the suppression of transonic buzz. Dampers may also be employed beneficially in wing-store cases of marginal stability.

Aircraft Flutter Analysis

Flutter analysis has evolved from the consideration of two or three degrees of freedom, at a time, by a hand calculation, prior to about 1950, to the analysis of the interaction of thirty or more vibration modes today through the use of large digital computers. The lack of computing capability in the early days forced the flutter engineer to carefully study the degrees of freedom available to him to ascertain which small group would likely lead to flutter, before undertaking the tedious task of finding the unstable roots. He postulated flutter mechanisms and investigated them analytically.

With the computer resources available today there is a tendency to include all possible modes in an analysis of flutter safety. This sometimes leads to difficulty in identifying the dominant physical mechanism causing flutter and in finding the most efficient way to modify the design to effect a solution.

Inertial-Elastic System

The theoretical analysis of flutter usually begins with a consideration of the dynamic behavior of the aircraft structure and its mass distribution in a gravity-free airless environment. An eigenvalue analysis provides the system resonant frequencies and the corresponding modes of natural vibration. These may be verified by direct experimentation on the completed aircraft by a ground vibration test.

Elastic properties.—The elastic properties of the free-free aircraft may be expressed as a flexibility matrix. (Each column of which is the distribution of deflections produced by a unit load applied at one loading point and reacted by rigid body inertia forces at all points. All deflections are measured relative to a common point or set of points in the physical structure). A flexibility matrix is the inverse of a stiffness matrix and may be calculated by finite element structural analysis methods.

Inertia properties.—The aircraft weight distribution is discretized into local masses and moments of inertia at the points employed in the flexibility matrix. (This may require the use of interpolation schemes).

Vibration mode analysis.—The above flexibility and inertia information is substituted into the matrix equation describing the dynamic oscillation of the conservative system. It is a set of unforced coupled second-order ordinary differential equations. The eigenvalues of its characteristic equation are extracted computationally and become the natural frequencies of the system. The eigenvectors (or mode shapes) associated with the eigenvalues then follow directly.

Coordinate systems for flutter analyses.—The theoretical vibration modes above are often employed in flutter analyses as the representative degrees of freedom of the system since they are orthogonal to each other and to the rigid body modes (or they are inertially uncoupled, i.e., inertia forces in one mode produce zero generalized forces in the others). They may not, however, be orthogonal to a control surface rotation degree of freedom when it is added as a general coordinate to describe control surface relative motion.

It is not necessary to employ the natural vibration modes as the describing degrees of freedom of the airplane, and in fact were not available in the early days of flutter analysis since they were then impossibly tedious to calculate. It is only required that the deflection describing modes be general enough to reproduce the important motions of the inertia-elastic system and the static aeroelastic system.

Notes: 1.) It may not be feasible to employ a sufficient number of natural vibration modes to adequately describe the static aeroelastic behavior of some low frequency flutter modes. In such cases it may be necessary to employ a smaller number of nonorthogonal modes specially tailored to include such effects.

The static aeroelastic deflection shapes due to AOA, pitch rate and control surface deflection make good candidates for inclusion with a set of elastic modes in analyses of flutter in which rigid-body motions are important, for example. If coordinates are employed that are not orthogonal, cross-coupling flexibility and inertia terms are present. Modern computers have no problem calculating and including these.

2.) Static aeroelastic problems are usually analysed in terms of the unreduced stiffness, (or flexibility), matrices of all load and deflection points on the aircraft structure rather than in terms of the reduced set of orthogonal elastic modes employed in flutter analysis. Though a small number of lower frequency elastic modes may adequately represent the dynamic motions involved in flutter, they will often not represent the elastic twist of the wing adequately for static aeroelastic analyses.

Unsteady Aerodynamics

Aircraft unsteady aerodynamics, at one value of nondimensionalized or reduced frequency, may be expressed as a matrix of complex aerodynamic forces on the set of contiguous elemental areas making up the thin lifting surfaces of wings, tails, control surfaces, etc. The differential pressures generating the forces are produced by the surface element motions: angular displacement and linear velocity normal to freestream flow.

The time lag between surface motion and pressure development is accounted for by the real and imaginary elements of the complex matrix.

The aerodynamic pressure distribution due to the motion of each mode, at one reduced frequency, is applied to all modes and integrated over the aircraft surface to yield the aerodynamic coefficients of a reduced set of flutter equations. This is the general procedure utilized with any general coordinates.

Detailed lifting surface computer programs are employed in generating the basic unsteady aerodynamic matrices, above. The primary methods in use today, for both steady and unsteady matrix prediction, are Strip Theory and Doublet Lattice for the subsonic flight regime and ZONA51 for the supersonic. In the transonic regime specialized codes are applied.

The analytical investigations of aircraft reported in this note, however, made use of MSC NASTRAN for the dynamic models, (structure-inertia systems), and unsteady Strip Theory and Doublet Lattice with steady-state weighting for the unsteady aerodynamics.

In discussing flutter prevention, however, a simpler implementation of unsteady aerodynamics has been employed in this note: incompressible two-dimensional unsteady aerodynamics operating on the plunge, pitch and control rotation degrees of freedom. This methodology provided the key to flutter analysis during the first fifty years of powered flight through its utilization in Strip Theory. Despite the lack of spanwise interference between sections in this theory it has been surprisingly effective. This may be due to the high aspect ratio of lifting surfaces common during this period.

Flutter Experience

The following cases of flutter have been chosen to illustrate the diversity and complexity of flutter mechanisms occurring in actual flight, encountered in wind-tunnel testing of new aircraft designs or found by analysis and corrected prior to flight.

Case 1: Effect of Wing-Store Distributions on Aileron/Wing Torsion Flutter

Aircraft description.—The twin-turbofan aircraft, see figure 1, has its engines mounted on the aft fuselage. Its swept low-wing has upper surface fences at 47 percent semi-span. Wing thickness varies from 10.5 percent at the root to 8 percent at the tip and sweep of the quarter-chord is 30 degrees. Conventional ailerons are actuated hydraulically with artificial feel and are almost irreversible.
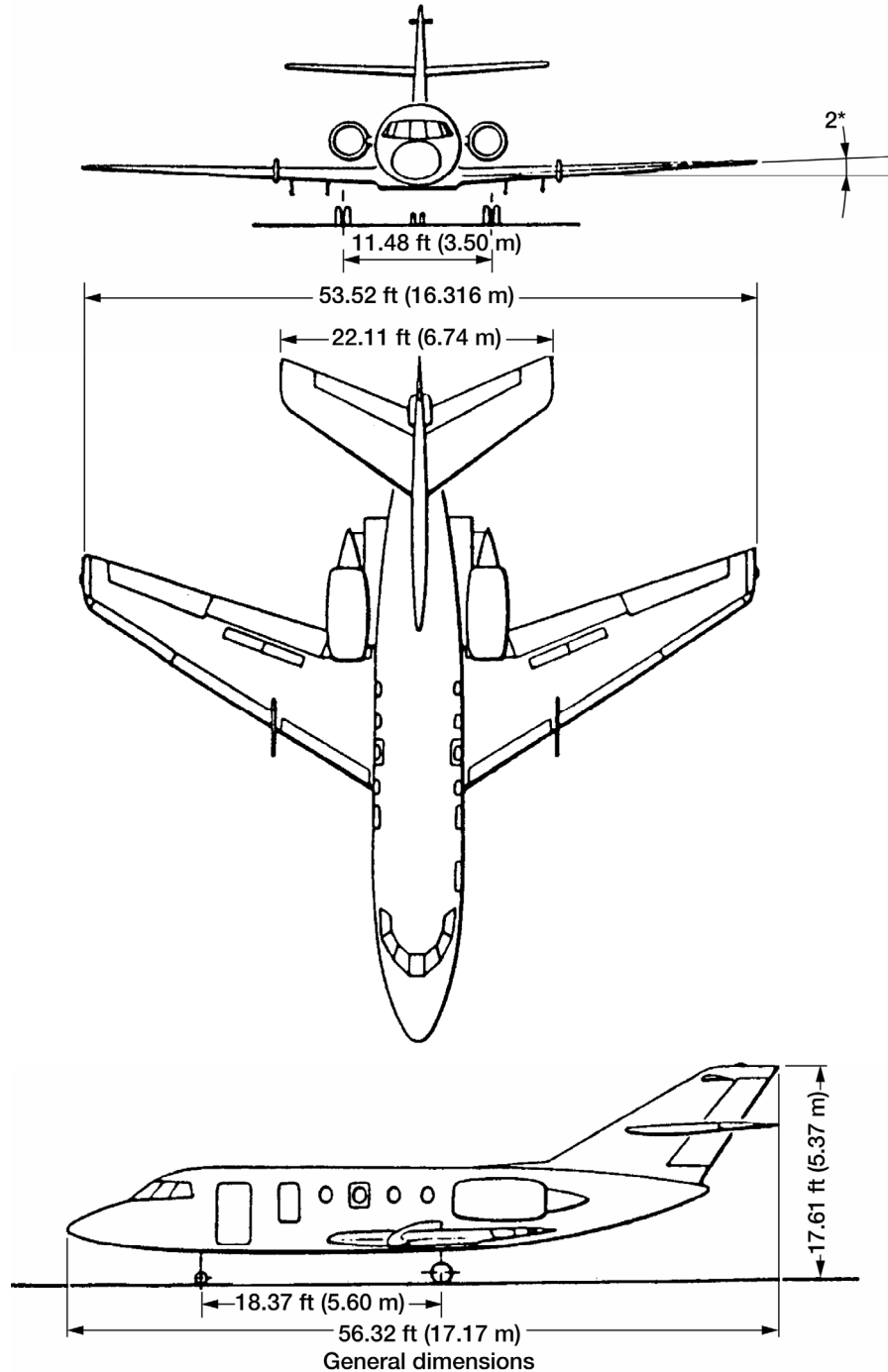
Figure 1.—Test aircraft for wing-store effect on Aileron/wing torsion flutter.

The swept vertical fin has a swept tailplane mounted at its semi-span.

- Maximum Mach Number = 0.80
- Maximum Cruise Speed = 461 knots TAS at 40,000 ft altitude

Though originally designed as a light commercial transport, it is currently employed in the military services of several countries. Two of its uses are as an aerial refueling trainer and maritime reconnaissance.

The configurations investigated, employed symmetrically-arranged inboard and outboard external store attachment points under the wing as is shown in figure 1 and table 1. Twenty-seven store configurations were considered.

The ailerons were not mass balanced and thus depended on a high irreversibility frequency and rotation mode damping to maintain aileron/wing coupled flutter margins. Ground vibration tests showed the following values:

TABLE 1.—SYMMETRIC VIBRATION MODES OF THE TEST AIRCRAFT

Hydraulic Power	Left Aileron		Right Aileron	
	Frequency Hz	Damping g	Frequency Hz	Damping g
On	49.3	0.06	50.3	0.05
Off	47.6	0.07	48.2	0.07

(Note: Vibration peak width at the half power point divided by the center frequency furnished the measured damping value, g).

FUEL TANKS EMPTY (SYMMETRIC MODES)

Frequency (Hz)	Vibration Mode Description
5.51	Wing 1st bending, A/P pitching
6.12	Wing 1st bending, A/P pitching
7.57	Stabilizer bending coupled with wing bending
10.57	Fuselage vertical bending-stabilizer bending
12.99	Fuselage vertical bending-engine pylon bending
15.77	Stabilizer bending
18.34	Wing 2nd bending-engine pitching
18.34	Engine pitching
31.23	Wing torsion
32.19	Wing torsion-aileron rotation
36.53	Wing 3rd bending
37.75	Elevator rotation (1 hydraulic system)
40.30	Elevator rotation (2 hydraulic system)
--	Higher-order wing torsion
55.01	Higher-order wing bending-torsion
--	Stabilizer 2nd bending
--	Stabilizer torsion

A twin hydraulic booster system rotated each aileron at its spanwise center. Each system also included a viscous damping circuit to prevent flutter.

Ground vibration tests also provided symmetric and antisymmetric overall vibration modes and natural frequencies for the aircraft with no fuel or stores, as described in tables 1 and 2. Note the outer wing torsion mode frequency identified during the antisymmetric tests as approximately 51 Hz. The above ground-measured aileron rotational modes for the various booster conditions range from 47.6 Hz through 50.3 Hz and exhibited g-damping levels of 0.05 to 0.07.

In the one configuration that was predicted to be flutter critical, near a frequency of 51 Hz, two unsymmetrical stores only were carried: of 300 and 140 lb weight respectively. These stores were carried on the outboard pylon stations.

Flutter experience.—Four flutter clearance programs were conducted on 27 store configurations. Most were symmetrical mixes of inboard and outboard stores on the four pylons. Analyses, ground and flight tests indicated no flutter within flight operational boundaries with all but one configuration, the only unsymmetrical one.

TABLE 2.—ANTISYMMETRIC VIBRATION MODES OF THE TEST
AIRCRAFT FUEL TANKS EMPTY (ANTISYMMETRIC MODES)

Frequency (Hz)	Vibration Mode Description
5.58	Fuselage torsion
6.33	Fuselage torsion-stabilizer rocking
7.43	Stabilizer rocking
9.62	Fuselage side bending-stabilizer rocking
12.23	Wing bending
13.85	Wing bending-fuselage side bending
17.05	Fin bending
20.66	Engine pitching
23.49	Rudder rotation (1 hydraulic system)
26.11	Rudder rotation (2 hydraulic system)
28.66	Wing 2nd bending
31.76	Wing torsion
40.47	Stabilizer bending
42.20	Elevator rotation (1 hydraulic system)
42.20	Elevator rotation (2 hydraulic system)
50.70	Higher order wing torsion
68.97	Stabilizer torsion

It consisted of one store per side located on the outboard pylon stations but of different weights (300 and 140 lb) and moments of inertia.

Analyses.—This configuration was analyzed as a complete aircraft, i.e., with each side described independently, using NASTRAN with Doublet Lattice unsteady aerodynamics. The analyses were conducted with aileron damping set at $g = 0.03$ and with the measured aileron rotation springs. Analyses were run with the full predicted unsteady aerodynamic aileron hinge moments and with hinge moments reduced to 50 percent of full value. Solutions were found for $M = 0.76$ over a range of altitudes from sea level to 40,000 ft.

The clean aircraft was entirely free of flutter with acceptable margins. With the unsymmetric stores on the outboard pylons only, the outer wing torsion mode coupled with the aileron rotation mode and resulted in flutter at approximately 51 Hz primarily involving motions on the light side, within the flight envelope, even though $g = 0.03$ had been included in the analysis.

Flight tests.—The unsymmetrical stores configuration was the first of the 27 configurations flight tested in each of the four test periods.

The instrumentation, see figure 2, emphasized wing structural strains and pylon store accelerations and recorded all control surface displacements.

Horizontal and vertical tail elastic strains were also recorded to permit the monitoring of any loss of empennage stability.

The strain monitoring gauges were added to give some indication of excessive load over a wide range of frequency and to make up, to a certain extent, for the lack of the large number of instruments usually found on prototype aircraft. Strains are proportional to structural deflection while accelerations are proportional to the product of deflection and frequency squared. Hence if an accelerometer is chosen to measure high frequency vibration, it will not pick up even large amplitude low frequency oscillations that could indicate large loads.

Since strain is directly indicative of structural damage, strain gauges can provide a limited but quantitative indication of excessive dynamic loads.

At the extreme edge of the flight envelope at 25,000 ft altitude the aileron rotation mode damping reduced from $g = 0.06$ to $g = 0.02$ over the last 50 Kts EAS, as determined by RDMDEC (random decrement) analysis of the test data. The test was repeated and gave the same result, thus in the interest of flight safety the aircraft was placarded (restricted) against flight with damping below the ground measured value.
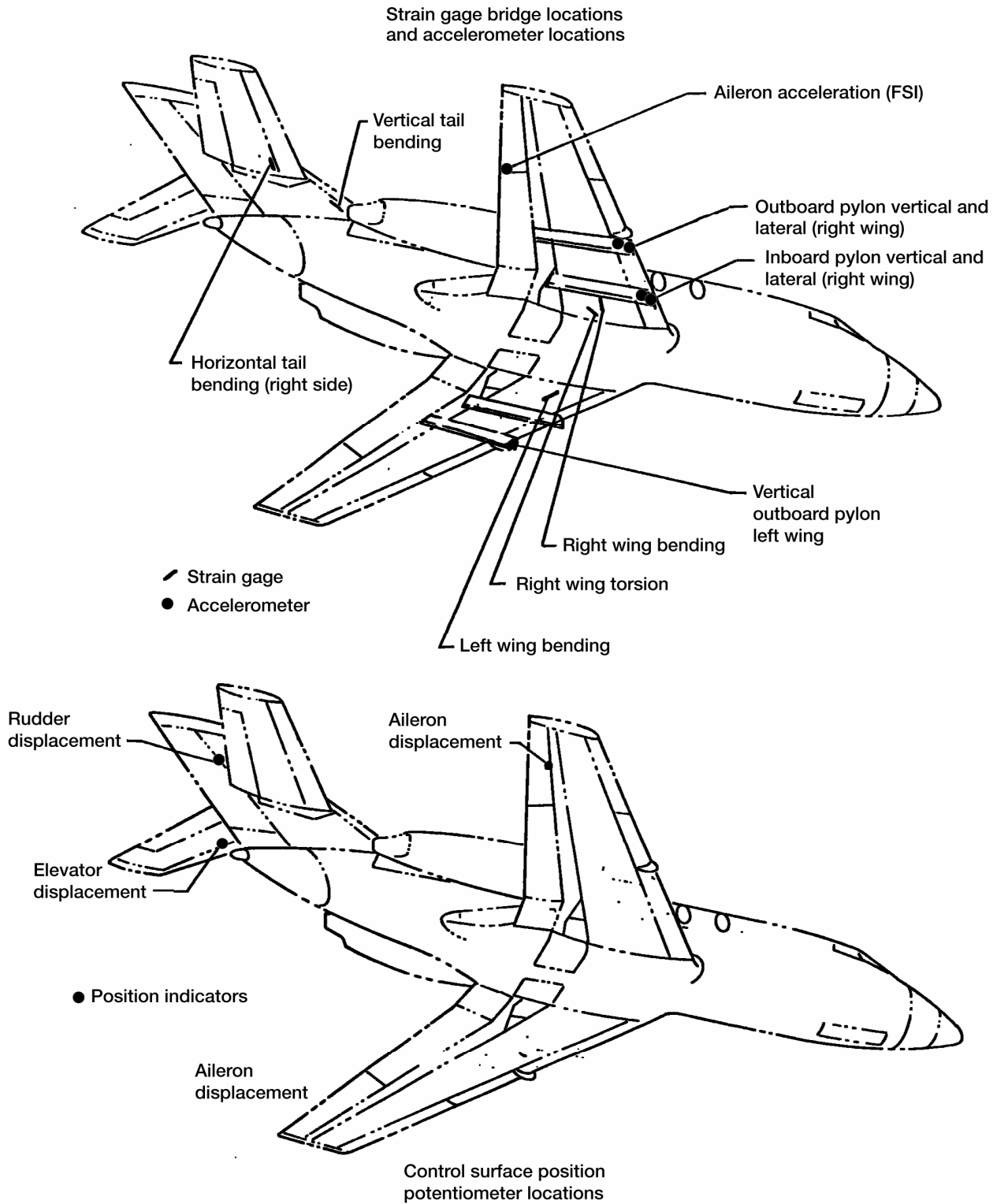
Figure 2.—Instrumentation layout for store-induced flutter flight tests.

With the stores, described above, on the outboard racks aileron/wing torsion flutter was predicted to occur. On the inboard racks the flutter disappeared.

Postulated flutter mechanism.—The presence of the light store on the outboard pylon led to the observed instability. Its light weight but significant moment of inertia produced a change to the outer wing torsion mode without significantly changing its frequency. This substantially increased the unbalanced mass/inertia coupling between the aileron rotation mode and outer wing torsion mode without increasing the frequency separation. The opposite side of the aircraft with the heavier store remained stable due to its increased frequency separation. A symmetric configuration of light stores on each side, had it existed, would have had a much lower flutter speed.

Corrective action taken.—The simple remedy to this problem was to restrict the airspeed for this configuration. The second choice was to move the stores to the inboard pylons where the problem did not exist.

Choice of arrangement made it possible for all 27 configurations in four subsequent programs to meet the full flight envelope of this aircraft without wing stores. The predicted most critical flutter cases were all flight flutter tested to the full design envelope, supported by FM telemetry and lattice filter analysis of the test results. These configurations, approximately ten aircraft, were FAA STC'd and are now operating under CAA regulations in the UK.

Case 2: Effect of Aerodynamic Balance on Vertical Fin/Rudder Flutter

Aircraft description.—A WWII light bomber with twin radial piston engines and an unswept shoulder-mounted wing of high aspect ratio (AR = 9.5) is the subject aircraft of Case 2 (see fig. 3). The aircraft was of metal monocoque construction except for the rudder and tabs which were fabric covered. The unswept fin and rudder and horizontal stabilizer and elevator were of conventional geometry.
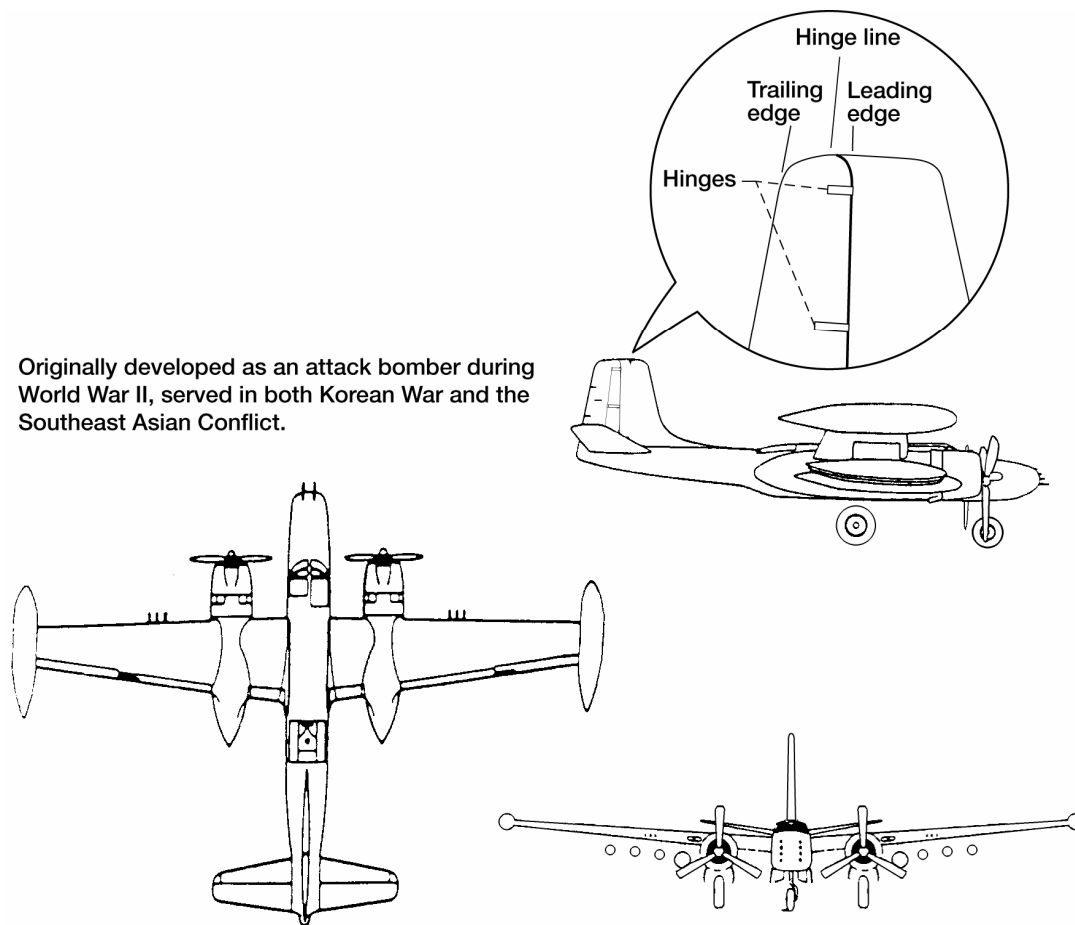
Figure 3.—Aircraft flight tested for effect of aerodynamic balance on vertical fin/rudder flutter.

$e = 0.4$				
k	T_β	T_z	P_z	P_β
0.16	$-1.94111 - 0.29845i$	$0.00851 - 0.31053i$	$-0.01542 - 1.55072i$	$-9.7045 - 1.0184i$
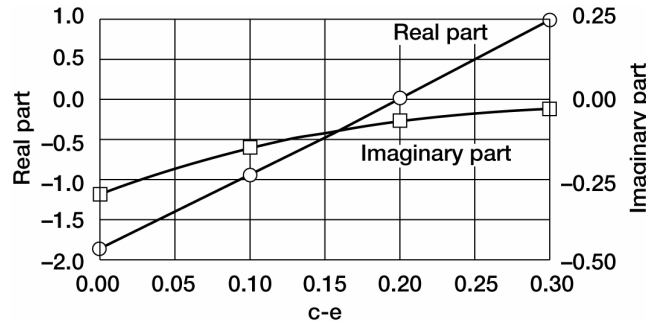
Figure 4.—Rudder unsteady aerodynamic hinge moment, T′, due to rudder deflection at k = 0.16.

The rudder, of approximately 35 percent chord, was marked by a very large distributed aerodynamic balance of approximately 8 percent of the fin and rudder chord.

The particular aircraft flutter tested was retrofitted for counterinsurgency service. Eight wing pylons were added for rocket and gun pods, bomblet dispensers and other external stores. The tip tanks were not installed during the reported test.

Maximum speed at 10,000 ft was 323 knots, true air speed (KTAS). The design dive speed was 370 knots, equivalent air speed (KEAS).w

Flutter experience.—The fin and rudder exhibited a limited amplitude flutter at 375 KEAS that did not induce structural failure and the aircraft landed normally. The flutter, at 5 KEAS faster than the design dive speed, oscillated at 12 Hz, and was of the fin bending/rudder rotation type.

The flight test had been conducted to examine the clean aircraft prior to the addition of external wing stores outboard of the propellers. The test was considered perfunctory, a test of the instrumentation, since no changes were known to have been made to the fuselage/empennage system. The test, however, did include tail instrumentation and was conducted so as to provide a slow build-up in airspeed.

Postulated flutter mechanism.—With little inertial coupling between the fin bending and rudder rotation modes, the mechanism of Case 3 is not likely to be the major cause of this unexpected flutter. With inertia coupling out of the picture aerodynamics became suspect.

The large distributed aerodynamic balance is somewhat unusual, but may be investigated by two-dimensional unsteady aerodynamics theory. Aerodynamic stiffness and damping of the rotation mode as the hinge-line progressively moves aft of the leading-edge of a control surface is provided by the equation in figure 4. The real part becomes the aerodynamic stiffness and the imaginary part is proportional to the damping.

At $k = 0.16$, and $e = 0.4$ the aerodynamic stiffness (real part) reduces to zero at $c = 0.58$ and the aerodynamic damping (imaginary part) reduces to approximately 1/3 the value it had with the hinge line at the rudder leading-edge. The distance from the leading-edge to the hinge line is $c - e = 0.18$ in terms of the half chord, b; that is, the hinge-line is 9 percent of the fin and rudder chord behind the control surface leading-edge.

The hinge-line on the bomber rudder is approximately at that chord station; thus it appears that the rotation mode frequency increase with airspeed will be relatively small. Furthermore, its modal damping is also quite small relative to that of a leading-edge hinged control surface.
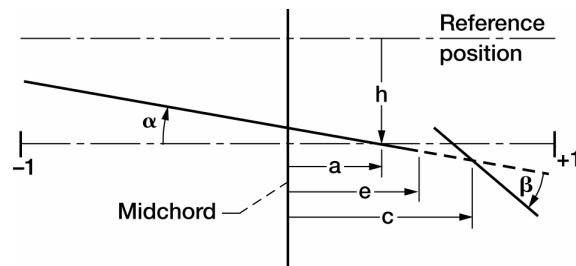
Hinge moment, T', due to control surface deflection, β, is given by:

$$\lambda = \frac{Kb}{SI} < T' = \pi\rho b^4 \omega^2 \left\{ \left[T_\beta - (c-e)(P_\beta + T_z) + (c-e^2)P_z \right] \beta \right\}$$

The reduced frequency $k = \dfrac{b\omega}{V} = 0.16$ at 12 Hz at the design dive speed gives the real and imaginary parts plotted below. Values for T_β, T_z, P_β, and P_z in the table below are adapted from Scanlan and Rosenbaum, reference 1.

It is postulated that a very slow growth of rotation frequency with forward speed led to a coalescence with the fin bending mode frequency just above the design dive speed. This coalescence, in conjunction with reduced rotation mode damping, led to the observed flutter.

Flutter corrective action.—The flutter took place at a speed almost outside of the operational overspeed envelope. A simple airspeed restriction would therefore be sufficient to meet airworthiness requirements. The nature of this flutter, however, is such that an increase in mechanical rotation-mode torsion spring stiffness would cause the flutter to occur at a lower airspeed, that could be well within the flight envelope.

This dangerous condition is a consequence of large aerodynamic balance and should be avoided.

Case 3: Vertical Fin/Rudder Flutter Despite Meeting Flutter Prevention Design Criteria

Among the rules that guide designers toward flutter-free configurations are those provided by the US CAA (Civil Aeronautics Administration) in the early 1950s. Some are presented in Airframe and Equipment Engineering Report 45, "Simplified Flutter Prevention Criteria for Personal Type Aircraft," by Rosenbaum and Vollmecke (ref. 2).

Its empennage design criteria for rudders recognize that flutter will most likely result from a coupling of rudder rotation with either the aft fuselage lateral bending or torsional natural modes.

It specifies a parallel axis criterion to prevent rudder coupling with aft fuselage lateral bending and a perpendicular axis criterion to prevent rudder coupling with aft fuselage torsion (see figs. 5 and 6).

The parallel axis criterion requires that the ratio, $\gamma = \dfrac{bS_\beta}{I}$, not exceed a value given in figure 5. Its parameters are as follows:

S_β, rudder static unbalance.
b, fin and rudder semi-chord.
I, rudder moment of inertia about the hinge axis.

The maximum allowable ratio is a function of the flutter speed factor (the inverse of a reduced frequency based on the aft fuselage natural bending frequency, f_h, the semi-chord and the design dive speed, V_D).

The perpendicular axis criterion is similar but requires the ratio, $\lambda = \dfrac{Kb}{IS}$, to be less than a value given in figure 6. Its parameters are as follows:

K, product of inertia of the rudder mass about the torsion and hinge axes.
b, fin and rudder semi-chord.
I, rudder moment of inertia about the hinge axis.
S, the distance from the torsion axis to the tip of the fin.
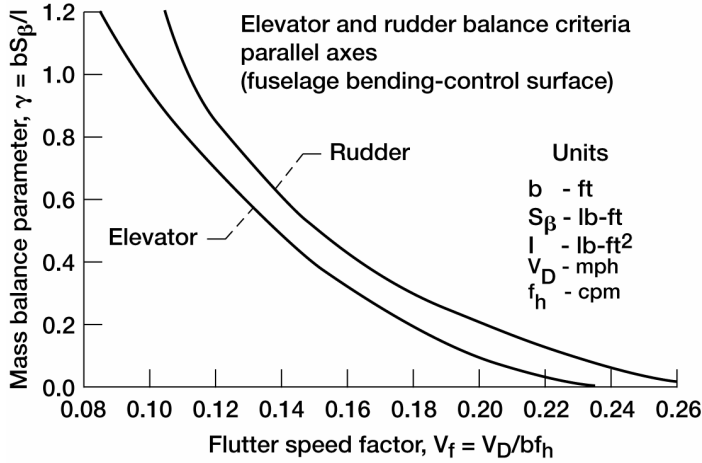
Figure 5.—Rudder mass-balance criterion for freedom from rudder rotation/fuselage side-bending flutter.
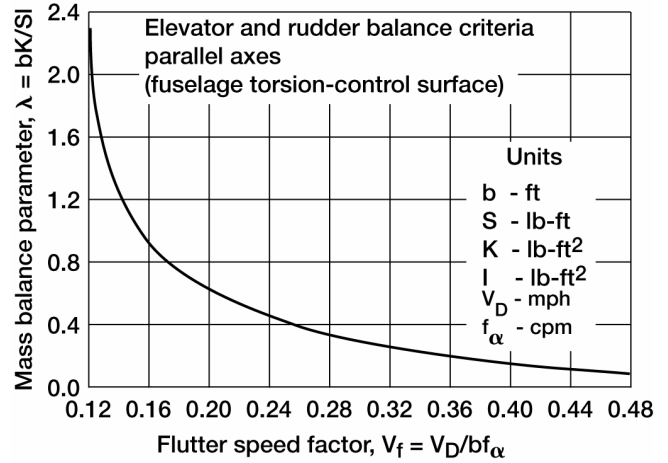
Figure 6.—Rudder mass-balance criterion for freedom from rudder rotation/fuselage torsion flutter.

The maximum allowable ratio is dictated by the flutter speed factor (or inverse of the reduced frequency at V_D based on the fuselage torsional frequency, f_α, and the fin and rudder semi-chord).

The present case indicates that even though the flutter design criteria, above, are met, flutter may still be possible.

Aircraft description.—A two-seat, twin-engined light aircraft, see figure 7, is the test aircraft in Case 3. The all metal unswept low-wing is of semi-monocoque construction. Its external skin surfaces are formed by chem-milling and stretching. The aircraft has a conventional tail with swept vertical surfaces and an conventional horizontal fixed stabilizer and elevator.

The swept fin and rudder are shown schematically in figure 8. Rudder mass balance was concentrated at the rudder tip to minimize the product of inertia of the rudder about the fuselage torsion and hinge axes with the smallest possible balance weight that would meet the perpendicular axis criterion.

$$K = m_r\, x_r\, y_r + m_{mb}\, x_{mb}\, y_{mb} \qquad (\text{lb ft}^2)$$

K must be such that $\lambda = \dfrac{Kb}{SI} <$ the value from figure 6 for $V_f = \dfrac{V_D}{bf_\alpha}$, where:

I = mass moment of inertia about the hinge line (lb ft^2)
b = $c_{midspan}/2$ (ft)
f_α = fuselage torsion mode *natural* frequency (cps)
V_D = design *dive* speed (mph)
S = effective fin span (ft)

Figure 7.—Test aircraft for vertical fin/rudder flutter despite adherence to flutter design criteria.
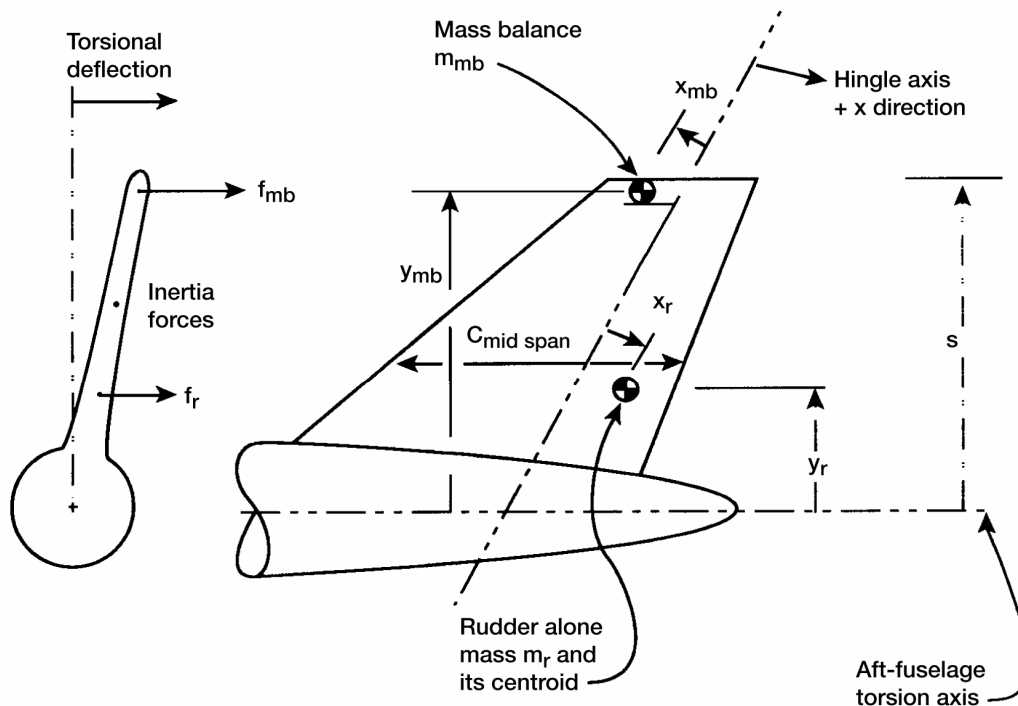
Figure 8.—Rudder rotation/fuselage torsion mode flutter prevention design criterion.

Flutter experience.—Vertical fin/rudder flutter was experienced in flight despite adherence to the flutter design criteria of CAA Rept 45.

Ground vibration testing disclosed a fin and rudder bending node line at approximately 60 percent fin span at a natural frequency near the inflight measured flutter frequency.

Postulated flutter mechanism.—In a rudder rotation/aft fuselage torsion flutter, locating a single rudder mass balance at the maximum distance from the fuselage torsion axis, i.e. at the rudder tip, yields the maximum compensating product of inertia per unit distance forward of the hinge line for that weight. (See fig. 8). The rudder was balanced in accordance with this logic.

In the flutter observed, however, the mode participating with the rudder rotation was not aft fuselage torsion but vertical fin and rudder lateral bending. The mode possessed a node line at 60 percent of the fin span as shown in figure 9. The tip located mass balance inertia force, in this case, is in a direction opposite to that of the inertia force
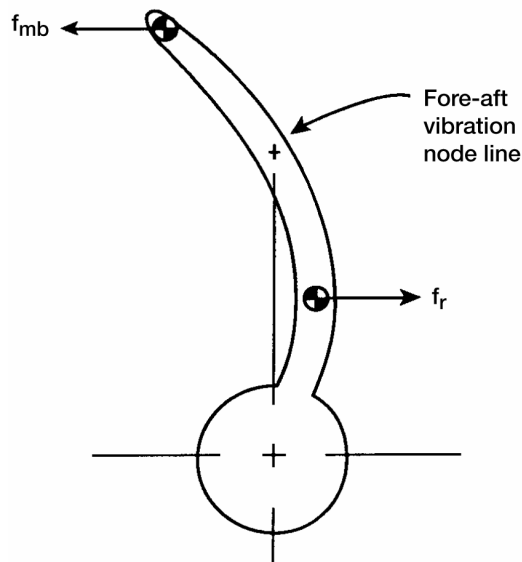
Figure 9.—Vertical fin and rudder bending mode.
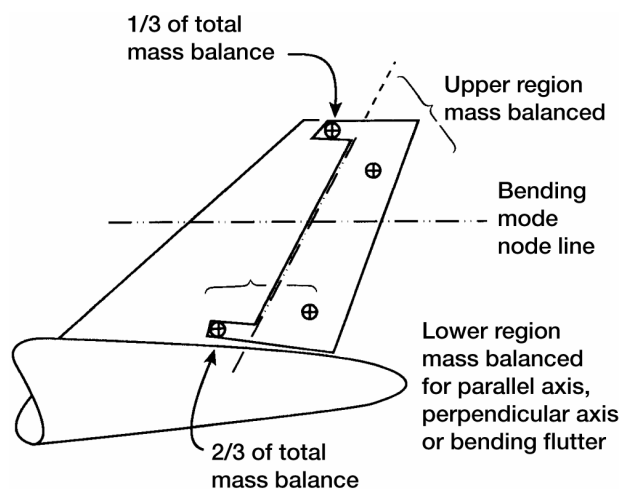
Figure 10.—Rudder rotation/vertical fin bending flutter cured by mass balance distributing.

on the rudder aft of the hinge line. Thus, instead of canceling the inertial hinge moment as it would in the case of fuselage torsion, it adds to it, and thereby strongly couples the bending mode to the rudder rotation mode. In other words, fin bending motion induces rudder rotation that in turn induces lateral airloads on the fin that amplify the fin bending motion. Thus, the precondition for flutter is in place.

Flutter corrective action.—With the flutter mode identified it became possible to neutralize it. Reducing the tip weight until it just balanced the fraction of rudder weight above the node line and adding a second weight near the bottom of the rudder to balance the rudder weight below the node line, as shown in figure 10, decoupled rudder rotation from fin and rudder bending.

Decoupling was due to the fact that bending mode induced accelerations produced balanced, (or zero), hinge moments separately both above and below the node line.

In the subject airplane, the balance weights were distributed 1/3 to the rudder tip and 2/3 to the rudder base. This redistribution of mass balance weights was slightly heavier than the original that covered only fuselage torsion coupling.

This exercise, in addition, illustrates the "flutter design rule" that control surface spanwise inertial hinge moment should be balanced locally at each span station by distributed balance weights when possible.

Case 4: Flutter of a Stabilator

Aircraft description.—The aircraft in Case 4 is a high-performance, single engine, two-seat (side-by-side), low-wing homebuilt monoplane of all-metal semi-monocoque construction and a conventional fin and rudder (see fig. 11). The design employed a *stabilator* (all moving tailplane hinged to the aft-fuselage with no elevator). The stabilator contained a *servotab* (trailing-edge tab geared to stabilator rotation).

To prevent flight-normal acceleration from producing inertia hinge moments, the first moment of the stabilator mass about its hinge-line was brought to zero by the use of a single centerline counterweight. (See fig. 12).

The maximum sea-level speed was 200 miles per hour. Flight tests were conducted to 230 miles per hour.

Flutter experience.—Following an in-flight failure, without witnesses, a speed placard of 180 mph was applied to all aircraft of this type. A second accident at very high speed produced similar damage and this time the flutter and departure of the stabilator were witnessed.

A flutter investigation, initiated by the designer, began with flight tests to calibrate flutter instrumentation. These were terminated at 190 mph despite the fact that the configuration had previously been flown to 230 mph. Dynamic results recorded at 160, 170, 180 and 190 mph showed a mode, consisting of symmetric pitch, stabilator rotation and first bending, to be losing damping with airspeed and to be approaching instability.
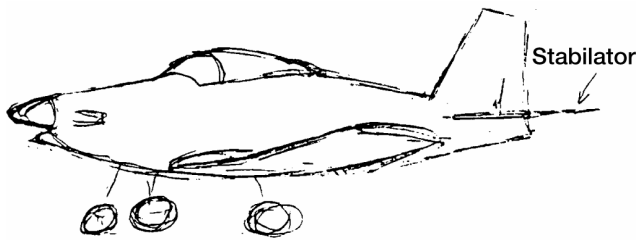
Figure 11.—Amateur built sport aircraft suffered stabilator flutter.
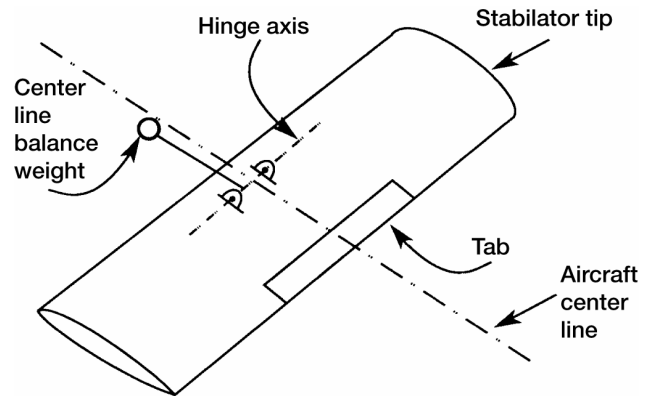
Figure 12.—Simplified schematic of stabilator, central balance weight and tab.
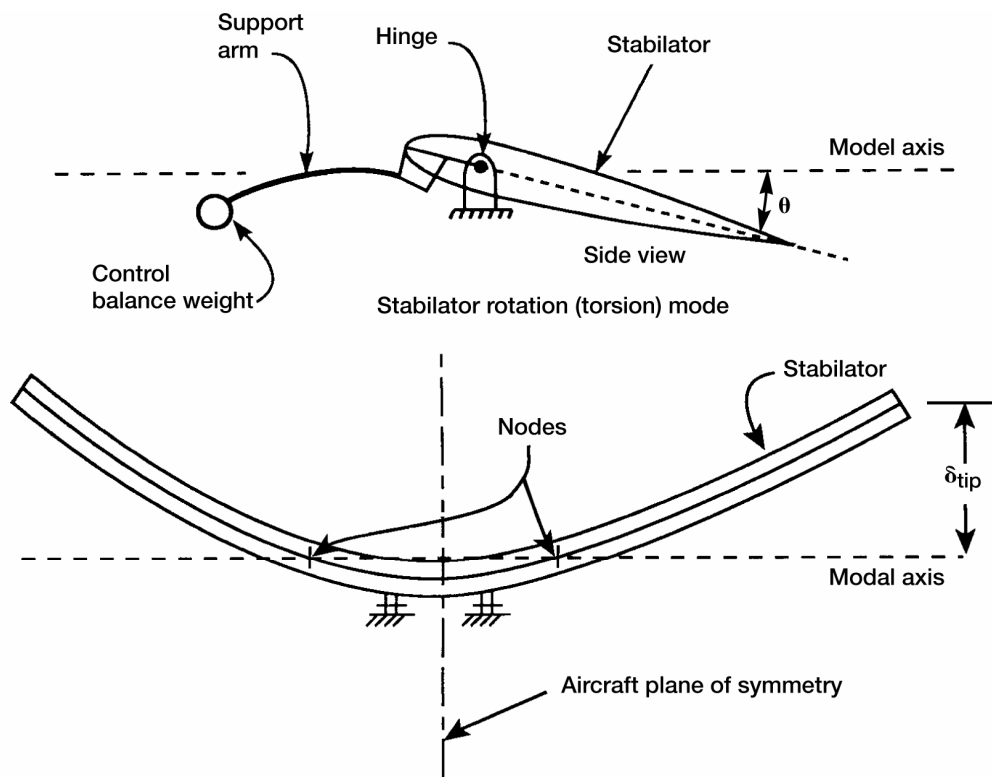
Figure 13.—Principal stabilator modes participating in the observed flutter.

An apparent cause of this was the center-line installed balance weight arm that supported the only balance weight on the stabilator. It was an L-shaped structure attached to the stabilator with its short side pointed down and long side, with the lead balance weight attached, pointed forward. (See figs. 12 and 13).

In the approaching flutter mode, at 31 Hz, the central mass-balance arm took on a cantilever bending oscillation reacted by an almost rigid rotation of the stabilator. (See fig. 13).

The flutter specialist suggested, based on ground vibration tests, that the balance arm be stiffened by a gusset across the L. Stiffening the support arm changed the rotation mode ground vibration frequency from 16 to 20 Hz.

Following the modification, in planning the flight tests with the stiffened balance arm, it was thought possible that the change might have made the flutter situation more critical, since it had been based on limited data and no analysis. The test series was therefore conducted in an orderly manner with a gradual build-up in flight speed.

During the flight tests, with the stiffened balance arm, the symmetric rotation mode coupled with the symmetric stabilator first bending mode and became unstable at 175 mph, or at a 15 mph lower speed than with the unstiffened balance arm. Fortunately, though the damage was severe, the aircraft remained flyable and made a safe landing.

The flutter specialist then advised the designer that the single central mass-balance configuration should be replaced by a more conservative, distributed balance, arrangement.

Following the logic outlined in the next section, the final modification moved one-third of the centerline mass balance to the stabilator tips, i.e. one-sixth to each tip. This cured the flutter problem and no flutter was experienced in flight tests to 231 mph. The aircraft was cleared to a never-exceed-speed of 210 mph.

Postulated flutter mechanism.—The rotation mode, described above, changed frequency with aircraft forward speed due to the aerodynamic hinge moment acting as a spring-to-ground. That is, the hinge moment due to surface unit rotation increased as the square of the forward speed. The stabilator bending mode, on the other hand, did not twist significantly with deflection and therefore did not encounter a spring-to-ground. Its frequency did not change significantly with aircraft forward speed.

Aside: Because surface vibration velocities normal to the wind are small in the rotation mode, its modal damping would be small if unaffected by other modes. Bending-mode surface normal velocities, however, are much larger and produce modal damping that grows linearly with aircraft forward speed increase, if not influenced by other modes.

It is clear that in streaming air the lower rotation-mode frequency will approach that of the bending mode at some forward speed. In addition, the oscillating rotation mode should be able to produce an aerodynamic force distribution that excites the bending mode. This is illustrated in figure 14.

Bending mode shape $\phi(y)$ for unit tip displacement, $\delta_{tip} = 1.0$ ft

Spanwise airload distribution, $\omega(y)$ due to unit torsion mode displacement, $\theta = 1$ rad

Product of bending mode shape and torsion mode induced spanwise load distribution
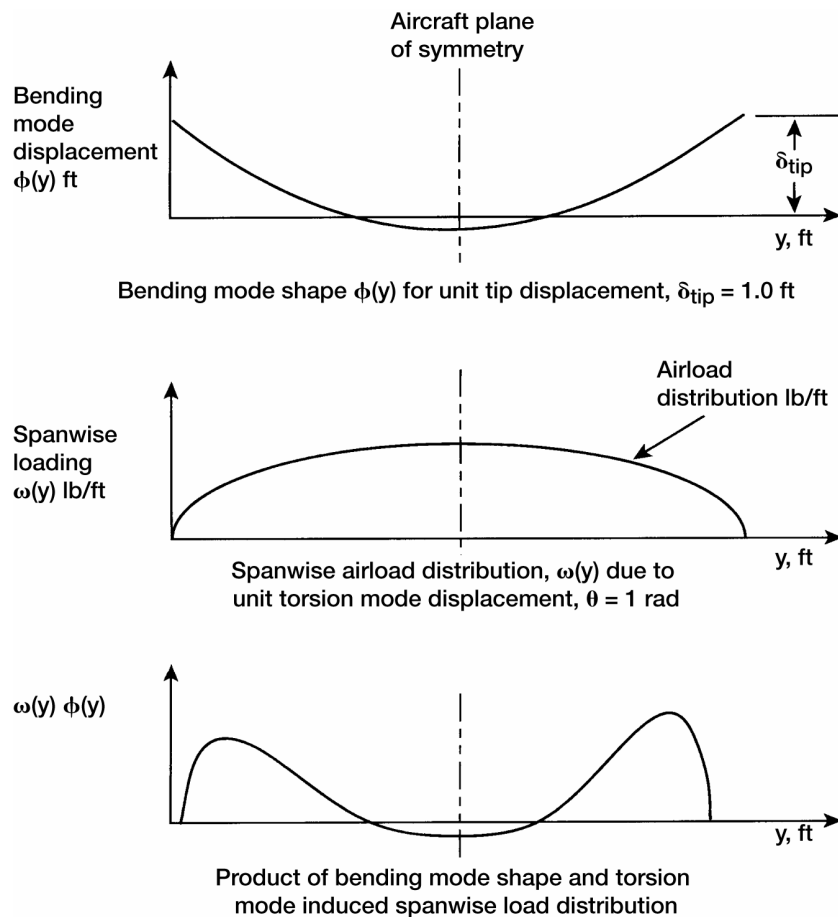
Figure 14.—Bending mode generalized force applied by rotation, (torsion), mode aerodynamics.

For one mode to influence another, its motion-produced force distribution must apply a nonzero *generalized force* to the other. The generalized force is defined in figure 14. It is clear from the figure that oscillations of the rotation mode will excite the bending mode at high forward speed.

If the rotation mode supplies an input generalized force to the bending mode at a frequency well below the bending-mode resonance, the responding bending-mode displacement will be essentially in phase with the input force and of amplitude dictated by bending-mode flexibility. (See fig. 15).

If the rotation mode supplies the input force at a frequency well above the bending-mode resonance, the bending mode-displacement response will be 180 degrees out of phase with the input force or will be in the opposite direction. Its amplitude is then dictated by the *generalized mass* of the bending mode resisting the input force.

The generalized mass of a mode is defined as follows:

$$G.M. = \int_{-y_{tip}}^{y_{tip}} m(y)\varphi^2(y)\,dy \quad m = \text{distributed mass, slugs/ft}$$

If, on the other hand, the rotation-mode-induced bending-mode generalized force has a frequency equal to the bending-mode resonant frequency, the bending-mode displacement will respond with a 90 degree lag to the input force, as shown in figure 15. Its amplitude will be dictated by the *viscous damping* reactive force in the bending mode. (The bending-mode viscous force is proportional to and opposes mode velocity.)
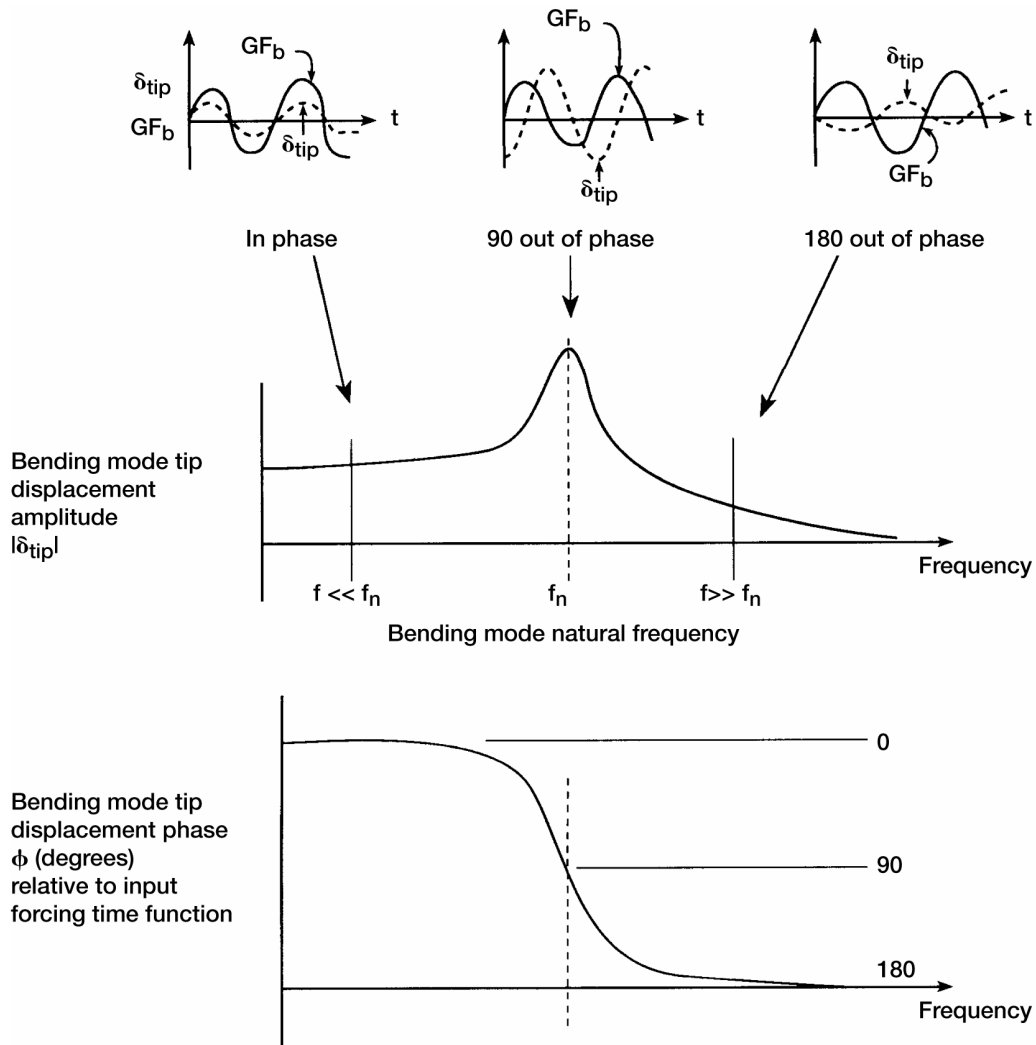
Figure 15.—Bending mode response to rotation, (torsion), mode generated forcing function, GF$_b$.

In other words, the rotation-induced generalized force in bending will be in phase with, not bending displacement, but bending velocity. By this means energy is input to the bending mode. The bending-mode amplitude will increase until its viscous resisting (or damping) force equals the bending generalized force input by the torsion mode.

An input force to a mode near its natural frequency from a driving mode is not sufficient to cause flutter (a dynamic instability). Instability requires the responding degree-of-freedom, in turn, to *feed back* a generalized force to the driving mode. In this way the increasing amplitude of the responding mode causes a continual increase in the driving-mode motion. The mutual reinforcement results in increases, without limit, of displacements in both modes, or a *dynamic divergence* or flutter.

In the present case of stabilator flutter the primary feedback was provided by the unbalanced first moment of section inertia about the hinge line produced in the outboard region of the tail surface by the bending mode. Due to the small normal acceleration of the centerline mass balance at its location in the bending mode, in this case, it could not react to this large inertial hinge-moment.

The feedback hinge-moment is in-phase with the rotation-mode angular velocity or in the direction to add energy. Thus the ingredients are in place to cause flutter. It is only necessary that the destabilizing energy being added to the system be larger than the bending-mode damping energy being removed.

Flutter corrective action assessment.—The movement of one-third of the mass balance to the stabilator tip effectively balanced the inertial hinge-moment generated in the bending mode. This essentially zeroed the feedback generalized force thereby neutralizing the flutter instability. This is another application of the *distributed mass balance* design rule.

Case 5: Wing-Aileron Flutter Due to Excessive Control Rotational Inertia

Aircraft description.—The subject aircraft of Case 5 is a low-wing, long-range naval patrol aircraft with four tractor propellers driven by turboprop engines mounted on an unswept wing of high aspect ratio. (See fig. 16). The all metal aircraft of semi-monocoque construction had a conventional unswept tail.

Control surfaces were hydraulically actuated with a reversion to manual control in the event of a failure. This meant that the control surfaces could be restrained by a rotation spring or treated as rotationally unrestrained in wind tunnel flutter tests.

The never exceed speed, V_{ne}, was 405 KEAS.

Note: This was a proposed new aircraft of increased capability based on an existing aircraft. Comparisons of characteristics with those of the original aircraft were therefore possible.

Flutter experience.—A 1/12 scale flutter model of the aircraft experienced violent wing tip torsion-mode flutter with aileron rotation participation. This took place at an equivalent full scale frequency of 17.1 Hz at a full scale flight speed of 417 KEAS.

A flutter analysis by the p-k Method, employing Doublet Lattice unsteady aerodynamics and making use of the FAMAS-MADOL computer system, confirmed the observed behavior. Free-free natural vibration modes of the aircraft that participated in the flutter are shown in figures 16 and 17.

The variations with flight speed of the aileron rotation and wing tip torsion-mode frequencies are shown in figure 18. The corresponding dampings of the coupled modes are shown in figure 19.

Flutter occurred despite the use of aileron mass balance to reduce the static unbalance to zero. The configuration included full wing fuel tanks and no external stores.

A number of distributions of mass balance weights along the aileron span were examined analytically, and it was concluded that the flutter problem could not be corrected solely by the use of mass balance. The moment of inertia of the basic aileron about the hinge line was so large that it became impractical even to overbalance the surface to uncouple the rotation mode. It became necessary to recommend a completely new lightweight aileron design to reduce rotational inertia.
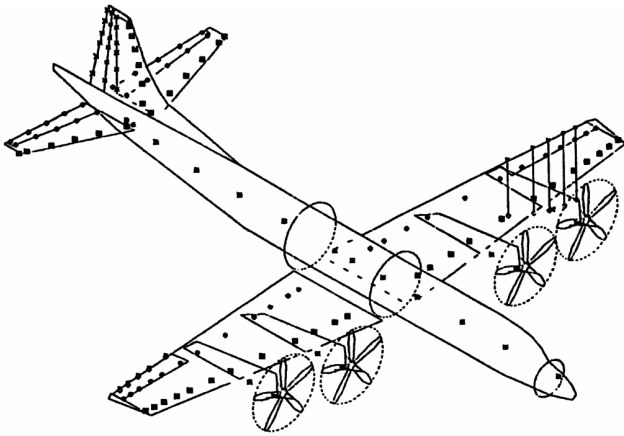
Figure 16.—Test aircraft model for wing/aileron flutter due to excessive control rotational inertia.
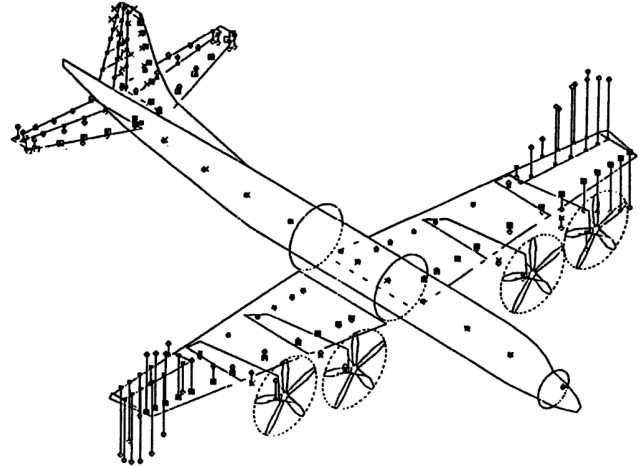
Figure 17.—Wing torsion mode that interacts with aileron rotation to produce flutter.
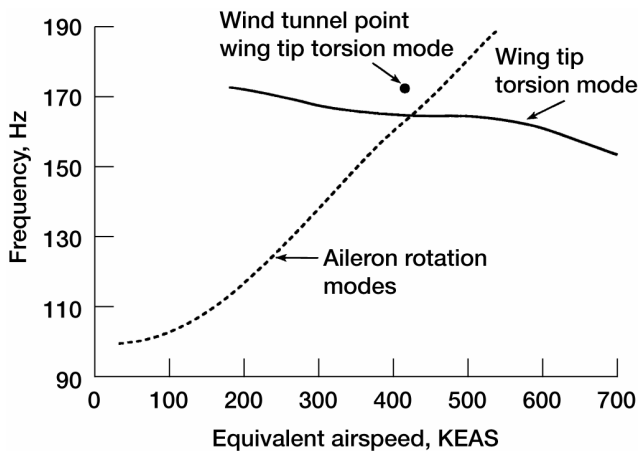
Figure 18.—Frequency versus airspeed prediction for the wind tunnel model.
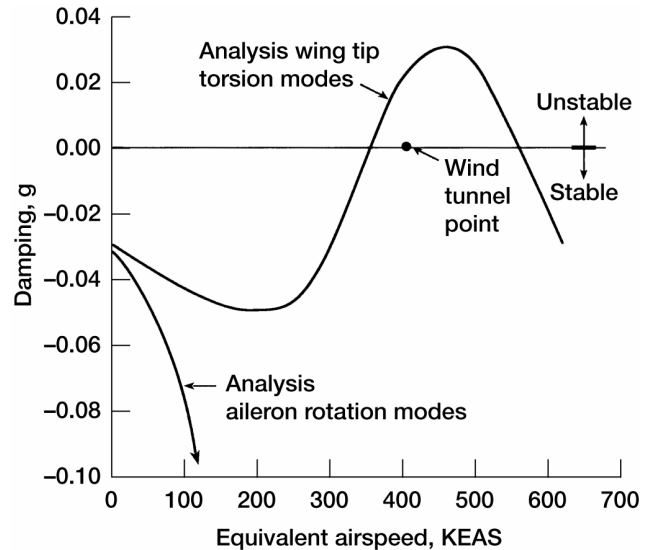
Figure 19.—Damping versus airspeed prediction and wind tunnel result.

Postulated flutter mechanism.—Inertial coupling of the plunge, pitch and control surface rotation degrees of freedom can be shown for rigid body motions as indicated in figure 20.

Control mass balancing (static balance) is accomplished by reducing the control surface mass offset arm to zero, $\bar{x}_\beta = 0$, so that $S_\beta = 0$. Examination of figure 20 then indicates that control rotation acceleration no longer produces vertical (or lift, L) inertia force and plunge acceleration, $\ddot{h}$, contributes no hinge moment (HM) to the control surface. Thus static balance uncouples the plunge and control rotation modes.

Control surface static balance, however, still permits control rotation acceleration to contribute pitching moment (M) to the section by virtue of the I_β term in the 2,3 matrix position and section pitch acceleration to produce hinge moment through the 3,2 term. Thus the pitch and control rotation degrees of freedom remain coupled even with statically balanced control surfaces. Control rotation/section pitch flutter thereby remains a possibility.

Elastic axis
Midchord
$b\bar{x}_w$
c.g. of wing-aileron
b
ab cb Aileron hinge
$h(x)$
$\alpha(x)$
$\beta(x)$
$b\bar{x}_\beta$
c.g. of aileron
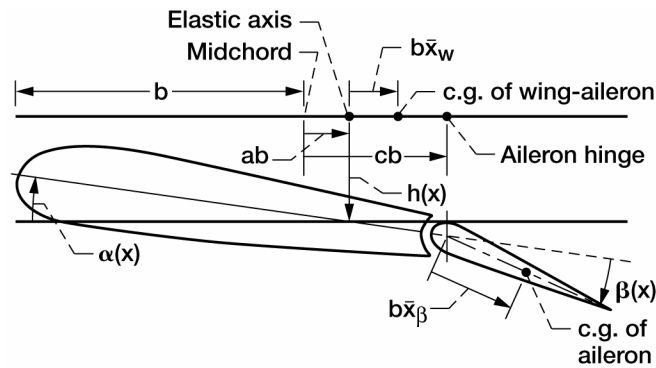
$$\left\{ \begin{array}{c} L \\ M \\ HM \end{array} \right\}_{\text{Inertia}} \quad \begin{bmatrix} M & S_w & S_\beta \\ S_w & I_w & c_1 S_\beta + I_\beta \\ S_\beta & c_1 S_\beta + I_\beta & I_\beta \end{bmatrix} \left\{ \begin{array}{c} \ddot{h} \\ \ddot{\alpha} \\ \ddot{\beta} \end{array} \right\}$$

where

b half chord

c_1 $(c - a)b$

S_β $M_\beta b \bar{x}_\beta$

S_w $Mb\bar{x}_w$

M_β mass of aileron per unit length

$b\bar{x}_\beta$ c.g. location of aileron measured from the hinge line, positive aft

M mass of wing-aileron per unit length

$b\bar{x}_w$ c.g. location of wing-aileron measured from the elastic axis, positive aft

I_w moment of inertia of wing-aileron per unit length about elastic axis

I_β moment of inertia of aileron per unit length about aileron hinge

Figure 20.—Inertia coupling of the plunge, h, pitch, α, and control rotation, β, degrees of freedom.

Overbalancing the control surface, i.e., by employing negative $\bar{x}_\beta$, may allow

$$c_1 S_\beta + I_\beta = 0$$

and this uncouples the pitch and control surface rotation modes. Such a remedy may, however, introduce coupling of the control surface and plunge modes that leads to a different form of instability.

If this occurs it may be necessary to redesign the control surface to reduce its moment of inertia about the hinge line.

Flutter corrective action assessment.—A region of unacceptable flutter stability with the original aileron design is shown in figure 21. Analysis of an aileron of reduced moment of inertia and 110 percent overbalance static first moment is shown in figure 22. The second design was judged to be marginally satisfactory.

Overbalance, in this case, is defined as an additive nose-heavy balance equal to 110 percent of the original tail-heavy balance without counterweights.
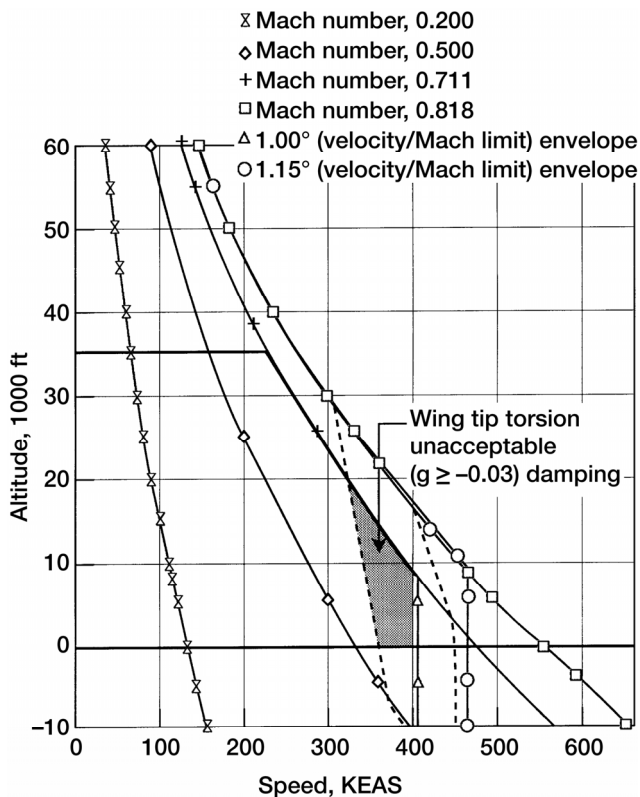
Figure 21.—Unacceptable flutter enclave for the nominal aileron.
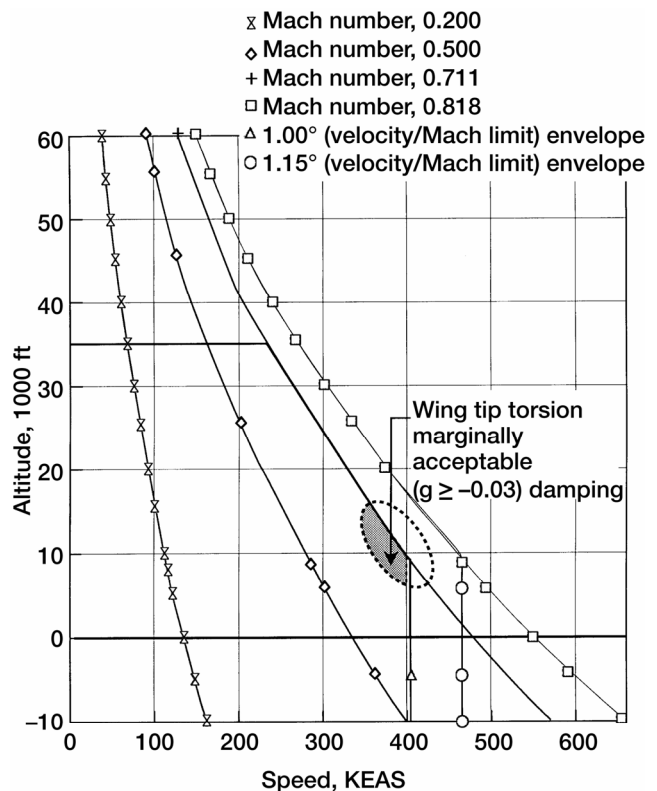
Figure 22.—Marginally acceptable flutter enclave for the new aileron.

Case 6: Elevon-Wing Torsion Flutter of a Delta Wing Model

This case, communicated to the authors by word of mouth, is included because of its similarity to Case 2. Both indicate the destabilizing effects of control surface aerodynamic balance.

Aircraft description.—A delta-wing wind tunnel model with its structure dynamically scaled to represent that of a full scale aircraft is the subject of Case 6. It had a single control surface per side that performed the functions of elevator and aileron. Such a surface is called an elevon.

The model was tested for flutter stability with the control surface, of constant size, hinged along the leading edge and along two chordwise positions aft of the leading edge.

Flutter Experience.—Three tests were performed of elevons of the same size, i.e., the same percent chord. The hinge axis was progressively moved aft from the leading edge in succeeding tests. This was expected to have the effect of increasing the aerodynamic balance, by the distributed balance method, and to progressively reduce hinge moment per unit control surface deflection.

In addition to the effect expected, however, a progressive decrease in flutter speed was noticed. This occurred even though a zero static mass balance condition was maintained in the three tests.

Postulated flutter mechanism.—It is suspected that the flutter mechanism is a coupling of an essentially wing-torsion mode with elevon rotation, and that an elevon rotation mechanical spring has been employed that raises the rotation-mode frequency to nearly that of the wing quasi-torsion mode.

The fact that the elevon is statically mass balanced does not uncouple the two modes, as is indicated in Case 5.

The I_β coupling still exists.

With the progressive aft movement of the hinge axis, the aerodynamic spring-to-ground reduces, eventually to zero, and thus is ineffective in splitting the frequencies of the two modes. In addition the damping of the rotation mode also reduces with aft movement of the hinge axis to about 1/3 its value with the hinge at the control surface leading edge.

It is this reduction in damping that is suspected as the cause of the gradually reducing flutter speed with hinge-axis aft movement.

References

1. Scanlan, Robert H.; and Rosenbaum, Robert: Introduction to the Study of Aircraft Vibration and Flutter. Dover Publications, New York, NY, 1968.
2. Rosenbaum, Robert: Simplified Flutter Prevention Criteria for Personal Type Aircraft. U.S. Civil Aeronautics Manual 3, Equipment Engineering Report No. 45, Supplement No. 11, 1952.

Flutter Prevention Handbook: A Preliminary Collection[*]

D.D. Liu, D. Sarhaddi, and F.M. Piolenc
ZONA Technology, Inc.
9489 E. Ironwood Square Drive, Suite 100
Scottsdale, Arizona 85258–4578

Part C: Flutter Occurrence on Eighteen High Performance Military Aircraft

William Roberts
Delta Dynamics, Inc.

Foreword

Abstract

This paper records the concurrent development of flutter analysis, numerical modeling techniques, ground vibration testing and in-flight flutter testing at three companies. Airplanes of 18 distinct types serve as illustrative examples, covering subsonic, supersonic and hypersonic regimes. Of these, half showed flaws in flutter design and half did not. Initially, analysis was not supplemented with scale model testing. As soon as scaled model technology was brought into regular use, the risk attendant on full dependence on analysis-namely that flutter might appear after production had begun-was steadily reduced. Several examples are included. Other major developments were the finite element methods for both structural and aerodynamic analysis. Piston theory, once available, found immediate application in the X15 with its Mach 7 speed. Another significant development was the use of item by

---

[*]This document was taken from the original report: Liu, D.D.; Sarhaddi, D.; and Piolenc, F.M.: Flutter Prevention Handbook: A Preliminary Collection, WL–TR–96–3111, 1996, first published by the Flight Dynamics Directorate, Wright Laboratory, Air Force Materiel Command, Wright-Patterson Air Force Base.

item structural scaling on a flutter model for the delta wing, Mach 3, F108, and its use on the Space Shuttle for development of a 1/4 scale model of the entire "stack" for early ground vibration tests. Three variables-stiffness, chordwise c.g. and control surface balance-were found to be the major determinants of success in preventing flutter. Satisfactory criteria based on this approach are given. The criteria show the great difficulty of building large airplanes with thin wings for use at high speed and show that accident rates are increased when the stiffness requirements are compromised.

The author's experience at the FAA sheds light on the distinct flutter prevention criteria applying to both military and civil aircraft. Civil transports are fail safe structures and in addition, damage identified by a Damage Tolerance Assessment is included in the flutter analysis. Flutter has nearly disappeared as a primary cause for an accident as a result of the complete program of flutter prevention. Because of its import on safety the stiffness criteria have also been useful in assessing new designs.

Introduction

This research presents actual case histories specially chosen for their fundamental content. There are many ways to learn flutter: a mentor is one way, extensive analytic experience is another. Some companies focus on approving the strength design, while others set forth the flutter requirements directly during preliminary design. Many of the cases from the history of flutter occur at a time when the approach was different from that now used. Thus the lesson drawn from each case is drawn from a time period where the context is also needed. While ground vibration tests (GVT) and flight flutter tests (FFT) have always been part of the design process, the scaled wind tunnel flutter models have not. Prior to use of the scaled models in wind tunnel tests, exceptional reliance was placed on the analyses, since a product was built and essentially readied for flight prior to conducting the essential flutter tests. There was obvious risk in this approach, and many of the cases presented will demonstrate this risk. The scaled model technology was clearly a response to this risk and came along at a definite point in the time history where the need was great. This permitted experimental determination of the adequacy of the design at a point in time when the essential information could still be acted on.

In this same vein, the analytical techniques were changing to introduce the structural and aerodynamic influence coefficients. Conclusions drawn regarding the technology prior to these developments would not be the same as those drawn following that development. For example, throughout the consideration of each case it is desirable to ask where might the fault lie that allowed flutter to occur. Was it the structural analysis, the aerodynamics, the flutter theory or in the testing technology. A surprising conclusion from the research was that the fault generally lay in but one of these areas—the portion of the flutter analysis devoted to the math model of structure. Unsteady aerodynamics was advanced via the influence coefficients appropriate for different flight regimes—just in time for the Mach 3 B70 and the Mach 3 F108. Piston theory was developed just in time for the X15 (see appendix B) with its Mach 7 performance. Another differentiation is to ask at what point was the design found to be not adequate and it was known that a change was required. This might occur following GVT or FFT or service experience. Each case answers these questions.

To the credit of the flutter designer, the experience of flutter has greatly diminished. Where 7 cases occurred to the F-100 in which one-half of the horizontal stabilizer was lost before control of the problem was obtained, experience in the civil transports has seen no such repetitive occurrences. Near total disappearance of flutter in transport category has occurred if one uses primary cause as a criterion. Flutter does occur as a result of instrumentation failure or as a result of structural failure but this means flutter is a secondary event, not the primary. Even these occurrences are very rare. In the general aviation fleet the picture is not as encouraging. Less rigorous regulation, design practice, maintenance and inspection result in repetitive failures in some fleets. The design challenge in both transports and general aviation is increased by increased speeds and altitudes. Altitude adds to the risk because, once upset occurs, the extent of overspeed can increase with altitude prior to regaining control.

Many of the designs covered in this history were the exceptional design challenges that pioneered new flight regimes. Covered are the first supersonic fighters, the first supersonic bomber, the Space Shuttle, and a hypersonic missile interceptor that reached Mach 10 in the lower atmosphere. One of the design challenges is the inclusion of trailing edge control surfaces that are not ballasted to prevent flutter but do so by the different approach of

increasing control surface stiffness and damping. Three of these early vehicles that prevented flutter without the use of ballast weights were the Xl5, B70 and the Space Shuttle.

At the FAA the essential function is to eliminate the fatal accidents. This is a practical goal since in 5 of the recent 10 years the number of fatalities was very nearly zero. To determine the root cause of the fatal accidents, many dynamic phenomena were identified and the question asked, what is their relationship to vehicle design. The most important of these relationships are described. In many cases it raises the question, is not flutter prevention a surrogate to prevention of many of these other phenomena. A possible answer to the question is provided in a plot (see appendix A) showing an attempted correlation of accident rates with speed and two other aeroelastic variables: stiffness and span. The correlations were successful and draw attention to the relationship of the accidents to aeroelasticity. Since the vehicles shown were certified as flutter free the correlation is presumably drawing attention to the difference between stiffness, airplane to airplane, in the design for flutter prevention, or to other phenomena which are stiffness related. This preliminary result cannot be used to conclude that a correlation has been established. Although 8 million departures and 92 accidents were recorded for 5 transports in the time frame 1987 to 1991, this is a too small data sample to provide a convincing correlation. But since the data were sufficiently ordered, it would be worthwhile to add more cases and to search for other causes that could verify or refute the relationship.

The study covers three topics, the presentation of the flutter story for each of 18 designs, flutter related events at the FAA, and flutter criteria. The study as a whole directs one's attention to vehicle stiffness—

1. as the major determinant required for flutter prevention,
2. for its involvement in other wide ranging dynamic phenomena and
3. that the flutter program probably is acting as a surrogate for prevention of other undesirable dynamic phenomena not directly addressed otherwise.

Case 1: North American Aviation F-100

This Air Superiority Fighter was the first fighter with the capability to achieve supersonic speeds in level flight. When the design was first flown, it did not have this capability. It was entered against designs from three other companies in the century series fighter competition. Each company had promised supersonic capability in level flight but this promise proved unattainable in their initial designs. North American immediately proceeded on its own to redesign to meet the 600 knot, 1.3 Mach number requirement by drag reductions. The other three companies chose to wait to renegotiate their contracts. The redesign consisted of four improvements: cockpit canopy, lip of the inlet engine duct, and reduced thicknesses to the horizontal and vertical stabilizers. The airfoil thicknesses were reduced from 7 to 3.5 percent. The changes to the horizontal and vertical stabilizers were especially challenging since the original design met its flutter requirements along the 600 knot leg only by restrictions limiting the use of

the afterburner. On takeoff and climb to 40,000 feet with afterburner followed by a dive to sea level with after-burner, the horizontal stabilizer would flutter. Either the right or the left half would separate from the airplane. This occurred on seven occasions. It was a result of afterburner heating that reached the horizontal stabilizer actuator, which provides actuation in pitch to control the all-moving surface. The heated hydraulic fluid was less stiff than fluid that was not heated. Fortunately the airplane could land safely with only 1/2 stabilizer.

Because of the obvious criticality of the configuration as first designed, the thinner horizontal stabilizer for supersonic speeds was subjected to further testing in a configuration expected to be flutter free. Testing was needed to the limit speed and also to the limit Mach number. Rather than model testing it was decided a more reliable answer could be obtained from full scale sled testing. Both critical dynamic pressure and critical Mach number could be reached by this test approach. The sled test was conducted at Edwards AFB on a full span surface with actuator and fairing and necessary support structure. The first test failed as a result of flutter, the model separated from the sled and, flying freely, reached an altitude of 500 feet above the desert before slowing and descending. But the occurrence of flutter was judged not to be related to the airplane design but to the manner of mounting the test structure on the sled. Following analysis and redesign of this unrelated case, subsequent sled tests substantiated freedom from flutter. A further requirement was to substantiate the test result with a flutter analysis. The initial flutter cases described above occurred in large part because the analysis for natural frequencies and mode shapes failed to match the ground vibration test results. A pitch mode appeared that had not been predicted. If a match could be obtained to the original ground test, then, taking that same analytical approach for the revised configuration, it could be expected that subsequently the ground test for the new configuration and the analysis would agree.

The configuration is presented in figure 1 showing an all-moving stabilizer with no elevator. An actuator at the centerline controls the pitch motion. The primary structure joining the two halves of the stabilizer is the large torque tube shown. A very large afterburner interferes with joining the two halves so that the torque tube is obliged to curve under the afterburner. The horizontal tail design is also unique in having its pitch axis elevated 7 inches above the midplane of the surface. The entire horizontal tail assembly is suspended from the fuselage pivots by the hanger shown in figures 2 and 3. The original analysis was a simplified bending torsion beam analysis with fixity assumed at the side of body. All the many deficiencies of this model were not suspected prior to the flutter cases. When the pitch mode showed up at a frequency significantly lower than the first torsion mode, this model was obviously invalid. The analysis had not attempted to describe the missing mode. The angle of attack amplitudes in both the pitch and torsion modes were large and accounted for both being unstable, figure 4. The most significant deficiency concerned the local flexibilities identified in figures 2 and 3—such local flexibilities were not part of the state of the
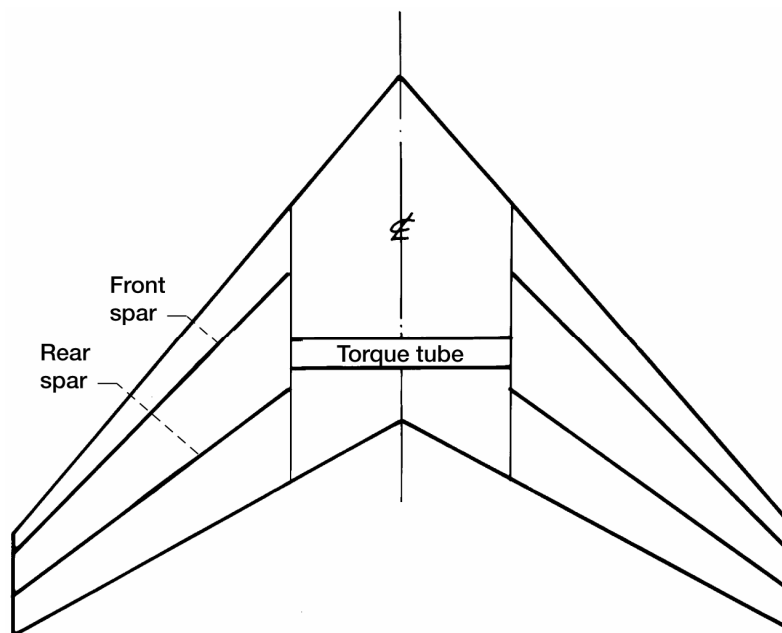
Figure 1.—Plan view F100 horizontal stabilizer.

art of flutter analysis in the early 1950s. Conceptually, the local flexibilities must describe flexibilities not included in either horizontal stabilizer bending or torsion or fuselage bending or torsion. The analyst could normally ignore the detail flexibilities of local structures for the case where two primary structures are joined at right angles. Not so for this case, here the primary structural box of the horizontal stabilizer outboard of the root was of generous dimensions but was reduced to the dimensions of a single 6 inch tube inboard of the side of the body. Another complication requiring improved methodology was the large coupling between all the fundamental motions, bending, torsion, pitch and fore and aft or in-plane chordwise motion. Closely spaced pitch and torsion modes and an extensive flutter history were the result of the extra flexibility in the root structure.
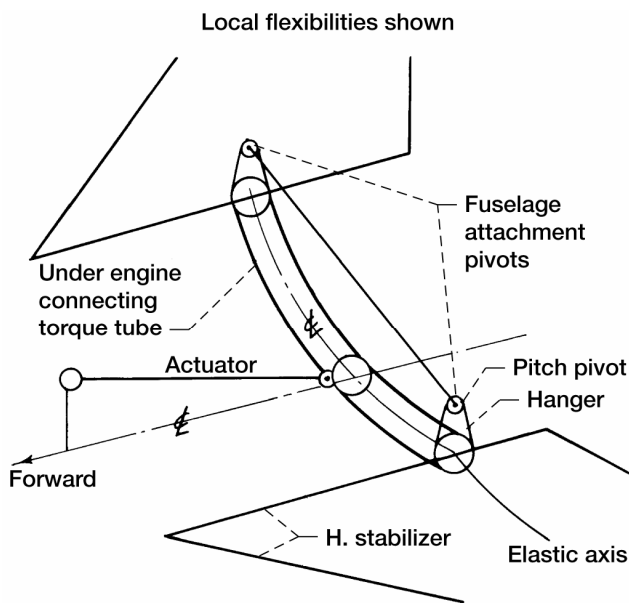
Figure 2.—Three-dimensional perspective (perspective view).
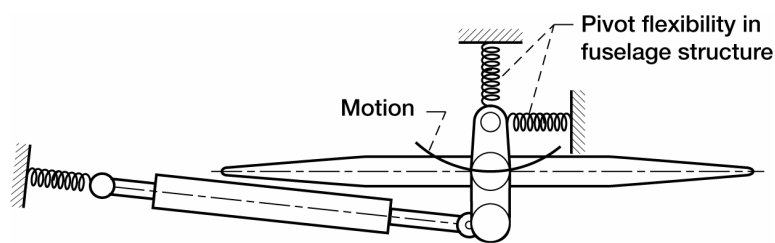
Figure 3.—Local flexibilities (side view).
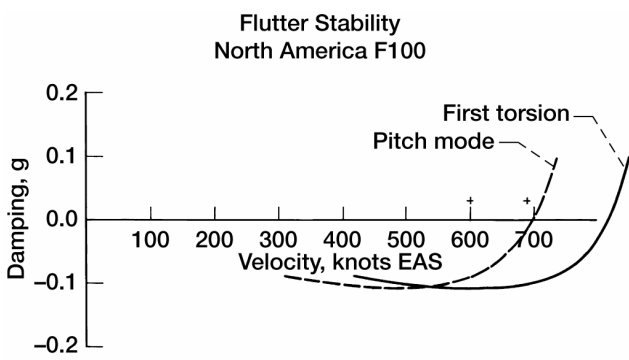
Figure 4.—Damping vs velocity, F100 horizontal stabilizer.

An expediency was chosen to obtain these local flexibilities from the original ground test results by iterating the analysis until matching modes and frequencies were obtained. An agreement to 2 or 3 percent was sought but the close coupling between pitch and torsion required a dozen iterations before suitable agreement was obtained. The need for describing a fore and aft mode had been encountered only rarely. Thus guidance was taken from an experimental result already in hand to determine the quantitative values for the structural flexibilities.

North American was following their own successful methods developed during the 1940s in which correspondence between analysis and test was clarified by defining coupled modes. The strip theory flutter analysis of Technical Report 4798 (ref. 1) had been augmented to be compatible with insertion of coupled modes of vibration rather than uncoupled modes. With this procedure a match can be seen directly in frequency and mode shape between analysis and ground test. Later the technology gravitated to component modes throughout the industry but in this later approach, clarity can be lost between analysis and test.

By the time this new design was to be frozen, a conservative procedure was chosen to provide an adequately stiff structure for the thin 3.5 percent thickness horizontal stabilizer. The original classical bending and torsion analysis was upgraded in parallel to the new analysis with bending, torsion, pitch and fore-and-aft modes. Whichever of these analyses provided the higher requirements was used at any location along the structural axis. The final result of the vibration and flutter analysis for the new configuration is seen in the g-V curve in figure 4. This unique result shows two unstable modes just beyond the required flutter speed with the more critical being the one with the lower frequency, a coupled pitch and fore-and-aft mode. Because of pivot points above the plane of the surface, the fore-and-aft mode contains a large pitch component.

What was learned.—The two important lessons were:

1) the development surrounding the concept of local flexibility and
2) the importance of rebuilding the analytical model to agree with the ground vibration test results. From the structural diagrams presented along with the description of the unique vibration modes, it can be seen immediately that no vague or approximate statement of the local flexibilities can possibly match the measured modes. All the local flexibilities must be precisely identified to obtain an accurate math model. An iterative method was developed whereby a correct set of vibration modes and frequencies could be defined using the results from the ground vibration test. This first example was based on 12 iterations which can be considered reasonable based on its importance to the design.

Case 2: North American F107

The F100 design was begun as a version of the F86; likewise the F107 was begun as a version of the F100. Wing and horizontal stabilizer were unchanged but the vertical was greatly enlarged as a result of a fatal accident to

the F100 in which the large diameter of the fuselage had reduced the effectiveness of the vertical stabilizer in a pullup. During flight test, the airplane diverged in yaw at high angles of attack. Thus yaw stability dictated a larger vertical stabilizer. The challenge of the empennage design in this case was that both the horizontal and vertical stabilizers were all moving surfaces; i.e., no trailing edge control surfaces. The speed altitude design envelope of the new aircraft was very greatly enlarged, to Mach 1.2 at sea level and 2.0 at altitude which naturally required greater stiffness in the wing and empennage. Figure 5 shows the layout of the all moving vertical stabilizer illustrating its relatively small footprint for the three point root restraint. Points 1 and 2 shown are the top and bottom of the spindle and point 3 is the location for the actuator connection.

With the experience of the F100 all moving horizontal surface as a foundation, the design of the all moving vertical stabilizer could reasonably have been expected to proceed without problems. The program was supported with a new low speed wind tunnel flutter model. The stiffness requirements for the model were easily established based on a long history of quantifying both the surface stiffness requirements and separately the root stiffness requirements. The wind tunnel program proceeded on the basis of the original stiffness requirements prior to the time that the GVT was conducted. However the GVT showed the all moving surface failed to meet its design targets for the torsion frequency. It was in fact a repeat on the vertical stabilizer of the problem seen on the F100 all moving horizontal stabilizer. The design requirements had been implemented in two steps:

1.) Conventional beam model for *EI* and *GJ*, and
2.) Root stiffness requirements at the 3 support points.

The original design analysis showed the design met the requirements. The root flexibility from the three point support was analyzed with a sufficiently advanced math model that avoided one pitfall. The elastic center of the three springs (a point load provides translation but not rotation) was determined and the surface elastic axis was located to pass through this centroid. In addition, the maximum and minimum principal axes of inertia representing the stiffness properties of the three point support were determined and the flutter analysis was based on this description.
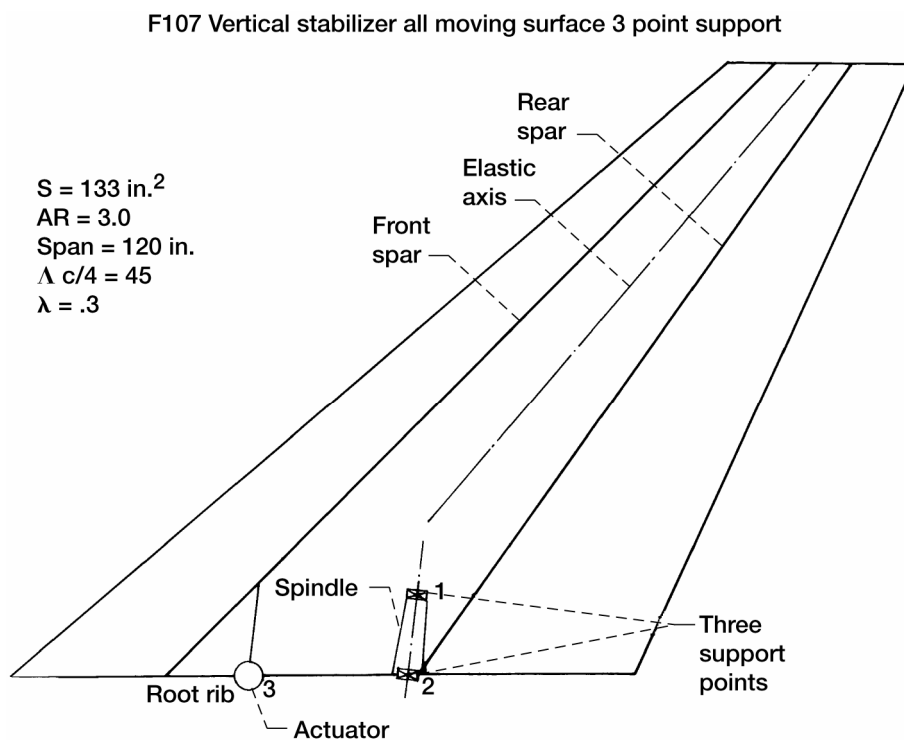
Figure 5.—F107 vertical stabilizer.

The low speed wind tunnel model was constructed only for the empennage. Flutter speeds obtained from the model showed that the flutter speeds were satisfactory in reaching the target flutter speeds of 1000 mph based on the chosen flutter design which included the 15 percent margin in speed.

The failure of the first flight article to reach the required natural frequency during GVT was a result of the additional local flexibility at the root beyond that described by the analytical model. Separate actuator stiffness tests had been conducted to verify the hydraulic actuator stiffness so that the areas questioned for the extra flexibility were either in the body supported 3 point restraint or in the surface locally in the vicinity of the three support points. Experience with the structural stiffness of the main box further out the span was not questioned as the torque box was of conventional design. In addition, allowance had been made for the shear lag reducing the dimensions in the transition zone from the main box to the much smaller dimensions at the 3 point support. Assessing the likely location of the extra flexibility as arising either in the body or in the surface at the root suggested that the nature of the structures problem was quite different between the two areas. In the body the structures were known, they were conventional, and the design group had excellent experience in meeting stiffness targets. Reviewing the root structure however showed that what had likely been missed was the ability of the covers to spread during bending and torsion as would be modeled by figure 6.

The design group recognized immediately that the necessary structure was missing and stiffened the root rib and boxed in the bearing areas to tie the two covers together. (This was not a simplified structure without ribs—just that the ribs and the structure surrounding the spindle did not meet the stiffness requirements.) The subsequent tests showed a return to the expected stiffnesses and agreement with the original design analysis.

The empennage flutter model represented a completely new design approach to the model structure. It was shown that a solid magnesium airfoil section would match both bending and torsion stiffness of the full scale structure based on an appropriate choice of thickness to chord ratio. This made the task of flutter model construction much simpler. In addition the 3 point support was modeled. The model construction using a solid magnesium cross section provided an excellent match to the analytic math model of the full scale design. The vibration modes were unique in that the first torsion and second bending modes of the surface were close in frequency and had node line patterns that could only be measured during GVT by a special test procedure. It was necessary to locate the shaker on one node line at the position that gave maximum excitation to the other mode as would be shown by a moment arm chosen to maximize the distance to the other node. At that point in time the vacuum pads had been developed

Vertical cross sections, F107

Notes:
1. Spanwise bending acting on internal spindle generates prying action on cover plates.

2. Local flexibilities shown were stiffened with a structural box lying on either side of spindle to tie covers together. Root rib stiffened as it also serves same function.

Spindle

Schematic
local flexibility
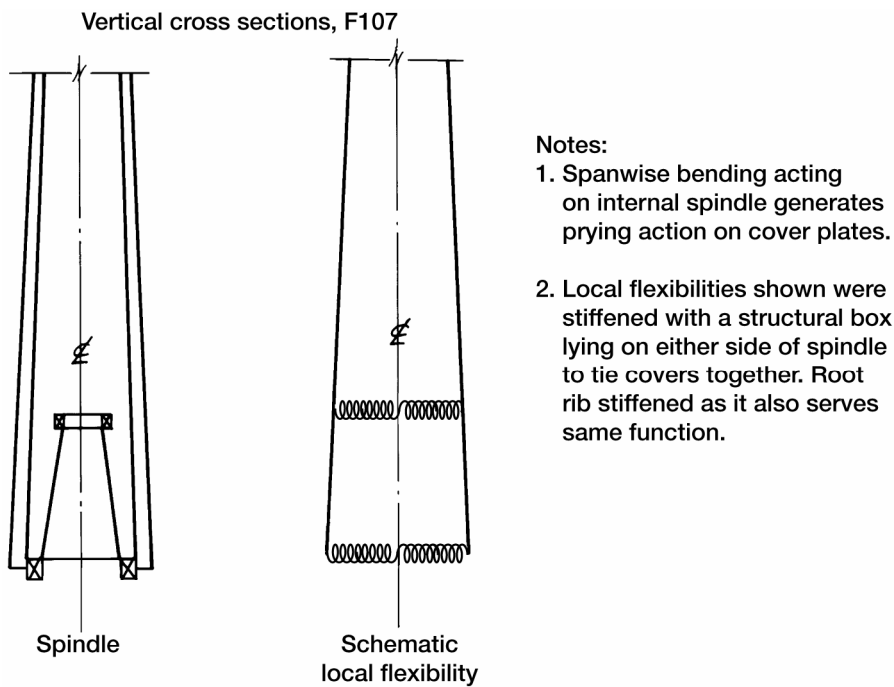
Figure 6.—Local flexibilities.
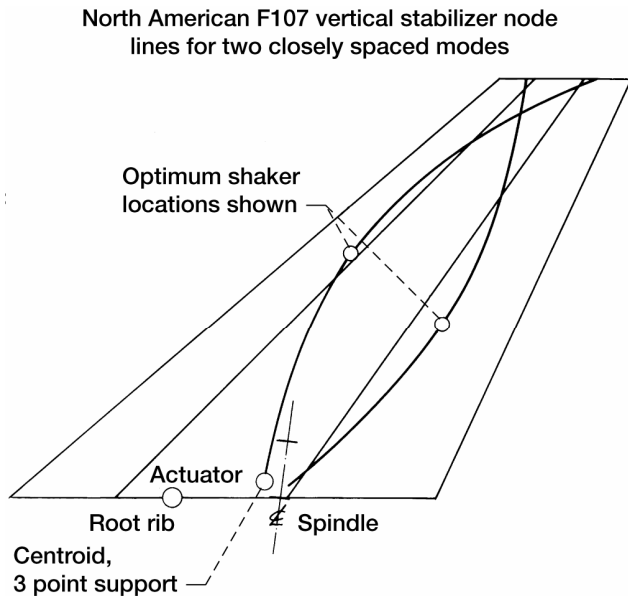
Figure 7.—F107 vertical stabilizer vibration nodal pattern.
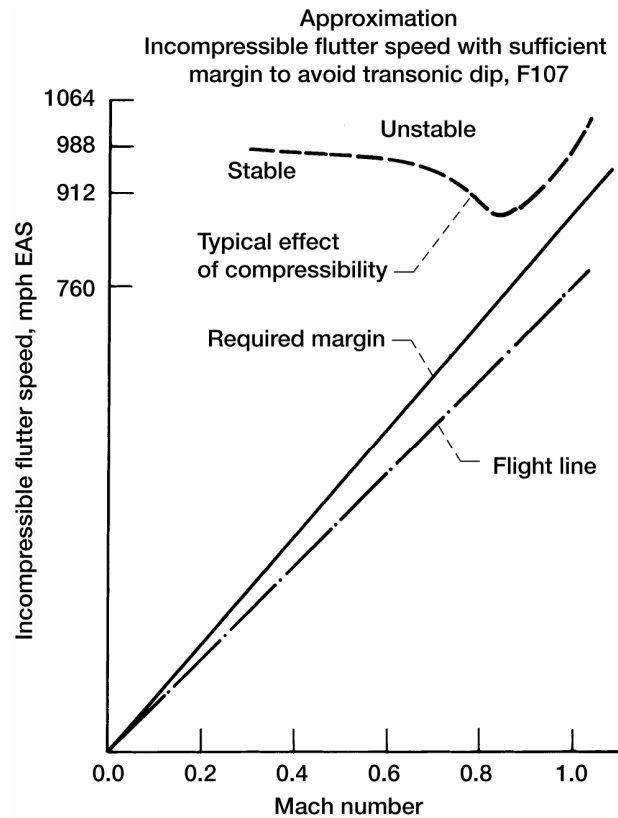
Figure 8.—F107 Flutter speed vs Mach number showing transonic dip.

that allowed the shaker to be attached at any point on the surface. Without that special test procedure, modes and frequencies were not repeatable when other shaker positions were used to verify results. Indeed both the node lines and natural frequencies wandered excessively without this approach of simultaneously maximizing the response in one mode while minimizing the response in the closeby mode. The node lines are shown in figure 7 and the necessary critical shaker locations are given. These had to be obtained by iteration so as to obtain stable modes and frequencies. It is a point of further interest that two close modal frequencies were also a feature of the F-100 horizontal stabilizer case described above. Although the wind tunnel model adequately covered this, the stiffness levels were the design values. Because the wind tunnel flutter model preceded the GVT, the problem it would uncover was not yet exposed.

The F107 was faulted for a failure to match a new incompressible flutter speed requirement of 1000 knots. The customer had previously imposed a target of 1000 mph requirement for bypassing the subsonic compressibility dip near Mach 0.85, see figure 8. The final wing flutter analyses had shown lesser flutter speeds than planned which was traced to a spoiler installation just forward of the flap. The addition to structural weight by the spoiler in a location far aft of the elastic axis was especially sensitive in reducing the flutter speed. A 1 percent further aft chordwise c.g. requires a 6 percent increase in wing stiffness to accommodate it. In this case the wing c.g. had moved from 40 to 46 percent of the chord in the region of the spoiler necessitating correspondingly large increases in wing stiffness. This sensitivity had not previously been included in the stiffness criterion. After validating the effect, it was added to the criterion. The argument was extended to chordwise c.g. forward of the reference 40 percent c.g. to show that the helicopter blade design solution of locating the chordwise c.g. at 25 percent chord cancelled the normal flutter requirements for torsional stiffness, see figure 9. Considerable optimization was completed to raise the wing flutter speed to the requested level for the least structural weight and it was found that relatively minor cover thickness increases in the outer 1/3 of the span would provide the increase requested.

Previous theoretical studies had already been completed to identify optimum placement of torsional stiffness spanwise. The results had been included in the stiffness criterion in the form of a weight equation that defined the weight of the torsion box needed for flutter, reversal or divergence. First attempts had been done merely by comparing several placements of additional material to find an optimum. The optimum result changes with taper ratio, the planform variable that measures the ratio of tip chord to root chord. But the task of optimizing each separate case was simplified when it was recognized that all cases could be defined by a constant stress-equivalent to constant strain energy. The optimum placement of torsional stiffness spanwise is illustrated by presenting the optimum mode shape in figure 10 for the divergence case.

The presentation of the stiffness criterion will be done later in two forms, the theoretical development in the section "Simplified Criterion for Torsional Stiffness Required for Flutter," and its accompanying weight equation, table 1. The latter form is especially useful for preliminary design. The criterion was also compared to the NASA flutter criterion and shown to correspond in the section "Similarities and Differences Between the Two Key Criteria." It makes an elegant alternative presentation with considerable insight to the overall aeroelastic design challenge.
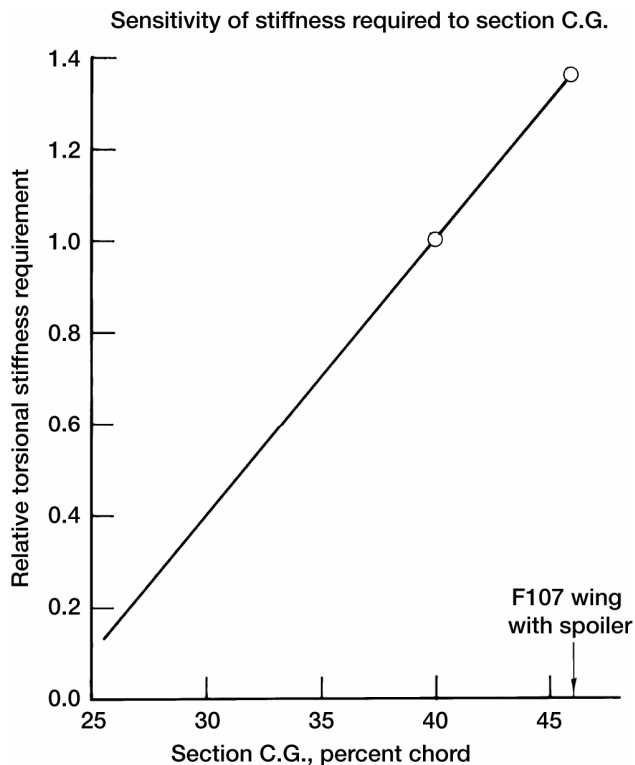
Figure 9.—Stiffness requirement vs chordwise center of gravity.
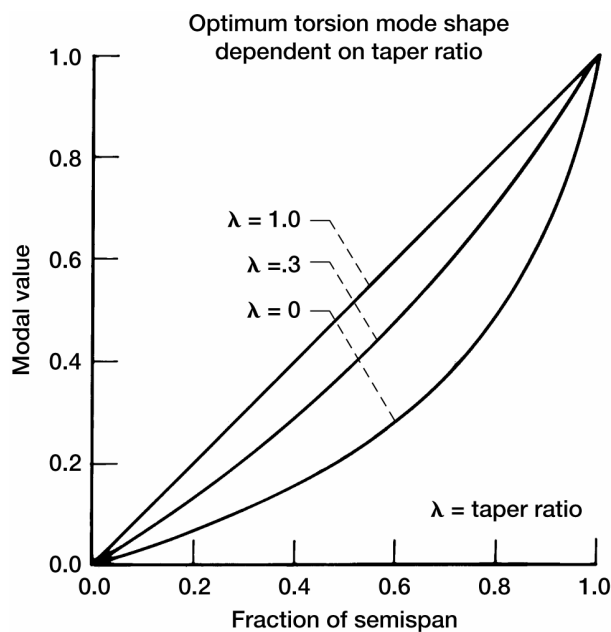
Figure 10.—Optimum mode shapes.

TABLE 1.—A WEIGHT EQUATION FOR FLUTTER

$$W = 1.1 f(\lambda) \frac{L^3}{(t/c)^2} e_e \frac{0.3845^2}{(a_0/k)^2} f(\Lambda) f(T) \frac{1 + 0.06g}{1.36}$$

W	=	weight of structural material around torque box, pound
$f(\lambda)$	=	$0.124 + 0.432\lambda$ variation with taper ratio, λ
e_e	=	effective eccentricity, $C_{l_\alpha} e q$ (see table 2)
L	=	structural semispan, along swept axis, ft.
t/c	=	structural thickness to chord ratio, structural direction, percent
a_o	=	dimensionless torque box area relative to rectangle enclosing airfoil
k	=	dimensionless torque box perimeter relative to chord
$f(\Lambda)$	=	$0.4 + 0.7 \cos\left(\Lambda_{0.25} - 10°\right)$ sweep correction
$f(T)$	=	$39 \times 10^6 \times \sigma/G$ modulus correction due to material or temperature
g	=	chordwise location of the section center of gravity, measured aft from a reference at 40 percent chord, as percentage chord.
G	=	shear modulus
σ	=	material density

TABLE 2.—SPECIAL CASE FOR DETERMINING EFFECTIVE ECCENTRICITY
AT ROOT ARISING FROM ROOT FLEXIBILITY

$$e_e = \frac{Kroot}{\overline{C}^2 L} \qquad \overline{C} = AVG \; CHORD \perp e.a.$$

What was learned.—The lessons learned were much more numerous for this supersonic fighter with Mach 1.2 capability at sea level and 2.0 capability at altitude even though this design was a duplicate in much of the configuration and structural design to that of the F100.

1.) To pass through transonic speeds and avoid the dip in flutter speeds at Mach 0.85 the customer would demand 1000 knot incompressible flutter speed instead of the previously accepted 1000 mph.

2.) The sensitivity to an aft c.g. on a lifting surface was established and shown to be a dominant variable. A 6 percent increase in stiffness was needed to accommodate an aft shift by 1 percent in chordwise c.g. This result was validated and shown to be consistent with the helicopter rotor blade design where the c.g. at the 25 percent point is free of a stiffness requirement. An addition was made to the stiffness criterion to accommodate the effects of aft c.g.'s.

3.) The missing element in the design of the all moving vertical stabilizer was the local flexibility surrounding each of the three restraints at the root. Structural loads on the surface could spread the covers on the structural box. Once the covers at the root were properly secured, one to the other, the measured stiffness returned to the predicted values called for in the original design. This deficiency in the approach occurred even though most of the design had been carefully validated step by step. The local flexibility at key points of the root restraint, the lesson learned in the case of the F-100 above, was of a different character from that of the previous case.

4.) The structural analysis was improved by a method to describe the three point support by an elastic center and axes of minimum and maximum stiffness. Other axes do not account for the existence of a minimum value of stiffness.

5.) A new procedure was developed for use in the GVT for separating closely spaced modes. If the shaker is located so as to minimize the excitation in one of the modes and maximize the excitation in the other, then a stable set of data can be obtained which can be validated by other shaker locations. Unless this is done, as the shaker is moved, mode shapes, node lines and natural frequencies can change radically. The state of the art for GVT had advanced to the point where the vacuum pads could be located at any point on the surface, a necessary development for this case.

6.) Using aluminum for the structural material of choice was adequate for this Mach 2.0 design. Structural temperatures did not exceed 205 degrees Fahrenheit at which point the loss in moduli did not exceed 5 percent.

7.) A technique for flutter model construction using a solid magnesium cross section for the structural design of the lifting surface simplified the time and cost of construction. The dynamically scaled magnesium model was designed to match full scale stiffness by varying the thickness.

8.) The optimum spanwise placement of torsional stiffness which had previously been solved, demonstrated its usefulness on the wing, horizontal and vertical stabilizers.

Assessing the State-of-the-Art Flutter Analysis in the 1940s and 1950s

During the decade of the 1940s and early 1950s prior to the widespread use of the scaled flutter models for low speed wind tunnel testing, the state-of-the-art consisted mainly of a stability analysis derived from energy methods using two dimensional unsteady aerodynamic derivatives in a strip theory format. Because all terms in the stability analysis were integrated spanwise the technique was referred to as three-dimensional, U.S. Army Technical Report 4798, reference 1. The approach was supported by the ground vibration test (GVT) and the flight flutter test (FFT). Since the latter two tests occur at the end of the design verification, it means that reliance on the analysis engendered sizeable risks. As we will show in this section, the hardware produced under these methods were generally successful. Between 1945 and extending all the way to 1950 North American successfully produced the following group of eight airplanes of mostly conventional designs: for the U.S. Navy, FJ-1, XSN2J, XAJ, XA2J; and for the USAF, F86, T28, B45 and later in the 1950 decade the Utility Transport UTX, later identified as the T39 and Sabreliner (see appendix B). These airplanes featured wings without sweepback (with the exception of the F86 Sabrejet and the UTX), small wing spans, relatively thick airfoil sections that provided for adequate torsional stiffness, speeds that reached as high as Mach 1.0 on the F-86, but otherwise conventional layouts and straight-forward structures. The flutter requirements were not very demanding because the configurations were such that extra structural material over and above the strength design was generally not required, although there were excep-tions. The approach used during the 1940s and the early 50s continues in use up to the present, but starting in 1955 lifting surface theories and aerodynamic influence coefficients gradually supplanted strip theory for designs for the higher speeds.

One might ask why such a simple approach had the capability to produce flutter-free hardware. Was it reasonable to expect that the design process for flutter based on simple theory would be successful? The major factors that promoted success using this approach were:

1.) Fundamental correctness of the underlying theory of unsteady aerodynamics was a proven technology,
2.) Structures technology adequate for uncomplicated structures, illustrated by the ability to calculate natural frequencies to the required 5 percent accuracy and
3.) NASA support for flutter that generally kept pace with the design requirements.

At North American the program for flutter prevention began in preliminary design by applying the criteria described later in this text.

a.) Torsional stiffness appropriate to each candidate configuration
b.) Chordwise c.g. control, a particularly sensitive flutter parameter for each of the lifting surfaces
c.) ballasted control surfaces by elements

The approach supported design in all speed ranges if the incompressible flutter speeds were adjusted upward to avoid the transonic dip (see fig. 8). The F86 and F100 series airplanes illustrated the successful use of the basic theory in speed ranges that included the transonic and low supersonic speeds. The kinds of problems that arose and their source will be shown. Only the specific problems are described for each of the designs. The recurring problems were mostly deficiencies in structural stiffness.

Case 3: F-86

The swept wing and empennage configurations required a derivation of the aerodynamic terms specifically tailored to the alteration of the slipstream angle of attack resulting from bending and torsion. Bending was no longer free of angle of attack change and torsion about the elastic axis was different from the slipstream angle. The derivation of the aerodynamic terms was done by two different methods, a velocity component method and a direct solution for flow along the slipstream. By 1947 the F86 had reached sonic speeds in a dive without benefit of flutter analysis valid for that speed range. Both the design and its flight testing were ahead of the flutter substantiation. In reality the design was substantiated by flight testing with the analysis following as rapidly as possible.

The design quickly progressed to carry a wide variety of underwing stores. Many of these configurations would not show satisfactory calculated flutter speeds. Extensive design studies, both analyses and tests, were conducted to define required pylon stiffness, safe store locations and upper limits to the gross weights and chordwise centers of gravity. Part of the requirement for scaled flutter models was the result of the need to more quickly and efficiently approve the large number of configurations based on the variety of stores and their many combinations. Anyone familiar with the weight of armament carried under the wing will appreciate the challenge to flutter stability.

Case 4: B-45

The ability to design a long range jet powered bomber is difficult technically. In order to reach the extended range needed for this bomber, ten thousand pound tip tanks were added to each wing tip. These were designed and substantiated by state of the art methods in the late 1940s using analysis, ground vibration test and flight flutter test. Stiffness was added in the outer wing panel to accommodate the extreme weight of the fuel tanks and the chordwise location of the c.g. was carefully optimized and controlled by bulkheads internal to the tip tanks. Adequate control of the c.g. was obtained in this way for any amount of fuel remaining. With partial fuel loads, fuel produces aft c.g.'s that cause unacceptably low flutter speeds. The power of the existing flutter methods was shown by this challenging design configuration.

Case 5: UTX, Also T-39, Later Commercial Version Became Sabreliner

This design was a utility transport for carriage of premium parts needed for repair of USAF airplanes. It was also configured for transport of VIPs. The airplane is a small twin engined jet with swept surfaces. The initial design was unique in that a normal elevator ballast weight design would not provide the required flutter speeds for the horizontal stabilizer. Neither balance by elements nor ballast concentrated near the tip had acceptable flutter speeds. The combination of modes defining the problem were first and second horizontal stabilizer bending, first torsion and elevator rotation and torsion. The coupling term for parallel axes does not completely decouple the elevator inertially from the torsion mode even when the elevator has 100 percent static balance $S_\beta = 0$. The term in question is

$$I_\beta + b(c - a)S_\beta \tag{1}$$

The residual quantity I_β remains and can only be suppressed by an elevator that is overbalanced, i.e. negative S_β. Because of the sensitivity shown by the analysis, the analysis was extended to include the aerodynamic overbalance and the hinge flexibility as a further safeguard. The elevator design included aerodynamic balance forward of the hingeline which results in longer hinges which provide translation of the hingeline - a conceivable complication. Methods to describe these variables were contained in USAF TR 5153 (ref. 2). Such overbalance is rarely required and, in addition, an optimum ballast location spanwise was also needed. Suitable flutter speeds were obtained once this was done. This problem was unscrambled during design with no schedule delay.

Case 6: XA2J-1 Navy Carrier Bomber
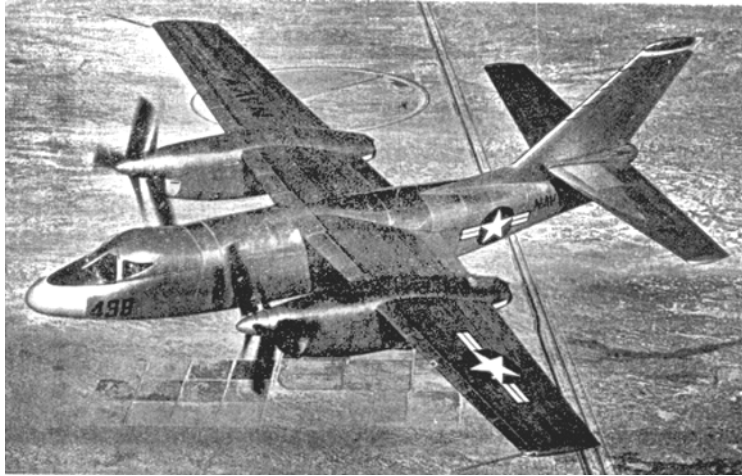
This jet powered turboprop was a heavy weight 52,000 pound bomber designed specifically for carrier operations. Large counter rotating propellers were required to absorb the 4000 horsepower from the jet engines. The design was unique in the extreme forward location of the propellers relative to the elastic axis. Flutter requirements could not be met based upon the results of the ground vibration test showing a low frequency for the stabilizer first torsion mode. The modal pattern indicated excess flexibility inboard of the root rib that arose from the ability to trim the complete horizontal stabilizer in pitch. Excess flexibility from the front spar carry through structure from left side to right side (see fig. 11). Trim was provided by a vertical ball screw actuator of adequately stiff design but the front spar carrythrough introduced extra flexibility by the extra freedom for rotation at the centerline. Both the extra flexibility and the extra degree of freedom were removed by a full depth carrythrough structure for the front spar that extended across the centerline from root rib to root rib.
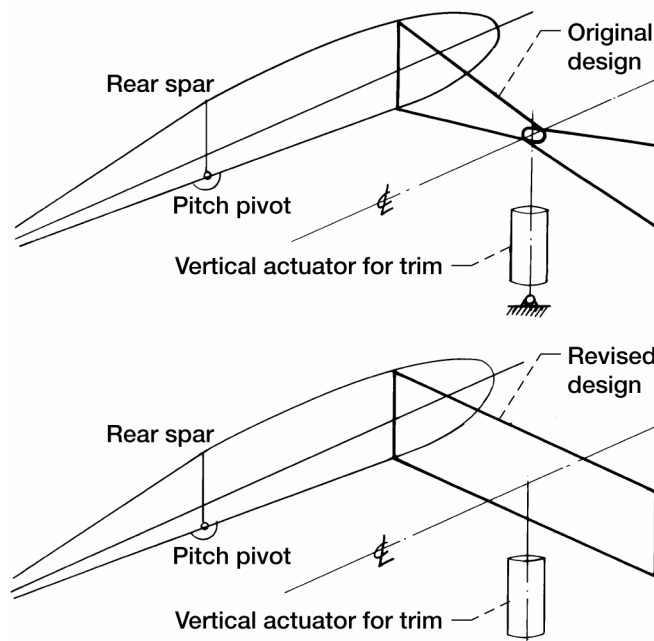
Figure 11.—XA2J-1 trimmable stabilizer showing front spar configurations.

Lessons learned.—This large and significant sample size of eight totally new vehicle designs and configurations were cleared for flutter based on an analytical approach buttressed by the ground vibration test and the flight flutter test. Since the latter two tests occur at the end of the design period, it means that confidence in the analysis was sufficient to accept the obvious risks. The basic approach was that of U.S. Army TR 4798 (ref. 1) and the strip theory it depends on. The reason for the success of this approach was partially a result of other aspects of the design that were accomplished prior to the flutter analysis:

a.) appropriate torsional stiffness, knowable at design inception
b.) ballasted control surfaces by elements
c.) chordwise c.g. control of all masses in the lifting surfaces; wing, horizontal and vertical stabilizers

Thus each of these eight designs had met these flutter design criteria prior to the beginning of the flutter analysis as a result of the work done in preliminary design. This examination of the state of the art flutter design for the time period up to 1955 shows the validity and practicality of the overall approach. The most difficult and time consuming design problems were the underwing stores on the F-86 and the large tip tanks on the B-45.

Summation: Cause of the Above Flutter Problems

The difficulties reported were of two types: 1) in-flight flutter and 2) necessary redesign prior to flight when GVT results showed unacceptable structural flexibility. Using the state-of-the-art information in the paragraph above, it can be seen that, procedural or substantive flaws in the accepted methods were not the source of either problem. For example, the state-of-the-art dependence on strip theory had been shown to be adequate and conservative on numerous occasions for determining flutter speeds by analysis. This included surfaces with aspect ratios as low as 3.5. In fact, the expected errors in the technique were seen as conservative. But when structural analyses were critically examined, it became clear that the structural math models were the source of both the flutter problems in flight and were the source of the GVT problems when targeted frequencies were not met. While conceptually the methods were in every sense adequate, the initial plans for the math model were often incomplete and important details of structural flexibility were omitted.

For swept wings of low aspect ratio and for all moving surfaces, a compromise had been accepted in using beam technology with structures cantilevered from a fixed root. The compromise was the use of beam theory for wings even of low aspect ratio, for wings with abrupt transitions in the structural box and for use on swept wings. Beyond these compromises in beam theory, there were also large assumptions made that the cantilever beam was fixed at the root. For the all moving surface or for the trimmable horizontal stabilizers, these variable root structures introduced a dominant flexibility. Use of finite element structural modeling technology was needed but was not yet a part of standard practice in flutter. A carefully executed finite element model would have solved all of these problems under favorable circumstance but even this technique would have missed a goodly portion of the instabilities without some foresight for new problems. If the fore and aft mode were the unstable mode, as it was in the case of the F100, then a finite element model does not solve this problem unless the math model is sufficiently complete to contain this degree of freedom. The difficulty with including all the flexibility introduced by the all moving stabilizer is answering the question of what degree of local flexibility needs modeling in joining two beams, the fuselage with the stabilizer. Hydraulic actuator flexibility is also critical because it concentrates load at a number of point elements. Framing these problems conceptually was needed to best exploit the added capability of FEM techniques. These flutter problems, mostly due to structures, suggested the following lessons learned:

For the F-100

1.) The analysis of natural modes and frequencies must match those from GVT.
2.) The GVT and the sled flutter test were needed to establish the critical mode: a coupled Mode combining pitch and fore and aft motion.

3.) Matching the analysis to the measured modes depended on an accurate description of local root flexibility. Although not generally a part of the state-of-the-art these flexibilities could be determined by iteration and reverse engineering.

For the F-107

4.) Structure surrounding the bearings that mount the vertical tail was inadequate to prevent excessive root flexibility caused by spreading of the cover plates. The root rib also functions to tie the covers together but initially was also too flexible. When corrected, the design then matched the analysis with no further change. Later the design was altered with greater thickness at the root to provide the necessary stiffness.

5.) The flutter design criterion of 1000 mph incompressible flutter speed was upgraded by the USAF just as the airplane was being readied for first flight. This required additional wing material. There were three other lessons attached to this portion of the problem:

    a.) One reason for not achieving the new 1000 knot incompressible flutter speed requirement was the relatively far aft chordwise c.g. at the spanwise location of the spoilers. These roll devices are located in the vicinity of 55 to 60 percent of the chord, inboard of half span, immediately ahead of the flaps.

    b.) The unique sensitivity of approximately 6:1, (6 percent increase in stiffness for 1 percent c.g. movement aft), was verified and added to the torsional stiffness criterion.

    c.) These problems are stated correctly as stiffness—not frequency problems.

For the XA2J-1

6.) For the trimmable horizontal stabilizer, extra front spar flexibility was a result of an unnecessary structural pivot at the centerline. Torsional deformation in pitch was considerably amplified by this feature. When the front spar was joined side to side with a full depth beam this extra flexibility was removed.

The flutter cases in flight and the unsatisfactory outcomes of the GVTs lead to the conclusion that the analytic descriptions of primary structure contained in the flutter analyses were insufficiently accurate and complete.

Case 7: F-108

This Mach 3 interceptor was a smaller version of the B70, shown in the above picture. Configuration and structural design were quite similar: a 65° delta wing with a forward canard surface and a structure of brazed steel honeycomb sandwich. The surfaces were so exceptionally thin that no possibility existed for ballast weights, instead a frequency criterion was imposed to obtain a trailing edge control surface of satisfactory stiffness. In considering how to model the surface, the analysis was conceived as being based on aerodynamic and structural influence coefficients. But the flutter model technology existing at that time would be a very poor representation. The idea of

concentrated stiffness at a single spar location was simply not acceptable. To model the diffuse structure on the other hand would require a new material were we to continue to use the more convenient low speed wind tunnel. First, it was desirable to set down a requirement without a presumed limitation to satisfy the desire to go with an accurate simulation. This approach led to a need to provide item-by-item simulation of the structure. And this in turn led to a need for a material with reduced moduli in tension and shear so that practical thicknesses could be used for skin, ribs and spars. The ratio of the two moduli, E to G, must also match that of the full scale article. Lastly, introduction of a totally new material meant it must be qualified as a structural material with a usable range of stresses and appropriate fatigue properties for use in a flutter model.

A plastics specialist had a very clear picture of how to meet these requirements and suggested that a material constructed in such a way as to be orthogonal in a material sense would provide the required internal structural similarity needed for a dynamic model—thereby providing the required ratio of E to G. The concept was implemented with microballs of bakelite which were joined with a plastic cement. The material had been developed to float on large reservoirs of petroleum to suppress evaporation of a volatile material. From the initial test, the material passed each requirement in turn. The material allowed the construction of a delta wing structure by item-by-item scaling of each individual component. In addition, it was shown to have usable fatigue properties and could be expected to provide a practical structure by permitting flutter amplitudes up to those that would be expected were flutter to occur near max expected amplitudes.

During qualification in the first low speed wind tunnel test, the model was lost at only half max tunnel speed while slowing the tunnel to test the ability to stop the flow. At approximately 55 mph the model rose to the ceiling of the wind tunnel, a distance of 3 feet, and was destroyed. The cause was the configuration of the flat plates designed to block the flow. Two plates at the level of the model, one on either side, are introduced to the flow by very rapid spring loaded "fly swatters." The centerline flow was not blocked but the flow further outboard was. The result was that the destabilizing canard near the tunnel centerline experienced increased flow and the stabilizing wing in the wake of the brakes experienced much diminished flow. This produced the pitch up that caused the model to rise and impact the tunnel ceiling. Cost at that time was a lost model worth $25,000. The model was immediately rebuilt and its performance as a flutter model met all requirements (following relocating the flat plates that partially block the flow). It was a pleasure to see full tip deflections occur during flutter without damage to the structure of the model. GVT results of the wind tunnel flutter model showed excellent match to those obtained analytically. Flutter speeds were found at the expected values and showed proper margin.

Lessons learned on the previous cases had shown the need for the scaled dynamic model and the delta wing showed the need for the item-by-item scaling. The material development needed to support the model allowed its use in a low speed tunnel.

Case 8: OV-10

The counter insurgency fighter, the OV-10, experienced flutter in flight test on 3 different occasions over a three year period and the contract was on the verge of cancellation when the source of the problem was determined by analysis. The configuration for this special design was an unconventional twin boom arrangement supporting the empennage. The design was compromised by locating the horizontal stabilizer between the two vertical tails rather
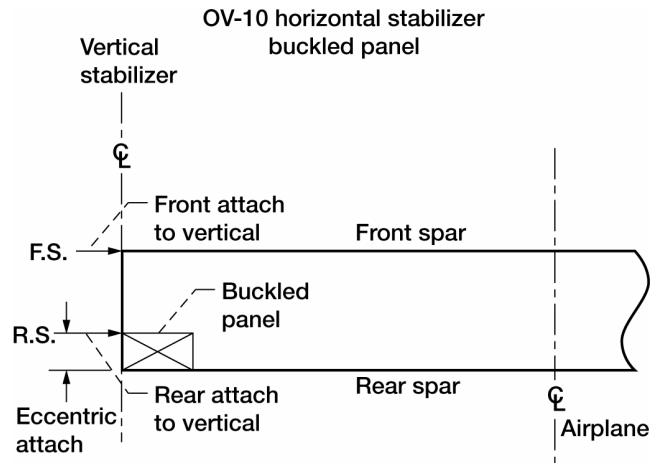
Figure 12.—OV-10 Coin buckled panel.

than a lower position between the tail booms. The two spars for the horizontal did not match the two spars for the vertical. As a result of the flutter instabilities in flight, flight measurements were made to determine the frequencies participating in the instability. These did not match those contained in the analytical model nor those from the ground vibration test. It was reasoned that the cause for different frequencies in flight relative to those measured on the ground was buckling of a panel at the root of the horizontal stabilizer where it attached to the vertical. The rear spar was not continuous due to the rear attach from the horizontal to the vertical stabilizer was forward of the horizontal rear spar location. Rear spar load was dumped into a skin panel for transfer to the eccentric attach. Further measurements showed this skin panel was buckled under flight loads resulting in a reduced stiffness to the key flutter mode, see figure 12. During the initial ground vibration test, agreement was obtained between the calculated and measured frequencies because both were describing an unbuckled panel. With the right idea in hand, the explanation of the lower measured frequency when the horizontal was under load was straightforward.

In summary, the structural problem concerned the load path at the rear spar of the horizontal stabilizer where it connects to the vertical stabilizer. A direct tie was prevented by the mismatched locations of these two spars. A large eccentricity was present where the two rear spars were joined. A shear panel transferred the load from the rear spar over to the attach point. Under load this panel would buckle; and its loss of stiffness was sufficient to cause flutter. It consumed nearly 3 years before the problem could be located.

Designs With Radically New Configurations

Three designs that departed radically from past practice were the F-108, B-70 and the Space Shuttle. B-70 was a long range Mach 3 strategic bomber with a 65° delta wing that lay inside the Mach 3 shock. The requirement for low drag resulted in a 3 percent wing thickness. Efficient structure required the use of a brazed steel honeycomb sandwich. Elevons serve for both roll and pitch control. To prevent bending across the large wing span, the elevons were segmented into 12 short segments. The full program included development of aerodynamic and structural influence coefficients and the construction of flutter models. Piston theory was also applied at the high Mach numbers. One problem common to all three designs centered on a major design improvement, trading increased control system restraint stiffness for ballast weights. The use of lead ballast was an established design practice on the control surfaces for flutter prevention because it decouples bending and torsion from control surface rotation. However, there are three major disadvantages to the use of lead ballast.

1.) A structure is needed forward of the hingeline to support the lead. Requirements for support include large load factors approaching 100 G limit load plus the test demonstration of the ability to carry 60 G for 500,000 cycles. These requirements apply to both civil and military airplanes, see references 3, 4, and 5.

2.) Control surface mass unbalance is matched with approximately equal mass unbalance forward of the hingeline. The weight of lead and the weight of structure are positioned far aft on the chord, a location that heavily penalizes flutter speeds.

3.) Design direction for high speed flight required thin airfoils which no longer provided adequate space for lead weights within the confines of the airfoil lines.

Exploring the fundamental question, for the same weight used to provide the lead ballast, is there a possibility that the control system stiffness could be made essentially equivalent to that of trailing edge structure, i.e., effectively "rigidly attached." (Trailing edge structure does not exhibit buzz.) If not, could sufficient damping also be added to accommodate the stiffened control system for whatever unacceptable flexibility still remained. Although designs without the use of lead ballast would also carry severe design penalties, ballast forward of the hingeline was literally no longer possible for very thin airfoil sections. Thus, solutions without the use of ballast were required. It is worthy of note that the all moving horizontal and vertical stabilizers are also compromised design solutions to circumvent the use of ballast weights.

The history of this development is not totally recorded. But a list of airplanes using this stiffness approach would include: F108, B70, Space Shuttle, AMD Falcon jet, and the Boeing series, 757, 767, and 777. The approach must account for different flight regimes, either subsonic or transonic, and for the civil transports cited, must account for the Federal Air Regulations requirements for fail safety. Requirements in the different flight regimes are considerably different because of the transonic control surface buzz phenomenon. Space Shuttle and B70 met the requirement

$$\frac{c\omega}{V} = 2.0 \tag{2}$$

where c is the average control surface chord length (hinge line to trailing edge), ω is the natural frequency in rotation (in radians/second), and V is the true airspeed (in feet/second).

While the AMD Falcon Jet had only a 30 Hertz aileron first rotation mode to meet the flutter speeds needed for subsonic flight, the level required for suppressing transonic buzz per the above criterion would have been possibly 5 times greater. A careful explanation for this difference is required. The buzz phenomenon is best understood as oscillating shocks that move in opposite directions on the upper and lower surfaces (implying different locations). Their different locations chordwise provide a large hinge moment that keeps the control surface oscillating constantly at high frequency. This phenomenon is seen generally at a very limited Mach range between 0.85 and 0.90. The variation from design to design is believed to be a function of the trailing edge angle between the straight lines of the upper and lower airfoil surface. The smaller the angle, the weaker the shock. Control surface buzz can be expected on any trailing edge control surface at transonic speeds and would normally reach such high amplitudes as to cause the flight to be immediately terminated. If the designer has chosen to proceed without damping added to the control surface, then the limit speed is set below the Mach number at which buzz begins and flight tests are conducted to demonstrate freedom from buzz. If the airplane limit speed includes Mach numbers greater than that for the onset of buzz, then dampers are incorporated in the design.

For Space Shuttle the buzz requirements were known as a result of the research completed on the B-70. Data had been assembled from known buzz cases, reduced to the dimensionless form shown in equation (1) and an envelope drawn to cover all the cases. In determining the stiffness in rotary motion of the control surface, the sketch shows the critical local structural flexibility at four points plus that of the actuator.
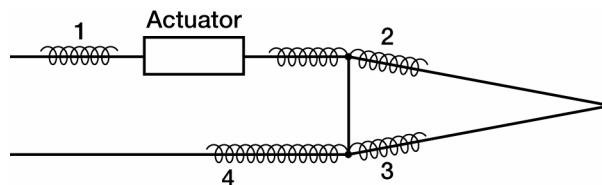
The extent of the structure brought into the calculation of local flexibilities is best determined from calculations in similar cases (supported by test data). Elevon supporting structure was extensively stiffened at all these locations and optimized for efficiency.

Space Shuttle also benefited from the torsional stiffness criterion presented in the paragraph "Simplified Criterion for Stiffness Required for Flutter." Space Shuttle wing and vertical tail were designed to this criterion and then extensively tested in five different wind tunnels for different Mach regimes to demonstrate freedom from flutter and buzz. At no point were changes made to the criteria or to the initial design. Thus these two design criteria were successfully applied to Space Shuttle.

Another application of lessons previously learned was utilized for Shuttle. NASA was concerned that the struts joining the four bodies led to large local flexibilities at their intersections with conventional structure. If a scaled model based on item-by-item scaling were built, the modal characteristics could be obtained much earlier. The vehicle dynamic characteristics pervaded many of the analyses on which safety depended. A 1/4 scale model was built and provided a 2 year lead time on the full scale GVT.

FAA Flutter Requirements for Unballasted Control Surfaces

Overall system complexity may consist of the supercritical airfoil, fly-by-wire, multiple actuators for a single control surface, and a primary flight computer, each with dual or triple redundancy. In addition, load alleviation, flutter suppression, gust suppression, unique control laws, overspeed protection and stability augmentation systems may be part of the design. The civil requirements have been under development for more than ten years and have reached a high degree of refinement. FAA requirements are continuously improved and developed but in the latest cases the following have been used:

1.) The loss of either stiffness or damping constraint needed to preclude flutter must be shown to be extremely improbable;

2.) Failures, malfunctions, or adverse conditions must be considered in showing compliance, including any single failure, any combination of failures not shown to be extremely improbable, latent failures not detected in normal operation, and any single hydraulic or electrical failure in combination with one actuator disconnect;

3.) Prior to every flight, conduct tests to expose latent actuator failures. During flight continuously monitor the primary flight control functions and monitor system configuration such as blocking and bypass modes;

4.) Latent failures not identifiable in preflight tests require the inclusion of a maintenance and inspection program in the certification maintenance requirements;

5.) Conduct hazard analysis to identify failure modes and latent failures;

6.) Force fight between actuators must be eliminated;

7.) Any damage or failure condition selected for investigation by FAR Part 25.571, 25.631, 25.671, 25.672 and 25.1309 must be considered. Failure modes from the primary flight computer (PFC), electrical, electronic, hydraulic and mechanical systems, their sensors and transducers, and feedback information to the PFC that could contribute to flutter must be considered. Failure probabilities must be based on previous experience.

8.) If a free surface cannot be shown to be free from flutter, then assurance must be provided that the surface will not become free.

Lessons Learned—Unballasted Control Surfaces

A major difference was shown between design at Mach numbers much less than transonic Mach numbers and design that requires penetration of the transonic region where buzz occurs.

Two criteria were used in the preliminary design stage for Space Shuttle, both of which were successful. If these had not been available, significant additional design time would have been required. Space Shuttle also benefited from an advanced modeling technology that provided early GVT results. Civil requirements for unballasted control surfaces include fail safety, damage tolerance; and failures, malfunctions and adverse conditions.

FAA and Flutter

The relationship of the FAA to flutter is best shown by relating some historical background, describing the applicable regulations and showing the extent each accident is covered, the corrective action and the overall depth of the many safety issues. Through in-depth study of the accidents a more thorough understanding of basic flight science has resulted. Topics to be covered include structural dynamics and flight dynamics, fail safety, reliability, maintenance with small flaws, flutter criteria including an Excel spread sheet, and the contrast in the required margins for the separate structural design tasks of stiffness and strength. The extent of the involvement of the various aeroelastic and dynamic phenomena has been far greater than expected with greatest involvement in the most serious accidents.

The history of the program to prevent flutter at the FAA is not consistent between transport category and general aviation. Because of the necessity to protect the passenger of an air carrier, requirements for transport category are extremely strict. This is not matched in general aviation because of the desire on the part of that community for greater design freedom and their desire to avoid burdensome regulations. So the history of occurrence of flutter between these classes of civil aviation is considerably different. History over the last 25 years shows freedom from whirl flutter that first appeared in 1955 in transport category was resolved very quickly. (Current regulations require evaluation of whirl flutter in both transports and general aviation.) Classical flutter has been observed in transport category on very rare occasions and then mainly as a result of a prior failure. Service difficulty reports required from air carrier operators provide only minimal information, and on the occurrence of flutter, a label "vibration" is used instead.

Serious flutter accidents do occur and have been catastrophic but almost always for the reason that another failure preceded flutter as the following cases will illustrate. Two examples are an Electra in Pennsylvania in 1983 and a Boeing 737 in Panama in 1991. In both cases the airplane was upset at high altitude due to a failure of the autopilot, direction finder or artificial horizon. The airplane entered a vertical dive and the flutter instability began as the airplane approached design dive speed. In both these cases flutter was so violent that the cockpit separated in flight. Another example, a Convair 580 elevator hinge pin failed leading to flutter of the horizontal stabilizer. This too was a catastrophic case in which the empennage separated in-flight and the airplane plunged into the North Sea. A catalog of flutter cases in the civil system would easily reach several dozen in transport category and many hundreds in general aviation.

The lesser regulation of the general aviation airplanes is best shown by the basic flutter requirements for the case where design dive speeds are less than 260 knots that lead only to the use of Report 45 "Simplified Flutter Prevention Criteria"; and for speeds greater than 260 knots that require only analysis or flight flutter test but not both. The higher accident rates and number of fatal accidents and number of fatalities in general aviation airplanes are all associated with the decision to impose lesser regulatory requirements. These lessened requirements lead directly to lesser safety. Various forms of dynamics that also depend on airframe stiffness would also help account for these lessened safety results. Reduced safety can be shown by the 2:1 difference in fleet safety depending on whether analysis *and* test were chosen to show compliance with freedom from flutter or analysis *or* test only. This choice is not available in transport category where a full flutter program is required: wind tunnel test, ground vibration test, flutter analysis and flight flutter test. The rigorous standards applicable to transport category likewise account for the excellent safety record achieved.

Accident Investigation

It would appear that no serious inroads on safety will occur without being grounded in the knowledge intentionally acquired from the fatal accidents. Current knowledge is faulted by the—

- repetitive occurrences of fatal accidents
- an unrecognized generic pattern with over 100 cases which has dominated the last several decades
- hidden dynamics because the accident investigations are shallow in this area
- new phenomena

Findings to date are of two kinds—
- the accident process itself. Once begun, the process tends to continue to completion, and
- fundamental additions to the aero sciences. This has been the most surprising part of the accident studies. The aero and structural instabilities interact with the weather, the vehicle and the pilot.

While there are many different components to the investigation itself—
- many failures, scattered debris
- a need to develop candidate scenarios from indirect evidence from the FDR, the ground marks and witnesses,

the main failure has been concentrating on the individual accidents without also integrating the whole of the body of knowledge. It is logical to breakdown the whole into several categories—
- propulsion, aerodynamics, systems and structures and
- those particular fleets with the highest number of accidents and the highest rates.

Thus the broadest possible role must be assigned to accident investigation—
- prevent repetitions of accidents of any one kind
- establish the involvement of structural and flight dynamics in the fatal accidents, currently estimated as 90 percent or more of the total number of cases
- using the label pilot error for primary cause in the majority of cases truncates the investigation short of determining vehicle deficiencies. In cases of repetitive accidents, it is only after the vehicle deficiencies are identified and corrected that the accidents stop.
- the on-site investigator must be trained to describe the important dynamics' clues.

See table 3 for an NTSB accident brief.

TABLE 3.—NTSB ACCIDENT BRIEF

BRIEFS OF ACCIDENTS

FILE DATE LOCATION AIRCRAFT INJURIES FLIGHT PILOT
F S MN PURPOSE

2-1134 9/11/66 NR MITCHELL OREG BEECH A35 CR- 1 0 0 NON COMMERCIAL PRIVATE
TIME-0920   N745B   PX 3 0 0 PLEASURE, PERSONAL AGE29
DAMAGE-DESTROYED   28 HOUR IN TYPE
NONINSTRU.RATED

TYPE OF ACCIDENT   PHASE OF OPERATION
AIRFRAME FAILURE IN FLIGHT   INFLIGHT - NORMAL CRUISE
COLLISION WITH GROUND/WATER   INFLIGHT UNCONTROLLED DESCENT
PROBABLE CAUSES
PILOT IN COMMAND - CONTINUED VFR FLIGHT INTO ADVERSE WEATHER CONDITIONS
PILOT IN COMMAND - SPATIAL DISORIENTATION
AIRFRAME - WING SPARS
MISCELLANEOUS ACTS, CONDITIONS - OVERLOAD FAILURE

FACTORS
WEATHER - LOW CEILING
WEATHER - TURBULENCE, ASSOCIATED W/CLOUDS AND THUNDERSTORMS
WEATHER BRIEFING - NO RECORD OF BRIEFING RECEIVED
WEATHER FORECAST - WEATHER SLIGHTLY WORSE THAN FORECAST

SKY CONDITION   CEILING AT ACCIDENT SITE
OVERCAST   300
VISIBILITY AT ACCIDENT SITE   PRECIPITATION AT ACCIDENT SITE
UNKNOWN/NOT REPORTED   NONE
OBSTRUCTIONS TO VISION AT ACCIDENT SITE   TYPE OF WEATHER CONDITIONS
NONE   IFR
TYPE OF FLIGHT PLAN
NONE
REMARKS - RIGHT WING AND LEFT RUDDERVATOR FAILED IN FLIGHT

TABLE 3.—Contiued.

Note: This authentic reproduction should be interpreted as follows:

File:	2-1134	type accid:	airframe failure in flight
Date:	9/11/66		collision with ground
location:	Mitchell OR	phase of operation	inflight-normal cruise
aircraft:	Beech A35		inflight-uncontrolled descent
Injury:	fatal/serious/minor	probable cause	continued visual flight rules
	cr 1 0 0		into adverse weather
	px 3 0 0		spatial disorientation
flight	non commercial		airframe wing spars
purpose	pleasure		overload failure
pilot	private pilot	factors	low ceiling, turbulence
	age 29		no briefing
	28hr in type		wx worse than forecast
	non instru. rated		overcase, ceiling 300
time	0920	type of weather	Instru. Flt. Rules
I.D.#	N745B	Remarks	Right Wing and Left Ruddevator failed in flight

In-Depth Substantiation of Findings

Findings from several decades of accident investigation provides a pretty good picture of the fundamentals. Data are given for the number of fatalities and the accident rates vs time, figures 13 and 14. The flight dynamics and structural dynamics showed one underlying fundamental phenomenon was occurring. Beginning with Instrument Meteorological Conditions (IMC) and turbulence, upset occurred in pitch, roll or yaw, singly or in combination. As long as the pilot was alert and arrested the divergent motion, safety was assured; but if permitted to persist, then overspeed was the next step in a process that led to stall or ground contact. Fifteen degrees nose down pitch held until a terminal velocity was approached showed that speeds of 160 to 180 percent of cruise speeds were obtained. Such speeds are well beyond the flutter speeds that reside just beyond 1.15 to 1.2 V_d.

TREND OF IMPROVEMENT IN ACCIDENT RATES

REFERENCE: **1992 YEAR IN REVIEW**
F.A.A. AVIATION SAFETY JOURNAL
VOL. 3, NO. 1

This underlying process that leads to fatal accidents was not known and accounts for one reason the fatalities have remained constant. The process is specific:

1.) IMC and turbulence
2.) upset and overspeed
3.) stall or ground contact

Other dynamic instabilities were found. The two rigid body modes of flight dynamics are the phugoid and the short period mode. Singly or in combination, these modes offer instabilities in certain circumstances that are difficult for the pilot to deal with. The oscillation in the phugoid mode obscures the flight path angle and the short period mode obscures the angle of attack.

The above descriptions of events have been identified in over 100 cases. Another kind of repetition had occurred in one general aviation fleet with 915 fatal accidents over a period of 40 years. Partly these repetitions were a result of the dynamics that lay hidden for many decades. The accident investigators were not specialists in this area, had not identified either of the four failure modes nor chose to deal with the repetitive occurrences. The dynamics involved in these accidents arose from longitudinal instabilities, lateral instabilities, the processes defined above, and imperfect structural design that allowed the root rib of the v-tail to fail.
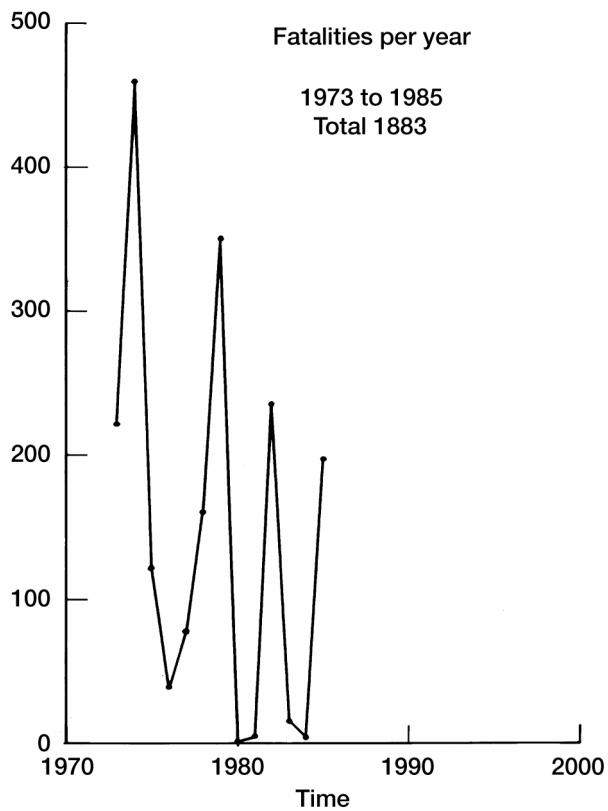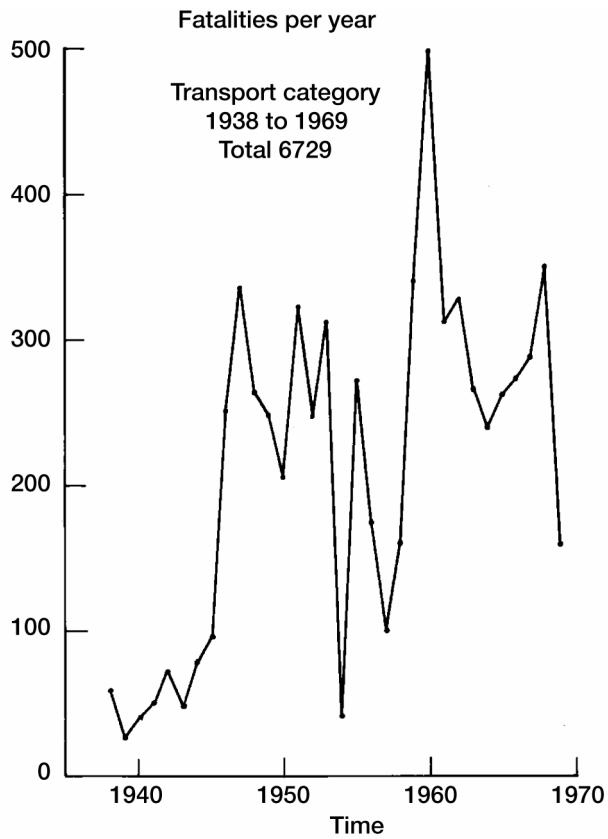
Figure 13.—Number of fatalities, U.S. scheduled air carriers.

Trend of improvements in accident rates

Reference: 1992 year in review
F.A.A. Aviation Safety Journal
Vol. 3, No. 1
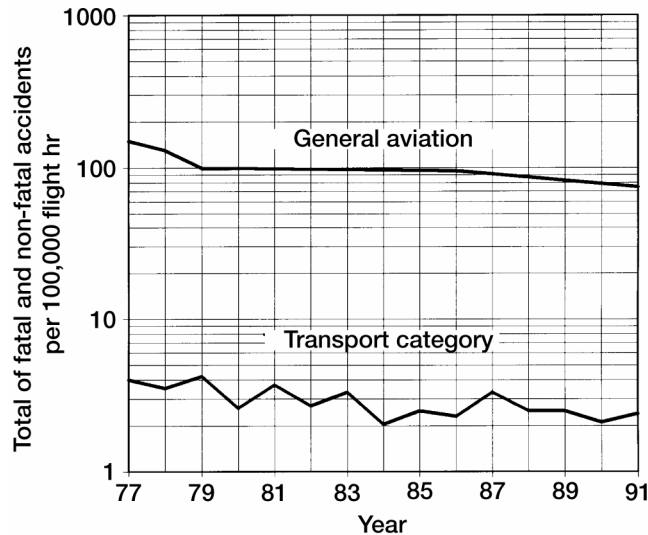
Figure 14.—Accident rates, U.S. scheduled air carriers.

In another example, 21 similar fatal accidents with a unique wreckage pattern occurred in one general aviation fleet. First along the wreckage path were two separate wing panels and two separate elevators. This indicates symmetric in-flight airframe failure. It was reasoned that no likely combination of gust and maneuver loads would exceed the measured strength in 21 cases (static test of the airframe showed a capability for 8 G ultimate load). A load amplification factor was derived that reached very high values on approach to a critical speed, see figure 15. The proof of concept was established both analytically and experimentally, figure 16. Thus this was a pivotal case leading to the development of the underlying process defined above: upset and overspeed and an explanation for repetitive failure in a single fleet with demonstrated 8 G capability. This was a major finding from the accident investigations which led to a significant advance in understanding the impact of lifting-surface structural flexibility on load magnification.

Accident reviews show two new flight phenomena. General aviation straight wing airplanes, on being upset in yaw, experience wing failure due to bending torsion divergence. This is compounded in those designs with slight sweepforward of the structural elastic axis. General aviation straight wing airplanes experience in-flight airframe failure when upset at high roll rates. Rapid roll tends to occur about the axis of minimum inertia in roll. In those airplanes where the axis is low at the nose and high at the tail, complete rollover finds the airplane at much higher angle of attack (AOA) inverted than the initial angle of attack. The much greater AOA inverted leads to IFAF.

Flutter design that meets the regulatory requirements may be acting as a surrogate for other stiffness related phenomena involved in fatal accidents. As a class fatal accidents exhibit more extreme loads and maneuvers than nonfatal accidents. The flexible airframe allows these loads to be amplified as previously discussed and generally suggest minimum margins. Repetitive accidents have featured each of the flagship fleets of the major general aviation manufacturers. It is suggested that the various dynamic phenomena are not recognized in the on-site investigations, that they lie hidden and that the repetitive accidents are a further indication of minimum margins.

Although the accident process was described, only in-depth substantiation is usable requiring a much longer investigation. It is not in the nature of complex relationships between owners, operators, manufacturers and government regulators that a simple unfolding of the events would suffice. The process of substantiation is moved forward in three steps, engineering findings, satisfactory explanations and development of consensus.
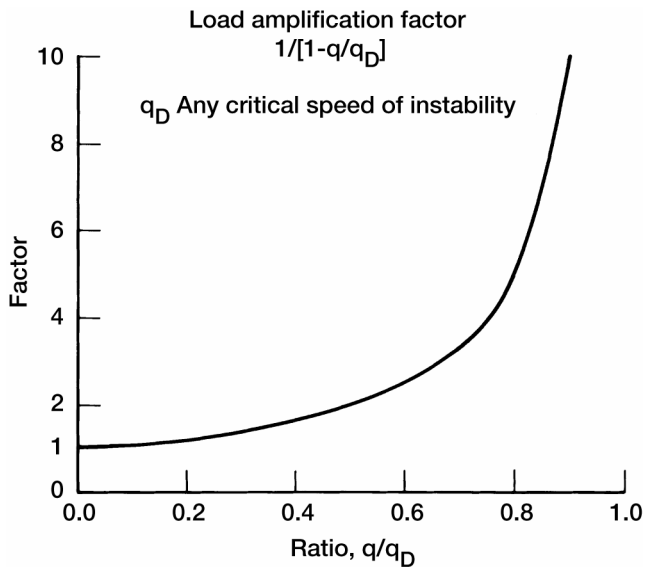
Figure 15.—Load amplification factor on close approach to a critical speed.
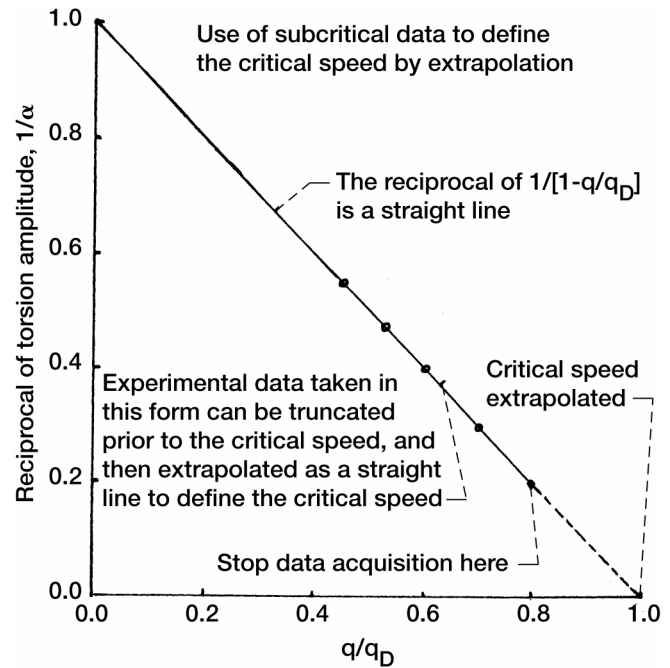
Figure 16.—Load amplification measured during experimental flutter testing.

Flutter Criteria

Several flutter criteria have been developed by the British, by NASA, by USAF, through a Navy contract and probably by each company separately as proprietary data. The objective of the criteria is to act as a surrogate for the flutter analysis, to cover all the key variables and to do so in the shortest possible time. Analysis of the criteria show several types exist:

1.) torsion influence coefficient at a strategic location spanwise, say 0.75 span
2.) torsion natural frequency expressed as a dimensionless variable
3.) torsional stiffness, a three dimensional measure of stiffness from root to tip
4.) for all moving surfaces, a stiffness criterion was developed that provides a balance between root flexibility and flexibility in the lifting surface

The two principal criteria are items 2) and 3) above. Both are torsional stiffness criteria but criteria that differ in the nature of their construction. The torsional frequency criterion is a measure of the important torsional stiffness of the main structural box extracted from the mode shape in the first torsion vibration mode. It measures a root to tip stiffness in a mode derived from an inertial load obtained from the mass moment of inertia distribution about the elastic axis. The torsional stiffness criterion by contrast is also a measure of the important torsional stiffness of the main structural box but it is extracted from the mode shape obtained in the calculation of the torsional divergence speed. It measures the root to tip stiffness in a mode derived from an aerodynamic load obtained from the aero moments that produce divergence.

The latter has proved effective for the following reasons:

1.) no need to change an original estimate up to the point of the completed design
2.) divergence mode shape used in the estimate is similar to the flutter mode shape

3.) the mode shape for flutter is determined by the aero moments more than by the inertial moments

4.) variables needed to determine required stiffness appear in the torsional stiffness criterion but not in the frequency criterion

The experience level associated with the stiffness criterion above has covered five decades of every conceivable design configuration. It is especially easy to apply. Solutions for optimum mode shape have been developed using the stiffness criterion to fulfill a need for an optimum solution for the flutter problem. Precise definition of permissible root flexibility for an all moving surface were accomplished using a variant of the stiffness criterion. Were a flutter program to produce an unsatisfactory result, the criterion has been reexamined and upgraded as needed. At the end of the presentation of this successful flutter criterion, a spread sheet is presented, table 4. It also contains a new technique for matrix iteration, a unique plus available from the spread sheet format. The result shortens the calculation.

TABLE 4.—TORSIONAL DIVERGENCE

	Chord			**Mode**	**Moment**	**Torsion Constant**	**ΣM/J ↑**		
	c inch	c^2		α_1	$\Sigma c^2 \alpha_1 \downarrow$	J inch^4	α_2	α_1/α_2
Tip	106.5	11342.25		1	11342.25	1256	32.06613	0.031186
	129.5	16770.25		0.718	23383.29	3271	23.03568	0.031169
	152.5	23256.25		0.4954	34904.44	6804	15.88701	0.031183
	175.5	30800.25		0.3354	45234.84	13085	10.75702	0.03118
	198.5	39402.25		0.2275	54198.85	22768	7.300022	0.031164
	221.5	49062.25		0.1534	61725.00	27218	4.919539	0.031182
	244.5	59780.25		0.08268	66667.63	57051	2.651738	0.03118
	267.5	71556.25		0.04624	69976.39	96829	1.483176	0.031176
	290.5	84390.25		0.0237	71976.44	159637	0.760496	0.031164
Root	313.5	98282.25		0.00965	72924.87	235530	0.30962	0.031167

0.031174 Avg.= K_D

Strip Theory:
$$L = 2\pi \alpha q c \, \Delta x$$

$$M = 2\pi \alpha q c^2 \, \Delta x \frac{(1/2 + a)}{2}$$

$$\Delta x = constant, = 102 \text{ inches}$$

$$K_D = \pi q (\Delta x)^2 (1/2 + a)/G = Avg.$$

$$V_D = \frac{262{,}670}{\Delta x} \sqrt{\frac{K_D}{(1/2 + a)}} = 829 \text{ mph, indicated incompressible}$$

$$e_e = \frac{3.45 \times 10^6 \times K_D}{(\Delta x)^2} = \frac{3.45 \times 10^6 \times 0.031174}{(102^2)} = 10.3$$

Note: Using Excel spreadsheet, convergence was easily obtained by continually adjusting α_1 to produce a constant value in the last column.

The design process is optimized by incorporating loads, flutter, strength, twist and camber solutions simultaneously into wing design. An optimum design is found by iteration. This was possible based on enhanced computer capability. It is almost mandatory for composite structure design as the design direction moved away from isotropic materials to anisotropic embedded fibers. Fibers in composite structures are subject to orientation in any direction and layered in such a way that sophisticated solutions could be found for each detail design requirement. It is a feature of this approach that a flutter analysis is incorporated in each design iteration. That analysis is sensitive as always to the torsional stiffness of the lifting surface and for a composite material this is provided by + and –45 degree fibers. The stiffness criterion provides a means to check the result at a tiny fraction of the time spent on iterating for the optimum, a process covered in preliminary design.

Simplified Criterion for Torsional Stiffness Required for Flutter

This criterion was constructed to include each known and significant flutter variable. The accuracy target for the criterion is to provide at initiation of a new design a level of stiffness required by the flutter phenomenon that would not require change during production design. For already completed designs, it directly measures the torsional stiffness built into that design. It permits an assessment of the design approach as executed by different design teams. When flutter occurs, it allows one to answer the question: was flutter due to a deficiency in stiffness. Using this measure of stiffness for both transports and general aviation airplanes, values of the effective eccentricity, e_e, are shown to increase proportionate to the dynamic pressure defined by the limit design speed. The starting point for the theoretical development is the work of Alexander Flax, The Influence of Structural Deformation on the Airplane Characteristics, Journal of Aeronautical Sciences, January 1945 (ref. 6). The divergence formula from this reference is:

$$q = \frac{\int GJ\theta'^2 dx}{\int c^2\theta^2 C_{l_\alpha} e\, dx} \tag{3}$$

where

q	=	dynamic pressure, psi
GJ	=	torsional stiffness of the wing cross section
θ	=	torsion mode shape, a function of span
θ'	=	first derivative of the modal parameter
C_{l_α}	=	lift curve slope
e	=	chordwise eccentricity between aerodynamic center and elastic axis
c	=	wing chord, inches
$\int dx$	=	indicates spanwise integration

Put the aerodynamic variables on the left and the structural variables on the right.

$$C_{l_\alpha}\, e\, q = \frac{\int GJ\theta'^2 dx}{\int c^2\theta^2 dx} \tag{4}$$

A label, the effective eccentricity, e_e, is attached to either grouping. For a completed design, the structural variables on the right-hand side result in a single number, a measure of the torsional stiffness of a lifting surface. This number defines the value of the criterion, a torsional stiffness index. Table 5 contains a list of 50 of these including most of the airplanes discussed in this paper. For preliminary design, the aerodynamic variables on the left side are also useful in defining a requirement.

TABLE 5.—TABLE OF STIFFNESS MEASURE, EFFECTIVE ECCENTRICITY
NORTH AMERICAN AVIATION

REPORT NA-54-619		DATE 6-8-54		***EXTENDED***

TABLE OF STIFFNESS MEASURE, EFFECTIVE ECCENTRICITY

WING		HORIZ. TAIL	
XF86	10.9	XF86	18.0
T-28	10.0	T-28	17.4
XAJ-l	8.6	XAJ-l	17.7
XA2J-l	8.8	XA2J-l	7.5
B45A	12.3	B45A SMALL	11.5
B45C	15.0	B45A EXTNDD	15.6
		ALL MOVING HORIZ TAIL	
F100A	16.0	YF100 (7%)	11.6
F100B	14.4	F100A (3.5%)	8.2
F107 ORIG	15.3	F100A REDES	11.7
F107 TIP DBLR	21.0	F107	12.0
XFJ-1	12.7		
FJ-2	13.0	T-38	10.0
FJ-4	13.4		
B47	10.0	ALL MOVING VERT. TAIL	
B51	6.3		
XF9l	3.1	F107 ORIG DES	15.3
F84	15.7	F107 AS BUILT	11.6
XF3Hl-l	14.5	F107 ROOT STIFFND	13.37
CONSTITUTION	3.7 (XR60-1)	F107 REDESIG 5 3/4% THICK @ROOT	
SNARK	13.8		17.6
DC-10	6.67		
B747	4.4		
B707-320	6.0		
L1011	9.13	L1011	5.7
DC-8	6.95		
AERO COMMANDER 680F			
	10.0		
SHUTTLE	10.0		
N156F	14.4		

Notes:
1. These stiffness measures can be used by reference to a vehicle in the same speed range.
2. These stiffness measures will correlate best if arrayed against their design limit speeds; in civil parlance, design dive speeds.
3. These stiffness measures were defined using strip theory. This would be characterized by a relatively more outboard load. It thereby emphasizes tip stiffness. A strip theory flutter analysis would do the same.
4. The variability is a result of the many different design groups controlling the design and the many different design limit speeds.
5. In some cases the flutter group has participated in the stiffness design and in some cases it has not.

The chordwise eccentricity for different aeroelastic problems is illustrated:
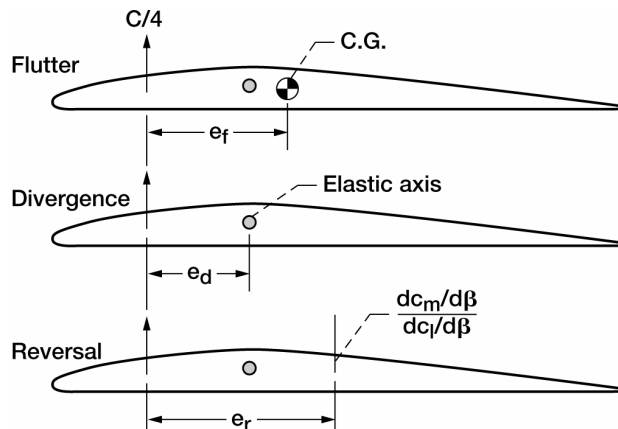
Their similarity is apparent. As the aerodynamic center moves aft from the quarter chord on approach to transonic and supersonic speeds, the eccentricity, *e*, identified in each figure is greatly diminished. For all three phenomena, both the aerodynamic center (a.c.) and the elastic axis (e.a.) remain the same. Flutter is sensitive to the c.g. position, divergence involves only the a.c. and the e.a.; and reversal depends on the center of pressure for trailing edge control surface movement. For a trailing edge control surface, however, the center of pressure for incremental lift moves to the midpoint of the control surface greatly increasing the eccentricity for reversal and effectively preventing the use of trailing edge controls at supersonic speeds for their normal spanwise position near the wing tip. The sensitivity to the eccentricity may not be immediately apparent, but an increase in eccentricity from a c.g. position at 40 percent chord to 46 percent chord resulted in a requirement for a 36 percent increase in stiffness. This describes an actual case that resulted from addition of a spoiler just forward of the trailing edge flap at midspan. The relatively heavy weight of the spoiler moved the c.g. significantly further aft on the chord. The sensitivity is shown in figure 9. In the original development of the torsional stiffness criterion it was necessary to extend the work beyond that of reference 6. A broad review of available flutter data was undertaken to find and quantify other variables important to flutter: area, aspect ratio, taper ratio, airfoil thickness, and the effect of aerodynamic heating on modulus. These variables naturally divide into those affecting the stiffness requirement directly and those affecting the structure and the resulting weight of the torque box. The two variables affecting stiffness are sweep, and the chordwise location of the sectional center of gravity. Variables affecting structural geometry and the weight of material in the torque box include thickness ratio, taper ratio, span, material, temperature environment and torque box efficiency. These variables are expressed in a form most easily used by preliminary design. To clarify the contributions of the many variables to either stiffness or weight, the variables are listed under the parameter affected:

Stiffness	Weight
lift curve slope	taper ratio
chordwise eccentricity	airfoil thickness/chord ratio
dynamic pressure	structural span
sweep angle at c/4	torque box efficiency, defined as the (dimensionless) torque box area divided by the (dimensionless) torque box perimeter

Thus the stiffness requirement in the form of the effective eccentricity becomes:

$$e_e = C_{l_\alpha}\, e\, q \times f\!\left(\Lambda_{c/4}\right) \tag{5}$$

where

$$f\!\left(\Lambda_{c/4}\right) = 0.4 + 0.7\cos\left(\Lambda_{c/4} - 10^\circ\right)$$

The extended definition of required stiffness is seen in the weight equation, table 1.

An extensive list of the stiffness indices has been kept as an historical accounting for a period of 5 decades. Although designs have been built on both jumbo jets and general aviation airplanes by different design teams that were later clearly seen as deficient in stiffness, the process is often self correcting as design teams encounter service difficulties and return to stiffness levels defined by the flutter community as a whole. A method was developed to measure the underlying fundamental requirement for flutter, torsional stiffness. An Excel spreadsheet example calculation is given in table 4.

The Space Shuttle preliminary design was prepared in this way. After flutter analysis, flutter model tests at subsonic, transonic and supersonic Mach numbers in five different wind tunnels, the design did not require change. The lifting surface on the SPRINT hypersonic missile interceptor with a dynamic pressure of 100,000 psf was also prepared from this criterion and, likewise, was proven successful at Mach 10 and elevated temperature in the lower atmosphere.

A recent calculation for wing, horizontal and vertical stabilizers of a new large jet transport showed the following values for the stiffness index:

Wing	8.84
Horizontal stabilizer	8.81
Vertical stabilizer	9.7

The design currently certified and flying showed relatively constant stiffness indices.

To apply the stiffness requirement to a particular wing design in a preliminary design proposal, 1000 candidates may be examined to locate an optimum design. Requirements from all disciplines are combined, summarized in terms of weight and using weight and configuration, performance is determined. The weight equation developed for flutter is thus one of many similar expressions developed for other disciplines.

Similarities and Differences Between the Two Key Criteria

The frequency criterion developed by NASA and used by USAF will be reformulated to allow comparison to the stiffness criterion presented above.

Square the frequency criterion:

$$\left[\frac{b\omega_\alpha}{V} \sqrt{\mu r_\alpha^2} \right]^2 = \frac{b^2 \omega_\alpha^2 \mu r_\alpha^2}{V^2} \tag{6}$$

Substitute $\dfrac{m}{\pi \rho b^2}$ for μ: $\qquad \dfrac{\omega_\alpha^2 m r_\alpha^2}{\pi \rho V^2}$

Substitute I_α for mr_α^2: $\qquad \dfrac{\omega_\alpha^2 I_\alpha}{\pi \rho V^2}$

Substitute K_α for $\omega_\alpha^2 I_\alpha$ and q for $\dfrac{1}{2}\rho V^2$: $\quad \dfrac{K_\alpha}{2\pi q}$

These kinds of simplified flutter criterion are used to assure an adequate level of torsional stiffness, the key design variable which places these aeroelastic instabilities well beyond the flight speeds. With all other conditions and requirements equal, designs of different size and configuration can be defined using the same value for the stiffness index used in a previous design. In the above comparison of the two criteria it was shown that the NASA frequency criterion requires that the torsional stiffness be increased proportionately to an increase in the dynamic pressure. Since it omits all other flutter variables it is insufficient and incomplete, as shown by the stiffness criterion in equation 2 and 3 and in table 1.

Lifting Surface Strength vs Stiffness Requirements

A comparison between strength requirements and stiffness requirements shows that in the normal design process for general aviation airplanes the strength requirements will also generally fulfill requirements for stiffness up to approximately 200 mph. Beyond that speed, stiffness requirements will likely exceed strength requirements and the design process must recognize the requirement for adequate torsional stiffness and what other flutter requirements may be needed. Margins of safety attached to strength and stiffness vary considerably. A long-standing factor of safety for strength requirements has been a factor of 1.5, but the civil stiffness requirements have

recently been reduced and now require only a flutter speed with a 15 percent margin above design dive speed. This equates to a stiffness factor of safety of only 32 percent ($1.15^2 - 1.0$). Consideration of the load amplification shown in figure 15 suggests there is no justification for this difference. Consideration of the correlation of accident rates with stiffness would also suggest a larger margin is needed on the stiffness related aspects of the design.

Examination of the weight equation for flutter given in table 1 shows three variables, squared or cubed, plus the velocity squared term included in the effective eccentricity. Each of these four exponents is to a one greater power than the corresponding exponents that would be used in a weight equation for strength.

Three quite different aspects of the regulatory standards will be presented next, the fail safety requirement applicable to flutter, the reliability standard and the effect of less than perfect maintenance characterized by small flaws.

Fail Safety

Flutter requirements are unique in requiring both fail safety and damage tolerance. Fail safety is a requirement that on the occurrence of any structural failure, no flutter will result. "Failure of any single element of structure ... any single failure in any flutter damper system must be considered ..., any other combinations of failures ... not shown to be extremely improbable" Reference FAR Part 25.629.

Damage Tolerance

Under FAR Part 25.629(d) Failures, Malfunctions and Adverse Conditions, "Any damage or failure conditions required or selected for investigation by 25.571 must be considered ... and any damage, failure, or malfunction considered under 25.631, 25.671, 25.672, and 25.1309 ... and discrete source damage conditions of 25.571(e)".

Reliability

The general requirement for reliability is that systems, equipment and components whose functioning is required must be designed to ensure:

1.) they perform their intended function under any foreseeable operating condition
2.) that the occurrence of any failure which would prevent continued safe flight and landing is extremely improbable.

The reliability standard is interpreted to mean that the probability of failure shall be less than 10^{-9} per flight hour. This standard of quality and excellence accounts for the safety in transport category, Reference FAR Part 25.1309. Deviation from this standard shows the consequences of maintenance with small flaws.

Maintenance With Small Flaws Leads to Fatal Accidents

A math model was constructed of a process of accruing small maintenance flaws over a period of time for the purpose of examining the question what size flaws and what number of flaws would account for two fatal accidents in a fleet of 500 transports in one year, a real case. A probabilistic approach based on normal distributions of loads and strength was used. Since propulsion, electrical, electronic, hydraulic, fuel and control systems are involved, it was assumed that the structural model could be used to represent failures in all systems. The following assumptions were made to start the system and the variable to be finally determined would be the size of the maintenance flaws:

1.) flaws accrue for a period of 6 years
2.) for a vehicle of 2,500,000 parts, 10 percent or 250,000 parts were capable of generating a fatal accident

3.) 1 percent of the maintenance actions were flawed. The number of maintenance actions (including inspection) covered 4,000 parts per 10,000 flight hours. If 1 percent were flawed, it meant 40 items were flawed in 10,000 hours of flight.

4.) 1 G static load plus gust and maneuver loads are normally distributed about 1 G. Strength is normally distributed about a mean to be determined

5.) actually two solutions are developed, one for the healthy airplane and one for the airplane with flaws, their difference defining the reduction in mean strength that would account for the two accidents.

6.) utilization of each airplane was 2400 hours per year, a total of 7,200,000 hours for 500 airplanes over 6 years. For two fatal accidents in the 6 years, this leads to an accident rate of 1 per 3,600,000 hours.

7.) the number of bad parts derived from the above data is 28,800 bad parts in 6 yrs. The part failure rate derived from the above two numbers is 10^{-11} per hour.

The results are graphed in figures 17 and 18. These two previously calculated failure rates are transformed into the number of standard deviations from the mean where the two distributions overlap. Failure rates are determined from figure 18 and their meaning is presented by the graph in figure 17 to show the extent of the overlap (where the two distributions overlap, the area formed is a measure of the probability of failure). As can be seen from figure 17, the area of overlap is so small that it is less than the width of the line representing the horizontal axis of the graph. The two distributions overlap where the standard deviation for each is 6.67, determined from figure 18. For comparison, the required failure rate for the original healthy airplane was also estimated in the same way. The number of good parts was 250,000 and the failure rate was taken exactly as the reliability standard, 1 fatal accident per 10^9 hours. In this case the part failure rate is the division of these two numbers, 1 per 2.5×10^{-14} hours. The math model provides an analysis that combines safety and maintenance. A too coarse screen to either instigate or withhold maintenance determines whether the product will meet the reliability standard or fall short, and whether fatal accidents will occur that would not otherwise have occurred. The total process is out of the range of perception and buried in numbers so small as to obscure their meaning. Thus effective maintenance depends on the mathematics of extremely remote events.
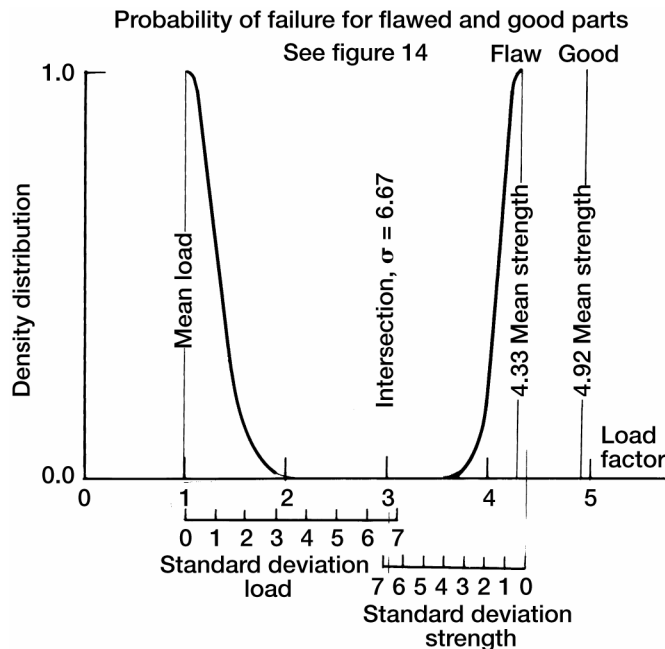
Figure 17.—Maintenance with small flaws.
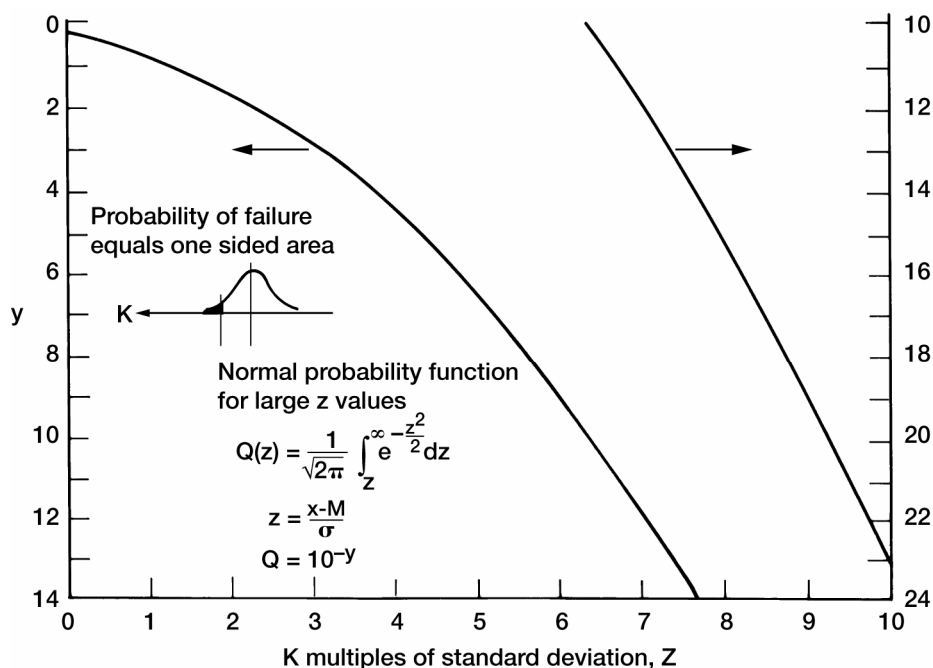
Figure 18.—Normal probability curves at large values of standard deviation.

The analysis shows that a reduction of 12 percent in mean strength led to an increased probability of the occurrence of the two fatal accident from 10^{-9} per flight hour to 10^{-6} per flight hour. Only a small loss in mean strength from 4.92 to 4.33 g for 28,800 bad parts produced a 1000 fold increase in risk. The exercise was supported by other analyses:

1.) analysis of the accidents and incidents in this 500 airplane fleet,
2.) a comparison of causes of fatal accidents in other major domestic fleets, and
3.) a critique by a recognized professional engineer for probability analyses

The analysis shows system safety depends on operations at the very limits of human perfection. Maintenance with small flaws greatly increases the probability of failure. The model was constructed with plausible inputs and subsequently checked as indicated. The analysis also suggests the system currently in operation in transport category lies far beyond what most engineers might have expected in terms of ruggedness and durability.

The analysis was a test of the ability to describe the source of two accidents in one fleet of 500 airplanes in a one year period—an actual case. The nature of the accidents were such as to identify the two accidents as maintenance related.

Conclusions

1.) The status of airplane flutter as it relates to the many safety issues has been reviewed. By the 1940s the method for conducting a flutter analysis had proven itself in many key high speed airplane developments. Prior to the time that the ground vibration test and the flight flutter test could be conducted, the design had been completed. In-service experience on these airplanes by the 1950s showed that sufficient problems arose that large risks were present that originated in the initial design and it was necessary to validate the design prior to manufacture and flight. The ability to build dynamic models and subject these to wind tunnel test has been demonstrated as early as

1940. This-off-the-shelf capability was considered the missing link therefore and the military customer pressed for its inclusion in each program.

2.) The flutter analysis depended on very accurate descriptions of unsteady aerodynamics and flexible structure of the special character needed for flutter prevention. In addition to dynamic scaled models using beam technology, finite element structural models and aerodynamic influence coefficients were developed during the 1950s to fulfill a need for improved techniques. The scaled models in low speed tunnels have proved to be a durable technology and when coupled with the full knowledge of the transonic dip, results from low speed tunnel tests were used to qualify airplanes for supersonic speeds.

3.) These two developments, the scaled dynamic model and the improvements in the flutter analysis, allowed the design and construction of advanced airplanes for all speed regimes free of flutter both in the initial flight testing and the later in-service usage.

4.) The cause of the flutter problems given were due mainly to a failure to completely describe local structural flexibilities at locations in primary structure where transitioning occurred to small local structures where loads became concentrated.

5.) An attempted correlation between accident rates and three aeroelastic variables, stiffness, span and speed suggested a relationship exists. The correlation is enticing but a solid physical relationship is not known. More work is needed to verify or refute the attempted correlation.

6.) Computing capability following the Fridens and the Marchants depended on IBM mainframes with their cost burden—a new model every year and the need to adapt all the programs with new software. At North American the computer was initially used 8 hours every day on optimizing new designs by Latin Squares for competitive bids on new contracts. The flutter equations played a key role in providing an optimum design with flutter requirements already incorporated.

Appendix A
Correlation of Accident Rates With Speed and Other Aeroelastic Variables
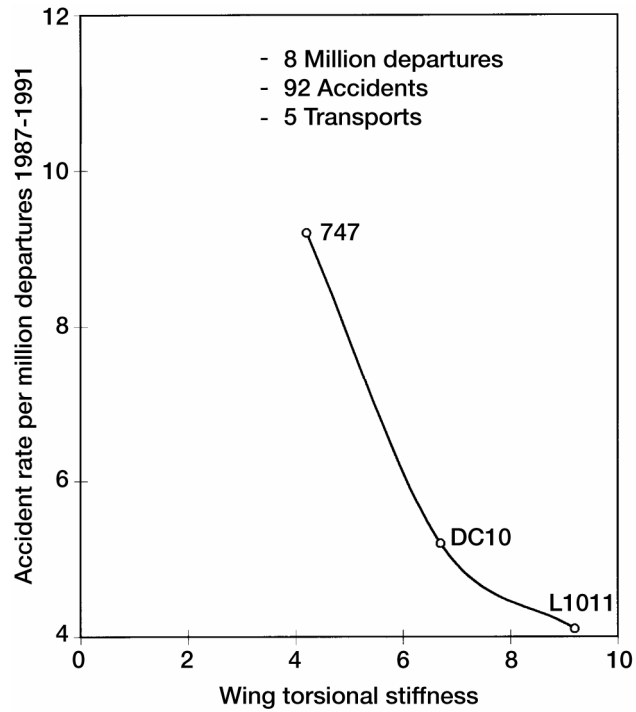
Figure A-1.—Correlation accident rate vs wing stiffness.
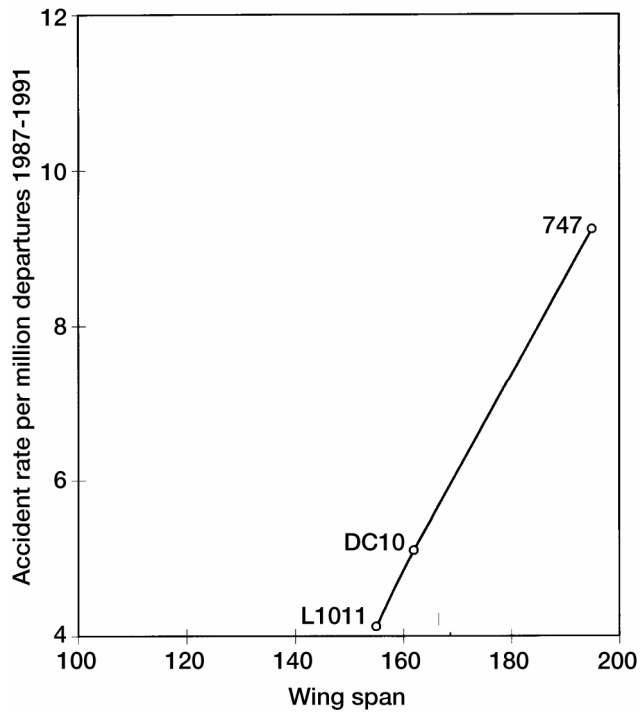
Figure A-2.—Correlation accident rate vs wing span.
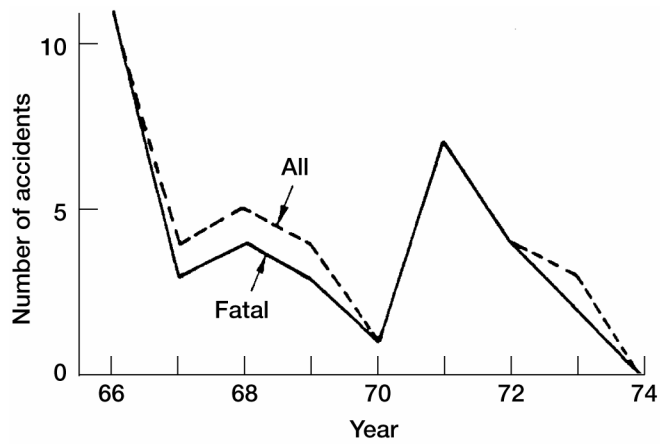
Figure A-3.—IFAF Accident history PA-24
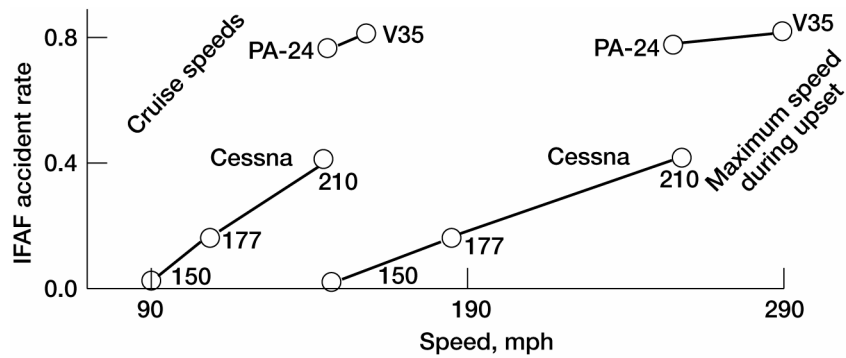
Figure A-4.—Effect of speed on accident rates for five fleets.

Appendix B
Aircraft Photos

Figure B–1.—X–15.

Figure B–2.—X–15A.
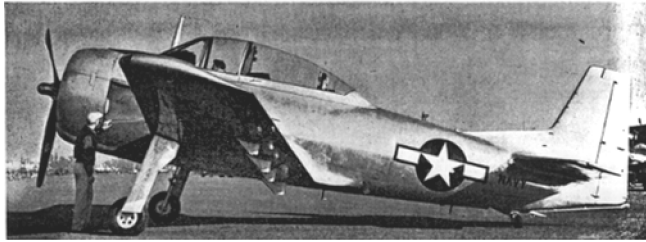
Figure B–3.—XSN2J.

Figure B–4.—T28 (side view).

Figure B–5.—T28 (perspective).

Figure B–6.—T38.

Figure B–7.—F–5E.

Figure B–8.—XFJ–2B Fury.

Figure B–9.—N–156F.

Figure B–10.—Space shuttle.

Figure B–11.—Sprint missile.

References

1. Smilg, B.; and Wasserman, L.S.: Application of Three-Dimensional Flutter Theory to Aircraft Structures. U.S. Army TR–4798, 1942.
2. U.S. Army TR–5153.
3. Airplane Strength and Rigidity Vibration, Flutter, and Divergence. MIL–A–8870, 1990.
4. Airworthiness Standards: Normal, Utility, Acrobatic, and Commuter Category Airplanes. Federal Aviation Regulations, part 23.
5. Airworthiness Standards: Transport Category Airplanes. Federal Aviation Regulations, part 25.
6. Flax, A.H.: The Influence of Structural Deformation on Airplane Characteristics. J. Aero. Sci., vol. 12, no. 1, 1945.

Bibliography

Harris, G.: Flutter Criteria for Preliminary Design. Engineering Report 2–53450/3R–467, Bureau of Naval Weapons Contract NOW 61–1072c, 1963.

Flutter Prevention Handbook: A Preliminary Collection[*]

D.D. Liu, D. Sarhaddi, and F.M. Piolenc
ZONA Technology, Inc.
9489 E. Ironwood Square Drive, Suite 100
Scottsdale, Arizona 85258–4578

Part D: Aeroservoelastic Instability, Case Study A

Raymond P. Peloubet, Jr.

Foreword

Abstract

The author presents two cases of aeroservoelastic instability, in which configurations that were flutter-stable without their flight control systems becomes unstable at certain regimes with the control systems engaged.

Part A discusses a high performance fighter with fly-by-wire control which showed antisymmetric oscillation in early flight tests. Flutter analysis and wind tunnel tests showed the aircraft minus flight control system was stable. The Nyquist Criterion was used to calculate the stability of the airplane with the control system engaged; it showed an unstable antisymmetric oscillation mode very close in frequency to that observed in flight. Calculated control loop gain adjustments were tested in flight and found to correct the problem.

Part B concerns a fighter prototype with fly-by-wire control which showed a pitching motion in a narrow range of high-subsonic Mach numbers, at a frequency well below that of the first symmetric vibration mode of the

---

structure and well above the rigid-body short-period mode. Subsequent flight tests showed that reducing the pitch loop gain eliminated the problem. Although the immediate problem was solved, two methods for measuring the open-loop frequency response function of the flight control system without actually opening the feedback loops were applied during flight tests. Both methods are explained and discussed.

Introduction

Flutter is an instability that is caused by the interaction of aerodynamic, elastic and inertia forces. The addition of servomechanism forces as a fourth set of interactive forces can cause a flutter stable configuration to become unstable. This type of instability has been labeled as an aeroservoelastic (ASE) instability.

The servomechanism forces are usually generated by control surface deflections which are produced by hydraulic actuators controlled by servo valves. The input to the servo valves is the sum of the inputs from the pilot and the feedback from flight control sensors which have been passed through flight control laws. The control laws can be mechanized either by analog or by digital systems. However, other types of servo mechanism forces, such as vectored thrust systems, can produce ASE instabilities.

An appreciation for the cause of ASE instabilities can be obtained by considering a typical design process. First, flight control laws are designed to cause the airplane to respond in the desired manner to pilot inputs throughout the airplane's operational envelope. These control laws are usually developed with the airplane considered to be rigid. Initially, the only flexibility effect considered is the modification of the stability derivatives due to aeroelasticity. The flight control law designer might take several steps to reduce the likelihood of encountering an ASE instability.

- Sensors might be located to minimize their response to certain natural modes of vibration. For example, vertical accelerometers might be located on the fuselage centerline close to a node line for the first fuselage bending mode. Similarly, pitch rate gyros might be located on the fuselage centerline near the maximum deflection on the first fuselage bending mode, where the slope would be zero and the pitch rate would be near zero.

- The flight control designer might select hydraulic actuators that have a low band pass. That is, the hydraulic actuator produces one degree of control surface deflection for one degree of command to the actuator for frequencies from zero to some cut-off frequency (for example, 3 Hz). Above the cut-off frequency, the actuator produces lower deflection which continues to decrease as the frequency increases.

- The flight control law designer can incorporate low pass filters in the control law which diminish the feedback signal for frequencies above some selected cut-off frequency, and/or notch filters which reduce the feedback signal in selected frequency bands.

However, in spite of these precautions, the response of one or more of the flight control sensors to the excitation of a structural natural mode of vibration might produce a feedback signal of sufficient magnitude and with the right phase angle to cause an ASE instability.

Sometimes it is difficult to determine if an instability encountered in flight is caused by flutter or ASE. That is, if the unstable boundary is approached at constant altitude by slowly increasing airspeed from the stable side of the boundary, the instability might first appear as constant amplitude oscillations for either type of instability. It is important to distinguish which type of instability is involved because the type of correction needed is different. If the instability is caused by flutter the needed correction might be to modify the structure, or the mass distribution, or the aerodynamic configuration (by adding vortex generators or fences, for example). If, on the other hand, the instability is an ASE instability, the solution is usually to modify the flight control system or control law.

If the flight control system lowers the flutter boundary by a small increment, modifications to the flight control system might only restore that small increment. Further incremental increases to the flutter boundary might well require "flutter type" modifications. If the flight control system increases the flutter boundary by a small increment,

further increases in the boundary might best be achieved by flutter type modifications. Sometimes, however, a modification to the flight control system or the addition of a separate independent control system can increase the flutter boundary substantially or remove it entirely. In these cases the control system is called a **flutter suppression system**.

A direct means of determining whether an instability encountered in flight is caused by flutter or ASE is to disengage the flight control system. This is a viable option if the ASE instability is caused by an autopilot and the pilot can override the autopilot with the basic flight controls. If, on the other hand, the instability is caused by a closed-loop flight control system in which small forces applied by the pilot to the flight controls produce large control surface deflections if the feedback loop is opened, disengaging the flight control system is not a viable option. That is, with the loop open, the pilot would be in danger of over controlling and subsequently losing control of the airplane. Furthermore, aircraft that are statically unstable and rely on the flight control system for stabilization would be statically unstable if the feedback loop were opened.

Methods used to distinguish a flutter instability from an ASE instability include:

(1) Comparing flutter analyses with ASE analyses,

(2) Conducting flight tests with a gradual reduction in flight control system gains (subject to flight control safety limitations) and

(3) Measuring the open-loop frequency functions in flight (without actually opening the flight control loop) at a sequence of flight conditions that approach the unstable boundary (this is discussed in Case Study A).

Case Study A Airplane Description

This case study is about a prototype of a highly maneuverable fighter aircraft that made its initial flight tests during the early part of the 1970 decade. One of the advanced technology concepts that it employed was the fly-by-wire flight control system. The connection between the cockpit controls and the servo valves for the hydraulic actuators for each control surface was electrical rather than mechanical. The conventional control systems at that time, transferred pilot-commanded deflections of the stick and rudder pedals via mechanical linkages to deflect the servo valves. The fly-by-wire system transformed pilot applied-stick and rudder forces into electrical signals which were sent to the servo valves by means of electrical lines. Pilot-applied stick forces produced deflections that were so small as to be virtually imperceptible, so the stick was called a **force stick**. The airplane was statically unstable over part of its operational envelope and the flight control system was used to stabilize the airplane.

The airplane with missiles mounted on the wing tip launchers is shown in figure 1. Control surfaces included flaperons on the wings, all-movable horizontal tail surfaces and a rudder. The locations of the servos that commanded the control surface actuators are shown. Electrical signals from the pilot controller and rudder pedals and the air data computer were input to the flight control computer which implemented the flight control laws. Electrical signals from the flight control computer were sent to the servos which commanded the control surface actuators. The airplane response to the control surface movement was sensed by the flight control sensors and the outputs of those sensors were returned to the flight control computer to close the loop. The flight control system had three primary loops:

- The longitudinal loop commanded the horizontal tail surfaces to move symmetrically; airplane response was sensed by the normal accelerometer, the pitch rate gyro and the angle of attack sensor.
- The roll loop commanded antisymmetric deflections of the flaperons and of the horizontal tail surfaces in the ratio of 1.0 degree flaperon to 0.25 degree horizontal tail; airplane response was sensed by the roll rate gyro.
- The yaw loop commanded the rudder and the airplane response was sensed by the roll rate gyro, the yaw rate gyro and the lateral accelerometer.
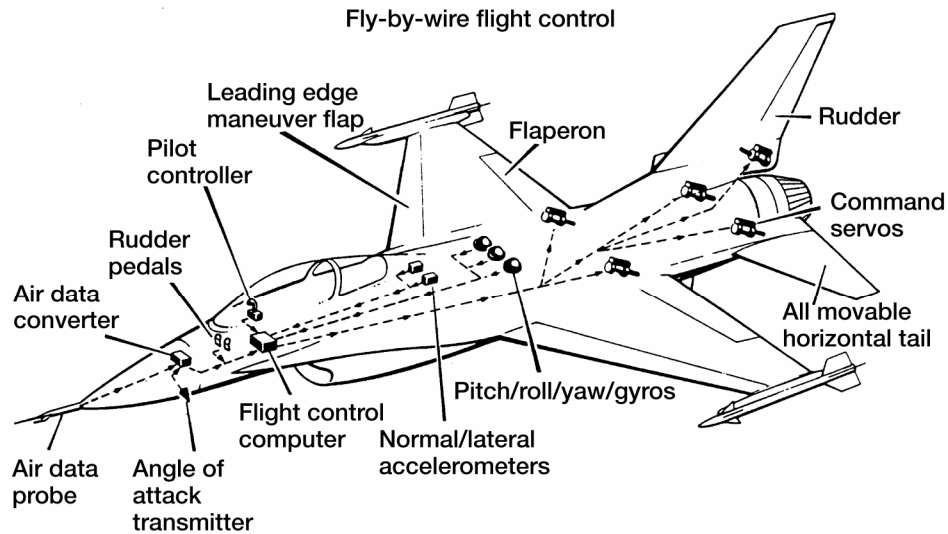
Figure 1.—Case study A airplane configuration.

Pre-Flight-Test Analyses and Tests

Flutter analyses were conducted without the flight control system. Analyses were conducted over a range of Mach numbers and altitudes. Several configurations of the airplane were analyzed, including configurations with and without wingtip missiles, for several fuel load conditions. These analyses indicated that the unaugmented (without the flight control system) airplane had at least a 20 percent flutter margin throughout its flight envelope.

Ground vibration tests were conducted with the airplane held by a soft suspension system. Hydraulic power was supplied to all control surface actuators but the feedback loops for all flight control system sensors were left open. With the tip missiles installed, the first two antisymmetric modes that were obtained by the ground vibration tests are shown in figure 2.

After the ground vibration tests, the finite element stiffness matrix of the airplane was modified to improve the correlation between computed and measured natural modes of vibration. Flutter analyses were repeated and they continued to show the unaugmented airplane to have at least a 20 percent flutter margin throughout its flight envelop.

A one-quarter scale flutter model of the airplane was tested on a cable system in the NASA Langley Transonic Dynamics Tunnel. The flight control system was not included in the model. The wind tunnel tests indicated that the unaugmented airplane with and without the tip missiles had at least a 20 percent flutter margin throughout its flight envelope.

Stability analyses of the airplane were conducted with the airplane considered to be a rigid body and with the flight control system engaged. Stability derivatives used in these analyses were modified to include the effects of static aeroelasticity. These analyses indicated that the augmented airplane was stable. Hence no aeroservo instabilities would be expected at any point in the flight envelope if the airplane were rigid.

Ground tests of the airplane were conducted with the airplane resting on its landing gear. An oscillatory input signal was applied to each set of control surfaces and the frequency of the input was varied over a broad range. Each control loop was opened, one at a time, and the open-loop frequency response function (FRF) (the ratio of feedback response to control surface input as a function of input frequency) was measured. Previous experience with this type of ground testing supported the belief at that time that if the magnitude of the measured frequency response function did not exceed 0.5 regardless of the phase angle, then the airplane would not experience any ASE instabilities in flight. These tests were conducted with the flight control system gains varied to simulate a large number of Mach-altitude flight conditions. These tests indicated that the airplane should be free of ASE instabilities throughout its flight envelope.

Mode #1 6.5 Hz

Mode #2 8.0 Hz
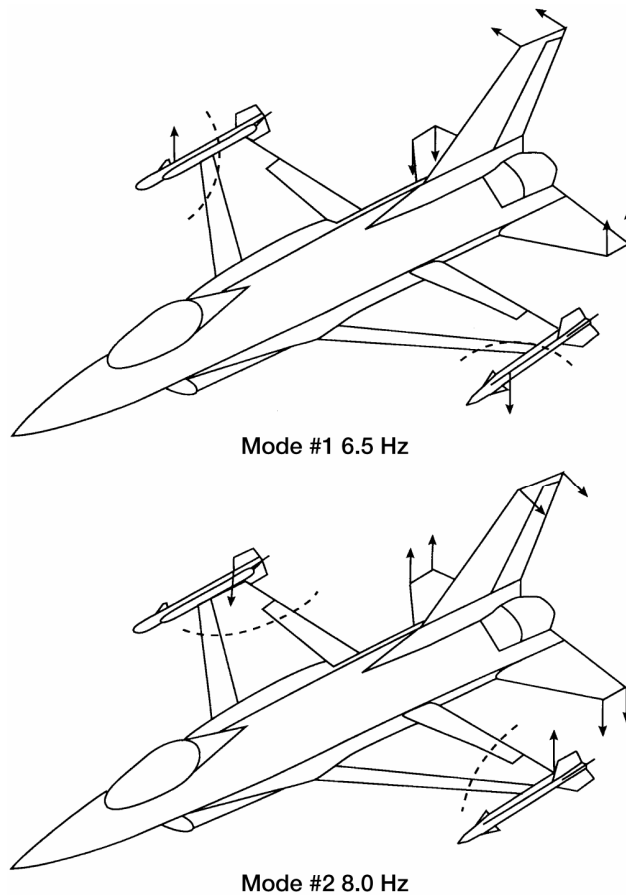
Figure 2.—Missiles on: missile pitch and first wing
bending modes.

An ASE analysis was conducted at one high Mach number, low altitude flight condition that was thought to be the most critical point. The results of these analyses indicated that the aircraft would be free of ASE instabilities at this flight condition. Subsequent post flight test analyses indicated that this flight condition was beyond the back side of the unstable region as predicted by analysis.

Flight Tests

Initial flights of the airplane were made with the wing tip missiles. In this configuration an antisymmetric oscillation at approximately 6.5 Hz was first experienced during flight number 8. The oscillation was experienced at the three flight conditions shown in figure 3. The airplane was being accelerated slowly at a constant altitude when the oscillation first began. The pilot climbed and reduced speed to get out of the unstable region. Then he climbed and increased Mach number until the instability was repeated. This operation was then repeated a third time.

The oscillation was again encountered during a sustained climb over a large altitude range on flight number 9, as shown in figure 3.

The instability was probed in a systematic manner on flight number 10. The airplane was flown at selected combinations of Mach number and altitude. These flight conditions were held constant while control surface pulses were applied. The roll pulse was the most effective in exciting the lowly damped response at 6.5 Hz as the unstable boundary was approached. But no excitation was required when the boundary was reached or exceeded. The unstable boundary at 20,000 feet was established. At 30,000 feet, however, the instability did not occur even for much higher Mach numbers.
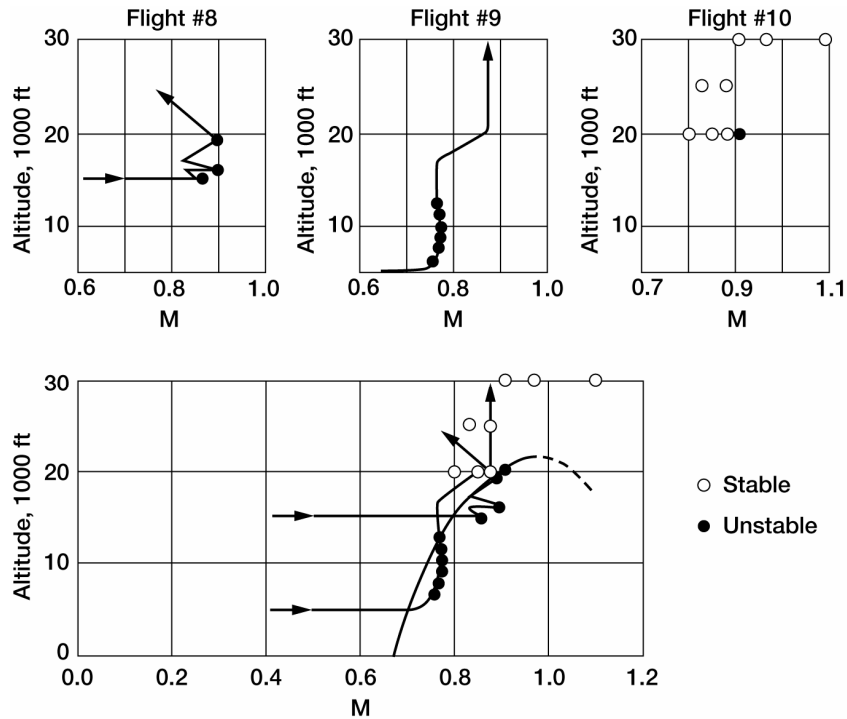
Figure 3.—Missile on: flight tests results with reference control system.

A composite of the stability data that was obtained during the three flights is shown in the lower part of figure 3. A line was drawn through the unstable points that were thought to be near the boundary of the instability and which divided all known stable flight conditions from all known unstable flight conditions. Since the instability did not exist at higher altitudes, the unstable boundary was expected to have a top and perhaps a back side as indicated by the dashed line continuation of the unstable boundary line.

During the 6.5 Hz antisymmetric oscillations, the output of the accelerometers mounted on the wing tip launchers, the horizontal tail tips and the vertical tail tip were consistent in magnitude and phase angle with the 6.5 Hz, first antisymmetric mode of vibration measured during the ground vibration tests and shown in figure 2.

Initially there was some uncertainty about whether the oscillations were caused by flutter or ASE. However, after a series of ASE analyses were conducted at 0.9 Mach number and sea level that indicated that the roll loop was causing an ASE instability, additional flight tests were conducted with systematic gain reductions in both the roll and yaw channels. These tests indicated that the instability no longer existed when the roll loop gain was reduced by 50 percent. There was no appreciable difference in the results when the yaw loop gain was reduced.

Post-Flight Analyses

To conduct the ASE analyses, it is desirable to add the flight control system equations to the equations of motion used to conduct flutter analyses. It is desirable because any change in stability can be attributed to the addition of the flight control equations and not be confused by the possibility that the change resulted from using a different method of analysis or a different modeling of the stiffness, mass or unsteady aerodynamics.

Unsteady aerodynamics are most conveniently expressed as a function of reduced frequency. Conventional V-g flutter analyses are conducted by constraining the equations of motion to harmonic motion, selecting a value of reduced frequency, computing the aerodynamic terms for the selected reduced frequency and then solving for the roots of the determinant of the equations of motion in the form of frequency and structural damping pairs. Using the selected reduced frequency, each frequency root can be used to compute a velocity associated with that root. The structural damping root can be plotted versus the velocity. By repeating this process for several selected reduced frequencies, each point on that curve can be interpreted to be the required structural damping to produce flutter at

the associated frequency. The point on the curve where the required structural damping agrees with the real structural damping is called the flutter point.

The flight control equations are usually expressed as a function of the Laplace variable. Hence, these equations can also be expressed as a function of frequency by substituting $i\omega$ for the Laplace variable s. For a selected velocity, frequency could be converted to reduced frequency so that the flight control equations could be expressed as a function of the reduced frequency to be compatible with the unsteady aerodynamics in the flutter equations. However, since velocity is an unknown variable in the flutter equations, only roots with velocity identical to the assumed velocity in the flight control equations would be valid solutions. Iterative methods would have to be applied in order to determine solutions that were compatible with the assumed value of velocity for the flight control equations.

A method for determining ASE stability characteristics was selected for the study airplane which employs the same equations of motion used in the flutter analysis. It requires selection of a velocity (Mach number, altitude and speed of sound) so the analyses can be conducted in the frequency domain. The flight control equations are combined with the flutter equations in the frequency domain. The stability of the closed loop system is determined by computing frequency response functions at selected flight conditions. The frequency response functions have a physical meaning and can be measured on the airplane.

The method of analysis is explained by referring to the block diagram of a closed loop single-input-single-output system shown in the upper left of figure 4. For the present application, consider an airplane with a flight control system consisting of only a roll loop and a single roll rate sensor. In the diagram, x_i would be the pilot commanded roll input signal. The symbol G would represent the transfer function relating roll rate response, x_o, to aileron deflection for the unaugmented airplane. The symbol H would represent the transfer function for the roll loop relating feedback response to the roll rate gyro input. The sensor response, x_o, to the pilot input for the closed loop system, expressed as a function of the Laplace variable, is

$$\frac{x_o}{x_i} = \frac{G}{1 + GH} \tag{1}$$

The stability of this closed-loop system can be assessed by determining whether the denominator $(1 + GH)$ has any zeros on the right hand side of the Laplace plane. If it has one or more zeros on the right-hand side, it is unstable. If it has no zeros on the right-hand side, it is stable. If a function of the Laplace variable is infinite at a value of the Laplace variable, it is said to have a pole at that value. Hence, if the function $(1 + GH)$ has a zero at some value of s on the right hand side of the Laplace variable plane, then the function $G/(1 + GH)$ has a pole at the same value of s.

The Nyquist criterion states that if a function of the Laplace variable is evaluated over a closed clockwise path that encloses the entire right hand side of the Laplace plane, the number of times (N) this function encloses the origin in the clockwise direction is equal to the difference between the number of zeros (Z) and the poles (P) on the right-hand side of the Laplace plane.

$$N = Z - P \tag{2}$$

The evaluation path is illustrated on the lower left part of figure 4. The path extends from the origin up the frequency axis to plus infinity. Then it follows a path that would be traced by a vector of infinite magnitude rotating from +90 degrees, to zero degrees, to –90 degrees. The path is then closed by following the frequency axis from minus infinity to zero. For this application the function $(1 + GH)$ would be evaluated for values of the Laplace variable along this path and plotted as illustrated by the lower center part of figure 4. In practice the function $(1+GH)$ would be plotted over a finite path along the frequency axis from zero to some selected positive upper frequency. The characteristics of the plot for higher frequencies and for the infinite magnitude part for the plot can usually be deduced. Also, since poles and zeros of the function $(1 + GH)$ are either real or appear as complex conjugate pairs, the plot of the function $(1 + GH)$ for negative frequencies is the mirror image of the plot for positive frequencies. The lower right part of figure 4 illustrates that the equivalent criteria is to determine the

s - Plane   1 + GH   GH

Z-P = N
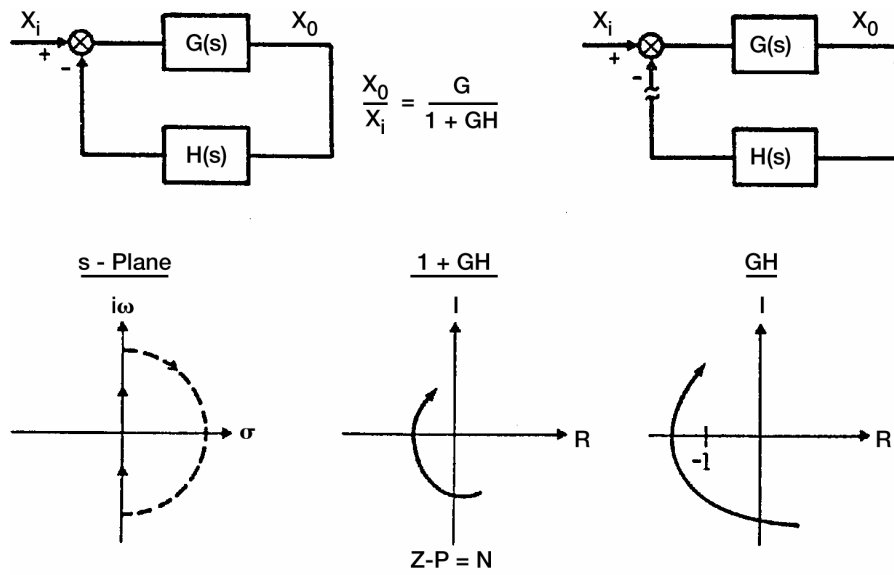
Figure 4.—Nyquist criteria.

number of clockwise enclosures of the minus one point by the function GH. And the upper right part of figure 4 illustrates that the physical interpretation of GH is the open-loop frequency response function relating the feedback to the pilot input. This is a measurable function.

By plotting the function GH, the number of enclosures of the minus one point can be determined. Hence, the number of zeros on the upper right quadrant of the Laplace plane can be computed

$$Z = N + P \tag{3}$$

The number of poles in GH is equal to the sum of the number of poles in G and H. If the unaugmented airplane is stable, G has no poles on the right-hand side of the Laplace plane. The number of poles on the right-hand side of H can be determined by inspecting the block diagram of the flight control system and usually there are none. So in practice, if the plot of GH shows no clockwise enclosures of the minus one point, the closed-loop system is stable. If the plot of GH shows one or more clockwise enclosures of the minus one point, the closed-loop system is unstable.

ASE stability was determined by computing the open-loop frequency response function over a frequency range from near zero to a selected upper frequency. The equations of motion employed rigid body side translation, roll and yaw and antisymmetric modes of vibration as generalized coordinates.

$$[A_{rs}]\{q_s\} = -\{A_{r\delta}\}\delta \tag{4}$$

where

$$A_{rs} = \left[1 - \left(\frac{\omega_r}{\omega}\right)^2 (1 + ig_r)\right] M_{rs} + Q_{rs} \quad r = s$$

$$= M_{rs} + Q_{rs} \quad r \neq s$$

$$A_{r\delta} = M_{r\delta} + Q_{r\delta}$$

In order to put the equations in the form usually employed in flutter analyses, they have been divided by $-\omega^2$.

$$Q_{rs} = \frac{1}{\omega^2} \int \phi_r \Delta p_s \, dS$$

$$Q_{r\delta} = \frac{1}{\omega^2} \iint \phi_r \Delta p_\delta \, dS$$

(5)

where S indicates the area of integration.

In equation (4) the structural damping in each mode can be assumed to be the same in every mode and treated as an unknown variable for the purpose of conducting flutter analyses. Setting the determinant of the left-hand side to zero and solving for the roots yields the variables that are plotted in the V-g type of flutter analysis.

Alternatively, the velocity, Mach number and altitude can be held constant and the determinant of the left-hand side of equation (4) can be computed as a function of frequency and plotted. The stability can be determined by the method of Landahl.

These analyses were conducted for the case study airplane at Mach 0.9 for several altitudes. The analyses indicated that the unaugmented airplane was stable.

A block diagram of the roll and yaw channels of the flight control system are shown on figure 5. The control system was an analog system. It had several gains that could be changed manually on the ground and it had gains that were computed as a function of the flight condition and changed automatically. The roll and yaw channels were essentially decoupled from the pitch channel. Two of the gains were varied as a function of the angle of attack and hence coupled with the pitch channel. However, these gains varied as a function of the steady angle of attack and provided virtually no dynamic coupling. The block labeled MGR is a manual gain in the roll channel; it was initially set at a value of 0.2. The block labeled M.G. is a manual gain in the aileron-rudder-interconnect; it was set a value of 1.0. The blocks labeled G_{ARI} and $G_\alpha/57.3$ are variable gains that are a function of the angle-of-attack. The block labeled F8 is a gain that varied as a function of the flight condition. The gains that varied as a function of the flight condition are tabulated in figure 6.
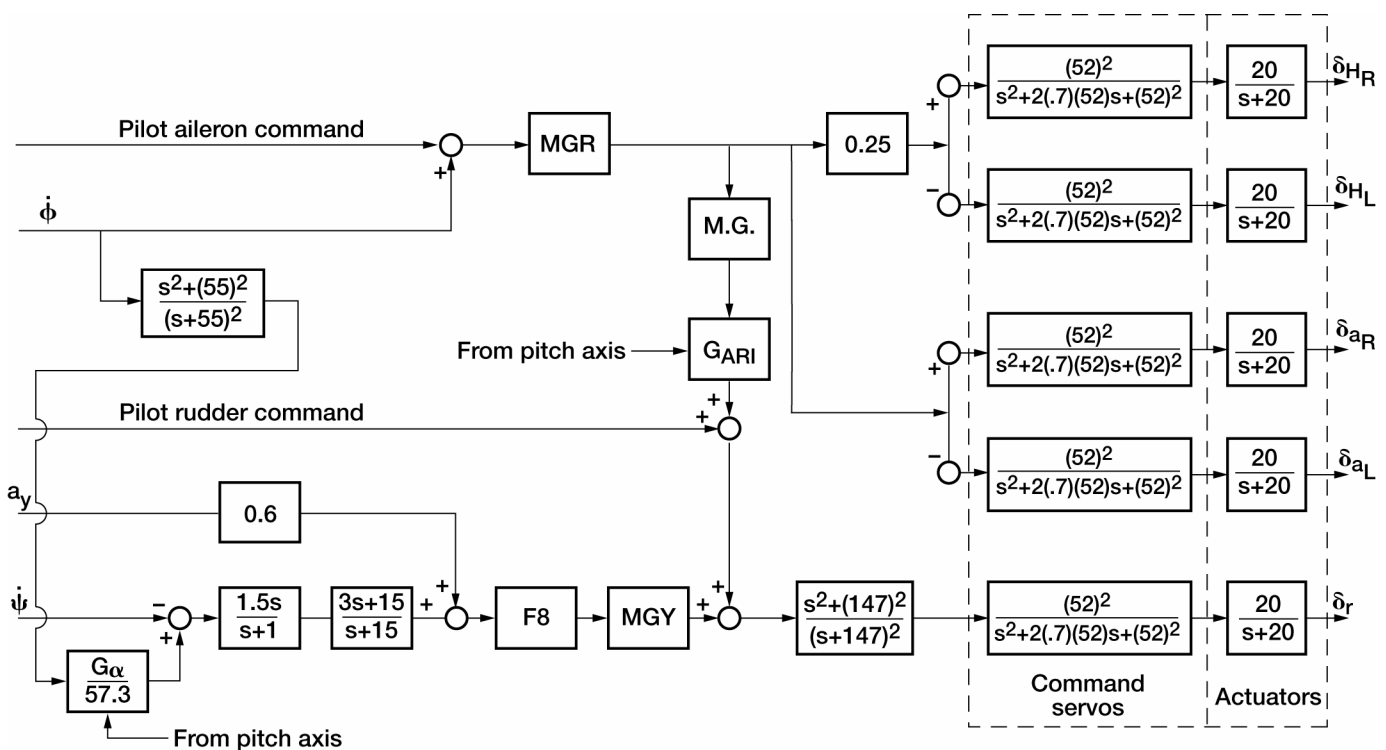
Figure 5.—Reference flight control system.

Figure 6 — Yaw loop (block diagram):

Inputs/outputs: δ_r → summing junction (+, −) → Airplane → outputs $\dot{\phi}$, $\dot{\psi}$, a_y

Feedback path blocks:
-1 ← $\dfrac{20}{s+20}$
$\dfrac{(52)^2}{s^2+2(.7)(52)s+(52)^2}$
$\dfrac{s^2+(147)^2}{(s+147)^2}$

Row 1: MGY — F8 — 0.6 — $\dfrac{(314)^2}{s^2+2(.6)(314)s+(314)^2}$ — Sensor

Row 2: MGY — F8 — $\dfrac{3s+15}{s+15}$ — $\dfrac{1.5s}{s+1}$ — $\dfrac{(314)^2}{s^2+2(.6)(314)s+(314)^2}$ — Sensor

Row 3: MGY — $\dfrac{1.5s}{s+1}$ — $\dfrac{G_\alpha}{57.3}$
F8 — $\dfrac{3s+15}{s+15}$ — $\dfrac{s^2+(55)^2}{(s+55)^2}$ — $\dfrac{(314)^2}{s^2+2(.6)(314)s+(314)^2}$ — Sensor

Row 4: G_{ARI} — M.G. — MGR — $\dfrac{(314)^2}{s^2+2(.6)(314)s+(314)^2}$ — Sensor

Lower left: δ_r → summing junction (+, −) → AP → Yaw

M = 0.9

Alt.	S.L.	5 K	15 K	20 K
F8	0.5	0.5	0.5	0.5
G/57.3	−.0105	−.0157	−.0262	−.0262
G_{ARI}	−.305	−.282	−.24	−.237

Figure 6.—Yaw loop.

The actuator was represented by a no-load, no-flow transfer function. The transfer function is different when the actuator is operating against a load and when high hydraulic flow rates are required. The no-load, no-flow transfer function was used because of its simplicity and because it was thought to be appropriate for predicting the onset of low amplitude ASE oscillations.

Similarly, the actuator stiffness was treated as a spring with constant stiffness. It was computed at a high frequency where the stiffness of the dynamic actuator approaches the stiffness of the hydraulic fluid. It appears in the equations of motion by way of the natural modes of vibration which were computed with a stiffness matrix in which each actuator spring was represented by a finite element.

The block diagram of the airplane with the yaw loop is shown in figure 6. Note that the sensor transfer functions have been added to the feedback loop. These transfer functions relate the sensor outputs to the airplane motion at the sensor locations. Note also that a minus one has been added so that the feedback signal subtracts from the pilot input. The flight control system block diagram in figure 5 shows the feedback signal adding to the pilot output. However, the negative sign is embedded in the feedback system or in the signs associated with control surface deflection.

The roll loop as used in the frequency response analyses is shown in figure 7. One degree of pilot commanded aileron produces one degree of aileron deflection plus 0.25 degrees of differential horizontal tail deflection.
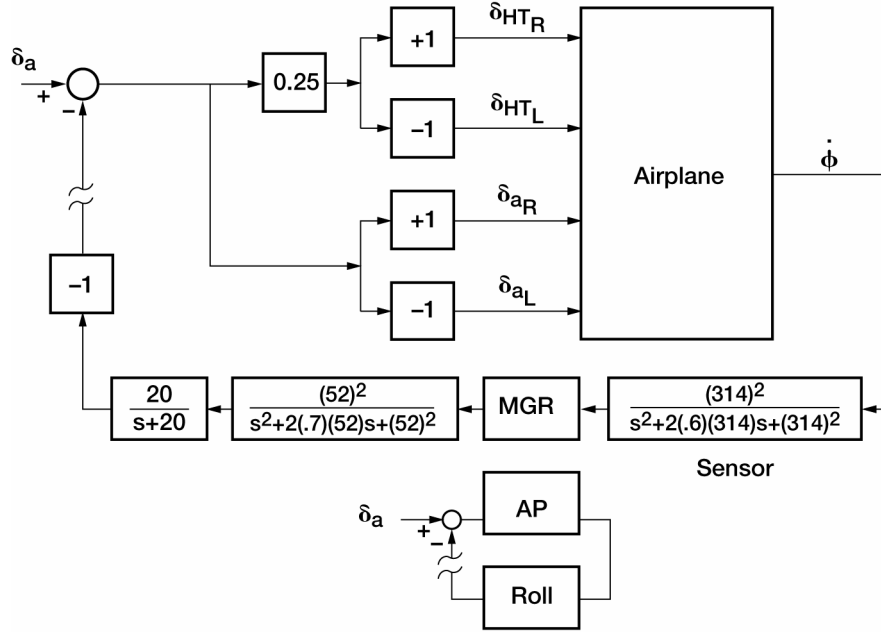
Figure 7.—Roll loop.

Equation (4) was used to compute the response of the generalized coordinates to rudder excitation.

$$\left\{ \frac{q_s}{\delta_r} \right\} = -\left[A_{rs} \right]^{-1} \left\{ A_{r\delta_r} \right\} \tag{6}$$

The frequency response function for each of the yaw loop sensors was computed as follows:

$$\frac{a_y}{\delta_r} = -\omega^2 \left[h_s \right] \left\{ \frac{q_s}{\delta_r} \right\}$$

$$\frac{\dot{\psi}}{\delta_r} = i\omega \left[\psi_s \right] \left\{ \frac{q_s}{\delta_r} \right\} \tag{7}$$

$$\frac{\dot{\phi}}{\delta_r} = i\omega \left[\phi_s \right] \left\{ \frac{q_s}{\delta_r} \right\}$$

where h_s is side deflection at the lateral accelerometer location,

Ψ_s is yaw deflection at the yaw rate gyro location,

φ_s is roll angle at the roll rate gyro location, for unit amount of generalized coordinates q_s.

The feedback at the point where the yaw loop is broken, shown in figure 6, can be expressed in the following form by substituting $i\omega$ for the Laplace variable s.

$$\frac{Feedback}{\delta_r} = T_{a_y}(\omega) \left(\frac{a_y}{\delta_r} \right) + T_{\dot{\psi}}(\omega) \left(\frac{\dot{\psi}}{\delta_r} \right) + T_{\dot{\phi}_Y}(\omega) \left(\frac{\dot{\phi}}{\delta_r} \right) \tag{8}$$

Substituting equation (7) into equation (8) yields the frequency response function relating the feedback in the yaw loop to rudder excitation with both the yaw and roll loops open. This function is plotted in polar form on the left side of figure 8 for Mach 0.9 sea level flight condition. The upper left part shows the function when only the three rigid body degrees of freedom (DOF) are used. This figure has two scales. All data plotted inside the unit circle have a scale from zero to unity. Outside the unit circle, the scale is from unity to 11.4. This figure shows no enclosures of the minus one point. It is concluded that if the yaw loop were closed, the rigid body representation of the airplane would have no ASE instabilities.
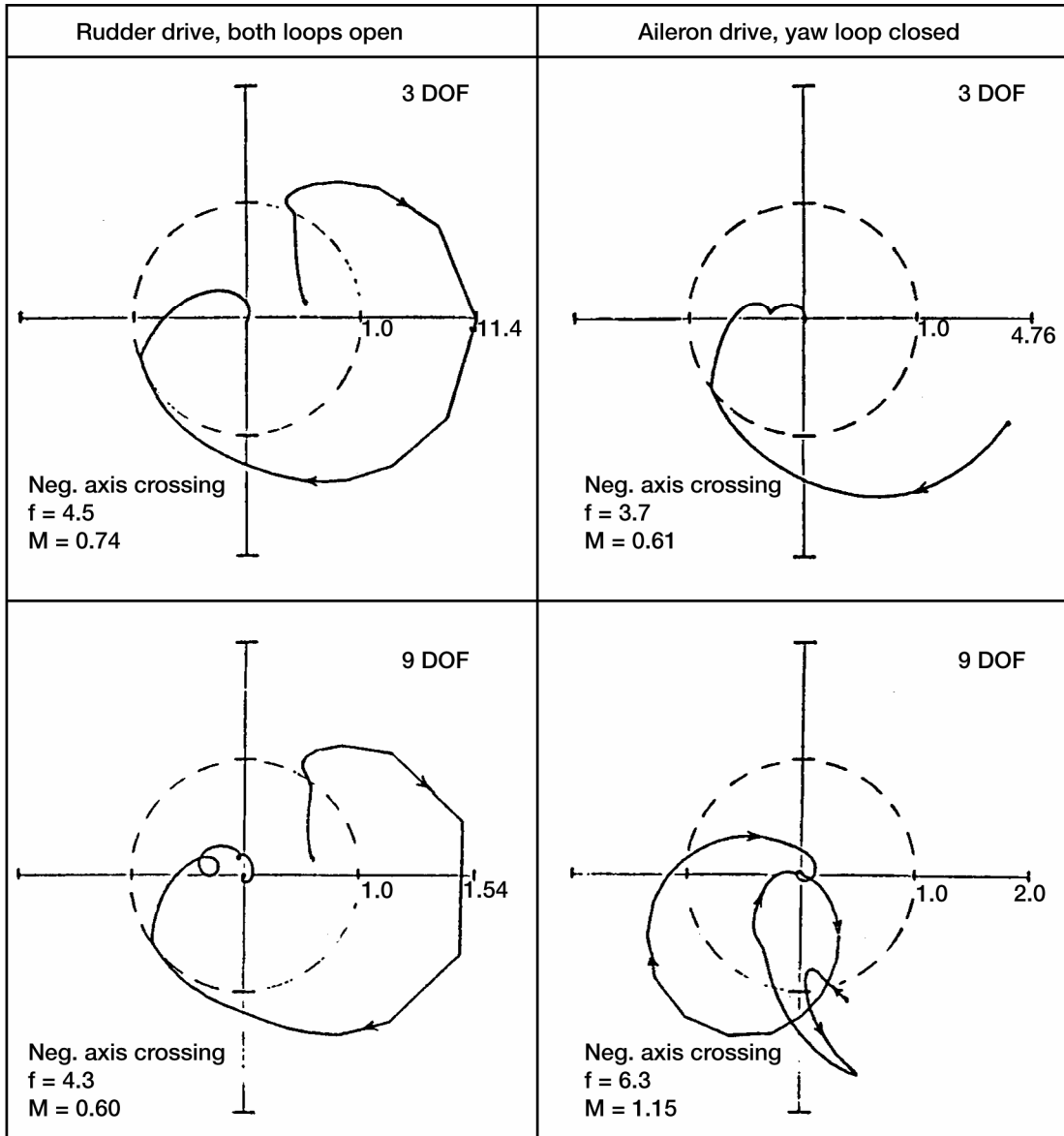
Figure 8.—Nyquist plots with yaw loop closed first, M = 0.9, sea level, missiles on, "flexible" stability derivatives, truncated GVT modes.

The figure in the lower left part of figure 8 shows the same frequency response data that was computed for a 9 DOF representation of the airplane. This representation has the same three rigid body DOF along with six natural modes of vibration DOF. The two antisymmetric modes of vibration shown in figure 2 are included in this analysis. This figure indicates that if the yaw loop were closed, the 9 DOF representation of the airplane would be stable. The stability margins of an airplane with a flight control system are usually expressed in terms of gain margin and phase margin. The gain margin requirement is usually 6 dB, which means that the overall gain in the open-loop FRF could be increased by a factor of 2 before the closed-loop system became unstable. This requirement is equivalent to the requirement that the maximum allowable magnitude of the open-loop FRF (with all other loops closed) where it crosses the negative real axis on a Nyquist plot, shall not exceed 0.5. The magnitude of the maximum negative axis crossing is tabulated in figure 8 along with the frequency at which the crossing occurs. The phase margin is defined as the angle between the negative real axis and the phase angle of the open-loop FRF where it crosses the unit circle. The phase margin requirement for a flight control system is usually ±60°. This means that the open-loop FRF phase angle (with all other loops closed) could be increased or decreased 60° before the closed-loop system became unstable. The phase margins can be estimated from the plots on figure 8.

The next step in the analysis is to close the yaw loop. The numerator of the left hand side of equation (8) is the rudder signal that was fed back and the denominator was the rudder signal that was input. Hence, the rudder signal that is fed back due to the sensor input, including the sign change at the summer, can be expressed as follows.

$$\delta_r = -T_{a_y}(\omega)a_y - T_{\dot\psi}(\omega)\dot\psi - T_{\dot\phi_Y}(\omega)\dot\phi \tag{9}$$

Expressing the lateral acceleration, yaw rate and roll rate in terms of the generalized coordinates, as indicated by equation (7) yields the following expression.

$$\delta_r = -T_{a_y}\lfloor -\omega^2 h_s \rfloor \{q_s\} - T_{\dot\psi}\lfloor i\omega\psi_s \rfloor \{q_s\} - T_{\dot\phi_Y}\lfloor i\omega\phi_s \rfloor \{q_s\}$$
$$= [T_{\delta_r}]\{q_s\} \tag{10}$$

Substituting equation (10) into (6) yields the equations of motion for the airplane with the yaw loop closed.

$$[A_{rs}]\{q_s\} = -\{A_{r\delta_r}\}[T_{\delta_r}]\{q_s\} = -[A_{\delta_r}]\{q_s\} \tag{11}$$

$$[A_{rs} + A_{\delta_r}]\{q_s\} = 0 \tag{12}$$

The Nyquist plots shown on the left side of figure 8 indicate that the airplane with the yaw loop closed would be stable at the Mach 0.9, sea level flight condition. Therefore, the closed loop system indicated by equation (12) is stable.

The equations of motion for the airplane with the yaw loop closed and excited by an oscillatory aileron command are as follows.

$$[A_{rs} + A_{\delta_r}]\{q_s\} = -\{A_{r\delta_a}\}\delta_a \tag{13}$$

where δ_a means aileron plus horizontal tail differential deflection in the ratio of one degree aileron to 0.25 degrees horizontal tail.

The generalized coordinate response per δ_a can be computed from equation (13) and used to compute the roll rate at the sensor location per δ_a.

$$\frac{\dot{\phi}}{\delta_a} = i\omega[\phi_s]\left\{\frac{q_s}{\delta_a}\right\} \tag{14}$$

Using figure 7, the ratio of aileron feedback, at the point where the loop is open, to the aileron command can be expressed as

$$\frac{Feedback}{\delta_a} = T_{\dot{\phi}_R}(\omega)\frac{\dot{\phi}}{\delta_a} \tag{15}$$

Substituting equation (14) into equation (15) yields the expression for the open loop feedback in the roll loop with the yaw loop closed. This frequency response function was computed and is shown plotted in polar form on the right side of figure 8.

The plot in the upper right-hand side of figure 8 is for the airplane represented with 3 DOF. This plot shows no clockwise enclosures of the minus one point. This plot indicates that the rigid airplane with both the yaw and roll loops closed would be stable.

The plot in the lower right-hand side of figure 8 is for the airplane represented with 9 DOF. This plot shows one clockwise enclosure of the minus one point. The negative axis crossing has a magnitude of 1.15 at a frequency of 6.3 Hz. The direction of increasing frequency is shown by arrow heads on each of the plots of figure 8. The plot in the lower right-hand side of figure 8 indicates that the 9 DOF representation of the airplane is unstable when both the yaw and roll loops are closed and that the frequency of the instability is near 6.3 Hz. This frequency is very close to the frequency of the instability that was observed during flight tests. The large loop on the plot with its maximum magnitude centered near a phase angle of –135 degrees, is associated with the response of mode one in figure 2. This antisymmetric mode has a large component of fuselage roll to balance the large inertia roll moment produced by the wing and tip missile motion.

Additional information can be obtained from the plot in the lower right-hand side of figure 8. Since the negative axis crossing has a magnitude of 1.15, a gain reduction in the roll channel of 1/1.15 would cause the open-loop frequency response to pass through the minus one point. Hence, neutral stability would occur for this reduced gain at this flight condition. That gain and any higher gain would cause the instability to occur. To reduce the gain so that the magnitude of the negative axis crossing was 0.5 (6 dB gain margin), the gain in the roll loop would have to be reduced by a factor of 0.5/1.15 or 44 percent.

The analysis was repeated with the control loops closed in the reverse order. The same conclusions with respect to ASE instability should be obtained. Only additional gain and phase information should be obtained. Plots of the open-loop frequency response function with the roll loop closed first are shown on figure 9. Referring to the lower left-hand side plot (9 DOF), it can be seen that the open-loop frequency response for the roll loop with both loops open shows a clockwise enclosure of the minus one point. The magnitude of the negative axis crossing is 1.06 and the frequency is 6.3 Hz. This plot indicates that closing the roll loop with the yaw loop open would still cause the ASE instability.

The plot on the lower right-hand side of figure 9 is the open-loop frequency response for the yaw loop with the roll loop closed. Since the left-hand plot shows the system to be unstable with the roll loop closed, the forward loop, G, (airplane with the roll loop closed) has one pole on the right-hand side of the Laplace plane. Substituting P equal one into the right-hand side of equation (3), it can be seen that N has to equal minus one in order for the number of zeros on the right hand side of the Laplace plane to be zero. That is the plot of the open-loop frequency response function for the yaw loop, with the roll loop closed, would have to produce one counterclockwise enclosure of the minus one point in order to conclude that the airplane with both loops closed was ASE stable. If it did not produce one counterclockwise enclosure of the minus one point, the airplane with both loops closed would be unstable.
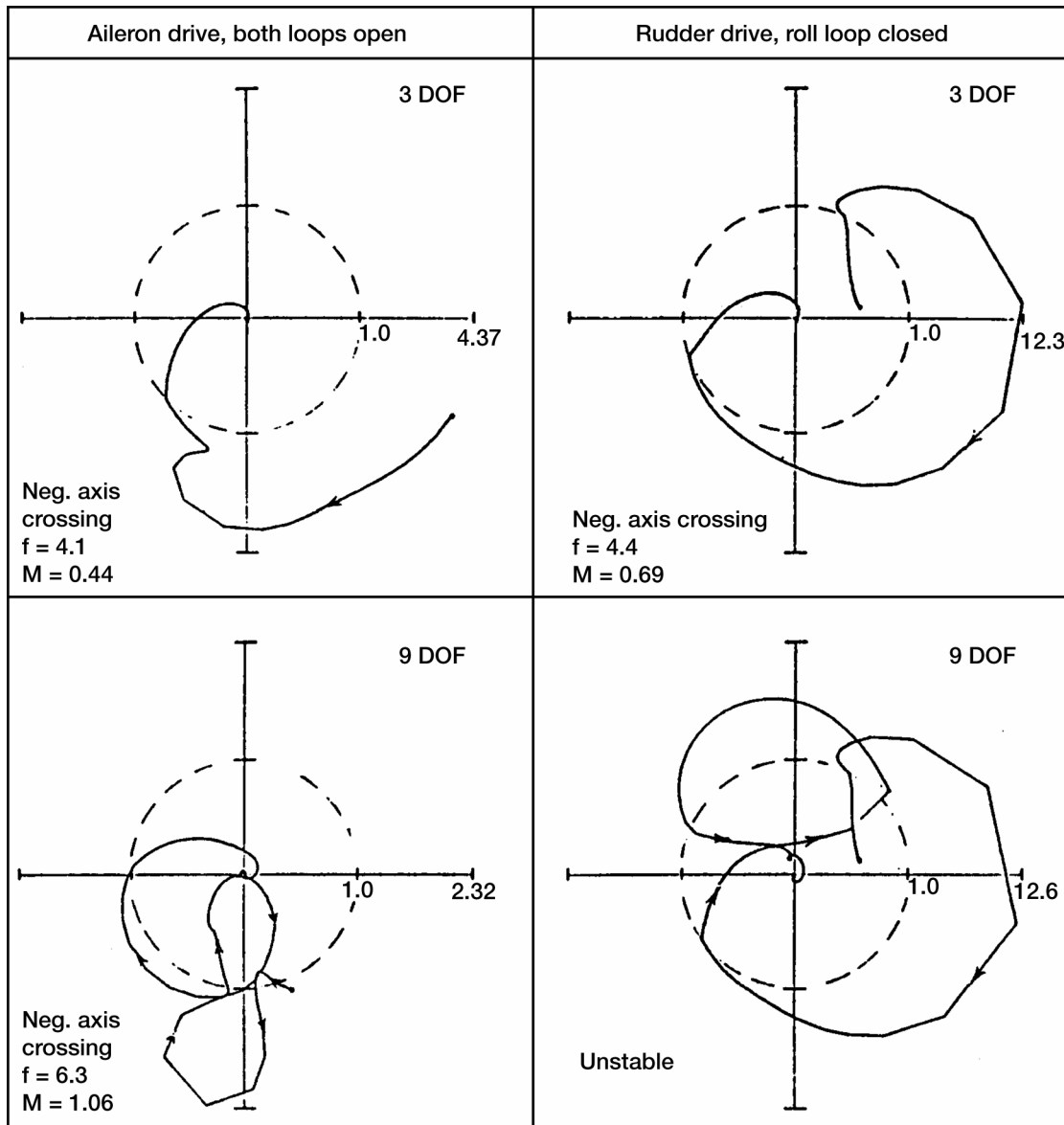
Figure 9.—Nyquist plots with roll loop closed first, M = 0.9, sea level, "flexible" stability derivatives, truncated GVT modes.

Returning to figure 9, the plot in the lower right hand side does show a counterclockwise loop but it does not enclose the minus one point. The counterclockwise loop has its maximum magnitude centered near a phase angle of approximately 100 degrees. Since a reduction in the yaw loop gain would reduce the magnitude of each point along radial lines from the origin, it can be seen that no amount of reduction of the gain in the yaw loop would cause the counterclockwise loop to enclose the minus one point. This plot confirms the conclusion that this airplane could be stabilized by reducing the gain in the roll loop but it could not be stabilized by reducing only the gain in the yaw loop. This conclusion was consistent with flight test results.

The two plots on the upper part of figure 9 show that the 3 DOF rigid body representation is stable with both loops closed. Therefore, regardless of the order in which the roll and yaw loops are closed the 3 DOF rigid representation indicates that the rigid airplane with both loops closed is stable and the 9 DOF representation indicates that the flexible airplane with both loops closed is unstable.

Although the analysis predicted the ASE instability which occurred during flight tests, the analysis did not predict as large a region of instability as was determined by flight tests. ASE analyses were conducted at Mach 0.9 at three altitudes, namely, sea level, 5,000 feet and 20,000 feet. Hence, the analysis indicated that the top of the unstable region was near 5,000 feet and the flight test data indicated that the top of the unstable region was at least as high as 20,000 feet.

Part of the unconservative characteristic of the analysis is attributed to the manner in which the computed aerodynamic terms for the rigid body DOF and the control surface aerodynamics were modified to agree with wind tunnel measured rigid stability derivatives corrected for aeroelastic effects. These stability derivatives were called flexible stability derivatives. The unsteady aerodynamic terms that were computed for the 3 DOF rigid body equations of motion were modified to agree with the flexible stability derivatives near zero frequency. When the 9 DOF analyses were conducted, six generalized coordinates representing six natural modes of vibration were added to the 3 DOF rigid body representation. All of the unsteady aerodynamic terms associated with the three rigid body modes in the 9 DOF analysis were the same as they were in the 3 DOF analysis (that is, corrected to agree with the flexible stability derivatives). No change was made to the computed unsteady aerodynamic terms that were produced by adding the six natural mode generalized coordinates. Hence, the six natural modes produced additional aeroelastic effects on the rigid body stability derivatives.

Later ASE analyses were conducted using the residual flexibility method. This method computes the residual flexibility that exists when a truncated set of natural modes are used in the equations of motion. The aeroelastic effects produced by the truncated set of natural modes plus the effect produced by the residual flexibility method provided the correct total aeroelastic effect. Hence, the computed unsteady aerodynamics for the rigid body DOF need only to be corrected to agree with wind tunnel based rigid stability derivatives.

A second method which approximated the residual flexibility method was also used. The aeroelastic effect contributed by the truncated set of natural modes was computed. This effect was subtracted from the total desired aeroelastic effect and the difference was applied to the rigid body stability derivatives. Hence, the sum of the modified rigid body aerodynamic terms plus the contribution produced by the truncated set of modes produced approximately the desired aeroelastic effect.

Later ASE analyses using these two methods for applying aeroelastic effects to the rigid body stability derivatives plus other refinements in the parameters used in the analyses improved the correlation between analysis and flight test data.

The ASE analysis conducted immediately after the ASE instability was encountered during flight tests provided assurance that the instability was an ASE instability, rather than flutter, and indicated that reducing the gain in the roll channel would restore stability. Although flight test experience indicated that a 50 percent reduction in the roll channel gain would stabilize the airplane, the selected correction consisted of reducing the roll channel gain to 60 percent of its original value and adding a notch filter to the roll channel. The notch filter was centered near 6.5 Hz and provided an additional gain reduction in a frequency band centered near 6.5 Hz.

Source of Additional Information

For a more in-depth description of the flight test experience, as well as a more detailed description of the ASE analyses that were conducted to improve the correlation between analysis and flight test results, the interested reader is directed to reference 1, from which most of the figures in the present work were taken. Subsequent ground testing that was conducted for the purpose of improving the ASE mathematical model is reported in reference 2.

The ASE instability for the Case Study A airplane was also reported in reference 3 at the 16th Structures, Structural Dynamics and Materials Conference. At the same meeting a similar ASE instability on a different airplane was reported in reference 4.

Recent ASE encounters through 1978, earlier close encounters, ASE analysis techniques, testing techniques, and design requirements are discussed in reference 5.

Aeroservoelastic Instability, Case Study B

Introduction

Most ASE instabilities occur near the frequency of a structural natural mode of vibration. The frequency of the ASE instability for the Case Study A airplane with wing tip missiles, was very close to the frequency of the first antisymmetric natural mode of vibration of the structure. At or near the frequency of a structural natural mode, a small amount of oscillatory control surface deflection can cause a large response in the natural mode and a large output from the flight control sensors. The flight control system designer is usually successful in designing the system so that it does not destabilize one of the airplanes rigid body natural frequencies.

However, the instability for the Case Study B airplane occurred at a frequency that was considerably below the lowest structural natural frequency and above the frequency of the rigid body short period mode. The frequency at which the instability occurred can be explained as the frequency at which the phase lag in the open-loop frequency response function (FRF) increased to 180° and the magnitude equaled or exceeded unity.

Case Study B complements Case Study A in that it demonstrates the use of one method of distinguishing a flutter instability from an ASE instability which was not applied in Case Study A. Specifically, Case Study B describes the measurement of the open loop FRF in flight.

Case Study B Airplane Description

The Case Study B airplane was a fighter prototype with a cranked delta wing planform. The configuration is shown in figure 10.

It had two sets of wing trailing edge control surfaces. The outboard control surfaces were called ailerons. They extended from an over-wing fairing that housed the aileron actuators to the wing tip missile launchers. The inboard surfaces, called elevons, could be actuated differentially as ailerons and symmetrically as elevators. The elevon actuators were located at the inboard end of each elevon in the fuselage. The airplane had a vertical tail with a full span trailing edge control surface called the rudder. The rudder actuator was located at the lower end of the rudder.
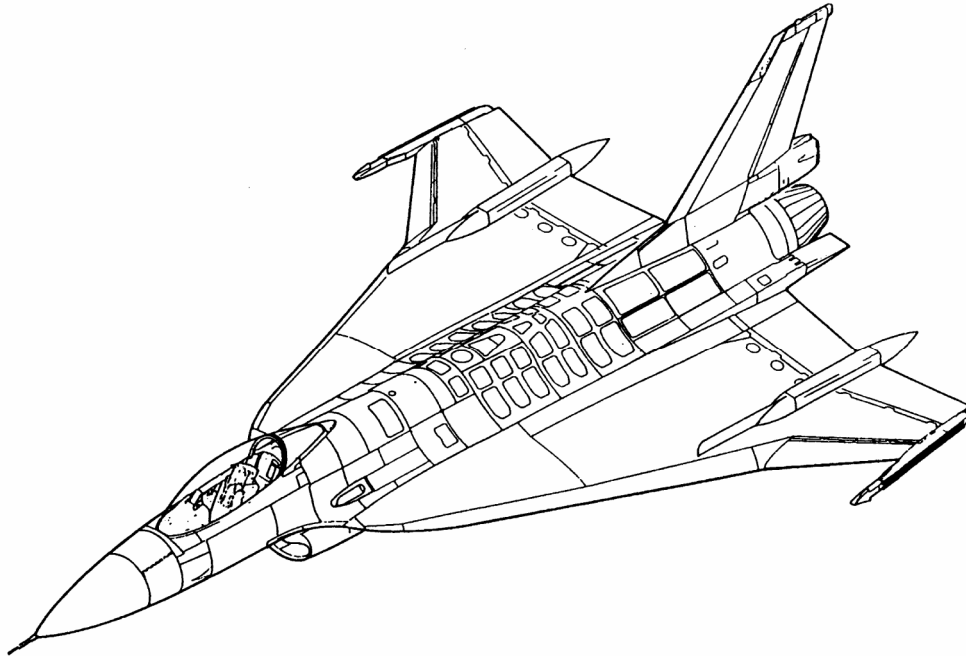
Figure 10.—Case study B airplane configuration.

Flight control was provided by an analog fly-by-wire system. Pilot inputs to the controller and the rudder pedals were transmitted electrically to the actuator servo valves. The servo valves and the actuators were combined into units called integrated servo actuators (ISAs), allowing the hydraulic fluid flow path between servo valves and actuators to be considerably shortened.

The airplane also had two sets of wing leading edge flap surfaces; these were not used for flight control.

The configuration carried missiles on wing tip launchers. Additional external stores were carried under the wing. Fuel was carried in the fuselage and in the wings.

Pre-Flight-Test Analyses and Tests

Flutter analyses, without the flight control system, were conducted with and without the tip missiles, for a wide range of fuel conditions and for many underwing store configurations. These analyses indicated that the airplane had at least a 20 percent flutter margin throughout its flight envelope.

Flutter model tests of the complete configuration without the flight control system were conducted in the NASA Langley Transonic Dynamics Tunnel. These tests indicated that the airplane without the flight control system had at least a 20 percent flutter margin through the transonic and low supersonic regions (to the wind tunnel limits).

Flight simulation studies indicated the airplane, with the flight control system engaged, to be stable throughout its flight envelope. These studies were conducted with the airplane considered to be a rigid body. Stability derivatives were determined by wind tunnel tests conducted with rigid models. The wind tunnel based stability derivatives were modified to account for aeroelastic effects.

ASE analyses were conducted. These analyses indicated that no ASE instabilities should be expected throughout the flight envelope. The symmetric ASE analyses for the basic configuration without underwing external stores, indicated that the lowest gain and phase margins occurred in a frequency range between 2.5 and 3.0 Hz. This frequency range is below the first symmetric structural natural mode frequency which was 5.6 Hz, and considerably above the airplane's short period mode frequency.

Flight Tests

During flight tests the pilot reported feeling a pitching motion of the airplane. It occurred in a narrow Mach number range between 0.9 and 0.95. It was experienced at all altitudes up to 40,000 feet. The oscillations were either constant amplitude oscillations or lowly damped oscillations. The frequency of the oscillations ranged from 2.0 to 2.5 Hz.

Several flights were conducted in an effort to find an aerodynamic oscillatory excitation mechanism as an explanation for the pitch oscillations. After these flight tests proved to be unsuccessful in determining the source of the oscillations, a decision was made to measure the open loop FRF in the flight control pitch channel, in flight. However, while preparations were being made to make these measurements, a second decision was made to reduce the gain in the pitch channel by 25 percent. Subsequent flight tests showed that a 25 percent reduction in the pitch channel gain eliminated the pitch oscillations. At this point the need to measure the open loop FRF in flight was considerably reduced. However, the plan to make the measurements was continued in order to obtain better visibility for other potential corrective actions.

The objective of measuring the open loop FRF is to determine the stability of the closed loop system, as illustrated in figure 11. A block diagram of a single input, single output closed loop system is shown on the upper left part of this figure. For this application, $G(s)$ represents the airplane transfer function and $H(s)$ represents the flight control pitch channel transfer function. The ratio of the feedback signal, $X_f(s)$, to the input signal, $X_i(s)$, is shown in the equation in the upper part of figure 11.

$$\frac{x_f(s)}{x_i(s)} = \frac{G(s)H(s)}{1 + G(s)H(s)}$$

Measuring open-loop frequency response function

With loop open   or   With loop-closed

$$G(\omega)H(\omega) = \frac{x_f(\omega)}{x_i(\omega)}$$

$$G(\omega)H(\omega) = \frac{x_f(\omega)}{x_e(\omega)} \text{ Direct method}$$

$$G(\omega)H(\omega) = \frac{T(\omega)}{1 - T(\omega)} \text{ Indirect method}$$

$$T(\omega) = \frac{x_f(\omega)}{x_i(\omega)}$$
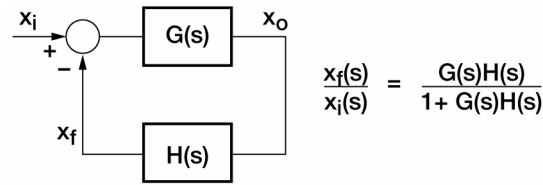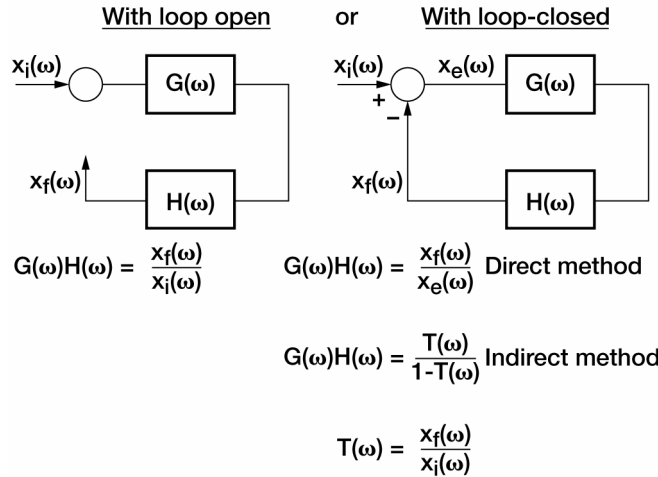
Figure 11.—Open-loop frequency response measurements.

The open-loop FRF can be measured by physically opening the feedback loop at the point at which it would subtract from the input signal. By applying an oscillatory input signal and measuring the oscillatory feedback signal, the open loop FRF relating the feedback signal to the input signal can be obtained, as illustrated by the block diagram and equation in the lower left part of figure 11.

It is not feasible to physically open the loop during flight tests because of the associated risks of losing control of the airplane. However, the open-loop FRF can be measured without physically opening the loop. Two methods for measuring the open-loop FRF with the loop closed are illustrated by the block diagram and the equations in the lower right part of figure 11.

To obtain the open-loop FRF by the direct method, an oscillatory input signal is applied and the FRF for the ratio of the feedback signal to the error signal x_e is measured. The error signal is the difference between the input signal and the feedback signal. This method is called the direct method because the open-loop FRF is measured directly and requires no subsequent algebraic operation.

To obtain the open-loop FRF by the indirect method, an oscillatory input signal is applied and the FRF for the ratio of the feedback signal to the input signal is measured. This closed-loop FRF is called T. By substituting frequency for the Laplace variable for the closed-loop transfer function equation at the top of figure 11 and substituting T for the left hand side of the equation, the equation can be solved for the product GH. This result is shown in the lower right part of figure 11 as T divided by $1 - T$ and is labeled the Indirect Method. This method is called the Indirect Method because the closed-loop FRF T is measured and the open-loop FRF is obtained as the algebraic ratio $T/(1 - T)$.

Both the direct and indirect methods were used to measure the open loop FRF with the loop closed, in flight. A block diagram of the pitch channel is shown in figure 12. The airplane block shows that the input to the airplane is the combined symmetric deflections of the elevons and the ailerons. The outputs of the flight control sensors were fed back through the pitch channel to produce the feedback signal. The flight control sensors were the angle of attack sensor, α, the vertical accelerometer, A_n, and the pitch rate gyro, Θ. During the FRF measurements, the excitation signal was applied through the autopilot while the pilot supplied input to maintain straight and level flight conditions at constant altitude and constant Mach number. The input signal was measured as the sum of the
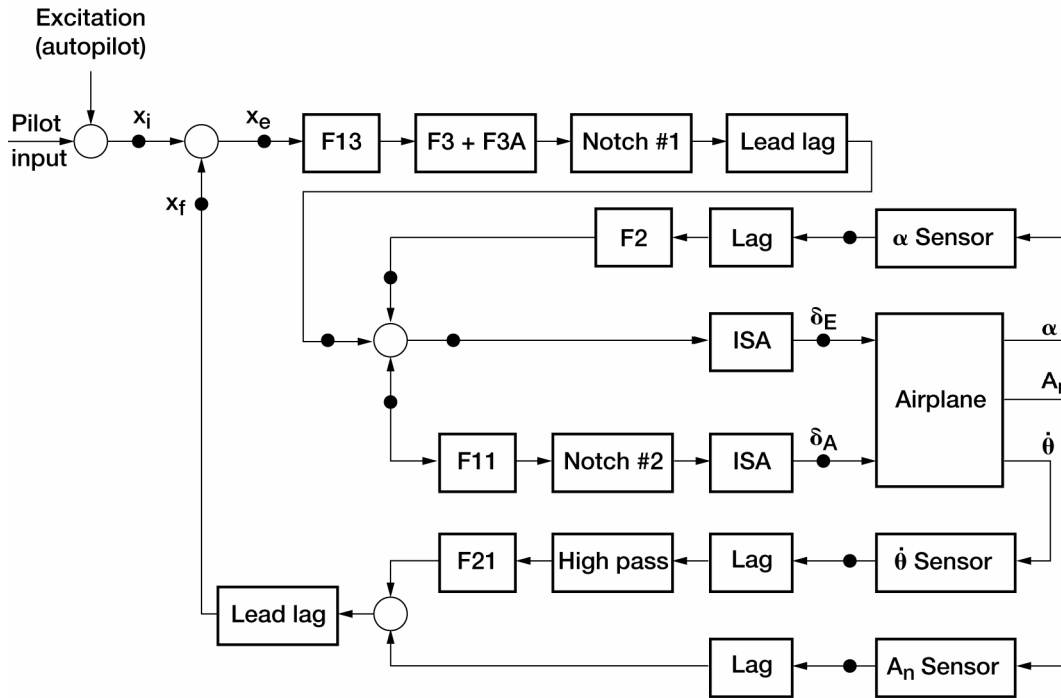
Figure 12.—Case study B flight control system pitch channel.

excitation signal and the pilot signal. The feedback signal was measured at the point before it was subtracted from the input signal to produce the error signal. The locations of the three signals that were measured are shown on the upper left part of the block diagram in figure 12 and labeled as x_i, x_e, and x_f.

The blocks in figure 12 that are labeled with an alphanumeric symbol beginning with the letter F are gains; both fixed and variable. The blocks labeled notch, lead lag, lag and high pass, indicate transfer functions for notch filters, lead lag functions, lag functions, and high pass filters. The blocks labeled ISA are the transfer functions for the integrated servo actuators. The blocks labeled sensors are the transfer functions for the angle-of-attack sensor, the pitch rate gyro sensor and the normal accelerometer sensor. The numerical value of the gains and the transfer functions are not given because the purpose of Case Study B is to show the results of measuring FRFs in flight; not to compare computed and measured FRFs. All gains were constant over the Mach number range from 0.85 to 1.0. Also, there was no variation in the transfer function blocks.

The FRF could be measured by applying the excitation at a discrete frequency and measuring the desired ratios at the discrete frequency. By repeating the measurements at a sufficient number of points the open-loop FRF could be produced. A more efficient method of measuring the FRF is by the use of a harmonic analyzer that employs the Fast Fourier Transform (FFT) algorithm. The FFT algorithm computes the discrete Fourier transform of a sequence of measurements equally spaced in time in a very efficient manner (minimum number of mathematical operations) if the number of time measurements is equal to a power of two (for example, 512 or 1024). A harmonic analyzer of this type was used to process the flight test data. This harmonic analyzer could accept 1024 measurements at equal time intervals and compute the FRF for the ratio of the two signals at 512 positive frequency points in approximately 0.03 second after the last of the two sets of data had been received. Hence, the FRF could be computed in virtually real time. Therefore, the excitation signal through the autopilot did not need to be a discrete frequency. Any type of input signal could be used and the harmonic analyzer could compute the FRF.

Two types of excitation are commonly used to measure FRFs. One is commonly called sine sweep excitation and the other is called random excitation. Sine sweep excitation applies an excitation signal at a discrete frequency and the frequency is slowly changed by sweeping from a selected minimum frequency to a selected maximum

frequency or vice versa. The random excitation method was selected for the Case Study B airplane. One reason for this selection is because the random excitation produces airplane motion that feels to the pilot as if he is flying in random turbulence. Hence, the ride comfort (or discomfort) and the degree of difficulty in maintaining straight and level flight appears to the pilot to be approximately the same from the beginning to the end of the applied excitation period. Whereas, during the sine sweep excitation the airplane response at the pilot station can vary to large degree as the frequency is slowly changed. Hence, the pilot feels like he is on a roller coaster ride with varying degrees of difficulty in maintaining straight and level flight throughout the frequency sweep.

The harmonic analyzer that was used, processed the data supplied to it in blocks called records. Each record consisted of 1024 measurements, for each of two signals, at equal time intervals. For this application the time intervals or sampling rate was set such that a record length was approximately 25 seconds. Hence the time interval was approximately 25/1024 or 0.0244 seconds. The FRF frequency increments were 1/25 or 0.04 Hz. Since 1024 data points are transformed into 512 positive frequency increments, the frequency range was from 0.04 Hz to (512)(0.04 Hz) or approximately 20 Hz. To improve the statistical accuracy the process was repeated for many records and the FRF data were averaged. To reduce the total time that the excitation was applied and to obtain better statistical accuracy, a new record was analyzed when 25 percent of new data had been added to the previous record and the oldest 25 percent of the previous record had been discarded. Using this 75 percent overlap on successive records, 32 records could be processed and averaged in a total excitation time of 220 seconds. These data are tabulated in figure 13.

A comparison of the open-loop FRF as obtained by the direct and indirect methods for one flight condition is also shown on figure 13. The FRFs are plotted in polar form or as Nyquist plots. The dotted circle on each plot is the unit circle. Although the frequency range was normally from zero to 20 Hz, the data are plotted up to 8 Hz. The data are plotted for negative feedback systems so the minus one point is the critical point. To describe the direction of the plot with increasing frequency it is noted that the magnitude of the plot at the low frequency end is greater than the unit circle and as the frequency is increased the magnitude of the plot approaches the center of the unit circle. Hence, the direction of the plot with increasing frequency is clockwise. It can be seen that the two methods for obtaining the open-loop FRF, with the loop closed, produce results that are very nearly the same. In particular, both methods show a negative axis crossing with a magnitude of approximately 0.63, at a frequency near 2.25 Hz.

Mach = 0.95
Altitude = 40K ft
Frequency Range = 0 to 20 Hz
Record Length per FRF = 25 sec.

No. of FRF Averages = 32
75% Overlap
Total Record Length = 220 sec.
Plot Window = 0 to 8 Hz
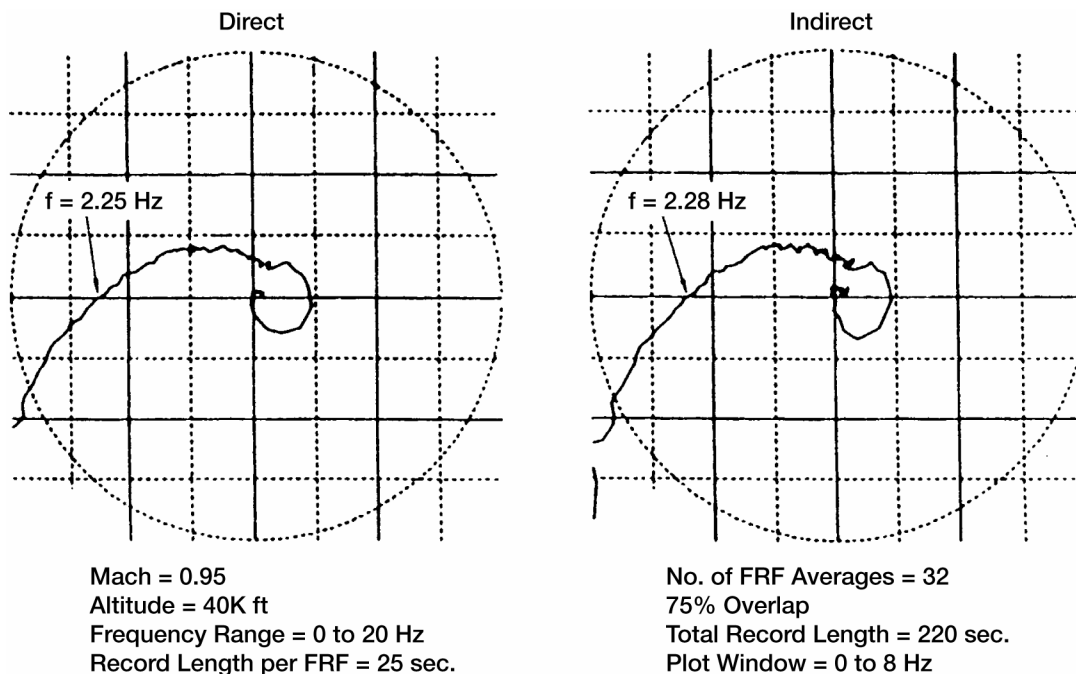
Figure 13.—Comparison of direct and indirect methods for measuring open-loop FRF.

Since the measurements were made with the gain in the pitch channel reduced to 75 percent of the value that it had when the pitch oscillations were experienced, the magnitude of all points would be expected to be increased by the ratio of 1/0.75 or 4/3 if the measurements had been made before the gain reduction had taken place. Hence, the magnitude of the negative axis crossing would have increased from 0.63 to 0.84. This magnitude is very close to unity and would indicate that the closed-loop system would be stable but lowly damped.

The flight conditions at which the open-loop FRF was measured are shown in figure 14. Measurements were made at three Mach numbers for each of the three altitudes and at six Mach numbers for one altitude.

Plots of the open-loop FRF obtained by the direct method at 40,000 feet for each of six Mach numbers are shown on figure 15. It can be seen that the negative axis crossing has the largest magnitude at 0.95 Mach number and that the magnitudes at lower Mach numbers are progressively lower. The magnitude of the crossing at the higher Mach number is also significantly lower. Hence, these plots show that the closed-loop system would be the closest to unstable at 0.95 Mach number.

The magnitude of the negative axis crossings, or the crossings with 180 degree phase angle, are plotted versus Mach number at 40,000 feet on figure 16. The measurements were made with various levels of excitation input that are identified as low, intermediate and high levels. The measurements that were made with and without wing fuel are identified on the plot. The scale on the left indicates the magnitude of the crossings with the pitch channel gain reduced to 75 percent of its original value. The scale on the right has been increased by a factor of 4/3 to show the magnitude of the crossing that would have existed, by implication, before the gain was reduced. It can be seen that the implied negative axis crossing was very close to unity at 0.95 Mach number before the gain was reduced. Since the measured negative axis crossing does not equal or exceed unity for the 100 percent gain implies that measurement error accounted for the short fall or that the measurements were not made at the critical Mach number. That is, if the measurements had been made for smaller Mach number variations near 0.95 Mach number, a Mach number might have been found that produced a negative axis crossing that equaled or exceeded unity. However, the data that were obtained were in agreement with the original observations that the pitch oscillations occurred in a narrow Mach number range between 2.0 and 2.5 Hz.

The magnitude of the negative axis crossings at 20,000 feet and 10,000 feet versus Mach number are shown in figures 17 and 18. These plots indicate the minimum stability occurred at 0.92 Mach number at these two altitudes.
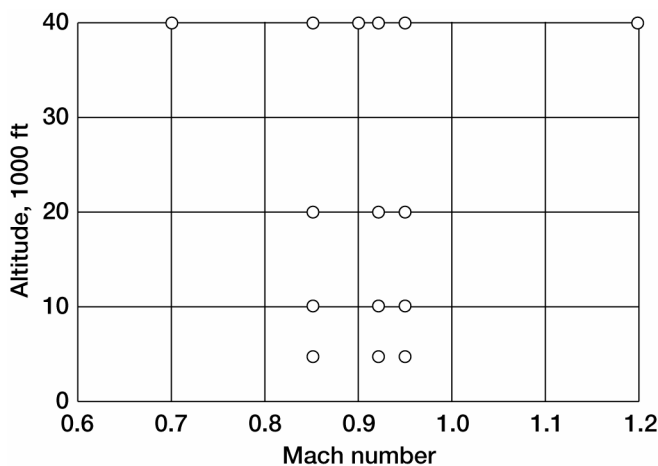
Figure 14.—Flight conditions at which open-loop FRF was measured.

Direct method, 40,000 ft
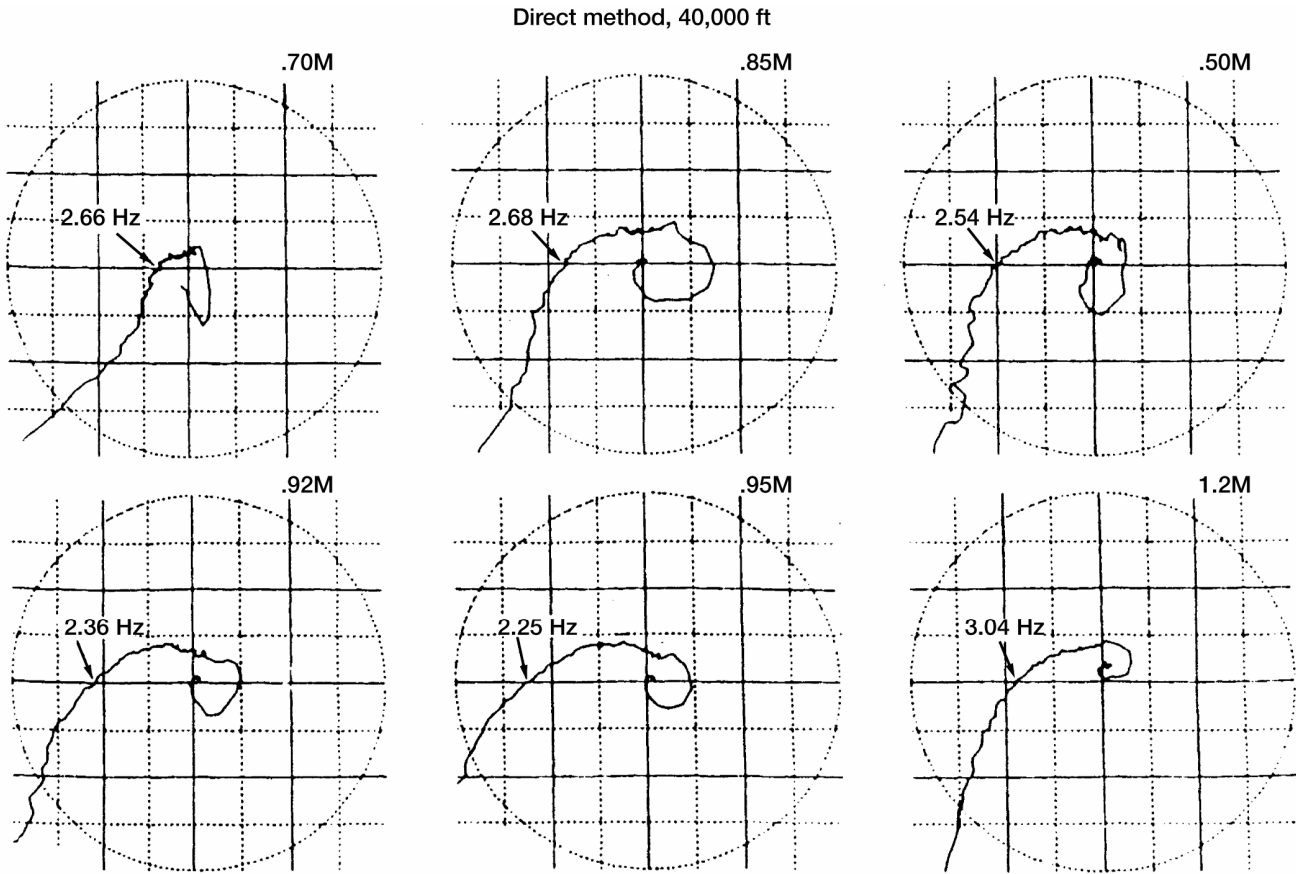
Figure 15.—Direct method FRF measurements at 40,000 ft showing maximum negative axis crossing near Mach 0.95.
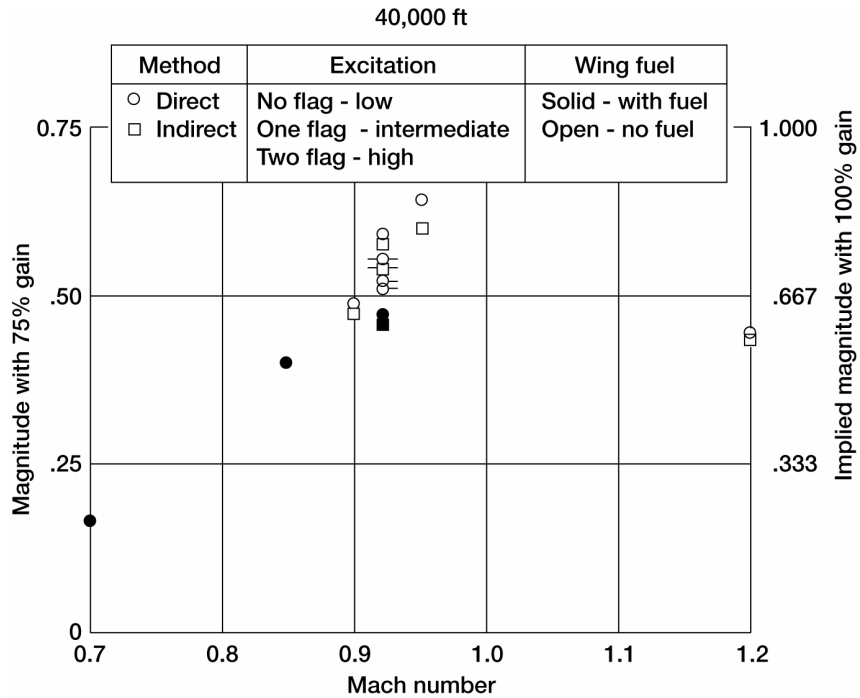
Figure 16.—Magnitude of negative-axis crossing vs. Mach number at 40,000 ft, showing maximum near Mach 0.95.

20,000 ft

Method	Excitation	Wing fuel
○ Direct	No flag - low	Solid - with fuel
□ Indirect	One flag - intermediate	Open - no fuel
	Two flag - high	

Magnitude with 75% gain

Implied magnitude with 100% gain
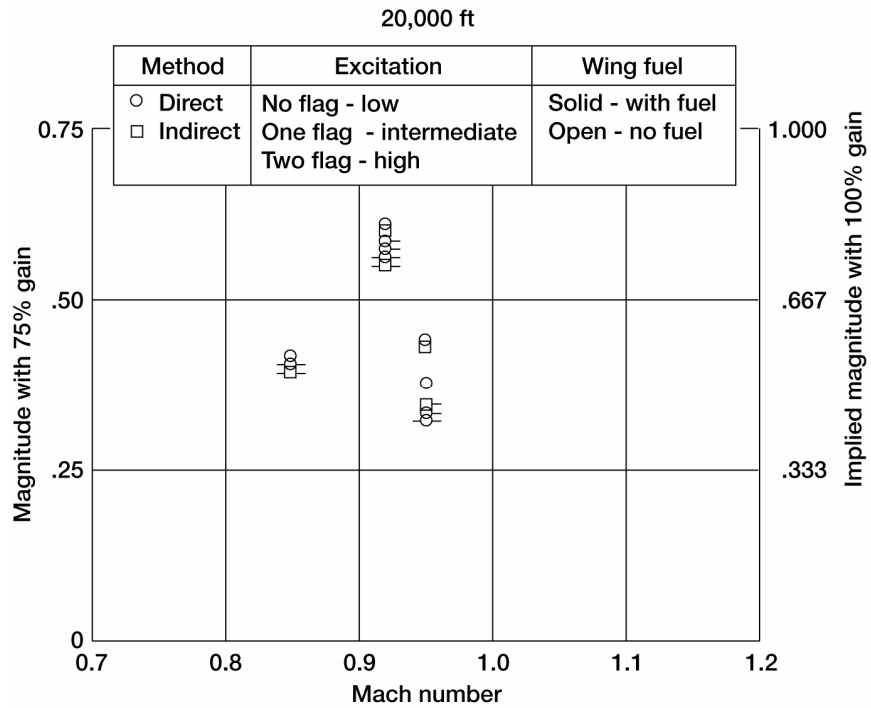
Mach number

Figure 17.—Magnitude of negative-axis crossing vs. Mach number at 20,000 ft, showing maximum near Mach 0.92.

10,000 ft

Method	Excitation	Wing fuel
○ Direct	No flag - low	Solid - with fuel
□ Indirect	One flag - intermediate	Open - no fuel
	Two flag - high	

Magnitude with 75% gain

Implied magnitude with 100% gain
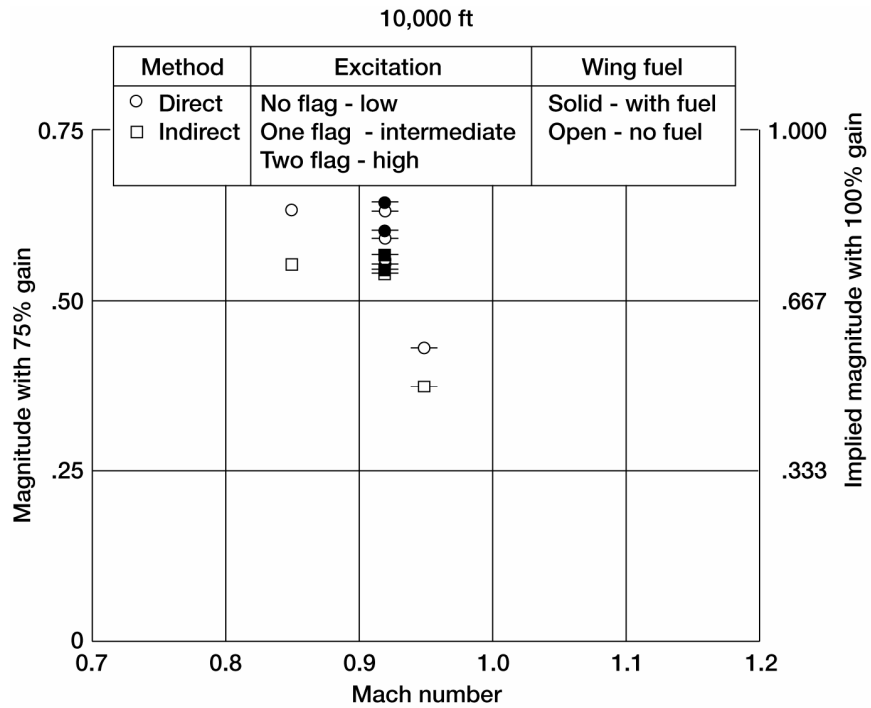
Mach number

Figure 18.—Magnitude of negative-axis crossing vs. Mach number at 10,000 ft, showing maximum near Mach 0.92.

Summary

The objective of measuring the open-loop FRF for the pitch channel, in flight, was to help diagnose the source of the pitch oscillations experienced by the pilot during flight testing in a narrow Mach number range between 0.9 and 0.95, in a frequency range between 2.0 and 2.5 Hz. Before the open-loop FRF was measured, flight tests were conducted with the pitch channel gain reduced to 75 percent of its original value. The pitch oscillations no longer occurred after the gain was reduced. Hence, the need for measuring the open-loop FRF in flight was highly reduced. However, the planned measurement of the open-loop FRF in flight was continued with the pitch channel gain reduced to 75 percent of its original value.

By looking at figure 15 and visualizing what the sequence of open-loop FRFs would look like if the magnitude of each point was increased by a factor of 4/3, it can be seen that the measurements with the original pitch channel gain would have shown the minus one point to be very nearly enclosed by a clockwise enclosure. It would have been clear that the pitch oscillations were caused by the flight control system and that a reduction of the pitch channel gain would have stabilized the pitch oscillations. These plots would also have shown that the lowest gain margins occurred in the Mach number range between 0.90 and 0.95 and that the frequency ranged from 2.54 Hz at Mach 0.9 to 2.25 at Mach number 0.95.

It would also have been clear from the sequence of plots in figure 15 that the pitching oscillations were not likely to be caused by flutter. If flutter were the source of the instability, a clockwise loop near a structural mode frequency would have been expected at a low dynamic pressure flight condition, such as Mach number 0.7 at 40,000 feet. If flutter were the source of the pitch oscillations, the magnitude of the structural mode loop would have increased and the frequency at which the largest magnitude in the loop occurred would have approached the 2.0 to 2.5 Hz range as the flutter boundary was approached. Figure 15 does not show these characteristics. One can therefore conclude that flutter was not the likely source of the pitch oscillations.

The ASE analyses that were conducted prior to the flight tests showed open-loop FRFs that were similar to the ones shown in figure 15 in that the negative axis crossing with the largest magnitude occurred in the frequency range between 2.5 and 3.0 Hz. However, the magnitude of the negative axis crossing was not sufficiently high to expect an instability in flight. The ASE analyses might have under predicted the magnitude of the negative axis crossing because the reduction in the control surface effectiveness due to aeroelasticity in the transonic range, might have been over predicted. If the control surface effectiveness, in the transonic region, was predicted to be lower than it actually was, this under prediction would lead to the ASE analyses predicting lower negative axis crossings. It would also encourage the flight control system designer to increase the pitch channel gain to compensate for the reduction in the control surface effectiveness.

As the frequency increases from zero to approximately 2.25 Hz, the phase lag in the pitch channel open loop FRF increases to 180 degrees. The phase lag is produced primarily by the ISA and the pitch channel. The oscillations were not caused by a rigid body natural frequency, such as the short period mode, or by a natural structural mode. Instead, they occurred because the gain in the open loop FRF was too high when the phase angle was 180 degrees. The frequency of the oscillation was determined by the frequency at which the phase angle reached 180 degrees.

It was demonstrated during these flight tests that the open-loop FRF can be measured without actually opening the loop. Both the direct and indirect methods were used. For this application, the two methods yielded virtually the same open-loop FRF measurement.

Source of Additional Information

The Case Study A airplane, without the tip missiles, encountered an instability in flight that was similar to the instability encountered by the Case Study B airplane. With the tip missiles removed from the Case Study A airplane, the first antisymmetric natural mode of the structure is 8.0 Hz. The Case Study A airplane without the tip missiles encountered an instability at a frequency near 3.5 Hz. This frequency is far below the first natural

frequency of the structure and above the rigid body natural frequency. This instability is reported in references 1, 2 and 3.

Techniques for measuring the open-loop FRF without physically opening the loop were developed and demonstrated during wind tunnel tests of a flutter model with a flutter suppression system. These techniques and the results obtained by applying them are described in references 6, 7 and 8. To the author's knowledge, the first time these techniques were applied to an airplane in flight was when these techniques were applied to the Case Study B airplane.

Lessons Learned

Some of the lessons learned from the experience gained from the Case Studies A and B are discussed.

Conduct ASE analyses at multiple flight conditions.—It is generally not sufficient to conduct ASE analyses only at maximum flight conditions. Flight control systems frequently employ variable gains that are scheduled to change as a function of flight conditions. Stability derivatives for a rigid airplane when plotted versus mach number frequently peak in the transonic region. Aeroelastic effects modify the stability derivatives for each flight condition. Hence, ASE analyses should be conducted for a sufficiently large number of flight conditions to ensure that the entire flight envelope has been adequately investigated.

Conduct ASE analyses for multiple external store configurations.—If the airplane carries external stores mounted on the wings, the natural modes of vibration can change with each store configuration. ASE instabilities can occur at different frequencies and at different flight conditions for different external store configurations. ASE analyses should be conducted for a sufficient number of store configurations to ensure that all possible external store configurations, including take-off store loadings and downloadings, have been adequately investigated.

Flight control system ground tests.—Open-loop FRF tests which are conducted on the airplane on the ground, should not be used, in lieu of ASE analyses, as a means of inferring ASE stability characteristics in flight. These tests are directly applicable only to the stability of the airplane on the ground. Open-loop FRF tests of the airplane on the ground (preferably supported by a soft suspension system to remove the effects of the landing gear) should be used to improve the correlation between the ASE mathematical model (without the aerodynamic representation) and the test data. One reason that ground tests are important is because flight control sensors are frequently located on the airplane where the response of the sensor is very low for one or more of the natural modes with the lowest frequencies. Hence, small errors in the computed mode shape at the sensor locations can make large percentage differences in the FRF.

Aeroelastic effects on stability derivatives.—The flight control system designer frequently conducts analyses with the airplane considered to be a rigid body. Stability derivatives are frequently obtained from wind tunnel tests of a rigid model. Hence these stability derivatives are sometimes called rigid stability derivatives. Aeroelastic effects are frequently computed by using a stiffness matrix representation of the airplane structure. The rigid stability derivatives modified by aeroelastic effects are sometimes called flexible stability derivatives. The flexible stability derivatives are used by the flight control designer.

When ASE analyses are conducted, the unsteady aerodynamic terms are computed. If only rigid body DOF are to be used in the analysis, the computed unsteady aerodynamic terms should be modified so that they agree with the flexible stability derivatives as the frequency approaches zero.

If both rigid body DOF and natural modes of vibration DOF are included in the ASE analysis, the modification of the rigid body unsteady aerodynamics varies with the number of natural modes included in the analysis. The same stiffness matrix that was used to conduct the static aeroelastic analysis should be used to compute the natural modes. If a lumped mass is located at each of the aerodynamic loading points used in the aeroelastic analysis, then the stiffness matrix is loaded with inertia loads in the vibration analysis at the same loading points used in the aeroelastic analysis. The maximum number of modes that can be computed is equal to the number of mass points. If all of the natural modes are included in the ASE analysis then the computed unsteady aerodynamic terms for the rigid body DOF should be modified to agree with the rigid stability derivatives as the frequency approaches zero. That is, the complete set of natural modes produces the same aeroelastic effect, as the frequency approaches zero, as the stiffness matrix produced in the aeroelastic analysis.

When a truncated set of modes (subset of the total number of modes) is used in the analysis (to reduce computational costs), only part of the stiffness effect is represented. If a truncated set of modes is used in the ASE analysis, the computed unsteady aerodynamic terms for the rigid body DOF should be modified, such that the sum of the aeroelastic effects in the modified rigid body aerodynamic terms plus the aeroelastic effect produced by the truncated set of modes, equals the correct total aeroelastic effect, as the frequency approaches zero. It should be noted that control surface aerodynamic terms are included when modifying computed unsteady aerodynamic terms for the rigid body DOF. Methods for making aerodynamic modifications are discussed in reference 1.

Measure open-loop FRF without physically opening the loop.—If an instability is encountered during flight tests the source of the instability is frequently in doubt. The measurement of the open-loop FRF at a series of speeds approaching the speed at which the instability was encountered, can be an effective means of determining whether the instability is primarily ASE or flutter. It is also useful in determining the changes needed to eliminate the instability.

References

1. Peloubet, R.P., Jr., et al.: Application of Three Aeroservoelastic Stability Analysis Techniques. AFFDL–TR–76–89, September 1976.
2. Peloubet, R.P., Jr., et al.: Ground Vibration Testing of Fighter Aircraft With Active Control Systems. AFFDL–TR–76–110, 1976.
3. Peloubet, R.P., Jr.: YF16 Active-Control-System/Structural Dynamics Interaction Instability. AIAA−1975−0823, 1975.
4. Arthurs, T.D.; and Gallagher, J.T.: Interaction Between Control Augmentation System and Airframe Dynamics on the YF−17. AIAA−1975−0824, 1975.
5. Felt, Larry R., et al.: Aeroservoelastic Encounters. J. Aircraft, vol. 16, no. 7, 1979, pp. 477–483.
6. Peloubet, R.P., Jr.; Haller, R.L.; and Bolding, R.M.: F−16 Flutter Suppression System Investigation Feasibility Study and Wind Tunnel Tests. J. Aircraft, vol. 19, no. 2, 1982, pp. 169–175.
7. Peloubet, R.P., Jr.; Haller, R.L.; and Bolding, R.M.: Wind Tunnel Demonstration of an Active Flutter Suppression System Using F−16 Model With Stores. AFWAL−TR−83−3046−VOL−2, 1984.
8. Peloubet, R.P., Jr.; Haller, R.L.; and Bolding, R.M.: Recent Developments in the F−16 Flutter Suppression With Active Control Program. J. Aircraft, vol. 21, no. 9, 1984, pp. 716–721.

Structural Testing for Static Failure, Flutter, and Other Scary Things[*]

Rodney H. Ricketts
National Aeronautics and Space Administration
Langley Research Center
Hampton, Virginia 23681–2199

Summary

Ground test and flight test methods are described that may be used to highlight potential structural problems that occur on aircraft. Primary interest is focused on light-weight general aviation airplanes. The structural problems described include static strength failure, aileron reversal, static divergence, and flutter. An example of each of the problems is discussed to illustrate how the data acquired during the tests may be used to predict the occurrence of the structural problem. While this report gives some rules of thumb for the prediction of structural problems, it is not intended to be used explicitly as a structural analysis handbook. However, many such handbooks are included in the reference list.

Introduction

All aircraft have inherent structural flexibilities that may contribute to the cause of many types of problems—some destructive in nature. These flexibilities may couple with aerodynamic forces, or with inertia forces to produce unwanted structural instabilities. To insure that these structural problems do not occur within the flight envelope, it is necessary to perform certain tests and/or analyses on the aircraft. A typical structural integrity verification program for a commercial aircraft includes the following elements: (1) extensive design-cycle analyses which may use computer simulations (called finite element models) to predict the response of the aircraft; (2) ground tests of the fabricated parts, both in the unassembled state and assembled to form the complete aircraft; (3) more analyses using the data acquired during the ground test to verify or calibrate the analytical results; (4) wind-tunnel tests of models which simulate the full scale article; and, finally (5) flight test of the completed aircraft throughout the flight envelope. Performing these tasks provides the safest means for verifying that the aircraft structure will hold together during operation.

This paper focuses on two of the above elements—namely, ground test and flight test techniques that may be used to predict the occurrence of potential structural problems. While methods are described herein that are applicable to all classes of aircraft, emphasis is placed on simple and inexpensive methods that may be used by individuals who are building their own general-aviation-class airplane. The problems that are discussed include static strength failure, aileron reversal, static divergence, and flutter. For each of these problem the following is given: a description of the problem; procedures for structural testing for the problem and an explanation of the use of the results; requirements set forth in the Federal Aviation Regulations as standards for airworthiness of the aircraft experiencing the problem; and an example of an application of the procedures used at the National Aeronautics and Space Administration (NASA) in ground, wind-tunnel, or flight tests. While this report gives some rules of thumb for the prediction of structural problems, it is not intended to be used explicitly as a structural analysis handbook. A more thorough discussion of these problems may be found in such books as references 1 to 3.

Static Strength Failure

Static strength failure is the interaction of aerodynamics, inertia, and strength. The interaction diagram shown in figure 1 illustrates the interaction by the shaded area. It is the condition where the aerodynamic and inertia loads

---

[*]This document was first published as Ricketts, R.H.: Structural Testing for Static Failure, Flutter and Other Scary Things. NASA TM–84606, 1983.

cause the structural stress to exceed the structural strength. At this condition the structure fails and is no longer capable of carrying the load. A failure can lead to catastrophic destruction of the aircraft.

A stress-strain curve for a typical metal is shown in figure 2. The curve shows three regions of interest. A region of linearity exists (segment AB) where the stress (related to applied load) is directly proportional to the strain (related to deformation) produced within the metal. When loaded and then unloaded within this region, the metal will return to a zero-strain (undeformed) condition. A region of nonlinearity exists (segment BE) where the material begins to yield (or permanently stretch) under additional load. Metal loaded into the yield region (point C) and then unloaded will return along line CD which is parallel to the original linear region line to a deformed condition—one with a permanent set (point 0). In this case, the linear region is shifted to the right, and the metal will respond along line DC when it is reloaded to point C. A region of failure exists (segment EF) where the ultimate strength of the metal is reached. The metal stretches rapidly to relieve the load and then fails at point F. Additional information is contained in reference 4.
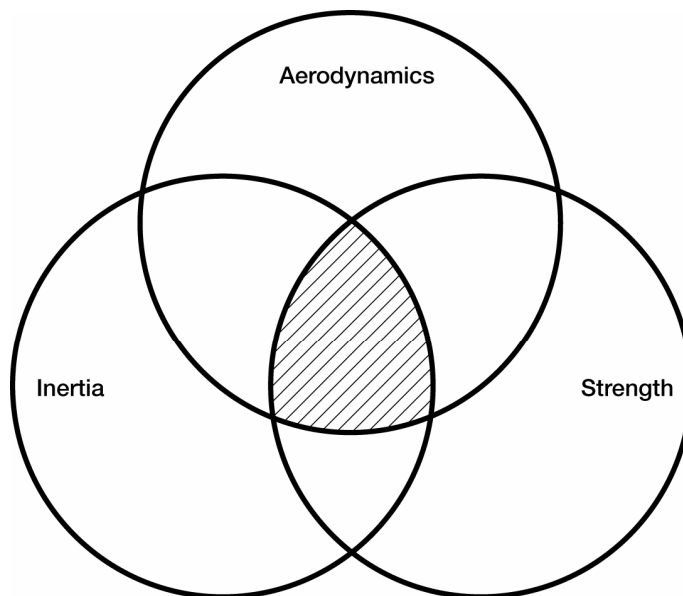
Figure 1.—Interaction diagram for static strength failure.
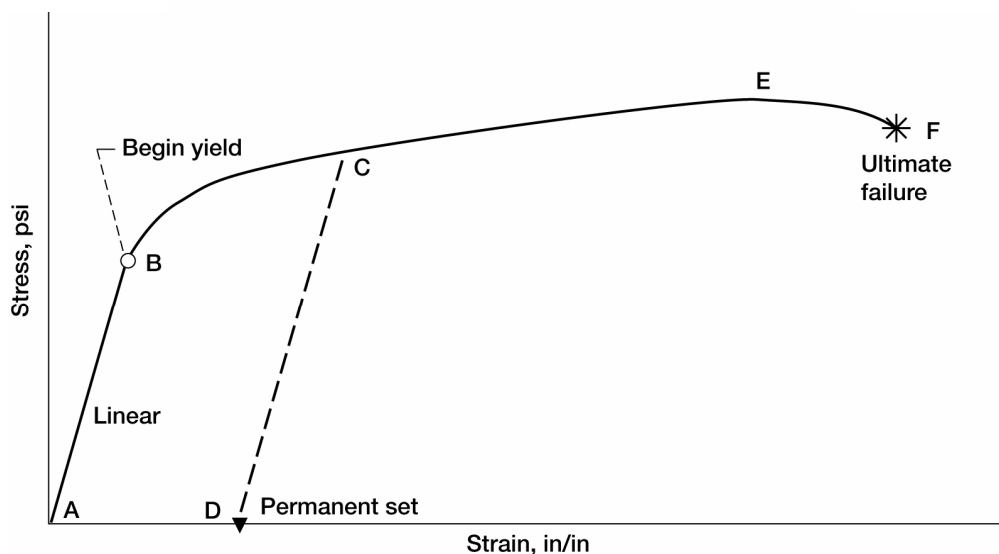
Figure 2.—Stress-strain diagram for a typical metal.

During ground tests for static failure, loads in the form of forces and/or moments are applied to the structure, the stresses that are produced in the structure are measured, and the resulting structural deformations are measured. These procedures are discussed in the following text.

Forces may be applied to the structure as either point or distributed loads. For point forces a weight pan as shown in figure 3(a) may be used to support the weights as they are applied. A loading pad may he used so as not to puncture the structure with the pan fixture. Another method of applying point forces is through the use of a hydraulic ram. Distributed forces which represent an aerodynamic or inertia load condition may be applied by distributing sandbags or bags filled with lead shot across the structure. An alternate method for applying distributed loads is through a whiffletree apparatus which attaches to the structure at several points as shown in figure 3(b). Forces then may be applied to the whiffletree using weights or a hydraulic ram.

A pure moment (couple) is produced when two equal loads are applied in opposite directions at different points on the structure. A torsional moment may he applied to a wing using two weight pans as shown in figure 4. One is attached to one end of a frame that snugly fits over the structure, while the other is attached to a cable routed over a pulley and connected to the other end of the frame. Equal weights are then applied to each weight pan. The moment is equivalent to the weight on either pan multiplied by the distance D between the attach points.

To measure the stress in a structure when it is loaded, small resistance wire gages connected in a Wheatstone bridge arrangement are used to measure the strain of the material. These strain gages, as they are called, are attached to the structure at specific locations, as shown in figure 5, and oriented in specific directions to measure such reactions as shear, bending moment, and torsion moment. Stress is proportional to strain in the linear range of the material (see fig. 2).

Structural deformations may be either linear (a displacement) or angular (a rotation) in nature. To measure a displacement a simple pointer attached to the structure and a scale attached to ground may be used. This method can give accuracy to 0.05 in. A slightly more accurate method requires a surveyor's level and a scale. The scale is hung from the structure and sighted with the level as shown in figure 6. This may give accuracy to 0.02 in. Mechanical dial gauges may be used to increase the accuracy of the measurements to 0.001 in.
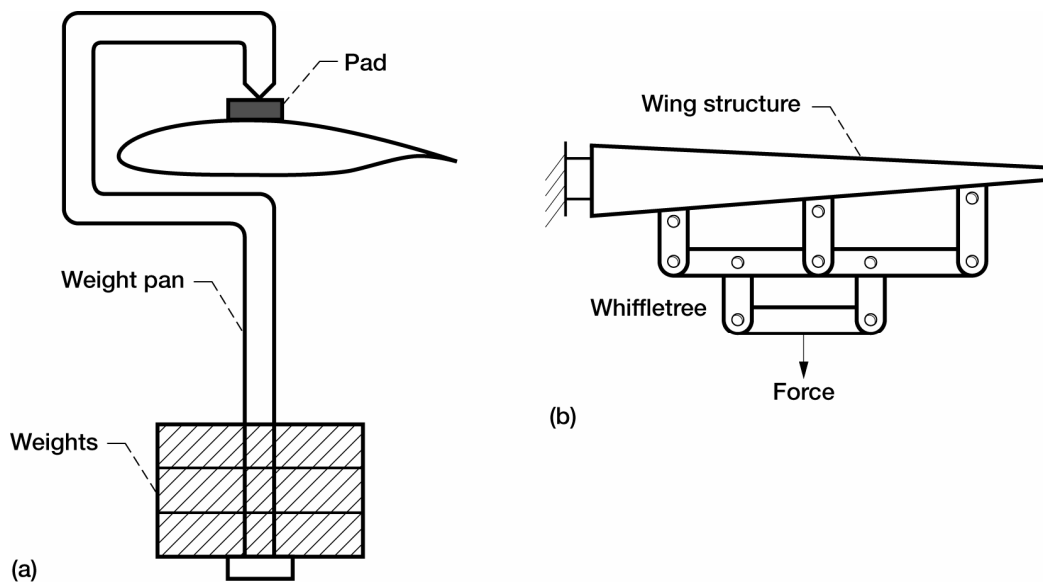
Figure 3.—Two loading fixtures for applying forces. (a) Weight pan. (b) Whiffletree.
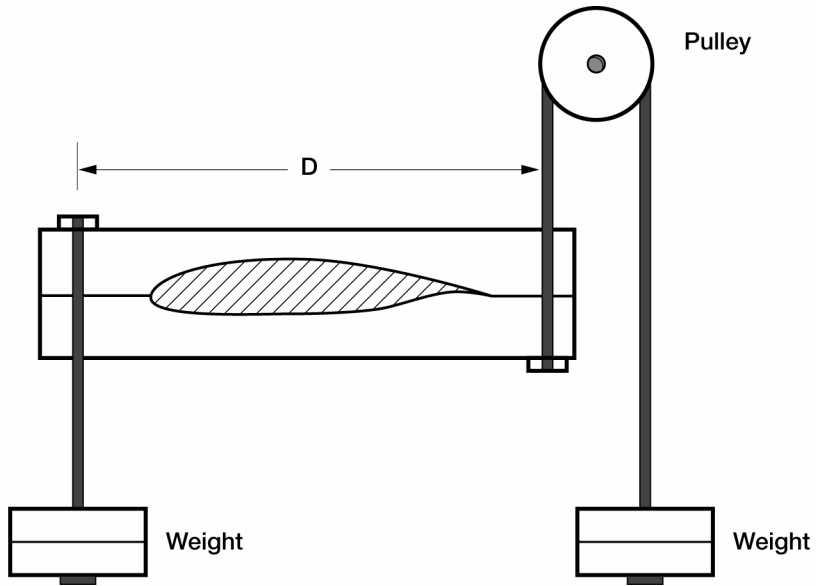
Figure 4.—A typical loading fixture for applying moments.
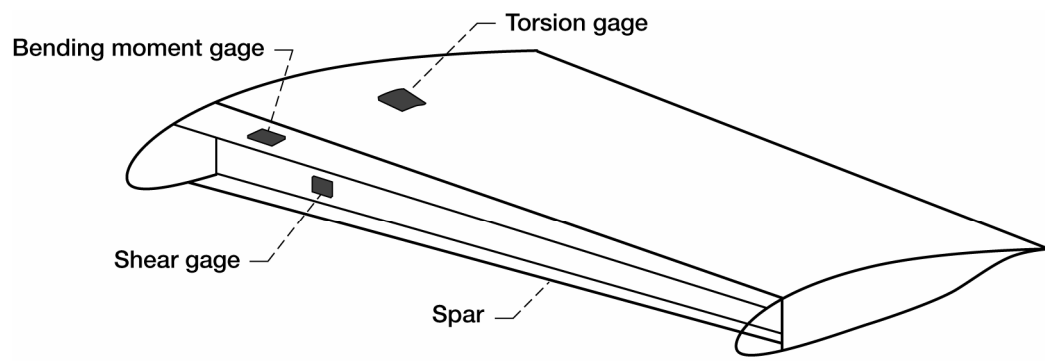
Figure 5.—Typical strain gage installation.
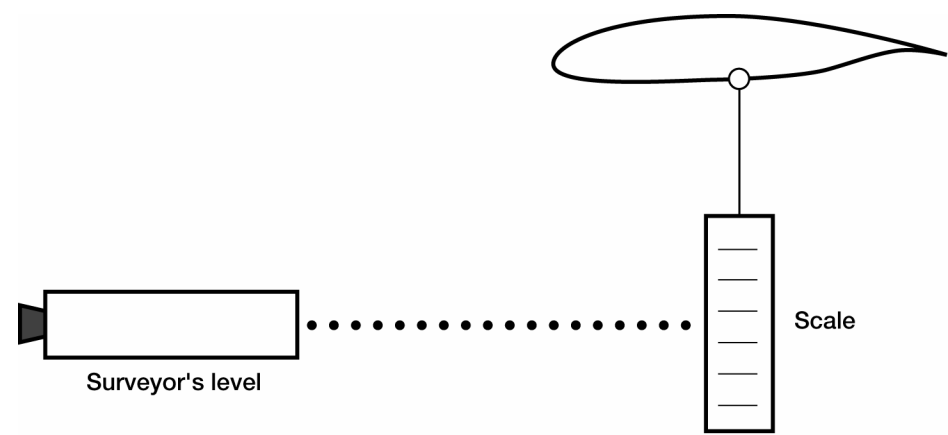
Figure 6.—A method for measuring displacements.

Three methods are presented for measuring a rotation. The simplest involves displacement measurements at two points at a distance L apart on the structure as shown in figure 7(a). For a small rotation, the angle θ is approximately equal to the tangent of the angle, or in other words, is equal to the sum of the displacements, Δl and Δ2, divided by the distance they are apart. That is,

$$\theta = (\Delta 1 + \Delta 2)/L .$$

Using another method which employs mirrors and a light source (a laser or simply a slide projector), rotation may he more accurately measured. The light is reflected by the mirror located on the structure to a wall some distance D away as shown in figure 7(b). As the structure rotates, the light is deflected a distance Δ such that θ = Δ/2D. The third method for measuring rotation is through the use of an inclinometer, either a bubble-type or an electrical accelerometer-type.

The federal standards for airworthiness of normal, utility, and acrobatic category aircraft are presented in Federal Aviation Regulations, Part 23 (ref. 5). To be certified by the Federal Aviation Administration (FAA) an airplane must pass certain ground tests for static strength. The aircraft must be able to withstand the application of limit loads—that is, the maximum loads expected during service—without permanent or excessive deformations. A permanent deformation may occur if the structure is loaded beyond the material yield point. In addition, the aircraft, must withstand the application of ultimate loads—that is, a load 1.5 times as large as the limit load—for at least three seconds without failure.

The flight envelope defines the flight conditions for which the aircraft has been designed. This envelope can be defined in terms of speed and load factor as shown in figure 8. Load factor is the ratio of total aerodynamic lift to total airplane weight. The envelope is bounded by values of maximum and minimum normal lift coefficients C_{N_A} which may be reached during take-off and landing, by maximum and minimum load factors N_z which may occur during maneuvers, and by maximum airspeed conditions which may occur during cruise or dive. The limit loads defined for ground tests must be the maximum load conditions experienced within this flight envelope.

Figure 9 shows the setup for the structural loads test of the NASA Langley Research Center DAST (Drones for Aerodynamic and Structural Testing) flight-test vehicle (see refs. 6 and 7). The vehicle is supported upside down along the fuselage so that the wing structure is loaded for a positive maneuver condition. Many loading pan fixtures are attached to the front and rear spars. Shot bags are placed in specific pans to simulate a flight load condition.

Data were acquired with strain gauges which were positioned to measure load L and bending moment BM. The data shown in figure 10 were acquired during the loading and unloading of many incremental loads. The data shown are linear (no yielding of the structure experienced) throughout the load range as is required.
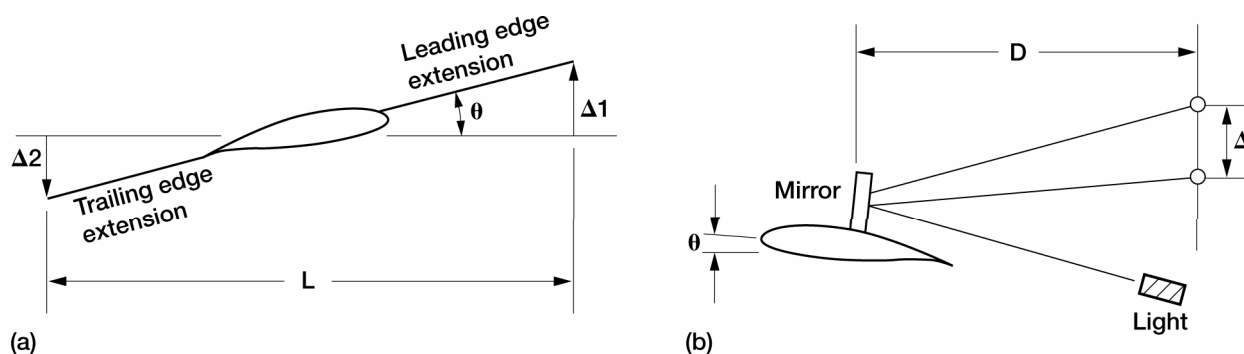
Figure 7.—Two methods for measuring rotations. (a) Displacement method. (b) Mirror method.
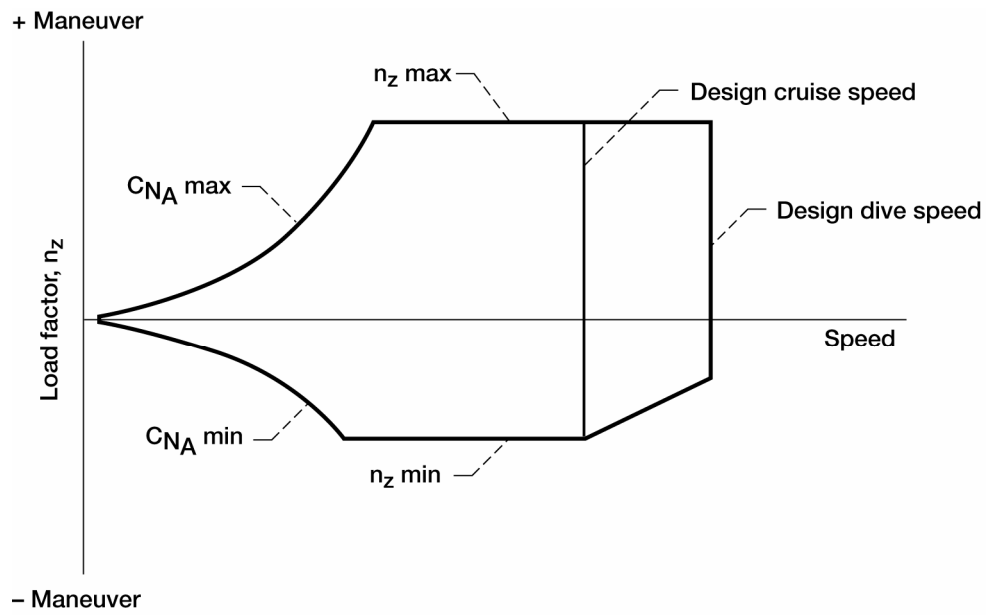
Figure 8.—Typical flight envelope in terms of speed and load factor.

Figure 9.—Structural strength test of DAST flight vehicle.
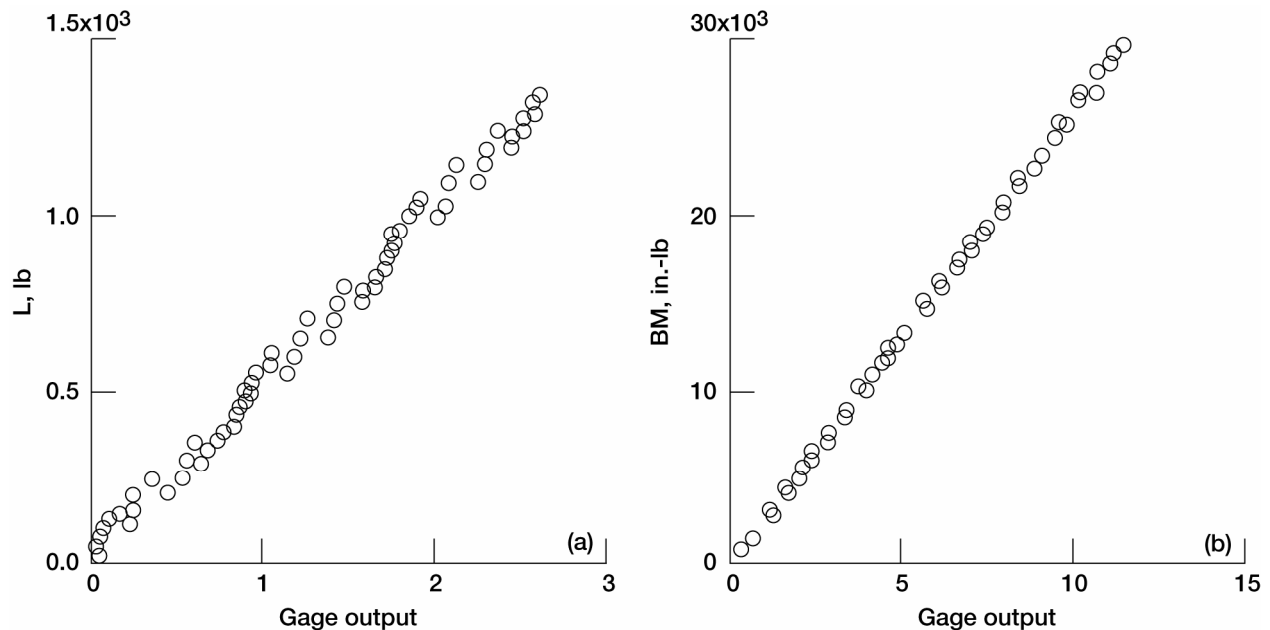
Figure 10.—Loads data measured on DAST flight vehicle. (a) Vertical load. (b) Bending moment.

Aileron Reversal

Aileron reversal is the condition in which the control surface aerodynamic forces twists the wing in such a manner that a zero rolling moment exists. Any further increase in speed will cause the aircraft to roll opposite to the stick motion—that is, a stick right command will cause the aircraft to roll to the left. This phenomenon is the interaction of aerodynamic structural elasticity as illustrated by the shaded area of figure 11.

Further explanation of aileron reversal is as follows. A deflection Δ of the control surface (positive for trailing edge deflected down) produces an incremental lift at the surface as illustrated in figure 12(a). Because the control is aft of the center of twist, a nose down pitching moment is produced which tends to decrease the wing angle of attack. Reducing the angle of attack causes a reduction in the wing contribution to lift. Normally, the total lift (wing plus control surface aerodynamics) is increased for a positive control deflection. However, if the elastic twist is large enough, the reduction in wing lift exactly equals the additional incremental lift caused by the control deflection. The total lift is unchanged in this case as illustrated in figure 12(b) by the neutral curve. For this condition no rolling moment is produced and the stick is ineffective. Increasing the aircraft speed will result in a decrease in total lift when the control is deflected and thus produces roll in the direction opposite that intended—that is, the reversal condition. Flight in this condition is possible if the pilot is able to reverse his thinking to push the stick right for a left roll. Recovery is achieved only by slowing down the speed.

During ground tests for aileron reversal evaluation, it is necessary to measure the torsional stiffness of the wing structure. The stiffness can be calculated from measurements of the twist angle made when the structure is loaded incrementally in torsion as illustrated in figure 4. For small twist angles θ at torsional loads T, the data is linear as illustrated in figure 13. The torsional stiffness k is equivalent to the inverse slope of the data.
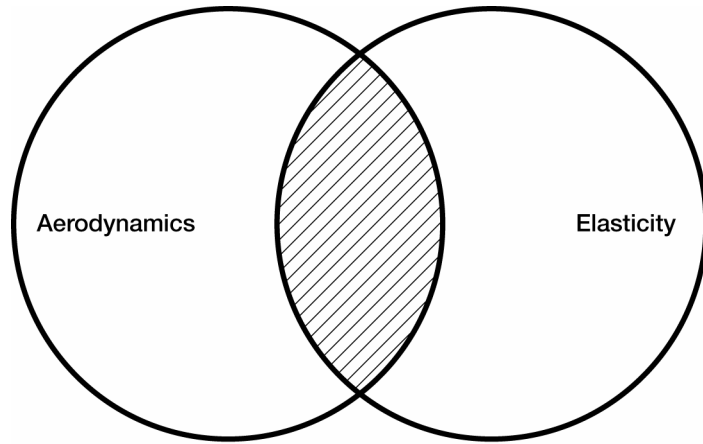
Figure 11.—Interaction diagram for aileron reversal.
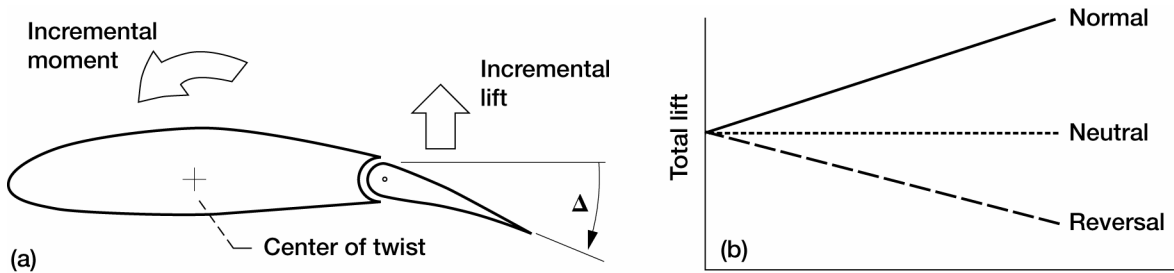
Figure 12.—Effect of control deflection on wing load and moment. (a) Incremental loads. (b) Total loads.
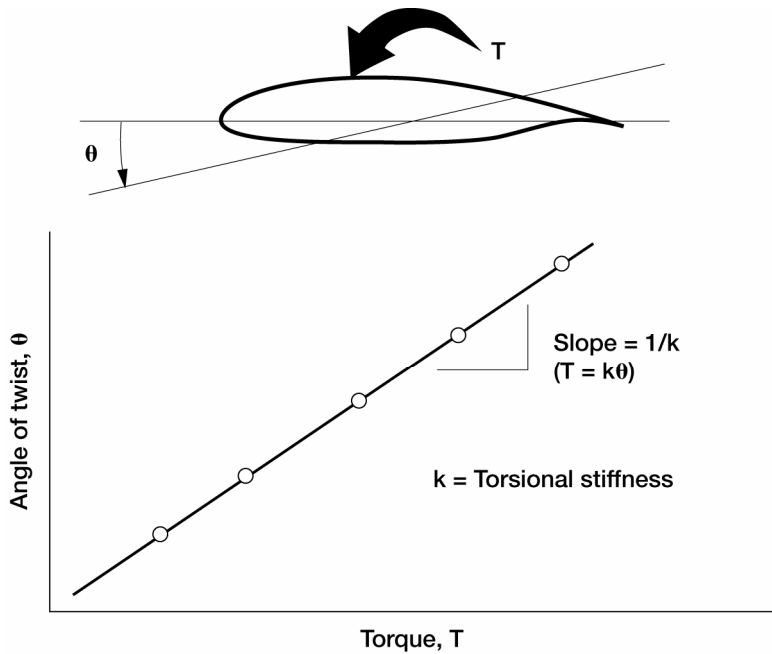
Figure 13.—Typical data curve for measuring wing torsional stiffness.

An aileron reversal dynamic pressure[†] can be calculated for a wing shown in figure 14 using the measured wing torsional stiffness k and a few other parameters. The other parameters include the coefficients of lift due to changes in angle of attack C_{L_α} and control deflection C_{L_β}, coefficient of moment about the mean aerodynamic center (*MAC*) due to control deflection C_{MAC_β}, the wing chord c and the wing area S. (The coefficients may be found in a typical airfoil handbook such as references 8 and 9). The equation for the reversal dynamic pressure q_R is

$$q_R = \frac{-C_{L_\beta} k}{C_{L_\alpha} C_{MAC_\beta} cS}$$

During flight test, data may be acquired to predict the dynamic pressure at which aileron reversal may occur. Measurements of roll rate and control surface displacement at various dynamic pressures may be used to extrapolate to the point of reversal—that is, the condition of zero roll rate per control surface deflection as shown in figure 16. Instrumentation normally used for the measurements include rate gyros, position potentiometer, strain gages, and tape recorders. However, equipment such as a horizon indicator or an inclinometer for measuring roll angle and a stop watch for measuring time may be used to calculate the roll rate. A stop for the control stick may be used to insure that the same control deflection is achieved at each data point.

FAR Part 23 requires that the airplane be free from control reversal throughout the flight envelope shown in figure 17 (simpler version of fig. 8). This may be shown by flight testing the aircraft to dive speeds without experiencing reversal. Or, by analysis, it may be shown that the aircraft is free from reversal up to 40 percent beyond cruise speeds or 20 percent beyond dive speeds, whichever is less.

Aileron reversal was measured on a quarter-scale wind-tunnel model of a fighter airplane (ref. 10). The aileron controls were located along the trailing edge at the wing tips of the arrow-wing planform. For the tests the model was supported on a sting in the middle of the NASA Langley Research Center Transonic Dynamics Tunnel (TDT) as shown in figure 18.

Rolling moment coefficients C_{L_δ} were measured using bending moment gages-positioned at the wing root. The moments were measured for three control deflection angles at each of three values of dynamic pressure transonic Mach numbers. The data are presented in figure 19 and show that the reversal dynamic pressure may be predicted by extrapolating the data to the zero-rolling-moment value.

$$q_R = \frac{-C_{L_\beta} k}{C_{L_\alpha} C_{MAC_\beta} cS}$$
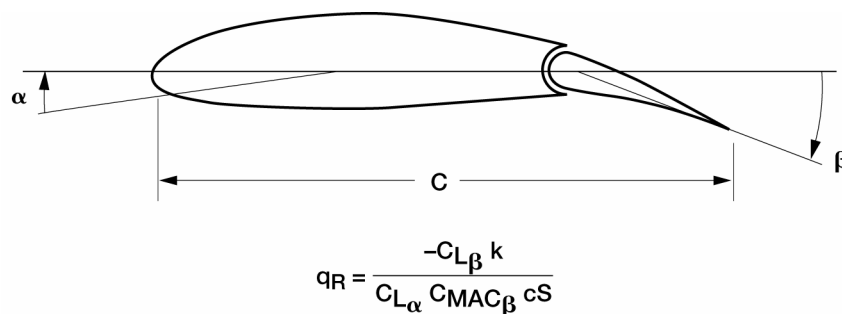
Figure 14.—Calculation of control reversal dynamic pressure.

[†]A short explanation of dynamic pressure is in order because it is the main parameter that is referenced when discussing aeroelastic problems. Dynamic pressure is defined as one-half the air density times the square of the true airspeed. This is also equal to one-half the air density at sea level times the square of equivalent airspeed. Because calibrated and indicated airspeeds are proportional to equivalent airspeed, dynamic pressure is proportional to the square of calibrated, or indicated, airspeed. Figure 15 shows the relationship between calibrated airspeed and true airspeed for altitudes to 40 000 ft.
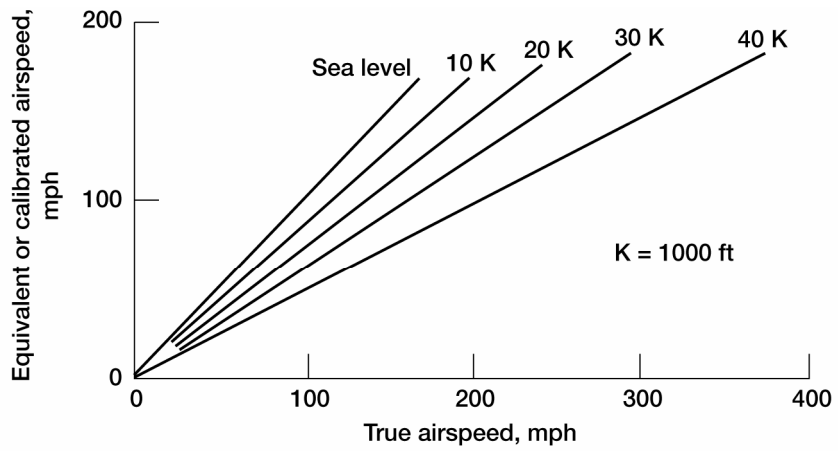
Figure 15.—Relationship between equivalent/calibrated airspeed and true airspeed at various altitudes.
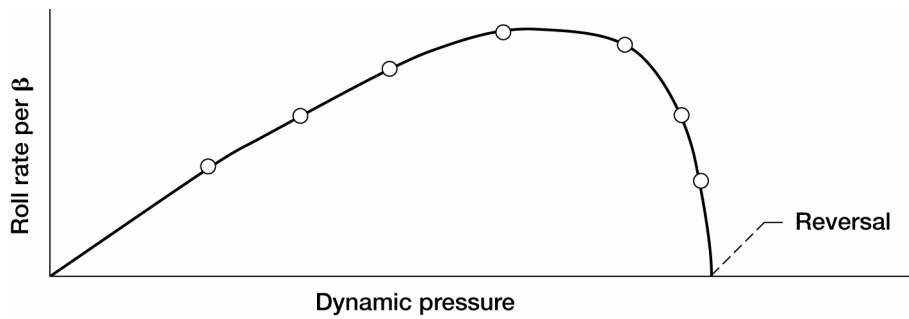
Figure 16.—Typical data measured to determine control reversal.
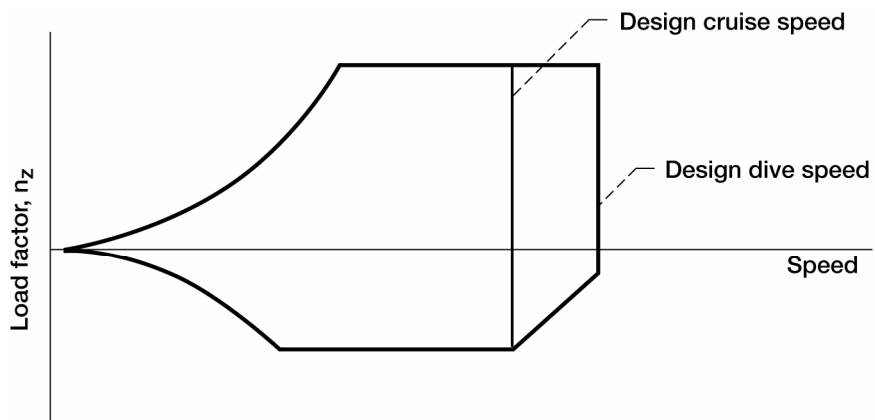
Figure 17.—Typical flight envelope showing relationship between cruise and dive speeds.
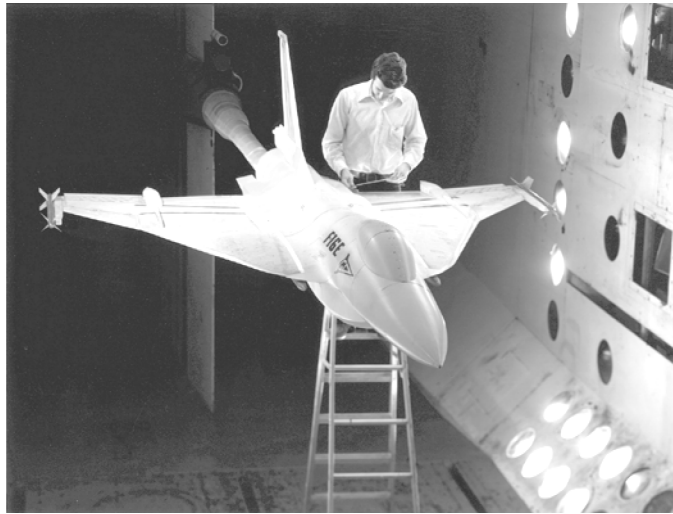
Figure 18.—Quarter-scale aeroelastic model mounted in TDT.
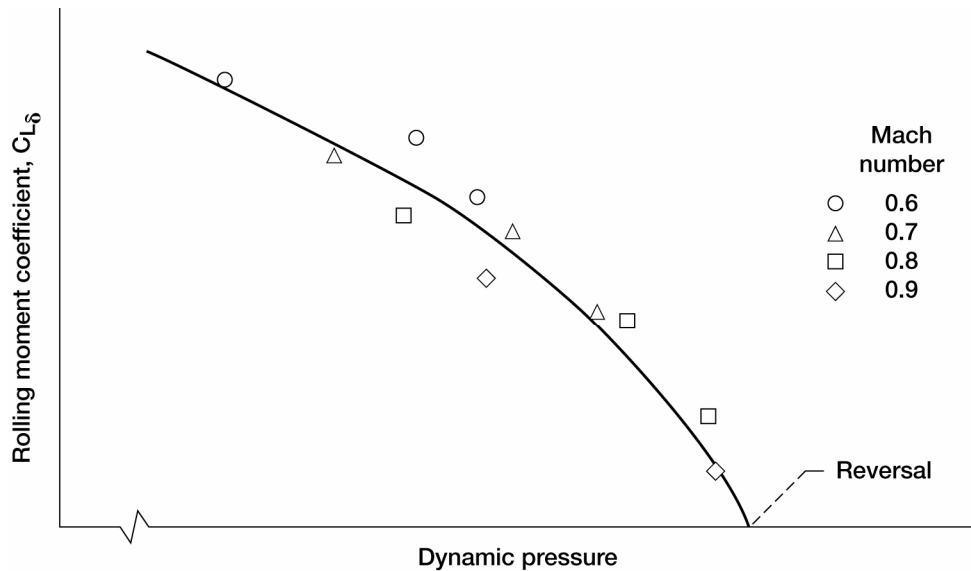
Figure 19.—Rolling moment coefficient measurements for predicting aileron reversal dynamic pressure.

Static Divergence

Static divergence of a lifting surface is a static instability which occurs when the aerodynamic moment on the surface exactly equals the structural elastic restoring moment. Therefore, it is the interaction of aerodynamics and elasticity as previously shown by the shaded area in figure 11. Divergence usually occurs on forward-swept surfaces (ref. 11) but also may occur on unswept or slight aft-swept surfaces. Divergence normally leads to catastrophic destruction of the lifting surface when the strength limits of the structure are reached.

Further explanation of divergence is as follows. The product of the resultant lift force illustrated in figure 20 and the distance e from the force to the elastic axis (effective rotation point of the structure) is equal to the aerodynamic torsional moment. For swept wings the relationship e between the lift forces and the local elastic axis locations inboard of the forces determines the twist of the elastic wing. For example, aft-swept wings twist nose down (washout) under load while forward-swept wings twist nose up (washin) under load. When the lift forces act

forward of the elastic axis (positive e), divergence can occur. Because forward sweep increases e and, therefore, the aerodynamic movement, forward-swept wings are more susceptible to static divergence than aft-swept wings.

The divergence dynamic pressure may be calculated from measurements made during ground test. It is necessary to measure the torsional stiffness k and the elastic axis location. To measure the torsional stiffness, the angle of twist of the structure is measured during the application of incremental torque loads as previously described. The torsional stiffness is inversely proportional to the slope of the acquired data as previously shown in figure 13.

The elastic axis EA is located by measuring the angle of twist of the structure during the application of a force load at various positions d along the chord. The elastic axis is the location at which an applied force creates pure displacement and no twist θ. An illustration of data acquired during such a test is shown in figure 21.

The divergence dynamic pressure q_D may be calculated from the following equation

$$q_D = k \big/ \left(C_{L_\alpha} e\, S \right)$$

where k is the torsional stiffness, e is the distance between the elastic axis location and the center of lift (normally assumed to be acting at the quarter-chord), C_{L_α} is the coefficient of lift due to angle of attack, and S is the wing area. This is illustrated in figure 22.
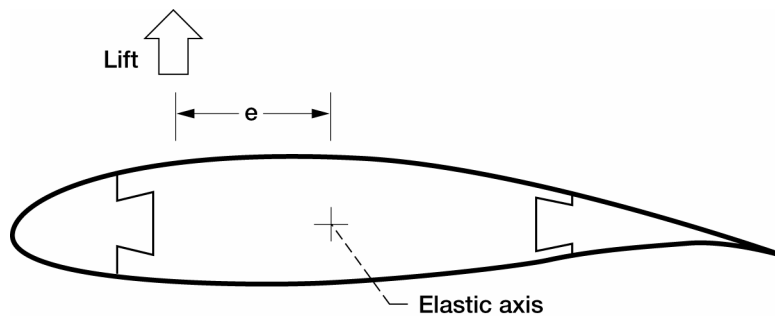
Figure 20.—Typical airfoil section showing relationship between lift and elastic axis.
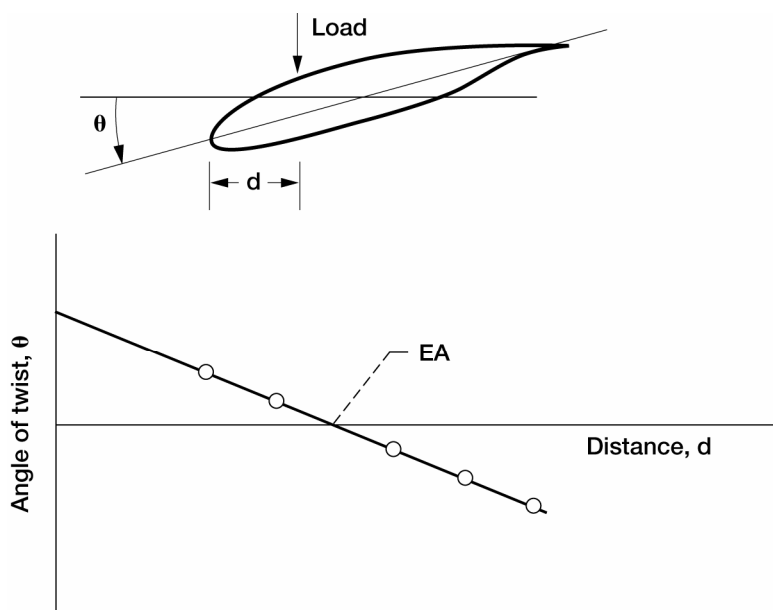
Figure 21.—Measurement of elastic axis (EA) location.
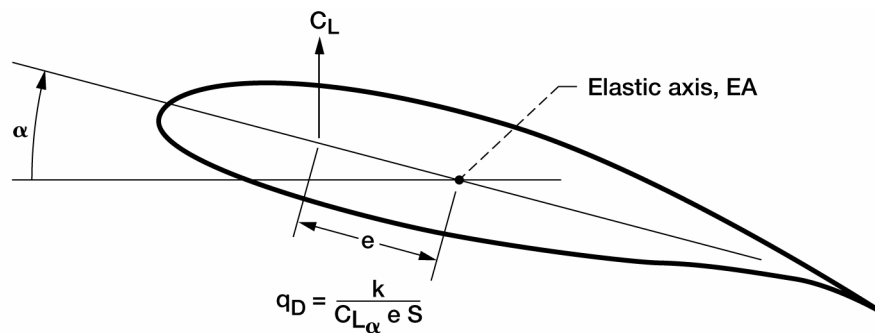
Figure 22.—Calculation of divergence dynamic pressure.
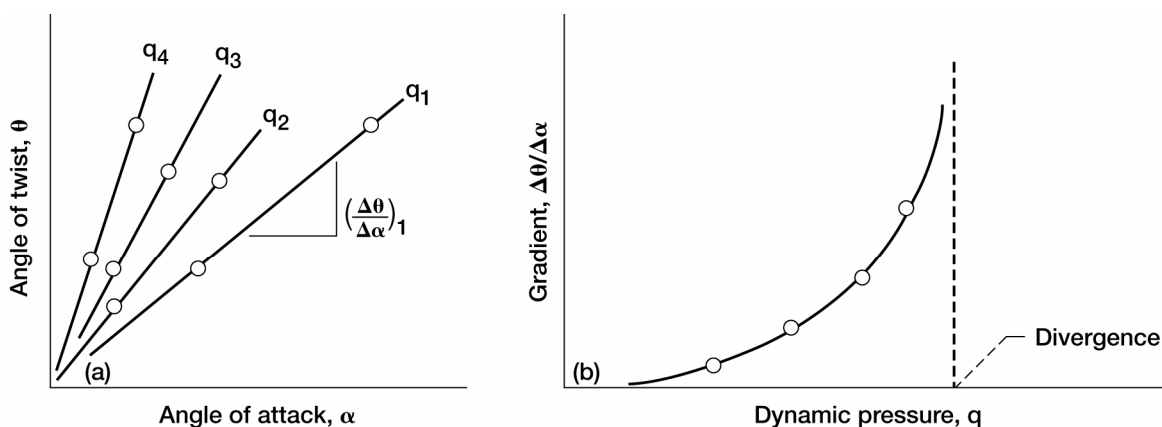
Figure 23.—Measurement of divergence dynamic pressure. (a) Twist-angle data. (b) Method of prediction.

Subcritical response of a lifting surface may be measured in flight to predict the conditions at which divergence will occur. The procedure is as follows. Wing twist angle θ is measured at several angles of attack α for various dynamic pressure conditions q. (The angle of attack may be varied while holding constant altitude and airspeed in a banked turn.) At each dynamic pressure a straight line is fitted through the twist/angle-of-attack data to determine the gradient (or slope) $\Delta\theta/\Delta\alpha$ as shown in figure 23(a). The gradients are larger at larger dynamic pressures and become infinite at divergence as shown in figure 23(b). Additional methods for predicting the divergence dynamic pressure from measured data are described in reference 11. Instrumentation that is needed include strain gauges calibrated to measure twist angle, angle-of-attack indicator and tape recorder to record the data. Alternately, a camera may be used to record the wing twist for post flight data reduction.

FAR Part 23 requires that the airplane be free from static divergence throughout the flight envelope. This may be shown by flight testing the aircraft at dive speeds without experiencing divergence. Or, by analysis which shows that the aircraft is free from divergence up to 40 percent beyond cruise speed or 20 percent beyond dive speed, whichever is less. These requirements are similar to those presented for aileron reversal (see fig. 17).

Static divergence was measured during wind-tunnel tests of the half-scale model of an experimental aircraft with a forward-swept wing shown in figure 24 (see ref. 12). The model consisted of an aeroelastically-tailored composite wing, half fuselage, and a closely-coupled canard. The model was mounted to a turntable on the sidewall of the TDT so that angle of attack could be varied to acquire load/angle-of-attack data for various dynamic pressure and Mach number conditions.

Subcritical response techniques were used to predict the divergence dynamic pressure boundary throughout the transonic Mach number range. The experimental predictions are compared in figure 25 with analytical predictions computed using structural finite element modeling techniques and several aerodynamic lifting surface theories. The range of analytical predictions is shown by the shaded area in the figure. The boundary has a minimum divergence dynamic pressure which occurs in the transonic region. (This is similar to typical flutter boundaries. Flutter is discussed in the following section.)

Figure 24.—Forward swept wing aeroelastic model mounted in TDT.
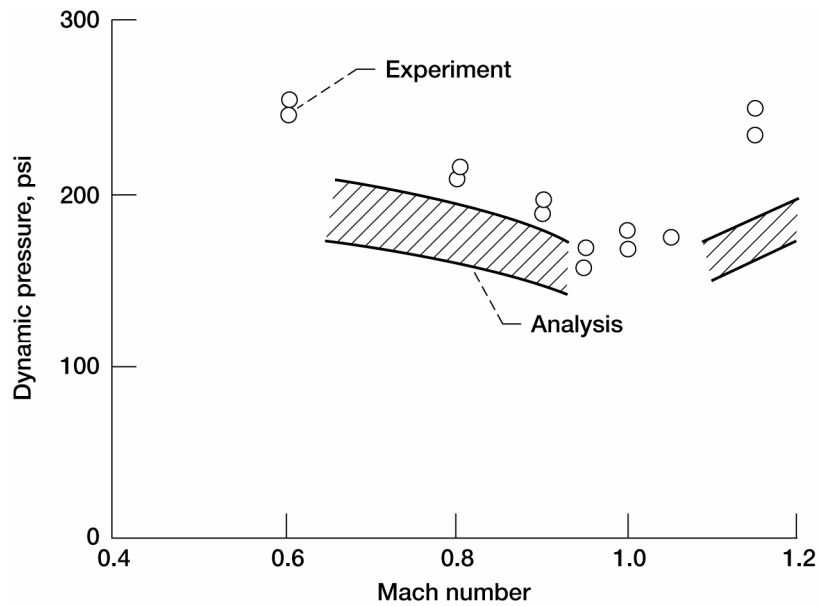
Figure 25.—Comparison of experimental and analytical results defining a static divergence boundary.

Flutter

Flutter is a dynamic instability which occurs when the aerodynamic, inertia, and elastic forces couple to cause a self-excited motion of a lifting surface. The flutter motion is sinusoidal and may be either constant or divergent in amplitude. Flutter, particularly that with divergent motions, may cause catastrophic destruction. The interaction of the three ingredients to flutter is shown by the shaded area in figure 26.

Further explanation of flutter is as follows. Time histories of typical structural responses are shown for three dynamic pressure conditions in figure 27(a). The time history for condition A shows motion that is damped and stable—that is, after a disturbance the amplitude decreases with time. The time history for condition B shows constant-amplitude motion that indicates neutral stability. The time history for condition C shows a divergent or unstable condition—that is, the amplitude increases with time. Both the neutral and unstable conditions represent flutter conditions.

In classical wing flutter the torsion mode coalesces (or couples) with the bending mode. The modal frequencies change with dynamic pressure as shown in figure 27(b). As the flutter dynamic pressure is approached the torsion frequency usually decreases substantially, and the bending frequency increases slightly. At flutter the two modes couple, and the wing oscillates at a single frequency. Typical conditions at which the time histories (A, B, and C) occur are indicated in the figure. Additional information is given in reference 13.

A simple flutter analysis of a lifting surface may be performed using strip theory aerodynamics and structural data. The aerodynamic parameters such as lift-curve slope and center of pressure location may be found in a typical aerodynamic handbook (ref. 8). The structural data, which includes the elastic axis location, mass properties, and vibration frequencies, may be acquired during ground test described as follows.

Measurement of the elastic axis location is performed as previously described. The angle of twist of the structure is measured for various load applications along the surface chord. Recall that the elastic axis is the load location which produces deflection but no angle of twist (see fig. 21).
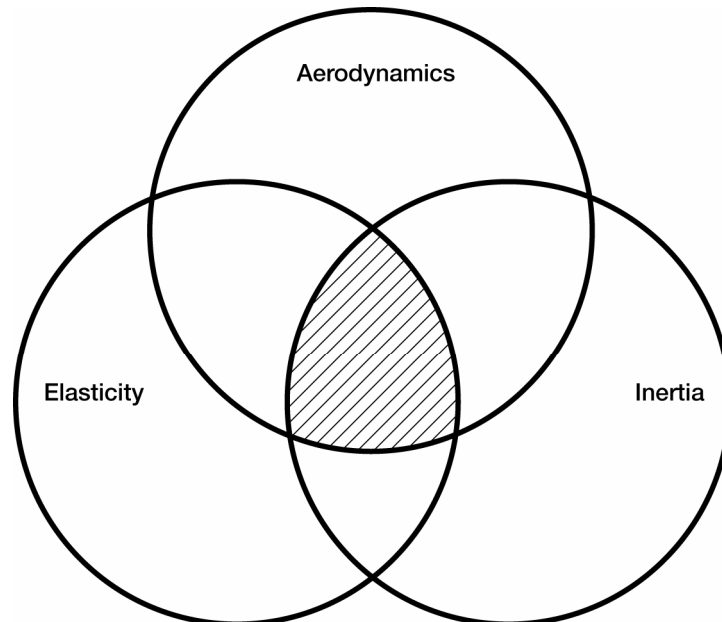
Figure 26.—Interaction diagram for flutter.
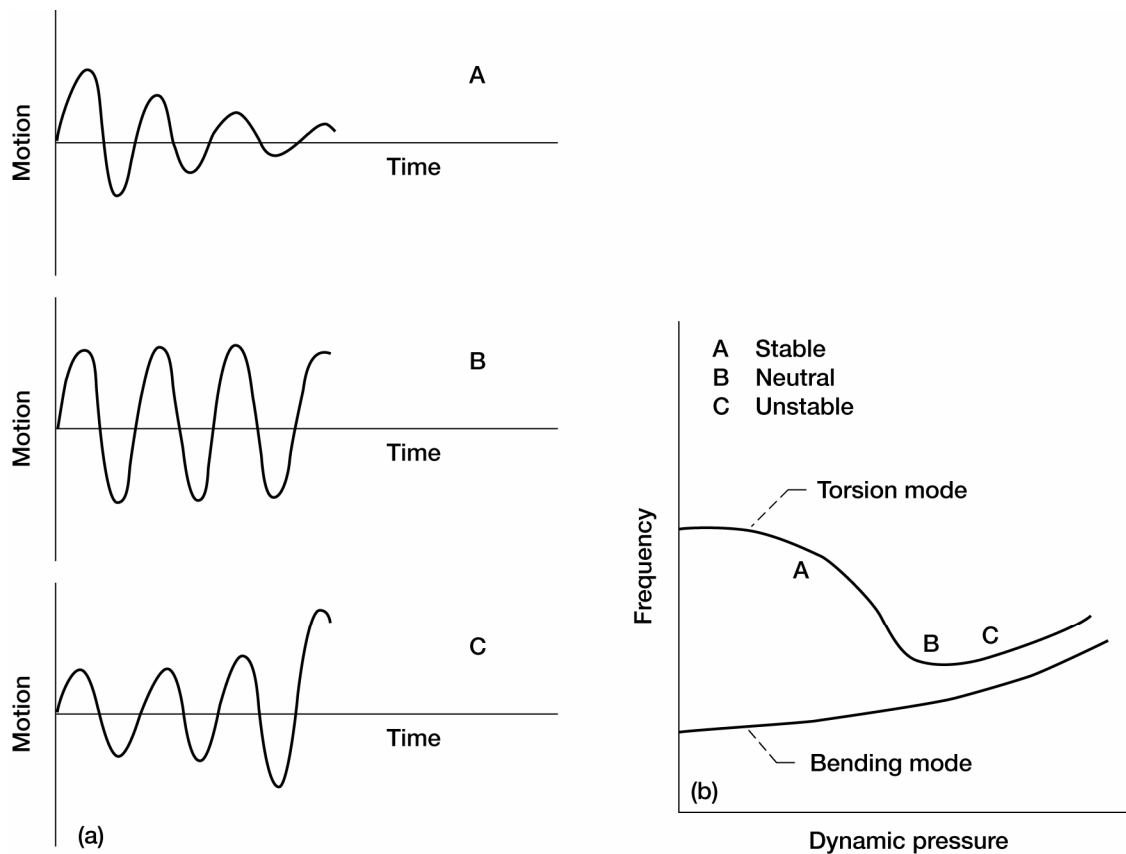
Figure 27.—Flutter stability of a typical wing structure. (a) Time histories. (b) Modal coupling.

The following mass properties may be measured in ground test: weight, center of gravity, and inertia. The weight of the surface may simply be measured with scales. The center of gravity CG may he located in terms of a distance x from the leading edge by balancing the surface on a "knife edge." The "knife edge" is moved until the point of balance is obtained as shown in figure 28(a). The pitch inertia of the surface may be measured using a bifilar pendulum—that is, a pendulum that has two filaments (or cables) as shown in figure 28(b). The cables are positioned symmetrically about the CG a distance d apart. The length ℓ of the cables should be at least ten times longer than d to maintain good accuracy. The period T (or time) that the surface moves through a complete cycle of oscillation may be measured with a stop watch. (The surface is displaced in twist on the cables about 30 degrees and released. Timing is begun as the surface passes a reference point and continues until the surface passes the reference point several times, usually ten or more. The period, or the average time for one cycle is computed by dividing the total time by the total number of cycles). The pitch inertia may be computed using the following equation

$$I = 2.444 \; W \; d^2 \, T^2 \big/ \ell, \;\; \text{lb-in.}$$

where the weight W is in units of pounds, lengths are in inches, and the period is in seconds.

Ground vibration testing which is performed to measure the natural vibration characteristics, particularly the resonant frequencies, of the structure, is described as follows. The structure to be tested must be supported so that the support mechanism does not influence the vibration characteristics of the structure alone. A good rule of thumb to follow is that the frequencies of the support modes should be on the order of ten percent of the frequency of the first structural mode. Often this can be achieved by simply deflating the tires of the aircraft. However, it may be necessary to suspend the aircraft on soft springs. The structure may also be supported as a pendulum with a low pendulum frequency. In this case the mode excitation force would he applied normal to the pendulum cable as shown in figure 29.
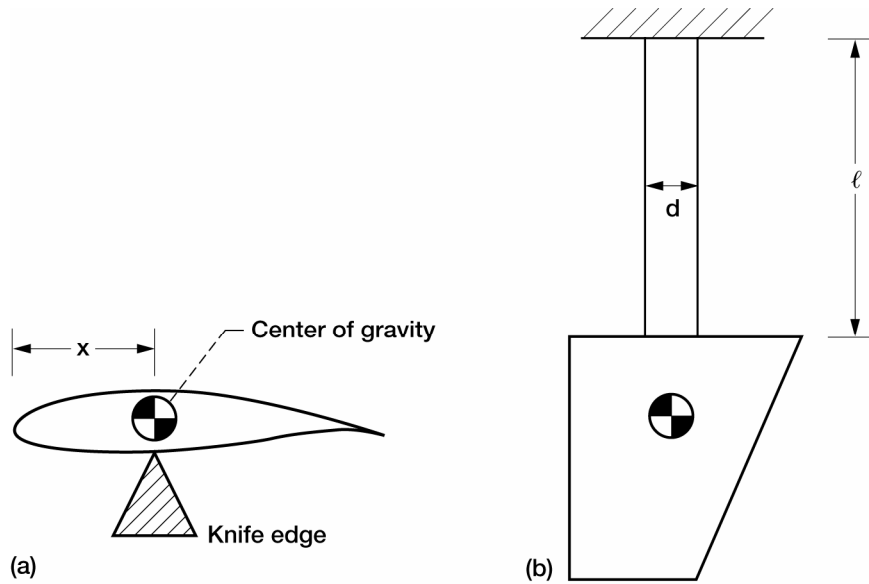
Figure 28.—Measurement of mass properties of wing. (a) Center of gravity.
(b) Pitch inertia.
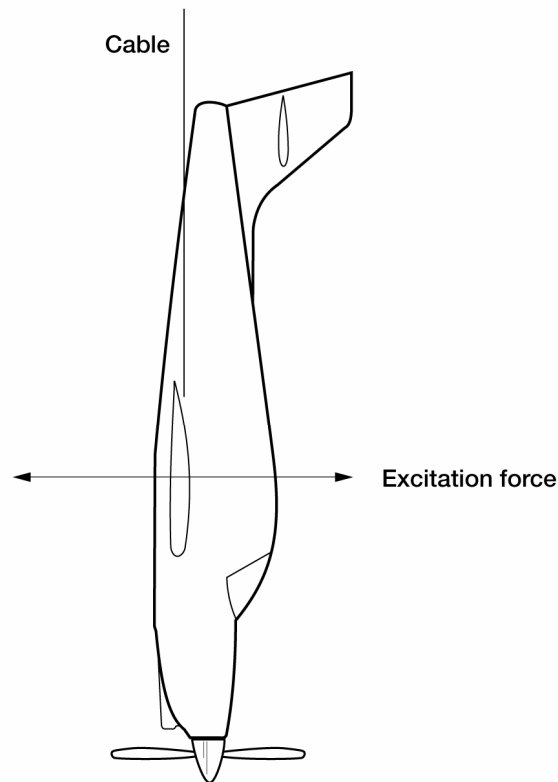
Figure 29.—Airplane support for ground vibration
test.

Equipment that may be used to sinusoidally excite the structure include electromagnetic shakers, pulsating air jets, and rotating masses. An electromagnetic shaker as illustrated in figure 30(a) may be used with an oscillator to drive it. A pulsating air jet device as illustrated in figure 30(b) may be easily fabricated using an air compressor to
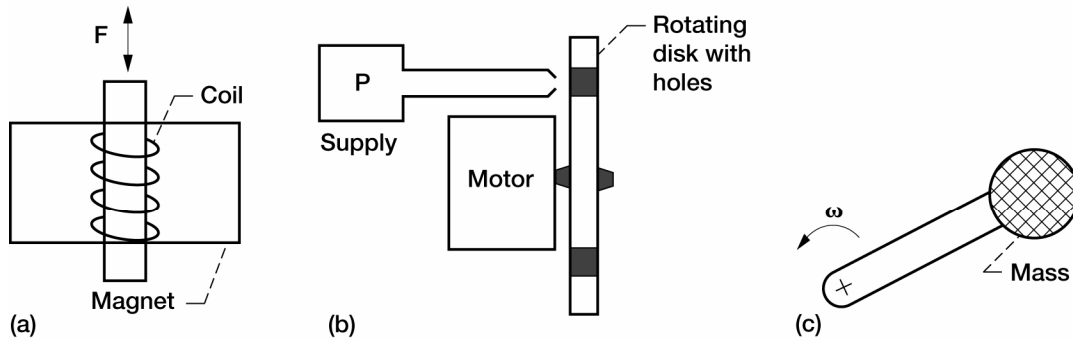
Figure 30.—Typical devices for exciting a structure. (a) Electromagnetic shaker. (b) Air shaker. (c) Rotating mass.

supply air which is directed toward the wing surface and deflected by a rotating disk with holes in it. The disk is driven by a variable speed motor. The air-jet device is particularly useful for lightweight structures because no additional mass is attached to the structure. A rotating-mass device as shown in figure 30(c) is the easiest shaker to fabricate. An eccentric weight is rotated using a variable speed motor. The vibration force is directly portional to the eccentricity e, the mass of the weight, and the square of the rotation frequency ω. It is important that neither the weight nor location of the device influence the frequencies of the structure.

Excitation of structures at their resonant, or natural, frequencies will cause the structural response of the structures to increase. The natural frequencies may be measure by exciting the structure with shaker equipment while slowly varying the excitation frequency and monitoring the structural response. The response may be monitored with an analyzer, strip chart, or, in some cases, visually. The frequencies at which the response is a maximum (see fig. 31) for constant shaker force are the natural frequencies of the structure. The value of the frequency may be determined with an oscilloscope, a strobe light, or, for frequencies less than three Hertz, a stop watch. It is also possible to use a timing light and tachometer attached to a running engine to measure the frequency of vibration of the structure.

A rule of thumb to follow for approximating the flutter speed of lifting surface with a conventional planform (zero to moderate aft sweep angles) uses a parameter called the flutter speed index FSI which is defined by the following equation:

$$FSI = V \big/ \left(b\omega\sqrt{\mu} \right)$$

where V is the flutter speed (feet per second), b is the length (feet) of the semichord at the three-quarter span, ω is the natural frequency (radians per second) of the torison mode, and μ is the ratio of the wing weight to the weight of the volume of air in a frustum of a cone enclosing the wing. For a constant chord wing μ is simply the wing weight per unit length w divided by π, the air density ρ, and the square of the semichord as illustrated in figure 32. The rule of thumb is that FSI is approximately equal to one-half at all altitudes. Thus, substituting the values of the parameters, including the air density at a particular altitude, into the equation for FSI equal to 0.5, the approximate flutter speed may be calculated. See reference 14 for additional information.

Flight testing for flutter (ref. 15) requires a flight plan to insure maximum safety. An example plan is shown in figure 33. The aircraft is tested at several velocities at each of several altitudes. Response of the aircraft to excitation may be monitored visually from the cockpit or from a chase plane, electronically using strain gages or accelerometers, or photographically using a movie camera mounted on the aircraft.
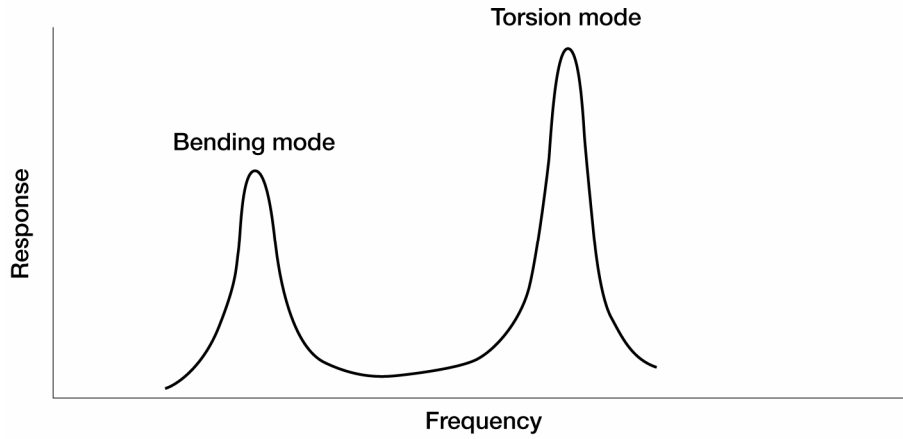
Figure 31.—Typical frequency response of wing structure.
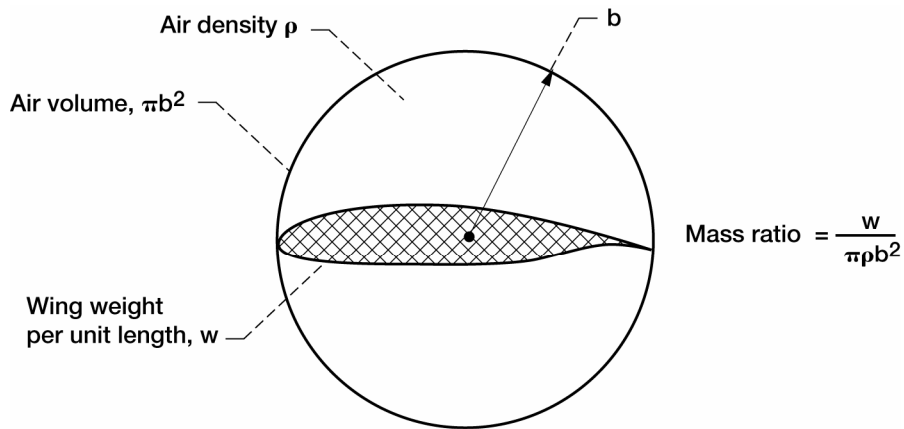
$$\text{Mass ratio} = \frac{w}{\pi \rho b^2}$$

Figure 32.—Mass ratio calculation.
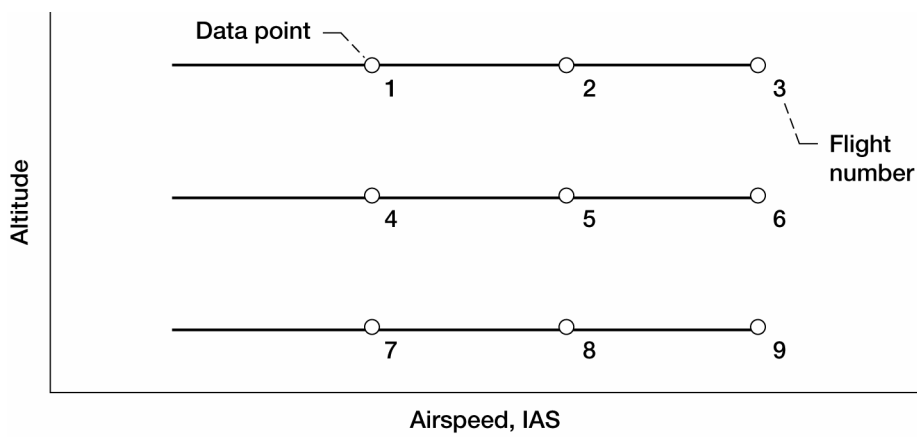
Figure 33.—Typical flight plan for flutter testing.

During flight tests the aircraft structure may be excited using a variety of methods. For a broad range of frequencies random ambients such as atmospheric turbulence or engine vibrations may be used in some cases. However, the level of excitation is not controllable and also is difficult to measure. For low frequencies (less than 10 Hz) pilot induced impulses from the controls may be used. For higher frequencies the excitations may be input to the structure through inertia or electromagnetic shakers attached to wing structure or control linkages. Another device that is often used is an aerodynamic vane attached to the wing tip as shown in figure 34 and driven by an electric motor or hydraulic actuator.

FAR Part 23 requires that the airplane be free from flutter throughout the flight envelope. This may be shown by flight testing the aircraft to dive speed without experiencing flutter. Or, by analysis, it may be shown that the aircraft is free from flutter up to 40 percent beyond cruise speed or 20 percent beyond dive speed, whichever is less. These requirements are similar to those presented for aileron reversal and static divergence (see fig. 17).

Ground test and flight test (ref. 16) of the experimental aircraft shown in figure 35 were conducted at Langley Research Center to determine the flutter speed of the horizontal tail so that laminar flow studies could be conducted on the aircraft wing. Ground vibration tests were conducted to measure the natural frequencies, mode shapes, generalized masses, and structural damping. The results were used in a flutter analysis which included lifting surface unsteady aerodynamics. The horizontal tail was instrumented with two accelerometers and then flight tested to record the tail response to random ambient turbulence.

Subcritical response techniques (ref. 17) were used on the recorded data to predict the flutter onset speed of the horizontal tail. One such technique is called the peak hold method which uses measured peak rms (root mean square) response at incremental frequencies throughout the frequency range of interest to predict flutter. As a flutter condition is approached, the peak increases in amplitude until, at flutter, it theoretically becomes infinite; or, in other words, at flutter, the inverse amplitude is zero. Results of data analysis using the peak hold method are shown in figure 36 for two different possible flutter modes. A 27 Hz mode is predicted to flutter at an airspeed of 235 mph. This speed is lower than that predicted for the 46 Hz mode. The aircraft speed was therefore limited to 205 mph to allow a 15 percent margin speed for overshoots during the laminar flow tests.
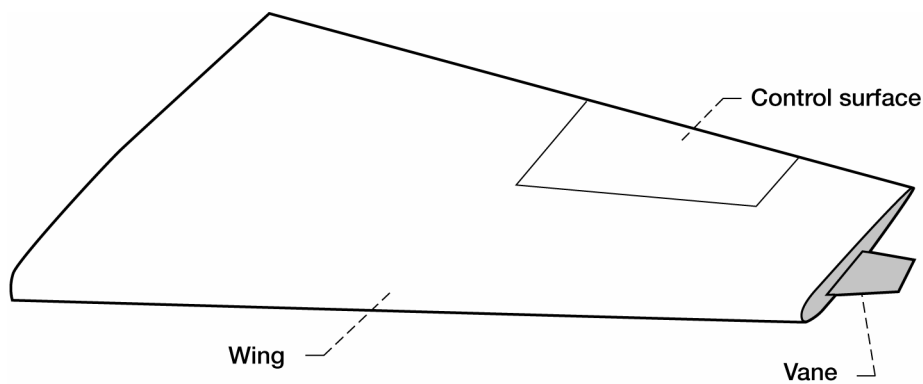
Figure 34.—Aerodynamic vane for structural mode excitation during flutter testing.

Figure 35.—Experimental aircraft for conducting laminar flow studies.
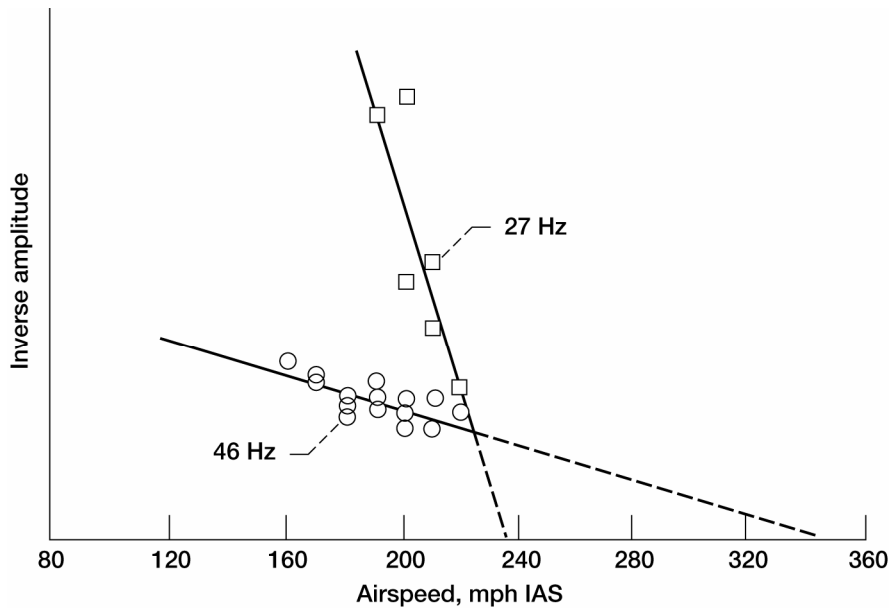
Figure 36.—Inverse amplitude data for predicting horizontal tail flutter.

Concluding Remarks

Ground test and flight test methods have been described that may be used to highlight potential structural problems that occur on aircraft. The structural problems described include static strength failure, aileron reversal, static divergence, and flutter. An example of each of the problems was discussed to illustrate how the data acquired during the tests may be used to predict the occurrence of the structural problem. Furthermore, the requirements that are set forth in the Federal Aviation Regulations to insure that each problem does not exist within the flight envelope were discussed.

References

1. Bisplinghoff, Raymond L.; Ashley, Holt; and Halfman, R.L.: Aeroelasticity. Second ed., Addison-Wesley Publishing Co., 1955.
2. Jones, W.P.: North Atlantic Treaty Organisation—Advisory Group for Aeronautical Research and Development: Manual on Aeroelasticity. Vols. I–VI, National Physical Laboratory, England, 1962.
3. Fung, Y.C.: An Introduction to the Theory of Aeroelasticity. Dover Publications, New York, NY, 1969.
6. Timoshenko, Stephen; and Young, D.H.: Elements of Strength of Materials. Fourth ed., Van Nostrand Company, Princeton, NJ, 1962.
7. Federal Aviation Regulations: Part 23, Airworthiness Standards, Normal, Utility, and Aerobatic Category Airplanes. Federal Aviation Administration, Washington, DC, 1974.
8. Murrow, H.N.; and Eckstrom, C.V.: Drones for Aerodynamic and Structural Testing (DAST)—A Status Report. J. Aircraft, vol. 16, no. 8, 1979, pp. 521–526.
9. Eckstrom, C.V.: Loads Calibrations of Strain Gage Bridges on the DAST Project Aeroelastic Research Wing (ARW–l). NASA TM–81889, 1980.
10. Abbott, Ira Herbert: Theory of Wing Sections, Including a Summary of Airfoil Data. Dover Publications, New York, NY, 1959.
9. Dommasch, Daniel O.; Sherby, Sydney S.; and Connolly, Thomas F.: Airplane Aerodynamics. Third ed., Pitman Publishing Corp., New York, NY, 1961.
10. Bensinger, C.T.: F–16E 1/4 Scale Flutter Model First Test (September 1981). General Dynamics/Fort Worth Division Report No. 400PR032, 1981.
11. Ricketts, R.H.; and Doggett, R.V., Jr.: Wind-Tunnel Experiments on Divergence of Forward-Swept Wings. NASA TP–1685, 1980.
12. Hertz, T.J., et al.: On the Track of Practical Forward-Swept Wings. Astro. Aeron., vol. 20, 1982, pp. 40–52.
13. Scanlan, Robert H.; and Rosenbaum, Robert: Introduction to the Study of Aircraft Vibration and Flutter. Dover Publications, New York, NY, 1968.
14. Harris, G.: Flutter Criteria for Preliminary Design. Report 2–53450/3R–467, Limg-Temco-Vought, Dallas, TX, 1969.
15. Flutter Testing Techniques. NASA SP–415, 1976.
16. Ricketts, R.H.; Cazier, F.W., Jr.; and Farmer, M.G.: Flutter Clearance of the Horizontal Tail of the Bellanca Skyrocket II Airplane. NASA TM–84528, 1982.
17. Ruhlin, C.L., et al.: Evaluation of Four Subcritical Response Methods for On-Line Prediction of Flutter Onset in Wind-Tunnel Tests. NASA TM–83278 (AIAA Paper 82–0644CP), 1982.

Flutter Model Technology[*]

Ron Busan[†]
Dynamic Engineering Inc.
703 Middle Ground Boulevard
Newport News, Virginia 23606

1.0 Introduction

Wind tunnel testing of dynamically scaled models plays a key role in assuring that new or modified aircraft will be free of flutter within their flight envelopes. Typically, about one-quarter of the total resources allocated to the flutter clearance of fighter type aircraft are for wind tunnel flutter model test programs. Dynamically scaled models are also widely used in research studies such as active control of aeroelastic response, buffet alleviation, and validation of theoretical or computational methods.

The purpose of this paper is to summarize the critical design considerations involved with designing and fabricating flutter model hardware once the basic requirements have been determined. An exhaustive treatment of all the analytical and testing considerations associated with flutter phenomena is beyond the scope of this work. Analytical and testing techniques will only be discussed with regard to their relation to the design, fabrication, and calibration of the hardware prior to tunnel testing.

The paper is organized as follows:

- Sections 2 and 3 present some design basics followed by a more detailed discussion of the design process for specific types of flutter model construction.
- Sections 4 through 7 discuss instrumentation, calibration techniques, load testing, and documentation.
- Section 8 is a case study of the design and analysis process for a set of supersonic flutter model components.

The design, analysis, fabrication, and calibration of flutter models involve many challenging and critical techniques. Engineers sometimes accuse the flutter model designer of practicing a mixture of intuition and art in addition to sound engineering practice. The intuition and art in many ways determine the eventual technical success of the model, but only if it is otherwise soundly engineered using techniques such as those presented in this paper.

All photographs included in this paper were supplied courtesy of Allied Aerospace, Newport News, Virginia.

2.0 Model Design Basics

2.1 Model Scaling

The selection of scale factors is a critical first step of any flutter model program. The first parameter to be selected is the model size, which determines the geometric scale factor, or the length ratio. It is usually desirable to make flutter models as large as possible for ease of fabrication and structural strength, as well as to make it easier to install instrumentation. Flutter models are typically larger relative to tunnel size than are conventional aerodynamic models. Although no absolute maximum ratio of model size to wind-tunnel size has been established, it is generally believed that it is desirable that the span of the model be less than 60 percent of the test section width for transonic

---

[*]This document was first published as Busan, Ron: Flutter Model Technology, WL–TR–97–3074, 1997, by the Flight Dynamics Directorate, Wright Laboratory, Air Force Materiel Command, Wright-Patterson Air Force Base.
[†]Currently at NASA Langley Research Center, Aeronautics Systems Engineering Branch, Systems Engineering Directorate, Hampton, Virginia 23681–2199.

tests where compressibility effects are important. Models for use at low speeds (compressibility effects not important) may have a larger span, perhaps as large as 75 percent of the test section width.

The fluid density is another parameter which is selected. Normally there will be one point in the full-scale operational envelope that will be simulated exactly during the wind-tunnel test. Testing will be conducted, of course, at other conditions, but the model will be slightly "out of scale." Generally, a density that is well up in the tunnel capability will be selected. The larger the test density for the model, the heavier the model can be made. Usually the heavier an aeroelastic model is, the easier it is to design and fabricate. Very lightweight structures are not only fragile, but are also costly to make and maintain.

For tests where compressibility effects are not important a wind-tunnel velocity will be selected to represent some full-scale velocity. These velocities can be the same or different in value. For tests where compressibility effects are important, there must be a match between model and full-scale Mach numbers so that the velocity scale factor becomes in effect a speed-of-sound scale factor.

There are essentially two classes of flutter models: low-speed models and high-speed models.

- For low speed models compressibility effects are not important, so the Mach number $(M = V/a)$ parameter is not matched between the model and the full-scale vehicle. The parameters that are always matched are the reduced frequency $(k = lw/V)$ and the mass ratio $(M = m/\rho V)$. It is also possible to match the Froude number $(F_N = V^2/lg)$, if that is desired. Froude number is an important parameter in instances where it is desirable to match static deflections of the vehicle due to gravity.
- For high speed models compressibility effects are important, and it is mandatory that the Mach numbers match. In addition, the reduced frequency and mass ratio will also be matched. It is not possible to satisfy Mach number, reduced frequency, and Froude number for a wind tunnel test with air as a test medium. It is possible, however, to match these parameters in another test medium, e.g., a nominal one-quarter size model tested in freon-12, which has a speed of sound (velocity) about one-half that of air, will satisfy these parameters. Due to environmental impact freon-12 is now being replaced with R134A at several test facilities.

2.2 Model Configurations

Most flutter models will fit into one of the following three configurations: component models, semispan models, or a model of the complete vehicle. For a particular aircraft program the models fabricated and tested will often progress through these configurations—initially starting with individual components, and ending with a model of the complete assembled vehicle.

Component models.—Component models are used to evaluate the dynamic characteristics of individual aircraft elements such as a wing, vertical tail, or horizontal. Since only an individual component is mounted in the tunnel, the scale factor can be larger, which often simplifies construction. Rudders and wing control surfaces will often be fabricated as separate elements, but are normally wind tunnel tested as part of a vertical tail or wing assembly. Component models are often mounted rigidly to a tunnel wall, although in some cases the attachment may incorporate springs or flexures to simulate a known mounting or actuator stiffness. Figure 2.2(a) shows a set of wing component flutter models.

Semispan models.—If the results of testing individual components and sub-assemblies yield satisfactory results, then a semispan model may be used to evaluate some of the interactions between components in the presence of a fuselage. Although a semispan model will not represent all the dynamic modes of the flight vehicle, it is considerably less expensive than a full model, and it will give significant information which cannot be obtained from individual component tests.

Complete vehicle.—A flutter model of the entire assembled vehicle configuration will yield results giving the most complete information about the dynamic characteristics of the flight vehicle. However, because of the
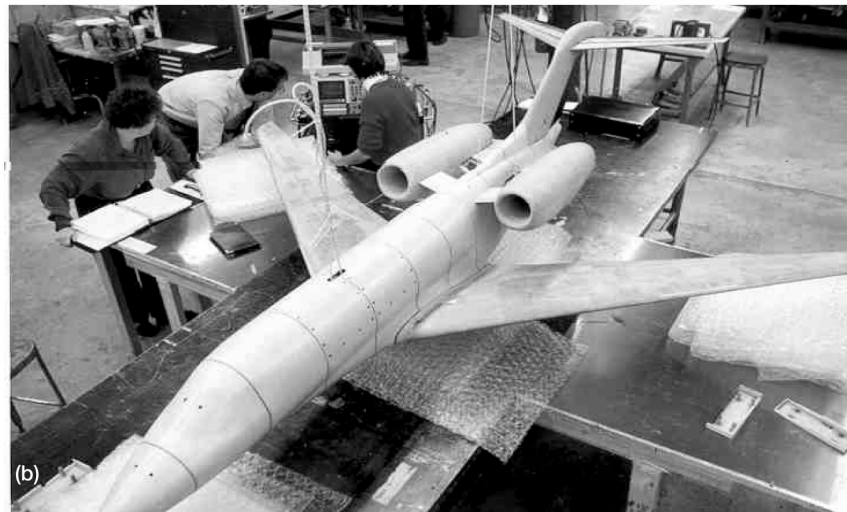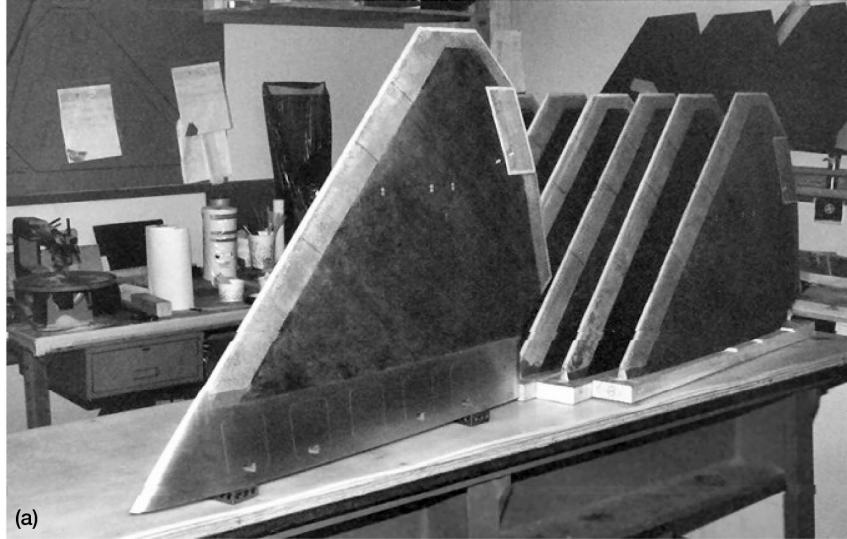
Figure 2.2.—(a) F-22 Supersonic wing flutter models. (b) Cessna Citation full span flutter model.

complexity of interactions between the various elements of the aircraft it may be difficult to interpret the results unless there has been previous testing of individual components. A flutter model of a complete aircraft assembly can also be relatively expensive, which is why models of simpler configurations will often be done to obtain preliminary data. Figure 2.2(b) is an example of a flutter model of a complete flight vehicle.

2.3 Model Mounting Systems

The mounting system for a flutter model must support the model in its proper position in the tunnel while simultaneously allowing sufficient motion so that the modes for the model can be evaluated. Support systems which have been used include cantilever mounts for individual components, stings, struts, four bar linkages, vertical rod and gimbal, cables, and 2-wire flying cable systems. Cantilevered models are used when it is not necessary to simulate the rigid body modes. In most cases the designer will attempt to have the mounting system allow three symmetric and three antisymmetric rigid body degrees of freedom with frequencies at least 30 percent below the lowest predicted flutter frequency.
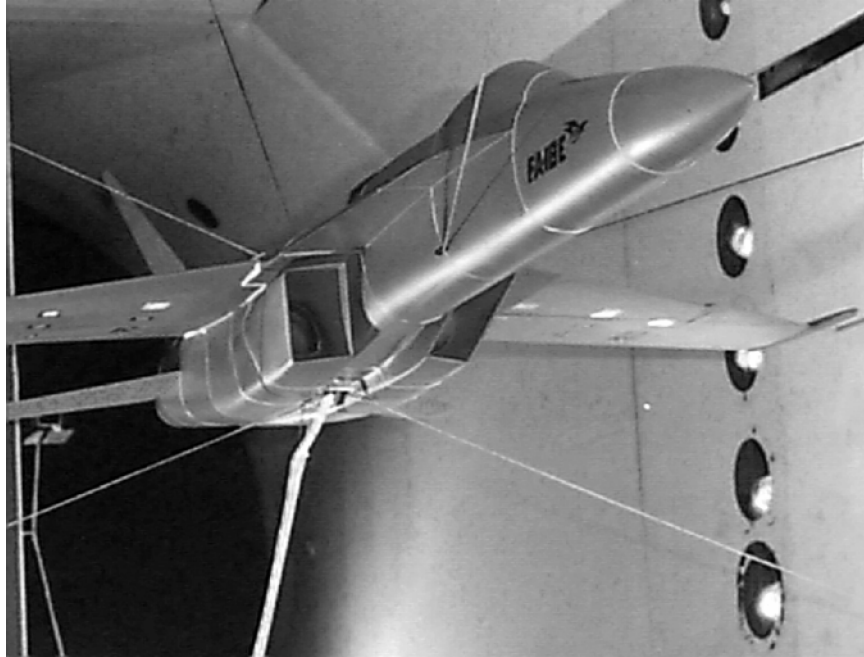
Figure 2.3.—F-18 E/F flutter model.

Each of the support mounting systems has particular advantages and disadvantages. Because this paper focuses on the flutter model components themselves, a detailed treatment of these support systems is beyond the scope of this report. Frequently the particular support mounting system used will be determined by the facility where testing will occur, and further information can be obtained from the facilities directly. Figure 2.3 shows an F–18E/F flutter model mounted on a cable/wire support system in the Transonic Dynamics Tunnel (TDT) at NASA Langley Research Center.

2.4 Types of Construction

The type of flutter model construction is usually determined by the specific test objectives (e.g., flutter trend studies, research, or flutter clearance of particular aircraft designs). The four basic types of construction are:

- plate
- beam/spar/pod
- stress skin
- replica

Simple trend studies or research can often be cost effectively evaluated using plate construction or a simplified beam/spar/pod model. Flutter clearance of aircraft designs will generally require more complicated beam/spar/pod models or stress skin/replica construction because of the need to accurately represent an actual aircraft structure.

The following paragraphs briefly describe each of these types of construction. A detailed discussion of the design parameters associated with each approach is contained in section 3.0.

Plate construction.—One method for matching the stiffness distribution of low aspect-ratio lifting surfaces is to use some variation of a plate as the main structural element. This approach has the advantage of providing a broad surface to which shaped elements can be mounted to simulate the proper external aerodynamic contour. Figures 2.4(a) and 2.4(b) show two views of a flutter model incorporating plate construction for the main wing.
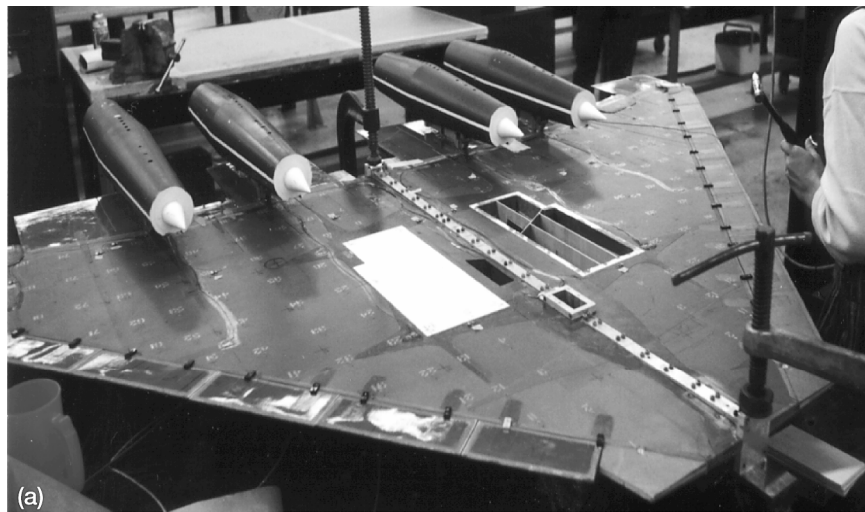
Figure 2.4.—(a) SST flutter model plate construction wing. (b) SST full flutter model assembly.

Since a constant thickness plate will rarely provide the required stiffness distribution, some means must be provided for varying the stiffness distribution across the plate. This can be done by "building up" sections of the plate to increase stiffness, making "cutouts" in the plate to reduce stiffness, "contouring" the surface of the plate, or some combination of each.

Beam/spar/pod construction.—Figures 2.4(c) through 2.4(f) illustrate beam/spar/pod flutter model construction. In this method a spar or beam element simulates the entire stiffness of the component. External "pods" attached to the spar provide the proper external aerodynamic shape. These pods typically have small gaps between them, with each pod attached to the spar at only one location. This minimizes the influence of the pods on the stiffness distribution of the component. The pods are normally constructed of lightweight materials, although "ballast weights" may be added later to properly simulate the mass properties of the overall component.
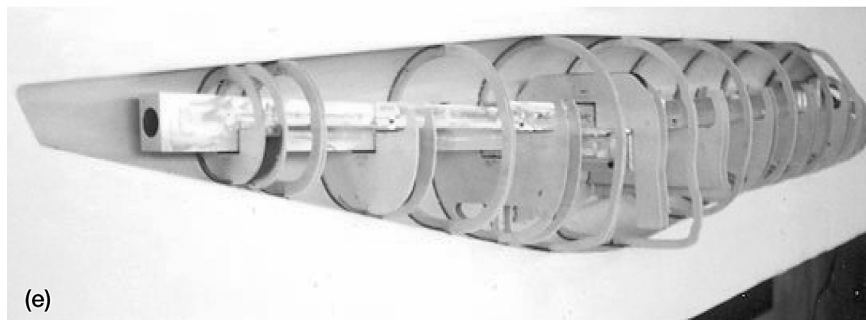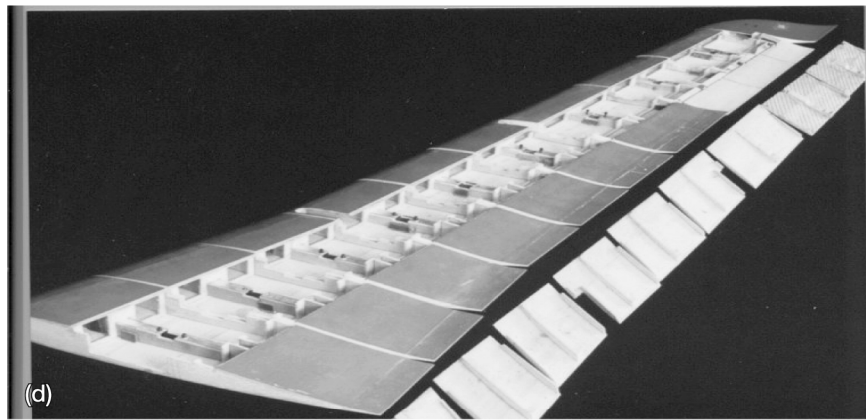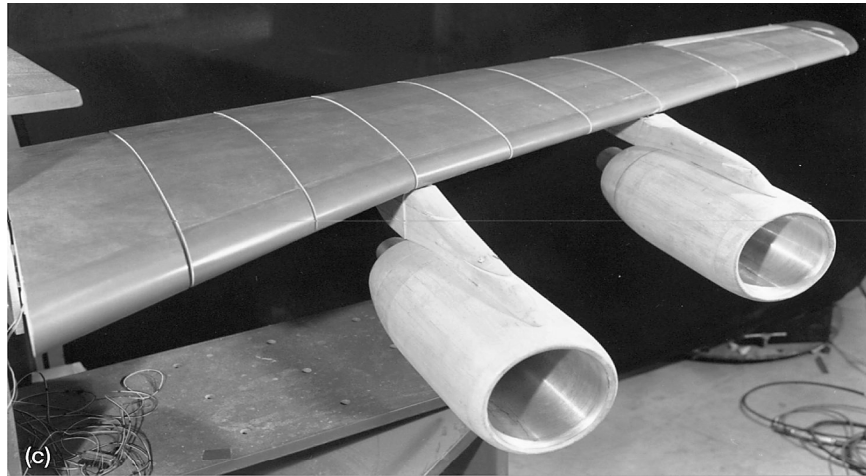
Figure 2.4.—(c) Assembled beam/spar/pod wing. (d) Details of wing pod construction. (e) Fuselage spar/pod construction.
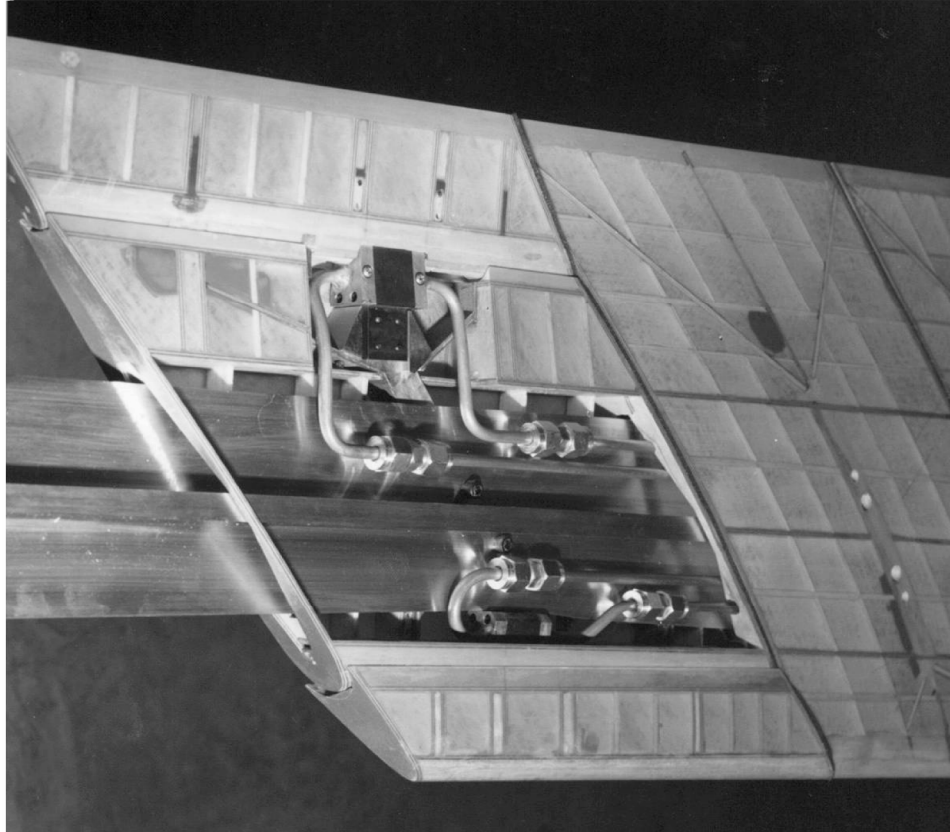
Figure 2.4.—(f) Close-up of spar/pod wing with actuated leading and trailing edge surfaces.

Stress skin construction.—For stress skin construction the skins forming the external contour carry a significant portion of the loads, and largely determine the dynamic characteristics of the model. Because the outer skin is intended to transmit loads, there are typically no "gaps" in the external shell. The core of a stress skin component will often be filled with a lightweight honeycomb or foam material. This type of construction is very common for high speed flutter models where the effects of "gaps" and discontinuities in the surface are much more critical to the flutter mechanisms. Figure 2.4(g) shows the internal structure for a stress skin vertical tail and rudder in the process of being fabricated.

Replica construction.—Replica construction involves duplicating the construction methodology for the full-scale design when making the model. Since almost all modern aircraft employ an integral skin/internal structure to transmit loads, this is typically a very difficult and costly construction method to use. Replica construction will almost always require extensive use of finite element modeling (FEM) because the interrelationship between skins and internal structure for the full-scale design is not always easy to assess. Except for very simple components replica construction often cannot be followed stringently because of unequal scaling factors, mounting constraints, and the particular requirements of the planned testing.
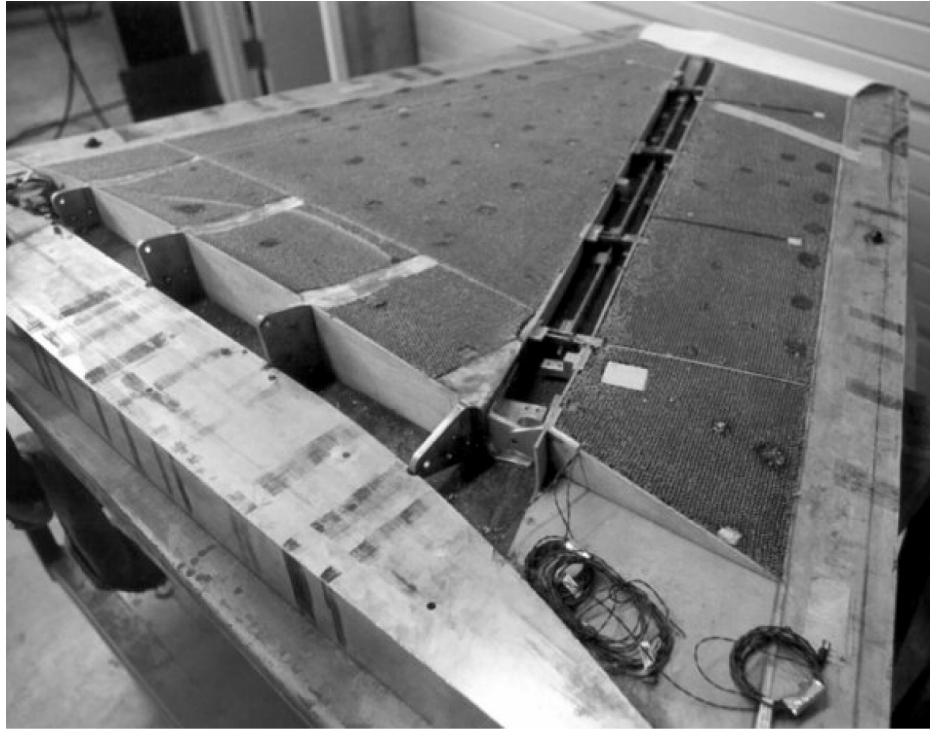
Figure 2.4.—(g) In-process construction of flutter model stress skin vertical tail.

2.5 Materials Used

The following table includes some materials frequently used in flutter model construction. "E" is the modulus of elasticity, "G" is the modulus of rigidity, and "F_{tu}" is ultimate tensile strength.

Material	E (psi)	G (psi)	Density (lb/in^3) Wt/Area (lb/in^2)	F_{tu} (lb/in^2)
2024 Aluminum	10.5×10^6	4.0×10^6	0.100	-----
Magnesium	6.5×10^6	2.4×10^6	.065	-----
Titanium	16.5×10^6	6.1×10^6	.163	-----
Steel	29.0×10^6	11.6×10^6	.280	-----
0–90° Fiberglass	3.5×10^6	$.40 \times 10^6$	.068	47,000
±45° Fiberglass	1.25×10^6	1.5×10^6	.068	20,000
0-90° Graphite	10.5×10^6	1.0×10^6	.057	90,000
±45° Graphite	3.8×10^6	4.0×10^6	.057	25,000
0–90° Kevlar	5.1×10^6	$.32 \times 10^6$	.048	75,000
±45° Kevlar	2.1×10^6	2.4×10^6	.048	30,000
Balsa (// to grain)	5000	200	.005	800
HRH 10–1/8 -1.8 Honeycomb	-----	-----	.00104	-----
HRH 10–1/8 - 3.0 Honeycomb	-----	-----	.00174	-----
1/64 in. Aircraft Plywood (3 ply)	-----	-----	.0004586	-----
1/32 in. Aircraft Plywood (3 ply)	-----	-----	.000926	-----
1/16 in. Aircraft Plywood (3 ply)	-----	-----	.001565	-----
1/8 in. Aircraft Plywood (5 ply)	-----	-----	.002372	-----
Tungsten	-----	-----	.67	-----

It should also be noted that the values in the table are averages. The values for metals do not vary much, but composite properties can deviate widely depending on the particular fibers used, the weave pattern, the layup process, etc. For example, the author is aware of a case where one graphite fabric was substituted for another. The brand of fibers, density, number of strands in each direction were all identical. The only thing that differed was the weave pattern, but this was enough to change the effective "E" value by 20 percent.

For composite layups it is a good practice to make up calibration samples using the same process planned for the spars. "E" and "G" values derived from such samples may vary significantly from those obtained from published data sheets. This is not to imply that manufacturers are not properly representing their products. Rather this is just a recognition of how "process dependent" the properties of composite layups can be. The flutter model designer must recognize and accommodate this reality of composite materials in flutter model applications.

There is also a common misconception that composites will always provide a stronger/stiffer structure for less overall weight. It is true that composites typically provide a better strength/stiffness to weight ratio when only one direction is important. However, in many cases spars or skins will experience loading in multiple directions, and it is necessary to design the structure with significant strength/stiffness along multiple axes. In these cases metal may prove to be more efficient not only because its material properties are isotropic, but also because the strength/ stiffness to volume ratio is typically better for metals than for composites. This can be a significant factor for highly loaded structures where the external contour is fixed.

This author is aware of several instances involving relatively thin members when the strongest/stiffest sandwich structure was obtained from steel skins over a honeycomb core. This was because the steel skins were thinner and thus had a greater average distance from the neutral axis. (The composite skins needed to be thicker, and as the skin thickness increases inward from the external geometry the effectiveness of the additional material decreases.)

The three most common composite materials used for flutter model construction are graphite, fiberglass, and Kevlar. Each of these has its own particular advantages and disadvantages.

Graphite.—Graphite materials generally provide a higher strength/stiffness to weight ratio than fiberglass. This is its primary advantage. The main disadvantage of graphite is its cost. Graphite also does not sand to quite as smooth a surface as fiberglass unless care is taken with regard to the resin content.

Graphite has an extremely low coefficient of thermal expansion. This can either be an advantage or a disadvantage depending on the requirements. If a graphite component is cured at elevated temperatures in an aluminum mold the resulting part will be larger because of the expansion of the mold. As the aluminum mold cools it will contract, but the graphite will not. This can cause difficulty in removing the part from the mold. For longer parts the dimensional changes may be significant enough that they will need to be accounted for during the design process.

Fiberglass.—Fiberglass is readily available, relatively inexpensive, and easy to work with. This is usually the first choice of composite materials unless the model requirements dictate otherwise. The main disadvantage of fiberglass is that it is somewhat heavier and not as stiff or strong as an equivalent weight of graphite.

Kevlar.—The main advantages of Kevlar is its toughness, abrasion resistance, and light weight. Graphite and fiberglass can be somewhat brittle, and individual fibers will fracture easily. Kevlar is much tougher, which is the reason it is frequently employed in bullet proof vests and lightweight armor for military applications. Generally the stiffness properties of Kevlar are less than graphite, but higher than fiberglass. Kevlar is also relatively expensive, and it is difficult to cut or sand because the individual fibers will resist shearing.

Kevlar is occasionally used in flutter models for applications where toughness is needed. Section 8.0 describes how it was used to solve a particular design challenge on a supersonic flutter model component.

Combinations of composite materials.—It is possible to mix the various composite materials together in a single layup to make the best use of the favorable characteristics of each. For example, the outer layer of the skins on some of the supersonic flutter model components described in section 8.0 was fiberglass fabric, and the remainder was graphite unidirectional tape. Whenever combinations of materials are put together it is advisable to make samples to ensure that there are no unforeseen difficulties. The initial skin layups just referred to curled up like potato chips because the fiberglass on the outer surface contracted significantly as the cured layup cooled, but the adjacent graphite did not. This made it necessary to use a vacuum "bag" to flatten out the skins and hold them tight against the core material while the adhesive bond was curing.

Fabrics, unidirectional tapes, and roving.—Woven fabrics are convenient to use for skin layups. Woven fabric also provides the most suitable external finish on a skin because interwoven fiber bundles are less likely to be pulled

loose from a scratch or scrape. For this reason a thin layer of woven fabric is often placed as the most exterior layer of the skin, even when the main layup consists primarily of unidirectional tape. Woven fabric also tends to be more isotropic with regard to its material properties. This inherently makes a skin layup made from woven fabric less likely to warp or have interlaminar stress problems.

Unidirectional tapes have the advantage of providing the highest strength and stiffness associated with a single direction. In applications where it is essential to achieve a strength or stiffness in one direction which is significantly higher than for others, unidirectional tape may be the best alternative. Some of the disadvantages of unidirectional tapes are:

- they are more subject to damage due to kinking of fibers or surface scrapes
- layups are more difficult to analyze with regard to stiffnesses and strengths in the off-axis directions
- they are normally only available pre-impregnated with resin
- warping of the skins is more likely due to the non-isotropic nature of the material
- they are much more sensitive to "fiber wash" (local changes in fiber orientation)

The previous table of material properties does not include any values for unidirectional composites. The reason for this is that unidirectional composites present greater challenges with regard to the stress analysis, and their properties are even more process dependent than fabrics. The very high published "E" values for unidirectional layups can only be achieved with careful control of the fabrication process. For example, the author is aware of a spar that was designed using an extensive amount of unidirectional graphite. The resulting spar stiffness was about 15 percent lower than expected due to small deviations in the mold pressure which caused the fibers to change their orientation slightly ("fiber wash"). Understanding and accounting for all the possible variables associated with a unidirectional composite layup can be a tedious process requiring multiple sample parts. While this may be warranted for mass production, it is usually not the most effective method to produce a flutter model component.

Roving consists of a continuous fiber bundle which can be used to create a composite structure using a filament winding machine. This approach is much more suited to mass production items for commercial industry. It is listed here only because it could be considered as an alternative fabrication method for certain simple spar configurations.

Dry versus pre-impregnated with resin.—Woven fabrics and roving are available as "dry" material consisting only of the fiber strands, or pre-impregnated with resin by the manufacturer. Unidirectional tape is normally only available pre-impregnated with resin. This is because the unidirectional fiber strands would simply fall apart if not "stuck" together with the resin. The following tables highlight the major advantages and disadvantages of using dry or pre-impregnated materials.

Dry:

Advantages	Disadvantages
Easy storage, and no shelf life considerations	Unidirectional tape not available
Can be cured at room temperature—and therefore can be used with wooden molds or patterns, wood internal structure, and low temperature adhesives	Resin content of final layup is a function of the particular fabrication procedure followed, thus making it more difficult to control

Pre-Impregnated With Resin:

Advantages	Disadvantages
Resin content of final layup very predictable	Must be stored in a freezer—has a limited shelf life
Unidirectional tape available	Usually must be cured at elevated temperatures—therefore usually must use composite or metal molds/patterns, and must consider temperature effects on wood and other materials subjected curing temperatures

3.0 Design Details

Sections 3.1 through 3.4 are descriptions of the design process for the four most common methods of flutter model construction. Section 3.5 deals with the specific subject of hinged control surfaces.

Figures 3.1(a), (b), and (c), as well as figures 3.2(gg), 3.2(i), and 3.2(j) were taken from or adapted from illustrations in chapter 12 of "Aeroelasticity" by Bisplinghoff, Ashley, and Halfman published by Addison-Wesley Publishing Company in 1955 (ref. 1). Some other figures in this section were based on sketches or illustrations found in undocumented material, or found in multiple references.

3.1. Plate Construction

Except for the most elementary of designs it is difficult to calculate a set of influence coefficients for a plate structure. Typically a finite element model (FEM) will be required to iterate to an acceptable design using plate construction.

Built-up plate structure.—A "built-up" plate structure is typically fabricated by bonding together constant thickness sheets of material as shown in figure 3.1(a). Aluminum and magnesium are the most common metal materials used in plate construction. For built-up plate construction composite materials can provide the design flexibility for adding plys to "tune" a plate structure up to match a particular stiffness distribution once the initial plate fabrication is complete. "Tuning" of flutter model structural elements is discussed in section 5.6.

Constant-thickness plate with cutouts.—A second approach is to start with a constant thickness plate which matches the "stiffest" portions of the target distribution. Other areas of the plate are then "cut out" to reduce the stiffness in the discrete areas corresponding to lower stiffnesses on the target distribution. Figure 3.1(b) shows a constant-thickness plate with circular cutouts. The shape, size, and number of plate cutouts is determined based on fabrication considerations, and on the particular configuration which the finite element model indicates will best match the targets. If larger and larger rectangular holes are used, the remaining plate structure will approach a beam network like that discussed in section 3.2.

Contoured plate.—Figure 3.1(c) shows a plate structure which has been contoured so that it varies in thickness over the area. For a metal plate this is typically done by computer numerically controlled (CNC) machining down from a constant-thickness piece of stock. For composites a constant-thickness plate could be CNC machined, but more typically the ply layup schedule is arranged so that the desired contour will be achieved without machining. If composite materials are used, the discussion in section 2.5 may be relevant.
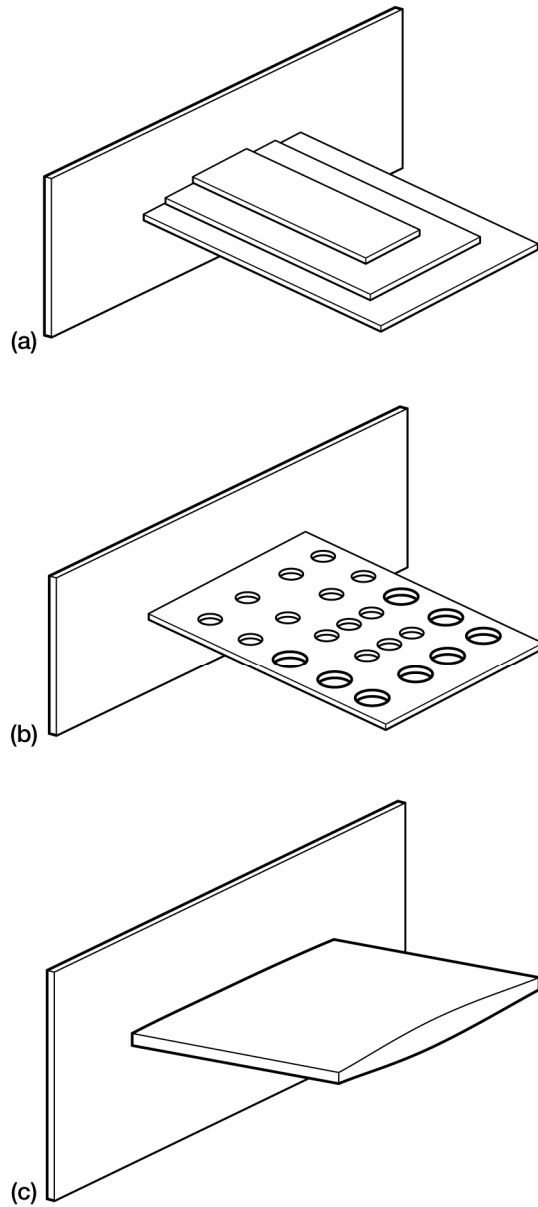
Figure 3.1.—(a) Build-up plate structure.
(b) Constant-thickness plate. (c) Contoured
plate structure.

3.2 Beam/Spar/Pod Construction

This section initially presents an extensive discussion of the parameters associated with designing flutter model spars and spar networks. The final portion of this section describes the different methods for modeling the external contour of each flutter model section ("pod").

Individual spar parameters.—As a general rule it is recommended that metals be considered first when attempting a flutter model spar design. However, a high GK/EI ratio, weight considerations, or stiffness targets changing drastically over the length of the spar may make it impractical to use metal in certain instances. In these cases composites may provide a simpler design solution. Generally the safest approach is to use fabrics. If the individual ply thickness is a small percentage of the average distance from the spar neutral axis and the total ply buildup, and if symmetric layups with alternating ply orientations are used, many of the potential problems associated with composites can be avoided. Often this approach will allow the composite to be treated as a pseudo-homogeneous material. For example, a graphite layup with 33 percent of the plys at a ±45° orientation and 67 percent of the plys at a 0-90° orientation (alternating between ±45° and 0–90°) will result in a layup whose material and strength properties can be predicted by weighting the values shown in the material properties table (i.e., $E_{layup} = 0.33\ (3.8 \times 10^6) + 0.67(10.5 \times 10^6) = 8.3 \times 10^6$ psi).

The following paragraphs describe some of the basic design considerations and options available when trying to design a particular spar or beam element to match bending and torsional stiffness requirements. The choices of material and the specific geometric configurations available provide a fairly extensive matrix of options. It is often possible to meet the target stiffness distributions with a variety of spar designs, with the choice of which is most appropriate often determined by weight, stress, or ease of fabrication considerations. The following sections present formulas for flanged rectangular spars, which are the most common spar configurations used in flutter models. The formulas defining the area moments of inertia for bending and torsional stiffness constants for a wide variety of other simple and complex geometric shapes can be found in standard textbooks such as "Roark's Formulas for Stress and Strain" by W.C. Young.

Geometric shape of main element.—The geometric shape of the main spar element is usually determined by the desired torsion to bending ratio, space envelope restrictions, and ease of fabrication. For a solid rectangular cross section of dimensions "*a*" and "*b*" where "*a*" is greater than "*b*" (ref. fig. 3.2(a)), the stiffnesses are determined by the following relationships:

$$EI_1 = (E\ a\ b^3)/12 \tag{3.2a}$$

$$EI_2 = (E\ b\ a^3)/12 \tag{3.2b}$$

$$GK = Ga\ b^3\ (1/3 - 0.21(b/a)(1 - ((b/a)^4)/12)) \tag{3.2c}$$

By varying the relationship between "*a*" and "*b*" it is often possible to match both bending target stiffnesses, or one bending and torsion. It is normally not possible to match all three at the same time without using some of the additional design variations discussed in the following sections.

In cases where the target GK/EI ratio is higher than can be achieved with a rectangular cross section, a circular cross section can be tried. The stiffnesses for a circular cross section of diameter "*d*" (ref. fig. 3.2(b)) are determined by the following relationships:

$$EI_1 = EI_2 = E\pi\ d^4/64 \tag{3.2d}$$

$$GK = G\pi\ d^4/32 \tag{3.2e}$$

Other geometric shapes are occasionally used. For high GK/EI ratios an ellipsoidal cross section may be a viable alternative when the envelope restrictions will not allow a circular cross section, or when it is desired to have the bending stiffness in one direction significantly different than the other.

Solid vs. hollow.—The formulas given in the previous section were for cross sections which are solid. Because the material furthest away from the neutral axis of the spar is most effective in determining the overall stiffness, hollow spars are often constructed to eliminate unnecessary weight. A second reason for using hollow spars is that it often allows alternate relatively inexpensive fabrication techniques (such as sheet metal bending and composite layups) to be used. The stiffnesses of a hollow circular cross section of outer diameter "$d1$" and inner diameter "$d2$" (ref. fig. 3.2(c)) are defined by the following:

$$EI_1 = EI_2 = E\pi\ (d1^4 - d2^4)/64 \tag{3.2f}$$

$$GK = G\pi\ (d1^4 - d2^4)/32 \tag{3.2g}$$

The stiffnesses of a hollow rectangular cross section with outside dimensions "a" and "b" and a constant wall thickness "t" (ref. fig. 3.2(d)) are defined by the following:

$$EI_1 = E\ (1/12)(a\ b^3 - (a - 2t)(b - 2t)^3) \tag{3.2h}$$

$$EI_2 = E\ (1/12)(b\ a^3 - (b - 2t)(a - 2t)^3) \tag{3.2i}$$

$$GK = G\ (2t(a - t)^2(b - t)^2)/(a + b - 2t) \tag{3.2j}$$

The previous equations assume that the no local buckling takes place, an assumption which is normally valid unless the wall thickness is extremely thin. A hollow spar design like that shown in figure 3.2(d) may pose some problems for construction, however. If constructed from sheet metal or a constant thickness composite layup in two halves, joints become a concern. For stress reasons and to adequately transfer strains a relatively large overlap region is preferable. If two "U-shaped" halves are joined together the wall thickness on the sides will not be the same as on the top and the bottom, and the above formulas are not applicable. The formulas for the case where the side and top/bottom thickness are different can be found in "Roark's Formulas for Stress and Strain." The formulas presented here were chosen because they are more applicable to the flanged spar designs discussed in the following section.

Flanges.—The addition of flanges to the basic geometric shape of the spar element adds a great deal of flexibility for matching widely varying target stiffness distributions. Flanges can be used to significantly increase the bending stiffness in one direction while adding very little to the other bending or torsional stiffnesses. This allows the following general design process to quickly iterate to a solution:

- Match the lower of the two bending stiffnesses (EI_1) and the torsional stiffness (GK) using the formulas for the central section of the spar only
- Compute the bending stiffness in the other direction (EI_2) resulting from the central section of the spar
- Add flanges to raise EI_2 up to the higher target value
- Calculate the additional contribution to EI_1 and GK due to the flanges to confirm that they are negligible. (If not negligible, then iterate through the process again after reducing the target EI_1 and GK values by the calculated flange contributions.)

The following formulas define the contribution of the flanges to the stiffness in each direction for a spar configuration defined as shown in figure 3.2(e). It should be noted that "t" is defined as being half the flange thickness. This is consistent with the common method of fabricating hollow spars in upper and lower halves, and bonding them together along the centerline of the flange.

$$EI_{1Flange} = (E(c - a)(2t)^3)/12 \tag{3.2k}$$

$$EI_{2Flange} = (E(2t)(c^3 - a^3)/12 \tag{3.2l}$$

$$GK_{Flange} = G\,(c - a)(2t)^3\,[1/3 - 0.21\,(2t/(c - a))\,[1 - (2t)^4/(12(c - a)^4)]] \tag{3.2m}$$

Note that the formulas and figures presented thus far all assume that dimension "*a*" is greater than "*b*", as shown in figure 3.2(f). It is possible to obtain a configuration which looks like figure 3.2(g). In this case the height "*b*" is greater than "*a*". To properly calculate the torsional stiffness the "*a*" in the *GK* formula for the central "box" must refer to the longer side.

It should also be noted that it will not always be possible to match particular target *GK*/*EI* ratios even when flanged spars are used. The subsequent discussion under the heading "High and Low Torsion to Bending Ratio Designs" presents a few alternatives which can be considered in the case of extremely high or low *GK*/*EI* ratios.

Constant section vs. tapering (overall dimensions or wall thickness).—The formulas presented define the stiffnesses of the spar at a particular cross section. Although occasionally a spar will have constant target stiffnesses over the entire length, it is more typical that the distributions will vary over the length of the spar. Matching of the target stiffness distributions will thus require that the cross section of the spar vary along its' length. Usually the target EI_1, EI_2, and *GK* values are determined at a series of discrete stations, the spar cross section is designed at each of these points, and the spar dimensions are transitioned between them. This results in a spar which will taper between adjacent sections.

If all the target stiffnesses are getting smaller in one direction along the spar, then the spar may taper smaller for all the defining dimensions. However, depending on how the stiffness ratios vary, it is also possible for the spar to have some dimensions which are increasing while others are decreasing.

It is also possible to vary the wall thickness "*t*" between adjacent sections. This might be done for a composite spar by gradually dropping off or adding plys to the overall layup. The load path should be carefully evaluated whenever this is done.

Whenever a varying stiffness distribution is being approximated by matching the design at discrete locations, care must be taken to evaluate what happens between the design stations. It is possible to accurately match the target distributions at discrete points and still have a very poor spar design. As an example, assume all three stiffness distributions vary linearly over the length of a rectangular spar from some nominal value at the root to zero at the tip. If the root stiffness values were used to define spar dimensions "*a*" and "*b*", and then these dimensions were straight line tapered to zero at the tip, a spar having dimensions of "*a*/2" and "*b*/2" at the midspan point will result. Using the formulas for a rectangular cross section, the resulting bending stiffness at the midspan would only be 1/16 of the root stiffness—which is considerably less than the 1/2 root stiffness target. Increasing the number of design points will reduce the error, but the areas of the spar between each design point will still be low in stiffness. A good check of a spar design is to calculate an average overall effective stiffness for the spar and compare that with a similar calculation based on target stiffnesses.

High and low torsion to bending ratio designs.—With the use of hollow circular spar cross sections and composite layups employing primarily ±45° ply orientations, it is possible to match *GK*/*EI* ratios not attainable with metal spars designed using the equations presented in the previous sections. Before the widespread use of composites, various designs for high *GK*/*EI* ratio metal spars were developed. One of these is illustrated in figure 3.2(gg). These are often relatively expensive designs because they require extensive machining with numerous thin web sections. The designs illustrated are also not conducive to fabrication with composites.

Occasionally the opposite problem presents itself. When it is desired to match bending stiffness in two directions with a very low torsional stiffness, spar cross sections employing multiple thin flanges can be used. Figure 3.2(h) illustrates one example of such a cross section.
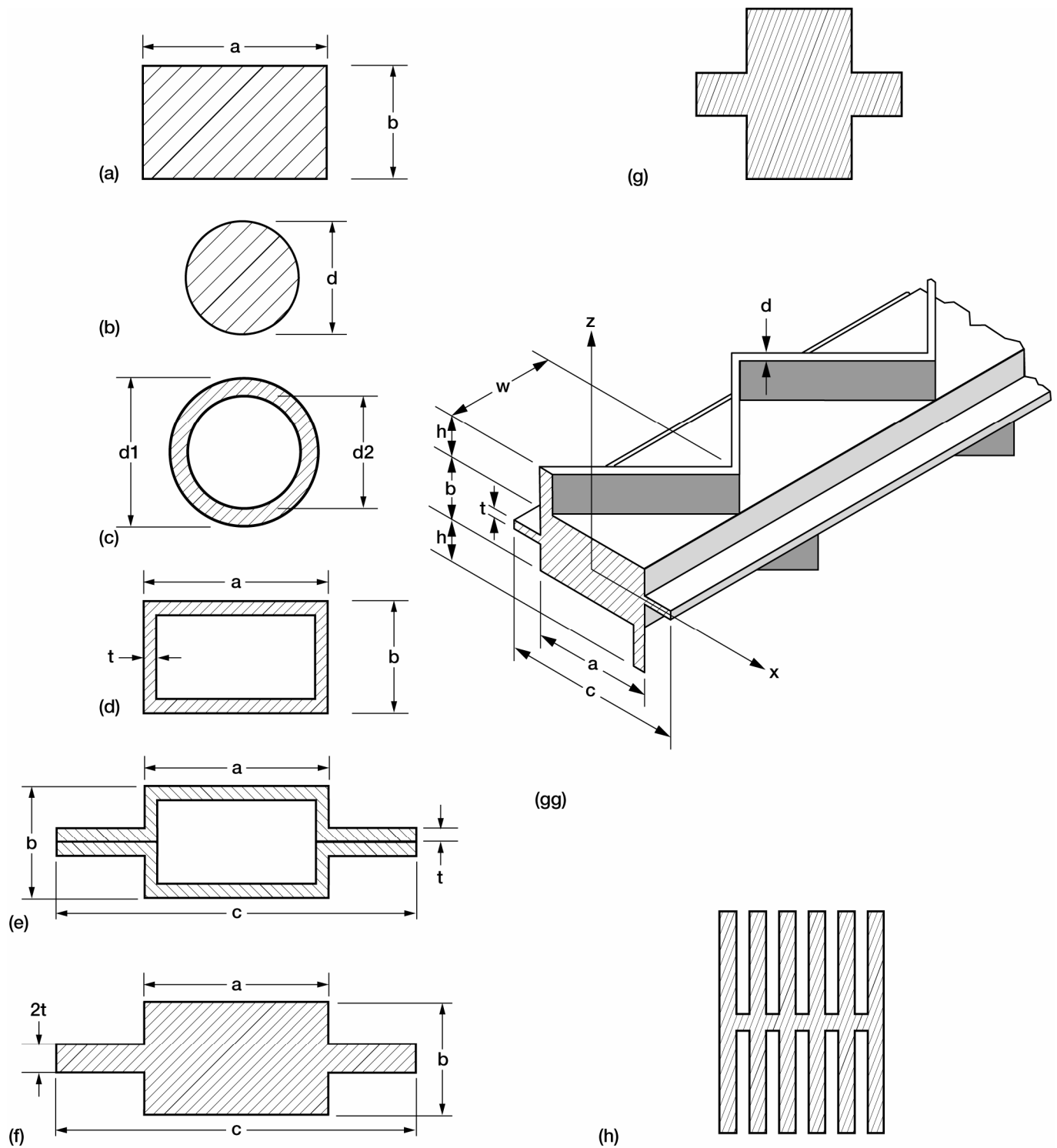
Figure 3.2.—(a) Rectangular cross-section (taken from ref. 1). (b) Circular cross-section (taken from ref. 1). (c) Hollow circular cross-section (taken from ref. 1). (d) Hollow rectangular cross-section. (e) Hollow flanged rectangular cross-section. (f) Solid flanged rectangular cross-section. (g) Special case for flanged cross-section. (gg) High torsional stiffness cross-section (taken from ref. 1). (h) Low torsional stiffness cross-section.

Built-up spar structures.—Individual spar elements can be combined in various ways to match the stiffness distributions for more complicated structures such as delta wing configuration aircraft. The following sub-sections highlight how this is done for a few basic approaches.

Two-spar torque-tube structure.—The material in this subsection largely consists of selective quotations from pages 727 through 731 of "Aeroelasticity" by Bisplinghoff, Ashley, and Halfman published by Addison-Wesley Publishing Company in 1955. Portions of this text, particularly chapter 12, are still excellent reference material relating to the subject of flutter model design and construction.

One type of structural arrangement in which the spar structure provides the entire stiffness requirements is the two-spar torque-tube structure shown in figure 3.2(i). The two spars provide the bending stiffness *EI*, whereas the torque tubes increase the torsional stiffness *GK* to the desired value. This structure cannot simply simulate a fore-and-aft bending stiffness distribution. It does, however, provide a differential-bending type of stiffness, as will be shown later. The torque tubes are very stiff in bending and ensure that the general deflection of the structure at a spanwise station can be described as a deflection at the elastic axis plus a rotation about it.

Since the torque tubes are perpendicular to the spars and do not contribute to the bending stiffness *EI*, the sum of the bending stiffnesses of the front and rear spars must at each station equal the desired stiffness:

$$EI_{target} = EI_{spar1} + EI_{spar2} \tag{3.2n}$$

Also, the relative sizes and locations of the spars must be such as to ensure the correct location of the local elastic enters. With the concept that the elastic center at a given section is the point at which a load would have to be applied to produce pure bending if the local conditions extended over the whole span, it can be shown that the moment of the spar stiffness *EI* about the elastic center must be zero:

$$(dist1)EI_{spar1} + (dist2)EI_{spar2} = 0 \tag{3.2o}$$

Thus, equation (3.2n) and (3.2o) govern the spacing and bending stiffnesses of the spars.

To obtain the desired torsional stiffnesses for the model it is necessary to supplement the torsional stiffnesses of the spars by installing suitable torque tubes. In most models of this type the major portion of the torsional stiffness comes from the torque tubes. It is important to recognize, however, that on multispar models (as well as on multi-spar wings) the differential bending of the spars also contributes to the torsional stiffness, although in a complicated fashion. Even in the absence of connections between the spars they will offer some restraint to an applied torque. The torsional restraint set up by differential bending of the spars is a function of the second moment of bending stiffness about the elastic center and the third derivative of the twist. If we take into account the fact that when the wing twists the spars twist also, it is apparent that each spar offers an additional torsional restraint about the spanwise axis proportional to its own *GK*.

The three requirements of total bending stiffness and its first and second moments about the elastic axis generally cannot be satisfied by the use of two parallel spars. If the simulation of differential bending at each spanwise station is of secondary importance, its over-all effect can be represented approximately by a reasonable location of the two straight spars. If the correct simulation of differential bending is of primary importance, or if the other stiffness requirements are difficult to obtain with two straight spars, it may be desirable to add a third spar over at least a portion of the model span rather than resort to kinked or offset spars.

Beam network.—For low aspect-ratio lifting surfaces the flexibility in the chordwise direction is often of the same order of magnitude as in the spanwise direction. The modes for these structures cannot be expressed in terms of bending and torsion about a single axis. They are typically complex deflection surfaces which must be expressed in terms of a series of structural influence coefficients. Except for the most elementary of designs it is difficult to calculate a set of influence coefficients for a beam network. Typically a FEM will be required to iterate to an acceptable design. Figure 3.2(j) shows an example of a beam network structure used to simulate the influence coefficients of a delta wing.

Outer contour sections.—It is usually necessary to represent the correct external shape for flutter model components to properly simulate the steady and unsteady airloads. As the internal support structure of the model

deflects under these airloads, the external shell should also deflect without significantly changing the stiffness properties of the model. Each approach to simulating the external contour has its own advantages and disadvantages.

Solid balsa or rigid foam.—Solid balsa has been used extensively in many flutter models because it is easy to contour and has a relatively low density. For flat plate models the balsa can be oriented with the grain perpendicular to the plate to minimize the additional stiffness added to the structure by the balsa. It is common practice to use an adhesive bond over the entire plate to attach the balsa. One of the disadvantages of using balsa or any type of wood on a flutter model is that the wood can absorb moisture. This can cause the wood to swell, which may distort the structure. To avoid this balsa sections are usually sealed to prevent moisture absorption. Sometimes model airplane silk or a thin layer of fiberglass is added to the outside surface of the balsa.

For low speed flutter models with internal spars it is common to divide the external shell into separate segments—each of which is then attached to the spar at a single point to minimize the impact of the segment on the stiffness distribution. A thin metal "U" clip may be added to facilitate attachment to the spar. Streamwise gaps intentionally left between the segments to prevent load transference between adjacent pieces can be filled with a low density compressible foam or bridged with thin latex rubber sheeting. Figure 3.2(k) shows typical construction for a segmented external shell attached to an internal spar.

In some cases low density foam is used as an alternative to balsa. Because of the extremely porous and rough surface, an external layer of fiberglass or model airplane silk is almost always added when foam is used.

Foam sandwich or egg-crate supported skins.—Foam sandwich or egg-crate supported skins can be used as an alternative to making solid segments of balsa or foam. Use of female wood molds allows fiberglass skins of the external contour to be laid up.

These skins can be kept relatively thin and lightweight using one of the following methods:

- incorporate balsa "egg-crate" support structure bonded to the inside surface of the skin
- make the outer skin a fiberglass/foam/fiberglass sandwich

In either case the internal support structure near the center of the segment typically includes a metal "u" clip to facilitate attachment to the spar. Figure 3.2(l) shows a cross section of this type of construction.

Rubber, RTV, or flexible foam.—To create a smooth external shell without gaps, very flexible materials are occasionally used. Ribs attached to internal spars can support thin latex sheets simulating the outer skin contour. Very little additional stiffness is added to the spars using this approach, but it is very difficult to control ballooning of the rubber skin above an airstream velocity of about ninety feet per second.

A flexible foam or an RTV material cured in molds can also be used to create the external shape on some flat plate and spar flutter models. A significant disadvantage to using rubber, RTV, or flexible foam on flutter models is that the damping of the model can be greatly increased. The availability of composites to create lightweight flutter components with smooth external surfaces has virtually eliminated the use of rubber in flutter model construction.

(i)

Torque tubes

Front spar

x

y

Rear spar

(j)

(k)

Metal U-clip to attach
upper half to spar

Balsa or foam sealed
or F/G on the outside
upper and lower halves

Hardpoints to attach
upper and lower
segment halves

Spar

(l)

Support
structure

Metal U-clip

Spar

Foam to seal
gaps between
segments
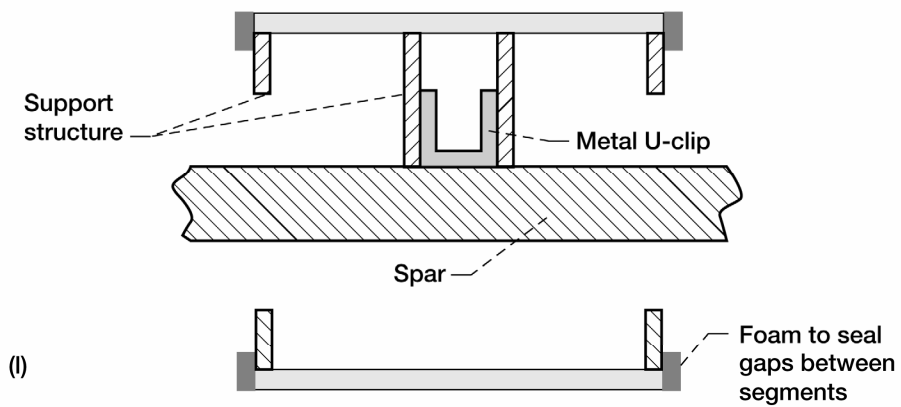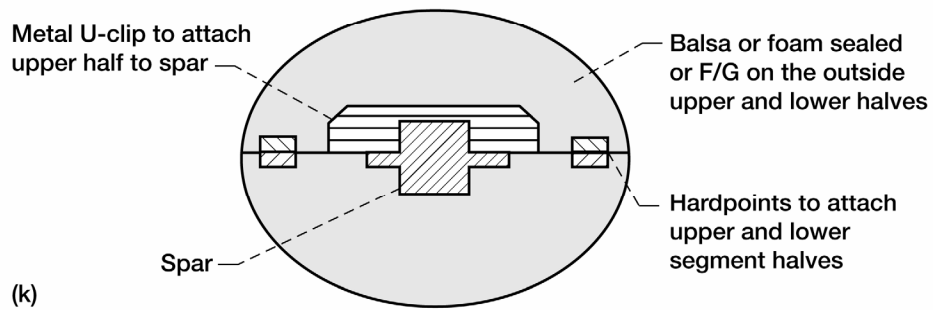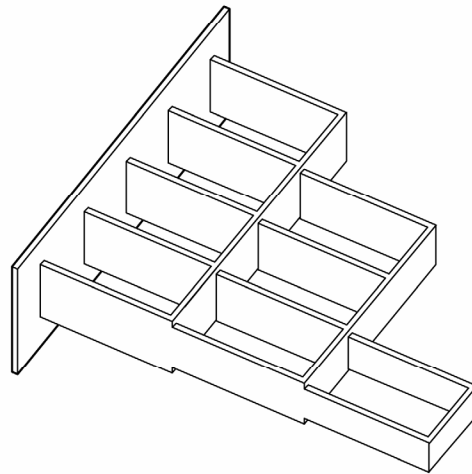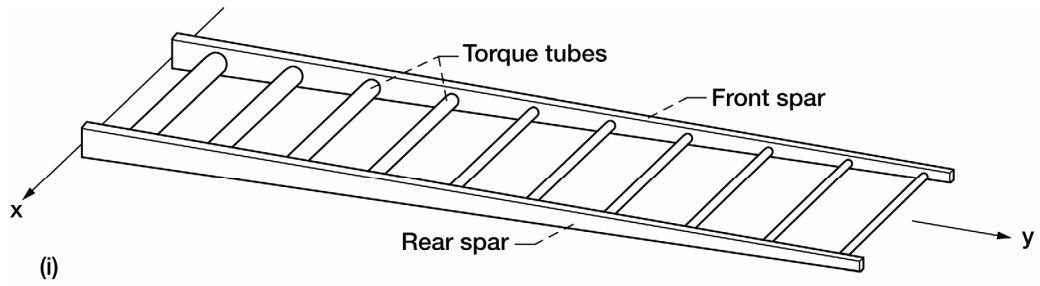
Figure 3.2.—(i) Two-spar torque-tube structure (taken from ref. 1). (j) Beam network structure
(adapted from ref. 1). (k) Fore/aft view of typical segmented construction. (l) Side view of
typical segmented construction.

3.3 Stress Skin Construction

Because modern aircraft are being designed with more extensive use of composites and honeycomb sandwich structures which tend to be lighter weight, it is becoming more difficult to produce an adequately scaled flutter model without the use of similar construction techniques. The following paragraphs will cover some of the key design considerations when attempting stress skin construction of flutter model components. The sub-sections under section 8.0 can be referenced for illustrative figures and a discussion of the design and analysis process used on a supersonic flutter model which employed stress skin construction.

Metal skins.—With the increasing use of fiberglass and graphite composites, metal skins are not often used in flutter models. The main reason for this is that it is very difficult to form metal skins into the complex contours found on many modern aircraft designs unless expensive molds and forming tools are used. However, metal skins have the advantage of being extremely predictable with regard to their material properties—and they provide an excellent external surface. Therefore, metal skins should at least be considered when the components involved have contours involving simple curves, or when then isotropic material properties present an advantage.

There are tradeoffs between the different design and fabrication considerations. Metal skins will occasionally still result in the best design. Aluminum and magnesium are the most common metals used for skins on flutter models.

Composite skins.—For the purposes of this paper composite skins will include discussion of graphite, fiberglass, and Kevlar. All of the materials are readily available and can be obtained as woven fabrics, unidirectional tapes, and roving. These materials can be pre-impregnated with resin, or they can be dry (for use in wet layups). Composite skins have the advantage of being relatively easy to form into the proper shape (as compared to metal skins).

Male patterns or female molds can be quickly fabricated from wood using CNC machining. Sometimes the wood molds or patterns are used directly for the process of laying up skins. At other times fiberglass female molds are laid up using a CNC machined male pattern. Female molds will maintain a better external surface finish and tighter control of external geometry than male patterns. Female molds are also frequently used as construction cradles for building up the structure inside the completed external skins.

The relative advantages and disadvantages of dry versus pre-impregnated materials must be weighed against the requirements of the particular flutter model and the experience of the individuals doing the fabrication. It is also possible to use a combination of the approaches. For some of the layups described in section 8.0 the outer layer of the skin was a layer of dry fiberglass fabric which had a measured amount of resin added to it, and the remainder of the layup was pre-impregnated unidirectional graphite tape. The entire layup was cured together at an elevated temperature.

3.4 Replica Construction

Replica construction involves duplicating the construction methodology for the full-scale design when making the model. This involves properly representing all structural members including skins, spars, longerons, etc. Generally this approach cannot be followed exactly because of unequal scaling factors, mounting constraints, and the particular requirements of the planned testing. However, it is becoming increasingly common to start with the full-scale design and to make some simplifications and changes while maintaining the basic relationship of skin layups and the main structural members. The design of the components described in section 8.0 followed this basic approach.

The previous discussions regarding stress skin and spars is generally applicable to replica construction. However, replica construction will typically require extensive use of finite element modeling since the assembled structures are usually too complicated to evaluate using handbook formulas.

3.5 Hinged Control Surfaces

Control surfaces on flutter models must be attached in some manner to the fuselage, main wing, or other structure. The hinges and bearings for the full scale design can be modeled with reduced-scale bearings and hinges, or with flexures. Usually the angular deflection and loading requirements for the control surfaces will determine which approach is used. Large angular deflections or actuated surfaces will usually require hinges or bearings. Relatively small angular deflections permit the use of flexures which have more predictable dynamic characteristics. Because flexures generally do not have sliding friction associated with the operation, the damping of a flexure attachment is much less than for a bearing or hinge. Less damping is a very desirable characteristic for most flutter model applications. The following three sections present a brief discussion of the most common approaches for control surface attachment, and some of the critical design considerations.

Hinge and bearing attachments.—For flutter models which incorporate actuated surfaces or large angular deflections it is often necessary to use hinges or bearings. The disadvantage of using hinges or bearings is that the friction and damping characteristics associated with these attachments must be evaluated and accounted for. Some of the factors which can significantly effect the friction and damping characteristics of hinges and bearings include:

- the difference between static friction and dynamic friction
- galling of similar materials
- differential thermal expansion of dissimilar materials
- wear of close-fitting moving parts
- vibration between close-fitting moving parts
- slight changes in alignment when parts are interchanged
- the effects of cleaners, lubricants, dirt, and dust

With hinges and bearings it is difficult to ensure that the frictional and damping characteristics of the attachment will remain constant under all circumstances. The hardware generally undergoes repeated model changes, experiences wear, and may be tested at different temperatures. The items listed above must be given due consideration, and any differences between the calibration setup and the tunnel installation taken into account. This is particularly true for simple pin-type hinges. Precision bearings properly installed will generally give more consistent results.

It is also desirable to eliminate "slop" or "free-play" in the system. With bearings and hinges this usually results in a "design tradeoff", because rotating attachments which are tight enough to have no "free-play" will tend to have increased friction and damping.

Simple beam flexures.—In certain cases simple beam flexures are used to simulate a hinge or bearing attachment. This is usually done when the anticipated deflections across the attachment are very small (i.e., if the target rotational spring rate is relatively high compared to the structure on either side). Standard beam formulas can be used to design these flexures and these formulas will give very predictable results when properly applied. However, the "back-up stiffness" of the structure to which the flexure is attached should be evaluated to see it this needs to be treated as another spring in series.

In cases where the anticipated deflections are somewhat larger, then the vertical/horizontal translation deflections of the beam inherently associated with a rotation may introduce undesirable modal characteristics. In these cases an alternate flexure arrangement should be considered.

X-type flexures.—An X-type flexure is an assembly of two crossed beam elements usually oriented perpendicular to each other. X-type flexures are used extensively in flutter models because they behave kinematically much more like a hinge or bearing than a single beam element, yet they retain the low damping characteristics of a flexure. The rotation point of an X-type flexure moves very little over relatively large angles. The vertical and horizontal translational stiffness of an X-type flexure can be kept relatively large compared to the rotational stiffness.

X-type flexures are typically made in two separate halves for ease of fabrication. Stainless steel is the most common material—although X-type flexures for flutter models have occasionally been fabricated from aluminum,

plastic, or composites. For metal flexures wire electric discharge machining (EDM) is an efficient means of fabrication. Figure 3.5(a) shows one half of an X-type flexure assembly. The figure shows sharp inside corners, but it is standard practice to include a radius on the actual hardware to reduce stress concentrations. Standard formulas for stress can be used to check whether a particular flexure design will have adequate factors of safety. Fatigue is a potential failure mode and may need to be evaluated, particularly if aluminum or other materials which exhibit poor fatigue characteristics are used.

If the desired rotational stiffness "k" (in-lb/rad) is known, and the angle "α", length "d" (inches), width "w" (inches), and modulus of elasticity "E"(psi) are assumed, then equation (3.5) can be used to obtain the required thickness "t" for an X-type flexure. This equation was derived based on superposition of simple beam formulas, and is therefore subject to similar restrictions (e.g., the individual flexure width "w" should be significantly less than "d", and should be of the same order of magnitude as the thickness "t"). Reference figure 3.5(a) for clarification of the dimensions.

$$t = [(6kd)/(wE(\sin \alpha))]^{1/3} \tag{3.5}$$

Figure 3.5(b) shows two halves of an X-type flexure assembled together in their final orientation. It is a good practice to make the attachment areas of the flexure at least one order of magnitude stiffer than the target springrate for the flexure. It is also advisable to design the flexures slightly overstiff—and then "tune" them down to the required value during calibration of the hardware.

(a)

(b)
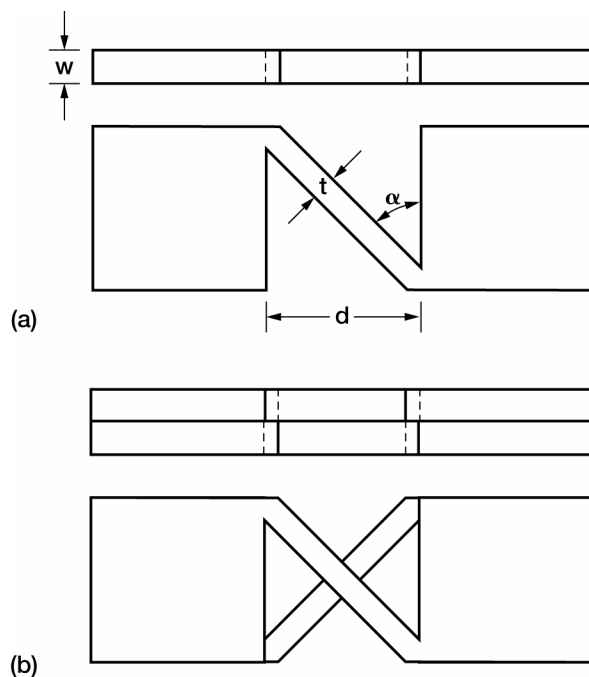
Figure 3.5.—(a) Half of X-type flexure. (b) Assembled X-type flexure.

4.0 Instrumentation

Instrumentation on flutter models may be added for any of the following reasons:

- to monitor loads at critical points in the model structure
- to help identify the modal patterns associated with particular components of the model
- to help identify phasing and relationships between the motions of different components
- to help identify shock locations and other aspects of the unsteady aerodynamics

The following three sections briefly discuss the most common types of instrumentation included on flutter models.

4.1 Strain Gage Bridges

Full strain gage bridges are often added to flutter model spars to monitor loads. The same gage output can also be used to determine the phasing for modal deflections. For stress skin structures gaging can be added directly to critical points on the component surface.

Sometimes strain gages are added to other elements such as the cross beam members in a X-type flexure. In these cases a half bridge is sometimes used because of space limitations. These bridges can be used to measure loads, but often they only provide the phasing for the rigid body modes of the control surface attached to the flexures.

4.2 Accelerometers

Accelerometers are frequently mounted at various locations within the flutter model structure to identify modal patterns and provide quantitative data for the motions. The positions of the accelerometers are usually chosen based on the anticipated mode shapes for the structure. For wing and control surface components the accelerometers are normally positioned to measure the acceleration perpendicular to the reference plane of the surface. For fuselage sections, nacelles, and other structures which may have significant motion in multiple directions, several accelerometers are often located close together with the measurement planes oriented orthogonal to each other.

4.3 Dynamic Pressure Transducers and Piezoelectric Strain Elements

Occasionally high speed stress skin flutter models will have dynamic pressure transducers located at various positions in the external skin contour. These transducers can be used to obtain quantitative pressure data which may be useful in identifying the location of the oscillating shock wave associated with some high speed flutter mechanisms. Figure 4.3 shows dynamic pressure transducers mounted in the structure of an aeroelastic model rotor blade.

Piezoelectric strain elements are currently being investigated for their usefulness on flutter models. These elements can be used as transducers to measure the direction and magnitudes of strains at particular locations. These elements can also have a voltage applied to them so that a strain is induced into the flutter model structure at specific locations. This application can be used to excite or modify the modal dynamics of a particular component.
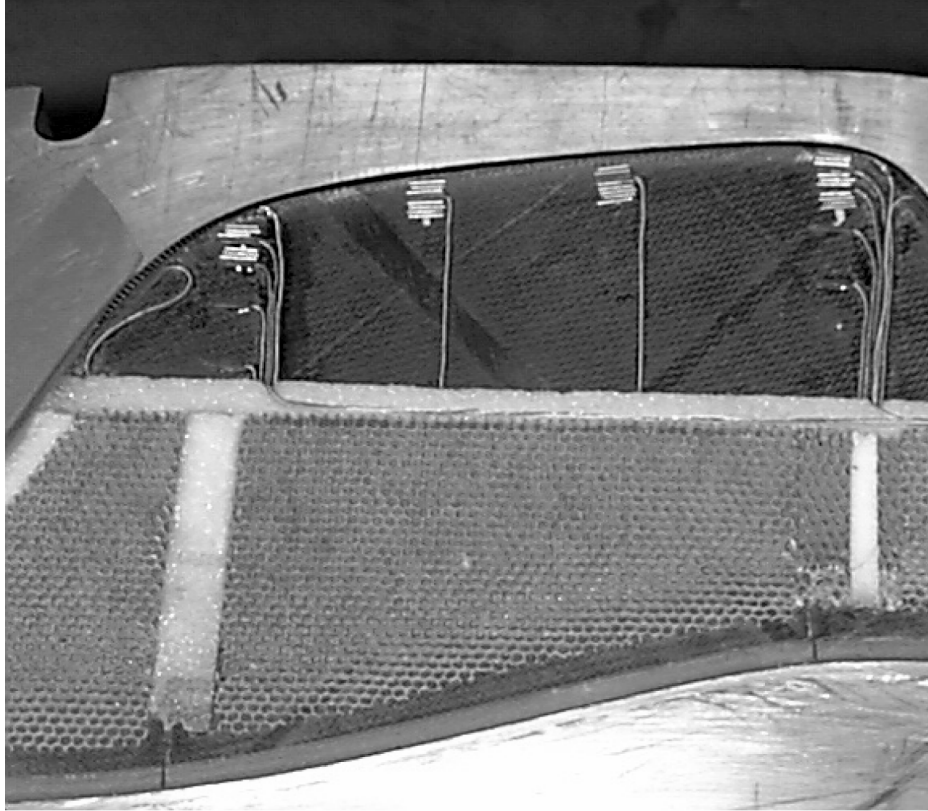
Figure 4.3.—Dynamic pressure transducers in an aeroelastic model rotor blade.

5.0 Model Calibration Techniques and "Tuning"

The information contained in this section addresses the most common calibration techniques used to measure the properties of samples and final flutter model hardware. Calibration is necessary because relatively small deviations in weight, machining tolerances, material properties, and a host of other variables can sometimes result in significant deviations from the original targets. These deviations can often be corrected for by "tuning" the final hardware.

5.1 Stiffness

Two methods are frequently used for measuring the stiffness distribution of flutter model components. The "mirror calibration" technique is a very efficient approach for spars and high aspect ratio elements. For low aspect surfaces which do not exhibit "beam-like" deflections it is usually necessary to use an approach involving structural influence coefficients.

"Mirror" deflections.—A convenient method for measuring the bending or torsional stiffness of a flutter model component which acts primarily like a beam is illustrated in figures 5.1(a) and 5.1(b). To obtain the stiffness between any two adjacent mirrors the following formulas were derived from basic beam formulas using superposition and small angle approximations. In addition to the variables indicated in the figures, "d" = distance between adjacent mirrors and "A" = distance from the mirror closest to load and the load application point. To be consistent with using the small angle approximation, the distance "L" should be at least two orders of magnitude larger that ΔZ or ΔY. In general, it is also a good idea to use multiple load increments and return to the initial "unloaded" position—so that any hysteresis or structural "creep" can be assessed.
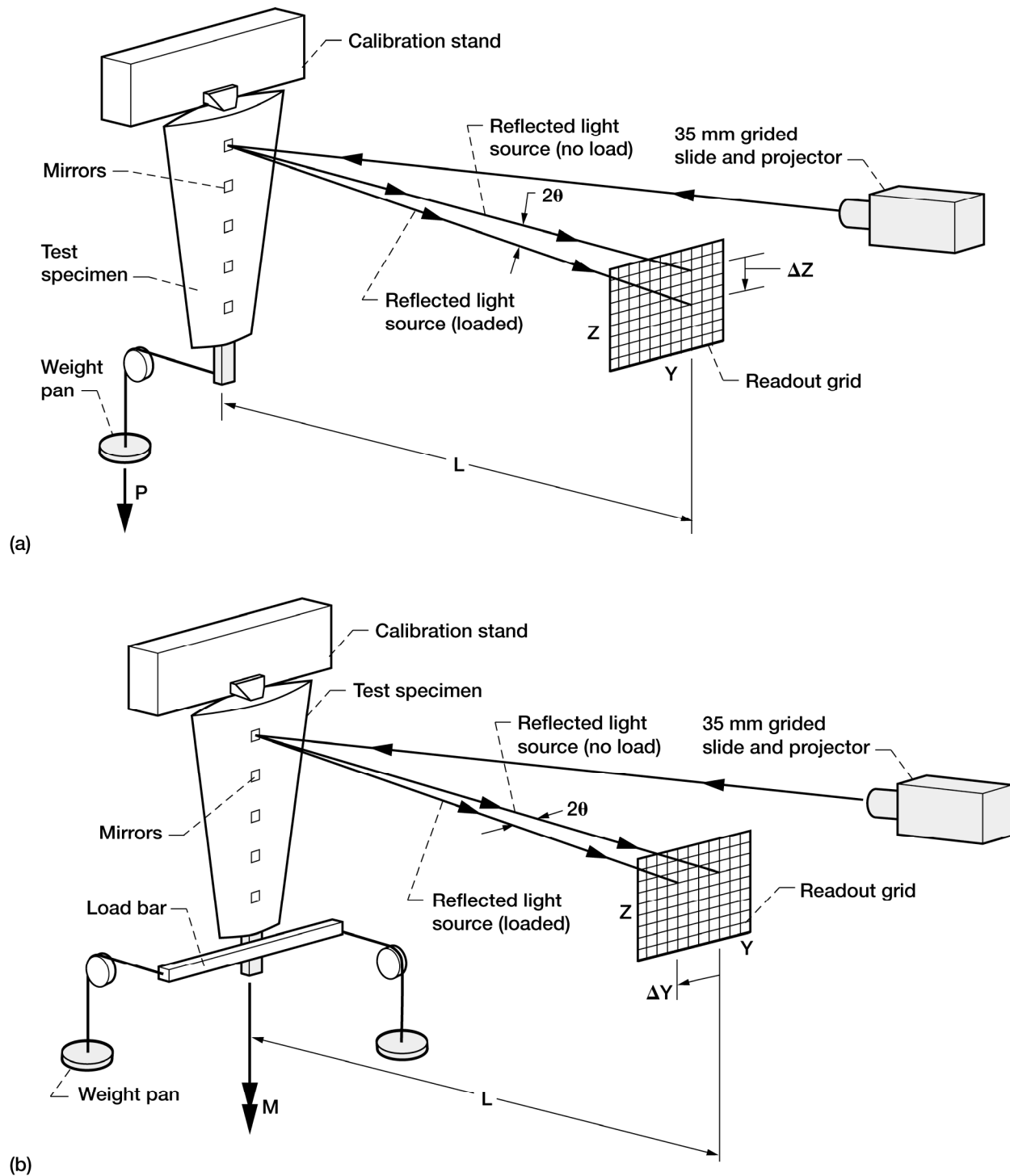
Figure 5.1.—Typical setup for measuring bending and torsional stiffness. (a) Bending stiffness. (b) Torsional stiffness.

Bending:

$$\theta/\# = \left(\Delta Z_{mirror\,1} - \Delta Z_{mirror\,2}\right)/2LP \tag{5.1.a}$$

$$EI = 1\big/\left(\theta/\#\right)\left[d^2/2 + A\,d\right] \tag{5.1.b}$$

Torsion:

$$\theta = \left(\Delta Y_{mirror\,1} - \Delta Y_{mirror\,2}\right)/2L \tag{5.1.c}$$

$$GJ = d\,M/\theta \tag{5.1.d}$$

Influence coefficients.—An alternate method for obtaining stiffness information is to place a distribution of load/measurement points on the component surface. If point loads are applied at each of these locations, and the deflection is measured at each location using a coordinate measuring machine or dial indicators, then it is possible to develop a set of structural influence coefficients defining the stiffness distribution for the component. A detailed treatment of this approach is beyond the scope of this paper, but the methodology can be found in any standard text dealing with complex structures. This approach for obtaining stiffness data is most applicable for delta wings or other structures which behave in a manner where the formulas derived from beam theory are not valid.

5.2 Mass and Inertia Properties

Overall mass and CG determinations.—Scales are employed to measure the mass of individual components. Electronic scales covering a variety of ranges can allow this data to be taken quickly, even when there is a large number of individual components.

Locating the center of gravity (CG) can be done in a number of ways. The part can be balanced on a knife-edge and the line formed by the edge is marked. If this is done with the knife-edge in several orientations the intersecting lines will locate the CG.

Sometimes parts can be suspended from one corner so that they hang freely. A plumb line hanging down from the same point will cross over the CG. If the process is repeated with the part hung from several different points, the intersection of the plumb line markings will locate the CG.

The previous two methods will give the required accuracy if done carefully. However, they are rather tedious and can require a significant amount of time if there is a large number of parts. Parts with rapidly curving surfaces and unusual shapes may also make these methods more difficult in practice.

An alternate method is to use a fixture such as the one illustrated in figure 5.2(a). If the part has weight "$W1$", the scale reading "$W2$" can be used to determine how far from the vertical stop the CG is located. (Reference equation (5.2a).) By orienting the part in two directions the CG can be located from two different edges or corners. This procedure is very efficient for doing large numbers of parts, and the CG location is typically repeatable within 0.020 in.

$$X1 = X2(1 - W2/W1) \tag{5.2a}$$

Measured mass moments of inertia.—There are a number of methods for experimentally measuring the mass moments of inertia for individual flutter model components or built-up assemblies. The most common method is to use some variation of a torsional pendulum. Torsional pendulums typically have a lightweight beam or platform suspended from wires or cables. The pendulum can be made to rotate about a vertical axis in an oscillating fashion. The frequency of oscillation is dependent on the effective torsional stiffness "K" resulting from the cables, the inertia of the beam or platform about the rotation axis, and the inertia of any object attached to the pendulum. The following equation allows the mass moment of inertia about an object's CG to be determined if the period is known. The period for one cycle can be determined by counting a reasonable number of cycles (i.e., 10 to 50) and timing with a stopwatch. A strobe light may prove useful in cases where the period is too short to effectively use the stop watch.

$$I_{object} = K(Mass_{pendulum} + Mass_{object})(period)^2 - I_{pendulum} \qquad (5.2b)$$

Figures 5.2(b) and 5.2(c) depict bi-filar and tri-filar pendulums respectively, the most commonly used configurations.
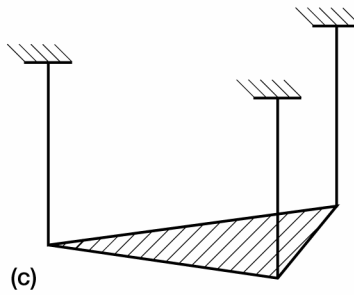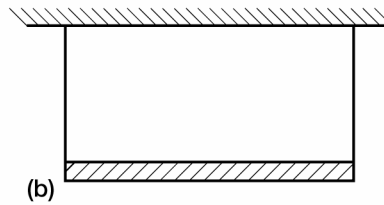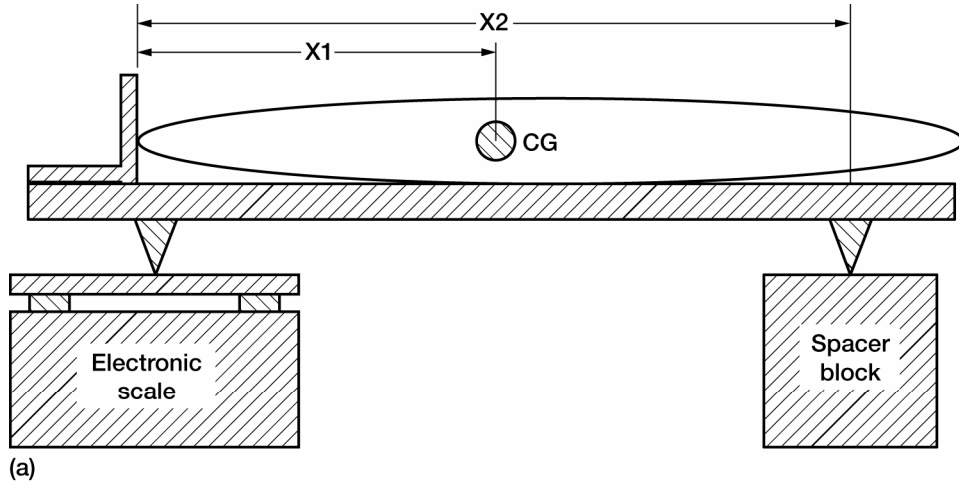
Figure 5.2.—(a) Setup for determining CG location using an electronic scale. (b) Bi-filar pendulum. (c) Tri-filar pendulum.

Tri-filar pendulums are generally more convenient to use because objects can often be placed directly on the triangular platform with no special provision for support. Occasionally the object is large enough that it cannot be positioned between the wires so that the CG of the object is located on the rotation axis of the pendulum. In these cases the object can sometimes be attached to the bottom of the pendulum using tape. However, care must be taken to ensure that the object moves rigidly with the platform, otherwise the measurements will not be accurate.

The accuracy of the measurement is directly related to the magnitude of the inertia being measured in comparison to the pendulum inertia. Therefore it is common to have pendulums of multiple sizes to optimize accuracy. A bi-filar is generally used when the component being measured is extremely lightweight. For a bi-filar with a beam of length "D" and cables of length "L" the torsional constant can be approximated using the following relationship ("g" is the acceleration due to gravity):

$$K_{bifilar} \sim (D^2 g)/(16\pi^2 L) \tag{5.2c}$$

Equation (5.2c) is not valid for tri-filars, and it should only be used as an approximation for bi-filars. The normal procedure for both bi-filars and trifilars is to calibrate them using bars, disks, or other shapes for which the mass moment of inertia can be accurately calculated. After recording the pendulum's period for each of two objects of a known mass and inertia, equation (5.2b) can be used to solve for the two unknowns, "K" and "$I_{pendulum}$". It is usually a good practice to perform the calibration using objects of very similar mass to that of the components to be measured. Depending on the particular wires or cables used for the pendulum the torsional constant "K" can vary slightly as a function of the combined mass of the pendulum and object being measured.

It is also important that the object's CG be placed on the pendulum's rotation axis with reasonable accuracy. If it is placed significantly "off-center" this may induce swinging of the pendulum. Any significant motion other than pure rotation can impact the accuracy of the measurement or calibration. Therefore it is normal practice to locate the component's CG as accurately as possible before measuring mass moment of inertia.

The mass of the air being moved by the object on the pendulum is normally negligible. However, in cases involving extremely lightweight surfaces it is occasionally desirable to try to account for the mass of air being moved. Sometimes this is done using a calculated value. However, it is also possible to construct a constant thickness flat plate of the same planform as the surface being measured. The difference between the calculated inertia of this flat plate and that determined for the flat plate using the pendulum will equal the contribution due to the air mass movement. This value can then be used to adjust the measured inertia of the original surface. Figure 5.2(d) shows the mass moment of inertia about the roll axis of a model being measured using a bi-filar pendulum.

Sectioned sample.—For stress skin construction of small to medium sized components, making a sample part is often done to fine tune the design process. The sample part must be checked for stiffness, overall mass properties, and the dynamic data discussed in the following sections. After these tests, the sample is often cut up into small sections. The mass properties of the individual sections can then be measured, compared with design values, and adjustments made prior to fabricating the final part.

Figure 5.2.—(d) Full model roll inertia measurement using bifilar pendulum.

5.3 Mounting Options

When evaluating frequencies and mode shapes there are various options available with regard to how the data is taken. The following two sections briefly discuss some of the most basic considerations associated with evaluating individual components versus assemblies, and cantilevered versus free-free mounting.

Individual components vs. assemblies.—The advantage of obtaining frequency and mode shape data for a single component is that the structure is usually relatively simple, and it is relatively easy to interpret the results for the isolated component. The disadvantage is that the mounting conditions and interactions with other components is usually neglected or must be idealized.

The advantage of obtaining frequency and mode shape data for an entire model assembly is that this represents how the hardware will be tested in the wind tunnel. Any interactions between various components will be reflected

in the results. The disadvantage is that it is often very difficult to interpret the results and interactions between components from the assembly data alone.

For all but the simplest of flutter models a combination of these two approaches is usually employed. Dynamic data is taken for the individual components in isolation. Then major subassemblies are built up with additional data taken at each stage. Normally the quantity of data taken for each component diminishes as the assemblies are built up. An individual component will normally have extensive mapping of node lines for all the frequencies of interest. At the subassembly and overall model assembly stage the data is usually restricted to obtaining frequencies and just enough acceleration or node line information to identify the mode associated with each frequency.

Cantilevered vs. free-free.—In cases where a component or subassembly is attached at one or two points with a relatively rigid joint it will probably be best to test the individual component or subassembly bolted or clamped to a rigid massive block. The attachments in the analytical model should be locked out to simulate this case for comparison. A wing with a single spar with a mounting block at the root is an example of a component which is commonly cantilever mounted. One disadvantage of cantilever mounting a component is that the effect of mass properties in the mounting area will not have a significant impact on the dynamic measurement results. Showing a good correlation of the mass properties in this area may then be more important for the overall model/FEM correlation (reference section 5.8).

In cases where the attachment of the individual component is through multiple attachments which have significant flexibility associated with them, cantilever mounting can give poor or misleading results. An example of this is a rudder attached at multiple hinge points, which also has a separate actuator link. Locking out the attachment points in the analytical model is likely to drastically change the predicted frequencies and mode shapes. Although it may be possible to take measurements to compare against this analytical case, the correlation may not be a good indication of what will occur for the installed condition with flexible attachments. For cases like this it is generally better to suspend the component by rubber bands or bungee chords and compare the measurements against the analytical model of the component in a "free-free" condition. Care should be taken to ensure that the attachment locations for the rubber bands or bungee chords do not significantly affect the modes. Attachments located on node lines are best. Dynamic data for the overall model assembly is normally done with the hardware suspended to simulate a free-free state. Figure 5.3(a) illustrates the concept of suspending an element to approximate a "free-free" condition. Figure 5.3(b) is an example of a flutter F–22 vertical tail suspended for evaluation of natural frequencies and mode shapes as described in sections 5.4 and 5.5.
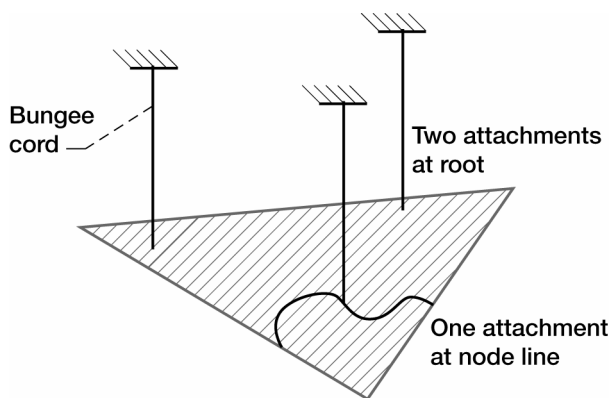
Figure 5.3.—(a) Typical setup for free-free testing.

Figure 5.3.—(b) Component suspended to simulate free-free condition.

5.4 Natural Frequency Determination

For determining the natural frequencies of flutter model components a frequency analyzer is the most common instrumentation used. The capabilities and operation of specific frequency analyzers varies, but all are capable of taking the input from one or more accelerometers mounted on the component surface and displaying the data in various formats. There are various brands of wax which allow an accelerometer to be temporarily attached to the component surface.

In some cases there are accelerometers permanently installed within the structure for the component to be used during wind tunnel testing. Using the output from such an accelerometer has the advantage of not adding additional mass to the component being evaluated. The results will also be directly comparable to what will be obtained during tunnel testing. Even when this approach is used it is advisable to make a check with a "roving" accelerometer positioned at various points on the component to ensure that frequencies/modes are not missed because the accelerometer was inadvertently positioned directly on a node line.

"Rap" test.—The simplest method for exciting the natural frequencies of the structure being tested is to give it a "rap" with a small impact hammer or a finger. Some practice is usually necessary to avoid making double hits, keeping the output within the gains set on the analyzer, etc. This method can be used for cantilever or "free-free" mounted structures, and it is often possible to get data within a few minutes.
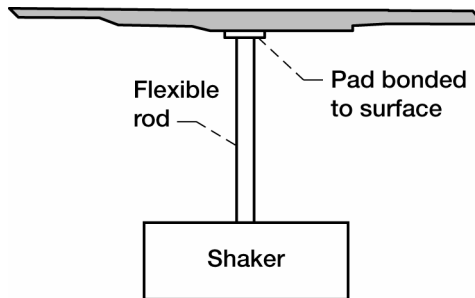
Figure 5.4.—Shaker attachment to surface.

Shaker excitation.—An alternate method for exciting the natural frequencies of the structure being tested is to mount the output rod from an electromagnetic shaker to the surface and drive it through the anticipated range of natural frequencies. The rod attached to the structure is normally lightweight, thin, and somewhat flexible in bending (e.g., a thin plastic rod or wooden dowel). Temporary attachment to the surface is usually done with a quick-drying epoxy adhesive which can be easily removed after the testing. This set up is illustrated in figure 5.4. A combination of random input to get mode locations followed by sine dwell for verification works well.

5.5 Mode Shapes

"Mode shape" refers to the characteristic motion associated with a particular natural frequency of a structure. "Node lines" are lines going through points on the structure which undergo no motion during deflection of the component. "Node lines" are also defined as the areas where the phase of the surface motion reverses and passes through zero. Figure 5.5(a) shows a node line for a structure undergoing bending.

The following four sections describe methods used to locate node lines and identify the mode shapes of flutter model components.

Salt or powder.—For relatively flat surfaces such as delta wings it is sometimes possible to use salt, sawdust, or some type of powder to make node lines visible. The powder should be a color which contrasts with the surface being checked. The powder is scattered over the surface, which is then excited at one of the natural frequencies using an electromagnetic exciter. The powder will gradually be bounced away from areas of high motion and collect along node lines.

Although quite simple in principle, this method tends to be difficult to get accurate results from most situations.

Mapping with impact hammer.—A common method for mapping node lines requires a frequency analyzer, an accelerometer mounted on the surface, and an "impact hammer" with an accelerometer in it. The method is briefly summarized below.

- Connect the output from the accelerometer attached to the surface to one data channel of the frequency analyzer
- Connect the output from the "impact hammer" to a second channel of the frequency analyzer
- Set the frequency analyzer to the desired frequency and display the phasing of the transfer function between the two channels of data (accelerometer and "impact hammer")
- Rap the surface with the "impact hammer" at points gradually moving across the surface—the points where the phasing passes through zero (reverses direction) correspond to a node line. These points can be marked with white-out or a wax pencil.

Although the above approach can be somewhat tedious, it requires a minimum of equipment and can give accurate results.

Accelerometer grid.—Sometimes a large number of accelerometers will be mounted to the external surface of a flutter model component (usually in a "grid" pattern) and an electromagnetic shaker used to excite a particular frequency. The acceleration data from each point on the grid where an accelerometer is located can be analyzed to
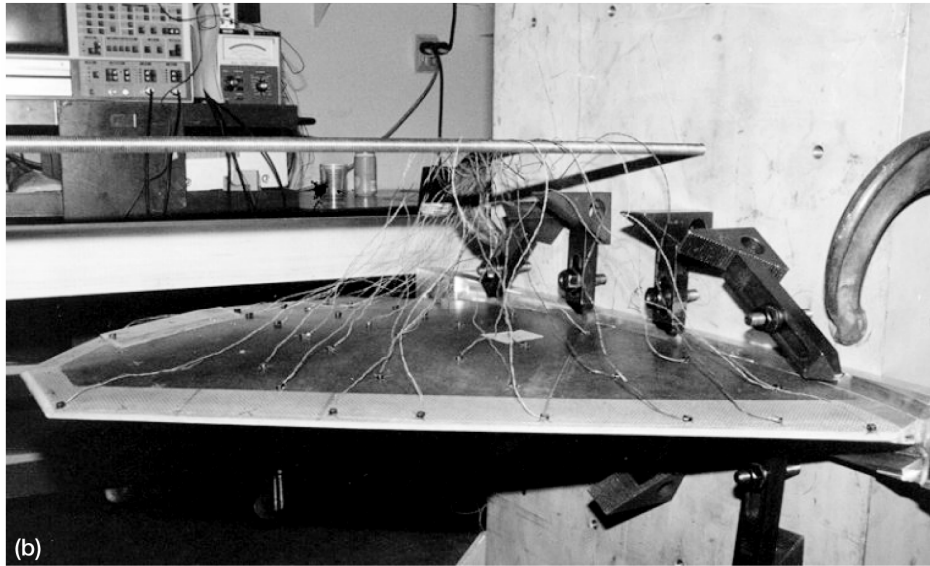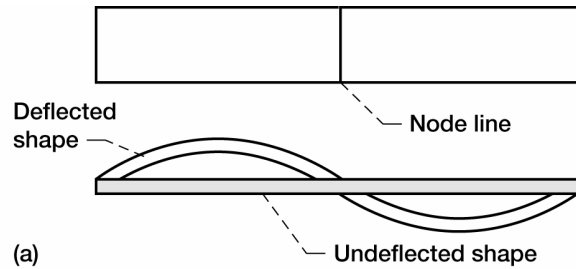
Figure 5.5.—(a) Example of bending node lines. (b) Accelerometer grid calibration set up.

give quantitative measurements of the surface motion. The main disadvantages of this approach are that the cost of the equipment necessary to obtain and analyze the data can be quite expensive. The weight of the accelerometer grid attached to the surface is also normally significant, and will change the frequencies. This effect must be taken into account analytically.

Figure 5.5(b) shows one example of an accelerometer grid calibration set up. Note that the wires from the accelerometers are supported to minimize the additional weight applied to the surface.

Laser scanning.—Laser scanning of a surface being excited at a particular frequency can give very good plots of deflections and node lines. This approach can give data similar to that obtained with an accelerometer grid. Laser scanning has the advantage of not introducing extra instrumentation mass to the component being tested. As the equipment used for this approach becomes more affordable it will probably be used more extensively.

5.6 Stiffness Tuning of Spars and Flexures

Spars and flexures are typically designed slightly "overstiff" because it is difficult to analytically account for all the variables involved with construction of a flutter model. It is normally easier to reduce the stiffness of a structural member than to increase it. When the stiffness or spring rate of a spar or flexure is initially measured using one of the techniques described in section 5.1, there will invariably be some deviations from the theoretical targets. If the member has been designed "overstiff" some material can be removed by sanding, filing, or grinding the spar or flexure. Many times it is possible to do this while the component is still set up for the stiffness calibration.

For metal spars the material properties are very consistent, so it is generally only necessary to design the spar two or three percent overstiff. For composite spars and flexures where the machining tolerance is a significant fraction of the overall thickness, it may be necessary to design the component as much as five or ten percent overstiff.

5.7 Mass Ballasting

Although detailed weight spreadsheets and an accurately controlled process for preparing composite layups and applying adhesive can result in very accurate weight predictions, it is still advisable whenever possible to initially design the sections of a flutter model to be five to fifteen percent underweight. Based on the stiffness calibrations and the initial mass property determinations it is then possible to "tune" the mass properties of each section to achieve a better match with the target values.

The following list summarizes the procedure generally used for mass ballasting a single flutter model component:

- Take initial weight, CG, and mass inertia measurements as described in section 5.3. Ideally the overall weight and mass inertia measurements will be less than the theoretical targets.
- Obtain multiple ballast weights (lead, tungsten, steel, etc.) equal to the difference between the target weight and the initial measure weight of the component.
- Position the ballast weights in or on the component so as to give the proper CG location.
- Check the mass inertia properties and adjust the positions to achieve the desired inertias (e.g., two or more identical weights moved equally outward from a single point can increase the mass moment of inertia without changing the overall weight or CG location).
- Permanently bond or attach the ballast weights in position and take final measurements for the mass and inertia properties.

5.8 FEM Correlation

Correlation of the finite element model (FEM) with the actual physical hardware is usually an important step in the flutter model design process. In an ideal case the FEM will represent the scaled design characteristics of the "real" aircraft, and the model hardware is tuned and ballasted to match. In most cases it is impossible to achieve a perfect correlation in this manner because of certain design tradeoffs that must be made to accommodate mounting the model, instrumentation requirements, safety factors, and practical limitations imposed by material properties and fabrication processes. The approach that is normally taken is to match the model hardware theoretical FEM as closely as is practical, and then to modify the FEM to match the hardware. This modified FEM is normally a second analytical model which is then directly compared to and validated by the wind tunnel test data. Additional modifications to this FEM may be made based on the wind tunnel test results.

Generally the FEM correlation process consists of matching the FEM of each individual component against the measured (calibrated) data from that component in isolation. Then the overall FEM is correlated to the overall assembled model calibration results.

6.0 Load Tests to Verify Structural Integrity

The design constraints imposed by having to meet scaled mass and stiffness distributions typically will not allow flutter models to meet strength requirements with large factors of safety. Some methods of construction used on flutter models also make it difficult to accurately predict stress levels—particularly since many of the components are relatively flexible compared to force models. For these reasons it is very common for load testing to be part of the "buyoff" criteria by which flutter model hardware is accepted.

6.1 Point Loads

Point loads are often used when the flutter model construction includes internal spars or structure which carry the majority of the loads. Loads applied at the appropriate locations can be used to verify the structural integrity of the spars, flexures, and bolted attachments. In cases where a point load must be applied to a composite structure, a metal or wood block may be temporarily bonded to the composite structure to act as an attachment point.

Weight pans and spring scales.—The most common method for applying point loads to flutter model components is through the use of weight pans. Weight pans can be attached with bolts, suspended from cables, or hung from a simple "S" hook as shown in figure 6.1(a). Occasionally, calibrated spring scales similar to those used by fishermen are used.

Hydraulic actuators.—In cases where the point loads to be applied are extremely high a hydraulic actuator can be used. Attachment to the structure is usually done by bolting directly to a spar or a metal hardpoint mounted in a composite structure. A load cell positioned between the hydraulic actuator and the model component can be used to measure the applied force. Figures 6.1(b) and 6.1(c) illustrate some typical test setups.
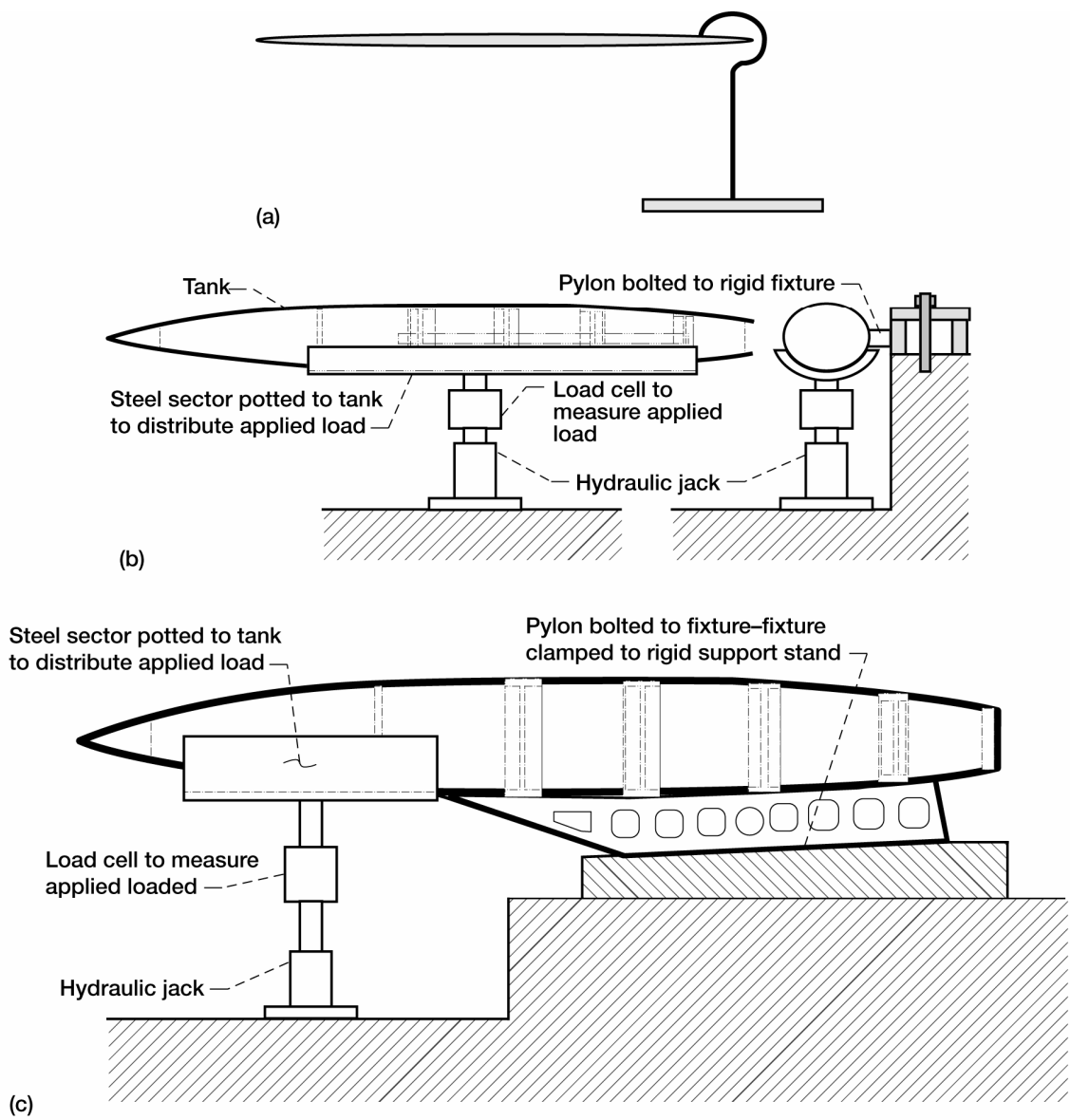
Figure 6.1.—(a) Typical weight pan. (b) External fuel tank and pylon combined side bending load test setup. (c) External fuel tank and pylon vertical load test setup.

6.2 Distributed Loads

Distributed loads can be applied to stressed-skin components or to the external panels mounted on internal spar structure. For some stressed-skin components it is necessary to apply distributed loads because loading at discrete points could damage the structure locally. For this reason distributed loads involve bags or bladders which will conform to the local contour of the surface to which the load is being applied.

Sandbags or bags of lead shot.—Bags filled with sand or lead shot provide a simple method for applying a distributed load to the surface of a flutter model component. Bags of a known weight can be added as necessary to achieve the required distribution. One advantage of this approach is that the distribution can be varied in different areas by stacking up different heights of bags. A disadvantage of this approach is that a considerable amount of weight may be involved, and if a failure should initiate, it will tend to progress catastrophically because the load is not self-relieving.

Water bladders.—Water bladders have an advantage over sand or lead shot bags in that it is possible to arrange the test so that the load is self-relieving. However, the disadvantage to using a single water bladder is that only a constant pressure distribution can be applied.

Water bladders were used successfully to apply distributed loads to the supersonic wing, vertical, and horizontal components described in section 8.0. The following description is for the particular setup used on the wing.

The purpose for performing the load test on the first production flutter model wing was to validate the handbook stress calculations and FEM stress analysis results for the wing design and to ensure that no critical failure modes were missed. A latex bladder filled with water was used to apply an even pressure distribution across the surface of the wing for the load test.

A fixture attached to the root end of the lower wing mold was used to mount the wing so that it was cantilevered 3/8 in. above the mold surface. The aileron was not installed on the sample. A bladder slightly larger than wing planform was formed by folding over a 0.030 in. thick latex rubber sheet and sealing the edges with vacuum bag tape. This flexible rubber bladder was placed in the 3/8 in. gap between the mold surface and the lower surface of the wing sample. A 0.008 in. thick piece of dry fiberglass fabric was placed between the bladder and the wing surface.

A series of wood blocks (2- by 2-in. cross-section) were positioned around the wing planform approximately 0.05 in. to 0.1 in. ahead of the LE, outboard of the tip, and behind the TE. These blocks were placed on top of the edges of the bladder and the fiberglass fabric, and clamped down to the mold. The fiberglass fabric was left quite loose to allow the rubber bladder to expand to completely fill the cavity formed by the mold surface on the bottom, the lower wing surface on the top, and the wooden blocks on the sides. This is illustrated in figure 6.2.
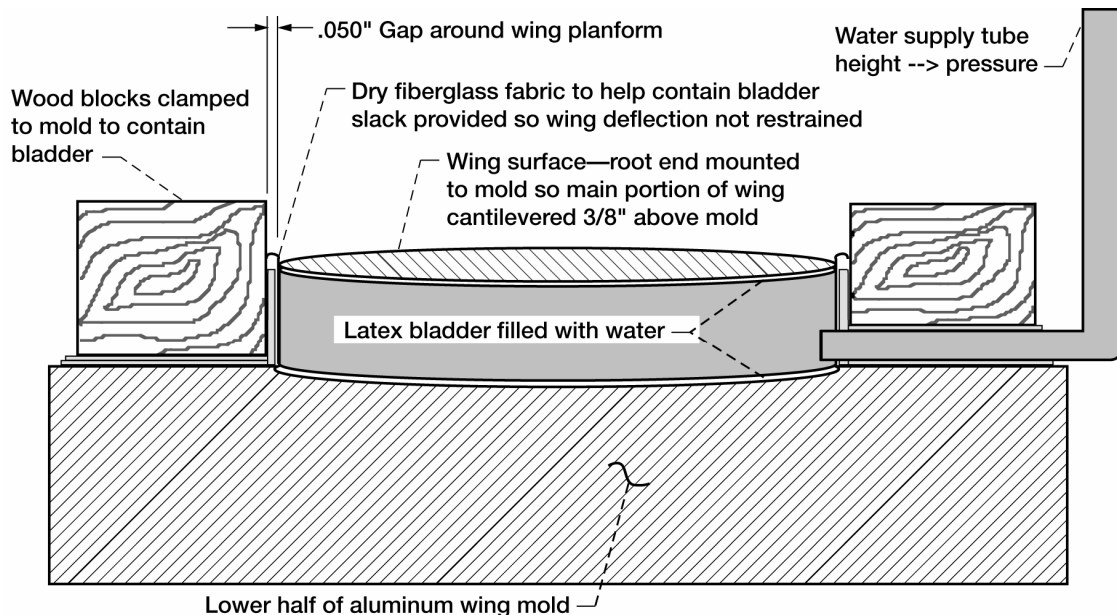
Figure 6.2.—Wing load test setup.

In the area of the aileron cut-out an aluminum plate with a fitting for tubing was used instead of a wooden block. Clear plastic 3/4 in. ID tubing was attached to this fitting and marked at one inch intervals along its length. This tubing extended straight up from the fixture to a height of 20 feet. Blue dye was added to water to make the level in the tube more visible. A video camera was used to document the load test procedure.

Water was poured into the clear plastic tube by a technician standing approximately 16 feet above the wing. The water was poured in small amounts and the resulting water level in the tube was noted. Initially there were occasional bubbles which traveled up the tube (from the small amount of remaining air trapped in the bladder).

The tip of the wing deflected upward with each increment of water added. A scale with inch markings mounted near the wing tip was used to check the surface deflection under load. The final wing design was tested to an applied load of four psi across the entire wing surface. Deflection at the maximum load was approximately 2.6 inches. After the wing was removed from the load fixture a visual examination and frequency checks confirmed that there was no damage or change in the dynamic characteristics of the wing.

One of the distinct advantages of using a water bladder as previously described is that the load is immediately reduced once failure occurs. In a test of a horizontal component taken to failure the compression surface of the composite structure buckled due to the core honeycomb failing in compression/shear. As soon as the failure began to occur the deflection of the surface increased a fraction of an inch. This small additional displacement of the surface equated to a relatively large volume increase in the latex bladder. The water from the vertical tube immediately entered the bladder and the pressure immediately dropped. This occurred quickly enough so that further progress of the component failure was halted. This made it very easy to identify the specific mode and location where the failure initiated.

7.0 Documentation

Documentation normally associated with a flutter model consists of a calibration report documenting all the measured properties of the model, a stress analysis report showing that the model meets all the safety criteria required by the test facility, and occasionally a stability analysis for the model installed on the particular support system to be used in the tunnel.

7.1 Calibration Report

The calibration report typically includes the measured mass and stiffness properties, the measured frequencies and mode shapes, and the documentation of any correlation work done to match the FEM to the measured data.

7.2 Stress Report

The stress analysis report typically consists of basic handbook calculations verifying the structural integrity of joints, fasteners, etc. as required by the particular wind tunnel test facility. For some models (particularly stressed skin or replica construction) the stress analysis may include stress distributions generated by a FEM.

The stress analysis report normally will also include the results from any load testing done on model components or assemblies.

7.3 Support System Stability Analysis

Frequently the support system/model assembly configuration will require a stability analysis to verify a safe operating envelope for the planned test conditions. Sometimes this analysis is done by the test facility, and sometimes it is done by the model design group. There are generally specific guidelines for a particular facility, and in some cases a custom analysis software package exists. If a support system stability analysis is done by the model design group then the results should be included in the documentation package for the model.

8.0 The Design and Analysis Process—A Case Study

This section describes the design and analysis process for portions of a supersonic flutter model developed by the author. This model program required stressed-skin construction for F-22 wings, horizontal tails, and vertical fins. These surfaces were tested as individual components cantilever mounted with root fairings to the wall of a blow-down wind tunnel facility. Due to large tunnel startup/shutdown shock loads and relatively high flutter frequencies, it was anticipated that only one or two flutter data points would be obtained from a component before it was damaged. Therefore, multiple test articles for each surface were fabricated and "tuned" to match a target set of dynamic specifications. In addition to the figures specifically referenced in this section of the paper, the hardware described is also pictured in figures 2.2(a), 5.2(d), 5.3(b), and 5.5(b).

Since the design of spar elements has already been covered extensively in section 3.2, the following subsections will concentrate on the design and analysis process for stressed-skin construction with an emphasis on one particular surface (the vertical stabilizer) and its associated design considerations.

8.1 Methodology for Converting Specifications

For each surface the simplified full scale layup for each segment of each skin was analyzed using a composite laminate analysis program to determine equivalent stiffnesses for the full layup in each direction. This stiffness was scaled by the desired scale factor and, using a PC spreadsheet routine, converted into a table of equivalent stiffnesses and corresponding skin thicknesses. (Model-scale skin thickness was not necessarily equal to the linear scale factor times full-scale thickness.) Based on the materials selected for the basic skin layups (reference section 8.2) proposed layups were developed and analyzed using the same laminate analysis software to match the equivalent skin stiffnesses in all directions as closely as possible.

After a skin layup was determined, the data for this layup and possible structure was input into weight and stress analysis spreadsheets which were developed for each surface. An overall evaluation of strength, mass properties, and stiffness sometimes resulted in conflicting requirements (i.e., to achieve the required stiffness might result in a mass distribution which did not match the target specification). When this occurred, the results and possible alternatives were discussed and analyzed. Modifications to the target specifications were necessary for all three surfaces, but these modifications were made in a way that preserved both the general characteristics of the flutter mechanism, and the proper relationship between critical modes.

The final model design specifications were then converted to the fabrication drawings and process control sheets used to produce the final hardware.

8.2 Material Selection and Property Verification

The model specification conversion process generated target layup stiffness, strength, and mass property requirements. To satisfy these requirements a prepreg unidirectional graphite was chosen as the primary skin layup constituent because of graphite's high stiffness-to-weight and strength-to-weight ratios. The thinnest readily available material (0.003 in. thick) was chosen to allow the greatest flexibility in developing specific layups to match targets. Continuous fabric was used on the outer layer of each layup to reduce the risk of bumps or scrapes causing local delaminations. Fiberglass was chosen because it was available in the thinnest stock (0.0015 in. thick).
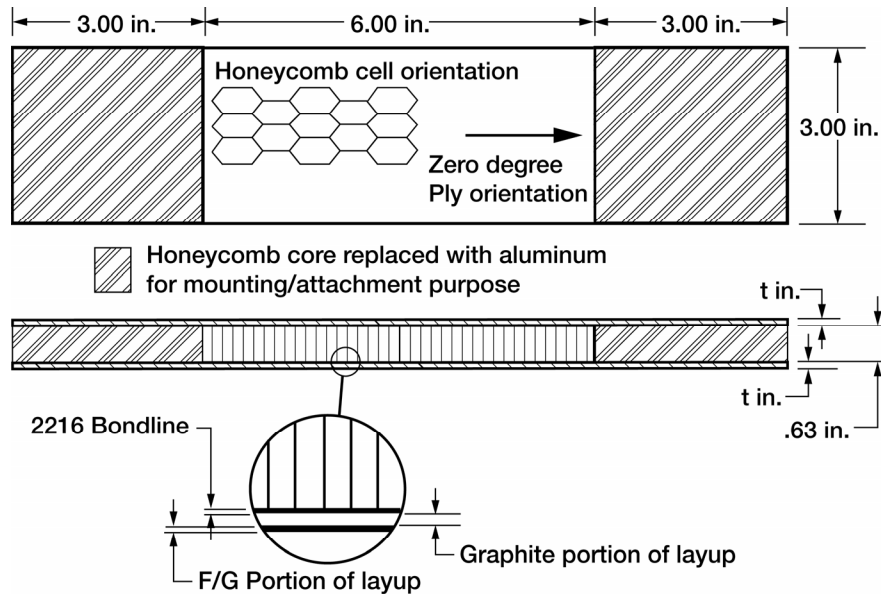
Figure 8.2.—Typical material test coupon.

Paper honeycomb core material was chosen because of its high strength-to-density ratio. The specific density used in each surface was determined based on a stress analysis of the composite surface at critical sections. Honeycomb in densities of 1.8, 3.0, and 6.0 pounds/cubic foot was used in the various surfaces.

After the initial selection of materials various sample coupons were used to verify the stiffness, density, and strength characteristics of each. A shear test was done on a layup of the unidirectional graphite to confirm shear strength. Sixteen sandwich coupons were made with fiberglass/graphite skins and cores of various grades of honeycomb. Figure 8.2 shows a typical coupon. The stiffness of these coupons was tested using the mirror calibration technique described in section 5.1. Each of the coupons was also load tested to failure to verify honeycomb core strength published values.

8.3 Stiffness and Strength Evaluation

The stiffness of the horizontal tailboom spar was tested using the mirror calibration technique, and also by measuring deflections with dial indicator gages (accurate to 0.0005 in.) as loads were applied. The stiffness of the production composite components was not directly measured. Determination of mass properties, frequencies, and node line positions was used to indirectly verify the stiffness of each component.

Mirror calibration was used to evaluate the horizontal actuator flexure stiffness when mounted in the tailboom. All other flexure stiffnesses were evaluated indirectly and modified based on frequency and mass property data. This was more consistent with the fact that the specified data were loop spring rates (they included the backup stiffness of the structure which the flexure was mounted to).

The strength of built up structures was initially evaluated by a stress analysis. Because of the extreme loading conditions anticipated for the test, proof load testing was also done on each surface and store. For the vertical fin, horizontal, and wing the surface was cantilevered at the root as it would be installed in the tunnel, and an even pressure was applied to the entire planform area using a water-filled latex bladder as described in section 6.2. For the external stores a hydraulic jack/load cell combination was used to apply loads as described in section 6.1.

8.4 Weight Evaluation and Control

Weight evaluation and control included the development of realistic weight targets during the design phase, control of weight during the fabrication phase, and verification for the final as-built surface.

Densities for materials commonly used for flutter model construction have been evaluated and tabulated during previous flutter model programs. For materials specific to this program, such as the prepreg unidirectional graphite and the fiberglass fabric wet layup, sample coupons were fabricated using the same processes anticipated for the actual hardware. The densities derived from these samples and from previously tabulated information were used to develop a weights spreadsheet for each component surface. The spreadsheet divided the surface into the individual weight cells defined by the surface FEM. For each cell the volume and density of individual items were separately tabulated. A typical weight cell would include data for some or all of the following:

- Upper skin layup
- Lower skin layup
- Honeycomb core
- Plywood rib or spar segments
- Aluminum or steel hardpoints
- Instrumentation & wiring
- Adhesive (glue)
- Ballast weights

The spreadsheet allowed weight, CG, and inertia evaluations for individual elements of a cell, cell totals, or combined values for the entire surface. Although the use of CAD solid modeling was helpful in assessing mass properties for various component elements, using it to evaluate the assembled component mass properties was not practical due to the level of detail required for the assessments. For example, the labels on figure 8.4 indicate individual elements of the internal wing structure—including various thicknesses of aircraft plywood and several densities of honeycomb core. For a typical element there was a specific weight of adhesive distributed over each of its six surfaces. The fabrication process for any wing included a two-page table just for recording the target and actual amount of glue applied per surface of all the individual core elements. Although keeping track of mass contributions at this level was tedious using spreadsheets, it was still more practical than trying to include the amount of CAD detail needed to obtain the same information using a solid CAD model.

Some of the initial sample surfaces were cut up into segments corresponding to the weight cells defined in the spreadsheets and the FEMs. The weights of individual segments were compared against predicted targets and, if necessary, adjustments were made to the targets and the written process sheets prior to fabrication of the production parts.

The mass properties (weight, CG, and inertias) for each production surface were measured and compared to the predicted values. For the wings a final adjustment was made by adding a small amount of ballast to each of the wings in the aileron cove area. The amount of ballast was chosen to produce the best matched set of final production wings.
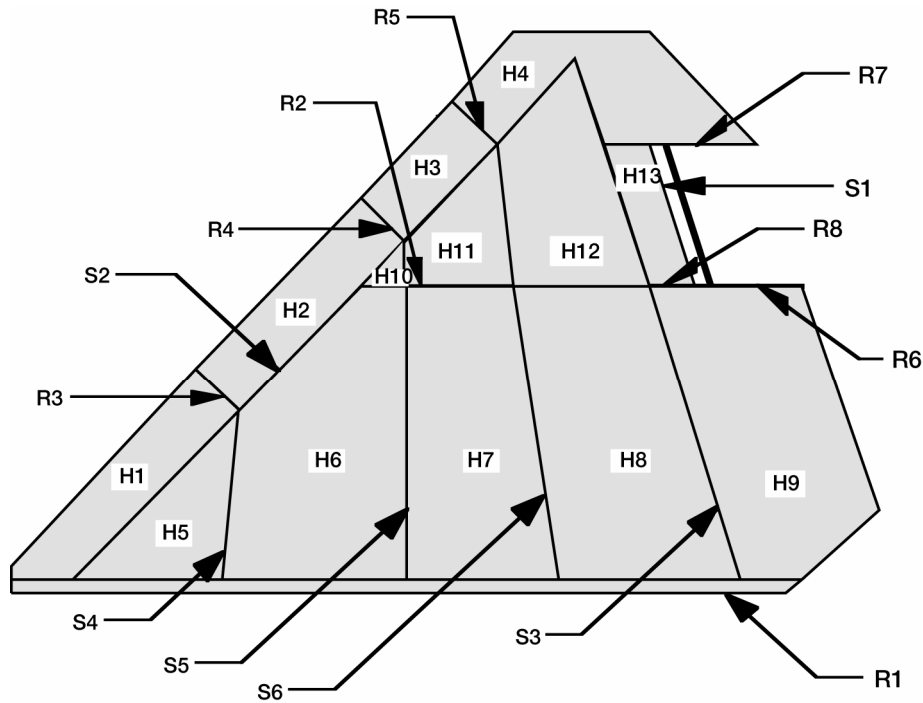
Figure 8.4.—Sample figure for glue weight control (wing fabrication process).

8.5 Model Scale FEM

Component geometry was taken from the full scale FEM data scaled to model scale. It was modified slightly to suit tunnel connection requirements. Internal geometry was simplified as much as possible without violating structural integrity or mode shapes.

The flutter model components were fabricated from fiberglass and graphite composite materials, paper honeycomb, balsa wood, plywood, steel, and aluminum. The composite materials and the paper honeycomb were orthotropic materials. The moduli of elasticity for all these materials were measured and the nominal values were included in the finite element models.

FEM generation and ground rules.—The purpose of the FEMs was twofold: first, to aid in the design of the flutter model so that the mass properties, stiffness distribution, natural frequencies, and mode shapes reasonably represented the full scale design, and second, to provide a high quality analytical model that closely matched the fabricated flutter model.

Mass distribution data was provided (in full scale) for all the components as a series of lumped masses. Data representing the stiffness distribution, frequencies, and mode shapes of the full scale aircraft were dynamically scaled, and the resulting mass and stiffness distributions were used as a guide to design the flutter model components.

Components were designed to match as closely as possible the scaled mass and stiffness distributions of the full scale aircraft. Operationally, this meant matching the first five mode shapes and frequencies to within 5 percent of the measured values.

FEM tuning.—Samples of each component (wing, horizontal, and vertical) were built. These samples were weighed and the mass properties (CG and inertias) were measured. Some samples were carefully cut along prescribed lines so that a detailed comparison of the mass distributions could be made. Results of the mass measurements were used to modify the mass distributions of the component FEMs to reflect more closely the fabricated parts. No structural influence coefficient measurements were made for any supersonic flutter model component. Overall stiffness was measured indirectly by matching mode shapes and natural frequencies.

The sample wing was experimentally tested to determine its natural frequencies and mode shapes in both the supported and unsupported configurations, with and without the aileron. The aileron itself was also tested to obtain unsupported frequencies, and again supported on flexures that were fixed to ground. All this data was used to modify the wing and aileron FEM to match more closely the fabricated parts.

The sample horizontal tail was also experimentally tested in both the supported and unsupported configurations. The horizontal tail was initially tested independently of the tailboom. The experimental data was used to tune the horizontal FEM, and more tuning was done later when the tailboom became available for testing. The tailboom was examined by itself, then with the horizontal attached to it. This information was used primarily to design and model the horizontal pitch spring.

The vertical tail sample components, fin and rudder, were tested individually and combined. The fin was tested by itself in both the supported and unsupported configurations. The rudder was tested unsupported, and then supported on the hinges that were fixed to ground. Then the fin and rudder combination was tested in both the supported and unsupported configurations. This data was used to tune the fin, rudder, actuator spring, and hinges of the vertical FEM.

8.6 Model Stress Analysis

The purpose of the stress analysis was to verify the structural integrity of the flutter model component designs so that they could perform their missions safely. Each surface was checked for tensile strength, compressive buckling, and core shear. Hinges, flexures, and screw fasteners were checked for load carrying capacity.

Satisfactory strength was an important part of the design criteria. It was necessary to ensure that each component of the flutter model could withstand the wind tunnel starting shocks, since no data could be obtained if the structure failed before achieving a flutter condition. Each component of the flutter model was designed to have a safety factor of 1.5 based on the ultimate strength of the material for the particular failure mode being assessed.

Applied loads were estimated initially from data provided in textbooks, and the design pressure was specified as 4.0 psi based on actual wind tunnel measurements. Although the skin of each surface had a factor of safety more than twice what was required based on ultimate tensile strength, preliminary load tests showed that the critical failure mode involved the compressive strength of the honeycomb core—not the tensile strength of the skin. The designs were then modified to incorporate a stronger (though somewhat heavier) core material that could survive a 4.0 psi average starting load.

Easy to apply, basic handbook equations were used to estimate the strength of the component designs. Some of the formulas, especially those pertaining to core buckling, came from the HEXCEL design manual. Later, when representative finite element models were generated, detailed stress distributions were computed for verification of the hand analyses.

Cross sections for critical stress areas were evaluated for each component. Section properties for complicated geometries were computed using the CAD system. A FORTRAN program was written that computed orthotropic properties for composite material lay-ups. Applied forces and moments were conservatively derived and used in the calculation of stress.

Material properties were obtained from a variety of sources including in-house testing. Material properties for standard structural materials like steel and aluminum were obtained from MIL HANDBOOK 5. For composite materials like fiberglass and graphite, some, but not all, material properties could be found in vendor (FIBERITE) catalogs. Data for the paper honeycomb core came from the HEXEL catalog. Other properties for composite materials, and for balsa and plywood, were obtained by performing calibration tests.

After the designs were approved, sample components were built. These samples underwent a variety of tests for mass properties, vibration characteristics, and strength. Eventually, the samples were tested to failure to measure their load carrying capability, and to ensure that all failure modes were accounted for.

8.7 Vertical Stabilizer Construction Details

As shown in figure 8.7(a) the vertical stabilizers were fabricated as individual fin and rudder components which were then assembled with flexure springs and a hingeline skirt.

Fin construction.—Figure 8.7(b) shows the basic internal structure of the vertical fin. The aluminum root rib had 1/4-20 keenserts and dowel holes installed to mount to the vertical fairing. In the hingeline area the rib had a pocket machined out to provide a mating surface for the rudder actuator flexure. Five aluminum rudder hinge hardpoints were bonded to the inside of one skin with additional plywood support structure. All other spar and stiffeners were 1/16 inch thick aircraft plywood. The location of the internal structural components was matched to the full scale aircraft wherever possible to maintain similar load transference paths and mass distributions. The paper honeycomb core density was three pounds per cubic foot.

Fin skins had fiberglass fabric outer layers and internal graphite unidirectional plys at specific orientations to match the desired stiffness and mass distributions. The layups for the upper and lower skins for the fin were not identical, but reflected the asymmetry of the full-scale aircraft vertical fin. Instrumentation included one accelerometer and two strain gage bridges.

Rudder construction.—The upper and lower rudder fiberglass and graphite skin layups were asymmetric, corresponding to that used on the full scale aircraft. Internal structure consisted primarily of balsa and plywood stiffeners. At each of the five rudder hinge locations an aluminum hardpoint was bonded to the skin, and a sixth larger aluminum hardpoint was bonded in to provide attachment for the rudder actuator flexure. The paper honeycomb core material had a density of 1.8 pounds per cubic foot. One accelerometer was installed in the rudder.

Mounting hardware.—The rudder is mounted to the vertical by X-flexures at five hinge point locations. Construction of the X-flexures is shown in figure 8.7(c). Two wire EDM stainless steel flexure webs are assembled with aluminum spacer blocks to create a flexure assembly. Each end of the X-flexure is mounted to a hardpoint in the vertical or rudder with two #4-40 flat head cap screws.

X-flexures were chosen to eliminate concerns about the friction and damping which would be present with pin or bearing attachments. The X-flexures provided a very low hingeline springrate, and a separate torsional flexure was used to model the rudder actuator stiffness. The outboard end of the rudder actuator flexure was attached to the rudder through a friction ring clamp with two set screws providing positive mechanical location. The root end of the actuator flexure was rigidly bolted to an extension of the aluminum root rib for the vertical.

The root rib of the vertical was attached to an aluminum vertical fairing assembly with twelve 1/4-20 socket head cap screws and two dowel pins. The vertical fairing assembly was in turn mounted to the interior window plate with ten 1/2-13 socket head cap screws. This vertical fairing assembly continued the external vertical contour inboard to the fuselage intersection plane. The fairing was machined from a single block of aluminum with six pockets on each surface to provide access to attachment bolts.

Hingeline skirts.—The magnitude of the start-up shocks and the size of the rudder resulted in a requirement for large bending moment loads to be transmitted across the rudder hingeline. Stress calculations indicated that the load would need to be distributed along the entire hingeline. Transference at a select number of points would locally overstress the skins of both the vertical and the rudder. A single layer of Kevlar fabric was bonded across the hingeline gap along the entire span of the rudder. This Kevlar "skirt" was impregnated with RTV resin in the gap area to allow it to remain flexible and not dampen the motion of the rudder surface within a +3.5° of deflection.

At approximately 3.5° the skirt on one surface would become taunt and transmit tensile loads between the rudder and the vertical. Along the opposing surface the gap closed so that the skins of the vertical and rudder made contact and transmitted compressive loads. A thin rubber strip bonded to the vertical side of the gap helped ensure that the compressive loads were more evenly distributed along the length of the hingeline. Figure 8.7(d) shows the hingeline area with the rudder in nominal position during testing and also at a rudder deflection of 3.5°. The bending moment produced by the start-up shock impinging on the rudder was taken out through tension in the skirt and compression through the skins. The shear loads were carried by the X-flexures located at the hinge points.

(a)

Graphite skin/ honeycomb core composite vertical

Rudder mounted with steel flexures

Aluminum vertical fairing

(b)

Plywood rib

HRH 10-1/8-3.0 honeycomb

2-part foam

Aluminum hardpoint

Plywood spar

Aluminum hardpoint

Aluminum hardpoint

Plywood spar

Plywood rib

Aluminum hardpoint

Aluminum hardpoint

Aluminum root rib

Plywood spar
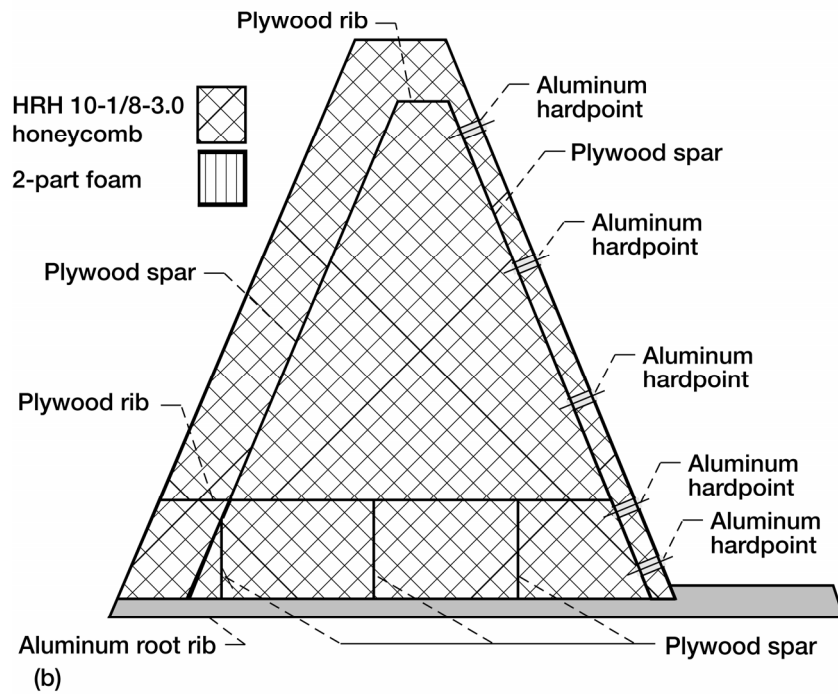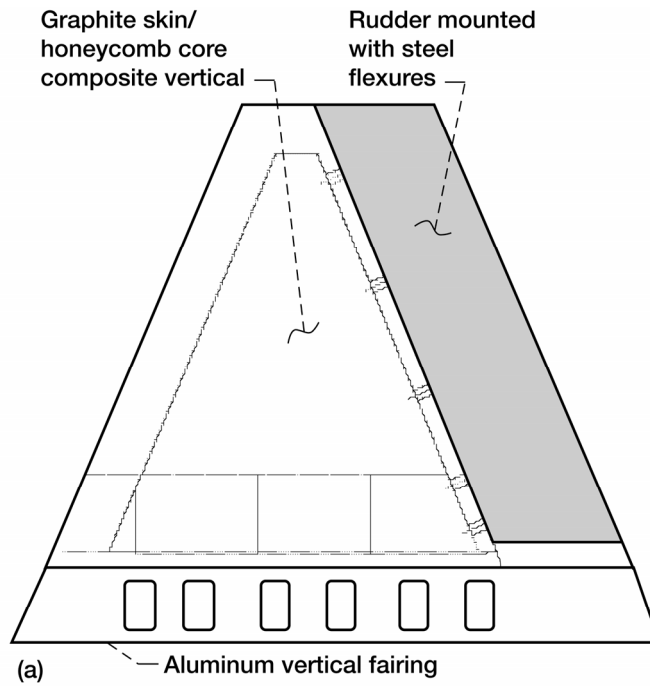
Figure 8.7.— (a) Vertical stabilizer assembly. (b) Internal fin structure.
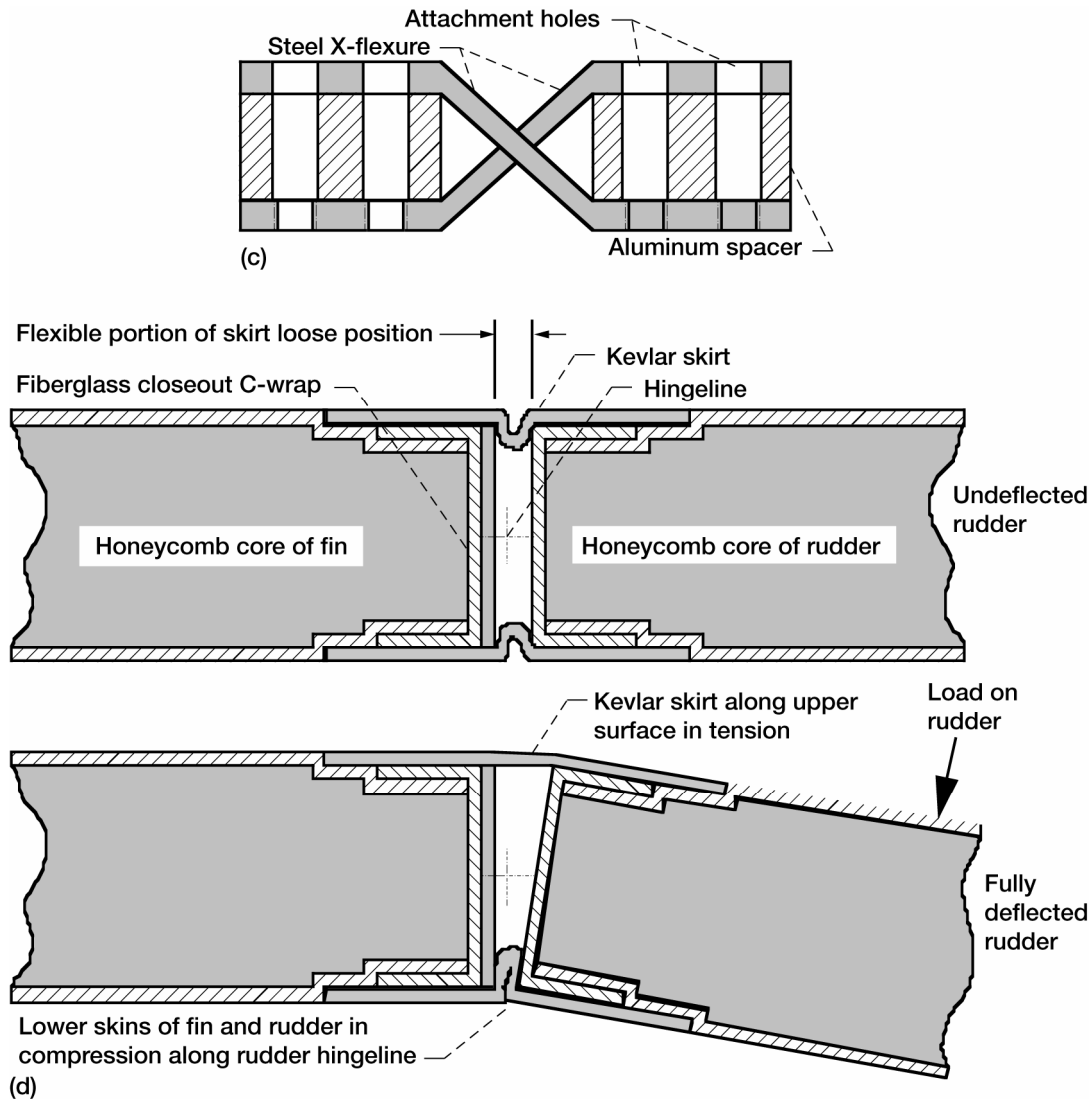
Figure 8.7.— (c) rudder X-flexure construction. (d) Rudder hingeline-skirt construction and load transference.

Rudder actuator stiffness.—The nominal rudder flexure configuration is shown in figure 8.7(e). The flexure is primarily a torsion flexure, although there is a small component of bending due to flexure centerline being offset from the hingeline. The square portion of the part acted as the actual flexure. The length of this square portion was extended to produce reduced stiffness flexure configurations. A 50 percent rudder flexure therefore has a two inch flexure length (twice the nominal).

Vertical ballast cases.—To test a second ballast condition for the vertical, lead foil tape (0.006 inches thick) was added to the exterior skin on the upper and lower surfaces of the vertical and rudders in the areas indicated in figure 8.7(f).
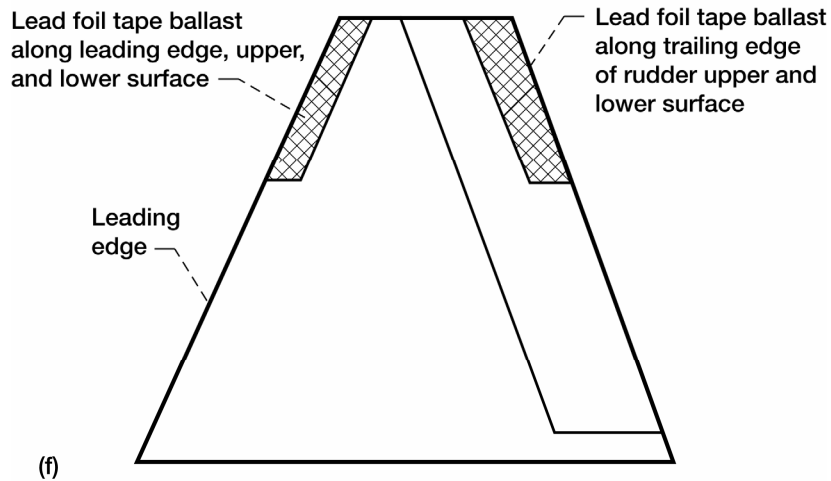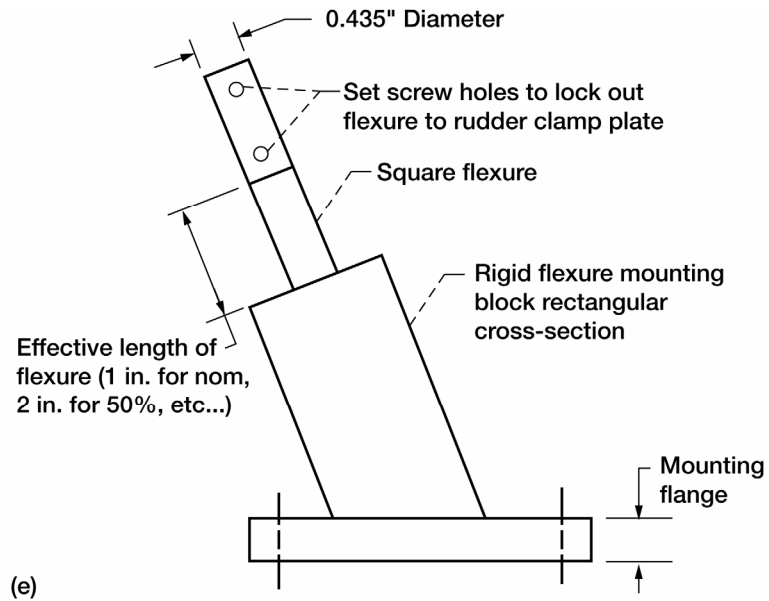
Figure 8.7.—(e) Rudder actuator flexure. (f) Location of additional ballast added to the verticals.

Conclusion of case study.—The F-22 supersonic flutter model components described in this case study were successfully tested at the Rye Canyon blow-down facility in Valencia California in 1994.

Reference

1. Bisplinghoff, Raymond L.; Ashley, Holt; and Halfman, Robert L.: Aeroelasticity, chap. 12. Addison-Wesley Publishing Co., Cambridge, MA, 1955.

Forced Vibration and Flutter Design Methodology[*]

Lynn E. Snyder and Donald W. Burns
Allison Gas Turbine Division
General Motors Corporation
Indianapolis, Indiana 46206

Introduction

Prevention of high cycle fatigue in turbomachinery components is the aim of the structural designer. High cycle fatigue considerations account for a significant percentage of development and operational costs of a gas turbine engine. In development, costly time delays and redesign efforts may be incurred due to high cycle fatigue failures of components. Decreased reliability, shortened time between overhauls, and increased need for spares may be associated with high cycle fatigue failures. These also add to the costs of operation of gas turbine engines. Based on the accumulated knowledge of the cause of high cycle fatigue, empirical and analytical design tools to aid the designer have been and continue to be developed. Proper application of these design aids leads to the ultimate goal of eliminating high cycle fatigue from gas turbine engines through judicious design of turbomachinery components.

This chapter will cover the aeroelastic principles and considerations of designing blades, disks and vanes to avoid high cycle fatigue failures. Two types of vibration that can cause high cycle fatigue, flutter and forced vibration, will first be defined and the basic governing equations discussed. Next, under forced vibration design the areas of source definition, types of components, vibratory mode shape definitions and basic steps in design for adequate high cycle fatigue life will be presented. For clarification a forced vibration design example will be shown using a high performance turbine blade/disk component. Finally, types of flutter, dominant flutter parameters, and flutter procedures and design parameters will be discussed. The overall emphasis of this chapter is on application to initial design of blades, disks and vanes of aeroeleastic criteria to prevent high cycle fatigue failures.

Characteristics of Flutter and Forced Vibration

The classification of the two types of vibration which can cause high cycle fatigue failures is delineated by the relationship between the component displacement and the forces acting on the component. Forced vibration is defined as an externally excited oscillating motion where there are forces acting on the component which are independent of the displacement. Where the nature of the forces acting on the component are functions of the displacement, velocity or acceleration of the component, and these forces feed energy into the system, the self-induced oscillations are classified as flutter. Therefore, to avoid forced vibration and flutter through design requires an accurate knowledge of the forces and the dynamic properties of the structural component involved.

A simplified view of the forces and the dynamic characteristics of the structural component are shown in figure 1. The basic equation of motion shown combines the structural dynamic properties on the left side of the equation with the forcing function on the right. The dynamic properties of the component are based upon the mass (M) and stiffness (K) matrices of the system from which natural undamped frequencies (ω) and mode shapes are determined. The force required to move the component in each mode shape is dependent on the structural damping (C) of the system.
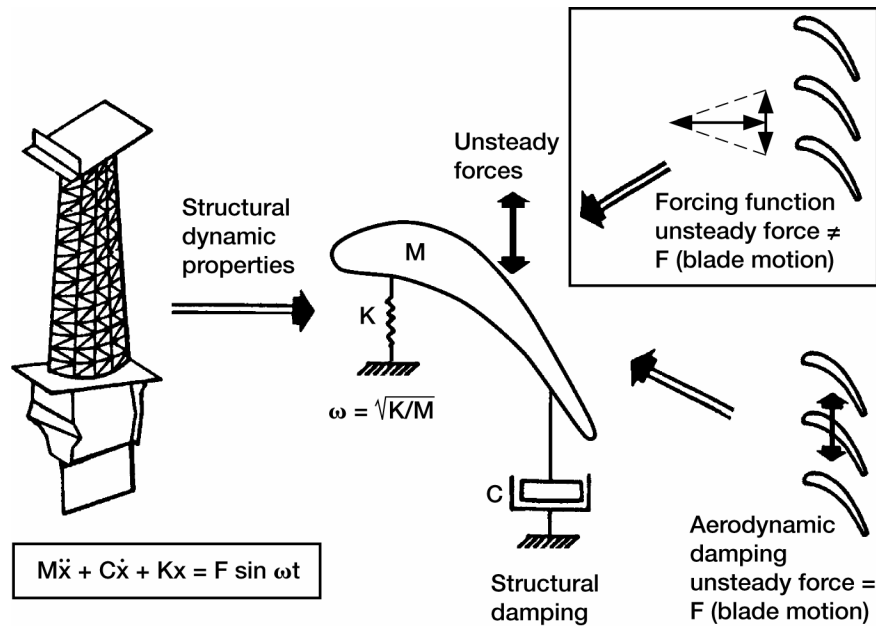
Figure 1.—Primary elements of flutter and forced vibration.

Definition of the forcing function is divided to distinguish between external and self-induced forces. External forcing functions which are independent of component displacement can be generated by such things as air flow nonuniformities or by mechanical mechanisms such as rub. The aerodynamic force which is created as a result of the component's displacement is classified as a self-induced force called aerodynamic damping. This self-induced force may either be stabilizing (positive aerodynamic damping) or destabilizing (negative aerodynamic damping).

For either forced vibration or flutter, the response (equilibrium amplitude) of the component is equal to the work done by the component. For forced vibration, the equilibrium amplitude is reached when the work done on the component by the external forcing function is equal to the work done by the structural damping force and by the aerodynamic damping force. This work balanced is expressed as:

$$\text{WORK/CYCLE)}_{\text{IN}} = \text{WORK/CYCLE)}_{\text{OUT}} \tag{1}$$

$$\text{WORK / CYCLE)}_{\substack{\text{FORCING} \\ \text{FUNCTION}}} = \text{WORK / CYCLE)}_{\substack{\text{STRUCTURAL} \\ \text{DAMPING}}} + \text{WORK / CYCLE)}_{\substack{\text{AERODYNAMIC} \\ \text{DAMPING}}} \tag{2}$$

For flutter, equilibrium is reached when the work on the component by the self-induced force, aerodynamic damping, is equal to and opposite in sign to the work done by the component by the structural damping force. This is expressed as:

$$\text{WORK / CYCLE)}_{\substack{\text{AERODYNAMIC} \\ \text{DAMPING}}} = -\text{WORK / CYCLE)}_{\substack{\text{STRUCTURAL} \\ \text{DAMPING}}} \tag{3}$$

The key elements of an analytical design system for aeroelastic response prediction is shown in figure 2. This system can be used to predict steady state (equilibrium) response of turbo-machinery components to forced response or flutter with the ultimate goal being elimination of high cycle fatigue failure in the design phase. The basic elements of the equation of motion are shown here with the structural dynamic properties on the left side and the forcing function on the right. The structural dynamics analyses used presently are based on finite element techniques and are able to accurately predict natural modes and frequencies of blade, disk and vane structures. Structural damping is defined by qualifying the various sources of damping such as material and interface friction. Recently structural damping has been measured by Srinivasan (ref. 1) and Jay (ref. 2). Damping materials have been

Structural dynamics analyses	Unsteady aerodynamics analyses
Prediction of natural modes and frequencies of structure, including effects of nonaxisymmetry	Provide time-dependent pressure distribution due to airfoil motion and/or flow nonuniformity

Aeroelastic analyses

Forced response prediction analysis
Flutter analyses

Goal: Avoidance in design phase
            of aeroelastic instability
            and limiting vibratory stress
            due to resonance

Structural damping model	Distortion analysis
Quantify sources of inherent damping such as material and interface friction Design rules for optimum application of damping materials	Prediction of strength of excitation source such as inlet distortion, upstream row wakes Attenuation of strength with distance from source

Figure 2.—Elements of an aeroelasticity design analysis.

identified for optimum application to various designs to improve flutter characteristics and/or reduce forced vibration responsiveness. D.I.G. Jones (ref. 3) gives an extensive list of efforts to increase/add structural damping to components. Prediction of the strength of the forcing function due to aerodynamic disturbances is also required. Research to acquire data and model such disturbances to provide an experimentally verified analytical prediction system has been carried out by Gallus (refs. 4 and 5). Research to develop unsteady aerodynamic analyses to calculate the time-dependent pressure distribution due to airfoil motion and/or flow uniformity has been conducted by Smith (ref. 6), and Caruthers (ref. 7). All of the elements shown are necessary to adequately design components for forced vibration or flutter considerations.

The preceding definitions and equations form the basis for the design systems used for preventing high cycle fatigue of gas turbine blades, disks and vanes. These design systems are largely centered on defining the sources and/or mechanism of forcing function generation and accurately predicting the aeroelastic properties of the component. The success of a design system is directly dependent on how well it can define these elements of forced vibration and flutter. Use of empirical relationships are still required as a substitute for exact definitions of some elements. Estimates of values of certain elements based on experience are needed. These approximations compromise the ability of the designer to completely avoid high cycle fatigue of blades, disks and vanes but are used to prevent most high cycle fatigue problems. As more exact definitions of these elements are obtained through experimental and analytical approaches, the designer will be able to more adequately attain the goal of elimination of high cycle fatigue failure in turbomachinery components.

Additional information on aeroelasticity can be found in references 8 through 11.

Forced Vibration Design

Forced vibration is the result of external forces acting on the blade, disk or vane component. The type of component geometry can be tailored to limit or lessen the effects of these forces through displacement limitation, frequency tuning, mode selection and/or damping control. Accurate calculation of the undamped natural frequencies and mode shapes is required to effect an acceptable geometry for forced response. These areas will be discussed and an example of the basic steps in forced vibration design will be presented in this section.

Sources of Unsteady Forces

The most common aerodynamic sources of forced vibration are shown in table 1. Aerodynamic sources due to structural blockages to the flow are mainly due to the upstream or downstream airfoil rows. Upstream vanes and struts create a periodic unsteady flow field for downstream rotating blade rows. Likewise the viscous flowfield of rotating blade rows creates a periodic unsteady flowfield for downstream stationary vanes and struts. Generally, vanes, struts, and blades are equally spaced circumferentially but if they are nonuniform in (a) circumferential location, (b) shape (i.e., thickness, camber, trailing edge thickness, chord), or (c) setting angle, for example, then the unsteady downstream flowfield will contain harmonics of the pattern which may coincide in the operating speed range of the engine with a natural frequency, of a downstream airfoil structure.

Downstream vanes and struts can also create a periodic unsteady flow field for upstream rotating blade rows. Likewise potential flow effects of rotating blade rows create a periodic unsteady flowfield for upstream vanes and struts.

Asymmetry in the stationary flowpath can cause unsteady forces on rotating (rotor) airfoils. Examples of flowpath asymmetry are (a) rotor off center, (b) non-circular case, and (c) rotor case tip treatment.

Circumferential inlet flow distortion can be a source of unsteady forces on rotating blade rows. A nonuniform inlet flow condition creates unsteady forces on the rotating (rotor) airfoils. The strength and harmonic content of the forcing function produced will be dependent on the magnitude of the velocity/pressure/temperature defect and the radial and circumferential extent of the distortion.

TABLE 1.—SOURCES OF UNSTEADY FORCES IN ROTATING
TURBOMACHINERY STRUCTURES

• Aerodynamic sources
• Upstream vanes/struts (blades)
• Downstream vanes/struts (blades)
• Asymmetry in flowpath geometry
• Circumferential inlet flow distortion (pressure, temperature, velocity)
• Rotating stall
• Local bleed extraction
• Mechanical sources
• Gear tooth meshes
• Rub

Circumferential inlet flow distortion taking the form of velocity, pressure or temperature variations at the inlet to the compressor or turbine can induce high sinusoidal forces through the length of the compressor or turbine. Crosswinds or ducting at the compressor inlet may produce distortion patterns of low order harmonic content. Combustor cans, because of the variations in operation, may produce temperature patterns of low order harmonic content. Even annular combustors may produce velocity/temperature patterns of low order harmonic content which are due to circumferential flow variations.

Rotating stall zones are another source of aerodynamic blockage which can produce high response in blade, disk, and vane components. Stall zones are formed when some blades reach a stall condition before others in the row. A zone(s) of retarded flow is formed which due to variations of angle of attack on either side of the zone begins to rotate opposite the rotor rotation direction. This speed of rotation has been observed to be less than the rotor speed. Thus, the zone(s) alternately stalls and unstalls the blades as it rotates. The number, magnitude, and extent of the zones and the relative speed between zone rotation and blade, disk or vanes determines the magnitude and frequencies of the forcing function available for component excitation. High stresses observed with this source of excitation can lead to quick failure of turbomachinery components.

Local bleed extraction, where air flow is not removed uniformly around the case circumference, may produce unsteady forcing functions which may excite natural modes of blade and disk components. Stages upstream and downstream of the bleed locations have been observed to respond to harmonics of the number of bleed ports.

Tooth meshing of a gear that is hard mounted on the same shaft is a common mechanical source of blade forced vibration excitation. Rotor blade failure is possible when the rotor system is excited in a natural mode in which

there is high vibratory stress at the blade root. The mechanism of this excitation can be illustrated by examining two examples.

Consider a rotating rigid rotor system vibrating in a fixed plane, the instantaneous direction of acceleration that is applied to each blade root differs from blade to blade for a total variation of 360° around the rotor. Each blade will resonate when its natural frequency (f_c) equals either the sum or difference of the rotor translation frequency (f_{TR}) and the rotational frequency (f_N).

$$f_c = f_{TR} \pm f_N \qquad (4)$$

This equation defines phase equality between the vibrating blade and the forcing function dynamics. If the rotor was not rotating only those blades which were normal to the plane of translation would be resonant due to common phase equality.

Gear tooth (N_T = number of teeth) meshing can be a source of such translation motion of the rotor system ($f_{TR} = N_T \times f_N$). Therefore whenever the blade frequency matches the order frequency due to the number of gear teeth plus or minus one, excitation is possible ($f_c = (N_T \times f_N) \pm f_N$ or $f_c = (N_T \pm 1) f_N$).

Considering the case of torsional vibration of a rigid rotor, all blades experience the same in-phase excitation forces at any instant, independent of whether the rotor is turning. Each blade will resonate when its natural frequency (f_c) equals the rotor torsional vibrating frequency.

$$f_c = f_{TR} \qquad (5)$$

Again, gear tooth meshing can be a source of such torsional motion of the rotor system ($f_{TR} = N_T \times f_N$). Therefore whenever the blade frequency matches the other frequency due to the number of gear teeth, excitation is possible.

Rub, as a source of forcing function, can produce high response in components. Contact of a rotor blade tip with the stationary casing locally, may cause an initial strain "spike" of the blade followed by strain decay in a natural mode. At its worst the rub excitation frequency will be equal to a blade natural frequency. Causes of contact may be related to rotor unbalance response, ovalizing of the case, casing vibration characterized by relative blade to case radial motion, casing droop, and nonuniform blade tip grind.

Types of Turbomachinery Blading

There are many types of turbomachine blades and vanes. Table 2 is a partial list of the types of blades and vanes. Each of these descriptors have a definite impact upon the dynamic properties of the components. They describe some aspect of the component design from how it is supported, general shape, structural geometry, material, to its aerodynamic design.

TABLE 2.—TYPES OF TURBOMACHINERY BLADES AND VANES

Blades	Vanes
Shrouded/shroudless	Cantilevered/inner banded
Axial/circumferential attachment	High/low aspect ratio
Stiff/flexible disk	Solid/hollow
High/low aspect ratio	Metal/ceramic
High/low speed	Compressor/turbine
Solid/hollow	High/low pressure ratio
Fixed/variable	
Metal/ceramic/composite	
High/low hub-to-tip radius ratio	
Compressor/turbine	
High/low pressure ratio	
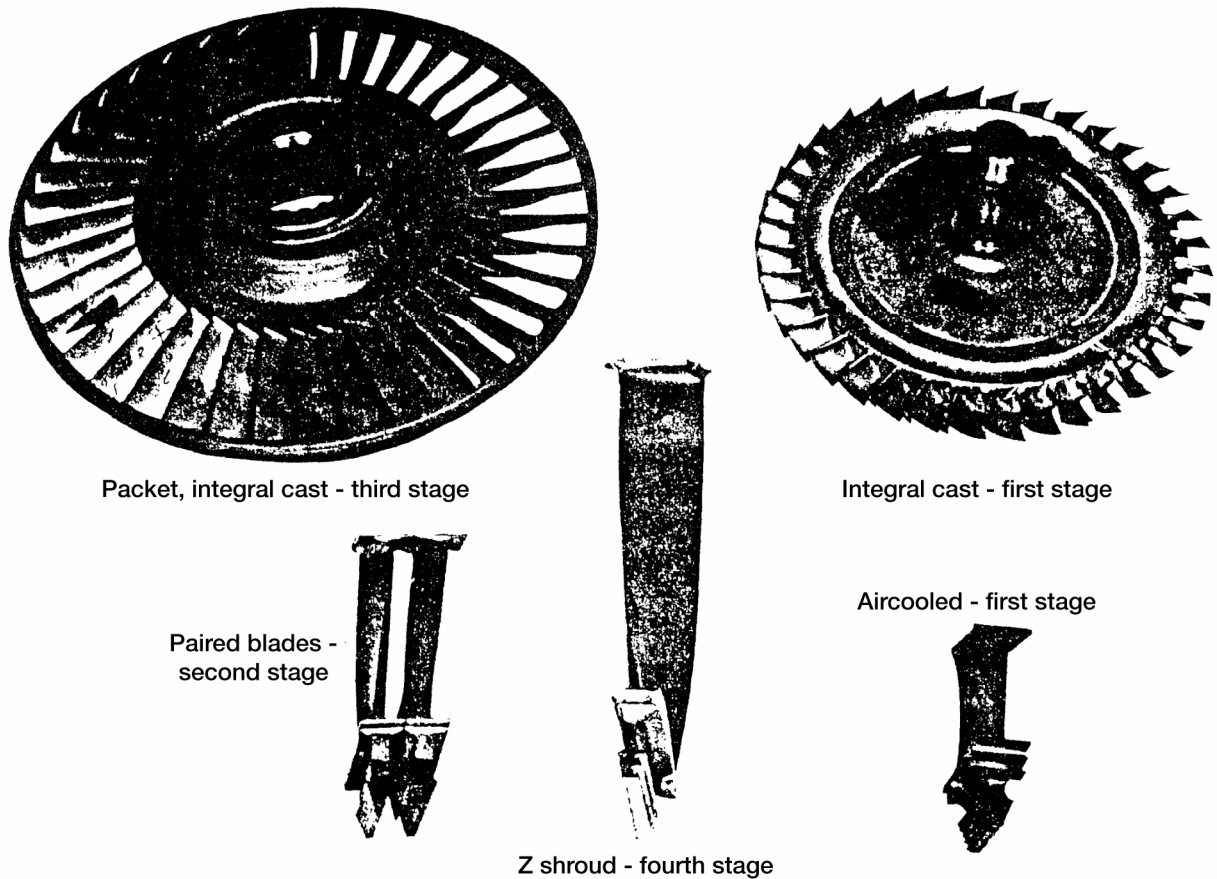
Figure 3.—Turbine blade configurations.

Some examples of turbine blade and disk geometries are presented in figure 3. As shown, blades may be integrally cast with blades or may be separate and have attachments at the blade root. The differences in dynamic characteristics of each of the blades must be accurately considered during the design of testing phases.

Natural Modes

Natural modes and frequencies of the components are defined by the physical geometry of the component. These natural modes are described by the location of node lines (zero motion) and general mode deflection. Generic types of natural modes are shown in figure 4.

The first, lowest frequency, mode of a beam-like component is that mode which has no nodes present on its unfixed surface. This is illustrated by the stiff disk and vane alone modes. For a blade or vane fixed at one end the motion is one of bending from side to side of the whole structure. The fixed blade or vane at both ends bends like a bow string in its first mode. For both types of fixity the second, third, etc. modes become more complex with node lines appearing on the blade or vane.

Actual holographic and calculated mode shapes for an unshrouded compressor blade are shown in figure 5. The fixity of this first stage compressor blade is at the bottom (hub) end of the airfoil. A variety of mode shapes characterized by node lines are identified as either basically bending (B), torsion (T), edgewise (EW), lyre (L) or chordwise bending, or complex (C). The finite element method used to calculate the frequency and mode shapes shows the excellent accuracy possible by analytical means. This ability to predict natural modes is necessary in order to have accurate forced response and flutter design systems.

Blades   Vanes

• Stiff Disk or circumferential attachment*

• Vane alone*

• Disk/blade**

+   −
−   +

• Vane/shroud assembly*

• Disk/blade/shroud**

+   −
−   +

*Modes 1, 2, 3 . . .

**Nodal diameters 0, 1, 2 . . . $\dfrac{NB}{2}$

For modes 1, 2, 3 . . .

NB = Number of blades
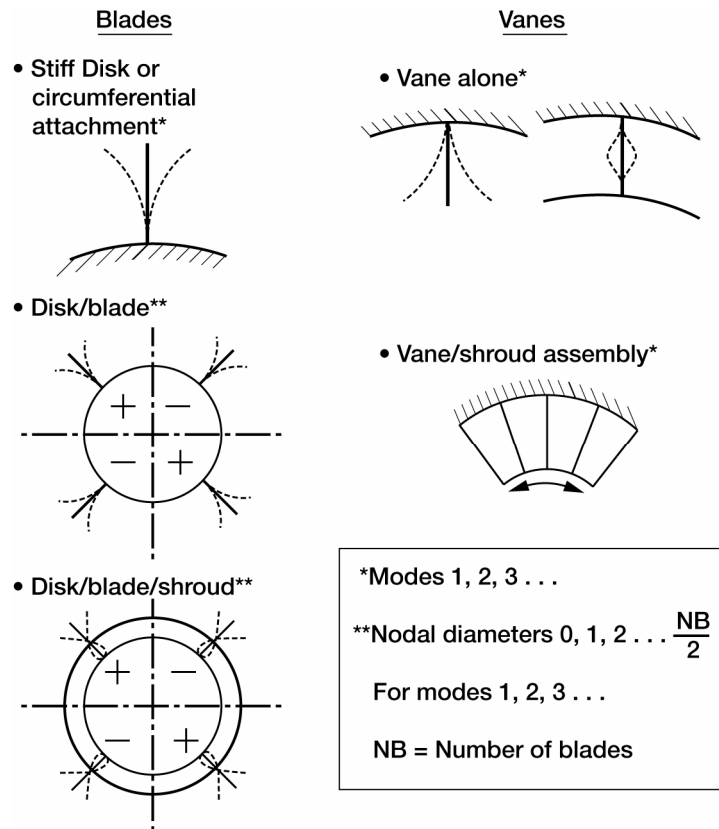
Figure 4.—Types of blade and vane vibratory modes.

When several blades or vanes are tied together and/or are a part of a flexible disk, the combined dynamic properties of the components couple to produce additional modes called system modes (see fig. 4). Packets of blades or vanes tied together have assembly modes in which combined bending/twisting of all blades take place at one natural frequency. Flexible disk natural mode shapes are characterized by line of zero motion across the diameter called nodal diameters (ND). These may couple with the blade natural modes to produce system modes with elements of motion from each component's natural mode but at a new natural frequency. Circumferential node lines also may describe higher frequency natural modes of blade/disk systems.

Holographic photographs (see fig. 6) of a blade/disk system illustrate the relationship between nodal diameter pattern and mode number. Three nodal diameter patterns are shown with the 3ND pattern family expanded for the first three modes. The second mode is characterized by one circumferential node while the third mode has two.
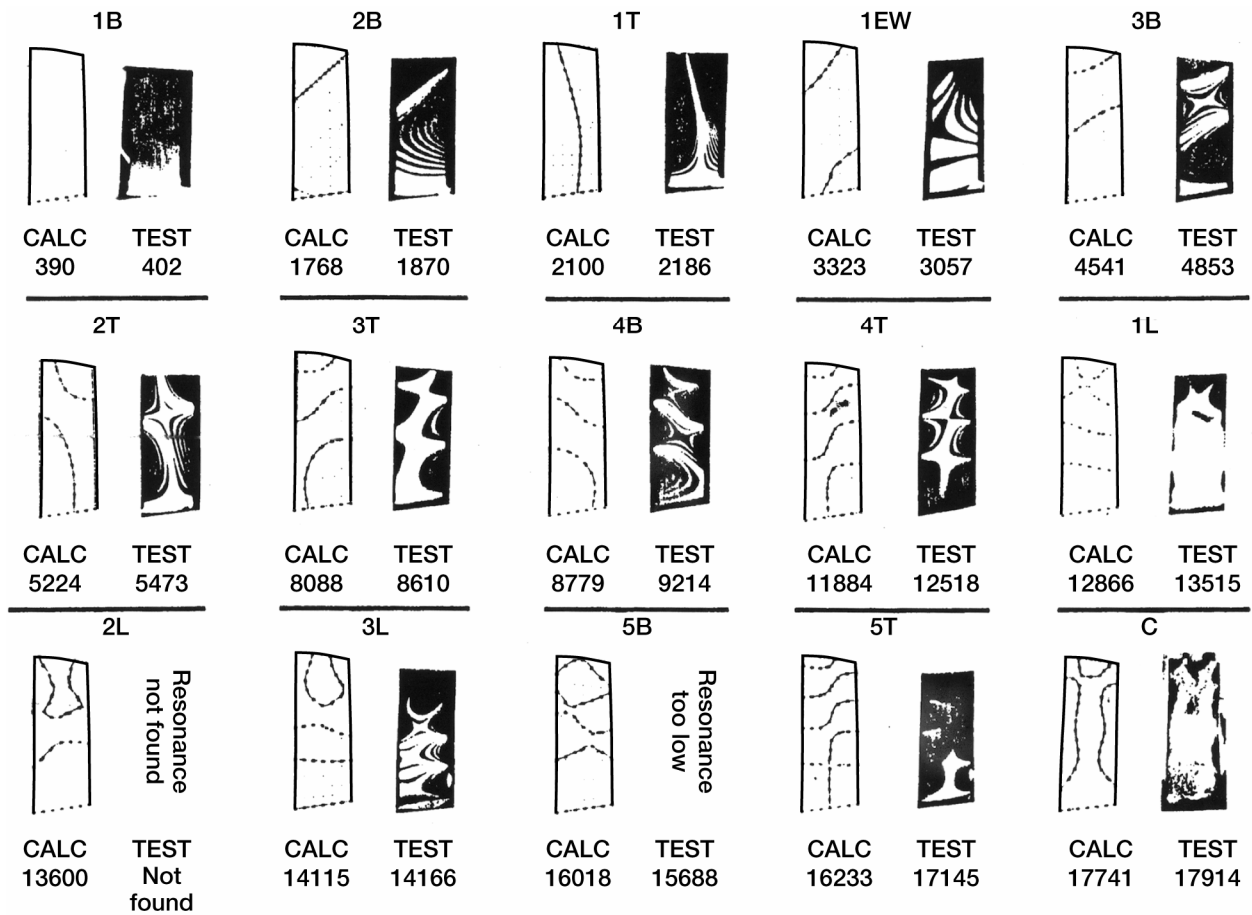
Figure 5.—Frequency and mode shape correlation.

2677 Hz
Mode 1, 3ND

2356 Hz
Mode 1, 2ND

6858 Hz
Mode 2, 3ND
— Circumferential node

2985 Hz
Mode 1, 4ND

Circumferential nodes

ND = Nodal diameter

13457 Hz
Mode 3, 3ND
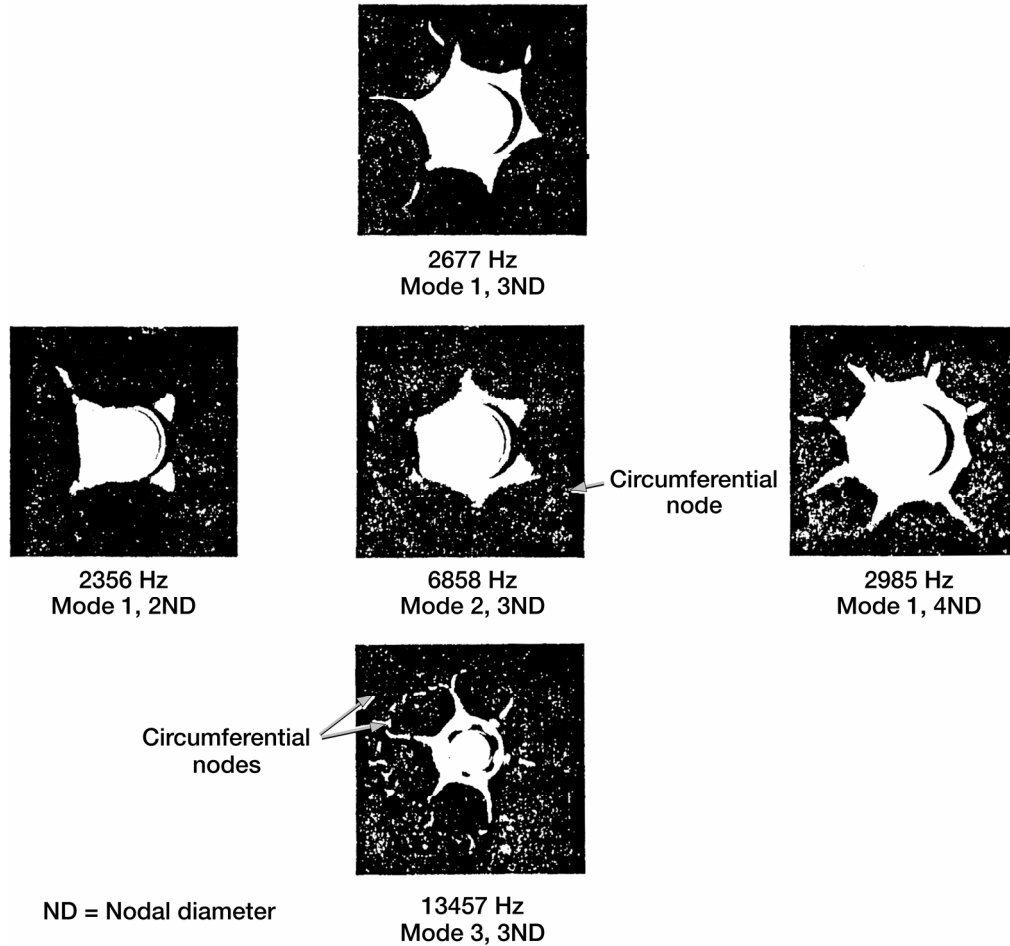
Figure 6.—Mode number and nodal diameter pattern.

Ten Steps of Forced Vibration Design

The ten basic steps in designing to prevent high cycle fatigue due to forced response are listed in figure 7. These steps involve evaluating the environment in which the component must operate (steps 1, 2, and 5), predicting the aeroelastic characteristics of the component (steps 3 to 8), investigating possible design changes (step 9), and finally the actual measurement of the dynamic response of the component in the engine environment (step 10). These steps will be illustrated by examining the design of a second stage gasifier turbine blade/ disk component. The choice of a turbine instead of a compressor component was arbitrary since the steps are the same for each.

The example blade is an aircooled design incorporating the features listed in figure 8. It is a shroudless blade which is integrally bonded to the disk. The hollow blade is a low aspect ratio (length to width) design, with twenty-two (22) airfoils in the stage. A nickel alloy which has good structural properties at high temperature and stress conditions is used in this design.

Step one calls for an identification of possible sources of excitation (forcing function) while step two requires the definition of the operating speed ranges the component will experience. For the example turbine the possible sources and speed ranges are shown in figure 9. Several sources of aerodynamic excitation exist and are listed. Two upstream and two downstream sources have been identified. Each of these sources creates a periodic forcing function relative to the rotating second stage blade/disk component. The relevant content of these forcing functions will be the harmonics associated with the second stage blade passing these stationary sources. The frequency of the forcing function is dependent upon the rotating speed of the second stage blade. The speeds of possible steady state

operation are between idle and design. Any resonance occurring below idle would be in a transient speed range implying lower chance of accumulating enough cycles for failure or maintaining high enough response to produce failure.

Step	1	Identify possible sources of excitation
Step	2	Determine operating speed ranges
Step	3	Calculate natural frequencies
Step	4	Construct resonance diagram
Step	5	Determine response amplitudes
Step	6	Calculate stress distribution
Step	7	Construct modified Goodman diagram
Step	8	Determine High Cycle Fatigue (HCF) life (finite or infinite)
Step	9	Redesign if HCF life is not infinite
Step	10	Conduct strain gaged rig/engine test to verify predicted response amplitudes

Figure 7.—Summary of basic steps in designing to prevent high cycle fatigue created by forced vibration.

Cooling air out

Features
• 3 Channel single-pass cooling
• Metered cooling air
• Tip discharge
• Wall-to-wall pin fins

Cooling air in   Metering tube
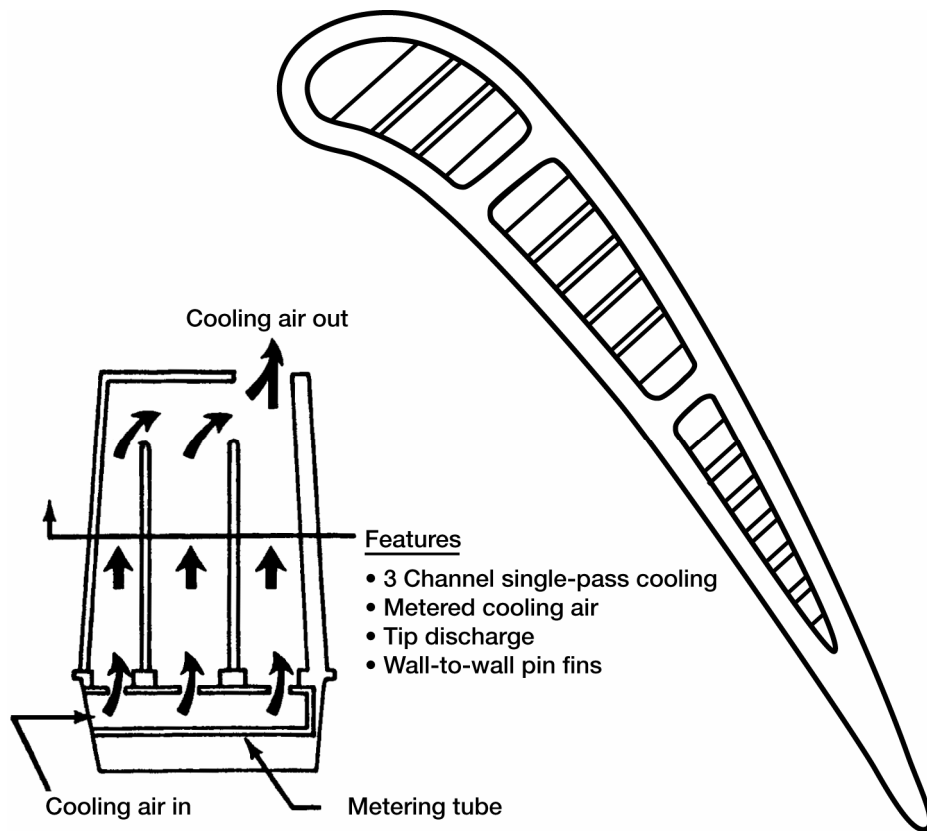
Figure 8.—Gas generator second stage blade cooling geometry.

Design speed = 48,500 RPM
Idle speed = 32,000 RPM
Disk boundary condition = spacer and disk
                         in constant contact

Sources:
13   1st stage vanes
19   2nd stage vanes
21   LP1 vanes
 5   Exit struts (not shown)
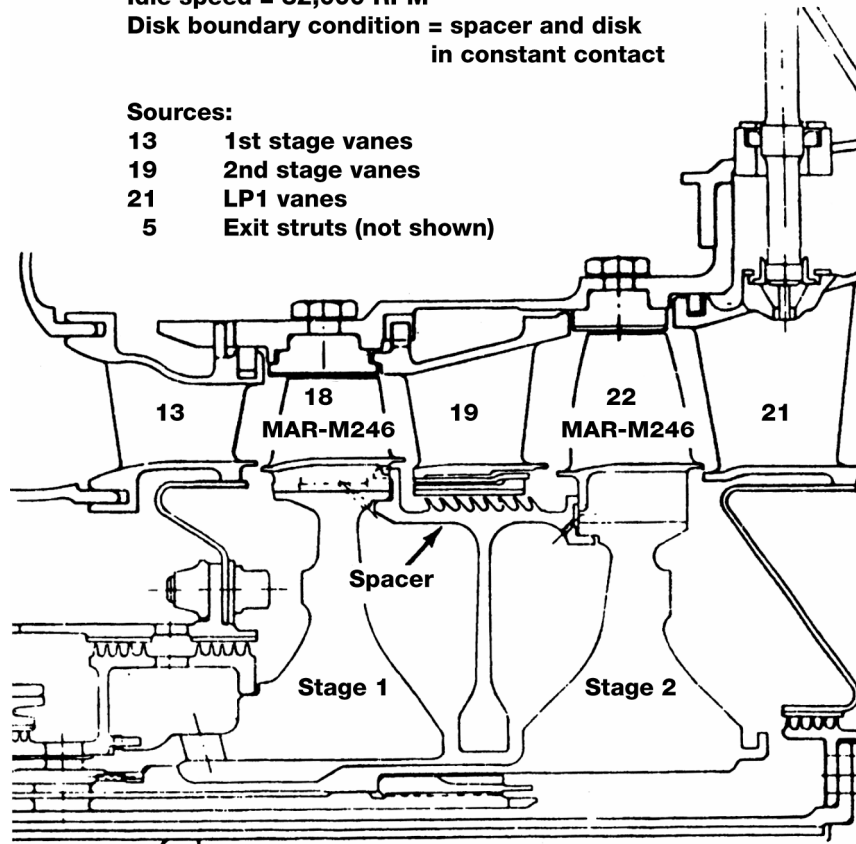
Figure 9.—Gas generator turbine general arrangement.

Figure 9 also notes that the spacer and disk have been designed to be in constant contact throughout the engine operating conditions. This contact limits the disk flexibility and eliminates the disk participation in the assembly modes. Therefore accurate prediction of natural modes, step 3, can be made for this type of design by modeling only the blade geometry and fixing the blade at the proper radial location.

The natural modes of a blade as complicated as this example, can be calculated using finite element techniques developed especially for rotating turbomachinery components. The natural frequencies of the blade have been calculated using a model constructed with triangular plate elements. The elements have been used to simulate the hollow airfoil, platform, and stalk geometry as shown in figure 10. The stiffness and mass matrices formed by these elements are solved to compute the natural frequencies. The more elements used, the closer to the actual blade is the mathematical model.

This method of calculation is shown to be accurate by the comparison of frequencies and mode shapes of test holograms with those of the finite element model. This comparison is for zero RPM and room temperature conditions. Additional calculations are made for various temperature and rotational speeds to determine natural modes at the actual operating conditions.

To determine if the natural frequency of a blade coincides with the frequency of a source, resonant condition, a resonance diagram is constructed (step 4). A resonance diagram relates frequency to rotational speed as shown in figure 11. Since the forcing function frequency is dependent on rotational speed, lines of concurrent frequencies can be drawn for various harmonics (i.e., 1, 2, 3,. . . 10,. . .13,. . .19,. . .21. . . sine waves per revolution of the rotor) of engine speed for which sources exist. Placing of the calculated natural frequencies on the diagram with the lines of concurrent frequencies, engine order lines, of the known sources, identifies possible resonant conditions of a component natural frequency coinciding with a forcing function, source frequency. In this example, a dropping of

natural frequency with rotor speed indicates that temperature effects are dominant over centrifugal stiffening within the operating speed range.
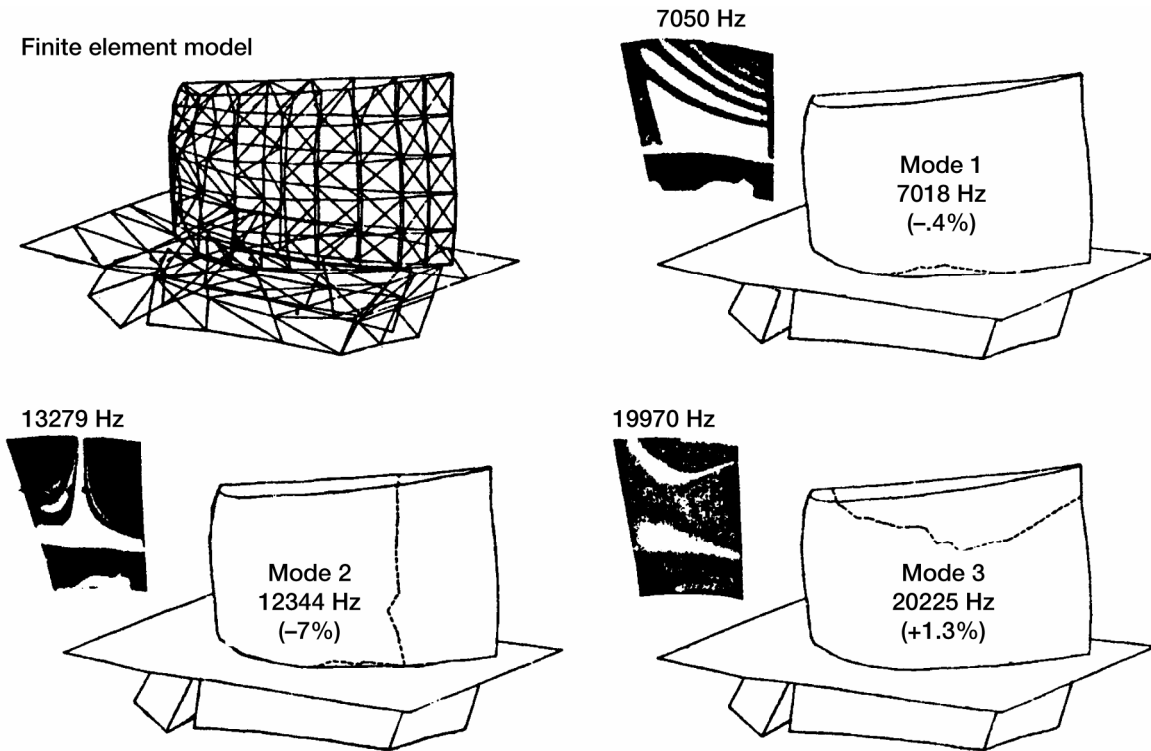
Figure 10.—Calculation of natural frequency for second stage blade.
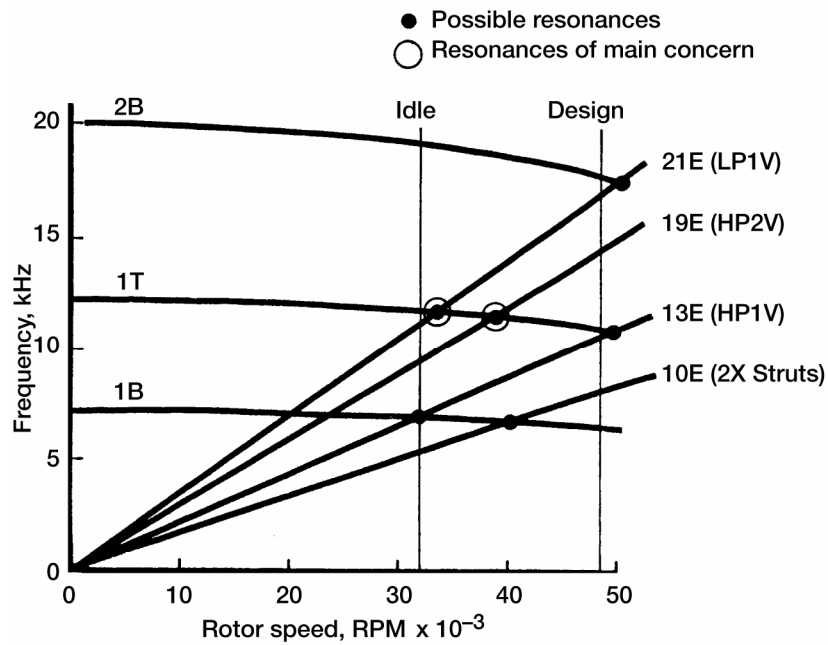
Figure 11.—Resonance diagram for second stage blade.

The possible resonant conditions are identified by intersection of natural frequencies and order lines which occur within or near to the steady state operating speed range. The strongest expected aerodynamic sources of excitation are those immediately upstream (in front of) and downstream (behind) the blade. The amount of response (step 5), depends not only on the strength of the forcing function, but also upon the aeroelastic characteristics of the component. For this example, the dynamic characteristics for the first torsional mode (1T), mode shape and damping are significant in determining possible response amplitudes.

The response of modes of blades due to aerodynamic sources of excitation have been empirically defined based on experience. This empiricism groups typical blades by common mode shape, damping, type of source, and distance from the source to correlate with response experience. The use of an empirical method for estimating response is due to a current inability to adequately predict the strength of the forcing functions produced and the damping present in the gas turbine environment.

For example, the response of first torsional modes of turbine blades due to an upstream vane source might be empirically defined as in figure 12. A plot of axial gap/vane axial chord (rate of decay of forcing function) versus the vane overall total to static expansion ratio (forcing function) may allow the designer to pick the combination of variables that will ensure a viable design. A range of blade gap/chord values is defined for the second stage based upon build up tolerances from engine to engine of the various rotor components. This range indicates that a maximum dynamic stress of six to ten thousand psi would be expected for the first torsional mode coincidence with the upstream vane order line.

The response of turbine blade modes to the turbine downstream vane source of excitation has been shown to be related to the variation of static pressure in front of the vane source, figure 13. $\Delta P/Q$ is a calculated value based on the aerodynamically predicted static pressure field created by the presence of the vane in the airflow stream. This pressure field is dependent upon aerodynamic characteristics (velocity triangles, mass flow, etc.) and vane cross-sectional geometry. Plotting $\Delta P/Q$ versus a normalized value of axial gap allows the designer to space (gap) the blade-vane row to avoid a large forcing function. A specified limit would be based upon turbine blade experience to date and represents the maximum value of $\Delta P/Q$ that is considered acceptable. The second stage blade range (based on build tolerances) indicates an acceptable value of $\Delta P/Q$ and thus indicates that a low response due to the third vane row is expected.
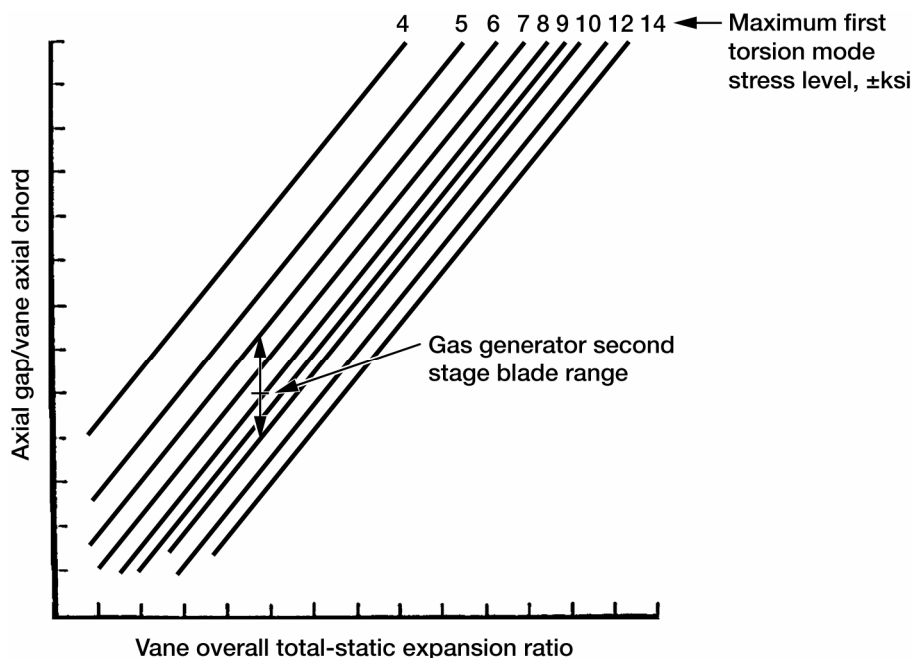
Figure 12.—Prediction of response due to second stage vane.

$$\Delta P/Q = \frac{\text{Maximum static pressure - minimum static pressure}}{\text{Dynamic head}}$$
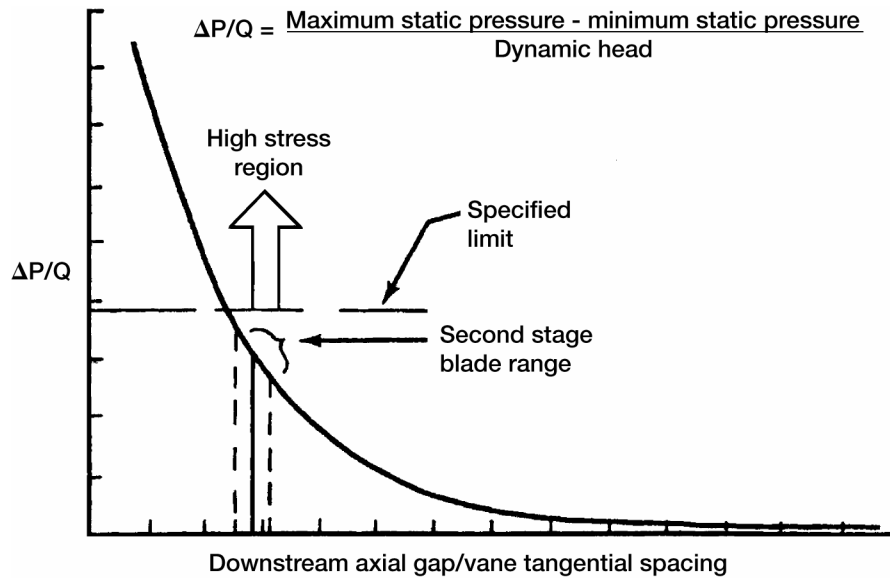
Figure 13.—Prediction of response due to third stage vane.

Calculation of dynamic stress distribution, step 6, is necessary for determining locations of maximum vibratory stress for high cycle fatigue assessment and as an aid in the placement of strain gages to measure strain due to blade motion during engine operation. A number of these gages placed in various positions on the airfoil can be used to qualify the relative responses of the blade at each location for each natural mode. A distribution of stress for each mode is thus identified.

An example of a first stage turbine blade stress distribution is shown in figures 14 and 15. The analytical results are based upon finite element calculations and show good correlation with test data. The results of the bench test are limited to the number of and direction of the gages, while the analytical results cover all locations and directions. Use of analytical stress distributions to pick a limited number of gage locations on the blade helps to ensure the best coverage of all modes of concern. It should be noted that one gage location may not cover all modes of concern since maximum locations vary with mode shape.

To determine the allowable vibratory stress for various locations on the blade a diagram relating the vibratory and steady state stress field is used, step 7. A typical modified Goodman diagram is shown in figure 16. Material properties are normally obtained through testing at several temperatures with smooth bar samples, no notches or fillets. From these properties mean ultimate strength at zero vibratory stress and mean fatigue strength at 10^7 cycles (or infinite life) of vibration at zero steady stress are placed on the diagram. A straight line is drawn between these two values which, for most materials, is a conservative mean fatigue strength as a function of loading (steady stress).

Parameters which can affect the distribution of mean fatigue strength and, thus allowable vibratory stress, are notch factor, data scatter, and temperature. These are illustrated in figure 17. The fatigue notch factor is related to a stress concentration factor which is a ratio of the maximum steady stress to the average steady stress of a particular geometry (notches, fillets, holes). The relationship between fatigue notch factor (K_f), and stress concentration factor (K_t), is dependent upon the notch sensitivity of the material. The one-sigma scatter, which is obtained from test data, accounts for variations in mean fatigue strength due to compositional changes of the material and processing differences from piece to piece. A minus three sigma (-3σ) value of fatigue strength used accounts for 99.865 percent of all pieces having a fatigue strength greater than this value. The temperature affects both the ultimate and fatigue strengths. The example shows a dip in fatigue strength with temperature which is characteristic of some alloys used in turbine blades.
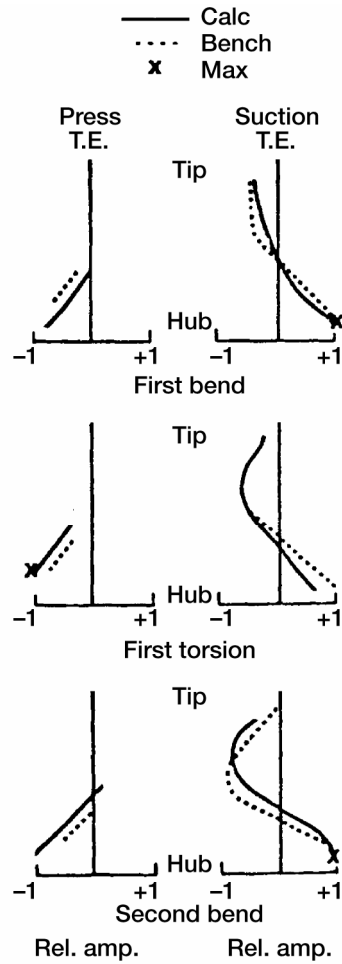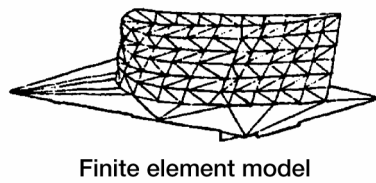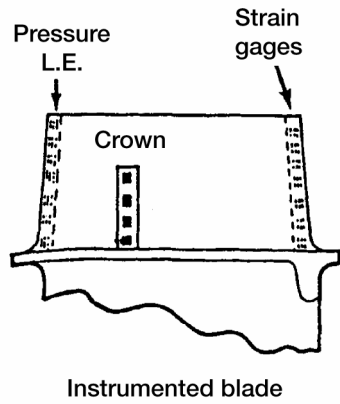
Figure 14.—Calculation of dynamic stress distribution for first stage blade–trailing edge.
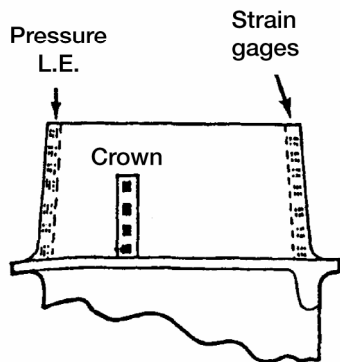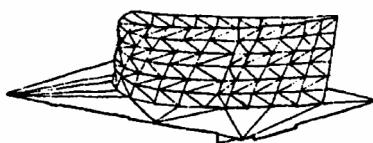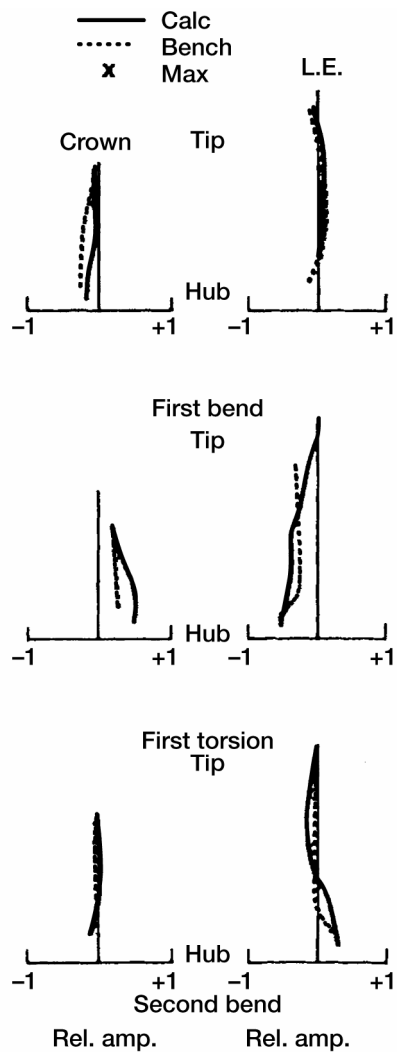
Figure 15.—Calculation of dynamic stress distribution for first stage blade–
leading edge and crown.
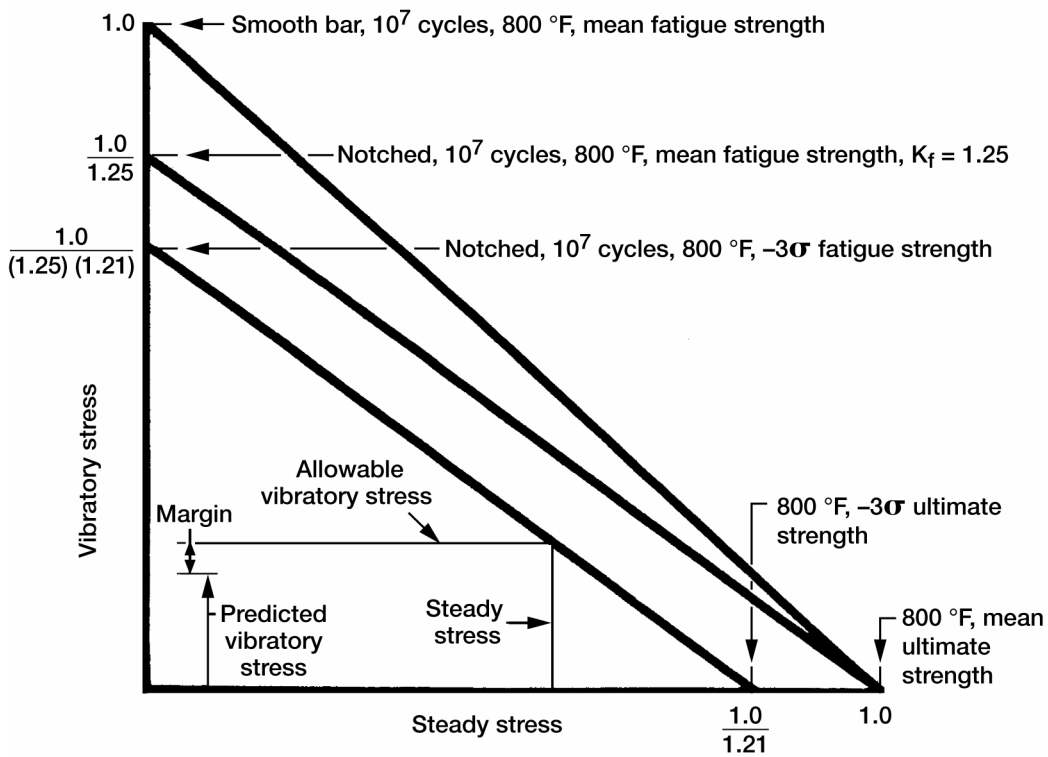
Figure 16.—Typical modified Goodman diagram.

Kt, stress concentration factor

- Fatigue notch factor, Kf, accounts for notches (fillets, nicks, FOD, holes)

Example on previous chart assumes σ = 7%
∴ −3σ = 21% degradation

- −3σ accounts for data scatter

- Temperature affects ultimate and fatigue strength
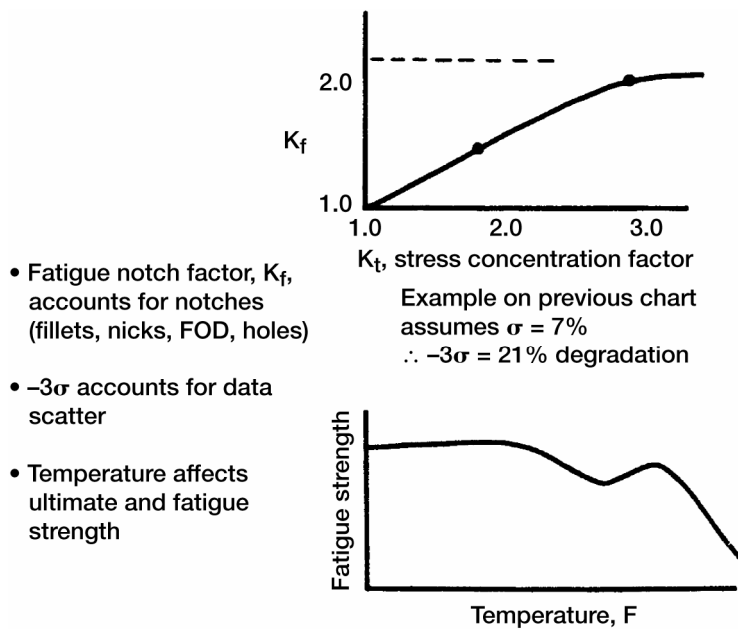
Figure 17.—Parameters which affect the allowable vibratory stress.

Returning to figure 16, degradation of the line representing the mean distribution of fatigue strength is made for notches, scatter and temperature. Where notches or fillets exist, it is necessary to degrade the mean fatigue strength by the notch fatigue factor (K_f). Lowering of both the mean fatigue and ultimate strengths for -3σ scatter effects is made. Temperature effects which also affect both fatigue and ultimate strengths was included initially in establishing their values. The lowest line now represents the distribution of fatigue strength versus steady stress at temperature for a specified notch factor and for which 99.865 percent of blades produced will have a greater strength.

This diagram is now entered at the steady stress value based on the resonance speed and specific component location of concern. The maximum allowable vibratory stress level for infinite life; 10^7 cycles in this case, is then read. The difference between the maximum allowable vibratory stress level and the predicted vibratory stress level is called the vibratory stress margin.

The modified Goodman diagram for the example second stage blade is based on MAR-M2465 material properties at 1300 °F, figure 18. The mean ultimate and the mean fatigue strengths are 142 and 31 thousand pounds per square inch (ksi) respectively. The one-sigma scatter for each strength is 8 and 2.2 ksi, respectively. The stress concentration factor (K_t) for the hub fillet radius is 1.36. For this material and fillet radius, this gives a notch factor (K_f) of 1.18. Degrading the mean strengths by the respective factors and entering the steady stress values for the two locations of concern, yields maximum allowable stresses of 15.3 and 14.3 ksi. These values of maximum allowable vibratory stress are above what is expected based upon evaluation of the upstream and down stream vane row sources. Thus, the high cycle fatigue life is predicted to be infinite and no redesign is required.

Redesign, step 9, was not necessary in this example, but if it had been, design changes such as those listed in table 3 would have been reviewed. Redesign considerations fall under the categories of changes to the source, component geometry, fixity, damping, material and possible maximum amplitude. Changing the proximity of sources may lower the forcing function strength and thus blade response. The frequency of resonance may be moved to occur outside the operating range by changing the number of sources and thus forcing function frequency. Geometry changes to the sources may be made to lower the disturbance factor (i.e., $\Delta P/Q$).
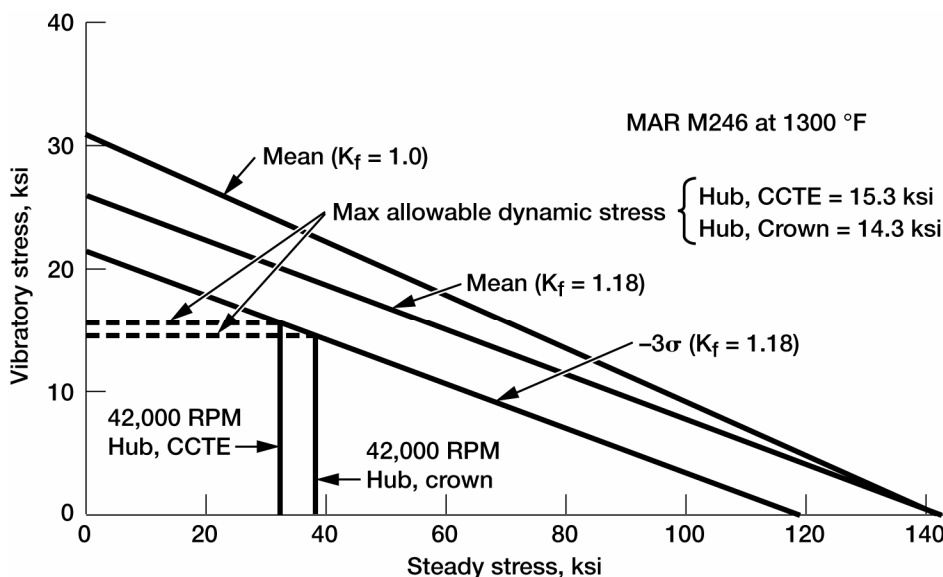
Figure 18.—Modified Goodman diagram for second stage blade.

TABLE 3.—TYPICAL FORCED VIBRATION
REDESIGN CONSIDERATIONS

• Proximity of sources (gap/chord, $\Delta P/Q$)
• Number of sources (resonance speed)
• Geometry of sources (lower disturbance)
• Geometry of resonant piece (stiffness and mass distributions)
• Boundary conditions (type of fixity)
• Increase system damping (coating, fixity)
• Amplitude limitation (shroud gap)
• Increase fatigue strength (geometry, material, temperature)

Component geometry changes such as variations in thickness or chord distribution which change stiffness and mass distributions can be used to raise or lower natural frequencies and thus move resonances above or below operating speed limits. Geometry modifications such as changing of fillet sizes or local thickening can be used to lower notch effects and thus increase allowable vibratory stress.

Changes to boundary conditions to raise or reduce fixity may be used to raise and lower natural frequencies, again to move resonances above or below operating speed limits. Some examples of fixity changes which affect blades and vanes include disk rim restraint as in our example, slot and tang restraint of vanes, blades and vanes cast rigidly to support structure, use of Z shrouds for turbine blades, pinned retentions for compressor blades and packeting of blades and vanes together. These changes may also increase or decrease damping by modifying the frictional losses. Damping may also be increased by application of a selected coating to the blade or vane surface.

Amplitude limitation has been used mainly in turbines to reduce the amount of response. Reducing gaps between adjacent shrouds will limit motion in modes where the adjacent blades are not in phase when at resonance. Application of a wear resistant coating to the shroud faces is usually required to limit material loss due to wear.

To maintain or increase fatigue strength material or processing changes may be required. Choosing materials which increase corrosion resistance, decrease notch sensitivity or increase temperature capability can help the designer to attain the necessary high cycle fatigue strength. Processes such as airfoil coating, peening, brazing, grinding, heat treating all affect fatigue strength and should be considered in the design process.

For the example chosen, testing to verify the predicted response amplitudes, step 10, was accomplished using a gasifier turbine rig with the instrumentation configuration shown in figure 19. The amount and location of the vibratory instrumentation to cover the rotating components is shown. The testing prior to rig running included determining frequencies, mode shapes, stress distributions and fatigue strengths for the second stage blade. Note that in the absence of the low pressure turbine, the third stage vane row was not present.

The vibratory responses of the second stage blade obtained during the gasifier test are shown on the predicted resonance diagram in figure 20. The two strain gage locations of crown and concave trailing edge are denoted by the circle and triangle symbols respectively. The percent gage sensitivity for the first torsion and first bend modes are bracketed directly below the symbols. The maximum vibratory allowables for these locations are ±14.3 and ±15.3 ksi.

Maximum measured stresses were ±6.3 to ±8.8 ksi for the 1T mode and upstream vane resonance. This compares to a ratioed maximum 1T response of ±13.3 ksi. The predicted response was estimated to be ±6 to 10 ksi. The design shows a minimum vibratory margin of 7.5 percent or ±1 ksi using the ±13.3 ksi as a maximum response.

Based on these measured responses this design should exhibit infinite high cycle fatigue life. Additional instrumented tests during actual engine running will assure that adequate HCF margin is present by better defining the vibratory response distribution (scatter) among blades.

This completes the discussion of forced response. Basic sources of excitation, component geometries, natural mode shapes and frequencies have been presented. Fundamental steps in designing for forced response included discussion of sources, environment, resonance and Goodman diagrams, calculation of natural frequencies, mode shapes and stress distributions, determination of response amplitudes and high cycle fatigue life, redesign considerations, and strain gage testing to verify the design.
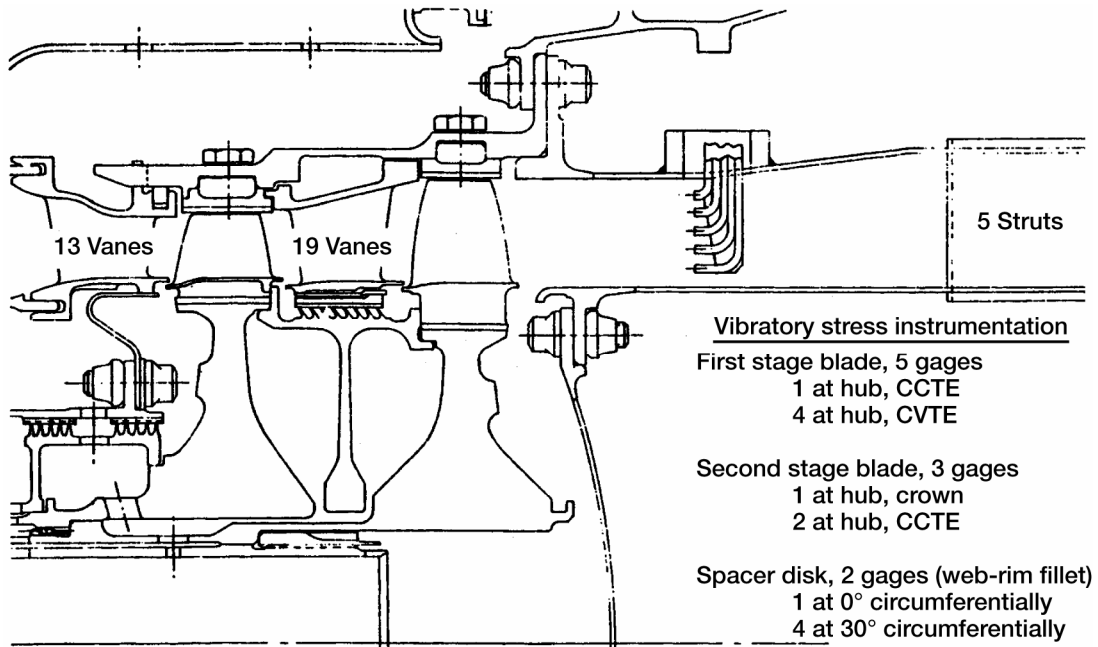
Figure 19.—Gasifier test configuration.

13 Vanes

19 Vanes

5 Struts

Vibratory stress instrumentation

First stage blade, 5 gages
1 at hub, CCTE
4 at hub, CVTE

Second stage blade, 3 gages
1 at hub, crown
2 at hub, CCTE

Spacer disk, 2 gages (web-rim fillet)
1 at 0° circumferentially
4 at 30° circumferentially
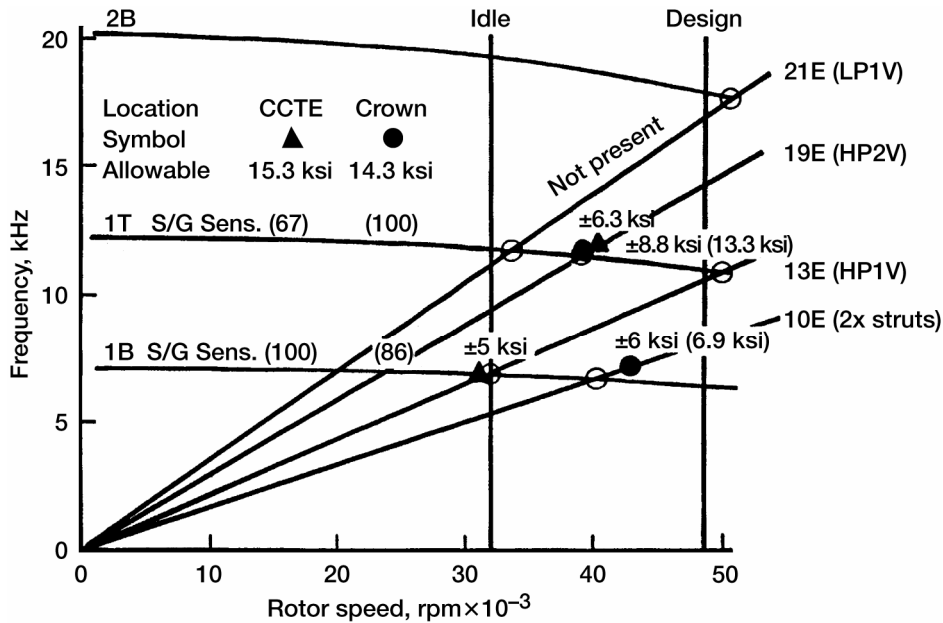
Figure 20.—Resonance diagram for second stage–gasifier test configuration.

Flutter Design

Designing to avoid flutter is an important part of the aeroelastic design process for aircraft engine fan and compressor blades. Although there is much more to be learned about turbomachinery flutter, there are basic principles that have been developed. In this section these principles will be presented. This presentation will contain a discussion of the types of fan/compressor flutter and the dominant design parameters associated with each. A

definition of the ideal flutter design system and the overall flutter design procedure will also be included. Finally, a detailed review of five types of fan/compressor flutter and empirical and analytical design systems for each will be presented.

Description of Flutter

The designer is interested in predicting the onset of flutter rather than predicting a specific vibratory response level as in forced vibration. As discussed earlier, the blade vibration present during flutter is not caused by an unsteady external force but instead by the fact that the blade is absorbing energy from the flow around the blade.

Once any random excitation causes a small vibration of the blade, if the blade aerodynamic damping is negative, the blade will absorb energy from the airstream as the blade vibrates. If the energy absorbed from the airstream is greater than that dissipated by the structural damping, the blade vibratory amplitude will increase with time until an energy balance is attained. Random excitation is always present at low levels in the turbomachinery environment. Thus predicting the onset of flutter entails predicting the aeroelastic conditions that exist when the absorbed energy due to negative aerodynamic damping equals the dissipated energy due to structural damping at the equilibrium vibratory stress level.

For most blade/disk/shroud systems, structural damping (i.e., frictional damping , material damping, etc.) is not large. Therefore, the stability (design) criterion essentially becomes positive aerodynamic damping. Aerodynamic damping is proportional to the nondimensional ratio of unsteady aerodynamic work/cycle to the average kinetic energy of the blade/disk/shroud system.

$$\delta_{\text{AERO}} = \text{AERODYNAMIC DAMPING} \sim \frac{\text{UNSTEADY AERODYNAMIC WORK}}{\text{BLADE/DISK/SHROUD KINETIC ENERGY}} \tag{6}$$

$$\delta_{AERO} = \frac{(\text{NB})(\text{ROOT}-TO-TIP \text{ INTEGRATED UNSTEADY WORK/CYCLE})}{(4)(\text{AVERAGE KINETIC ENERGY OF B - D - S SYSTEM})} \tag{7}$$

The criterion for stability requires that the unsteady aerodynamic work/cycle remain positive (i.e., system is not absorbing energy). The unsteady aerodynamic work/cycle is the integral over one vibratory cycle of the product of the in-phase components of unsteady force (pressure times area) and unsteady displacement.

$$= \int F_0 \exp\{i(\omega t + \phi)\} \, d(h_0 \exp\{i\omega t\}) \tag{8}$$

$$= \int_0^{2\pi} \underbrace{F_0 \exp\{i(\omega t + \phi)\}}_{\substack{\text{RESULTANT UNSTEADY} \\ \text{FORCE}}} \quad i \quad \underbrace{h_0 \exp\{i\omega t\} \, d(\omega t)}_{\substack{\text{VIBRATORY} \\ \text{DISPLACEMENT}}} \tag{9}$$

$$\underbrace{\phantom{= \int_0^{2\pi} F_0 \exp\{i(\omega t + \phi)\} \quad i \quad h_0 \exp\{i\omega t\} \, d(\omega t)}}_{\text{In-phase components}}$$

Thus positive aerodynamic damping is related to the aerodynamic characteristics of the flow field (unsteady forces) and vibratory mode shape (displacement).

Dependence upon the flow field is noted by the names given to five types of fan/compressor flutter which have been observed and reported during the last thirty-five years. These five are presented in figure 21 on a compressor performance map. Each of these types of flutter is characterized by a distinct aerodynamic flow field condition. Each of these types will be discussed later with respect to avoidance of flutter in design. References for this section are Carta (ref. 12) and Snyder (ref. 13).
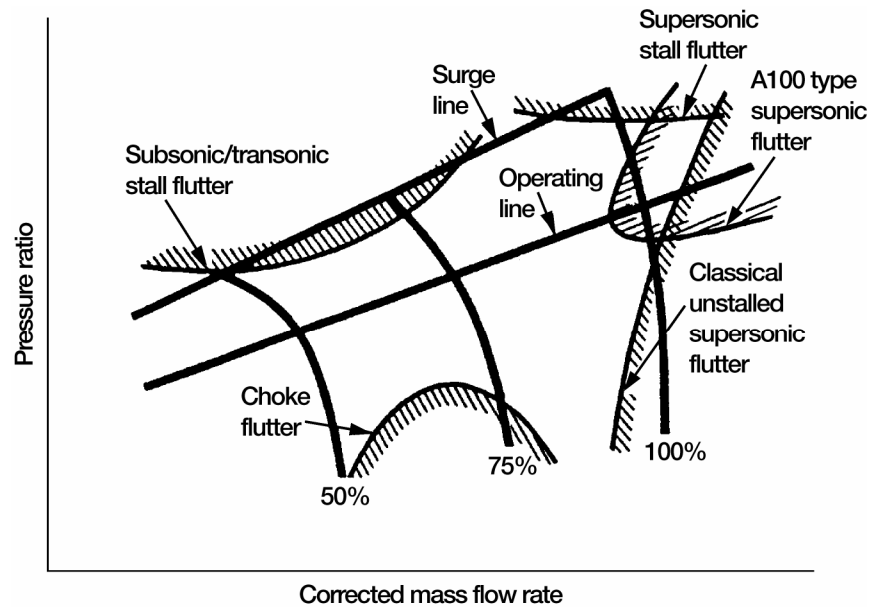
Figure 21.—Types of fan/compressor flutter.

Dominant Design Parameters

Since the distinct flutter regimes are identified by the type of flow present, it is not surprising that four of the five dominant flutter design parameters involve aerodynamic terms. The five are as follows:

1. Reduced velocity
2. Mach number
3. Blade loading parameter
4. Static pressure/density
5. Vibratory mode shape

The fifth parameter, vibratory mode shape, is necessary since the vibratory displacement directly affects the magnitude and sign of the unsteady aerodynamic work per cycle. All five design parameters are pertinent to each type of flutter and are important elements of the flutter design system.

The first two dominant design parameters are dimensionless and appear in the governing equations for unsteady flow over a vibrating airfoil. Mach number is a parameter which describes the nature of the unsteady flow field whether it be subsonic, transonic or supersonic. It has been seen that Mach number and reduced velocity are key parameters in correlating flutter data and developing empirical design systems. Reduced velocity is defined as the ratio of relative inlet velocity to the product of blade vibratory frequency and blade semi-chord length.

$$\text{REDUCED VELOCITY} = \frac{V}{b\omega} \tag{10}$$

Decreasing this parameter is stabilizing. In general, the reduced velocity parameter is between 1 and 5 at the flutter stability boundary. Examination of the unsteady flow equations for flow through a cascade of airfoils shows that the unsteady flow terms are important for these levels of reduced velocity.

Blade loading parameters have also been used in correlations of flutter data. Incidence or nondimensional incidence, pressure ratio, diffusion factor and margin to choke are parameters which have been used to describe the

blade loading. Blade shape geometry descriptors such as leading edge radius, maximum thickness/chord ratio and the maximum thickness location also indicate the magnitude and distribution of aerodynamic loading.

Either static density or pressure can be used as a design parameter if static temperature is held constant and the flow of a perfect gas, $p = \rho RT$, is being considered. The primary effect of changing air density (or pressure) is a proportional change in unsteady aerodynamic work/cycle and therefore in aerodynamic damping.

Increasing the gas density is stabilizing if aerodynamic damping is positive. Likewise, increasing the gas density is destabilizing if aerodynamic damping is negative. An indirect effect of changing gas density is that of changing the flutter mode shape which is a weak function of mass ratio. Thus, aerodynamic damping is also a function of density through the effect of air density on the flutter mode shape. Aerodynamic damping is also a function of density through the effect of density on the Reynolds number and the effect of Reynolds number on the unsteady flow field.

The final dominant design parameter is vibratory mode shape. The unsteady aerodynamic work per cycle of blade motion is a function of both the unsteady surface pressure created by the blade's motion in the air flow and the vibratory mode shape. Thus, since the blade unsteady surface pressure distribution is also a function of the blade mode shape (motion), the aerodynamic damping is a strong function of the vibratory mode shape. Vibratory mode shape may be described as pure bending or torsion of the airfoil or a coupling of bending and torsion. Rigid body bending or translation of the airfoil is displacement of the airfoil perpendicular to the minimum moment of inertia axis. Rigid body torsion or pitching is rotation of the airfoil about the minimum polar moment of inertia axis. Some cases of flutter have been encountered in a chordwise bending with node lines nearly perpendicular to the airfoil chord. Since blade modes generally contain chordwise bending, bending and torsion motions, the modes can best be described in terms of a generalized mode shape where motion perpendicular to the mean line is expressed as a function of radial and chordwise position.

References for this section are Pines (ref. 14) and Theodeorsen (ref. 15).

Design System and Steps

This dependence of flutter on vibratory mode shape is illustrated in figure 22 in the definition of the ideal flutter design system, an experimentally verified analytical prediction system. Classical supersonic unstalled flutter is one type of flutter for which such a design system exists. The analysis which is a part of an ideal flutter design system considers the mode shape and frequency for each nodal diameter of each mode. It also considers both forward and backward traveling wave directions (ref. 16). There is a least stable nodal diameter and wave direction for each mode and of these there is a least stable mode (i.e., mode 2) for the structure. The design system must accurately calculate the aerodynamic damping and corresponding flutter mode shape for each of these modes in order to predict the stability of the blade. Stability is determined by maintaining positive total damping (i.e., above dashed line) for all modes and all nodal diameters and wave directions. Furthermore, the aerodynamic damping must be determined at the least stable fan/compressor steady state aerodynamic operating point. The impact of the steady state aerodynamic operating point will be discussed in more detail in later sections.

The three steps in the flutter design procedure are outlined in figure 23. The first step is to perform the aerodynamic design of the blade and to obtain the pertinent aerodynamic parameters that have an impact on aerodynamic damping. This should be accomplished at the most critical points within the predicted operating envelope of the engine. The definition of the modal displacement and frequencies of the blade/disk/shroud system is the next step. This can be done by conducting a structural dynamic analysis using a finite element model of the blade/disk/shroud system to determine the modal frequencies and mode shapes of the natural modes of the system (i.e., ND = 0, 1, 2, . . . for modes 1, 2, 3,. . .). The final step is to conduct the analysis to combine the steady state aerodynamics and dynamics results and conduct a flutter analysis (unsteady aerodynamics analysis plus stability analysis). Depending on the type of flutter this analysis may entail an actual calculation of the aerodynamic damping (e.g., classical supersonic unstalled flutter) for each mode or may involve an empirical correlation of flutter data (stalled flutter) using the dominant design parameters.
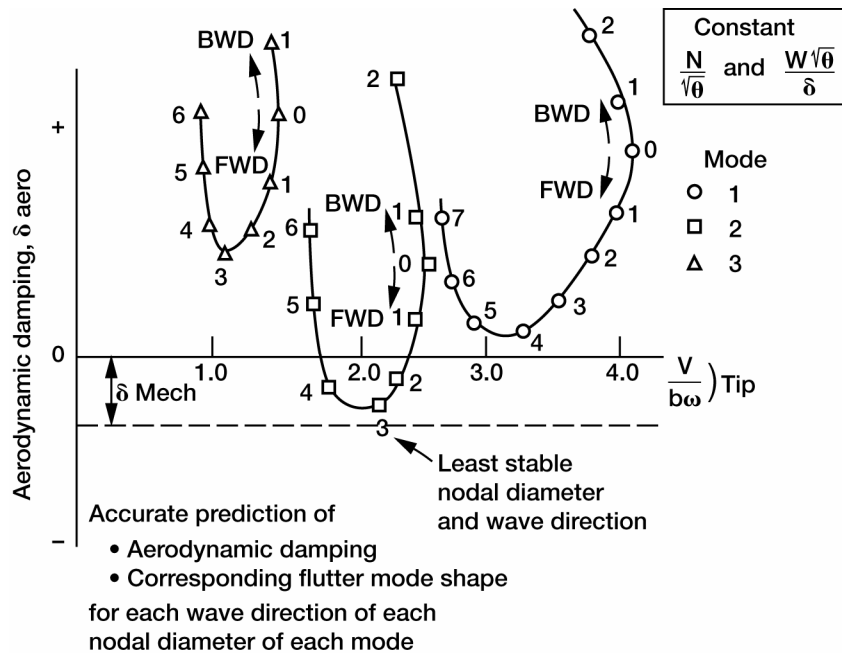
Figure 22.—Definition of ideal flutter design system.

Step 1 –

Design   **Aerodynamic design and analysis**
<u>Design</u>   <u>Analysis</u>

- Pressure ratio/stage   - Relative velocity and Mach number
- Specific flow   - Blade camber and chord
                                        - Incidence, D_f, margin to choke
- $\dfrac{H}{T}\Big)_{\text{inlet and exit}}$ - Static air temperature
                                        - Static air density and pressure
- Flowpath type
- Blade aspect ratio
- Thickness/chord ratio
- Blade series
- Taper ratio

Step 2 –   **Blade structural design and analysis**

<u>Design</u>   <u>Analysis</u>

- Blade material   - Steady stress
- No. of shrouds   - Blade/(disk/shroud) vibratory mode
                                        shapes and frequencies

Step 3 –   **Flutter analysis and redesign**

<u>Analysis</u>   <u>Redesign</u>

- Blade stability margin   - Change aspect ratio
                                           or
                                        - Change blade thickness
                                           or
                                        - Change taper ratio
                                           or
                                        - Change shroud location

Figure 23.—Flutter design procedure.

If the blade is predicted to exhibit flutter within the desired operating range, a redesign effort must be initiated. Changes are usually in the form of geometry modifications which not only affect the system modal characteristics (displacement and frequency) but also the flow characteristics (velocity and blade loading). These changes are aimed at obtaining a design which exhibits stability, positive total damping, throughout the engine operating environment.

Detailed Review, Types of Flutter and Design

The types of flutter will now be discussed with respect to the dominant design parameters and the available analytical tools. The purpose of this discussion is to demonstrate how to avoid fan/compressor flutter through judicious design. Five types of flutter and the location of their boundaries on a compressor map are shown in figure 21. The order of discussion will be subsonic/transonic stall flutter, classical unstalled supersonic flutter, A100 supersonic flutter, choke flutter and supersonic stall flutter.

The first documented type of turbomachinery flutter, subsonic/transonic stall, was first reported almost at the same time that the performance of the first axial compressor was reported. At first, this type of flutter was confused with rotating stall. Characteristics of the subsonic/transonic stall flutter vibratory stress response are nonintegral order, sporadic amplitude with time, stress holds or increases with increasing stage loading and blades vibrate at different frequencies and amplitudes in same mode, whether bending, torsion or coupled modes.

All five dominant flutter design parameters are needed to describe subsonic/transonic stall flutter (S/TSF). By its very name, S/TSF is dependent on Mach number. The shape of the flutter boundary on the compressor map shows its dependence on a blade loading parameter such as incidence or diffusion factor. The simplest S/TSF design system is a correlation of flutter and no flutter data on a plot of reduced velocity versus a blade loading parameter such as incidence (see fig. 24). Experience has shown that with such a correlation with parameters chosen at a representative spanwise location it is possible to separate most of the flutter and no flutter data with a curved line. This curve is then called the flutter boundary. The relationship between points A and C on the flutter boundary on the compressor map and the same points on the design system flutter boundary are shown. This example shows that S/TSF flutter can prevent acceleration along the operating line of the compressor. For the case where the boundary falls between the operating line and surge line the flutter boundary can become a limiting characteristic of the compressor performance if distortion, increased density or temperature or changes in the operating line occur. The design goal is to have all points on the surge line be below the flutter boundary with an adequate margin.
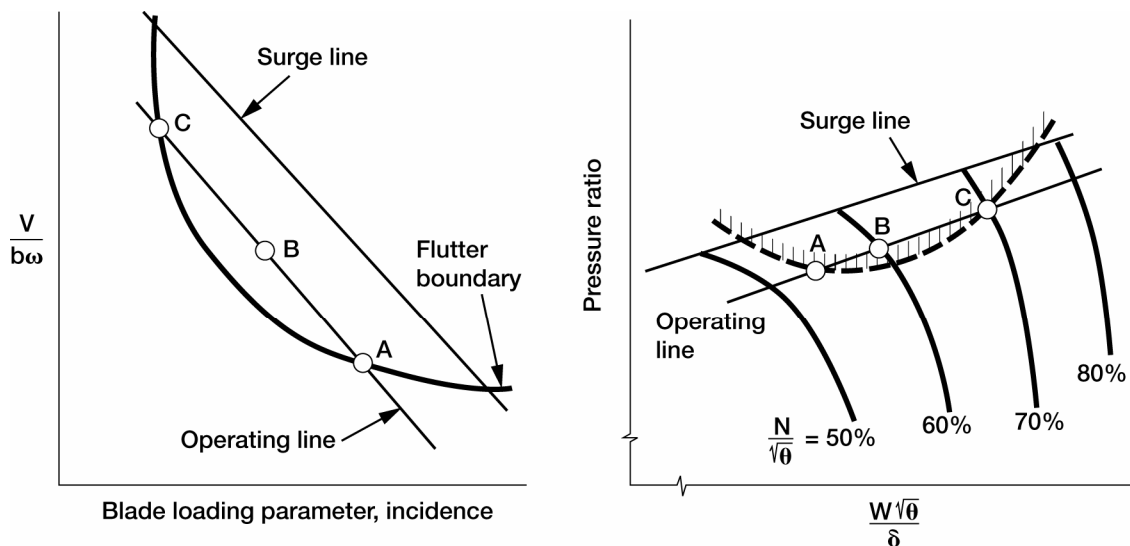
Figure 24.—Subsonic/transonic stall flutter design system using reduced velocity and blade loading parameter.
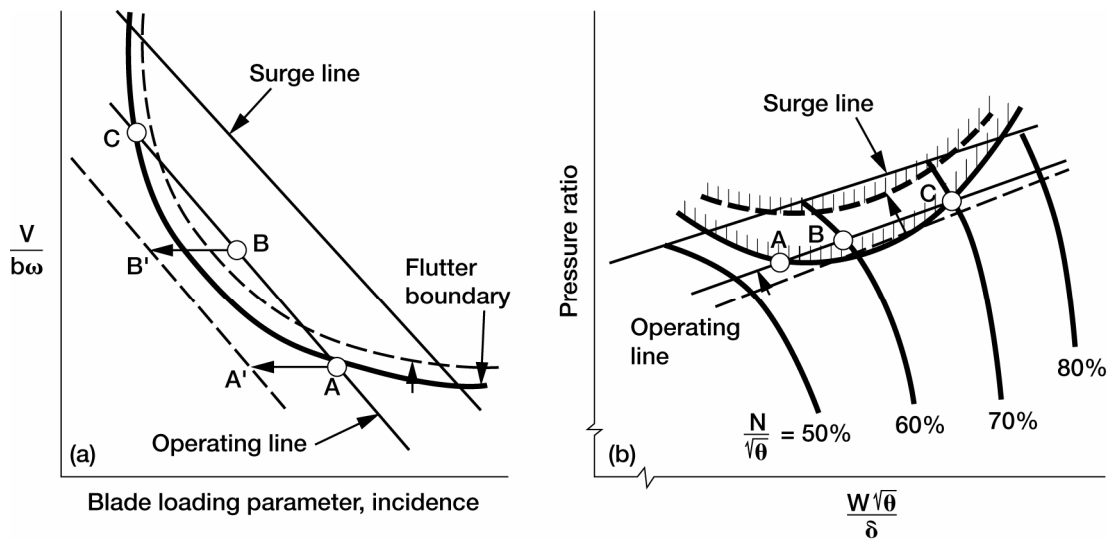
Figure 25.—Stabilizing effect of lowering blade loading parameter.

Based on this empirical design system, a blade design may be stabilized by lowering the blade loading parameter. This may be accomplished by modifying the position of the operating line as shown in figure 25a. This change may be made through rescheduling stators or retwisting the airfoil. Likewise, by changing the blade shape, the position of the flutter boundary may be moved. Such changes to shape would include leading edge radius, recamber of leading edge, blade thickness and maximum thickness location. All of the above changes demonstrate the effect of lowering the blade loading parameters (i.e., diffusion factor, incidence) to increase the stability of the blade in the operating environment (fig. 25b).

Another way of avoiding a potential flutter problem suggested by this empirical design system is to lower the reduced velocity. This is most commonly done by increasing the product of semi-chord times frequency, $b\omega$. Increasing the chord or lowering blade thickening, adding part span shrouds (also called snubbers, dampers, bumpers, and clappers) or changing taper ratio have been used. Use of composite materials have been made to change the material modulus/density ratio to increase frequency. The effects of increasing $b\omega$ are shown graphically in figure 26. The change shows up as a relocation of the operating and surge lines in the correlation plot (fig. 26a) while it is a shift in the flutter boundary on the performance map.

Blade inlet static density (or static pressure) changes may occur as the aircraft changes altitude and/or flight speed or as the engine changes speed. As discussed earlier aerodynamic damping is proportional to static density. If the aerodynamic damping is positive, increases in static density are further stabilizing. If the aerodynamic damping is negative, decreases in static density are stabilizing. The latter is shown in figure 27 on both the compressor map and the S/TSF design system as shifts-in flutter boundary. Changes in aircraft altitude and/or flight speed also affect blade inlet static temperature. However, to properly predict the independent effects of density and temperature changes, they should be considered independently. After they are considered independently, the two effects can be combined.

Changes in blade inlet static temperature affect the relationship between Mach number and velocity. If Mach number is held constant and static temperature is decreased, velocity is decreased and, therefore, reduced velocity is reduced. Thus, reducing static temperature and holding static density will be stabilizing. The effect of such a change is shown on both the compressor map and the S/TSF design system plot in figure 28.

In gas turbine engine applications, temperature and density changes generally occur simultaneously. Such is the case as aircraft flight speed is changed. As aircraft flight speed is increased, the blade inlet static temperature increases, corrected speed drops if there is a mechanical speed limiter and blade inlet static density increases. These effects can cause a S/TSF boundary to move nearer to the compressor operating region, while at the same time causing the engine operating point to move closer to the S/TSF region. This is illustrated in figure 29.
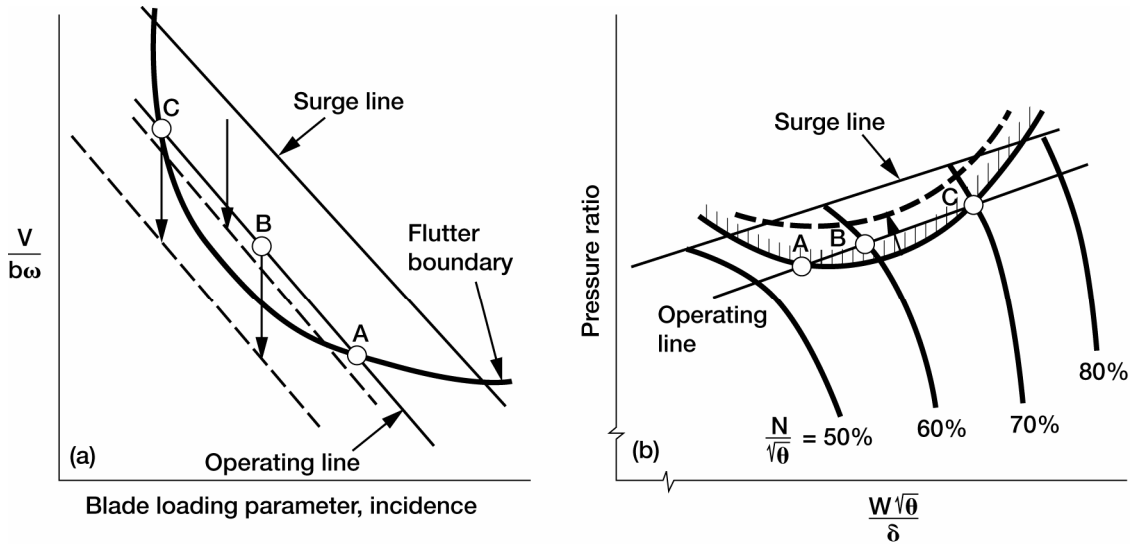
Figure 26.—Stabilizing effect of increasing the product bω.
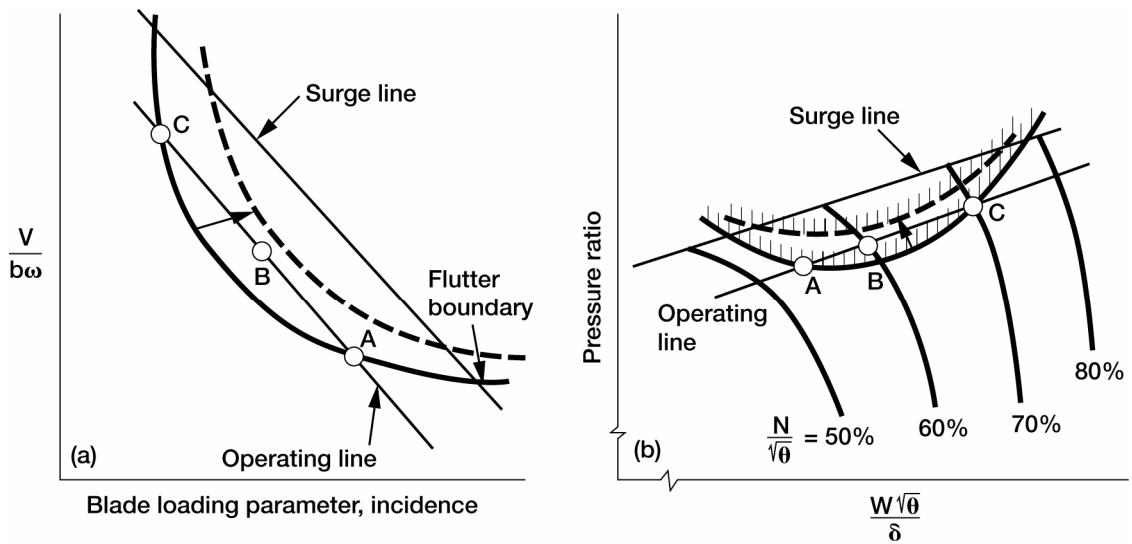
Figure 27.—Stabilizing effect of lowering static pressure/density at constant static temperature.
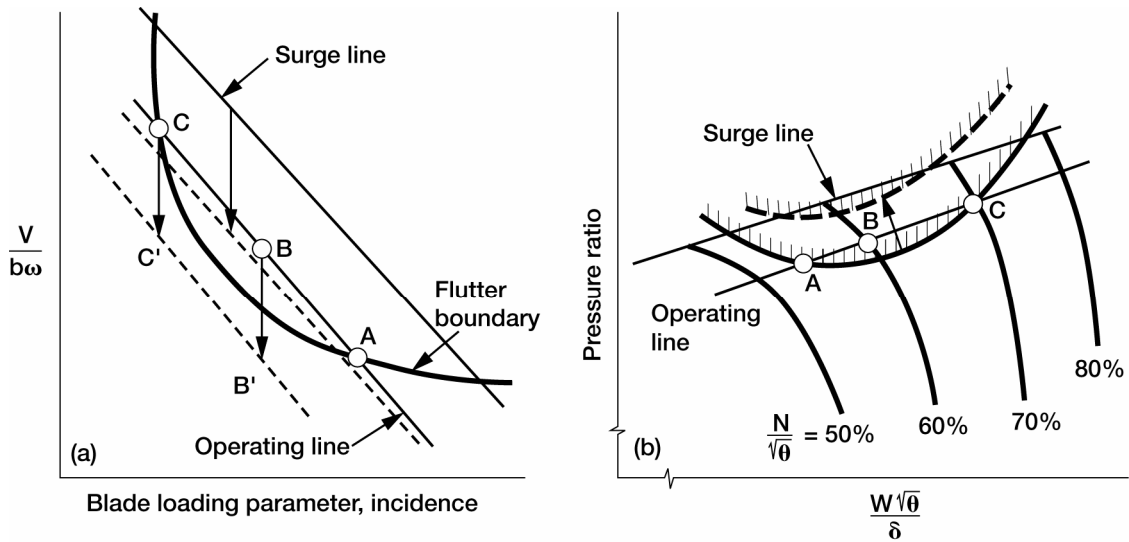
Figure 28.—Stabilizing effect of reducing inlet static temperature at constant static density.
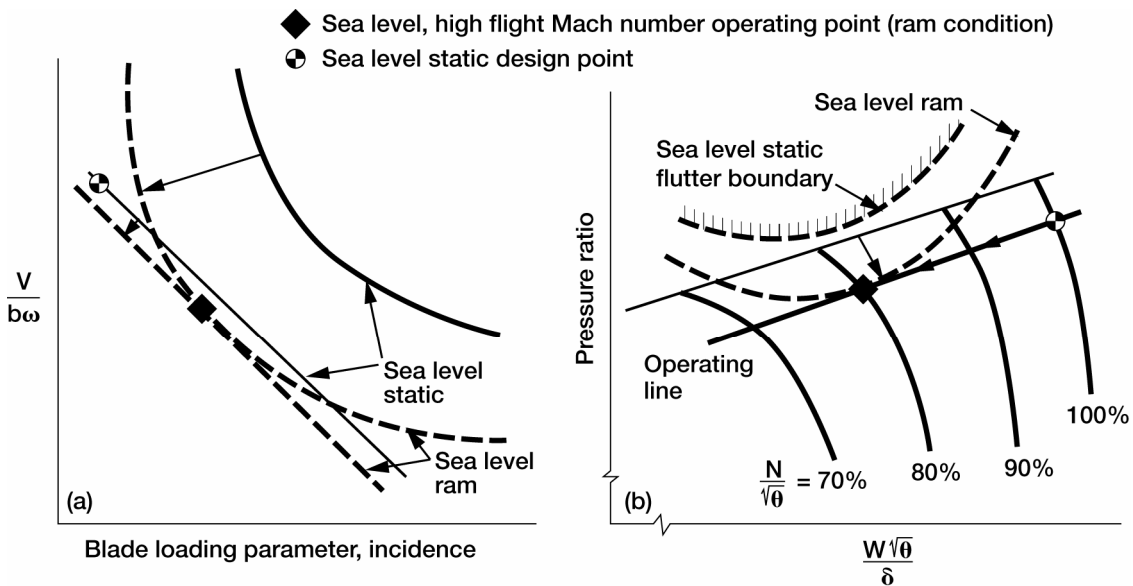
Figure 29.—Consideration of subsonic/transonic stall flutter in fan/front compressor stages at sea level ram conditions.

Sufficient flutter margin must be designed into a new compressor or fan such that flutter will not be encountered under any aircraft operating point.

Vibratory mode shape is a dominant S/TSF design parameter. For a given reduced velocity a bending mode is much more stable than a torsional mode (fig. 30a) with node-line located at mid-chord. This implies the need of the designer to evaluate the S/TSF flutter margins of both bending and torsion modes. If bending and torsion modes are coupled by the presence of a flexible disk or part span or tip shroud, the ratio of bending to torsional motion and the phase angle between them must be considered in the flutter analysis. This is illustrated in figure 30b.
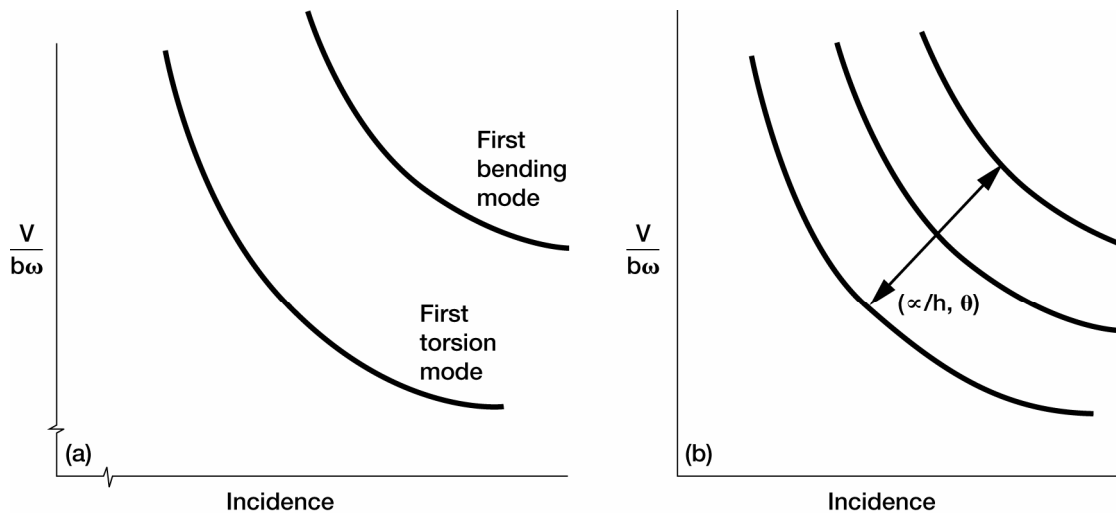
Figure 30.—Effect of mode shape on subsonic/transonic stall flutter. (a) Shroudless blades. (b) Shrouded blades.

For subsonic/transonic stall flutter information, see references 17 through 31.

Classical unstalled supersonic flutter (USF) is a design concern if a significant portion of the blade has supersonic relative inlet flow. The term unstalled is used because USF is encountered at the lowest corrected speed when the stage is operating at the lowest pressure ratio. Classical is used because of its similarity to classical aircraft wing flutter. The stress boundary is very steep with respect to speed as shown in figure 21, thus, preventing higher speed operation. The stress level does not usually fluctuate with time and all blades vibrate at a common frequency unlike S/TSF. Experience to date has been predominately in torsional modes but has occurred in coupled bending/torsion modes or chordwise bending modes. Four dominant design parameters are used to describe USF. They are reduced velocity, Mach number, vibratory mode shape, and static pressure/density.

The simplest classical unstalled supersonic flutter design system consists of plotting available classical USF data on a plot of reduced velocity versus inlet Mach number and drawing a curve (flutter boundary) which best separates the flutter and no flutter data points (fig. 31). The flutter data points should be about this curve, while the no flutter data points should be below the line. The design system can be applied to new designs by calculating the parameters reduced velocity and Mach number for points along the compressor operating line and then plotting the operating line on the design system plot. No classical USF is predicted if the operating line is below the flutter boundary.

As in the case of subsonic/transonic stall flutter, increasing the product $b\omega$ is stabilizing for classical supersonic unstalled flutter. The effect of increasing $b\omega$ is to push the flutter boundary to higher operating speeds. This is illustrated in figure 32. The slope of the "new" operating line on the design plot is inversely proportional to $b\omega$. For successful designs, the flutter boundary is beyond the highest expected operating speed.

Classical unstalled supersonic flutter is the one type of flutter for which a reasonably accurate analytical design system exists. This analytical design system parallels the ideal flutter design system. The existing analytical design system contains a blade-disk-shroud vibrational analysis, an unsteady, flat plate, cascade analysis, and an aerodynamic damping calculation. The result is the capability to calculate the aerodynamic damping for each mode (and nodal diameter if necessary) of a compressor blade/disk assembly. A typical plot of the resulting data is shown in figure 22.

The effect on classical USF of lowering static density at constant static temperature is stabilizing since aerodynamic damping is proportional to blade inlet static density. This stabilizing effect is shown on both the empirical and analytical design systems in figure 33. In each case three points are shown: The original flutter point, the same operating point after the decrease in static density, and a new flutter free operating point at higher rotor speed.
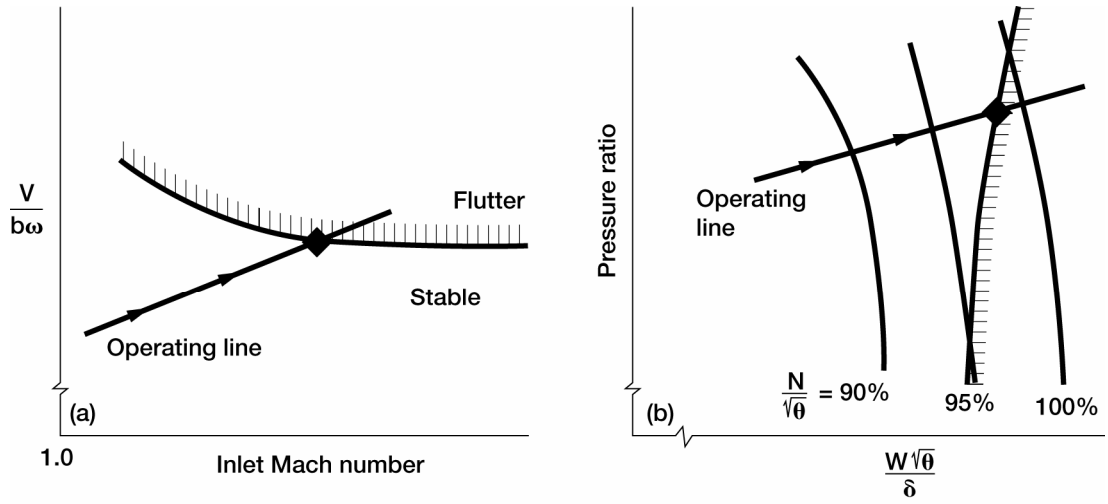
Figure 31.—Classical unstalled supersonic flutter design system using reduced velocity and Mach number.
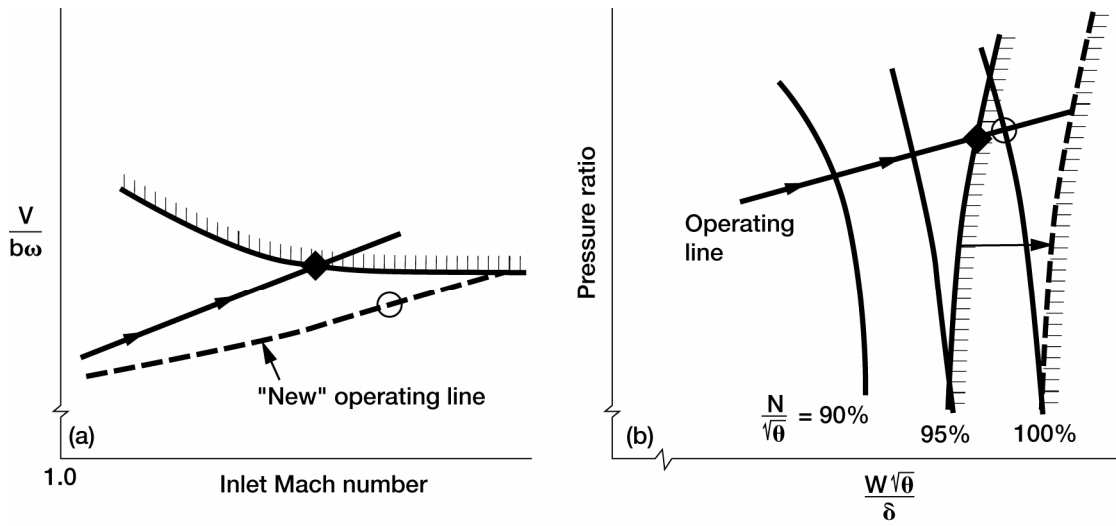
Figure 32.—Stabilizing effect of increasing the product $b\omega$.
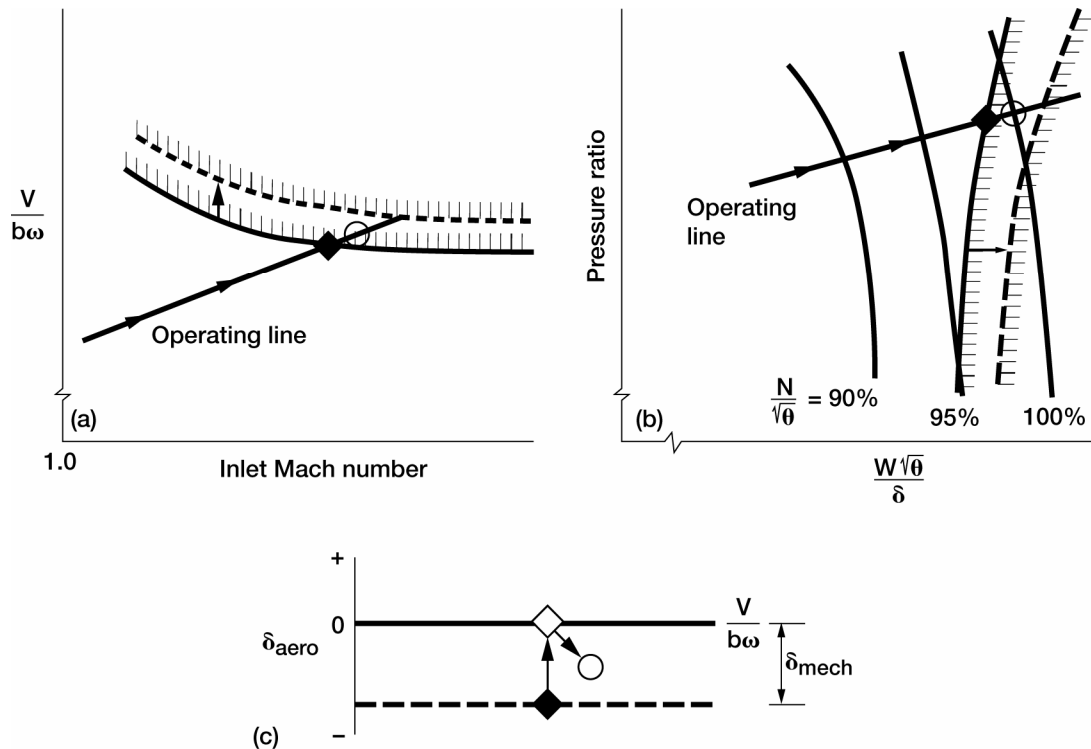
Figure 33.—Stabilizing effect of lowering static pressure/density at constant static temperature.

Since reducing inlet static temperature at constant corrected rotor speed causes the mechanical rotor speed and, hence, blade inlet relative velocity to decrease, the effect of reducing inlet static temperature at constant static density is stabilizing for classical USF. The result of such a change is to move the flutter boundary to a higher speed. This is illustrated in figure 34 on both empirical and analytical design system.

For classical unstalled supersonic flutter see references 6, 13, 32 through 46.

A third type of fan/compressor flutter, which has been identified, is A100 type supersonic flutter, reference 47. This was identified as a torsional mode flutter of a shroudless blade. The flutter boundary for this type of flutter is unlike the other types of flutter, indicating that the unsteady aerodynamics of this type of flutter are unique. Looking at figure 21, a moderate pressure ratio at constant corrected speed is destabilizing, while at sufficiently higher pressure ratio the effect of the same change is stabilizing. However, though unique in boundary it is very similar to USF. The outer portion of the blade is supersonic. The stress boundary is steep. All blades vibrate at the same frequency and interblade phase angle. The reduced velocity/inlet Mach number empirical method also predicts this instability. Varying of $b\omega$, static pressure/density and inlet static temperature produces similar effects as those observed with USF.

Choke flutter received its name from the close proximity of the flutter boundary and the choke operating region of the compressor. This boundary can be encountered during part speed operation, figure 21. Blades are usually operating at negative incidences in the transonic flow regime. In this near choke condition, in-passage shocks with associated flow separation are thought to influence the aeroelastic characteristics and thus the blade stability. Recently, modal aerodynamic solution codes which analytically predict aerodynamic damping as in the ideal flutter design system and the USF analytical design system have been developed for choke flutter. The crucial element in these codes is the development of the transonic unsteady aerodynamic programs. Improvement in this area is presently underway and will benefit the designer in predicting the occurrence of choke flutter. Experimental data has been correlated much like S/TSF data as a function of reduced velocity and incidence. Reducing solidity has been found to increase stability due to increases in incidence. As with S/TSF lowering reduced velocity, static pressure/density and inlet static temperature are stabilizing effects. Choke flutter has been observed in both bending and torsional modes.

$$\frac{V}{b\omega}$$

"New" operating line

(a)

1.0

Inlet Mach number

Pressure ratio

Operating line

$$\frac{N}{\sqrt{\theta}} = 90\%$$ 95%   100%

(b)

$$\frac{W\sqrt{\theta}}{\delta}$$

+

0

δ_{aero}

$$\frac{V}{b\omega}$$ δ_{mech}

(c)   −
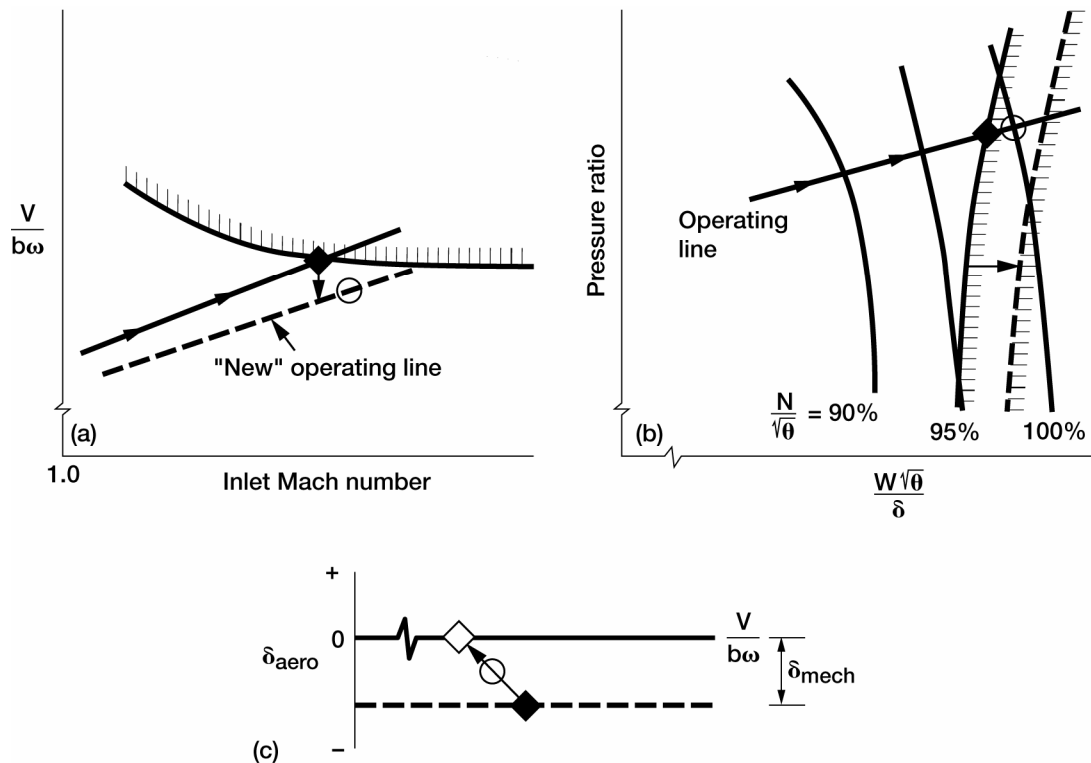
Figure 34.—Stabilizing effect of reducing inlet static pressure.

For choke flutter see references 48 through 51.

The last type of flutter to be discussed will be supersonic stall flutter. The position of this flutter boundary on the compressor map is suggested by the title. This flutter is like unstalled supersonic flutter in that all blades vibrate at a common frequency. Experience indicates that the mode is generally first bending. An analytical design approach which determines the unsteady aerodynamic force, aerodynamic damping, as a function of interblade phase angle has been developed for the designer by Adamczyk (see ref. 52). The authors use two dimensional actuator disk theory in which flow separation is represented through rotor loss and deviation-angle correlations. The analysis is for the fundamental mode bending of shroudless blades. Based on experimental data, in reference 53, blade stability is increased by increases in $b\omega$ and reduction in blade loading. The presence of strong shocks is indicated to have an effect on this type of flutter, reference 54. This effect is one of destabilizing for both bending and torsional motions and as such may be expected to lower the back pressure at which this flutter first occurs. Flow separation was observed to exist, in reference 55, for a cascade of airfoils representing the airfoils exhibiting flutter above 105 percent speed in reference 53.

This concludes the discussion of forced vibration and flutter design methodology. Design principles have been presented to aid the designer of turbomachinery in understanding the mechanisms involved and in properly evaluating the crucial components of turbomachinery. Effective application of the design steps for both forced vibration and flutter are necessary to limit the occurrences of high cycle fatigue failure in new turbine engine designs. Research is continuing at this time to define and model the unsteady flow fields and forces present during forced vibration and flutter. As knowledge is acquired, experimental and theoretical, and combined to develop better analytical predictions tools, the possibility of eliminating high cycle fatigue from turbine engines in design is increased and costs decreased.

References

1. Srinivasan, A.V.; Cutts, D.G.; and Sridhar, S.: Turbojet Engine Blade Damping; Final Report. NASA CR–l65406, 1981.
2. Jay, R.L.; and Burns, D.W.: Bladed Disk Response Study. Draft Final Report Number AFWAL–TR–83–2050 under Air Force Contract F336l5–79–C–2045, July 1983.
3. Jones, D.I.G.; Henderson, J.P.; and Rogers, L.C.: Viscoelastic Damping in USAF Applications. Damping Effects in Aerospace Structures, AGARD–CP–277, 1979.
4. Gallus, H.E.; Lambertz, J.; and Wallmann, T.: Blade Row Interaction in an Axial-Flow Subsonic Compressor Stage. ASME Paper 79–GT–92, 1979.
5. Gallus, H.E.; Grollius, H.; and Lambertz, J.: Influence of Blade Number Ratio and Blade Row Spacing on Axial-Flow Compressor Stator Blade Dynamic Load and Stage Sound Pressure Level. Trans. ASME J. Eng. Power, vol. 104, no. 3, 1982, pp. 633–641.
6. Smith, S.N.: Discrete Frequency Sound Generation in Axial Flow Turbomachines. ARC R&M 3709, University of Cambridge, 1973.
7. Caruthers, J.E.: Aerodynamic Analysis of Cascaded Airfoils in Unsteady Rotational Flow. Paper presented at the Second International Symposium on Aeroelasticity in Turbomachines, Lausanne, Switzerland, Sept. 1980.
8. Scanlan, Robert H.; and Rosenbaum, Robert: Introduction to the Study of Aircraft Vibration and Flutter. The Macmillan Co., New York, NY, 1951.
9. Bisplinghoff, Raymond L.; Ashley, Holt; and Halfman, Robert L.: Aeroelasticity. Addison-Wesley Publishing Co., Cambridge, MA, 1955.
10. Bisplinghoff, R.L.; and Ashley, Holt: Principles of Aeroelasticity. John Wiley & Sons, New York, NY, 1962.
11. Fung, Y.C.: An Introduction to the Theory of Aeroelasticity. John Wiley & Sons, New York, NY, 1955.
12. Carta, F.O.: A Parametric Study of Coupled Blade-Disk-Shroud Flutter Instabilities in Turbojet Engine Rotors. United Aircraft Research Laboratories Report E2l1529–l, 1966.
13. Snyder, L.E.; and Commerford, G.L.: Supersonic Unstalled Flutter in Fan Rotors; Analytical and Experimental Results. Trans. ASME Ser. A J. Eng. Power, vol. 96, no. 4, 1974, pp. 379–386.
14. Pines, S.: An Elementary Explanation of the Flutter Mechanism. Proceedings of the National Specialists Meeting on Dynamics and Aeroelasticity, Inst. of the Aeronautical Sciences, Ft. Worth, Texas, November 1958, pp. 52–58.
15. Theodorsen, Theodore: General Theory of Aerodynamic Instability and the Mechanism of Flutter. NACA–TR–496, 1935.
16. Campbell, W., Protection of Steam Turbine Disc Wheels from Axial Vibration, ASMA Paper No. 1920, May 26, 1924.
17. Shannon, J.F., Vibration Problems in Gas Turbines, Centrifugal, and Axial-Flow Compressors, A.B.C. R&M No. 2226, 1945.
18. Graham, Robert W.; and Costilow Guentert, Eleanor: Compressor Stall and Blade Vibration. Aerodynamic Design of Axial-Flow Compressors, NASA SP–36, Ch. XI, 1965, pp. 311–330.
19. Huppert, Merle C.; Calvert, Howard F.; and Meyer, André J.: Experimental Investigation of Rotating Stall and Blade Vibration in the Axial-Flow Compressor of a Turbojet Engine. NACA RM E54A08, 1954.
20. Pearson, H.: The Aerodynamics of Compressor Blade Vibration, Fourth Anglo-American Aeronautical Conference, London, 16–17 September 1953, pp. 127–162.
21. Sisto, F.: Stall Flutter in Cascades. J. Aero. Sci., vol. 20, no. 9, 1953, pp. 598–604.
22. Sisto, F.: Linearized Theory of Nonstationary Cascades at Fully Stalled or Supercavitated Conditions, ZAMM, vol. 47, no. 8, 1967, pp. 531–542.
23. Sisto, F.; and Ni, R.H.: Quasi-Static Moment Measurements for Airfoils in an Annular Cascade. J. Aircraft, vol. 9, no. 4, 1972.
24. Sisto, F.; and Perumal, P.V.K.: Lift and Moment Prediction for an Oscillating Airfoil With a Moving Separation Point. ASME Paper 74–GT–28, 1974.
25. Schnittger, J.R.: Single Degree of Freedom Flutter of Compressor Blades in Separated Flow. J. Aero. Sci., vol. 21, no. 1, 1954, pp. 27–36.
26. Carter, A.D.S.: A Theoretical Investigation of the Factors Affecting Stalling Flutter of Compressor Blades. National Gas Turbine Establishment Report No. R.172, C.P. No. 265, 1955.
27. Carter, A.D.S., et al.: An Experimental Investigation of the Blade Vibratory Stresses in a Single-Stage Compressor. National Gas Turbine Establishment Report No. R.174, C.P. No. 266, 1955.
28. Armstrong, E.K.; and Stevenson, R.E.: Some Practical Aspects of Compressor Blade Vibration. J. R. Aeronaut. Soc., vol. 64, no. 591, 1960, pp. 117–130.
29. Rowe, J.R.; and Mendelson, A.: Experimental Investigation of Blade Flutter in an Annular Cascade. NACA TN 3581, 1955.
30. Halfman, Robert L.; Johnson, H.C.; and Haley, S.M.: Evaluation of High-Angle-of Attack Aerodynamic-Derivative Data and Stall-Flutter Prediction Techniques. NACA TN 2533, 1951.
31. Jeffers II, James D.; and Meece, Carl E., Jr.: F100 Fan Stall Flutter Problem Review and Solution, J. Aircraft, vol. 12, no. 4, 1975, pp. 350–357.
32. Snyder, L.E.: Supersonic Unstalled Torsional Flutter. Aeroelasticity in Turbomachines; Proceedings of Conference on Effects of Aeroelasticity, S. Fleeter, ed., Indianapolis, IN, 1972, pp. 164–195.
33. Mikolajczak, A.A., et al.: Advances in Fan and Compressor Blade Flutter Analysis and Prediction, J. Aircraft, vol. 12, no. 4, 1975, pp. 325–332.
34. Garrick, I.E.; and Rubinow, S.I.: Flutter and Oscillating Air-Force Calculations for an Airfoil in a Two-Dimensional Supersonic Flow, NACA–TR–846, 1946.
35. Whitehead, D.S.: Force and Moment Coefficients for Vibrating Aerofoils in Cascade. ARC R&M 3254, 1972.

36. Verdon, J.M.: Unsteady Aerodynamics of a Finite Supersonic Cascade With Subsonic Axial Flow. J. Appl. Mech. Trans. ASME, vol. 40, series E, no. 3, 1973, pp. 667–671.
37. Verdon, J.M.: Further Developments in the Aerodynamic Analysis of Unsteady Supersonic Cascades. ASME Papers No. 77–GT–44 and 77–GT–45, 1977.
38. Brix, C.W., Jr.; and Platzer, M.F.: Theoretical Investigation of Supersonic Flow Past Oscillating Cascades With Subsonic Leading-Edge Locus. AIAA Paper 74–14, 1974.
39. Caruthers, J.E.: Theoretical Analysis of Unsteady Supersonic Flow Around Harmonically Oscillating Turbofan Cascades. Ph.D. Thesis, Georgia Institute of Technology, Sept. 1976.
40. Nagashima, T. and Whitehead, P.S., Aerodynamic Forces and Moments for Vibrating Supersonic Cascade Blades, University of Cambridge, Department of Engineering Report CUED/A-Turbo/TR59, 1974.
41. Goldstein, M.E.: Cascade With Subsonic Leading-Edge Locus. AIAA J., vol. 13, 1975, pp. 1117–1119.
42. Ni, R.H.; and Sisto, F.: Numerical Computation of Nonstationary Aerodynamics of Flat Plate Cascades in Compressible Flow. ASME Paper No. 75–GT–5, 1975.
43. Fleeter, S., et al.: Experimental Determination of the Unsteady Aerodynamics in a Controlled Oscillating Cascade. ASME Paper 76–GT–l7, 1976.
44. Adamczyk, J.J.; Goldstein, M.E.; and Hartmann M.J..: Supersonic Unstalled Flutter; Aerodynamic Loading of Thin Airfoils Induced by Cascade Motion. NASA TM–79001, 1978.
45. Adamczyk, J.J.; and Goldstein, M.E.: Unsteady Flow in a Supersonic Cascade With Subsonic Leading-Edge Locus, AIAA J., vol. 16, no. 12, 1978.
46. Halliwell, D.G.: The Characteristics, Prediction and Test Analysis of Supersonic Flutter in Turbofan Engines. Proceedings of a Conference of the Vibrations in Rotating Machinery, Cambridge, England, 1976, pp. 181–185.
47. Troha, W.; and Swain, K.: Composite Inlays Increase Flutter Resistance of Turbine Engine Fan Blades. ASME Paper 76–GT–29, 1976.
48. Carter, A.D.S: Some Preliminary Notes on the Flutter of Axial Compressor Blades. National Gas Turbine Establishment Report No. M.181, 1953.
49. Carter, A.D.S.; and Kilpatrick, D.A.: Self-Excited Vibration of Axial-Flow Compressor Blades. Proceedings of the Institution of Mechanical Engineers, vol. 171, 1957, pp. 245–281.
50. Schneider, P.: Analysis of J85–21 Compressor Aerodynamic Flutter Data. NASA CR–159795, 1980.
51. Justras, R., Hi, N., and Post, R., Experimental Analysis of Blade Instability-A Flutter Data Correlation for Turbomachinery Blading, AFWAL–TR–82–2008, March 1982.
52. Adamczyk, J.J.; Stevans, W.; and Jutras, R.: Supersonic Stall Flutter of High-Speed Fans. ASME Paper 81–GT–l84, 1981.
53. Ruggeri, R.S.; and Benser, W.A.: Performance of a Highly Loaded Two-Stage Axial-Flow Fan. NASA TM X–3076, 1974.
54. Goldstein, M.E.; Braun, Willis; and Adamczyk, J.J.: Unsteady Flow in a Supersonic Cascade With Strong In-Passage Shocks. J. Fluid Mech., vol. 83, part 3, 1977, pp. 569–604.
55. Riffel, R.E.; and Rothrock, M.D.: Experimental Determination of Unsteady Blade Element Aerodynamics in Cascades. Volume 2: Translation Mode Cascade; Final Report. NASA CR–l65l66, 1980.

Aeroelasticity in Axial Flow Turbomachines[*]

Dr. Robert E. Kielb
GE Aircraft Engines
Cincinnati, Ohio

and

Dr. Mehmet Imregun[†]
Imperial College
London, United Kingdom

Introduction

Dr. Kielb will present six sections, five of which describe methods for aeroelastic design of turbomachinery blading. The sixth section examines experimental methods to evaluate aeroelastic behavior, with emphasis on full scale engine testing. The design sections start with a description of the selection of aeroelastic models used during the conceptual, preliminary and detailed design phases. The two most critical aeroelastic phenomena to consider in design are flutter and forced response. The flutter design sections contain a description of the steps in the design process and give examples of typical steady and unsteady pressure distributions, mode shapes, and work distributions over the airfoil surfaces. The sensitivity of stability calculations to variations in the steady aerodynamic loads and mode shapes are also described. The forced response design sections begin with a description of the design analysis process. Excitations due to wakes, bow waves (potential), shock waves, and inlet distortion are described in detail. Examples of typical forced response calculations are provided, including sensitivity to variations in the input parameters. The probabilistic design section examines the role of statistical methods in the aeromechanical design process and describes methods being currently developed. In the damping section damping mechanisms are described with emphasis on platform damper analysis methods. The section on full scale engine testing begins with a description of vibration measurement techniques and the methods of defining the limiting vibratory stresses. Next, characteristics of typical vibratory stress signals for flutter, forced response, and transient response are reviewed. The section concludes with a description of stress mapping techniques.

Acknowledgments

1.0 Aeroelastic Models

This monograph begins with a discussion of the importance of aeroelasticity and the consequences of a poor design (high cycle fatigue) in turbomachinery design and development. Emphasis is placed on blade aeroelasticity. After the aeroelastic design process is reviewed, the monograph addresses different types of unsteady aerodynamic, structural, and aeroelastic models.

The primary design concern for aviation gas turbines is pilot and passenger safety. Aeroelastic excitation can result in excessive blade vibration, which can cause blades to fail in high cycle fatigue (HCF). A severe aeroelastic failure can result in a complete blade separation and loss of thrust, but the blade is usually designed to be contained and the engine is designed to be shut down gracefully. As a result, aeroelastic failures on multi-engine commercial aircraft are not usually safety concerns. However, on single engine military aircraft the loss of a blade can mean the loss of an aircraft.

The impact of aeroelastically induced failures has been primarily economic. Precise quantitative data on the cost of these failures is not available, however, some related information has been presented in the open literature. Various surveys of previous engine development programs have found that HCF problems account for between 10 percent and 40 percent of the total problems. However, HCF also occurs in field service. In fact, it was found that only half of the HCF problems are encountered in development testing. The "average" engine model was found to have approximately 2.5 serious HCF problems in its lifetime. A survey of commercial engine maintenance cost found that 5 percent was due to HCF failures. In looking into the future, an estimate of the next 20 years of military development and field usage found that the HCF related costs could exceed 2 billion US dollars if the state of technology stagnated. Needless to say, the minimization of aeroelastically related failures is of great interest to engine companies and users.

As mentioned above an aeroelastic problem can result in an entire blade separation. However, this is not typically the case. Figure 1-1 shows the type of failures experienced by blades. The most destructive failure, loss of an entire blade, can usually be attributed to the 1F or 1T mode. It can cause high unbalance, significant secondary damage and is very costly to repair. A good practice is to design the blade to have the vibratory critical point to be in the airfoil, and not in the dovetail or shank. This is commonly called "weak link" criteria. The 2T or higher order bending modes usually result in a loss of the outer portion of the airfoil. This results in a measurable unbalance,
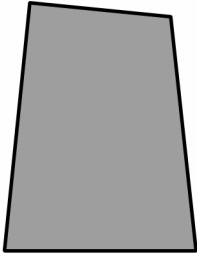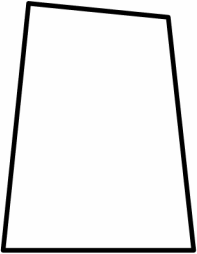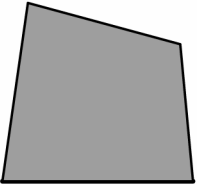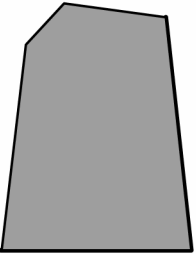
Description	Loss of entire airfoil and/or dovetail and/or disk tang	Loss of outer portion of airfoil	Loss of tip leading or trailing edge
Vibratory mode	First bending or first torsion	Second torsion or higher order bending mode	Panel (stripe) modes or higher order torsion mode
Effects	High unbalance, containment, significant secondary damage, high cost	Measurable unbalance, some secondary damage, moderate cost	Undetectable, minimal repair

Figure 1-1.—Damage severity.

some secondary damage, and moderate repair cost. The stripe and higher order torsion modes usually result in the loss of a blade tip. This is typically undetectable to the pilot and is only found by inspection. Repair costs are relatively modest.

Blade design always starts with the "hot" aerodynamic definition, hot meaning the position of the blade at design conditions of speed and temperature. After the initial aerodynamic definition is completed, the initial aeroelastic evaluation is conducted. In addition to evaluating mechanical design criteria, this is when the Campbell Diagram is used to set frequency margins and crossing speeds, and where the preliminary flutter criteria are evaluated. At this point heat transfer and acoustic evaluations are also made. Iterations between the aerodynamic, heat transfer, acoustics, mechanical, and aeroelastic design groups produce the final hot definition. At this point the hot-to-cold analysis is used to produce the definition of the "as-manufactured" blade. This is also when the detailed flutter and forced response analyses are conducted. Note that detailed analysis are not conducted on all blades and vanes of a new engine design. In fact, the detailed analyses, described in later sections, are only conducted in areas of concern, which may be only 3 airfoils of an 8 stage compressor. Also, for these 3 airfoils only 1 or 2 modes may be given a detailed aeroelastic analysis.

The primary aeromechanical design concerns are flutter margin, frequency placement, forced response, stall overstress capability, leading edge durability, and attachment strength. Ideally the flutter boundary is placed at a location in the compressor map which cannot be achieved. This is commonly called stall protected, that is, the compressor would stall before the flutter boundary was reached. It is more common in recent designs to have a relatively large stall margin. This has made it more difficult to place the flutter boundary such that the blade is stall protected. As a result it is more common to design for adequate flutter margin. The "adequacy" is determined by the migration of the operating line due to engine-to-engine variations, altitude effects, transient operation, and engine deterioration. Both empirical and detailed analysis methods are used to determine flutter margin.

Frequency placement is done with a Campbell Diagram and is based on past experience. That is, the Campbell Diagram is used to display the resonant crossings, and experience is used to identify acceptable, marginal, and unacceptable crossings. Detailed resonant response analyses are typically conducted for the marginal crossings. A transient response which must be considered is a compressor stall overstress. That is, the blade must be able to survive a compressor stall. That is, it does not contact adjacent vane rows and does not experience any permanent plastic deformation.

Since the blade leading edge experiences an environment which can cause erosion and contains high speed objects which can cause damage, special attention is given to the leading edge in blade design. That is, the blade is designed such that the critical vibratory locations are not on the leading edge. Then, it is usually assumed that the leading edge is damaged (a level of damage at which the blade should be able to operate). This damaged leading edge is re-evaluated to see if it now becomes the critical vibratory location. If so, the leading edge is usually thickened, much to the chagrin of the aerodynamic designer.

Another area of the blade that requires extra attention is the attachment. It is good design practice to design the dovetail to be stronger than the neck and the neck to be stronger than the airfoil. In the event of a failure a smaller mass will be released. As previously mentioned this is usually called "weak link" criteria. The interface between the blade dovetail and the disk attachment slot is complex. The steady stresses are relatively high, which means that it plots on the right side of the Goodman Diagram where there is little vibratory stress allowable.

Flutter is primarily seen in fans, front and middle compressor blades, and high aspect ratio low pressure turbine stages. Flutter is not a concern for HPT blades. The types of flutter observed in turbomachinery blading are usually shown on a compressor map (fig. 1-2). Flutter rarely occurs at, or near, the design point, where the flow is "clean". The most common type is high operating line flutter, which is usually called "stall flutter" (although the blade is not aerodynamically stalled). This is seen in fans and front compressor stages.

The next most common type of flutter is "supersonic unstalled flutter" which is commonly seen in shrouded fans. The current design approach is to provide for corrected speed margin between the flutter boundary and the maximum corrected speed which can be experienced by the engine. Since this is commonly at the top of climb for commercial aircraft fans, this can be difficult to simulate in a ground test. Choke flutter is a less common, low operating line type of flutter experienced by middle and rear compressor stages.
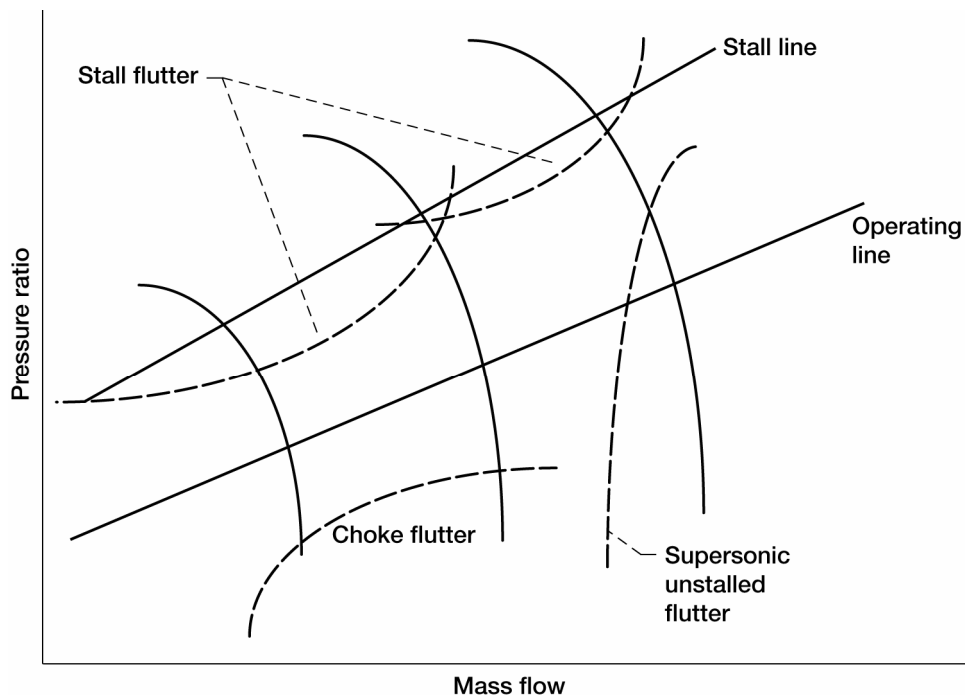
Figure 1-2.—Types of flutter.

Blades are in a rich environment for dynamic excitation. In addition to self-excited flutter, there are a plethora of external excitations of either aerodynamic or mechanical origin. There are three temporal types of forced response: synchronous, non-synchronous and transient. Synchronous excitation can be aerodynamic (e.g., wakes) or mechanical (e.g., tip rubs). Non-synchronous excitation is primarily aerodynamic in origin. The transient loads of interest are compressor stall loads and bird impact. In subsequent sections these excitation types are discussed in greater detail.

Although unsteady aerodynamic models have been in development since the 1950's, it has only been in the last 10 years that they have been useful in blade design. The reason is that it has been found that a very precise analysis is needed. The simpler models of the past may have captured the important physics of the problem, but could not model the subtle effects needed for a design analysis. Three dimensional effects are significant. Therefore, a three-dimensional or quasi-three-dimensional unsteady aerodynamic model is necessary. The quasi-three-dimensional model involves stacking quasi-two-dimensional analysis to cover the entire span. A quasi-two-dimensional analysis (streamtube contraction) is usually necessary to get accurate solutions. Although a nonlinear steady analysis is always performed, either a linear or non-linear unsteady analysis can be chosen. Studies have shown that most turbomachinery aeroelastic problems are linear. There are two types of nonlinear analysis: time domain and frequency domain, with the former being the most common. Inviscid (Euler) or viscous (Navier-Stokes) analysis are available. It has (surprisingly) been found that inviscid models have done a good job of modeling some "stall" flutter. Most unsteady aerodynamic models assume that all blades have the same amplitude and mode shape. The only difference between blades is a constant phase shift between one blade and its neighboring blade. This is usually defined by the interblade phase angle or nodal diameter. Some unsteady aerodynamic models model a single passage and use phase-shifted boundary conditions, while others model multiple passages. Until recently all unsteady aerodynamic analysis modeled an isolated blade row. The assumption being that adjacent blade rows have little influence on the displacement induced (flutter) unsteady pressures. However, recent studies have shown that the adjacent airfoils can have significant effects. Although the multi-stage models are not currently used in design, they are under development. These models are discussed in great detail in subsequent sections.

Structural models used in blade design are universally finite element based. The most common approach is to assume that all blades are identical and model either a single blade (fixed at the attachment) or a pie-section of the bladed disk (or blisk). When the pie-section method is chosen, either axisymmetric or cyclic symmetric boundary

conditions can be applied on the edge surfaces of the pie. This also applies to blades with mid or tip shrouds. The cyclic symmetric approach is necessary for shrouded blades or when the disk plays a significant role in the mode shape. The term "system mode" is usually used to describe this situation. Recently, reduced order models have been developed to speed up solution times. Another computational intensive approach is to model the entire bladed disk assembly. As with the unsteady aerodynamic models, the structural models can be either linear or nonlinear, and can be solved in either the frequency or time domains. For shroudless, damperless blades the linear approach is entirely adequate. A friction damper analysis always requires a nonlinear approach. The flutter or forced response analysis of a shrouded blade, assuming no shroud damping, can use a linear method. But, if a prediction of shroud damping is required, a nonlinear method is necessary.

Aeroelastic analysis of turbomachinery blading is somewhat simpler than that for other aeroelastic components, such as aircraft wings and helicopter rotors, in one important aspect. Flutter and resonant response usually involves a single mode and the frequency and mode shapes are only minimally affected by the aerodynamic loads. The primary reason for this is mass ratio, defined as the ratio of the mass per unit span of the structure divided by the mass per unit span of a cylinder of air circumscribing the leading and trailing edges. For turbomachinery blading the mass ratio is typically one order of magnitude higher than that for aircraft wings. Because the aerodynamic loads of turbomachinery blades do not significantly effect frequency or mode shape, uncoupled aeroelastic models have been very popular. In this frequency domain approach the real frequency and mode shape is calculated with a finite element model with no unsteady aerodynamic loads. The frequencies and mode shapes are the inputs to the unsteady aerodynamic analysis. A modal flutter or forced response analysis is then conducted. In some cases an iteration on frequency may be accomplished. Coupled, time domain models have also been developed. In this approach the structural and aerodynamic problem is solved simultaneously. Two coupled methods are available. One method expands the blade motion in terms of eigenmodes and integrates in time. The other method utilizes physical blade coordinates.

The current "production" method used in industry is to structurally model one blade. The frequencies and mode shapes are input to the unsteady aerodynamic model of one passage. A modal aeroelastic problem is then solved.

2.0 Flutter Design Analysis

Although analytical methods for turbomachinery flutter analysis have been under development for over forty years, the design approach has remained primarily empirical. This approach has relied on traditional aeroelastic parameters such as reduced frequency, Mach number, and incidence. However, in the last 10 years computational methods have been incorporated into the flutter design system. This section begins with an examination of the equations controlling flutter and forced response. This is followed with a discussion of the types of flutter and the empirical design system. The bulk of this section addresses detailed flutter analysis.

Figure 2-1 displays the equations controlling the motion of a single DOF torsional oscillator (e.g., an airfoil) which is excited by an aerodynamic moment. The "structural" properties are defined by the torsional stiffness, K, and the angular inertia, I. The structural damping is assumed to be zero. The aerodynamic moment contains motion dependent terms and terms which are independent of motion which are commonly called the "gust" terms. In many aeroelastic problems, especially for turbomachinery blading, the aerodynamic inertia is much smaller than the structural inertia and the aerodynamic stiffness is much smaller than the structural stiffness. The result is that the aerodynamic forces have very little effect on the natural frequency (also the mode shape for multi-DOF systems). On the contrary the structural damping is commonly very small (in this example, zero) and the aerodynamic damping term, A_D, is dominant. The simple solution to this equation, also shown in figure 2-1, contains the homogeneous solution (flutter problem) and the particular solution (forced response problem). Of course, the homogeneous solution must have a decaying behavior (stable) for the particular solution to have a practical meaning. For the homogeneous solution to be stable the aerodynamic damping must be positive. Thus, the primary goal in a flutter analysis is to determine the sign of the aerodynamic damping. If this system is stable, one can then proceed to calculate the forced response. Typically the resonant response, where the denominator of the bottom equation is minimized, is of most interest. The magnitude of the gust force and the aerodynamic damping are the controlling parameters.

Equation of Motion: $\qquad I\ddot{\Theta} + K\Theta = M$

Aerodynamic Moment: $\qquad M = -A_I\ddot{\Theta} - A_D\dot{\Theta} - A_K\Theta + A_G\sin(\omega_f t)$

$$(I + A_I)\,\ddot{\Theta} + A_D\dot{\Theta} + (K + A_K)\,\Theta = A_G\sin(\omega_f t)$$

Solution: $\quad \Theta = R_H\,e^{-Dt}\sin(\omega_D t + \phi_H) + R_P\sin(\omega_f t + \phi_P)$

Where: $\qquad\qquad\qquad\qquad D = \dfrac{A_D}{(I + A_I)}$

$$R_P = \frac{A_G}{\sqrt{\left[K + A_K - (I + A_I)\omega_f^2\right]^2 + (A_D\omega_f)^2}}$$

Figure 2-1.—Flutter and forced response–SDOF equations.

As stated in section 1, flutter is primarily seen in fans, front and middle compressor blades, and high aspect ratio low pressure turbine stages. Flutter is not a concern for HPT blades. The types of flutter observed in turbomachinery blading are usually shown on a compressor map (fig. 1-2). Flutter rarely occurs at, or near, the design point, where the flow is "clean". The most common type is high operating line flutter, which is usually called "stall flutter" (although the blade is not aerodynamically stalled). This is seen in fans and front compressor stages. A design practice of the past was to require that the flutter boundary be "stall protected", that is, the compressor would stall before the flutter boundary was reached. Recent improvement in blade design have increased the stall margin to the point where it is difficult or impossible to achieve stall protection. As a result, the current approach is to provide enough "flutter margin" to handle engine-to-engine variation, deterioration effects, and transient operation.

The next most common type of flutter is "supersonic unstalled flutter" which is commonly seen in shrouded fans. The current design approach is to provide for corrected speed margin between the flutter boundary and the maximum corrected speed which can be experienced by the engine. Since this is commonly at the top of climb for commercial aircraft fans, this can be difficult to simulate in a ground test. Choke flutter is a less common, low operating line, type of flutter experienced by middle and rear compressor stages.

As previously stated the preliminary design system for flutter is empirical. For stall flutter, reduced frequency, incidence, and mode shape are the most common design parameters. The boundary is defined by previous successful and unsuccessful blades. A typical preliminary design process is shown in figure 2-2. Here the reduced velocity and incidence at a fixed spanwise location are plotted for a range of speeds for a given operating line. This is usually done for the nominal operating line and for the stall line and compared with the flutter boundary. If the stall line is entirely in the stable region, the design is accepted. If the nominal operating line is stable and the stall line penetrates the boundary, the plot can be used to estimate the flutter margin and the corrected speed with the minimum margin. Note that for 1F stall flutter the boundary is very dependent on mode shape. Most blade designers use a mode shape parameter which quantifies the level of pitching in the 1F mode. Typically, as the level of pitching increases, the blade is more unstable. For supersonic unstalled flutter the most common design parameters are mode shape, reduced frequency and Mach number. For low pressure turbine blades the parameters are mode shape, reduced frequency, and a blade loading parameter.

Unsteady CFD analysis is used to conduct detailed flutter analysis. Because of the complexity of this type of analysis, it is only conducted for selected blades. It is wise to always perform detailed analysis on first stage fans, first stage compressors, and last stage low pressure turbine blades. In addition, blades which are shown to be marginal in preliminary design should receive a detailed analysis. Figure 2-3 displays an approach for unsteady CFD analysis. Although blades never flutter at the design point, this is a good condition with which to baseline the analysis. High and low operating line points should then be run. Next, an overspeed condition on the nominal line should be run. Finally, a part speed condition should be run at both the nominal and high operating lines. For all of

these points you will need to have the blade "hot" shape, the frequencies and mode shapes (first 4 modes are sufficient), and the steady aerodynamic condition (for a linearized method). The unsteady CFD analysis is then conducted for a range of interblade phase angles. The unsteady pressures are then integrated with the blade motion to determine the work per cycle or aerodynamic damping. An example of the results of this approach is shown in figure 2-4.

Figures 2-5 through 2-8 give a two-dimensional example of a detailed analysis for supersonic unstalled flutter. Figure 2-5 displays the steady solution. The mode shape (mode 2), shown in figure 2-6, is primarily a rigid body pitching about a point approximately 50 percent chord downstream of the trailing edge. The work per unit span is shown in figure 2-7 for a range of interblade phase angles for the first two modes. As can be seen, the blade is stable.
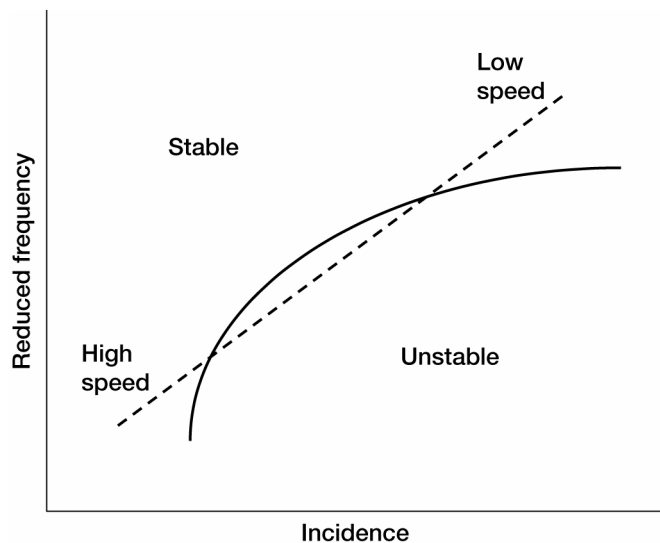
Figure 2-2.—Flutter analysis preliminary design.
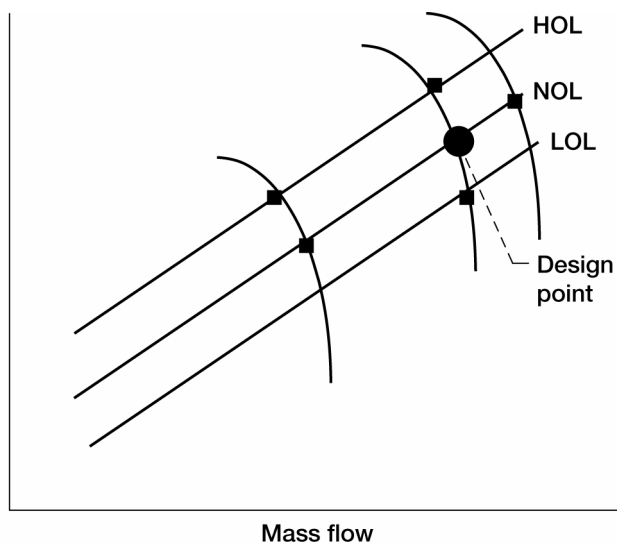
Figure 2-3.—Detailed flutter analysis.
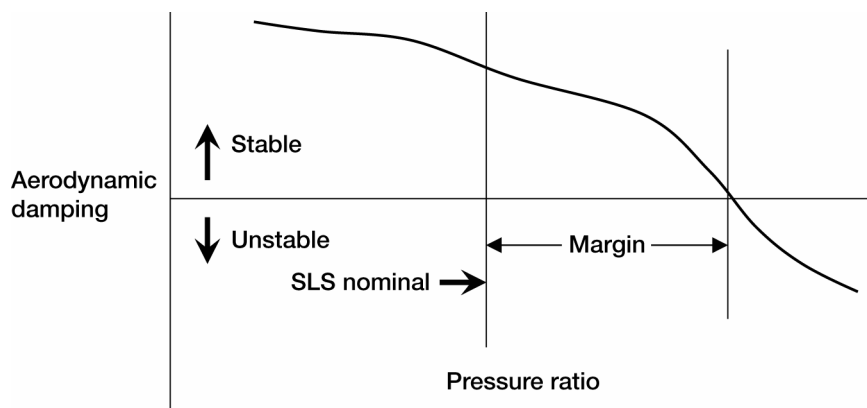
Figure 2-4.—Detailed flutter analysis–pressure ratio margin.

Steady aerodynamics
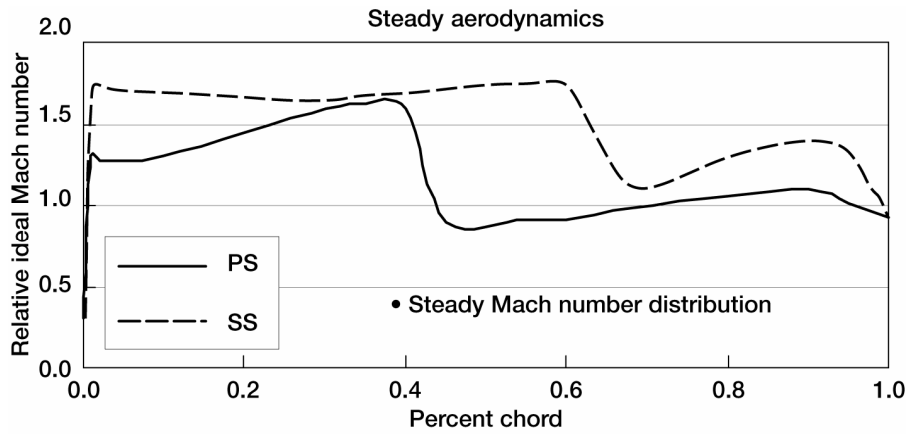
Figure 2-5.—Detailed flutter analysis–example–aero condition.
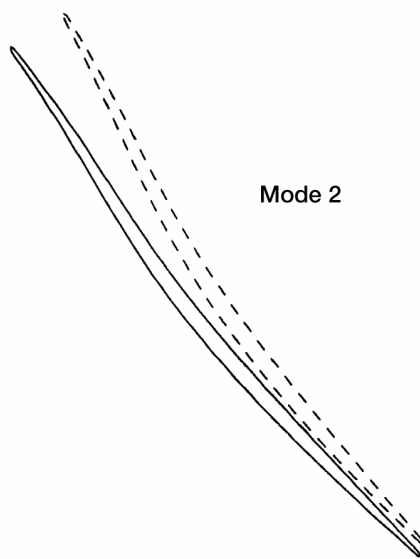
Figure 2-6.—Detailed flutter analysis–
example–mode shape.
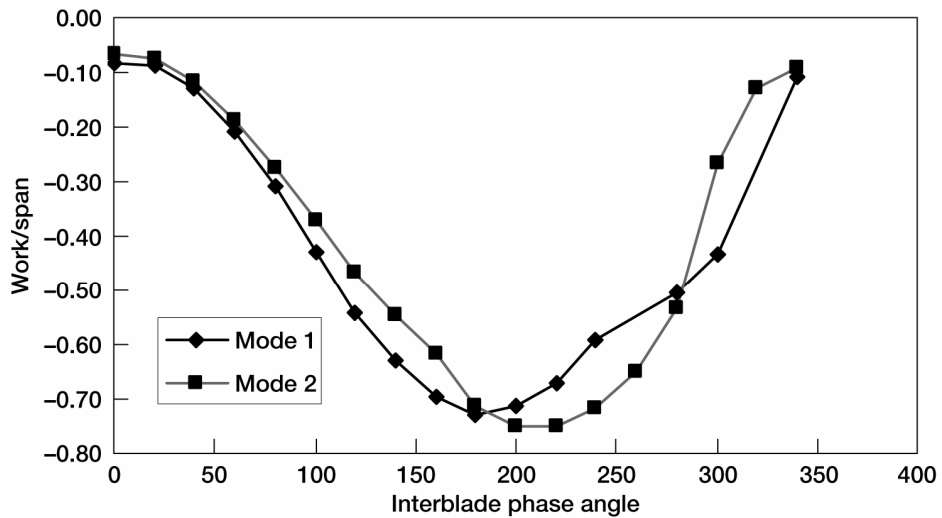
Figure 2-7.—Detailed flutter analysis–example–stability.

Effect of pitching axis.
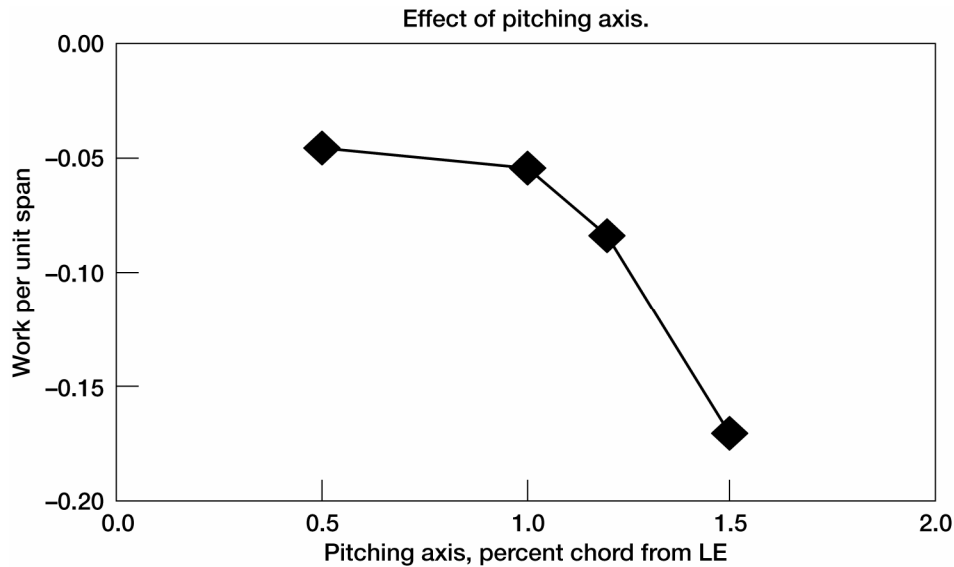
Figure 2-8.—Detailed flutter analysis–example–mode shape sensitivity.

Examples of sensitivity to mode shape are shown in figures 2-8, 2-9, and 2-10. Figure 2-8 shows the change in work for the same example of figure 2-7. Here the pitching axis is moved forward until it is at midchord (pure torsion). As can be seen, this is a destabilizing effect. Figures 2-9 and 2-10 display a more complete study of mode shape sensitivity for an LPT blade. A useful linear technique has been used to construct this plot. A two-dimensional linearized unsteady aerodynamic analysis was conducted for three different motions: translation in the axial direction, translation in the circumferential direction and rotation about the leading edge. From these three solutions a solution can be constructed for rotation about any point in the plane where the critical (flutter) values of reduced frequency are determined. This plot is useful in blade design by determining "good" mode shapes. That is, locations of the pitching axis that have relatively low values of critical reduced frequency and are in areas of low gradient. Figure 2-9 shows the values of critical reduced velocity for pitching axes in the vicinity of the blade. As can be seen, there is an order of magnitude difference in critical reduced velocity depending on the location of the pitching axis. The leading edge and trailing edge locations have relatively low values and the location of approximately 25 percent chord has the highest value. Figure 2-10 is a zoomed out view of the same data to investigate the translational modes. That is, when the pitching axis is infinitely far from the blade, the vibratory motion is a pure translation. Note that a pitching axis distant from the blade along the engine axis produces a circumferential translation. Other relationships are given in the table. The most stable motion is when the blade translates in the axial direction and the most unstable motion is when the blade translates in the circumferential direction.

It is also useful to plot the local work over the surface of the blade to determine where the "bad" and "good" work is being generated. If your design is unstable this information can be used to define redesigns which maximize the stabilizing work and minimize the destabilizing work. Figure 2-11 is an example of a plot of the work per unit span as a function of span.

An example of the sensitivity of flutter to the steady aerodynamic loads is shown in figure 2-12. Again, this is the same two-dimensional case examined in figures 2-6 through 2-9. In this case, the passage shock meets the blade surface at about 42 percent chord on the pressure side and 64 percent chord on the suction side (see fig. 2-5). Figure 2-12 displays the details of the unsteady behavior on the pressure side, which was found to have more influence on flutter behavior. First examine the variation of unsteady pressure with chord. It is obvious that the unsteady pressure at the foot of the shock is dominant. The phase plot is normalized such that 1 is equivalent to 180 degrees of phase shift. The small diagram to the right of the plot gives the phase definition with respect to work done on the blade, 0 and 180 are neutral, –90 is the most unstable phase, and +90 is the most stable phase. The phase is near zero from the leading edge to the shock, where it quickly rises to almost +180 degrees. Aft of the shock the phase approaches zero and slowly rises to approximately 60 degrees at the trailing edge. The "local" work is also near zero from the leading edge to the shock. At the shock negative work (stable) is done. From the shock to the trailing edge

additional negative work is done. The cumulative work plot shows how the negative work increases from the leading edge to the trailing edge. The total work done by the pressure side unsteady forces is stabilizing. Now contrast this with the data shown in figure 2-13. The only difference between conditions in figures 2-12 and 2-13 is that an improved steady analysis was conducted and it resulted in the shock being moved to approximately 36 percent chord (from 42 percent). Although the magnitude of the unsteady pressure is still dominant at the shock, the phase is now drastically different. The phase is "stable" from the leading edge to the shock. At the shock the phase is very near –90 degrees which is the most unstable phase. Aft of the shock the phase again becomes stable except for a small region around 87 percent of chord. Thus, a 6 percent change in shock position has resulted in the phase at the shock changing from neutral to the most unstable.
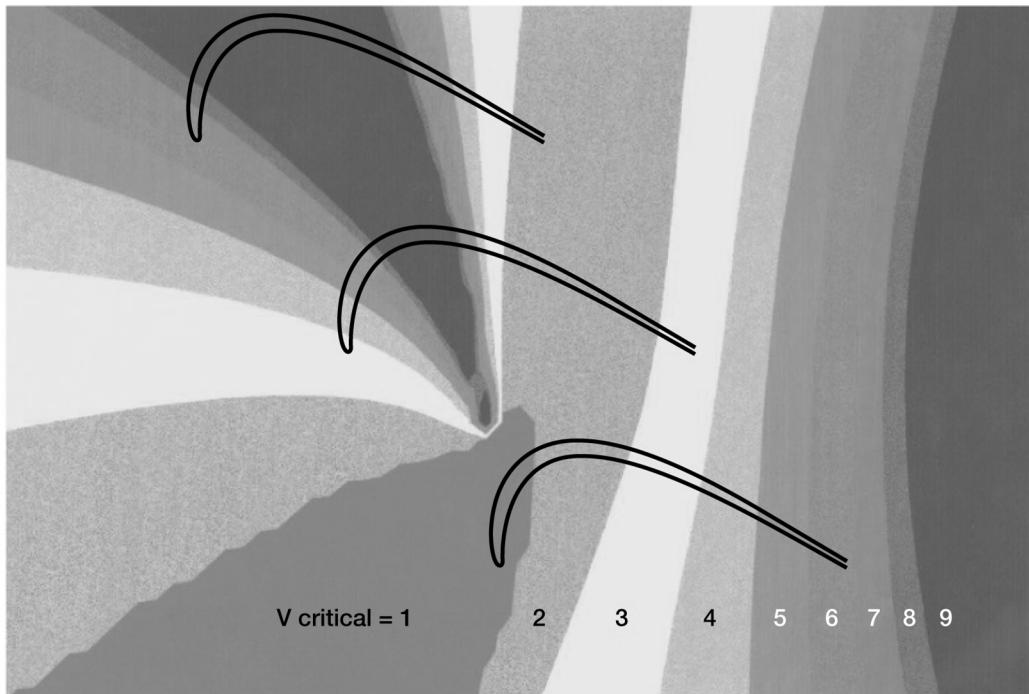
Figure 2-9.—Detailed flutter analysis–example–LPT mode shape sensitivity.
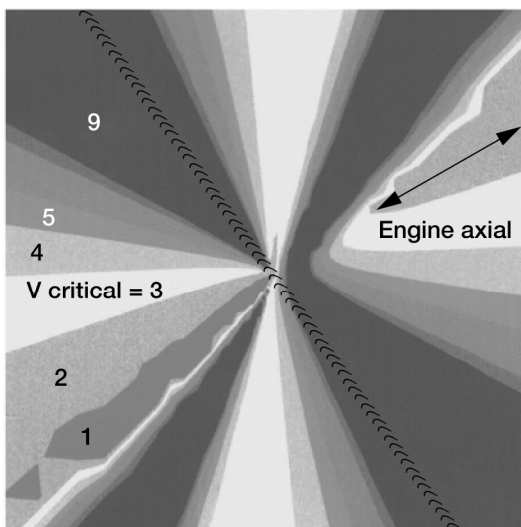
Pitching axis location	Type of "bending"	V critical
Engine axial	Circumferential	2
Engine circumferential	Axial	9
Blade chordwise	Flexwise	4
Normal to chord	Chordwise	3

Figure 2-10.—Detailed flutter analysis–example–LPT mode shape sensitivity.
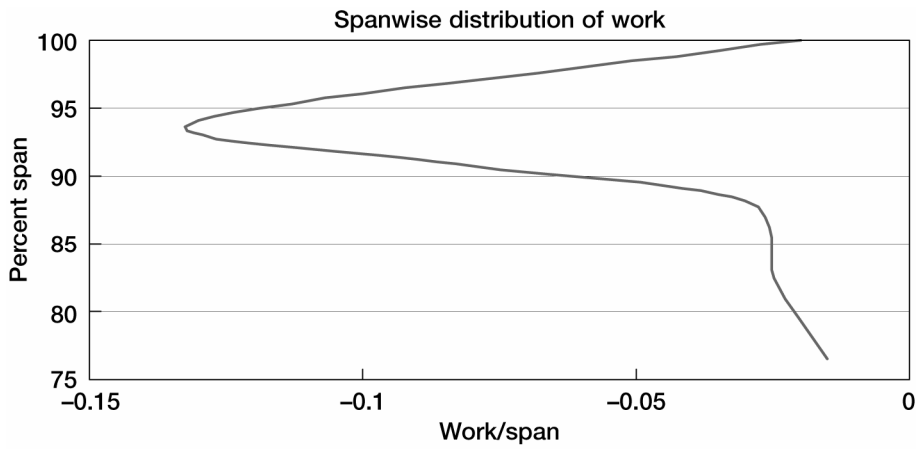
Figure 2-11.—Detailed flutter analysis–example–work versus span.
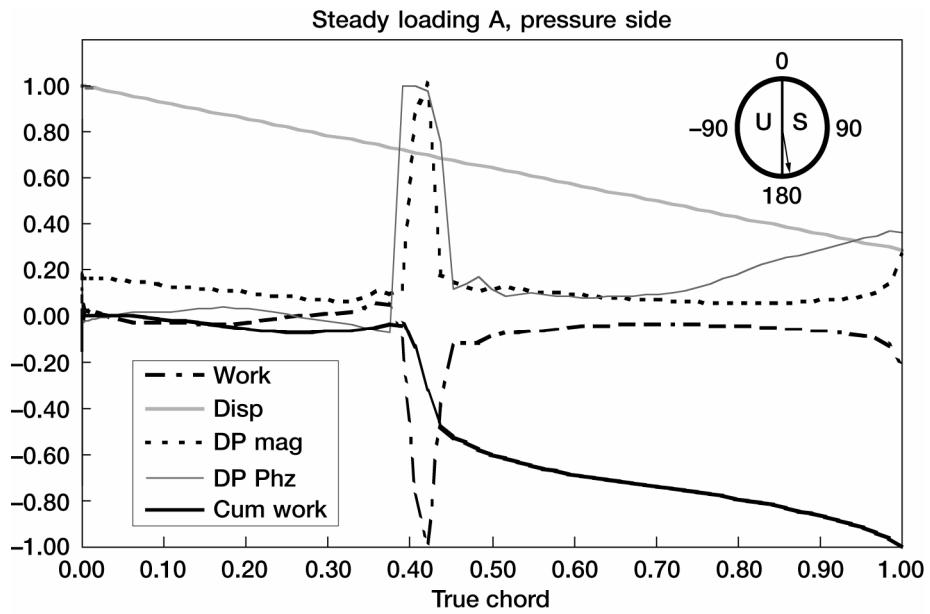
Figure 2-12.—Detailed flutter analysis–example–sensitivity to steady loads A.
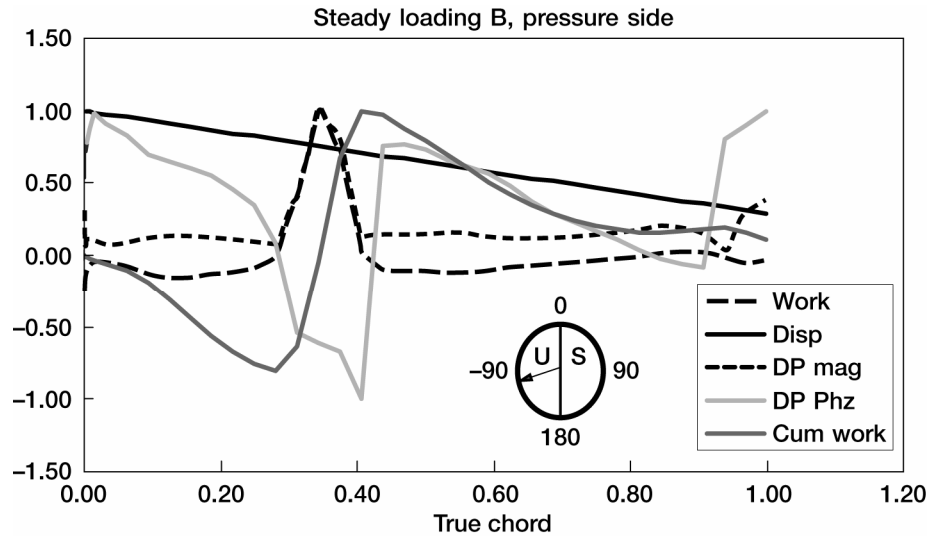
Figure 2-13.—Detailed flutter analysis–example–sensitivity to steady loads B.

3.0 Forced Response Analysis-1

This section begins with a description of preliminary design analysis for turbomachinery blading with emphasis on the Campbell diagram. This is followed by a discussion of detailed forced response analysis. Blade excitation due to upstream wakes, potential fields, shocks, and inlet distortion is highlighted.

The SDOF equations shown in figure 3-1 were discussed in section 2 with respect to the flutter problem. For the flutter problem we are primarily interested in the sign of D, which determines the blade stability. This is relatively easy compared to the forced response problem, where we are primarily interested in the amplitude of the resonant response. Even with simplifying assumptions (fig. 3-1), we must accurately calculate at least ζ, A_G, and A_D. This is a very difficult task. Consider the case of an upstream vane wake exciting a downstream blade. First, the steady wake of the upstream airfoil must be determined. As this downstream blade is passing through the wake the unsteady pressures on the blade must be calculated. Since the blade is vibrating, the unsteady pressures due to this motion must also be included. Not shown in the equations of figure 3-1 is the structural damping. Its determination is of the same order of difficulty as that of the unsteady pressures. Finally, all of these ingredients must come together in a forced response model. Therefore, it should not be surprising that for most resonant response analyses, the expected accuracy is not high. An absolute response prediction within a factor of 2 of the measured value is many times considered to be "good" agreement. As a result most forced response analyses are relative. That is, an analysis is conducted for a baseline case for which the measured response is known. The desired response analysis is then compared with the baseline case.

The complexity of forced response analysis is one reason that detailed response analysis has been included in the blade design process only in the last ten years. It is also the reason that the primary design procedure does not include response analyses. The Campbell Diagram is the most important tool in blade aeromechanical design. It is used to avoid resonances, or to place resonances at speeds for which low excitations are expected.

As shown in figure 3-2, resonant response is avoided or minimized by controlling the stimulus or by changing the blade frequency. The stimulus can be controlled by changing the count (frequency), or changing the strength of the stimulus (e.g., axial spacing, variable geometry position, or distortion magnitude). The most common method of modifying blade frequency is to tailor the thickness versus span. In addition, other design variables which affect frequency are aspect ratio, taper, solidity, and radius ratio. A more drastic design modification to raise frequency (and add damping) is to add a mid-span or tip shroud.

A typical Campbell Diagram for a wide chord fan blade is shown in figure 3-3. Here the 1F mode has been placed to give adequate margin to 1/rev and a low speed crossing of the 2/rev. The 2F mode has been placed to minimize the speed of the 3/rev crossing. The 1T crossing has a high speed 4/rev crossing. It would be desirable to spread the 1T and 2F frequencies such that the 1T/4 crossing is above redline speed and the 2F/3 is at a lower speed. However, this is very difficult to accomplish for a solid Titanium blade.

- Assume aerodynamic mass and stiffness are zero
- Assume structural damping is zero

$$R_P = \frac{A_G}{A_D \omega_n} \qquad \zeta = \frac{A_D}{2 \omega_n I}$$

$$R_P = \frac{A_G}{K} \frac{1}{2\zeta}$$

Figure 3-1.—Resonant response.

- Stimulus control
  - Blade and vane counts
  - Axial spacing
  - Variable geometry schedule
  - Distortion level
  - Bleed port locations
- Frequency control
  - Aspect ratio
  - Taper
  - Solidity
  - Radius ratio
  - Shrouds

Figure 3-2.—Forced response analysis preliminary design.
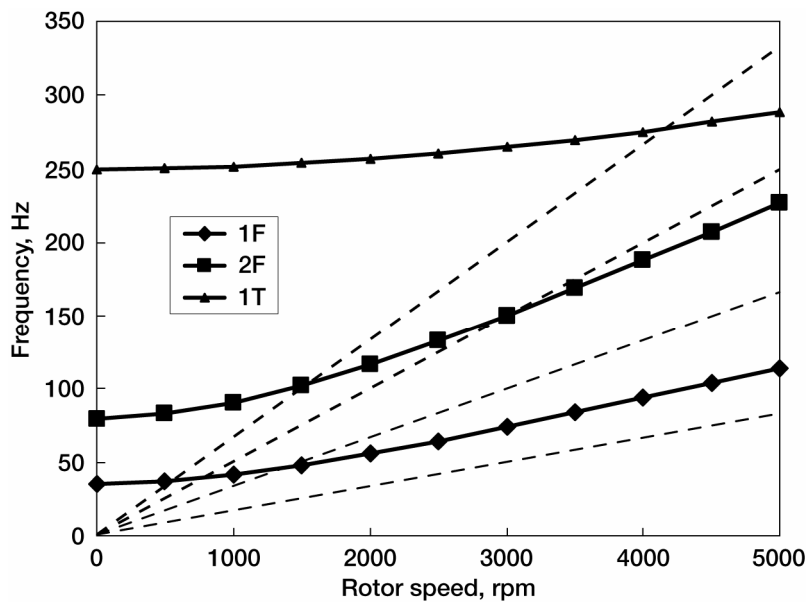
Figure 3-3.—Campbell diagram.

- Frequencies and mode shapes
- Unsteady blade loads due to blade motion
- Flow defects
- Fourier analysis of flow defect
- Unsteady blade loads due to flow defect
- Structural damping
- Modal response analysis
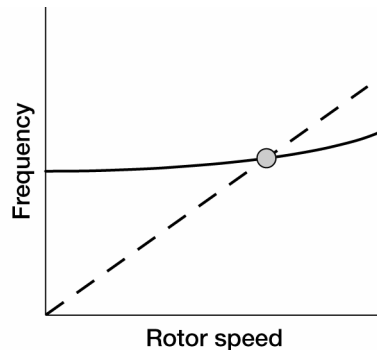
Figure 3-4.—Detailed forced response analysis.

The main ingredients to a detailed forced response analysis have been previously mentioned. Figure 3-4 lists the specific tasks for conducting a decoupled, linearized analysis. "Decoupled" refers to separate analysis for the flow defect (e.g. wake) and the blade response. That is, a steady analysis is conducted to determine the flow defect. These results are an input to the blade analysis to calculate the unsteady pressures on the blade and subsequently, the blade response.

Figure 3-5 displays the complex flows which produce flow defects. First consider compressor wakes as shown in figure 3-6. In the reference frame of the upstream airfoil which produces the wake, the wake is primarily a region of low velocity flow. However, seen in the reference frame of the downstream airfoil, the flow defect is primarily a perturbation in the flow angle. As shown in the figure this flow angle perturbation is usually sharp. When Fourier analyzed it can contain significant amplitude in the harmonics. The fundamental frequency and first harmonic must be considered on the Campbell Diagram. The second harmonic does not usually cause a significant response, however, this excitation can sometimes be seen in blade response testing.

The velocity diagrams for turbine wakes are shown in figure 3-7. Here the situation is significantly different from that of the compressor. That is, the velocity deficit in the upstream reference frame is seen primarily as a perturbation in the flow velocity in the reference frame of the downstream airfoil. There is little change in the flow angle.

There have been two common methods to characterize the wake: empirical and computational. Figure 3-8 gives an example of an empirical wake model where the wake is characterized by the velocity deficit, W, and the width, δ. These parameters are usually empirically determined from measured wakes and normalized by the airfoil loss coefficient. Hyperbolic secant and Gaussian models are commonly used to express the azimuthal variation. An empirical model for streamwise decay is also shown in figure 3-8. Figure 3-9 shows a comparison of a prediction (solid line) and measurement (symbols). The result that the prediction is narrower and deeper than the measurement is not uncommon. Fortunately, these two errors counteract each other during the Fourier analysis process.

In the last 5 years it has become more common to use a steady CFD analysis to determine the blade wakes. Figure 3-10 shows the results of a CFD analysis downstream of a fan blade and its comparison with an empirical model.

Figure 3-5.—Flow defects.

Compressor vector diagram
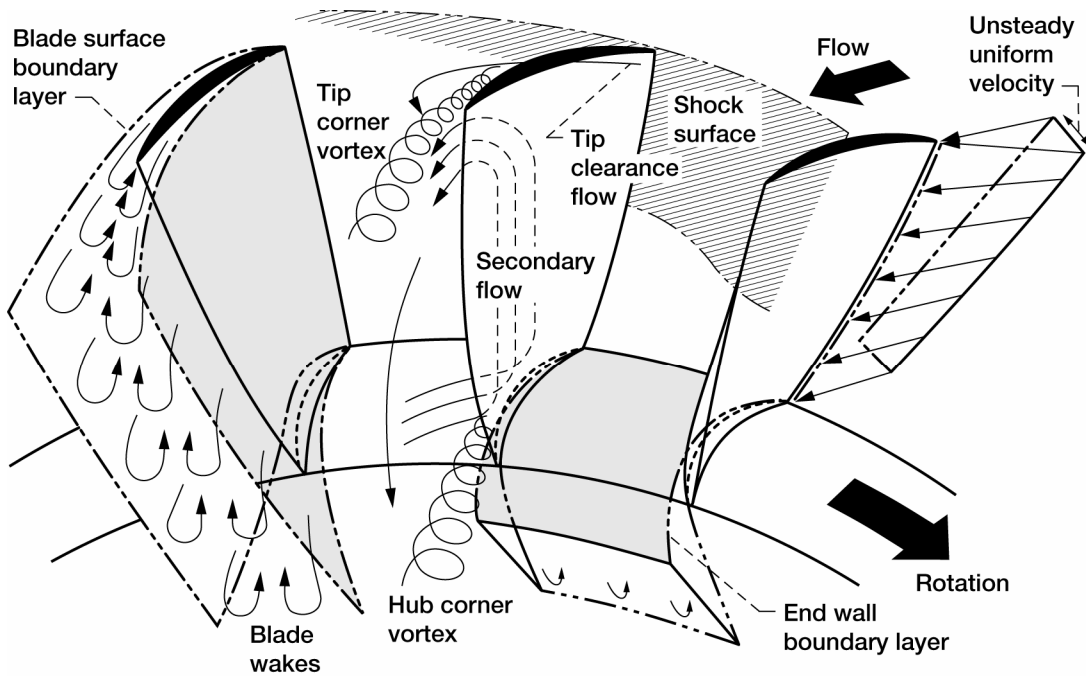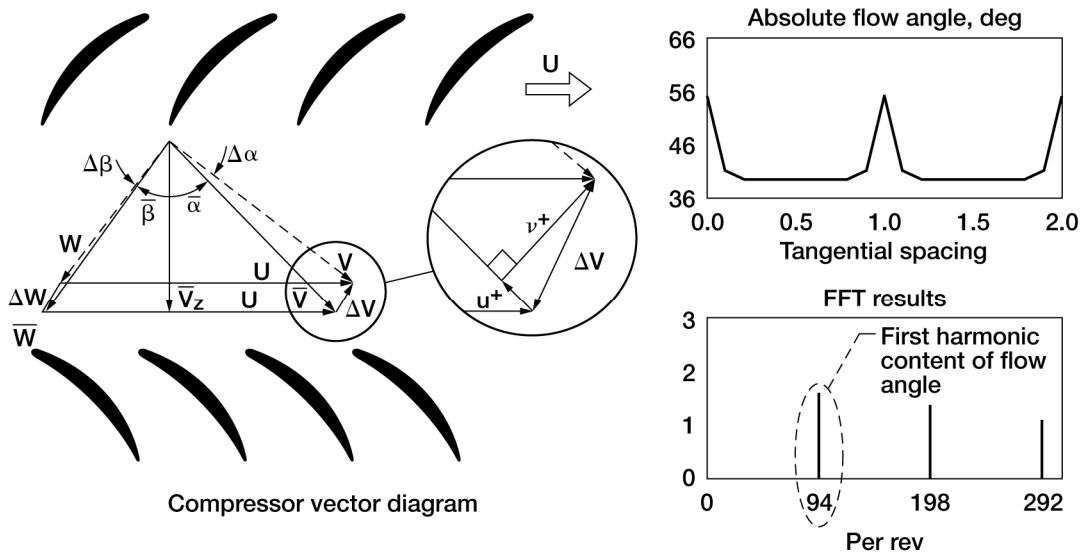
Figure 3-6.—Compressor wakes.
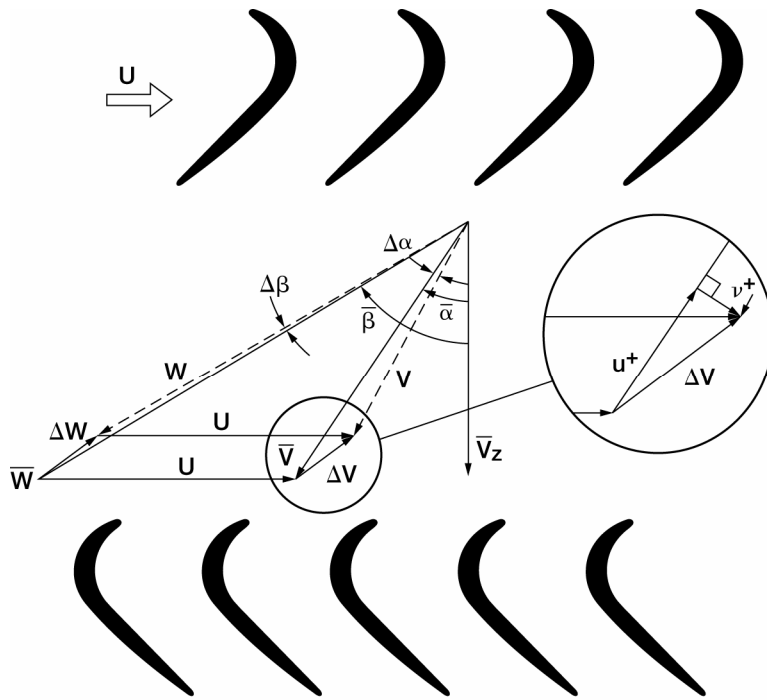
Figure 3-7.—Turbine wakes.

- Strength based on loss coefficient
- Azimuthal variation
  - Hyperbolic secant
  - Gaussian
- Streamwise decay
  - $W = (ax + b)/(cx + 1)$

Velocity

Azimuthal distance
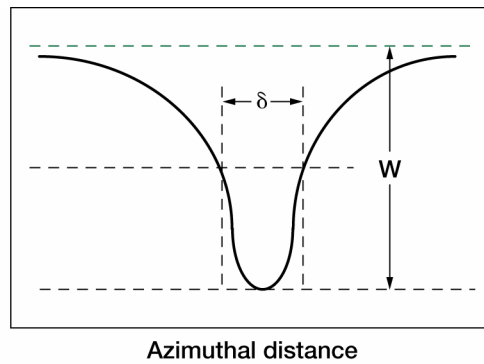
Figure 3-8.—Empirical wake model.
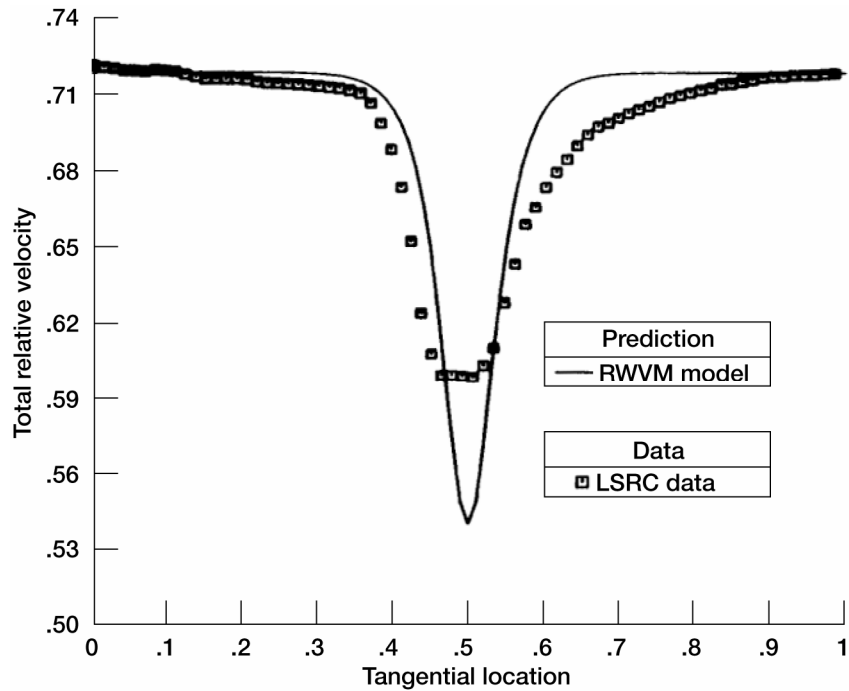
Figure 3-9.—Empirical wake model–comparison of prediction with measurement.
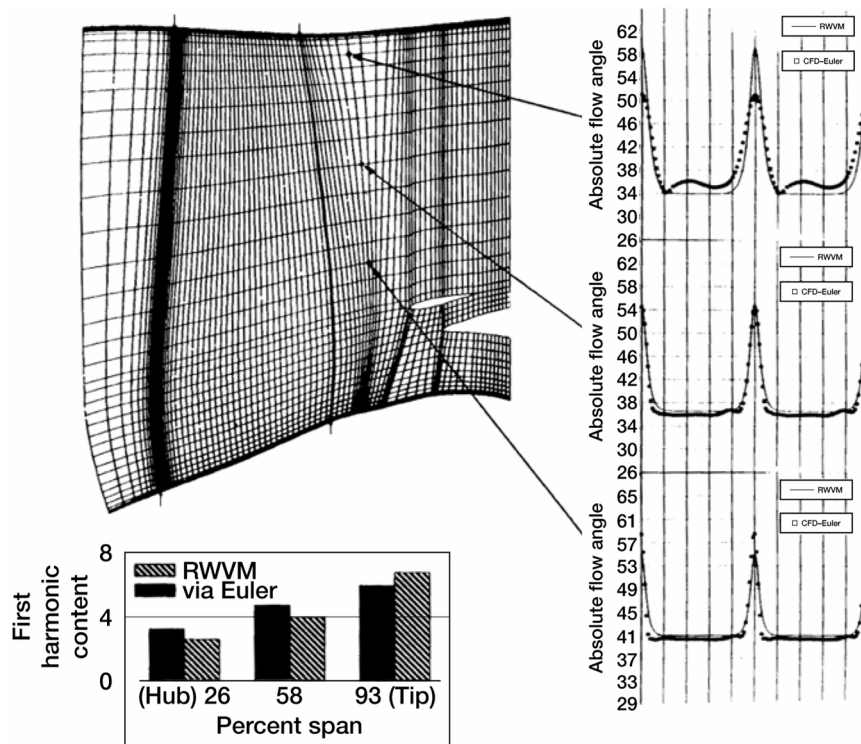
Figure 3-10.—Comparison of empirical (RWVM) and CFD wake predictions.
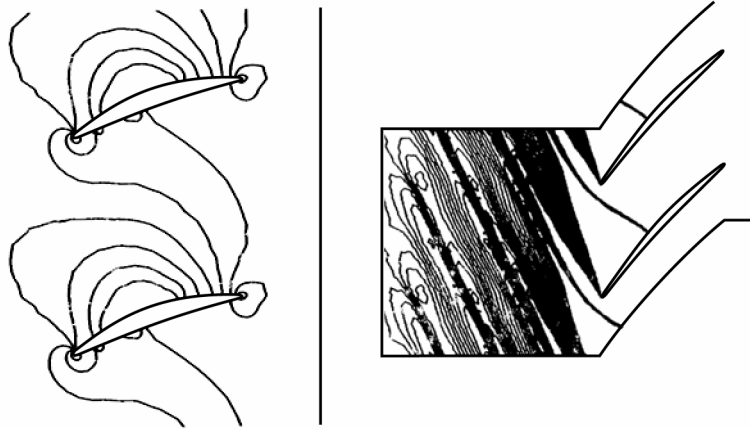
Figure 3-11.—Example of bow waves–pressure distribution.

$$\Delta P \approx e^{\frac{-2\pi DZ/GAP}{\sqrt{1-M^2}}}$$

	M
——	0.0
— —	0.3
- - -	0.6
—·—·	0.9
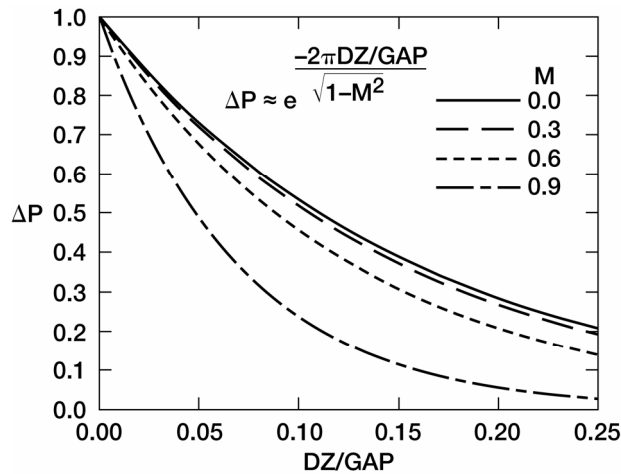
Figure 3-12.—Bow waves–axial decay.

The next type of flow defect to be considered are pressure disturbances. Figure 3-11 shows two very different examples of pressure disturbances. On the left is the potential field produced by a subsonic airfoil which generates upstream and downstream pressure disturbances. On the right is pressure disturbance generated by an unstarted supersonic passage of a fan. In this case a leading edge shock can extend upstream of the fan rotor. This excitation source has been found to cause cracking of the inlet guide vanes of military fans.

For a two-dimensional subsonic potential pressure disturbance the axial decay is easily estimated from the equation shown in figure 3-12. DZ is the axial distance and GAP is the circumferential spacing of adjacent airfoils. Examples of the circumferential variation in static pressure as a function of axial position are shown in figure 3-13 for a turbine frame (left) and a fan blade (right). It should be noted that a potential disturbance can be "amplified" by an intervening vane row. This must be considered when predicting the response of a blade row due to down-stream frame struts when there is a vane row in between the frame and the blade.

Of course the wakes and pressure disturbances do not act independently. Figure 3-14 shows the results of a study of the wake/potential interaction experienced by a turbine blade which is excited by an upstream turbine vane. Two loading conditions for the blade were considered. On the left is the low load condition in which the wake and potential produce blade forces that constructively interfere. However, for the high load condition (right) the wake and the potential produce forces that destructively interfere and produce a much smaller net blade load.
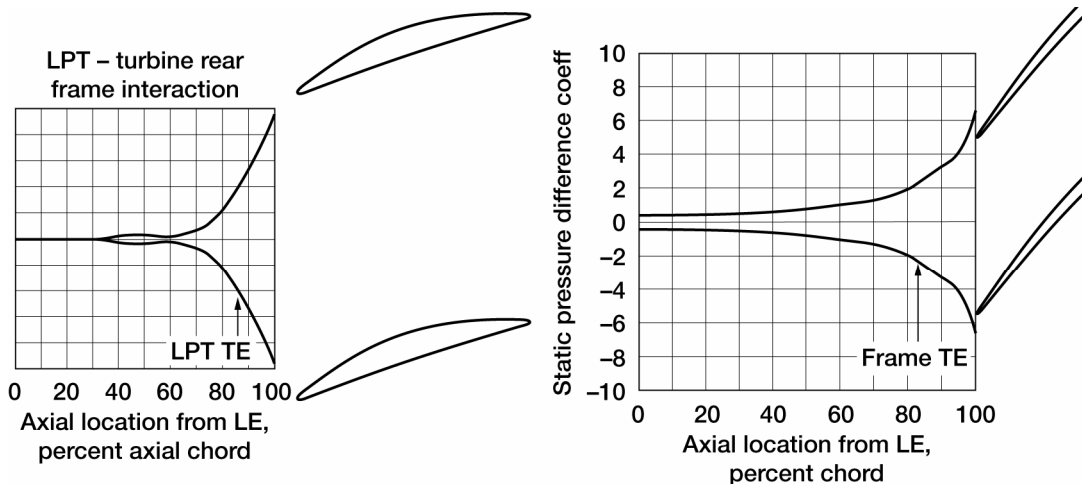
Figure 3-13.—Example of bow waves–circumferential static pressure difference.
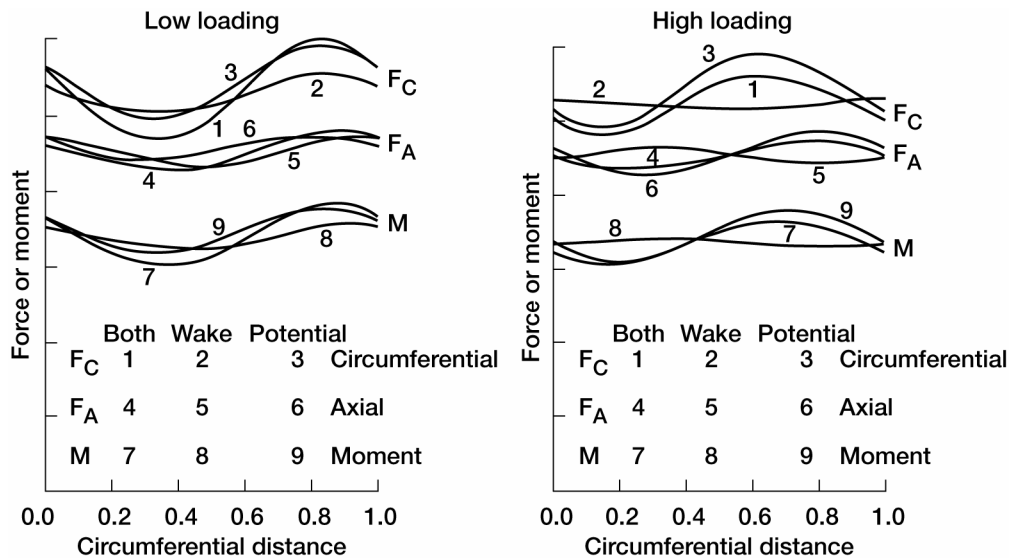
Figure 3-14.—Wake/potential interaction.

In past HPT and LPT designs the wake and potential disturbances produced the only significant excitation in HPT's and in LPT's. Recent advanced turbine designs have produced significant shock excitations. One new type of shock excitation, shown in figures 3-15 and 3-16, has been experienced on high speed vaneless turbines. Here the trailing edge shock emitted by the HP blade impacts the leading edge of the downstream LP blade.

The wake, potential, and shock produced excitations discussed above have relatively high frequency content and generally excite high order modes. A significantly different type of excitation is produced by inlet distortion. No inlet is exactly symmetric and most inlets, especially military, are significantly non-symmetric. This in itself produces a nonuniform flow field at the fan face. In addition, environmental crosswinds produce additional nonuniformities. A significant crosswind combined with a low forward aircraft velocity can cause a massive separation of the inlet which produces a significant excitation source to the fan. This is one reason for requiring a significant 1/rev, 2/rev, and 3/rev margin on the Campbell Diagram. For military aircraft flight maneuvers also cause inlet flow nonuniformities.

Currently there has been little success with using CFD inlet models to predict distortions. Therefore, the distortion level and patterns are measured during scale model inlet tests and sometimes in flight tests. Development tests for commercial engines use auxiliary fans to simulate environmental winds. For military engines "distortion" screens are used in development testing. Figure 3-17 gives an example of a forced response prediction for a 1F 3/rev

resonant response due to inlet distortion for an in-flight maneuver and a takeoff condition. On the left is shown the harmonic perturbation in flow angle as a function of span. The plots on the right side show the predicted and measured stress response. Unusually good agreement is seen.

Some studies have been conducted concerning the sensitivity of forced response predictions to perturbations. Figure 3-18 shows a study of the change in the steady flow on the unsteady pressure and the modal force. On the left is shown the two steady flows considered. As can be seen there is only a 5 percent change in the chordwise position of the shock. The apparently small effect on the predicted unsteady pressure distribution is shown on the right. The surprise is that this small change in unsteady pressure produces a 67 percent change in the modal force.

Figure 3-19 shows the unsteady pressures (difference of pressure and suction side) on a fan blade due to a distortion screen. The predictions of a three-dimensional CFD analysis are compared with those of a "stacked" two-dimensional analysis. Also shown are the measurements from a rotating test.
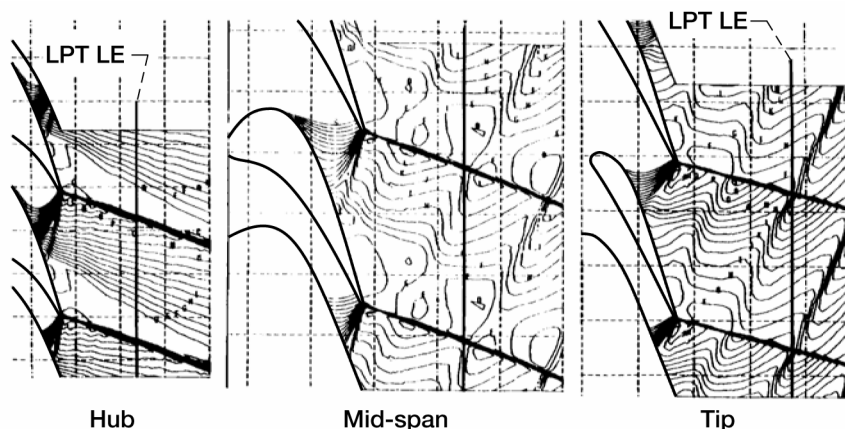
Figure 3-15.—Vaneless HP/LP shock interaction.
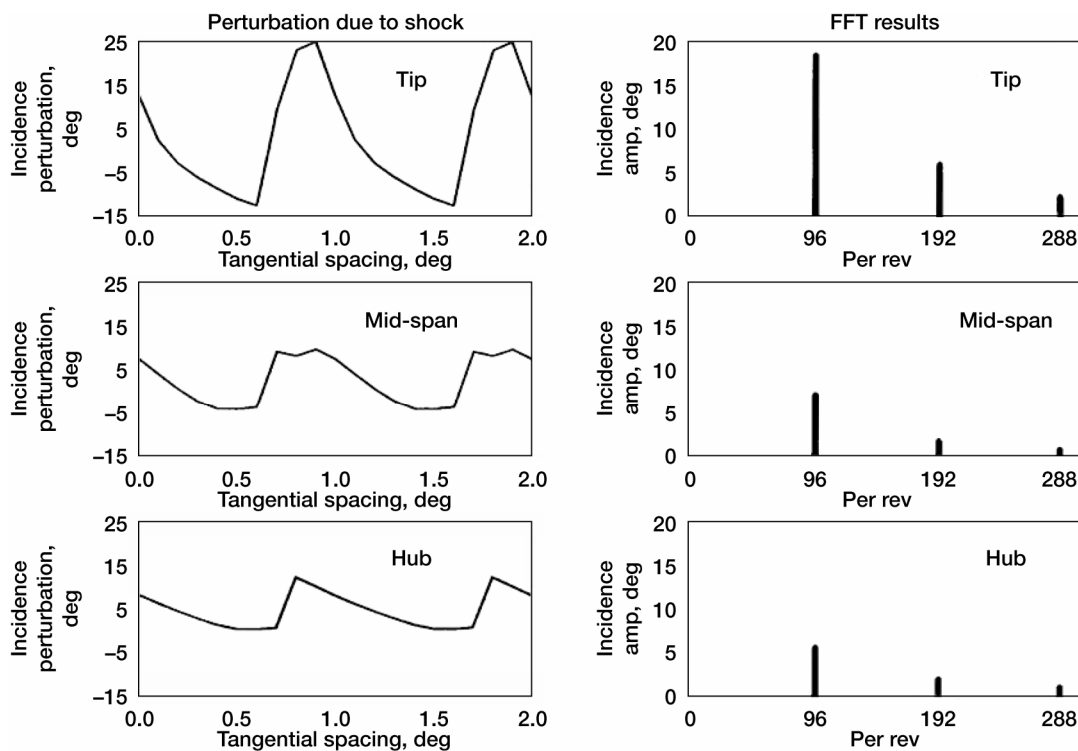
Figure 3-16.—Shock excitation–harmonic content.
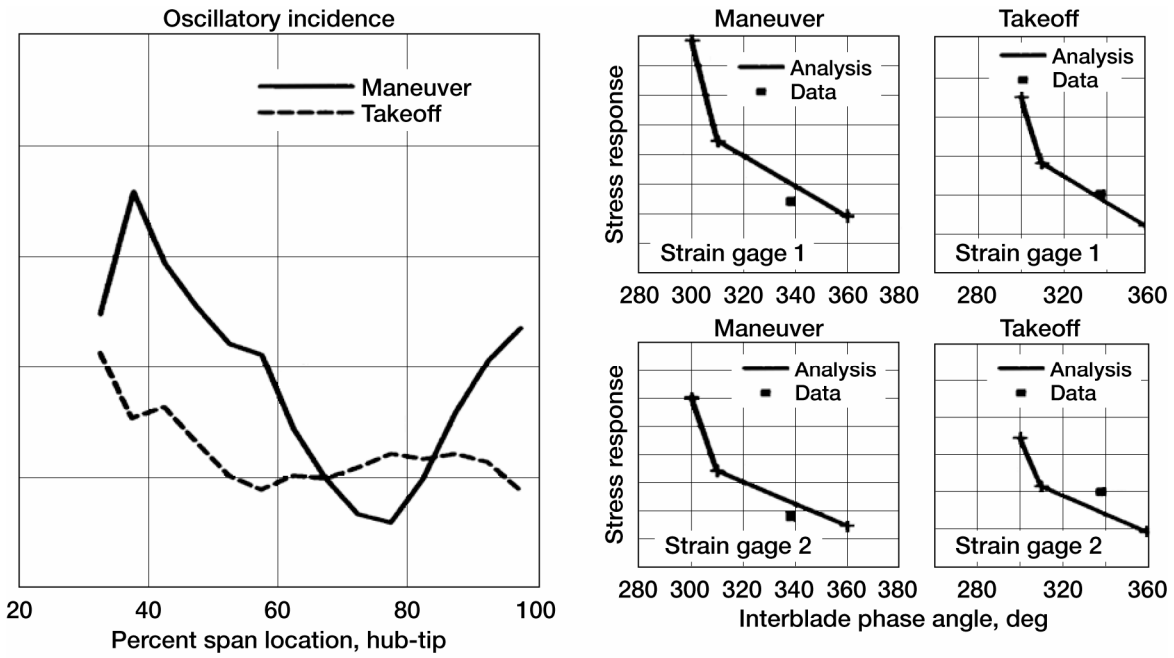
Figure 3-17.—Flow angle fluctuation due to inlet distortion. 3/R velocity perturbation and response prediction for maneuver and takeoff conditions.
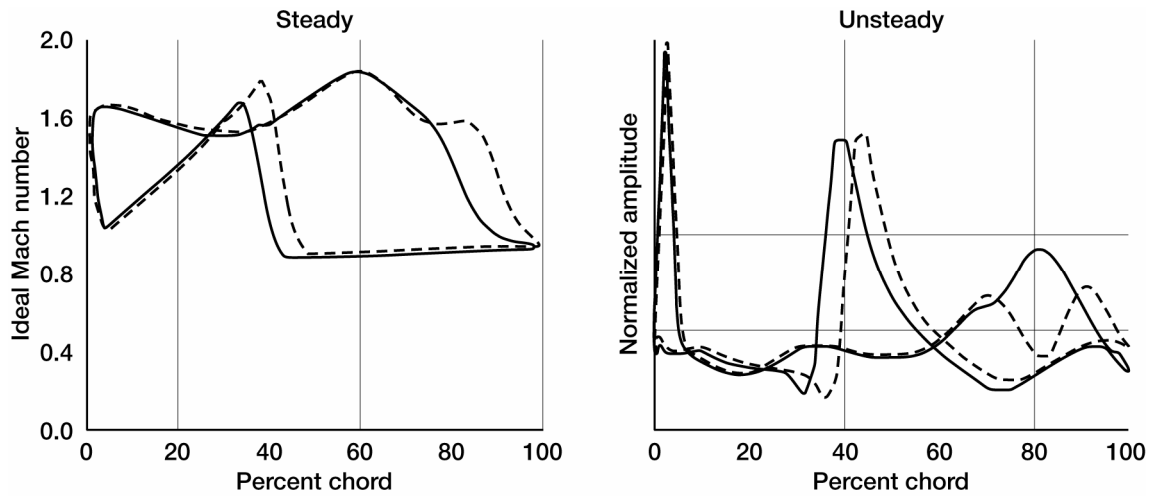
Figure 3-18.—Sensitivity of modal force to steady aero solution.
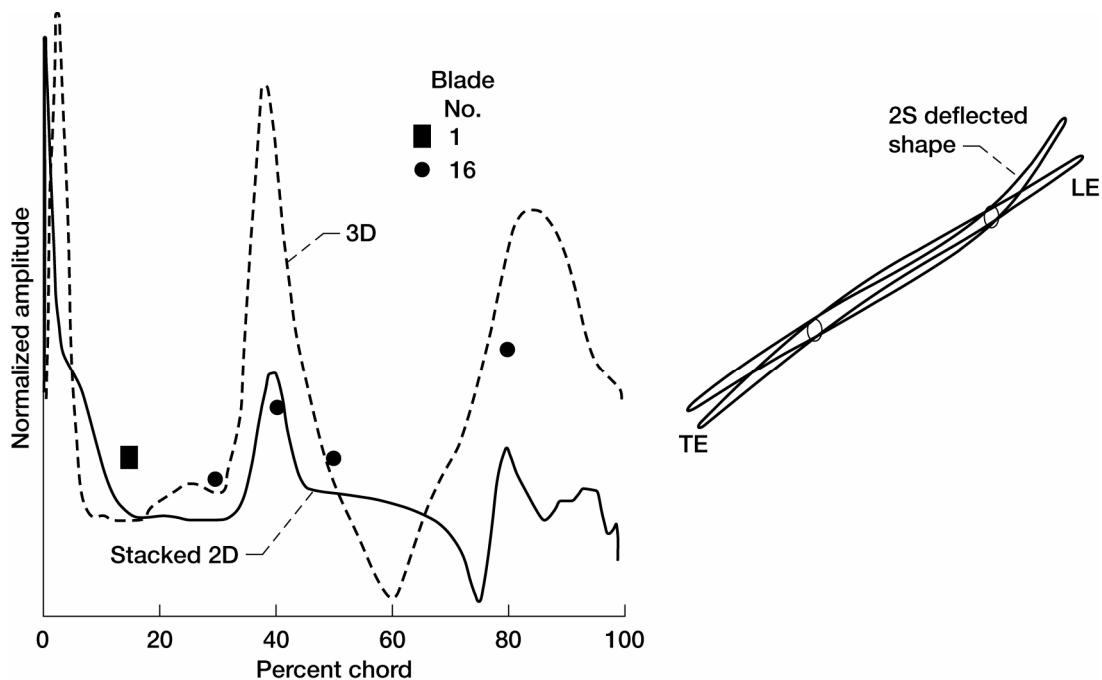
Figure 3-19.—Unsteady pressure–3D versus 2D.

4.0 Forced Response Analysis-2

The section begins with a brief description of applying the modal analysis method to forced response predictions. This is followed by a simple numerical example. Discussions of prediction accuracy and additional complicating factors are then given. The final part of this section deals with probabilistic approaches for aeroelastic design and assessment.

A typical linear, modal, forced response analysis (shown in fig. 4-1) starts with a finite element model which is used to determine the steady position of the blade at the speed of interest, the stress stiffening matrix, and the frequencies and mode shapes. The mode shapes are usually normalized such that the modal mass is 1 and the modal stiffness is equal to the square of frequency. Next the aerodynamic damping is determined, using the same procedures as are used for the flutter problem. This consists of calculating the dot product of the unsteady pressures (induced by the blade motion) and the mode shape. This produces the local work, which is integrated over the blade surfaces to determine the total (real) work. The aerodynamic damping is related to the real part of the work. The structural damping is determined from experience, analysis, bench test data, or deduced from engine data. The modal force is then calculated with the same procedure, but now using the unsteady pressures induced by the flow defect. The modal response is then determined by the equation shown in figure 4-1. To determine local stress the finite element mode shape is used.

Figure 4-2 gives a quantitative example of a 1T/4 forced response calculation. A Titanium rectangular blade with a span of 3 feet, an aspect ratio of 3, and a thickness/chord ratio of 0.05 is considered. A finite element analysis was run and the results are shown in figure 4-2. The critical vibratory amplitude was determined by calculating the modal amplitude at which the highest local vibratory stress is on the Goodman Diagram minimum life curve. The aerodynamic damping was calculated with an unsteady CFD code for the 1T mode. The structural damping was assumed to be negligible. A steady CFD analysis was conducted on the upstream strut producing the wakes. The Fourier analysis of the wake profile resulted in a 40 percent amplitude of the fundamental frequency content. For

this amplitude the effective oscillatory incidence was + and –2.5 degrees. This was the upstream boundary condition for the unsteady CFD analysis used to predict the unsteady pressures over the surface of the blade. The modal force was determined by integrating the pressures with the mode shape. The equation on figure 4-1 was used to determine the modal amplitude, which was 33 percent of the allowable value.

Even with many simplifying assumptions, to perform an accurate forced response analysis we must accurately calculate at least ζ, A_G and A_D. This is a very difficult task. Figure 4-3 shows a typical comparison of predicted and measured resonant response for a fan operating behind distortion screens. As can be seen, the accuracy ranges from excellent to poor and is modal dependent.

- Obtain modal stiffness, K, from FE analysis
  (usually modal mass is normalized to 1, then $K = \omega_n^2$)

- Dot product of local unsteady pressure and mode shape

- Integrate over surface of blade to obtain modal force, A_G

- Add structural damping and aerodynamic damping to obtain total modal damping, ζ

- Solve SDOF response equation

$$R_P = \frac{A_G}{K}\ \frac{1}{2\zeta}$$

Figure 4-1.—Modal response analysis.

- Blade description: l = 3 ft, l/c = 3, t/c = 0.05, titanium

- FE results: 1T, 270 Hz, I = 0.108 slug-ft^2, K = 3.1 E5 ft-lb/rad, critical vibratory amplitude = 0.15 rad

- Unsteady blade loads due to blade motion

  A_D = 1.83 ft-lb-sec/rad

  ζ = 0.0025 (Q = 200)

- Flow defect

  4 identical wakes per revolution at blade LE

  Wake depth = 50% of flow velocity

  Wake width = 0.5 in.

- Fourier analysis of flow defect

  4/revolution content is 40%

  Oscillatory incidence at blade LE:
  + and – 2.5 deg.

- Unsteady blade loads due to flow defect

  A_G = 155 ft-lb

- Structural damping: None

- Modal response analysis:

  R_P = 0.05 rad

  33% of critical vibratory amplitude

Figure 4-2.—Forced response prediction–example–1T 4/revolution.

Mode/stimulus	Predicted response (2D CFD) (% of stress limit)	Measured response (% of stress limit)
1-F/3 revolution	128	127
2-S/8 revolution	26	104
2-T/8 revolution	70	112

Figure 4-3.—Example of comparison of test results with pre-test predictions–resonant response.

- Flow defects
  Secondary flows (passage vortices)
  Multi-stage
  Flow discontinuities (bleed ports, steps)
  Acoustic
  Manufacturing tolerances
- Unsteady blade loads
  Multi-stage
  Manufacturing tolerances
- Response
  Manufacturing tolerances (mistuning)
  Damping (interfaces)
  Engine "system" coupling

Figure 4-4.—Additional complicating factors.

In addition to the complexities mentioned above, there are other complicating factors in calculating forced response (fig. 4-4). The ability to predict the flow defects is complicated by secondary flows, multi-stage effects, discontinuities in the flow path, acoustic interactions, and variations due to manufacturing tolerances. The unsteady analysis is primarily complicated by multi-stage effects and manufacturing tolerances. The response problem is complicated by "mistuning" effects and interface damping. Mistuning means that the blades have different natural frequencies and do not respond identically. The damping at interfaces such as mid-span and tip shrouds has been found to be very sensitive to small changes. Finally, the mode may include more than the blade and disk. Some modes couple with the entire engine structure.

An important parameter related to forced response is "hot spot". One definition of the hot spot parameter is the maximum local strain normalized by the total strain energy. It has been found that this parameter can vary significantly by changing the blade design slightly, such as moving the chordwise location of maximum thickness. In addition, the hot spot can vary significantly from blade to blade. A study was performed to determine which parameters drive these strain distributions or hot spots. Figure 4-5 shows the hot spot sensitivities as a function of tmax/c, t leading edge, t trailing edge and tmax as a percent of chord for the tip, root, and pitch sections. A plus one standard deviation change is independently made for each of the design parameters. The vertical axis represents the change in the hot spot parameter. A positive change means an increasing hot spot parameter which means a higher local maximum strain. It can be seen that tmax/c has a significant effect at the tip. As expected, a thickening of the tip greatly reduces the hot spot parameter. Unexpectedly, the opposite behavior is seen at the pitch section. The other significant effect is due to tmax as a percentage of chord. As can be seen, this has a beneficial effect as the location of the maximum airfoil thickness is moved forward. Historically the airfoil maximum thickness (tmax) was located at approximately 50 percent chord. In an effort to achieve better performance this was moved to 60 percent chord. It was subsequently found that this increased the hot spot sensitivity. These predicted sensitivities compare well with those found manually in 20 design iterations.

Next is a discussion of "probabilistic design" and "probabilistic assessment". The background is set by defining the aeromechanical design concerns, and then by listing a comprehensive set of variability factors which affect the aeromechanical response over the life of a compressor airfoil. It is shown how manufacturing variability is one of these factors. Next, the classical design approach is shown with emphasis on how manufacturing variability is considered. Finally, the new probabilistic design approach is described.

Figure 4-6 shows the most important aeromechanical analysis parameters. The four parameters of most interest are steady stress, modal frequencies, mode shapes and modal strain distributions. Manufacturing variations effect all of these quantities. The steady stress is limited to provide for some vibratory capability. This is especially true for the blade leading edge. Modal frequencies are predominately used to set adequate margin to known excitation sources. The required margins are based on experience on the effect of manufacturing variability on frequency. The

modal frequencies are also used to ensure that modes have adequate frequency separation. When modes are too close together a high level of variability can be seen in blade response. Reduced velocities are flutter parameters which are also affected by frequency variation. Flutter is also affected by the mode shape. Hot spots are areas of locally high vibratory strain and they can be significantly affected by manufacturing variation.

The classical aeromechanical design approach for blades uses deterministic design analysis to analyze the nominal blade geometry. Manufacturing variability is taken into account by requiring margins, or applying Factors of Safety, when compared to design criteria. Distributions of design analysis parameters, such as blade frequency, are not estimated. The margins and Factors of Safety are "calibrated" by experience from previous successful and unsuccessful designs. Of course, this approach has been used in engineering design since the early days of design analysis. The downside of this approach is that it is typically overly conservative and can reject good designs. Alternatively, this approach can be unconservative and allow bad designs to make their way to production.

In the probabilistic design process the design analysis considers the distribution of blades that will be produced from a given design by a given process. These distributions will be evaluated against probabilistic criteria. The evaluation will generally be a probability that criteria will be violated. The process is expected to minimize the chances for under- or over-conservative design. The result is a high quality, robust product. Figures 4-7 through 4-9 show an example of the process for blade frequencies. Factors of safety are generally based on past experience and consequently are parametric and may not necessarily be physics based. For example a 10 percent margin may be insufficient, adequate or overkill. Unfortunately only when it is insufficient does it get peoples attention.

Figure 4-5.—Vibratory strain hot spot–sensitivities.

- Steady stress
- Leading edge ruggedness
- Frequency margin to known excitations
- Frequency separation criteria
- Reduced velocities
- Mode shape parameters
- Hot spot for panel vibratory modes

Figure 4-6.—Blade HCF–classical design criteria.

- Maximum thickness/chord versus span
- Chord versus span
- Leading edge thickness versus span
- Trailing edge thickness versus span
- Maximum thickness versus chord versus span
- Airfoil fillets
- Stagger angle versus span
- Tilt and lean
- Material properties

Figure 4-7.—Key airfoil characteristics for cantilevered titanium airfoils.
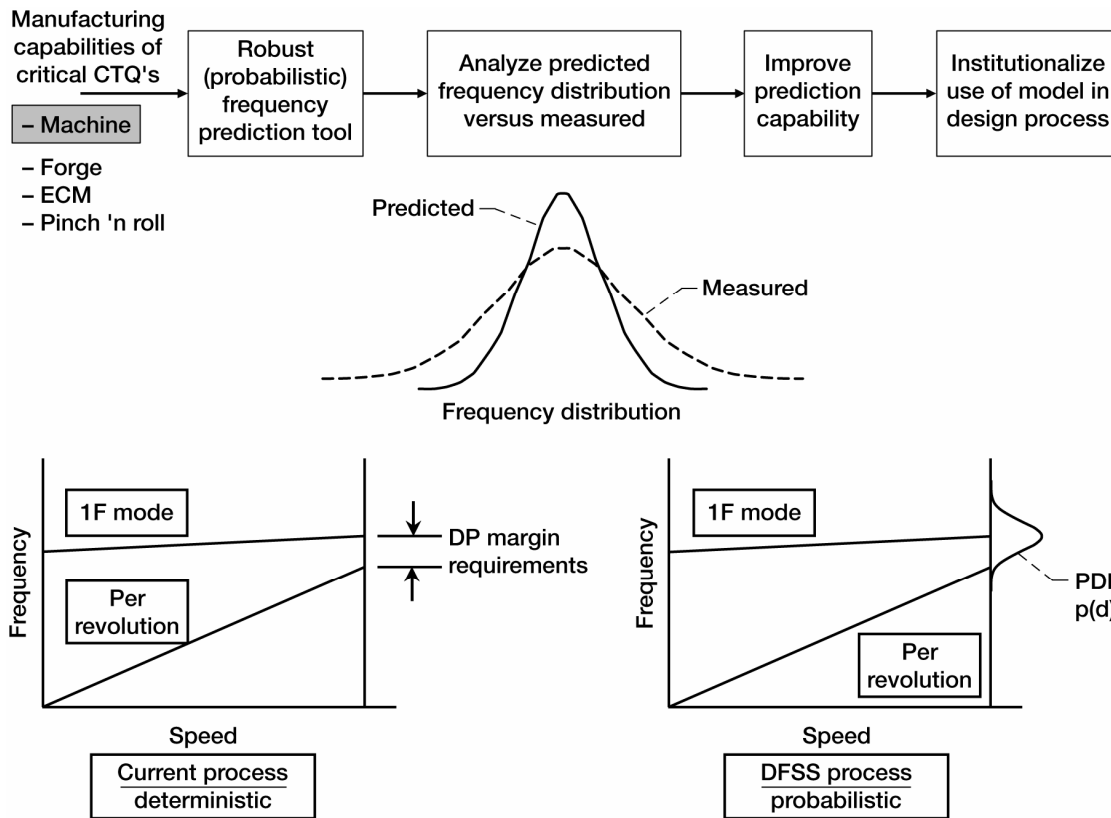
Figure 4-8.—Frequency prediction philosophy.

The classical aeromechanical design approach for blades uses deterministic design analysis to analyze the nominal blade geometry. Manufacturing variability is taken into account by requiring margins, or applying Factors of Safety, when compared to design criteria. Distributions of design analysis parameters, such as blade frequency, are not estimated. The margins and Factors of Safety are "calibrated" by experience from previous successful and unsuccessful designs. Of course, this approach has been used in engineering design since the early days of design analysis. The downside of this approach is that it is typically overly conservative and can reject good designs. Alternatively, this approach can be unconservative and allow bad designs to make their way to production.

In the probabilistic design process the design analysis considers the distribution of blades that will be produced from a given design by a given process. These distributions will be evaluated against probabilistic criteria. The evaluation will generally be a probability that criteria will be violated. The process is expected to minimize the chances for under- or over-conservative design. The result is a high quality, robust product. Figures 4-7 through 4-9 show an example of the process for blade frequencies. Factors of safety are generally based on past experience and consequently are parametric and may not necessarily be physics based. For example a 10 percent margin may be insufficient, adequate or overkill. Unfortunately only when it is insufficient does it get peoples attention.

Figure 4-7 shows a minimal set of blade geometry parameters which are key to determining the success of a design. As such, the effect of manufacturing variation on these parameters is important and must be controlled. The maximum thickness/chord and chord are usually used to set steady stress and frequency margins. The edge thicknesses determine the ability to withstand damage. The location of the maximum thickness as a function of chord plays a significant role in controlling the hot spots. An adequate airfoil/platform fillet is necessary to control stress concentrations. Stagger angle is a controlling parameter for flutter. Tilt and lean are used to control the root steady stress of the airfoil. Material selection is based on low cycle and high cycle fatigue strength, modulus/density ratio, temperature capability, damage sensitivity, wear/fretting sensitivity, and cost.

Figure 4-8 shows how the process can be institutionalized for the frequency placement of a machined blade. The probabilistic frequency prediction tool relies heavily on finite element analysis. These predictions will be

compared with measured frequencies to define the key variables affecting frequencies, and for calibration purposes. In application, this probabilistic design tool will be used to predict the distribution of frequencies for comparison with the known excitation sources. The probability that a blade will have a natural frequency which approaches the excitation frequency will then be calculated to determine the adequacy of the design. Here the margin is based on process capability and design intent, not past experience. Thus the potential exists to open up tolerances to create a more producible design that meets design intent.

As an example, figure 4-9 shows a conventionally designed blade in which the mean frequency was required to have 10 percent margin to the excitation frequency. The example shown is an unconservative design in that 0.4 percent of the blades will have frequencies at, or below, the excitation frequency. On the contrary, the probabilistically designed blade has caused a much tighter frequency spread. Although the mean frequency is less than that of the conventionally designed blade, this optimal design has virtually no blades with frequencies at, or below, the excitation frequency.

A comparison between a deterministic and probabilistic approach for leading edge durability is shown in figure 4-10. Five variabilities are considered. First, consider the variation in blade amplitude. One deterministic approach assumes that all blades are vibrating at the limiting allowable amplitude. In the probabilistic approach the
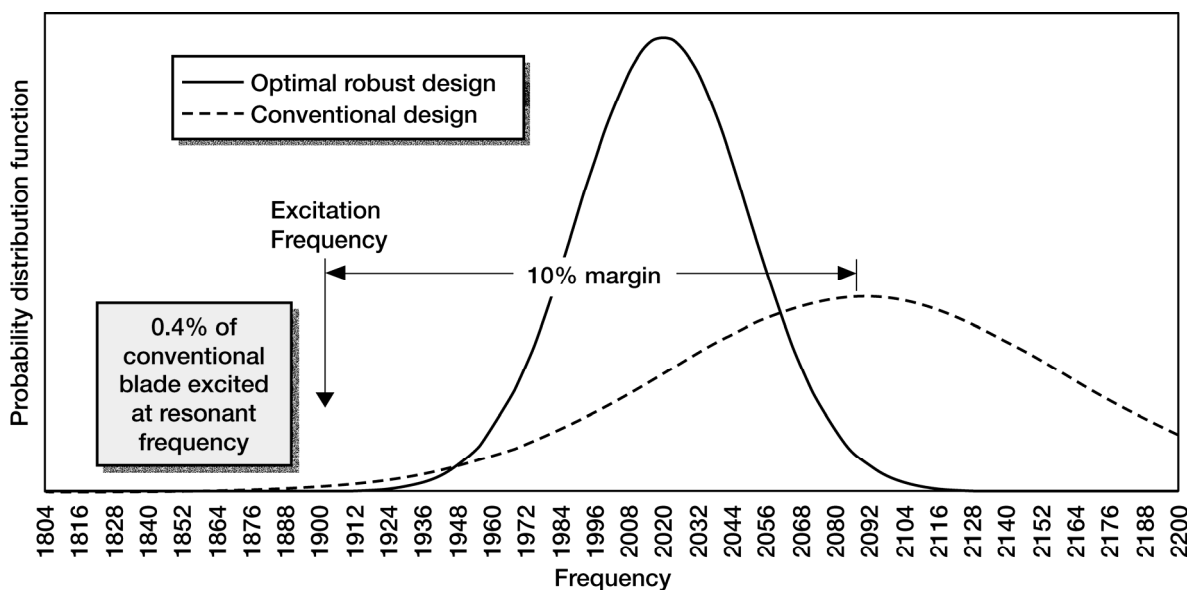
Figure 4-9.—Example of robust design with minimized probability of resonant crossing.

	Current method	DFR method
Blade amplitude	All blades 35% at critical location	Assume max amp use mistuning code for variation
LE strain distribution	Same for all blades	Varies due to blade Tol's (couples with hot spot)
LE damage	Same everywhere	Distributions from field data
Material properties	–3 sigma	Distributions from material data
Life	Bench test empirical	Probabilistic fracture mechanics
Output	Go/no go	Probability of exceeding threshold

Figure 4-10.—Fracture screening–blade leading edge damage capability.

blade to blade amplitude variability is predicted by a "mistuning" method. Next, consider the leading edge strain distribution. Both approaches use finite element methods to predict the strain distribution. In the deterministic approach the strain distribution for a nominal blade is usually applied to all blades. In the probabilistic approach the variation in leading edge distribution is a function of manufacturing tolerances and is similar to the previous discussion on hot spot variation. Next consider leading edge damage. One deterministic approach is to pick the desired damage severity and shape, and assume that it is equally likely at all locations on the leading edge. The probabilistic approach utilizes measured distributions of severity and locations from similar blades in similar field applications. Finally, consider the high cycle fatigue capability of a damaged leading edge. The current approach is to use "minimum property" bench test data. One probabilistic approach is to use the same bench test data but to use a "probabilistic Goodman Diagram". Another probabilistic approach is to utilize probabilistic fracture mechanics. The output of the deterministic and probabilistic methods is significantly different. In the deterministic approach the output is "go/no go" with respect to the ability of a blade design to operate with an assumed level of damage. In the probabilistic approach the output is the probability of failure for the population of blades (of a given design) when operated with assumed damage distributions.

In blade design there is currently no criteria or analysis directly related to blade-to-blade variability in vibratory amplitude. In fact, almost all detailed design analysis assumes that all blades are identical, and respond identically. Figure 4-11 displays a histogram of over 200 cases of light probe data. Considered is the maximum-to-average blade amplitude for each case. As can be seen the variation ranges from 1 to 3.4. In 7 percent of the cases the maximum-to-average is greater than 2. The objective of a probabilistic approach to this problem (high response variability) is to utilize mistuning analysis tools to identify the design parameters causing high variation and to use this knowledge to design low sensitivity bladed disks and blisks.

Another application of probabilistic methods is in certification testing. The current procedure utilizes an instrumented engine test(s) to measure the vibratory responses of a few blades. From this measured response a "Percent Limits" is determined for all blades for all modes of interest. Blade-to-blade variability and engine-to-engine variability are considered by applying safety factors. The measured Percent Limits are compared with the allowable Percent Limits. This process can be greatly improved by combining the limited measured engine responses with analysis, previous experience, and bench and rig tests and conducting computer simulations. The

Histogram of max/avg blade response
255 data sets
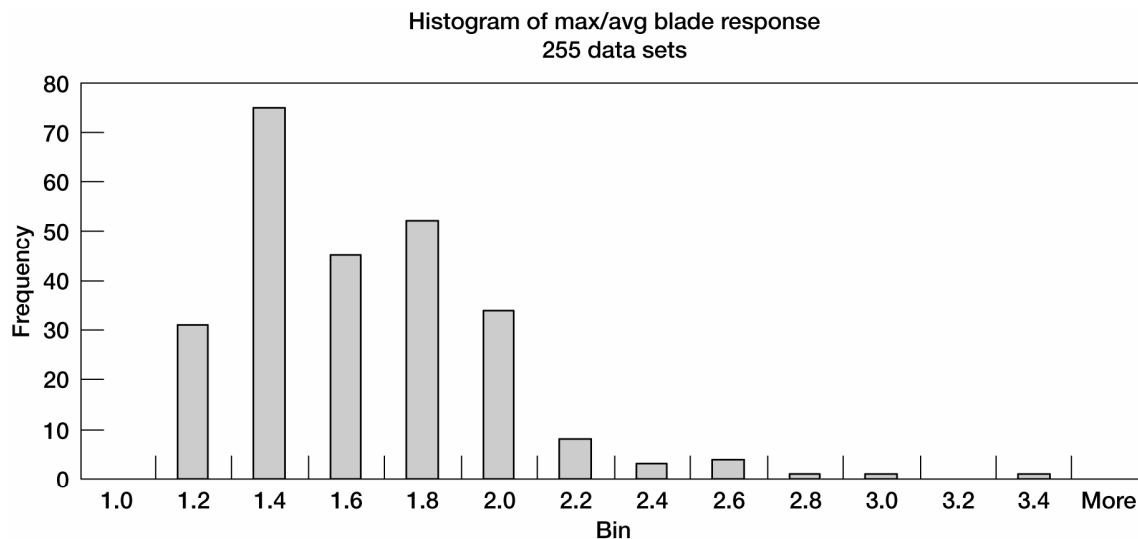
- Primary objective–design blisks and bladed disks to have low sensitivity to mistuning

- Replace current empirical factor with predicted distributions (input to fracture screening)

Figure 4-11.—Blade-to-blade amplitude variation.

simulation includes all known variability's and the defined field usage to determine the probability of blade failure. Thus, the current (nebulous) Percent Limits is replaced with a meaningful probability of failure.

Figure 4-12 shows the many factors which can have an effect on airfoil high cycle fatigue. Two important, and all encompassing, categories of blade response variability are manufacturing and assembly variation and wear and environmental variation. Examples of manufacturing effects are geometric variation in vanes, fit-up variation between struts and flaps, misrigged variable geometry and inlet variation. Examples of wear effects are dovetail wear, shroud wear and tip rub.

Figures 4-13 and 4-14 give an example of an application of this probabilistic assessment approach. A fan blade with leading edge damage was considered. Since this is a case with a significant amount of instrumented engine test data and field experience, measured distributions of vibratory stress and leading edge damage were available. The results of this study were used to make decisions concerning allowable field configurations. The variables were shroud angle, dampers, shroud wear, and leading edge cutback. Figure 4-13 outlines the Monte Carlo simulation technique. For every possible configuration the simulation was run for 30,000 engines. The results are shown in figure 4-14.
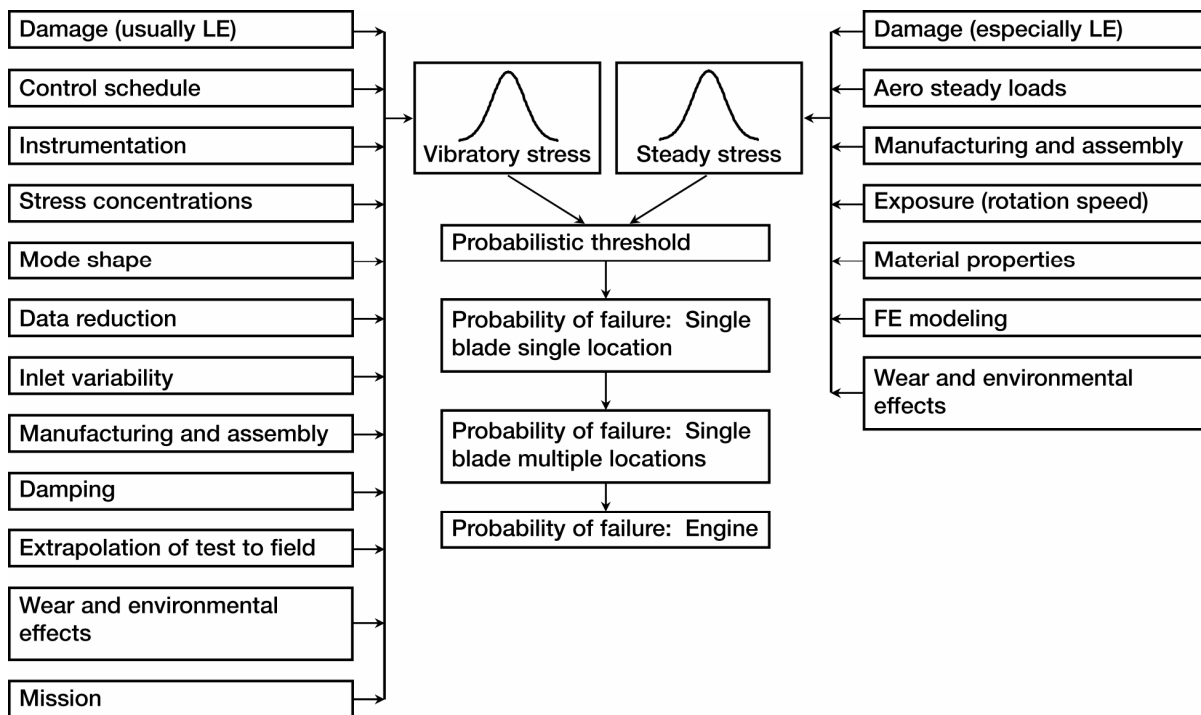
Figure 4-12.—Probabilistic assessment variability factors affecting blade response.
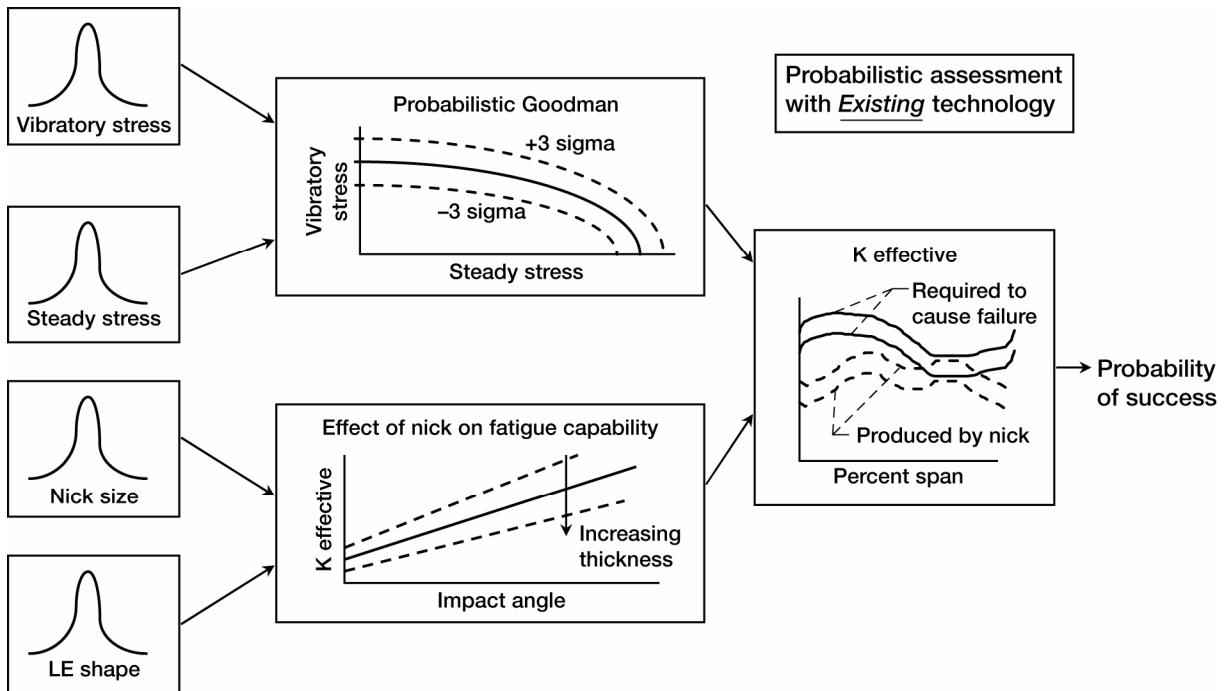
Figure 4-13.—Probability assessment example fan blade with LE nick.

Predicted failures per 1000 engines
No LE cutback

No wear

| Damper | Shroud angle | |
	Lo	Hi
N	2.27 FF	0.10
Y	0.17	0.00

With wear

| Damper | Shroud angle | |
	Lo	Hi
N	5.70	0.23 FF
Y	0.53	0.00

With LE cutback

No wear

| Damper | Shroud angle | |
	Lo	Hi
N	0.47	0.00
Y	0.10	0.00

With wear

| Damper | Shroud angle | |
	Lo	Hi
N	1.87	0.07
Y	0.10	0.00

Figure 4-14.—Probabilistic assessment results.

5.0 Damping Characteristics

The authors thank Dr. K.Y. Sanliturk for his valuable contribution to the friction damping part of this section.

This section begins with a discussion of the importance of understanding damping mechanisms in turbomachinery blading. Next the three primary sources of damping (aerodynamic, friction, and hysteretic) are discussed. Since nearly all turbomachinery has at least one stage which includes a blade friction damper, this section describes types of friction dampers and design analysis methods. The section concludes with a description of advanced damping systems currently being developed. In this section damping is usually defined in terms of the critical damping ratio (usually zeta).

Unlike mass and stiffness properties, damping properties are not easy to model in a general fashion. For this reason, damping models tend to be application specific. For instance, in classical vibration analysis one tends to use the viscous critical damping ratio, $\zeta = c/c_0$, which is suitable for impact modeling where c is the damping coefficient and c_0 is called the critical damping. This particular model is based on the practical observation that most freely vibrating systems eventually die out and reduce to zero motion. Indeed, the solution of the equation of motion yields terms of the type $e^{-\varsigma\omega_n t}$, where ω_n is the natural frequency and t is time, a feature which ensures that the time histories will decay for positive damping. It is also common to study damping mechanisms by examining the energy dissipated per vibration cycle under a harmonic loading. Often, force vs. displacement or stress vs. strain curves are used to determine the amount of energy dissipated by internal hysteresis. Such considerations lead to the definition of loss factor, η. The loss factor approach allows the use of complex stiffnesses: the real part is due to the system's true stiffness while the imaginary part represents damping. This is known as hysteretic damping.

Aerodynamic damping is due to the motion-dependent air loading on the blade. If a time history of the response is available, it can be evaluated by calculating the logarithmic decrement, δ, of the response. Basically, this is the decay rate between successive cycles of vibration. At resonance, the inertia and stiffness properties tend to cancel each other out and hence, the magnitude of the response is controlled by the amount of damping. Under this condition, all damping models can be shown to be equivalent to each other.

$$\zeta = \frac{\eta}{2} = \frac{\delta}{2\pi} = \frac{0.5}{Q}$$

It is very difficult to design blading which is free from being excited at its natural frequencies. Therefore, damping is required to limit resonant responses. Shown on figure 5-1 is an experimental Campbell Diagram for a blisk.[1] As can be seen there are numerous modes excited by numerous forcing functions. Although following good design practices can result in resonant crossings which minimize the likelihood of an unacceptable response, the existence of reliable damping systems greatly decreases the risk of high cycle fatigue failures. For most blading the primary source of damping is aerodynamic, which is typically less than 1 percent of critical damping for the first flap (1F) mode, and is much less for higher modes of vibration. Not only do current design trends increase the usage of low damping designs such as blisks, but there is also a trend to design lower aspect ratio blades. Lower aspect ratio designs result in more modes (and closer spaced, modal compression) being excited.

When a blade is in flutter, the aerodynamic damping is negative. However, in most situations the blade is significantly far away from the flutter boundary and there is positive aerodynamic damping. For damperless, shroudless blades the only sources of damping are aerodynamic, root friction, and hysteretic (internal material). For large blades it has been found that the aerodynamic usually dominates for the 1F, first torsion (1T), and second torsion (2T) modes. Although there is very little measured data on damping in dovetail and firtree attachments, the trends show that it is smaller than aerodynamic damping for the 1T and 2T modes, and is greater than the aerodynamic damping for the second and third bending modes (2F and 3F). Although hysteretic damping is proportional to the square of frequency, even for the higher frequency stripe modes this internal material damping is negligible. For blisks it has been found that the total damping is similar to that of bladed disks. For the higher modes blisks usually

---

[1]A bladed-disk in which the blades and the disk are machined together from a single piece. Blisks are very lightly damped because there are no losses at the blade root which is an integral part of the disk.

have less total damping than an equivalent bladed disk. It should be noted that a well designed friction damper can result in values of critical damping ratio greater than 2 percent.

First, a word of warning concerning figure 5-2. This figure is intended to give very approximate values of damping, and is to be used only to gain a basic understanding of the importance of the various sources of damping for turbomachinery blading. This table lists typical values of damping (in terms of the amplification factor Q) determined from analysis, bench test, rig test, or engine test. The aerodynamic damping is predominantly from computations, the attachment (dovetails, firtrees) friction and hysteretic data is from bench test. The friction damper data is for a "well-designed" turbine blade platform damper. Note that poorly designed friction dampers can have much higher values of amplification factor. The total system damping data on the bottom of the figure is from engine tests for a wide variety of fan and compressor (inserted) blades. Damping determined from engine test data is determined using the "half-power" technique and should be considered to be contaminated by blade mistuning effects. With this warning in mind, the dovetail damping can be inferred from comparing this data with the aerodynamic damping values. Finally, it should be noted that shrouded blades are not considered on this figure. Mid-span and tip shrouds can serve as excellent dampers and produce effective damping performance equal to that of platform friction dampers.

- Numerous strong forcing functions exist which cannot be avoided

- The primary damping source, aerodynamic, is generally small and unreliable

- Future trends make the problem worse
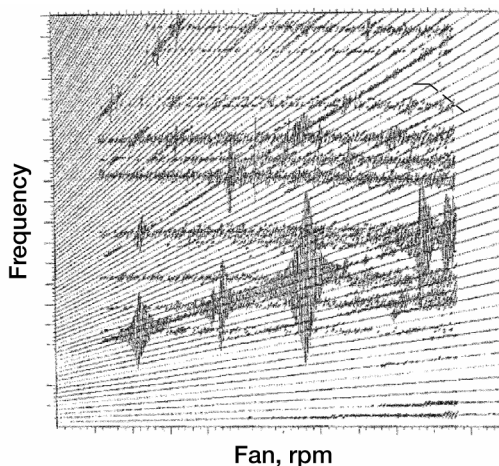
Figure 5-1.—Motivation for damping.

(Q's)

Mode	Aerodynamic	Attachment friction	Hysteretic (titanium)	Friction dampers
1F	50-100	100-500	1000-2800	15-30
1T	100-200		5500-6500	
2F	300-1000		1200-4000	
2T	100-200			
2S	300-2000			

Total system damping
(inserted blades, from engine SG data)

Mode	Total Q
1F	30-130
2F and 3F	80-100
1T and 2T	20-190
2S and 3S	60-150

Figure 5-2.—Turbomachinery blade damping–data and lore.

The most common type of damper for turbomachinery blading is the platform friction damper which is used in most high pressure turbine blades and some fan, compressor, and low pressure turbine blades. The damper is usually a piece of metal which is centrifugally loaded against the bottom surface of the platform(s). There are two basic types of platform damper, blade-to-blade and blade-to-ground. In the blade-to-blade damper the damper piece simultaneously loads the platforms of two adjacent blades. The differential motion between the two blades results in a slipping of the surfaces between the damper and the two blade platforms. In the blade-to-ground damper the damper piece is supported in some manner to the disk, or another part mated to the disk. The damper is then loaded against the underside of one blade platform. The differential motion of the blade and the disk results in the slipping of the damper and blade platform surfaces. Some companies require platform dampers on all high pressure turbine blades. The platform damper is usually most effective for the first bending mode. Looking at a typical high pressure turbine (HPT) blade Campbell diagram will reveal that the 1F mode intersects approximately the 10th engine order line at high speed. Since the number of upstream vanes, or number of fuel nozzles is always larger than 10, you may wonder why a damper is mandatory. The answer is that as an engine ages in the field, burning, erosion and wear result in the generation of low engine order excitation. The best example is a partial vane burn-out. Having an effective platform damper will allow a first stage high pressure turbine blade to withstand the excitation produced by time induced flow nonuniformities.

The "split-ring" type damper has been used for many years in gears. A ring rides in a circumferential groove in the gear. The ring is cut at one circumferential location to allow it to rub against the gear at all circumferential locations. In the turbomachinery application the "split-ring" can be either a relatively rigid ring or a relatively soft sheet metal ring. It is most commonly used in blisks or for the rotating side of a labyrinth seal tooth ring. For blisks this type of damper has been shown to be effective for the low nodal diameter, lower order modes.

Although the primary purpose of mid-span and tip shrouds (a.k.a. snubbers and dampers) is to raise the frequency of high aspect ratio blades, these devices can be very effective dampers. Design analysis techniques are now being developed to maximize damping. However, the dynamics of the shroud interface are very complicated, and engine test data has shown that the damping can be very sensitive to subtle changes in the shroud interface conditions.

Although most aeroelastic analyses for turbomachinery blading are approximated well with linear models, the friction damper is inherently a nonlinear device, requiring a nonlinear analysis. When friction dampers were first introduced the assumption was that the damper is always in a slipping condition when the blade is vibrating. As a result the approach to increase the amount of damping was to increase the level of the damping force, $\mu*N$. Since it was easier to change the damper dynamic weight than the friction coefficient, this method was chosen to increase damper effectiveness. Many times this resulted in a damper which was actually less effective. The reason is that, as the damper dynamic weight increased, the damper became stuck during most, if not all, of the vibratory cycle. This was the motivation for the development of nonlinear damper models which considered the stick/slip nature of the blade/damper interface during the vibratory cycle. Figure 5-3 shows the first-generation physical and mathematical models used to investigate damper dynamics. The airfoil is modeled as a single degree-of-freedom oscillator and the damper is modeled as a Coulomb friction force tied to ground by a spring. When the mass is displaced the damper "sticks" until the spring force equals $\mu*N$, at which point the damper "slips" with a constant damper force. The slipping occurs until the mass reaches its maximum displacement. The mass then moves in the opposite direction and the damper sticks until the spring force equals negative $\mu*N$, when the damper begins to slip. This stick-slip behavior is repeated every vibratory cycle.

Figure 5-4 illustrates the dependence of damper effectiveness on the normal force. When the normal force is zero, the damper has no effect and the vibratory stress is only limited by the other damping in the system. With a relatively small normal force the damper slips during most of the vibratory cycle, produces some damping, and reduces the peak vibratory stress. As the normal force is further increased, it is found that the damping effectiveness increases until a point, and then begins to loose effectiveness. It has been found that this point of optimal damper effectiveness is when the damper is slipping for approximately half of the vibratory cycle. At some point the normal force is high enough that the damper sticks during the entire vibratory cycle. Thus, the damper has become a stiffener and changes the frequency and mode shape of the blade, but provides no damping. Note, that this is not always undesirable. For example, a stuck platform damper can change the mode shape to reduce the amount of vibratory stress in the blade shank or dovetail. If the mode of interest is critical in this area, the stuck platform
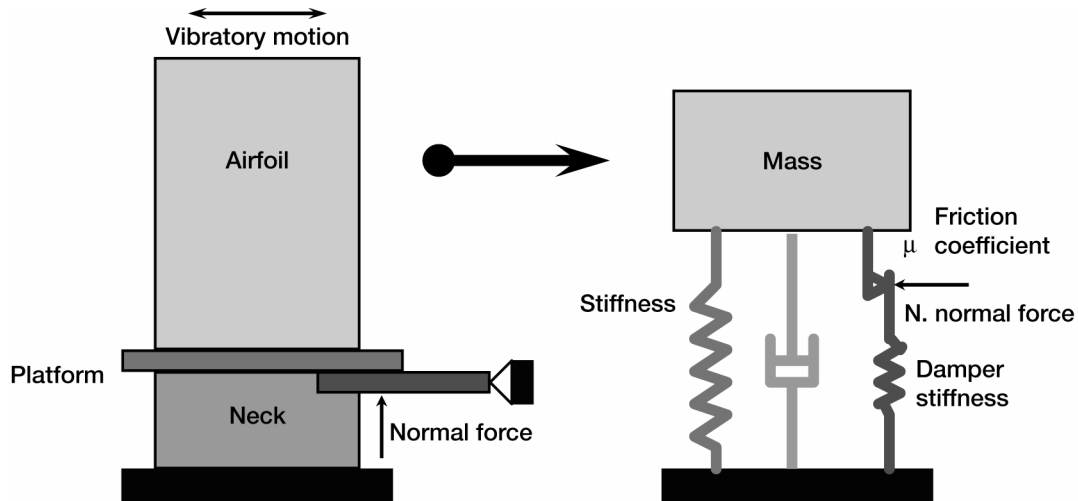
Figure 5-3.—Platform damper physical and math models.
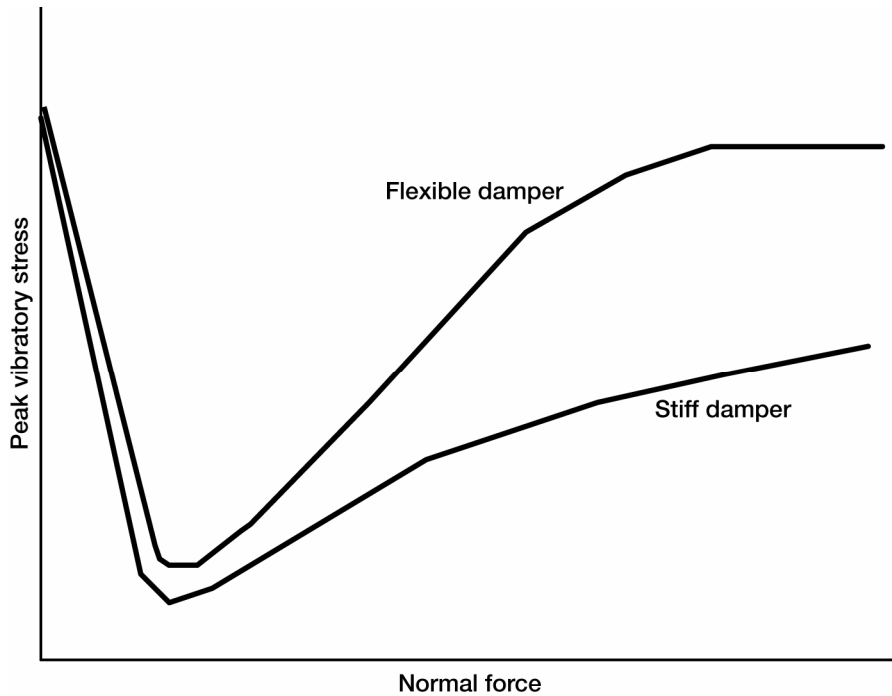
Figure 5-4.—Characteristics of platform friction dampers.

damper (but really a stiffener) may be beneficial. Also shown in figure 5-4 is the difference between a flexible and stiff damper. With all other parameters constant, it is always beneficial to make the damper as stiff as possible. However, the damper stiffness is usually dependent on its weight.

When comparing analytical predictions with experimental data it is usually found that good agreement is found up to normal forces near the optimal value. At normal forces significantly beyond this value, the experimental data usually shows lower peak vibratory force (more effective damper) than predicted. A common explanation is that at high normal forces, when a simple model says that the damper is stuck, there is actually micro-slip behavior at the interface of the two surfaces. Because of this behavior, it is common practice to design a damper with a normal force somewhat higher than the optimal value.

To design an "optimal" damper normal force the magnitude of the excitation force must be known. In many cases the damper must be designed before the engine has been tested and the excitation force is unknown. Figure 5-5 illustrates a characteristic of friction dampers which may be considered when designing a damper with an unknown excitation force. First consider the medium weight damper curve. For low excitation forces the damper is always stuck, and hence shows a linear relationship between force and response. At some point the damper starts to slip. As the force continues to increase, the response stays relatively constant over a relatively broad range of force. As the force again increases a point is reached where the damper is slipping over most of the vibratory cycle. From this point onward, the slope of the curve is near that of the low force region. It has also been found that the value of "plateau" region is dependent on the damper dynamic weight. Thus, if the allowable vibratory response is known, the damper weight can be designed to be as close to the allowable value as possible. This approach increases the range over which the damper is effective.

As previously mentioned, friction dampers and ring dampers are usually more effective in the lower order modes. A need exists, especially on blisks, to provide damping for higher modes which have little motion at the blade root. A number of different techniques, especially viscoelastic, have been shown to be effective in bench tests. The viscoelastic damper involves getting the material to be strained in shear. Particle damping involves small particles which impact each other and rub against one another as the blade vibrates. The difference between powder and particles is somewhat arbitrary and has been based on the size of the particles and the physical mechanism involved. It is thought that powder dampers include some of the same mechanisms of both the particle and viscoelastic dampers. For approximately 20 years, piezoceramic crystals have been used to excite blades, and passive piezoceramic dampers are currently being used in sporting equipment, such as skis. Therefore, there has been some interest in applying this technology to blades.
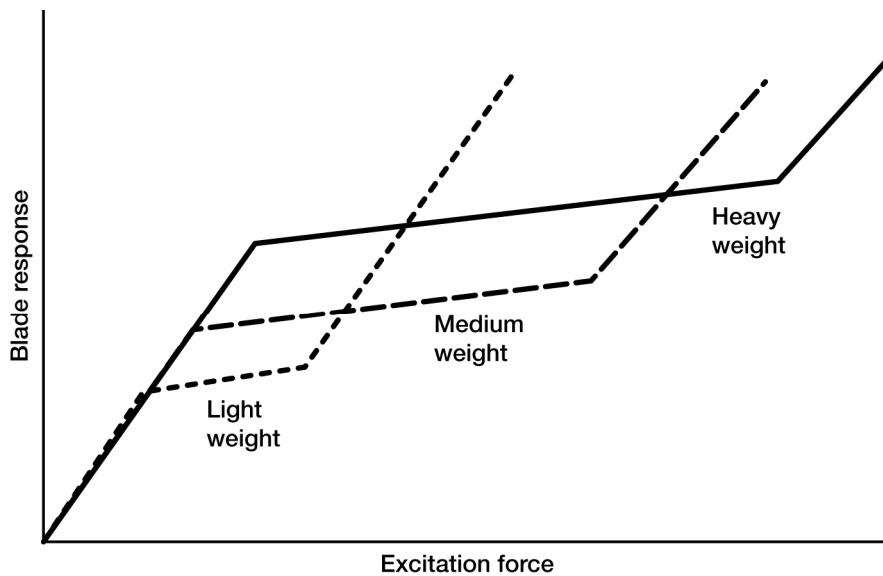
Figure 5-5.—Damper performance curves.

- Viscoelastic, particle, powder, passive piezoceramic

- Viscoelastic constrained layer damping treatment
  - Applied to blade surface
  - Designed for 2S mode and demonstrated very effective in bench test
  - Could not withstand the centrifugal G field

- Test of viscoelastic material in hollow blade was ineffective for 2S mode
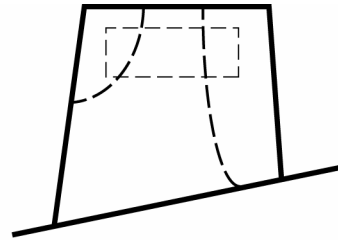
Measured Q's

Mode	Blade H			Blade X		
	Untreated	CLDT	Ratio	Untreated	CLDT	Ratio
1F	2222	389	5.7	827	331	2.5
1T	843	122	6.9	527	331	1.6
2F	2405	131	18.4	728	102	7.1
2S	1195	101	11.8	530	58	9.1

Figure 5-6.—Advanced damping methods.

Figure 5-6 gives the results of attempts to apply viscoelastic damping to a blisk airfoil. A viscoelastic material and constraining layer were applied to two blades (H and X) with the goal of damping the second stripe (2S) mode. The bench test results show that this method was very effective in damping the 2S and 2F mode and less effective on the 1F and 1T mode. Also, note that a fighter engine has used constrained layer viscoelastic damping on the inlet guide vanes (non-rotating) for over 20 years. However, a rotating test of the above application showed that it could not withstand the centrifugal force field. In another damping attempt, the cavities of an existing hollow airfoil were filled with a viscoelastic material and tested with negative results. The conclusion is that a constrained layer viscoelastic damper can be effective if properly designed and placed in the airfoil. The major remaining problem is how to execute this design without degrading the structural integrity to a point which defeats the purpose of reducing the vibratory amplitudes.

Related to the subject of damping is vibration control. Although active control of blade vibrations is not thought to be practically desirable, the notion of adaptive control is under consideration. In adaptive control a non-intrusive sensor monitors blade vibrations. When the blade vibrations exceed prescribed limits, the engine control system takes an action designed to reduce vibrations. Examples of possible actions are not allowing the engine to operate steady state in a prescribed speed range (speed avoidance), or adjusting the variable geometry of the engine to reduce the forcing function.

Due to reduced weight requirements, the use of damping to control the maximum vibration amplitudes is a very attractive route. It is no exaggeration to say that the two main aeroelastic phenomena, flutter and forced response, are controlled by damping. Flutter occurs when the sum of the aerodynamic and mechanical damping becomes negative, indicating that energy is being fed into the structure.

The amplitude of the forced response is controlled by the total force to total damping ratio. It is clear that either the excitation force needs to be reduced or the damping must be increased. An accurate determination of both aerodynamic and mechanical damping can be extremely difficult. Both quantities not only vary from mode to mode, but also can be significantly non-linear with respect to vibration amplitude.

As can be shown from figure 5-7, many sources of damping exist. However, broadly speaking, the basic damping mechanisms are poorly understood in most cases. Although some approaches have been tried during engine development programs, the consensus appears to be that current technology and understanding are not sufficient to use damping for active vibration control. However, although the exact damping mechanisms are still not fully understood, friction dampers provide an effective means of reducing forced response vibration levels.

A typical application of the dry damping concept in gas turbines is the so-called friction damper which is, essentially, a small piece of metal loaded by the centrifugal force against the underside of the platforms of two adjacent blades as shown in figure 5-8. If the damper is too light, the normal force will be small and so will be the friction force. In this case, the damper will not be able to dissipate enough energy. On the other hand, if the damper

- Aerodynamic damping
- Internal energy dissipation
    –Inherent material damping
    –Filler materials, particle dampers
    –Coatings (ceramic, enamels)
    –Constrained layer damping (viscoelastic materials)
- Friction damping
    –Metal-to-metal contact devices at roots and shrouds
- Viscous dampers
    –External fluid dampers
- Smart materials
    –Strain-voltage generating materials for active and passive control

Figure 5-7.—Damping sources.
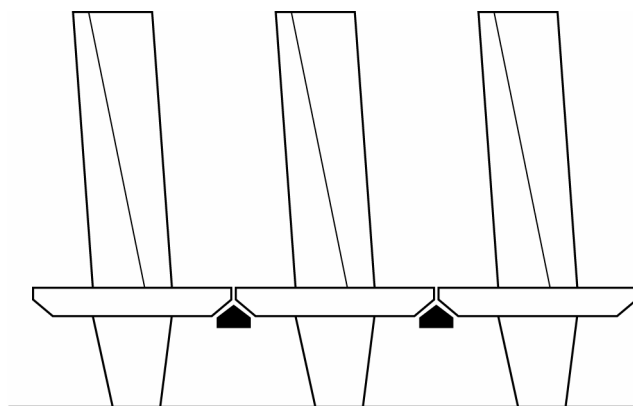
- FDs are placed at the blade roots (or at shroud interfaces).

Figure 5-8.—Friction damping modeling.

$$F = kX \text{ if } F < F_{critical}$$

$$F = \begin{cases} sX - tX^2 & \text{if } 0 < X < s/2t \\ s^2/4t & \text{if } X \geq -s/2t \end{cases}$$

Macro slip

Micro slip
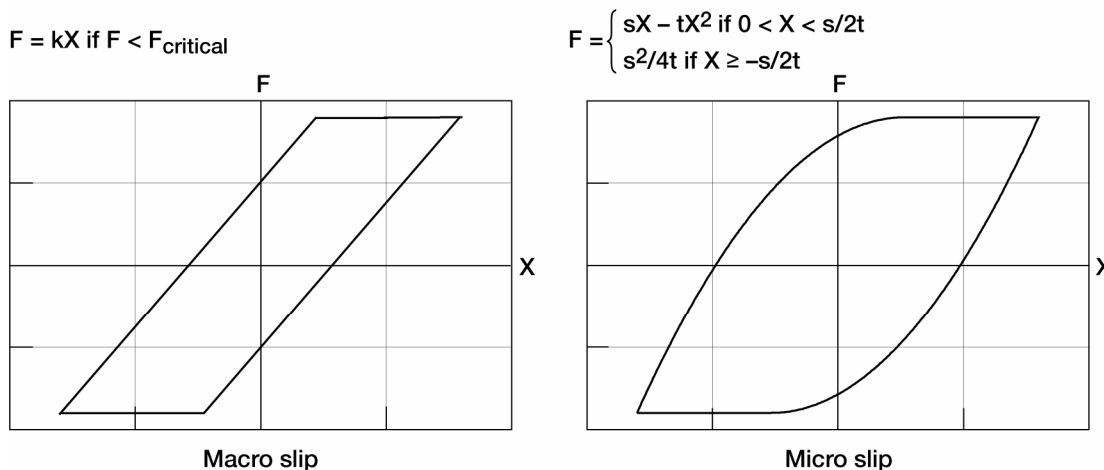
- Significant non-linear behaviour
- The aim is to obtain a representative relationship between the friction force and the vibration amplitude

Figure 5-9.—Force versus displacement characteristic.

is too heavy, the normal force will be too high and no relative friction motion will take place. Therefore, the main design criterion is to determine the optimum damper weight that will produce optimum relative displacement that will give maximum energy dissipation by friction. In practice, the amount of displacement is very small and vibration mode-dependent. It is not unusual to place several dampers per blade so that at least one damper is effective.

A characteristic of non-linear systems is the dependence of the response on the vibration amplitude. In the case of a friction damper, the key issue is the determination of the friction force at a given amplitude. Several modeling techniques, ranging from Hertzian contact to semi-empirical formulations, have been used by the researchers. The overall shape of the force-displacement curve, the so-called hysteresis loop, is likely to remain the same for most practical cases. Two models exist for this basic shape and are shown in figure 5-9. The macro-slip model consists of a linear spring and a dry friction element. Until the force reaches the critical level, the force-displacement relationship remains linear. When the force reaches this critical value, its magnitude remains constant regardless of further increases in the displacement values.

• Elliptical relative contact motion.
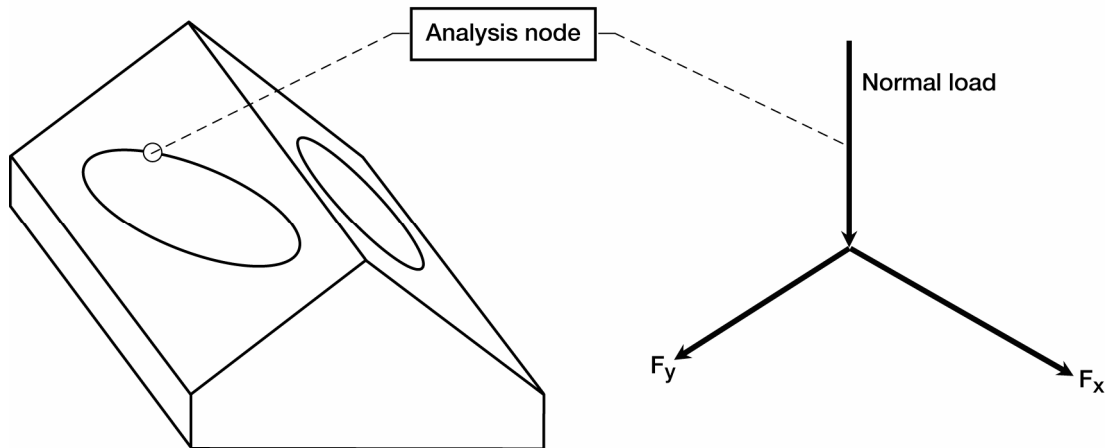
Figure 5-10.—Example: Cottage roof damper.

Also shown in figure 5-9 is a more refined version, the micro-slip model, that considers the effect of partial slip at some parts of the interface before the gross slip occurs. The parameters s and t depend on several factors, such as the effective contact area, surface asperity, friction coefficient, etc.

A major modeling problem is the determination of the actual relative motion that gives rise to friction damping. Several modeling levels, ranging from point contact to full three-dimensional motion, are possible. In the example shown in figure 5-10, a relative elliptic motion is considered on the inclined surface of the damper. It should be noted that the normal (and friction) forces are not necessarily the same for the left and right surfaces. Once an analysis node is defined on the elliptical path, the friction forces in the xy plane of the surface can be defined by considering the static and dynamic cases. Once this is done, the variation of the friction forces with amplitude is obtained using a semi-empirical method. A hybrid macro/micro slip model is used and the required coefficients are determined by laboratory measurements.

6.0 Full Scale Engine Testing

This section begins with a description of test vehicles used in aeroelastic research and engine development, but the remainder of the section deals with full scale engine testing for aeroelastic verification of blade designs. Previous sections described the complexity of aeroelastic design analysis. Although we have, and use, sophisticated design analysis tools, test validation of new engine designs will be required for many years to come. Therefore, it is important to have an understanding of instrumentation, test methods, and how to interpret the test results. These subjects will be briefly discussed in this section.

Spin rigs, linear cascades, and annular cascades are primarily used in research. However, spin rigs are occasionally used in damper development. Component rigs are mostly used for concept development. The primary experimental tools in engine development are core, full engine, and flight tests. Flight tests for commercial engines are conducted on "flying test beds." For military engines instrumented (aeroelastic) flight tests are not usually conducted. Flight envelope effects are typically explored in an altitude test facility.

Shown in figure 6-1 is an experimental Campbell Diagram. This is usually constructed by performing a slow engine acceleration or deceleration. A Fourier analysis of the measured blade response is then performed at regular speed intervals. At each speed the significant components of blade response are plotted as a vertical line at the response frequency. The height of the vertical line is proportional to the amplitude of response. The specific data shown in figure 6-1 is for a slow acceleration of a fan blade on a high operating line. As can be seen there are three obvious aeromechanical responses. As the speed reaches 2000 rpm the blade enters a region of stall flutter. Notice that the frequency is not synchronous with the rotor speed. From the measured frequency and comparison with finite element analysis or bench test, it is known that this is the second blade mode. The number of nodal diameters
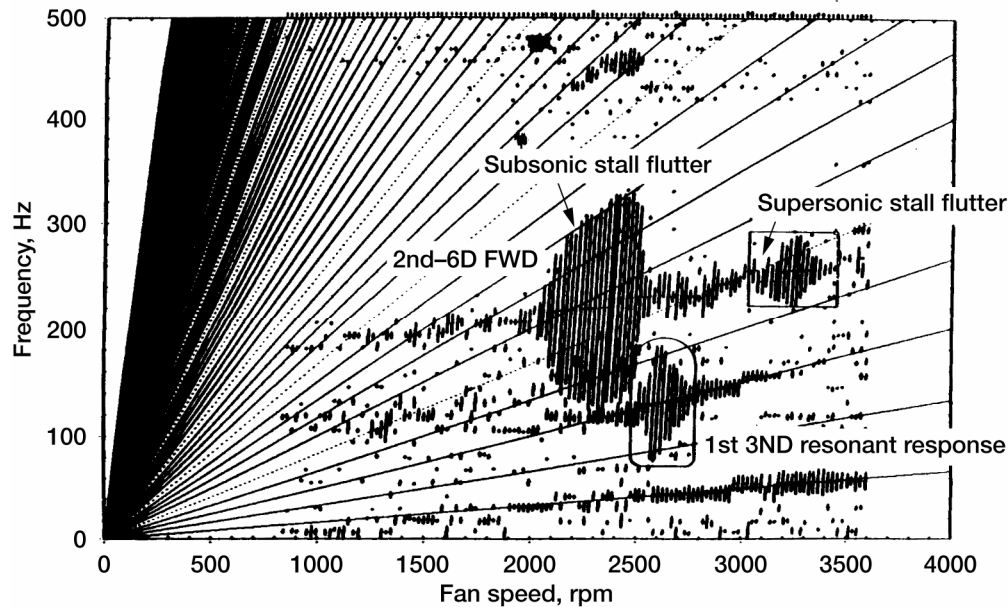
Figure 6-1.—Experimental Campbell diagram.

is usually determined from non-rotating instrumentation such as light probes or casing pressure transducers. The number of nodal diameters is determined by comparing the Doppler shifted stationary frequency with the rotating blade frequency. Also, note the small region of 460 Hz response at 2400 rpm. This frequency is exactly double that of the flutter frequency which suggests that the flutter response is not exactly sinusoidal.

Returning to figure 6-1, the blade exits stall flutter at a speed of approximately 2500 rpm and immediately enters a region of first mode 3/rev forced response. Notice that this response is synchronous with the rotor speed and the blade response tracks the 3/rev line, not the blade natural frequency. The behavior in which flutter is apparently suppressed by a resonant response is seen quite often, but now well understood. As the engine continues to accelerate the blade leaves the 3/rev response and enters a second flutter region at approximately 3100 rpm. The final response of interest in figure 6-1 is the 1/rev response. This is an off-resonant response of primarily the first mode. This response is generally low in amplitude, unless the frequency 1/rev margin of the lowest frequency mode at high speed is inadequate.

Two primary methods of measuring blade vibrations during engine tests are strain gages and light probes. Strain gages and the necessary electrical leads are directly applied to the blade surface. The leads are routed down the airfoil and out of the flowpath where the signal is transformed to the nonrotating reference frame by a slip ring or telemetry system. Although up to 4 strain gages are applied per blade, and up to 4 blades per stage are instrumented, fewer numbers are usually used. (Note that there have been research tests with all of the blades strain gaged). Therefore, a limited set of data is produced.

Light probes have been developed to measure **all** blades. A light probe senses the arrival of the blade tips and compares the actual arrival time with the expected time assuming that the blade is not vibrating. The difference of expected and actual arrival times is used to determine the tip vibration. This process works well for non-synchronous vibration. For synchronous vibration the vibrating blade is at the same point in its vibratory cycle every time that it passes under the light probe. Therefore, the vibration appears to be a steady deformation. Two methods have been used to get around this difficulty. The "phase-shift" method takes advantage of the fact that there is a 180 degree phase shift as a structure goes through a resonance. In this method a slow acceleration is conducted and the apparent steady deformation is recorded as the blade passes through the resonance. This data is used to deduce the vibration amplitude. A more sophisticated method is to use multiple light probes circumferentially. In this method the blade is sampled multiple times per vibratory cycle and this data is used to determine the vibratory amplitude.

To help prevent failures in development testing, blade vibration amplitudes should be monitored real time and the allowable vibratory amplitudes should be determined prior to test. An example of this is shown in figures 6-2 and 6-3. First the steady stresses are determined, usually with a finite element analysis. Figure 6-2 shows the steady radial stresses for a turbine blade at the root of the blade. The total stress is the sum of the thermal, centrifugal, and gas bending stresses. Also, shown in figure 6-2 are the normalized vibratory radial stresses. The steady and vibratory stresses are plotted on a Goodman Diagram (fig. 6-3) to determine the critical area and the limiting vibratory stress. The critical location (in this case point C) is usually placed on the 10^7 minimum life line. Now the limiting vibratory stress at the strain gage location (point S) is determined. To be conservative the allowable stress is generally defined as 50 percent of this limiting stress. Note that this is a simple two-dimensional example. In practice all points in the blade and all components of stress must be considered. Also, the allowables should be defined as a function of speed. For light probes a similar procedure is used, except that a finite element model is used to relate tip displacement to blade stress.

The various aeroelastic phenomenon experienced by blades show different character in their strain gage signals. First consider flutter as shown in figure 6-4. As previously mentioned the flutter frequency is not synchronous with the rotor speed. One method of "mapping" fans and compressors is to throttle the machine at a constant speed. A variable nozzle is commonly used. As the flutter boundary is approached the strain gage signal shows a low ampli-tude, high modulation, and other blades are vibrating at slightly different frequencies. As the flutter boundary is penetrated the amplitude increases significantly, the modulation decreases and the blades lock into a system mode, where the blades are at the same frequency, and there is a constant phase angle between blades.

When throttling the machine as described above, a different non-synchronous response is sometimes seen and is shown as the top chart in figure 6-5. It has the same appearance as incipient flutter. That is, a low amplitude and high modulation, but as the machine is throttled further, the amplitude increases, but blade row does not lock into a system mode. The modulation is high and the blades vibrate at their individual natural frequencies. Also, the excitation appears to have a rather broad frequency content in that the first four modes are usually excited. This response is thought to be similar to wing buffeting at high angles of attack and is sometimes called "separated flow vibrations". The third type of throttled behavior is compressor stall and its precursor, rotating stall. The bottom chart in figure 6-5 is a blade response during rotating stall.
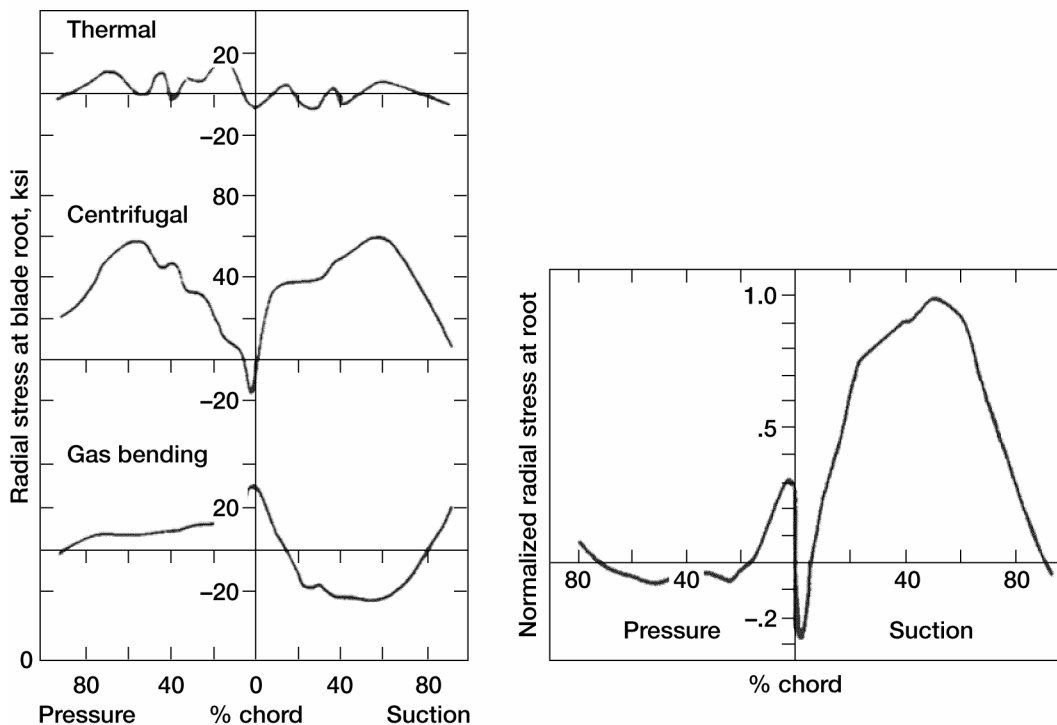
Figure 6-2.—Steady and vibratory stresses.
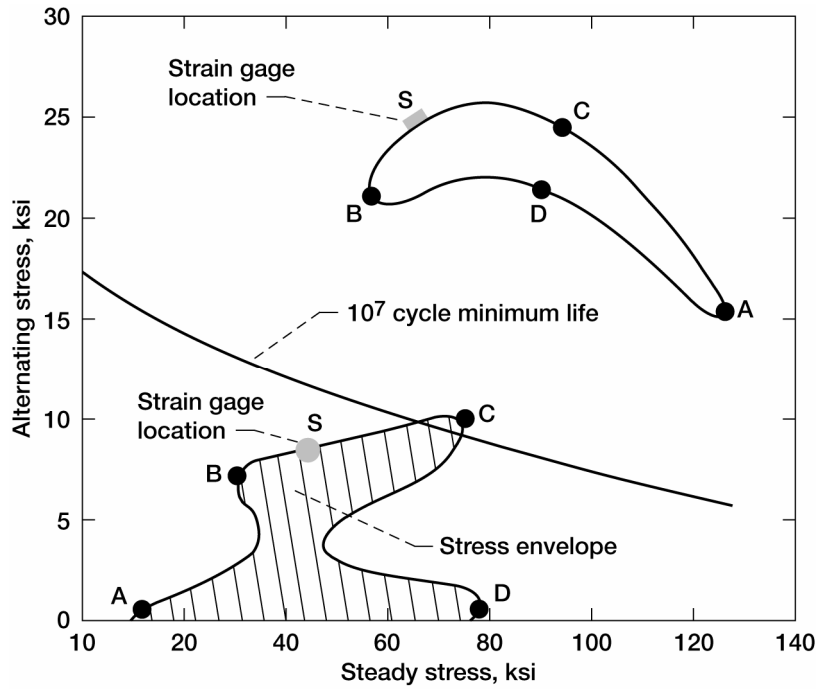
Figure 6-3.—Goodman diagram/allowable stress, vibratory stress.
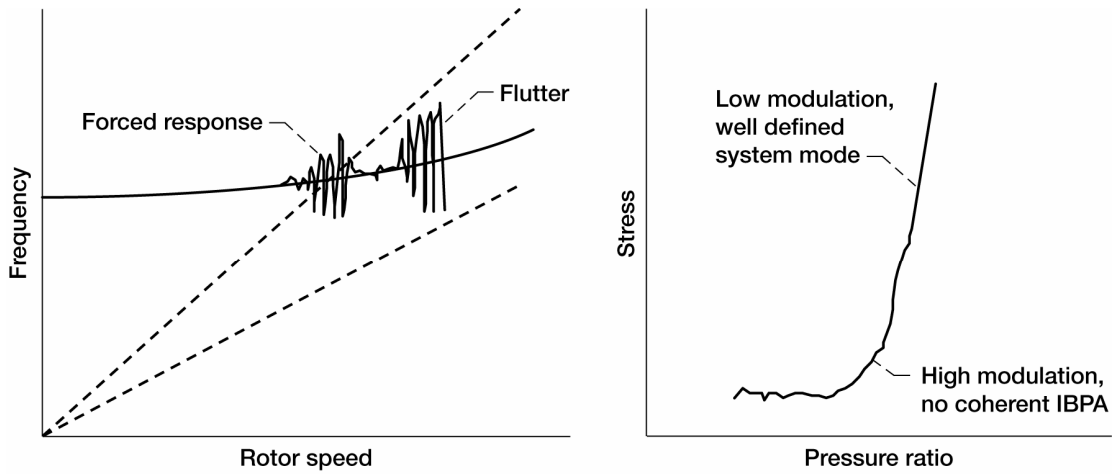
Figure 6-4.—Characteristics of blade vibratory signals–flutter.
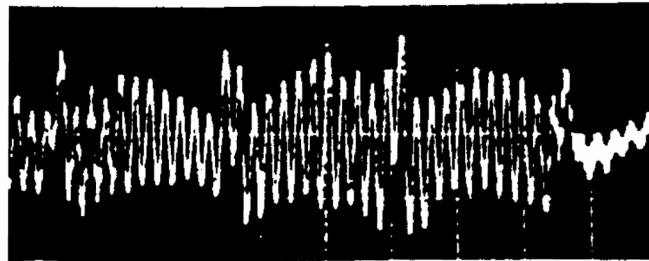
Figure 6-5.—Characteristics of blade vibratory signals–forced response–
non-synchronous.

(8/rev)

1 rev   (14/rev)

1 rev   7 cycle
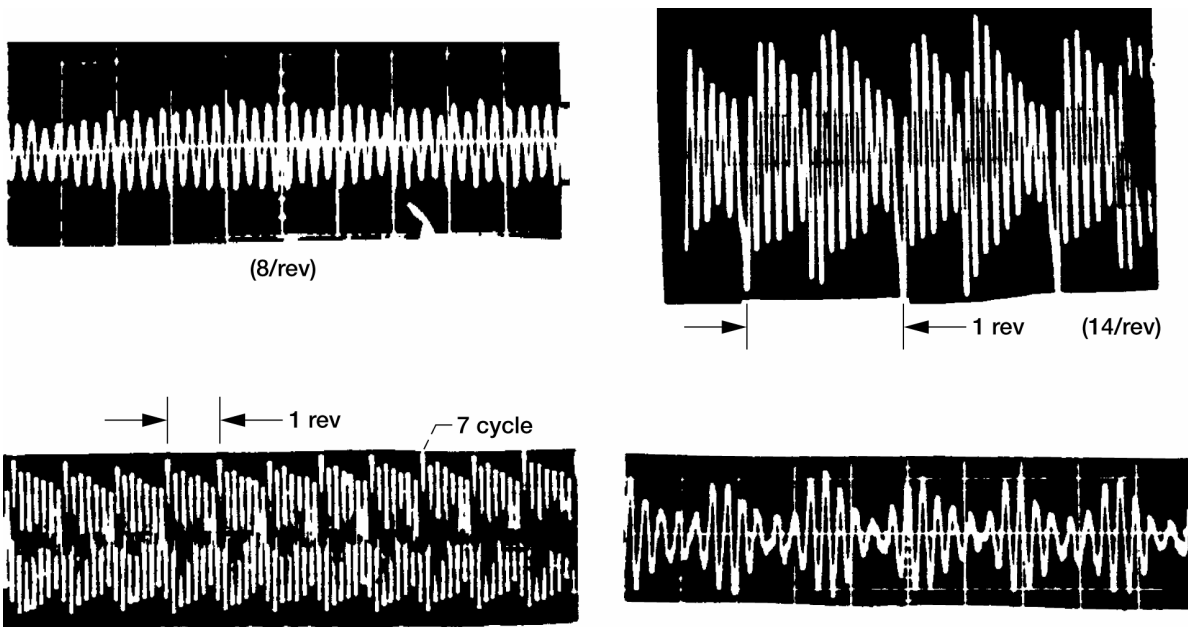
Figure 6-6.—Characteristics of blade vibratory signals–forced response–synchronous.

There are many different types of synchronous response signals. Four of these are shown in figure 6-6. The top left shows a simple 8/rev resonance. The bottom left chart shows the response signal when one of the vanes has been misassembled. The wake from this misassembled vane is experienced once per revolution and the modal frequency is approximately 7/rev. Note that the response of an HPT blade to a single burned out vane has a similar appearance. The chart on the top right show a single mode response to a mechanical excitation where the tip rubs the case twice per revolution and the modal frequency is approximately 14/rev. The chart on the bottom right is an obvious case of beating. This can occur when the damping is very low and the excitation frequency is near to the natural frequency, or when the blade is excited by two excitation sources very close in frequency.

Whereas figure 6-6 shows single mode responses, figure 6-7 shows twin mode responses. That is there are two resonant crossings at the same speed. The top response displays the signal appearance when the low frequency
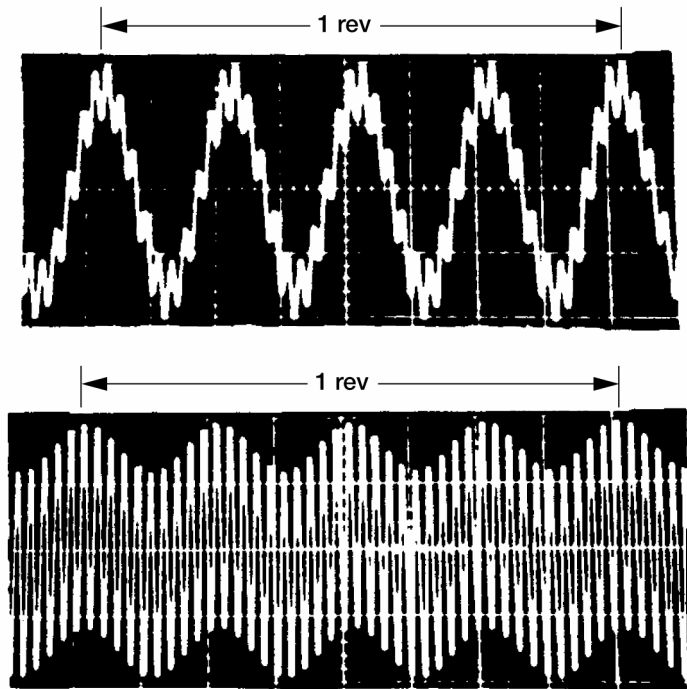
Figure 6-7.—Characteristics of blade vibratory signals–forced response–synchronous.

mode has the higher amplitude. The opposite situation is shown in the lower signal display. If it is known that there are two strong excitation sources such as 4 struts and 40 vanes, a good design practice is to not have any two modes with the same frequency ratio (in this case 10).

The final example of a blade response signal is shown in figure 6-8. Displayed here is the blade response to an entire compressor stall. In this case it is a four pulse stall where the blade sees a very high transient load. It is not unusual for these transient responses to be nearly twice of the vibratory limits. In compressor design it is important to estimate the axial displacements due to stall loads. This is a key parameter in setting axial spacing between airfoil rows.

If everything is constant except the inlet density and the forced response problem is linear, the response amplitude should be a linear function of density. However, it is found from experience that the dependency is usually somewhere between a square root and linear dependency. One reason is that other variables are changed. An example of how temperature and variable geometry position are related is shown in figure 6-9. The figure on the left is a Campbell Diagram showing a 2S vane mode being excited by a 22/rev (downstream rotor) at RS1 and a 20/rev (upstream rotor) at RS2. Since the variable geometry is scheduled on corrected speed, not physical speed, the resonant crossing can be seen at various positions of the vanes which are exciting the blades. The middle diagram shows the vane position (stagger angle) as a function of physical speed. The schedule including points B and E is for a nominal inlet condition. The low inlet temperature schedule includes points C and F. The high inlet temperature schedule includes points A and D. The effect this has on the vibratory stress is shown in the chart on the right. As expected the vibratory stress decreases as the vane is opened (lower stagger angle). Also, the 22/rev crossing causes higher response amplitudes than the 20/rev crossing. Not that it is unusual for the downstream excitation source to result in a higher response than the upstream excitation source. One reason is that the 22/rev crossings occur at more closed vane angles.
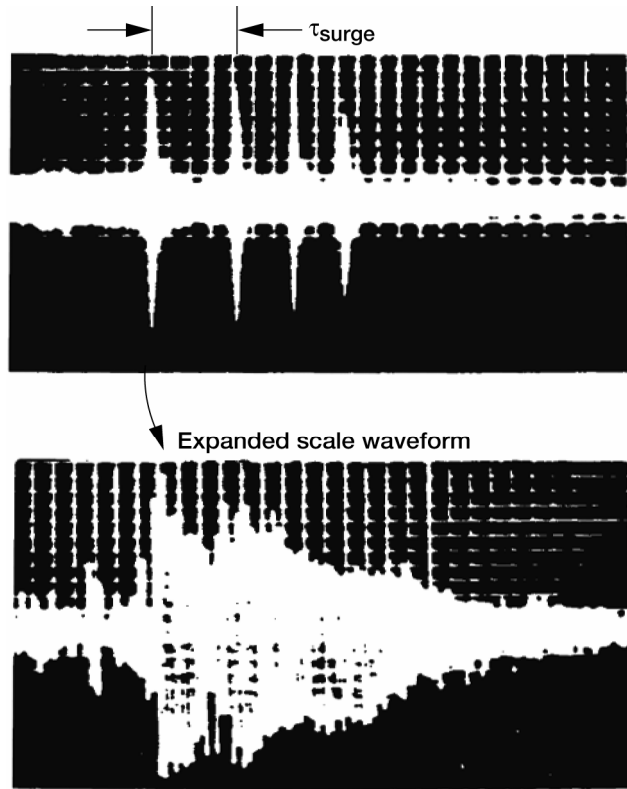
Figure 6-8.—Characteristics of blade vibratory signals–transient.

- Density effect
  - Dynamic pressure = $1/2 \rho V^2$
  - In practice, $\sigma \propto \rho^n$, where $0.5 < n < 1.0$
- Temperature–variable geometry effect
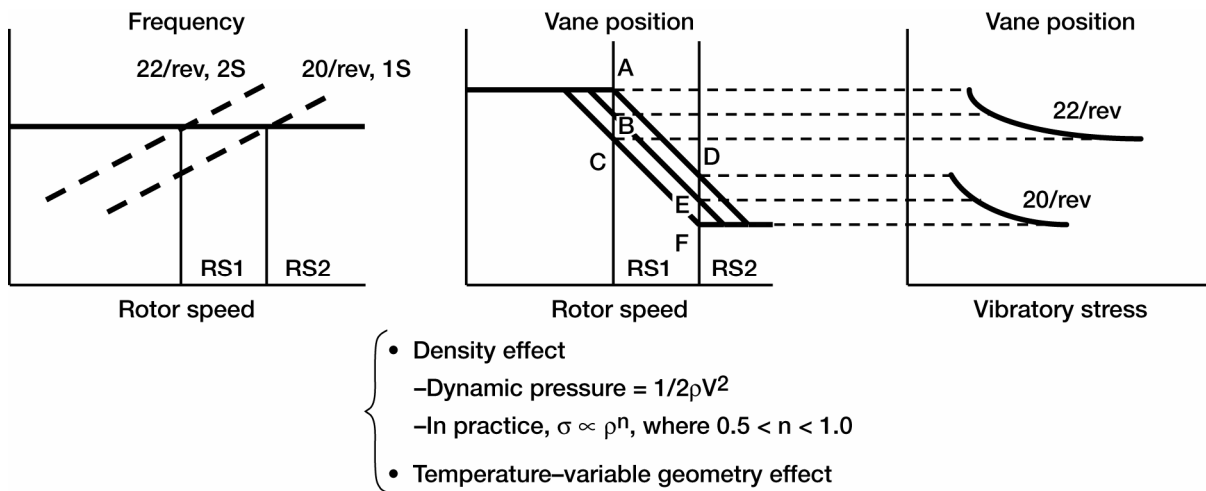
Figure 6-9.—Forced response–sensitivity to temperature and density.

There are so many variables (important test variables are listed on fig. 6-10) in turbomachinery aeroelastics that it is practically impossible to measure all combinations in full scale engine tests. Therefore good planning is necessary to maximize the usefulness of the measured data. If component rig data is available this can be used to identify the location of flutter boundaries and significant resonant crossings. In mapping responses over the flight envelope it is best to consider variations in inlet pressure and temperature than to simply run the extreme corners of the flight envelope. For flutter it is important to run to the maximum corrected speed. To reach this condition on a

- Rotor speed

- Variable geometry

- Pressure and temperature

- Maximum corrected speed

- Maximum pressure

- Distortion screens
    - ID radial
    - OD radial
    - 180 degree
    - "Flight" screens (based on scaled inlet testing)
    - "Special screens"

Figure 6-10.—Stress mapping–test matrix.

ground test usually requires special test procedures. The primary instrumentation systems, strain gages and light probes, have been previously discussed. However, it is important to point out here that the instrumentation mortality should be considered in test planning. For example, the important aeroelastic test points should be near the beginning of the test, when there is a high probability that the instrumentation will still be working. In addition, certain conditions, such as high speed, high temperature, and high pressure can be very damaging to the instrumentation and should be conducted last in the aeroelastic test sequence.

Bibliography on Supersonic Through-Flow Fan Aeroelasticity

John K. Ramsey
National Aeronautics and Space Administration
Glenn Research Center
Cleveland, Ohio 44135

In the late 1980's and early 1990's there was an increased interest in providing efficient supersonic propulsion technology for supersonic transport applications. One concept that showed promise was the supersonic throughflow fan (SSTF) engine. A detailed description of this engine and its benefits, as well as associated research, is given in references 1 and 2 and is described briefly here. This engine concept (see fig. 1) was anticipated to realize a 12 percent improvement in installed specific fuel consumption and a 25 percent reduction in installed weight compared with a nonafterburning turbofan. The SSTF processes the intake airflow at supersonic throughflow velocities, thereby eliminating the need for a conventional supersonic inlet system. Thus, the inlet weight reduction realized by using the SSTF was estimated to be about one-half that of conventional supersonic inlets. Other advantages include fewer fan stages required to achieve a given pressure ratio, less boundary-layer bleed drag, better pressure recovery, and better matching of bypass ratio variations to flight Mach number.

Experimental research on the SSTF concept was extremely limited prior to NASA's research efforts in the late 1980's and early 1990's. The following bibliography lists aeroelasticity related publications applicable to the supersonic throughflow fan.
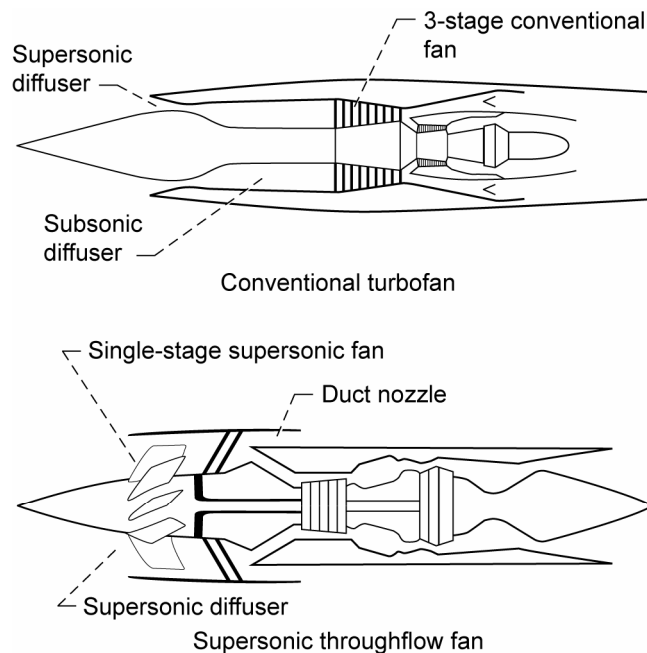
Figure 1.—Supersonic throughflow fan engine.

References

1. Franciscus, Leo C.: The Supersonic Through-Flow Turbofan for High Mach Propulsion. NASA TM–100114, (AIAA–87–2050) 1987.
2. Aeropropulsion '87. Session 6—High-Speed Propulsion Technology. NASA CP–10003, 1987.

Bibliography

Caruthers, J.E.: Theoretical Analysis of Unsteady Supersonic Flow Around Harmonically Oscillating Turbofan Cascades. Ph.D. Thesis, Georgia Inst. of Tech., 1976.

Chalkley, H.G.: A Study of Supersonic Cascade Flutter. NTIS AD–745838, Naval Postgraduate School, Monterey, CA, 1972.

Drake, D.G.: The Oscillating Two-Dimensional Aerofoil Between Porous Walls. Aeronaut. Q., vol. 8, no. 3, 1957, pp. 226–239.

Giordano, Daniel D.; and Fleeter, Sanford: Investigation of Oscillating Airfoil Shock Phenomena. AIAA Paper 90–0695, 1990.

Giordano, Daniel D.; and Fleeter, Sanford: Supersonic Axial Flow Oscillating Cascade Shock Motion and Unsteady Aerodynamic Moment. Int. J. Turbo Jet Eng., vol. 12, no. 2, 1995, pp. 79–98.

Gorelov, D.N.: Lattice of Plates in an Unsteady Supersonic Flow. Fluid Dynamics (English transl.), vol. 1, no. 4, 1966, pp. 34–39.

Hanada, T.; and Namba, M.: Unsteady Aerodynamic Analysis of Supersonic Through-Flow Fan With Vibrating Blades Under Non-Zero Mean Loading. J. Sound Vib., vol. 194, no. 5, 1996, pp. 709–750.

Hanada, Toshiya; and Namba, Masanobu: Unsteady Lifting Surface Theory Based on Double Linearization Concept for Supersonic Through-Flow Fan. NKGBD, vol. 60, no. 569, 1994, pp. 161–168.

Hanada, Toshiya; and Namiba, Masanobu: Double Linearization Theory for Supersonic Through-Flow Fan. Memoirs of the Faculty of Engineering, Kyushu Univ., vol. 53, no. 3, 1993, pp. 151–179.

Huff, Dennis L.; and Reddy, T.S.R.: Numerical Analysis of Supersonic Flow Through Oscillating Cascade Sections by Using a Deforming Grid. NASA TM–102053 (AIAA Paper 89–2805), 1989.

Huff, Dennis L.; and Reddy, T.S.R.: Numerical Simulations of Supersonic Flow Through Oscillating Cascade Sections. NASA TM–103100, 1990.

Jacquet-Richardet, G.; and Henry, R.: Flutter Analysis of Plate-Like Rotating Blades. IFTOMM 3rd Int. Conference on Rotordynamics, Sept. 9–12, 1990, Lyon, France.

Kielb, R.E.; and Ramsey, J.K.: Flutter of a Fan Blade in Supersonic Axial Flow. J. Turbomachinery (ASME Paper 88–GT–78), vol. 111, no. 4, 1989, pp. 462–467.

Lane, F.: Supersonic Flow Past on Oscillating Cascade With Supersonic Leading-Edge Locus. J. Aero. Sci., vol. 24, no. 1, 1957, pp. 65–66.

Miles, J.W.: The Compressible Flow Past an Oscillating Airfoil in a Wind Tunnel. J. Aero. Sci., vol. 23, no. 7, 1956, pp. 671–678.

Nagashima, T.; and Whitehead, D.S.: Linearized Supersonic Unsteady Flow in Cascades. ARC R&M 3811, 1977.

Namba, M.; and Hanada, T.: Lifting Surface Theory for Supersonic Through-Flow Fan. 10th International Symposium on Air Breathing Engines, Nottingham, England, 1991, pp. 669–677.

Namba, Masanobu; and Hanada, T.: Unsteady Lifting Surface Theory for Supersonic Through-Flow Fan. JSME Int. J., series B, vol. 37, no. 4, 1994, pp. 760–768.

Nishiyama, T.; and Kikuchi, M.: Theoretical Analysis for Unsteady Characteristics of Oscillating Cascade Aerofoils in Supersonic Flows. The Technology Reports of the Tohoku University, vol. 38, no. 2, Dec. 1973, pp. 565–597.

Platzer, M.F.; and Chalkley, H.G.: Theoretical Investigation of Supersonic Cascade Flutter and Related Interference Problems. AIAA Paper 72–0377, 1972.

Ramsey, John K.; and Kielb, Robert E.: A Computer Program for Calculating Unsteady Aerodynamic Coefficients for Cascades in Supersonic Axial Flow. NASA TM–100204, 1987.

Ramsey, John K.: Influence of Thickness and Camber on the Aeroelastic Stability of Supersonic Throughflow Fans: An Engineering Approach. NASA TM–101949, 1989.

Ramsey, J.K.: Influence of Thickness and Camber on the Aeroelastic Stability of Supersonic Throughflow Fans. J. Propul. P., vol. 7, 1991, pp. 404–411.

Ramsey, John K.: Semi-Nonlinear Code for Calculating Unsteady Aerodynamic Coefficients for Cascades in Supersonic Axial Flow. Users and Programmers Manual. NASA TM–102573, 1991.

Ramsey, John K.; and Erwin, Dan: Comparison of Theoretical and Experimental Unsteady Aerodynamics of Linear Oscillating Cascade With Supersonic Leading-Edge Locus. NASA/TM—2004-211820, 2004.

Reddy, T.S.R., et al.: Analysis of Cascades Using a Two Dimensional Euler Aeroelastic Solver. AIAA Paper 92–2370, 1992.

Reddy, T.S.R.; Bakhle, M.A.; and Huff, D.L.: Flutter Analysis of a Supersonic Cascade in Time Domain Using an ADI Euler Solver. NASA TM–105625, 1992.

Reddy, T.S.R., et al.: Flutter Analysis of Supersonic Axial Flow Cascades Using a High Resolution Euler Solver. Part 1: Formulation and Validation. NASA TM–105798, 1992.

Spara, Karen Michelle: Aerodynamic Detuning and Aeroelasticity of a Supersonic Turbomachine Rotor. Master's Thesis, Purdue Univ., 1988.

Spara, Karen M.; and Fleeter, Sanford: Supersonic Turbomachine Rotor Flutter Control By Aerodynamic Detuning. AIAA Paper 89–2685, 1989.

Spara, Karen M.; and Fleeter, Sanford: Aerodynamic Detuning for Control of Supersonic Rotor Forced Response. AIAA–1990–2018, 1990.

Spara, K.M.; and Fleeter, S.: Aerodynamic Detuning for Control of Supersonic Rotor Forced Response. Comput. Mech., vol. 12, no. 5, 1993, pp. 315–327.

Toshimitsu, Kazuhiko; Iwai, Sellichi; and Namba, Masanobu: Double Linearization Theory of Three-Dimensional Cascades With Vibrating Blades Under Spanwise-Nonuniform Mean Loading (Supersonic Leading-Edge Locus Cascade). JSME Int. J., series B, vol. 38, no. 4, 1995, pp. 582–592.

Bibliography on the Aeroelasticity of Labyrinth Seals

National Aeronautics and Space Administration
Glenn Research Center
Cleveland, Ohio 44135

The following bibliography was excerpted from the Engineering Design Guide, Volume 1A, Rotating Machinery, NASA Glenn Research Center.

Bibliography

Alford, J.S.: Protection of Labyrinth Seals From Flexural Vibration. ASME J. Eng. Power, vol. 86, 1964, pp. 141–147.

Abbott, D.R.: Advances in Labyrinth Seal Aeroelastic Instability Prediction and Prevention. ASME Paper 80–GT–151, 1980.

Alford, J.S.: Labyrinth Seal Designs Have Benefited From Development and Service Experience. SAE Paper 710435, 1971.

Alford, J.S.: Nature, Causes, and Prevention of Labyrinth Air Seal Failures, J. Aircraft, vol. 12, 1975, pp. 313–318.

Alford, J.S.: Protecting Turbomachinery From Unstable and Oscillatory Flows. ASME J. Eng. Power, vol. 89, 1967, pp. 513–527.

Campbell, W.: Protection of Steam Turbine Disk Wheels From Axial Vibration. Proceedings of the ASME Conference 1924, Paper no. 1920, 1924.

Ehrich, F.: Aeroelastic Instability in Labyrinth Seals. ASME Paper 68–GT–32, 1968.

Halila, E.E.; Lenahan, D.T.; Thomas, T.T.: Energy Efficient Engine High Pressure Turbine Test Hardware Detailed Design Report. NASA CR–167955, 1982.

Lewis, D.A.; Platt, C.E.; and Smith, E.B.: Aeroelastic Instability in F100 Labyrinth Air Seals. AIAA Paper 78–1087, 1978.

Stodola, Aurel: Steam and Gas Turbines, With a Supplement on the Prospects of the Thermal Prime Mover. McGraw-Hill, New York, NY, 1927 (reprinted 1945).

Influence of Pitch Axis Location and Orientation
on Rotor Aeroelastic Stability[*]

Wen-Liu Miao
Sikorsky Aircraft Division
United Technologies Corporation
Stratford, Connecticut 06601

Abstract

The aeroelastic and aeromechanical stability problems of the rotor and the coupled rotor-airframe system are reviewed. The interrelationship of the various subcategories of aeroelastic stability is discussed. The key element that influences the rotor aeroelastic stability, namely the spacial location and orientation of the blade pitch axis, is illustrated. Design parameters that enhance the stability characteristics are discussed.

Nomenclature

a Lift curve slope

A Induced flow parameter, $\dfrac{\pi\sigma}{6}\left[\sqrt{1+\dfrac{12\theta}{\pi\sigma}}-1\right]$

c Blade chord

C_{d_o} Profile drag coefficient

$C_{\beta\zeta}$ Coefficient of lag velocity term in the flap equation

I Rigid blade flap and lead-lag inertia

I_β Rigid blade flap inertia

I_θ Rigid blade pitch inertia

K_β Total flap hinge spring rate at $\theta = 0$

$K_{\beta b}$ Flap spring rate at blade root

$K_{\beta h}$ Flap spring rate at hub

K_ζ Total lead-lag hinge spring rate

$K_{\zeta b}$ Lead-lag spring rate at blade root

$K_{\zeta h}$ Lead-lag spring rate at hub

p	Nondimensional flatwise frequency
r	Blade radial coordinate
R	Rotor radius, also variable elastic coupling parameter
β, β_0	Blade flap angle, steady coning
β_{B-H}	Built-in flexbeam-to-hub cone angle
β_{BL-B}	Built-in blade-to-flexbeam cone angle
γ	Lock number
θ, θ_0	Blade pitch angle, collective pitch
θ_{B-H}	Built-in flexbeam-to-hub pitch angle
θ_{BL-B}	Built-in blade-to-flexbeam pitch angle
θ_ζ	Blade pitch-lag coupling
ρ	Air density
σ	Rotor solidity, real part of eigenvalue
Φ_i	Induced flow angle
ω	Frequency, imaginary part of eigenvalue
$\omega_{1\beta}$	Blade first flatwise mode frequency
$\omega_{1\zeta}$	Blade first edgewise mode frequency
$\omega_\zeta, \overline{\omega}_\zeta$	Blade edgewise frequency, nondimensional frequency
$\omega_\theta, \overline{\omega}_\theta$	Blade torsion frequency, nondimensional frequency
Ω	Rotor speed
ζ	Blade lag angle
$\Delta(\ )$	Equilibrium perturbation quantities

Introduction

The helicopter rotor aeroelastic stability problem can be classified into two prime categories: rotor stability and coupled rotor-airframe stability. This division is due to the fact that a stable rotor can encounter instability when coupled with the airframe. In other words, there is a class of aeroelastic stability problems that can be analyzed with rotor degrees-of-freedom in the rotating system alone and there is another class that requires both the rotating and the non-rotating coordinates to describe the total system adequately.

Loewy (ref. 1) provided a first comprehensive review and a basic description of these two types while discussing various dynamic and aeroelastic problems associated with V/STOL vehicles in general, and helicopters in particular. More recent reviews by Friedmann (refs. 2 and 3) emphasized the role of geometric nonlinearities, due to

moderate deflections, in rotary-wing aeroelasticity together with the treatment of the aeroelastic problems in forward flight and the role of unsteady aerodynamics. Ormiston (ref. 4), in his review of the hingeless and bearingless rotor stability, in hover, provided an excellent description of the theoretical and experimental investigations of these instabilities with emphasis on the physical interpretation of the intricacies of the aeroelastic couplings and their effect on stability.

The rotor aeroelastic stability problem has received a considerable amount of attention during the past two decades. This is due to an intensified interest in the hingeless and/or bearingless rotor systems in the helicopter industry and government organizations. However, the physical simplicity and significant parts reduction of the hingeless/bearingless rotor designs are achieved by having a much more complex system in terms of defining and analyzing the rotor aeroelastic couplings as compared to the more analyzable articulated rotors. In fact, it is desirable to deliberately introduce aeroelastic couplings through design parameters so that the aeroelastic stability is enhanced. A good example of this is the MBB BO-105 hingeless rotor system. This design has a substantial amount of aeroelastic coupling (ref. 5) that enables the helicopter to operate in a stable mode with neither blade lead-lag dampers nor landing gear oleos. The Westland WG-13 had adopted the design philosophy of minimizing these couplings (ref. 6) resulting in a hingeless rotor system that has lag dampers.

Johnson (refs. 7 and 8) provided a thorough discussion of the rotor aeroelastic stability problem with emphasis on theoretical treatment to elucidate the causes. It is the purpose of this paper to give an overview of the aeroelastic stability problem, the interrelationships of the subcategories and the way the important design parameters affect the stability.

It is worth mentioning that there is another class of aeroelastic stability problems that involves the active feedback such as the automatic flight control system (AFCS) (ref. 9) or the engine fuel control system (ref. 10). They are not covered in this document.

Rotor Stability

Rotor blade flapping stability has been studied quite exhaustively through the years e.g. (refs. 11 to 13). This stability, however, is associated with advance ratios greater than 2, and is of academic interest only. Stall flutter is another vexing "instability" that is a single degree-of-freedom phenomenon involving primarily blade pitch or torsion in a nonlinear aerodynamic environment. This phenomenon (ref. 14) is best characterized as an excessive response of a limit-cycle nature. With improvement in the airfoil-design and the blade tip shape (ref. 15), this nettlesome problem, which has imposed limits on the thrust coefficient and advance ratio plane due to the sharp rise in control loads when stall is encountered, has not been a limiting factor in helicopter design of late. Since flapping stability is not a concern of practical helicopters and stall flutter is more of a loads issue, they will not be discussed further in this document.

Pitch-Flap Flutter

Just like the fixed wings, the rotor blades are susceptible to the kind of classical bending torsion flutter (ref. 16). The typical analysis for the rotating blade employs a two-degree-of-freedom model with one freedom being rigid blade flapping about an offset hinge (equivalent spring-hinge for a hingeless rotor) and the other a rigid body pitch motion about a feathering axis, since the control system is usually the softest element in the torsion motion (ref. 17). The key parameters that control the flutter boundary are the torsion natural frequency and the chordwise distance of the blade CG (center of gravity) to the section aerodynamic center. Figure 1, replotted from reference 18, shows the effect of the torsional frequency and aft CG on the flutter boundary for the BO-105 hingeless rotor blade. As expected, as the non-rotating torsional frequency moves closer to the first flatwise mode frequency of 1.12 per rev, the blade is more prone to the pitch-flap flutter. At the coalescence, it is least tolerant to the aft CG offset. It is worth noting that rotor blades are typically mass balanced about the quarter chord for loads considerations and therefore are generally free from flutter.
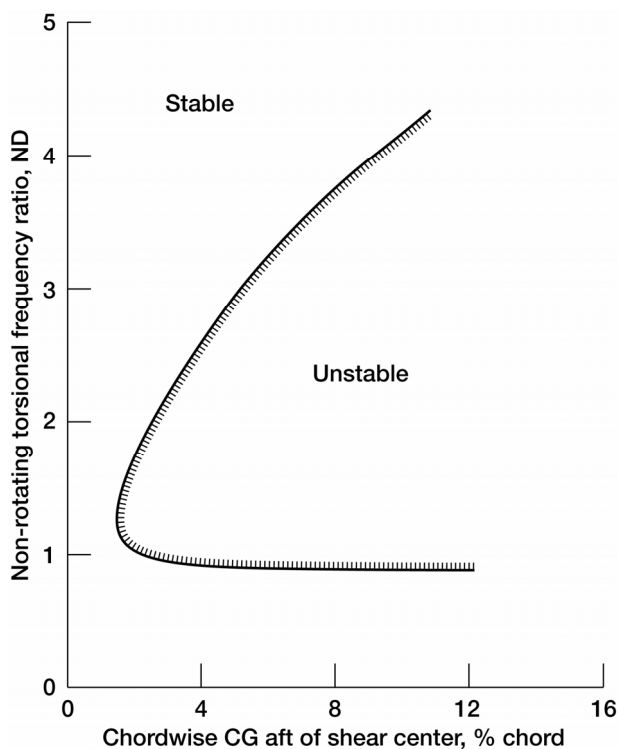
Figure 1.—Effect of torsional frequency and aft CG on
pitch-flap flutter (replotted from ref. 18). (The original
version of this figure was published by the Advisory
Group for Aerospace Research and Development,
North Atlantic Treaty Organization (AGARD/NATO) in
Strehlow, H.; and Enenkl, B.: Aeroelastic Design
Considerations in the Development of Helicopters.
AGARD Conference Proceedings CP–354, Aeroelastic
Design Considerations in the Preliminary Design of
Aircraft, 1983. Used with permission.)

Since the torsional frequency is a critical parameter in the flutter considerations, large, steady bending deflections should have a profound effect on the blade flutter characteristics due to the increase in the pitch inertia from the steady deflections. To illustrate this point, consider a blade with a pitch axis and coincidental flap-lag hinges as shown in figure 2. The blade has a steady flapping deflection of β_0. The mass, dm, is undergoing a lag acceleration of $r\beta_0\ddot{\theta}$ resulting from a positive pitch acceleration. The inertia force, $dm \cdot r\beta_0\ddot{\theta}$, acting towards the leading edge with a moment arm of $r\beta_0$ produces a nose down pitching moment of $\int dm \cdot (r\beta_0)^2 \ddot{\theta}$. This is precisely the inertia restoring moment when viewing the mass, dm, being displaced from the pitch axis by a distance of $r\beta_0$ thereby increasing the pitch inertia by $\int dm \cdot (r\beta_0)^2$, or $\beta_0^2 I_\beta$. Since the pitch inertia is of the order of magnitude of 1.5 and the flapping inertia 1200, the term $\beta_0^2 I_\beta$ quickly dominates the total pitch inertia and would reduce the torsion frequency. However, as shown in figure 2, the inertia force due to a positive pitch acceleration not only produces a restoring nose down pitch moment, it also produces a lead moment of $\int dm \cdot r\beta_0\ddot{\theta} \cdot r$, or $\beta_0 I_\beta\ddot{\theta}$. That is to say that there will be lead-lag motion as well as pitch motion. In other words, the dynamic system requires that both lead-lag and pitch degrees-of-freedom be considered in order to assess the coning effect on the torsion frequency properly. The equations for this dynamically coupled system are as following:

$$\begin{bmatrix} I_\theta + \beta_0^2 I_\beta & \beta_0\left(I_\theta + I_\beta\right) \\ \beta_0\left(I_\theta + I_\beta\right) & I_\beta \end{bmatrix}\begin{Bmatrix} \ddot{\theta} \\ \ddot{\zeta} \end{Bmatrix} + \begin{bmatrix} I_\theta\omega_\theta^2 & 0 \\ 0 & I_\beta\omega_\zeta^2 \end{bmatrix}\begin{Bmatrix} \theta \\ \zeta \end{Bmatrix} = 0$$

Pitch moment due to $dm \cdot r\,\beta_o\,\ddot{\theta}$ is: $\int dm \cdot r\,\beta_o\,\ddot{\theta} \cdot r\,\beta_o = \beta_o^2\,I_\beta\,\ddot{\theta}$

Lead moment due to $dm \cdot r\,\beta_o\,\ddot{\theta}$ is: $\int dm \cdot r\,\beta_o\,\ddot{\theta} \cdot r = \beta_o\,I_\beta\,\ddot{\theta}$
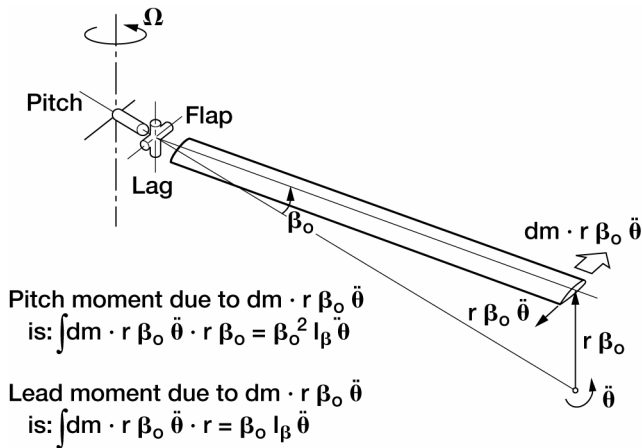
Figure 2.—Effect of steady deflection on pitch moment of inertia and accompanying pitch-lag coupling.
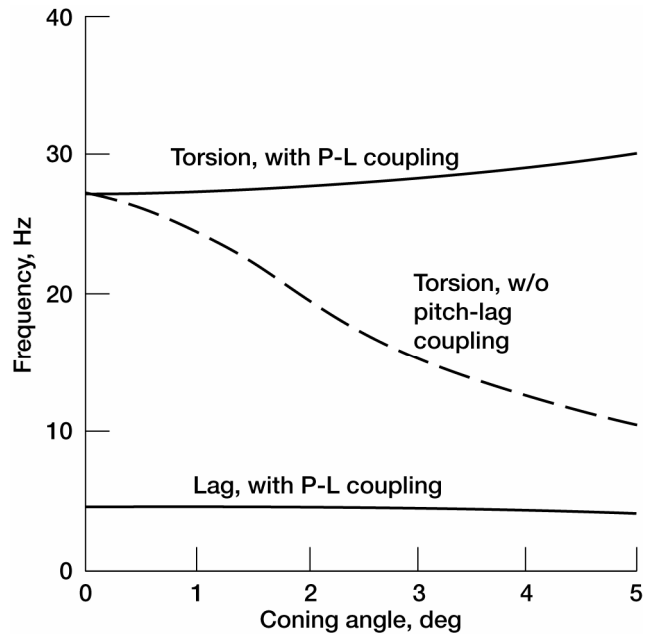
Figure 3.—Effect of dynamic pitch-lag coupling on the torsion frequency.

The coupled frequencies for a typical blade are shown in figure 3 as a function of the coning angle. It is evident that the torsion frequency, instead of decreasing rapidly with coning angle as shown by the dashed line when only the pitch degree-of-freedom is considered, is increased with increasing coning angle due to the dynamic coupling with the lead-lag degree-of-freedom. It is interesting to note that the pitch-flap flutter analysis that does not take into account the pitch inertia increase due to steady deflections, when necessary, actually gives a better approximation of the torsion frequency for flutter assessment.

It is clear, however, as analyses become more refined and take into account more coupling terms due to steady deflections as pointed out in reference 1, it is necessary to include the blade lag degree-of-freedom to conduct a proper pitch-flap flutter assessment.

Pitch-Lag Stability

Chou (ref. 19) described the first encounter of the pitch-lag instability of a helicopter rotor blade. The term pitch-lag may be a misnomer since the critical degrees-of-freedom involved are flap and lag motions, although the critical parameter that caused instability is a kinematic pitch-lag coupling which produces nose up pitch motion when the blade leads forward.

The mechanism of this instability is summarized in reference 19 as follows: "As the blade moves forward in the lead-lag plane (decreasing lag angle) the pitch angle increases. This increase in pitch produces an additional lift force and the blade flaps up. This upward flapping in turn produces a forward Coriolis force which tends to push the blade further forward. If the moment of this Coriolis force is larger than the lag damper moment, the net damping is negative and the blade will have self-excited vibration." This physical insight is remarkable because the stability criterion derived from this consideration is the same as that from the more elaborate flap-lag aeroelastic equations. It is clear that this so-called pitch-lag stability is actually the modern day flap-lag stability with pitch-lag couplings.

Figure 4.—Math model for flap-lag dynamic analysis (from ref. 20).

In the figure:

$R \equiv K_\beta/K_{\beta_b} = K_\zeta/K_{\zeta_b}$

$K_\beta = 1/(1/K_{\beta_h} + 1/K_{\beta_b})$, $K_\zeta = 1/(1/K_{\zeta_h} + 1/K_{\zeta_b})$

$R = 1$: Pitch I/B of flap and lag

$R = 0$: Pitch O/B of flap and lag

Flap-Lag Stability

Ormiston and Hodges (ref. 20) conducted a comprehensive theoretical study of the flap-lag-stability for rotor blades in hover. They extended Young's (ref. 21) equivalent hinge concept to represent both the blade flap and lag degrees-of-freedom. As shown in figure 4, the mathematical model also distinguishes the bending stiffnesses between those inboard of the pitch bearing and those outboard. An R factor is used to denote the distribution of the bending stiffnesses as noted in the figure. The resulting flap and lag perturbation equations, taken from reference 4, are:

$$
\begin{bmatrix} 1 & 0 \\ 0 & 1 \end{bmatrix} \begin{Bmatrix} \Delta\beta'' \\ \Delta\zeta'' \end{Bmatrix} + \frac{\gamma}{8} \begin{bmatrix} 1 & 0 \\ 0 & \dfrac{2C_{d_o}}{a} + \Theta_0\Phi_i \end{bmatrix} \begin{Bmatrix} \Delta\beta' \\ \Delta\zeta' \end{Bmatrix} + \begin{bmatrix} 1 + \dfrac{K_\beta}{I\Omega^2} & 0 \\ 0 & \dfrac{K_\zeta}{I\Omega^2} \end{bmatrix} \begin{Bmatrix} \Delta\beta \\ \Delta\zeta \end{Bmatrix} + \underbrace{\begin{bmatrix} 0 & 2\beta_0 \\ -2\beta_0 & 0 \end{bmatrix} \begin{Bmatrix} \Delta\beta' \\ \Delta\zeta' \end{Bmatrix}}_{\substack{\text{inertial} \\ \text{coupling}}}
$$

$$
+ \underbrace{\frac{\gamma}{8} \begin{bmatrix} 0 & \Phi_i - 2\Theta_0 \\ \Theta_0 - 2\Phi_i & 0 \end{bmatrix} \begin{Bmatrix} \Delta\beta' \\ \Delta\zeta' \end{Bmatrix}}_{\substack{\text{aerodynamic} \\ \text{coupling}}} + \underbrace{R\Theta_0 \begin{bmatrix} 0 & \dfrac{K_\zeta - K_\beta}{I\Omega^2} \\ \dfrac{K_\zeta - K_\beta}{I\Omega^2} & 0 \end{bmatrix} \begin{Bmatrix} \Delta\beta \\ \Delta\zeta \end{Bmatrix}}_{\substack{\text{structural} \\ \text{coupling}}} = \frac{\gamma}{8} \begin{Bmatrix} 1 \\ -\Phi_i \end{Bmatrix} \Delta\Theta
$$

Note that for blades that do not have structural coupling ($R = 0$), the prime couplings for the flap and lag motions are the velocity terms due to inertia (Coriolis) and aerodynamics. Of particular interest is the flap moment due to lag velocity:

$$
C_{\beta\zeta} = 2\beta_0 + \frac{\gamma}{8}(\Phi_i - 2\Theta_0) \approx \frac{\gamma}{8}(-\Phi_i)
$$

since

$$
\beta_0 \approx \frac{\gamma}{8}(\Theta_0 - \Phi_i).
$$

The induced inflow angle Φ_i is, of course, a function of thrust, or pitch angle. This coupling is relatively weak and becomes substantial only at relatively large pitch angles. Figure 5, from reference 20, shows the flap-lag stability as a function of the flap and lag frequencies and pitch angle. For the worst possible frequency combination (both flap and lag frequencies equal to $\sqrt{4/3}$), instability occurs when the pitch angle exceeds 0.193 rad, or 11.1°. For rotors with a blade inplane natural frequency ratio less than 0.9 or greater than 1.5, flap-lag instability is not possible for a practical blade pitch range.

Figure 6, also from reference 20 demonstrates the powerful effect of structural coupling. With more bending stiffness inboard of the pitch bearing, the unstable region shifts to a higher inplane frequency. Introducing pitch-lag kinematic coupling changes the stability characteristics of the stiff-inplane rotor drastically for different R values. Figure 7 (from ref. 20) shows that for a stiff-inplane rotor with an edgewise frequency of 1.4, the pitch-lag coupling that eliminates the instability at one R factor will destabilize the blade at another R value. As for the soft-inplane rotor, negative pitch-lag coupling is always stabilizing, and positive pitch-lag coupling is strongly destabilizing for all values of R. Reference 20 also describes the effect of pitch-flap coupling on flap-lag stability.

It becomes quite obvious that since the flap-lag stability is very much dependent on the pitch-lag and pitch-flap couplings as well as the spanwise distribution of the bending stiffnesses with respect to the radial location of the pitch bearing, one would expect that a proper assessment of the flap-lag stability should have torsion as an indispensable degree-of-freedom. As mentioned earlier, the lag degree-of-freedom is necessary for the assessment of pitch-flap flutter as well. Rotor stability is truly a flap-lag-torsion phenomenon.
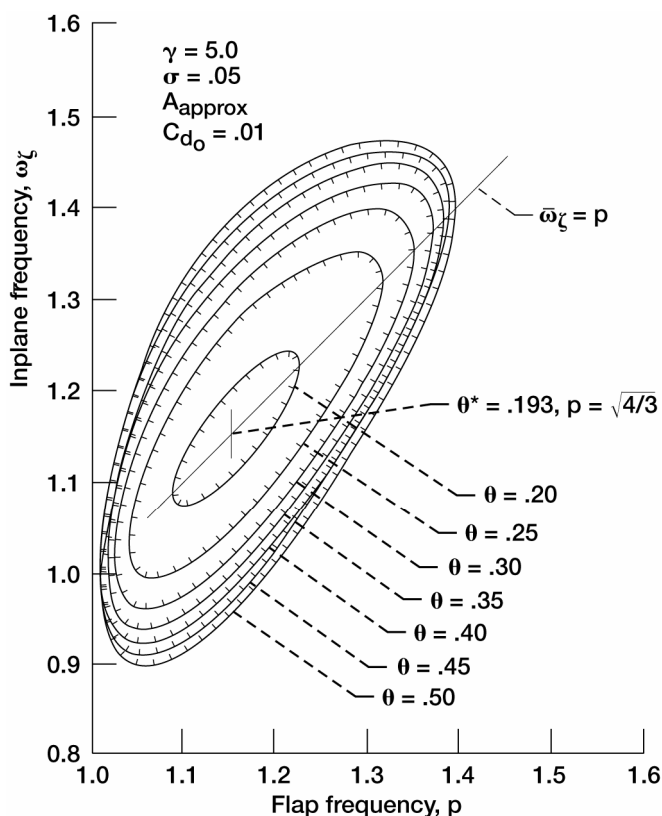
Figure 5.—Effect of collective pitch on flap-lag stability. (The original version of this figure first appeared in Ormiston, R.A.; and Hodges, D.H.: Linear Flap-Lag Dynamics of Hingeless Rotor Blades in Hover. J. Amer. Helicopter Soc., vol. 17, no. 2, 1972. Copyright American Helicopter Society; used with permission.)
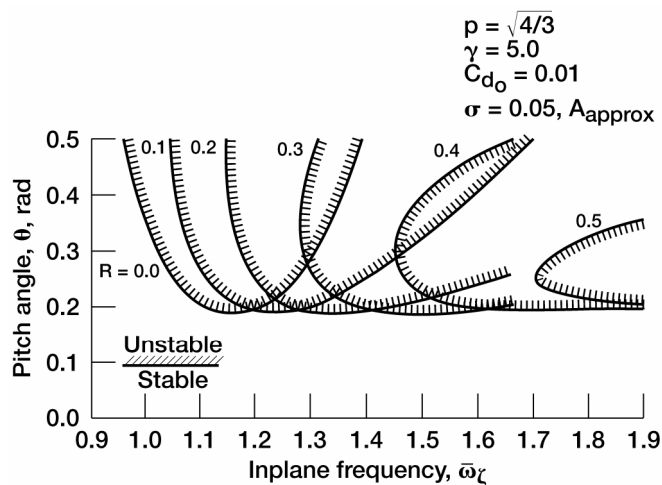
Figure 6.—Effect of structural coupling on flap-lag stability, rigid torsion. (The original version of this figure first appeared in Ormiston, R.A.; and Hodges, D.H.: Linear Flap-Lag Dynamics of Hingeless Rotor Blades in Hover. J. Amer. Helicopter Soc., vol. 17, no. 2, 1972. Copyright American Helicopter Society; used with permission.)
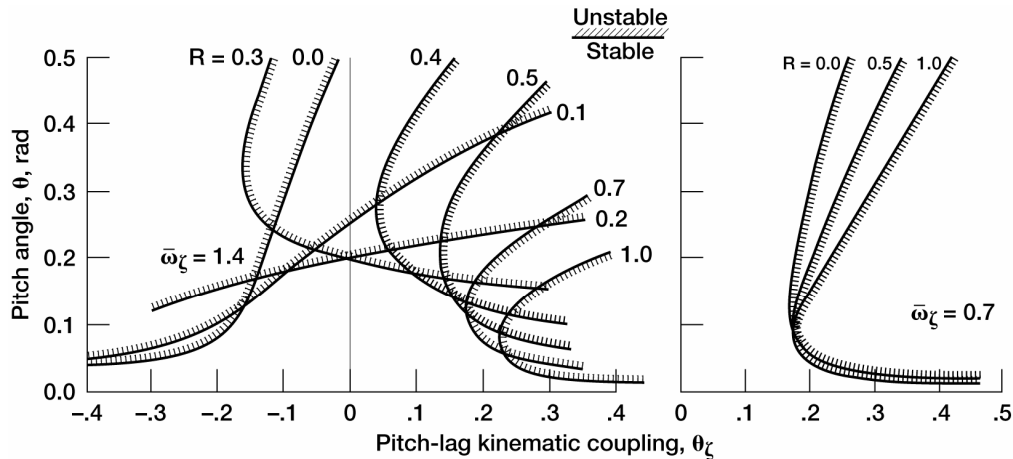
Figure 7.—Effect of pitch-lag coupling on flap-lag stability. (The original version of this figure first appeared in Ormiston, R.A.; and Hodges, D.H.: Linear Flap-Lag Dynamics of Hingeless Rotor Blades in Hover. J. Amer. Helicopter Soc., vol. 17, no. 2, 1972. Copyright American Helicopter Society; used with permission.)

Pitch-Flap-Lag Stability

Houbolt and Brooks (ref. 22) provided the first comprehensive linear flap-lag-torsion equations of motion. The first effort toward the nonlinear flap-lag-torsion problem for a fully elastic blade was the derivation of nonlinear equations of motion by Arcidiacono (ref. 23). The equations were reasonably detailed and complete with some nonlinear inertial terms deleted. Hodges and Dowell (ref. 24) derived the complete nonlinear equations using both Hamilton's principle and the Newtonian method. An extensive study of the flap-lag-torsion stability using these equations was conducted by Hodges and Ormiston and presented in reference 25.

Figure 8, replotted from reference 25, shows the stability boundaries, similar to those shown in figure 6, as affected by the R factor with a blade torsion frequency of 5/rev. From a comparison of the boundaries shown in figures 6 and 8, the effect of torsion is quite obvious.

The torsion degree-of-freedom affects stability in two ways: the dynamic response of torsion and the flap-lag couplings produced by the torsional flexibility. Reference 25 further explores this by comparing the stability of the coupled flap-lag-torsion system with those obtained with the torsion dynamics eliminated. Figure 9, from reference 25, shows that for a torsion frequency greater than 3, the calculated modal damping values for the flap-lag-torsion case are identical to those for the "modified flap-lag" case. In other words, the prime influence of torsion is almost entirely due to the bending-torsion couplings produced by torsion flexibility. As long as the couplings are properly taken care of, dynamics of torsion is not very significant until the torsion frequency is very low. This echoes the sensitivities of stability to the R factor shown previously. The value of R is indirectly a measure of the spacial orientation of the pitch axis. This orientation determines the magnitude of the pitch-lag and pitch-flap couplings which ultimately translate into flap-lag couplings and affect the blade flap-lag-torsion stability.

To illustrate this, let us consider a case of R equals 0.5, i.e., 50 percent of the bending stiffness is inboard of the pitch axis while the other half outboard. Figure 10 shows schematically that the pitch axis is a distance Z_1 above the rotor disc plane due to the flapwise bending flexibility inboard of the pitch axis, while the blade elastic axis is another distance Z_2 above the pitch axis due to further flapwise bending outboard of the pitch axis under load. Similar bending in the edgewise direction can also occur, but for clarity is not shown in figure 10. Now consider an inplane force, for example, an induced drag force, acting through the moment arm of Z_2 producing a pitching moment. The magnitude of this moment is directly proportional to the vertical deflection Z_2. If the bending stiffness distribution is changed to be entirely inboard of the pitch axis, then under the same vertical load the pitch axis will coincide with the blade elastic axis, or, the distance Z_2 becomes zero. The bending-torsion coupling is thus eliminated. Conversely, with the bending flexibility entirely outboard of the pitch axis, the pitch axis will remain in the disc plane, whereas the blade tip will be a sum total of Z_1 and Z_2 above the pitch axis. The resultant bending-torsion coupling is doubled.
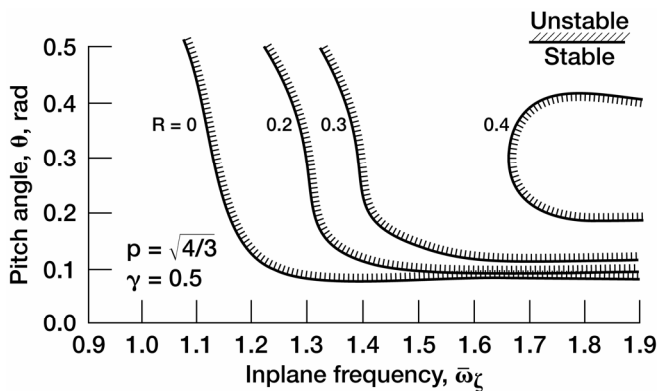
Figure 8.—Effect of structural coupling on flap-lag-torsion stability, $\bar{\omega}_\theta = 5.0$ (replotted from ref. 25).
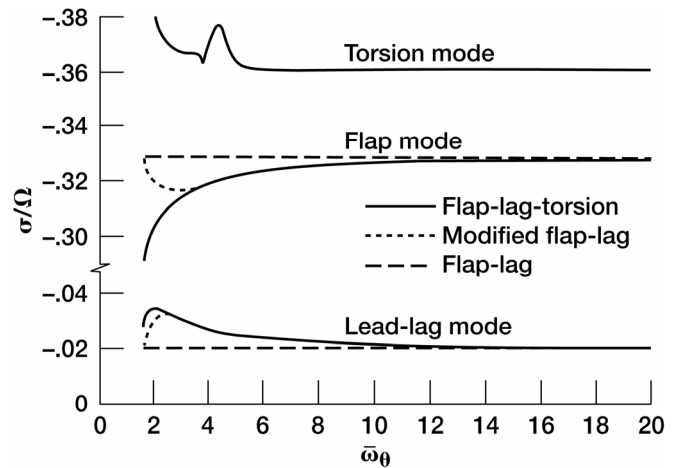
Figure 9.—Effect of torsion dynamics on the flap-lag-torsion stability.
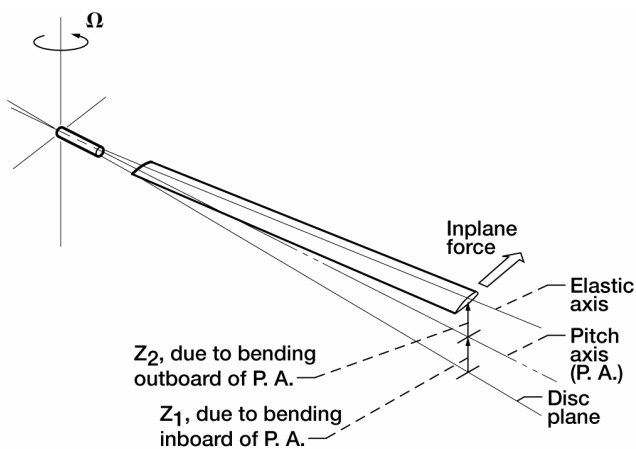
Figure 10.—Schematic of the orientation of the pitch axis with respect to the disc plane and blade elastic axis due to flapwise bending both inboard and outboard of the pitch axis.
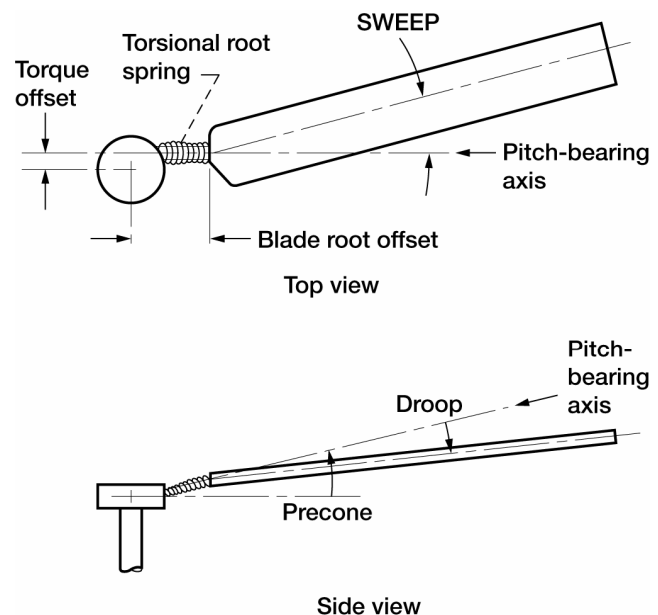
Figure 11.—Orientation of precone, droop, torque offset, and blade root offset.

In order to control the spatial orientation of the pitch axis, practical rotor designs use geometric parameters such as precone and droop for vertical orientation and torque offset and sweep for horizontal orientation. These parameters are shown schematically in figure 11. Precone was first explored analytically and experimentally by Burkam and Miao (ref. 26) in their coupled rotor-airframe stability investigation. Droop (negative) was adopted later in Boeing's YUH-61A hingeless rotor design (ref. 27). Experimental investigation of the flap-lag-torsion stability of the rotor has been carried out by the U.S. Army Aeromechanics Laboratory for a number of years (ref. 4) and the correlation of test with analysis is generally good.

To summarize, the rotor stability problem is truly a coupled flap-lag-torsion phenomenon. However, with proper understanding and approximations of the aeroelastic couplings, a simplified analysis can be used to deal with the specific problem at hand. As a general rule, beneficial couplings exist through hub geometry to stabilize the prime mode of instability, inplane lead-lag motion.

Rotor-Airframe Stability

As mentioned earlier, while rotor stability can be described entirely by the rotating system coordinates, the rotor-airframe stability can only be described by a mixture of rotating and fixed system coordinates. Even if a rotor system is free from pitch-flap-lag rotor instabilities, the coupled rotor-airframe system can be unstable. Perhaps the most well known rotor-airframe instability is the one first described by Coleman (ref. 28) and known as mechanical instability or ground resonance. The essential degrees-of-freedom are the lead-lag motion of the rotor blades and airframe modes that contain the inplane motions of the hub. Ground resonance occurs when the frequency of the regressive lead-lag mode (one of the two cyclic lead-lag modes viewed in the fixed system) coalesces with the natural frequency of the airframe mode that contains sufficient inplane hub motion. The mechanism that creates instability is as follows: an imbalance in centrifugal force is created by the cyclic lead-lag motion and this force excites the rotor hub at the regressive lag mode frequency of $\Omega - \omega_\zeta$. Airframe responds to this excitation when the airframe mode frequency is near or equal to $\Omega - \omega_\zeta$. The hub inplane motion thus created in turn excites the rotor resulting in more blade lead-lag motion when the phase is correct. Coleman was able to analyze this problem correctly without consideration of the blade flap motion and the associated aerodynamics, hence the name mechanical instability. This phenomenon, however, is a subset of the rotor-airframe instability problem which can occur in the air (or off the ground) as well as on the ground. And is sometimes known as air and ground resonance or aeromechanical stability, first coined in reference 29.

Definition of Problem

One way of describing the air and ground resonance problem is to examine the variation of the frequency of the cyclic lead-lag mode, the regressive lag mode to be precise, as a function of the rotor rotational speed. Figure 12 shows the $\Omega - \omega_\zeta$ frequency for a typical hinged rotor and a typical soft-inplane hingeless rotor. Since the lag frequency for a typical hinged rotor with 5 percent hinge offset is around 0.3/rev, the regressive lag mode frequency starts at zero and is proportional to the rotor speed with a ratio of 0.7. The non-rotating inplane frequency for a typical soft-inplane hingeless rotor at 0.7/rev, on the other hand, is of a finite value. At some rotor speed, the two are equal and thereafter the rotor speed will be greater than the inplane frequency. The regressive lag mode frequency of interest, therefore, starts at some rotor speed then increases with increasing rotor speed and is below the typical hinged rotor frequency line as shown in figure 12.

Figure 12 also shows two typical airframe mode frequencies with mode no. 1 in resonance with the hinged rotor regressive lag mode at the typical rotor operating speed and mode no. 2 with the hingeless rotor. For aircraft on the ground, mode no.1 typically involves the aircraft rigid body lateral-roll motion while no. 2 the longitudinal-pitch motion. This brings up another important factor that has paramount influence on the rotor-airframe stability, namely, the mass ratio of the rotor to the airframe. Longitudinal-pitch mode of the airframe normally is not as unstable as the lateral-roll mode simply because the airframe inertia in pitch is larger.

For aircraft in the air, or off the ground, the airframe rigid body mode frequencies are controlled by the rotor cyclic flapping stiffness. Figure 13 shows the calculated *in vacuo* frequencies of a typical hingeless rotor helicopter with six degrees-of-freedom: two cyclic lead-lag, two cyclic flap, and airframe rigid body pitch and roll. The regressive flap mode at around 0.1/rev resulted from the cyclic flap degrees-of-freedom couples with the two rigid body degrees-of-freedom. As a consequence, there are three coupled modes: a zero frequency rigid body pitch-roll mode, a regressive flap-pitch-roll mode with pitch more dominant than roll, and a regressive flap-roll-pitch mode with roll being the dominant component. The potential resonance points of the latter two modes with the regressive lag mode are the subject of the air resonance stability.

A couple of points worth noting here. The frequencies for the coupled regressive flap and airframe pitch and roll modes remain at a similar frequency range for either the hinged or the hingeless rotors since the difference in
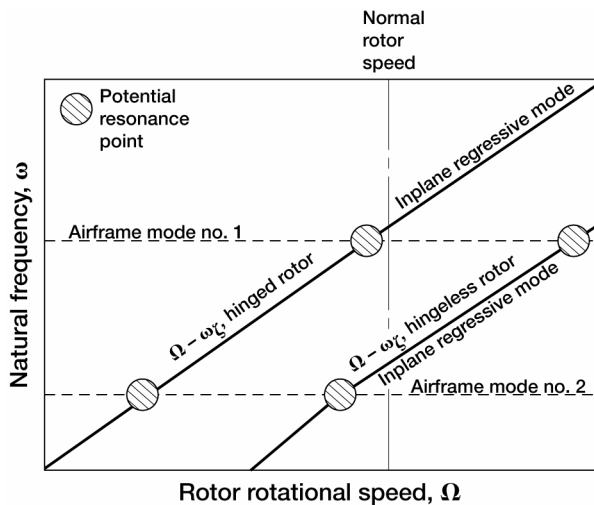
Figure 12.—Potential resonance characteristics of hinged and hingeless rotor helicopters.
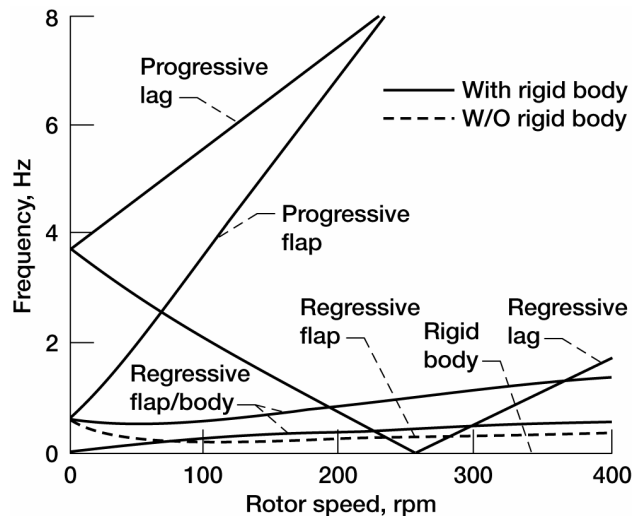
Figure 13.—Resonance characteristics of a typical hingeless rotor helicopter in air.

the flap frequency is about 0.1/rev. This puts the potential air resonance points with the hinged rotor way beyond the normal operating rotor speed range, and it is therefore not a problem. Since the airframe modes have substantial flap motion, the inclusion of the aerodynamics becomes indispensable.

Source of Damping

The aerodynamic forces introduce additional coupling terms, be it stiffness or damping, that can significantly alter the nature of the rotor-airframe stability behavior. The most significant is the fact that the powerful aerodynamic flap damping provides the inherent damping in the air resonance stability mode. Reference 26 discussed in detail how the flap damping is coupled into the airframe rigid body motions. Figure 14, from reference 26, illustrates the inherent damping available as a function of the flap frequency ratio. Two facts become obvious. First, the choice of the flap frequency will affect the available damping. Typical non-articulated rotor has much higher aerodynamic damping and therefore aerodynamics is indispensable.

Second, because of the importance of the flap motion, means of inducing favorable flapwise response into the aeromechanical stability mode, which consists of primarily the blade lead-lag motion with airframe participation, is of utmost importance. The more favorable flapwise response, the more stable the coupled rotor-airframe system.

Before getting into the discussion of design parameters that may improve rotor-airframe stability, the distinction between rotor stability and rotor-airframe stability should be made. As shown in figure 15 (from ref. 26), the calculated modal damping for the $\Omega - \omega_\zeta$ mode shows two possible regions of instability: one at low collective and the other at high collective. Also shown in dashed line is the lead-lag mode modal damping calculated without the airframe degrees-of-freedom. Although the shape of the curve is similar to the $\Omega - \omega_\zeta$ mode at low collective, it is stable without the airframe motions.

This is verified by the model test results. Figure 16, also from reference 26, shows the time histories for a point at the high collective boundary. After the air resonance mode is excited, the blade lead-lag motion measured in the rotating system is divergent in the rotating system frequency. Likewise, the body pitch and roll motions are divergent in the fixed system frequency. The key is the procedure of arresting this instability by snubbing out the body pitch and roll motion. After the model is snubbed, the pitch and roll oscillations go to zero and the inplane blade bending quickly decays. In other words, without the airframe body degrees-of-freedom participating in the air resonance mode, the regressive lag mode is stable by itself.
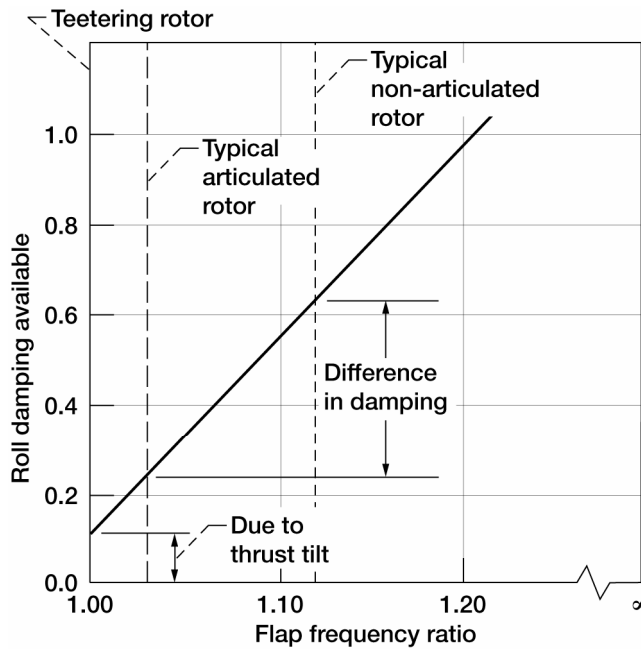
Figure 14.—Source of aerodynamic damping for air and ground resonance. (The original version of this figure first appeared in Burkham, J.E.; and Miao, W.: Exploration of Aeroelastic Stability Boundaries With a Soft-Inplane Hingeless-Rotor Model. J. Amer. Helicopter Soc., vol. 17, 1972. Copyright American Helicopter Society; used with permission.)
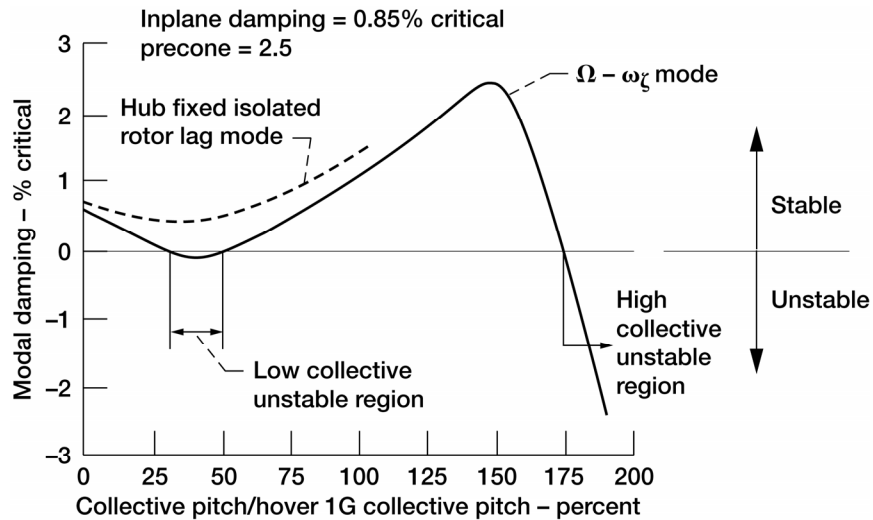
Figure 15.—Comparison of rotor stability and rotor-airframe stability. (The original version of this figure first appeared in Burkham, J.E.; and Miao, W.: Exploration of Aeroelastic Stability Boundaries With a Soft-Inplane Hingeless-Rotor Model. J. Amer. Helicopter Soc., vol. 17, 1972. Copyright American Helicopter Society; used with permission.)
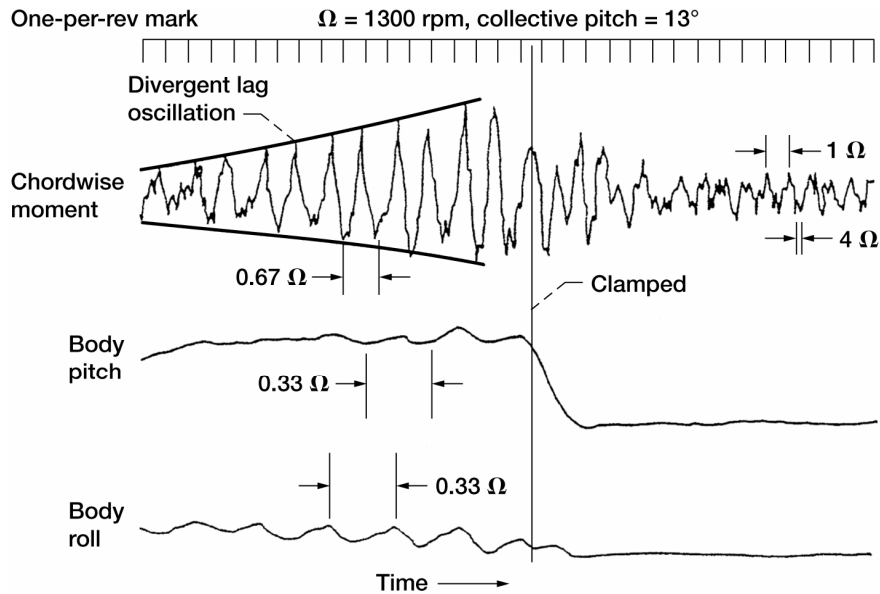
Figure 16.—Time histories of rotor-airframe aeromechanical instability. (The original
version of this figure first appeared in Burkham, J.E.; and Miao, W.: Exploration
of Aeroelastic Stability Boundaries With a Soft-Inplane Hingeless-Rotor Model.
J. Amer. Helicopter Soc., vol. 17, 1972. Copyright American Helicopter Society;
used with permission.)

It is clear that there are additional coupling terms between the rotor degrees-of-freedom and the airframe. One
prime example is the thrust tilted by the cyclic flap motions. It will produce a pitch or roll moment on the airframe
in the direction of the rotor disc tilt caused by the cyclic flapping. This negative aerodynamic spring which couples
the cyclic flapping with airframe pitch and roll has a profound effect on the coupled mode frequencies and
dampings.

The point of all this discussion is to raise a word of caution. Design parameters that enhance rotor stability in
general will enhance rotor-airframe stability. However, their effect should be evaluated specifically for the coupled
rotor-airframe system (ref. 30) because of the existence of the additional couplings between the rotor and airframe.

Useful Design Parameters

As previously mentioned, the key to a successful rotor design from the stability standpoint is to incorporate
favorable couplings to capitalize on the flap damping. Orientation of the pitch axis in space is the prime considera-
tion because of the eventual flap motion coupled into the lead-lag motion through the pitch-flap and the pitch-lag
couplings. Hub geometries that can affect the spacial orientation are shown in figure 11 earlier.

Figure 17, from reference 26, shows the calculated effect of precone on air resonance mode stability. As shown,
zero precone is more stable than 2.5° precone configuration. The negative precone is even better. Stability bound-
aries determined by tests of the model described in reference 26 with three different precone values, figure 18,
substantiated the analytic sensitivity. The YUH-61A hingeless rotor system, although dynamically similar to the
BO-105, has zero precone instead of the 2.5° precone of the BO-105 rotor. As a result, its air resonance mode stabil-
ity is quite good (ref. 27). This sensitivity has been further substantiated by the extensive model tests carried out as
part of the Army/Boeing Bearingless Main rotor program (ref. 31). Figure 19, from reference 32, clearly shows the
beneficial effect introduced by reduced precone, or beam-to-hub coning angle.
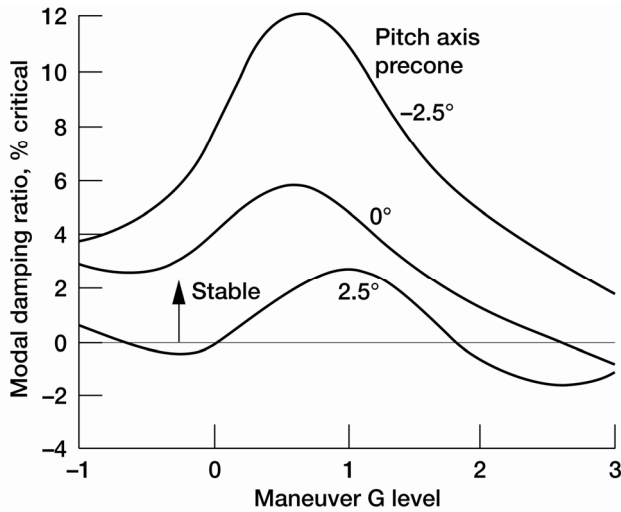
Figure 17.—Effect of pitch axis precone on air resonance stability. (The original version of this figure first appeared in Burkham, J.E.; and Miao, W.: Exploration of Aeroelastic Stability Boundaries With a Soft-Inplane Hingeless-Rotor Model. J. Amer. Helicopter Soc., vol. 17, 1972. Copyright American Helicopter Society; used with permission.)
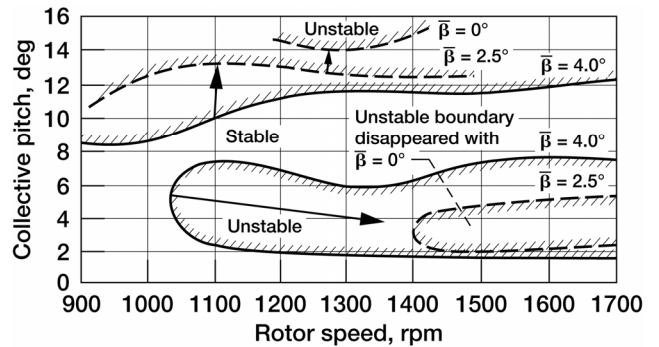

Figure 18.—Effect of precone on test stability boundaries. (The original version of this figure first appeared in Burkham, J.E.; and Miao, W.: Exploration of Aeroelastic Stability Boundaries With a Soft-Inplane Hingeless-Rotor Model. J. Amer. Helicopter Soc., vol. 17, 1972. Copyright American Helicopter Society; used with permission.)
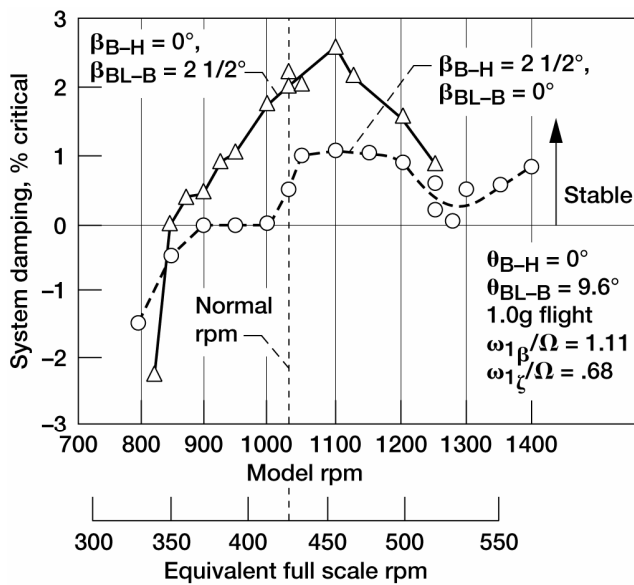
Figure 19.—Effect of beam-to-hub coning angle on air resonance stability. (The original version of this figure was published by the Advisory Group for Aerospace Research and Development, North Atlantic Treaty Organization (AGARD/NATO) in Miao, W.; and Blackwell, R.H.: Aeroelastic Considerations in the Design of High Speed Rotors. AGARD Conference Proceedings CP–354, Aeroelastic Design Considerations in the Preliminary Design of Aircraft, 1983. Used with permission.)
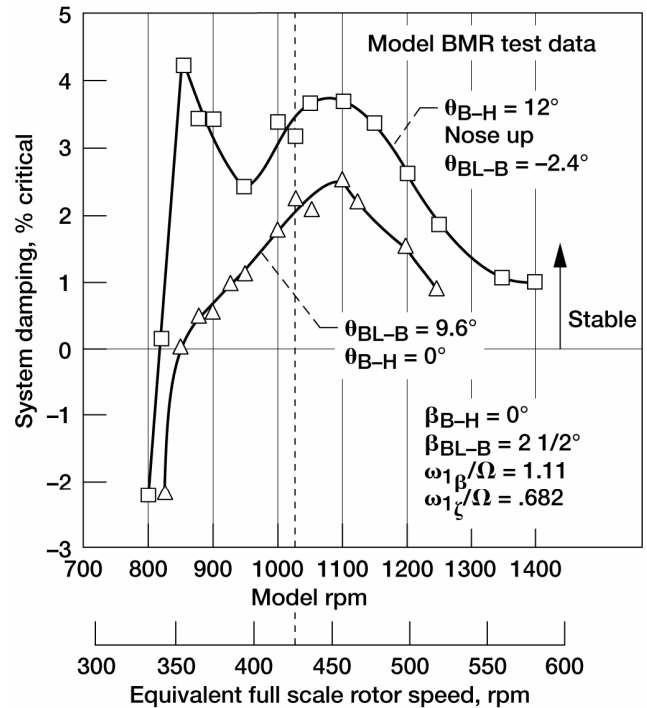
Figure 20.—Effect of beam-to-hub pitch angle on air resonance stability. (The original version of this figure was published by the Advisory Group for Aerospace Research and Development, North Atlantic Treaty Organization (AGARD/NATO) in Miao, W.; and Blackwell, R.H.: Aeroelastic Considerations in the Design of High Speed Rotors. AGARD Conference Proceedings CP–354, Aeroelastic Design Considerations in the Preliminary Design of Aircraft, 1983. Used with permission.)

Rotating the blade cross-sectional principal axes, flapwise and chordwise, about the spanwise pitch axis so that they do not coincide with the inertial axes is one direct way of introducing flap-lag coupling (ref. 33). For a bearingless type of rotor, this can be accomplished by introducing a flexbeam-to-hub pitch angle and/or blade-to-flexbeam pitch angle. The model test data shown in figure 20, from reference 32 are for two configurations. Although both configurations had a resultant blade pitch angle of 9.6°, one configuration achieved this with a beam-to-hub pitch angle of zero and the blade-to-beam pitch angle of 9.6° while the other configuration had a beam-to-hub pitch angle of 12° and the blade-to-beam pitch angle of –2.4°. The latter configuration intuitively possesses more flap-lag coupling than the former, and, as the test data in figure 20 show, it is considerably more stable.

Since the blade pitch motion contributes to the coupling, control system stiffness will also be an important design parameter, as is the location of the pitch arm and push rod attachment point. In summary, the design parameters to be considered, in addition to the control system stiffness and the location of pitch arm and push rod attachment point, are the flapwise stiffness, the chordwise stiffness, precone, droop, torque offset, sweep, beam-to-hub pitch angle, and blade-to-beam pitch angle.

Concluding Remarks

Rotor stability is truly a coupled pitch-flap-lag phenomenon. To assess the problem properly, all three blade motions not only have to be considered, but have to be considered meticulously (refs. 34 and 35). However, simplified analysis which treats only the flap-lag or the pitch-flap motions can provide useful insight to the problems at hand. This is so only when the aeroelastic couplings due to the blade torsion deflection are properly understood and are properly represented in the simplified analyses. Ironically, to understand the analytic trend from the fully coupled pitch-flap-lag analysis, one has to have firm understanding of these intricate aeroelastic couplings.

Rotor stability can be enhanced through judicious use of design parameters that provide favorable aeroelastic couplings. Substantial progress has been made in the understanding of the interplay of these couplings. The aggressive design approach of utilizing these favorable couplings may not be as risky as it appeared to be fifteen years ago.

Rotor-airframe stability is an entirely different problem from the rotor stability problem. Although, in general, design parameters that enhance rotor stability should be beneficial to rotor-airframe stability, it is a good practice to verify their effect for the coupled rotor-airframe case. The prime factor that affects both rotor and rotor-airframe stability is the spacial location and orientation of the pitch axis. A general rule is to place this axis inboard of all the bending flexibility, so that bending-torsion couplings, namely pitch-flap and pitch-lag, can be maximized. The pitch axis should also be oriented as far away from the equilibrium position of the blade as practical so that beneficial couplings are maximized.

References

1. Loewy, R.G.: Review of Rotary-Wing V/STOL Dynamic and Aeroelastic Problems. J. Am. Helicopter Soc. (AIAA Paper 69–0202), vol. 14, no. 3, 1969, pp. 3–23.
2. Friedmann, Peretz P.: Formulation and Solution of Rotary-Wing Aeroelastic Stability and Response Problems. Vertica, vol. 7, no. 2, 1983, pp. 101–141.
3. Friedmann, Peretz P.: Recent Developments in Rotary-Wing Aeroelasticity. J. Aircraft, vol. 14, no. 11, 1977, pp. 1027–1041.
4. Ormiston, Robert A.: Investigations of Hingeless Rotor Stability. Vertica, vol. 7, no. 2, 1983, pp. 143–811.
5. Huber, H.B.: Effect of Torsion-Flap-Lag Coupling on Hingeless Rotor Stability. 29th Annual National V/STOL Forum, American Helicopter Society, Washington, DC, 1973.
6. Hansford, R.E.; and Simons, I.A.: Torsion-Flap-Lag Coupling on Helicopter Rotor Blades. J. Am. Helicopter Soc., vol. 18, no. 4, 1973, pp. 2–12.
7. Johnson, Wayne: Helicopter Theory. Princeton University Press, Princeton, NJ, 1980.
8. Johnson, W.: Recent Developments in the Dynamics of Advanced Rotor Systems. NASA TM–86669, 1985.
9. Kuczynski, W.A.; Sissingh, G.J.; and Sharpe, D.L.: Hingeless Rotor—Experimental Frequency Response and Dynamic Characteristics With Hub Moment Feedback Controls. 28th Annual National Forum, American Helicopter Society, Washington, DC, 1972.

10. Fredrickson, C.; Rumford, K.; and Stephenson, C.: Factors Affecting Fuel Control Stability of a Turbine Engine and Helicopter Rotor Drive System. 27th Annual National V/STOL Forum, American Helicopter Society, Washington, DC, 1971.
11. Horvay, G.: Rotor Blade Flapping Motion. Quart. Appl. Math., vol. 5, no. 2, 1947, pp. 149–167.
12. Lowis, O.J.: The Stability of Rotor Blade Flapping Motion at High Tip Speed Ratios. ARC R&M 3544, 1963.
13. Peters, D.A.; and Hohenemser, K.H.: Application of the Floquet Transition Matrix to Problems of Lifting Rotor Stability. J. Am. Helicopter Soc., vol. 16, no. 2, 1971, pp. 25–33.
14. Tarzanin, F.J., Jr.: Prediction of Control Loads Due to Blade Stall. 27th Annual National V/STOL Forum, American Helicopter Society, Washington, DC, 1972.
15. Blackwell, R.H.; and Merick, P.H.: Effect of Blade Design Parameters on Helicopter Stall Boundaries. 30th Annual National V/STOL Forum, American Helicopter Society, Washington, DC, 1974.
16. Bisplinghoff, Raymond L.; Ashley, Holt; and Halfman, Robert L.: Aeroelasticity. Addison-Wesley Publishing Co., Cambridge, MA, 1955.
17. Miller, R.H.: Helicopter Blade Vibration and Flutter. J. Am. Helicopter Soc., Washington, DC, 1956.
18. Strehlow, H.; and Enenkl, B.: Aeroelastic Design Considerations in the Development of Helicopters. AGARD CP–354, 1983.
19. Chou, Pei Chi: Pitch-Lag Instability of Helicopter Rotors. JAHS Index 1956–1960, 1958.
20. Ormiston, Robert A.; and Hodges, Dewey H.: Linear Flap-Lag Dynamics of Hingeless Helicopter Rotor Blades in Hover. J. Am. Helicopter Soc., vol. 17, no. 2, 1972, pp. 2–14.
21. Young, Maurice I.: A Simplified Theory of Hingeless Rotors With Application to Tandem Helicopters. Proceedings of the 18th Annual National Forum, American Helicopter Society, Washington, DC, 1962, pp. 38–45.
22. Houbolt, John C.; and Brooks, George W.: Differential Equations of Motion for Combined Flapwise Bending, Chordwise Bending, and Torsion of Twisted Nonuniform Rotor Blades. NACA TR–1346 (NACA TN–3905), 1958.
23. Arcidiacono, P.J.: Prediction of Rotor Instability at High Forward Speeds. Volume 1—Steady Flight Differential Equations of Motion for a Flexible Helicopter Blade With Chordwise Mass Unbalance. USAAVLABS–TR–68–18A, 1969.
24. Hodges, D.H.; and Dowell, E.H.: Nonlinear Equations of Motion for the Elastic Bending and Torsion of Twisted Nonuniform Rotor Blades. NASA TN D–7818, 1974.
25. Hodges, Dewey H.; and Ormiston, Robert A.: Stability of Elastic Bending and Torsion of Uniform Cantilever Rotor Blades in Hover With Variable Structural Coupling. NASA TN D–8192, 1976.
26. Burkam, John E.; and Miao, Wen-Liu: Exploration of Aeroelastic Stability Boundaries With a Soft-Inplane Hingeless-Rotor Model. J. Am. Helicopter Soc., vol. 17, no. 4, 1972, pp. 27–35.
27. Miao, W.L.; Edwards, T.; and Brandt, D.E.: Investigation of Aeroelastic Stability Phenomena of a Helicopter by In-Flight Shake Test. NASA SP–415, 1976.
28. Coleman, Robert P.; and Feingold, Arnold M.: Theory of Self-Excited Mechanical Oscillations of Helicopter Rotors With Hinged Blades. NACA TR–1351, 1993.
29. Lytwyn, R.T.; Miao, W.; and Woitsch, W.: Airborne and Ground Resonance of Hingeless Rotors. J. Am. Helicopter Soc., vol. 16, no. 2, 1971, pp. 2–9.
30. Ormiston, Robert A.: Aeromechanical Stability of Soft Inplane Hingeless Rotor Helicopters. 3rd Eur. Rotorcraft and Powered Lift Aircraft Forum, Aix-en-Provence, Paper no. 25, 1977 (also Ormiston, Robert A.: Aeromechanical Stability of Soft Inplane Hingeless Rotor Helicopters. NASA Ames Research Center, 1977).
31. Staley, J.A.; Gabel, R.; and MacDonald, H.I.: Full Scale Ground and Air Resonance Testing of the Army–Boeing Vertol Bearingless Main Rotor. Proceedings of the 35th Annual National Forum of the American Helicopter Society, AHS 79–23, 1979.
32. Miao, W.L.; and Blackwell, R.H.: Aeroelastic Considerations in the Design of High Speed Rotors. AGARD CP–354, 1983.
33. Ormiston, R.A.: Concepts for Improving Hingeless Rotor Stability. Proceedings of the Symposium on Rotor Technology, Essington, PA, 1976.
34. Sopher, R.; and Cassarino, S.J.: Effects of Analytical Modeling Assumptions on the Predicted Stability of a Model Hingeless Rotor. Proceedings of the 41st Annual Forum, American Helicopter Society, Fort Worth, TX, 1985, pp. 85–99.
35. Friedmann, P.P.; and Kottapalli, S.B.R.: Coupled Flap-Lag-Torsional Dynamics of Hingeless Rotor Blades in Forward Flight. J. Am Helicopter Soc., vol. 27, no. 4, 1982, pp. 28–36.

Airframe Structural Dynamic Considerations
in Rotor Design Optimization[*]

Raymond G. Kvaternik
National Aeronautics and Space Administration
Langley Research Center
Hampton, Virginia 23681–2199

T. Sreekanta Murthy
Planning Research Corporation
Hampton, Virginia 23665

Summary

The paper gives an overview and discussion of those aspects of airframe structural dynamics that have a strong influence on rotor design optimization. Primary emphasis is on vibration requirements. The vibration problem is described, the key vibratory forces are identified, the role of airframe response in rotor design is summarized, and the types of constraints which need to be imposed on rotor design due to airframe dynamics are discussed. The paper concludes with some considerations of ground and air resonance constraints on rotor design.

Introduction

The helicopter design process is a combination of all the major engineering disciplines aimed at meeting a wide variety of requirements (fig. 1). Clearly, the design process is multidisciplinary in nature. Although not indicated in figure 1, the design process is also interdisciplinary in character. Because of the complexity of the total design problem, the tendency has been to address the design problems in each of the contributing disciplinary areas as though they were independent (see, for example, figs. 2 and 3). Thus, the design process has been traditionally treated as a sequence of essentially independent design activities. It is clear that such a sequential approach does not, in general, lead to a design which is optimum with respect to all the disciplines. A truly effective design process requires an integrated multidisciplinary approach which fosters the necessary synergism. Structural optimization techniques, if properly brought to bear by the design engineer, could play a key role in establishing such an integrated approach to helicopter design.

The NASA Langley Research Center and the Army Aerostructures Directorate have recently undertaken a major research program which is aimed at developing an integrated, multidisciplinary, optimization-based approach for rotorcraft design (ref. 1). Initial attention under this program is being directed to design optimization of rotors only, with the airframe design assumed to be prescribed and therefore not subject to design changes. As a further expedient, the airframe is also assumed to be decoupled from the rotor and the influence of airframe dynamics is to be accounted for in terms of design requirements (constraints) on the rotor blades. The purpose of this paper is to provide an overview and discussion, both in rather broad terms, of those aspects of airframe structural dynamics that have a strong influence on rotor design optimization. Primary emphasis is on vibration requirements. The vibration problem is described, the key vibratory forces are identified, the role of airframe response in rotor design is summarized, and the types of constraints which need to be imposed on a rotor design due to airframe dynamics are discussed. The paper concludes with some considerations of ground and air resonance constraints on rotor design.

---

[*]This document was first published as Kvaternik, Raymond G.; and Murthy, T. Sreekanta: Airframe Structural Dynamic Considerations in Rotor Design Optimization. NASA TM–101646, 1989.

Disciplines

Aerodynamics
Aeroacoustics
Dynamics
Controls
Structures
Weights
Materials
Aeroelasticity
Propulsion
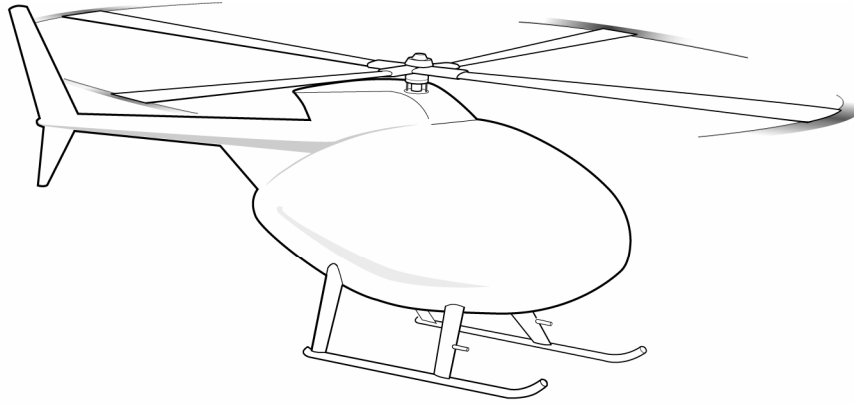
Requirements

Performance
Flight envelope
Economics
Mission
Noise
Life
Vibration
Stability and control
Manufacturability

Figure 1.—The interdisciplinary nature of helicopter design.

Impact loads

Flexible swashplate

Flexible blades coupled modes

Flexible linkages

Structural modes

Black boxes
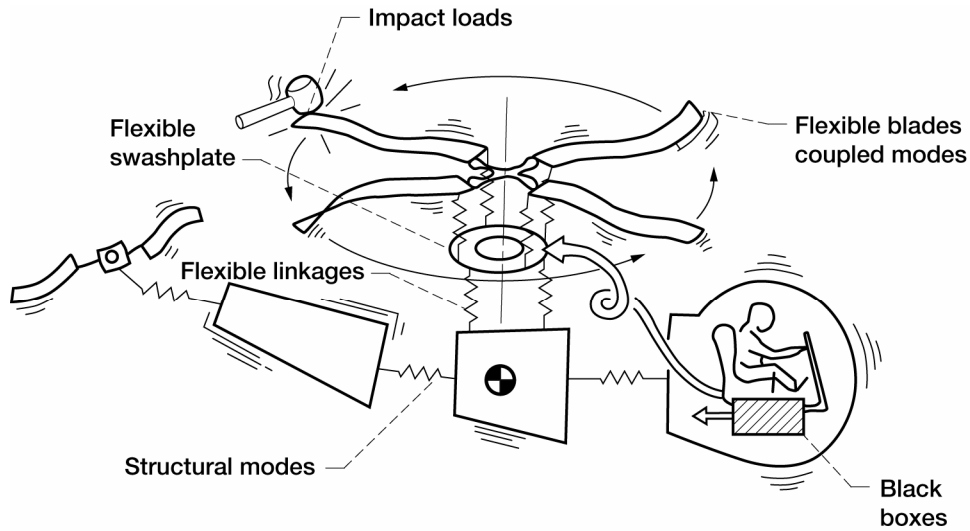
Figure 2.—The helicopter as might be viewed by a dynamicist.

Tip vortex induced dynamic stall

Airfoil dynamic stall

Lift stall– moment stall

Yawed flow

Tail rotor/main rotor wake interaction

Reversed flow

Shock pulse shock stall

Pylon-hub-engine turbulent wake

Wing body interference

Blade vortex "slap"
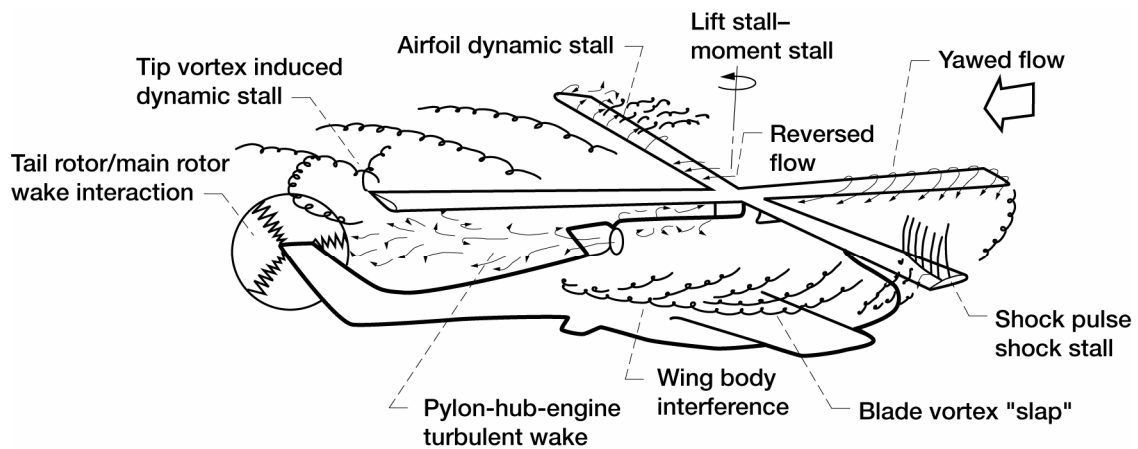
Figure 3.—The helicopter as might be viewed by an aerodynamicist.

Vibrations: The Problem

Helicopters are susceptible to vibrations due to the inherent cyclic nature of the airloads acting on the rotor blades. The vibrations normally pervade both the rotor and the airframe (fig. 4) and can seriously degrade both service life and ride qualities. Vibrations also frequently limit the maximum speed in forward flight. While considerable progress has been made over the past forty years in reducing the level of vibrations in helicopters, the reduction has, for the most part, been achieved through the use of add-on vibration control devices. These devices, while quite effective in reducing vibrations, have usually had significant weight penalties associated with them.

Even though excessive vibrations have plagued virtually all new helicopter development programs, until recently, helicopter manufacturers have relied little on analysis during design in their efforts to limit vibrations. With only a few exceptions, helicopters have been designed to performance requirements while relying on past experience to account for vibrations. Excessive vibrations were then "tinkered out" during ground and flight testing. However, because of the vibration problems encountered during two recent major helicopter development programs, there has emerged a consensus within the industry on the need to account for vibrations more rigorously during both the analytical and experimental phases of design. This need has resulted in the subject of helicopter vibrations receiving considerably increased attention in recent years (ref. 2). The goal (unofficially) set down by the industry is to achieve the vibration levels associated with fixed-wing aircraft, the so-called "jet smooth" ride (ref. 3). To achieve this goal will require the development of advanced design analysis methodologies and attendant computational procedures which properly and adequately take into account vibrations requirements. These procedures will also have to account for the interdisciplinary nature of the design process.
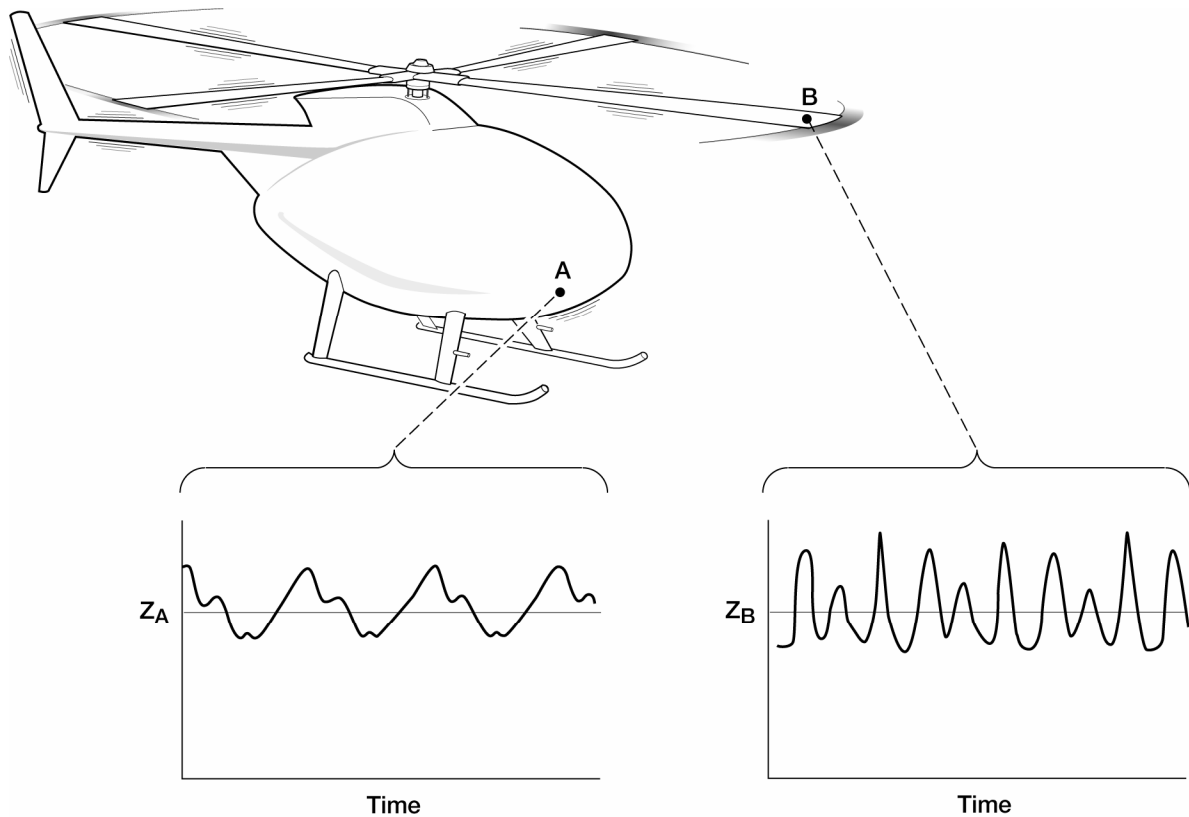
Figure 4.—Steady-state vibrations of flexible helicopter in steady flight.

Vibration design can be broadly classified into three interdependent activities: (1) Use of traditional design techniques to select rotor and airframe parameters which yield low inherent vibrations; (2) Design of vibration control devices to (further) reduce rotor and airframe vibrations; and (3) Vibration testing to verify design concepts and to compensate for any deficiencies in analytical capabilities. The interactive nature of these activities is depicted in figure 5. The diagram indicates that the helicopter vibration design cycle involves analytical and experimental considerations of the rotor, the airframe, and the coupling between the rotor and the airframe. This paper is concerned with only the first of the three activities noted above, that is, the use of traditional rotor and airframe design techniques to limit inherent vibrations.

Various types of analyses are used to support rotor and airframe design work. Special- and general-purpose rotor aeroelastic analysis codes are used to evaluate designs for acceptable rotor/hub vibratory loads. Finite-element models of varying complexity are used to verify adequate placement of airframe natural frequencies with respect to rotor excitation frequencies. Comprehensive rotorcraft aeroelastic analyses suitable for use in vibrations design work and which account for the coupling between the rotor and the airframe are under development. These efforts include both improving existing analyses and developing new analyses. Those analyses which have become available have not yet reached the level of maturity required for use in practical design work.
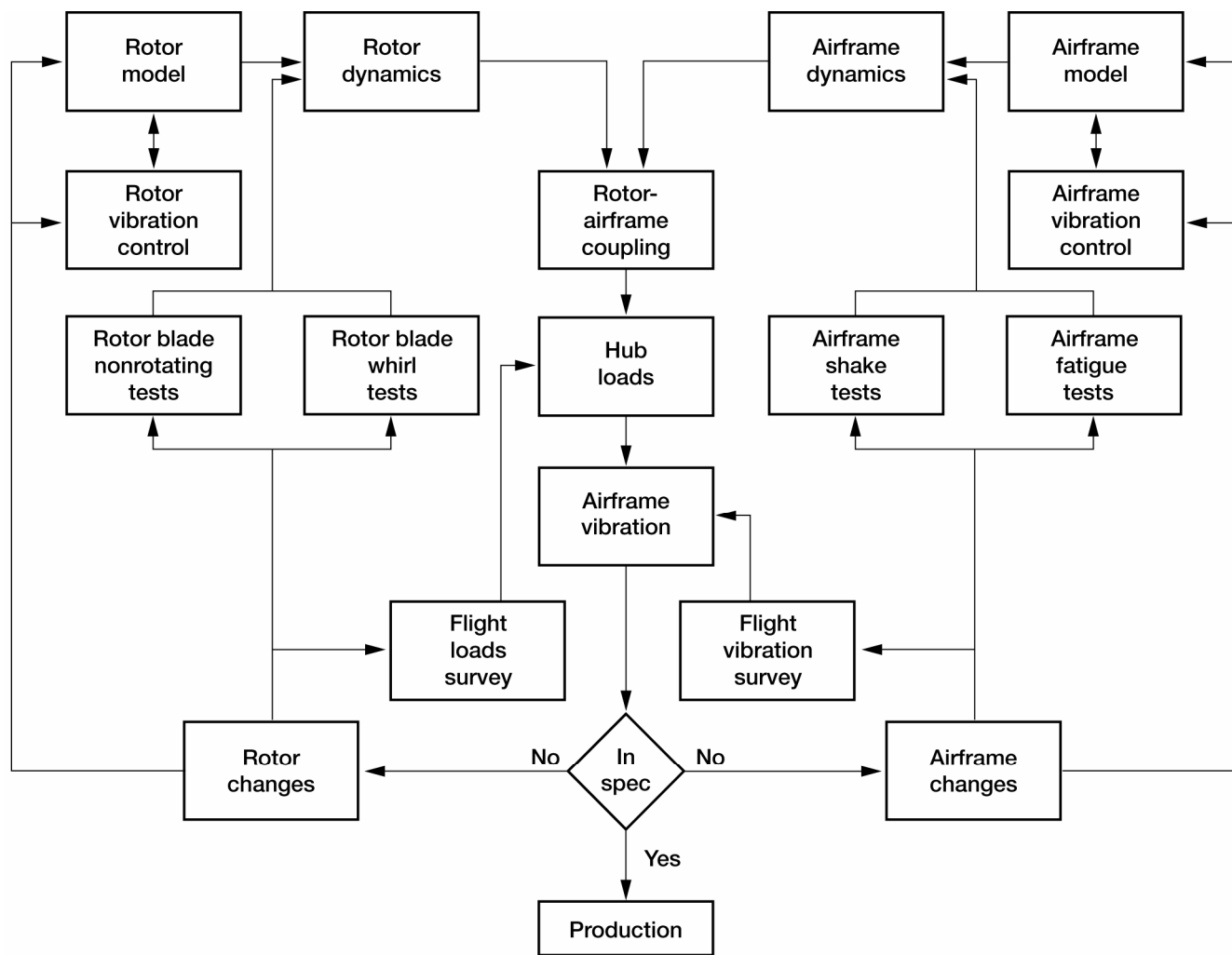
Figure 5.—One view of the helicopter vibration design cycle.

Key Vibratory Forces

The most significant vibrations arising in a helicopter are caused by the cyclic airloads acting on the blades of the main rotor. These loads are transmitted to the hub and down the shaft into the airframe as vibratory forces and moments. There are also other generally less important sources of vibration such as the tail rotor and the impingement of the main rotor wake on the tailboom and empennage. For steady-state flight conditions, the vibratory loads acting both on the rotor and on the airframe are periodic (fig. 4). The harmonic content of these periodic loads is indicated in figure 6. The periodic airloads acting on the rotor blades contain frequencies Ω, 2Ω, 3Ω, . . . , $n\Omega$, where Ω is the rotor rotational speed in radians per second. The loads which are transmitted from the rotor to the airframe are also periodic. However, if the blades are perfectly matched (as assumed here), the shears and moments acting at the roots of the individual blades sum in such a way that the resultant forces and moments which act on the airframe occur only at frequencies which are integer multiples of $N\Omega$ (the so-called blade passage frequency), where N is the number of blades. Thus, the airframe is excited by forces which are at frequencies $N\Omega$, $2N\Omega$, $3N\Omega$, . . . , $nN\Omega$. The oscillatory forces which act on the airframe at the frequencies $nN\Omega$ are generated by blade oscillatory forces which occur at frequencies $nN\Omega$ and $(nN \pm 1)\,\Omega$ when viewed in a coordinate system which is rotating with the blade. Because the magnitude of the harmonic airloads generally decreases with increasing harmonic number, the lower harmonics of the blade airloads are usually more important with respect to vibrations than the higher harmonics. For the airframe then, the largest vibratory forces acting on the airframe are usually those occurring at the frequency $N\Omega$.

Periodic airloads acting on rotor blades contain frequencies Ω, 2Ω, 3Ω, 4Ω, . . .

Rotor forces transmitted to airframe contain frequencies $N\Omega$, $2N\Omega$, $3N\Omega$, . . .

Ω = Rotor rotational speed
N = Number of blades
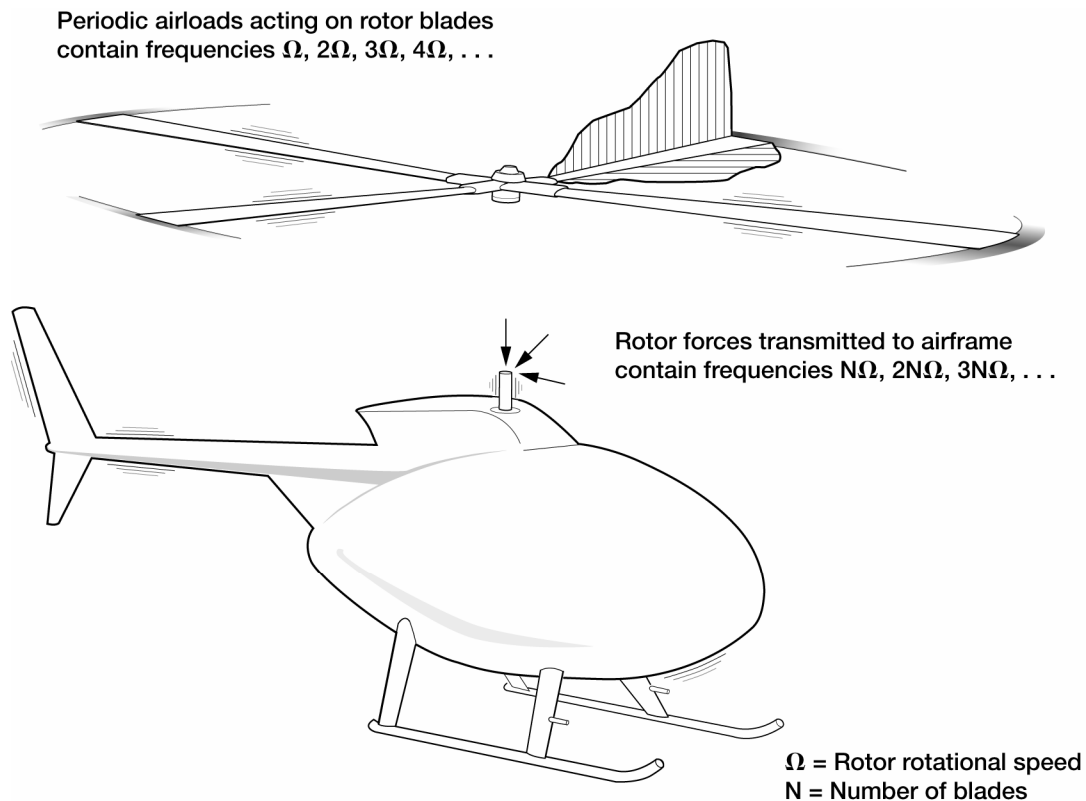
Figure 6.—Oscillatory forces important in helicopter vibrations.

Role of Airframe Response

The major source of vibrations in helicopters, as already mentioned, arises from the cyclic airloads acting on the blades of the main rotor. The dynamic characteristics of the rotor and the airframe and the coupling of these two systems determine the manner in which the helicopter responds dynamically to these oscillatory loads. It has long been recognized that the dynamic (and aerodynamic) interaction between the rotor and the airframe is important in analysis of helicopter vibrations. However, the complexity of the problem is so overwhelming that it has been customary to compute the blade (and hence rotor) vibratory loads assuming that the rotor is operating in a trimmed flight condition but with its hub fixed. The loads are then applied to separate analytical models of the rotor and the airframe for determining their respective vibratory responses. It is clear that this approach cannot account for the dynamic interactions between the rotor and the airframe. A simplified view of how the rotor and the airframe interact to produce vibrations is depicted in figure 7. Due to the periodic nature of the airloads acting on the blades of a rotor, the blades respond dynamically and the resulting vibratory loads are transmitted to the airframe causing it to respond. The resulting airframe motions cause the hub to vibrate which alters the aerodynamic loading on the blades and hence the loads transmitted to the airframe. Depending on the type and configuration of the hub, this interaction can substantially affect the vibrations in both the rotor and the airframe.

Because of increasing demands for further reductions in vibrations to achieve the goal of a "jet smooth" ride, it is now recognized that the simplistic approach described above for accounting for vibrations during design is no longer adequate. Analysis methods which accurately account for the coupling between the rotor and the airframe must be employed in design analyses. Practical computational implementations of the analysis methods are also needed. As previously mentioned, comprehensive rotorcraft aeroelastic analyses suitable for vibrations design work and which account for the coupling between the rotor and the airframe are under development. The problem of defining computational procedures for the coupled system which are suitable for use during structural design is also being addressed. For example, reference 4 establishes foundations for the adequate representation and treatment of the airframe structure in design analysis of helicopter vibrations.
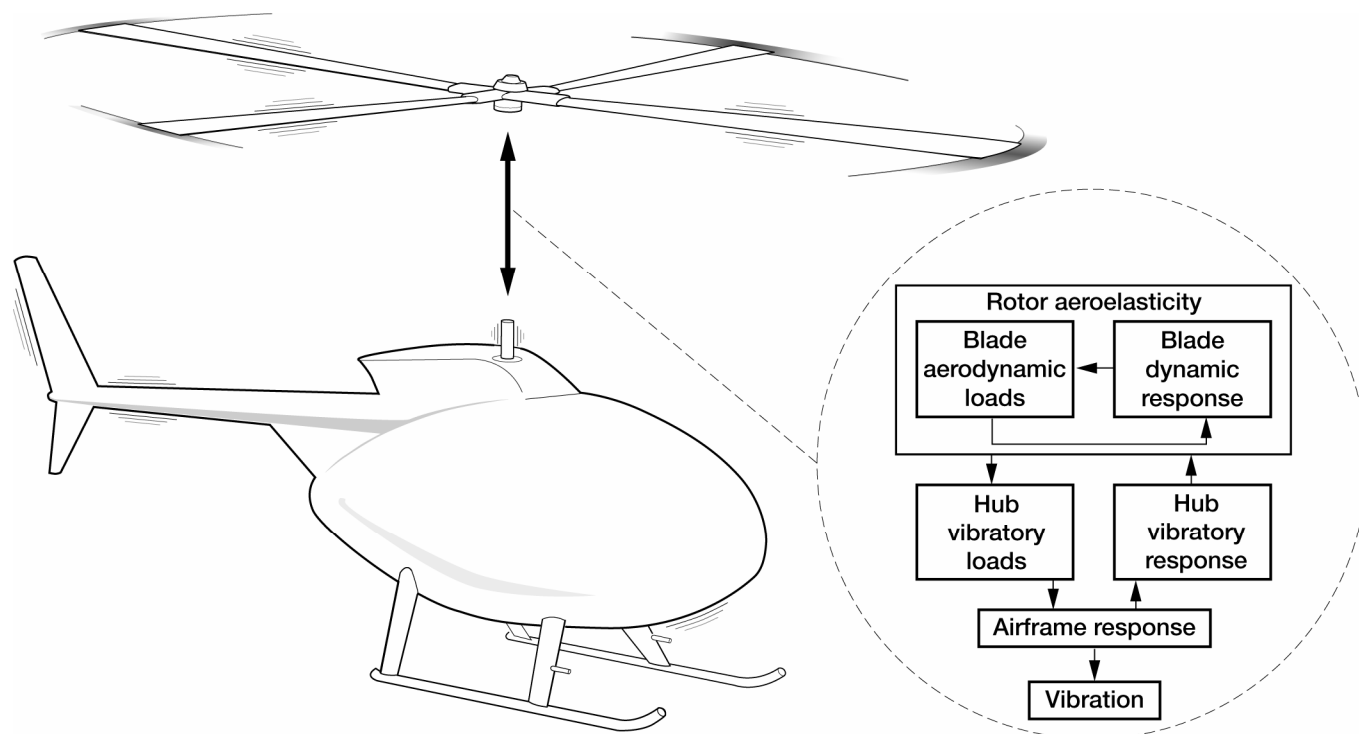
Figure 7.—A simplified view of rotor-airframe interaction in producing vibrations.

Among the practical methods for calculating the vibrations of a rotor and an airframe as a single system, those methods that are based on impedance matching techniques which effect a solution in the frequency domain rather than in the time domain appear to be better suited for use in design work. The impedance coupling technique has been widely used for the vibration analysis of mechanical systems which are composed of an assembly of point-connected components. While the method has been known to the helicopter community for many years and has been employed in analysis of helicopter vibrations (see, for example, refs. 5 to 7), it has not been used extensively in design to limit vibrations. In the application of the method to the solution of the coupled rotor-airframe problem, a trimmed flight condition must first be established for the aircraft. The loads acting on the airframe at the hub are then given by the sum of the rotor hub vibratory loads (both forces and moments) calculated by assuming that the hub is fixed at the attitude angles determined by the trim solution and a (linear) correction term which accounts for small oscillatory hub motions away from trim. The gross vibratory forces exerted by the rotor on the airframe are given by the fixed-hub forces. The fixed-hub forces come from the solution of the underlying nonlinear aeroelastic equations for the rotor with the hub fixed at the attitude angles determined from a trim solution. The correction term is the so-called rotor hub impedance matrix and represents a correction to the gross rotor forces resulting from small motions of the rotor from equilibrium. The rotor impedance matrix is obtained by imposing small oscillatory motions on each of the rotor hub degrees of freedom at the airframe excitation frequencies which are of interest (i.e., $N\Omega$) and calculating the resulting hub loads required to maintain that motion. Changes in the vibratory hub loads per unit hub motion in each rotor hub degree of freedom are then computed. These loads constitute the columns of the impedance matrix. (For zero forcing frequency the impedance matrix reduces to the familiar stiffness matrix). The rotor hub impedance matrix is square, generally complex, and of a size equal to the total number of degrees of freedom associated with the interface point(s) between the rotor system and the airframe system. For a single point interface, such as at the point where the hub is connected to the shaft, the maximum number of degrees of freedom is six. The impedance matrix of the airframe at its interface with the rotor is calculated in a similar manner. Compatibility relations are then written for the interface forces and displacements leading to a set of coupled equations in terms of impedances. The resulting "harmonic balance" equations are a set of simultaneous linear algebraic equations which are solved for the hub motions, from which the airframe (and rotor) vibrations are computed.

Constraints Imposed on Rotor Design

As mentioned earlier, in this paper the airframe structure is assumed to be prescribed and not subject to design changes. Now the design of a rotor which, when coupled to an existing airframe, will result in low vibration levels in the airframe requires knowledge of the latter's dynamic characteristics. Because the airframe design is fixed, it is assumed that its dynamic description in terms of both its frequency response characteristics and its frequencies, mode shapes, and modal structural damping are known. It is also assumed that the airframe hub impedance can be computed for the excitation frequencies of interest (which depend on the number of blades and the rotor rotational speed). The purpose of this section is to identify the types of constraints which airframe dynamics imposes on rotor design from the perspective of vibrations requirements.

The requirement for low vibratory response of the airframe to excitation from the rotor necessitates: (1) Insuring that none of the frequencies of the major airframe modes is close to the predominant rotor exciting frequencies; and (2) Minimizing the rotor induced loads which are transmitted to the airframe.

The proximity of airframe modal frequencies to rotor exciting frequencies as well as the level of airframe vibratory response under excitation are usually determined by inspection of frequency response functions which are computed (or measured) for the airframe structure. Frequency response curves typically have the form depicted in figure 8, which shows the airframe response (usually the acceleration in g's) at some point (and direction) as a function of hub excitation frequency. Usually, many curves of this kind are generated corresponding to each unique combination of the location of the excitation point (the hub is assumed in these discussions) on the airframe, the type (force or moment) and direction (vertical, lateral, etc.) of excitation, and the response points and directions of interest. The "peaks" on the curve occur at the natural frequencies of the airframe; the higher peaks correspond to modes which are major contributors to the total response. The "valleys" represent low levels of response.
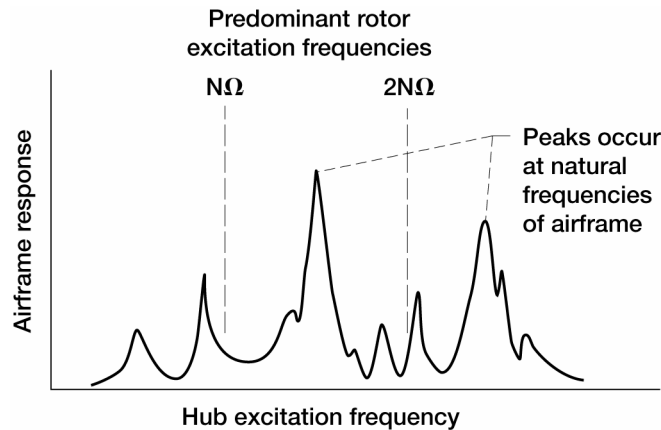
Figure 8.—Typical variation of airframe response with hub excitation frequency.

As previously mentioned, the oscillatory loads acting on the airframe occur at integer multiples of $N\Omega$. Because the magnitude of these loads typically decreases with increasing harmonic number, usually only $N\Omega$ (and sometimes $2N\Omega$) need be considered in practice, as suggested by figure 8. Now the number of blades and the rotor rotational speed are generally determined by aerodynamic requirements early in design. Usual practice is to then design the airframe to avoid any frequencies which would result in either resonance or high amplification at $N\Omega$ (and perhaps $2N\Omega$). However, because the airframe design is assumed to be fixed, the design requirement here is to select N and Ω such that the rotor excitation frequencies $N\Omega$ and $2N\Omega$ are sufficiently removed from the frequencies of the major airframe modes.

The airframe natural frequencies are strongly dependent on the dynamic characteristics of the rotor and thus its effect needs to be included in the calculated (or measured) frequency response functions for the airframe. To satisfy this requirement, the mechanical impedance of the rotor is usually taken into account approximately by including an "equivalent" rotor mass in the airframe finite-element model. If the airframe design is assumed to be fixed, it may be inappropriate to require recalculation of the airframe frequency response functions at each iteration in the rotor design optimization process to account for the changing rotor weight. However, because the weight of the initial rotor design will usually not be too much different from the weight of the final design, an equivalent rotor mass based on the initial weight can be used in the calculation of the frequency responses for the (fixed) airframe design.

Once adequate separation of the rotor exciting frequencies from the major airframe natural frequencies has been established, the remaining step to achieving low vibratory response in the airframe is the reduction of the magnitude (with due attention to phase) of the rotor oscillatory forces and moments which are transmitted to the airframe. This, in effect, requires the reduction of the resultant vibratory shears and moments acting at the roots of the individual blades. There are several design approaches which may be employed to effect this reduction. Some of these are discussed below.

Traditional rotor blade design practice for the reduction of blade vibratory response under airload excitation is based on the criterion of blade frequency placement. The objective in this approach is to maintain adequate separation between the rotating natural frequencies of the blade modes and the frequencies of the periodic airloads acting on the rotor blades over the operating range of rotor rotational speeds. This assessment is usually done with the aid of a blade frequency diagram, such as the one shown in figure 9 for an articulated rotor. The figure shows the variation of the blade frequencies with rotor rotational speed. The radial lines emanating from the origin represent aerodynamic excitation frequencies which occur at harmonics of the rotor speed. Whenever a natural frequency of the blade coincides with one of the lines representing a harmonic of rotor speed, the blade is in a state
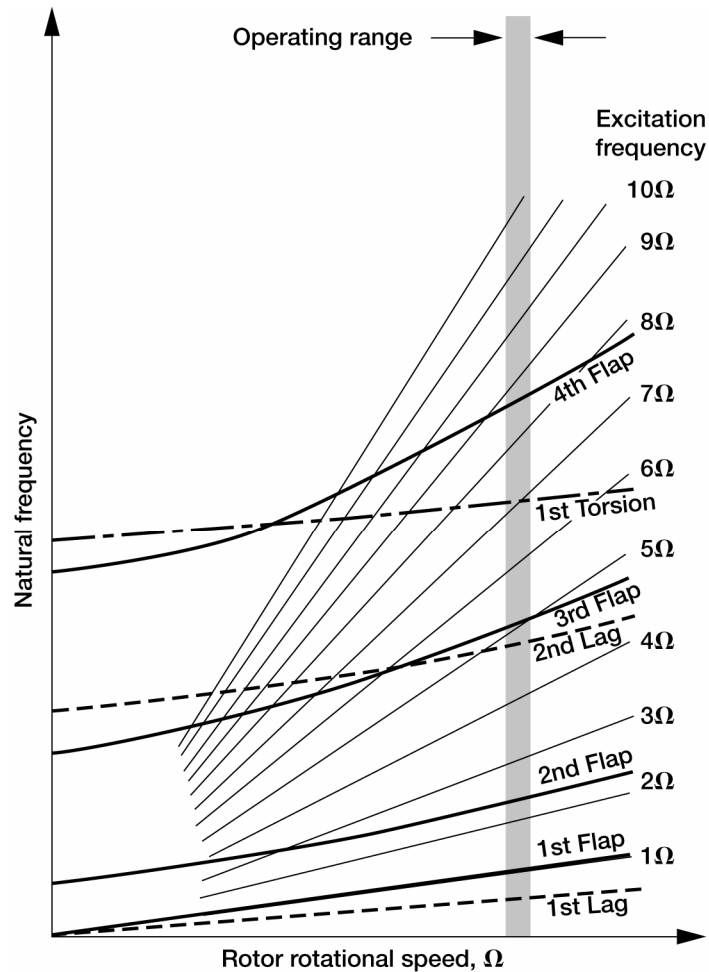
Figure 9.—Typical variation of blade natural frequencies with rotor speed for articulated rotor.

of resonance. Whether the blade responds excessively at resonance depends on whether there is sufficient aerodynamic excitation at that frequency to drive the mode in question and on the amount of structural and aerodynamic damping which is present. As already pointed out, the rotor loads transmitted to the airframe occur at frequencies $nN\Omega$ (see fig. 8). These loads are a result of the blade vibratory responses which, when viewed in a rotating coordinate system, have frequencies $nN\Omega$ and $(nN \pm 1)\Omega$. This suggests that for a low vibration airframe the design requirement for blade frequency placement is to maintain adequate separation of the blade frequencies from $nN\Omega$ and $(nN \pm 1)\Omega$. This will require placing upper and lower bound constraints on the frequencies of the blade modes. However, because the magnitude of the harmonic airloads generally decreases with increasing harmonic number, attention to only the lower harmonics corresponding to $n = 1,2$ would probably suffice in design work.

A blade design which is optimized for blade frequency placement does not guarantee a low vibration airframe. If this approach does not prove adequate, resort must be made to other approaches. Most alternative methods which appear to be well suited for design optimization work are based on directly reducing the resultant shears and moments which act at the roots of the individual blades, rather than indirectly by the method of frequency placement. Such alternative methods could be employed either subsequent to, or in lieu of, a blade design based on the frequency placement criterion, depending on the particular formulation. If such methods are employed as an adjunct to the use of a frequency-based approach, the design established based on frequency placement would provide the initial design for the direct minimization of the blade root shears and moments. The required blade root shears and moments can be calculated using blade aeroelastic analyses formulated to compute such quantities. However, because the aeroelastic equations which underlie these analyses are normally highly nonlinear, such an approach may not be well suited to optimization work where repetitive analyses are required. Approaches based on the use of estimates for the blade root shears and moments which are computed by means of simpler (approximate) expressions probably need to be employed if such methods are to gain acceptance in rotor design optimization work. Two such expressions which appear to be well suited to serve in this capacity have been described in the literature (see, for example, refs. 8 to 10). The expressions, one for "modal shears" and the other for "modal vibration indices," are contributors to the complete expression for the blade root shear obtained from a solution of the equation of motion for the generalized response of the ith blade mode to harmonic airload excitation. The modal shear expression is the simpler of the two and only requires knowledge of the blade mass distribution and its natural modes and frequencies. The vibration indices are directly dependent on the modal shears, but also require knowledge of the blade generalized mass, the aerodynamic forcing function, and the dynamic amplification factor for the blade. Whichever type of expression is used, it would need to be evaluated only for the blade modes which are major contributors to the blade vibratory response. Also, in the calculation of the generalized aerodynamic force which appears in the expression for the vibration indices, an approximate aerodynamic loading would be assumed to simplify the computations.

Depending on the formulation of the optimization problem, it may be useful to impose constraints on the resultant forces and moments which are transmitted to the airframe rather than on the shears and moments which act at the roots of the individual blades. As previously mentioned, for a coupled rotor-airframe system in a trimmed flight condition, the loads acting on the airframe at the hub are given by the sum of the rotor hub loads calculated assuming that the hub is fixed and a correction term dependent on the rotor hub impedance matrix. If one were dealing with the coupled system, it would be appropriate to impose constraints on the resultant forces. However, for the rotor design problem in which the rotor is assumed to be decoupled from the airframe, use of the fixed-hub forces alone is appropriate. Because the fixed-hub forces give the gross vibratory loads acting on the airframe, these should give a good approximation to the total transmitted load.

The computations for blade frequencies which lead to frequency diagrams such as that shown in figure 9 are usually based on the assumption of a fixed hub; that is, the impedance (resistance) presented to the rotor by the airframe at the hub is taken to be infinite. In practice the impedance is finite and it is well known that in this situation the blade natural frequencies and mode shapes can be substantially different from what they are for a fixed hub. In this case, the effects of hub flexibility should probably be included in any calculation of the blade modes and frequencies. This can be done by determining the relevant airframe hub impedance matrix (or some approximation to it) and including it in an appropriately formulated blade dynamic analysis (see, for example, refs. 11 and 12). The inclusion of hub flexibility in the blade dynamic analysis should lead to improved estimates of frequencies for use in a blade frequency placement approach. The corresponding blade modes should also be improved and could be used in rotor aeroelastic analyses to calculate improved estimates of the blade root shears and moments and fixed-hub rotor forces which are employed in constraint equations.

Several types of vibration problems involving the coupling of the rotor/engine/drive train combination with the airframe have been encountered in helicopter development programs (see, for example, ref. 13 and references cited therein). This experience has shown that some blade frequencies may be substantially affected by the dynamics of the drive train system. This suggests that the impedance characteristics of the drive train at the rotor hub may also

have to be included in the determination of the blade modes and frequencies. If the drive system is considered part of the airframe (which design is assumed fixed), then it may impose an additional constraint on the permissible range of values of rotor speed for a new rotor design. This is because the dynamic characteristics of the drive system (e.g., shaft critical speeds) are usually matched to the rotor/engine/airframe system during design.

Ground and Air Resonance

Aeromechanical instabilities are phenomena in which the inertial coupling between the motion of the first inplane blade mode and any airframe mode that involves hub motion in the plane of the rotor produces a growing oscillation. This may occur on the ground (ground resonance) or in flight (air resonance). Because the airframe dynamics play an important role in these instabilities, it seems appropriate to briefly address rotor design requirements as they might be affected by consideration of these instabilities.

Early studies of ground resonance (ref. 14) showed that this type of instability can occur only when the rotating natural frequency of the blade's first inplane mode, ω_L, is less than the rotor rotational speed, Ω, and when the difference between the rotor speed and this blade frequency, $\Omega - \omega_L$, coincides with, or is close to, a frequency of one of the airframe modes having inplane hub motion. Thus, ground resonance is only a problem on articulated and soft-inplane hingeless rotors, both of which have $\omega_L < \Omega$. The instability is purely mechanical, deriving its energy from the shaft torque, and does not develop from aerodynamic forces. (However, aerodynamic forces may affect the level of damping.) The critical airframe modes in ground resonance are typically those associated with essentially rolling and pitching motions on the landing gear.

Air resonance is a similar type of instability which can occur when a helicopter is in flight (see, for example, ref. 15). Both stiff-inplane ($\omega_L > \Omega$) and soft-inplane ($\omega_L < \Omega$) rotors can be susceptible. The instability, if it occurs, is associated with a frequency coalescence of the absolute value of the quantity $\Omega - \omega_L$ with the frequency of an airframe mode containing inplane hub motion. However, unlike ground resonance where the dominant stiffness arises from the landing gear structure, the frequency of the critical airframe mode in the case of air resonance is determined primarily by the aerodynamic stiffness associated with the blade flapping motion. Air resonance is generally not a problem in articulated and stiff-inplane hingeless rotors but must be considered for soft-inplane hingeless rotors.

Assessment of both ground and air resonance can be made from plots of the type shown in figure 10, which illustrates how the pertinent airframe and rotor mode frequencies (all expressed with respect to a fixed coordinate system) vary with rotational speed for both hingeless and articulated rotors. For simplicity, the uncoupled rotor and airframe frequencies are shown in figure 10. The open circles denote points of frequency coalescence between the critical rotor modes and an airframe frequency and are regions of potential instability. The amount of structural or viscoelastic damping present determines whether the system responds excessively at resonance and goes unstable. The rotor design requirement is to insure that, within the operating speed range of the rotor, there are no coincidences of the frequency of the critical rotor mode with an airframe mode and that sufficient damping is present.
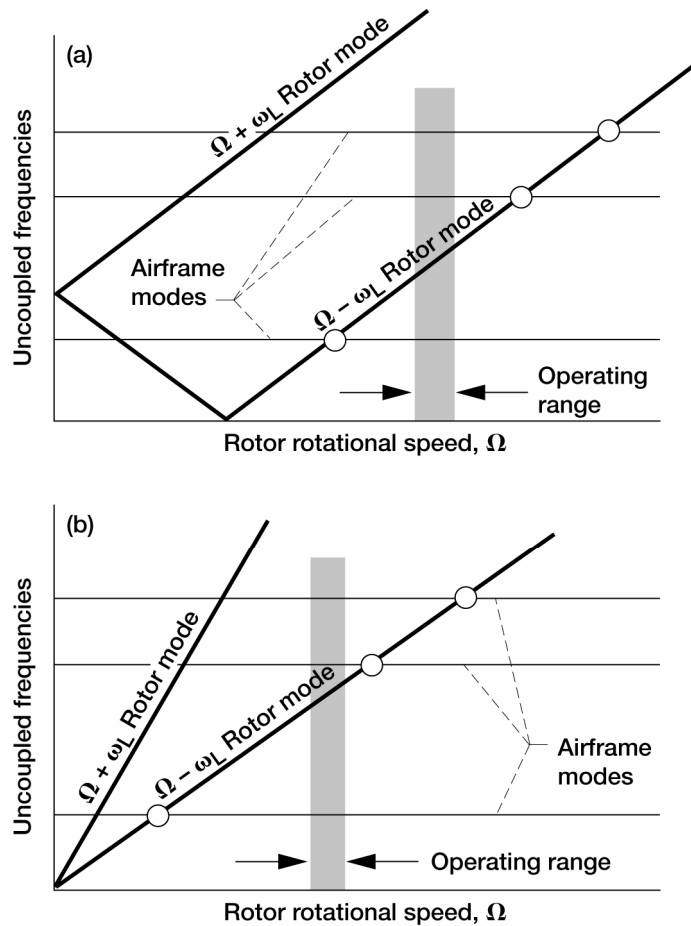
Figure 10.—Typical variation of uncoupled rotor and airframe frequencies with rotor rotational speed for assessment of ground and air resonance. (a) Hingeless rotor. (b) Articulated rotor.

Concluding Remarks

An overview and discussion has been presented of those aspects of airframe structural dynamics that have a strong influence on rotor design optimization. Primary emphasis was placed on vibration requirements. The vibration problem was described, the key vibratory forces were identified, the role of airframe response in rotor design was summarized, and the types of constraints which need to be imposed on rotor design due to airframe dynamics were discussed. Some considerations of the influence of ground and air resonance on rotor design were also discussed.

References

1. Adelman, Howard M.; and Mantay, Wayne R.: Integrated Multidisciplinary Optimization of Rotorcraft: A Plan for Development. NASA TM−101617 (AVSCOM−TM−89−B−004), 1989.
2. Kvaternik, Raymond G.; Bartlett, Felton D., Jr.; and Cline, John H.: A Summary of Recent NASA/Army Contributions to Rotorcraft Vibrations and Structural Dynamics Technology. NASA/Army Rotorcraft Technology Conference, NASA CP− 2495−VOL−1, 1988, pp. 71−179.

3. Gabel, R.: The Future: When Helicopter Smooth Surpasses Jet Smooth. Keynote Address, AHS National Specialists' Meeting on Helicopter Vibration, Hartford, CT, 1981.
4. Kvaternik, R.G.; and Walton, W.C., Jr.: A Formulation of Rotor-Airframe Coupling for Design Analysis of Vibrations of Helicopter Airframes. NASA RP–1089, 1982.
5. Gerstenberger, W.; and Wood, E.R.: Analysis of Helicopter Aeroelastic Characteristics in High-Speed Flight. AIAA J., vol. 1, 1963, pp. 2366–2381.
6. Novak, M.E.: Rotating Elements in the Direction Stiffness Method of Dynamic Analysis With Extensions to Computer Graphics. Shock Vib. Bull. 40, pt. 4, 1969, pp. 41–46.
7. Staley, J.A.; and Sciarra, J.J.: Coupled Rotor/Airframe Vibration Prediction Methods. Rotorcraft Dynamics, NASA SP–352, 1974, pp. 81–90.
8. Blackwell, R.H., Jr.: Blade Design for Reduced Helicopter Vibrations. J. Am. Helicopter Soc., vol. 28, no. 3, 1983, pp. 33–41.
9. Davis, M.W.; and Weller, W.H.: Application of Design Optimization Techniques to Rotor Dynamics Problems. Presented at the 42nd Annual National Forum of the American Helicopter Society, Washington, DC, 1986, pp. 27–44.
10. Taylor, R.B.: Helicopter Rotor Blade Design for Minimum Vibration; Final Report. NASA CR–3825, 1984.
11. Weller, W.H.; and Mineck, R.E.: An Improved Computational Procedure for Determining Helicopter Rotor Blade Natural Modes. NASA TM–78670, 1978.
12. Buffalano, A.C.; and Wood, E.R.: Parametric Investigation of the Aerodynamic and Aeroelastic Characteristics of Articulated and Rigid (Hingeless) Helicopter Rotor Systems. TRECOM–TR–64–15, 1964.
13. Twomey, W.J.: Review of Engine/Airframe/Drive Train Dynamic Interface Development Problems. Proceedings of the AHS Specialists' Meeting on Helicopter Propulsion Systems, American Helicopter Society, Washington, DC, 1980.
14. Coleman, Robert P.; and Feingold, Arnold M.: Theory of Self-Excited Mechanical Oscillations of Helicopter Rotors With Hinged Blades. NACA–TR–1351 (Supersedes NACA TN 3844), 1958.
15. Donham, R.E.; Cardinale, S.V.; and Sachs, I.B.: Ground and Air Resonance Characteristics of Soft In-Plane Rigidrotor System. J. Am. Helicopter Soc., vol. 14, no. 4, 1969, pp. 33–41.

Fundamental Dynamic Considerations in Tilt-Proprotor VTOL Aircraft Design—I[*]

Troy M. Gaffey and Ying G. Yen
Bell Helicopter Company
Fort Worth, Texas 76101

Raymond G. Kvaternik
National Aeronautics and Space Administration
Langley Research Center
Hampton, Virginia 23681–2199

Introductory Remarks

Tiltrotor aircraft operating at high speeds in the airplane mode of flight can exhibit a variety of dynamic aeroelastic phenomena that are driven by the aerodynamic forces and moments generated by the large proprotors characterizing such configurations. In particular, these aircraft are susceptible to a proprotor/pylon aeroelastic instability akin to propeller whirl flutter. Such an instability was first encountered during full-scale testing of the Bell XV-3 tiltrotor in the NASA Ames 40- by 80-foot Wind Tunnel in 1962. Extensive analytical and experimental studies of small dynamically scaled models were conducted by Bell subsequent to this incident and led to both an explanation for and a means of eliminating the instability. Both government and industry undertook a number of other studies in the subject area over the next decade or so. Taken as a whole, these early studies helped to establish key elements of the technology base needed to later successfully address the issue of proprotor/pylon/wing aeroelastic stability in the design of the Bell XV-15 tiltrotor research aircraft in the mid-1970s, the Bell/Boeing V-22 Osprey in the mid-1980s, and the Bell/Agusta BA609 in the late 1990s.

The Aeroelasticity Branch at NASA Langley Research Center has been actively involved in tiltrotor aeroelastic research since 1968, when a joint NASA/Bell test of a 0.133-scale semi-span dynamic aeroelastic model of a proposed Bell tiltrotor design (designated the Model 266) was conducted in the Transonic Dynamics Tunnel. The results of this investigation were reported by T.M. Gaffey, J.G. Yen, and R.G. Kvaternik in a paper entitled "Analysis and Model Tests of the Proprotor Dynamics of a Tilt-Proprotor VTOL Aircraft" that was presented at the Air Force V/STOL Technology and Planning Conference in Las Vegas, NV, September 23–25, 1969. Although the paper addresses a specific tiltrotor design, the discussion of key structural and kinematic design parameters and design guidelines for ensuring acceptable proprotor/pylon/wing stability and blade flapping response is not applicable only to the Model 266. This is so because the structural dynamics of the wing and the blades are presented and discussed in terms of their nondimensional per-rev natural frequencies (i.e., their natural frequencies divided by the rotor rotational speed). Because of the broader applicability of this discussion, this section of the paper is reproduced below.

Fundamental Dynamic Considerations

Proprotor Flapping

In the airplane mode a freely flapping proprotor will develop a flapping angle with respect to its shaft if the aircraft is pitched or yawed or if operated at a steady angle of attack. This flapping is due to two aerodynamic effects. If the shaft has an angle of attack with respect to the freestream, the blades experience a cyclic variation in

---

[*]This document was excerpted from Gaffey, T.M.; Yen, J.G.; and Kvaternik, R.G.: Analysis and Model Tests of the Proprotor Dynamics of a Tilt-Proprotor VTOL Aircraft. Presented at the Air Force V/STOL Technology and Planning Conference, Las Vegas, Nevada, Sep. 23–25, 1969. Used with permission.

local angle of attack. The resulting one-per-rev flapping moment causes the tip-path plane to precess until the local blade angle of attack is constant around the azimuth. If the shaft has a pitching or yawing rate, the proprotor lags the shaft motion in order to generate the aerodynamic flapping moment required to precess the rotor at the shaft angular rate.

Flapping amplitude.—The amplitude of flapping resulting from shaft angle of attack and angular rate is approximated by equations (1) and (2), respectively. These are for a freely flapping rotor without flapping hinge offset, flapping restraint, or pitch-flap coupling.

$$\partial\beta/\partial\alpha_{shaft} = \tan^2\phi_{3/4} \tag{1}$$

and

$$\partial\beta/\partial\alpha_{shaft} = 16/\gamma\Omega\cos\phi_{3/4} \tag{2}$$

where $\phi_{3/4}$ is the inflow angle at the blade three-quarter radius and γ is the blade Lock number.

Insight into the significance of proprotor flapping can be gained by considering the magnitude of these derivatives at an inflow ratio of $\lambda = V/\Omega R = 1.0$, i.e., at a propeller advance ratio of $J = \pi$. This would correspond to 350 knots for a typical design. At this advance ratio the inflow angle at the three-quarter radius, $\phi_{3/4}$, is 53 degrees. Using XV-3 proprotor parameters for this example, the angle-of-attack derivative, $\partial\beta/\partial\alpha$, is 1.77 degrees/degree and the angular rate derivative is 0.665 degrees/degree per second. At an inflow ratio of $\lambda = 1$, angles of attack of up to 6 to 7 degrees and angular rates of 15 degrees per second can be encountered in maneuvers with consequent large flapping.

A large flapping amplitude is not, by itself, a problem. But the accommodation of large flapping amplitudes does pose a problem since it requires a longer mast to provide greater flapping clearance. A long mast reduces proprotor stability and flight mode stability since it increases the arm over which destabilizing proprotor inplane shear forces act. Other design problems, such as providing sufficient hub flapping clearance, may also arise. In general, it has been found that some means must be provided to reduce flapping amplitudes in airplane mode. The amount of reduction depends on a trade-off between flapping, blade loads, proprotor stability, and flight mode stability.

Methods of reducing flapping.—A number of means are available to keep proprotor flapping to an acceptable level. Among those investigated are: flapping restraint, pitch-flap coupling, and automatic flapping feedback. Both the angle-of-attack and rate derivatives may be reduced by using flapping restraint, flapping hinge offset, or pitch-flap coupling to detune the rotor blade from the normal flapping natural frequency of one per rev. Equation (3) gives the angle-of-attack derivative as a function of the flapping natural frequency, $\overline{\omega}_\beta$.

$$\partial\beta/\partial\alpha = \frac{\tan^2\phi_{3/4}}{\sqrt{1+\left[\dfrac{8\left(\overline{\omega}_\beta{}^2-1\right)}{\gamma\cos\phi_{3/4}}\right]}} \tag{3}$$

A similar expression is available for the rate derivative.

In equation (3) $\overline{\omega}_\beta$ is the flapping natural frequency in cycles per revolution given by

$$\overline{\omega}_\beta = \frac{\omega_\beta}{\Omega} = \sqrt{1 + \frac{3}{2}\frac{e}{R} + \frac{K_b}{I_b\Omega^2} + \frac{\gamma\tan\delta_3}{8\cos\phi_{3/4}}} \qquad (4)$$

From (4) it follows that flapping hinge offset, flapping restraint, or pitch-flap coupling separately or in combination may be used to vary the flapping natural frequency. Either positive or negative pitch-flap coupling may be used since they are equally effective in reducing flapping. Also, it is evident from equation (2) that rate flapping can be reduced by employing lightweight rotor blades, i.e., blades with a high Lock number.

Automatic flapping feedback is an attractive approach to controlling the flapping amplitude. Either aircraft attitude or blade flapping can be sensed and an appropriate pitch change made using the cyclic pitch system. In theory, flapping can be nearly eliminated using flapping feedback. However, this method requires lateral cyclic pitch to be incorporated in the design. Normally only longitudinal cyclic pitch control is required on tilt-proprotor aircraft.

All of the means of reducing flapping affect other dynamic considerations, principally blade loads and proprotor stability. In selecting the means to be used, these other effects must also be considered.

Flapping restraint: Flapping restraint (or flapping hinge offset) affects rotor stability and blade loads as well as reducing flapping. For moderate values of flapping restraint proprotor stability is increased, which makes this approach very attractive. However, high blade loads are incurred by even moderate values of flapping restraint. The use of flapping restraint implies that hub and blade out-of-plane moments will be generated. At the high inflow angles associated with propeller operation these are accompanied by inplane moments. It is the blade stresses arising from the inplane moments which pose a restriction on the use of flapping restraint. Figure 4(a) summarizes the results of Bell studies of the use of flapping restraint. These have shown that the amount of restraint required to constrain flapping is in excess of that allowed by blade load considerations.

Pitch-flap coupling: Pitch-flap coupling has a negligible effect on blade loads but reduces proprotor-pylon stability. The reduction in flapping obtained with pitch-flap coupling, along with the effect on stability, is shown in figure 4(b). Blade motion stability considerations dictate whether positive or negative pitch-flap coupling should be employed. For proprotors with the first inplane frequency slightly above one per rev, positive pitch-flap coupling must be used. The converse is true for rotors having the first inplane frequency below one per rev.

Automatic flapping control: Application of this method is limited by transient flapping control requirements and by proprotor stability considerations. Figure 4(c) shows the reduction of steady-state flapping as a function of the static gain. Steady-state flapping can be nearly eliminated using nominal static gains. The effect on transient flapping and stability is illustrated by the time history of a model's flapping response to a step pitch input representing a sudden gust. Note that little reduction in peak transient flapping is observed and that the system damping is reduced. Compensating networks can be used to mitigate the destabilizing effects but these must be varied with rpm and airspeed to be effective. Probably the controlling consideration is reliability of automatic controls.
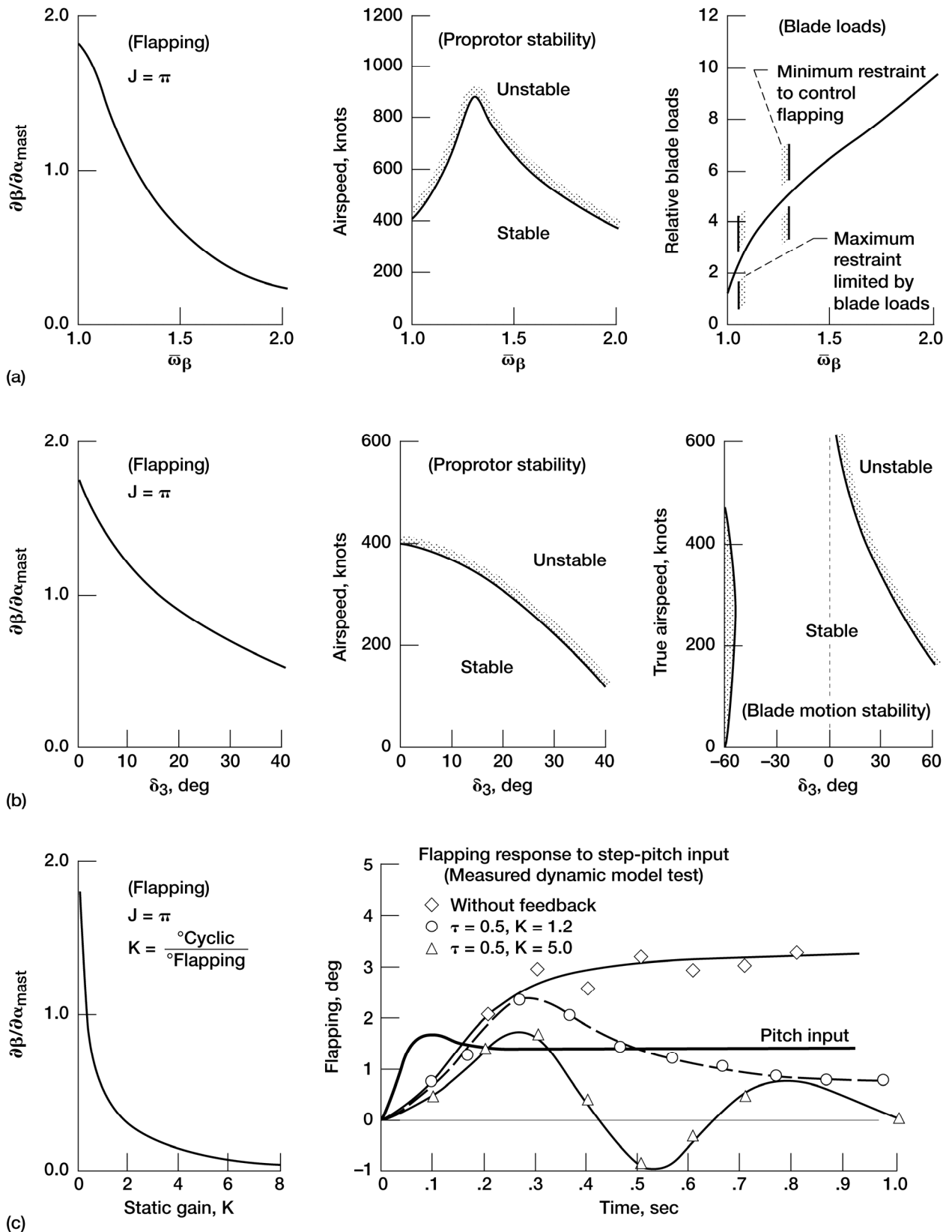
Figure 4.—Flapping control selection considerations. (a) Flapping restraint. (b) Pitch-flap coupling. (c) Automatic flapping control.

Proprotor Stability

Superficial considerations might at first lead one to believe that design considerations for proprotor stability are the same as those for propeller-whirl flutter. This is not entirely the case because of the proprotor's flapping and feathering degrees of freedom. Additional complications arise with the proprotor from the more flexible blades, pitch-flap and pitch-lag couplings, and control system flexibility and feedback. These give rise to the possibility of instabilities other than the familiar propeller autoprecession.

When all the possible factors affecting proprotor stability are considered, the task of providing the required stability may seem nearly insurmountable. However, analytical and experimental investigations have generated analytical tools which can be used with confidence to predict proprotor stability. Furthermore, design guidelines similar to those available for other types of flutter have been established.

Mechanism of proprotor instability.—The basic cause of proprotor instability is the same as that of propeller whirl flutter—the aerodynamic forces generated by precession. However, the proprotor's flapping degree of freedom causes basic differences in the nature of the proprotor's precession generated aerodynamic forces. This leads to basic differences in the nature of proprotor instability as well as to differences in design solutions. For example, pylon damping has a strong stabilizing influence on propeller whirl flutter but only has a small effect on proprotor stability.

The mechanism of proprotor instability can be understood by considering the proprotor inplane shear forces generated by pylon pitching. These are plotted in figure 5 as a function of the pitching frequency. Two mast lengths are indicated to show the influence of translational damping. Note that for a freely flapping proprotor moments cannot be transferred at the hub. Only inplane shear forces act on the pylon.

The most significant feature shown in figure 5 is the positive value of C_{Z_q} for pitching frequencies below 0.6 cycles per rev. This means that the proprotor contributes large negative damping to pylon pitching modes whose frequency is below 0.6 cycles per rev at $J = \pi$. The pitch frequency at which C_{Z_q} contributes negative damping increases with increasing airspeed. At the same time the C_{Z_α} derivative acts so as to reduce the pylon natural frequency in pitch. Note that translational damping (compare $h/R = 0.5$ to $h/R = 0.3$) has only a small effect on the pitch frequency at which C_{Z_q} becomes positive.

The effect of the proprotor inplane shear force on the stability of a three degree-of-freedom proprotor/pylon system is shown in figure 6. The system consists of a proprotor with longitudinal and lateral tip-path plane freedom, mounted on a pylon with pitching freedom only. Arrows indicate the root motion with increasing airspeed.

At low airspeeds the damping of the pylon pitch mode is seen to be increased by the proprotor. This is due to translational damping. But as airspeed increases both the frequency and the damping of the pylon mode decrease and the mode becomes unstable.

The modes labeled $\Omega \pm \omega_\beta$ in figure 6 are the tip-path-plane precessional modes. These may be explained as follows: A proprotor has two uncoupled flapping modes. In the rotating system they have the same natural frequency, ω_β, but one involves precession in the direction of rotation; the other, precession opposite to the direction of rotation. Without flapping restraint or pitch-flap coupling the natural frequency, $\overline{\omega}_\beta$, is one per rev; flapping restraint and pitch-flap coupling raise or lower the flapping natural frequency in accordance with equation (4). For example, the flapping natural frequency of the Model 266 proprotor, which has a pitch-flap coupling ratio of 0.414 ($\delta_3 = -22\ 1/2°$), is 0.875/rev at low inflow angles and decreases with airspeed.
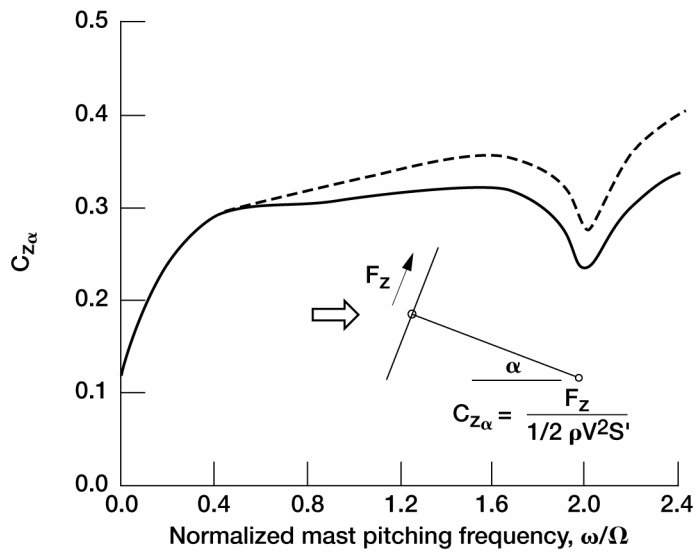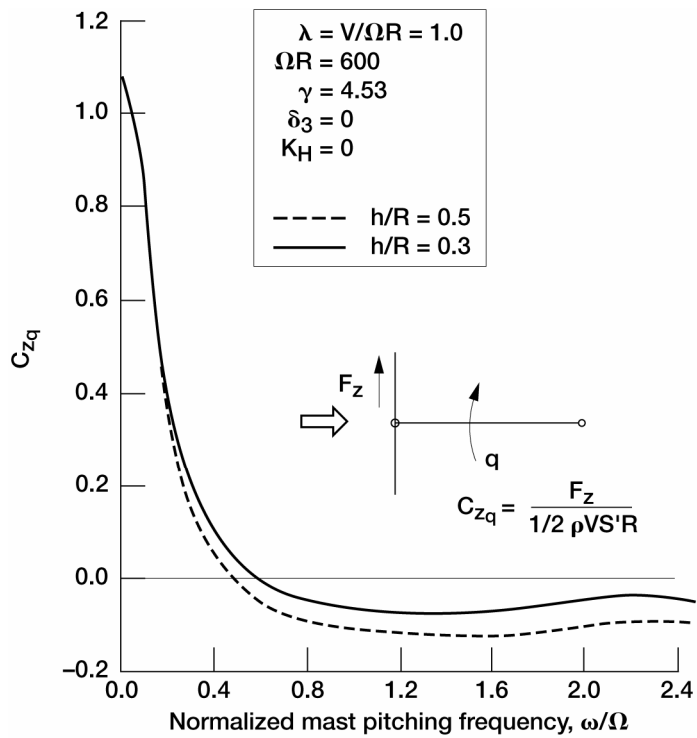
Figure 5.—Proprotor inplane shear derivatives.
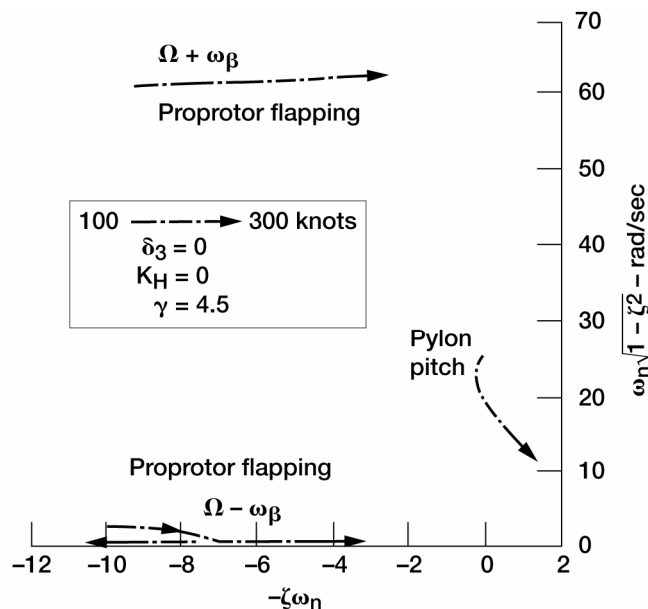
Figure 6.—Root locus of three-degree-of-freedom system.

Both of the uncoupled flapping modes are aerodynamically damped with the damping ratio given by equation (5) below:

$$\zeta_\beta = \frac{\gamma \cos \phi_{3/4}}{16 \overline{\omega}_\beta} \tag{5}$$

The damping ratio of the Model 266 proprotor flapping modes is 0.32 at low inflows and decreases with airspeed.

Viewed in the nonrotating system the flapping mode precessing opposite to the direction of rotation appears as a low frequency precession of the tip-path plane at a frequency of $\Omega - \omega_\beta$. For the Model 266 proprotor the nonrotating system frequency is 0.125 per rev and is a forward precession of the tip-path-plane. (For flapping restraint or negative pitch-flap coupling this mode is a backward precession.) The flapping mode which precesses in the direction of rotation has a frequency of $\Omega + \omega_\beta$ and is a forward precession of the tip-path-plane. The dip in C_{Z_α} at about 2/rev in figure 5 is due to the $\Omega + \omega_\beta$ mode.

Under certain conditions the flapping modes may also become unstable. The XV–3 proprotor instability in the 1962 wind tunnel test was a flapping mode. It involved large amounts of proprotor flapping with simultaneous pylon pitching and yawing at a very low frequency, 0.7 cycles per second or 0.13 cycles per rev. It was of limit amplitude. Flapping mode instability only occurs for very soft pylon mountings and high values of pitch-flap coupling or flapping restraint.

Design guidelines.—Useful design guidelines can be established by considering the influence of various structural and kinematic parameters on proprotor stability. Since the proprotors will generally be wing-tip mounted the wing torsion, beam and chordwise stiffnesses have a strong influence on stability. Pylon yawing stiffness can also have a strong influence under certain conditions. The particular influence of each of these wing parameters will be established by building up a proprotor-wing-pylon system from the simple three degree-of-freedom system.

The wing torsional degree-of-freedom corresponds to pylon pitching for proprotors rigidly attached to the wing tip. For a three degree-of-freedom system the stability is essentially a function of the pylon pitch (or wing torsion)

static natural frequency. This is shown in figure 7(a). Mast length or pylon stiffness by themselves have only a small effect on the stability. A long mast combined with a pylon pitch stiffness that gives the same natural frequency is more stable because of the disc translational damping. However, the increase in stability is slight because of the large proprotor negative damping contribution to the pylon when the pylon frequency falls below the positive C_{Z_q} threshold (see fig. 5). Consequently, the use of as short a mast as is possible, consistent with other design considerations, is desirable in tilt-proprotor designs. At the same time the wing structural design should be selected to achieve the highest possible torsional stiffness.

Pylon isotropy has a much smaller effect on proprotor stability than it does on propeller-whirl flutter. The effect of pylon isotropy is shown in figure 7(b). Here the stability boundary for a geometrically isotropic system is shown as a function of the ratio of the pylon yaw to pitch static natural frequency. Perfectly isotropic pylons will have reduced stability, but if the frequency ratio is greater than 1.2 the effect of adding the yaw degree of freedom is negligible. This is provided the yaw stiffness is greater than that of the pitch. For pylons rigidly attached to the wing tips the pylon yaw stiffness will normally be 5 to 10 times that of the wing torsion stiffness.

Wing beam freedom can have a stabilizing or destabilizing effect on stability, depending on its frequency ratio with respect to pylon pitching. This is shown in figure 7(c). Normally wing beam strength requirements for tilt-proprotor aircraft will result in wing beam frequency ratios of about 0.35 to 0.5 cycles per rev. In that range prop-rotor stability is not highly sensitive to variations in beam stiffness. Wing beam stiffness can be established on a strength basis alone.

Normal wing chordwise frequency ratios have a negligible effect on proprotor stability. This is illustrated in figure 7(d). Degradation of stability is observed only when the chord frequency is below 0.6 per rev. For most wing designs the chordwise stiffness will be at least 3 to 4 times that of the beam, giving chord frequency ratios of 0.7 to 1.0. For the designer, the principal problem encountered with the wing chord mode is keeping it out of 1-per-rev resonance.

Proprotor parameters such as flapping restraint have a strong influence on proprotor stability. The effect of these parameters was shown earlier in figure 4. For proprotor stability the highest flapping restraint possible, consistent with blade load considerations, should be used. The smallest value of pitch-flap coupling that will give acceptable transient flapping control should then be selected. Blade motion stability considerations will dictate whether positive or negative pitch-flap coupling should be employed.

The effect of blade flexibility on proprotor stability is illustrated in figure 7(e) as a function of the first inplane natural frequency at a collective pitch corresponding to $\lambda = 1$. Blade inplane frequencies above one per rev are seen to have a slightly stabilizing influence while those below one per rev are destabilizing. Blade frequencies below 1.0 per rev cause mechanical instability due to coupling with wing modes.

Figure 7(f) shows the stabilizing influence of altitude on proprotor stability. This can be advantageous in selecting design airspeeds.

The proprotor-wing-pylon system used to illustrate the proprotor stability design guidelines given above consisted of a cantilevered wing. In evaluating proprotor stability characteristics the free-flight motions of the aircraft must be considered. As is normal practice in stability investigations the free-flight modes may be treated as being symmetric and antisymmetric, where the symmetry or antisymmetry is about the longitudinal axis. Bell studies show that the free-flight modes are more stable than those of the cantilevered wing. This is illustrated in figure 8 where the damping of the wing beam mode is shown as a function of airspeed for a cantilevered wing mode and a symmetric free-flight mode.

The increased stability of the symmetric free-flight mode compared to that of the cantilevered wing mode is due to fuselage pitching out of phase with the pylon pitching as well as to the higher free-flight frequency. This produces less pylon pitching in space for a given hub shear. Note that even higher stability is predicted when the airframe aerodynamics are accounted for. This increased damping will be realized if the fuselage and empennage bending natural frequencies are higher than those of the wing beam mode.
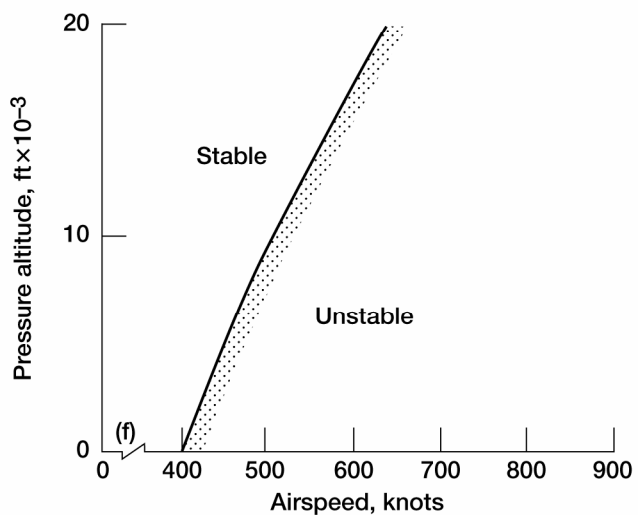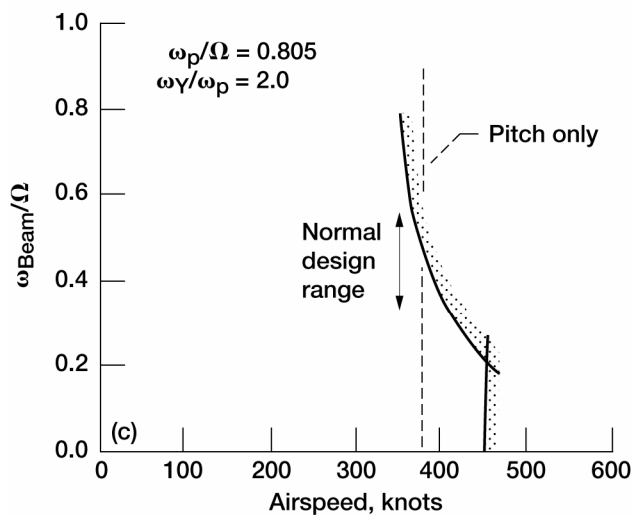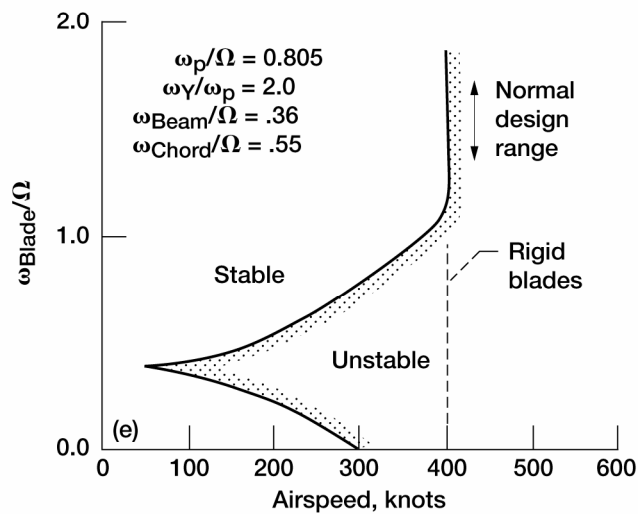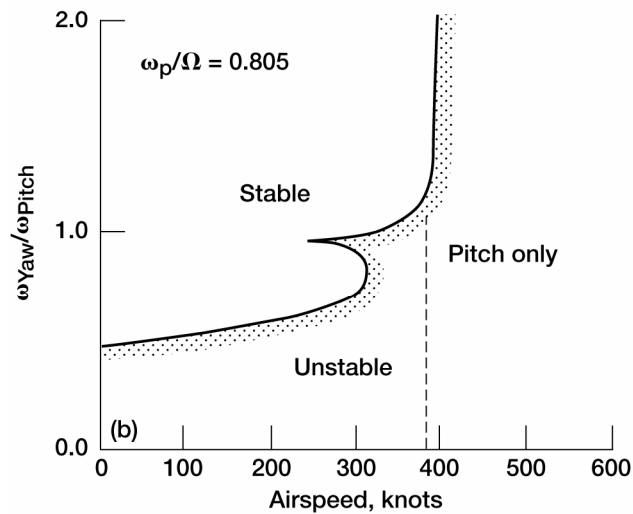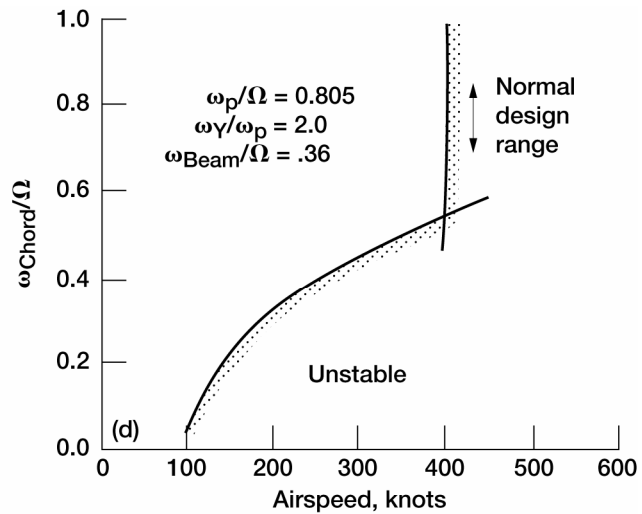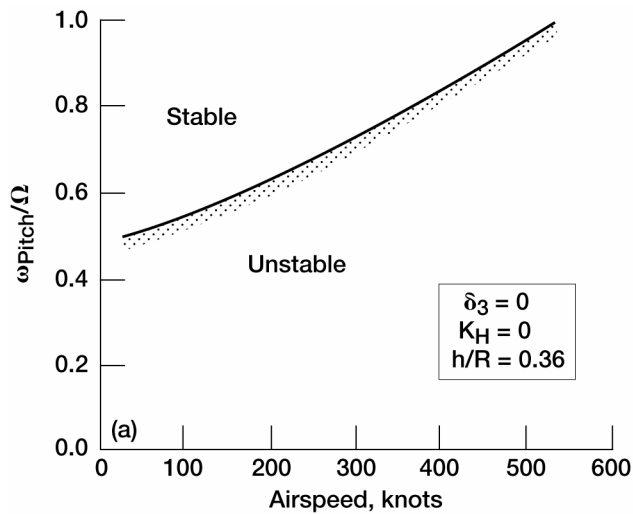
Figure 7.—Proprotor stability design considerations. (a) Pylon pitch. (b) Pylon isotropy. (c) Wing beam freedom. (d) Wing chord freedom. (e) Blade flexibility. (f) Altitude.
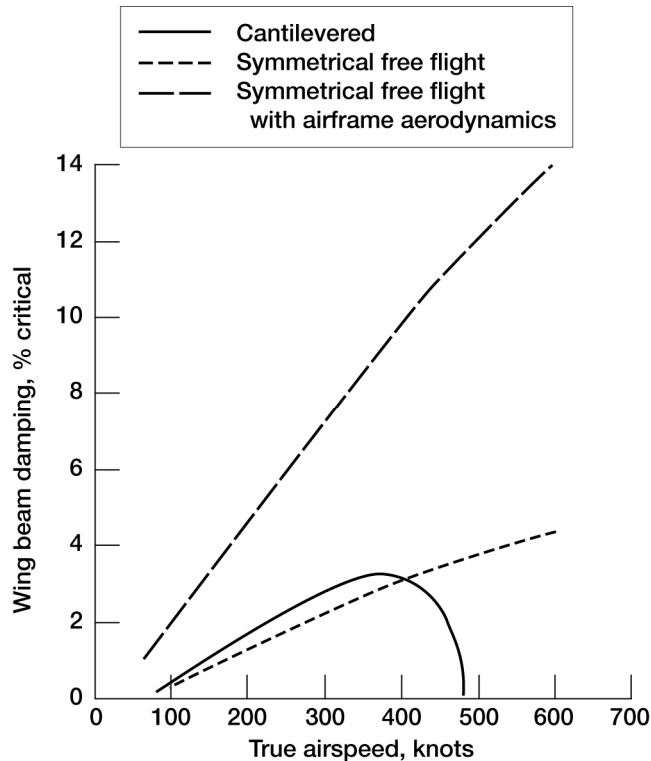
Figure 8.—Wing beam mode damping versus airspeed.

It is clear from the discussion above that the wing torsional stiffness is the most significant structural factor affecting proprotor stability. If flapping considerations could be ignored, a very high level of proprotor stability could be readily achieved with the wing stiffnesses resulting from strength requirements. In practice, however, pitch-flap coupling is necessary to reduce flapping amplitudes to an acceptable level. Studies show that when flapping reduction is considered, the wing stiffness from strength considerations generally provides an adequate margin of proprotor stability for designs with maximum speeds of less than 300 knots at sea level. For designs with higher maximum speeds some form of stability augmentation is required.

Means of Augmenting Proprotor Stability.—There are two basic approaches to augmenting proprotor stability: (1) increased structural stiffness and (2) blade pitch control feedback. The choice of methods depends on the design flight envelope and on factors such as stiffness requirements to avoid proximity to resonance, and system reliability.

Increasing the wing torsional stiffness beyond that stiffness required for strength will provide an increase in stability. In some designs increased stiffness may be necessary in order to move the wing torsion mode away from one-per-rev resonance, and thereby indirectly increase stability. There are two factors limiting the application of this approach: increased wing structural weight and decreased stability of the aircraft short period mode. Twisting of the wing increases the destabilizing proprotor forces, thus decreasing the stability of the short period flight mode. In considering the stiffness approach for high-speed tilt-proprotor designs, the requirement for increased tail volume must be considered.

Blade pitch control feedback, such as swashplate-pylon coupling, offers the possibility of increasing the aircraft flight mode stability as well as the proprotor stability. There are several methods of accomplishing blade pitch control feedback. The principle role employed is that of divorcing the rotor control plane from the pylon angular motion so that it remains fixed in space when the pylon pitches or yaws.

Focused Rotor is a name coined by Bell for one method of providing blade pitch control feedback. The focused rotor principle is illustrated in figure 9. One significant advantage of the focused rotor device is that the control plane and the focal mast are the same, thus referencing pitch-flap coupling to the control plane which reduces the destabilizing effect of pitch-flap coupling on stability.
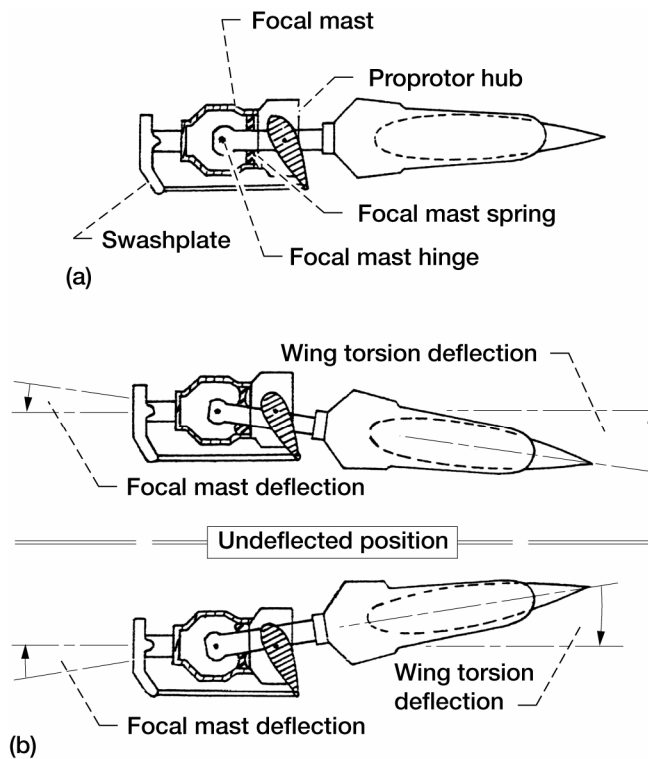
Figure 9.—Focused rotor schematic. (a) Components. (b) Principle of operation.

The principle by which the focused rotor provides an increase in stability can be explained as follows: When the wing vibrates in the fundamental beam mode (the mode which normally becomes unstable) the focal mast pitches opposite to the wing torsional deflection. The focal mast spring is selected so that the focal mast angular deflection is equal to that of the wing torsional angular deflection. Thus at the wing beam mode frequency the swashplate has no angular motion in space and precessional airloads are not generated.

The effect of the focused rotor on proprotor stability is shown in figure 10. Note that two new modes are introduced. These are the coupled focal mast pitch and yaw modes. The decoupling of the proprotor and wing pylon modes is evident by the small change in frequency of the wing modes with airspeed.

As in the case with all control feedback systems, while some modes are stabilized, stability of others is degraded. Generally this is a function of the feedback "gain." In the case of the focused rotor the gain is proportional to the reciprocal of the focal mast hinge spring rate. Figure 11 shows the system stability versus the reciprocal of the spring rate; i.e., zero corresponds to the focal hinge being locked out.

For low gains the mode of instability is that of the wing beam (that is also the mode of instability with the focal hinge locked out) with the stability of the beam mode increasing with increased gain. However, for high gains, the mode of instability changes and becomes one involving the blade inplane mode and the focal mast mode. This aeromechanical instability occurs if the focal mast frequency is equal to the blade inplane frequency plus one per rev. In practice the focal mast frequency can be located between four and five per rev by using a short focal mast and a high focal hinge spring rate. The optimum spring rate will be one whose reciprocal is below the apex of the stability boundary in figure 11.
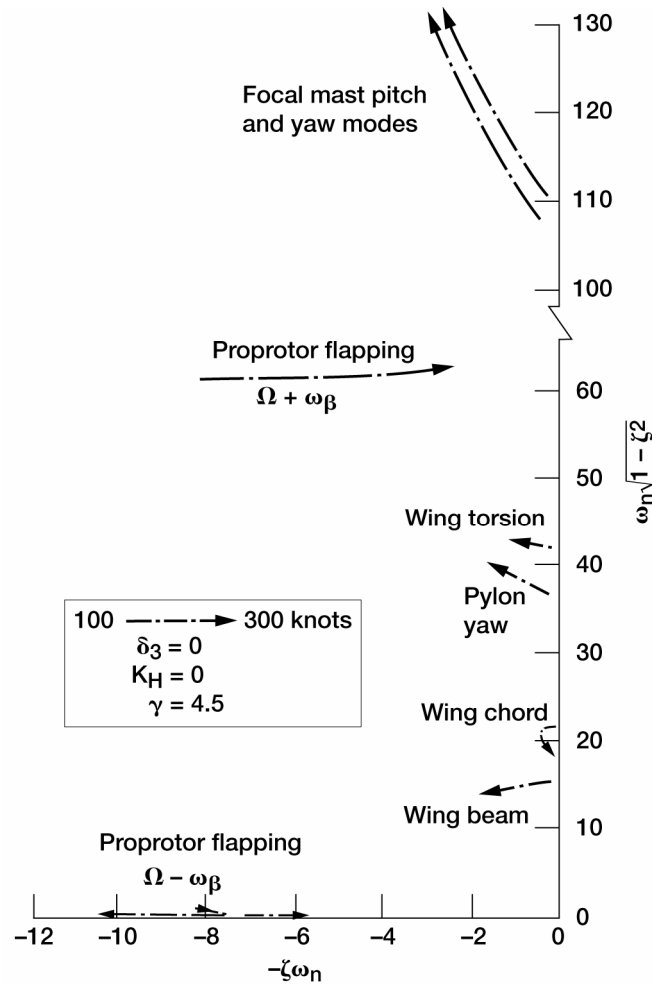
Figure 10.—Root locus with focused rotor.

Blade control feedback using automatic system has been suggested by a number of investigators. This is based on using gyros and accelerometers to feedback pylon angular and linear displacements and rates. The stability potential of this method is very high provided compensating networks are employed to prevent instability in higher frequency modes. It is also possible to combine such a system with flapping and aircraft attitude feedback to provide complete control over the problems of flapping, proprotor stability, and aircraft flight mode stability.
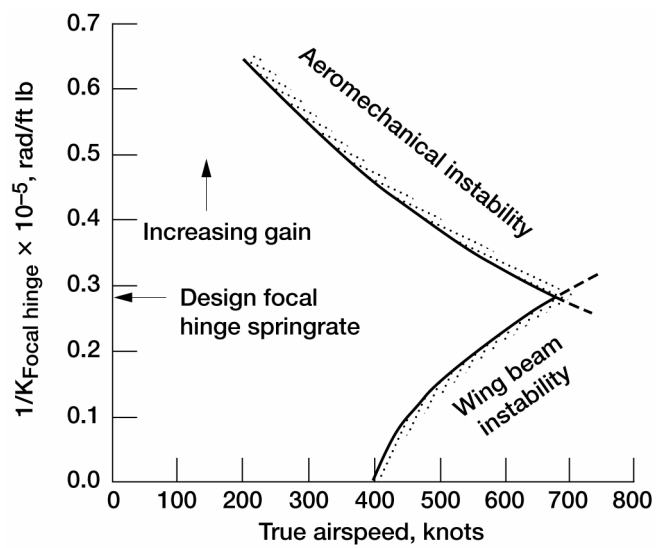
Figure 11.—Effect of focused rotor "gain" on stability.

Fundamental Dynamic Considerations in Tilt-Proprotor VTOL Aircraft Design—II[*]

Raymond G. Kvaternik
National Aeronautics and Space Administration
Langley Research Center
Hampton, Virginia 23681–2199

Tiltrotor aircraft operating at high speeds in the airplane mode of flight can exhibit a variety of dynamic aeroelastic phenomena that are driven by the aerodynamic forces and moments generated by the large proprotors characterizing such configurations. In particular, these aircraft are susceptible to a proprotor/pylon aeroelastic instability akin to propeller whirl flutter. Such an instability was first encountered during full-scale testing of the Bell XV-3 tiltrotor in the NASA Ames 40- by 80-foot Wind Tunnel in 1962. Extensive analytical and experimental studies of small dynamically scaled models were conducted by Bell subsequent to this incident and led to both an explanation for and a means of eliminating the instability. Both government and industry undertook a number of additional fundamental studies in the subject area over the next decade or so. These early studies helped to establish key elements of the technology base needed to successfully address the issue of proprotor/pylon/wing aeroelastic stability during design.

The Aeroelasticity Branch at NASA Langley Research Center has been involved in tiltrotor aeroelastic research since 1968, when a joint NASA/Bell test of a 0.133-scale semi-span dynamic aeroelastic model of a proposed Bell tiltrotor design (designated the Model 266) was conducted in the Transonic Dynamics Tunnel (TDT). Several other cooperative experimental studies were conducted in the TDT over the next several years using a variety of models. The analytical and experimental work conducted as part of these investigations was documented in a Ph.D. dissertation (R.G. Kvaternik: "Studies in Tilt-Rotor VTOL Aircraft Aeroelasticity," Case Western Reserve University, June 1973). Chapter 4 of this treatise contains the results of extensive analytical trend studies that were conducted to identify the effects of key structural design parameters on proprotor/pylon/wing stability, the proprotor-generated hub forces and moments governing system stability, and rotor flapping behavior. Although the specific configuration chosen to be the basis of these parametric studies is the Bell Model 266, the results are presented and discussed in a manner providing useful design guidelines that are not limited to this specific design. Because of the broader applicability of this discussion, this chapter of the dissertation is reproduced below.

Analytical Trend Studies

Introduction

Proprotor/pylon instability, like propeller/nacelle whirl flutter, is an instability associated with the high advance ratios typically encountered in high-speed flight and, as in propeller whirl flutter, pylon/wing stiffness and damping have a major influence on stability. However, because of the blade flapping and pitch-change freedoms available to the proprotor, pylon support stiffness and damping are not the only parameters governing stability. Design parameters associated with the rotor configuration, such as proprotor type, pitch-flap coupling, and blade flapping restraint also assume a major role in determining the resultant stability or instability of the proprotor/pylon/wing system. Although the design values of these particular parameters are generally dictated by considerations other than stability their influence on the stability of the overall system must nevertheless be assessed. The additional freedoms in which a proprotor is able to respond can also give rise to a dynamic environment in which the

---

[*]This document was excerpted from Kvaternik, Raymond George: Studies in Tilt-Rotor VTOL Aircraft Aeroelasticity. Ph.D. dissertation, Case Western Reserve University, 1973. Used with permission.

proprotor/pylon/wing system can exhibit instabilities in modes other than the familiar propeller/nacelle precessional mode. In particular, depending on the characteristics of the system, instabilities associated with either the proprotor, pylon, or wing modes can occur. The possibility that two unstable response modes can occur simultaneously, or nearly so, also exists.[1] This leads to so-called "bi-modal" instabilities in which the pylon responds in a steady or continuously changing Lissajous pattern. Other aircraft characteristics which explicitly depend upon the dynamic behavior of the proprotor must also be considered. These include steady-state flapping, transient flapping required to generate the airload moments to precess the proprotor in response to aircraft maneuvers, and the destabilizing shear forces which accompany any precessional motion of the proprotor. These shears can destabilize the aircraft short period and Dutch roll modes in the same manner as the proprotor/pylon/wing elastic system.

This chapter will present the principal findings of some generalized trend studies shedding additional light on the role of several system design parameters on proprotor/pylon stability, frequency response characteristics of the proprotor-generated shear forces and moments, and proprotor flapping. The specific configuration chosen to form the basis of these parametric studies is the Bell Model 266 tilt-proprotor design developed during the Army Composite Aircraft Program in 1966 and 1967. Attention herein is directed to considerations of the right-hand proprotor/pylon/wing system taken to be cantilevered at the wing root with the proprotor fully converted forward.

The chapter is divided into five sections. Some of the distinguishing design features of the Model 266 are presented first. Proprotor/pylon instability involves an intimate coupling between certain proprotor flapping modes and pylon motions. The nature of this coupling is briefly discussed in the next section. This is followed by funda-mental considerations of proprotor/pylon instability as affected by pylon/wing stiffness and damping, pitch-flap coupling, blade flapping restraint, and blade flapping frequency. Sections presenting the frequency response characteristics of the proprotor shears and moments and blade flapping conclude the chapter.

The trend studies included in this chapter have been selected with a view toward delineating some of the salient dynamic response characteristics of a proprotor/pylon/wing system. The frequency response characteristics of the shear forces and moments and blade flapping will, where appropriate, be examined in light of their effects on proprotor/pylon stability, aircraft rigid-body stability, and flapping behavior.

Some Characteristic Design Features of the Model 266

The Model 266 represents a design evolution of the XV-3 convertiplane. It has two, three-bladed, contra-rotating proprotors of semi-rigid, teetering, or seesaw type in which the blades are rigidly attached to the yoke spindles of a non-underslung hub/yoke assembly. The hub assembly is in turn gimbal-mounted to the drive shaft (mast) to permit flapping or tilting of the tip-path-plane relative to the mast. Blade feathering motion is provided by pitch-change bearings housed in the blade grips. The blade centrifugal force is carried to the yoke by a retention strap inside the spindle bore. Three degrees of precone are-built into the hub yoke spindles to minimize steady blade out-of-plane bending moments and reduce feathering bearing loads. The blades are relatively stiff inplane, the lowest frequency being above the rotor rotational speed for all operating ranges. In the airplane mode the first inplane frequency is about 1.5 cycles/rev. A non-symmetric hub-flapping restraint (which is equivalent to blade flapping restraint) located in the non-rotating system is employed to improve the aircraft control power and response characteristics in pitch while operating in the helicopter mode. Its location in the fixed system implies that pitching moments are produced directly as a result of tilting the proprotor disc, thereby augmenting control moments from tilting of the thrust vector.

Blade pitch control is effected through a conventional helicopter-type swashplate assembly. The pitch links are connected to pitch horns on the trailing edge of the blades so that when the blades flap up the blade pitch increases, that is, positive pitch-flap coupling (negative δ_3) is employed in contrast to the more conventional negative pitch-flap coupling (positive δ_3). Pitch-flap coupling is employed on proprotors to reduce first harmonic flapping.

---

[1]See, for example, refs. 1 and 2.

Although either positive or negative δ_3 will reduce one-per-rev flapping, considerations of blade flap-lag stability (ref. 3) dictate the use of negative δ_3 on the Model 266.

The propulsion system consists of a T64 free turbine engine and associated gearbox located in each of the wing tip mounted pylons. The effect of the opposing requirements of high blade twist and low solidity in cruise and low twist with high solidity in helicopter flight are minimized by reducing the rotor rpm in the airplane cruise mode, thereby increasing propulsive efficiency.

Some of the primary design parameters of the Model 266 are summarized in table 1. The interested reader will find a more detailed account of the Model 266 design in the state-of-the-art paper by Wernicke (ref. 4). Complete documentation of the design may be found in reference 5. The particular physical parameters employed in the analytical trend studies are given in table 2.

TABLE 1.—MODEL 266 DESIGN PARAMETERS

WEIGHTS	
Design gross weight	28000 lb
Payload	6600 lb
VTOL overload gross	35000 lb
STOL overload gross	40000 lb
PROPROTOR SYSTEM	
Direction of rotation	Inboard Up
Diameter	38.5 ft
Chord	1.92 ft
Number blades/proprotor	3
Disc loading (Hover, DGW)	12.0 lb/ft^2
Solidity	0.095
RPM schedule	
Helicopter mode	387 to 408 rpm
Conversion mode	298 to 382 rpm
Airplane mode	238 to 298 rpm
Lock number	4.54
Pitch-flap coupling (δ_3)	Max. −22.5°
	Min. −18°
Maximum flapping angle	±9.5°
Blade aerodynamic twist	−43.5°
Longitudinal hub restraint	1500 ft-lb/deg
Lateral hub restraint	250 ft-lb/deg
WING SYSTEM	
Span	49.6 ft
Taper ratio (c_r/c_t)	1.1
Airfoil section	
Root chord	NACA 64A223
Tip chord	NACA 64A219
Wing loading (DGW)	73.3 lb/ft
Aspect ratio	6.43
Forward sweep (1/4 chord)	6.2°
DESIGN FACTORS (DGW)	
Airspeed (knots)	V_C V_L
Helicopter	160 184
Conversion	200 230
Airplane	360 414
Limit load factor	
Helicopter	+2.5g, −0.5g
Conversion	+2.5g, −0.5g
Airplane	+4.0g, −1.0g

TABLE 2.—PHYSICAL PARAMETERS
EMPLOYED IN TREND STUDIES

M_R	43.8 slugs
M_P	87.5 slugs
I_B	791 slug-ft^2
I_{cg} (pylon)	580 slug-ft^2
H	6.92 ft[*]
$\bar{h}$	2.60 ft[*]
$\bar{c}$	1.10 ft
R	19.25 ft
β_o	0°
C	1.92 ft
ρ	0.00238 slug-ft^3[*]
a_o	5.73
η_1	0.0
η_2	1.0
K_1	0.0[*]
ε	0°[*]
Pylon support stiffness and damping $\begin{cases} K_H \\ \delta_3 \\ \begin{cases} K_{pitch} \\ K_{yaw} \\ K_{beam} \\ K_{chord} \\ g \end{cases} \end{cases}$	Varied

[*] Unless noted otherwise

The Rotor/Pylon Dynamic System

(a) Flapping modes of a gimbaled proprotor.—A three-bladed semi-rigid proprotor such as on the Model 266 has two uncoupled rigid body flapping modes. In the rotating coordinate system these two modes have the same frequency and damping but one involves precession in the direction of rotor rotation and the other precession opposite to the direction of rotor rotation. Their frequency and damping are given by

$$\overline{\omega}_\beta \equiv \frac{\omega_\beta}{\Omega} = \left[1 + \frac{K_H}{I_R \Omega^2} + \frac{1}{2} \gamma B_3 \tan\delta_3 \right]^{1/2} \tag{1}$$

$$\zeta_\beta = \frac{\gamma A_5}{4\overline{\omega}_b} \tag{2}$$

Note that in the absence of flapping restraint and pitch-flap coupling the natural frequency of these modes in the rotating system is one-per-rev (1/rev). Use of flapping restraint in conjunction with positive or negative pitch-flap coupling raises or lowers the natural frequency of these modes from l/rev. It is of interest to examine these modes as they would appear to an observer in the non-rotating system. With reference to the sketch below the required transformation from rotating system
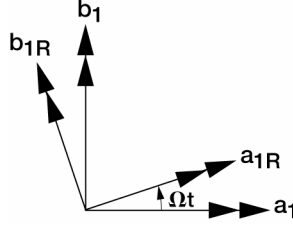
tip-path-plane coordinates a_{1R}, b_{1R} to fixed system tip-path-plane coordinates a_1, b_1 is given by

$$a_1 = a_{1R}\cos\Omega t - b_{1R}\sin\Omega t$$

$$b_1 = a_{1R}\sin\Omega t + b_{1R}\cos\Omega t$$

(3)

A forward whirl precessional motion of the tip-path-plane in the rotating system can be written as

$$a_{1R} = \bar{a}\cos\omega_\beta t$$

$$b_{1R} = \bar{a}\sin\omega_\beta t$$

(4)

where ω_β is the flapping natural frequency defined by equation (1) and $\bar{a}$ is the amplitude of whirl. Substituting equation (4) into equation (3) and making use of trigonometric identities,

$$a_1 = \frac{\bar{a}}{2}\left[\cos(\omega_\beta - \Omega)t + \cos(\omega_\beta + \Omega)t - \cos(\omega_\beta - \Omega)t + \cos(\omega_\beta + \Omega)t\right]$$

$$b_1 = \frac{\bar{a}}{2}\left[\sin(\omega_\beta + \Omega)t - \sin(\omega_\beta - \Omega)t + \sin(\omega_\beta - \Omega)t + \sin(\omega_\beta + \Omega)t\right]$$

(5)

Equation (5) reduce to

$$a_1 = \bar{a}\cos(\omega_\beta + \Omega)t$$

$$b_1 = \bar{a}\sin(\omega_\beta + \Omega)t$$

(6)

Equation (6) indicate that a forward whirl in the rotating system transforms to a forward whirl in the fixed system if ω_β is greater than, equal to, or less than Ω.

A backward whirl precessional motion of the tip-path-plane in the rotating system can be written as

$$a_{1R} = \bar{a}\cos\omega_\beta t$$

$$b_{1R} = -\bar{a}\sin\omega_\beta t$$

(7)

Substituting equation (7) into equation (3) and proceeding as above yields

$$a_1 = \bar{a}\cos(\omega_\beta - \Omega)t$$

$$b_1 = -\bar{a}\sin(\omega_\beta - \Omega)t$$

(8)

as the motion in the fixed system. Note that for the case of backward whirl in the rotating system the motion observed in the fixed system is a backward whirl if $\omega_\beta > \Omega$, a steady longitudinal tilt of the tip-path-plane if $\omega_\beta = \Omega$ and a forward whirl if $\omega_\beta < \Omega$.

The above considerations are also directly applicable to the blade inplane whirl modes which "appear" in the rotating system as a forward and backward whirl of the cg of the displaced blades.

In the fixed system, the flapping modes manifest themselves as a weaving or wobbling of the tip-path-plane in the forward or backward directions. For the particular combination of positive pitch-flap coupling and hub restraint employed on the Model 266 the flapping natural frequency in the rotating system at low airspeeds is 0.875 cycles/rev and decreases with increasing airspeed while the associated damping is about 30 percent of critical and also decreases with airspeed. In the fixed system these flapping modes constitute a low frequency forward precession of the tip-path-plane at 0.125 cycles/rev and a high frequency forward precession at 1.875 cycles/rev.

In the absence of precone (steady-state coning for the case of a rotor with offset flapping hinges) the flapping modes can not flutter by themselves. However, in the presence of precone these modes can be destabilized. In particular, positive precone has a destabilizing effect upon the high frequency flapping mode and negative precone is destabilizing upon the low frequency flapping mode. For rotor rpm typical of proprotor cruise operations the precone required for instability is much larger than that which exists in practice and these precone-induced flapping instabilities are mainly of academic interest.

For completeness, it should be pointed out that the rigid body flapping modes can also be destabilized by coupling with blade inplane elastic bending, the coupling in one such instability being associated with the sign of the pitch-flap coupling ratio and another being caused by elastic coning in the presence of control system/ blade torsion flexibility. A comprehensive treatment of these types of instabilities is given in references 3 and 6.

Before closing this discussion on flapping it should be noted that the flapping due to small mast angle of attack is a 1/rev <u>forced response</u> in which the blades flap with respect to the swashplate so as to minimize the cyclic variation in blade section angle of attack around the azimuth. This flapping appears as a steady longitudinal and/or lateral tilt of the tip-path-plane in the fixed system. The flapping <u>natural frequency</u>, ω_β, is the frequency of the transient motion which would be observed in the rotating system if the tip-path-plane of steady l/rev flapping were set into motion by "plucking."

(b) The role of pylon freedoms.—The rigid body flapping modes of a stiff inplane proprotor with zero precone can not flutter by themselves. When this proprotor is mounted on a pylon which has freedom of motion, both the pylon modes and the flapping modes can be destabilized. Since angular motions of the pylon represent angular motions of the control plane in space for a proprotor having the swashplate rigidly attached to the pylon, pylon motions and flapping motions are strongly coupled. In addition to the familiar pylon whirl instability associated with one of the pylon modes and occurring near a pylon-mode coupled natural frequency the shear forces can destabilize the flapping modes. A flapping mode instability appears as a whirl of the tip-path-plane and pylon near a tip-path-plane coupled natural frequency with large flapping in space. (The XV–3 instability encountered in the Ames tunnel in 1962 was in a low-frequency, backward whirl flapping mode.) In general the low-frequency flapping mode can be destabilized for relatively low pylon support stiffnesses in combination with large values of flapping restraint or positive δ_3. The high-frequency flapping mode can be destabilized if the pylon support stiffnesses are such as to place the pylon mode frequencies close to the second flapping mode frequency.

Several aspects of rotor/pylon mode coupling will be brought out in the following sections.

Proprotor/Pylon Instability

Because of the additional flapping and feathering freedoms available to a proprotor and the many rotor design parameters which can influence stability the dynamic characteristics of the typical proprotor are such that various types of instabilities associated with the proprotor/pylon/wing system can occur. The influence of several structural and kinematic parameters on proprotor/pylon stability will be presented here in a manner which will hopefully provide useful design guidelines. The results are based on a mathematical model developed for an idealized proprotor/pylon/wing system. Since the wing is taken as cantilevered at its root the results are, of course, not indicative of stability in free-flight. These results do however, represent a lower bound on stability for the Model 266 since its free-flight stability is increased compared to that of the cantilevered wing. Wing elasticity is accounted for in terms of equivalent wing tip spring rates referenced to the pylon mast/conversion axis intersection.

To insure a blade flapping frequency independent of azimuth a symmetric hub restraint was employed in the trend studies. Mach number effects, except in one case, are neglected.

(a) Pylon support stiffness.—Proprotor/pylon combinations employing proprotors with more than two blades are generally rigidly mounted to the wing tips to take maximum advantage of the stiffness and damping inherent in the wing structure. The effective wing support conditions at the pylon/wing junction will then have a strong influence on stability. In such an arrangement the pylon freedoms are equivalent to certain wing freedoms: pylon pitch to wing torsion, pylon yaw to the rotational component of wing inplane bending, etc. The effects of several of these pylon support stiffnesses on proprotor/pylon stability will be established below in the manner of reference 7 by sequentially adding pylon degrees of freedom to the basic tip-path-plane pitch and yaw-degrees of freedom of the proprotor. These results generally extend those of reference 7 in that both flapping restraint and pitch-flap coupling are taken to be non-zero (representing a more realistic proprotor design condition), damping effects are indicated, and several additional features are included.

Pylon pitch: The stability of the three degree-of-freedom system which includes the pylon pitch (wing torsion) degree of freedom is given in figure 1. The flutter speed is plotted as a function of the uncoupled pylon pitch static natural frequency[2] normalized on the proprotor speed at which the stability calculations were made. Instability occurs in the pylon pitch mode,[3] being driven by the destabilizing shear force component inphase with the pitch rate. This illustrates that a proprotor can be dynamically destabilized in a single plane, in contrast to a propeller/ nacelle combination. At the higher pitch frequencies reflective of current design practice, pylon damping is seen to have a negligible stabilizing effect.
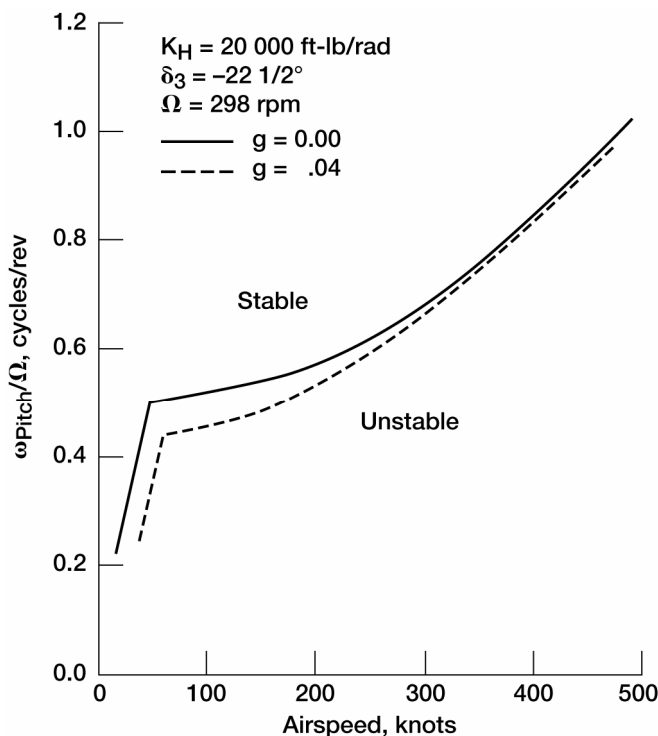
Figure 1.—Effect of pylon pitch stiffness on stability.

---

[2]The uncoupled static natural frequency is taken to be that observed in the transient response resulting from statically displacing the system in the degree of freedom in question and releasing it, all other degrees of freedom being "locked out" with zero rotor rpm.

[3]Mode designations herein are based on the uncoupled mode motion which predominates in the coupled mode.

Pylon Yaw: The effects of adding the pylon yaw degree of freedom to the 3° of freedom system are indicated in figure 2 for the case of $\omega_{pitch}/\Omega = 0.80$. Here the flutter speed is given as a function of the ratio of uncoupled pylon yaw natural frequency to uncoupled pylon pitch natural frequency. The dramatically destabilizing effects of pylon isotropy are clearly evident in the extended region of instability along the line representing a stiffness ratio of unity. Pylon damping is seen to be quite effective in stabilizing the system under isotropic and near isotropic support conditions but has only a small effect for non-isotropic support conditions.

For pylon yaw-to-pitch frequency ratios below 0.75/rev flutter is in the pylon yaw mode, with the pylon and tip-path-plane precessing in the forward whirl direction near the pylon yaw coupled natural frequency. As the frequency ratio is increased beyond 0.75/rev the flutter mode initially changes to a backward whirl associated with the pylon pitch mode and then, at 1.4/rev, changes back to a forward whirl but remaining associated with the pylon pitch mode. Note that if the frequency ratio is greater than about 1.5 the effect of adding the yaw degree of freedom (i.e., the freedom in the stiffer direction) is negligible. This is further illustrated by including the stability boundary for the case of no pylon yaw freedom. For pylons which are rigidly attached to the wing tips the yaw-to-pitch frequency ratio will normally be about 2.0 to 3.0. For the Model 266 this ratio is 2.24.

As a sidelight, results based on the use of a representative section aerodynamic theory are also shown. This theory lumps the aerodynamic loading at some "representative" blade radial station in a manner not unlike the so-called typical section approaches employed in early fixed-wing flutter analyses. The specific results shown indicate that the location of the "correct" representative section moves inboard on the blades as the flutter airspeed increases.
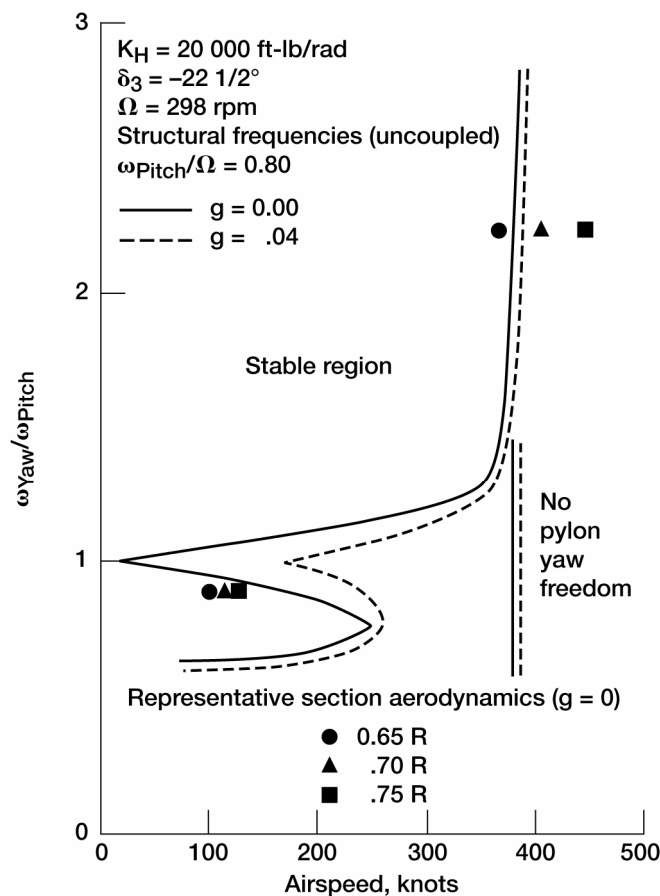
Figure 2.—Effect of pylon yaw stiffness on stability.

Wing Beam: The addition of the wing beam degree of freedom ($\equiv$ vertical translational component of wing vertical bending) to a pylon which has freedom in pitch permits the wing beam freedom to couple with pylon pitch to create two pylon/wing modes of motion: a so-called inphase mode in which the pylon pitching motion and wing vertical displacement are in the same direction and an out-of-phase mode in which the pitching motion of the pylon is in a direction opposite to that of the wing vertical displacement. Each of these coupled modes is characterized by the predominance of an uncoupled mode: the former by wing vertical displacement and the latter by pylon pitching (wing torsion). For descriptive purposes the inphase coupled pylon/wing mode in which wing vertical bending predominates will be herein designated as the wing beam mode and the out-of-phase coupled pylon/wing mode in which pylon pitching (wing torsion) motion predominates will be designated as the pylon pitch (or wing torsion) mode. These designations are also prompted by frequency considerations: the inphase mode has a frequency near the uncoupled wing vertical bending natural frequency and the out-of-phase mode oscillates near the uncoupled pylon pitch (wing torsion) natural frequency. The wing beam mode is equivalent to a pure pitching motion about a node located aft of the pylon physical pivot; the pylon pitch mode is equivalent to a pure pitching motion about a node between the proprotor disc and the physical pivot.

The effect of adding the wing beam degree of freedom to the 4° of freedom system above can be stabilizing or destabilizing depending on its frequency ratio with respect to pylon pitch. This is illustrated in figure 3. At very low levels of wing beam frequency the pylon motion involves mainly vertical translation, with very little precession of the proprotor in space. The precession-generated shears, which constitute the destabilizing forces, are thus initially dominated by the stabilizing damping contribution associated with hub translational motion. This does not represent a viable design solution however, since the corresponding wing stiffnesses would be too low to satisfy basic strength requirements. Flutter at these low stiffness levels occurs in the wing beam mode, the pylon/rotor combination executing a forward whirl precession. As the wing beam frequency is increased the stability initially decreases quite rapidly because the coupling between wing beam and pylon pitch increases, the coupling having the dual effect of moving the effective pivot forward toward the physical pivot, thereby reducing hub translational damping, and reducing the effective pylon pitch stiffness. The stability continues to decrease as wing beam frequency is further increased because the wing beam mode begins to couple with the low frequency $(\Omega - \omega_\beta)$ flapping mode. In this region $(0.10 < \omega_{beam}/\Omega < 0.40)$ the instability is still in the wing beam mode with the pylon/rotor combination executing a forward precessional whirl motion. Because of the strong coupling with a flapping mode a considerable amount of flapping (in space) distinguishes the flutter mode in this region. If ω_β were equal to Ω the frequency of the low frequency flapping mode in the fixed system would be zero, there would be no coupling with this mode and the elongated region of instability shown in figure 3 about $\omega_{beam}/\Omega = 0.25$ would not occur.[4] As wing beam frequency is increased beyond 0.70/rev an abrupt reduction in stability occurs in a small range of frequency about 0.80/rev, the reduction being quite large for zero damping. For no damping the instability is in the pylon pitch mode (the out-of-phase coupled pylon/wing mode) with large flapping in space. When pitch is out of phase with wing beam motion the effective pylon pitch stiffness increases with increasing wing beam stiffness until the pylon pitch mode couples with the high frequency $(\Omega + \omega_\beta)$ flapping mode. Unusual features of the flutter mode are the whirl direction: the pylon exhibits a backward precessional whirl while the tip-path-plane whirls in the forward direction relative to space. For nonzero damping only a slight reduction in stability occurs; flutter is in the wing beam mode with both the pylon and tip-path-plane whirling in the forward direction. For wing beam frequencies beyond 0.80/rev the flutter modes for both values of damping are identical, a forward whirl in the wing beam mode.

Wing Chord: The effects of adding the fore-and-aft translational component of wing inplane bending ($\equiv$ wing chord) to the 5° of freedom system are summarized in figure 4. As wing chord stiffness is increased the flutter mode changes from a forward whirl in the pylon yaw mode to a forward whirl in the wing beam mode. Because of this change in flutter mode, pylon damping has no effect upon stability beyond $\omega_{chord}/\Omega = 0.30$. Wing chord frequency ratios beyond about 0.5/rev are seen to have a negligible influence upon stability.

---

[4]See figure 7c of ref. 7.
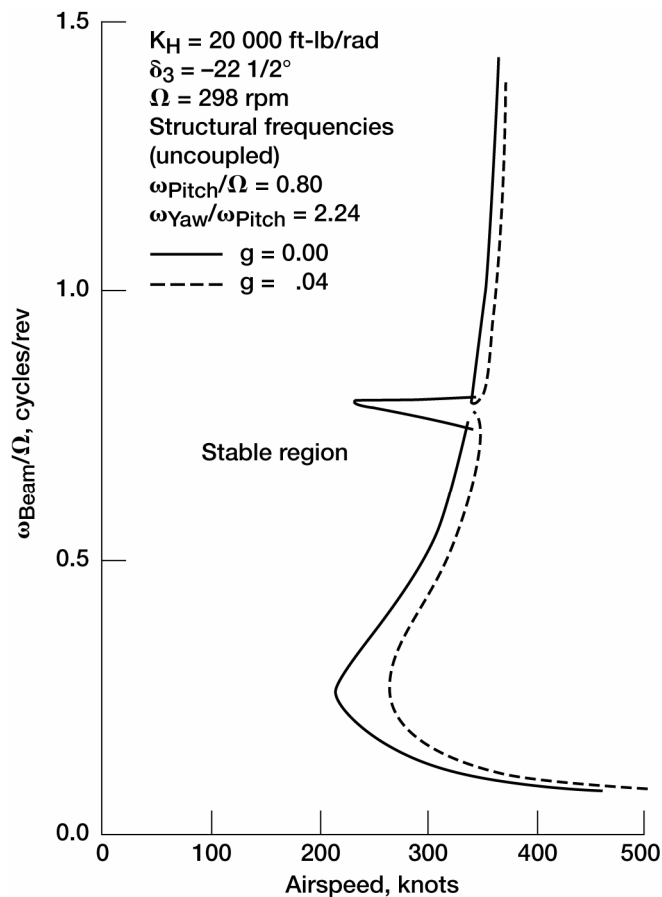
Figure 3.—Effect of wing vertical bending stiffness on stability.
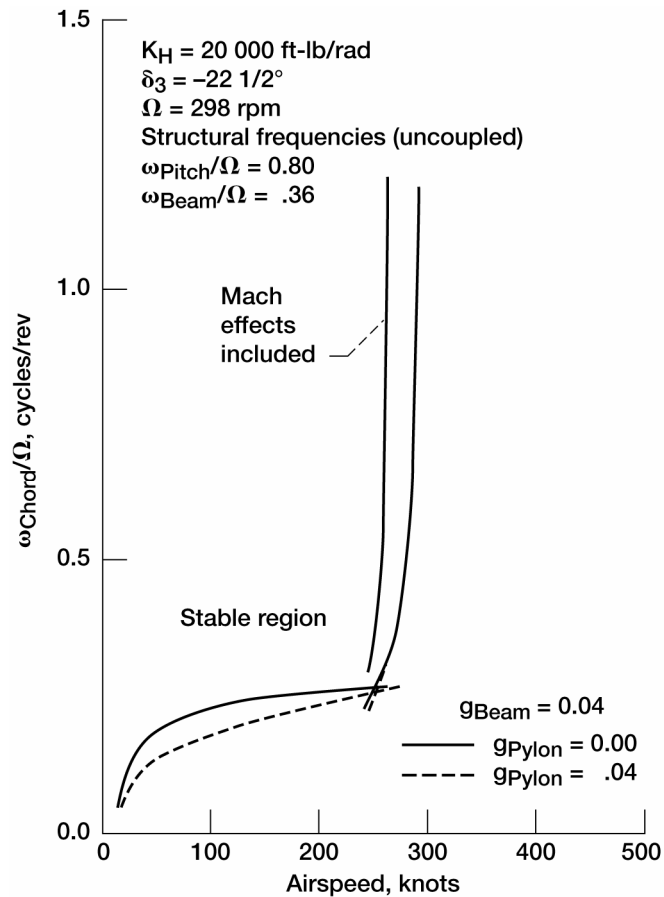
Figure 4.—Effect of wing chordwise stiffness on stability.

The effects of Mach number upon stability axe indicated for the region of chord frequencies greater than 0.3/rev. Both the Prandtl-Glauert and compressible flow aspect ratio corrections are reflected in the Mach-number-corrected results. As might be expected, stability is decreased.

(b) Pitch-flap coupling.—Considerations of blade flapping while operating in the high-speed proprotor mode generally indicate that flapping amplitudes must be reduced. One means of effecting a reduction in flapping is through the use of pitch-flap coupling (δ_3). Either positive or negative pitch-flap coupling ($-\delta_3$ or $+\delta_3$) is effective in reducing flapping. The effects of δ_3 on the stability of the 4° of freedom proprotor/pylon system for the case of non-isotropic pylon supports for two values of hub restraint and two rotor rpm are displayed in figure 5. The destabilizing effects of large positive or negative δ_3 on proprotor/pylon stability are noteworthy and constitute the most significant feature of δ_3 as regards proprotor/pylon stability. It should be pointed out that the wide range of δ_3 values shown was chosen to better illustrate the effects of δ_3 on stability. The maximum values of positive or negative δ_3 are in practice dictated by considerations of blade flap-lag stability and static divergence (ref. 3) and generally fall well within the extremes shown.

(c) Flapping restraint.—A summary of the results concerning the effect of flapping restraint (as reflected in the blade flapping natural frequency) on proprotor/pylon stability is given in figure 6 for both the four and five degree-of-freedom systems. δ_3 was set to zero so that the uncoupled flapping natural frequency would be independent of aerodynamic conditions. For the 4° of freedom case maximum stability occurs at a blade flapping natural frequency of about 1.12 cycles/rev. This is in agreement with the results of Young and Lytwyn (ref. 1) who analytically demonstrated that the pylon support stiffness and/or damping requirements for prevention of whirl flutter are a
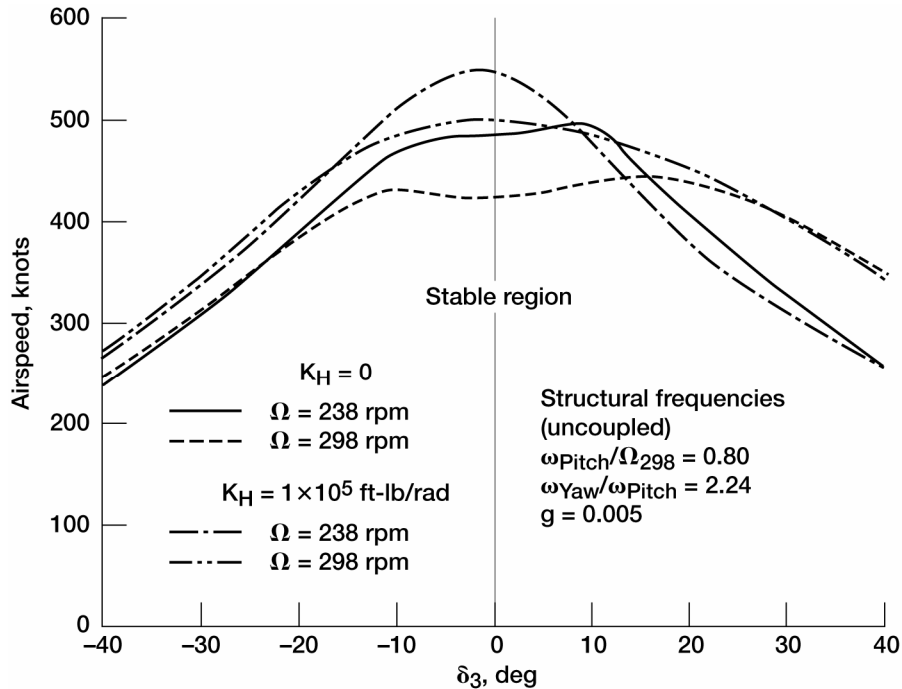
Figure 5.—Effect of δ_3 on stability of four degree-of-freedom system.

minimum when the blade fundamental flapping natural frequency is 1.1 to 1.2 cycles/rev.[5] It is of interest to describe the change in flutter mode as flapping frequency is increased from 1/rev. This will be done with the aid of root loci showing the frequency and damping variation with airspeed for each of the modes of the system, arrows indicating the direction of root movement with increasing airspeed. The root designation selected for the root loci plots was suggested by the fact that each of the coupled modes of the system is characterized by the predominance of an uncoupled mode.

For frequencies below about 1.09 cycles/rev flutter is in the forward whirl pylon pitch mode. The root locus for the particular case of $\omega_\beta/\Omega = 1.0$ given in figure 7. Flutter occurs in the low frequency ($\omega_\beta - \Omega$) flapping mode for $\omega_\beta/\Omega > 1.09$ (fig. 8), the pylon/rotor combination precessing in the backward whirl direction. It is to be noted that these whirl directions are also in agreement with the findings of reference 1.

Figure 6 also shows the effects of including the wing beam degree of freedom. Maximum stability occurs at about $\omega_\beta/\Omega = 1.14$, indicating that a "design optimum" in the sense of reference 1 also exists in the more general case which includes wing vertical bending. Note that wing beam freedom is slightly destabilizing at low values of ω_β/Ω and stabilizing at higher values of ω_β/Ω. This is associated with the flutter mode shape. At low blade flapping frequencies wing beam motion is inphase with pylon pitch thereby reducing the effective pitch stiffness relative to the case for no wing beam freedom. This is destabilizing on proprotor/pylon stability. At the higher flapping frequencies pylon pitch and wing beam are out of phase with each other, effectively stiffening the pylon in pitch, which is stabilizing.

---

[5]Reference 1 established this optimum on the basis of considerations on a rotor having centrally hinged flapping blades restrained by springs. More recently, ref. 8 demonstrated that this optimum also exists when the flapping restraint is achieved through a combination of hinge offset and spring restraint.
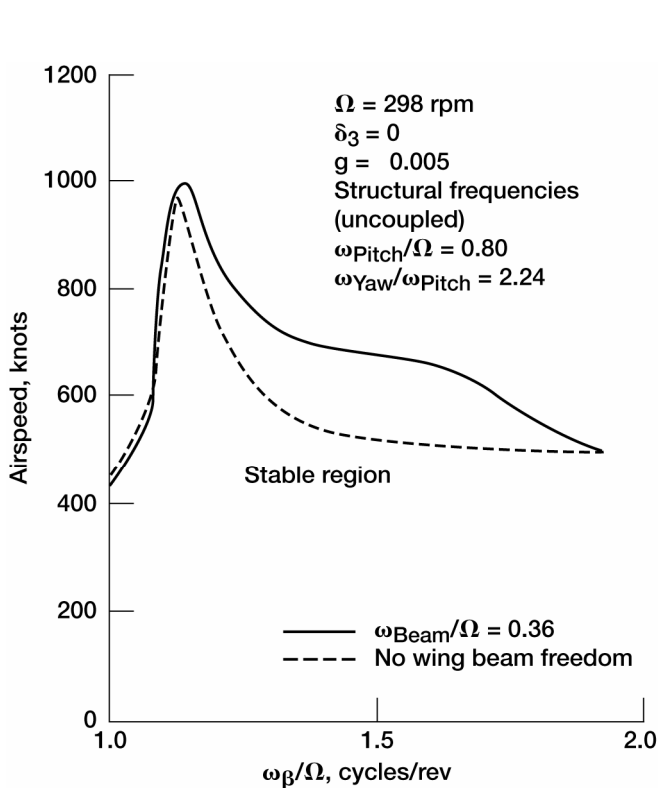
Figure 6.—Effect of blade flapping natural frequency on proprotor/pylon stability.
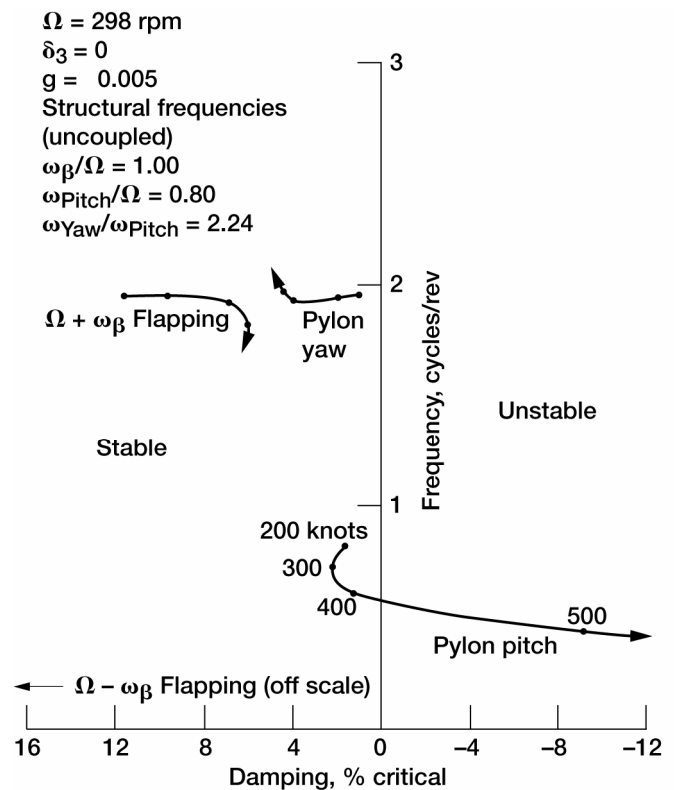
Figure 7.—Root locus for four degree-of-freedom proprotor/pylon system ($\omega_\beta/\Omega = 1.00$).
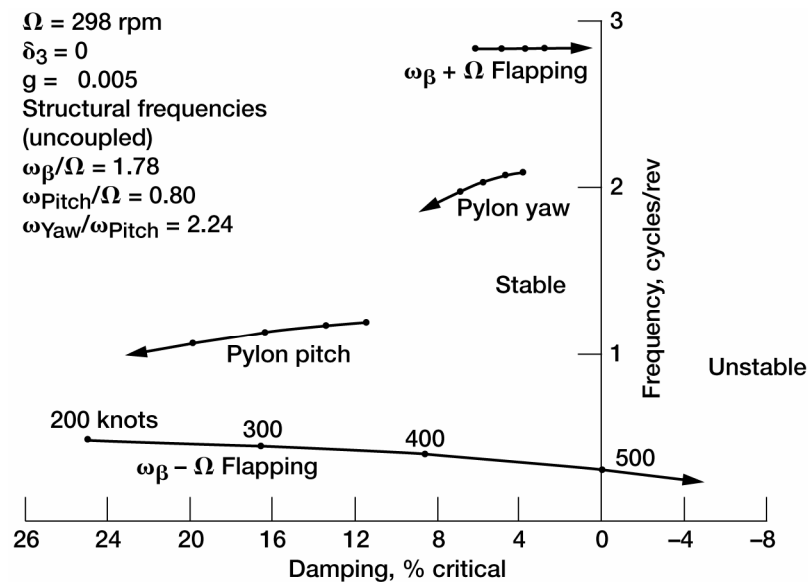
Figure 8.—Root locus for four degree-of-freedom proprotor/pylon system ($\omega_\beta/\Omega = 1.78$).

The variation in flutter mode and direction of pylon whirl with increasing flapping frequency is of particular interest in this case, there being several such changes. Below $\omega_\beta/\Omega = 1.09$ flutter is in the wing beam mode with the pylon/rotor combination precessing in the forward whirl direction. For ω_β/Ω between 1.09 and 1.16 a backward whirl instability in the pylon pitch mode occurs. The high frequency ($\omega_\beta + \Omega$) flapping mode is unstable for ω_β/Ω between 1.16 and 1.65, the whirl now being again in the forward direction. Beyond 1.65 flutter is in the low frequency ($\omega_\beta - \Omega$) flapping mode, the whirl now occurring in the backward precessional direction. Root loci showing the root movement leading to each of these flutter modes are presented in figures 9 to 12.

The maximum value of flapping restraint which can be employed in practice is dictated by considerations of allowable blade loads.[6] This generally limits the maximum flapping frequency (for $\delta_3 = 0$) to values well below 1.5 cycles/rev, depending on the particular design. The results of figure 6 are thus for the most part mainly of academic interest.
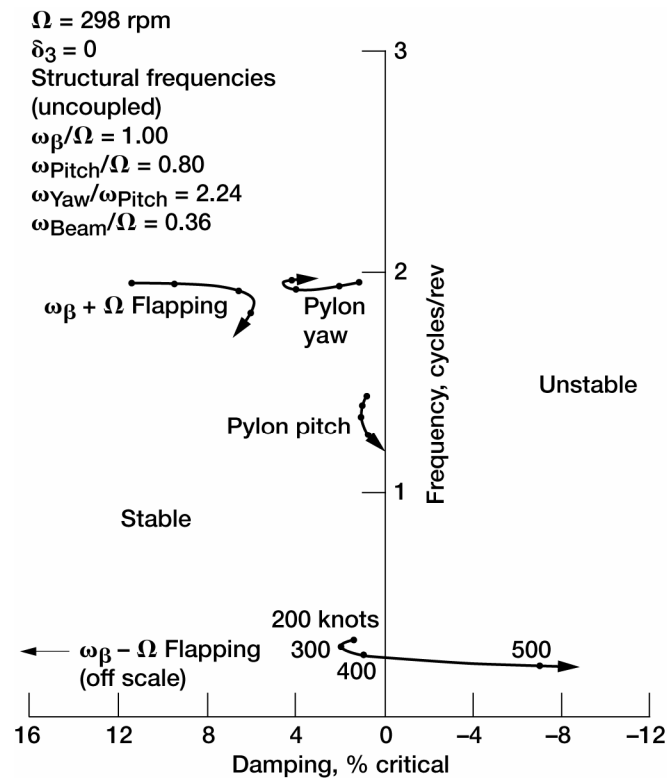
Figure 9.—Root locus for five degree-of-freedom prop-rotor/pylon system ($\omega_\beta/\Omega = 1.00$).

[6]See, for example, the "Review and Discussion" of ref. 1 by Wernicke and Gaffey which forms an integral part of that reference.
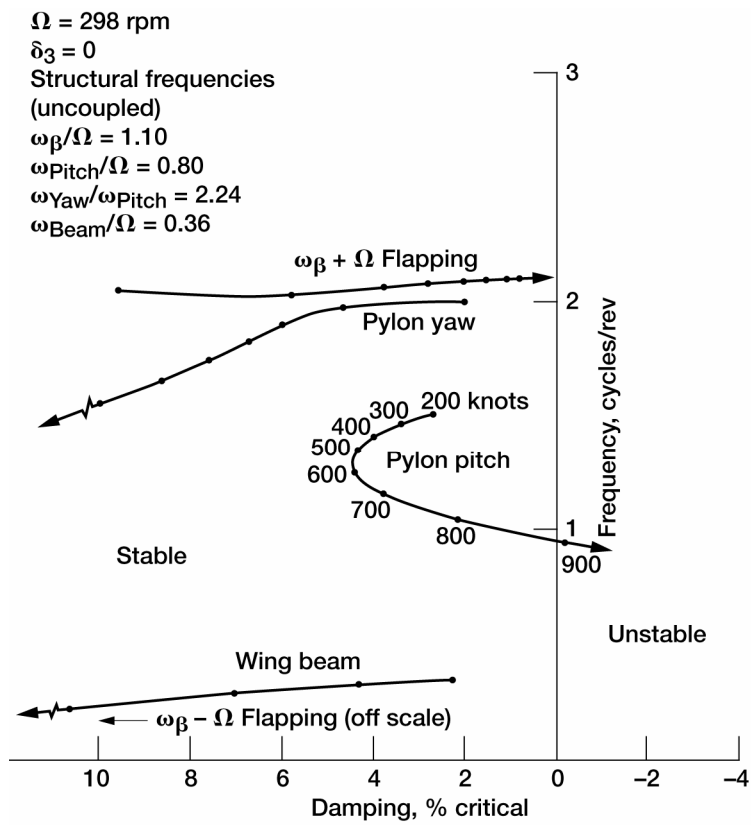
Figure 10.—Root locus for five degree-of-freedom proprotor/pylon system ($\omega_\beta/\Omega = 1.10$).
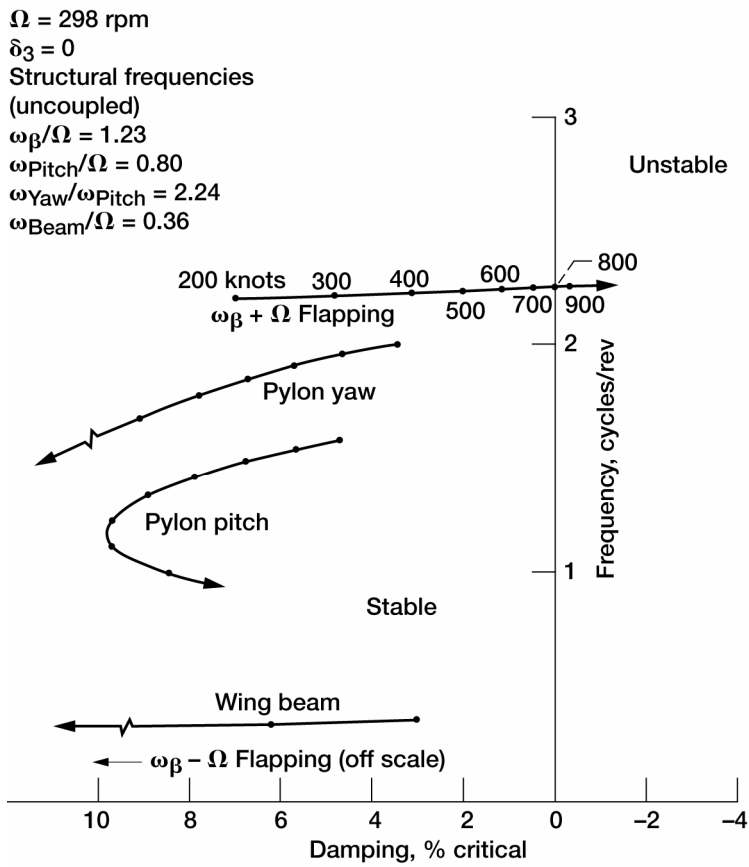
Figure 11.—Root locus for five degree-of-freedom proprotor/pylon system ($\omega_\beta/\Omega = 1.23$).
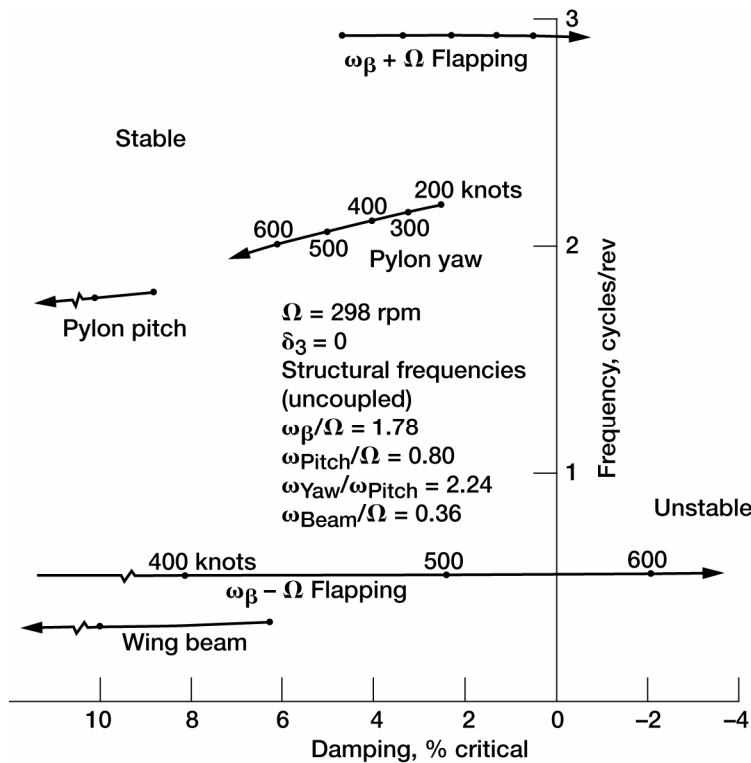
Figure 12.—Root locus for five degree-of-freedom proprotor/pylon system ($\omega_\beta/\Omega = 1.78$).

(d) Effects of pitch-flap coupling on stability of the five degree-of-freedom system.—An indication of the effects of δ_3 on proprotor/pylon stability for the case in which wing beam freedom is included are displayed in figure 13. The sharp reduction in stability associated with large values of δ_3 arise from the coupling of the wing beam mode with the low-frequency flapping mode, the frequency of which in the fixed system is increased by positive or negative δ_3. In each case shown, flutter is in the wing beam mode with the direction of pylon whirl being determined by the flapping natural frequency as indicated. The flapping frequency at which stability is a maximum occurs in the range 1.02 to 1.05 cycles/rev for the range of parameters studied. This suggests that an optimum flapping frequency in the sense of reference 1 also exists for $\delta_3 \neq 0$ and for K_H/δ_3 combinations.[7]

Frequency Response Characteristics of Proprotor Shear Force and Moment Derivatives

Airload moments are required to precess a proprotor in response to pylon oscillatory motions. At high advance ratios these moments are accompanied by shear forces which are phased with the pylon motion such that they tend to increase its pitching or yawing velocity and hence constitute negative damping on the pylon motions. These shears are the primary forces which destabilize the proprotor/pylon/wing elastic system and the aircraft rigid body modes.

Disturbances occurring in flight can, depending on their frequency content, excite the elastic proprotor/pylon/ wing system or the aircraft rigid body modes in an oscillatory manner. Any motions of this type effectively

---

[7]Young and Lytwyn did not consider δ_3 effects.
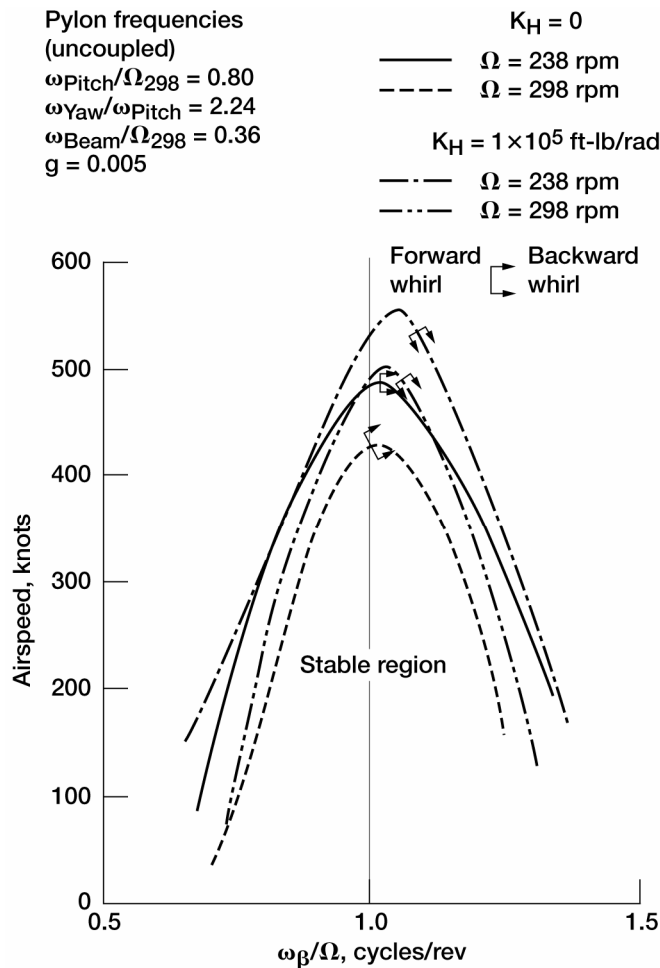
Figure 13.—Effect of flapping frequency on stability of five
degree-of-freedom proprotor/pylon system.

represent oscillatory motions of the proprotor mast (control axis) in space. Since the proprotor-generated forces and moments are a function of these oscillatory motions it is of interest to examine the dependency of the frequency response characteristics of these forces and moments on several system design parameters.

Proprotor inplane shear forces are proportional to the tip-path-plane precessional rate in space. Now the relationship of the proprotor response in space to that of the control plane (swashplate) is quite complicated, depending on the proprotor inertial properties, airspeed, rpm, flapping restraint, pitch-flap coupling, and control feedbacks. Consequently both proprotor/pylon stability and aircraft rigid-body stability will be sensitive to those parameters which affect proprotor response. The effect of several such parameters on the frequency response characteristics of these forces and moments will be delineated below by examining their variation during sinusoidal pitching oscillations of the pylon.[8] Attention is directed to the pitch plane only since, neglecting flow asymmetries and assuming a symmetric hub restraint, the forces and moments generated by yawing oscillations follow directly from the pitch results by virtue of symmetry.

The majority of these studies are for a velocity of 350 knots and a rotor speed of 238 rpm. This represents a tip inflow ratio ($V/\Omega R$) of 1.23. Although this is somewhat larger than that consistent with maximum propulsive efficiency in the high-speed cruise mode of flight, it is a value which can be realized in an overspeed flight

---

[8]This is equivalent to control axis pitching motions if the swashplate is fixed to the mast.

condition. Also, during wind-tunnel tests of scaled models (in which the full-scale $V/\Omega R$ is maintained) testing is done beyond scaled flight speeds to establish margins of safety.

The resultant shears and moments acting on a harmonically oscillating proprotor are algebraically complex quantities indicating that components proportional to both pitch angle and pitch rate contribute to their absolute value. To facilitate the interpretation of these forces and moments they will be separated into the above-mentioned components in the studies to be presented below. The separation of the normal force and pitching moment into components inphase with pitch angle and pitch rate is schematically illustrated in the sketch below.

$\partial H/\partial \alpha_m$

$\partial M/\partial \alpha_m$ α_m

$\alpha = \alpha_m \sin \omega_p t$

$\partial H/\partial q$ q

$\partial M/\partial q$

$\dot\alpha = \alpha_m \omega_p \cos \omega_p t = q \cos \omega_p t$
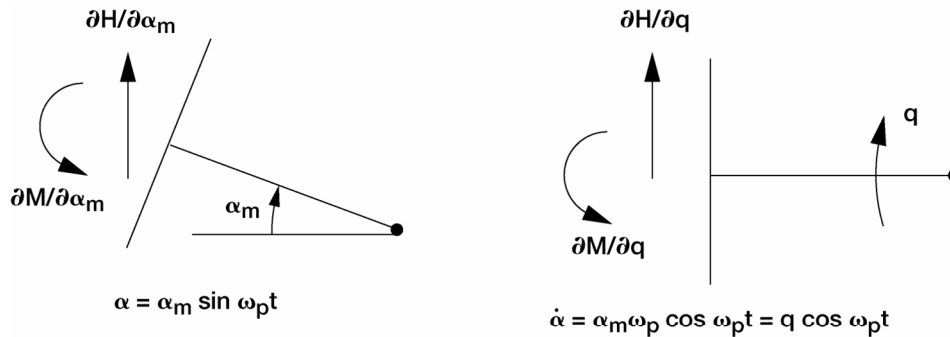
The components proportional to pitch angle are normalized by the maximum pitch amplitude α_m while the components proportional to pitch rate are normalized by the maximum pitch rate q (= $\alpha_m \omega_p$). Normalized in this manner the forces and moments assume the form of derivatives. With reference to the *H*-force components, the $\partial H/\partial \alpha_m$ term is the portion of the total *H*-force which is inphase or 180° out-of-phase with the pylon pitch displacement. When it is inphase with the pitch displacement it acts as a negative spring force tending to reduce the effective pylon pitch stiffness; when it is 180° out-of-phase with the pylon displacement it acts as a positive spring force, tending to increase the pylon pitch stiffness. $\partial H/\partial \alpha_m$ is a maximum at $\alpha = \alpha_m$ and zero when $\alpha = 0$. The $\partial H/\partial q$ term is the component of the total *H*-force which is inphase or 180° out-of-phase with the pylon pitch rate. It constitutes a negative (destabilizing) damping on the pylon pitching motion when it is inphase with the pitching velocity and positive damping when it is 180° out-of-phase with the pitching velocity. $\partial H/\partial q$ is a maximum when $\alpha = 0$ and zero when $\alpha = \alpha_m$. The sign convention which will be employed in the graphical results is given in figure 14.

z

$\alpha, \dot\alpha$

y

x

N H

b_1 β Y

M

a_1
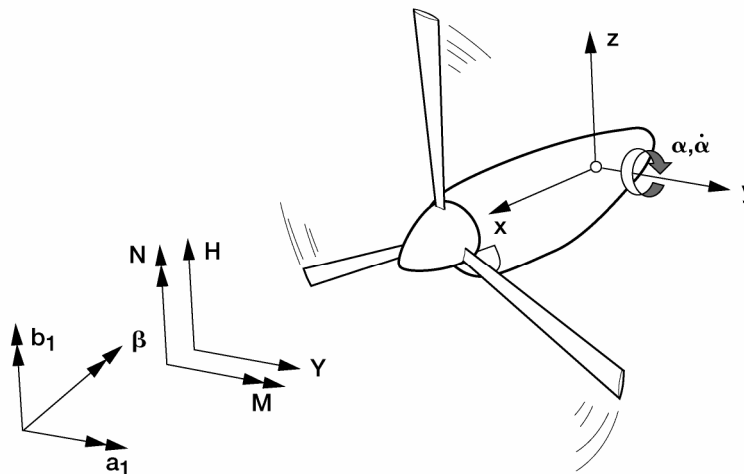
Figure 14.—Sign convention employed for presentation of proprotor force and moment derivatives and proprotor flapping derivatives.

(a) Proprotor rotational speed.—The frequency response characteristics of the shear forces and moments for two values of rpm are shown in figure 15. Consider the variation of the normal force component. The proprotor contributes large negative damping to pylon motions of low frequency. If the pylon coupled natural frequency falls within this range (below 2.5 cps for $\Omega = 300$ rpm, for example) the negative damping from the *H*-force will at some forward speed exceed the inherent structural damping and any positive aerodynamic damping and instability will result. As frequency is increased the negative damping decreases and eventually becomes positive. Simultaneously, $\partial H/\partial\alpha_m$ increases in a manner to reduce the pylon natural frequency in pitch. Hence, even if the pylon coupled natural frequency is sufficiently high to ensure a stabilizing contribution from $\partial H/\partial q$, the increasing negative spring effect of $\partial H/\partial\alpha_m$ with increasing airspeed (see fig. 16a) will act so as to reduce the pylon coupled natural frequency until $\partial H/\partial q$ becomes destabilizing and the negative damping effect is finally able to overcome the combined positive damping. This is precisely the mechanism by which the pylon pitch mode was driven unstable in the results for the 3° of freedom system shown in figure 1.

The magnitude and phase of $\partial H/\partial\alpha_m$ and $\partial H/\partial q$ are seen to be strongly dependent on the pylon pitch frequency and hence on the magnitude and phase of the tip-path-plane response $\left(\dot{a}_1\right)$ relative to the motion of the pylon mast $\left(\dot{\alpha}\right)$. For a steady continuous pitching motion in which $\omega_p = 0$, $\dot{a}_1$ is zero and $\partial H/\partial q$ contributes a large negative damping force to pylon motions. When the pylon is oscillating $\dot{a}_1$ is not zero. The tip-path-plane response can be quite large if the pylon is excited at one of the fixed-system flapping natural frequencies. The crests and troughs apparent in the response curves are associated with the fixed system flapping modes. For the particular rotor parameters indicated, $\partial H/\partial\alpha_m$ and $\partial H/\partial q$ become more destabilizing at pylon frequencies near $\Omega - \omega_\beta$ while for pylon frequencies near $\Omega + \omega_\beta$ $\partial H/\partial\alpha_m$ becomes less destabilizing and $\partial H/\partial q$ becomes less stabilizing. This implies that parameters which alter the proprotor flapping natural frequency can significantly affect the stability of both the pylon modes and the flapping modes. The results presented earlier in figures 6 to 12 are indicative of these effects for the case of flapping restraint.

At low pylon pitch frequencies the proprotor tip-path-plane is essentially inphase with the pylon angle ($a_1 \approx 0$) and the total *H*-force is predominantly inphase with the pitch rate. The damping component of the *H*-force then predominates at low pylon frequencies. As the pylon frequency is increased the proprotor disc begins to lag the pylon motion more and more until the tip-path-plane eventually assumes a fixed vertical orientation in space, being unable to respond fast enough to the high frequency pylon oscillations. The total *H*-force is then predominantly inphase with the pylon pitch displacement and the destabilizing forces act on the pylon primarily in the sense of a negative spring. Summarizing, the effect of the proprotor on pylon oscillations is to reduce both damping and frequency, the negative damping predominating at low pylon frequencies and a negative spring term predominating at higher pylon frequencies.

Note that as the proprotor rpm is increased the pitch frequency at which $\partial H/\partial q$ becomes stabilizing increases, implying that increased pylon stiffness and/or damping would be required to maintain the same level of stability as rpm increases.

Considerations similar to those above are generally applicable to the pitching moment response characteristics shown in figure 15c. Since proprotors usually have some type of flapping restraint (in the form of a spring, flex-hinge or offset flapping hinge) these moments can be transferred to the pylon and, with reference to figure 15c, can contribute either a stabilizing or destabilizing influence on pylon motions. For the particular conditions indicated $\partial H/\partial q$ is destabilizing for pylon pitch frequencies located near the fixed system flapping mode frequencies; the opposite is true for $\partial H/\partial\alpha_m$. The corresponding side force and yawing moment response characteristics are presented in figures 15b and d.

Tilt-proprotor aircraft are generally designed to have contra-rotating rotors in order to minimize the coupling between longitudinal and lateral rigid body motions. In this case, the side forces and yawing moments cancel out during aircraft pitching motions while the normal forces and pitching moments sum to zero during yawing motions.
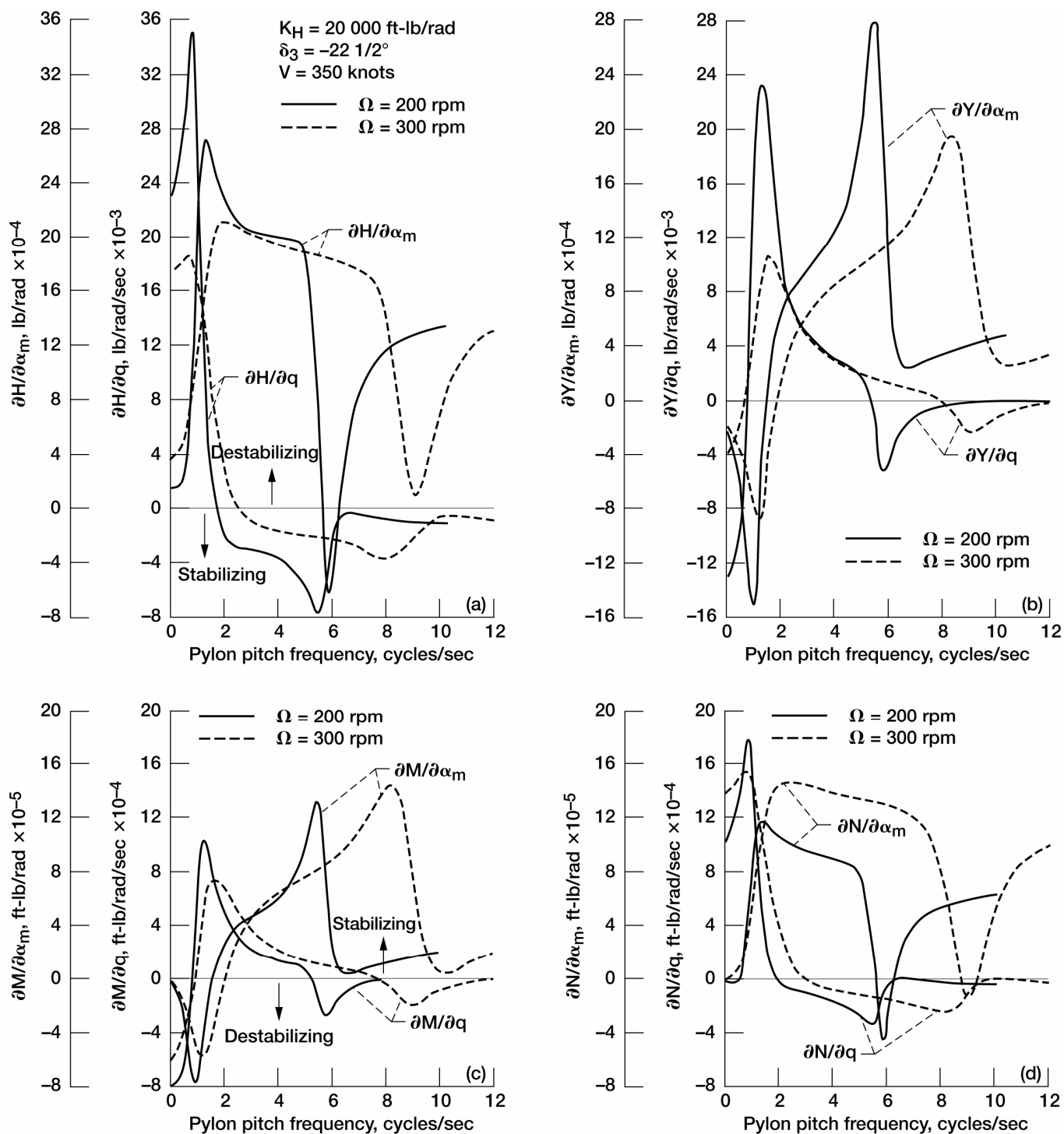
Figure 15.—Effect of proprotor rotational speed on frequency response of shear force and moment derivatives. (a) Normal force. (b) Side force. (c) Pitching moment. (d) Yawing moment.
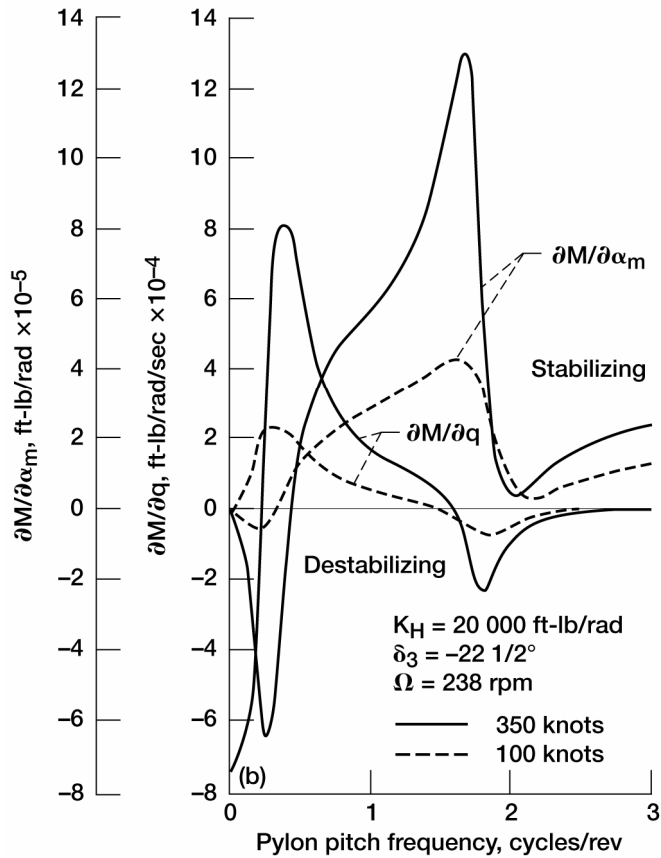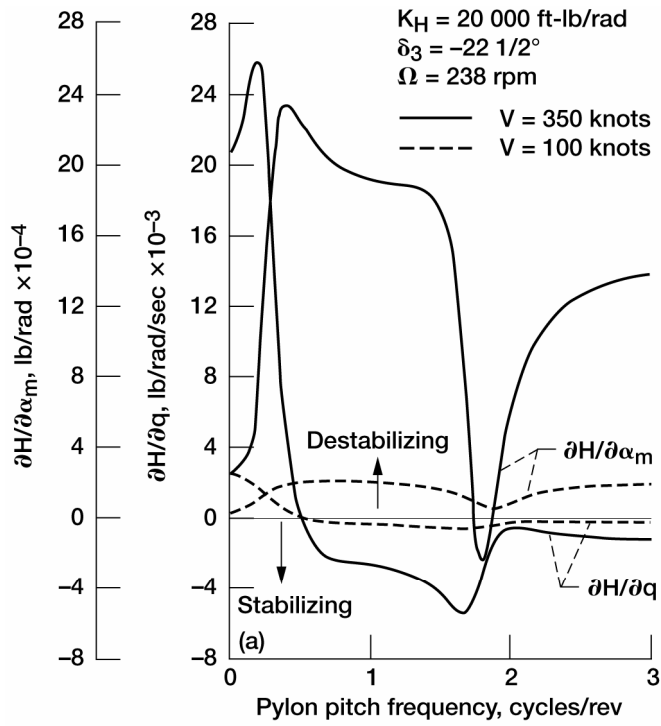
Figure 16.—Effect of airspeed on frequency response of shear force and moment derivatives. (a) Normal force. (b) Pitching moment.

(b) Airspeed.—The effects of forward flight velocity on the frequency response of the normal force and pitching moment are shown in figure 16. Since the rotor rpm will remain fixed the pylon pitch frequency is normalized on the rpm, in accordance with customary practice in rotary-wing dynamics. The effect of increased airspeed is seen to be an increase in the magnitude of the forces and moments, as might have been expected. There is a negligible influence on the pylon pitch frequency at which $\partial H/\partial q$ contributes positive damping, in contrast to the case of increasing rotor rpm. This suggests that the destabilizing effects of increasing airspeed are solely a result of the increasing magnitude of $\partial H/\partial \alpha_m$ and $\partial H/\partial q$.

(c) Pitch-flap coupling.—The negative damping contributed by the proprotor is a function of the amplitude and phase of the tip-path-plane response relative to the motion of the control axis. Two factors which increase the rotor response rate are $+\delta_3$ and K_H since they both act to increase the flapping natural frequency. The effect of δ_3 on the frequency response of the normal force and pitching moment derivatives for the case of zero hub restraint are shown in figure 17. For $\delta_3 = 0$, –22 1/2°, and +22 1/2°, the corresponding flapping natural frequencies in the rotating system are 1.0, 0.74, and 1.2 cycles/rev, respectively. These modes occur at fixed system frequencies of $\left| \Omega \pm \omega_\beta \right|$ and lead to the crests and troughs seen in the response curves at those frequencies. There is no low-frequency peak for $\delta_3 = 0$ because this mode has zero frequency in the fixed system. Note that the use of δ_3 decreases the destabilizing $\partial H/\partial \alpha_m$ forces at low pylon frequencies but increases the $\partial H/\partial q$ forces. This indicates that δ_3 is destabilizing on the aircraft short period mode. At higher frequencies δ_3 can be stabilizing or destabilizing relative to the $\delta_3 = 0$ case depending on the pylon frequency.

The destabilizing effect of δ_3 on proprotor/pylon stability demonstrated earlier in figure 5 can be explained with reference to figure 17b. As airspeed increases $\partial H/\partial \alpha_m$ decreases the pylon pitch stiffness more and more until $\partial H/\partial q$ becomes destabilizing. The magnitude of $\partial H/\partial q$ is larger for $\delta_3 \neq 0$ and hence can more quickly exceed the net positive damping in the system as pylon frequency continues to be reduced. Alternatively, this may be viewed as the pylon being destabilizing by coupling with the low-frequency flapping mode at a lower airspeed since increased δ_3 moves this frequency to the right.

The frequency of the second flapping mode either increases or decreases depending on whether δ_3 is positive or negative. The design consideration of separating the pylon modes from the flapping modes indicates that careful attention must be directed to the system coupled frequency spectrum when employing either positive or negative δ_3.

(d) Flapping restraint.—The increase in the proprotor response rate due to flapping restraint can be stabilizing or destabilizing depending on its value and the frequency of pylon oscillation. This is brought out in figure 18. Increased K_H is seen to lessen the destabilizing effect of $\partial H/\partial q$ at low frequencies ($\partial H/\partial q$ even become stabilizing for very large values of K_H) but decreases its stabilizing effect at intermediate pitch frequencies.

It is of interest to examine the variation of the zero pitch-frequency force and moment derivatives with flapping restraint and interpret the limiting conditions of infinite flapping restraint in light of the results shown for a propeller in figure 14 which were obtained by simple physical considerations. These results are summarized in figure 19 for three values of δ_3. As K_H is increased to "infinity" the derivatives will be asymptotic to the propeller limits indicated. It is seen that $\partial Y/\partial \alpha_m$ and $\partial M/\partial \alpha_m$ go to zero while $\partial H/\partial \alpha_m$, $\partial H/\partial q$, $\partial Y/\partial q$, $\partial M/\partial q$, $\partial N/\partial \alpha_m$, and $\partial N/\partial q$ approach non-zero limits. The limiting directions are also in agreement with those shown in figure 14. Note that of all the non-zero limiting values all are small except $\partial H/\partial \alpha_m$ and $\partial N/\partial \alpha_m$. Hence of the forces and moments which can destabilize the backward whirl mode only $\partial N/\partial \alpha_m$ (and $\partial M/\partial \psi_m$) are of sufficient magnitude to do so. This then constitutes another "proof" that the cross-stiffness moments are the driving terms for backward whirl flutter of a propeller.
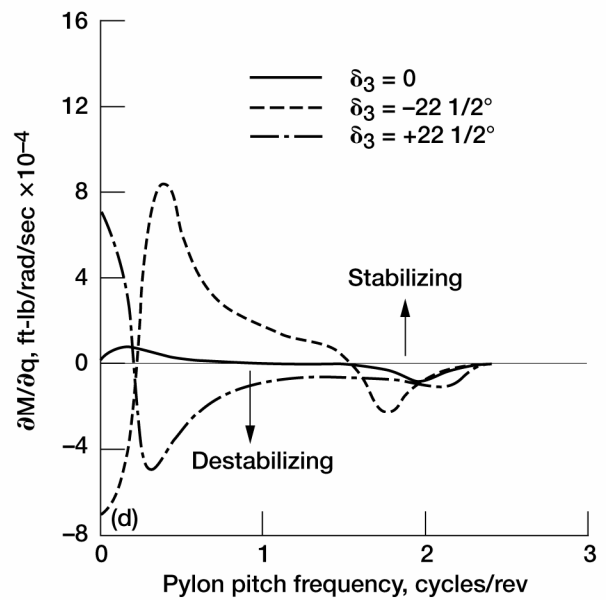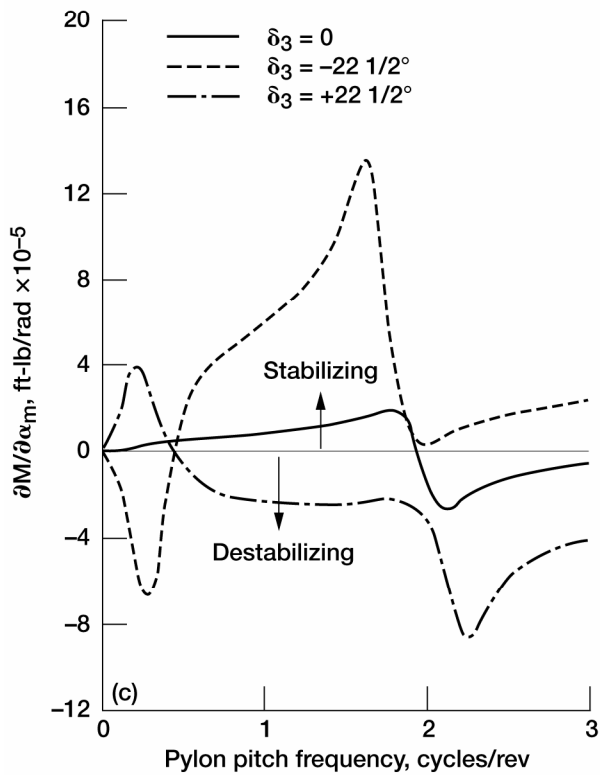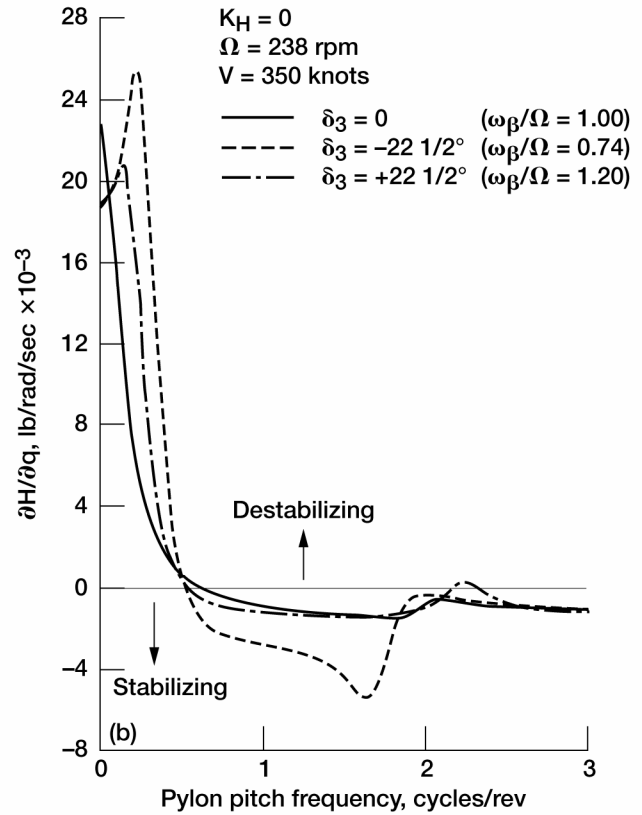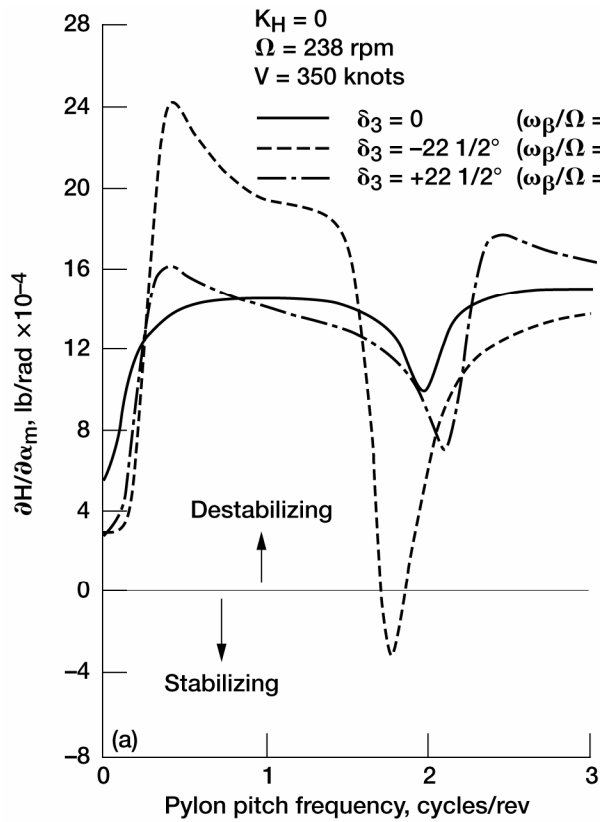
Figure 17.—Effect of δ_3 on frequency response of normal force and pitching moment derivatives. (a) Normal force due to pitch angle. (b) Normal force due to pitch rate. (c) Pitching moment due to pitch angle. (d) Pitching moment due to pitch rate.
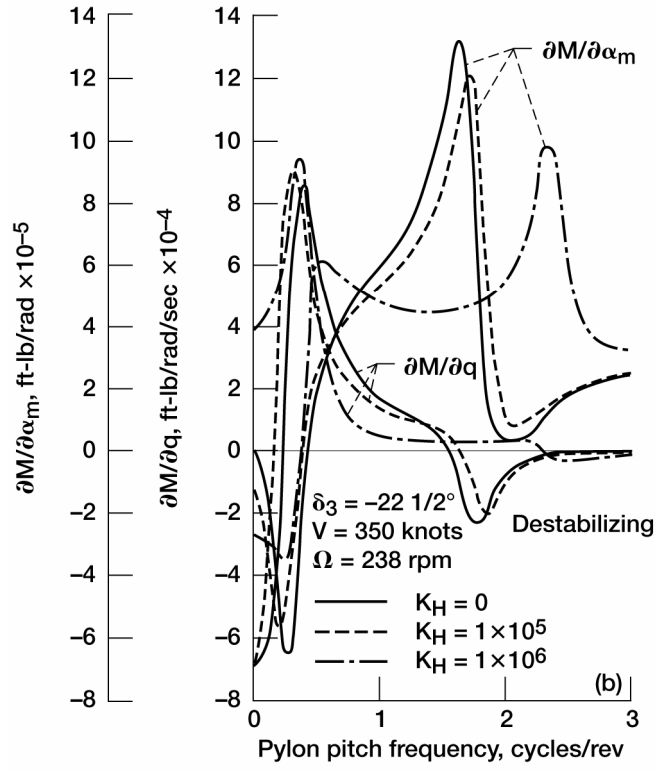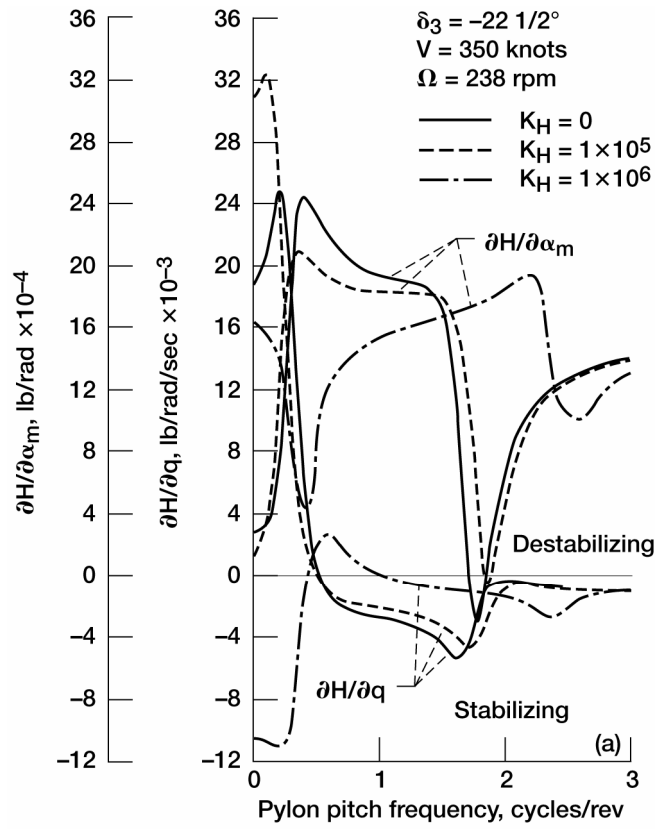
Figure 18.—Effect of hub restraint on normal force and pitching moment frequency response. (a) Normal force. (b) Pitching moment.
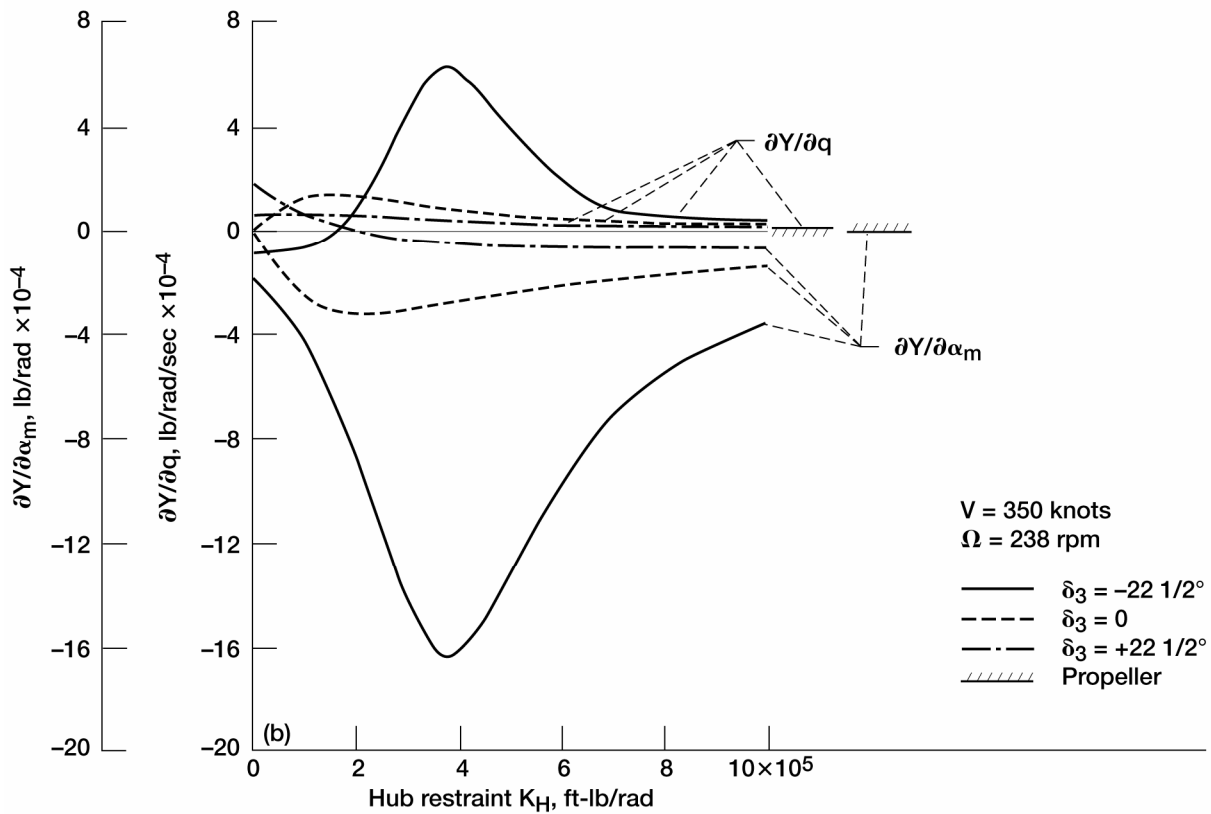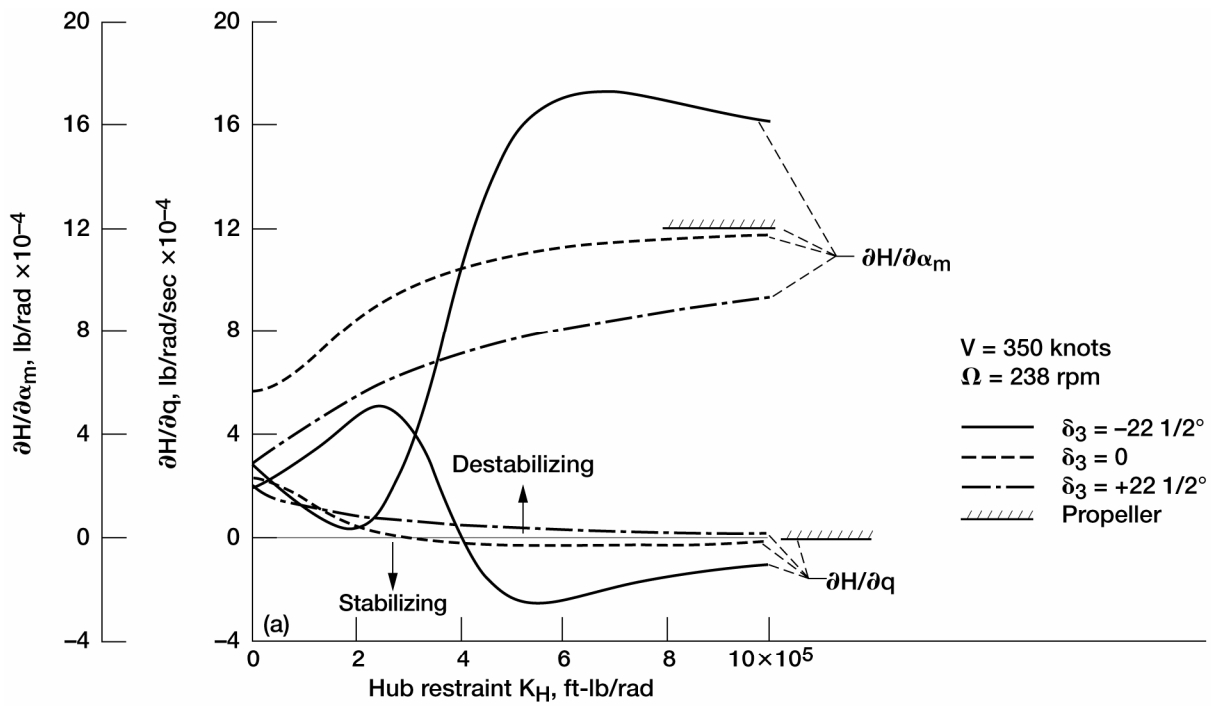
Figure 19.—Variation of zero frequency shear force and moment derivatives with hub restraint. (a) Normal force. (b) Side force.
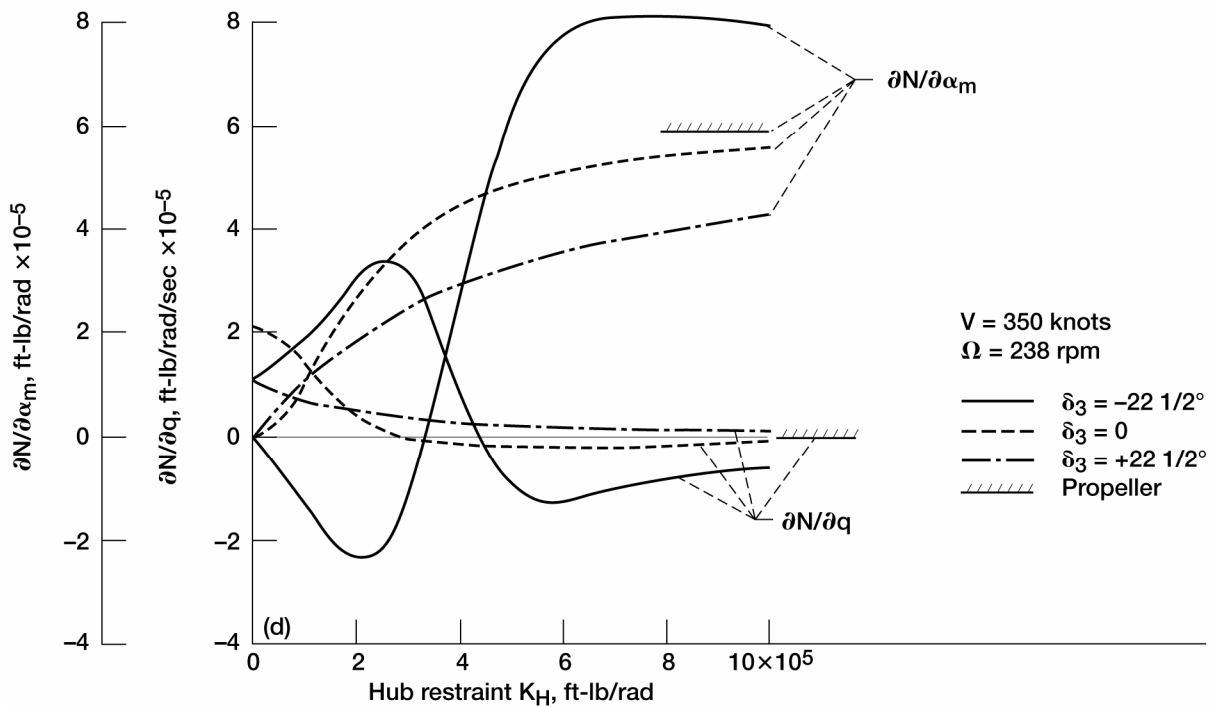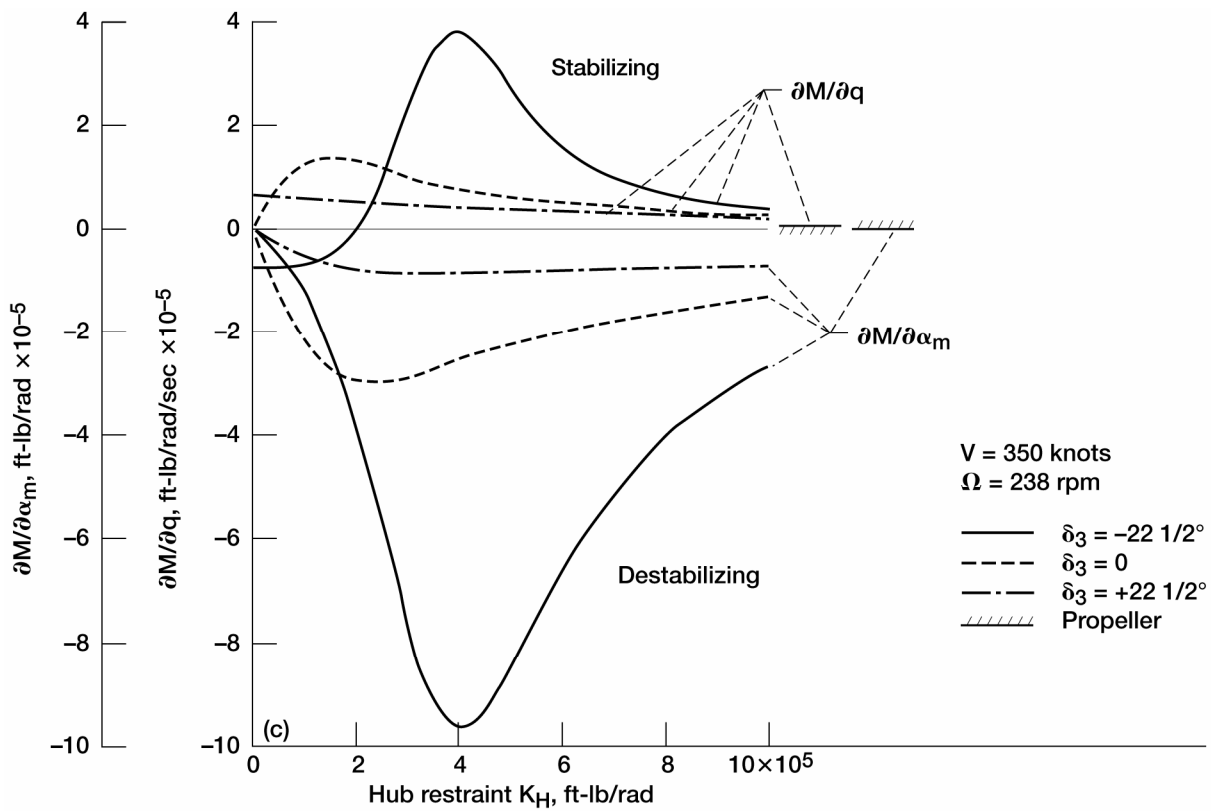
Figure 19.—Concluded. (c) Pitching moment. (d) Yawing moment.

(e) Shaft length.—Figure 20 illustrates the effect of shaft length on the normal force and pitching moment frequency response behavior of a proprotor and propeller. Since these results are for a forced response of the proprotor/pylon system the differences between the results for h = 6.92 and h = 0 are indicative of the aerodynamic damping associated with transverse velocities of the proprotor or propeller hub. Increasing the shaft length is stabilizing in the sense that hub translational damping is increased. This has already been shown analytically in refs. 9 to 11 for the case of a propeller. If the changes in inertia which accompany increases in shaft length are accounted for, the stabilizing effect due to increased hub translational damping is essentially negated by the destabilizing effect of a decrease in the effective pylon support stiffness in pitch and yaw so that the net stability of the system is basically unchanged.[9] It is to be noted that this conclusion is not in agreement with that of reference 11 which found that the net stability of the system was significantly increased even if the increase in system inertia was taken into account.

For the case of a proprotor the net effect of increased shaft length is highly destabilizing on whirl flutter. This is a consequence of the frequency response characteristics of the proprotor *H*-forces. With reference to figure 20a it is seen that for pylon pitch frequencies beyond about 0.5 cycles/rev increased shaft length is aerodynamically stabilizing. However, as airspeed increases the increasing negative spring effect of $\partial H/\partial \alpha_m$ reduces the pylon frequency until $\partial H/\partial q$ becomes destabilizing. In this range of pylon frequencies increases in shaft length are seen to have a negligible aerodynamic effect. Since the effective pylon pitch stiffness has been reduced the net effect of increased shaft length is destabilizing.

The propeller forces and moments are constant with frequency of excitation because there is no lag of the propeller disc relative to its shaft. This also causes $\partial H/\partial \alpha_m$ to be independent of shaft length. Recalling that $\partial M/\partial q$ is a function of the disc pitch rate in space shaft length has no effect on this derivative. $\partial M/\partial \alpha_m$ is of course identically zero for a propeller.

(f) Altitude.—The manner in which the zero frequency normal force derivatives vary with altitude are given in figure 21. $\partial H/\partial q$ increases with altitude. This implies a destabilizing effect of the inplane shears on the aircraft short period and Dutch roll modes. Since the horizontal and vertical tail contributions to aircraft damping in pitch and yaw remain relatively constant with altitude the proprotor contribution to these aircraft motions becomes increasingly destabilizing with altitude. The decreasing magnitude of $\partial H/\partial \alpha_m$ with increasing altitude indicates that aircraft longitudinal and lateral static stability are increased with altitude.

(g) Proprotor stabilization by blade pitch control feedback.—Inplane shears generated by proprotor precession in response to pylon motion are the cause of instability. These forces are dependent on the motion of the tip-path-plane in space, or, what is equivalent, the motion of the tip-path-plane relative to the swashplate (control plane). The preceding results were based on the assumption that the centerline of the mast and the control axis were identical, since the swashplate was taken to be rigidly affixed to the shaft. When the shaft pitches the swashplate follows. This induces blade angle of attack changes, resulting in precessional airload moments which are accompanied by destabilizing shear forces. If the proprotor could be uncoupled from the pylon or swashplate motions in a way which would minimize the angular motion of the proprotor control axis in space the destabilizing shears could be reduced. The direct approach of increasing pylon support stiffness is limited by weight considerations. Since it is the control plane and not the mast which determines proprotor behavior in space, various means for accomplishing this uncoupling based on the use of blade pitch control feedback are possible. A mechanical displacement uncoupling scheme, termed "swashplate/pylon coupling" will be employed here to illustrate the effectiveness of such a technique. Swashplate/pylon coupling (refs. 2 and 12) is based on a mechanical arrangement whereby the swashplate angular displacement relative to the mast during oscillatory motions of the pylon is opposite to that of the pylon tilt.

---

[9]These results are not shown herein.
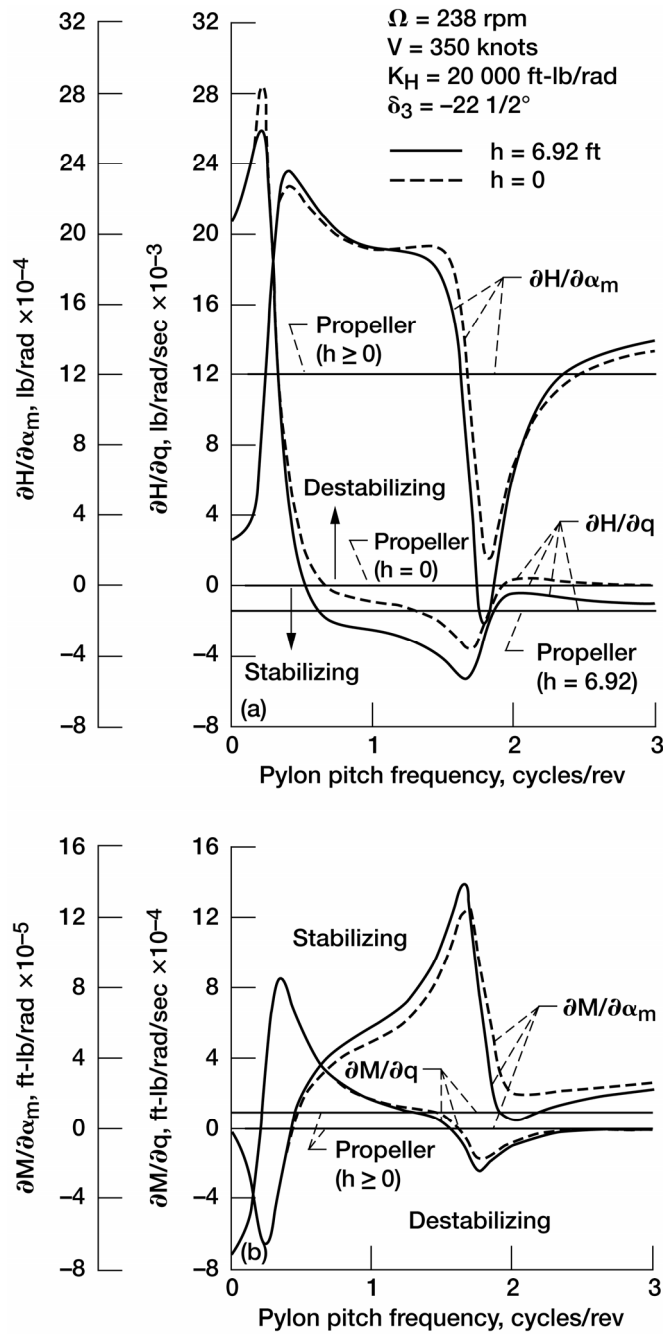
Figure 20.—Effect of shaft length on frequency response of proprotor and propeller force and moment derivatives. (a) Normal force. (b) Pitching moment.
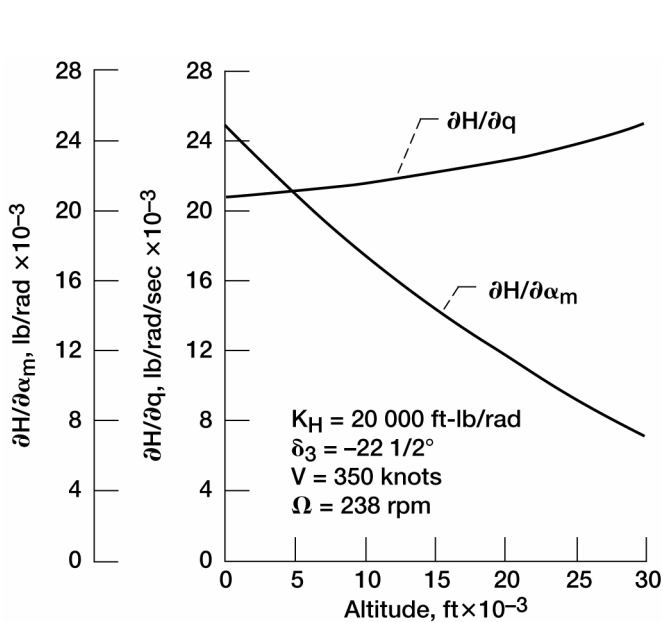
Figure 21.—Effect of altitude on zero frequency normal force derivatives.
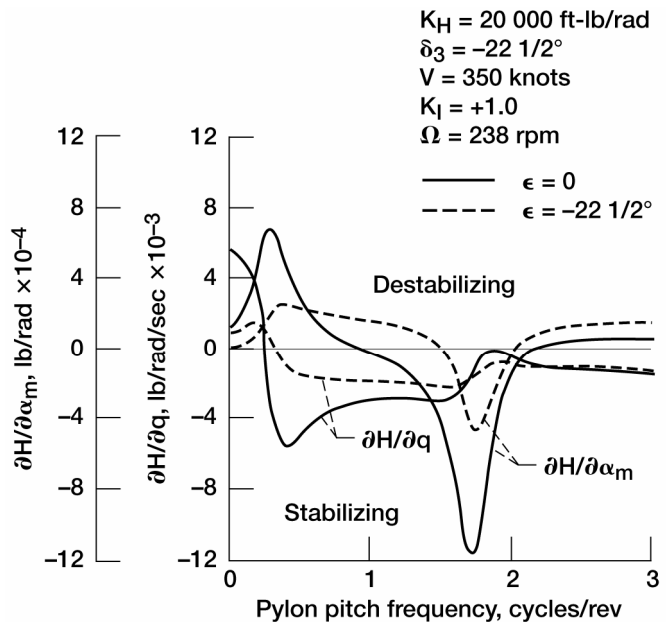
Figure 22.—Effect of swashplate/pylon coupling and control phasing on normal force frequency response.

Results indicative of the effectiveness of a blade pitch control feedback based on longitudinal swashplate/pylon coupling are shown in figure 22. For the coupling ratio used ($K_1 = +1.0$) the tip-path-plane remains essentially vertically oriented in space. These results are to be compared with the corresponding results in figure 20a for the case of no coupling. The significant stabilizing effects are readily apparent.

If $\delta_3 \neq 0$ (or, more generally, if $\omega_\beta/\Omega \neq 1$) the effective control axis is rotated and a swashplate command for a longitudinal tilt of the tip-path-plane will also cause the tip-path-plane to tilt laterally. Control phasing is incorporated into the swashplate/pylon mechanism to phase the swashplate and tip-path-plane in a manner which will eliminate this cross-coupling between longitudinal and lateral tip-path-plane motions in a given flight condition. This phasing is accomplished by adjusting the control linkages such that the swashplate control inputs to the pitch horns appear on the blades at an azimuth position more retarded or advanced than the swashplate tilt, which is the source of the control deflection, depending on whether ω_β/Ω is greater than or less than one. The effectiveness of swashplate/pylon coupling is generally increased by the use of control phasing. Figure 22 also shows the results of using a phasing equal to the δ_3 angle in conjunction with $K_1 = +1.0$.

(h) Zero frequency shear force characteristics during proprotor feathering.—Whereas aircraft rigid body dynamic stability considerations dictate the tail requirements for tilt-rotor operation in the high-speed cruise mode, tail requirements for a folding proprotor are dictated by considerations of static stability. This is due to the nature of the response characteristics of the shear forces during the feathering sequence of transition. An indication of the magnitude of the *H*-forces during this period at an airspeed which is representative of the transition speed is given in figure 23.

No transient effects are included. It is seen that as the rotors are stopped the flight condition of minimum static margin is encountered because angle-of-attack stability decreases by an increasing amount as $\partial H/\partial \alpha_m$ increases.
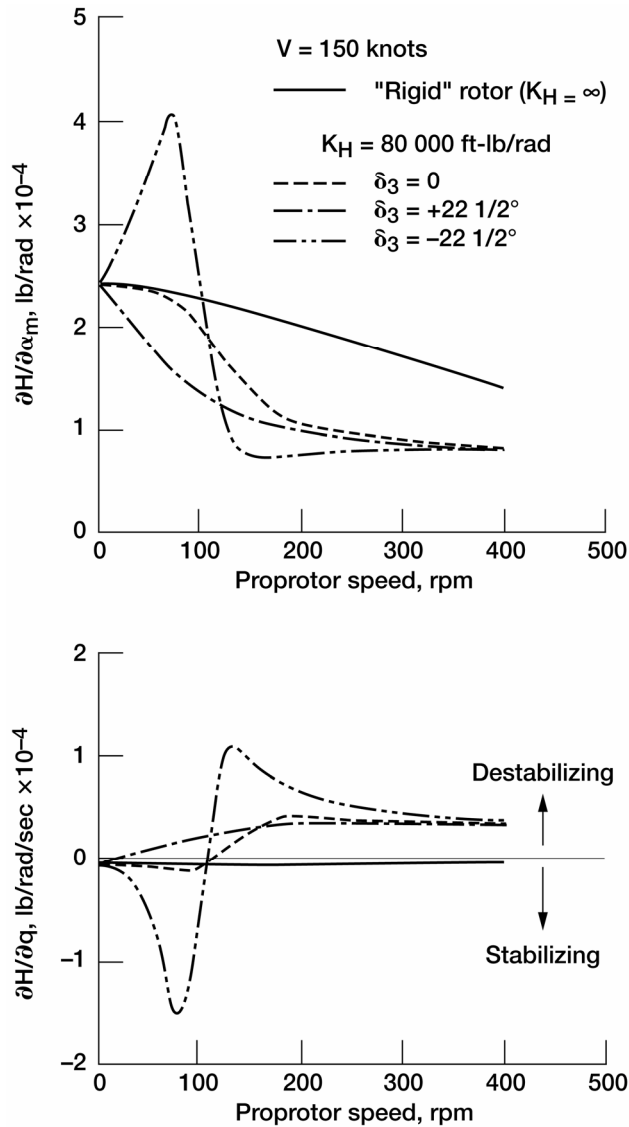
Figure 23.— Variation of zero frequency normal force
derivative with rotor rpm.

The corresponding results for a proprotor with infinite flapping restraint (i.e., a propeller) are shown for comparison. At rpm typical of proprotor operation (200 to 400 rpm) $\partial H/\partial\alpha_m$ is small relative to that of a propeller because flapping reduces 1/rev airload moments and hence $\partial H/\partial\alpha_m$. $\partial H/\partial q$ on the other hand is large since airload moments are required to precess the proprotor. The situation for a propeller in the same range of rpm is reversed, $\partial H/\partial\alpha_m$ is large and $\partial H/\partial q$ is small. The corresponding limiting values of $\partial H/\partial\alpha_m$ and $\partial H/\partial q$ at $\Omega = 0$ for the proprotor and propeller are identical because with flapping identically zero at $\Omega = 0$ (see fig. 29) the proprotor is effectively a propeller. Note that positive hub translational damping also exists for $\Omega = 0$. The peak in the curves for $\delta_3 = -22\ 1/2°$ is related to the flapping associated with passing through the flapping natural frequency (see fig. 29).

Proprotor Flapping Characteristics

Blade flapping is designed into rotor systems to relieve unbalanced moments across the rotor disc, to provide a means of controlling the aircraft longitudinally and laterally in hover and low-speed helicopter flight, and to relieve 1/rev blade-root bending moments in the airplane mode. During airplane mode operations a flapping proprotor will develop a flapping angle with respect to a plane normal to the shaft if the aircraft is pitched or yawed, as in a maneuver, or if operated at a steady angle of attack or sideslip, as in trimmed 1g flight. Flapping during maneuvers performed at high advance ratios can lead to especially large flapping angles because at the large inflow angles associated with high advance ratios the perturbation forces contributing to the precessing moment are reduced, and the proprotor must flap more to generate enough moment to precess the proprotor.

When the mast is given an angular displacement with respect to the freestream velocity, cyclic variations in blade section angle of attack are produced. The resulting 1/rev flapping moments cause the tip-path-plane to precess to a new steady-state position relative to the mast such that the aerodynamic moments are either balanced by the hub spring moments (if $K_H \neq 0$) or are zero (if $K_H = 0$).

The value of this steady-state tip-path-plane flapping angle can be written as a function of ω_β/Ω in the form

$$\frac{\partial \beta}{\partial \alpha_m} = \frac{\lambda^2 A_3}{\left[A_5^2 + \frac{4}{\gamma^2} \left(\overline{\omega}_\beta^2 - 1 \right)^2 \right]^{1/2}} \tag{9}$$

where, using equation (1),

$$\overline{\omega}_\beta^2 - 1 = \frac{K_H}{I_R \Omega^2} + \frac{1}{2} \gamma B_3 \tan \delta_3 \tag{10}$$

Under oscillatory conditions the flapping derivatives, like the force and moment derivatives, are mathematically complex quantities having components proportional to both pitch angle and pitch rate.

Considerations other than flapping per se dictate that some means be employed to reduce the flapping amplitude during airplane mode operations. Several means for reducing flapping are available to the designer (ref. 7). These include the use of flapping restraint, hinge offset, pitch-flap coupling, and blade pitch control feedback mechanisms. The first three reduce flapping by detuning the blade flapping natural frequency from 1/rev according to equation (9), thereby removing it from 1/rev resonance with the cyclic airloads due to shaft angle of attack. The influence of several of these methods will be presented below following the sign convention indicated in figure 14.

The variation of the total flapping derivative $\partial \beta / \partial \alpha_m$ with airspeed[10] and the effectiveness of δ_3 in reducing flapping are brought out in figure 24. If no δ_3 is employed the flapping derivative increases rapidly with airspeed. Positive δ_3 is seen to be somewhat more effective in reducing flapping than negative δ_3.

The effects of δ_3 on $\partial \beta / \partial \alpha_m$ for a fixed airspeed are illustrated in figure 25. For zero hub restraint the flapping curve is symmetric about $\delta_3 = 0$ and both positive and negative δ_3 are just as effective in reducing flapping. This can also be seen with reference to equations (9) and (10). However, K_H in conjunction with negative δ_3 reduces the effectiveness of negative δ_3 while K_H in conjunction with positive δ_3 increases the effectiveness of positive δ_3.

---

[10]δ_3 was held fixed as airspeed was increased.
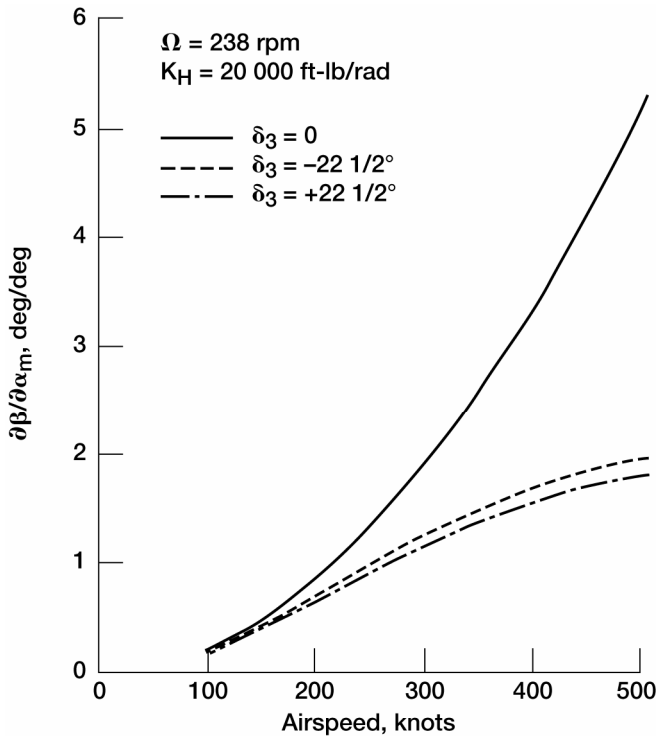
Figure 24.—Variation of total blade flapping derivative with airspeed.
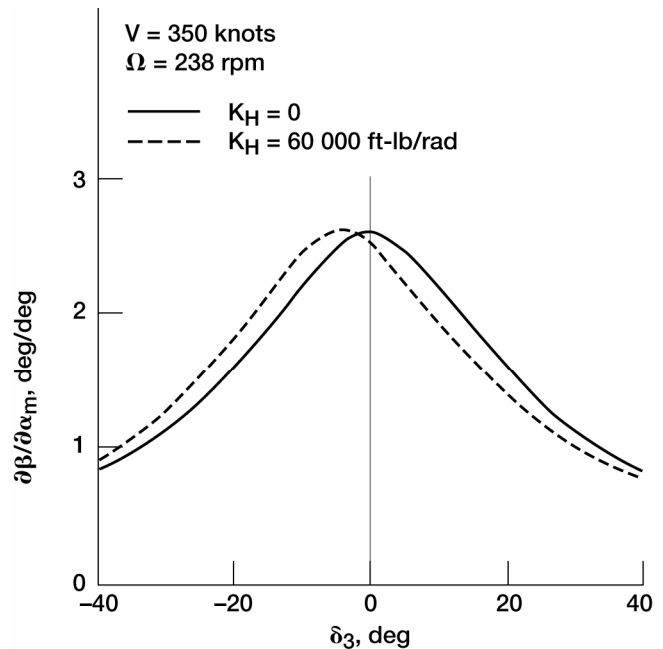
Figure 25.—Effect of δ_3 on blade flapping.

The left result in figure 26 indicates that large values of flapping restraint axe quite effective in reducing flapping. However, as pointed out earlier, blade loads generally limit the maximum flapping restraint which can be employed in practice. Pitch-flap coupling (δ_3) has a negligible effect on blade loads and can be equally effective in reducing flapping, as reference to the result in the right half of figure 26 will verify.

The tip-path-plane derivatives corresponding to figure 26 are given in figure 27 as a function of the flapping natural frequency. The sign of the longitudinal tip-path-plane derivative $\partial a_1/\partial \alpha_m$ is constant with ω_β/Ω such that the rotor disc is flapped aft at the top for a nose-up pitch attitude. A reversal in the sign of the lateral flapping derivative $\partial b_1/\partial \alpha_m$ occurs at a flapping frequency of 1/rev. As the sketches indicate, below 1/rev the tip-path-plane is flapped laterally outboard, away from the wing leading edge while for $\omega_\beta/\Omega > 1$/rev the tip-path-plane flaps laterally inboard toward the wing leading edge. Since 1g trimmed cruise flight will result in some positive mast angle of attack, wing/rotor 3/rev aerodynamic interference and attendant vibrations are minimized if the tip-path-plane flaps away from the wing leading edge (assuming cyclic pitch is not available for this purpose). On this basis, if $\omega_\beta/\Omega > 1$ the proprotors should turn inboard-down, and if $\omega_\beta/\Omega < 1$, inboard-up. The effective dihedral is also increased if $\omega_\beta/\Omega < 1$ and the direction of rotation is inboard-up. Note that as ω_β/Ω is increased both $\partial a_1/\partial \alpha_m$ and $\partial b_1/\partial \alpha_m$ approach zero, as they should for the limiting case of a propeller.

The frequency response characteristics of the tip-path-plane flapping derivatives are illustrated in figure 28. As pylon pitch frequency is increased from zero the magnitude and phase of the derivatives vary considerably. The crests and troughs evident in the response curves occur at the fixed system flapping mode frequencies. At high pylon frequencies $\partial b_1/\partial \alpha_m$ approaches zero and $\partial a_1/\partial \alpha_m$ approaches the negative of the pylon pitch angle. As pointed out earlier this is a consequence of the pylon oscillating too fast for the rotor to respond and the tip-path-plane remains essentially fixed in space. Both $\partial a_1/\partial q$ and $\partial b_1/\partial q$ approach zero with increasing frequency.
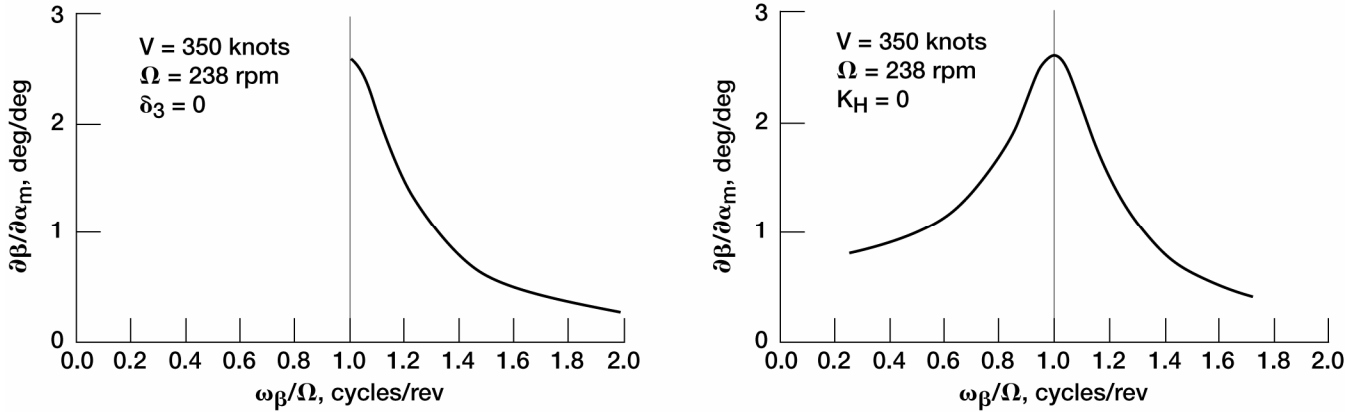
Figure 26.—Variation of blade flapping with flapping natural frequency.
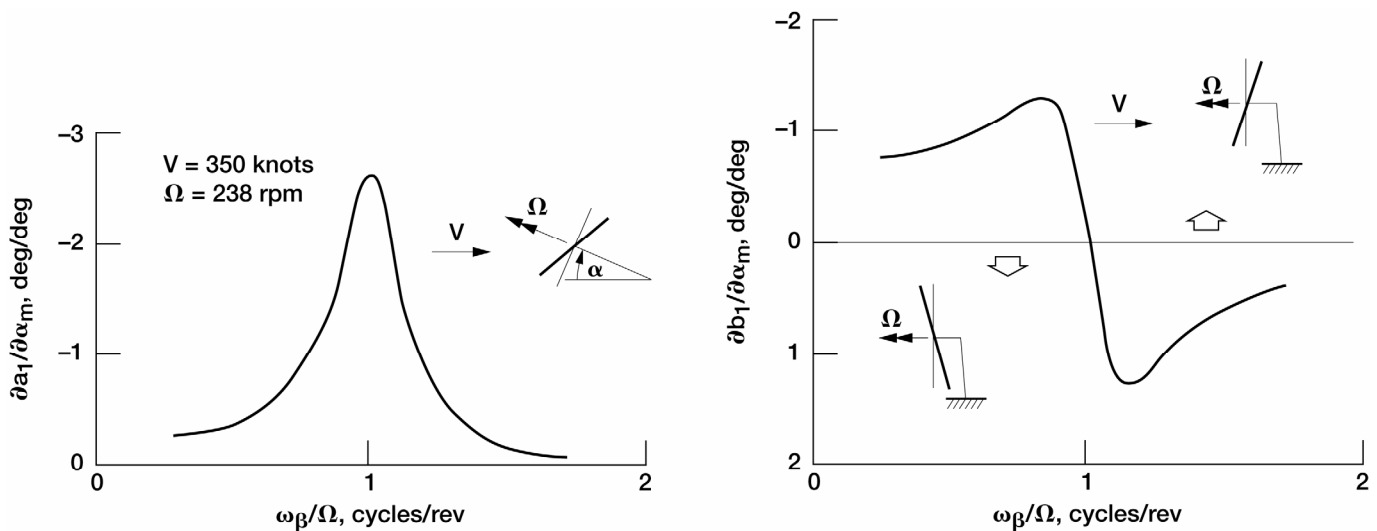
Figure 27.—Tip-path-plane flapping derivative variation with blade flapping frequency.

The effect of employing a swashplate/pylon coupling ratio of +1.0 in conjunction with a control phasing equal to the δ_3 angle are included in figure 28 for the case of zero pylon pitch frequency. $\partial a_1/\partial \alpha_m$ is seen to be about equal to the negative of the pitch angle indicating that the tip-path-plane is vertically oriented in space. $\partial b_1/\partial \alpha_m$ is almost zero so there is little lateral flapping.

The flapping behavior of a proprotor at low rpm, such as that which might be experienced during the feathering sequence of transition for a folding proprotor aircraft, constitutes an important design consideration. For $\omega_\beta/\Omega = 1.0$, equation (9) becomes

$$\frac{\partial \beta}{\partial \alpha_m} = \lambda^2 \frac{A_3}{A_5} = 1.8\lambda^2 \tag{11}$$

As the proprotor slows down the inflow angle increases and flapping sensitivity to changes in shaft angle of attack increases rapidly in accordance with equation (11). Figure 29 gives an indication of the flapping sensitivity to angle of attack as a function of rotor rpm for three values of δ_3. Steady-state values are given. The peaks in the response curves occur when the rotor rpm is in resonance with the blade flapping natural frequency, the maximum amplitudes being determined by the amount of flap damping.
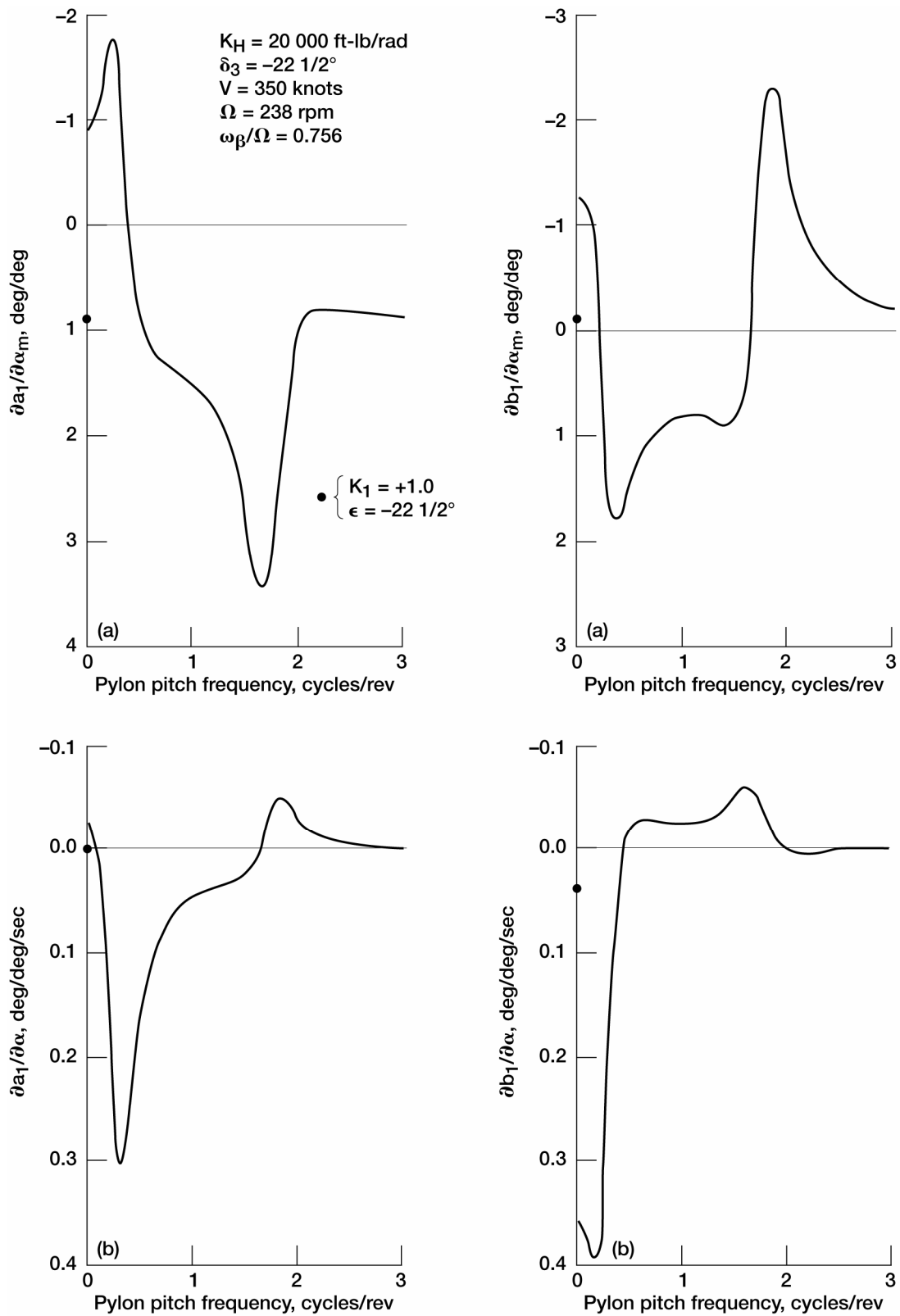
Figure 28.—Frequency response of tip-path-plane flapping derivatives. (a) Pitch angle components. (b) Pitch rate components.
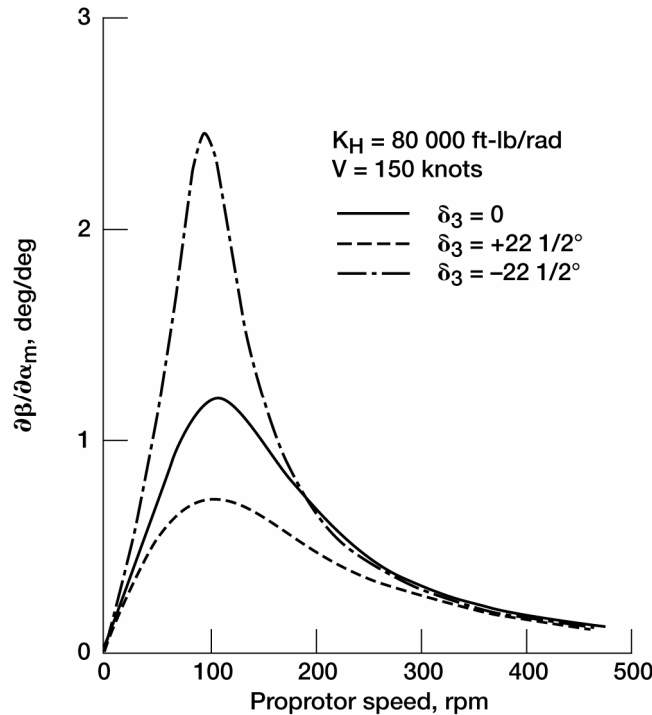
Figure 29.—Variation of steady-state flapping derivative with rotor rpm.

References

1. Lytwyn, R.T.; and Young, M.I.: The Influence of Blade Flapping Restraint on the Dynamic Stability of Low Disk Loading Propeller-Rotors. J. Am. Helicopter Soc., vol. 12, 1967, pp. 38–42.
2. Hall, W.E.: Prop-Rotor Stability at High Advance Ratios. J. Am. Helicopter Soc., vol. 11, 1966, pp. 11–26.
3. Gaffey, T.M.: The Effect of Positive Pitch-Flap Coupling. J. Am. Helicopter Soc., vol. 14, 1969, pp. 49–67.
4. Wernicke, K.G.: Tilt Proprotor Composite Aircraft, Design State of the Art. J. Am. Helicopter Soc., vol. 14, no. 2, 1969, pp. 10–25.
5. Exploratory Definition Final Report, Model 266 Composite Aircraft Program, Bell Helicopter Company, Report Nos. 266–099–201 through 223, July 1967.
6. Hohenemser, K.H.: On a Type of Low-Advance-Ratio Blade Flapping Instability of Three-or-More Bladed Rotors Without Drag Hinges, Proc. of the 13th Annual National Forum of the American Helicopter Society, May 1957.
7. Gaffey, T.M.; J.G. Yen; and R.G. Kvaternik: Analysis and Model Tests of the Proprotor Dynamics of a Tilt-Proprotor VTOL Aircraft, Presented at the Air Force V/STOL Technology and Planning Conference, Las Vegas, Nevada, September 1969.
8. Rao, K.V.K.; and Sundararajan, D.: Whirl Flutter of Flapped Blade Rotor Systems. NAL–TN–18, 1969.
9. Reed, Wilmer H., III; and Bland, Samual R.: An Analytical Treatment of Aircraft Propeller Precession Instability. NASA TN D–659, 1961.
10. Houbolt, J.C.; and Reed, W.H., III: Propeller-Nacelle Whirl Flutter. J. Aero. Sci., vol. 29, no. 3, 1962, pp. 333–346.
11. Sewall, John L.: An Analytical Trend Study of Propeller Whirl Instability. NASA TN D–996, 1962.
12. Edenborough, H.K.: Investigation of Tilt-Rotor VTOL Aircraft Rotor-Pylon Stability. J. Aircraft, vol. 5, no. 6, 1968, pp. 97–105.

Parametric Studies for Tiltrotor Aeroelastic Stability in High-Speed Flight[*]

Mark W. Nixon
U.S. Army Aerostructures Directorate
NASA Langley Research Center
Hampton, Virginia 23665

Abstract

The influence of several system design parameters on tiltrotor aeroelastic stability is examined for the high-speed (axial) flight mode. The results are based on a math model in which the wing is assumed to be cantilevered and is represented by beam finite elements having vertical bending, chordwise bending, and torsional degrees of freedom. A quasi-steady aerodynamic model is used for both the wing and rotor system. Coupling of the rotor flapping modes with the wing elastic modes produces a whirl motion, typical of tiltrotors, that can become unstable at high speeds. The sensitivity of this instability with respect to rotor frequencies, wing stiffnesses, and forward wing sweep is examined. Some important new trends are identified regarding the role of blade lag dynamics and forward wing sweep in tiltrotor aeroelastic stability. Two important conclusions based on these trend studies are that the blade lag frequency may be tuned to improve tiltrotor stability, and forward wing sweep is destabilizing because of changes in rotor force components associated with the sweep.

Nomenclature

b, c, t	wing beam, chord, and torsion modes
C_T	rotor thrust coefficient
EI_b	wing section beamwise stiffness
EI_c	wing section chordwise stiffness
GJ	wing section torsional stiffness
V^*	flight velocity normalized by blade tip speed
V_f^*	V^* at flutter
β_0	rotor collective flap degree of freedom
β_{1c}	rotor cyclic flap degree of freedom
β_{1s}	rotor cyclic flap degree of freedom
$\beta + 1$	high-frequency rotor flap mode
$\beta - 1$	low-frequency rotor flap mode
δ_3	blade pitch-flap coupling angle
ζ	percent critical damping
ζ_0	rotor collective lag degree of freedom
$\dot{\zeta}_0$	rotor collective lag velocity
ζ_{1c}	rotor cyclic lag degree of freedom

ζ_{1s}	rotor cyclic lag degree of freedom
$\zeta + 1$	high frequency rotor lag mode
$\zeta - 1$	low frequency rotor lag mode
Λ	wing sweep angle, negative forward
ν_β	blade flap rotating in-vacuum frequency
ν_ζ	blade lag rotating in-vacuum frequency
ω/Ω	frequency normalized by rotor rotation rate
$[p]$	progressive mode
$[r]$	regressive mode

Introduction

The tiltrotor aircraft has been a subject of renewed interest because of its ability to combine vertical takeoff and landing capability with efficient long-range and high-speed cruise flight capability. Its conversion from high-speed axial flight to helicopter flight is illustrated in figure 1. As shown, this aircraft is similar to a conventional fixed-wing aircraft in appearance, but has a rotor system mounted to a pylon at each wing tip. The pylons are rotated to change between axial and helicopter flight modes.

In high-speed axial flight, the tiltrotor is subject to an instability known as proprotor whirl flutter. High inflow through the rotor in this configuration results in large inplane motion-dependent rotor forces. The inplane forces for a tiltrotor are much larger than those typically associated with conventional propeller-driven aircraft because of the blade flap and lag motions which are usually exhibited by the rotors. The motion-dependent rotor forces act to reduce damping in the wing, resulting in greater wing motion and therefore greater pylon and hub motion. The rotor forces and wing/pylon motion augment each other with increasing airspeed to the point where the rotor forces may become destabilizing, ultimately driving the rotor/pylon/wing system unstable.

The stability of the tiltrotor in high-speed axial flight was a subject of great interest in the 1960's and early 1970's when the first prototypes of this aircraft were under development. Several early investigations of the aeroelastic behavior of tiltrotor aircraft having straight wings were performed using pylon-pivot models. These models approximate the wing as a system of springs and masses located at the effective pylon pivot point. The earliest work with application to tiltrotors was directed at hinged or flexible propeller systems (refs. 1 and 2). The analysis developed through this research effort, as well as other analyses of the time, had difficulty predicting forward whirl flutter in several instances in which it was obtained experimentally with small models. These problems were highlighted in the review made by Reed (ref. 3). A study by Young and Lytwyn (ref. 4) showed that the fundamental (in-vacuum) blade flapping frequency could be tuned to maximize stability of a tiltrotor system. The optimum tuning was approximately 1.1 to 1.2 per rev, which implies a requirement for an increase in flapping restraint for an articulated or gimballed rotor system. Because an increase in flapping restraint increases blade loads, in practice the applicability of blade tuning is limited (ref. 5). The results of an experimental and analytical investigation conducted on a scale model of the XV-3 tiltrotor were reported by Edenborough (ref. 6). His analysis used a math model which included a wing beamwise translation degree of freedom in addition to the conventional pylon pitch and yaw freedoms. The effects of several major parameters on stability were identified: an increase in pylon pitch and yaw stiffnesses is stabilizing, use of blade pitch-flap coupling (δ_3) is destabilizing, and increased flapping restraint is stabilizing. These trends were substantiated analytically by DeLarm (ref. 7) using a similar mathematical model. A study of the effects of steady-state coning angle and hinge damping by Kaza (ref. 8) showed that these parameters can also have a significant influence on stability. The results of extensive parametric studies were reported by Kvaternick (refs. 9 to 11). The math model used in these latter studies included all six degrees of freedom at the pylon pivot point, but generally only the pylon pitch, yaw, and beam degrees of freedom were used. These studies verified trends discussed previously and reported some important new trends: wing aerodynamics are stabilizing, unsteady aerodynamics are stabilizing, windmilling configuration is conservative (power-on case is more stable), high precone is destabilizing, both positive and negative δ_3 are destabilizing, and blade lag dynamics can have an important influence on stability.
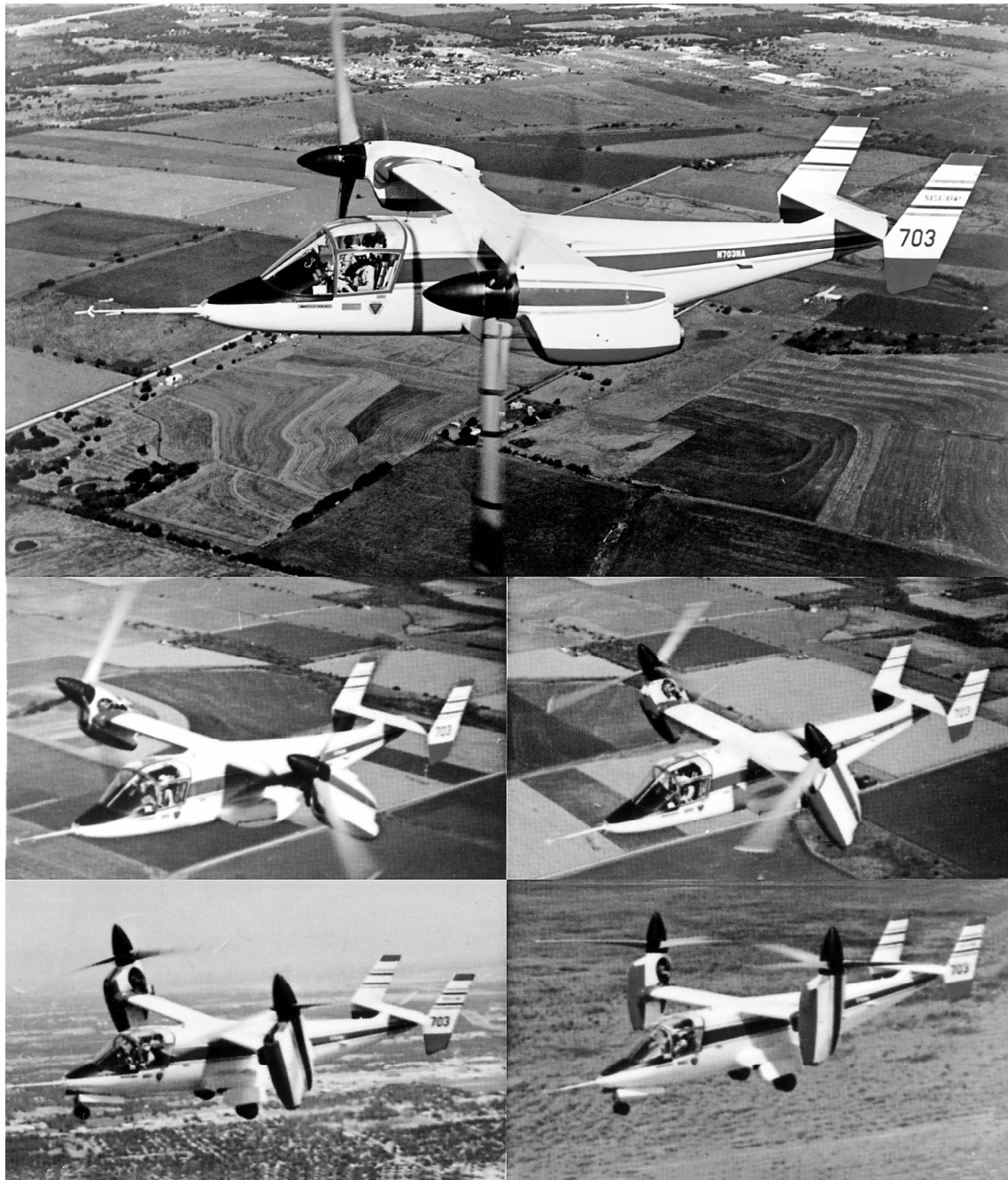
Figure 1.—Geometry of the tiltrotor model.

A more comprehensive math model which included a modal representation for the wing was developed by Johnson (ref. 12). This model was applicable only to axial flight and included nine degrees of freedom: six for the three-bladed rotor system and three for the three fundamental wing modes. Analytical results obtained with this model correlated well with the results of fullscale proprotor tests. Johnson later extended this math model to include elastic blade characteristics and helicopter and conversion modes of operation (refs. 13 and 14) These models formed the basic theory for the tiltrotor model in CAMRAD (refs. 15, 16, and 17), which is one of the few comprehensive rotorcraft codes to allow treatment of a tiltrotor aircraft.

While the studies mentioned above describe most of the tiltrotor dynamic behavior trends, they do not always provide a physical explanation for the observed behavior. In addition, there has been little investigation of the role of lag dynamics in stability. Further, although wing sweep has been recently considered as a means of increasing tiltrotor cruise velocities (ref. 18), there apparently has been no consideration of the influence of wing sweep on aeroelastic stability.

The objective of this paper is to ascertain the tiltrotor system design parameters which are important to aeroelastic stability and to determine their influence on stability in the high-speed axial flight mode using a recently-developed analysis. The present paper describes only briefly the math model and theory underlying the analysis, focusing instead on a discussion of the results obtained using the analysis. In particular, the discussion includes the frequency and damping characteristics of a baseline system, the Bell 25-ft diameter proprotor mounted on a cantilever wing (ref. 12), as well as the effects of several key system design parameters on stability of the baseline system. These include: blade frequencies, wing stiffnesses, wing sweep, and blade pitch-flap coupling. All cases assume that the rotor is operating in the autorotation state, which means that the rotor torque does not transfer to the wing and that the wing vertical bending rotation degree of freedom at the wing tip (pylon roll) does not contribute to rotor inplane motion.

Description of the Math Model

A three-bladed gimballed rotor system is assumed. The rotor aerodynamic model is quasi-steady and assumes a constant lift curve slope with Mach number corrections. The structural model is a rigid blade flaplag model. For a gimballed rotor system in flap, the rotor tip path plane may tilt like an articulated system hinged at the center of rotation, but must cone like a hingeless system about a virtual flap hinge. In cyclic lag, the rotor acts like a hingeless system with deflections defined about a virtual lag hinge, but in collective lag the blades are free. Perturbations of the rotor speed are considered which have been shown in past studies to have a significant influence on tiltrotor stability. The rotor system has six degrees of freedom (β_0, β_{1c}, β_{1s}, ζ_0, ζ_{1c}, ζ_{1s}) and associated equations of motion. The wing-tip motion contributes terms to the rotor equations, and the net rotor forces are in-turn applied to the wing tip. The wing model is represented by beam finite elements having vertical bending, chordwise bending, and torsional degrees of freedom. The wing lift is included in the wing equations through a quasisteady aerodynamic model with Mach number corrections. The wing and rotor systems are coupled through the degrees of freedom associated with the wing-tip node. The force terms of both the rotor and wing equations contain motion dependent terms which are brought into the system mass, damping and stiffness matrices. The steady forces are then set to zero and the resulting system of equations is solved using standard eigenvalue techniques to obtain its frequency and damping characteristics. The accuracy of the analysis was verified through comparison of results with those reported by Kvaternik (ref. 9) and Johnson (ref. 12).

Frequency and Damping Characteristics of the Baseline System

The important in-vacuum frequencies of the baseline wing and rotor system are listed in table 1. The cyclic lag frequency changes with collective pitch (and therefore forward flight velocity) so its baseline value is represented by a curve as shown in figure 2. The in-vacuum cyclic flap frequency is related to the gimbal dynamics, and does not change with collective pitch. The collective flap frequency is dominated by the rotational stiffness contribution, and thus changes very little with the collective pitch. Since this mode has a high frequency the small changes as a function of collective pitch setting are neglected. Additional data is reported by Johnson (ref. 12).

TABLE 1.—FREQUENCIES OF
THE BASELINE SYSTEM

Rotating Blade Freq. (per rev) In vacuum	
ν_β	1.02
ν_{β_0}	1.85
ν_ζ	see fig. 2
ν_{ζ_0}	0
Wing freq. (per rev)	
beam	0.42
chord	0.70
torsion	1.30
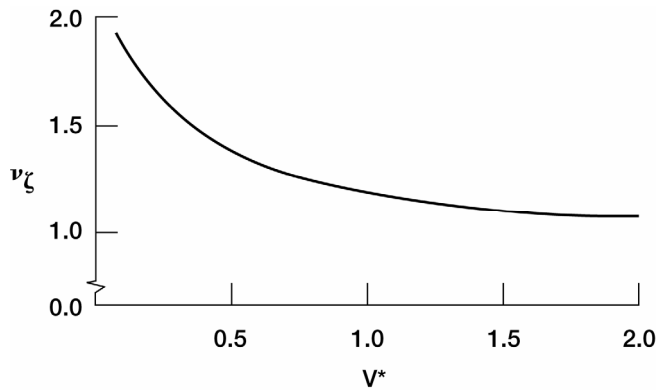
Figure 2.—Blade lag frequency as a function of velocity.

Now consider the system with aerodynamics. The frequency and damping of the wing and rotor modes for the baseline system are shown as a function of forward flight velocity in figure 3. Since ν_β is less than 1.0 in air, the $\beta - 1$ mode is progressive. The frequencies of the $\beta - 1$ and $\zeta - 1$ modes cross the fundamental wing mode frequencies and affect the damping of the wing modes. Abrupt changes of damping occur in the beam and chord modes where $\zeta - 1$ crosses those wing frequencies, and the beam and chord mode damping decrease rapidly as the $\beta - 1$ frequency approaches those wing frequencies. The chord mode has a damping valley because the $\zeta - 1$ mode damping is lower than the chord mode damping at the velocity where the frequencies cross. Conversely, the beam mode has a damping peak because the $\zeta - 1$ mode damping is greater than the beam mode damping at the velocity where those frequencies cross. Further indication of this transfer of damping from the lag mode is offered in figure 4, where the baseline lag frequency curve has been arbitrarily shifted up by a factor of 1.05. As shown, the increase in lag frequency shifts the crossing with the chord frequency to a higher velocity where the corresponding chord mode damping is now lower than the $\zeta - 1$ mode damping. The result is a damping peak in the chord mode rather than a damping valley.
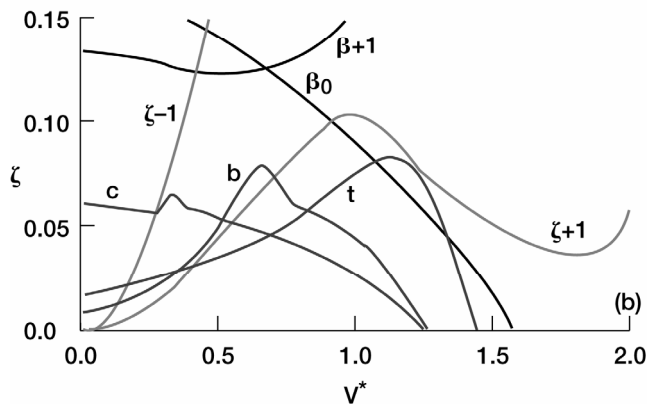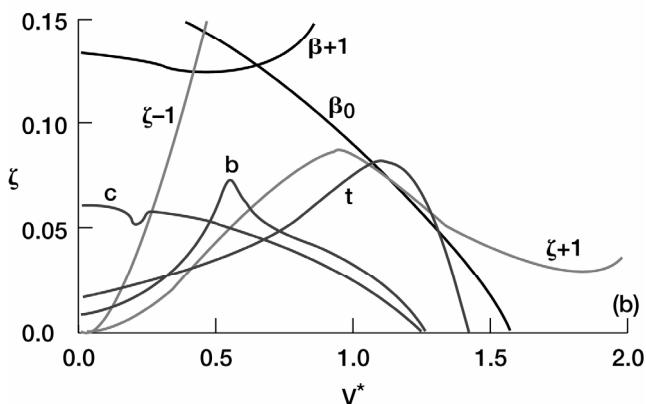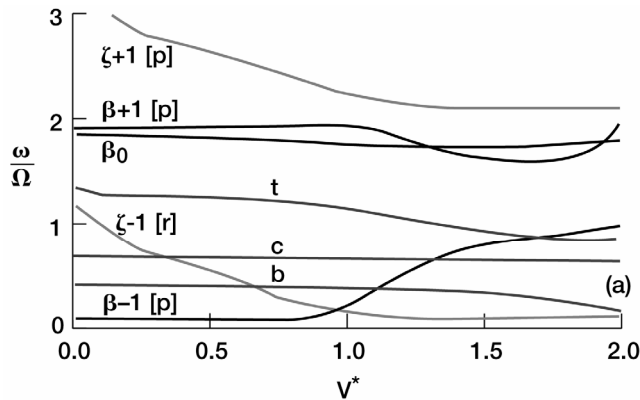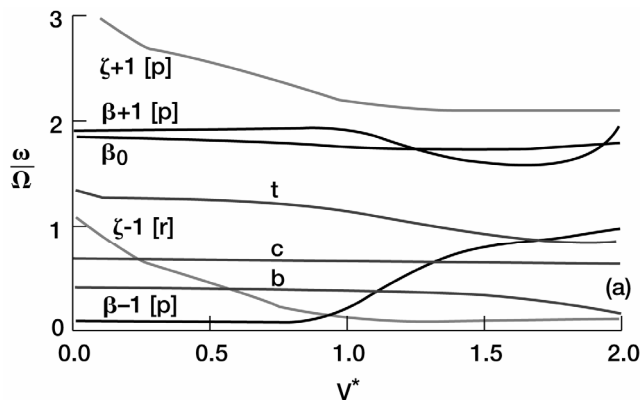
Figure 3.—Frequency and damping as a function of
velocity for the baseline (1.0 ν_β, 1.0 ν_ζ) system.
(a) Frequency. (b) Damping.

Figure 4.—Frequency and damping as a function of
velocity for ν_ζ increased by the factor 1.05.
(a) Frequency. (b) Damping.

Rotor Frequency

In this section, the influence of rotor in-vacuum flap and lag frequencies on tiltrotor stability is examined in more detail. The mass and inertia properties are held fixed, so the increase in vacuum flap frequency can be developed only through an increase in the gimbal hub spring. The lag frequency increase would be obtained through increases in the blade stiffnesses (both flap and lag). The baseline flap frequency is parametrically varied from 0.9 to 2.5 of its original value (the lower factor of 0.9, while physically unobtainable for flap in vacuum, is used to provide continuity of the trends). Because the lag frequency changes as a function of velocity, for this study the lag frequency was varied by shifting the baseline lag frequency curve by a factor ranging from 0.9 to 2.5. Extreme variations of flap and lag frequency are unlikely to be obtainable in design practice, but they are of academic interest so that physical reasoning of the trends within the design range may be established. The in-vacuum flap and lag frequency variations were performed independently, meaning that the flap frequency was held at its baseline value while lag frequency was varied, and vice versa. In addition to showing the direct effects of flutter speed as a function of flap and lag frequency, this study will provide insight into the flutter mechanism. By better understanding this mechanism, the rotor and wing properties may be selected to enhance tiltrotor stability.

The results of sweeping through values of ν_β and ν_ζ on the baseline tiltrotor configuration are illustrated in figures 5 and 6, respectively. Several observations based on these plots are described in the following numbered paragraphs (italicized). The paragraphs also include explanations (non-italicized) which are based on a sequence of frequency and critical damping plots reflecting parametric changes in the flap and lag frequencies. The results of changing flap frequency are shown in figures 7 and 8 while the results of changing lag frequency are shown in figures 9 and 10.
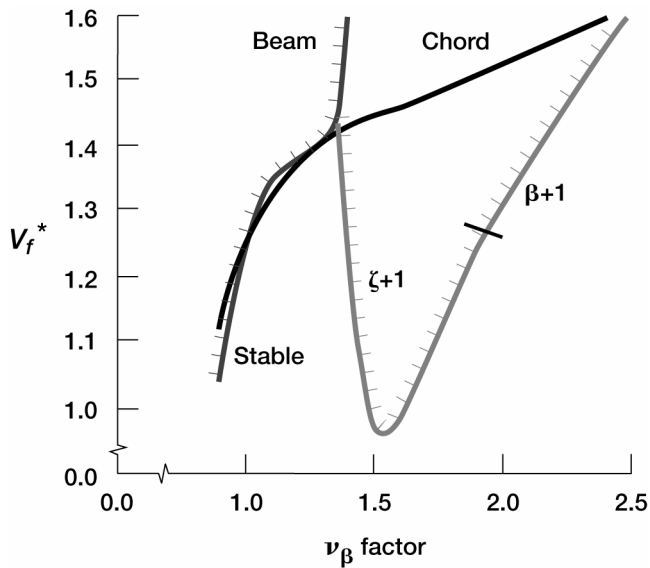
Figure 5.—Flutter velocity as a function of ν_β factor.
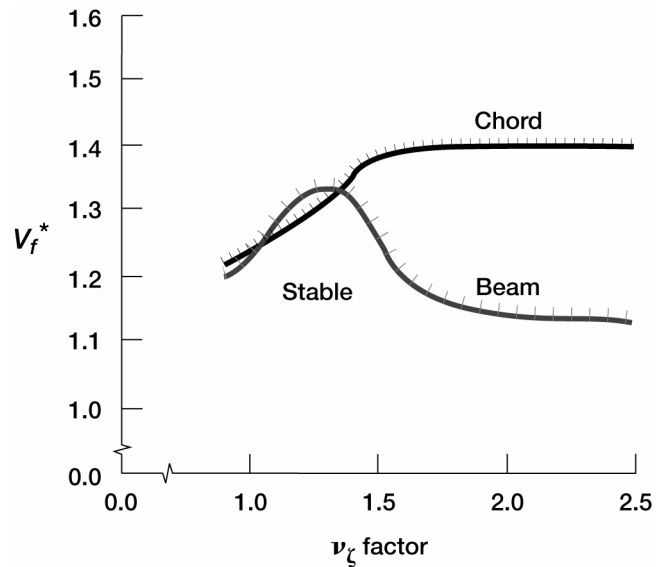
Figure 6.—Flutter velocity as a function of ν_ζ factor.
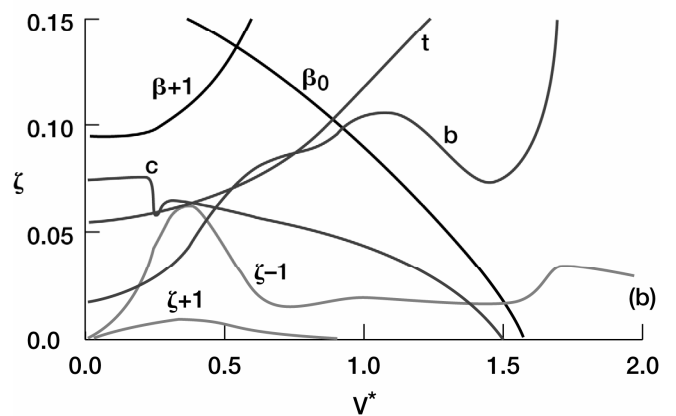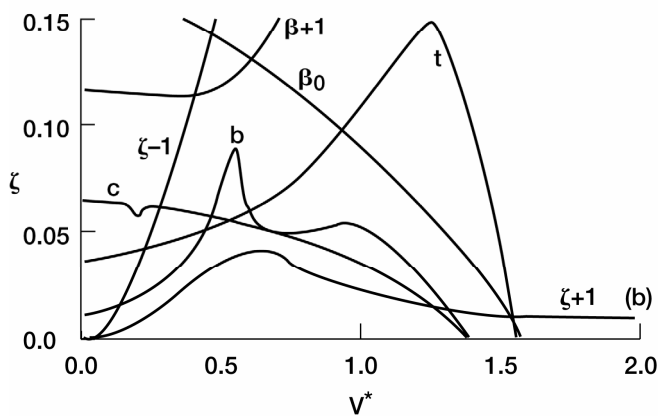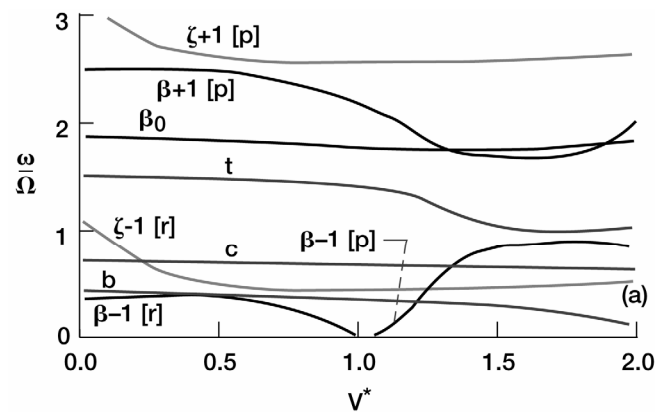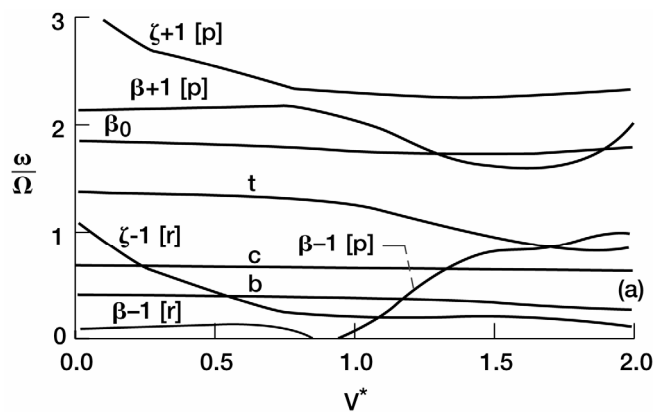
Figure 7.—Frequency and damping as a function of velocity for 1.2 ν_β. (a) Frequency. (b) Damping.

Figure 8.—Frequency and damping as a function of velocity for 1.5 ν_β. (a) Frequency. (b) Damping.
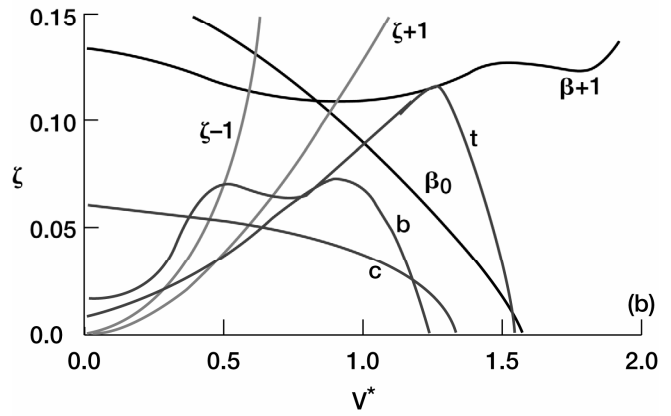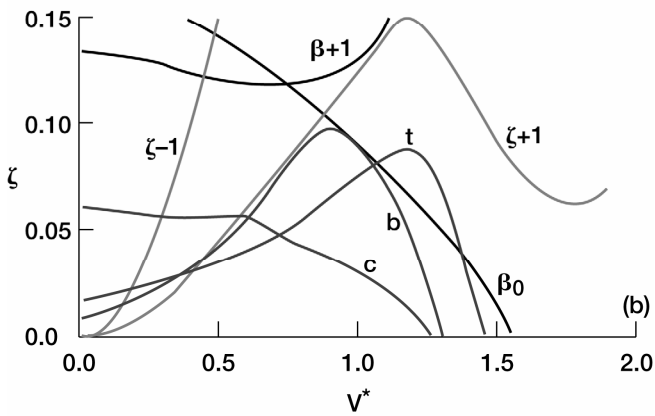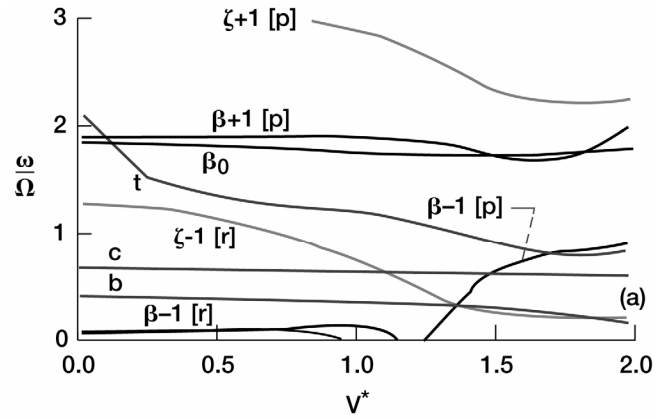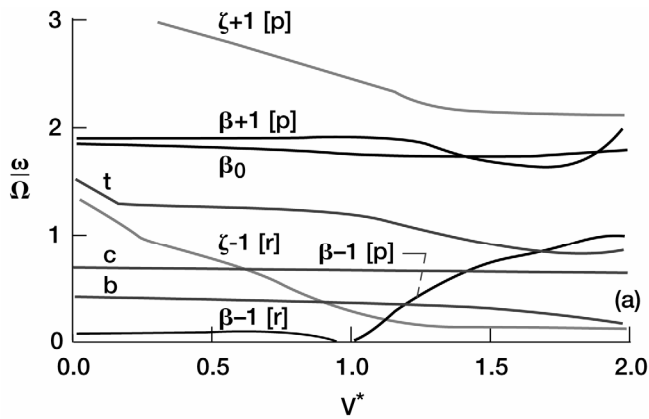
Figure 9.—Frequency and damping as a function of velocity for 1.2 ν_ζ. (a) Frequency. (b) Damping.

Figure 10.—Frequency and damping as a function of velocity for 1.5 ν_ζ. (a) Frequency. (b) Damping.

1. *As shown in figure 5, the beam and chord mode V_f^* rise sharply with an increase in ν_β at low values of ν_β* (ν_β *factors 0.9 to 1.2*). There are two effects working here. One is a decrease in the $\beta - 1$ frequency, and the other is an increase in the wing torsion frequency. The decrease of the $\beta - 1$ frequency increases the velocity at which it crosses above the $\zeta - 1$ frequency (note sequence of figs. 3, 7, and 8). As long as the $\zeta - 1$ frequency remains between the beam mode frequency and the $\beta - 1$ frequency there is little interaction between the flapping and wing motions. The low lag frequency acts like a barrier, preventing coalescence of the low flap frequency with the beam mode, until the low flap frequency is able to cross above it. Notice that in figure 5 the $\beta - 1$ mode changes from a progressive mode at $10\nu_\beta$ (fig. 3) to a regressive mode at higher ν_β and low velocities (figs. 7 and 8). This is because the δ_3 effect is small at low velocities, so the effective rotating frequency is above 1.0 until the δ_3 effect lowers it. As ν_β increases it takes progressively higher velocities to lower the effective flap frequency, which is why the transition from the regressive to progressive flap mode occurs at increasingly higher velocities. The increase in torsion frequency further separates the beam and torsion modes, which is stabilizing as will be shown later in the wing frequency study.

2. *As shown in figure 5, a $\zeta + 1$ mode instability occurs at high ν_β factors (ν_β factor above 1.2).* The flutter speed, V_f^*, drops sharply over the range $1.2\nu_\beta$ to $1.6\nu_\beta$ then increases over the range $1.6\nu_\beta$ to $2.5\nu_\beta$. The rotor instability shifts from a $\zeta + 1$ mode to a $\beta + 1$ mode at about $1.9\nu_\beta$. A $\zeta + 1$ rotor instability occurs above about $1.2\nu_\beta$ because of a flap and lag frequency coalescence in the rotating frame. In the fixed frame the high frequency modes cross which results in an instability in the highest frequency rotor mode, $\zeta + 1$. As ν_β increases beyond $1.6\nu_\beta$ (these plots not shown), the $\beta + 1$ frequency first crosses the $\zeta + 1$ frequency curve then coalesces weakly with it as it falls below the $\zeta + 1$ frequency. The weakening of the coalescence gives a higher V_f^* for the $\zeta + 1$ instability.

Further increases in ν_β result in the rotor instability shifting from the $\zeta + 1$ mode to the $\beta + 1$ mode. This occurs at the ν_β where the $\beta + 1$ frequency becomes higher than the $\zeta + 1$ frequency.

3. *As shown in figure 5, the wing beam mode does not become unstable above about 1.4ν_β.* There are two reasons for this. First, the flap and lag modes become highly coupled due to the coalescence of those frequencies (as discussed above) so there is only a slight destabilizing influence of the blade flap mode on the beam mode. The second reason is the increased separation of the wing beam and torsion frequencies which has a stabilizing effect on the wing mode (notice increase in torsion frequency in sequence of figs. 3, 7, and 9, even at low velocities). As ν_β increases, the torsion frequency also increases because of mechanical coupling between the rotor flap and wing torsion motions.

4. *As shown in figure 5, the wing chord mode can become unstable even at high ν_β factors.* This is because the chord mode is not strongly coupled to any other modes. Its flutter speed continues to increase as ν_β increases due to decreasing interaction with the rotor flapping mode. It should be noted that the chord mode may be more strongly coupled with the beam and torsion modes in the free flight condition (not considered in the present study) through inertial coupling.

5. *As shown in figure 6, the chord mode V_f^* increases with increases in ν_ζ factor, until about 1.5ν_ζ, then does not increase further.* At low values of ν_ζ factor the damping in the chord mode is strongly influenced by the location of the $\zeta - 1$ frequency with respect to the chord frequency, particularly when there are no other frequencies between the two. Each subsequent change in the lag frequency creates a large change in the chord mode V_f^* (notice where the $\zeta - 1$ frequency crosses the chord frequency in the sequence of figs. 3, 9, 10). As the lag frequency factor increases above 1.5, the $\zeta - 1$ frequency becomes higher than the torsion frequency for most velocities, so there is little influence of further increases in ν_ζ factor on the chord mode instability.

6. *As shown in figure 6, the beam mode V_f^* first increases with ν_ζ factor, reaches a maximum, then decreases with ν_ζ factor to a value lower than that for the baseline configuration (1.0ν_ζ).* The beam mode V_f^* initially increases with ν_ζ factor because damping of this mode is increased through coalescence of the beam frequency with the $\zeta - 1$ frequency (note where the $\beta - 1$ and $\zeta - 1$ frequencies cross in relation to the beam mode frequency in the sequence of figs. 3, 9, and 10). As the lag frequency increases, the $\zeta - 1$ mode crosses the beam mode at higher velocity, where there is more damping available to be transferred to the beam mode. With further increases in ν_ζ factor the $\beta - 1$ frequency coalesces with the beam frequency without any interference from the $\zeta - 1$ frequency (fig. 10). The coalescence between the beam and $\beta - 1$ frequencies becomes dominant as ν_ζ (continues to increase, resulting in a large decrease in the beam mode V_f^*. Also of interest is the trend of the beam mode flutter curve with respect to ν_ζ in comparison with that of the chord mode (see fig. 6). As noted previously, the beam mode instability becomes flap mode dominated at about 1.3ν_ζ, which corresponds to the peak in its flutter curve. The chord mode instability becomes flap mode dominated at about l.7ν_ζ, which corresponds to the plateau in its flutter curve. The instability of the beam mode becomes flap mode dominated at a lower ν_ζ factor than the chord mode because its frequency is closer to the $\beta - 1$ frequency than is the chord mode frequency. The beam mode flutter curve eventually levels off at a very high ν_ζ factor, above that at which the chord mode levels off, because the beam mode is coupled to the torsion mode through the wing-chordwise mass offset. The beam mode flutter continues to be influenced by the lag frequency until the $\zeta - 1$ frequency ceases to cross or coalesce with the torsion frequency.

7. *As shown in figure 6, the chord V_f^* is lower than the beam V_f^* over the range of l.0ν_ζ to 1.4ν_ζ.* This is because there is increased damping in the beam mode due to its interaction with the lag mode. As shown in the sequence of figures 3 and 9, the $\zeta - 1$ frequency crosses the beam mode frequency at increasingly higher velocities as the ν_ζ factor is increased in this range (1.0 to 1.4 ν_ζ). With higher velocity there is greater damping in the lag mode, some of which is transferred to the beam mode during the frequency coalescence. Little increase in damping is introduced into the chord mode because of the low velocity at which those frequencies cross. Thus, for the cited range of ν_β factor, the chord mode instability occurs before the beam mode instability.

The most significant results of the rotor frequency study are that optimum flap and lag frequencies exist which can significantly increase the flutter velocity of tiltrotor systems. The flutter velocity is shown in figure 5 to increase from 1.23 to about 1.42 by increasing the flap frequency by a factor of 1.35, and in figure 6 from 1.23 to about 1.33 by increasing the lag frequency by a factor of 1.35. These represent increases in flutter velocity of about 13 percent

for the flap case and about 8 percent for the lag case. The results associated with tuning of the lag frequency are especially important because tuning of the lag frequency has more practical relevance than does tuning of the flap frequency. This is because tiltrotor systems have been stiff-inplane so that an increase in inplane stiffness would not have a severe impact on loads.

It is also important to note that the stability improvements presented above came about because of the coalescence of certain frequencies. The low rotor frequencies ($\beta - 1$ and $\zeta - 1$) are important system design parameters, as their placement with respect to each other as well as the fundamental wing modes can greatly improve or degrade the stability of the system. Based on the rotor frequency study, a general rule is to design the $\zeta - 1$ frequency to fall between the $\beta - 1$ frequency and the lowest fundamental wing mode in the velocity range preceding the flutter velocity. The lag frequency in this case couples with the flap frequency, delaying its interaction with the wing modes. An even better solution is to have the low lag frequency cross the lowest fundamental wing mode just as that mode begins to coalesce with the low flap frequency. In this case, the damping of the wing mode is increased by the lag mode, delaying the instability to a higher velocity. For maximum influence, the lag frequency should cross the wing mode at the highest possible velocity (but before the flap mode drives an instability). This will maximize the damping in the lag mode which is then available to be transferred.

Based on the results of the above study, as well as results of other studies not reported here, there are three main mechanisms which are responsible for instability. These may be described as lag-dominated whirl flutter, flap-dominated whirl flutter, and rotor resonance. In lag-dominated whirl flutter, the lag mode weakens the coupling of the flap and wing modes while increasing the coupling between the flap and lag motions themselves. As a result, the stability of the system is more sensitive to lag motion related forces than to flap motion related forces. In flap-dominated whirl flutter the flap motion becomes highly coupled with one or more wing modes and there is negligible coupling with the lag motion. Rotor resonance is characterized by coalescence of the high frequency flap and lag modes, which results in an instability of the higher frequency mode.

Wing Frequency

The effects of the wing beam, chord, and torsion frequencies on tiltrotor stability are examined in this section. The wing frequencies, as given in table 1, are altered through parametric variation of the wing baseline stiffnesses. In the first part of this study, the variations are performed independently, as they were in the rotor frequency study. In the second part of this study, combined changes in wing stiffnesses are examined.

The results of independent variations of the three wing stiffnesses by factors of 0.50 to 1.50 of the baseline value are shown in the plots of figures 11 to13. The plots show the change in flutter speed for each of the three wing modes for each case. These results indicate that the flutter velocity is more dependent on the placement of the wing frequencies relative to each other than on the placement of the wing frequencies relative to the rotor frequencies. This is most evident for the case of torsional stiffness variation (fig. 11). The beam mode stability is greatly reduced by a reduction in the torsion stiffness. The rotor frequency study showed that the beam stability changes relative to changes in the beam or rotor frequencies. Since the rotor frequencies and beam mode frequency are unchanged for variations of torsion stiffness, the reduced beam mode stability must instead be due to placement of the torsion frequency relative to the beam frequency. Based on the above reasoning, the beam mode flutter speed would be expected to decrease rather than increase with an increase in beam stiffness. This is indeed the case as is illustrated in figure 12.

The chord mode flutter velocity is shown to increase with an increase in chord stiffness in figure 13, while the flutter velocities of the beam and torsion modes remain relatively constant. The change in flutter velocity of the chord mode is less dramatic than was shown for the beam mode in the previous two cases. This is because the chord mode is not highly coupled to either of the other two wing modes, and the extent of stiffness variation does not move the chord frequency above or below the other wing frequencies. Since the chord mode is not highly coupled to either the beam or torsion modes, placement of the chord mode frequency with respect to the other wing frequencies is less important.
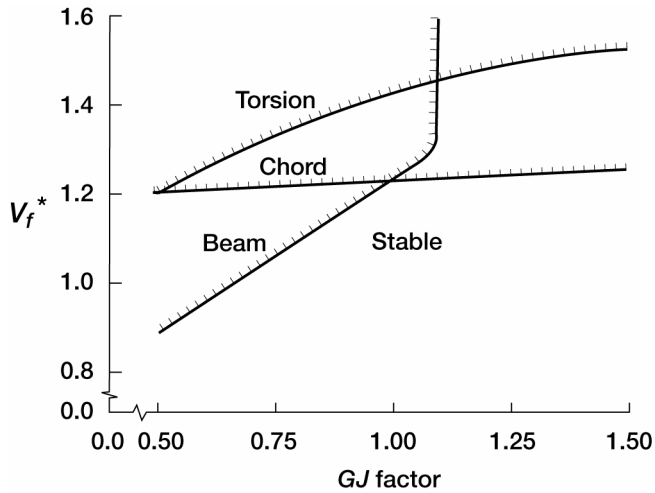
Figure 11.—Flutter velocity of the wing modes with
parametric variations of wing torsion stiffness.
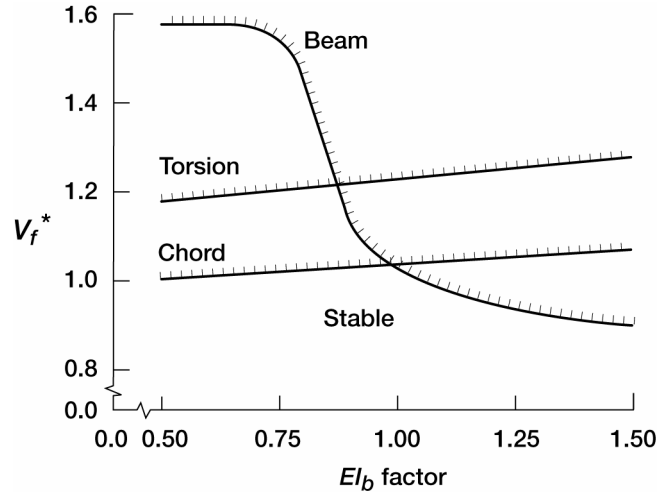
Figure 12.—Flutter velocity of the wing modes with
parametric variations of wing beam stiffness.
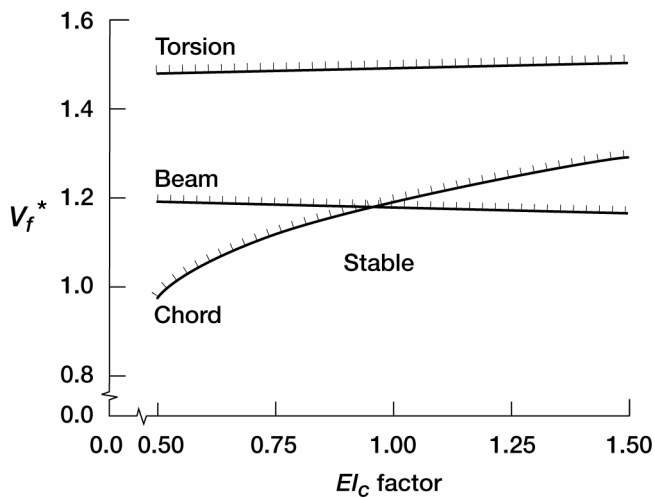
Figure 13.—Flutter velocity of the wing modes with
parametric variations of wing chord stiffness.
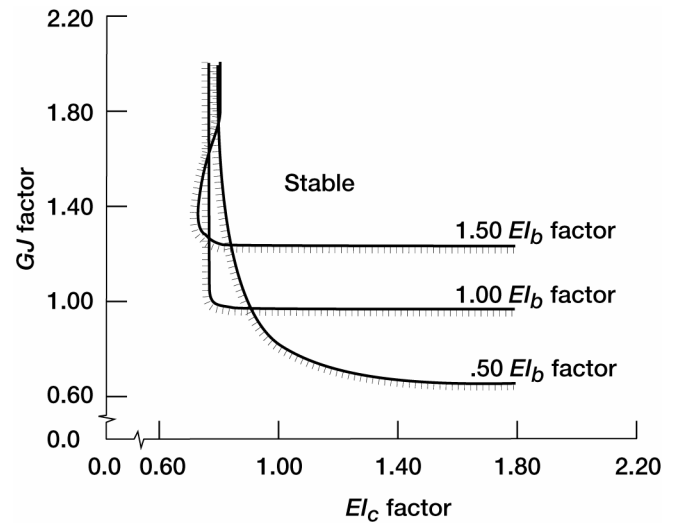
Figure 14.—Stability boundaries of constant $V_f^* = 1.23$
for combined stiffness variations.

As was shown in figure 3, the flutter velocity of the baseline tiltrotor system is about 1.23. In the next study, the combinations of wing stiffness required to maintain flutter at $V^* = 1.23$ are examined. Three flutter boundaries, corresponding to constant beam stiffness values ranging from 0.50 to 1.50 of the baseline value, are shown in figure 14. Each curve represents the combination of torsion and chord stiffness (shown as a factor of the baseline value) required to maintain the baseline flutter velocity. As the beam stiffness is increased the minimum required torsion stiffness also increases (for EI_c above the 1.0 factor). This supports earlier findings that stability is improved through increased separation between the beam and torsion frequencies. The plot also shows that the chord stiffness requirements are almost constant for GJ factors above about 0.8.

The most significant result of the wing frequency study is that the wing torsion to beam frequency ratio is an important design parameter for a tiltrotor system. It is clear that the separation between these frequencies has greater importance than the placement of the beam frequency relative to the rotor frequencies. If this were not the case then the flutter velocity would increase with an increase in beam frequency (because of an increased separation between the flap and beam frequencies) rather than decrease (because of increased participation of torsion in the beam

mode). It is also noteworthy that the chord frequency significantly influences only the chord mode V_f^*. Thus, it is possible to improve the chord mode V_f^* independently of the beam mode V_f^*, and vice versa. Since the chord mode instability occurs at a velocity very close to that associated with the beam mode, any design changes aimed at increasing the stability of the complete system must take both modes into account.

Forward Swept Wing

This study examines the effects of sweeping the baseline wing forward. The pylon and rotor system remains oriented in the flow direction the same as for a straight wing. The sweep is varied while maintaining wing length (measured along the elastic axis), streamwise chord length, and rotor radius constant. While both wing length and rotor radius cannot be maintained constant with sweep on an actual tiltrotor aircraft due to rotor-fuselage clearance requirements, this assumption is employed in the analysis to isolate the effects of forward sweep. Divergence of the system was considered, but was found to occur at velocities much higher than those associated with flutter, even at high wing sweeps. This is not surprising because 1) the wing stiffnesses associated with tilt rotors are much higher than that associated with conventional fixed wing aircraft, and 2) the flutter boundaries associated with tilt rotors are lower than those associated with conventional fixed wing aircraft (primarily due to the large rotor flapping motion).

The influence of wing forward sweep on flutter is illustrated in figure 15. This plot shows that the beam and chord mode V_f^* come together for the swept wing, with a reduction in system flutter velocity of about 8 percent over a sweep from zero to –45°. The cause of this reduction has two possible sources: the change in wing frequencies due to a shift in pylon mass or the change in perturbation force components due to reorientation of the rotor with respect to the wing. The wing frequencies are altered by the change in pylon first and second mass moments of inertia in pitch about the wing elastic axis. This primarily effects the wing torsion frequency which increases with sweep. Based on the wing frequency parametric study, this should increase the beam mode V_f^* because of the increased separation between the beam and torsion frequencies. The plot of figure 15 shows that the beam mode V_f^* is not increased. Hence, the wing frequency change must not be the dominating influence for the beam or chord mode instabilities. This is confirmed in figure 16 which shows the beam mode instability boundaries for two cases: one with the normal orientation of the wing pylon in the flow direction (and a corresponding decrease in torsion frequency) and one with the pylon mass distribution remaining the same as for the straight wing (as if the pylon orientation with respect to the wing was unchanged by sweep) such that the wing frequencies are nearly constant with respect to sweep. As shown, the beam mode V_f^* decreases even further with the baseline wing frequencies, indicating that the wing frequency changes associated with sweep have a stabilizing influence. The decrease in flutter velocity must then be attributed to a change in the destabilizing forces from the rotor.
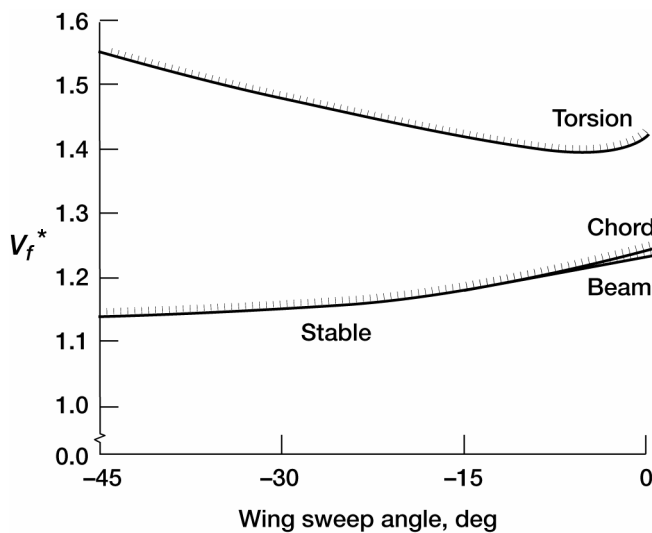
Figure 15.—Flutter of the swept forward wing.
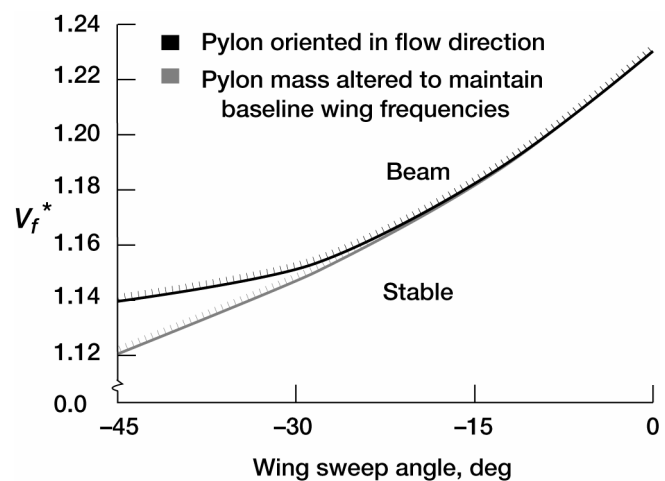
Figure 16.—Beam mode flutter of the swept wing for two pylon orientation cases.
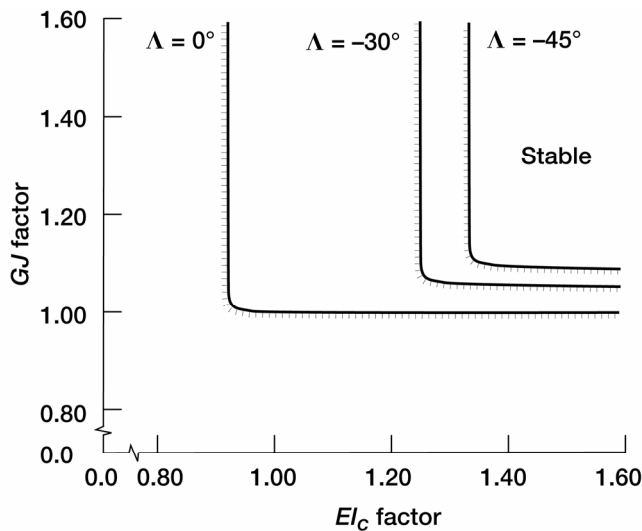
Figure 17.—Torsion and chordwise stiffness requirements for maintaining straight-wing flutter velocity.
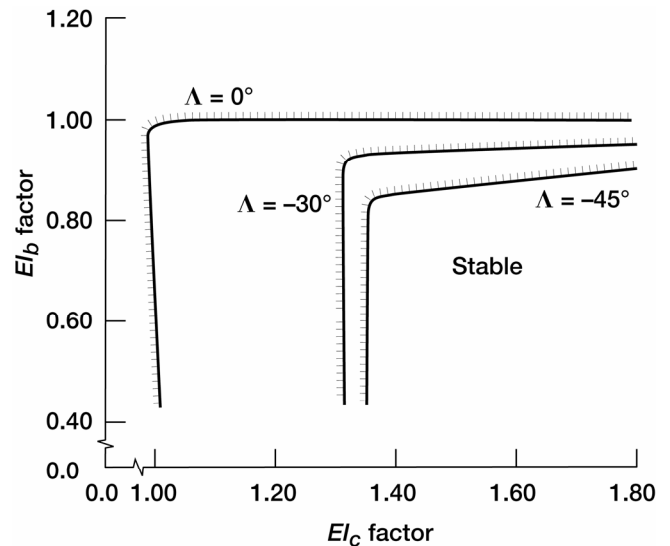
Figure 18.—Beamwise and chordwise stiffness requirements for maintaining straight-wing flutter velocity.

In figures 17 and 18, the stiffness changes required to maintain the straight wing flutter velocity ($V_f^* = 1.23$) for the swept wing are shown. The plot of figure 17 shows that a substantial increase in chord stiffness is required to maintain $V_f^* = 1.23$, while only a slight increase in torsional stiffness is required. The chord stiffness increase maintains the chord mode V_f^* while the torsion stiffness increase maintains the beam mode V_f^*. Based on the results of the previous section, it might be assumed that an increase in beam stiffness is required to overcome the additional destabilizing force components associated with wing sweep if one desires to maintain the straight wing flutter velocity. However, the plot of figure 18 shows that a decrease in beam stiffness of roughly 10 to 15 percent is required. The two plots of figures 17 and 18 suggest that the ratio of wing torsion to beam frequency is still an important factor even with wing sweep. The additional destabilizing forces associated with wing sweep couple these two modes more than for the straight wing case. While the coupling between the torsion and beam modes is through the pylon and rotor mass offset for the straight wing, these modes are additionally coupled through the rotor system forces when wing sweep is introduced. With increased coupling, the requirement for frequency separation between the modes is increased. The wing sweep tends to increase the frequency separation, but not enough to overcome the rotor force coupling effects, so the net effect is decreased flutter velocities. The torsion and beam modes remain largely uncoupled from the chord mode. For the chord mode, a substantial increase in chord stiffness is the only alternative for maintaining straight wing flutter velocity at large forward wing sweep angles.

Pitch-Flap Coupling

Pitch-flap coupling is an important and necessary parameter for basic tiltrotor designs because of flap clearance considerations. There are four basic methods for obtaining adequate flap clearance of the blade from the wing. One is an adjustment of the mast length, the second is an increase of flapping restraint, the third is use of forward wing sweep, and the fourth is employment of kinematic pitch-flap coupling. Extension of the mast length is very desta-bilizing while increase of flapping restraint drives blade loads to an unacceptable level. The destabilizing effects of forward wing sweep have been discussed in the previous section. The employment of pitch-flap coupling can significantly reduce blade flapping with negligible effect on the blade loads, but it also has a destabilizing effect on stability. Positive pitch-flap coupling (here defined as blade flap up producing blade pitch up) is given by negative δ_3 and decreases flap frequency while negative pitchflap coupling is given by positive δ_3 and increases flap frequency.
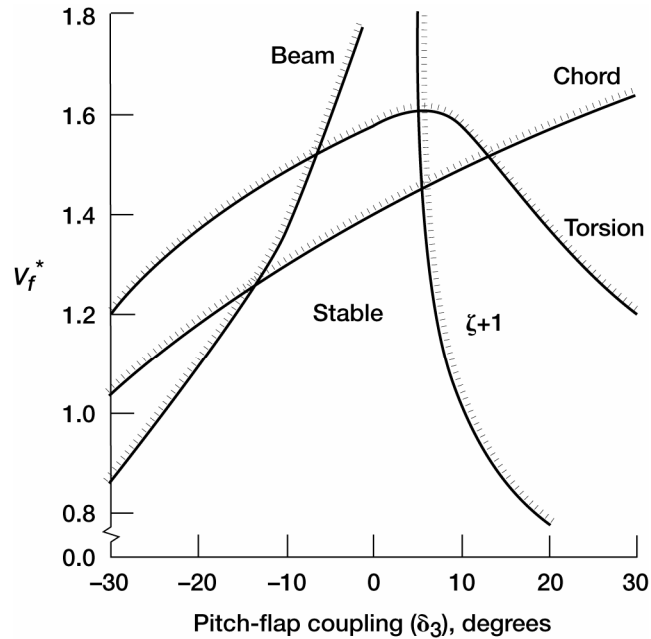
Figure 19.—Flutter velocity boundaries as a function of
the pitch-flap coupling.

The plot of figure 19 shows the flutter velocity boundaries associated with changes of δ_3 (the baseline config-uration has $\delta_3 = -15°$). This plot shows that negative δ_3 is more suitable with respect to stability considerations than positive δ_3, which is generally true for stiff-inplane rotor systems as reported by Gaffey (ref. 17). As shown, positive δ_3 results in a rotor instability at relatively low values of δ_3. This instability is best explained by consider-ing the blade frequencies in the rotating system. The rotor instability is caused by resonance of the blade flap and lag frequencies. The resonance occurs because the lag frequency of a stiff-inplane rotor decreases with velocity (discussed in rotor frequency section) while the flap frequency increases (because of positive δ_3) until at some velocity, the two coincide. With negative δ_3 the effective flap frequency decreases with velocity, so it never meets the lag frequency in the velocity range of interest.

The plot of figure 19 also shows that the mode of instability changes from a chord mode at small negative δ_3 to a beam mode at large negative δ_3. While both the chord and beam modes are stabilized with decreasing negative δ_3, the beam mode is stabilized more than the chord mode because of increased separation between the torsion and beam frequencies (decreased negative δ_3 increases the flap frequency which increases the torsion frequency). Consequently, there is a range of negative δ_3 where the chord mode instability becomes critical.

Conclusions

The influences of several key system design parameters on tiltrotor aeroelastic stability in the high-speed axial flight mode have been examined. The findings have substantiated earlier work performed by other research-ers as well as identified some new trends and the physical reasonings behind them. Some of the important past conclusions which have been substantiated are as follows:

1.) Beam and torsion frequency separation has a large influence on stability of the beam mode.

2.) Negative δ_3 is more effective than positive δ_3 with respect to stability considerations for a stiff-inplane rotor system.

The results of this study have also identified and explained at least two important effects which have not been previously discussed in the open literature:

1.) Lag frequency tuning appears to be a practical method for increasing axial flight flutter velocities. The blade lag frequency may be selected to reduce the coupling of the β – 1 and wing beam modes, thereby increasing the wing beam mode damping.

2.) An increase in forward wing sweep is destabilizing. This is because of an increase in the rotor destabilizing force components in the beam and chord directions. The wing frequency changes associated with the reorientation of the pylon with sweep have a stabilizing influence on the beam mode, but this effect is dominated by the rotor force changes.

References

1. Naylor, H.F.W.; and Richardson, J.R.: Whirl Flutter of Propellers With Hinged Blades. REPT.–24, Engineering Research Associates, Toronto, Canada, 1962.
2. Bandler, P.A., et al.: Whirl Flutter of Propellers With Flexible Twisted Blades. REPT.–43, Engineering Research Associates, Toronto, Canada, 1963.
3. Reed, Wilmer H., III: Propeller-Rotor Whirl Flutter: A State-of-the-Art Review. J. Sound Vib., vol. 4, no. 3, 1966, pp. 526–544.
4. Lytwyn, R.T.; and Young, M.I.: The Influence of Blade Flapping Restraint on the Dynamic Stability of Low Disk Loading Propeller-Rotors. J. Am. Helicopter Soc., vol. 12, 1967, pp. 38–42.
5. Gaffey, T.M.; and Wernicke, K.G.: Review and Discussion of "The Influence of Blade Flapping Restraint on the Dynamic Stability of Low Disk Loading Propeller-Rotors." J. Am. Helicopter Soc., vol. 12, 1967, pp. 55–60.
6. Edenborough, H.K.: Investigation of Tilt-Rotor VTOL Aircraft Rotor-Pylon Stability. J. Aircraft, vol. 5, no. 6, 1968, pp. 97–105.
7. DeLarm, Leon: Whirl Flutter and Divergence Aspects of Tilt-Wing and Tilt-Rotor Aircraft. U.S. Air Force V/STOL Technology Planning Conference, Las Vegas, Nevada, September 1969.
8. Kaza, Krishna Rao Venkata: Effect of Steady State Coning Angle and Damping on Whirl Flutter Stability. J. Aircraft, vol. 10, no. 11, 1973, pp. 664–669.
9. Kvaternik, Raymond G.: Studies in Tilt-Rotor VTOL Aircraft Aeroelasticity. Ph.D. Thesis, Case Western Reserve Univ., 1973.
10. Kvaternik, R.G.: Experimental and Analytical Studies in Tilt-Rotor Aeroelasticity. Proceedings of the Specialists Meeting on Rotorcraft Dynamics, Moffett Field, CA, 1974.
11. Kvaternik, R.G.: A Review of Some Tilt-Rotor Aeroelastic Research at NASA-Langley. J. Aircraft, vol. 13, 1976, pp. 357–363.
12. Johnson, W.: Dynamics of Tilting Proprotor Aircraft in Cruise Flight. NASA TN D–7677, 1974.
13. Johnson, W.: Analytical Model for Tilting Proprotor Aircraft Dynamics, Including Blade Torsion and Coupled Bending Modes, and Conversion Mode Operation. NASA TM X–62369, 1974.
14. Johnson, W.: Analytical Modeling Requirements for Tilting Proprotor Aircraft Dynamics. NASA TN D–8013, 1975.
15. Johnson, W.: A Comprehensive Analytical Model of Rotorcraft Aerodynamics and Dynamics. Part 1: Analysis Development. NASA TM–81182, 1980.
16. Johnson, W.: A Comprehensive Analytical Model of Rotorcraft Aerodynamics and Dynamics. Part 2: User's Manual. NASA TM–81183, 1980.
17. Johnson, W.: A Comprehensive Analytical Model of Rotorcraft Aerodynamics and Dynamics. Part 3: Program Manual. NASA TM–81184, 1980.
18. Schneider, John; and Wilkerson, Joseph: Advanced Rotorcraft V/STOL—Technology Needs for the High-Speed Rotorcraft. AIAA Paper 90–3298, 1990.
19. Gaffey, T.M., Yen, J.G., and Kvaternik, R.G.: Analysis and Model Tests of the Proprotor Dynamics of a Tilt-Proprotor VTOL Aircraft. U.S. Air Force V/STOL Technology and Planning Conference, Las Vegas, Nevada, September 1969.

Review of Propeller-Rotor Whirl Flutter[*]

Wilmer H. Reed III
National Aeronautics and Space Administration
Langley Research Center
Hampton, Virginia 23681

Summary

A survey is made of the state of the art of propeller-whirl flutter—a precession-type instability that can occur on a flexibly mounted aircraft engine-propeller combination. This report reviews the literature relating to this problem from the time it first became of concern on conventional turboprop and V/STOL aircraft.

Included in the survey are a description of the basic mechanism of whirl flutter, a summary of generalized trend studies on idealized systems, the status of methods for predicting propeller aerodynamic coefficients, the effects of flapping hinged blades and twisted flexible blades on whirl flutter, and some approaches for including propeller whirl modes as a part of the flutter evaluation for complete aircraft. Also, brief consideration is given to the response of flexibly mounted propeller-nacelle systems to random atmospheric turbulence.

Whirl flutter of conventional propeller-nacelle systems is now a reasonably well understood phenomenon and amenable to analysis. For propeller-rotor systems with flapping blades, however, comparisons between experiment and theory suggest the need for further refinements in the mathematical model.

Introduction

Although the phenomenon known as propeller-whirl flutter—a dynamic instability that can occur in a flexibly mounted aircraft engine-propeller combination—was discovered analytically by Taylor and Browne (ref. 1) in 1938, it was not until its "rediscovery" in 1960 that it was identified as a problem of practical concern.

Following the loss of two turboprop aircraft it was established in wind-tunnel investigations (ref. 2) at NASA Langley Research Center that propeller-whirl flutter could have occurred if the nacelle stiffness was severely reduced, for example, by a structural failure. In the undamaged condition the aircraft had an adequate margin of safety from whirl flutter. In addition to this wind-tunnel investigation for a specific configuration, some generalized trend studies were also conducted at Langley Research Center in order to identify and study the basic parameters involved in propeller-whirl flutter. (See refs. 3 to 6.)

As a result of these experiences on a turboprop aircraft, and the fact that VTOL configurations are likely to have unconventional propeller-rotor systems, whirl flutter has now become a design consideration on new propeller-driven aircraft. These considerations are reflected in recent amendments to U.S. Civil Air Regulations (ref. 7) which require that whirl flutter be included as a part of the dynamic evaluation of transport aircraft, and that no flutter shall occur as a result of failure of any single element of an engine mount structure.

The purpose of this report is to review work relating to propeller whirl flutter since the time the phenomenon became the subject of intensive investigation in 1960. The material presented herein essentially follows that given by the author in a recent review article (ref. 8) on the subject but with some additional background information included for completeness.

---

[*]This document was first published as Reed, W.H., III: Review of Propeller-Rotor Whirl Flutter. NASA TR R–264, 1967.

Following a description of the basic mechanism of propeller whirl flutter, the report summarizes some principal findings of generalized trend studies for idealized systems, next reviews the status of propeller aerodynamic coefficients used for the prediction of whirl flutter, and then illustrates how whirl stability of an idealized system can be altered by the use of propeller-rotors with hinged blades or highly flexible twisted blades. The next two sections deal with the question of incorporating propeller whirl modes into analytical and wind-tunnel flutter studies of the aircraft treated as a complete system. Finally, consideration is given to dynamic loads associated with the response of a flexibly mounted propeller-nacelle system to random atmospheric turbulence.

Nomenclature

a distance between nacelle pivot point and plane of propeller in propeller radii

C_T thrust coefficient, $\dfrac{Thrust}{\rho\left(\dfrac{\Omega}{2\pi}\right)^2 (2R)^4}$

c_θ nacelle viscous damping coefficient in pitch direction

c_ψ nacelle viscous damping coefficient in yaw direction

EI_2 bending stiffness of cantilevered nacelle in pitch direction

e hinge offset distance of flapping-blade propeller

$F + iG$ oscillating lift function

$H_{\theta,u}$ frequency response function giving response in θ to unit sinusoidal input in u/V

$H_{\theta,v}$ frequency response function giving response in θ to unit sinusoidal input in v/V

$H_{\theta,w}$ frequency response function giving response in θ to unit sinusoidal input in w/V

h wing bending deflection

I total moment of inertia of propeller-nacelle system about pivot

I_x mass moment of inertia of propeller about rotation axis

J advance ratio, $\dfrac{\pi V}{\Omega R}$

K_θ effective linear spring constants of cantilevered nacelle in pitch direction

K_ψ effective linear spring constants of cantilevered nacelle in yaw direction

L_y total aerodynamic force due to propeller in y direction

L_z total aerodynamic force due to propeller in z direction

M_y total aerodynamic moment due to propeller about y axis

M_z total aerodynamic moment due to propeller about z axis

R blade tip radius

r	radius of propeller blade section from rotational axis
S_θ	torsional spring constant in pitch direction
S_ψ	torsional spring constant in yaw direction
t	time
u,v,w	components of gust velocity (see fig. 15)
V	forward flight speed
x,y,z	coordinate axes (see fig. 3)
z_1	natural mode shape of nacelle pitch mode
α	angle of attack
α_1	wing torsion angle
α_T	inclination of thrust axis
ζ	viscous damping of engine mount system relative to critical damping
θ	pitch angle of propeller axis
θ_1	inclination of propeller axis for unit deflection in natural pitch mode z_1
μ	damping ratio of whirl mode (positive – unstable, negative – stable)
ρ	air density
$\Phi_u, \Phi_w, \Phi_\theta$	power spectra and cross spectra, where subscripts denote the associated time histories
ψ	yaw angle of propeller axis
Ω	propeller rotational frequency
ω	whirl frequency
ω_b	cantilever fundamental frequency of nonrotating propeller blade
ω_h	uncoupled wing bending frequency with rigidly attached nacelle and nonrotating propeller
ω_θ	fundamental natural frequency in pitch with nonrotating propeller
ω_ψ	fundamental natural frequency in yaw with nonrotating propeller
ω_1	first coupled natural wing bending frequency

A dot over a symbol denotes differentiation with respect to time.

Mechanism of Propeller Whirl Flutter

Idealized System

To introduce the basic ingredients of propeller whirl flutter, the idealized systems shown schematically in figure 1 will be used. On the left side of the figure the powerplant and nacelle structure are represented by a cantilever beam having continuous arbitrary distribution of mass and stiffness; on the right is shown an equivalent representation in which a rigid powerplant structure is assumed to be spring-restrained about a pivot located a distance a behind the propeller.

When the cantilever system is approximated by a single pitch mode and a single yaw mode the two systems are exactly equivalent. For example, the cantilever system has an effective pivot distance a which is simply $1/\theta_1$, where θ_1 is the inclination of the propeller axis corresponding to a unit deflection in the natural pitch mode z_1. This and other equivalent relations between the two systems are established in reference 4.

The governing equations of motion for the idealized system may be derived from Lagrange's dynamic equation (see ref. 4.) For the pivoted -powerplant system these equations are as follows:

The origin of the various forces and moments acting on the system are indicated above the equations. Note that in addition to the usual inertia, damping, and elastic forces, the spinning propeller introduces gyroscopic and aerodynamic forces. Since these latter two forces are distinguishing features of propeller whirl flutter they will be discussed in greater detail in the following subsections.

Role of Propeller Gyroscopic Forces

The influence of gyroscopic forces on the natural vibration modes of the idealized system can be illustrated with the aid of figure 2. When the propeller is not rotating, and aerodynamic and damping forces are neglected, natural vibrations of the system can occur independently about either the pitch axis or the yaw axis as shown by the left-hand side of figure 2.
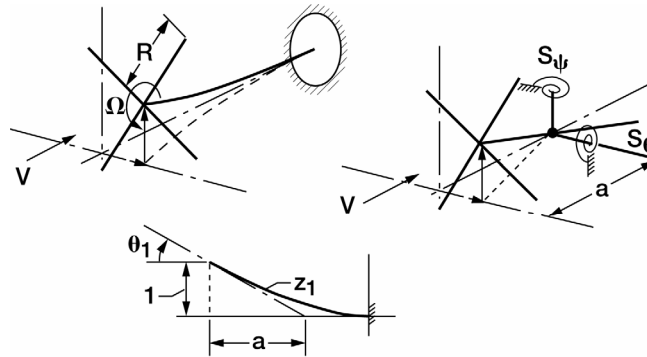
Equivalence:

$$\frac{1}{\theta_1} \qquad \text{Equivalent to} \qquad a$$

$$K_\theta = \int EI_2 \, z_1''^2 \, dx \qquad \text{Equivalent to} \qquad \frac{S_\theta}{a^2}$$

Etc.

Figure 1.—Idealized propeller-nacelle systems (ref. 4).
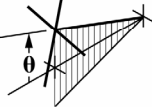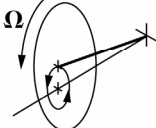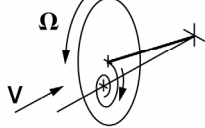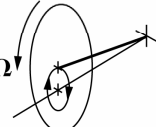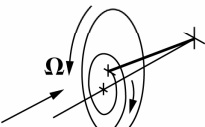
Figure 2.—Natural vibration modes of system with rigid propeller.

When the propeller is rotating, however, the natural vibration modes cannot be excited independently, but are coupled by gyroscopic action of the spinning propeller. The natural modes of the system are then characterized by whirl or precession modes in reference to the manner in which the propeller hub whirls or precesses about the static thrust axis. These modes are so indicated by the center sketch in figure 2; again aerodynamic and damping forces have been neglected. Even for systems having symmetrical stiffness properties, the natural whirl frequencies would be different. The higher frequency mode is defined as the forward whirl mode and is associated with a whirl of the hub in the direction of propeller rotation. Similarly, the lower frequency mode is defined as the backward whirl mode and is associated with a whirl opposite to that of propeller rotation.

Role of Propeller Aerodynamic Forces

Since whirl modes produce angle-of-attack changes on blade elements of the propeller, aerodynamic forces are generated; these are the forces that provide the mechanism for instability. This instability for rigid-blade systems invariably occurs in the backward whirl mode. When the propeller blades have flap hinges or are very flexible, however, an instability in the forward mode is possible.

The sketches on the right-hand side of figure 2 give an example of the manner in which the system would respond in the backward whirl mode following a disturbance such as a gust. When the airstream velocity is less than the whirl flutter velocity V_{crit}, the path traced by the propeller hub is a spiral that converges to the original static equilibrium position. When the flutter speed is exceeded, however, a small disturbance will result in a diverging spiral motion of the hub which will continue to build up until the structure fails or its motion becomes limited by nonlinearities.

Some fundamental properties of the aerodynamics of a pitching and yawing propeller can be demonstrated, as in reference 9, by consideration of a propeller blade element. In figure 3 are shown the propeller force and moment vectors that can be significant. Drag forces on the blade element have been neglected. Also, the propeller thrust force is omitted from the figure because, as will be discussed later, thrust has only a small effect on whirl flutter. The vectors shown in figure 3 arise as a result of three distinct types of motions associated with a whirl mode: angular displacement of the propeller shaft in pitch (or yaw), the rate of change of pitch (or yaw) angle, and lateral
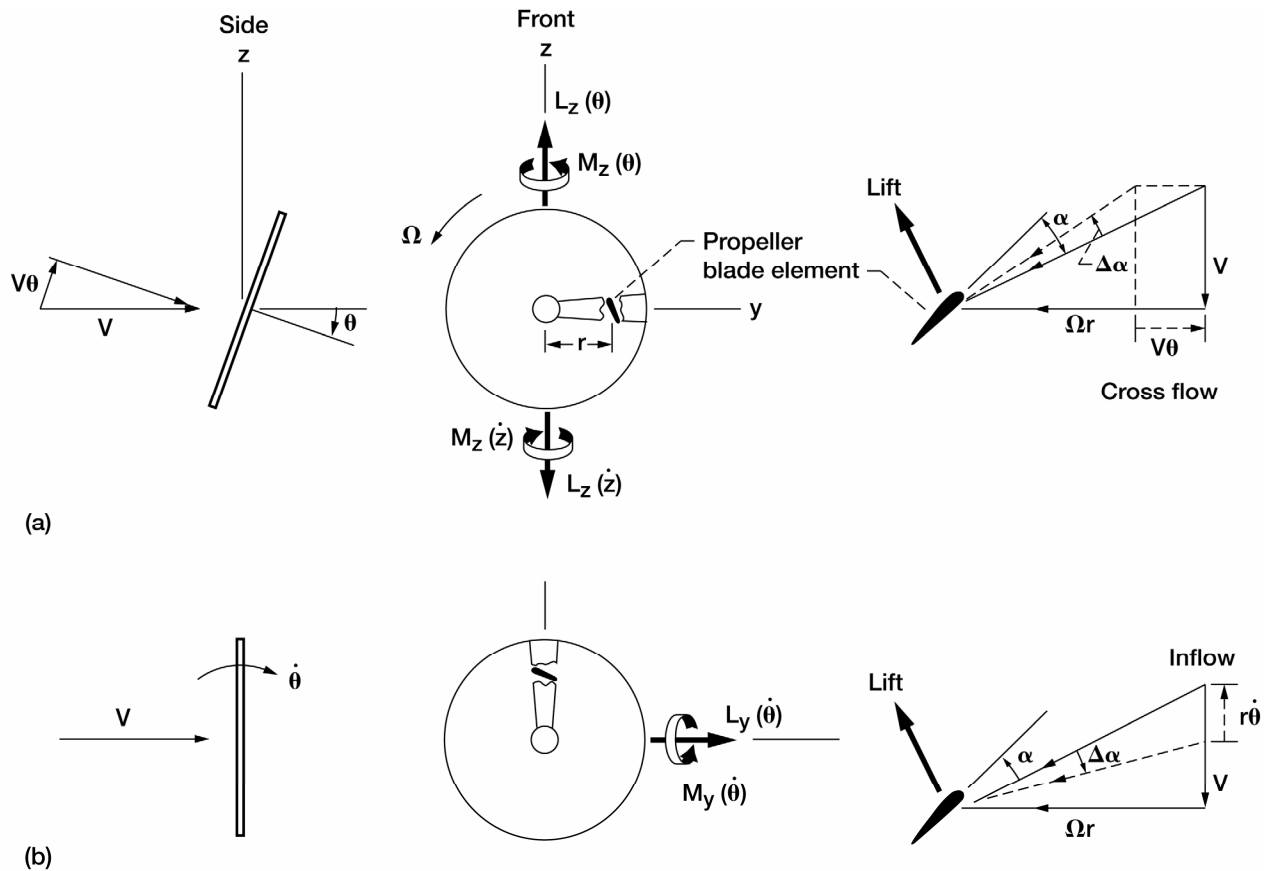
Figure 3.—Aerodynamic forces and moments on a pitching and plunging propeller at zero thrust. (a) Pitch. (b) Pitch rate.

(or vertical) velocity of the shaft. Because of symmetry, only motions in one plane need be considered; the pitch plane is shown in figure 3. It should be noted, however, that interference effects of a nearby wing can result in unsymmetrical aerodynamic forces on the propeller.

When the propeller shaft is inclined at an angle θ relative to the free stream, the forward velocity has a cross-flow component V_θ in the plane of the propeller disk. With reference to the sketch of a blade element in figure 3(a), it can be seen that on the up-going side of the propeller disk, this cross-flow velocity component tends to reduce both the relative velocity and the angle of attack of the blades; alternatively, blade elements on the down-going side of the propeller disk experience an increase in relative velocity and angle of attack. If the lift force on a blade element due to these angle-of-attack and velocity changes is resolved into components parallel and normal to the propeller disk plane and these components then integrated over a cycle of propeller rotation, the net effect is a vertical force $L_z(\theta)$ and a yaw moment $M_z(\theta)$ having the directions indicated in figure 3(a). Note that the vertical force is in a direction to increase the pitch angle and therefore opposes the structural spring restoring force—a fact which makes possible the occurrence of a static divergence for very low levels of mount system stiffness.

The yawing moment due to pitch $M_z(\theta)$ may be interpreted as a cross-stiffness term. This important term is the driving moment of propeller whirl flutter. Note that it produces a moment which is in the same direction as the yawing velocity for the backward whirl mode. Thus, this term acts as negative (destabilizing) aerodynamic damping which must be compensated by other positive damping forces if the system is to be stable. The aerodynamic part of the total damping available for this purpose may be found in the force $L_z(\dot{z})$ and in the moment $M_y(\dot{\theta})$ produced by the rate terms $\dot{z}$ and $\dot{\theta}$, respectively. The damping force $L_z(\dot{z})$ is equal and opposite to the vertical force due to pitch $L_z(\theta)$, but is associated with the effective angle $\dot{z}/V$ ($\dot{z} = a\dot{\theta}$ a for pivoting system) rather than with the geometric angle θ. During whirl the yawing moment $M_z(\dot{z})$ associated with vertical velocity is in phase with the yaw angle and therefore acts as an aerodynamic stiffness term.

The damping due to pitch rate $M_y(\dot{\theta})$ (fig. 3(b)) arises because of velocity components normal to the propeller disk. From the blade element diagram in figure 3(b) it can be seen that the inflow velocity due to pitch rate $r\dot{\theta}$ results in an increased angle of attack on blade elements in the disk area above the horizontal pitch axis and a decreased angle of attack in regions below the pitch axis. The integrated effects produce a direct damping moment $M_y(\dot{\theta})$ and across-damping force $L_y(\dot{\theta})$. This cross-damping force behaves as a stiffness term in the yaw plane in a manner similar to that of the cross-damping moment $M_z(\dot{z})$. Except for conditions near static divergence, the stiffnesses associated with these cross-damping terms, as well as the term $L_z(\theta)$, are small relative to the structural stiffness of the powerplant mount.

In summary, the propeller aerodynamic term important with regard to whirl flutter is the yaw moment due to pitch, or equivalently, the pitch moment due to yaw. This cross-stiffness moment drives the system in the backward whirl mode and is resisted by the aerodynamic and structural damping moments. At the critical whirl flutter speed, the energy input by the aerodynamic driving moment is exactly balanced by the energy absorbed by damping, such that oscillations of the system become self-sustaining (or neutrally stable).

Whirl Flutter Characteristics of Two-Degree-of-Freedom Systems

Generalized Studies

The basic phenomenon of propeller whirl flutter for systems that comprise a rigid propeller and a flexibly mounted powerplant, such as that illustrated in figure 1, is now reasonably well understood. The stability characteristics of such systems have been investigated analytically over a rather broad range of parameters (refs. 3, 4, and 5). In addition, wind-tunnel studies have been conducted (ref. 6) to evaluate the theoretical prediction of propeller aerodynamic derivatives as well as whirl flutter stability boundaries.

A general finding of these studies is that whirl flutter is strongly dependent on such system parameters as stiffness, damping, pivot location, and propeller advance ratio. The influence of these and other parameters on whirl flutter stability boundaries for the two-degree-of-freedom system is briefly summarized in the following subsections.

Stiffness and Speed Stability Boundaries

Some typical whirl flutter stability boundaries presented in reference 4 illustrate the combined effects of stiffness, flight speed, and propeller advance ratio for a particular system. The system used for illustration was two times stiffer in yaw than in pitch and had an effective pivot point located $a/R = 0.585$ behind the propeller disk. Figure 4 shows the system stability boundaries for the following three cases of practical importance: constant propeller speed, constant advance ratio, and constant stiffness.

Constant propeller speed.—The first condition represents the usual constant-propeller speed flight operation; the associated stiffness-airspeed stability boundary is shown on the left side of figure 4. At the lower airspeeds the stiffness required to prevent whirl flutter is relatively low. As speed is increased larger stiffnesses are required for stability, and for sufficiently high speeds stability becomes governed by static divergence instead of flutter.
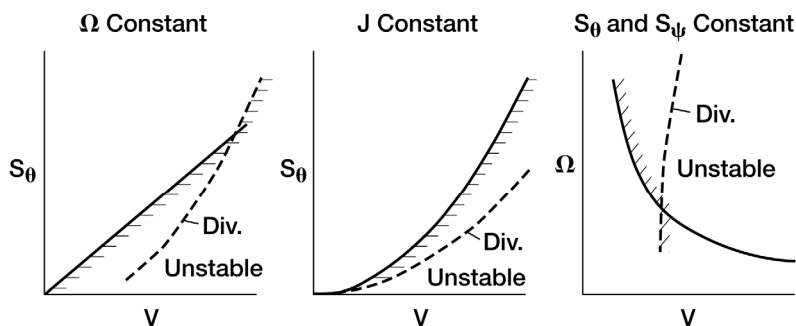
Figure 4.—Illustrative stiffness and speed boundaries (ref. 4).

Constant advance ratio.—The condition for constant advance ratio, illustrated by the plot in the center of figure 4, corresponds to a windmilling propeller having a fixed blade angle. The use of windmilling propellers is a convenient wind-tunnel test procedure and can be justified on the basis that propeller thrust generally has a small effect on whirl flutter. Again, these stability boundary plots depict the variation of stiffness required to prevent whirl flutter as a function of airspeed. In this case, however, the curves are parabolas—that is, S_θ is proportional to V^2 or, in other words, S_θ varies linearly with dynamic pressure. Note that, in contrast to the previous case, divergence would not be encountered for this particular choice of system parameters.

Constant stiffness.—Finally, with stiffness held constant the stability boundaries involving propeller speed and forward speed are illustrated on the right side of figure 4. The unstable region is above and to the right. An important implication of the plot is that for operation on the nearly vertical portion of the curves a large change in propeller speed can occur without altering the critical speed appreciably, but that for operation on the nearly horizontal portion of the curve, the critical speed is quite sensitive to small changes in propeller speed; however, at these lower propeller speeds the instability is governed by static divergence rather than by whirl flutter.

Stiffness Ratio

Some additional typical whirl flutter trends are illustrated in figure 5. On the left side of the figure is plotted the critical pitch stiffness against the critical yaw stiffness for a given combination of forward speed, damping, and other system parameters. The stability boundaries are indicated by the shaded lines, and the lines radiating from the origin represent lines of constant stiffness ratio. Note in particular that the whirl flutter boundary is extended along the diagonal ray $S_\theta = S_\psi$; this indicates that if a system had equal pitch and yaw stiffnesses it would be more prone to flutter than if one of the stiffnesses was appreciably reduced. The shape as well as the location of this curve, however, may be altered appreciably by the amount of structural damping in the system (see ref. 4). The lines that intersect each end of this boundary denote the stiffnesses required to prevent static divergence of the system.

Nacelle Damping

The center plot in figure 5 indicates the powerful stabilizing influence which mechanical damping usually has on whirl flutter. Because of this important influence, it is not feasible to neglect damping in whirl flutter analyses, as is frequently done in wing flutter analyses—to do so would in many cases result in a gross underestimation of the flutter speed. To predict whirl flutter in practical applications it is therefore desirable to obtain an accurate estimate of the powerplant-mount system damping. Damping measurement obtained during ground vibration test on an engine suspension system is discussed in reference 9. It is of interest to note that since the damping of the rubber engine mounts varied with temperature, a correction factor was determined by measuring the damping characteristics of the mount at elevated temperatures in an environmental chamber.
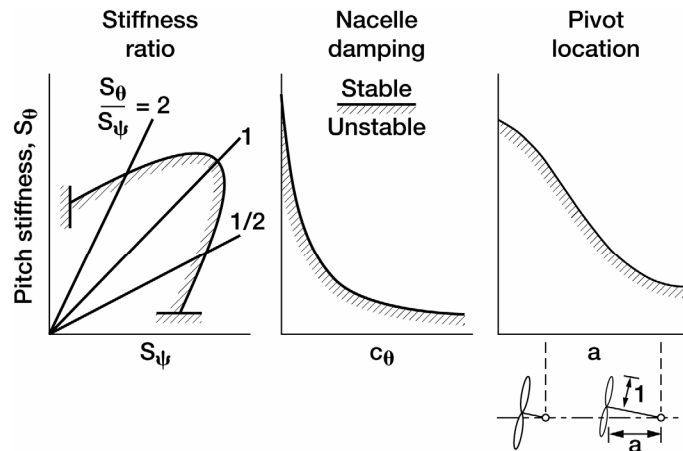
Figure 5.—Résumé of propeller-whirl trend studies.

Pivot Location

The effect of location of the pivot axes on whirl stability is illustrated on the right side of figure 5. Note that moving the pivot location aft has a significant stabilizing influence. This fact, incidentally, can be attributed to the aerodynamic damping force associated with the transverse velocity of the propeller hub, that is, $L_z(\dot{z})$ in the notation of figure 3. In addition to reducing the required stiffness, moving the pivot aft tends to make the system less sensitive to changes in structural damping, because aerodynamic forces then become the predominant source of damping.

Propeller Aerodynamics

As previously discussed, the pitching and yawing oscillations that accompany propeller-nacelle whirl motions produce aerodynamic forces on the propeller which in turn provide the driving mechanism for instability. Several methods are available for predicting the aerodynamic forces and moments required in a whirl flutter analysis. Ribner's analysis (ref. 10) of yawed propellers has long been used in studies of aircraft stability and is equally useful in propeller whirl flutter studies. (See, for example, ref. 3.) Houbolt's strip theory analysis (see ref. 4) lacks some of the refinements of Ribner's method, but is simpler to apply and appears to give comparable results. Both theories involve the assumption of quasi-steady aerodynamic forces and small angle-of-attack changes.

Measured Derivatives

To evaluate theoretical methods for predicting propeller whirl flutter, an experimental investigation was conducted (ref. 6) in which both whirl flutter boundaries and propeller aerodynamic derivatives were measured. The wind-tunnel model, which resembled the previously described idealized mathematical model, consisted of a windmilling propeller mounted on an isolated nacelle having symmetrical stiffness in pitch and yaw. Typical results from the study are presented in figure 6 which shows the nacelle damping ratio required to prevent flutter plotted against a nondimensional velocity. The calculated flutter boundaries were determined on the basis of three sets of aerodynamic derivatives: the theoretical derivatives derived by the methods of references 4 and 10, and the actual derivatives as measured on the model. Note that the calculations based on measured derivatives are in excellent agreement with the experimental data, whereas those based on theoretical derivatives follow the same trends but tend to underestimate the observed flutter speed.
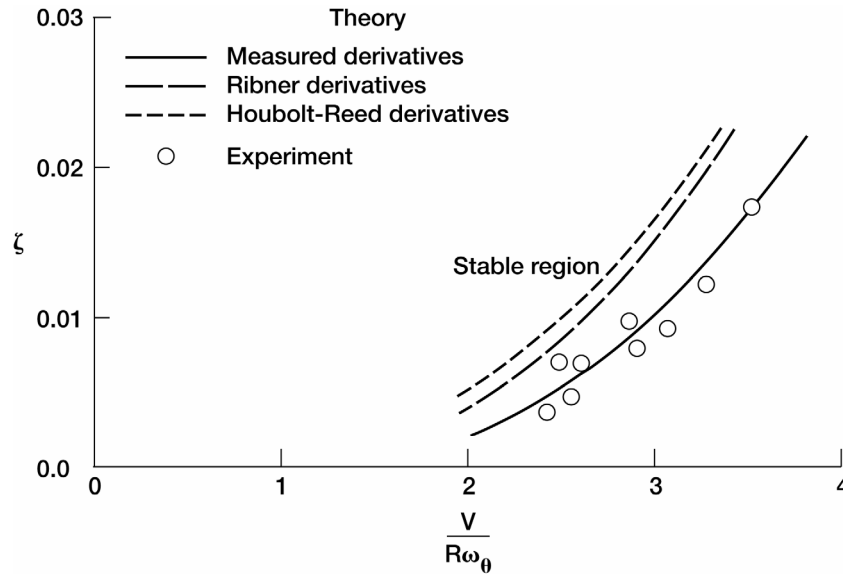
Figure 6.—Comparison of theoretical and experimental whirl-flutter
boundaries for an axisymmetric system with rigid propeller (ref. 6).

Unsteady Flow

The differences in the flutter boundaries based on theoretical and measured derivatives may in part be due to unsteady aerodynamic effects. It can be shown that aerodynamic phase lags associated with the oscillatory wake have a stabilizing effect on the usual backward-mode whirl flutter. The theoretical derivatives used in figure 6 were modified to account for phase lags on the basis of the Theodorsen circulation function $F + iG$ for two-dimensional airfoils. This approximation is good for very large advance ratios; however, for smaller advance ratios, the circulation function is significantly altered because of the helical pattern of the wake.

Studies (refs. 11 and 12) indicate that for low advance ratios the phase lag for a propeller can be much larger than would be predicted by the classical $F + iG$ function for two-dimensional airfoils. It is interesting to note that for lowest advance ratios investigated in reference 6 ($J = 1.3$) the measured phase lag was 24° as compared with a maximum possible theoretical value, based on Theodorsen's function, of 13°.

Thrust

It has been established theoretically that propeller thrust has a relatively insignificant effect on whirl flutter stability for conventional rigid propellers under high-speed flight conditions. This fact greatly simplifies the construction and testing of wind-tunnel models in that it permits the use of windmilling rather than thrusting propellers. In a theoretical investigation of the effects of propeller thrust on whirl flutter (ref. 13), it is shown that thrust causes large deviations in the propeller derivatives at low-speed high-thrust flight states, such as take-off. However, at higher forward speeds where whirl flutter normally occurs, the deviation between aerodynamic coefficients for thrusting and windmilling propellers is usually less than 5 percent. Similar conclusions are found in reference 14 on the basis of experimental coefficients obtained on a thrusting propeller.
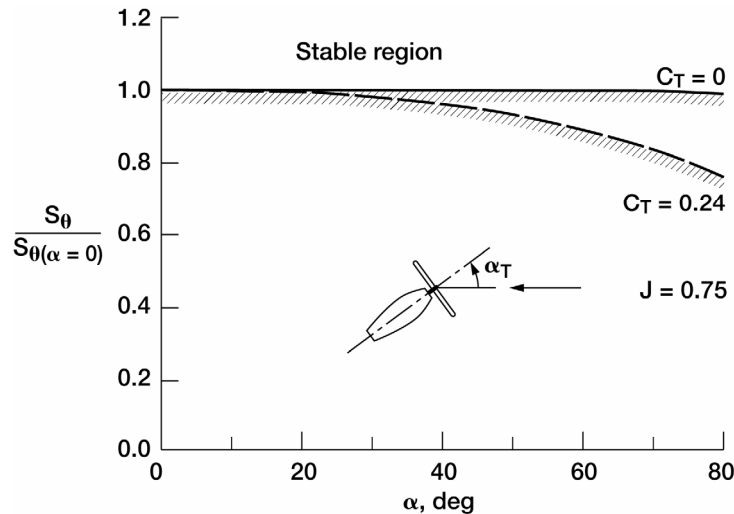
Figure 7.—Effect of inflow angle on stiffness required to prevent whirl flutter (ref. 14).

High Inflow Angles

In the transition maneuver of VTOL aircraft from vertical to horizontal flight the inflow angle—that is, the angle between the thrust axis and the airstream α_T—may be as large as 90°. At these high angles the propeller aerodynamic derivatives are likely to have values that differ markedly from those corresponding to high-speed flight conditions (see refs. 15 and 16.) Since whirl flutter is usually considered to be a relatively high-speed flight phenomenon it is of interest to explore the possibility of encountering whirl flutter in low-speed flight during transition. This question was briefly examined in reference 14. On the basis of whirl flutter calculations, which utilized experimental propeller derivatives and a simple axisymmetric nacelle, angle-of-attack effects were found to be stabilizing in that the stiffness required to prevent flutter at high inflow angles was slightly less than that required at low angles. These results are summarized in figure 7 for a windmilling and a thrusting propeller.

Nonrigid Propeller Rotors

The generalized studies of classical propeller whirl flutter in references 3 to 6 were restricted to rigid propellers. This assumption is reasonable for conventional propeller-driven aircraft; however, V/STOL designs often incorporate articulated and flexible propeller-rotor systems that are compromises between the long flexible blades of a helicopter rotor and the short stiff blades of an aircraft propeller. It is therefore of interest to consider the manner in which whirl flutter might be altered by the use of nonrigid propeller-rotor systems. Of equal interest is the question of how rotor mechanical instability—an instability fed by energy of the rotating rotor rather than by the airstream—might be altered by the inclusion of aerodynamic forces associated with propeller whirl.

Flapping Blades

Recent studies.—The effects of flapping hinged blades on whirl flutter have been examined in several recent studies. In a generalized study (ref. 17), a considerable number of parametric variations were investigated analytically and some complementary test data presented for a low-speed wind-tunnel model. An analysis of a whirl-flutter type of instability that was encountered on the XV-3 aircraft—a VTOL configuration with two-bladed see-saw propeller-rotor system—is presented in reference 18. This analysis included, in addition to blade flapping, the effects of control coupling between the rotor and the pylon mounting structure.
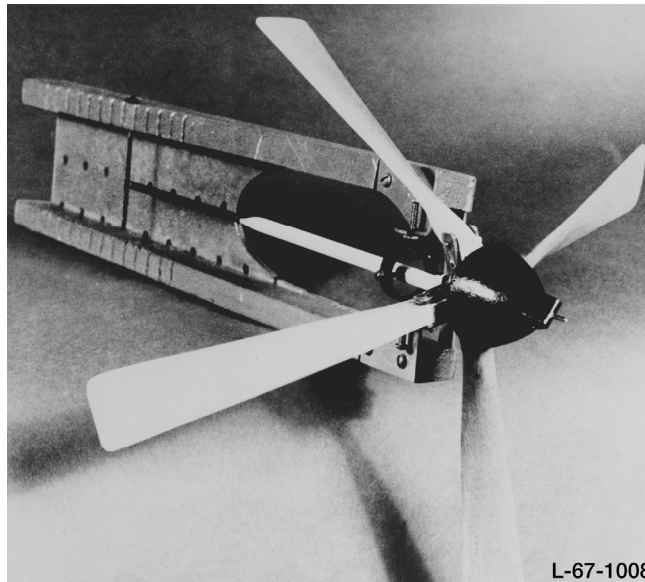
**Figure 8.—Flapping-blade propeller-whirl model
investigated in reference 14.**

The remainder of this section will concern a brief exploratory study of whirl flutter on the simple flapping blade model discussed in reference 14.

Wind-tunnel model.—The model, shown in figure 8, consisted of a windmilling propeller attached to a rod which has freedom to pitch and yaw about a set of gimbal axes. The system had symmetrical stiffness that could be controlled by varying tension in a spring connected axially at the other end of the rod. Each propeller blade was attached to the hub by means of two pins, such that when both pins were in position the blades were fixed, and when one of the pins was removed the other pin became a flap hinge. In this way the blades could be hinged at either 8 or 13 percent of the propeller radius from the spin axis.

Experimental stability boundaries.—Whirl-flutter boundaries for the flapping-blade and fixed-blade conditions are presented in figure 9. During the test the model encountered both forward and backward whirl instabilities. The system became unstable in the backward mode for the fixed blade and the 13-percent hinge offset, but instability developed in the forward mode with the smaller hinge offset of 8 percent. Note that for flutter in the backward mode, blade flapping had a significant stabilizing influence; the opposite conclusion is indicated for flutter in the forward mode. In addition to the frequency differences, other changes in the system behavior were observed. Whereas backward whirl instability was accompanied by divergent motions as would be predicted by linear theory, forward whirl instability was characterized by amplitude-limited motions which could be excited when the disturbing force exceeded a threshold level.

Comparisons with theory.—Results of a theoretical analysis of the flapping-blade model are also shown in figure 9. This analysis, based on the method of reference 17 and considered further in reference 8, involves four degrees of freedom as follows: pitch and yaw of the propeller disk about the gimbal axis and cyclic flapping of the blades in the pitch and yaw directions normal to the propeller.

From roots of the characteristic equation associated with these four degrees of freedom, the calculated frequency and damping of the flapping-blade whirl modes are as presented in figure 10 for the case of a 13 percent hinge offset. These roots are plotted against the ratio of propeller rotational frequency Ω to the pitch frequency of the system with a nonrotating propeller. Since the propeller is windmilling, Ω is proportional to the airstream velocity. Note from the plot of damping, that the stability of all but one of the modes increases continuously with increasing Ω. The critical mode in this case (identified as ② in fig. 10) becomes neutrally stable when $\Omega/\omega_\theta = 7.5$. The whirl mode shapes calculated at the propeller frequency ratio corresponding to flutter are also indicated in figure 10. Note the relatively small contribution of blade flapping present in the unstable mode.
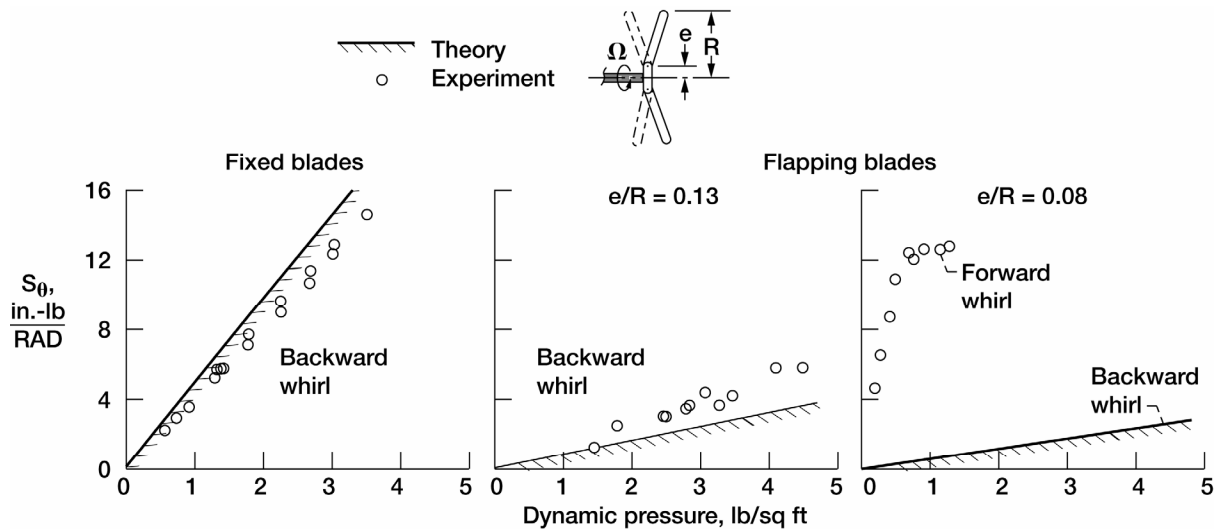
Figure 9.—Comparison of calculated and measured whirl-flutter boundaries for flapping-blade model investigated in reference 14.
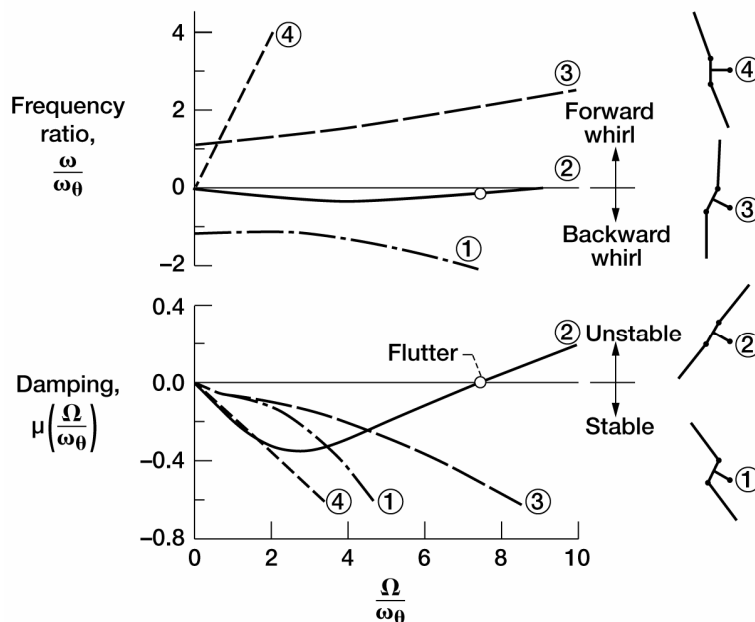
Figure 10.—Calculated flapping-blade whirl modes for e/R = 0.13 (ref. 8).

The theory and experiment shown in figure 9 are in reasonable agreement for the two cases where flutter occurred in the backward whirl mode, that is, for the fixed blades and the flapping blades with a 13 percent hinge offset. However, the theory did not predict the forward whirl mode instability encountered with the 8 percent hinge offset (see plot on right side of fig. 9.) It should be noted that in reference 17 a similar forward whirl mode instability was observed on a flapping-blade model which, again, theory did not predict. By modifying the theory in order to introduce an arbitrary phase lag in the propeller aerodynamic forces, a forward mode instability could be predicted; the required phase lag was 30°. For the configuration in figure 9, however, phase lags as high as 45° were assumed (see ref. 8), but the predicted instability always developed in the backward whirl mode. It therefore appears that this mathematical model lacks some of the ingredients needed to predict the whirl stability characteristics of flapping-blade systems.

Flexible Twisted Blades

General.—Bending deformations of a twisted propeller blade differ from those of the previously discussed flapping blade in a fundamental way. Whereas the flapping motion of a hinged blade was assumed to be normal to the propeller plane, the bending motion of a flexible blade with twist has components of displacement in the propeller plane as well as components normal to the plane. The relative contribution of these two components to a bending vibration mode of the blade will depend on such factors as its geometric pitch angle and the spanwise location of the root chord (i.e., the hub diameter).

The in-plane motions permitted by blade flexibility make possible the occurrence of another class of self-excited vibrations which, unlike propeller-whirl flutter, is purely mechanical in origin. This phenomenon, popularly called ground resonance, has received considerable attention in helicopter studies (e.g., refs. 19 and 20) and has also been recognized as a potential problem on tilt-wing V/STOL configurations (ref. 21).

A recent study of the interaction between propeller-whirl flutter and mechanical instabilities on systems having flexible twisted propellers is presented in reference 22. In this study, as in reference 17 for hinged propellers, a considerable number of parametric variations were analyzed theoretically and wind-tunnel tests were conducted on a simple low-speed wind-tunnel model.

The mathematical and physical models considered in this study consisted of an axisymmetrical nacelle and a flexible twisted propeller having a rigid hub and three or more uniform constant-chord blades. The relevant blade bending modes which can couple with whirl flutter are shown to be cyclic "pitch" and cyclic "yaw" motions in which the tip path plane is pitched or yawed because of blade bending. Each of these modes has associated with it an in-plane component of displacement. The flexible-blade mode illustrated in the following sketch is the pitch mode accompanied by in-plane bending. It is found that coning motions of the blades do not couple with the modes involved in the whirl instabilities and, consequently, this mode was not included in the analysis.
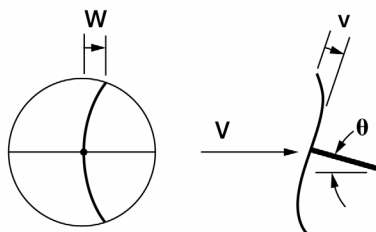
Mechanical instability in vacuo.—Some principal findings of the studies in reference 22 are presented in figures 11 and 12 of this report. Figure 11 shows the stability characteristics of one of the configurations analyzed for a condition of zero damping and without aerodynamic forces (e.g., as in a vacuum). There is close similarity between these plots and the Coleman frequency diagrams for mechanical instability (ref. 19). As the propeller rotational speed Ω increases, a point is reached where two of the frequencies coalesce, resulting in two modes at the same frequency, one of which is damped and the other unstable. This point, denoted by A in the figure, marks the beginning of a region of mechanical instability in a forward whirl mode.

Effects of air density.—Figure 12 shows the effects of adding aerodynamic forces to the stability analyses by progressively increasing air density from zero, the value assumed in figure 11. (Point A in fig. 11 lies on the zero density curve in fig. 12.) Stability boundaries are presented in figure 12 as plots of blade frequency against nacelle frequency for both forward and backward whirl modes. Boundaries for the forward mode originate from a mechanical instability; those for the backward mode originate from a whirl-flutter instability.
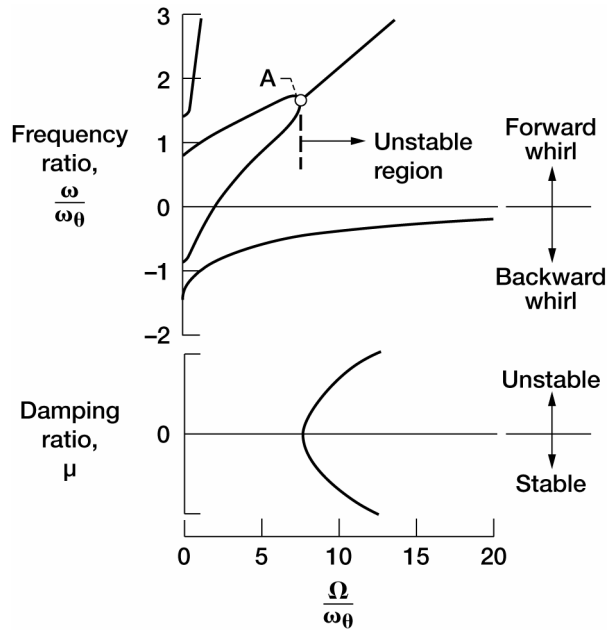
Figure 11.—Mechanical instability of system with flexible propeller in vacuo (ref. 22).
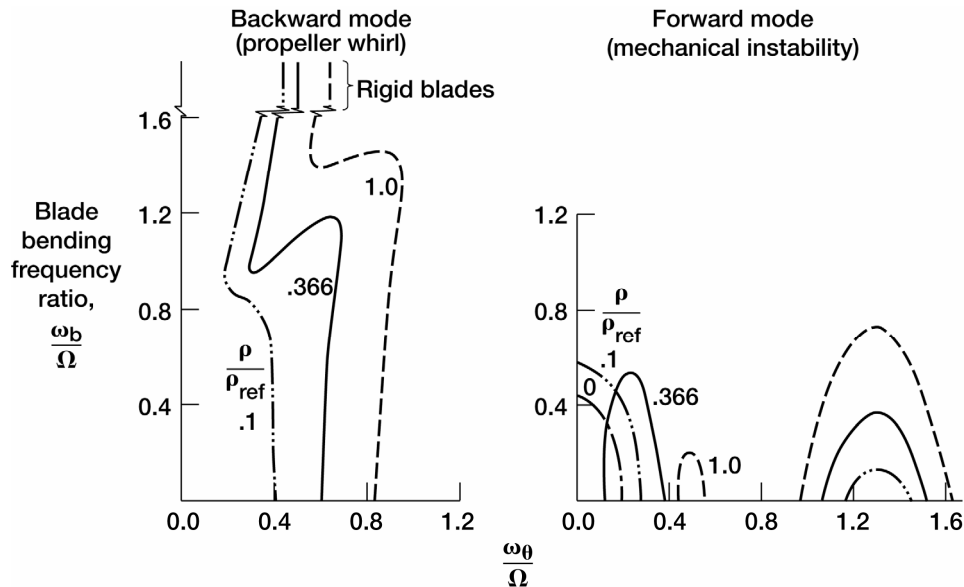
Figure 12.—Effect of air density on stability of system with a flexible-blade propeller (ref. 22).

Note (fig. 12) that in the forward whirl mode as air density increases two regions of instability develop. The region that has the higher values of ω_θ/Ω is not of practical significance because the rate of growth of the unstable motions involved was found to be extremely low and would be eliminated by a small amount of structural damping. The other region of instability in the forward whirl mode is made worse initially as density increases, but with further increase in density the area of instability is reduced and eventually eliminated. It is interesting to note from

this figure that the system encounters mechanical instabilities only if the nonrotating blade natural frequency ω_b is less than the rotational frequency of the propeller.

With regard to propeller-whirl flutter—indicated by the stability boundaries for the backward mode—it appears that blade flexibility has relatively little effect except in a region where the blade frequency parameter ω_b/Ω is near unity. The asymptotic boundaries for a rigid propeller are also shown for comparison.

Remarks on the Inclusion of Propeller-Whirl Modes in Wing Flutter Analyses

General Considerations

Although the idealized propeller-nacelle systems treated thus far in this report have been useful in explaining basic aspects of whirl flutter, more complex representations are usually required to evaluate the flutter characteristics of actual systems. Of particular interest is the effect of wing flexibility on whirl-flutter stability, and conversely, the effect of propeller-whirl modes on flutter stability of the wing. The purpose of this section will be to first discuss some general trend studies relating to the effects of wing flexibility on whirl flutter and then to review briefly some cases wherein whirl modes have been incorporated into the flutter clearance analysis for specific aircraft.

An Analog Trend Study

It has been found that when a propeller-nacelle system is mounted on a flexible wing the whirl-flutter speed is generally higher than if the system were mounted on a rigid back-up structure. The wing in this instance tends to act as a damped-mass oscillator, capable of absorbing energy from the whirl mode. This observation may not apply, however, in cases where the wing flutter speed with rigidly attached nacelles is close to the whirl-flutter speed of the isolated propeller-nacelle system.

This tendency for the aerodynamic forces on a flexible wing to stabilize whirl flutter has been demonstrated in an analog computer study (ref. 23). Typical results from that study are presented in figure 13 for three cases: (a) a rigid wing, (b) a wing having freedom to translate vertically, and (c) a wing having freedom to translate and rotate about an elastic axis. In the latter two cases, aerodynamic forces are assumed to act on the wing as well as on the propeller.

Consider first the case of a rigid wing. Features of this stability boundary are typical of those found in reference 4 and discussed previously with reference to figure 5. Again, it is to be noted that the boundary is extended along the diagonal ray $S_\theta = S_\psi$ such that the symmetrical system, indicated by point A in figure 13(a), is the most critical from the standpoint of whirl flutter. The points at which this curve terminates are the static divergence boundaries for the system.

When the wing has freedom to oscillate in vertical translation (fig. 13(b)) it can be seen that its effect on whirl flutter is always stabilizing. This increased stability can be attributed to aerodynamic damping forces on the wing. It is of particular interest to note the "neck-down" portion of the curve where the stabilizing influence of the wing is most pronounced. At the points labeled B, the whirl frequency ω coincides with the wing bending frequency ω_h so that whirl motions of the propeller-nacelle system tend to drive the wing at a resonant amplitude. It is suggested in reference 23 that the wing may be considered analogous to a tuned damper which absorbs greatest energy when the system frequency is close to the tuned frequency of the damper.

In the third case shown in figure 13(c) the wing vibration mode involves coupled bending and torsion motions. The frequency of the first coupled wing mode ω_1 is approximately the same as the uncoupled bending frequency ω_h discussed previously, but the mode shape indicates strong coupling between the bending and twisting motions h and α. The stability boundary for this condition illustrates an exception to the generally observed trend that wing flexibility stabilizes whirl flutter. It should be noted that the maximum stiffness S_θ required occurs in the vicinity of point C where the wing fundamental coupled frequency ω_1 and the nacelle yaw frequency ω_ψ, are the same. Since the wing mode involves pitching of the propeller, point C may be regarded as a coincidence of "pitch" and yaw frequencies for the flexible wing just as point A was for the rigid wing. In both instances the region of instability is extended at these points where the pitch and yaw frequencies coincide.
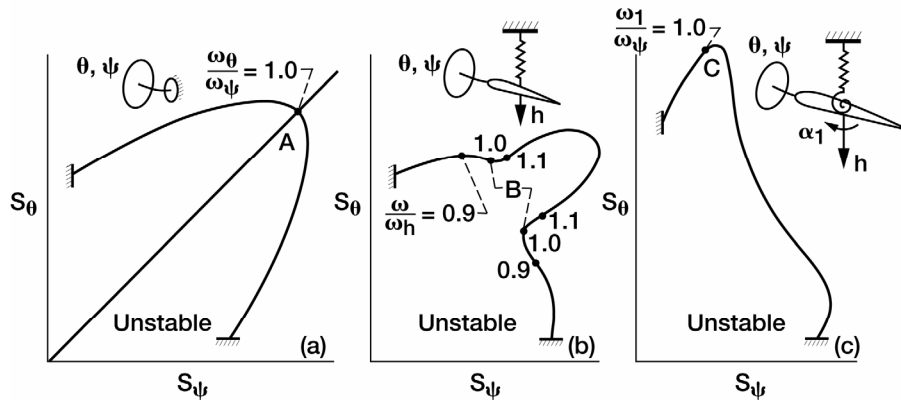
Figure 13.—Influence of wing flexibility on whirl flutter (adapted from ref. 23).
(a) Rigid wing. (b) Wing bending mode. (c) Wing bending torsion mode.

Thus, a general conclusion of these studies is that a flexible wing has a stabilizing effect on propeller-whirl flutter except possibly in a region where the uncoupled yaw frequency is close to a wing torsion frequency. Beneficial effects of a wing on whirl flutter have also been reported in references 24 and 25.

Typical Procedures

Analysis of components.—To investigate the flutter characteristics of an aircraft configuration at the preliminary design stage, the following two-phase approach is commonly employed: In the first phase the major components of the aircraft are analyzed individually. For example, on a propeller driven aircraft parametric studies of whirl flutter would be made with the assumption that the propeller-nacelle system is flexibly mounted on a rigid wing structure. These trend studies would include not only the normal mount structure but also various simulated mount failure conditions. Similarly, wing flutter would be studied by assuming that the nacelle -powerplant mass is rigidly attached to the flexible wing.

Then, in the second phase the equations of motion for each component are coupled together and the flutter characteristics of the complete aircraft examined. Usually, a minimum number of parameters are varied in this second phase. Some practical applications of such a flutter analysis procedure may be found in references 25 and 26 for the XC-142A and in reference 9 for the CL-44.

Choice of modes.—The advantage of making flutter trend studies on isolated components as a preliminary to computations for the complete aircraft can be readily appreciated when one considers the large number of modes that are generally necessary to adequately represent the coupled wing-nacelle system. Flutter analyses, such as discussed in reference 9 for the CL–44, serve to illustrate this point. Each of four powerplant packages on this aircraft can be defined in terms of four degrees of freedom-pitch and yaw rotations about a set of perpendicular axes, and vertical and horizontal translation along these axes-giving a total of 16 degrees of freedom. Since all four engines rotate in the same sense, there is a cross-coupling effect between the symmetric and the antisymmetric wing modes. It may therefore be necessary to consider an asymmetric system; that is, simultaneously include both symmetric and antisymmetric modes in the flutter analysis. Thus, with 16 nacelle modes combined with possibly 10 or 15 wing modes, the flutter analysis may require up to 30 degrees of freedom. For the XC-142A flutter analysis discussed in reference 25, 27 degrees of freedom were included.

Equations of such large order obviously require high-speed computing equipment for solution. However, even with high-speed digital computers, ill-conditioned equations which may exist result in computational difficulties.
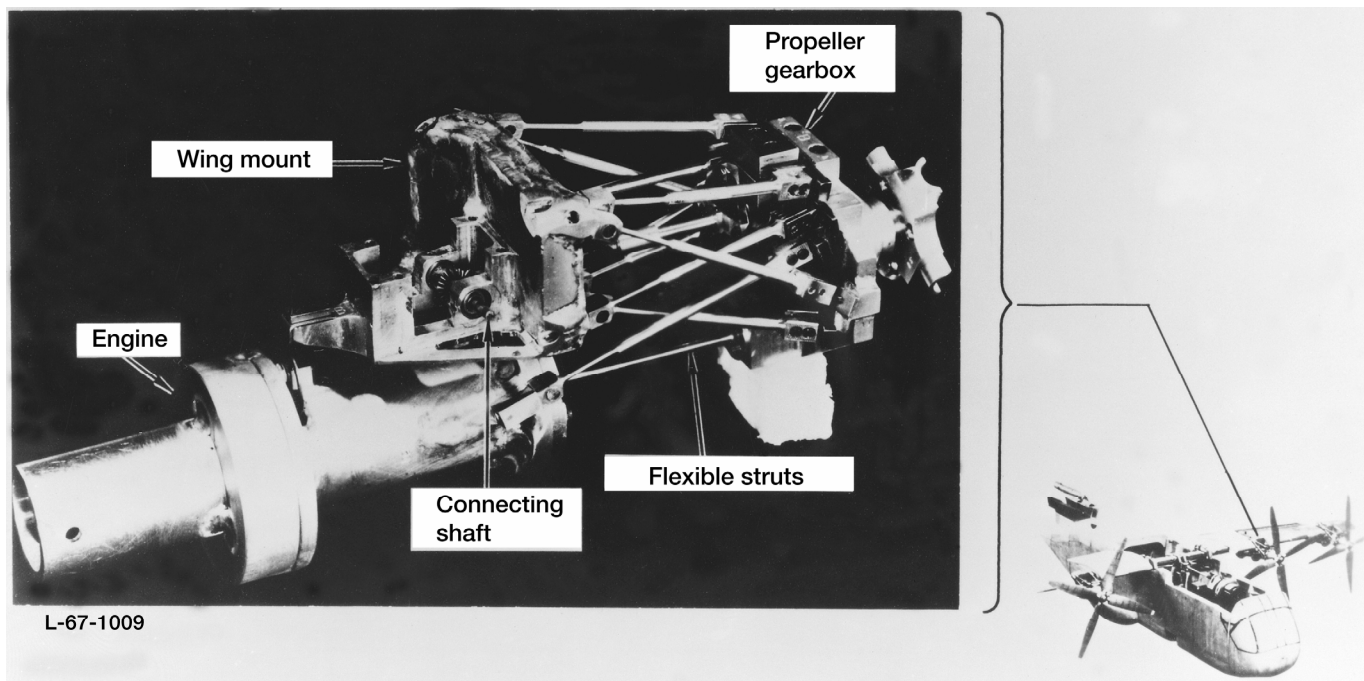
Figure 14.—Engine-gearbox-propeller system used on 1/10-scale dynamic model of XC-142A aircraft (ref. 26).

Aeroelastic Models

Wind-tunnel tests of aeroelastic models are commonly employed to supplement analytical investigations of flutter. A recent example of a wind-tunnel program in which propeller-whirl dynamics were carefully simulated in the flutter model is reported in reference 26.

This investigation involved tests of a 1/10-scale aeroelastic model of the XC–142A VTOL aircraft. Each of four engine-gearbox-propeller systems were dynamically scaled on the model. The propellers, although nonpowered, were shafted together to insure that all turned at the same speed. The remarkable degree of detail achieved in the dynamic simulation of the engine-gearbox system is apparent in figure 14. The gearbox is connected to the engine by a multiredundant strut arrangement on the model in the same manner as it is on the aircraft. The flexibility of each strut as well as the overall flexibility between the engine and the gearbox are accurately scaled in the model. The authors of reference 26 stated that the simulation of this one component represented the most difficult design problem on the model.

A design requirement for the XC-142A was that no flutter occur, as a result of failure of any single structural element (see ref. 7.) Therefore, in the model tests a failure of various strut members was simulated by simply removing the strut in question. The strut failure conditions that were actually simulated on the dynamic model were selected on the basis of analysis. It is interesting to note that in some cases an increase in calculated whirl-flutter speed occurred as a result of a strut failure.

Response to Random Atmospheric Turbulence

Previous sections of this report have dealt with factors that affect the stability of propeller-powerplant systems. A problem of interest related to dynamic loads and fatigue is the response of such systems to gusts and turbulence in the atmosphere. These loads may be significant even though the system is operating well on the stable side of its whirl-flutter boundary.
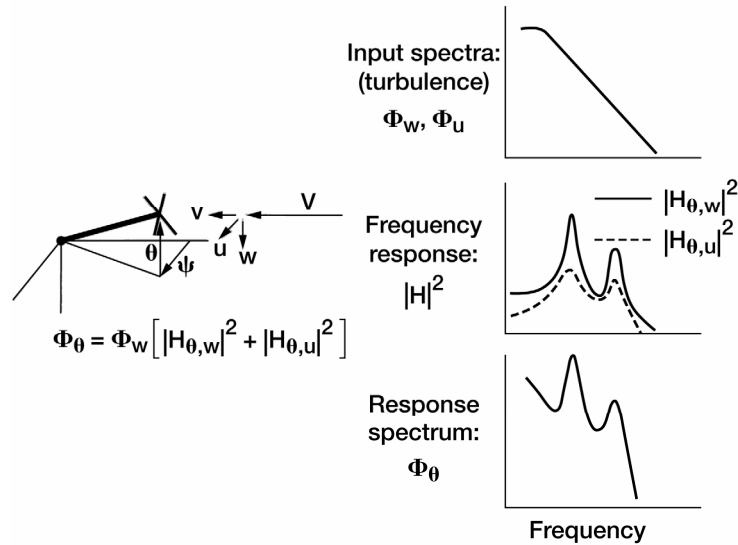
Figure 15.—Response of propeller-nacelle system to random turbulence (ref. 14).

The gust response problem for a flexibly mounted propeller-powerplant system is briefly considered in reference 14 and a method of analysis suggested. Figure 15, taken from reference 14, shows the free-stream velocity represented components $u(t)$, $v(t)$, and $w(t)$. These time-dependent velocities produce unsteady forces and moments on the propeller which in turn cause pitch and yaw deflections $\theta(t)$ and $\psi(t)$ of the flexibly mounted system. If turbulence is considered to be a stationary random process, a solution can be obtained for the response of the system to multiple random inputs $u(t)$, $v(t)$, and $w(t)$. The analysis requires specifications of the power spectra and cross spectra of the inputs, together with a set of frequency-response functions which define the response of the system to sinusoidal variations of the gust velocity components. If the turbulence is assumed to be isotropic, the cross-spectrum terms of the input become zero and the equation for the power spectrum of response of the system, in pitch, for example, can be written

$$\Phi_\theta = \Phi_w \left(\left| H_{\theta,w} \right|^2 + \left| H_{\theta,u} \right|^2 \right)$$

where Φ_w is the power spectrum of the u and w components of turbulence and $H_{\theta,u}$ and $H_{\theta,w}$ represent the response in pitch to unit-amplitude sinusoidal u and w inputs. The variation of θ due to fluctuations of the longitudinal velocity v, that is, $H_{\theta,v}$, has been neglected. The derivation of these equations may be found in reference 14.

The way in which typical power spectra and frequency-response functions for a system might vary with frequency is indicated graphically in figure 15. It should be mentioned that the frequency-response function $H_{\theta,u}$—that is, the response in a vertical plane due to a lateral gust input—is a measure of the aerodynamic and gyroscopic coupling produced by the propeller. The two peaks in the response spectrum occur at the backward and forward whirl frequencies. Of these, the peak associated with the backward whirl mode is the larger for two reasons: (1) this mode is more lightly damped than the forward mode, and (2) being at a lower frequency the mode experiences a higher level of the input turbulence spectrum.

Concluding Remarks

A survey is made of the state of the art of propeller-whirl flutter—a precession-type instability that can occur on a flexibly mounted aircraft engine-propeller combination. This report reviews the literature relating to this problem from the time it first became of concern on conventional turboprop and V/STOL aircraft.

Included in the survey are a description of the basic mechanism of whirl flutter, a summary of generalized trend studies on idealized systems, the status of methods for predicting propeller aerodynamic coefficients, the effects of flapping hinged blades and twisted flexible blades on whirl flutter, and some approaches for including propeller-whirl modes as a part of the flutter evaluation for complete aircraft. Also, brief consideration is given to the response of flexibly mounted propeller-nacelle systems to random atmospheric turbulence.

Whirl flutter of conventional propeller-nacelle systems is now a reasonably well understood phenomenon and amenable to analysis. For propeller-rotor systems with flapping blades, however, comparison between experiment and theory suggests the need for further refinements in the mathematical model.

Langley Research Center,
National Aeronautics and Space Administration,
Langley Station, Hampton, Va., February 1, 1967,
721-02-00-06-23.

References

1. Taylor, E.S.; and Browne, K.A.: Vibration Isolation of Aircraft Power Plants. J. Aero. Sci., vol. 6, no. 2, 1938, pp. 43–49.
2. Abbott, Frank T., Jr.; Kelly, H. Neale; and Hampton, Kenneth D.: Investigation of Propeller—Power-Plant Autoprecession Boundaries for a Dynamic-Aeroelastic Model of a Four-Engine Turboprop Transport Airplane. NASA TN D–1806, 1963.
3. Reed, Wilmer H., III; and Bland, Samuel R.: An Analytical Treatment of Aircraft Propeller Precession Instability. NASA TN D–659, 1961.
4. Houbolt, John C.; and Reed, Wilmer H., III: Propeller-Nacelle Whirl Flutter. J. Aerospace Sci., vol. 29, no. 3, 1962, pp. 333–346.
5. Sewall, John L.: An Analytical Trend Study of Propeller Whirl Instability. NASA TN D–996, 1962.
6. Bland, Samuel R.; and Bennett, Robert M.: Wind-Tunnel Measurement of Propeller Whirl-Flutter Speeds and Static-Stability Derivatives and Comparison With Theory. NASA D–1807, 1963.
7. Anon.: Airplane Airworthiness; Transport Categories—Flutter, Deformation, and Vibration Requirements. Civil Air Regulations Amendment 4b–16, FAA, Aug. 31, 1964.
8. Reed, W.H., III: Propeller-Rotor Whirl Flutter—A State-of-the-Art Review. J. Sound Vib., vol. 4, 1966, pp. 526–544.
9. Baker, K.E.; Smith, R.; and Toulson, K.W.: Notes on Propeller Whirl Flutter. Can. Aeronaut. Space J., vol. 11, 1965, pp. 305–313.
10. Ribner, Herbert S.: Propellers in Yaw. NACA–TR–820 (Supersedes NACA ARR 3L09), 1945.
11. Loewy, R.G.: A Two-Dimensional Approximation to the Unsteady Aerodynamics of Rotary Wings. J. Aero. Sci., vol. 24, no. 2, 1957, pp. 81–92.
12. Timman, R.; and Van de Vooren, A.I.: Flutter of a Helicopter Rotor Rotating in Its Own Wake. J. Aero. Sci., vol. 24, no. 9, 1957, pp. 694–702.
13. Ravera, R.J.: Effects of Steady State Blade Angle of Attack on Propeller Whirl-Flutter. Grumman Aircraft Eng. Corp. Rept. ADR 06–01–63.1, July 1963.
14. Bennett, R.M.; and Reed, W.H., III: Propeller Whirl Flutter Considerations for V/STOL Aircraft. ATRECOM CAL/TRECOM Symposium Proceedings, vol. II, 1963. Available from the Center for Aerospace Information.
15. De Young, J.: Propeller at High Incidence. J. Aircraft (AIAA Paper 64–169), vol. 2, 1965, pp. 241–250.
16. Shenkman, Albert M.: Generalized Performance of Conventional Propellers for VTOL/STOL Aircraft. Hamilton Standard Report No. HS–1829, 1958.
17. Naylor, H.F.W.; and Richardson, J.R.: Whirl Flutter of Propellers With Hinged Blades. REPT.–24, Engineering Research Associates, Toronto, ON, 1962.
18. Hall, W.E., Jr.: Prop-Rotor Stability at High Advance Ratios. J. Am. Helicopter Soc., vol. 11, 1966, pp. 11–26.
19. Coleman, Robert P.; and Feingold, Arnold M.: Theory of Self-Excited Mechanical Oscillations of Helicopter Rotors With Hinged Blades. NACA–TR–1351 (Supersedes NACA TN–3844), 1958.
20. Brooks, George Warren: The Mechanical Instability and Forced Response of Rotors on Multiple-Degree-of-Freedom Supports. Ph.D. Thesis, Princeton Univ., 1961.
21. Loewy, R.G.; and Yntema, R.T.: Some Aeroelastic Problems of Tilt-Wing VTOL Aircraft. J. Am. Helicopter Soc., vol. 3, no. 1, 1958, pp. 35–57.

22. Bandler, P.A., et al.: Whirl Flutter of Propellers With Flexible Twisted Blades. Rept.–43, Engineering Research Associates, Toronto, ON, 1963.

23. Zwann, R.J.; and Bergh, H.: Propeller-Nacelle Flutter of the Lockheed Electra Aircraft. National Lucht-en Ruimtevaart-Laboratorium Report F–288, 1962.

24. Bennett, R. M.; and Bland, Samuel R.: Experimental and Analytical Investigation of Propeller Whirl Flutter of a Power Plant on a Flexible Wing. NASA TN D–2399, 1964.

25. Head, A.L., Jr.: A Review of the Structural Dynamic Characteristics of the XC−142A Aircraft. CAL/TRECOM Symposium Proceedings, vol. II, 1963. Available from the Center for Aerospace Information.

26. Head, A.L., Jr.; and Smith, W.D.: Dynamic Model Testing of the XC−142A Aircraft. Proceedings of Symposium on Aeroelastic and Dynamic Modeling Technology, 1964, pp. 723–762.

Bibliography on Propfan Aeroelasticity

John K. Ramsey
National Aeronautics and Space Administration
Glenn Research Center
Cleveland, Ohio 44135

In the early 1970's, fuel prices increased substantially, adversely affecting airline budgets. In response to this situation, NASA and industry began research efforts to develop advanced turboprops, known as propfans, to improve aircraft fuel efficiency. Propfans are characterized by thin highly swept blades as shown in figure 1. The propfan, when combined with the turbine engine, could provide improved fuel efficiency compared to an equivalent-technology turbofan engine.

It was recognized that efficiency could be improved by removing the swirl created by single-rotation propfans. To accomplish this, NASA and industry began research on both tractor and pusher counterrotating propfans, wherein the aft blade row would recover the swirl. The counterrotating propfan could also provide increased power over a single-rotating propfan of the same tip diameter. Shown in figure 2, is a pusher configuration of a counterrotating propfan, known as the counterrotating unducted fan.

The following bibliography lists aeroelasticity related publications applicable to the propfan.

Figure 1.—Single rotation profan.

Figure 2.—Counterrotating profan configuration known as counterrotating unducted fan.

Bibliography

August, Richard; and Kaza, Krishna Rae V.: Vibration, Performance, Flutter and Forced Response Characteristics of a Large-Scale Propfan and Its Aeroelastic Model. NASA TM–101322 (AIAA Paper 88–3155), 1988.

August, Richard: Vibration and Flutter Analysis of the SR–7L Large-Scale Propfan. Lewis Structures Technology Conference, Volume 1: Structural Dynamics, 1988, pp. 379–392.

August, Richard; and Kaza, Krishna Rao V.: Vibration and Flutter Characteristics of the SR7L Large-Scale Propfan. NASA TM–100272, 1988.

Bakhle, Milind A.; Reddy, T.S.; and Theo, G., Jr.: Time Domain Flutter Analysis of Cascades Using a Full-Potential Solver. AIAA J. (AIAA–1990–0984), vol. 30, no. 1, 1992, pp. 163–170.

Bakhle, M.A.; and Reddy, T.S.R.: Unsteady Aerodynamics and Flutter of Propfans Using a Three-Dimensional Full-Potential Solver. AIAA Paper 93–1633, 1993.

Bansal, P.N., et al.: Analysis and Test Evaluation of the Dynamic Response and Stability of Three Advanced Turboprop Models; Final Report. NASA CR–174814, 1985.

Bartos, K.F.; and Ernst, M.A.: Evaluation of MARC for the Analysis of Rotating Composition Blades. NASA TM–4423, 1993.

Besson, J.M.; and Petot, D.: Dynamic Behavior of a Propfan. ONERA TP No. 1984–122, 1984.

Billman, L.C., et al.: Large Scale Prop-Fan Structural Design Study. Volume 1: Initial Concepts. NASA CR–174992, 1988.

Billman L.C., et al.: Large Scale Prop-Fan Structural Design Study. Volume 2: Preliminary Design of SR–7. NASA CR–174993, 1988.

Campbell, William A., et al.: Large-Scale Advanced Prop-Fan (LAP) High Speed Wind Tunnel Test Report. NASA CR–182125, 1988.

Chamis, C.C.; and Aiello, R.A.: Tensile Buckling of Advanced Turboprops. J. Aircraft, vol. 20, 1983, pp. 907–912.

Chi, R.M.: Separated Flow Unsteady Aerodynamics for Propfan Applications. AIAA–1984–0874, 1984.

Cornell, R.W.; and Rothman, E.A.: Structural Design and Analysis of Prop-Fan Blades. AIAA–1979–1116, 1979.

Crawley, Edward F.; and Ducharme, Eric H.: Velocity Scaled Aeroelastic Testing of Advanced Turboprops. ASME Paper 87–GT–209, 1987.

Crawley, E.F.; and Ducharme, E.H.: Parametric Trends in the Flutter of Advanced Turboprops. ASME Paper 89–GT–280, 1990.

Degeorge, C.L.; Turnberg, J.E.; and Wainauski, J.E.: A Report on the Initial Testing of the Large Scale Advanced Prop-Fan. AIAA–1986–1551, 1986.

Degeorge, C.L.: Large-Scale Advanced Prop-Fan (LAP) Technology Assessment Report. NASA CR–182142, 1988.

Ernst, Michael A.; and Lawrence, Charles: Hub Flexibility Effects on Propfan Vibration. NASA TM–89900, 1987.

Fertis, D.G., et al.: Parametric Studies of Advanced Turboprops. J. Propul. Pow., vol. 6, no. 1, 1990, pp. 58–62.

Graber, Edwin J.: Overview of NASA PTA Propfan Flight Test Program. Aeropropulsion 1987, 1987, pp. 363–382.

Hagar, Roy D.; and Vrabel, Deborah: Advanced Turboprop Project. NASA SP–495, 1988.

Hirschbein, Murray, et al.: Structural and Aeroelastic Analysis of the SR–7L Propfan. NASA TM–86877, 1985.

Hwang, Ching-Chywan: Propfan Supersonic Panel Method Analysis and Flutter Predictions. Ph.D. Thesis, Purdue Univ., 1990.

Joo, Gene; and Lee, Hae-Kyung: Dynamic Response and Aeroelastic Analysis of a Propeller Blade of a Prop-Fan Engine. Proceedings of the 28th Aircraft Symposium. Tokyo, Japan, 1990, pp. 84–87.

Kaza, K.R.V.; and Kielb, R.E.: Coupled Bending-Bending-Torsion Flutter of a Mistuned Cascade With Nonuniform Blades. NASA TM–82813 (AIAA–1982–0726), 1982.

Kaza, K.R.V.; and Kielb, R.E.: Effects of Warping and Pretwist on Torsional Vibration of Rotating Beams. J. Appl. Mech. Trans. ASME, vol. 51, no. 14, 1984, pp. 913–920.

Kaza, Krishna Rao V., et al.: Analytical and Experimental Investigation of Mistuning in Propfan Flutter. NASA TM–88959 (AIAA Paper 87–0739), 1987.

Kaza, Krishna Rao V., et al.: Aeroelastic Response of Metallic and Composite Propfan Models in Yawed Flow. NASA TM–100964 (AIAA Paper 88–3154), 1988.

Kaza, Krishna Rao V.: Development of Aeroelastic Analysis Methods for Turborotors and Propfans, Including Mistuning. NASA Lewis Research Center, Structures Technology, Volume 1: Structural Dynamics, 1988, pp. 247–262.

Kaza, K.R.V.; and Reddy, T.S.R.: Assessment of Semi-Empirical Dynamic Stall Models for Turboprop Stall Calculations. NASA Tech Briefs, vol. 13, no. 1, 1989, p. 77.

Kaza, Krishna Rao V.: Turbomachinery Aeroelasticity at NASA Lewis Research Center. NASA Langley Research Center, Transonic Unsteady Aerodynamics and Aeroelasticity 1987, part 2, 1989, pp. 571–603.

Kaza, K.R.V., et al.: Predicting Flutter of a Propfan. NASA Tech Briefs, vol. 13, no. 7, 1989, p. 74.

Kaza, K.R.V., et al.: Analytical Flutter Investigation of a Composite Propfan Model. J. Aircraft (NASA TM–88944 and AIAA Paper 87–0738), vol. 26, no. 8, 1989, pp. 772–780.

Keith, Theo G., Jr.; and Reddy, T.S.R.: Aeroelastic Stability and Response of Rotating Structures; Final Report. NASA CR–202647, 1996.

Kurkov, A.P.: Optical Measurement of Unducted Fan Blade Deflections. J. Turbomachinery, vol. 112, 1990, pp. 751–758.

Kurkov, A.P.; and Mehmed, O.: Optical Measurements of Unducted Fan Flutter. J. Turbomachinery, vol. 115, 1993, pp. 189–196.

Kurkov, Anatole P..: Optical Measurement of Propeller Blade Deflections. NASA TP–2841, 1998.

Lawrence, C.; and Kielb, R.E.: Nonlinear Displacement Analysis of Advanced Propeller Structures Using NASTRAN. NASA TM–83737, 1984.

Lawrence, C., et al.: A NASTRAN Primer for the Analysis of Rotating Flexible Blades. NASA TM–89861, 1987.

Mahajan, Aparajit J., et al.: Aeroelastic Stability Analyses of Two Counter Rotating Propfan Designs for a Cruise Missile Model. NASA TM–105268 (AIAA Paper 92–2218), 1992.

Mehmed, O., et al.: Bending-Torsion Flutter of a Highly Swept Advanced Turboprop. NASA TM–82975, 1981.

Mehmed, O.; and Kaza, K.R.V.: Experimental Classical Flutter Results of a Composite Advanced Turboprop Model. NASA TM–88792, 1986.

Mehmed, Oral: Propfan Model Wind Tunnel Aeroelastic Research Results. NASA Lewis Research Center, Structures Technology, Volume 1: Structural Dynamics, 1988, pp. 273–286.

Mehmed, Oral; and Murthy, Durbha V.: Experimental Investigation of Propfan Aeroelastic Response in Off-Axis Flow With Mistuning. J. Propul. Pow. (AIAA Paper 88–3153 and NASA TM–101320), vol. 7, no. 1, 1991, pp. 90–98.

Mehmed, Oral; and Kurkov, Anatole P.: Experimental Investigation of Counter-Rotating Propfan Flutter at Cruise Conditions. J. Propul. Pow. (AIAA Paper 93–1632), vol. 10, no. 3, pp. 343–347 1994, pp. 343–347.

Murthy, Durbha V.; and Kaza, Krishna Rao V.: A Semianalytical Technique for Sensitivity Analysis of Unsteady Aerodynamic Computations. J. Aircraft (NASA TM–100810 and AIAA Paper 88–2377), vol. 28, no. 8, 1991, pp. 481–488.

Murthy, Durbha V.; and Kaza, Krishna Rao V.: Application of a Semianalytical Technique for Sensitivity Analysis of Unsteady Aerodynamic Computations. AIAA–1988–2377, 1988.

Murthy, Durbha V.; and Kaza, Krishna Rao V.: A Computational Procedure for Automated Flutter Analysis. Commun. Appl. Numer. Methods (NASA TM–100171), vol. 5, no. 1, 1989, pp. 29–37.

Nitzsche, F.: Whirl-Flutter Suppression in Advanced Turboprops and Propfans by Active Control Techniques. J. Aircraft, vol. 31, no. 3, 1994, pp. 713–719.

Nitzsche, Fred: Insights on the Whirl-Flutter Phenomena of Advanced Turboprops and Propfans. J. Aircraft, vol. 28, no. 7, 1991, pp. 463–470.

Nitzsche, F.: Whirl-Flutter Investigation on an Advanced Turboprop Configuration. J. Aircraft, vol. 26, no. 10, 1989, pp. 939–946.

Podboy, Gary G.; and Krupar, Martin J.: Laser Velocimeter Measurements of the Flow Field Generated by a Forward-Swept Propfan During Flutter. NASA TM–106195, 1993.

Ramsey, J.K.; and Kaza, K.R.V.: Concentrated Mass Effects on the Flutter of a Composite Advanced Turboprop Model. NASA TM–88854, 1986.

Reddy, T.S.R.; and Kaza, K.R.V.: A Comparative Study of Some Dynamic Stall Models. NASA TM–88917, 1987.

Reddy, T.S.R.: Stall Flutter Analysis of Propfans. NASA Lewis Research Center, Structures Technology, Volume 1: Structural Dynamics, 1988, pp. 405–419.

Reddy, T.S.R.; Srivastava, Rakesh; and Kaza, Krishna Rao V.: The Effects of Rotational Flow, Viscosity, Thickness, and Shape on Transonic Flutter Dip Phenomena. NASA TM–100811 (AIAA Paper 88–2348), 1988.

Reddy, T.S.R.; and Kaza, K.R.V.: Analysis of an Unswept Propfan Blade With a Semiempirical Dynamic Stall Model. NASA TM–4083, 1989.

Reddy, T.S.R.; and Mehmed, Oral: Aeroelastic Analysis of Prop Fan Blades With a Semiempirical Dynamic Stall Model. AIAA Paper 89–2695, 1989.

Reddy, T.S.R., et al.: APPLE—An Aeroelastic Analysis System for Turbomachines and Propfans. AIAA Paper 92–4712, 1992.

Reddy, T.S.R., et al.: A Review of Recent Aeroelastic Analysis Methods for Propulsion at NASA Lewis Research Center. NASA TP–3406, 1993.

Reddy, T.S.R.: Aeroelastic Analysis Methods for Turbomachines and Propfans. Proceedings of the International Symposium of Recent Advances in Aerospace Sciences and Engineering, vol. 1, Interline Publishing, Bangalore, India, 1993, pp. 208–219. Available from Interline Publishing.

Reddy, T.S.R.; and Lucero, John M.: ASTROP2 Users Manual: A Program for Aeroelastic Stability Analysis of Propfans. NASA TM–107195, 1996.

Smith, Arthur F.: Analysis and Test Evaluation of the Dynamic Stability of Three Advanced Turboprop Models at Zero Forward Speed; Final Report. NASA CR–175025, 1985.

Smith, Arthur F.: Analysis and Test Evaluation of the Dynamic Response and Stability of Three Advanced Turboprop Models at Low Forward Speed; Final Report. NASA CR–175026, 1985.

Smith, A.F.; and Brooks, B.M.: Dynamic Response and Stability of a Composite Prop-Fan Model; Final Report. NASA CR–179528, 1986.

Smith Arthur F.; and Brooks, Bennett M.: Dynamic Response of Two Composite Prop-Fan Models on a Nacelle/Wing/Fuselage Half Model; Final Report. NASA CR–179589, 1986.

Srinivasan, A.V.; and Fulton, G.B.: Advanced Turboprop Vibratory Characteristics; Final Report. NASA CR–174708, 1984.

Srinivasan, A.V.; Kielb, R.E.; and Lawrence, C.: Dynamic Characteristics of an Assembly of Prop-Fan Blades. ASME Paper 85–GT–134, 1986.

Srivastava, R., et al.: Application of an Efficient Hybrid Scheme for Aeroelastic Analysis of Advanced Propellers. J. Propul. Pow., vol. 7, no. 5, 1991, pp. 767–775.

Srivastava, R.; Reddy, T.S.R.; and Mehmed, O.: Aeroelastic Analysis of Advanced Propellers Using an Efficient Euler Solver. AIAA Paper 92–0488, 1992.

Srivastava, R.; Reddy, T.S.R.; and Mehmed, O.: A Numerical Classical Flutter Analysis of Advanced Propellers. AIAA–1992–2118, 1992.

Srivastava, R.; and Mehmed, O.: On the Static Stability of Forward Swept Propfans. AIAA Paper 93–1634, 1993.

Srivastava, R., et al.: Flutter Analysis of Propfans Using a Three-Dimensional Euler Solver. J. Propul. Pow. (AIAA Paper 94–1549), vol. 12, no. 2, 1996, pp. 267–273.

Sun, Xiaofeng; and Hu, Zongan: On Aeroelasticity and Aeroacoustics of Propfan. J. Aerospace Pow., vol. 2, 1987, pp. 299–302.

Turnberg, J.E.: Unstalled Flutter Stability Predictions and Comparisons to Test Data for a Composite Prop-Fan Model; Final Report. NASA CR–179512, 1986.

Violette, John A.; Sullivan, William E.; and Turnberg, Jay E.: Large-Scale Advanced Prop-Fan (LAP) Blade Design; Topical Contractor Report. NASA CR–174790, 1984.

Williams, M.H.; and Hwang, C.-C.: Three Dimensional Unsteady Aerodynamics and Aeroelastic Response of Advanced Turboprops. AIAA Paper 86–0846, 1986.

Williams, Marc H.: Aeroelastic Effects of Alternate Blade Sweep on Advanced Propfan Rotor. ASME Paper 87–WA/AERO–8, 1987.

Panel Flutter[*]

E.H. Dowell
Princeton University
Princeton, New Jersey 08544

Foreword

NASA experience has indicated a need for uniform criteria for the design of space vehicles. Accordingly, criteria are being developed in the following areas of technology:

Environment
Structures
Guidance and Control
Chemical Propulsion

A list of all published monographs in this series can be found at the end of this document.

These monographs are to be regarded as *guides* to the formulation of design requirements and specifications by NASA Centers and project offices.

This monograph was prepared under the cognizance of the Langley Research Center. The Task Manager was G. W. Jones, Jr. The author was E. H. Dowell of Princeton University. A number of other individuals assisted in developing the material and reviewing the drafts. In particular, the significant contributions made by the following are hereby acknowledged: C. P. Berry, D. L. Keeton, and D. A. Stewart of McDonnell Douglas Corporation; J. Dugundji of Massachusetts Institute of Technology; L. D. Guy of NASA Langley Research Center; M. H. Lock of The Aerospace Corporation; M. H. Shirk of U.S. Air Force Flight Dynamics Laboratory; and H. M. Voss of Boeing.

NASA plans to update this monograph periodically as appropriate. Comments and recommended changes in the technical content are invited and should be forwarded to the attention of the Structural Systems Office, Langley Research Center, Hampton, Virginia 23365.

June 1972

Guide to the Use of This Monograph

The purpose of this monograph is to provide a uniform basis for design of flightworthy structure. It summarizes for use in space vehicle development the significant experience and knowledge accumulated in research, development, and operational programs to date. It can be used to improve consistency in design, efficiency of the design effort, and confidence in the structure. This monograph consists of three major sections preceded by a brief INTRODUCTION, section 1, and complemented by a list of REFERENCES.

The STATE OF THE ART, section 2, reviews and assesses current design practices and identifies important aspects of the present state of technology. Selected references are cited to supply supporting information. This section serves as a survey of the subject that provides background material and prepares a proper technological base for the CRITERIA and RECOMMENDED PRACTICES.

The CRITERIA, section 3, state *what* rules, guides, or limitations must be imposed to ensure flightworthiness. The criteria can serve as a checklist for guiding a design or assessing its adequacy.

The RECOMMENDED PRACTICES, section 4, state *how* to satisfy the criteria. Whenever possible, the best procedure is described; when this cannot be done, appropriate references are suggested. These practices, in conjunction with the criteria, provide guidance to the formulation of requirements for vehicle design and evaluation.

---

[*]This document was first published as Dowell, E.H.: Panel Flutter. NASA SP–8004, 1964 (revised 1972).

1. Introduction

Panel flutter is a self-excited, dynamic-aeroelastic instability of thin plate or shell-like components of a vehicle. It occurs most frequently, though not exclusively, in a supersonic flow. At subsonic speeds, the instability more often takes the form of a static divergence or aeroelastic buckling. Flutter is caused and maintained by an interaction among the aerodynamic, inertial, and elastic forces of the system. Initially, the amplitude of the motion of an unstable panel increases exponentially with time, although frequently the amplitude is limited because of nonlinearities, usually structural.

Panels are normally designed to avoid flutter. If it should occur during flight, however, then limited-amplitude and limited-duration flutter may be tolerated for some vehicles as long as the amplitude and duration do not cause: (1) structural failure of the panel or supporting structure due to fatigue, (2) functional failure of equipment attached to the structure, or (3) excessive noise levels in space vehicle compartments near the fluttering panel.

Panel flutter has occurred on a number of flight vehicles. Early experience, largely aircraft, is surveyed in reference 1. More recently, panel flutter has occurred on the X-15 during flight operation (ref. 2), during wind tunnel tests in the development program of the X-20 (refs. 3 through 5), on Titan II and III (ref. 6), and on the S-IVB (ref. 7).

The structural damage resulting from panel flutter was judged destructive on the X-15 and the X-20. The structure of these vehicles was stiffened to prevent panel flutter throughout the flight envelope. For the Titans and S-IVB, the flutter was judged nondestructive because it was determined that the severity and duration of the flutter would not be great enough to degrade unacceptably the structural integrity of the panel. Hence, no stiffening was added (and no weight penalty incurred) to prevent flutter of these panels.

This monograph is concerned with the prediction of panel flutter, determination of its occurrence, design for its prevention, and evaluation of its severity. Theoretical analyses recommended for the prediction of flutter stability boundaries, vibration amplitudes, and frequencies for several types of panels are described. Vibration tests and wind tunnel tests are recommended for certain panels and environmental flow conditions to provide information for design or verification of analysis. Appropriate design margins on flutter stability boundaries are given and general criteria are presented for evaluating the severity of possible short-duration, limited-amplitude panel flutter on non-reusable vehicles.

The occurrence of flutter in a particular panel configuration depends upon the mass, damping, and stiffness of the panel; local Mach number, dynamic pressure, density; in-plane flow angularity; and, for some conditions, boundary layer profile and thickness. The parameters affecting panel stiffness which are reflected in panel natural frequencies include the panel length, thickness, material modulus, length-to-width ratio, edge conditions, curvature, orthotropy (variation in stiffness with direction), in-plane loads, transverse pressure differential across the panel, and acoustic cavity (closed-in space) beneath the panel. For some configurations geometric imperfections in the panel may be important as well.

Related NASA design criteria monographs include those on natural vibration modal analysis (ref. 8); structural vibration prediction (ref. 9); and flutter, buzz, and divergence of lifting surfaces (ref. 10).

2. State of the Art

One of the difficulties in assessing the state of the art with respect to panel flutter is the large number of parameters which may be important for any particular application. References 11 and 12 present some of the historical background of the problem. More recent surveys are those of references 13 and 14, which give bibliographies complete to the time of publication. Much of this state-of-the-art section is based on reference 15, dealing with theoretical aspects of panel flutter, and reference 16, which is concerned primarily with the experimental aspects and theoretical-experimental correlation of the problem. Two additional general references that are of great use are reference 17, which is a survey of the literature on free vibrations of plates, and reference 18, which gives simplified criteria in graphical form for most, though not all, of those parameters which may be important for panel flutter design. Little previous knowledge of the subject is assumed on the part of the reader of reference 18, and the

premise is that no panel shall be permitted to experience flutter; however, reference 18 provides no method for the inclusion of boundary layer effects, for handling orthotropy and damping, or for handling pressurized or buckled panels accurately.

Some background knowledge of the physical nature of the panel-flutter problem is useful for assessing the state of the art. The flutter boundary is commonly defined as the variation with Mach number of the dynamic pressure at which the onset of panel flutter begins (refs. 19 to 22). Below the flutter boundary, random oscillations of the panel occur which have predominant frequency components near the panel's lower natural frequencies. These oscillations are the panel response to pressure fluctuations in the turbulent boundary layer (i.e., "noise"). The amplitudes of the oscillations are normally some small fraction of the panel thickness. As the flutter boundary is exceeded at some critical dynamic pressure, called the flutter dynamic pressure, q_f, the oscillation becomes nearly sinusoidal with an amplitude that tends to increase with the dynamic pressure and approaches or exceeds the plate thickness. One major limitation of the present state of the art is the lack of data covering an extensive range of dynamic pressure, q, greater than q_f particularly at supersonic speeds. However, limited data of this type have been obtained for S-IVB type panels (ref. 23).

Flutter onset is more a matter of definition than it is some point which can be determined with great precision. Using the best available techniques, the onset can be estimated within about 10 percent of the dynamic pressure (ref. 21). There has been some effort to obtain a more precise experimental determination of the flutter boundary by using admittance techniques and the concept of a linear plate impedance (ref. 24).

The behavior of panels after flutter onset is largely dominated by system nonlinearities, the most prominent of which is the nonlinear structural coupling between bending and stretching of the plate. The plate stretches as it bends, thereby inducing a tension in the plate. Limited-amplitude, post-flutter onset oscillation results from a balance between the (unstable) linear-plate and fluid forces and this tension force, which increases the effective plate stiffness. Qualitative estimates of the flutter amplitude that account for this balance can be made by order-of-magnitude considerations (ref. 25).

Not a great deal of study has been directed toward flutter failure mechanisms; however, at least two are readily identifiable and have occurred in practice. If the flutter-induced stress level exceeds the yield stress of the plate material, then catastrophic or rapid failure occurs; on the other hand, even a relatively low stress level stemming from a sustained period of flutter can induce fatigue or long-term failure. Fatigue life can be estimated if the stress level and frequency of the oscillation are known. Current analytical methods are inadequate for predicting failure mechanisms; hence, wind tunnel or flight flutter tests must be conducted for this purpose.

Current practice is to design a panel to avoid any flutter. However, should flutter occur during developmental testing or flight operation, the designer has, on occasion, exercised the option of demonstrating that flutter is nondestructive rather than redesigning the panel. This approach is normally only attempted for short-lived, nonreusable operational vehicles.

2.1 Consideration of Flutter in Panel Design

Conventional practice in the initial structural design of panels has been to design each panel to withstand the steady and dynamic load environments it is expected to encounter with little or no consideration given to a possible panel-flutter instability. However, certain rules-of-thumb have been developed which lead to increased resistance to panel flutter without the necessity of detailed analysis or testing.

2.1.1 Flutter-resistant design.—Minimum-gage panels are particularly flutter-prone. Conversely, panels designed to withstand large static (e.g., compressive, lateral) or dynamic (e.g., acoustic, bending) loads are apt to be so thick that flutter is not likely to occur. Because of the many possible panel configurations, general guidelines to flutter-resistant panel design have not been well documented in the literature. Nevertheless, the following guidelines for flutter-resistant design have emerged:

- Align short edges of rectangular panels parallel to the airflow, and stiffeners in stiffened panels also parallel to the flow, and where feasible, provide extra stiffening of edge supports perpendicular to the panel stiffeners.
- Avoid designs having closely spaced natural frequencies, or natural frequencies which are abnormally sensitive to any parameter.
- Where panel configurations cause flutter behavior that is sensitive to structural damping or geometrical imperfections, make design changes to eliminate this sensitivity. (Normally, such changes involve the separation of closely spaced natural frequencies.)
- Panel curvature perpendicular to the direction of airflow is beneficial, but curvature in the same direction as the flow is to be avoided.
- In order to avoid destabilizing loads, design panels for compressive loads to have the loading in the spanwise rather than streamwise direction.

2.1.2 Flutter margins and conservative assumption.—Generally speaking, the ability to predict panel flutter by experimental and theoretical means has improved greatly in the past ten years. However, there are still panel configurations, loadings, and flow conditions for which the understanding of and ability to predict panel flutter are lacking. Hence, the current practice is to use conservative assumptions for panel or flow parameters to ensure an adequate panel design. In addition, a margin on flutter dynamic pressure is often specified to allow for the uncertainty in some instances as to what constitutes a conservative assumption (i.e., an assumption which leads to the prediction of a lower flutter dynamic pressure than that encountered in practice). By tradition, and also on the basis of the differences observed between the results of theory and experiment, a margin of 50 percent on flutter dynamic pressure is frequently used.

An overly conservative assumption or several moderately conservative assumptions which have a cumulative effect, may result in an excessively thick (hence, heavy) structure. The designer has several alternatives to avoid an excessive weight penalty. First, he may make basic changes in the panel design that will result in flutter resistance with no weight penalty. This is usually impossible because conventional practice is to design the basic structural configuration initially on the basis of other load conditions.

Secondly, the designer may use more accurate (but usually more complicated) methods to estimate the flutter dynamic pressure and hence reduce the uncertainty and conservatism in the determination of flutter dynamic pressure, due to overly conservative assumptions. This is frequently done and leads to a hierarchy of methods ranging from theoretical analyses to wind-tunnel model testing to flight testing of the full-scale structure.

Lastly, if it has become clear from flight test data that flutter does occur, but that it may not be damaging, the designer, rather than redesign the vehicle, may attempt to demonstrate that such flutter does not compromise the integrity of the vehicle or its mission. This demonstration requires the determination of the flutter dynamic pressure and the panel amplitude and frequency in the flutter regime (i.e., beyond the flutter boundary), so that a fatigue or failure analysis can be made to assess the damage potential of the flutter. Such a demonstration has occasionally been made on short-lived, nonreusable vehicles. The potential damage may take the form of excessive noise or excessive vibration, as well as structural fatigue. No generally agreed upon margins for these types of damage have been developed.

2.1.3 Panel flutter prediction in preliminary design.—Many designers predict panel flutter boundaries in preliminary design through the use of design charts based upon theoretical and experimental data for certain panel configurations and flow conditions. In addition to reference 18, which contains such design charts, special mention should be made of references 26 to 28.

Reference 26 contains empirical and theoretical results for flat, rectangular panels under compressive loads in terms of flutter dynamic pressure (at high Mach number) versus panel length/width ratio. Equivalent length/width ratios for orthotropic panels (panels with different but constant stiffness in two directions) are given in terms of isotropic panels (panels with same stiffness in all directions). Although the limitations of these results with respect to Mach number and unknown variations in test conditions are now well appreciated, this document continues to be widely used.

Reference 27 provides additional data of the type presented in reference 26 and also presents a discussion of the accuracy and usefulness of such data.

Design charts are developed in reference 28 for rectangular, isotropic panels (again at high Mach numbers) on the verge of buckling (a critical design condition) using theoretical methods. Correlations with a limited quantity of experimental data are offered to support the theoretical results. A limitation of the theoretical methods is the necessity of specifying the structural damping of the panel. Also, caution is required in applying the results of references 18 and 26 to 28 at low supersonic-transonic Mach numbers and for pressurized or buckled panels where the simplified nondimensional correlating parameters used in these references are inadequate.

Nevertheless, results such as those given in references 18 and 26 to 28 are useful for preliminary evaluation of panel flutter if one keeps in mind the limitations of the data and approaches. These sources are frequently used to make an initial assessment of all panels in an effort to identify those which require more detailed study. If a flutter-dynamic-pressure margin of 2 or more is indicated for some panels, these panels are often considered to pose no serious flutter problem. The number of different possible panel configurations subject to varying flow conditions usually make a comprehensive study of each configuration impossible. Hence some simple screening method such as that just described must be used to identify those panels most likely to encounter flutter so that the design effort can be most effectively expended.

2.2 Panel Flutter Analysis

It is essential to examine the structural and aerodynamic parameters systematically and assess their relative importance to, and our present ability to predict their effect on, panel flutter. Parameters in the former category characterize the mass, stiffness, and damping of the panel or, alternatively, the modal mass, natural frequencies, and damping of the structure; parameters in the latter category describe the nature of the flow (e.g., subsonic or supersonic Mach number, mass density, and dynamic pressure).

2.2.1 Structural parameters.—The importance of the structural parameters for any specific panel flutter analysis can be assessed by noting their effect on the panel's natural frequencies. The ability to determine accurately the effect of these parameters on flutter can be measured by the accuracy with which the natural frequencies of the panel can be predicted. The effect of the structural parameters on the panel's natural modes and frequencies can be determined either theoretically or experimentally. Normally, the most efficient procedure is to use theoretical methods to as great extent as possible with occasional experimental checks to verify the accuracy of the theoretical model. Typical methods of analysis used are Rayleigh-Ritz, Galerkin, finite-difference, and finite-element methods as well as exact solutions to the structural equilibrium equations (refs. 8 to 10, 17, and 29 to 32).

The following structural parameters are adequately handled by classical linear plate or shell theory: plate thickness, modulus of elasticity, length, length-to-width ratio (refs. 19, 20, 29, and 30), acoustic cavity effect (ref. 19), orthotropy (refs. 26 and 33 to 40), and, for many cases, flexural boundary conditions (refs. 17, 38, 39, and 41) and spanwise curvature (refs. 42 to 45).

For simple isotropic panels, plate thickness, modulus of elasticity, and length are usually combined with flutter dynamic pressure into a single nondimensional parameter.

$$\lambda_f^* = 24\left(1 - v^2\right)q_f a^3 \Big/ Eh^3 \tag{1}$$

where v is the Poisson's ratio of the panel material, a is the panel span, E is the material modulus of elasticity, and h is panel thickness. For such panels, flutter is characterized by λ_f^* exceeding some critical number determined by aerodynamic parameters. For more complex panels, λ_f^* is also a function of the remaining structural parameters (refs. 15 and 16).

The simplest procedure for mathematically modeling panels with elastic supports will normally be to judge the flexibility of these supports by measuring the natural frequencies (perhaps only the fundamental panel mode) and selecting the theoretical support flexibility which will best match the measured natural frequencies. Linear structural

theory is also used to determine the effects of in-plane mechanical or thermal loads if they do not cause buckling. The degree of in-plane as well as out-of-plane support conditions is determined experimentally for such loads through a vibration test, the simplest procedure, although a buckling test can also be used.

Nonlinear structural theory is required to predict the natural frequencies of panels with loads which cause buckling, panels with curvature in the direction of flow (which will consequently have aerodynamic preloading due to their inherent geometry), or panels under pressurization (refs. 15, 26, and 46 to 48). This requirement is necessary because there are substantial changes with changes in stress in the natural frequencies of panels subjected to a significant pre-flutter static stress. Structures sensitive to geometric imperfections also require a nonlinear treatment (refs. 45 and 49). Nonlinear theory is always required to predict the limit-cycle amplitude and stresses of any panel that has penetrated into the flutter regime.

Because no reliable theory is available for predicting structural damping, it can only be determined from experiment, either by the decay or frequency-bandwidth method (ref. 9).

With regard to structural theory for orthotropic panels (an important consideration for many practical designs), the situation is somewhat complex. If a panel is truly orthotropic, then a well developed linear structural theory is available for determining the panel's natural modes and frequencies (refs. 26 and 32 to 40). The corresponding nonlinear theory, although basically understood (ref. 17), has not been applied to the panel flutter problem, and hence no capability exists for handling buckling, pressurization, or streamwise curvature of orthotropic plates. An orthotropic model of a panel is usually acceptable if the wavelength of the flutter mode (or distance between nodal lines) is large compared to the distance between stiffeners or other discontinuities.

If an orthotropic model is inappropriate, the only recourse is to use a more complicated model which treats the structure in terms of its individual components.

Finite-element, finite-difference, or component mode methods may be used for analyzing these more complicated models (refs. 8, 9, and 17). The principal criterion of success is the ability to compute the natural panel modes and frequencies accurately. For some stiffened panels the eccentricity of the stiffeners may be important to its flutter behavior. Although this parameter has been widely studied for its effect on buckling, reference 50 is one of the few which discuss its effect on flutter.

It is usually desirable to verify the theoretical predictions of frequencies and modes by measurement. If the theoretical model proves to be inaccurate, these measurements may sometimes replace the theoretically predicted natural frequencies and modes in the flutter analysis. (See section 2.4.) For some panels, the number of natural modes required for an accurate flutter analysis may be too large to measure in practice. Orthotropic panels or those with large length-to-width ratio are typical.

Finally, various types of panels can be ranked approximately in order of the precision with which theory and/or tests can predict the onset and severity of their panel flutter oscillations. This is roughly the same order in which one can accurately determine the panels' natural modes and frequencies. The main difficulty lies in predicting panel stiffness, and perhaps the most difficult parameters to evaluate are (1) variable stiffness (e.g., orthotropy or determination of equivalent orthotropy of built-up panels); (2) the effective stiffness of buckled plates; (3) curvature; and (4) panel boundary support conditions particularly for variable-stiffness, loaded plates whose stiffness may be sensitive to support conditions.

An approximate ranking of various panel types in order of their increasing difficulty of prediction of panel flutter onset and severity is given in the following listing. In constructing this list we distinguish between geometric factors and types of panel loadings.

- Geometric Factors
  - (a) Flat, isotropic panels
  - (b) Flat, orthotropic panels
  - (c) Flat, stringer-stiffened panels
  - (d) Isotropic panels with spanwise curvature
  - (e) Isotropic panels with streamwise curvature

- Loadings
  - (a) In-plane loads below buckling

      (b)   Pressurization

      (c)   In-plane loads beyond buckling

    Nonlinear flutter theory is required to determine the panel flutter boundary for isotropic panels with streamwise curvature or panels under pressurization or under compressive loads beyond the buckling load, and to determine such panels' natural modes and frequencies. Nonlinear flutter theory is also required for any panel geometry or loading to calculate flutter stress levels and frequencies. Nonrectangular planform shapes will offer analytical difficulty with some theoretical methods (e.g., Rayleigh-Ritz or Galerkin); however, the accuracy of the basic theory normally is not affected significantly.

    2.2.2 Aerodynamic parameters.—There has been almost exclusive reliance on theoretical methods to evaluate the aerodynamic parameters and assess their effect on panel flutter. Attempts have been made to evaluate aerodynamic theory by measuring aerodynamic pressures over rigid, sinusoidally deformed surfaces and also over oscillating panels, for comparison with theory (e.g., ref. 51). These measurements, and the construction of accurate models, have proven to be quite difficult. The experiments nevertheless appear to have yielded limited verification of the aerodynamic theory or, at least, they have not invalidated it. Confidence in the theory is based largely upon airfoil experience and the indirect evidence of flutter results; the aerodynamic theory appears basically sound.

    There are essentially three levels of aerodynamic theory, available: (1) a quasi-steady, two-dimensional or "piston" theory appropriate to high supersonic Mach number (refs. 29 and 30); (2) an unsteady (linearized, inviscid) theory (refs. 48, 52, and 53) appropriate from zero up to high supersonic Mach number; and (3) an unsteady, shear-flow theory which accounts for the variable, mean-velocity profile due to boundary-layer effects (ref. 54). The last theory is generally most needed at transonic to low supersonic Mach numbers or when there are thick boundary layers. The first theory is the simplest but also has the smallest range of applicability and hence is the least accurate. The second and third theories offer systematic improvements and include the first or first and second as special cases.

    For very high Mach numbers or relatively blunt vehicle configurations, one must use the aerodynamic variables (e.g., Mach number, etc.) appropriate to the local flow field over the panel, which may be substantially different from the free-stream values. The important aerodynamic parameters are generally the local values of Mach number, dynamic pressure, and density, the in-plane flow angularity, and for some flow conditions the boundary-layer velocity profile and thickness.

    The aerodynamic theory in any of its several forms is most reliable at high supersonic Mach number and when the boundary layer is so thin that it may be neglected. For such flow conditions, the quasi-steady, two-dimensional aerodynamic theory is quite accurate. As the Mach number decreases to 2 or less, the quasi-steady or piston-theory analysis no longer accurately predicts the aerodynamic forces on an oscillating plate for the following reasons: (1) the three-dimensionality of the flow field becomes important when $(M^2-1)^{1/2}$ times the panel aspect ratio is less than 1, and (2) the unsteadiness of the flow field gives rise to significant phase shifts between aerodynamic force and panel deformation, which can be accurately described only by a fully unsteady theory. Such phase shifts may give rise to negative aerodynamic damping in a given panel mode, which in turn leads to an instability in that mode. This so-called single-degree-of-freedom instability, which usually only occurs for $M < \sqrt{2}$, is more sensitive to various parameters than the flutter which occurs at a higher Mach number.

    In particular, structural damping or boundary layer effects tend to provide positive damping to offset or diminish the negative aerodynamic damping and may result in substantial increases in the dynamic pressure at which flutter occurs. For high-Machnumber, coalescent flutter (typically a coupling of two panel modes by the in-phase aerodynamic forces leading to a merging or coalescing of two panel modal frequencies), these parameters are much less important. Some authors (refs. 55 and 56) have suggested that quasi-steady, two-dimensional theory may be used for $M \geq 1.6$ for all length-to-width-ratios, *a/b*, and for $M \geq 1.3$ if $a/b \geq 2$. These conclusions were based on analytical and experimental results for panels with all edges restrained.

    As for boundary layer effects, recent theoretical advances (ref. 54) show considerable promise and give results in reasonable agreement with the best available experimental data (refs. 21 and 22). Because of the newness of this complex theory, it has not been used extensively.

When "piston theory" or quasi-steady, two-dimensional theory is applicable, the Mach number may be incorporated into a non-dimensional flutter parameter, $\lambda \equiv \lambda_f^* / M$ or $\lambda \equiv \lambda_f^* / \left(M^2 - 1\right)^{1/2}$ (see refs. 15 and 16 and sec. 2.2.1).

2.2.3 Assessment of panel flutter theory.—In summary, linear flutter theory is useful and may be employed with confidence for determining the flutter stability boundary for unbuckled, unpressurized panels which undergo rapidly destructive flutter and which have no streamwise curvature or significant boundary layer effects. This assessment applies if the structural theory that is used adequately describes the natural modes and frequencies of the panel. Linear theory for these conditions has been verified by comparison with experiment (see section 2.4).

Nonlinear flutter theory has been developed to the extent that it is now practical to use to account for the parameters of buckling, pressurization, and streamwise curvature. This also has been verified by comparison with experiment although such comparisons are less extensive than those available for the verification of linear theory. The nonlinear theory may also be used to determine flutter amplitudes, stresses, and frequencies from which the severity of the flutter oscillation may be evaluated (e.g., prediction of fatigue life). Unfortunately, no systematic experimental data are available to assess the quantitative validity of the theory in this regard. Available experimental data are only adequate for qualitative comparisons of results and to that limited extent show agreement with theory.

There are a number of different mathematical techniques available for use in flutter analysis. Among these are modal analyses (Galerkin or Rayleigh-Ritz), finite-difference, finite-element, and Laplace transform methods and also so-called "exact solutions" which utilize the method of separation of variables and the classical exponential-factor method for solving ordinary differential equations with constant coefficients. All of these methods have been employed successfully for linear flutter analysis using "piston-theory" aerodynamics. Modal and Laplace transform methods have been used with the full linearized potential-flow aerodynamic theory and, in principle, the finite-difference and finite-element methods could be used as well, though to date they have not. Only the modal method has been used with the boundary-layer aerodynamic theory. Also, only the modal method has been used with a nonlinear structural theory, although, again, the finite-difference and finite-element methods could also be used.

The linear panel-flutter problem is usually treated by determining the complex eigenvalues (i.e., complex frequencies whose negative imaginary parts indicate flutter) as a function of dynamic pressure. For nonlinear flutter analyses, time histories of the limited amplitude motion are normally calculated. Reference 15 discusses the advantages and disadvantages of these mathematical methods in greater detail.

Aerodynamic theory is generally accurate, with the possible exception of accounting for boundary layer effects. Recent advances in the aerodynamic theory to account for boundary layer effects suggest that this may soon be in hand; however, verification of the theory by additional comparisons with experimental data is still needed. At present, the use of experimental flutter data is the most accurate means of predicting or assessing boundary layer effects. In terms of increasing complexity, high-Mach-number flows are the simplest, low supersonic-transonic flows are more difficult, and flows with significant boundary layer effects (usually in the transonic regime) are the most difficult of all to handle theoretically.

Few mathematical methods for determining the aerodynamic pressures on a fluttering panel are available. An analytical expression for pressure is known as "piston theory" or quasi-steady, two-dimensional theory. The "Mach Box" method and also Laplace and Fourier transform methods have been used for the linearized inviscid aerodynamic theory. Only the Fourier transform combined with a finite-difference approach has been used for boundary layer effects (see refs. 15 and 54 for details).

2.3 Panel Flutter Tests

Vibration testing of panels to determine modes and frequencies is valuable for assessing the adequacy or accuracy of the structural theory used in flutter analyses, and it is essential on new panel configurations for which no previous experience exists. Such testing frequently provides useful information for evaluating the theoretical model; that is, the test results (modes and frequencies) can be used to determine how well the stiffness of the theoretical model simulates the stiffness of the real panel.

Wind-tunnel and flight-panel flutter testing are very valuable, but unfortunately, very expensive. It may be impossible to scale all of the significant parameters in a given wind tunnel facility if a panel design is substantially affected by a large number of parameters. Hence, partially scaled tests may be necessary, with theory used to assess the effect of the unscaled parameters.

2.3.1 Wind-tunnel panel-flutter testing.—Wind-tunnel flutter testing is essential to evaluate boundary layer effects and to determine amplitudes, stresses, and frequency of the flutter oscillation. High-Mach-number flows are the most difficult to simulate properly because of the high temperatures and low dynamic pressures that accompany such flows in most wind tunnels. Early flutter experiments (pre-1963) lacked adequate control or failed to measure all important parameters to be simulated. Even today great care must be exercised in order to perform meaningful tests. Because full-scale panels can frequently be mounted in a wind tunnel and because panel flutter frequently does not result in major structural failure, there has been a tendency to make greater use of wind tunnel tests of flight hardware panels as proof tests rather than to use flight tests for this purpose.

The success of a wind-tunnel flutter test is largely determined before the test specimen is placed in the tunnel. The first step, and often the most difficult, is the construction of the panel models and their boundary support without inducing significant prestresses. Experience has shown that bench vibration tests to determine panel natural frequencies and modes are excellent indicators of the quality of panel construction and support simulation. Conventional practice is to use acoustic excitation for vibration tests and to measure structural responses with strain gages and capacitance or inductance-deflection transducers.

Normally, the next step is to determine the sensitivity of the model to environmental factors, particularly static pressure loadings and thermal stresses due to a temperature differential between the model and its support. Changes in material modulus of elasticity at very high temperatures may also be significant. These effects may require considerable effort to control and measure in the wind tunnel. Hence, the sensitivity of the panel to these factors is usually determined early in the experimental program by bench vibration tests prior to wind tunnel test.

Another concern may be the dynamics of the air in an enclosed cavity beneath the plate (acoustic cavity). However, available theory may be used to establish a cavity size which will ensure a valid test simulation (refs. 19 and 57).

Next, an appropriate wind tunnel is chosen. In practice, the choice is often rather limited. A wind tunnel with the appropriate Mach number range (usually supersonic), of size sufficient to avoid aerodynamic wall interference on the panel, with adequate dynamic pressure range and with good control over tunnel temperature is desired.

Two techniques have been used for mounting the panel in the wind tunnel: (1) wall mount; and (2) splitter plate. Generally, the former is more desirable because of easier access to the model, though its use may be impractical in some tunnels.

Instrumentation is chosen so that the temperature of the panel model and support, pressure differential across the model, and plate deflection, strain, and frequency can be measured (e.g., thermocouples, pressure transducers, strain gages, and capacitance or inductance-deflection transducers). Lightweight, if possible noncontacting, instrumentation is used which will not alter the dynamic characteristics of the plate nor disturb the aerodynamic flow.

Once the model is installed in the tunnel, the test is then normally carried out by increasing dynamic pressure while holding a fixed Mach number. Other experimental techniques have been employed, however. Some experimenters (ref. 58) have varied the Mach number while holding the stagnation pressure constant. Others (ref. 59) have penetrated the flutter regime at constant stagnation pressure by heating the panel to induce compressive thermal stresses which decrease the plate stiffness. In the latter investigations, blowdown wind tunnels were employed. Changing stagnation pressure in precise steps in these tunnels is impractical. Although the use of a blowdown tunnel is feasible, it is difficult to determine and control the plate environment, particularly with regard to thermal stresses and static pressure loading.

When extrapolating from existing data to predict flutter on new panel designs, or when planning an experimental program, it is important to consider the appropriate scaling laws. Because it is frequently possible to test a geometrically full-scale panel in a wind tunnel, there is sometimes an unfortunate and unfounded belief that complete full-scale simulation has been achieved. This is rarely the case. Usually thermal stresses, pressurization loads, flow density, boundary layer, and/or other parameters can not all be correctly scaled. Hence, one must rely upon theory to assess the effects of some of these variables or sacrifice the full-scale geometry to help scale other variables correctly. A valuable general discussion of these problems which is applicable to panel flutter is given in reference 60.

If the effect of some parameter is thought to be well understood and accurately predictable by theory, it has proven to be wise to sacrifice proper scaling of that parameter in a test, if necessary, to obtain a more nearly true scaling for some other parameter which is not as well understood. References 16 and 19 to 22 should be consulted for detailed discussions of testing techniques.

2.3.2 Flight flutter testing.—Relatively few flight tests have been made solely for panel flutter. Generally, panels have been instrumented with strain gages or accelerometers to check for panel vibration response whether due to flutter or other causes. The difficulties of flight test beyond those of wind-tunnel test are largely those of data retrieval from a remote source and the associated telemetry problems (ref. 9). No adequate documentation of flight-test technique is available in the open literature; however, discussion of flight test results are available in references 61 to 63 for the X-15, S-IVB, and Atlas Centaur panels. The pre-flight test preparation is substantially the same as that for pre-wind tunnel test. It should be pointed out that flight flutter tests can only determine whether flutter occurs within the flight envelope but cannot demonstrate that the desired flutter margin has been achieved.

2.4 Correlation of Analytical and Test Results

Comparisons of results obtained from theoretical analyses with results from flutter tests for various panels help to demonstrate the capabilities and limitations of both theory and tests and give insight into the confidence with which present state-of-the-art techniques can determine panel-flutter boundaries and the nature of panel flutter. Reference 16 presents extensive correlation between theory and experiment for certain typical classes of panel geometries and loading conditions. These are listed and the results summarized in the following paragraphs. Also summarized are additional comparisons for buckled plates (refs. 64 and 65), for cylindrical shells (ref. 66), conical shells (ref. 67), orthotropic panels (ref. 39), and boundary layer effects (ref. 54).

Flat plates.—In general, linear structural theory coupled with an aerodynamic theory chosen to fit the Mach number range and including cavity effects, where applicable, agrees well with experiment in the determination of the flutter boundary (refs. 19, 21, 22, and 56). A possible exception is the effect of a fluid boundary layer, although limited experimental-theoretical correlations are encouraging (ref. 54).

Flat plates under static pressure loads.—A flat plate exposed to a transverse pressure load undergoes a static deformation in its middle surface, causing membrane stresses and associated stretching which induce middle surface curvature and a change in natural frequencies. These changes can be determined by nonlinear structural theory. Reasonable agreement between theory and experiment, both for natural frequencies and prediction of the flutter boundary, has been obtained by assuming zero in-plane edge restraint, which is probably typical for flat panels of practical construction (ref. 41).

Flat plates under compressive in-plane loads.—In general, reasonable agreement between theory and experiment for the flutter boundary has been obtained by at least two methods. In the first, nonlinear structural theory (nonlinear stiffness) is used with quasi-steady aerodynamic theory appropriate for the high Mach number of the tests and the assumption of values of in-plane edge restraint inferred from the measured static Euler buckling load (ref. 41). In the second method, a linear-plate structural theory is combined with quasi-steady aerodynamic theory and an appropriate model of structural damping (ref. 20, 64, and 65). See references 20 and 68 for a discussion of pressurized, buckled plates. It should be mentioned that the available comparisons between theory and experiment apply to a limited range of panel geometries and types.

Orthotropic panels.—The comparisons of theory and experiment shown in reference 39 are typical of much recent work on orthotropic panels. In general, satisfactory agreement between theory and experiment appears feasible, provided careful attention is paid to items such as panel boundary conditions and determination of natural modes and frequencies. The boundary conditions are important because many practical orthotropic panels have significant support flexibility along edges perpendicular to the direction of largest stiffness. Accurate mode shapes and frequencies for complicated built-up panels typical of orthotropic panels must often be determined by careful experimental measurements (ref. 5) to obtain sufficient accuracy for panel flutter analysis that correlates well with flutter test results. In more recent work on stressed orthotropic plates (ref. 33), it has been found that flutter theory and experiment are not in satisfactory agreement, and it has been suggested that structural damping should be

included in the analysis to resolve the discrepancy. It has been determined that, generally, the direction of maximum stiffness should be aligned with the direction of airflow to obtain the largest flutter dynamic pressure.

Curved plates.—For the limited data available for which comparisons have been made (curvature in the flow direction) there are several quantitative discrepancies between theory and experiment (refs. 25 and 69); however, the qualitative (trend) shapes of the flutter boundaries from theory and experiment are in reasonable agreement. It is felt that the chief sources of the discrepancies were that the very thin plates tested (h = 0.008 in.) were sensitive to manufacturing imperfections and possibly thermal stresses and that the in-plane edge supports had unaccounted-for flexibility that affected the curved panel.

Cylindrical and conical shells.—The correlation between theory and experiment regarding cylindrical and conical shells presents a rather confused picture. A number of comparisons have been made using various types of aerodynamic and structural theories and, in general, the agreement of theory with experiment at low supersonic Mach number has been poor, with some theoretical values for dynamic pressure substantially higher than those obtained experimentally for the flutter boundary, while other theory yields lower values (ref. 70). At high Mach number $M \simeq 3$, theory and limited test data agree fairly well for unpressurized shells (refs. 71 to 73). It has been shown theoretically that cylindrical panels are sensitive to small imperfections on the order of the shell thickness which change the flutter characteristics of these panels in a manner which may account for some of the differences between theory and experiment for pressurized shells (ref. 45). For one recent study (ref. 66), the results indicate that linear shell theory used with quasi-steady, two-dimensional aerodynamics is satisfactory for predicting flutter onset, but nonlinear theory is required to predict accurately the flutter mode and frequency (see also ref. 74). Only quasi-steady aerodynamic theory has been used in flutter analyses to date for comparison with experiment, although a more accurate aerodynamic theory is available (refs. 75 to 78). Limited experimental flutter data have been obtained for a pressurized conical shell at high Mach number, and comparison with theory gives results similar to those for a cylindrical shell (ref. 67). Very recent experiments have suggested the importance of the fluid boundary layer in determining whether the flutter is catastrophically destructive or of a limited-amplitude, nondestructive type (ref. 79).

Systematic, unclassified experimental flutter data which may be correlated with theory do not exist for edge conditions, planform geometry, cavity effect, structural damping, geometric imperfections, angle-of-flow, multibay panels, or post-flutter stress amplitudes. Edge conditions and planform geometry effects should be adequately described theoretically if their effect on panel natural modes and frequencies can be predicted. The cavity effect is thought to be adequately handled by theory on the basis of theoretical prediction of measured panel/cavity natural frequencies (ref. 19). If measured values of structural damping and/or geometric imperfections are used, then flutter theory is probably reliable at least for qualitative trend studies. On physical grounds, the angle-of-flow effect should be adequately handled by flutter theory (ref. 36) if an appropriate aerodynamic analysis is employed. Multibay effects are not likely to be important but the flutter theory for multibay effects (refs. 80 to 82) should be fundamentally neither more nor less reliable than for a single isolated panel. The quantitative accuracy of nonlinear flutter theory for predicting post-flutter stress amplitudes remains an open question in the absence of adequate experimental data.

3. Criteria

The panels of space vehicles which are exposed to a flow shall be designed to be free of flutter at all dynamic pressures up to 1.5 times the local dynamic pressure expected to be encountered at any Mach number within the normal operating flight envelope and during aborts from normal operating conditions. Flutter of limited amplitude and short duration, occurring during flight on panels of a nonreusable space vehicle, shall not necessitate redesign if it can be demonstrated that no fatigue failure of any structural panels, no functional failure of equipment, and no excessive noise levels in compartments near a fluttering panel will occur during the vehicle mission lifetime. Adequacy of the space vehicle panels with respect to these criteria shall be demonstrated by a suitable combination of analysis and tests.

3.1 Analyses and Model Tests

Analysis shall be considered adequate for predicting the onset of panel flutter as defined by dynamic-pressure flutter boundaries if: (1) the structural portion of the analysis adequately predicts the panel's natural modes and frequencies under anticipated critical environmental conditions, and (2) an aerodynamic theory appropriate to the relevant Mach number range and panel geometry is employed. Conservative assumptions shall be employed for any structural or aerodynamic parameter where precise knowledge concerning its magnitude or effect is unavailable. When flutter boundaries are determined solely or partially by wind tunnel test, as far as possible, all significant flight parameters shall be conservatively simulated by the model and the wind tunnel. If no previous experience exists for a given panel type, natural modes and frequencies under anticipated critical environmental conditions, including thermal, mechanical, and pressure loads, shall be determined by vibration tests before flutter analyses or flutter tests are undertaken.

Analyses and/or model tests shall account for the effects of at least the following factors:

- Mass, damping, and stiffness of the panel
- Local Mach number
- Local dynamic pressure
- Local density
- In-plane flow angularity
- Boundary layer profile and thickness (where applicable)

Simulation of panel stiffness shall include the effects of at least the following factors:

- Panel thickness, length, and material modulus
- Length-to-width ratio
- Edge conditions (in-plane and out-of-plane, as required)
- Curvature
- Orthotropy
- Thermally induced and mechanically applied in-plane loads
- Static pressure differential across the panel
- Acoustic cavity beneath the panel

Where previous analytical or test data exist for panels of similar structural configuration and edge support conditions in a similar environment, such data shall be acceptable in lieu of further tests.

3.2 Flight Tests

During developmental flight tests, instrumentation for detecting panel flutter shall be installed on flutter-critical panels of one or more vehicles. For panels for which a verification of ability to withstand nondestructive, limited-amplitude flutter is desired, the instrumentation shall be sufficient to determine clearance with other equipment, maximum stress amplitudes, and frequencies of vibration.

3.3 Nondestructive, Limited-Amplitude Flutter

When on a nonreusable space vehicle, flutter of limited amplitude and short duration is thought to have occurred and verification of ability to withstand the flutter is desired in lieu of redesign, the following procedure shall be utilized. Amplitudes and frequencies of suspected nondestructive, limited-amplitude flutter shall be determined by wind tunnel or flight flutter test unless it can be shown that theory can be used to adequately interpolate

or extrapolate existing test data. The data thus obtained shall be utilized to establish that the limited-amplitude flutter is nondestructive in that, for each case, chosen margins exist on fatigue life, noise levels, and vibration amplitudes and frequencies of the fluttering panel.

4. Recommended Practices

The design goal with respect to panel flutter should be to prevent flutter from occurring while using the lightest possible structure that will withstand the expected load and other environments. The general recommended procedure is to utilize, in initial design, good design practices for flutter-resistant panels. Because of the many possible panel configurations, however, it is difficult to provide general guidelines for flutter-resistant design. Nevertheless, some good practices have emerged. Examples are as follows:

- Short edges of rectangular panels should be aligned parallel to the airflow.
- Stiffeners should be aligned parallel to the airflow and extra stiffening of edge supports perpendicular to the panel stiffeners should be provided, if possible.
- Panel designs with closely spaced natural frequencies or whose natural frequencies are abnormally sensitive to any parameter, should be avoided.
- Serious consideration should be given to changing panel designs to eliminate flutter behavior that is sensitive to structural damping or geometric imperfections. This normally implies design changes that will separate closely spaced natural frequencies.
- Panel curvature perpendicular to the direction of the airflow, as opposed to the same direction as the flow, should be incorporated in the design.
- Spanwise rather than streamwise loading should be directed for panels under compressive loading, since loads in the streamwise direction are destabilizing.

The panel design should be checked for panel-flutter susceptibility by use of design charts, where applicable, such as those contained in references 18, 27, and 28. For these panels whose flutter margins fall below a factor of 2 on dynamic pressure, this check should be supplemented by a systematic flutter investigation (section 4.1), utilizing an efficient combination of analysis and model tests to determine the flutter margin.

Under conditions of known sensitivity or high uncertainty relative to the state of the art, good judgment may require a systematic flutter investigation for panels having margins of 2 or larger as determined by design charts. Note that there is no assurance that use of the data of references 18, 27, and 28 will provide a conservative estimate of the possible occurrence of flutter. Hence, considerable judgment is required in assessing the results obtained from such sources for a given panel design. If flutter is still predicted after the systematic flutter investigation, the design should be modified and the analysis and model tests of the modified design iterated until the panel-flutter behavior meets the criteria of section 3.

4.1 Analyses and Model Tests

The first step in a systematic flutter evaluation should be to determine by analysis or test the natural modes and frequencies of the panel, including the significant effects of likely design variations of thickness, material modulus, length, length-to-width ratio, edge conditions, thermally induced and mechanically applied in-plane loads, static pressure differential, curvature, orthotropy, and acoustic cavity beneath the plate. Secondly, the panel's flutter dynamic pressure should be determined from theory using an appropriate aerodynamic model and local aerodynamic flow parameters.

If the theoretical result, using an initial choice of conservative estimates of the structural stiffness parameters (or equivalently, the panel's natural modes and frequencies) and aerodynamic parameters, indicates that flutter will exist for dynamic pressures less than 1.5 times the maximum expected dynamic pressure at any Mach number within the

flight envelope, then a systematic effort should be made to improve the accuracy of the analysis by removing some of the conservative assumptions in order to establish the required flutter margin. A conservative assumption is defined as one that results in the prediction of a lower dynamic pressure for destructive flutter or a higher stress level (for a given dynamic pressure) for limited-amplitude, nondestructive flutter. Unconservative assumptions should be avoided.

If the analysis still fails to establish the required margin, then such a margin should be established by wind tunnel test, or the panel should be redesigned.

For panels with flutter margins not adequately established by design charts, the simplest type of analysis or test that will verify that the panel satisfies the design critieria should be used. Specific conservative (and simplifying) assumptions derived from references 1 to 89 are summarized in table I (appendix) for structural parameters and in table II (appendix) for aerodynamic parameters.

The parameters presented in tables I and II are accompanied by pertinent comments concerning their relative importance and means of evaluating their effect on flutter, recommendations for conservative, simplifying assumptions, and citations of the most valuable references containing information with respect to each parameter.

Theoretical flutter analyses should be made employing conservative assumptions for all parameters as recommended in tables I and II. References 15, 16, 29, 30, and 52 should be consulted for their general recommendations on theoretical methods and references 16 and 19 to 22 for their recommendations on experimental methods. Good judgment is required in balancing the gain in simplicity of analysis or test for a given conservative assumption versus the loss in predicted flutter margin.

Prior to model flutter tests, principal normal modes and frequencies of the panel should be determined by vibration tests. The flutter tests should be planned to simulate accurately but conservatively all structural parameters determined to be significant for panel natural modes and frequencies as well as the aerodynamic parameters, dynamic pressure, flow Mach number, and flow density (where the latter is determined to be important). Furthermore, if boundary layer effects are used to obtain the flutter margin, boundary layer profile and thickness also should be accurately but conservatively simulated.

If simulating all important parameters proves impossible, careful attention should be given to identifying and simulating those parameters for which theory is known to be inaccurate for a particular panel configuration. The simulated conditions should be at least as severe as the anticipated operating conditions. Whenever possible, a continuous-flow rather than a blowdown wind tunnel should be used to obtain better control over environmental factors such as temperature, static pressure differential, etc. For the remaining unsimulated parameters, theory should be used to interpolate or extrapolate the flutter test results.

If it is determined by wind tunnel test that flutter occurs at dynamic pressures below the required flutter margin, then the design should be altered to prevent flutter (e.g., panel thickness should be increased). The previous design process should be repeated until an adequate flutter margin is established by analyses or tests, including a substantial effort to resolve any discrepancy between test and analysis.

4.1.1 Structural Parameters

Where prior experience or the use of table I and the references cited therein do not provide a basis for judging a particular structural parameter's importance to panel flutter, the importance of the parameter should be assessed by evaluating its effect on panel natural modes and frequencies. If a parameter has a small effect on the natural modes and frequencies, then it can normally be neglected as far as flutter is concerned.

Where feasible, the accuracy of theoretical structural models used in the flutter analysis should be verified by vibration tests. Any of the standard methods of vibration and flutter analysis (refs. 8 to 10) are recommended, provided they accurately predict panel natural modes and frequencies for a given panel configuration. Recommended methods include Galerkin, Rayleigh-Ritz, finite-element, and finite-difference. When significant differences exist between measured and theoretical panel natural frequencies, measured values should be employed in the flutter analysis to the extent possible. If structural damping is thought to be important, it should be measured for the principal natural panel modes and incorporated into the flutter analysis or the value of damping used in the analysis should be demonstrated to be smaller than in the actual structure (ref. 9).

Normally, it will be necessary to use an analysis that models panel nonlinear stiffness (refs. 15, 47, and 48), when accounting for the effects of streamwise curvature, panel buckling, pressurization, or when predicting flutter stress amplitudes to verify the nondestructiveness of flutter (section 4.3). In-plane panel boundary supports (and hence, nonlinear stiffnesses) should be adequately simulated in flutter tests conducted to derive this information. Before wind tunnel testing, however, the degree of in-plane panel-boundary support should be verified by vibration tests of buckled panels or panels under static pressure differential.

4.1.2 Aerodynamic Parameters.—An aerodynamic theory appropriate to the Mach number and panel geometry should be used in the flutter analysis. Generally, for $M > 2$, the "piston theory" or quasi-steady, two-dimensional aerodynamic theory should be used if the effective aerodynamic aspect ratio is greater than 1 (refs. 29 and 30). A conservative estimate of the effective aspect ratio is the geometric aspect ratio multiplied by $(M^2-1)^{1/2}$, e.g., for a rectangular flat plate it is $(M^2-1)^{1/2} b/a$.

For simple panels with all edges restrained, the quasi-steady, two-dimensional theory (ignoring aerodynamic damping) may be used for $M \geq 1.6$ for all length-to-width ratios (a/b), and for $M \geq 1.3$ for $a/b \geq 2$ (refs. 55 and 56). For lower Mach numbers, the full three-dimensional, unsteady, potential flow theory (refs. 47 and 49 to 53) should be used. Even this theory may be quantitatively inaccurate if boundary layer effects are significant. Initially, it should be assumed there is no flutter stabilization due to boundary layer effects; if found necessary to demonstrate an adequate flutter margin, the boundary layer effect must be verified by flutter test. Table II lists recommended conservative assumptions for the aerodynamic parameters, and references for further study.

As far as possible, local flow conditions over the panel throughout its operating flight envelope should be adequately represented in both theoretical and experimental studies. The accuracy of representation required should be determined by reviewing table II and its listed references.

It will generally be impossible to simulate simultaneously, in a given wind tunnel, Mach number, dynamic pressure, and flow density, even if the test specimen is a full-scale panel under appropriate thermal loads, pressurization, etc. (in itself a rather unlikely circumstance). Normally, the requirement on flow density may be relaxed; however, if the mismatch between wind tunnel and flight-trajectory flow density is a factor of 3 or more, theoretical calculations should be made to assess the possible importance of the mismatch (refs. 48 and 52).

4.2 Flight Tests

The selection of panels to be instrumented in the flight test should be based on the extent to which the predicted flutter margins exceed the design criteria margins. Critical panels are those whose flutter margins have been previously established to be less than 2. Under conditions of known sensitivity or high uncertainty relative to the state of the art, the instrumentation of panels with higher margins should be considered.

Critical panels should be instrumented sufficiently to measure all significant structural and aerodynamic parameters including, where necessary, panel and support temperatures, static pressure differential, in-plane loading, Mach numbers, dynamic pressure, air density, and boundary layer thickness. The flight-test data obtained will permit correlation with ground data and the formulation of appropriate corrective action for flutter suppression or alleviation as required. The recommended flight test measurements are in addition to those required to detect the presence or absence of flutter. Flight tests using techniques such as those discussed in references 61 to 63 are recommended.

4.3 Nondestructive, Limited-Amplitude Flutter

If flutter is detected during the flight test of a short-lived, nonreusable space vehicle, the designer may choose to demonstrate that the flutter is nondestructive rather than redesign the panel. For the former alternative, nonlinear theory, if available, may be applied over a range of dynamic pressures (from the flutter dynamic pressure to 1.5 times the anticipated maximum dynamic pressure over the flight envelope) to estimate panel flutter amplitudes, stresses, and frequencies of oscillation. The theoretical model should include, where feasible, in-plane edge support

conditions (or more generally, nonlinear structural stiffnesses) which have been verified experimentally by vibration tests, buckling tests, or static pressure loading. These flutter calculations should be verified experimentally by wind tunnel or flight tests conducted to obtain panel flutter amplitudes and resulting panel stresses of a sufficient number of points over the flight envelope to establish the validity of the theoretical results. If the theoretical model is inadequate or unavailable, the preceding information should be determined experimentally either by wind tunnel or flight test at a sufficient number of additional points to permit the designer to ascertain that the structural integrity of the panel under limited-amplitude flutter is assured. These analyses and tests will normally be in addition to those previously conducted before the discovery of flutter during flight test.

Once the panel flutter stresses and frequencies of oscillation have been determined, fatigue life, vibration levels of nearby sensitive components, and noise levels should be determined by standard methods (refs. 9 and 83 to 85). At least one panel should be tested sufficiently to ensure that no failure due to any of the above means is possible under actual operating conditions.

Instrumentation should be sufficient to measure all significant structural and aerodynamic parameters including, where necessary, panel and support temperatures, static pressure differential, in-plane loading, Mach number, dynamic pressure, air density, and boundary layer thickness. The recommended flight test measurements are in addition to those required to determine clearance with other equipment, maximum-stress amplitudes, and vibration frequencies.

Appendix
Important Structural and Aerodynamic Parameters

TABLE I.—STRUCTURAL PARAMETERS

Parameter	Comments	Recommended Conservative Assumptions	References
Panel thickness	Specified for a given panel configuration; however, it is frequently the design parameter to be determined if the dynamic pressure below which flutter shall not occur is specified. For simple isotropic panels at high Mach number, flutter dynamic pressure is approximately proportional to thickness cubed.	Use smaller thickness	All, but particularly refs. 18, 27, 28
Modulus of elasticity	For simple isotropic panels, flutter dynamic pressure will be approximately proportional to modulus.	Use smaller modulus	All, but particularly refs. 18, 27, 28
Panel length	For simple isotropic panels at high Mach number, the flutter dynamic pressure will be approximately proportional to the inverse cube of length for fixed length-to-width ratio.	Use larger length	All, but particularly refs. 18, 27, 28
Panel length-to-width ratio	Easy to simulate experimentally and theory generally reliable. For $a/b < 0.1$, plate is effectively two-dimensional, $a/b \equiv 0$; for large a/b, $a/b > 10$, normalize dynamic pressure with b and extrapolate to higher a/b, assuming no significant changes with a.	Use smaller a/b for given a or larger a/b for given b	18 to 20, 27 to 30, 52, and 56
Edge conditions	Should be assessed by natural vibration tests whenever feasible; may be particularly sensitive to some combinations of other variables (e.g., loaded or stiffened plates). In-plane as well as out-of-plane boundary conditions should be considered.	Use out-of-plane boundary conditions of lesser restraint. For in-plane boundary conditions situation is somewhat more delicate; rely on theory as guide to conservative assumptions. Usually use lesser in-plane restraint.	17, 38, 39, and 41
Orthotropic or stiffened plates	A basic question is whether a given plate may be considered effectively orthotropic and how stiffness constants may be determined. Orthotropicity may make estimation of support conditions for panel edges perpendicular to greater stiffness extremely important. Plate also becomes more sensitive to angle of flow. For a plate with greater stiffness in flow direction, panel will usually behave like a panel with small a/b and for greater stiffness perpendicular to flow, like an equivalent isotropic plate with large a/b.	If large angle-of-flow variations anticipated, assume direction of greater stiffness will align perpendicular to flow.	3 to 5, 26, 33 to 40, 50, and 86

TABLE I.— (Continued)

Parameter	Comments	Recommended Conservative Assumptions	References
Orthotropic or stiffened plates (Cont.)	Theory reliable if equivalent stiffnesses and edge conditions are known or, alternatively, if natural modes and frequencies are known. Particularly careful attention to edge support modeling required for experiments. Panels which are eccentrically stiffened frequently cannot be treated as equivalent orthotropic plates.		
Pressurization	In-plane support conditions are important; measurement of natural frequencies and/or static deflection under pressure load is convenient means for assessing in-plane edge support. Theory (nonlinear) is reliable and the loading is moderately easy to simulate experimentally. May be difficult to determine the pressure load actually present	For flat plate assume zero pressure; for curved plates, assume pressure acts in opposition to curvature. Quantitative effect will be small if static deflection under load is much less than plate thickness for flat plate or rise height for curved plate	41, 47, and 68
In-plane loads	Loads may be of thermal or mechanical origin. Whenever feasible measure natural frequencies under such loads to determine effective-in-plane edge conditions (for alternative, see Pressurization); theory used for flutter determination should accurately predict natural frequencies and buckling conditions. For some panel configurations, linear theory will predict the flutter dynamic pressure to be zero. Design changes should be made to these configurations if possible. May be difficult to determine in-plane loads actually present	Ignore spanwise in-plane loads. If streamwise loads are tensile, ignore them. If compressive, assume buckling will occur. For loads substantially below buckling load, quantitative effect will be small	15, 20, 28, 41, 47, 59, and 68. Ref. 28 contains useful preliminary design charts for varying a/b, in-plane loads, edge conditions, and structural damping at high Mach number
Spanwise curvature	In-plane support conditions along the streamwise edge are extremely important; for small restraint, flutter dynamic pressure increases while for nearly rigid restraint it decreases. Limiting case of complete cylindrical shell has proven sensitive to several parameters (e.g., pressurization and geometric imperfections). Theory is qualitatively reliable; experiments will usually be required. Panels may be flutter-free to small disturbances, but not if subjected to large ones	Quantitative effect is small if rise height is only a few panel thicknesses or less. Usually conservative to ignore curvature for typical (flexible) in-plane support conditions	42 to 45 and 70 to 79
Streamwise curvature	In-plane support conditions are important as well as static aerodynamic pre-loading prior to flutter. Theory (nonlinear) is qualitatively reliable; experiments will usually be required	Quantitative effect of curvature is small if rise height is only a few panel thicknesses or less. Conservative to assume larger rise height than actual, though this may not be practical	25, 46, and 69

TABLE I.—(Concluded)

Parameter	Comments	Recommended Conservative Assumptions	References
Structural damping	Trouble is indicated if this parameter is important; configurations determined to be theoretically sensitive to structural damping will generally be sensitive to other parameters as well (e.g., boundary layer effects, pressuri-zation, and geometrical imperfections). Damping must be determined by experiment.	Assume no structural damping	9, 20, 28, 30, and 60
Odd planform geometries	Too many possibilities for specific recommendations. Consult references for some guidance	(See Comments)	9, 17 (general), 13, 14 (circular, elliptic), 87 (parallelogramic), and 88 (triangular)
Acoustic cavity	Theory very reliable in predicting effect on panel natural frequencies; hence, thought to be adequately handled by theory for flutter purposes. Simple to incorporate into modal flutter analysis	Quantitative effect small for cavity depths greater than panel length and width. Conservative to ignore cavity effect for single-degree-of-freedom flutter. Otherwise assume smaller cavity depth and use one-term acoustic model. See references	19 and 57
Multi-bay panels	Unimportant unless a large number of nearly identical panel bays; most significant in low supersonic, transonic regime	For spanwise arrays, treat as a single bay panel	80 to 82
Geometric imperfections	Only important in exceptional circumstances (e.g., cylindrical shell under loads and buckled plates). If less than one plate thickness, effect of imperfections is usually small. Will be difficult to determine imperfections actually present	For a flat plate, ignore them	45 and 49
Fatigue life	Analysis must use nonlinear theory. Experiments must penetrate into flutter regime. No systematic experimental data presently available to evaluate theory, which is in rapid state of development	Underestimate non-linear stiffness, (e.g., assume zero in-plane edge restraint for flat plates)	41, 47, 48, 83, and 85

TABLE II.—AERODYNAMIC PARAMETERS

Parameter	Comments	Recommended Conservative Assumptions	References
Dynamic pressure	Essential ingredient in any theory or test; at high M, q and M may be combined into single parameter, q/M or $q/(M^2 - 1)^{1/2}$	Use larger values, though this is not usually practical	All, but particularly refs. 18, 27, and 28
Mach number	Theory reliable if boundary layer effects are negligible; must always be simulated in tests. However, for large M, q_f proportional to M	None possible	19, 21, 22, 48 and 52
Flow density	Normally not a very sensitive parameter; sometimes becomes important at transonic, low supersonic speeds or for structures with closely spaced natural frequencies. Theory reliable; difficult to simulate experimentally	Use smaller values for a given dynamic pressure	19, 21, 22, 48, and 52
Angle of flow	Important if nominal direction of flow is aligned with direction of highest panel stiffness. Theory probably reliable though little systematic experimental data for comparison and validation. May be difficult to determine angle of flow actually present	Assume nominal direction of flow is aligned with direction of lowest panel stiffness	36 and 86
Boundary layer	Important for single-degree-of-freedom flutter at low supersonic-transonic speeds and, more generally, whenever damping forces are significant. Experiment requires careful simulation of boundary layer profile and thickness; theory under rapid development but not yet reliable for routine use. May be difficult to determine boundary layer characteristics actually present	Ignore or use thinner boundary layer	21, 22, 54, and 89

References

1. Mirowitz, L.I.; Schweiker, J.W.; and Zimmerman, N.H.: Panel Flutter Survey and Design Criteria. ATC−ARTC−32, 1962.
2. Bohon, Herman L.: Panel Flutter Tests on Full-Scale X−l 5 Lower Vertical Stabilizer at Mach Number of 3.0. NASA TN D−1385, 1962.
3. Rich, R.L.: Preliminary Skin Panel Flutter Tests. Document D2−8148, 1962. Available from the Boeing Company.
4. Mortvedt, R. L.; and Wagner, R. T.: Transonic, Supersonic Panel Flutter Test. The Boeing Company, Document D2-81095, 1964. (Available from DDC as AD 441-741)
5. Golden, C.T.; Hager, T.R.; and Sherman, L.L.: Orthotropic Panel Flutter Analysis Correlation. Document D2−81301, 1964.
6. Anon.: 624A Panel Flutter Analysis. U. S. Air Force, Space Systems Division CR-64-87, May 1964. (Available from DDC as AD 600-417)
7. Nichols, J.J.: Saturn V, S−IVB Panel Flutter Qualification Test Final Report. NASA TN D−5439, 1969.
8. Archer, J.S.: Natural Vibration Modal Analysis. NASA SP−80l2, 1968.
9. Archer, J.S.: NASA Space Vehicle Design Criteria (Structures)—Structural Vibration Prediction. NASA SP−8050, 1970.
10. NASA Space Vehicle Design Criteria (Structures). NASA SP−8003, sec. 1, 1964.
11. Fung, Y.C.B.: A Summary of the Theories and Experiments on Panel Flutter. AFOSR−TN−60−224, 1960.
12. Bolotin, Vladimir Vasil'evich: Nonconservative Problems of the Theory of Elastic Stability. MacMillan Co., New York, NY, 1963.
13. Johns, D.J.: A Survey on Panel Flutter. AGARD−AR−1, 1965.
14. Johns, D.J.: A Panel Flutter Review. AGARD Manual on Aeroelasticity, ch. 7, pt. 3, 1969.
15. Dowell, E.H.: Nonlinear Analysis of the Flutter of Plates and Shells. Fluid-Solid Interaction, American Society of Mechanical Engineers, Winter Annual Meeting, Symposium, Pittsburgh, PA, 1967.
16. Dowell, E.H.: Panel Flutter—A Review of the Aeroelastic Stability of Plates and Shells. AIAA J., vol. 8, no. 3, 1970, pp. 385–399.
17. Leissa, A.W.: Vibration of Plates. NASA SP−160, 1969.
18. Lemley, C.E.: Design Criteria for the Prediction of Panel Flutter. AFFDL−TR−67−140, vols. I and II, 1968. Available from the Air Force Flight Dynamics Lab.
19. Dowell, E.H.; and Voss, H.M.: Theoretical and Experimental Panel Flutter Studies in the Mach Number Range 1.0 to 5.0. AIAA J., vol. 3, 1965, pp. 2292–2304.
20. Hess, R.W.: Experimental and Analytical Investigation of the Flutter of Flat Built-Up Panels Under Streamwise Inplane Load. NASA TR−R−330, 1970.
21. Gaspers, P.A., Jr.; Muhlstein, L., Jr.; and Riddle, D.W.: An Experimental Study of the Influence of the Turbulent Boundary Layer on Panel Flutter. NASA TN D−4486, 1968.
22. Gaspers, P.A., Jr.; Muhlstein, L., Jr.; and Petroff, D.N.: Further Experimental Results on the Influence of the Turbulent Boundary Layer on Panel Flutter. NASA TN D−5798, 1970.
23. Kappus, H.P.; Lemley, C.E.; and Zimmerman, N.H.: An Experimental Investigation of High Amplitude Flutter. NASA CR− 1837, 1971.
24. Muhlstein, L., Jr.: A Forced-Vibration Technique for Investigation of Panel Flutter. AIAA−1966−769, 1966.
25. Dowell, E.H.: Nonlinear Flutter of Curved Plates. AIAA J., vol. 7, no. 3, 1969, pp. 424–431.
26. Kordes, Eldon E.; Tuovila, Weimer J.; and Guy, Lawrence D.: Flutter Research on Skin Panels. NASA TN D−451, 1960.
27. Hess, Robert W.; and Gibson, Frederick W.: Experimental Investigation of the Effects of Compressive Stress on the Flutter of a Curved Panel and a Flat Panel at Supersonic Mach Numbers. NASA TN D−1386, 1962.
28. Shore, C.P.: Flutter Design Charts for Biaxially Loaded Isotropic Panels. J. Aircraft, vol. 7, no. 4, 1970, pp. 325–329.
29. Hedgepeth, J.M.: Flutter of Rectangular Simply Supported Panels at High Supersonic Speeds. J. Aero. Sci., vol. 24, no. 8, 1957, pp. 563–573.
30. Dugundji, John: Theoretical Considerations of Panel Flutter at High Supersonic Mach Numbers. AIAA J., vol. 4, no. 7, 1966, pp. 1257–1266. (See also Errata and Addenda, AIAA J., vol. 7, no. 8, 1969, pp. 1663–1664.)
31. Olson, M.D.: Finite Elements Applied to Panel Flutter. AIAA J., vol. 5, no. 12, 1967, pp. 2267–2270.
32. Shideler, J.L.; and Weeks, G.E.: Effect of Edge Loadings on the Vibration of Rectangular Plates With Various Boundary Conditions. NASA TN D−2815, 1965.
33. Bohon, H.L.; and Heard, W.L., Jr.: Natural Vibration and Flutter of Elastically Supported Corrugation Stiffened Panels—Experiment and Theory. NASA TN D−5986, 1970.
34. Erickson, L.L.: Supersonic Flutter of Sandwich Panels—Effects of Face Sheet Bonding Stiffness, Rotary Inertia, and Orthotropic Core Shear Stiffness. NASA TN D−6427, 1971.
35. Erickson, L.L.: Supersonic Flutter of Flat Rectangular Orthotropic Panels Elastically Restrained Against Edge Rotation. NASA TN D−3500, 1966.
36. Gaspers, P.A., Jr.; and Redd, B.: A Theoretical Analysis of the Flutter of Orthotropic Panels Exposed to a High Supersonic Stream of Arbitrary Direction. NASA TN D−355l, 1966.
37. Calligeros, J.M.; and Dugundji, J.: Effects of Orthotropicity Orientation on Supersonic Panel Flutter. AIAA J., vol. 1, no. 9, 1963, pp. 2180–2182.
38. Anderson, M.S.; and Bohon, H.L.: Role of Boundary Conditions on Flutter of Orthotropic Panels. AIAA J., vol. 4, no. 7, 1966, pp. 1241–1248.

39. Anderson, M.S.; Bohon, H.L.; and Heard, W.L., Jr.: Flutter Design of Stiffened-Skin Panels for Hypersonic Aircraft. NASA TN D−5555, 1969.
40. Stroud, W. Jefferson: Elastic Constants for Bending and Twisting of Corrugation-Stiffened Panels. NASA TR R−166, 1963.
41. Dowell, E.H.; and Ventres, C.S.: Comparison of Theory and Experiment for Nonlinear Flutter of Loaded Plates. AIAA J., vol. 8, no. 11, 1970. pp. 2022−2030.
42. Dixon, S.C.; and Hudson, M.L.: Supersonic Asymmetric Flutter and Divergence of Truncated Conical Shells With Ring Supported Edges. NASA TN D−6223, 1971.
43. Dixon, S.C.; and Hudson, M.L.: Flutter, Vibration, and Buckling of Truncated Orthotropic Conical Shells With Generalized Elastic Edge Restraint. NASA TN D−5759, 1970.
44. Voss, H.M.: The Effect of an External Supersonic Flow on the Vibration Characteristics of Thin Cylindrical Shells. J. Aerospace Sci., vol. 28, no. 12, 1961, pp. 945−956.
45. Barr, G.W.; and Stearman, R.O.: Aeroelastic Stability Characteristics of Cylindrical Shells Considering Imperfections and Edge Constraint. AIAA J., vol. 7, no. 5, 1969, pp. 912−919.
46. Dowell, Earl H.: Nonlinear Flutter of Curved Plates, II. AIAA J., vol. 8, no. 2, 1970, pp. 259−261.
47. Dowell, E.H.: Nonlinear Oscillations of a Fluttering Plate, AIAA J., vol. 4, no. 7, 1966, pp. 1267−1275.
48. Dowell, E.H.: Nonlinear Oscillations of a Fluttering Plate, II. AIAA J., vol. 5, no. 10, 1967, pp. 1856−1862.
49. Dowell, E.H.: Flutter of Buckled Plates at Zero Dynamic Pressure. AIAA J., vol. 8, no. 3, 1970, pp. 583−584.
50. McElman, J.A.; Mikulas, M.M.; and Stein, M.: Static and Dynamic Effects of Eccentric Stiffening of Plates and Cylindrical Shells. AIAA J., vol. 4, no. 5, 1966, pp. 887−894.
51. Beranek, R.G.; and Muhlstein, L., Jr.: Experimental Investigation of the Influence of the Turbulent Boundary Layer on the Pressure Distribution Over a Rigid Two Dimensional Wavy Wall. NASA TN D−6477, 1971.
52. Cunningham, H.J.: Flutter Analysis of Flat Rectangular Panels Based on Three-Dimensional Supersonic Unsteady Potential Flow. NASA TR R−256, 1967.
53. Dowell, E.H.: Generalized Aerodynamic Forces on a Flexible Plate Undergoing Transient Motion. Quart. Appl. Math., vol. 24, no. 4, 1967, pp. 331−338.
54. Dowell, E.H.: Generalized Aerodynamic Forces on a Flexible Plate Undergoing Transient Motion in a Shear Flow With an Application to Panel Flutter. AIAA J., vol. 9, no. 5, 1971, pp. 834−841.
55. Bohon, H.L.; and Dixon, S.C.: Some Recent Developments in Flutter of Flat Panels. J. Aircraft, vol. 1, no. 5, 1964, pp. 280−288.
56. Dixon, S.C.: Comparison of Panel Flutter Results From Approximate Aerodynamic Theory With Results From Exact Inviscid Theory and Experiment. NASA TN D−3649, 1966.
57. Ketter, D.J.: Coupled Panel/Cavity Vibrations. AIAA J., vol. 3, no. 11, 1965, pp. 2162−2164.
58. Fung, Y.C.; and Lock, M.H: Comparative Experimental and Theoretical Studies of the Flutter of Flat Panels in a Low Supersonic Flow. AFOSR TN−670, 1961.
59. Dixon, S.C.; Shideler, J.L.; and Shore, C.P.: Flutter at Mach 3 of Thermally Stressed Panels and Comparison With Theory for Panels With Edge Rotational Restraint. NASA TN D−3498, 1966.
60. Dugundji, J.; and Calligeros, J.M.: Similarity Laws for Aerothermoelastic Testing. J. Aerospace Sci., vol. 29, no. 8, 1962, pp. 935−950.
61. Kordes, E.E.; and Noll, R.B.: Flight Flutter Results for Flat Rectangular Panels. NASA TN D−1058, 1962.
62. Anon.: Saturn V Launch Vehicle Flight Evaluation Report: AS−502 Apollo 6 Mission. NASA TM X−61038 (MPR−SAT−FE−68−3), 1968.
63. Lall, T.R.: Interstage Adapter Panel Flutter on Atlas-Centaur AC−2, AC−3, and AC−4 Vehicles. NASA TM X−l179, 1965.
64. Shore, C.P.: Effects of Structural Damping on Flutter of Stressed Panels. NASA TN D−4990, 1969.
65. Shore, C.P.: Experimental Investigation of Flutter at Mach 3 of Rotationally Restrained Panels and Comparison With Theory. NASA TN D−5508, 1969.
66. Kobayashi, S.; and Matsuzaki, Y.: A Theoretical and Experimental Study of Supersonic Panel Flutter of Circular Cylindrical Shells. Proceedings of the Eighth International Symposium on Space Technology and Science, Tokyo, Japan, 1969, pp. 281−290.
67. Dixon, S.C.; and Miserentino, R.: Vibration and Flutter Tests of a Pressurized Thin-Walled Truncated Conical Shell. NASA TN D−6106, 1971.
68. Ventres, C.S.: Flutter of a Buckled Plate Exposed to a Static Pressure Differential. AIAA J., vol. 9, no. 5, 1971, pp. 958−960.
69. Anderson, W.J.: Experiments on the Flutter of Flat and Slightly Curved Panels at M = 2.81. AFOSR TN−2996, 1962.
70. Stearman, R.O.: An Experimental Study on the Aeroelastic Stability of Thin Cylindrical Shells at the Lower Supersonic Mach Numbers. AFOSR 66−2828, 1966.
71. Fung, Y.C.; Lock, M.H.; and Stearman, R.O.: Ames Tests on the Flutter of Cylindrical Shells. SM 62−37, 1962.
72. Fung, Y.C.; and Olson, M.D.: Supersonic Flutter of Circular Cylindrical Shells Subjected to Internal Pressure and Axial Compression. AIAA J., vol. 4, no. 5, 1966.
73. Fung, Y.C.; and Olson, M.D: Comparing Theory and Experiment for the Supersonic Flutter of Circular Cylindrical Shells. AIAA J., vol. 5, no. 10, 1967, pp. 1849−1856.
74. Evensen, D.A.; and Olson, M.D.: Nonlinear Flutter of a Circular Cylindrical Shell in Supersonic Flow. NASA TN D−4265, 1967.
75. Dowell, E.H.: Generalized Aerodynamic Forces on a Flexible Cylindrical Shell Undergoing Transient Motion. Quart. Appl. Math., vol. 26, no. 3, 1968, pp. 343−353.
76. Parthan, S.; and Johns, D.J.: Vibration and Flutter of Unstiffened and Orthogonally Stiffened Circular Cylindrical Shells. Loughborough Univ. of Technology, Dept. of Transport Technology TT−7106, vols. I and II, 1971.

77. LeClerc, J.: Study of the Flutter of Thin Cylindrical Shells Within the Framework of the Linearized Potential Theory. I—Determination of Aerodynamic Forces. J. de Mechanique, vol. 9, 1970, pp. 111–154.

78. LeClerc, J.: Study of the Flutter of Thin Cylindrical Shells Within the Framework of the Theory of Linearized Supersonic Potential. II. J. de Mechanique, vol. 9, 1970, pp. 213–265.

79. Barr, G., et al.: Recent Contributions to Experiments on Cylindrical Shell Panel Flutter. AIAA–1971–0328, 1971.

80. Dowell, E.: Flutter of Multibay Panels at High Supersonic Speeds. AIAA J., vol. 2, no. 10, 1964, pp. 1805–1814.

81. Kobett, D.R.: Flutter of Multiple-Streamwise Bay Rectangular Panels at Low Supersonic Mach Numbers. NASA CR–538, 1966.

82. Farkas, E.F.; and Lock, M.H.: Flutter of Two-Bay Flat Panels of Infinite Span at Supersonic Mach Number. AIAA J., vol. 3, no. 9, 1965, pp. 1692–1697.

83. Bellinfante, R.J.; and Christensen, R.H.: Some Considerations in the Fatigue Design of Launch and Spacecraft Structures. NASA CR–242, 1965.

84. Lyon, R.H.: Random Noise and Vibration in Space Vehicles. Shock and Vibration Information Center Report SVM–1, 1967.

85. Dowell, E.H.: Fatigue Life Estimation of Fluttering Panels. AIAA J., vol. 8, no. 10, 1970, pp. 1879–1881.

86. Bohon, H.L.; and Shore, C.P.: Application of Recent Panel Flutter Research to the Space Shuttle. Part II—Influence of Edge Clips and Flow Angularity. NASA Space Shuttle Technology Conference, Vol. III—Dynamics and Aeroelasticity, NASA TM X–2274, 1971, pp. 247–264.

87. Durvasula, S.: Flutter of Simply Supported, Parallelogrammic, Flat Panels in Supersonic Flow. AIAA J., vol. 5, no. 9, 1967, pp. 1668–1673.

88. Wais, Edward Arthur: The Flutter of a Triangular Panel. Ph.D. Thesis, Univ. of Southern Calif., 1969.

89. Gaspers, P.A., Jr.: Application of Recent Panel Flutter Research to the Space Shuttle. Part I—Boundary Layer and Hypersonic Effects. NASA Space Shuttle and Technology Conference, Vol. III—Dynamics and Aeroelasticity, NASA TM X–2274, 1971, pp. 231–245.

Design Procedures for Flutter-Free Surface Panels[*]

Robert M. Laurenson and J.I. McPherson
McDonnell Douglas Astronautics Company–East
St. Louis, Missouri 63166

Foreword

The result of this investigation, as presented in this document, is an approach for the design of lightweight external surface panel configurations to preclude panel flutter. The McDonnell Douglas program manager during the initial phase of the investigation was Mr. J.I. McPherson with Dr. Robert M. Laurenson serving in this capacity during the latter portion of the study. In support of this investigation, a survey was made of the current panel flutter work being conducted at academic institutions, governmental agencies, and industrial firms. The information obtained during this survey aided in the definition of the design procedures presented in this document. The participation of the following individuals in this data gathering effort is acknowledged: Eugene F. Baird, Grumman Aerospace Corporation, Bethpage, New York 11714; J.B. Bartley, Boeing Commercial Airplane Company, Seattle, Washington 98124; Charles F. Coe, NASA Ames Research Center, Moffett Field, California 94035; Lt. Col. Duane M. Davis, Department of the Air Force, Air Force Flight Dynamics Laboratory, Wright-Patterson Air Force Base, Ohio 45433; Earl H. Dowell, Princeton University, Princeton, New Jersey 08540; Gordon Getline, Convair Aerospace Division, General Dynamics, San Diego, California 92138; G.E. Kahre, McDonnell Douglas Astronautics Company–West, McDonnell Douglas Corporation, Huntington Beach, California 92467; R.H. Lassen, Space Division, Rockwell International, Downey, California 90241; C.E. Lemley, McDonnell Aircraft Company, McDonnell Douglas Corporation, St. Louis, Missouri 63166; J. Wayne Sawyer, NASA Langley Research Center, Hampton, Virginia 23665; Ronald O. Stearman, The University of Texas of Austin, Austin, Texas 78712; A.C. Tracy, Douglas Aircraft Company, McDonnell Douglas Corporation, Long Beach, California 90846; and J.E. Wignot, Lockheed–California Company, Burbank, California 91503.

Summary

An approach for the design of lightweight external surface panel configurations to preclude panel flutter has been developed. Design procedures were developed for flat orthotropic panels under the interacting influence of parameters such as support flexibility, inplane loads, pressure differential, and flow angularity. The relationships required to define these design procedures were based on theoretical panel flutter analyses. Where possible, the design procedures were verified through comparison with available experimental panel flutter data.

1. Introduction

Future high velocity cruise aircraft and reusable entry vehicles must cope with environments which place severe thermal and structural demands on the external surfaces. Prevention of panel flutter in these external surfaces is one of many problems which designers must face. Traditionally, external panels have been designed by strength, buckling, and fatigue considerations and then checked for panel flutter performance. Such a procedure often leads to "flutter fixes" and additional weight for panel flutter prevention.

To permit consideration of panel flutter early in the design process, design procedures have been developed in a format useful to designers without prior panel flutter experience. The major emphasis is placed on development of flutter design procedures and their application to metallic panels with orthotropic stiffness characteristics and a variety of edge support conditions from nearly free to fully clamped. The panels may also be subjected to various

[*]This document was first published as Laurenson, R.M.; and Mcpherson, J.I.: Design Procedures for Flutter-Free Surface Panels. NASA CR–2801, 1977.
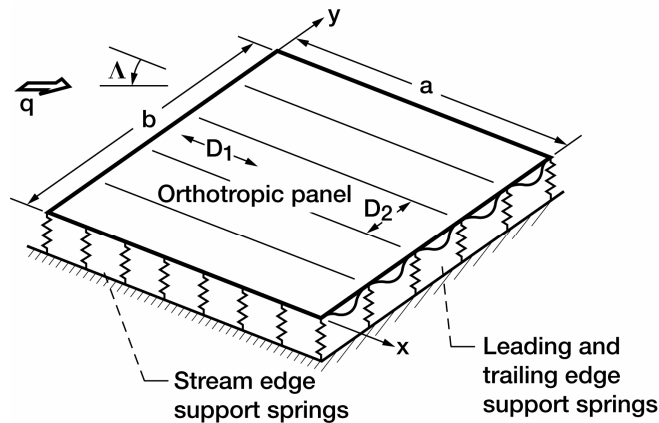
Figure 1.—Surface panel configuration.

loading and flow conditions. Additionally, results are also presented for surface panels attached to primary structure by an elastic coupling medium. For either panel configuration it should be emphasized that although these design procedures are useful in preliminary design, detailed flutter analyses and/or tests may be necessary to verify the final design of critical panel configurations.

A wealth of theoretical panel flutter investigations and wind tunnel data exists in the literature. The theoretical approaches were employed to establish the trends and relationships required to define these panel flutter design procedures. Experimental flutter data were used to verify the design criteria which are presented in the form of flutter-free panel design boundaries. The flat, orthotropic panel configuration to which this approach has application is illustrated in figure 1. The influence of such interacting parameters as flow angularity, support flexibility, inplane loading, orthotropic panel stiffness characteristics, damping, and static pressure differential on the flutter of external surface panels is included in these procedures.

Interest in the establishment of panel flutter design procedures has been high for a number of years. An initial attempt to define such procedures is given in reference 1. In that document, a panel flutter design boundary is defined which envelopes the available experimental data from both unstiffened and corrugation stiffened panels.

Modifications and refinements to this design approach have continued (refs. 2 and 3). In 1964, and later in a revised form in 1972, the National Aeronautics and Space Administration issued a formal design monograph (ref. 4) to be used as a guide in the formulation of design requirements and specifications dealing with panel flutter. Reference 4 does not provide detailed procedures to be followed for the design of flutter free surface panels but rather the philosophy to be followed during the design process. Reference 5, published in 1968, gives simplified criteria in graphical form for many of the parameters important for panel flutter design; however, effects of panel orthotropy, edge support flexibility, and damping are not included. The panel flutter design procedures presented in this report are extensions of the previously mentioned design approaches. Additional parameters such as panel orthotropy, edge support flexibility, flow angularity, and damping, as understood in the current state of the art, are included in a graphical format which should be useful to designers without prior panel flutter experience.

2. Symbols

Definitions of the major symbols required for the application of the panel flutter design procedures are given below. Symbols not having general usage throughout this report are defined as they are introduced.

a, b	Panel length in x and y directions, respectively; m
D	Isotropic panel stiffness parameter; N-m
D_f	Damping factor (eq. (41))

D_1, D_2, D_{12}	Orthotropic panel stiffness parameters; N-m
E	Young's modulus of panel material; N/m^2
E_c	Panel edge rotational restraint coefficient
$f(M)$	Mach number correction factor (fig. 7)
FP	Flutter Parameter
g	Structural damping coefficient
g_T	Total damping coefficient
G	Shear modulus of panel material; N/m^2
GP	Geometry Parameter
h	Isotropic panel thickness; m
h_{eq}	Equivalent isotropic panel thickness (eq. (39)); m
$\overline{K}_{LT}$	Nondimensional leading and trailing edge support stiffness parameter
$\overline{K}_{LT}*$	Nondimensional stiffness parameter $\overline{K}_{LT}$ modified for presence of flow angularity (eq. (29))
$\overline{K}_S$	Nondimensional stream edge support stiffness parameter
$\overline{K}_S*$	Nondimensional stiffness parameter $\overline{K}_S$ modified for presence of flow angularity (eq. (28))
M	Mach number
N_{CR}	Critical buckling load; N/m
N_1	Inplane load in x direction; N/m
P_f	Nondimensional pressure differential parameter (eq. (38))
P_{CR}	Buckling load ratio (eq. (12))
q	Free stream dynamic pressure; Pa
Q_p	Pressure differential correction factor (fig. 6)
S_{LT}	Leading and trailing edge support parameter (eq. (22))
$S_{LT}*$	Support parameter S_{LT} modified for presence of flow angularity (eq. (30))
t	Time
α	Equation (4)
γ	Panel mass density per area
Δg	Differential damping coefficient (eq. (42))
Δp	Static pressure differential; Pa
λ	Flow parameter (eq. (6))
ν	Poisson's ratio of panel material

The International System of Units (SI) has been used throughout this report. The appropriate quantities are defined as follows:

Quantity	Unit	SI Symbol
length	meter	m
force	newton	N
pressure	pascal	Pa

Abbreviations for the following prefixes have been employed for multiples of units in this report.

Prefix	Multiplying Factor	Abbreviation
milli	10^{-3}	m
kilo	10^{3}	k
mega	10^{6}	M
giga	10^{9}	G

3. Flutter-Free Panel Design Boundaries

To allow designers without prior panel flutter experience to consider panel flutter early in the design process, flutter-free panel design boundaries have been developed in terms of a nondimensional panel geometry parameter *GP* and a nondimensional flutter parameter *FP*. Effects of interacting parameters such as panel size, panel stiffness characteristics and panel support conditions are included in the geometry parameter. The flutter parameter contains the effects of free-stream dynamic pressure and Mach number.

The initial definition of the geometry and flutter parameters and their relationship was based on a two mode solution for flutter of simply supported orthotropic panels. The following assumed panel deflection satisfies simply supported boundary conditions

$$w(x,y,t) = W_{11}(t)\sin\left(\frac{\pi x}{a}\right)\sin\left(\frac{\pi y}{b}\right) + W_{21}(t)\sin\left(\frac{2\pi x}{a}\right)\sin\left(\frac{\pi y}{b}\right) \tag{1}$$

The basic partial differential equation for flutter of an orthotropic panel (ref. 6) is of the form

$$D_1\frac{\partial^4 w}{\partial x^4} + 2D_{12}\frac{\partial^4 w}{\partial x^2 \partial y^2} + D_2\frac{\partial^4 w}{2_{\partial y}^2} + \frac{2q}{f(M)}\frac{\partial w}{\partial x} + \gamma\frac{\partial^2 w}{\partial t^2} = 0 \tag{2}$$

where the aerodynamic loading has been assumed to be given by two-dimensional static aerodynamics. Employing the assumed panel deflection of equation (1), a Galerkin solution to the above yields the following set of ordinary differential equations:

$$\left(\frac{\pi}{a}\right)^4\left[D_1 + 2D_{12}\left(\frac{a}{b}\right)^2 + D_2\left(\frac{a}{b}\right)^4\right]W_{11} - \frac{16q}{3f(M)a}W_{21} + \gamma\ddot{W}_{11} = 0$$

$$\left(\frac{\pi}{a}\right)^4\left[16D_1 + 8D_{12}\left(\frac{a}{b}\right)^2 + D_2\left(\frac{a}{b}\right)^4\right]W_{21} + \frac{16q}{3f(M)a}W_{11} + \gamma\ddot{W}_{21} = 0 \tag{3}$$

Assuming a solution to equation (3) of the form

$$W_{n1}(t) = \overline{W}_{n1}e^{\alpha t} \tag{4}$$

and solving the corresponding characteristic equation yields the following two mode flutter solution

$$\lambda = \frac{3\pi^4}{16}\left[15 + 6\left(\frac{D_{12}}{D_1}\right)\left(\frac{a}{b}\right)^2\right] \tag{5}$$

In equation (5), the flow parameter λ is expressed as

$$\lambda = \frac{2q\,a^3}{D_1\,f(M)} \tag{6}$$

The geometry and flutter parameters are arbitrarily defined as

$$GP = \frac{a}{b}\sqrt{\frac{D_{12}}{D_1}} \tag{7}$$

and

$$FP = \frac{D_1\,f(M)}{q\,a^3} \tag{8}$$

Combining equations (7) and (8) with equation (5) yields the following relationship between *GP* and *FP* for simply supported panels

$$FP = \frac{0.0365}{5 + 2(GP)^2} \tag{9}$$

A second approximate flutter solution, referred to as the preflutter solution, has been presented in several documents such as reference 7. This approximate solution is very accurate for simply supported panels for values of *GP* > 0.1 and results in the following relationship between *GP* and *FP*

$$FP = \frac{0.0593}{\left(5 + GP^2\right)\sqrt{4 + 2(GP)^2}} \tag{10}$$

Results from the two mode solution and the preflutter solution are presented in figure 2 where *GP* is shown as a function of *FP*. Both solutions have the same trends; however, the two mode solution lacks sufficient accuracy for design purposes and the preflutter solution is not applicable to panels with edge supports which approach a fully clamped condition.

Since the approximate solutions were insufficient for design purposes, reliance was placed on more detailed flutter analyses of panels with boundary condition combinations which varied from nearly free to fully clamped to obtain the final flutter-free panel design boundaries shown in figure 3. These analyses included both closed form solutions and well converged modal solutions so that accurate results were used to develop the boundaries. As the effects of different parameters such as inplane loading, flow angularity, and support flexibility were considered it became necessary to redefine the geometry and flutter parameters to maintain the relationship between these two parameters given by the flutter-free panel design boundaries shown in figure 3. The required expressions for *GP* and *FP* were determined by combined analysis and curve fitting of experimental data. This approach was followed to duplicate the trends obtained in detailed theoretical and experimental panel flutter investigations reported in the literature.
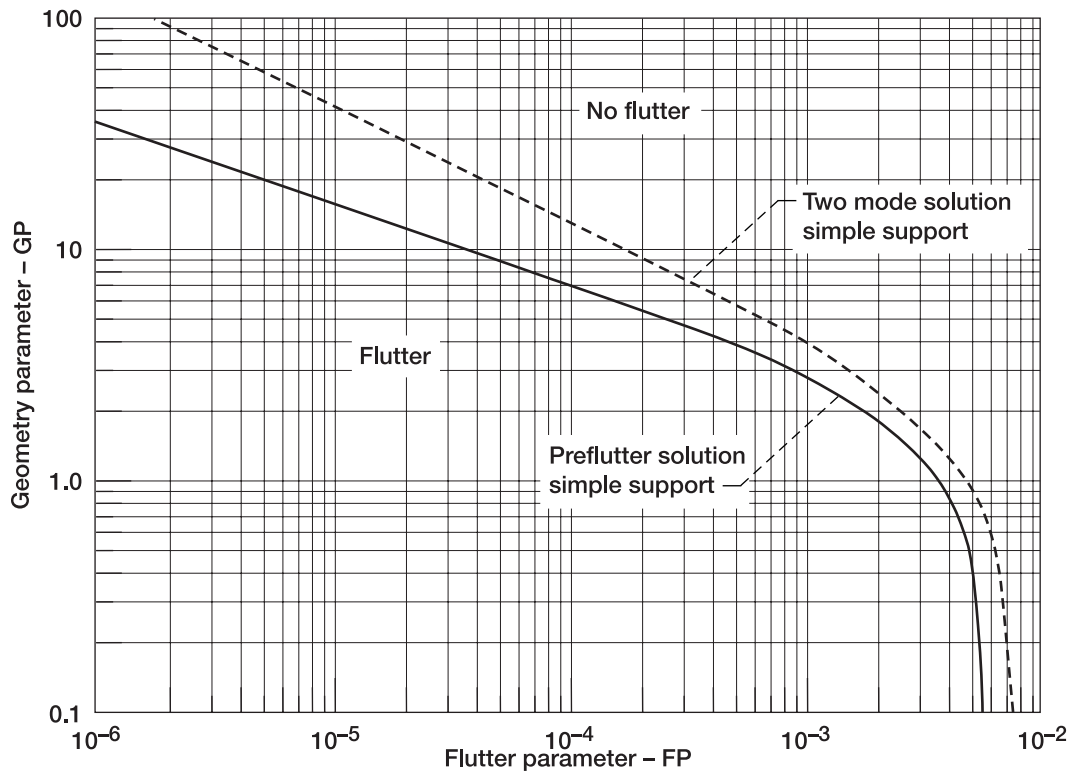
Figure 2.—Flutter-free panel design boundaries from approximate solutions.
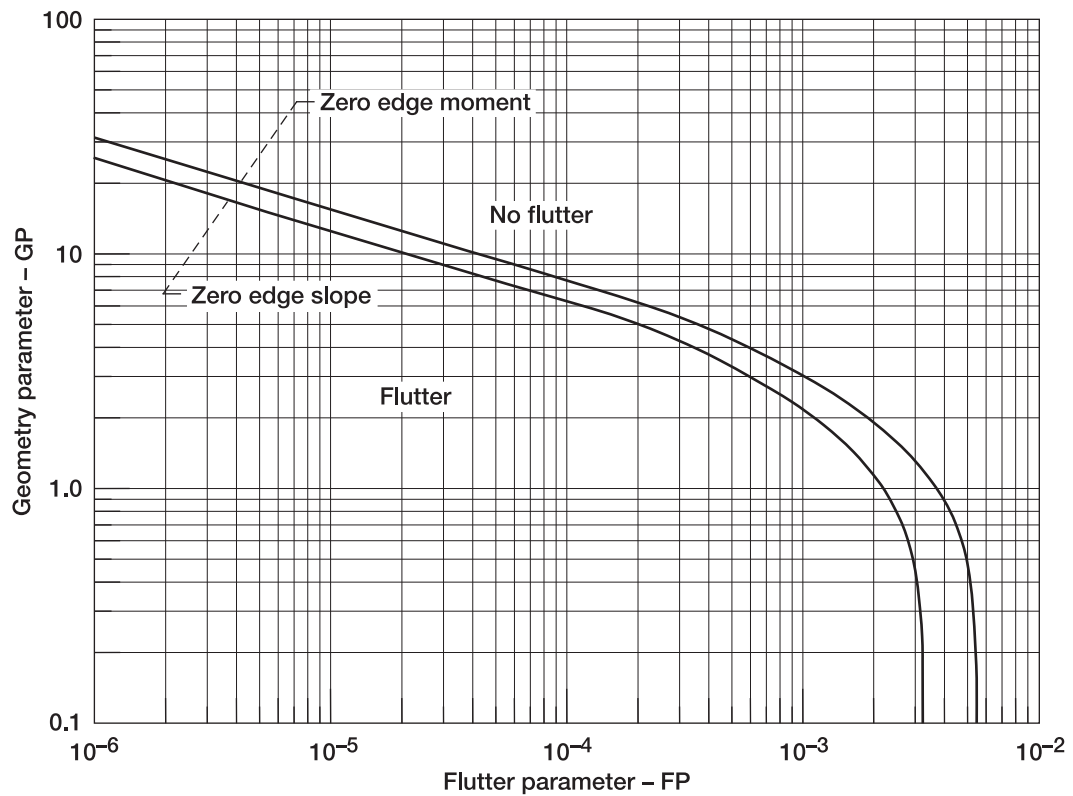
Figure 3.—Flutter-free panel design boundaries.

As an example, the two mode flutter solution was extended to include the influence of inplane loads. This analysis resulted in a definition for *GP* to be used when inplane loads are present. To be specific, it can be shown that the two mode solution, including the influence of an inplane load in the direction of flow, N_1, takes the form

$$\lambda = \frac{3\pi^4}{16}\left\{15 + 6\frac{D_{12}}{D_1}\left(\frac{a}{b}\right)^2(1 - P_{CR}) - 3P_{CR}\left[1 + \frac{D_2}{D_1}\left(\frac{a}{b}\right)^4\right]\right\} \tag{11}$$

In equation (11) P_{CR} is the ratio of the inplane load N_1 to the buckling load N_{CR}. Thus,

$$P_{CR} = N_1 / N_{CR} \tag{12}$$

Comparing equations (5) and (11) reveals that the second term of equation (11) indicates a new definition for *GP* of the form

$$GP = \frac{a}{b}\sqrt{\frac{D_{12}}{D_1}(1 - P_{CR})} \tag{13}$$

As will be discussed in section 4.3, equation (13) is in fact the form for *GP* that was selected to account for the presence of inplane loads. For a panel with inplane loads, modifications to the *FP* relationship of equation (8) were then made by correlating flutter predictions with available experimental data.

For ease of computer application and to assist the designer in making accurate determinations of *FP* once *GP* has been calculated, analytical expressions of the design boundaries were determined by curve fitting techniques. These expressions take the form

$$FP = \frac{E_c}{5 + 2(GP)^2 + 0.18(GP)^3} \tag{14}$$

where E_c is the panel edge rotational restraint coefficient defined as

$$E_c = 0.016 \tag{15}$$

for a panel with zero edge slope and

$$E_c = 0.027 \tag{16}$$

for a panel with zero edge moment. Thus for a given value of *GP*, the corresponding magnitude of *FP* may be obtained from equation (14) with the appropriate E_c.

The relationship of equation (14) is valid over the range of *GP*'s between slightly more than zero (0.1) and 5.0. For values of *GP* lower than 0.1, the coefficient E_c is defined as

$$E_c = 0.0157 \tag{17}$$

for a panel with zero edge slope and

$$E_c = 0.0292 \tag{18}$$

for a panel with zero edge moment.

4. Design Boundary Application

The steps required in the application of the flutter-free panel design boundary during preliminary design of lightweight external surface panels are detailed in this section. Parameters which are included in this design approach as they influence panel flutter are:

- Panel aspect ratio
- Panel orthotropic properties
- Support flexibility
- Inplane loads
- Static pressure differential
- Flow angularity
- Structural damping

Verification of these design procedures is addressed in section 6.

In the application of the flutter-free panel design boundary, the basic approach involves the determination of the magnitude of *GP* for the panel configuration of interest. The design boundary (fig. 3) is then entered with this value and the corresponding magnitude of *FP* obtained. With this value of the Flutter Parameter, the flutter critical flight condition may be defined. The forms taken by the parameters *FP* and *GP* depend on the particular situation under consideration. Definition of these parameters and their application in conjunction with the design boundary is detailed in the following sections.

The steps required for application of the panel flutter design procedure during the design of lightweight surface panels are summarized in figure 4. The basic geometry data required are the panel length *a*, width *b*, and ortho-tropic stiffness properties D_1, D_2, and D_{12}. A number of techniques for the determination of these panel stiffness

parameters are presented in appendix A. For an isotropic panel these three panel stiffness properties are equal and are expressed as

$$D = \frac{h^3 E}{12(1 - \nu^2)} \tag{19}$$

When the influence of deflectional support flexibility is to be included in the design the nondimensional stream edge stiffness parameter $\overline{K}_S$ and/or leading and trailing edge parameter $\overline{K}_{LT}$ are required. These quantities are defined for a number of support conditions in appendix B.

Several options available for use with the flutter-free panel design boundary are indicated in figure 4. This is to aid the designer in selecting the correct procedures to be followed when applying these panel flutter design criteria. For each option, reference is made in the figure to the report section detailing the application of the design boundary to a particular panel configuration. A number of examples detailing the use of these panel design procedures are discussed in section 5.

The procedures to be followed in defining the magnitude of the geometry parameter for the panel configuration of interest are presented in the following sections. With this quantity, the flutter parameter is obtained from the flutter-free panel design boundary. This value of *FP* is then used to obtain the critical dynamic pressure parameter $q/f(M)$, where *q* is the free stream dynamic pressure and *f(M)* is the Mach number correction factor.

Modifications to the dynamic pressure parameter for a static pressure difference across the panel are covered in section 4.4. As discussed in section 4.5, the quantity $q/f(M)$ may require modification to account for the presence of significant structural damping in the system. With this modified dynamic pressure parameter, the flutter critical dynamic pressure is obtained with the procedures detailed in section 4.6.
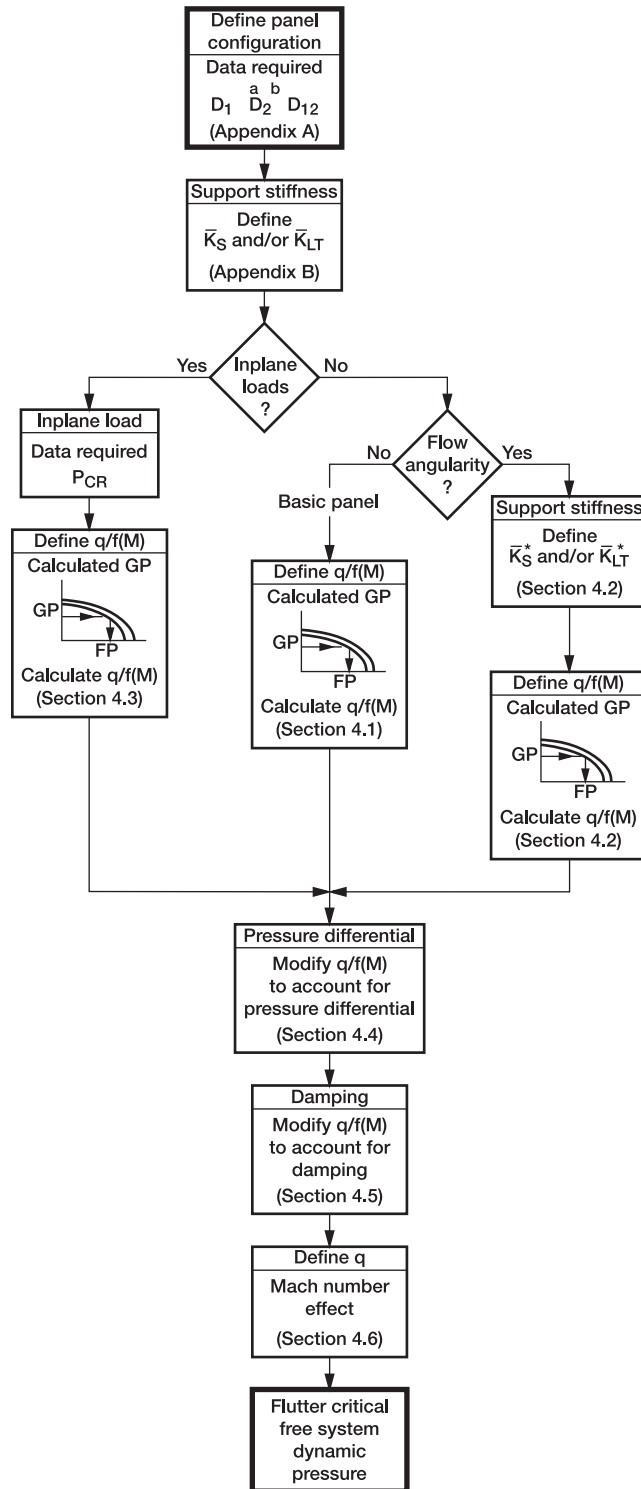
Figure 4.—Panel design procedure.

4.1 Basic Panel

For an orthotropic panel with no inplane load and zero flow angularity, the geometry and flutter parameters are defined as

$$GP = \frac{a}{b}\sqrt{\frac{D_{12}/D_1}{1 + C^2/\overline{K}_S}} \tag{20}$$

and

$$FP = S_{LT}\frac{D_1\,f(M)}{q\,a^3} \tag{21}$$

In equation (20), $\overline{K}_S$ is the nondimensional stream edge deflectional support stiffness and in equation (21) S_{LT} is the leading and trailing edge support parameter expressed as

$$S_{LT} = e^{-\left(\frac{71}{12\overline{K}_{LT}+\overline{K}_{LT}{}^2}\right)^{1/2}} + e^{\left(\frac{-2\overline{K}_{LT}}{(a/b)^2(D_{12}/D_1)}\right)} \tag{22}$$

where $\overline{K}_{LT}$ is the nondimensional stiffness parameter associated with the leading and trailing edge support flexibility. Additionally, the quantity C required in equation (20) is defined by the following expression

$$C = \sqrt{\frac{D_{12}{}^2}{D_1\,D_2}} \tag{23}$$

In this application the concept of support flexibility refers to a panel edge which is not completely restrained against deflections normal to the panel. Thus, in this case the panel boundary condition is less rigid than either a simply supported or clamped edge. Appendix B contains a number of procedures which may be employed to determine the magnitudes of the nondimensional edge support parameters $\overline{K}_S$ and $\overline{K}_{LT}$. For panel configurations with unequal flexible supports on opposite edges an average value of the nondimensional edge support parameters $\overline{K}_S$ and $\overline{K}_{LT}$ should be used except for values of $\overline{K}_{LT}$ less than about five. At values of $\overline{K}_{LT}$ less than five a flutter analysis should be conducted since theory (ref. 8) indicates large reductions in flutter margins can occur at low values of $\overline{K}_{LT}$ for unequal supports at the panel leading and trailing edges.

The theoretical trends presented in reference 9, of flutter critical flow conditions versus leading and trailing edge support stiffness, were employed in obtaining the equation (22) definition of S_{LT}. The modifying term $C^2/\overline{K}_S$ present in equation (20), which accounts for the stream edge support stiffness, was obtained by matching the experimental trends presented in reference 10.

As the stream edge deflectional support stiffness $\overline{K}_S$ approaches infinity the quantity $C^2/\overline{K}_S$ approaches zero and equation (20) becomes

$$GP = \frac{a}{b}\sqrt{\frac{D_{12}}{D_1}} \tag{24}$$

Likewise, for a $\overline{K}_{LT}$ approaching infinity, the magnitude of S_{LT} approaches one and equation (21) may be written as

$$FP = \frac{D_1 \ f(M)}{q \ a^3} \tag{25}$$

With the magnitude of GP defined with either equation (20) or (24), the corresponding value for FP is obtained from the design boundaries in figure 3.[†]

The dynamic pressure parameter $q/f(M)$ may be determined as appropriate, from equation (21) or (25). Potential modifications to $q/f(M)$ for static pressure differential are presented in section 4.4 and for structural damping are covered in section 4.5. The evaluation of $f(M)$ allowing definition of the flutter critical dynamic pressure is discussed in section 4.6.

4.2 Flow Angularity

For flow at an angle, and with edge flexibility included, the geometry and flutter parameters are defined as

$$GP = \frac{a}{b} \sqrt{\frac{D_{12}/D_1}{1+C^2/\overline{K}_S^*} \left[\cos^2 (\Lambda) + \frac{D_1}{D_2} \left(\frac{b}{a} \right)^4 \sin^2 (\Lambda) \right]} \tag{26}$$

and

$$FP = \frac{D_1 \ f(M)}{qa^3} \frac{S_{LT}^*}{\cos^2 (\Lambda) + \frac{D_1}{D_2} \left(\frac{b}{a} \right)^3 \sin^2 (\Lambda)} \tag{27}$$

In equations (26) and (27), Λ is the magnitude of flow angularity shown in figure 1 and $\overline{K}_S^*$ and S_{LT}^* are edge support flexibility parameters modified to account for the flow angularity.

The modified nondimensional edge support stiffness parameters including the influence of flow angularity are given as

$$\overline{K}_S^* = \frac{1}{\dfrac{\cos^2 (\Lambda)}{\overline{K}_S} + \dfrac{\sin^2 (\Lambda)}{\overline{K}_{LT}}} \tag{28}$$

and

$$\overline{K}_{LT}^* = \frac{1}{\dfrac{\sin^2 (\Lambda)}{\overline{K}_S} + \dfrac{\cos^2 (\Lambda)}{\overline{K}_{LT}}} \tag{29}$$

[†]Choice of the design boundary is dependent on the degree of rotational restraint along the panel edges. Most panels are probably adequately represented by the zero edge slope boundary; however, a more conservative design results from the zero moment boundary.

The modified leading and trailing edge support parameter S^*_{LT} is of the form

$$S^*_{LT} = e^{-\left(\frac{71}{12\overline{K}^*_{LT} + \overline{K}^{*2}_{LT}}\right)^{1/2}} + e^{\left(\frac{-2\overline{K}^*_{LT}}{(a/b)^2 (D_{12}/D_1)}\right)} + e^{-0.25\overline{K}_{LT}} \sin(2\Lambda) \tag{30}$$

The expressions for GP and FP given by equations (26) and (27) were chosen to assure correct results for a flow angle of 90°. That is, for a 90° flow angle, the a and b panel dimensions and the panel stiffness properties are properly interchanged. The combination of flow angularity and panel edge support flexibility has been expressed in terms of effective edge support stiffness parallel and perpendicular to the flow. Thus, the modified edge support stiffness parameters of equations (28) and (29) are based on the assumption that the leading and trailing edge springs act in parallel with the stream edge springs. The last term of equation (30) is included to match the experimental trends for panels with flow angularity such as presented in reference 11.

For panel configurations which include both edge support flexibility and flow angularity, the application of equations (28) through (30) in combination with the relations presented for FP and GP can result in inaccurate flutter predictions. This occurs when the second term in the expression for S^*_{LT} (eq. (22)) is not small when compared to the magnitude of the first term. To overcome this difficulty, an equivalent nondimensional leading and trailing edge support stiffness was defined as

$$\overline{K}^{eq}_{LT} = \sqrt{\frac{71}{\ln^2 (S_{LT})} + 36} - 6 \tag{31}$$

where S_{LT} is obtained from equation (22) for the particular value of $\overline{K}_{LT}$. The magnitudes of GP and FP are then obtained from equations (26) and (27) where S^*_{LT} and $\overline{K}^*_S$ are based on the quantities $\overline{K}_S$ and $\overline{K}^{eq}_{LT}$.

For configurations where the edge support stiffness parameters $\overline{K}_S$ and $\overline{K}_{LT}$ approach infinity (total edge deflection restraint), equations (26) and (27) become

$$GP = \frac{a}{b} \sqrt{\frac{D_{12}}{D_1} \left[\cos^2 (\Lambda) + \frac{D_1}{D_2} \left(\frac{b}{a}\right)^4 \sin^2 (\Lambda) \right]} \tag{32}$$

and

$$FP = \frac{D_1 \, f(M)}{q \, a^3} \left[\frac{1}{\cos^2 (\Lambda) + \frac{D_1}{D_2} \left(\frac{b}{a}\right)^3 \sin^2 (\Lambda)} \right] \tag{33}$$

It should be noted that the definitions for the geometry and flutter parameters and the edge support stiffness parameters are based on data at flow angles of zero and in the range from about 15 to 90°. Analysis (ref. 6) indicates that slight variations in flow angle in the region of zero to 15° can have large effects on flutter conditions. Due to lack of experimental flutter data for flow angles of zero to 15° some uncertainty exists about the validity of the current design approach in this region. When effects of flow angularity are to be included a conservative design can be obtained if the panel is considered for both zero and 90° flow and the design based on the worst case.

With the magnitude of FP obtained for the appropriate deflection edge support condition, the dynamic pressure parameter $q/f(M)$ can be evaluated. The effects of static pressure differential, section 4.4; structural damping, section 4.5; and Mach number, section 4.6, should be examined and included in the determination of the flutter critical dynamic pressure when significant.

4.3 Inplane Loads

The flutter-free panel design boundary has application to panels subjected to inplane loading if the flow is parallel to the x axis. In addition, the panel stream edges may have either total deflectional restraint or some edge support flexibility as defined by $\overline{K}_S$. The leading and trailing edges are assumed to have complete deflectional restraint. Figure 5 illustrates a panel subjected to inplane loading.

For this configuration the geometry parameter is given as

$$GP = \frac{a}{b}\sqrt{\frac{D_{12}}{D_1}\frac{1-P_{CR}}{1+C^2/\overline{K}_S}} \tag{34}$$

and the corresponding expression for the flutter parameter is

$$FP = \frac{D_1\, f(M)}{q\, a^3}\left[\frac{1}{1+\left(P_{CR}\right)^{2b/a}\left(\dfrac{D_1}{D_2}\right)\left(2\pi\,\dfrac{b}{a}\right)^2}\right] \tag{35}$$

The quantity P_{CR}, equations (34) and (35), is the ratio of the inplane load N_1 in the x direction to the critical buckling load N_{CR}. Thus

$$P_{CR} = N_1/N_{CR} \tag{36}$$

As indicated in section 3.0 by equation (13), the basic form for GP including the influence of inplane loads is based on the two mode flutter solution. The $C^2/\overline{K}_S$ term in equation (34) was added to yield results consistent with equation (20). The form of the flutter parameter given by equation (35) was obtained by matching trends in experimental panel flutter data, primarily from reference 12.

To make flutter predictions for a panel with inplane loading, the magnitude of N_{CR} is required for use in equation (36). Evaluation of this buckling load parameter must account for both the N_1 and N_2 loadings (fig. 5), Procedures for obtaining N_{CR} are presented in references 13 and 14.
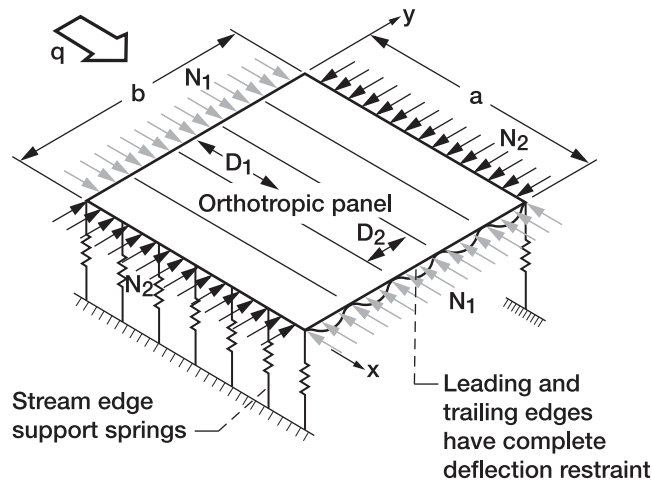
Figure 5.—Panel with inplane loading.

Often in preliminary design neither the magnitude of the inplane loads nor the critical buckling load are known with any degree of confidence. As indicated in reference 15, for a given panel configuration subjected to inplane loading, the minimum dynamic pressure for panel flutter occurs at the transition point between an unbuckled and buckled panel. Thus, a conservative approach, when the effects of inplane loading are desired, would be to assume a value for P_{CR} of one. Equation (34) shows that when P_{CR} equals one the geometry parameter equals zero. In this situation the magnitude of the flutter parameter may be obtained from equation (14). The flutter critical dynamic pressure is then obtained from equation (35).

The design approach is limited to panel configurations with normal inplane loads and does not account for the possibility of inplane shear loading. A recent theoretical investigation of this question of combined normal and shear inplane loads is presented in reference 16. The conclusion of this study is that designs for panels at buckling due to inplane shear or combinations of inplane shear and normal loads will be conservative if it is assumed that the panels buckle due to N_1 alone.

With the established value of FP, the magnitude of $q/f(M)$ is determined from equation (35). The flutter critical dynamic pressure q is then obtained after consideration of the effects of static pressure differential, section 4.4; structural damping, section 4.5; and Mach number, section 4.6.

4.4 Static Pressure Differential

It has been shown experimentally (refs. 17 and 18) that a static pressure differential Δp across the panel has a significant effect on the panel flutter boundary. This effect is due to the inplane stresses that are induced by this pressure differential. These stresses are always tensile regardless of the direction in which Δp acts and increase the effective stiffness of the panel. Thus, the effect of this differential pressure is to raise the panel's flutter boundary.

In reference 17, the effect of a pressure differential is described through a nondimensional parameter given as

$$P = \frac{\Delta p \, a^4}{D \, h} \tag{37}$$

where an isotropic panel is assumed. For an orthotropic panel an analogous nondimensional parameter of the form

$$P_f = \frac{\Delta p \, a^4}{D_1 h_{eq}} \tag{38}$$

has been defined. In this expression h_{eq} is an equivalent isotropic panel thickness quantity related to the orthotropic panel stiffness properties and is defined as

$$h_{eq} = \frac{1}{2}\left(\sqrt[3]{\frac{12 \, D_1}{E}} + \sqrt[3]{\frac{12 \, D_2}{E}} \right) \tag{39}$$

The dynamic pressure parameter including the influence of a static pressure differential becomes

$$\frac{q_p}{f(M)} = Q_p \frac{q}{f(M)} \tag{40}$$

where Q_p is the ratio of the dynamic pressure parameter $q_p/f(M)$, which includes the effects of Δ_p, to $q/f(M)$ which does not include pressure differential effects. Shown in figure 6, as a function of P_f, is the parameter Q_p for panels with several length to width ratios. These trends are based on experimental data discussed in references 17 and 18.
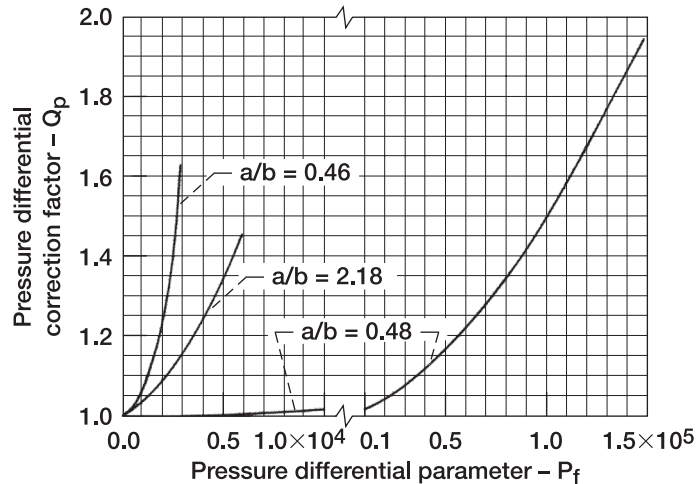
Figure 6.—Pressure differential correction factor.

The results summarized in figure 6 form the basis for including the influence of a Δp in the panel design. Following the determination of the flutter critical parameter $q/f(M)$, as covered in the preceding sections, the magnitude of P_f is calculated from equation (38). With this value of P_f, the appropriate Q_p is obtained from figure 6 and the updated quantity $q_p/f(M)$ obtained.

4.5 Structural Damping

The influence of structural damping in a panel system with inplane loading is accounted for through a damping factor D_f defined as

$$D_f = [1 + 100\, P_{CR}\, \Delta g] \tag{41}$$

In the above, P_{CR} is the buckling load ratio of equation (36) and the quantity Δg is expressed as

$$\Delta g = g - 0.01 \tag{42}$$

where g is the damping coefficient assumed in the system.

With the definition of D_f, equation (41), the dynamic pressure parameter including the influence of damping is obtained from the following relationship.

$$\frac{q_d}{f(M)} = D_f\, \frac{q}{f(M)} \tag{43}$$

The quantity $q/f(M)$ in equation (43) is the result of the flutter prediction employing the flutter-free design boundary as discussed in the previous sections, and $q_d/f(M)$ is the updated quantity including the effects of damping.

The quantity Δg is defined as indicated by equation (42) because application of the design procedures produce results which compare well with theoretical results for panels with inplane loading and panel damping represented by a structural damping coefficient of 0.01. Thus, results obtained from the design boundary may be thought of as including "nominal" damping of this magnitude. The parameter Δg is introduced in the damping factor to account for panel damping which is higher than this nominal value.

The above form of D_f was obtained through comparison with the results of references 15 and 19. These references present trends, obtained during detailed theoretical investigations, of flutter critical flow conditions as influenced by inplane loading and structural damping.

4.6 Mach Number Effect

Use of the dynamic pressure parameter $q/f(M)$ to describe the flutter critical free stream flow conditions is based on the commonly used linear piston theory, reference 20, to represent the aerodynamic forces acting on the panel. As indicated in reference 20, experience has shown that use of this aerodynamic theory in conjunction with $f(M)$ defined as

$$f(M) = \sqrt{M^2 - 1} \tag{44}$$

yields flutter boundaries that exhibit excellent agreement with those given by more refined theories, provided the Mach number is higher than approximately 1.6 to 2.0.

For application with the flutter-free panel design boundary, $f(M)$ is assumed to take the form of equation (44) for Mach numbers greater than 2.0 and is defined as shown in figure 7 for Mach numbers in the range of 1.0 to 2.0. These curves were derived from experimental data discussed in reference 18. Following determination of the parameter $q/f(M)$ through application of the design boundary and including modifications for potential static pressure differential and damping effects, the flutter critical free stream dynamic pressure is obtained for the Mach number correction factor defined by either equation (44) or figure 7.

5. Example Applications of Design Procedure

Several examples are presented which illustrate the use of the panel design procedures detailed in section 4.0. Both isotropic and orthotropic panels with various combinations of support conditions, inplane loading, and flow angularity are discussed. In all cases, it has been assumed that the applicable factors of safety have been considered in arriving at the stated free stream dynamic pressure requirements.
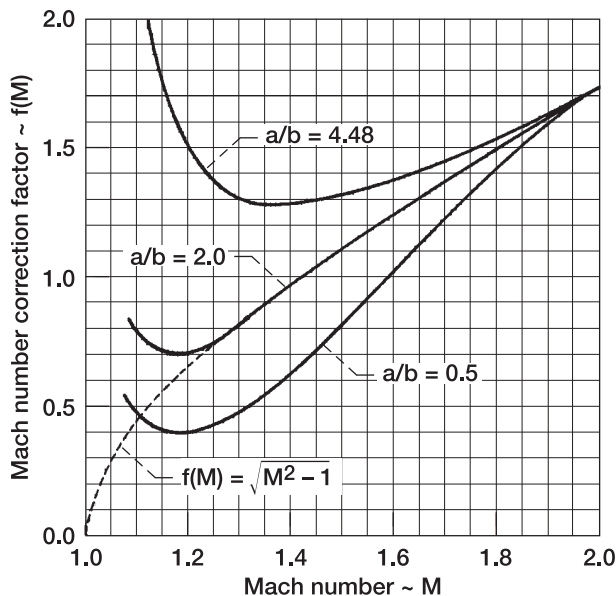
Figure 7.—Mach number correction factor.

5.1 Uniform Panel With Inplane Loads

It is desired to determine the thickness of a uniform aluminum panel required to preclude flutter when the panel is subjected to an inplane load that is 75 percent of its buckling load. A sketch of the panel is shown in figure 8 and details of this configuration are as follows:

Simply supported panel
- a = 0.25 m
- b = 0.65 m
- E = 69 GN/m^2
- P_{CR} = 0.75
- M = 2.5
- q = 40 kPa

Figure 4 shows that the design approach for a panel with inplane loading is detailed in section 4.3. For an isotropic panel, the panel stiffness properties D_1 and D_{12} are equal and equation (34) becomes

$$GP = \frac{a}{b}\sqrt{1 - P_{CR}}$$

The above expression also reflects that for a panel simply supported at all edges, the quantity $\overline{K}_S$ approaches infinity and thus, the $C^2/\overline{K}_S$ term of equation (34) approaches zero. Thus the magnitude of the geometry parameter for this particular panel configuration becomes:

$$GP = 0.192$$

From equation (14) with an E_c of 0.027 or from figure 3, the magnitude of the flutter parameter is determined to be

$$FP = 0.00532$$

From equation (35) the panel stiffness parameter to preclude flutter may be expressed as

$$D = \frac{FP\,q\,a^3}{f(M)}\left[1 + (P_{CR})^{2b/a}\;\left(2\pi\frac{b}{a}\right)^2\right]$$

where q is the free stream dynamic pressure requirement. Note that it has been assumed that no modifications to the dynamic pressure which account for damping or pressure differential effects are required. The Mach number correction factor (sec. 4.6) is given as
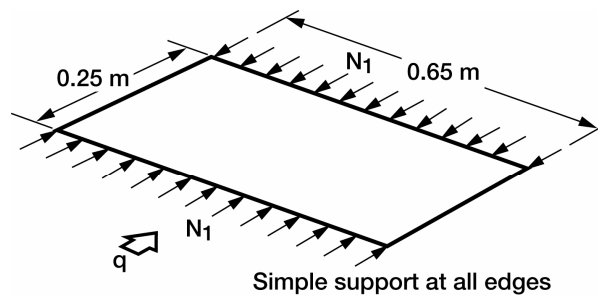
Figure 8.—Uniform panel with inplane loading.

$$f(M) = \sqrt{M^2 - 1} = 2.29$$

and the resulting panel stiffness requirement becomes

$$D = 88.26 \text{ N-m}$$

For an isotropic panel, the panel stiffness is expressed as

$$D = \frac{h^3 E}{12 \left(1 - v^2\right)}$$

where E is the material modulus of elasticity, h the panel thickness, and v the material Poisson's ratio. Using a value of 0.3 for v, the panel thickness requirement to preclude flutter becomes

$$h = 2.4 \text{ mm}$$

5.2 Elastically Supported Orthotropic Panel

An orthotropic panel simply supported at the leading and trailing edges and elastically supported at the stream edges as shown in figure 9 is to be evaluated for flutter. The influence of stream edge flexibility on the flutter critical dynamic pressure at a Mach number of 1.7 is required to aid in the definition of the support springs. The physical characteristics for the panel are as follows:

a	=	0.45 m
b	=	0.90 m
E	=	70 GN/m^2
D_1	=	10 N-m
D_2	=	2000 N-m
D_{12}	=	750 N-m
Δp	=	2kPa
K_D	=	range of 2 to 20 MN/m/m

Zero flow angle

From figure 4 the design procedure to be followed in this instance is detailed in section 4.1. The expressions for the geometry and flutter parameters are given by equations (20) and (21):

$$GP = \frac{a}{b} \sqrt{\frac{D_{12}/D_1}{1 + C^2/\overline{K}_S}}$$

$$FP = \frac{D_1 \, f(M)}{q \, a^3}$$

The fact that the leading and trailing edges have complete deflectional restraint (simply supported) has been reflected in the above by setting the nondimensional support parameter S_{LT} (eq. (22)) equal to one. Thus, for the particular panel configuration of interest
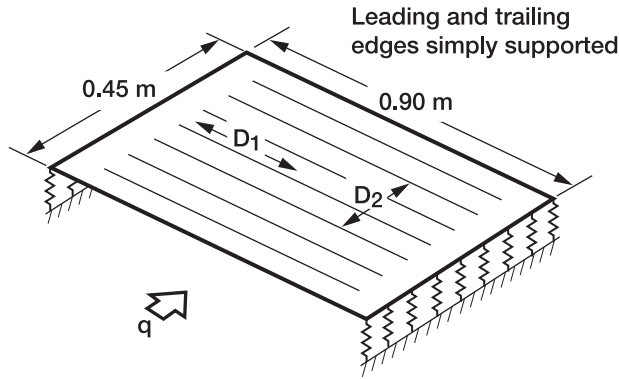
Figure 9.—Elastically supported orthotropic panel.

$$GP = \frac{1}{2}\sqrt{\frac{75}{1+28.13/\overline{K}_S}}$$

$$\frac{q}{f(M)} = \frac{109.7}{FP}$$

It is assumed that the stream edge supports take the form of a running spring. From figure B2 of appendix B the nondimensional support stiffness is given as

$$\overline{K}_S = \frac{K_D\, b^3}{\pi^3\, D_2}$$

which becomes

$$\overline{K}_S = 1.18 \times 10^{-5}\, K_D$$

for the configuration under consideration.

From figure 7, with an a over b ratio of one half and a Mach number of 1.7, the Mach number correction factor has a magnitude of

$$f(M) = 1.23$$

From equation (38), the pressure differential parameter is

$$P_f = \frac{\Delta p\, a^4}{D_1\, h_{eq}}$$

where h_{eq} is given by equation (39) and has the following value for this particular configuration

$$h_{eq} = 4.1 \text{ mm}$$

Thus, the pressure differential parameter becomes

$$P_f = 2000$$

and from figure 6 the pressure differential correction factor is determined to be

$$Q_p = 1.2$$

Combining the above, the relationship between the flutter critical dynamic pressure and the flutter parameter is given as

$$q = \frac{109.7}{FP} f(M) Qp = \frac{167.3}{FP}$$

The resulting influence of the stream edge support stiffness on the critical dynamic pressure is illustrated in figure 10. It must be noted that since GP is always less than five, the corresponding values for FP are obtained from equation (14). The zero moment boundary condition value of E_c is employed for the calculations summarized in figure 10.

5.3 Orthotropic Panel With Flow Angularity

The flutter sensitivity of a clamped orthotropic panel to angular flow is to be evaluated. Physical characteristics of the panel in question, shown in figure 11, are as follows:

a = 1.1 m
b = 0.7 m
D_1 = 2500 N-m
D_2 = 10 N-m
D_{12} = 50 N-m
M = 3.5
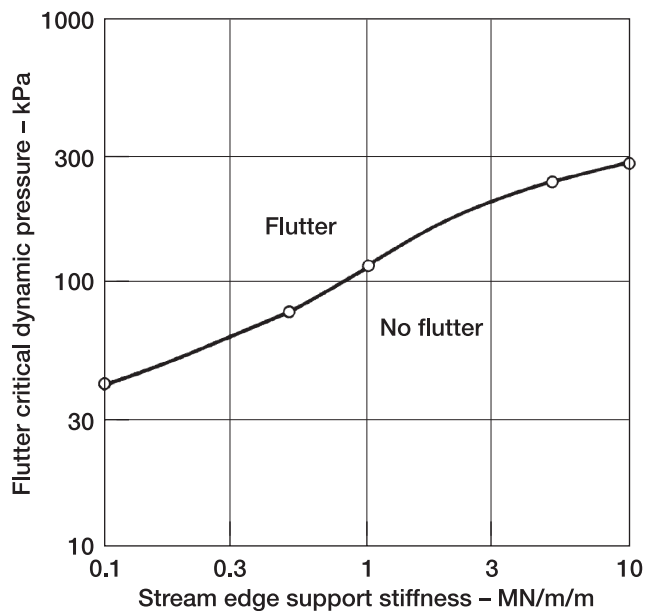
Figure 10.—Flutter critical dynamic pressure versus edge support stiffness.
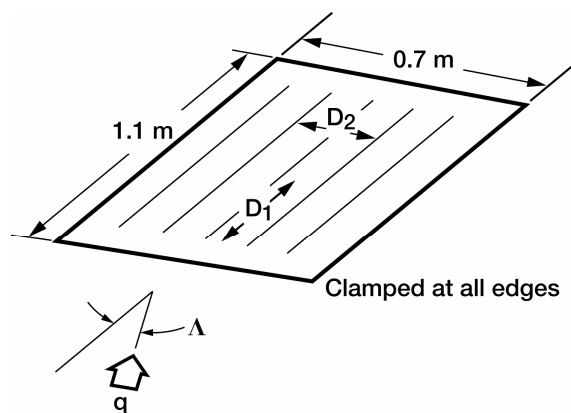
Figure 11.—Orthotropic panel with flow angularity.

From figure 4 the procedures of interest for this case are presented in section 4.2. For a panel with complete deflectional restraint (fully clamped) the desired relationships for *GP* and *FP* are given by equations (32) and (33). These relationships become

$$GP = 0.222\sqrt{\cos^2(\Lambda) + 41\sin^2(\Lambda)}$$

and

$$q = \frac{6300}{FP\left[\cos^2(\Lambda) + 64.4\sin^2(\Lambda)\right]}$$

for this particular panel configuration. Reflected in the above expression for the flutter critical *q* is the evaluation of the Mach number correction factor from equation (44).

$$f(M) = \sqrt{M^2 - 1} = 3.354$$

K_D (MN/m/m)	$\overline{K}_S$	*GP*	*FP*	*q* (kPa)
0.1	1.18	0.87	4.07×10^{-3}	41
0.5	5.9	1.80	2.15×10^{-3}	78
1	11.8	2.35	1.46×10^{-3}	114
5	59	3.56	7.00×10^{-4}	239
10	118	3.89	5.88×10^{-4}	284

The preceding expression for *GP* has been evaluated for various magnitudes of flow angularity Λ. The corresponding value for *FP* was obtained from equation (14) using the zero slope boundary condition value for E_c. The flutter critical dynamic pressure was then obtained and the resulting relationship between *q* and Λ is shown in figure 12.

Λ (deg)	*GP*	*FP*	*q* (kPa)
0	0.222	0.00302	2086
15	0.426	0.00298	403
30	0.736	0.00260	146
45	1.017	0.00221	87
60	1.236	0.00191	68
75	1.374	0.00179	60
90	1.421	0.00167	59
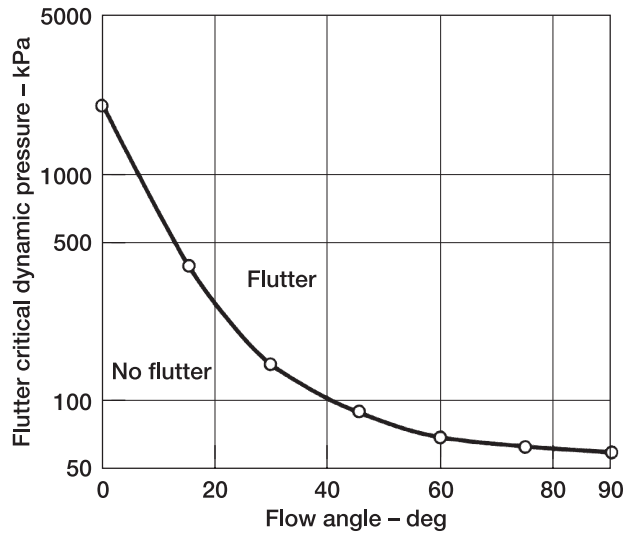
Figure 12.—Flutter critical dynamic pressure versus flow
angularity.

6. Design Boundary Verification

The preceding section describes a design approach, in conjunction with the flutter-free panel design boundary, developed for use in the preliminary design of flutter free lightweight external panels. In this section, the validity of the approach, as it applies to various panel configurations, is evaluated by comparing results from the preliminary design predictions with appropriate existing experimental data. Where no experimental data exist, comparisons are made with the results of detailed theoretical analyses. The experimental panel flutter data employed in the following sections are tabulated in appendix D and cross-referenced to the appropriate figures in the following sections.

6.1 Basic Panel

A large amount of experimental and flight flutter data for the basic panel configuration is available. In this context, "basic" panel configuration refers to a flat orthotropic panel (fig. 1) with either complete edge deflectional restraint or edge support flexibility effects. The influence of additional parameters such as flow angularity, inplane loads, etc., is considered in later sections.

The panel flutter data for the basic panel configuration obtained from references 10, 18, and 21 are shown in figure 13. The data of references 18 and 21 are for isotropic panels with total edge deflection restraints. As seen in figure 13, a majority of these data compare well with the flutter-free panel design boundary. The reference 18 data were obtained for a number of uniform panels of the same thickness and length to width ratios. For this panel configuration, the 37 experimental data points (represented by the straight line connecting the circular symbols) all fall within the flutter boundary. The data of reference 21 are for clamped isotropic panels of varying thickness and length to width ratios. These experimental results also compare well with the design boundary.

Data from an experimental investigation on the flutter characteristics of orthotropic panels are given in reference 10. These results are for a wide variety of panel configurations and stream edge flexibility support conditions. Their comparison with the flutter-free panel design boundary shows the boundary to be conservative. Indicated in figure 13 is the importance of the $C^2/\overline{K}_S$ term in the geometry parameter of equation (20). The solid points shown in this figure present the reference 10 data without accounting for the stream edge support flexibility while the open symbols include the influence of this support flexibility. It can be seen that when the edge flexibility effects are neglected the design boundary is very unconservative.

The lack of experimental data for panels with leading and trailing edge support flexibility precludes the comparison of the design boundary with test data. As an alternate, predictions obtained through application of the

flutter-free panel design boundary are compared with theoretical results of reference 9. This comparison is shown in figure 14 and as can be seen there is adequate correlation between the trends obtained with the design boundary and the theoretical results of reference 9.
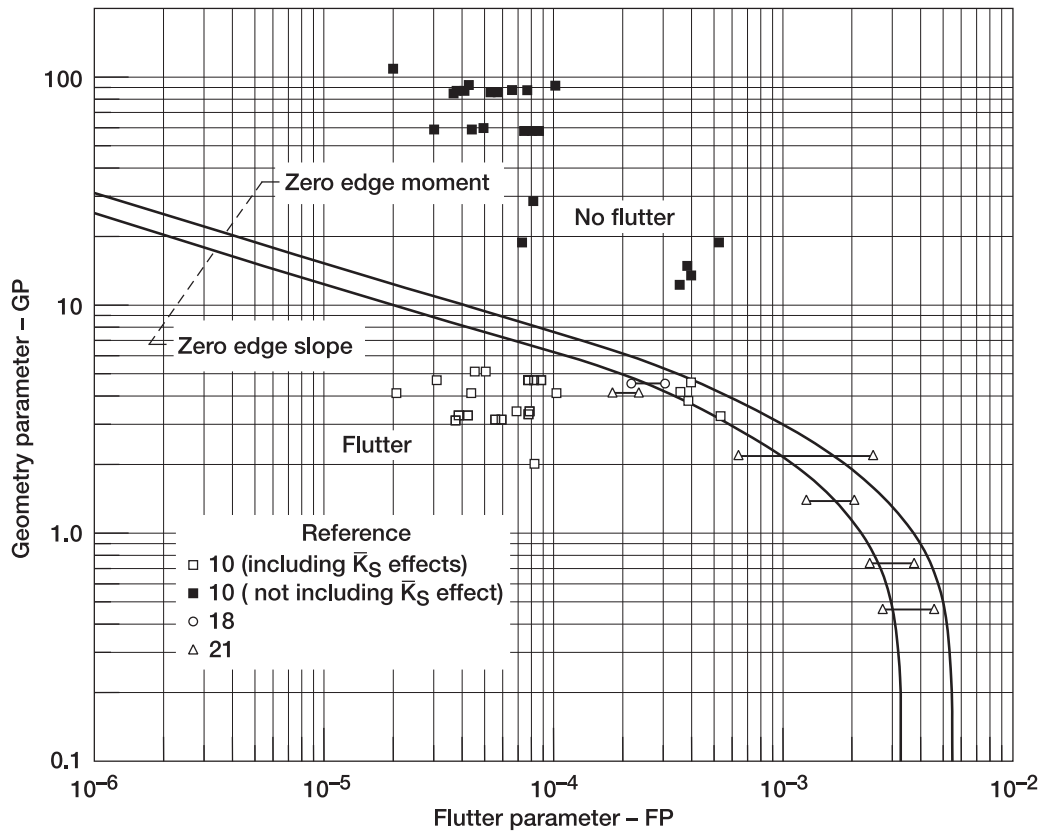
Figure 13.—Flutter data for basic panel configurations.
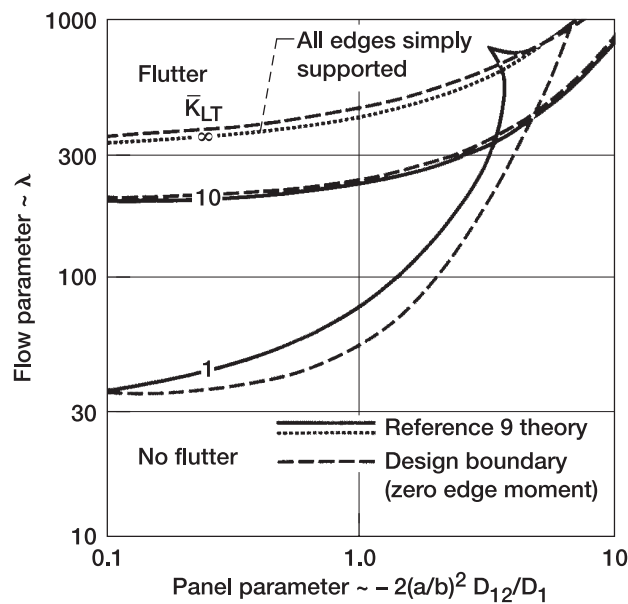
Figure 14.—Correlation with reference 9 theoretical results.

6.2 Flow Angularity

A limited amount of experimental flutter data, as presented in references 8, 11, and 22, exist for panels exposed to flow not parallel to one side. Note that the results presented in reference 22 are a duplication of the reference 11 information. All of these data, except for panel 1 of reference 11, are for orthotropic panels with leading and trailing edge support flexibility with respect to zero angle flow. The panel 1 configuration was an orthotropic panel clamped along all sides.

Comparison of these data with the design boundary is shown in figure 15. As can be seen, for a majority of these experimental data the correlation with the design boundary is conservative. Shown in figure 16 are the experimental and predicted λ's as a function of flow angle for the panel 2 (ref. 11) data. This figure illustrates the adequacy of the design approach in predicting the influence of flow angle on the flutter critical flow conditions of an orthotropic panel.
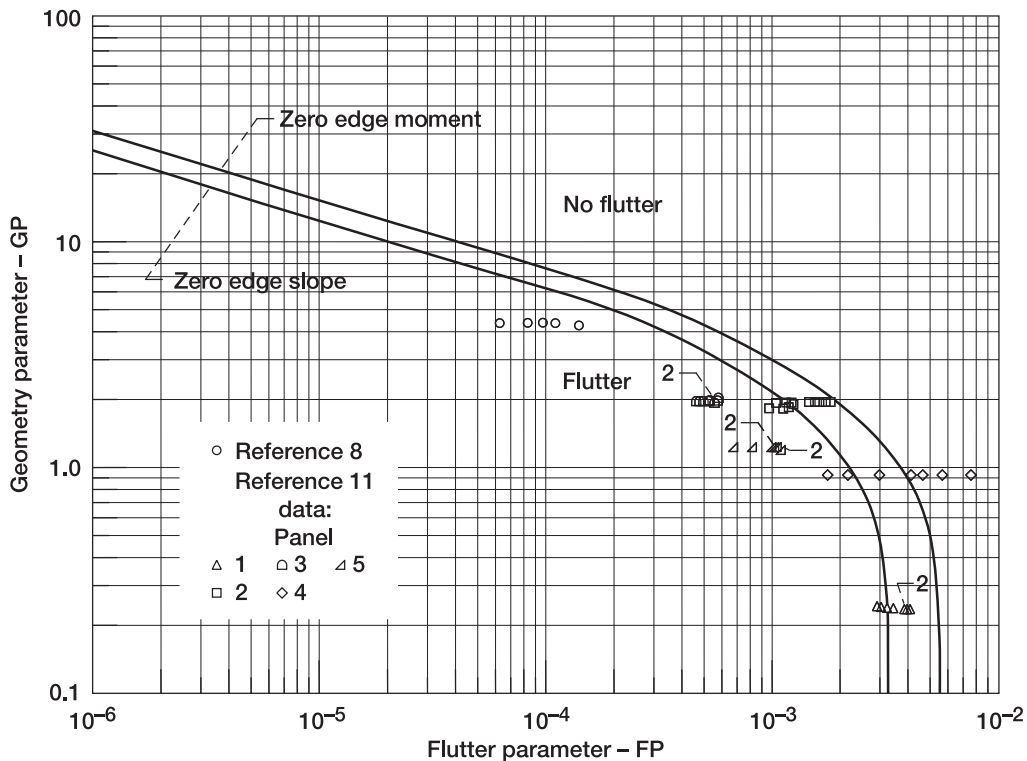
Figure 15.—Panel flutter data including influence of flow angularity.
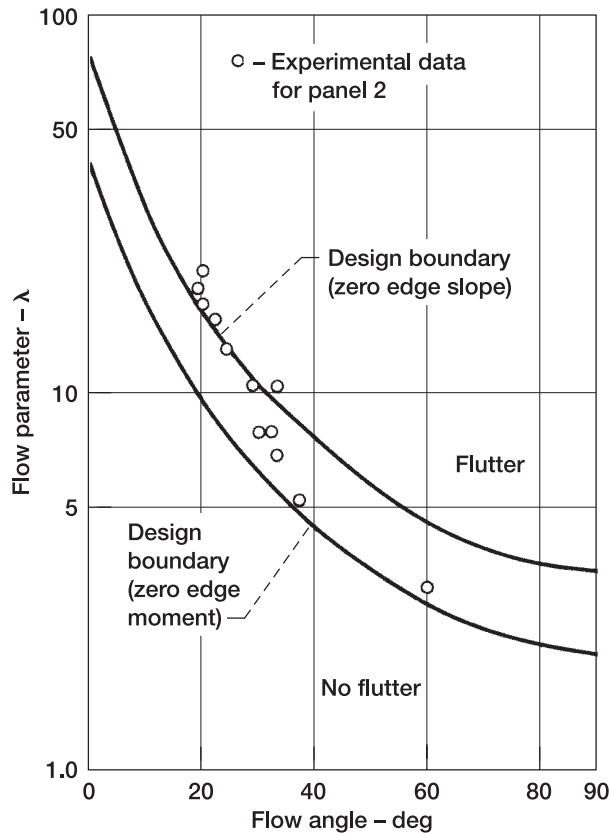
Figure 16.—Correlation with reference 11 experimental results.

6.3 Inplane Loads

Experimental data obtained during an extensive wind tunnel test program conducted to evaluate the influence of inplane loads on panel flutter (ref. 12) are compared with the design boundary in figure 17. These data are for isotropic panels with a wide range of panel *a* over *b* ratios. During the test program mechanical inplane loading was introduced by hydraulic actuators. As indicated in this figure, the correlation between these data and the flutter-free panel design boundary is conservative. It is assumed in reference 12 that the test panels have complete deflectional support at the edges. However a review of the test setup indicates that some stream edge support flexibility existed. This effect, as presented in table D-6 was included in the calculation of GP for the data shown in figure 17.

Additional experimental panel flutter results, including the influence of inplane loads, are given in references 7, 19, and 23 through 26. Test data as presented in these references are plotted on the panel design boundary in figure 18. The overall comparison between these data and the design boundary is in general conservative. For all these panels the inplane loads are the result of panel aerodynamic heating. The data shown on figure 18 are for isotropic panels except those discussed in references 7 and 26.
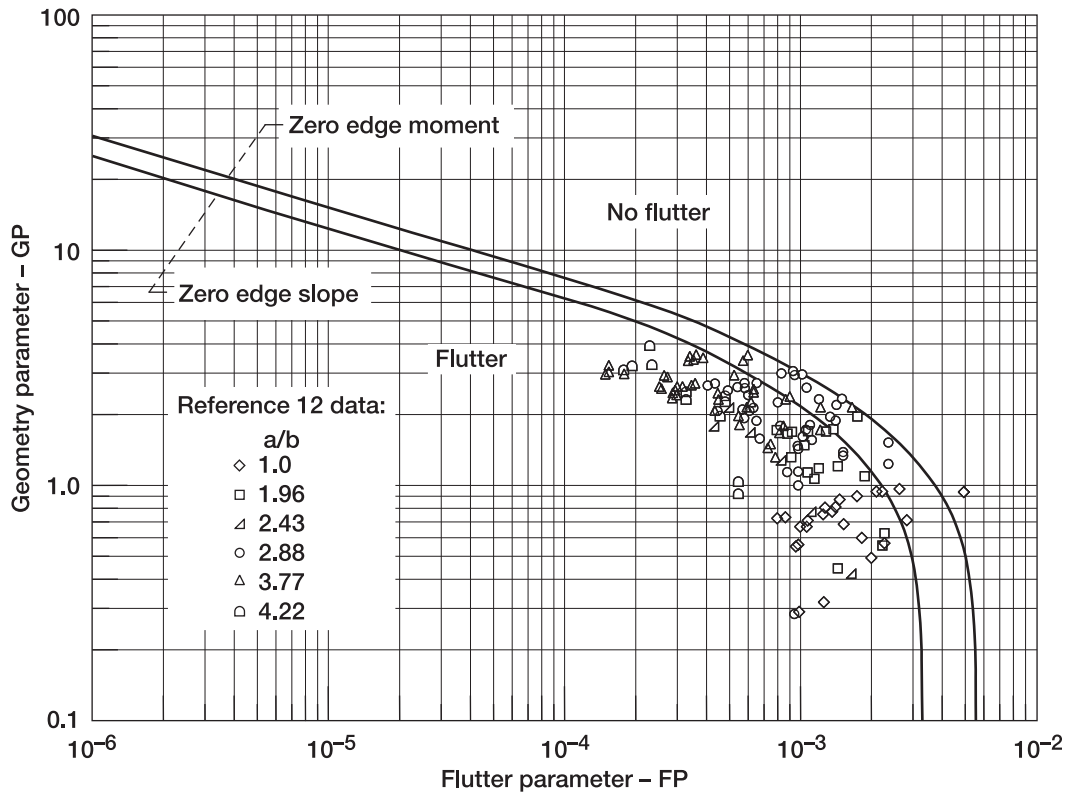
Figure 17.—Flutter data for panels with various a over b ratios and inplane loads.
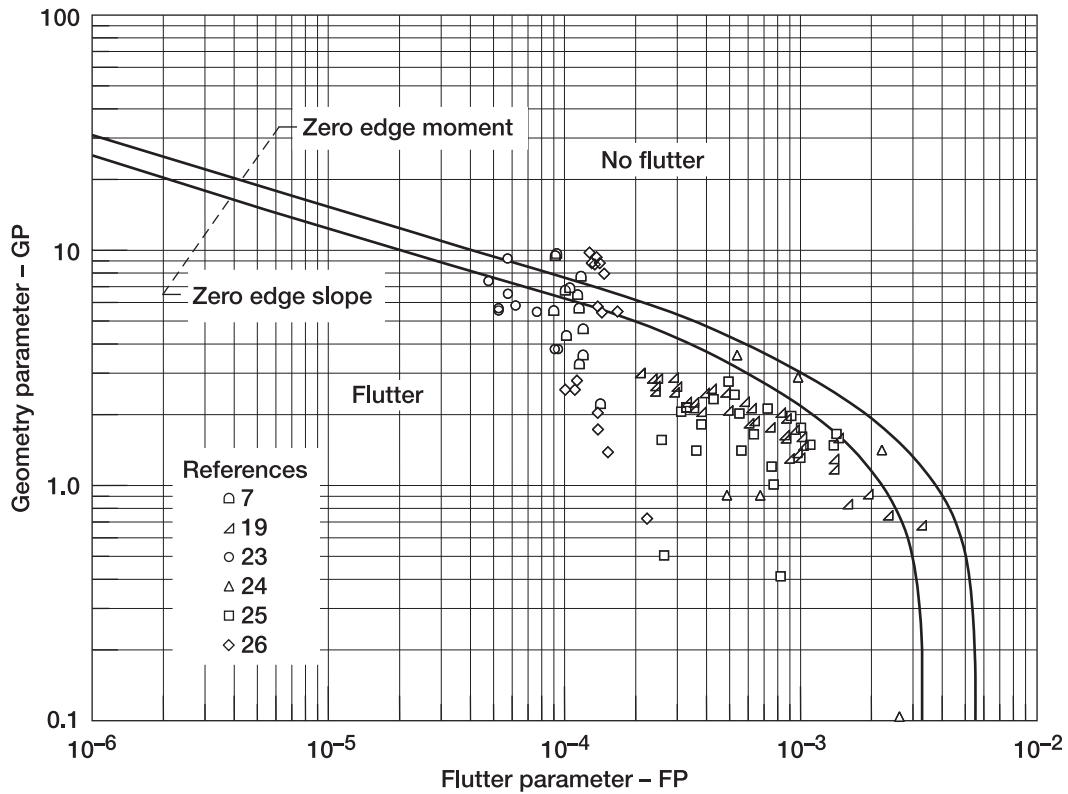
Figure 18.—Panel flutter data including influence of inplane loads.

6.4 Static Pressure Differential

The design procedure to be followed in evaluating the influence on panel flutter of a pressure differential is based on experimental results presented in references 17 and 18. These wind tunnel data were obtained for isotropic panels having complete restraint (clamped or simply supported) at the panel boundaries.

Limited amounts of additional data including pressure differential effects are available for correlation with the recommended design approach. The available data (ref. 10) are compared with the design boundary in figure 19. These data are for a highly orthotropic panel with stream edge support flexibility and an a over b ratio of one.

The closed symbols are for this experimental data before the pressure differential correction factor Q_p has been applied. Application of the procedures of section 4.4 to modify the experimental $q/f(M)$ value by the appropriate magnitude of Q_p results in the comparison with the design boundary as indicated by the open symbols in figure 19.

Other data with pressure differential effects included are available in reference 10. However, these configurations result in magnitudes for the pressure differential parameter P_f which exceed the range covered in figure 6. This indicates that the design procedure of section 4.4 is limited to panel configurations whose characteristics result in magnitudes of P_f covered by figure 6.
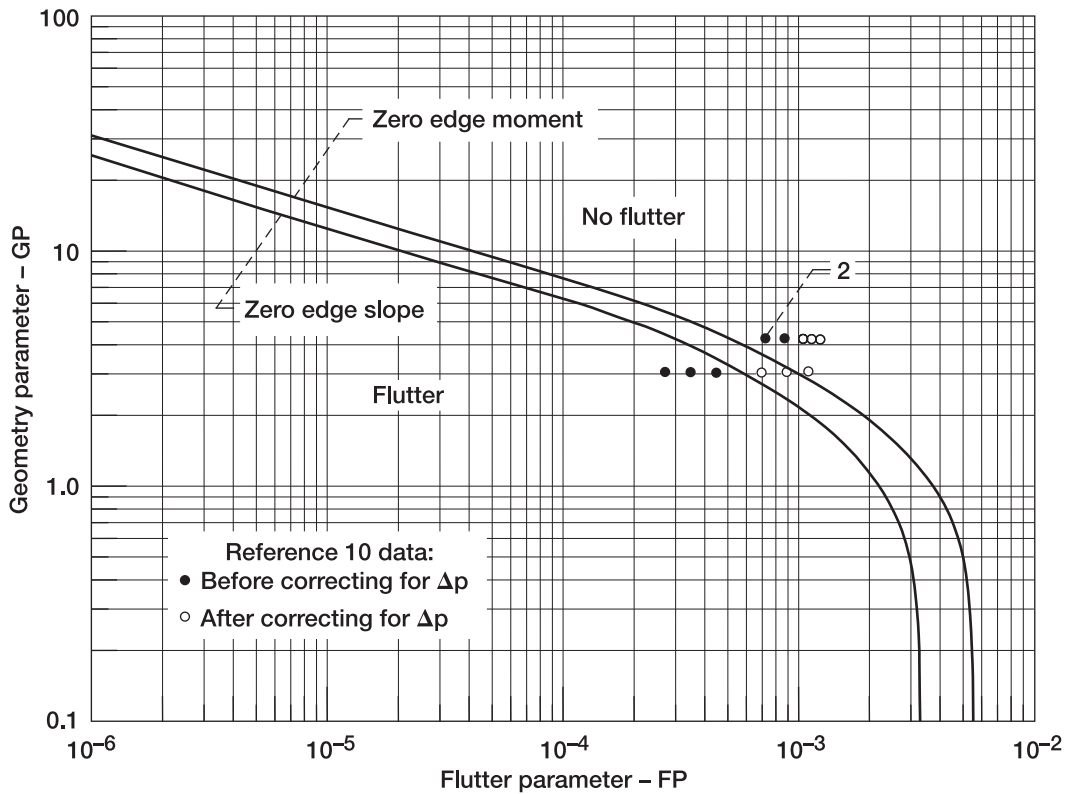
Figure 19.—Panel flutter data including the influence of static pressure differential.

6.5 Structural Damping

A procedure is described in section 4.5 which allows evaluation of the influence of structural damping in combination with inplane loads. With this procedure the dynamic pressure parameter $q/f(M)$ obtained through application of the design boundary is modified by the damping factor D_f (eq. (41)) to account for the presence of the damping.

For a panel with inplane loading, results obtained from application of the flutter-free panel design boundary with no added damping compare well with detailed theoretical analyses that include a structural damping coefficient of 0.01. Such a comparison is shown in figure 20, where both experimental data and theoretical results for a clamped panel detailed in reference 19 are shown. Thus, results obtained from the design boundary may be thought of as including "nominal" structural damping on the order of 0.01. For panels having higher damping characteristics ($g > 0.01$) and inplane loads, the damping factor D_f as defined by equation (41) is to be employed.

Many data points for panels with inplane loading shown in figure 17 appear quite conservative. As discussed in reference 12, significant structural damping, up to five percent, was measured for a number of the panels. The presence of such magnitudes of damping can have a large influence on the flutter susceptibility of panels with inplane loading. Referring to equation (41), the damping factor is dependent on the magnitudes of both the structural damping and inplane loading. Figure 21 shows the influence of structural damping on panel 4 of reference 12. The lower flutter boundary results from the design boundary ($g = 0.01$) and the upper boundary results from the damping factor D_f defined by equation (41). The good agreement between the experimental data and the predicted boundary for the average measured structural damping $g = 0.028$ indicates that equation (41) is sufficiently accurate for flutter design of panels with significant structural damping.
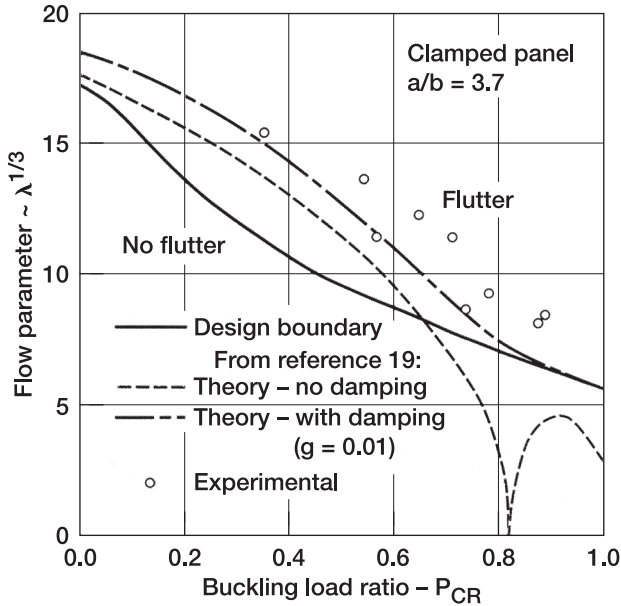
Figure 20.—Correlation with reference 19 clamped panel results.
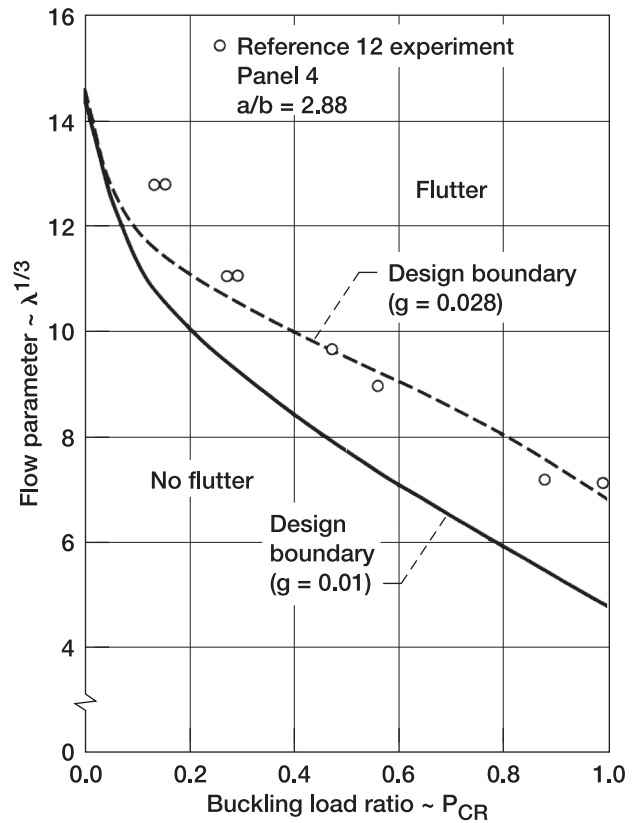
Figure 21.—Influence of high structural damping for a panel with inplane loading.

6.6 Mach Number Effect

The definition of the Mach number correction factor $f(M)$ as given in figure 7 is based on experimental panel flutter results in the low supersonic Mach number regime. The trends illustrated in figure 7 are established in reference 18 and are based on results obtained during wind tunnel test programs such as those discussed in references 18 and 21.

Further verification of these relationships between $f(M)$ and Mach number is illustrated in figure 22. Here data obtained during extensive panel flutter test programs detailed in references 27 and 28 are compared with predictions obtained with the flutter-free panel design boundary when modified by $f(M)$. The data from reference 27 are for a clamped isotropic panel while those of reference 28 were obtained for a panel having less than a fully clamped boundary condition. The spread in test data indicated in figure 22 for a particular Mach number is related to the boundary layer thickness at the test conditions.
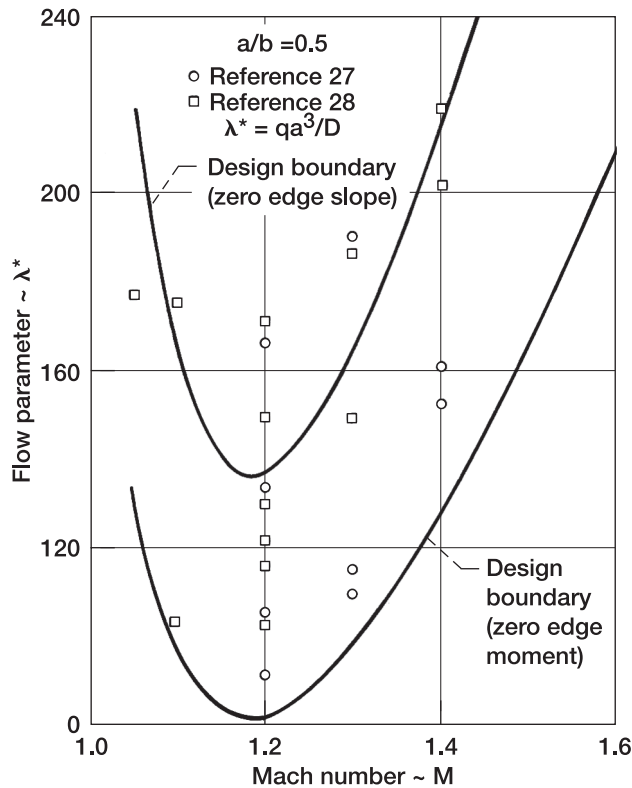
Figure 22.—Panel flutter data in low supersonic regime.

7. Concluding Remarks

Criteria and procedures for their application in the preliminary design of flutter free lightweight external surface panels have been presented in a format which permits their use by individuals without prior panel flutter experience. The major area of application for these procedures is in the design of orthotropic metallic panels which stand off from primary structure. Examples which illustrate the use of these criteria and procedures are given.

The panel design approach presented in this report is a logical extension of previous work done in this area. The design criteria account for most of the interacting parameters which significantly influence panel susceptibility to flutter. Parameters included in these design procedures are

- Panel aspect ratio
- Panel orthotropic properties
- Support flexibility
- Inplane loads
- Static pressure differential
- Flow angularity
- Structural damping

The validity of the flutter-free panel design boundary (fig. 3) and its application (section 4.0) to preliminary panel design has been demonstrated by comparison of predicted flutter results with experimental data. Included in this verification process are data for panels ranging from isotropic to those having highly orthotropic stiffness characteristics. In addition, data for panels including the influence of parameters such as edge support conditions, inplane loads, flow angularity, etc., were available and used. As discussed in section 6.0, application of the design procedures resulted in the conservative prediction of flutter points for a vast majority of the existing experimental data.

External panels on discrete flexible supports are being strongly considered for use as a high performance vehicle thermal protection system. The influence of this type of support condition was not incorporated into the design procedure due to a limited availability of information (ref. 29) for this configuration. Further theoretical considerations and corresponding panel flutter test programs are needed to investigate this support condition.

Limited experimental data exist for the flutter of orthotropic panels including the influence of flow angularity. In addition, no data exist for panels subjected to the combined conditions of inplane loads and flow angularity. Comprehensive theoretical investigations of these aspects of the panel flutter problem have been conducted and are documented in the literature. Further testing to provide the data needed to evaluate these theoretical results is required.

Appendix A
Orthotropic Panel Stiffness Parameters

Of basic importance to the use of the flutter-free panel design boundary is knowledge of the panel orthotropic stiffness properties. A number of techniques which may be employed to obtain these quantities are presented in this appendix.

For panels with closed corrugations (fig. A1(a)) the use of the procedures detailed in reference 30 are recommended. Determination of the panel stiffness properties for the other two configurations shown in figure A1 is discussed in reference 31. For a panel with equidistant ribs (fig. A1(b)) reference 31 gives the following expressions for D_1, D_2, and D_{12}

$$D_1 = \frac{Eh^3}{12\left(1-v^2\right)} \frac{\ell}{\left[\ell - t + (h/H)^3 t\right]}$$

$$D_2 = \frac{EI_1}{\ell} \tag{A1}$$

$$D_{12} = \frac{Eh^3}{12\left(1-v^2\right)} + \frac{GJ}{\ell}$$

where I_1 is the moment of inertia of the cross-hatched area defined in figure A1(b) and GJ is the torsional rigidity of one rib.

The stiffness properties for the corrugated sheet (fig. A1(c)) as defined in reference 31 are expressed as

$$D_1 = \frac{\ell}{s} \frac{Eh^3}{12\left(1-v^2\right)}$$

$$D_2 = EI_1 \tag{A2}$$

$$D_{12} = \frac{s}{\ell} \frac{Eh^3}{12(1+v)}$$

where

$$s \approx \ell\left[1 + \left(\frac{\pi H}{2\ell}\right)^2\right] \tag{A3}$$

and

$$I_1 = \frac{H^2 h}{2}\left[1 - \frac{0.81}{1 + 0.625\,(H/\ell)^2}\right] \tag{A4}$$
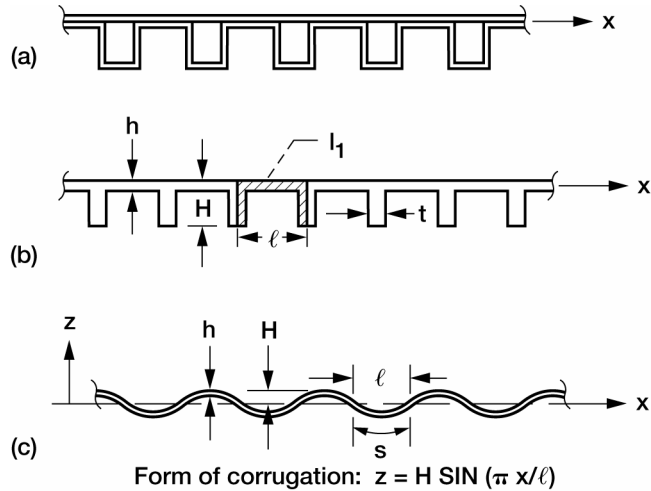
Figure A1.—Orthotropic panel configurations. (a) Closed corrugations. (b) Equidistant ribs. (c) Corrugated sheet.

An approach for obtaining initial estimates for the stiffness properties of an orthotropic panel is implied by Timoshenko in reference 31. With this approach, the panel bending rigidities are related to the properties of a beam of unit width. Thus, considering the case illustrated in figure Al(b), we have

$$D_1 = \frac{Eh^3}{12}$$

$$D_2 = \frac{EI_1}{\ell}$$

(A5)

where I_1 has previously been defined. Following the approach mentioned in reference 31, the quantity D_{12} is then estimated as

$$D_{12} = \sqrt{D_1 D_2}$$

The above is not a recommended procedure for general usage, but does allow initial estimates of the panel's stiffness characteristics to be readily made.

Experimental procedures for obtaining these panel parameters are discussed in references 32 and 33. These experimental approaches do not have application during preliminary design, but are mentioned here for completeness.

Appendix B
Edge Support Stiffness Expressions

Techniques have been developed for the estimation of the nondimensional stiffness parameters for various panel edge support configurations. An energy approach is used to obtain these expressions. In this approach, for an assumed deflection pattern, the strain energy stored in an idealized support spring configuration (fig. B1) is equated to the energy stored in the configuration of interest.

A summary of these results is given in figure B2. Expressions are presented in this figure for the support stiffnesses along with sketches defining each support's geometric characteristics. The results presented in figure B2 are for support springs located along the panel stream edges as illustrated in figure B1. Similar expressions for leading and trailing edge support springs are obtained by interchanging the geometric quantities associated with the panel coordinate system. The stiffness expressions are given in the nondimensional form required for application with the flutter-free panel design boundary.

A summary of the stiffness properties for a number of support clips or standoffs is presented in figure B3. These quantities are presented in terms of the stiffness associated with a discrete spring. The corresponding running or line spring for a number of K_d discrete springs is defined as

$$K_D = \frac{N K_d}{a} \tag{B1}$$

where N is the number of discrete springs located down the panel side of length a.

To illustrate the procedure that was employed to obtain the information presented in figure B2, the analysis of an edge support panel (support condition 3) will be presented in detail. Referring to figure Bl, the strain energy stored in the idealized support springs is given as

$$U_I = \frac{1}{2} \int_0^a K_D w^2 dx$$

$$= C^2 \frac{a}{4} K_D \tag{B2}$$

where it has been assumed that the deflection at the support springs is given as

$$w = C \sin \frac{\pi x}{a} \tag{B3}$$

Introducing the nondimensional spring rate notation

$$\overline{K}_D = \frac{K_D b^3}{\pi^3 D_2} \tag{B4}$$
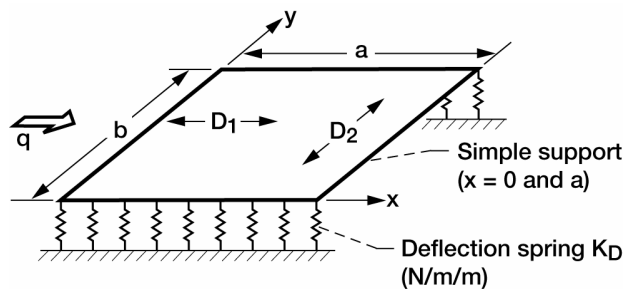
Figure B1.—Idealized stream edge spring supports.

Support Condition	Support Type	Support Configuration	Nondimensional Support Stiffness
1	Running Spring		$$\overline{K}_s = \frac{K_D b^3}{\pi^3 D_2}$$
2	Discrete Spring		$$\overline{K}_s = \frac{2}{a}\frac{K_d}{D_2}\left(\frac{b}{\pi}\right)^3 \sum_j \sin^2\left(\frac{\pi x_j}{a}\right)$$
3	Edge Support Panel		$$\overline{K}_s = \frac{D_o}{D_2}\left(\frac{b}{\pi}\right)^3 l\left[\frac{17}{35}\left(\frac{\pi}{a}\right)^4 + \frac{12}{5}\left(\frac{\pi}{al}\right)^2 + \frac{3}{l^4}\right]$$
4	Tapered Edge Support Panel		$$\overline{K}_s = \alpha\left(\frac{b}{\pi}\right)^3 l\left[\frac{17}{35}\left(\frac{\pi}{a}\right)^4 + \frac{12}{5}\left(\frac{\pi}{al}\right)^2 + \frac{3}{l^4}\right]$$ where $$\alpha = \frac{1}{20}\left(\frac{s}{l}\right)^3 + \frac{D_o}{D_2}\left[1 - \frac{1}{20}\left(\frac{s}{l}\right)^3\right]$$
5	Doubler		$$\overline{K}_s = \frac{EI_o}{D_2}\left(\frac{b}{a}\right)^3\left(\frac{\pi}{a}\right)$$

Figure B2.—Nondimensional stream edge support stiffness expressions.

equation (B2) becomes

$$U_I = C^2 \frac{a}{4} \left(\frac{\pi}{b}\right)^3 D_2 \ \overline{K}_D \qquad \text{(B5)}$$

Since for stream edge support flexibility we have

$$\overline{K}_S = \overline{K}_D \qquad \text{(B6)}$$

equation (B5) may be written as

$$U_I = C^2 \frac{a}{4} \left(\frac{\pi}{b}\right)^3 D_2 \ \overline{K}_S \qquad \text{(B7)}$$
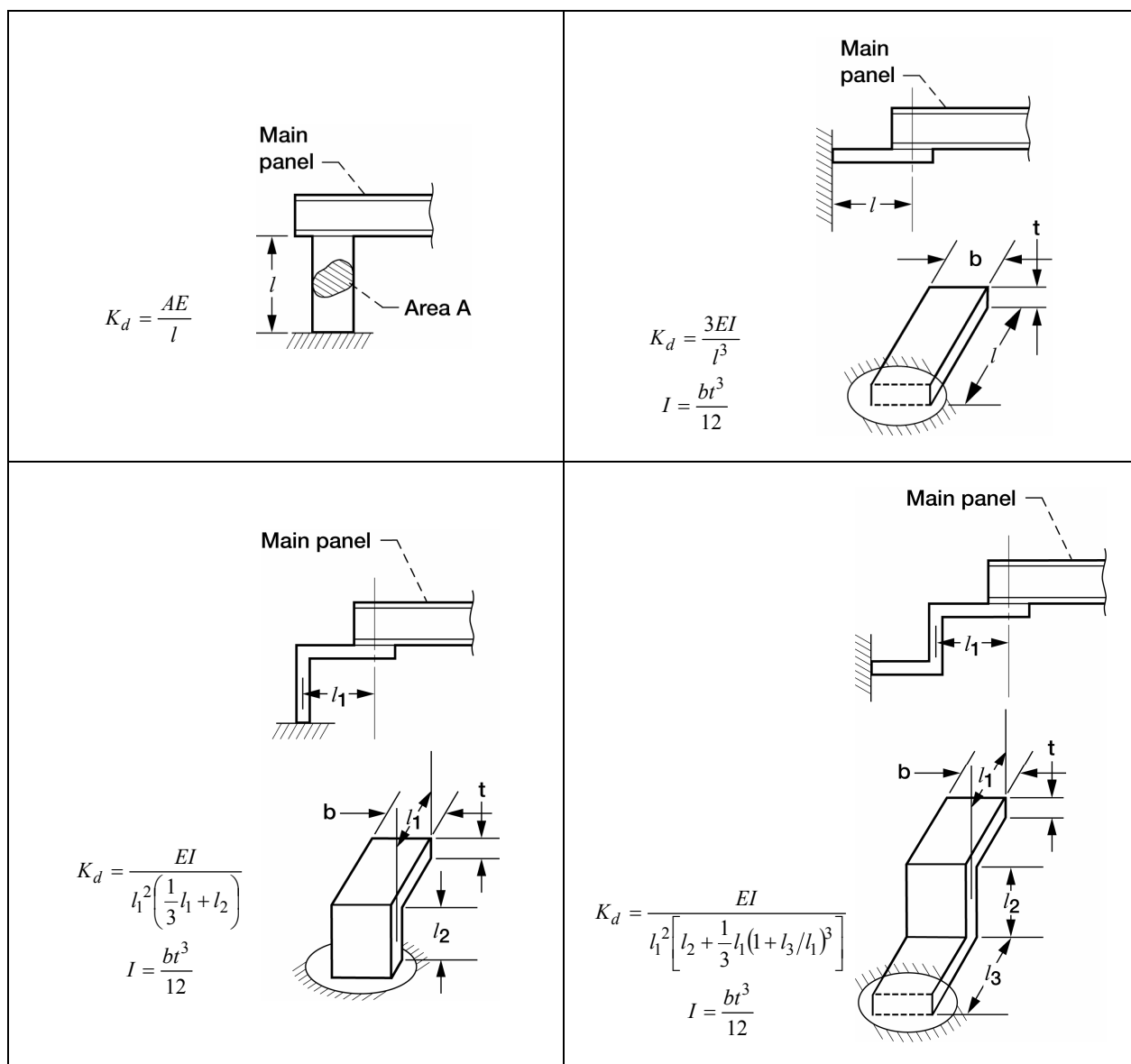
Figure B3.—Stiffness of panel edge support springs.

For the edge support panel illustrated in figure B4 the energy stored in the edge panel is given by

$$U_S = \frac{1}{2} D_o \int_0^{\ell} \int_0^a \left\{ \left(\frac{\partial^2 w}{\partial x^2} + \frac{\partial^2 w}{\partial y^2} \right)^2 - 2(1-\nu) \left[\frac{\partial^2 w}{\partial x^2} \frac{\partial^2 w}{\partial y^2} - \left(\frac{\partial^2 w}{\partial x \, \partial y} \right)^2 \right] \right\} dx \, dy \tag{B8}$$

It is assumed that the deflection throughout the edge panel is given as

$$w = \frac{C}{2} \left[3 \frac{y}{\ell} - \left(\frac{y}{\ell} \right)^3 \right] \sin \frac{\pi x}{a} \tag{B9}$$

The use of this deflection shape is analogous to assuming that the main panel is infinitely stiff relative to the stiffness of the edge panel in the y direction. Combining equations (B8) and (B9) yields the following expression for the strain energy stored in the edge panel:

$$U_S = \frac{1}{4} C^2 D_o \frac{a\ell}{4} \left[\frac{68}{35} \left(\frac{\pi}{a} \right)^4 + \frac{48}{5} \left(\frac{\pi}{a\ell} \right)^2 + 12 \frac{1}{\ell^4} \right] \tag{B10}$$

Equating equations (B10) and (B7), the expression for the nondimensional stiffness of an edge support panel becomes

$$\overline{K}_S = \ell \frac{D_o}{D_2} \left(\frac{b}{\pi} \right)^3 \left[\frac{17}{35} \left(\frac{\pi}{a} \right)^4 + \frac{12}{5} \left(\frac{\pi}{a\ell} \right)^2 + \frac{3}{\ell^4} \right] \tag{B11}$$
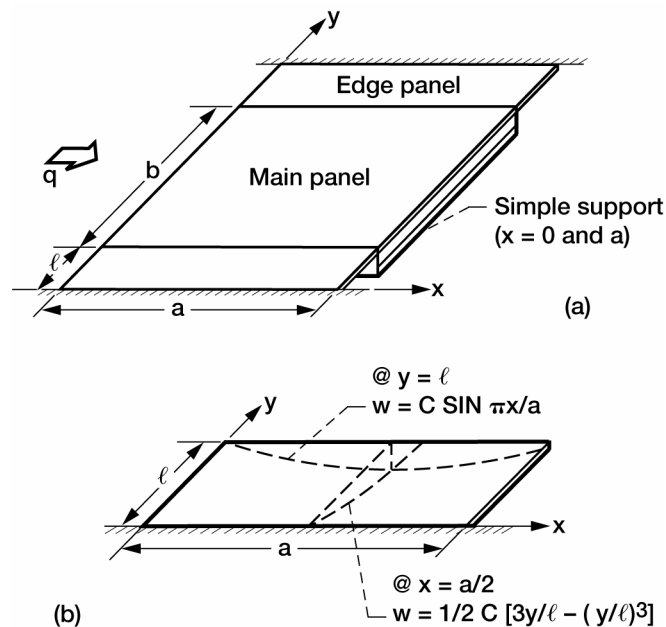
Figure B4.—Edge support panel. (a) Overall configuration.
(b) Assumed deflection pattern.

Appendix C
Panel on Elastic Foundation

The question of the flutter sensitivity of a panel on an elastic foundation falls into two categories. The first of these, with a rigid substructure, is illustrated in figure C1(a). It consists of a flexible panel exposed to the flow while supported by an elastic medium or foundation. This elastic foundation is in turn mounted to an essentially rigid base. In the second, the lower surface of the elastic medium is mounted to a second flexible panel or elastic substructure as shown in figure Cl(b). These two different configurations are treated separately in the following sections.

C.1 Rigid Substructure

In the absence of damping it can be shown (ref. 34) that the critical flow conditions for flutter of a simply supported isotropic panel resting on an elastic foundation with a rigid substructure are unaffected by the foundation. In reference 34 a Winkler foundation model was employed wherein a point load on the foundation gives rise to a deflection at the same point but nowhere else. The distinction between this Winkler foundation representation and a foundation model which allows deflections at points surrounding a point load is discussed in reference 35.

The fact that a Winkler foundation has no influence on the flutter of a simply supported panel, can be explained by the way in which the foundation contributes to the panel dynamic characteristics. The effect of the foundation is to increase the panel natural frequencies, but not to change the frequency separation between the various modes. This results in the same flutter q for a given panel configuration with or without the elastic foundation. As discussed in reference 34, when aerodynamic damping or an effective structural damping (viscous type) is included in the analysis the flutter conditions can be significantly affected by the foundation depending upon the magnitude of the foundation stiffness.
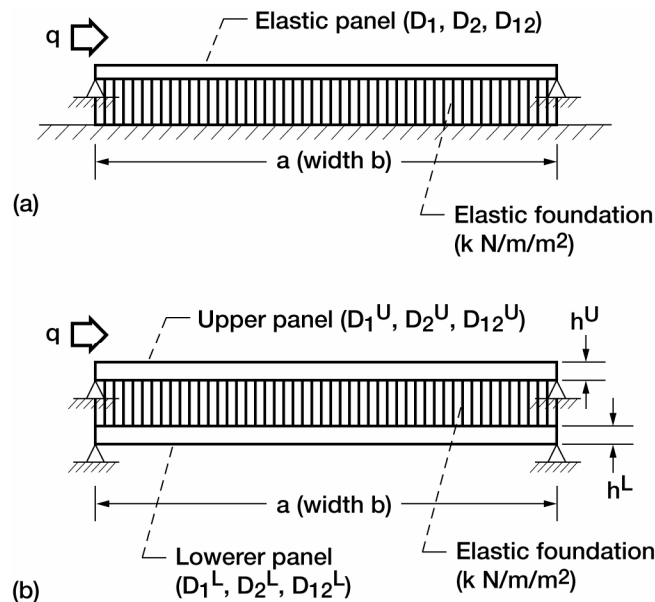
Figure C1.—Panel on elastic foundation. (a) Rigid substructure. (b) Elastic substructure.

Results of a two mode flutter solution for an isotropic panel presented in reference 34 have been extended to the case of an orthotropic panel resting on an elastic foundation. These results are expressed as

$$\lambda = 18.26 \left\{ \left[15 + 6\frac{D_{12}}{D_1}\left(\frac{a}{b}\right)^2 \right]^2 + 2g_T^2 \left[17 + 10\frac{D_{12}}{D_1}\left(\frac{a}{b}\right)^2 + \frac{D_2}{D_1}\left(\frac{a}{b}\right)^4 + 2K \right] \right\}^{1/2} \qquad (C1)$$

where λ is defined by equation (6). In this expression, g_T is a damping coefficient which combines both aerodynamic and structural damping, K is the elastic foundation stiffness parameter given as

$$K = \frac{k\,a^4}{\pi^4 D_1} \qquad (C2)$$

with other quantities defined in figure C1(a).

The design procedure for this panel configuration employs the flutter-free panel design boundary to estimate a flutter critical condition neglecting g_T and elastic foundation effects. With equation (C1), the ratio of flow parameters with and without elastic foundation and damping effects is obtained. The critical parameter obtained from the design boundary is then modified by this ratio to account for damping and foundation stiffness.

Results obtained from this approach for a panel configuration with a rigid substructure are shown in figure C2. The relationship between the flow parameter ratio λ/λ_o obtained from equation (C1) as a function of the nondimensional foundation parameter K (eq. (C2)) and damping is illustrated. In this context λ_o is the flow parameter at flutter neglecting damping and elastic foundation effects while λ is the corresponding parameter including these effects. These results are compared with the analytical results from reference 34.
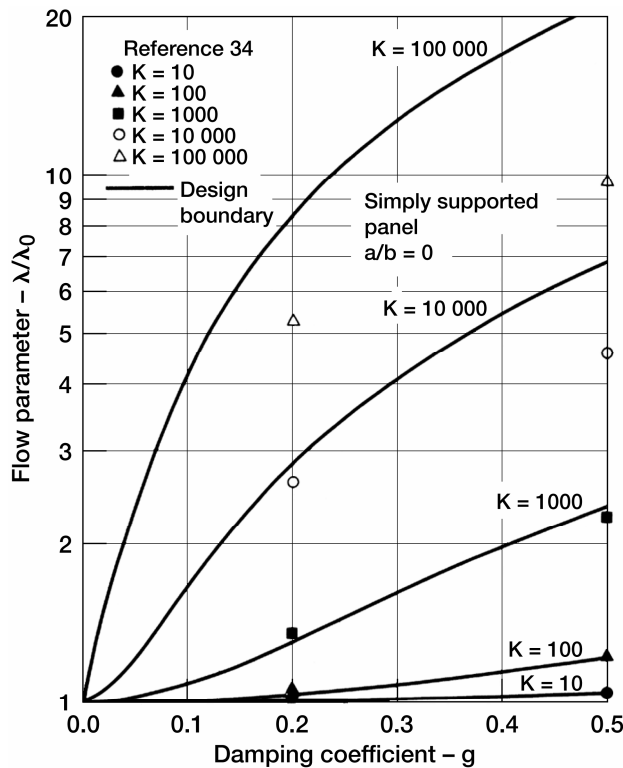
Figure C2.—Comparison of two mode solution including elastic foundation effects with reference 34 results.

As indicated by the data presented in figure C2, this procedure has application only at lower values of K ($K \leq 1000$). It must be emphasized that this approach has the inherent limitations of a two mode flutter solution and a reliable panel design effort must include a detailed flutter analysis including the influence of the elastic foundation.

C.2 Elastic Substructure

Theoretical considerations for two parallel isotropic simply supported elastic panels interconnected by an elastic medium are given in references 36 and 37. Results shown in these references illustrate the complex interplay between the stiffness characteristics of the elastic medium, panel configurations, and magnitude of inplane loading. Representation of these complex interactions in terms of design criteria does not appear feasible. However, the two mode theoretical approach of references 36 and 37 has been modified for orthotropic panels and additional panel flutter trends obtained.

Following the analytical procedure of references 36 and 37 and neglecting the influence of inplane loads, the two mode solution for parallel, elastically interconnected simply supported orthotropic panels is

$$
\pi^4 \frac{ab}{4}
\begin{bmatrix}
\dfrac{D_1^U}{a^4}\left[1+2\left(\dfrac{D_{12}}{D_1}\right)^U\left(\dfrac{a}{b}\right)^2+\left(\dfrac{D_2}{D_1}\right)^U\left(\dfrac{a}{b}\right)^4\right] & -\dfrac{16q}{3f(M)a} & 0 & 0 \\[2ex]
\dfrac{16q}{3f(M)a} & \dfrac{D_1^U}{a^4}\left[16+8\left(\dfrac{D_{12}}{D_1}\right)^U\left(\dfrac{a}{b}\right)^2+\left(\dfrac{D_2}{D_1}\right)^U\left(\dfrac{a}{b}\right)^4\right] & 0 & 0 \\[2ex]
0 & 0 & \dfrac{D_1^L}{a^4}\left[1+2\left(\dfrac{D_{12}}{D_1}\right)^L\left(\dfrac{a}{b}\right)^2+\left(\dfrac{D_2}{D_1}\right)^L\left(\dfrac{a}{b}\right)^4\right] & 0 \\[2ex]
0 & 0 & 0 & \dfrac{D_1^L}{a^4}\left[16+8\left(\dfrac{D_{12}}{D_2}\right)^L\left(\dfrac{a}{b}\right)^2+\left(\dfrac{D_2}{D_1}\right)^L\left(\dfrac{a}{b}\right)^4\right]
\end{bmatrix} W
$$

$$
+\frac{ab}{4}
\begin{bmatrix}
\bar{\rho}^U & 0 & 0 & 0 \\
0 & \bar{\rho}^U & 0 & 0 \\
0 & 0 & \bar{\rho}^L & 0 \\
0 & 0 & 0 & \bar{\rho}^L
\end{bmatrix}\ddot{W}
+\frac{ab}{4}
\begin{bmatrix}
k & 0 & -k & 0 \\
0 & k & 0 & -k \\
-k & 0 & k & 0 \\
0 & -k & 0 & k
\end{bmatrix}W = 0
\tag{C3}
$$

where $\bar{\rho}$ is the mass per unit area for the particular panel. In figure C1(b) the superscripts U and L refer to the upper and lower panels, respectively. The form of equation (C3) assumes deflection solutions for the upper panel as follows

$$w^U(x,y,t) = W^U_{11}(t)\sin\left(\frac{\pi x}{a}\right)\sin\left(\frac{\pi y}{b}\right) + W^U_{21}(t)\sin\left(\frac{2\pi x}{a}\right)\sin\left(\frac{\pi y}{b}\right) \tag{C4}$$

with similar expressions for the lower panel.

Equation (C3) is nondimensionalized with respect to the lower panel by employing the following relationships

$$D^U_1 = \varepsilon D^L_1 \qquad \lambda = \frac{2qa^3}{f(M)D^L_1}$$

$$\bar\rho^U = \eta \bar\rho^L \qquad K = \frac{k\,a^4}{\pi^4 D^L_1} \tag{C5}$$

Thus, equation (C3) may be written as

$$\frac{\pi^4 D^L_1}{\bar\rho^L a^4}\left[\begin{array}{cccc}
\left[1+2\left(\dfrac{D_{12}}{D_2}\right)^U\left(\dfrac{a}{b}\right)^2+\left(\dfrac{D_2}{D_1}\right)^U\left(\dfrac{a}{b}\right)^4\right]\varepsilon+K & \dfrac{8}{3}\dfrac{\lambda}{\pi^4} & -K & 0 \\[3mm]
-\dfrac{8}{3}\dfrac{\lambda}{\pi^4} & \left[16+8\left(\dfrac{D_{12}}{D_1}\right)^U\left(\dfrac{a}{b}\right)^2+\left(\dfrac{D_2}{D_1}\right)^U\left(\dfrac{a}{b}\right)^4\right]\varepsilon+K & 0 & -K \\[3mm]
-K & 0 & \left[1+2\left(\dfrac{D_{12}}{D_1}\right)^L\left(\dfrac{a}{b}\right)^2+\left(\dfrac{D_2}{D_1}\right)^L\left(\dfrac{a}{b}\right)^4\right]+K & 0 \\[3mm]
0 & -K & 0 & \left[16+8\left(\dfrac{D_{12}}{D_1}\right)^L\left(\dfrac{a}{b}\right)^2+\left(\dfrac{D_2}{D_1}\right)^L\left(\dfrac{a}{b}\right)^4\right]+K
\end{array}\right]W$$

$$+ \begin{bmatrix} \eta & 0 & 0 & 0 \\ 0 & \eta & 0 & 0 \\ 0 & 0 & 1 & 0 \\ 0 & 0 & 0 & 1 \end{bmatrix}\ddot{W} = 0 \tag{C6}$$

The eigenvalue problem associated with equation (C6) was formulated and programmed on the digital computer. An interactive procedure was then used to obtain the flutter critical λ for a given panel configuration. In this procedure the value of λ is systematically varied and the lowest value of λ for which two of the eigenvalues coalesce is sought. The procedure was used to generate trends for flutter of coupled orthotropic panels. These trends are presented so that the designer is aware of the potential flutter problems with parallel elastically coupled panels.

Typical results for interconnected parallel panels are illustrated in figure C3 where the critical flow parameter λ as a function of panel a over b ratio and elastic medium stiffness is shown for identical upper and lower isotropic panels ($\varepsilon = \eta = 1.0$). As can be seen there is a significant dip in the critical flow parameter as a function of the a over b ratio. A plot of the elastic medium stiffness versus panel aspect ratio for this dip in critical λ is given in figure C4.

A portion of the results presented in figure C3 can be compared with the data presented in reference 37. Shown on figure C3 is the comparison which indicates that the trends presented here are consistent with the reference 37 results.

If it is assumed that the two panels have different thicknesses, but are constructed of the same material, the quantities ε and η of equation (C5) become

$$\varepsilon = T_r{}^3$$
$$\eta = T_r$$

(C7)

where T_r is the thickness ratio expressed as

$$T_r = h^U \big/ h^L$$

(C8)
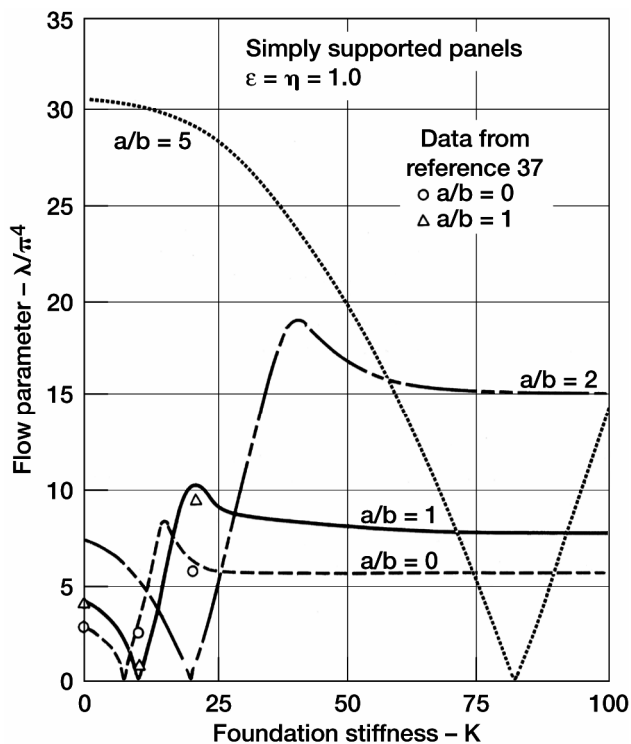
Figure C3.—Flutter results for equal parallel elastically interconnected isotropic panels.
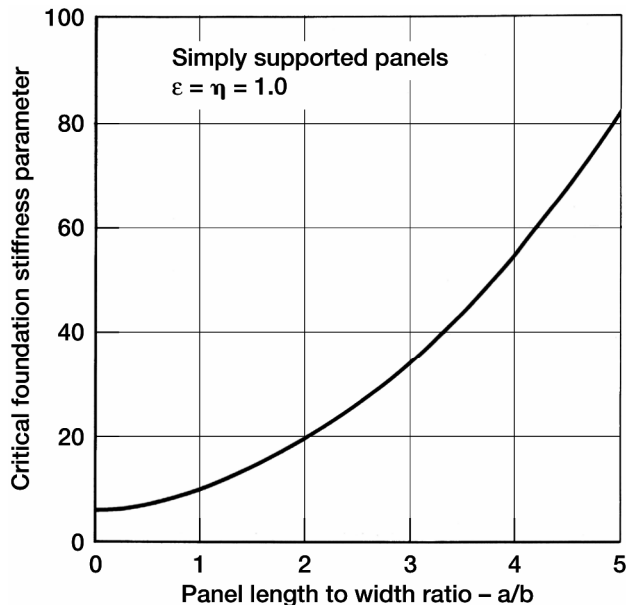
Figure C4.—Flutter critical foundation stiffness parameter as a function of length to width ratio for equal isotropic panels.

Two mode results for an upper panel having twice and half the thickness of the lower panel are compared with results for equal panel thicknesses in figure C5. These configurations have a critical foundation stiffness parameter K values which result in low values for the flow parameter at flutter.

An analysis of elastically interconnected panels representative of the space shuttle thermal protection system is presented in reference 38. In this configuration the upper panel consists of a relatively thick ceramic tile. Included in this investigation is the influence of several individual tiles supported by a common lower panel and interaction between adjacent tiles. The designer is referred to this work for detailed discussions of this type of panel configuration.

In the absence of more extensive theoretical and/or experimental results, the above two mode approach allows the evaluation of trends for parallel panel configurations. These procedures could be employed during preliminary design, but as with the case of a rigid substructure, detailed flutter studies must be conducted during later design efforts.
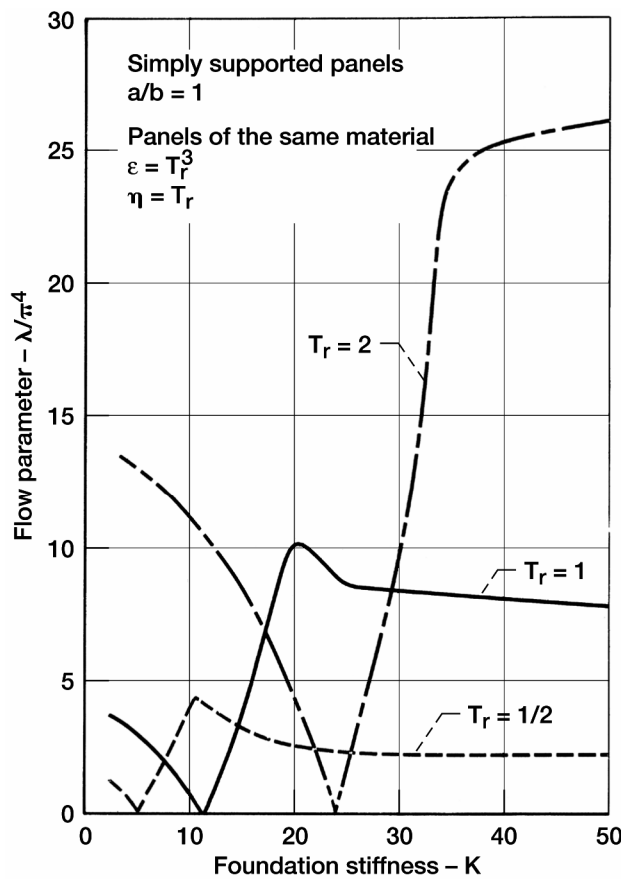
Figure C5.—Flutter results for parallel elastically interconnected isotropic panels having varying thickness ratios.

Appendix D
Panel Flutter Test Data

A tabulation of the experimental panel flutter data used in the verification of the flutter-free panel design boundary, section 6.0, is presented on the following pages. In each case, the panel configuration (isotropic or orthotropic, flow angularity, inplane loads, etc.) is indicated. A separate table is given for the data obtained from a particular reference for a given panel configuration. Also presented is a cross reference with the figure number of section 6.0 in which each set of data is plotted.

TABLE D1.—PANEL FLUTTER DATA FROM REFERENCE 10
Orthotropic panel with stream edge support flexibility. Data shown in figure 13.

Panel No.	Support Condition	$\overline{K}_S$	a (m)	b (m)	D_1 (N-m)	D_2 (N-m)	D_{12} (N-m)
U-1	3	5.0	0.61	0.61	0.35	204	52
U-2	3	2.5	.61	.61	1.03	1640	376
V-1	3	3.7	.61	.61	1.9	2180	344
V-4	3	3.4	.61	.61	5.4	5420	1190
H-1	3	.8	.61	.61	.94	4150	798
S-1	4	1.5	.946	.441	1.15	2700	856
S-2	4	.7	.946	.408	1.19	5350	1760
S-3	4	.7	.946	.408	1.25	5060	1800
S-4	4	.7	.946	.408	1.33	4790	1840
S-5	4	1.5	.946	.441	1.02	3060	800
S-6	4	1.5	.946	.441	.33	987	258
S-7	4	1.5	.946	.441	.37	870	277
S-8	4	.7	.946	.408	.94	6800	1520
S-9	4	.7	.946	.408	.31	2200	490
S-10	4	.7	.946	.408	.47	5460	1210

Note: Support condition definition and $\overline{K}_S$ calculation based on figure B2, appendix B and $\lambda = \dfrac{2q\,a^3}{D_1 f(M)}$.

TABLE D1.—Concluded. PANEL FLUTTER DATA FROM REFERENCE 10

Panel No.	M	q (k Pa)	$GP^{(1)}$	$GP^{(2)}$	FP (x 10^{-5})
U-1	2.83	11.4	12.19	4.16	35.8
U-2	1.63	10.0	19.11	3.25	53.5
U-2	3.0	162.8	19.11	3.25	7.88
V-1	1.63	24.6	13.46	4.56	40.1
V-4	1.63	72.3	14.84	3.80	38.8
H-1	3.0	138.8	29.14	2.03	8.43
S-1	1.57	18.4	58.52	4.65	8.97
S-1	1.85	25.1	58.52	4 65	8.43
S-1	2.1	32.4	58.52	4.65	7.73
S-2	1.57	21.3	89.17	3.38	8.04
S-2	1.85	31.4	89.17	3.38	6.98
S-3	1.85	53.3	87.99	3.25	4.31
S-3	2.1	69.4	87.99	3.25	3.93
S-4	1.57	49.8	86.24	3.13	3.85
S-4	1.85	41.1	86.24	3.13	5.95
S-4	2.1	51.4	86.24	3.13	5.64
S-5	2.1	43.3	60.08	5.12	5.14
S-6	2.1	15.6	59.98	5.12	4.61
S-7	1.57	16.8	58.69	4.64	3.16
S-8	2.1	45.9	93.24	4.10	4.46
S-9	2.1	6.4	92.18	4.11	10.47
S-10	1.57	32.0	117.65	4.12	2.11

Notes: 1. GP not corrected for $C^2/\overline{K}_S$ term.

2. GP corrected for $C^2/\overline{K}_S$ term.

TABLE D2.—PANEL FLUTTER DATA FROM REFERENCE 18
Isotropic panel supported at all edges
Data shown in figure 13

E = 69 GN/m^2
h = 0.81 mm
a = 0.762 m
b = 0.17 m
GP = 4.48

Panel No.	Log No.	M	q (kPa)	FP (x 10^{-4})
10	17	1.4	30.6	2.9
10	19	1.3	32.3	2.8
10	20	1.2	33.5	3.1
10	21	1.2	38.3	2.7
10	23	1.2	38.3	2.7
10	24	1.1	55.1	2.7
4	19	1.4	30.4	2.9
4	21	1.3	31.1	2.9
4	26	1.2	40.6	2.6
4	57	1.4	35.9	2.5
4	70	1.4	32.3	2.8
5	6	1.4	33.0	2.7
5	7	1.33	32.0	2.8
5	8	1.2	40.7	2.5
5	9	1.35	32.3	2.8
5	16	1.3	30.9	2.9
5	18	1.4	32.3	2.8
5	19	1.3	29.9	3.0
5	20	1.3	34.5	2.6
5	21	1.2	35.9	2.9
5	25	1.3	29.4	3.0
5	26	1.3	32.3	2.8
5	27	1.4	31.1	2.9
5	28	1.4	34.5	2.7
5	36	1.3	32.1	2.8
5	37	1.2	38.1	2.7
5	38	1.3	32.3	2.8
5	54	1.3	35.4	2.6
5	82	1.3	37.8	2.4
5	83	1.2	43.8	2.4
5	84	1.3	39.7	2.3
6	6	1.4	35.2	2.6
6	7	1.3	34.2	2.6
6	8	1.2	40.0	2.7
6	14	1.3	39.5	2.3
6	35	1.3	41.2	2.2
6	36	1.3	41.4	2.2

TABLE D3.—PANEL FLUTTER DATA FROM REFERENCE 21
Isotropic panel supported at all edges. Data shown in figure 13

Panel 10–20–20

a = 0.216 m b = 0.470 m
D = 0.75 N-m GP = 0.46

M	q (kPa)	FP (x 10^{-3})
2.0	29.44–36.82	4.40–3.52
3.0	59.29–61.71	3.57–3.43

Panel 10–20–16

a = 0.216 m b = 0.470 m
D = 0.39 N-m GP = 0.46

M	q (kPa)	FP (x 10^{-3})
2.0	17.17–19.65	3.87-3.37
3.0	23.72–29.65	4.57-3.66

Panel 10–20–12

a = 0.216 m b = 0.470 m
D = 0.16 N-m GP = 0.46

M	q (kPa)	FP (x 10^{-3})
2.0	7.38–8.58	3.80–3.26
3.0	11.86–14.83	3.79–3.03
4.0	20.14–22.62	3.05–2.72
5.0	26.21–27.31	2.97–2.85

Note: The q data presented in this table were taken from figure 16 of reference 21.

Panel 15–20–20

a = 0.343 m b = 0.470 m
D = 0.75 N-m GP = 0.73

M	q (kPa)	FP (x 10^{-3})
2.0	11.03-12.27	2.93-2.64
2.5	14.20-17.79	3.01-2.41
3.0	14.20-16.62	3.72-3.18

Panel 20–15–20

a = 0.470 m b = 0.343 m
D = 0.75 N-m GP = 1.37

M	q (kPa)	FP (x 10^{-3})
2.0	8.58–9.79	1.47-1.28
3.0	10.68–11.86	1.92-1.73
4.0	17.58–20.13	1.60-1.40
4.5	15.51–17.24	2.05-1.85

Panel 20–10–25

a = 0.470 m b = 0.216 m
D = 1.47 N-m GP = 2.18

M	q (kPa)	FP (x 10^{-3})
2.0	9.79-11.03	2.51-2.23
2.5	17.79-22.20	1.83-1.46
3.0	23.72-26.61	1.69-1.51

Panel 20–10–20

a = 0.470 m b = 0.216 m
D = 0.75 N-m GP = 2.18

M	q (kPa)	FP (x 10^{-4})
2.0	14.75–19.65	8.51–6.40
3.0	23.72–26.68	8.66–7.70

Panel 20–10–16

a = 0.470 m b = 0.216 m
D = 0.39 N-m GP = 2.18

M	q (kPa)	FP (x 10^{-4})
2.0	7.38–9.79	8.73–6.58
2.5	8.89–10.69	9.58–7.97
3.0	9.48–11.86	11.09–8.87
3.5	11.31–13.17	11.03–9.47
4.0	13.86–15.10	10.39–9.53
4.5	11.24–12.06	14.51–13.52
5.0	22.75–25.02	8.00–7.28

TABLE D3.—Concluded. PANEL FLUTTER DATA
FROM REFERENCE 21

Panel 20–06–12

a = 0.470 m b = 0.114 m
D = 0.16 N-m GP = 4.11

M	q (kPa)	FP (x 10^{-4})
2.0	12.27–14.75	2.21–1.84
3.0	20.75–23.72	2.14–1.87
4.0	25.17–30.20	2.41–2.01

TABLE D4.—PANEL FLUTTER DATA FROM REFERENCE 8
Orthotropic panel with flow angularity
Data shown in figure 15

a = 0.48 m
b = 0.48 m
$\overline{K}_{LT}$ = 1.94
D_{12}/D_1 = 0.17
D_2/D_1 = 0.00026

Λ (deg)	λ	GP	FP (x 10^{-4})
30	11.50	3.26	1.42
45	8.90	3.32	1.12
60	7.05	3.34	1.02
75	7.05	3.34	.86
90	8.16	3.35	.64

Note: The above data were taken from figure 6 of reference 8 with

a normalization factor on λ of 371 where $\lambda = \dfrac{2qa^3}{D_1 f(M)}$

TABLE D5.—PANEL FLUTTER DATA FROM REFERENCE 11
Orthotropic panel with flow angularity
Data shown in figures 15 and 16

Panel	a (m)	a/b	D (N-m)	D_1/D_2	D_{12}/D_2	$\overline{K}_{LT}$	M
1	0.572	5.	0.0982	755	1.5	Clamped	2
2	.356	.933	.405	420	137.	1.13	2
3	.356	.933	.405	420	137.	1.13	2
4	.356	.933	.405	420	137.	.252	2
5	.356	.933	.405	270	137.	.698	2

Panel 1			
Λ (deg)	q (kPa)	GP	FP (x 10^{-3})
31.6	77.0	0.23	3.8
32.5	72.7	.23	3.9
33.5	68.4	.23	4.0
36.2	64.2	.23	3.9
46.	56.4	.23	3.4
46.	60.0	.24	3.2
50.	58.1	.24	3.0
57.	53.0	.24	2.9

Note: The q's presented in this table were calculated from $q/f(M)$ data provided by
Peter Shyprykevich, Grumman Aerospace Corporation. This information is summarized
in figures 11 through 15, reference 11.

TABLE D5.—Concluded. PANEL FLUTTER DATA FROM REFERENCE 11

Panel 2

Λ (deg)	q (kPa)	GP	FP (x 10⁻³)
19.	61.5	1.81	1.13
19.8	68.3	1.82	.97
19.8	56.4	1.82	1.17
21.7	51.2	1.84	1.16
24.2	42.6	1.87	1.23
28.8	34.2	1.90	1.24
30.2	25.6	1.91	1.57
32.	25.6	1.92	1.47
33.1	34.2	1.92	1.05
33.2	22.2	1.92	1.62
37.2	17.0	1.93	1.84
59.5	10.3	1.96	1.71

Panel 3

Λ (deg)	q (kPa)	GP	FP (x 10⁻⁴)
35.6	85.5	1.93	3.87
36.1	76.7	1.93	4.23
36.5	85.5	1.93	3.75
39.	68.2	1.94	4.33
41.8	59.7	1.94	4.53
46.8	59.7	1.95	3.94
49.1	51.3	1.95	4.33
54.	42.8	1.96	4.61
64.8	34.3	1.97	4.66
69.4	30.7	1.97	4.88
90.5	27.4	1.97	4.74

Panel 4

Λ (deg)	q (kPa)	GP	FP (x 10⁻³)
16.3	25.7	0.92	4.27
17.1	34.3	.92	3.02
17.9	17.1	.92	5.73
18.5	42.8	.92	2.20
19.3	51.4	.93	1.74
21.2	17.1	.93	4.64
25.4	8.6	.93	7.47

Panel 5

Λ (deg)	q (kPa)	GP	FP (x 10⁻³)
15.5	85.6	1.17	1.11
17.	77.0	1.18	1.11
20.5	68.4	1.19	1.01
23.	60.0	1.19	1.01
26.	51.4	1.20	1.02
30.	42.8	1.20	1.03
40.5	34.3	1.21	.83
58.3	25.7	1.21	.68

TABLE D6.—PANEL FLUTTER DATA FROM REFERENCE 12
Isotropic panel supported at all edges with inplane loads
Data shown in figures 17 and 21

Panel 1

$a = 0.343$ m		$b = 0.343$ m	
$D = 7.085$ N-m		$M = 1.96$	

$$\overline{K}_s = 968$$

P_{CR}	q (kPa)	GP	FP (x 10^{-3})
0.13	66.6	0.932	2.66
.17	61.1	.911	2.26
.18	61.7	.905	2.11
.24	51.4	.871	1.76
.27	51.4	.854	1.49
.48	33.7	.721	.87
.50	33.7	.707	.81
.57	20.0	.655	1.07
.58	20.6	.648	1.01
.70	14.6	.547	1.00
.71	14.6	.538	.97
.92	8.6	.283	1.00

Panel 2

$a = 0.622$ m		$b = 0.318$ m	
$D = 13.839$ N-m		$M = 1.96$	

$$\overline{K}_s = 43.4$$

P_{CR}	q (kPa)	GP	FP (x 10^{-3})
0.03	42.5	1.90	1.77
.29	22.6	1.63	1.10
.56	15.6	1.28	.93
.63	8.8	1.18	1.48
.71	6.2	1.04	1.89
.95	6.2	.43	1.45

Note: For all panels the P_{CR} and q data were obtained from information shown in figure 9, reference 12.

TABLE D6.—Continued. PANEL FLUTTER DATA FROM REFERENCE 12

Panel 3

$a = 0.622$ m		$b = 0.257$ m	
$D = 13.839$ N-m		$M = 1.96$	

$$\overline{K}_S = 22.8$$

P_{CR}	q (kPa)	GP	FP ($\times 10^{-3}$)
0.21	65.7	2.11	0.52
.46	47.4	1.74	.45
.53	30.4	1.62	.64
.72	18.6	1.25	.85
.90	11.9	.75	1.14
.97	7.6	.41	1.68

Panel 4

$a = 0.622$ m		$b = 0.216$ m	
$D = 7.085$ N-m		$M = 1.96$	

$$\overline{K}_S = 25.7$$

P_{CR}	q (kPa)	GP	FP ($\times 10^{-3}$)
0.13	51.6	2.64	0.45
.15	51.6	2.60	.42
.27	33.6	2.41	.51
.29	33.6	2.38	.49
.47	22.3	2.06	.58
.56	17.8	1.87	.67
.88	9.2	.98	1.01
.99	9.1	.28	.95

TABLE D6.—Continued. PANEL FLUTTER DATA FROM REFERENCE 12

Panel 5

a = 0.622 m $\qquad$ b = 0.165 m

D = 3.628 N-m $\qquad$ M = 1.96

$\overline{K}_S$ = 21.6

P_{CR}	q (kPa)	GP	FP ($\times 10^{-4}$)
0.25	68.6	3.19	1.59
.38	60.4	2.90	1.58
.38	51.2	2.90	1.86
.39	60.4	2.88	1.57
.41	34.1	2.83	2.73
.43	50.4	2.78	1.82
.50	23.8	2.61	3.65
.52	23.9	2.55	3.59
.68	17.0	2.08	4.58
.70	17.1	2.02	4.51
.88	8.8	1.28	8.03

Panel 6

a = 0.622 m $\qquad$ b = 0.148 m

D = 3.628 N-m $\qquad$ M = 1.96

$\overline{K}_S$ = 14.3

P_{CR}	q (kPa)	GP	FP ($\times 10^{-4}$)
0.10	60.3	3.85	2.41
.38	43.1	3.20	2.44
.41	51.7	3.12	1.99
.49	34.6	2.90	2.84
.64	26.3	2.44	3.44
.66	26.3	2.37	3.41
.68	17.7	2.30	5.02
.69	18.0	2.26	4.91
.78	18.0	1.91	4.73
.94	14.3	1.00	5.61
.95	14.3	.91	5.59

TABLE D6.—Continued. PANEL FLUTTER DATA FROM REFERENCE 12

Panel 7

$a = 0.343$ m $\qquad$ $b = 0.343$ m

$D = 13.839$ N-m $\qquad$ $M = 1.96$

$$\overline{K}_S = 545$$

P_{CR}	q (kPa)	GP	FP $(\times 10^{-4})$
0.16	57.9	0.916	4.97
.39	63.8	.780	1.29
.39	57.9	.780	1.43
.42	52.0	.761	1.40
.51	34.1	.699	1.50
.52	17.5	.692	2.83
.54	42.6	.678	1.08
.58	26.0	.647	1.56
.66	17.5	.583	1.82
.69	12.6	.556	2.31
.77	11.7	.479	2.02
.90	13.8	.316	1.27

Panel 8

$a = 0.622$ m $\qquad$ $b = 0.318$ m

$D = 29.007$ N-m $\qquad$ $M = 1.96$

$$\overline{K}_S = 21.6$$

P_{CR}	q (kPa)	GP	FP $(\times 10^{-3})$
0.23	75.8	1.68	0.81
.24	42.8	1.67	1.40
.26	42.8	1.64	1.32
.27	58.0	1.63	.94
.29	57.7	1.61	.90
.63	22.6	1.16	1.21
.65	22.6	1.13	1.17
.70	17.5	1.05	1.42
.72	22.0	1.01	1.10
.90	8.6	.60	2.30
.92	8.6	.54	2.26

TABLE D6.—Continued. PANEL FLUTTER DATA FROM REFERENCE 12

Panel 9

a = 0.622 m b = 0.216 m
D = 13.839 N-m M = 1.96

$\overline{K}_S$ = 10.2

P_{CR}	q (kPa)	GP	FP (x10^{-3})
0.09	76.5	2.62	0.67
.12	76.2	2.58	.61
.15	76.2	2.53	.56
.39	60.7	2.15	.46
.40	60.1	2.13	.46
.44	40.4	2.06	.65
.46	40.4	2.02	.64
.53	40.7	1.88	.59
.58	20.2	1.78	1.13
.60	29.9	1.74	.75
.63	19.9	1.67	1.09
.67	19.9	1.58	1.06
.69	29.9	1.53	.69
.71	8.5	1.48	2.40
.73	20.2	1.43	.99
.74	19.9	1.40	1.00
.76	12.6	1.35	1.56
.78	12.6	1.29	1.54
.81	7.9	1.20	2.40

Panel 10

a = 0.622 m b = 0.165 m
D = 7.085 N-m M = 1.96

$\overline{K}_S$ = 8.45

P_{CR}	q (kPa)	GP	FP (x10^{-3})
0.05	51.2	3.47	0.62
.14	43.1	3.31	.58
.37	35.0	2.83	.54
.53	25.5	2.44	.65
.55	25.2	2.39	.65
.58	17.7	2.31	.91
.61	25.2	2.23	.63
.61	17.7	2.23	.89
.67	9.0	2.05	1.70
.67	12.2	2.05	1.25
.68	25.4	2.02	.60
.78	11.6	1.67	1.25

TABLE D6.—Continued. PANEL FLUTTER DATA FROM REFERENCE 12

Panel 11

a = 0.662 m b = 0.216 m
D = 7.085 N-m M = 1.96

$\overline{K}_S$ = 22.3

P_{CR}	q (kPa)	GP	FP (x10^{-3})
0.01	35.0	2.98	0.97
.02	30.1	2.97	1.03
.05	30.1	2.92	.85
.13	20.6	2.80	.95
.27	13.6	2.56	1.09
.42	7.9	2.28	1.54
.43	9.6	2.26	1.25
.43	7.7	2.26	1.56
.49	7.7	2.14	1.47
.62	7.0	1.85	1.44
.74	8.2	1.53	1.13
.86	8.5	1.12	1.00
.86	9.5	1.12	.90

Panel 12

a = 0.622 m b = 0.165 m
D = 7.085 N-m M = 1.96

$\overline{K}_S$ = 9.96

P_{CR}	q (kPa)	GP	FP (x10^{-4})
0.06	82.3	3.48	3.71
.08	82.3	3.45	3.49
.13	65.3	3.35	3.92
.15	69.3	3.31	3.55
.17	68.7	3.27	3.47
.49	52.6	2.57	3.25
.49	65.1	2.57	2.63
.51	54.2	2.52	3.11
.53	54.2	2.46	3.07
.53	61.9	2.46	2.69
.56	52.7	2.38	3.10
.57	53.8	2.36	3.01
.58	34.4	2.33	4.68
.58	53.8	2.33	2.99
.60	34.3	2.27	4.64
.72	26.5	1.90	5.62
.76	26.2	1.76	5.57
.78	16.5	1.68	8.76
.80	17.0	1.61	8.42
.84	18.4	1.44	7.64
.85	18.7	1.39	7.48

TABLE D6.—Concluded. PANEL FLUTTER DATA FROM REFERENCE 12
Panel 13

$a = 0.622$ m $b = 0.216$ m
$D = 7.085$ N-m $M = 1.96$

$\overline{K}_S = 14.1$

P_{CR}	q (kPa)	GP	FP ($\times 10^{-3}$)
0.11	41.6	2.63	0.59
.17	34.4	2.54	.60
.21	38.4	2.47	.50
.30	26.3	2.33	.62
.37	17.8	2.21	.82
.54	8.8	1.89	1.37

TABLE D7.—PANEL FLUTTER DATA FROM REFERENCE 7
Orthotropic panels with spring supported stream edges and inplane loads
Data shown in figure 18
Panel I

$a = 0.605$ m $b = 0.605$ m
$D_1 = 1$ N-m $D_2 = 1640$ N-m
$D_{12} = 376$ N-m $\overline{K}_S = 63$

$M = 3$

Test	P_{CR}	q (kPa)	GP	FP ($\times 10^{-4}$)
1	0.74	110	6.42	1.15
1	.92	101	3.56	1.24
2	.40	134	9.76	.95
2	.71	115	6.79	1.10
4	.72	118	6.67	1.07
5	.43	137	9.51	.93
6	.61	106	7.87	1.19
8	.80	107	5.63	1.18

Note: P_{CR}'s determined from information shown in figure 8, reference 7.

Panel II

$a = 0.605$ m $b = 0.605$ m
$D_1 = 0.94$ N-m $D_2 = 4150$ N-m
$D_{12} = 798$ N-m $\overline{K}_S = 6.9$

Test	P_{CR}	q (kPa)	GP	FP ($\times 10^{-4}$)
15	0.38	98	4.62	1.22
16	.09	131	5.60	.92
17	.45	117	4.35	1.02
17	.69	102	3.27	1.17
18	.86	83	2.20	1.44

Note: P_{CR}'s determined from information shown in figure 9, reference 7.

TABLE D8.—PANEL FLUTTER DATA FROM REFERENCE 19
Isotropic panel with inplane loads
Data shown in figures 18 and 20

$E = 72.4$ GN/m^2
$a = 0.66$ m
$M = 3$

Partially Clamped Panel
$a/b = 3.3$

h (mm)	P_{CR}	q (kPa)	GP	FP (x 10^{-3})
1.4	0.44	117	2.47	0.43
1.4	.62	69	2.03	.63
2.03	.63	158	2.01	.84
2.03	.78	138	1.55	.88
2.03	.77	117	1.58	1.04
2.03	.85	83	1.28	1.40
2.03	.94	69	.81	1.61

Partially Clamped Panel
$a/b = 3.3$

h (mm)	P_{CR}	q (kPa)	GP	FP (x 10^{-3})
1.32	0.39	179	2.58	0.25
1.37	.56	117	2.19	.37
1.37	.29	234	2.78	.24
1.37	.39	165	2.58	.30
1.40	.29	234	2.78	.26
1.60	.59	186	2.11	.36
2.59	.85	220	1.28	1.09
2.59	.88	165	1.14	1.44
2.59	.93	117	.87	1.99
2.59	.95	96	.74	2.38
2.59	.96	69	.66	3.30

Note: P_{CR}'s based on information shown in figures 10 and 11, reference 19.

TABLE D8.—Concluded. PANEL FLUTTER DATA FROM REFERENCE 19

Fully Clamped Panel
$a/b = 3.3$

h (mm)	P_{CR}	q (kPa)	GP	FP (x 10^{-3})
1.35	0.26	186	2.84	0.30
1.35	.46	110	2.42	.40
1.35	.56	69	2.19	.59
1.37	.61	83	2.06	.50
1.60	.76	69	1.62	.87
1.60	.69	96	1.84	.65
1.65	.70	110	1.81	.62
1.65	.47	165	2.40	.49
1.93	.74	110	1.68	.96
1.93	.81	96	1.44	1.06
2.59	.79	172	1.51	1.45

Fully Clamped Panel
$a/b = 3.7$

h (mm)	P_{CR}	q (kPa)	GP	FP (x 10^{-3})
1.37	0.36	269	2.96	0.21
1.37	.55	200	2.48	.25
1.37	.65	138	2.19	.34
1.37	.71	117	1.99	.39
1.62	.57	269	2.43	.30
1.62	.78	96	1.74	.75
1.62	.74	83	1.89	.89
1.62	.87	69	1.34	1.01
1.62	.88	76	1.28	.91

TABLE D9.—PANEL FLUTTER DATA FROM REFERENCE 23
Supported isotropic panel with inplane loads
Data shown in figure 18

$M = 3$
$E = 72.4 \text{ GN/m}^2$

Panel	Test	h (mm)	a (m)	b (m)	P_{CR}	q (kPa)	GP	FP (x 10^{-5})
2-A	1	0.64	0.686	0.0686	0.58	177	6.48	5.78
2-A	5	.81	.686	.0686	.86	212	3.74	9.59
2-A	6	.81	.686	.0686	.86	216	3.74	9.41
4-A	8	.64	.66	.066	.46	240	7.35	4.84
4-A	9	.64	.66	.066	.71	144	5.39	7.89

$M = 3$
$E = 200 \text{ GN/m}^2$

Panel	Test	h (mm)	a (m)	b (m)	P_{CR}	q (kPa)	GP	FP (x 10^{-5})
4-S$_2$	3	0.51	0.711	0.0711	0.68	237	5.66	5.37
4-S$_2$	4	.51	.711	.0711	.69	237	5.57	5.37
4-S$_2$	5	.51	.711	.0711	.66	199	5.83	6.41
4-S$_2$	6	.51	.711	.0711	.15	231	9.23	5.93

Note: P_{CR}'s based on information presented in table I, reference 23.

TABLE D10.—PANEL FLUTTER DATA FROM REFERENCE 24
Clamped isotropic panel with inplane loads
Data shown in figure 18

$a = 0.635$ m
$b = 0.159$ m
$E = 72.4 \text{ GN/m}^2$
$M = 3.0$

Test	h (mm)	P_{CR}	q (kPa)	GP	FP (x 10^{-3})
2	1.6	0.20	240.8	3.58	0.54
3	1.6	.95	166.1	.89	.48
4	1.6	.95	119.2	.89	.67
5	2.06	.51	214.0	2.80	.99
6	2.06	.88	78.5	1.39	2.24
7	3.18	1.00	236.5	0.0	2.61

Note: Determination of P_{CR}'s based on information given in figure 14, reference 24.

TABLE D1l.—PANEL FLUTTER DATA FROM REFERENCE 25
Supported isotropic panel with inplane loads
Data shown in figure 18

$a = 0.661$ m
$E = 72.4$ GN/m^2
$M = 3$
$a/b = 2.5$

Test	*h* (mm)	P_{CR}	*q* (kPa)	*GP*	*FP* (x 10^{-3})
1	1.6	0.96	129.5	0.50	0.26
2	1.6	.56	187.2	1.66	.26
3	1.8	.29	141.0	2.11	.73
4	1.8	.39	93.8	1.95	.92
5	1.8	.52	70.9	1.73	1.03
6	2.62	.56	151.3	1.66	1.41
8	2.62	.65	140.3	1.48	1.38
10	2.62	.77	232.0	1.20	.75
11	2.62	.65	174.3	1.48	1.11

Note: P_{CR}'s based on information presented on figure 7, reference 25.

$a/b = 2.9$

Test	*h* (mm)	P_{CR}	*q* (kPa)	*GP*	*FP* (x 10^{-4})
1	2.06	0.52	235.6	2.01	5.49
2	2.06	.77	187.	1.39	5.61
3	2.06	.88	128.1	1.00	7.61
6	2.06	.98	111.8	.41	8.20
7	1.35	.50	117.5	2.05	3.15
8	1.35	.77	80.4	1.39	3.66
9	1.35	.09	152.7	2.77	5.02
10	1.6	.62	146.3	1.79	3.78
11	1.6	.31	146.	2.41	5.36
12	1.6	.69	81.9	1.61	6.37
13	1.6	.34	176.	2.36	4.25

Note: P_{CR}'s based on information presented on figure 8, reference 25.

TABLE Dl2.—PANEL FLUTTER DATA FROM REFERENCE 26
Orthotropic panels with spring supported stream edges and inplane loads
Data shown in figure 18

Panel III

$a = 0.605$ m $\qquad$ $b = 0.605$ m
$D_1 = 2.4$ N-m $\qquad$ $D_2 = 2130$ N-m
$D_{12} = 500$ N-m $\qquad$ $\overline{K}_S = 89$

$M = 3$

Test	P_{CR}	q (kPa)	GP	FP (x 10^{-4})
2	0.54	204	7.86	1.48
3	.42	221	8.83	1.38
4	.44	225	8.68	1.35
5	.36	220	9.28	1.39
6	.42	213	8.83	1.43
7	.30	232	9.70	1.32
7	.78	179	5.44	1.67
7	.78	201	5.44	1.49
7	.75	212	5.79	1.41

Note: P_{CR}'s determined from information shown in figure 8(a), reference 26.

Panel IV

$a = 0.483$ m $\qquad$ $b = 0.483$ m
$D_1 = 0.87$ N-m $\qquad$ $D_2 = 3380$ N-m
$D_{12} = 556$ N-m $\qquad$ $\overline{K}_S = 2.1$

$M = 3$

Test	P_{CR}	q (kPa)	GP	FP (x 10^{-4})
1	0.77	154	1.70	1.41
1	.85	141	1.37	1.54
2	.49	190	2.53	1.15
3	.68	153	2.00	1.42
4	.50	213	2.50	1.02
5	.39	191	2.76	1.14
5	.96	95	.71	2.28

Note: P_{CR}'s determined from information shown in figure 8(b), reference 26.

TABLE D13.—PANEL FLUTTER DATA FROM REFERENCE 10
Orthotropic panel with stream edge support flexibility
and pressure differential effects
Data shown in figure 19

Panel V-5

$a = 0.61$ m $b = 0.61$ m
$D_1 = 2.4$ N-m $D_2 = 1960$ N-m
$D_{12} = 433$ N-m $\overline{K}_S = 4.3$

$E = 73$ GN/m^2

M	Δp (kPa)	q (kPa)	GP	$FP^{(1)}$ (x 10^{-4})	$FP^{(2)}$ (x 10^{-3})
1.63	0.24	14.2	4.19	8.81	1.26
1.84	−.24	22.1	4.19	7.27	1.04
1.96	−.29	24.5	4.19	7.25	1.16

Panel V-2

$a = 0.61$ m $b = 0.61$ m
$D_1 = 1.46$ N-m $D_2 = 3560$ N-m
$D_{12} = 464$ N-m $\overline{K}_S = 1.2$

$E = 214$ GN/m^2

M	Δp (kPa)	q (kPa)	GP	$FP^{(1)}$ (x 10^{-4})	$FP^{(2)}$ (x 10^{-3})
1.63	−0.24	27.80	2.99	2.73	0.697
1.84	.24	28.01	2.99	3.49	.890
1.96	−.24	24.08	2.99	4.49	1.144

Notes: 1. *FP* not corrected for Δp effects.
        2. *FP* corrected for Δp effects.

TABLE D14.—PANEL FLUTTER DATA FROM REFERENCE 27
Isotropic panel at low supersonic flow
Data shown in figure 22

$a = 0.229$ m
$b = 0.457$ m
$h = 1.019$ mm
$E = 38.6$ GN/m^2

M	δ (mm)	q (kPa)
1.05	24.13	50.3
1.1	26.16	49.6
1.1	7.62	29.2
1.2	25.91	48.7
1.2	19.56	42.3
1.2	13.21	36.7
1.2	11.68	34.2
1.2	8.64	32.9
1.2	7.11	29.0
1.3	24.38	52.6
1.3	7.11	42.2
1.4	22.61	61.8
1.4	6.86	56.9

Note: The quantity δ is the boundary layer thickness at the
test conditions.

TABLE D15.—PANEL FLUTTER DATA FROM REFERENCE 28
Isotropic panel at low supersonic flow
Data shown in figure 22

$a = 0.229$ m
$b = 0.457$ m
$h = 0.488$ mm
$E = 144.8$ GN/m^2

M	δ (mm)	q (kPa)
1.2	28.96	19.3
1.2	20.83	15.6
1.2	16.76	12.3
1.2	11.68	10.6
1.3	29.21	22.2
1.3	9.65	13.4
1.3	8.13	12.7
1.4	11.94	18.7
1.4	8.64	17.7

Note: The quantity δ is the boundary layer thickness at the
test conditions.

References

1. Kordes, Eldon E.; Tuovila, Weimer J.; and Guy, Lawrence D.: Flutter Research on Skin Panels. NASA TN D–45l, 1960.
2. Mirowitz, L.I.; Schweiker, J.W.; and Zimmerman, N.H.: Panel Flutter Survey and Design Criteria. ATC–ARTC–32, 1962.
3. Kordes, Eldon E.; and Noll, Richard B.: Theoretical Flutter Analysis of Flat Rectangular Panels in Uniform Coplanar Flow With Arbitrary Direction. NASA TN D–1156, 1962.
4. Dowell, E.H.: Panel Flutter; NASA Space Vehicle Design Criteria. NASA SP–8004, Revised ed., 1972.
5. Lemley, C.E.: Design Criteria for the Prediction and Prevention of Panel Flutter. Vols. I and II, AFFDL–TR–67–140, 1968. Available from the Air Force Flight Dynamics Lab.
6. Bohon, Herman L.: Flutter of Flat Rectangular Orthotropic Panels With Biaxial Loading and Arbitrary Flow Direction. NASA TN D–1949, 1963.
7. Bohon, Herman L.: Experimental Flutter Results for Corrugation-Stiffened Panels at Mach Number of 3. NASA TN D–2293, 1964.
8. Bohon, Herman L.; and Shore, Charles P.: Application of Recent Panel Flutter Research to the Space Shuttle. NASA TM X–2274, pt. II, 1971, pp. 247–264.
9. Anderson, M.S.; and Bohon, H.L.: Role of Boundary Conditions on Flutter of Orthotropic Panels. AIAA J., vol. 4, no. 7, 1966, pp. 1241–1248.
10. Weidman, Deene J.: Experimental Flutter Results for Corrugation-Stiffened and Unstiffened Panels. NASA TN D–3301, 1966.
11. Shyprykevich, P.: Experimental Investigation of Orthotropic Panel Flutter at Arbitrary Yaw Angles, and Comparison With Theory. NASA CR–2265, 1973.
12. Hess, Robert W.: Experimental and Analytical Investigation of the Flutter of Flat Built-Up Panels Under Streamwise Inplane Load. NASA TR R–330, 1970.
13. Roark, Raymond Jefferson: Formulas for Stress and Strain. Third ed., McGraw-Hill, New York, NY, 1954.
14. Timoshenko, Stephen P.; and Gere, James M.: Theory of Elastic Stability. Second ed., McGraw-Hill, New York, NY, 1961.
15. Shore, C.P.: Flutter Design Charts for Biaxially Loaded Isotropic Panels. J. Aircraft, vol. 7, no. 4, 1970, pp. 325–329.
16. Sawyer, J.W.: Supersonic Flutter of Panels Loaded With Inplane Shear. NASA TN D–7888, 1975.
17. Dowell, E.H.: Panel Flutter—A Review of the Aeroelastic Stability of Plates and Shells. AIAA J., vol. 8, no. 3, 1970, pp. 385–399.
18. Kappus, H.P.; Lemley, C.E.; and Zimmerman, N.H.: An Experimental Investigation of High Amplitude Panel Flutter. NASA CR–l837, 1971.
19. Shore, Charles P.: Experimental Investigation of Flutter at Mach 3 of Rotationally Restrained Panels and Comparison With Theory. NASA TN D–5508, 1969.
20. Hedgepeth, J.M.: Flutter of Rectangular Simply Supported Panels at High Supersonic Speeds. J. Aero. Sci., vol. 24, no. 8, 1957, pp. 563–573, 1957.
21. Dowell, E.H.; and Voss, H.M.: Theoretical and Experimental Panel Flutter Studies in the Mach Number Range 1.0 to 5.0. AIAA J., vol. 3, no. 12, 1965, pp. 2292–2304.
22. Shyprykevich, P.; and Sawyer, J.W.: Orthotropic Panel Flutter at Arbitrary Yaw Angles—Experiment and Correlation With Theory. AIAA–1973–0192, 1973.
23. Guy, Lawrence D.; and Bohon, Herman L.: Flutter of Aerodynamically Heated Aluminum-Alloy and Stainless-Steel Panels With Length-Width Ratio of 10 at Mach Number of 3.0. NASA TN D–1353, 1962.
24. Dixon, Sidney C.: Application of Transtability Concept to Flutter of Finite Panels and Experimental Results. NASA TN D–1948, 1963.
25. Shideler, John L.; Dixon, Sidney C.; and Shore, Charles P.: Flutter at Mach 3 of Thermally Stressed Panels and Comparison With Theory for Panels With Edge Rotational Restraint. NASA TN D–3498, 1966.
26. Bohon, Herman L.: Flutter of Corrugation-Stiffened Panels at Mach 3 and Comparison with Theory. NASA TN D–4321, 1968.
27. Gaspers, Peter A., Jr.; Muhlstein, L., Jr.; and Riddle, D.W.: An Experimental Study of the Influence of the Turbulent Boundary Layer on Panel Flutter. NASA TN D–4486, 1968.
28. Gaspers, Peter A., Jr.; Muhlstein, Lado, Jr.; and Petroff, Daniel N.: Further Experimental Results on the Influence of the Turbulent Boundary Layer on Panel Flutter. NASA TN D–5798, 1970.
29. Stein, M.: Flutter of Panels on Discrete Flexible Supports; Analysis of Three Different Panel-Support Configurations. NASA TN D–7443, 1974.
30. Stroud, W. Jefferson: Elastic Constants for Bending and Twisting of Corrugation-Stiffened Panels. NASA TR R–166, 1963.
31. Timoshenko, Stephen; and Woinowsky-Krieger, S.: Theory of Plates and Shells. Second ed., McGraw-Hill Book Co., 1959.
32. Hoppmann, W.H.: Bending of Orthogonally Stiffened Plates. J. Appl. Mech. Trans. ASME, vol. 22, no. 2, 1955, pp. 267–271.
33. Beckett, R.E.; Dohrmann, R.J.; and Ives, K.D.: An Experimental Method for Determining the Elastic Constants of Orthogonally Stiffened Plates. Proceedings of the First International Congress on Experimental Mechanics, Pergamon Press, New York, NY, 1963, pp. 129–148.
34. Dugundji, J.: Theoretical Considerations of Panel Flutter at High Supersonic Mach Numbers. AIAA J., vol. 4, no. 7, 1966, pp. 1257–1266.
35. Dowell, E.H.: Dynamic Analysis of an Elastic Plate on a Thin, Elastic Foundation. J. Sound Vib., vol. 35, no. 3, 1974, pp. 343–360.
36. McElman, J.A.: Flutter of Two Parallel Flat Plates Connected by an Elastic Medium. AIAA J., vol. 2, no. 2, 1964, pp. 377–379.

37. Johns, D.J.; and Taylor, P.W.: Vibration and Flutter of Parallel Flat Plates Connected by an Elastic Medium. Paper presented at 11th Materials and Structural Dynamics, American Institute of Aeronautics and Astronautics and American Society of Mechanical Engineers, Structures, Structural Dynamics and Materials Conference, Denver, CO, 1970, pp. 25–35.

38. Dowell, E.H.: Vibration and Flutter Analysis of Reusable Surface Insulation Panels. J. Spacecr. Rockets, vol. 12, 1975, pp. 44–50.

Bibliography

Bisplinghoff, Raymond L.; and Ashley, Holt: Principles of Aeroelasticity. John Wiley & Sons, New York, NY, 1962.

Bohon, Herman L.: Panel Flutter Tests on Full-Scale X–l5 Lower Vertical Stabilizer at Mach Number of 3.0. NASA TN D–1385, 1962.

Bohon, H.L.; and Dixon, S.C.: Some Recent Developments in Flutter of Flat Panels. J. Aircraft, vol. 1, no. 5, 1964, pp. 280–288.

Bohon, Herman L.; Anderson, Melvin S.; and Heard, Walter L., Jr.: Flutter Design of Stiffened-Skin Panels for Hypersonic Aircraft. NASA TN D–5555, 1969.

Chopra, Inderjit: Flutter of a Panel Supported on an Elastic Foundation. AIAA J., vol. 13, no. 5, 1975, pp. 687–688.

Cunningham, Herbert J.: Flutter Analysis of Flat Rectangular Panels Based on Three-Dimensional Supersonic Unsteady Potential Flow. NASA TR R–256, 1967.

Dixon, Sidney C.; Griffith, George E.; and Bohon, Herman L.: Experimental Investigation of Mach Number 3.0 of the Effects of Thermal Stress and Buckling on the Flutter of Four-Bay Aluminum Alloy Panels With Length-Width Ratios of 10. NASA TN D–921, 1961.

Dixon, Sidney C.: Experimental Investigation at Mach Number 3.0 of Effects of Thermal Stress and Buckling on Flutter Characteristics of Flat Single-Bay Panels of Length-Width Ratio 0.96. NASA TN D–l485, 1962.

Dixon, Sidney C.; and Shore, Charles P.: Effects of Differential Pressure, Thermal Stress, and Buckling on Flutter of Flat Panels With Length-Width Ratio of 2. NASA TN D–2047, 1963.

Dixon, Sidney C.: Comparison of Panel Flutter Results From Approximate Aerodynamic Theory With Results From Exact Inviscid Theory and Experiment. NASA TN D–3649, 1966.

Dixon, S.C.; and Shore, C.P.: State of the Art for Panel Flutter as Applied to Space Shuttle Heat Shields. Space Transportation System Technology Symposium, NASA TM X–52876, vol. II, 1970, pp. 199–221.

Dowell, E.H.; and Voss, H.M.: The Effect of a Cavity on Panel Vibration. AIAA J., vol. 1, no. 2, 1963, pp. 476–477.

Dowell, E.H.; and Voss, H.M.: Effect of Aerodynamic Damping on Flutter of Thin Panels. AIAA J., vol. 2, no. 1, 1964, pp. 119–120.

Dowell, E.H.: Nonlinear Oscillations of a Fluttering Plate. AIAA J., vol. 4, no. 7, 1966, pp. 1267–1275.

Dowell, E.H.: Theoretical-Experimental Correlation of Plate Flutter Boundaries at Low Supersonic Speeds. AIAA J., vol. 6, no. 9, 1968, pp. 1810–1811.

Dowell, E.H.; and Ventres, C.S.: Comparison of Theory and Experiment for Nonlinear Flutter of Loaded Plates. AIAA J., vol. 8, no. 11, 1970, pp. 2022–2030.

Dowell, E.H.: Flutter of Buckled Plates at Zero Dynamic Pressure. AIAA J., vol. 8, no. 3, 1970, pp. 583–584.

Dugundji, John; Dowell, Earl; and Perkin, Brian: Subsonic Flutter of Panels on Continuous Elastic Foundations. AIAA J., vol. 1, no. 5, l963, pp. 1146–1154.

Durvasula, S.: Flutter of Simply Supported, Parallelogrammic, Flat Plates in Supersonic Flow. AIAA J., vol. 5, no. 9, 1967, pp. 1668–1673.

Eisley, J.G.; and Luessen, G.: Flutter of Thin Plates Under Combined Shear and Normal Edge Forces. AIAA J., vol. 1, no. 3, 1963, pp. 620–626.

Ellen, C.H.: Influence of Structural Damping on Panel Flutter. AIAA J., vol. 6, no. 11, 1968, pp. 2169–2174.

Erickson, Larry L.: Supersonic Flutter of Flat Rectangular Orthotropic Panels Elastically Restrained Against Edge Rotation. NASA TN D–3500, 1966.

Fralich, Robert W.: Postbuckling Effects on the Flutter of Simply Supported Rectangular Panels at Supersonic Speeds. NASA TN D–1615, 1963.

Fung, Y.C.: On Corrugation-Stiffened Panels. California Institute of Technology, Pasadena, CA, 1962.

Gaspers, Peter A., Jr.; and Redd, Bass: A Theoretical Analysis of the Flutter of Orthotropic Panels Exposed to a High Supersonic Stream of Arbitrary Direction. NASA TN D–3551, 1966.

Heard, Walter L., Jr.; and Schaeffer, H.G.: Flutter of a Simply Supported Panel Subjected to a Nonlinear Temperature Distribution and Supersonic Flow. AIAA–1965–112, 1965.

Heard, Walter L., Jr.; and Bohon, Herman L.: Natural Vibration and Flutter of Elastically Supported Corrugation-Stiffened Panels— Experiment and Theory. NASA TN D–5986, 1970.

Hess, Robert W.; and Gibson, Frederick W.: Experimental Investigation of the Effects of Compressive Stress on the Flutter of a Curved Panel and a Flat Panel at Supersonic Mach Numbers. NASA TN D–1386, 1962.

Johns, D.J.; and Parks, P.C.: Effect of Structural Damping on Panel Flutter. Aircraft Eng., vol. 32, no. 380, 1960, pp. 304–307.

Johns, D.J.: Static Instability of Rectangular Orthotropic Panels Subjected to Uniform In-Plane Loads and Deflection-Dependent Lateral Loads. ARC R&M No. 3569, 1969.

Kobett, D.R.; and Zeydel, E.F.E.: Flutter of Flat Plates With Partially Clamped Edges in the Low Supersonic Region. AIAA J., vol. 3, no. 1, 1965, pp. 17–22.

Kordes, Eldon E.; and Noll, Richard B.: Flight Flutter Results for Flat Rectangular Panels. NASA TN D–l058, 1962.

Leissa, A.W.: Vibration of Plates. NASA SP–160, 1969.

Pride, Richard A.; Royster, Dick M.; and Helms, Bobbie F.: Design, Tests, and Analysis of a Hot Structure for Lifting Reentry Vehicles. NASA TN D−2186, 1964.

Pritchard, A.J.: Stability Boundaries for a Two-Dimensional Panel. AIAA J., vol. 6, no. 8, 1968, pp. 1590−1592.

Sawyer, J.W.: Flutter of Elastically Supported Orthotropic Panels Including the Effects of Flow Angle. NASA TN D−7491, 1974.

Schaeffer, Harry G.; and Heard, Walter L., Jr.: Supersonic Flutter of a Thermally Stressed Flat Panel With Uniform Edge Loads. NASA TN D−3077, 1965.

Shore, Charles P.: Effects of Structural Damping on Flutter of Stressed Panels. NASA TN D−4990, 1969.

Shore, Charles P.: Flutter Analysis of Two Parallel Elastically Coupled Flat Plates. NASA TN D−8085, 1975.

Sikand, Harmohan Singh; and Libove, Charles: Supersonic Flutter of a Thermally Stressed Flat Plate With Edge Stiffeners. NASA CR−1574, 1970.

Sylvester, Maurice A.; and Baker, John E.: Some Experimental Studies of Panel Flutter at Mach Number 1.3. NACA TN 3914, 1957.

Sylvester, Maurice A.: Experimental Studies of Flutter of Buckled Rectangular Panels at Mach Numbers From 1.2 to 3.0 Including Effects of Pressure Differential and of Panel Width-Length Ratio. NASA TN D−833, 1960.

Ventres, C.S.: Flutter of a Buckled Plate Exposed to a Static Pressure Differential. AIAA J., vol. 9, no. 5, 1971, pp. 958−960.

Weeks, George E.; and Schideler, John L.: Effect of Edge Loadings on the Vibration of Rectangular Plates With Various Boundary Conditions. NASA TN D−2815, 1965.

Zimmerman, N.H.; and Lemley, C.E.: Cavity Effect on Panel Flutter—Just How Significant? The Shock and Vibration Bulletin, BULL−40−PT−4, 1969.

Design Criteria for the Prediction and Prevention of Panel Flutter—Volume I: Criteria Presentation[*]

Clark E. Lemley
McDonnell Aircraft Company
McDonnell Douglas Corporation
St. Louis, Missouri 63166

Foreword

This report, prepared by the Structural Dynamics Department of the Engineering Technology Division of McDonnell Douglas Corporation, covers work performed under Air Force Contract AF33(615)–5295. The contract was sponsored by the Air Force Flight Dynamics Laboratory, Air Force Systems Command, Wright-Patterson Air Force Base, Ohio. This work was done to provide improved panel flutter design criteria for aircraft and aerospace vehicles as part of the exploratory research program of the Air Force Systems Command. This research was conducted under Project No. 1370, "Dynamic Problems in Flight Vehicles," and Task No. 137003, "Prediction and Prevention of Aerothermoelastic Problems." This report covers work conducted from August 1966 to November 1967. The work was administered by Mr. Michael H. Shirk of the Vehicle Dynamics Division.

The program was managed by Dr. Norman Zimmerman. Dr. Clark E. Lemley was the principal investigator. Significant technical contributions to the program were made by Mr. Bobby R. Scheller, Structural Dynamics Engineer.

This manuscript was release by the author in January 1968 for publication.

This technical report has been reviewed and is approved.

Walter J. Mykytow
Asst. for Research and Technology
Vehicle Dynamics Division

Abstract

The program described in this report was performed to bring together all available data from wind tunnel test, flight test, vibration test, thermal test, and theoretical investigations to form comprehensive panel flutter design criteria. Procedures were developed which are applicable to the environment and various panel structural arrangements for transonic, supersonic, and hypersonic aircraft; aerospace reentry vehicles, and boosters.

This report presents a set of criteria for the design of flutter-free panels. The design procedure provides for initially establishing the required thickness at neutral stability of a flat, unstressed, unswept panel. Thickness corrections are then made to account for various parameters that are known to affect panel flutter boundaries.

Reference 1 presents the results of background investigations and supplemental analyses that provide the bases for establishing the criteria of this report. An extensive bibliography is also presented in reference 1.

---

[*]This document was first published as Lemley, Clark E.: Design Criteria for the Prediction and Prevention of Panel Flutter. Volume I: Criteria Presentation. AFFDL–TR–67–140, vol. I, 1968.

Nomenclature

D Plate Bending stiffness $\left(= \dfrac{Et^3}{12\left(1-v^2\right)} \right)$

d Cavity depth

d_o Static deflection

E Modulus of elasticity

$f(M)$ Mach number correction factor

h_o Crown height of curved panel

ℓ Panel length (streamwise)

M Mach number

N Curvature parameter $\left(= \dfrac{h_o}{t_B} \right)$

N_x Inplane load (= $\sigma_x t$) per unit length in the x-direction

N_y Inplane load (=$\sigma_y t$) per unit length in the y-direction

P_{cav} Cavity pressure

Δp Differential pressure between opposite panel surfaces

q Dynamic pressure $\left(= \tfrac{1}{2}\rho V^2 \right)$

R Radius of curvature

s Core thickness, honeycomb panel

t Panel thickness

ΔT Differential temperature

V Velocity

w Panel width

α Angle of attack of panel

α_T Thermal coefficient of expansion

β Compressibility parameter $\left(= \sqrt{M^2 - 1} \right)$

θ Sector angle of cylindrically curved panel

Λ Yaw or sweep angle

v Poisson's ratio

ρ	Mass density of air
σ	Inplane stress
Φ	Nondimensional panel flutter parameter $\left[= \left(\dfrac{f(M)E}{q} \right)^{1/3} \dfrac{t}{\ell} \right]$

Subscripts

B	Baseline
b	Buckling
cav	cavity
C	Corrected
cr	Critical
D	Design value
eq	Equivalent
f	Face sheet, honeycomb panel
L	Local
max	Maximum
N	Curvature
Δp	Differential pressure
ss	Simply supported
ΔT	Differential temperature
x	x-direction (parallel to air flow)
y	y-direction (perpendicular to air flow)
Λ	Yaw or sweep
∞	Free stream

1 Introduction

Panel flutter is a self-excited, aeroelastic instability that may occur when a panel is exposed to a supersonic airstream. During flutter the panel oscillates in a direction normal to its plane and the amplitude of motion usually increases until limited by inplane stresses. The consequences of panel flutter cannot be reliably predicted, but the serious effects that have been encountered include very high noise levels within occupied compartments as well as panel failure due to fatigue.

A considerable amount of work, both experimental and theoretical, has been done during the last two decades not only to obtain insight into the phenomenon but to develop procedures for the prediction and prevention of panel

flutter. This report presents the results of an extensive investigation to determine the state of the art in panel flutter, and from that basis, to formulate a comprehensive set of design criteria. The investigation consisted not only of literature review but also of personal consultation with individuals who have made significant contributions in the field. The report further brings together data from wind tunnel test, flight test, vibration test, and theoretical investigation, and presents methods that have been developed to provide procedures, criteria, and guidelines for designing panels.

The criteria may be applied directly under the following conditions:

(a) The skin panels are of uniform thickness and rectangular in shape.

(b) All edges are supported, that is, either clamped or simply supported.

(c) The panels are flat or cylindrically curved.

(d) Inplane (membrane) stress may exist in the panel whether due to flight loading, unequal static pressures on the two faces, or unequal temperature between the panel and its support structure.

(e) A small volume of air may be contained behind the panel (cavity effect).

(f) The flow conditions (Mach number and dynamic pressure) local to the surface of the panels are known.

(g) Flow angularity (yaw or sweep) across the face of the panel is known.

(h) The inplane (membrane) restraint exerted on the panel at the supported edges is considered to be fully effective; the supports do not yield and thereby allow stress buildup in the panel.

The treatment of conditions not covered above are discussed later in this monograph. The work is presented in two parts. This monograph is the working document that explains the design approach and presents panel design criteria. Reference 1 presents background information that has provided the basis for development of the criteria.

This report is organized in a manner that permits the designer to arrange his data in a logical manner and then proceed step by step with panel design.

Section 2 presents brief discussions of the parameters that are taken into account in panel design; this provides the designer with better insight into some of the problem areas.

Section 3 presents the design approach together with the charts and curves to be used in establishing panel physical parameters.

Section 4 discusses several areas that are closely related to the criteria of section 3 although not specifically covered there.

Section 5 describes some special considerations in the panel design problem; notable in this section are margins of safety and design of panels in critical locations.

Section 6 presents two examples of typical panel design problems that illustrate the application of the design criteria. In addition, panel thicknesses obtained with these criteria are compared with actual modifications that were made to remedy two previous incidences of panel flutter; it is indicated that the criteria would have provided flutter-free panels of the approximate gauges that were used for the final fixes.

The notation and symbols are defined at the beginning of this monograph.

2 Parameters That Affect Panel Flutter Boundaries

This section presents a discussion of the parameters that affect the flutter speeds of skin panels. The first group of parameters listed, items (*a*) through (*ℓ*) are sufficiently well understood to be included in this set of design criteria. This report presents sufficient data to support complete panel design, but detailed discussions of the parameters and their treatment is given in reference 1. The remaining factors, listed under Other Parameters, are known to affect flutter speeds but criteria cannot be presented at this time because theoretical results are inconclusive and experimental data are incomplete.

2.1 Parameters Included in These Criteria

The following are taken into account in the application of the panel design criteria:

a. Dynamic Pressure (*q*)

The aerodynamic forces that cause panel flutter are, in the flight regimes that are adapted to analysis, proportional to dynamic pressure. It has proven to be advantageous to include the dynamic pressure directly in primary design parameters. This trend has been followed in these criteria and therefore dynamic pressure is implicit in the application of the criteria.

b. Mach Number (*M*)

The Mach number of the impinging airstream has a strong influence on the spatial distribution, magnitude, and time-phasing of the aerodynamic pressures that are exerted on a vibrating panel. This criterion presents a Mach number correction factor $f(M)$ that is derived from experimental data and replaces the usual compressibility factor $\sqrt{M^2 - 1}$ between $M = 1$ and $M = 2$. The basis for the Mach number correction factor is given in section 3 of reference 1.

c. Angle-of-Attack (α)

If a panel is inclined to the prevailing airstream, the flow conditions at the surface of the panel (local conditions) are different from those of the free stream; furthermore a static airload Δp may be induced if the volume behind the panel is not vented to the stream. The effect of the angle of attack is taken into account by using local values of M and q and by taking into account the differential pressure.

d. Length-to-Width Ratio (*ℓ/w*)

The planform dimensions of a panel affect flutter boundaries in the sense that an increase in streamwise length (width constant) is destabilizing. The length-to-width parameter ℓ/w has been chosen as a primary design parameter and the ℓ/w effect is implicit in the criteria presentations.

e. Flow Angularity (Λ)

The flutter speed of a rectangular panel changes when the panel is yawed to the free stream wind velocity. Both theory and experiment show that flow angularity is somewhat stabilizing when $\ell/w > 1$ but is strongly destabilizing when $\ell/w < 1$. These criteria call for thickness increase to account for flow angularity when $\ell/w < 1$; the criterion tends to be conservative for $\ell/w > 1$ in that no thickness decrease is called out to account for flow angularity. These guides are based on data that is presented in section III of reference 1.

f. Edge Conditions

A simply supported (unstressed) panel flutters at a lower airspeed than a panel with clamped edges. The clamped panel, is used as a standard in these criteria, and a correction is shown to account for simply supported edges. For real panels, the edge conditions usually lie somewhere between the two extremes and guidelines are presented for treating the intermediate cases.

g. Curvature

Many applications of skin panels require simple, cylindrical curvature in one direction. The frequencies of the lower modes, and hence flutter speeds, may be different from those of the equivalent flat panel. These criteria treat the simply curved panel configuration in which stream flow passes axially (i.e., parallel to a generator) along the panel. The curvature in this case tends to raise the flutter boundary. The case in which flow is perpendicular to the generators of a singly curved panel is not covered in these criteria but is discussed in section III of reference 1.

h. Buckling

Panel buckling is a condition in which inplane compressive stresses cause some (in most cases the lower) modal frequency to be reduced to zero. While buckled, the structure is described as being in a state of indifferent equilibrium; experience has shown that the flutter speed of a panel on the verge of buckling (in which large static deflections have not yet occurred) has a minimum value very near this critical stress condition. The basis for the criterion presented here is the experimental evidence that a buckled panel required about twice the thickness for stability of an unstressed panel. Further discussions are given in reference 1.

i. Inplane Stress (σ)

As stated in the previous paragraphs, the critical compressive stress causes a panel to flutter at very nearly its lowest flutter speed. In addition, compressive inplane stress less than critical causes a flutter speed that is larger than the buckled value but smaller than the flutter speed for the unstressed panel; likewise tensile stress causes a larger flutter speed and is therefore stabilizing. Inplane stress may be caused by vehicle loads, temperature change or may be built in during manufacture. These criteria account for various combinations of streamwise and cross-stream stresses on the assumption that the stress is uniform along each edge.

j. Differential Temperature (ΔT)

A difference in temperature between a panel and its supporting structure causes thermal stresses that are compressive when the panel is hotter and tensile when the structure is hotter. These stresses are assumed to be uniform if the panel temperature is uniform and are treated by the methods developed for inplane stresses discussed previously. The criterion considers only the case of compressive thermal stress.

k. Differential Pressure (Δp)

Differential pressure denotes a condition whereby different static pressures exist on the two surfaces of a panel. The primary effect on panel flutter is due to the inplane stresses that are induced in resisting the pressure difference. For flat panels, the induced stresses are always tensile regardless of whether Δp acts inward or outward, and by (i) above would raise flutter speeds. The criteria presented in this report apply to flat panels. (If a cylindrically curved panel of radius R and thickness t is subjected to Δp, the circumferential stress is

approximated by $\sigma = \dfrac{R\Delta p}{t}$; it is compressive if Δp acts inward and tensile if Δp acts outward. The computed value of stress can be used as described in (i) above).

l. Cavity Effect

Air that is entrapped in a sealed-off volume behind a panel acts as a mechanical spring to increase the effective stiffness, and hence the frequency, of the fundamental panel mode. Some higher ordered modes are also affected but to a negligible degree. The cavity therefore diminishes the separation between modal frequencies and may lower the speed at which panel flutter occurs. In accounting for this effect, the cavity volume is interpreted as the gross volume of the constrained air, thus leading to the equivalent cavity depth

$$d = \frac{\text{actual cavity volume}}{\ell w}$$

The volume is not to be construed as the projected volume directly beneath the panel unless this is the volume actually enclosed.

2.2 Other Parameters

The following parameters have been treated in the literature and are known to affect panel flutter speeds; as noted previously, however, reliable quantitative design guides cannot yet be formulated.

a. Orthotropicity

A panel that has unequal bending stiffnesses in orthogonal directions is described as being orthotropic. The condition of orthotropicity may be caused by beading or corrugation stiffening.

b. Damping

Mechanical damping may be caused by friction in built up structures, by material losses, or by the application of commercially available damping material. Although damping does provide a mechanism for energy absorption, and hence might always be expected to raise flutter speeds, there are also cases in which friction lowers flutter speeds by introducing a phase shift between flutter critical vibration modes. Therefore the overall role of damping requires better definition.

c. Boundary Layer

The boundary layer adjacent to the exposed panel surface has been shown to appreciably raise flutter speeds under certain flow conditions. However, knowledge at the present time precludes criteria formulation.

3 Design Criteria

The set of criteria presented here is an attempt to substantially reduce the uncertainty that has been inherent in existing design techniques by incorporating existing knowledge in a revised and reoriented set of design guidelines. The design criteria are based on stability boundaries, that is, the condition of no flutter is the basis for design. Factors of safety in design are not included in this section but are discussed separately in section 5.

The nondimensional panel flutter parameter

$$\phi = \left[\frac{\beta E}{q}\right]^{1/3} t/\ell$$

has gained wide usage and is used in these criteria with some modification. In its most familiar application to flat panels, the critical value of ϕ is specified as a function of length-to-width ratio (see ref. 2 for example) and any combination of β, q, E, t and ℓ giving the specified ϕ will cause a panel to be neutrally stable.

Note, however, that as M approaches the value 1, β approaches zero. This untenable situation would require that the panel have prohibitively large thickness to prevent flutter at low transonic Mach numbers. In this document, therefore, β has been replaced by a Mach number correction factor $f(M)$ that is derived from published experimental data. The function $f(M)$ is shown versus Mach number in figure 1, and is seen to coincide with β for $M > 2$. (This curve was derived from experimental data obtained with a panel for which $\ell/w = 0.5$ and is discussed in section III of ref. 1; as additional data become available it may be possible to define the variation in $f(M)$ with ℓ/w.) The nondimensional panel flutter parameter that will be used in this set of criteria thus has the modified form

$$\phi_B = \left[\frac{f(M)E}{q}\right]^{1/3} \left(\frac{t_B}{\ell}\right)$$

and t_B is a "baseline" design thickness. These concepts are described in the following paragraphs.

The design procedure is oriented for the designer who must specify a panel thickness that will preclude flutter throughout the vehicle flight environment. To this end, the designer must first be furnished data in the following three basic categories:

(a) Flight conditions
(b) Physical Data and Geometry
(c) Environmental Conditions

The parameters that were discussed in section 1 are now separated and grouped in table I within these three categories.

TABLE I.—GROUPING OF PARAMETERS THAT AFFECT FLUTTER SPEED

(a) Flight Conditions	(b) Physical Data and Geometry	(c) Environmental Conditions
Mach number	Young's modulus	Inplane stress
Dynamic pressure	Length	Differential pressure
Angle-of-attack	Width	Differential temperature
Flow angularity	Length-to-width ratio Curvature Cavity Edge conditions Thickness (to be determined)	
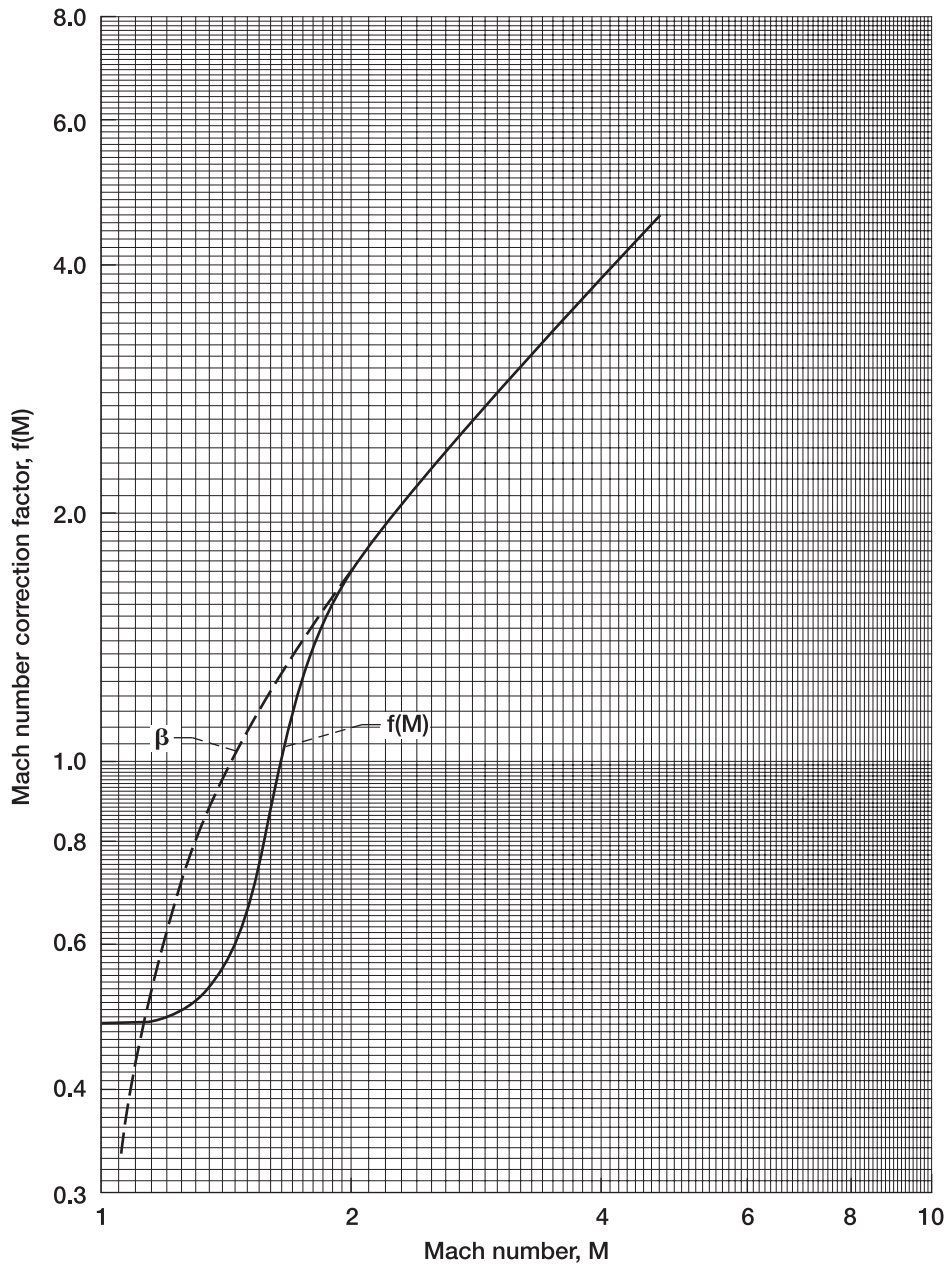
Figure 1.—Mach number correction factor versus Mach number.

The remainder or this section is used to describe step-by-step procedures that account for the above listed parameters in the overall set of criteria.

3.1 Step (1)—Flight Data, ℓ/w

The known quantities that enable the beginning of design are

Mach number (M)
Dynamic pressure (q)
Planform dimensions, length (ℓ), and width (w)

and are to be used as follows:

(a) Establish the aerodynamic quantity $[q/f(M)]$ for the flight envelope of the vehicle. Since the designer usually possesses flight data as altitude-Mach number or he can easily convert to this form, this step is facilitated by plotting the data directly on the prepared graph of figure 2. This figure was constructed by using $f(M)$ from figure 1. together with pertinent dynamic pressure-Mach number relationships from reference 3. The most adverse panel flutter environment usually occurs at $[q/f(M)]_{max}$ although other trajectory points may require investigation. Any other flight loading condition, either aerodynamic or thermal, that can cause panel buckling must be considered in the design. If the panel will be flown at or very near zero angle of attack, proceed to step (2).

(b) If the panel will be inclined to the airstream, go to step (4) before continuing with step (2) below.
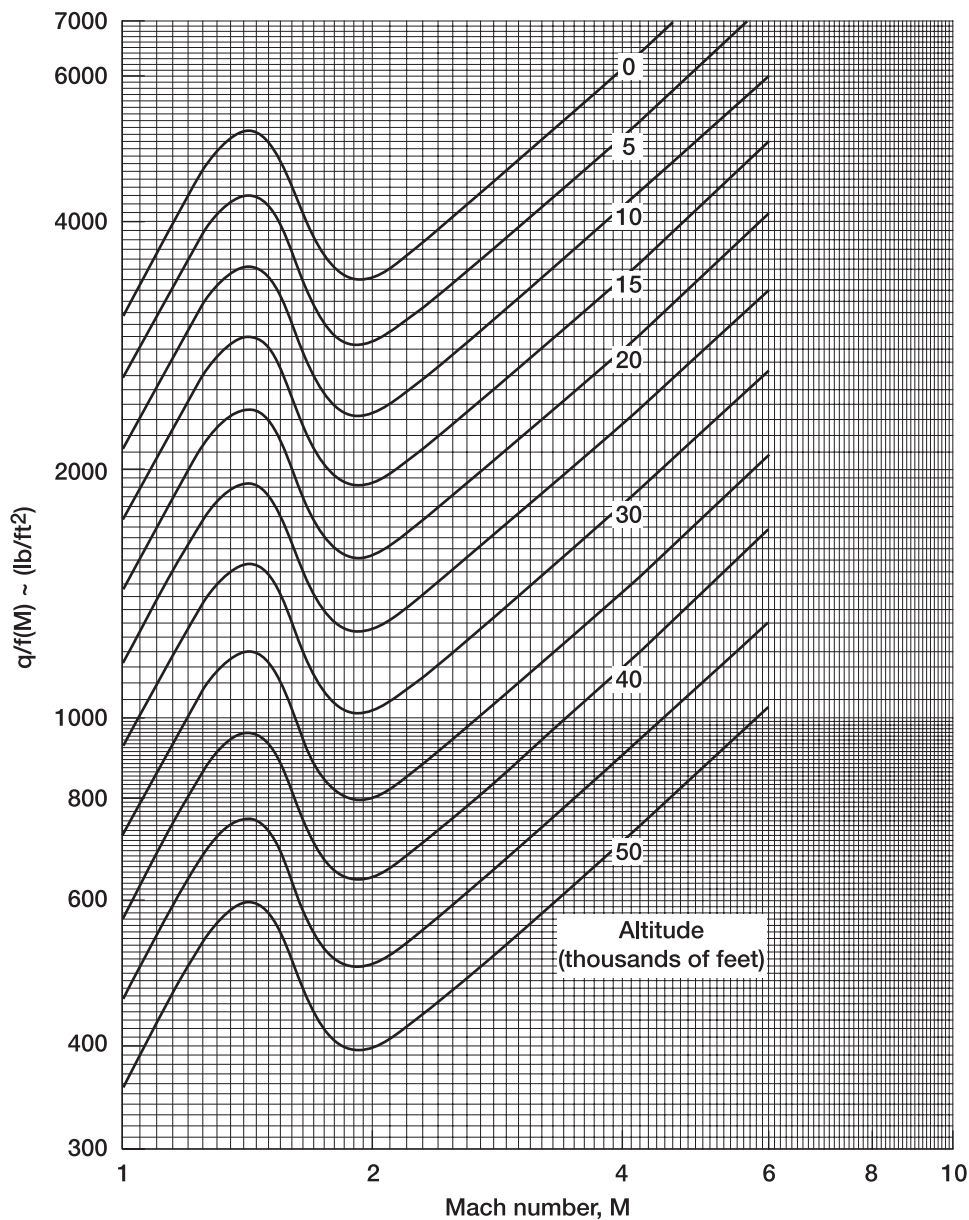
Figure 2.—Plot of q/f(M) versus Mach number with parametric variation in altitude.

3.2 Step (2)—"Flat" Panel Design

Proceed with the assumption that the panel will be clamped on all edges, flat, unswept and unstressed. Determine the panel thickness t_B that is required for neutral stability from the flight data used in step (1). (Thickness corrections for deviations from the ideal flat conditions will be made in step (3).)

The value t_B is obtained by using the "baseline" panel flutter parameter ϕ_B that is shown in figure 3. This parameter, which is of the same nondimensional form that is now widely accepted, is

$$\phi_B = \left(\frac{f(M)E}{q} \right)^{1/3} \left(\frac{t_B}{\ell} \right)$$

This plot is adapted from experimental data given in references 2 and 4 together with a theoretical extrapolation from plots given in reference 5. It is expedient to rewrite the parameter as follows:

$$\phi_B^3 = \underbrace{\left(\frac{f(M)}{q} \right)}_{\text{Aerodynamic}} \times \underbrace{E\left(\frac{t_B}{\ell} \right)^3}_{\text{Structural}}$$

and by using the data from figure 3, the relationships shown in figure 4 are obtained. This data, plotted in the form that shows $[q/f(M)]$ as the ordinate (as it also was in fig. 2) presents the opportunity of graphically determining the value of t_B required for neutral stability. In addition to the flight path data that was developed in step (1), it is assumed that the quantities
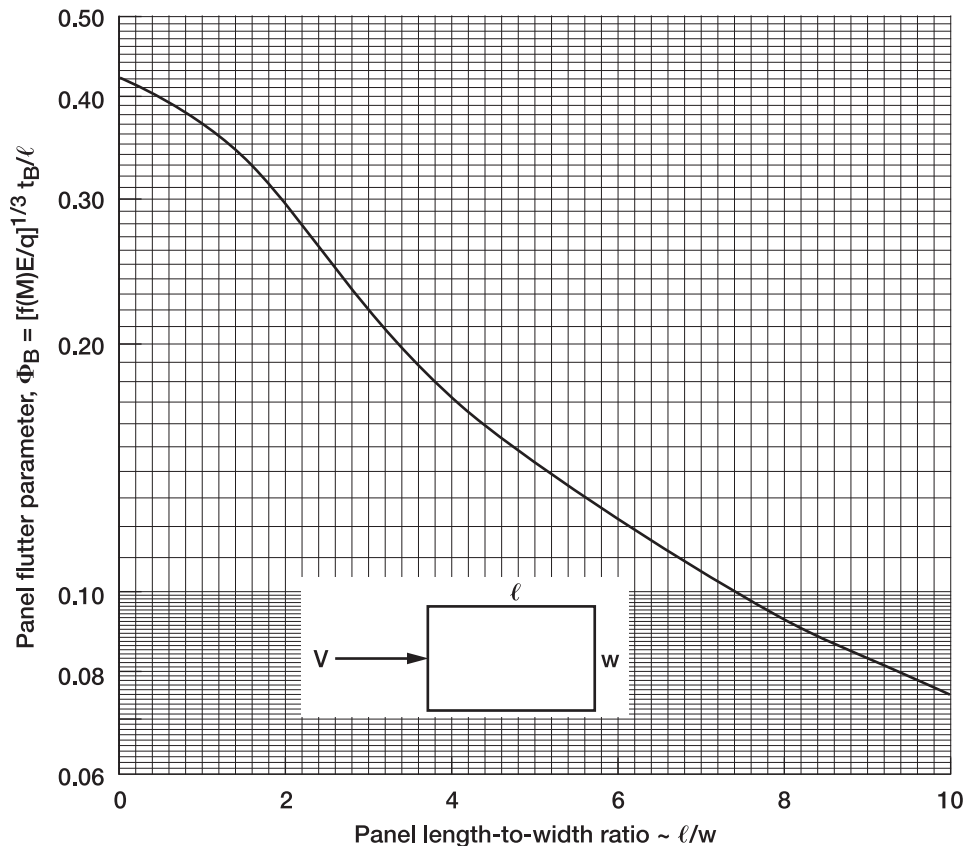
Figure 3.—"Baseline" design curve.
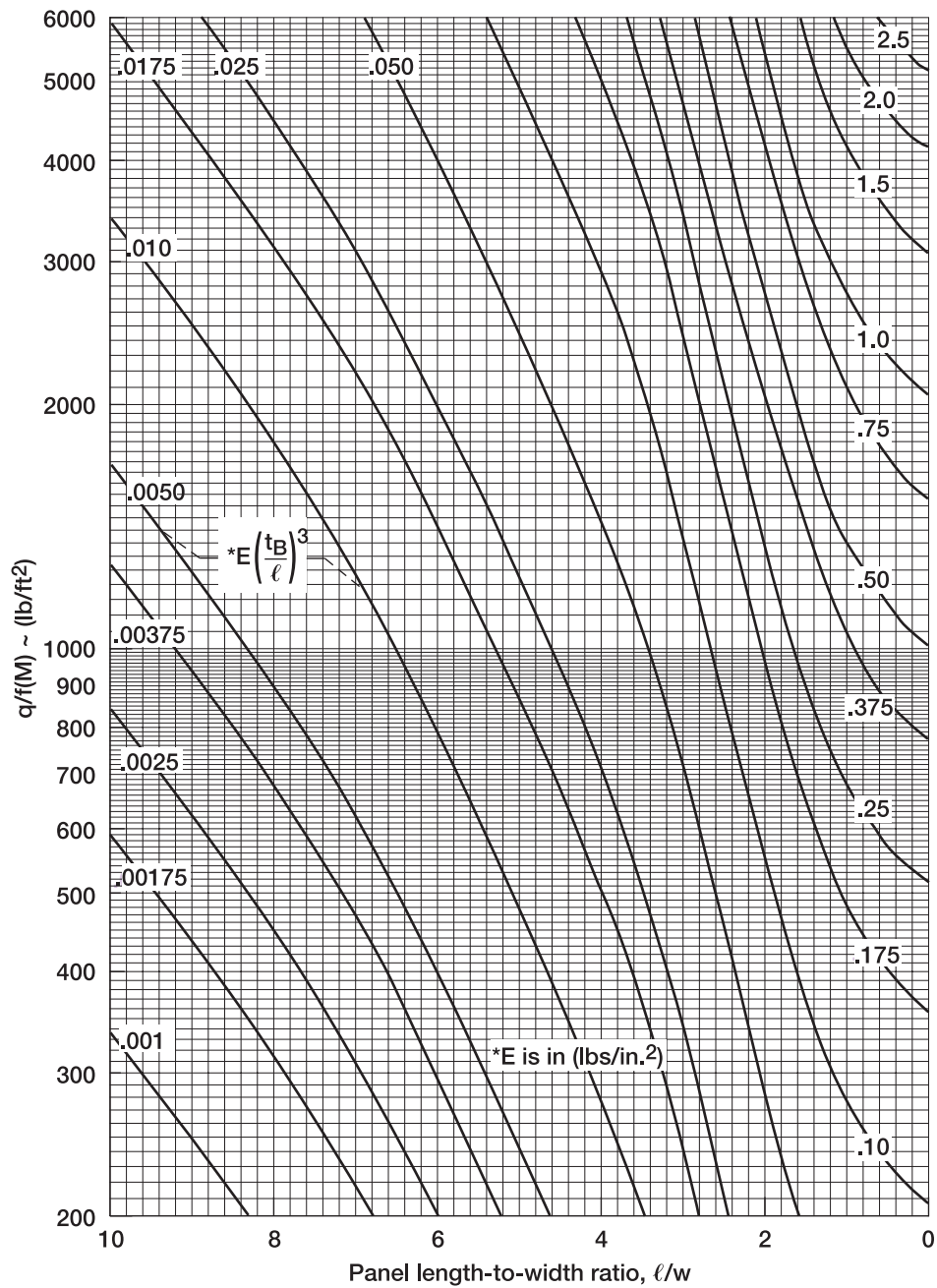
Figure 4.—Aerodynamic parameter q/f(M) versus ℓ/w with variation in structural parameter $E\left(\dfrac{t_B}{\ell}\right)^3$.

Modulus (E),
length (ℓ),
width (w)

have also been specified.

We now combine figures 2 and 4 by matching the ordinates to obtain the composite graph shown as figure 5. Given the maximum value of [$q/f(M)$] from step (1) and the length-width ratio ℓ/w, the required value of the structural term

$$E\left(\frac{t_B}{\ell}\right)^3$$

is found from the intersection of two lines that are constructed as explained in the following sample design case: [An example problem is shown in figure 5 for a typical flight envelope that has been drawn on Curve (B) to establish [$q/f(M)$]$_{max}$. A horizontal line is passed through this peak value. A vertical line is drawn on Curve (A) through the value of ℓ/w for the subject panel ($\ell/w = 3$ in the sample problem). The intersection of the two lines is found, by interpolation, to be

$$E\left(\frac{t_B}{\ell}\right)^3 = 0.31$$

so that the "baseline" design thickness for the sample design is

$$t_B = \left(0.31/E\right)^{1/3}\ell \ .$$

This concludes the second step.
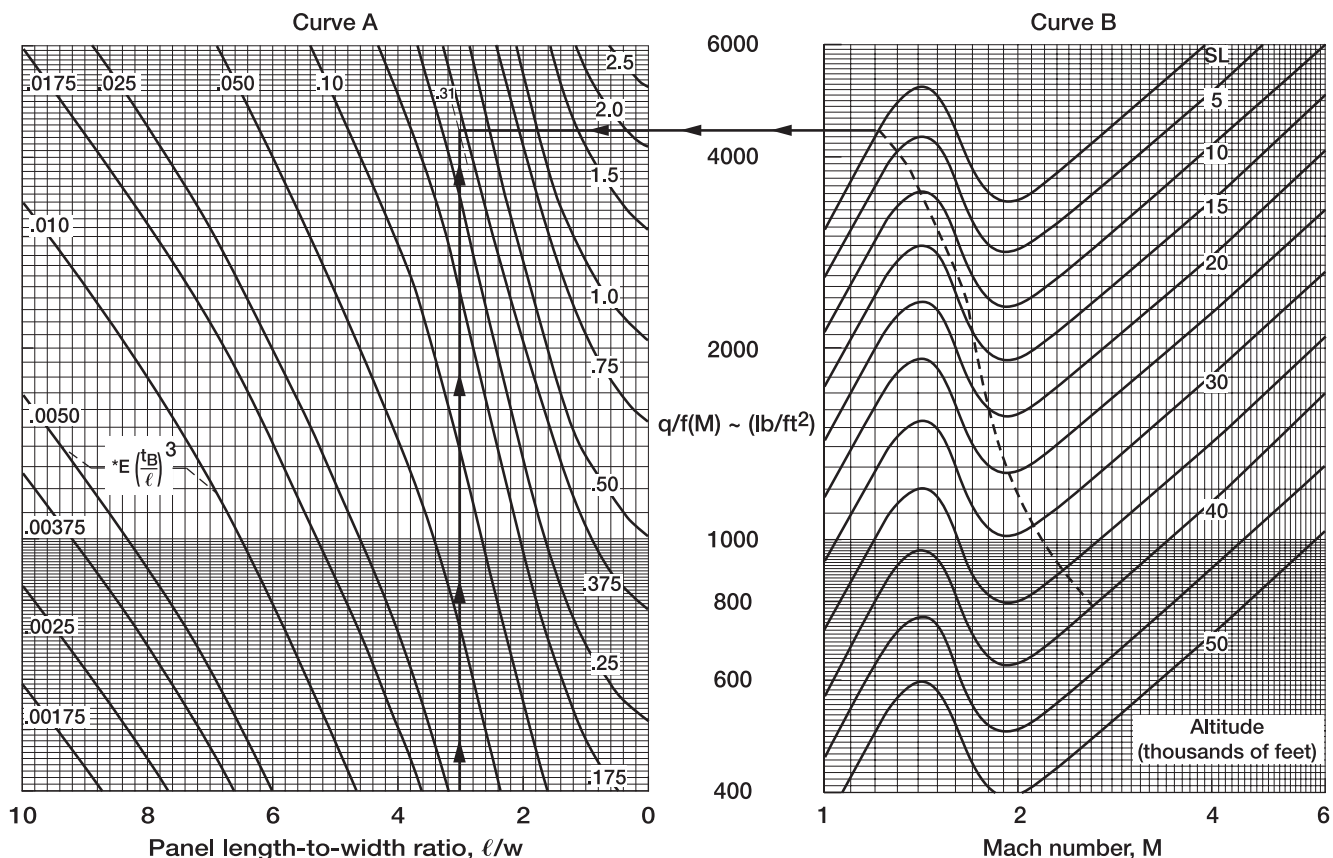
Figure 5.—Flat panel design curves. Curve A; [*E is in lbs/in.^{2}]. Curve B; [– – – – Hypothetical flight envelope].

3.3 Step (3)—Thickness Requirement

The flat panel thickness value t_B has now been established. If the anticipated service condition of the panel happens to be flat, clamped, unswept and unstressed, then the design is complete, and t_B is the panel thickness required for neutral stability. This is unlikely, however.

We direct our attention back to the parameters that were listed in Columns (b) and (c) of table I. We assume that each of the parameters that is not yet accounted for will cause a change in panel stability that can be represented by a correction in panel thickness. If the parameter destabilizes the panel, then panel thickness should be increased; likewise a stabilizing effect would cause a decrease in required panel thickness. It was assumed, in establishing thickness correction factors that are shown in the remaining figures, that interaction between parameters is small compared to the primary influence of a parameter itself. This step results in a corrected thickness t_C obtained from t_B and the thickness correction factors.

Thickness correction factors and procedures for their determination are as follows:

Curvature t_N/t_B Figure 6

Procedure:

Determine the baseline thickness t_B. For a cylindrically curved panel with the flow orientation shown on figure 6, determine the crown height distance h_o from the geometrical relationship

$$h_o = R\left(1 - \cos\left(\frac{\theta}{2}\right)\right) = R - \sqrt{R^2 - \left(\frac{w}{2}\right)^2}$$

Compute the curvature parameter

$$N = h_o/t_B$$

and enter figure 6 to obtain t_N/t_B.
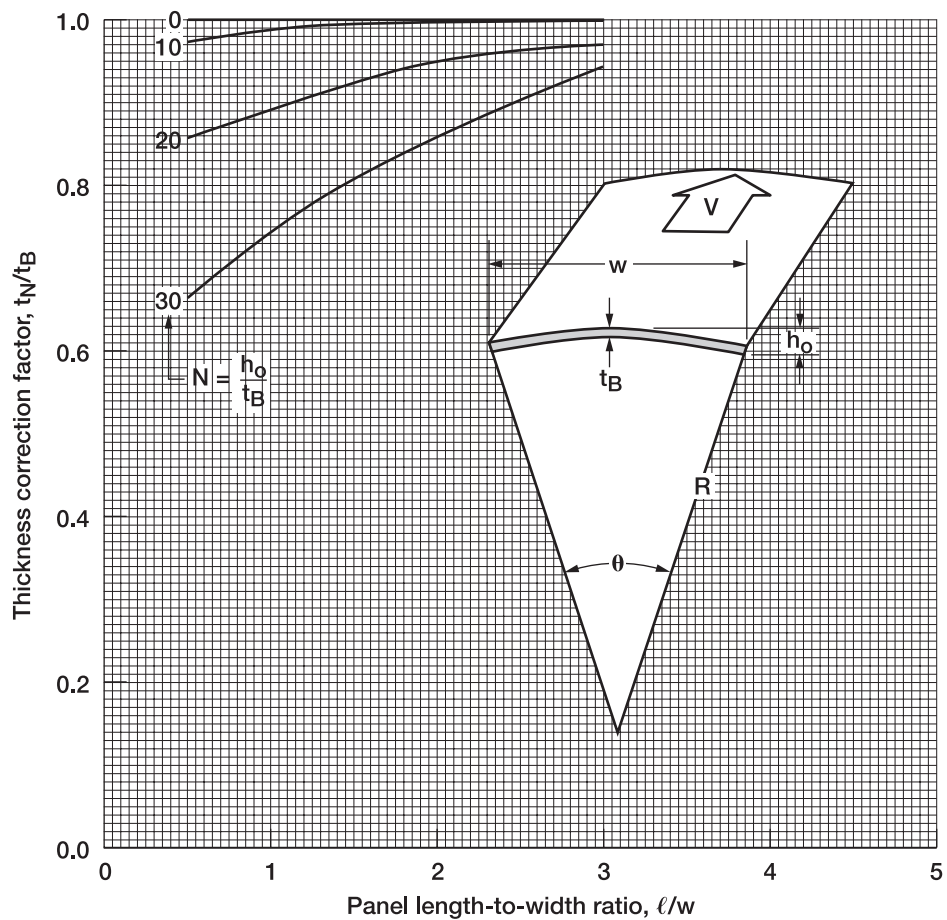
Figure 6.—Thickness correction factor for curvature.

Procedure:

Make thickness correction for flow angularity Λ only if $\ell/w < 1$. The dimension ℓ is the one most nearly aligned with the flow since the correction t_Λ/t_B is only applied to rectangular panels when $\Lambda \leq 45°$. The thickness correction factor is obtained from figure 7. (The effect of flow angularity for $\ell/w > 1$ is shown in reference 1 to be slightly stabilizing; therefore no thickness correction is recommended.)
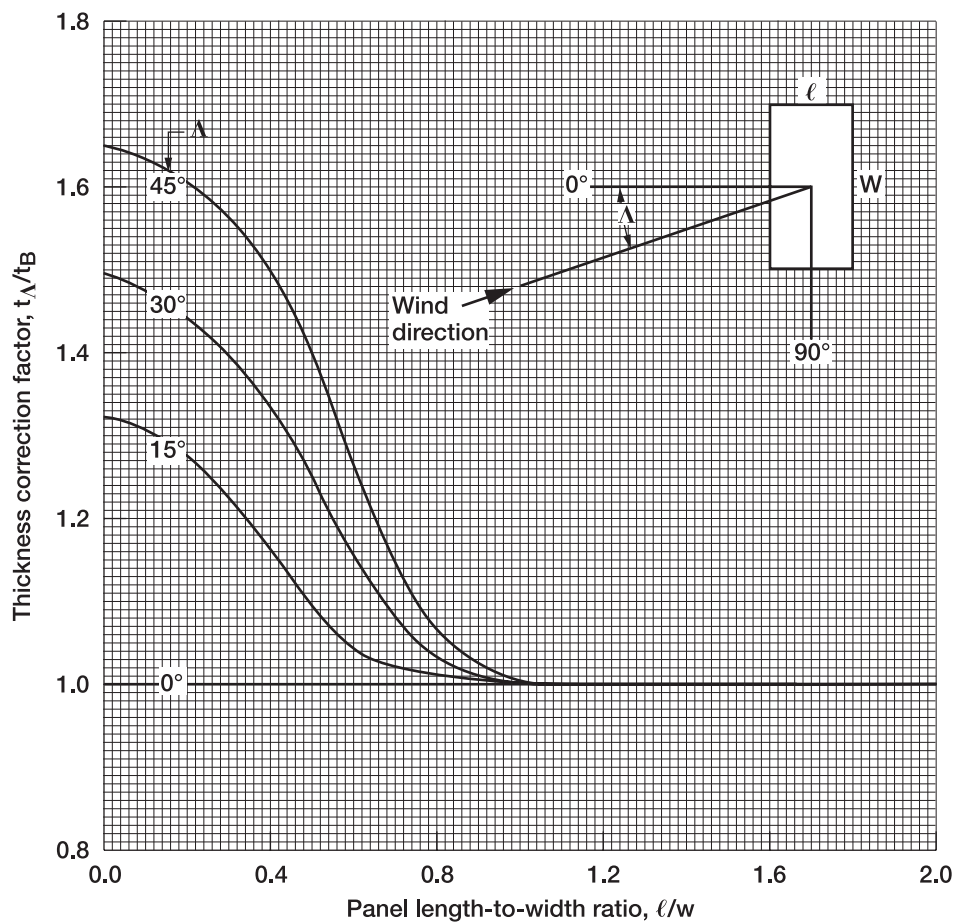
Figure 7.—Thickness correction factor for flow angularity.
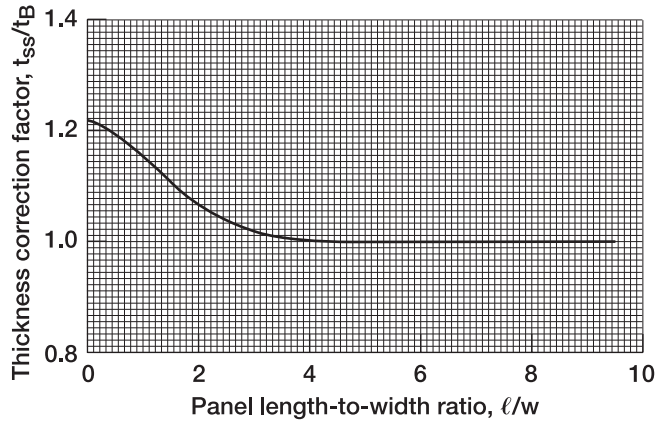
Figure 8.—Thickness correction factor for a simply
supported panel.

Simply-supported edges t_{ss}/t_B Figure 8

Procedure:

Use this correction if panel edge supports are less than fully clamped. The baseline thickness t_B assumes clamped edges and figure 8 provides a thickness correction t_{ss}/t_B for a panel whose edges are not restrained in rotation. For intermediate cases, choose a value of the correction factor between 1 and the value of t_{ss}/t_B. The value chosen will depend on the method by which the panel is attached to support structure. For example, closely spaced rivets or screws would justify the use of a value of 1.0, whereas sparsely spaced fasteners would call for a value near the curve. In most cases the clamped edge approximation is believed to be adequate.

Inplane stress (tension) t_σ/t_B Figure 9

Procedure:

Tensile stress is stabilizing and is most easily handled as an apparent increase in the panel modulus in the amount

$$E_{effective} = E\left(1 + \frac{N_x}{N_{x_{cr}}}\right)$$

A thickness correction factor has been derived from this relationship and is presented in figure 9 as a plot of t_σ/t_B versus $N_x/N_{x_{cr}}$. The tension load is applied in the stream direction and the cross-stream load is zero; it is recommended, however, that this correction be used even if tension load also occurs in the cross stream direction.

(The designer may obtain values of $N_{x_{cr}}$ from figs. 11 and 13.)
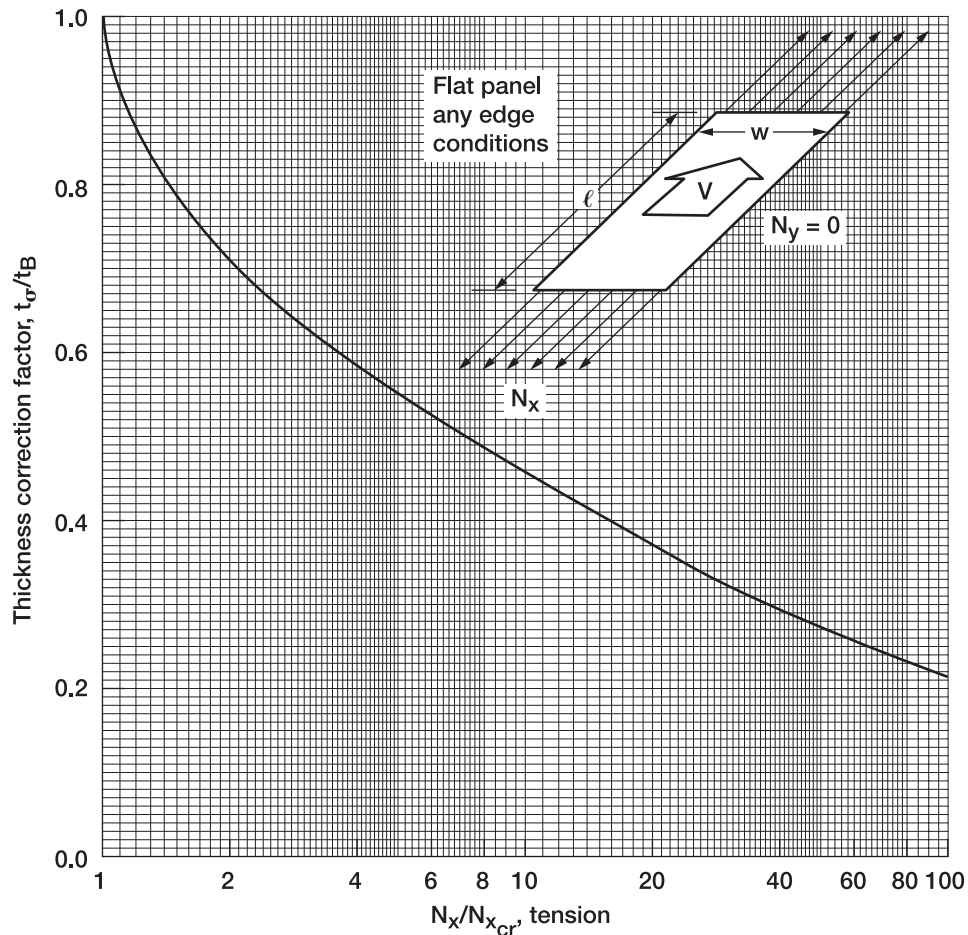
Figure 9.—Thickness correction factor for stress (tension).

Inplane stress (compression) t_σ/t_B Figures 10 through 14

Procedure:

The method of obtaining the thickness correction for longitudinal compressive stress is accomplished in three steps:

(1) Determine the anticipated inplane loads N_x (streamwise) and N_y (cross-stream) that will occur during the critical portion of flight.

(2) Determine the critical value of streamwise load $N_{x_{cr}}$ for the panel based upon edge conditions, ℓ/w, and the ratio N_y/N_x. (For aid in determining $N_{x_{cr}}$ see item (4) below.)

(3) Using the computed value $N_x/N_{x_{cr}}$, enter figure 10 and obtain the thickness correction factor t_σ/t_B. (On the basis of experimental data that is discussed in ref. 1, the curve of figure 10 assumes that the critical flutter speed occurs when panel compressive stress is between 80 percent and 100 percent of the still air buckling stress. Therefore the flat
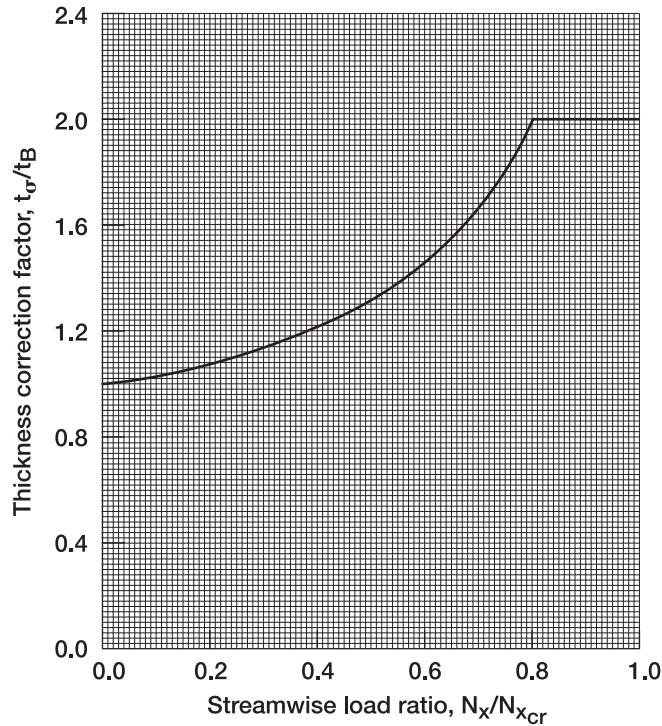
Figure 10.—Thickness correction factor for inplane
stress (compression).

portion between $N_x/N_{x_{cr}} = 0.8$ and 1.0 provides maximum thickness correction. The remainder of the curve is obtained by adjusting the values of the theoretical curve shown in figure 20 of ref. 1 downward to 0.8 $N_x/N_{x_{cr}}$.)

(4) Figures 11, 12, 13 and 14 have been included to assist in determining $N_{x_{cr}}$. These curves present $N_{x_{cr}} / \left(\pi^2 D / \ell^2 \right)$ versus ℓ/w for clamped and simply supported panels for the loading conditions $N_y = 0$ and $N_y = N_x$. It is recommended that the designer inter-polate among the four cases if he feels that his panel edge supports and loading do not identically match any of the examples presented. (As an example, suppose that a panel of $\ell/w = 3$ is estimated to have edge bending stiffness that is roughly intermediate between simply supported and clamped edge conditions; furthermore, the inplane stress at the critical flight condition is estimated to be $N_y = 0.5N_x$. Linear interpolation gives a value

$$N_{x_{cr}} \Big/ \frac{\pi^2 D}{\ell^2} = 33.3$$

as indicated by the following chart.)

Demonstration of linear interpolation to obtain value of $N_{x_{cr}} / \frac{\pi^2 D}{\ell^2}$ for panel with $\ell/w = 3$

SS*	C1**
$N_y = 0$	
23 (Figure 13)	65 (Figure 11)

SS	C1
$N_y = N_x$	
10 (Figure 14)	35 (Figure 12)

Average

44
(Intermediate
edge restraint)

22.5
(Intermediate
edge restraint)

Average yields

$$N_{x_{cr}} / \frac{\pi^2 D}{\ell^2} = 33.3$$

(Intermediate edge
restraint and $N_y = 0.5 \, N_x$)

SS* - simply supported edges
C1** - clamped edges
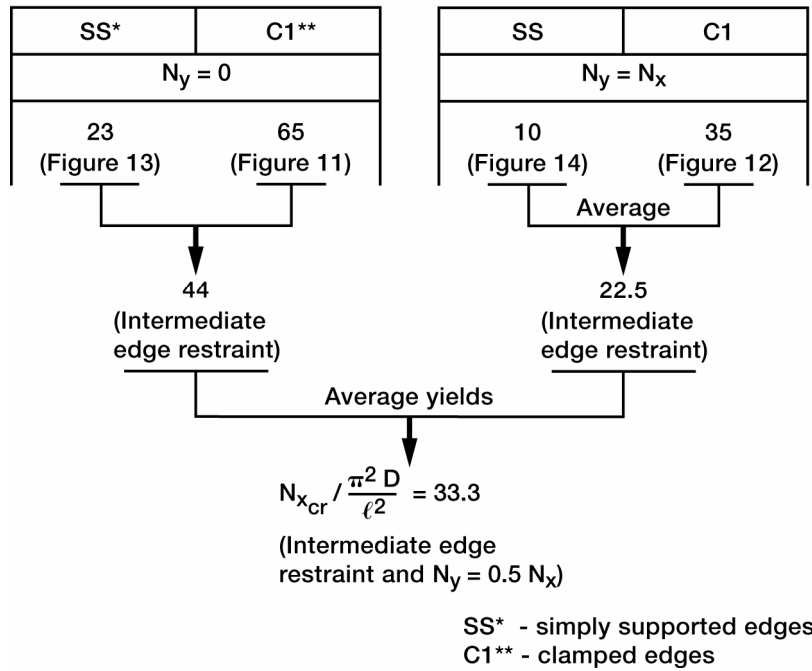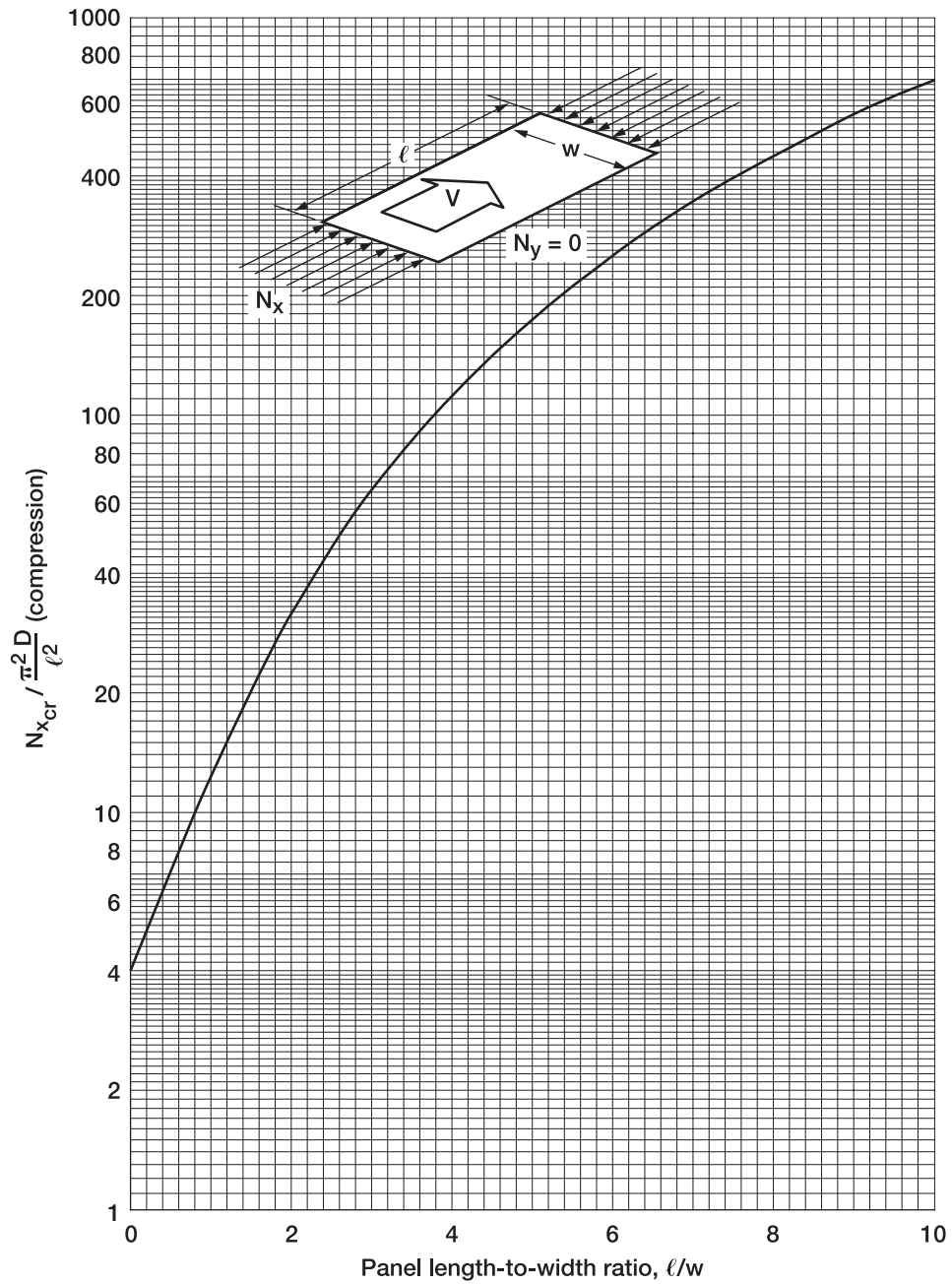
Figure 11.—Critical inplane compression load for clamped panel, $N_y = 0$.
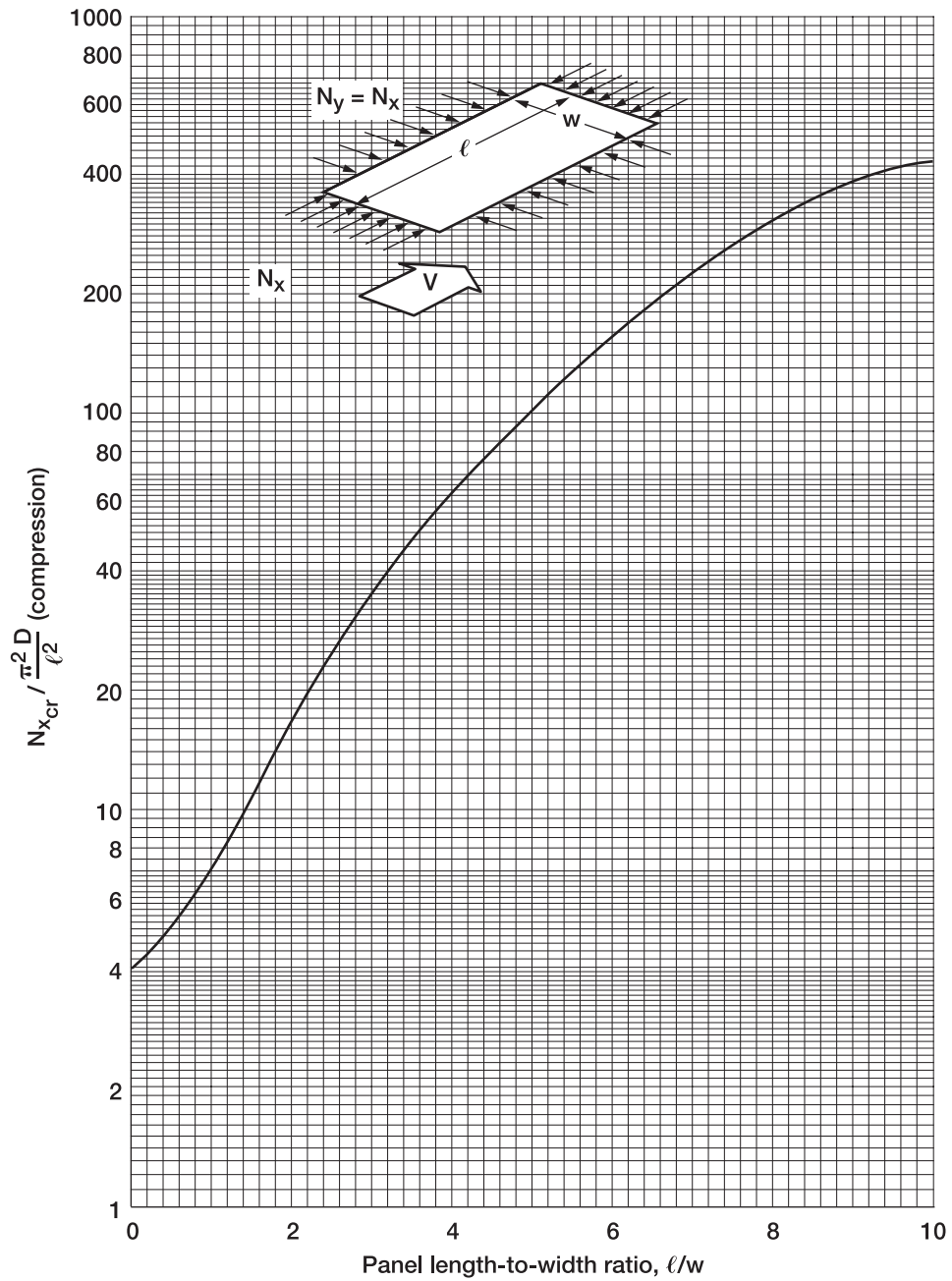
Figure 12.—Critical inplane compression load for clamped panel, $N_x = N_y$.
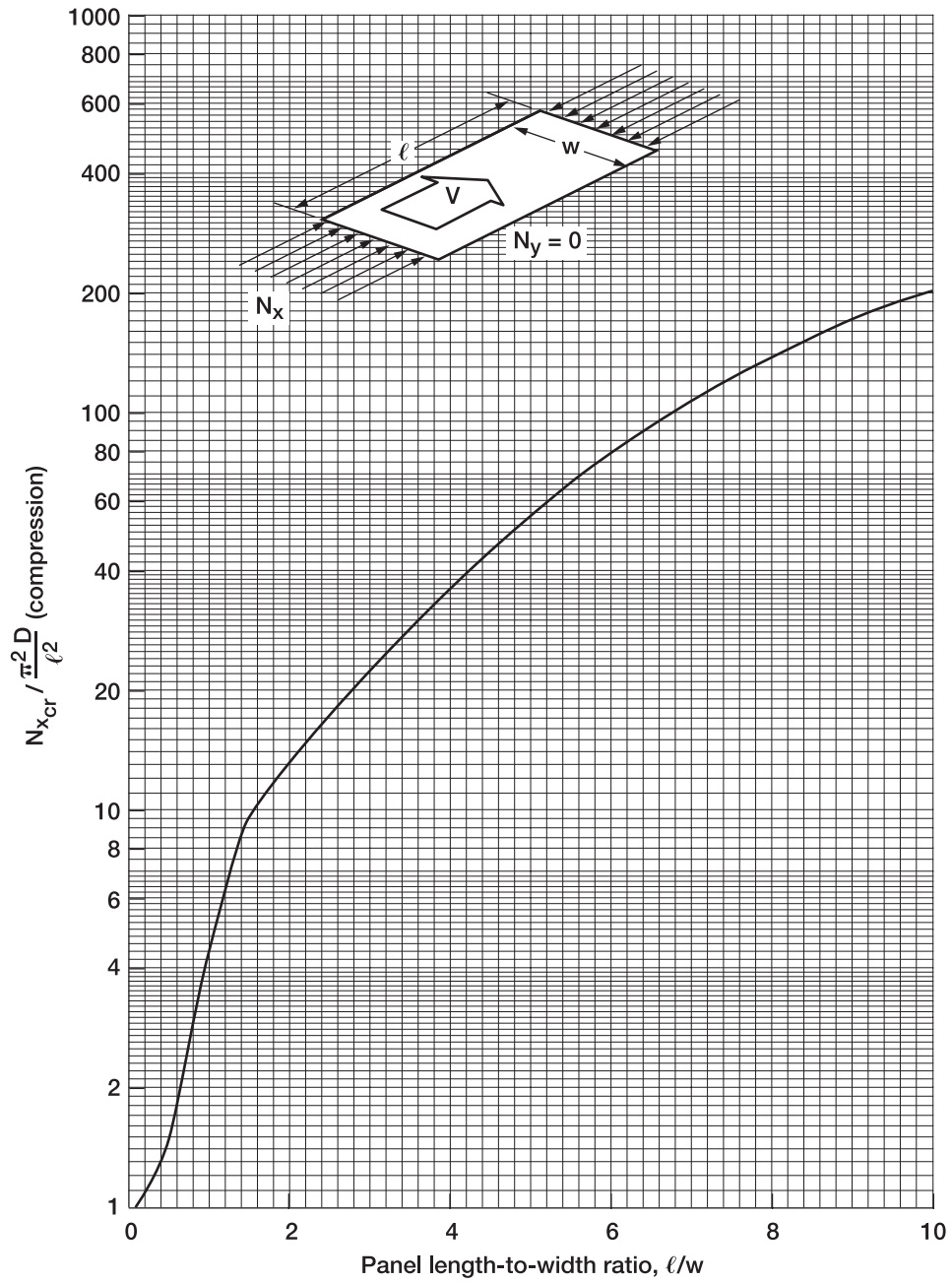
Figure 13.—Critical inplane compression load for simply supported panel, $N_y = 0$.
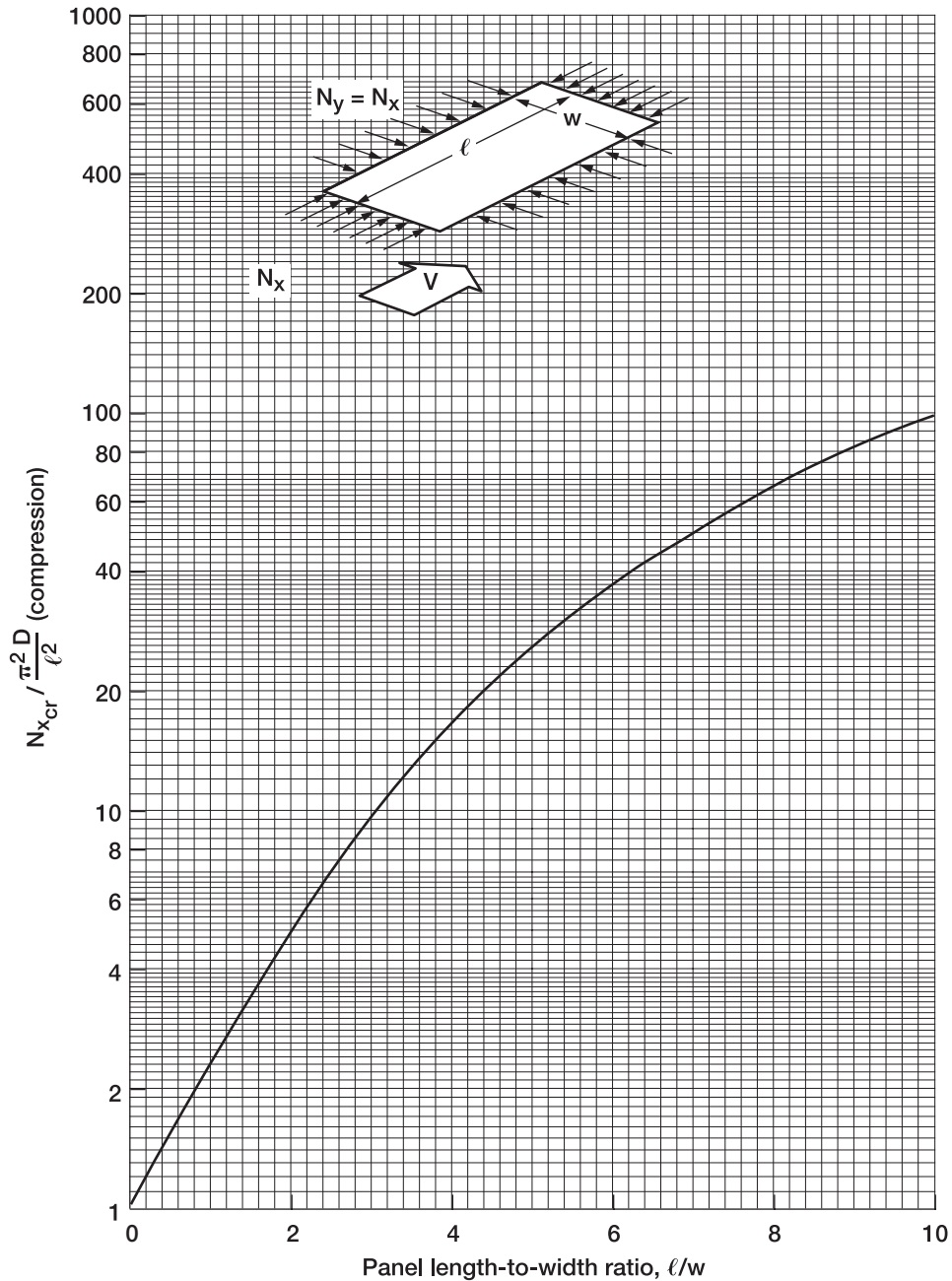
Figure 14.—Critical inplane compression load for simply supported panel, $N_y = N_x$.

Buckling t_b/t_B Figures 11 through 14

Procedure:

Experimental evidence from studies of inplane stress indicate that the lowest flutter speed for a stressed panel occurs when N_x is at or near $N_{x_{buckling}}$. Therefore, a panel that will be buckled during the critical portion of its flight requires a thickness correction $t_b/t_B = 2$. (This is the maximum correction factor from the curve of figure 10.). Assume that $N_{x_{buckling}} = N_{x_{cr}}$ so that critical load values can be obtained from figures 11, 12, 13, and 14.

Procedure:

To account for unequal pressures on opposite faces of a flat panel,

(1) Compute the value of the parameter $\Delta p \bigg/ E\left(\dfrac{t_B}{\ell}\right)^4$ from the design data; with ℓ/w enter figure 15 to find the parameter d_o/t_B.

(2) With the value of d_o/t_B and ℓ/w, enter figure 16 to find the thickness correction factor $t_{\Delta p}/t_B$.
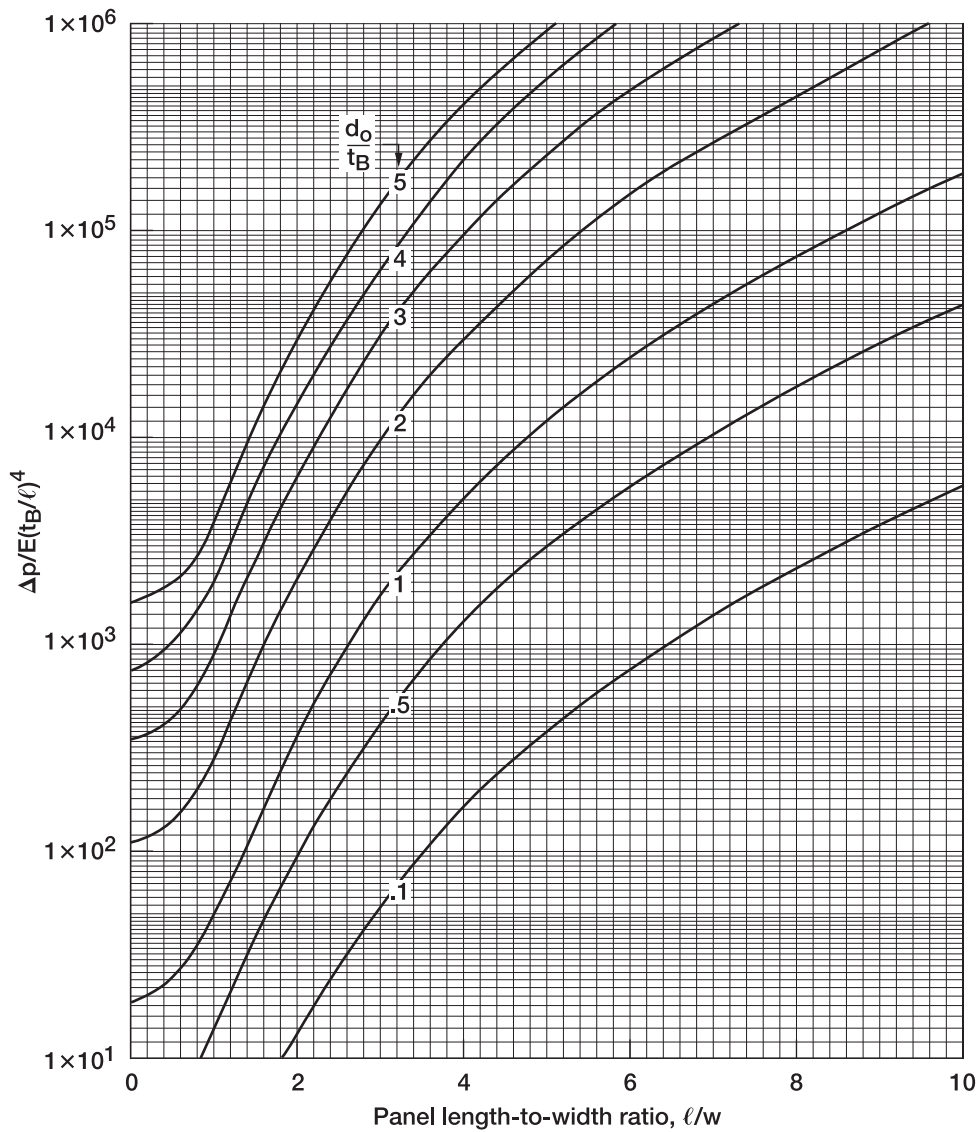
Figure 15.—Relationship between d_o/t_B, Δp, and panel geometric-physical characteristics.
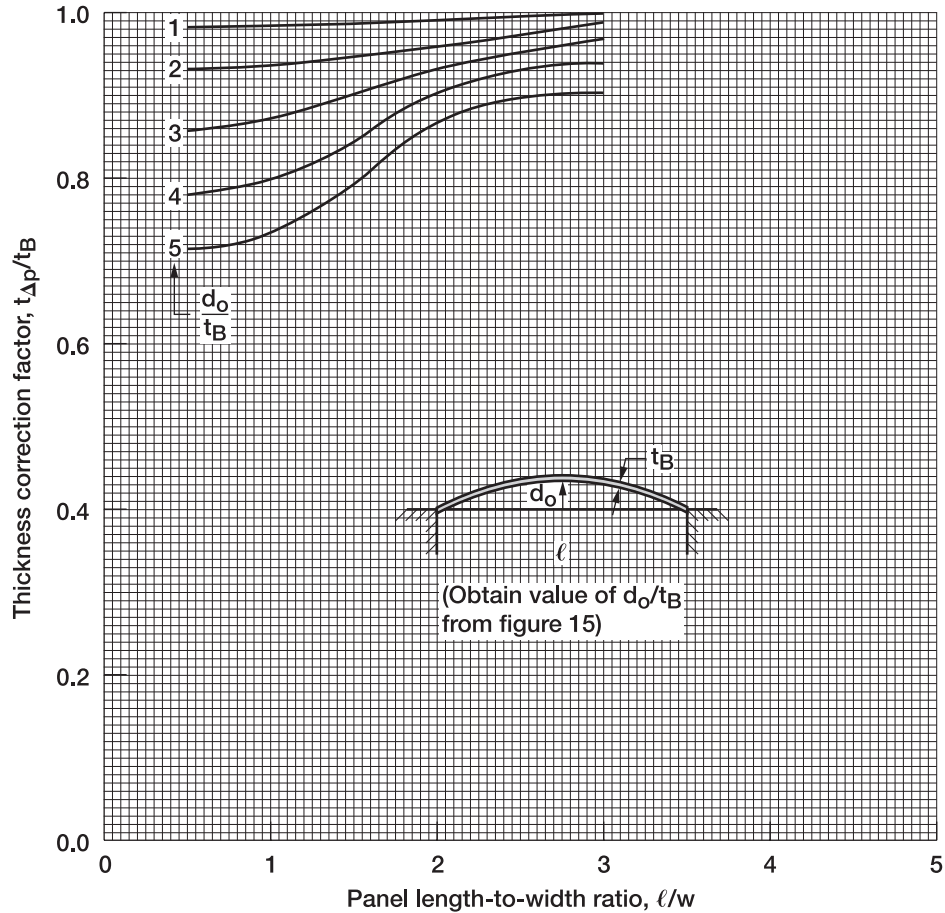
Figure 16.—Thickness correction factor for differential pressure.

Differential temperature $t_{\Delta T}/t_B$ Figures 17 through 19

Procedure:

This correction applies to a panel whose edges are restrained against inplane motion; the panel temperature is higher by an amount ΔT than its supporting structure. The critical value of differential temperature ΔT_{cr} is that value at which the panel buckles.

(1) Enter figure 17 or 18 with ℓ, t_B and ℓ/w to determine $\alpha_T \Delta T_{cr}$ in which α_T is the thermal coefficient of expansion for panel material.

(2) Compute $\Delta T/\Delta T_{cr}$ and enter figure 19 to find $t_{\Delta T}/t_B$.
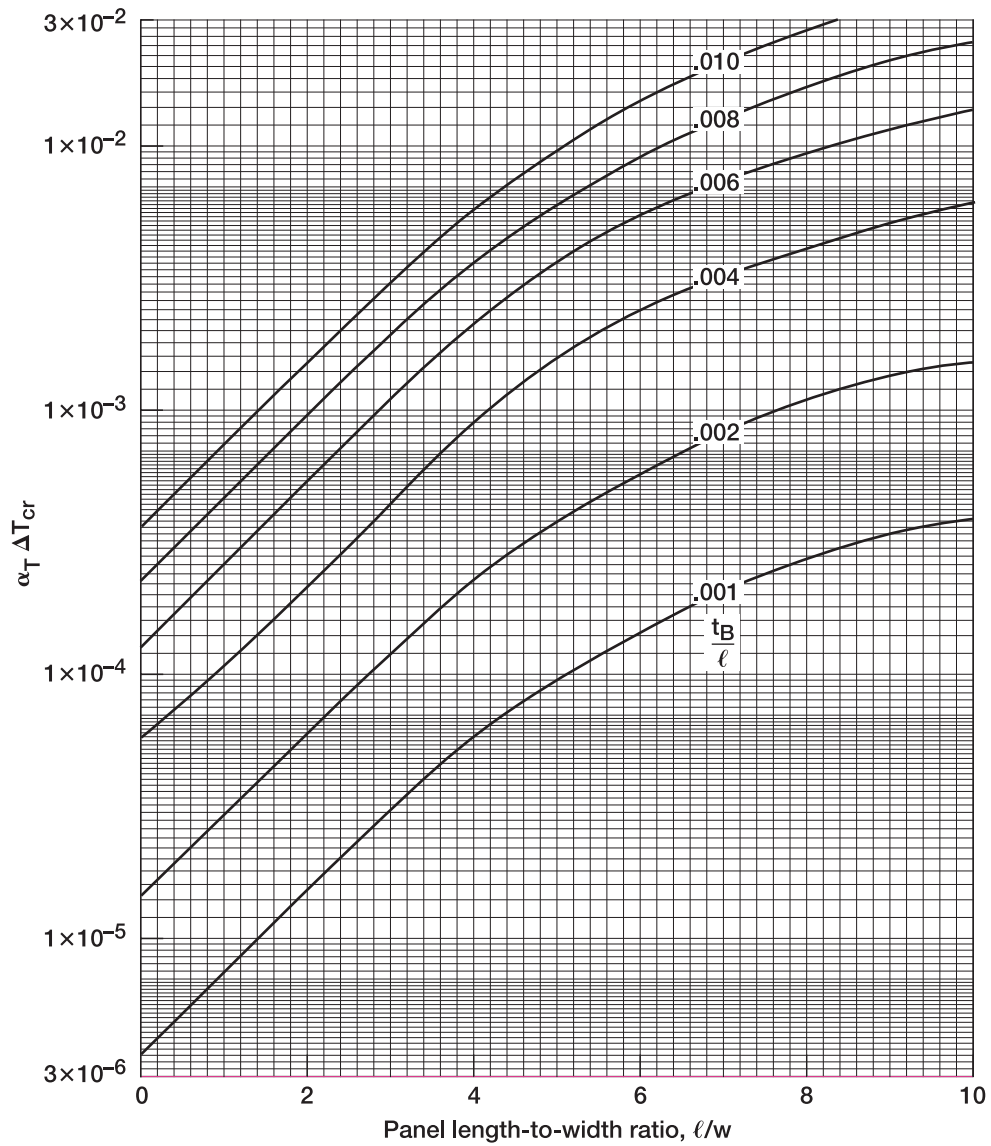
Figure 17.—Critical differential temperature of clamped panel with restrained edges.
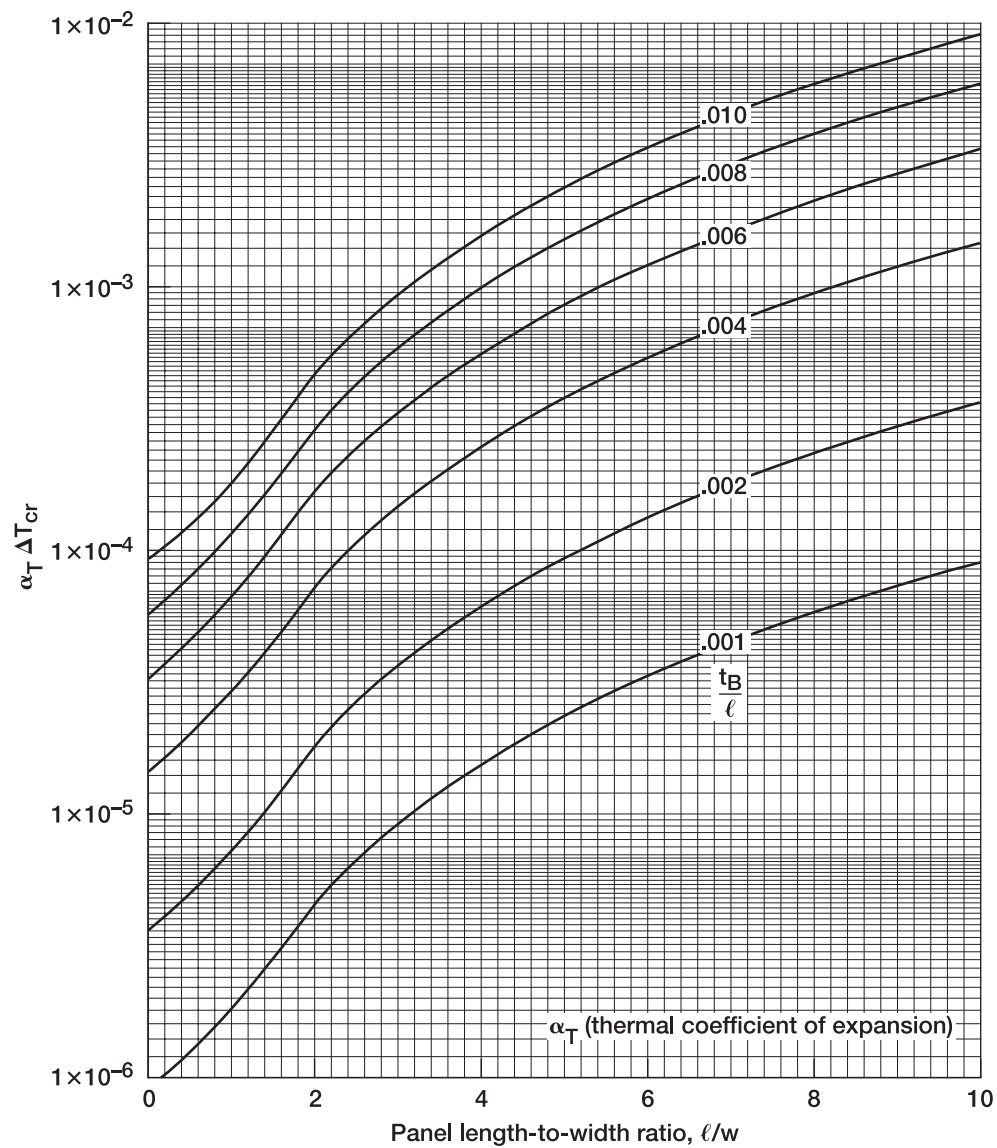
Figure 18.—Critical differential temperature of simply supported rectangular panel with restrained edges.
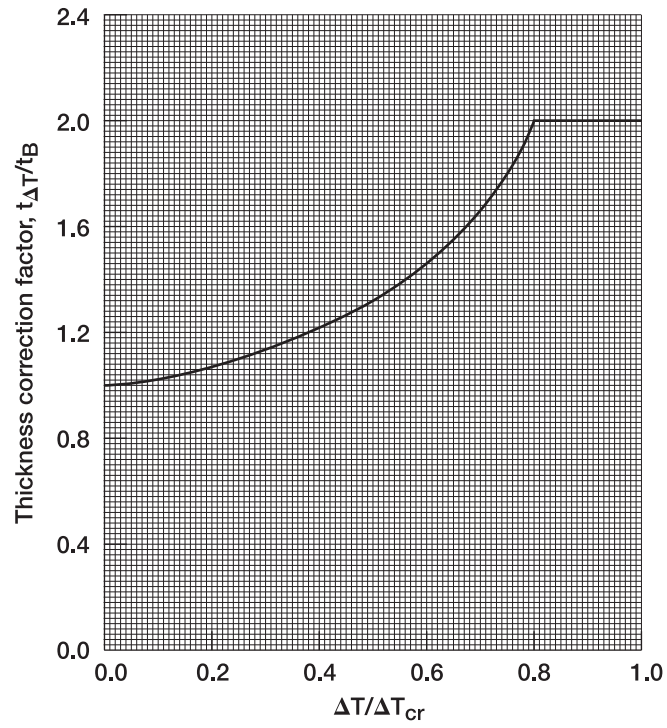
Figure 19.—Thickness correction factor for differential temperature.

Cavity t_{cav}/t_B Figure 20

Procedure:

This correction applies if the panel encloses a volume of air that is not vented to the atmosphere. The volume of the cavity is written in the form (ℓwd) in which d is an equivalent cavity depth. Compute the quantity

$$P_{cav}(\ell^4/Dd)$$

and enter figure 20 to determine t_{cav}/t_B.
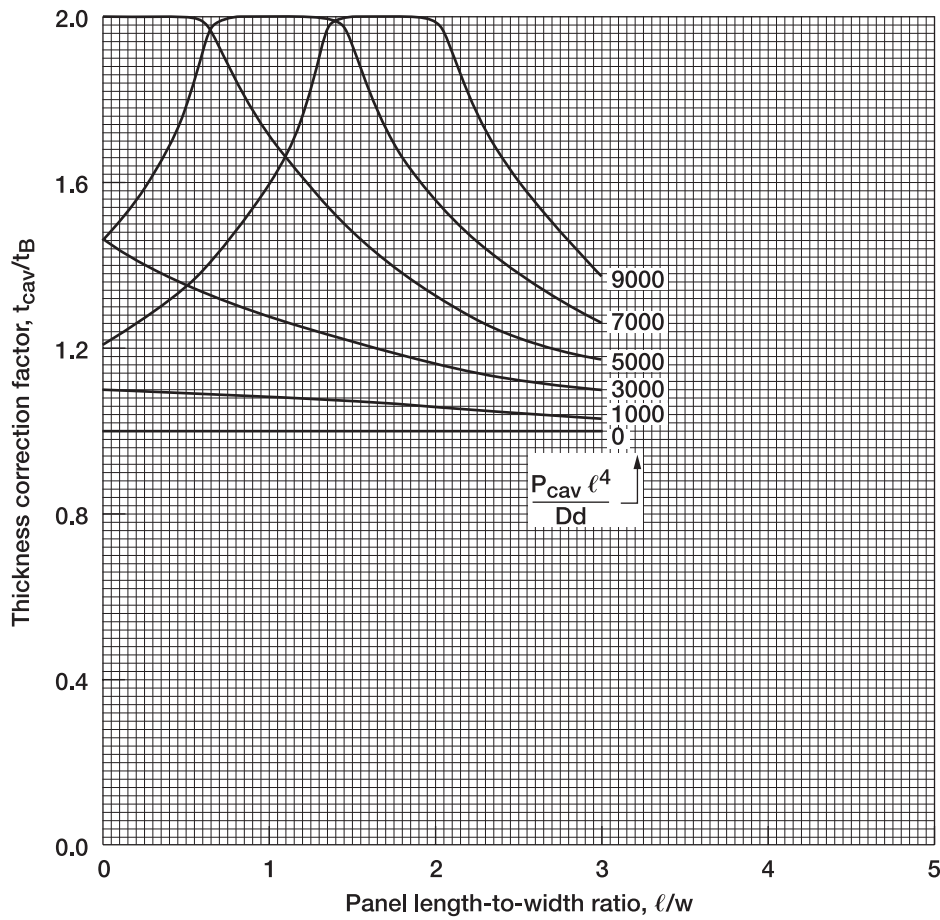
Figure 20.—Thickness correction for an enclosed cavity.

Determination of corrected thickness t_C

The final value of thickness t_C is obtained by multiplying all thickness correction factors by the "baseline" thickness, viz.,

$$t_C = t_B (t_1/t_B)(t_2/t_B) --- (t_i/t_B)$$

The maximum value of the corrected thickness is limited to

$$t_C = 2\left(\frac{t_\Lambda}{t_B}\right) t_B$$

Use of the factor 2 as a maximum value recognizes that the "worst case" flutter susceptibility cannot be compounded; this fact is substantiated by experimental data as shown in the plots of reference 4 for example. Flow angularity, however, does influence flutter boundaries even at the minimum flutter speeds.

3.4 Step (4)—Angle of Attack

If the panel is inclined to the airstream then the angle of attack α is used to establish local values of Mach number (M_L) and dynamic pressure (q_L). The quantity

$$[q/f(M)]_L = q_L/f(M_L)$$

must be computed for a sufficient portion of the flight envelope to insure that the critical (maximizing) value is obtained. This value is then used to enter Curve (a) of figure 5, and hence to determine the value of $E\left(\dfrac{t_b}{\ell}\right)^3$. (It is suggested that the conversion from free stream to local be obtained by using directly charts of $(q/\beta)_L / (q/\beta)_\infty$ such as shown in figure 3(a) of ref. 6.)

The design now proceeds back to Step (2).

4 Related Areas

The conditions under which the criteria in this report are directly applicable are discussed in section 1. The purpose of this section is to discuss certain areas in which the criteria are not directly applicable, but may be used indirectly to design flutter-free panels. These closely related areas include (1) built-up isotropic panels (such as honeycomb), and (2) panels whose edge supports do not restrain inplane motion. Before discussing these conditions individually, the designer is reminded that the dominating factor that determines panel flutter behavior is the inter-relationship of the natural frequencies. Therefore, if analyses (or the judgment and experience of the designer) are able to predict how the panel still air frequencies will behave, the trend of the variation in flutter speed can be estimated by one of the assumed mode methods described in section IV, part 2 of reference 1.

4.1 Built-Up Isotropic Panels

The most important example of a built-up, isotropic panel is honeycomb which consists of a low density core (middle layer) sandwiched between two flat face sheets. The core serves to stabilize the relative positions of the face sheets in a structural configuration that is much more rigid in bending than is a single panel with the combined thickness of the two faces. A flexural stiffness that is analogous to the plate stiffness D for a flat panel is obtained from the Young's modulus E, the face sheet thickness t_f, the core thickness s and by neglecting the bending rigidity of the core.

Figure 21 shows the honeycomb configuration. The equivalent plate bending stiffnesses are

(a) if t_f and s are of the same order of magnitude,

$$D_h = \frac{E}{2(1-v^2)}\left[t_f(s+t_f)^2 + \frac{1}{3}t_f^3\right]$$

and

(b) if $s \gg t_f$,

$$D_h = \frac{E}{2(1-v^2)}t_f s^2$$

These stiffnesses lead to the following equivalent thicknesses (for a flat plate):

(a) t_f and s same order of magnitude,

$$t_{eq}^3 = 6t_f(s+t_f)^2 + 2t_f^3$$

and

(b) if $s \gg t_f$,

$$t_{eq}^3 = 6t_f s^2$$

Frequencies of the equivalent uniform thickness skin panel would not be the same, but the frequency ratios between modes would be, i.e., we preserve basic stiffness level and frequency ratios. Once the equivalent thickness has been obtained, criteria charts can be used as before.
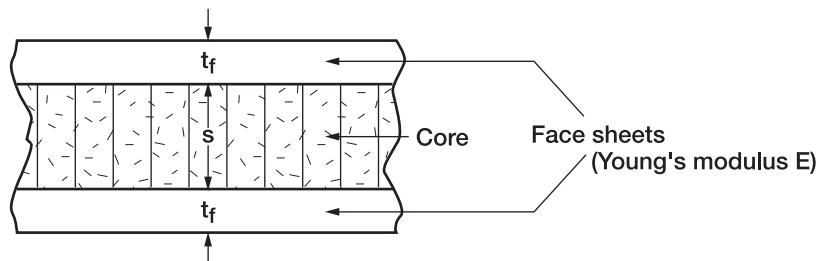
Figure 21.—Honeycomb configuration for analyzing stiffness.

4.2 Negligible Inplane Edge Restraint

If the edge support structures offer negligible inplane restraint (as, for example, in the case of a heat shield panel that is allowed to expand thermally), the basic criteria are even easier to apply. Under this condition no corrections need be made for any effects resulting from induced inplane stress. Thus no correction is needed for induced inplane stress resulting from flight loading, differential pressure, or differential temperature.

5 Special Considerations

Previous sections have presented criteria for the design of panels that will be free of flutter even though subjected to environments and conditions that are known to affect flutter boundaries. This section presents further guidance and assistance in accomplishing the final design in certain areas that cannot be as clearly defined. These areas include safety factors, panels recommended for closer study, weight saving, and use of testing as a design tool.

5.1 Factors of Safety

The criteria presented in section 3 include a certain degree of conservatism, as a result of encompassing some scatter in basic test data (see, for example, fig. 4 of ref. 1). Consequently, the design thickness obtained from using the criteria is expected to be slightly greater than required for a given set of designing conditions. Inasmuch as the amount of such conservatism cannot be defined, the design thickness obtained from section 3 is considered as the "neutral" value to which additional margins against flutter must be added. This subsection discusses panel flutter margins, and presents some guidelines that will be useful in establishing a design philosophy.

Factors of safety are imposed to provide assurance of design integrity in spite of uncertainties in basic theory, as well as the possibility of unexpected and/or underestimated environmental conditions. Panel flutter, being a relatively new discipline, is not as well understood as the classical lifting surface flutter. Furthermore, a greater number of parameters significantly affect panel flutter boundaries and some of these are difficult to assess prior to flight. The aerospace designer is always faced with the problem of trading off weight against mission objectives and crew safety. In the case of panel flutter, the need for a rationale to assist in design decisions is clearly evident.

There are three basic considerations which must logically be accounted for in establishing a flutter margin philosophy, namely, the uncertainties involved, the consequences of a panel flutter, and the consequences of over-design. These are discussed below and are followed by a set of guidelines recommended for incorporating safety factors in panel design.

a. Uncertainties involved

The various factors that may cause uncertainties in determining flutter boundaries are as follows:

(1) *Accuracy of Analytical Predictions*—The ability of the basic analytical tools depends upon how well the mechanisms are understood and how well the mathematical idealizations describe the mechanisms.

(2) *Ability to Predict Values of the Parameters that Affect Panel Flutter*—The parameters can be separated into two basic groupings with a distinct line of demarcation between them. The first grouping contains those parameters whose values can be predicted with a high confidence level. These include the vehicle Mach-altitude flight envelope and the panel material properties, length, width, thickness, sweep, and curvature. The other grouping, well separated from the first, contains those parameters whose values are more nebulous and more difficult to predict. These include parameters such as induced inplane loads, differential pressure, differential temperature, angle of attack, boundary layer, as well as any remaining parameters discussed in section 3.

b. Consequences of panel flutter

The consequences of panel flutter encompass a very wide spectrum and are listed below in the order of increasing severity:

(1) **No Deleterious Effects**—Experience indicates that some panels may flutter for prolonged periods of time without adverse effects.

(2) **Undesirable Noise Only**—Some panels on flight vehicles may flutter and be bothersome only because of the noise generated by the flutter.

(3) **Fatigue Cracks Develop, Requiring Panel Replacement**—Panel flutter amplitude and time duration may combine to cause fatigue damage; this normally requires panel replacement, repair, or modification.

(4) **Panel Fails in Flight—No Significant Influence on Mission or Flight Safety**—Failure may occur on a panel serving only a minor functional role; its loss does not result in subsequent damage to other important vehicle comments.

(5) **Panel Failure in Flight Jeopardizes Mission and Flight Safety**—Failure may occur on panel serving a major functional role. Or, failure of an otherwise insignificant panel may result in subsequent damage to some other important vehicle component.

c. Consequences of overdesign

Overdesign adds unnecessary weight thus imposing unwarranted performance penalties on the vehicle. Certainly the failure of some panels on a vehicle can have serious consequences, and panel integrity would be the overriding consideration from a flight safety standpoint. However, the temptation to make the same kind of trade-offs and to use the same safety factors for all panels would cause intolerable performance penalties, and should be avoided.

d. Recommended safety factors

It is now necessary to incorporate the previous basic considerations into a workable set of design guidelines. Obviously all panels on a vehicle will not be considered safety-of-flight critical; likewise, all panels will not be considered noncritical. In a similar sense, the condition of a panel during flight can be estimated more reliably in some cases than in others. Therefore, a rationale is required that assigns different safety factors to the different panels and the foregoing considerations suggest that a workable set of guidelines may be set up in a matrix format with the rows representing the degree of uncertainty of the panel condition and the columns representing weight/ safety tradeoffs. This format was employed in the preparation of table II, where recommended panel flutter safety factors are presented.

In using table II, the designer multiplies the thickness determined from the criteria of section 3 by an appropriate factor to obtain a specified design thickness. The table has purposely been made flexible enough to encompass varying depths of preliminary investigation which the designer might wish to employ during various phases of vehicle design. The minimal depth (Baseline Design Criteria only) might be employed in the early advanced design phase where time limitations permit only cursory studies. In the detailed design phase the designer will probe more extensively into the problem and will employ the overall criteria to a much greater extent (Baseline Criteria, plus all applicable corrections and careful assessment of the parameters involved). In addition to these extremes, intermediate depths of investigations are included. The bases for selection of the numerical values assigned for the safety factors are discussed in the following paragraphs.

The factors 3.75 and 2.25 at the upper right of table II are the maximum recommended safety factors obtained by accounting for uncertainties in all the parameters that affect flutter boundaries beyond baseline design. The "worst case" to be guarded against in practice depends on the length-to-width ratio. When $\ell/w < 1$, a worst case may be caused for example by a combination of buckling and flow angularity; buckling, without sweep requires that the baseline panel thickness be doubled (see fig. 10). The maximum thickness correction factor due to sweep for a panel of very low ℓ/w (i.e., $\ell/w \to 0$) is 1.65 and occurs for $\Lambda = 45°$ (see fig. 7). Inasmuch as safety of flight is involved, a velocity margin of 20 percent is provided by applying an additional factor 1.13 to the thickness. Therefore, the thickness multiplier $2 \times 1.65 \times 1.13 \cong 3.75$ is used for the case $\ell/w < 1$ when no knowledge is assumed for any parameters other than flight conditions and baseline panel properties. The flow angularity correction becomes 1.0 when $\ell/w \geq 1.0$ (see fig. 7); thus the corresponding thickness multiplier for $\ell/w \geq 1$ is $2.0 \times 1.13 \cong 2.25$.

TABLE II.—RECOMMENDED PANEL FLUTTER SAFETY FACTORS

Multiply thickness (t_B or t_C) determined by Criteria of section 3 by appropriate factor at right below to obtain recommended design thickness (t_D).	TRADE OFF	
	Weight ◄──────► Safety of Flight	
	CONSIDERATIONS	
CRITERIA THICKNESS SPECIFIED BY:	Non-critical (Excessive weight penalties override minor consequences of panel flutter.)	Critical (Serious consequences of panel failures override weight penalties.)
1. Baseline Design Criteria only.	1.70 ($\ell/w < 1$)	3.75 ($\ell/w < 1$)
2. Baseline Design Criteria plus use of sweep correction.	1.30 ($\ell/w \geq 1$)	2.25 ($\ell/w \geq 1$)
3. Baseline Design Criteria plus use of both sweep and curvature corrections.	1.30	2.25
*4. Baseline Design Criteria plus use of all corrections from section 3. Requires careful assessment of all parameters involved.	1.30	2.25
	1.00	**1.25

DECREASING UNCERTAINTIES ↓

*The corrected thickness t_C obtained from the complete criteria of section 3 cannot exceed twice the baseline value t_B (see section 3, part 3).

**The design thickness t_D for this case need not exceed 3.75 t_B for $\ell/w < 1$ or 2.25 t_B for $\ell/w \geq 1$.

NOTE: The safety factors presented herein are not to be construed as specification requirements. The use in design of safety factors other than required by formal specifications should be requested through the procuring agency.

The factors 1.70 (for $\ell/w < 1$) and 1.30 (for $\ell/w \geq 1$) at the upper left were obtained by using approximately 25 percent of the thickness margins used for the most conservative case discussed in the preceding paragraph. It is felt justified to dismiss the possibility that a worst combination of conditions would prevail and inasmuch as the panel is noncritical, the justification reflects a tradeoff in accepting the remote possibility of minor panel flutter incidences in order to avoid excessive weight penalties.

The factor 1.00 at the lower left represents the opposite extreme from the most conservative factor (3.75). It assumes full use of the criteria and the consequences of panel flutter would be minor.

The factor 1.25 at the lower right is based on a velocity margin of 40 percent instead of the 20 percent velocity margin used for other critical cases. This is based on the premise that careful assessment of all parameters involved does not necessarily insure that the assessed values are the same as the actual values encountered in flight and may result in a worse actual environment than the predicted environment. The other critical cases (20 percent velocity margin) have already assumed the worst possible environment.

The other factors shown in table II are natural extensions of the factors established for line 1 and they fall between the extremes at the corners of the matrix.

All of the factors shown in table II are believed to be consistent with the present state-of-the-art and the various tradeoffs which must be realistically included in panel design.

NOTE: The safety factors presented herein are not to be construed as specification requirements. The use in design of safety factors other than required by formal specifications should be requested through the procuring agency.

5.2 Panels Recommended for Closer Study

Panels that are not designed to carry static or maneuvering loads are often made very thin to preserve weight; as a consequence, such panels are found to be the source of many noise problems and fatigue failures. Therefore, it is recommended that all non-structural panels receive close scrutiny.

Some panels may be designed initially in anticipation of some inflight stabilizing condition (such as pressurization or tension stress). The possibility of a temporary or permanent change in the anticipated condition should be considered in initial design.

Built-up panels are usually sufficiently stiff in bending that they only need cursory investigations. Therefore, the single thickness panel should receive most of the designer's attention.

Although sufficient data were not available to define a criterion for boundary layer in this report, some designers believe that aft fuselage panels are not susceptible to flutter because of the thicker boundary layer. It is hoped that further research will soon clarify the problem of boundary layer.

5.3 Some Minimum Weight Configurations

The following weight savings ideas may be employed to advantage:

(a) Less thickness is required to preclude flutter if the panel is incorporated into the design with the short side in the streamwise direction rather than the long side (see fig. 22).

(b) Stiffeners or corrugations running streamwise will result in a lighter structure to prevent panel flutter (see fig. 23).
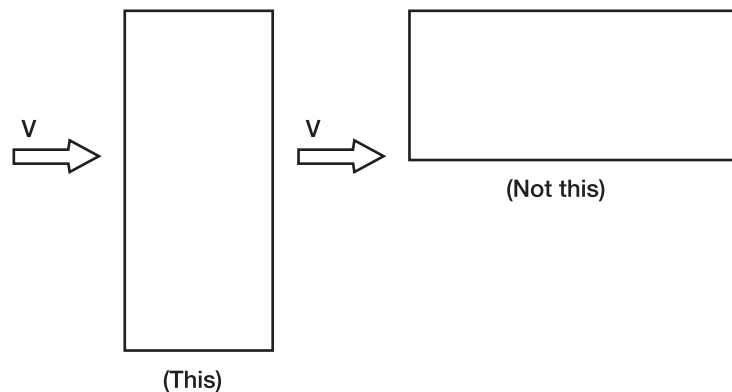
Figure 22.—Orientation of a rectangular panel for minimum weight.
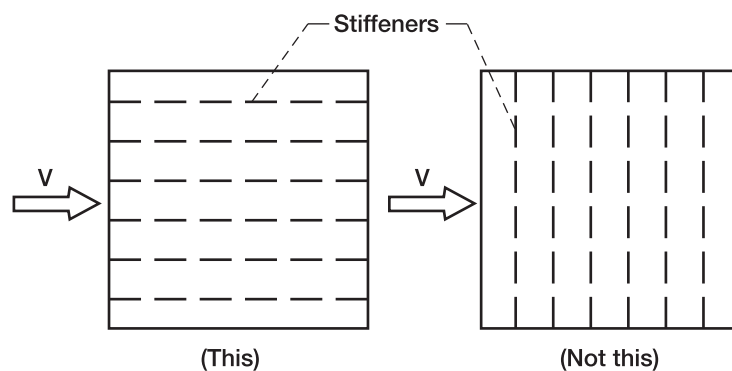
Figure 23.—Orientation of stiffeners to obtain higher flutter speed.

5.4 The Role of Testing in Panel Design

Testing should be used to verify panel integrity when a design is not covered by existing criteria or as justification for specifying lesser thicknesses than those specified by the criteria.

Panel flutter is caused by an intricate interaction between structural and aerodynamic forces. Furthermore the panel dynamics, and hence flutter speeds, may be influenced by flight conditions and vehicle loads; therefore a careful assessment of the extent to which actual service conditions can be simulated in the laboratory is the first step toward defining a meaningful test program. Air loads, thermal stresses, Mach number, and panel geometry, for example, may all combine to influence the minimum flutter speed.

Vibration tests and wind tunnel tests are of primary interest here and their uses are discussed in the following paragraphs:

(a) Vibration tests

A large portion of the uncertainty in panel flutter analysis can be traced directly to structural causes; that is, the structural analysis is inadequate to accurately predict panel dynamics. Therefore, the structural features that determine panel dynamics can be conveniently checked by a direct measurement of the panel natural frequencies. A panel test fixture that incorporates as many parameters as are deemed necessary can be employed (1) to check the accuracy of the theory used or (2) to obtain natural frequencies (and possibly mode shapes) for use in flutter analysis. The vibration test may provide sufficient confidence that design may proceed without further tests; if not, a wind tunnel test may be required.

(b) Wind tunnel tests

A wind tunnel test provides the closest simulation of flight conditions that can be attained on the ground and therefore also provides the greatest assurance of design integrity. The cost may be very large, however, and the usefulness of the test is directly related to the degree of flight simulation that is attained. The designer will consider scaling, choice of wind tunnel, type of fixture, measurement of parameters, and related problems. Mach number cannot be scaled so that the flight Mach numbers of concern must be duplicated in the wind tunnel. Aerodynamic heating can be induced artificially as can inplane stresses and differential pressure. In many respects the formulation of a good wind tunnel test program poses problems as formidable as the prototype design itself. However, the results of the test should provide a very high level of confidence in the final design.

6 Sample Designs and Evaluation of Criteria

This concluding section deals with application of the criteria to panel design problems and is divided into two parts. The first part traces the step-by-step design of two hypothetical panels for a particular flight trajectory. The second part applies the criteria to two actual instances of panel flutter and the results are compared with the fixes that were made to correct the flutter conditions.

6.1 Panel Design Problems

The use of the thickness correction curves presented in section 3 will be demonstrated with two hypothetical design problems. The flight path of the vehicle is shown in figure 5 where a maximum value of $q/f(M)$ is obtained at sea level for M = 1.15. In the sample design problems that follow, the panels will be assumed to have zero angle of attack so that corrections for local flow conditions will not be included.

(a) Find the thickness required to prevent flutter of the aluminum panels, shown in figure 24, which is representative of a panel on a wing or stabilator yawed to the free stream flow.

ℓ = 10 in.
w = 20 in.
E = 10.3×10⁶ lb/in²
Λ = 30°
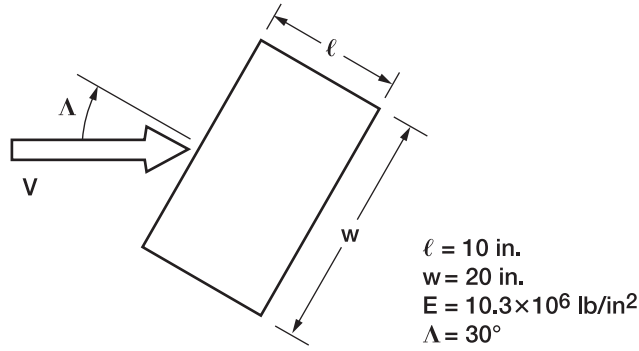
Figure 24.—Panel configuration for sample design number 1.

Using figure 5 with a $\dfrac{\ell}{w}$ of 1/2 yields a value of

$$E\left(\frac{t_B}{\ell}\right)^3 = 1.92$$

from which the "baseline" thickness is determined as

$$t_B = \ell^3 \sqrt{\frac{1.92}{E}} = 0.057 \text{ in.}$$

(It should be noted that E is Young's modulus in lb/in² in the above equation)

The required thickness, t_R, is obtained by multiplying t_B by the thickness correction factor for yaw, t_Λ/t_B. The value of t_Λ/t_B determined from figure 7 is 1.24 which results in a t_R of

$$t_R = \frac{t_\Lambda}{t_B} t_B = (1.24)(0.057) = 0.071 \text{ in.}$$

(b) Assuming a curved steel panel orientated with the flow as shown in figure 25, find the panel design thickness for a noncritical installation. Using the value of $E\left(\dfrac{t_B}{\ell}\right)^3$ of 1.92 obtained from sample problem (a) results in a "baseline" panel thickness of

$$t_B = \ell^3 \sqrt{\left[\frac{1.92}{E}\right]} = 0.040 \text{ in.}$$

The curvature parameter $N = \dfrac{h_o}{t_B}$ is computed from

$$N = \frac{h_o}{t_B} = \frac{R - \sqrt{R^2 - \left(\frac{w}{2}\right)^2}}{t_B} = R\left(1 - \cos\frac{\theta}{2}\right)$$

which gives a value of $N = 12.5$ for this case.
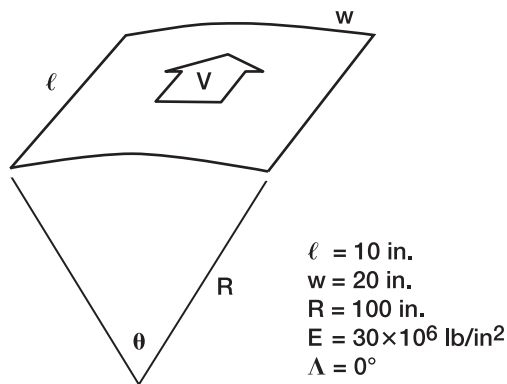
Figure 25.—Panel configuration for sample design number 2.

ℓ = 10 in.
w = 20 in.
R = 100 in.
E = 30×10^6 lb/in^2
Λ = 0°

Using figure 6, the thickness correction factor for curvature $\left(\dfrac{t_N}{t_B} = 0.95\right)$ is obtained. By using the noncritical safety factor 1.30 obtained from item 3 of table II, the design thickness of the panel is determined from

$$t_D = (0.95)(1.30)(0.040) = 0.0495 \text{ in.}$$

In the above design problems it should be noted that additional thickness correction factors would have to be included to account for the effect of inplane stress, differential pressure, cavity, edge conditions, or local flow conditions.

6.2 Evaluation of Design Criteria

Two cases of panel flutter that have occurred on different supersonic aircraft are studied here; the available data for these cases is used in the design criteria of section 3 to arrive at recommended thicknesses which are then compared with actual "fixes" that were made to alleviate the flutter problems.

(a) First case, flat panel

Location—Side fuselage, vicinity of cockpit
Symptoms—Noise and fatigue cracks
Panel Length—6.50 in.
Length-to-width ratio—approx. 0.32
Young's Modulus—10×10^6 psi
Skin thickness—0.032 in.
Most severe flutter conditions—$M = 1.25$
$h = 8k$ ft
$[q/f(M)]_{cr}$—approx. 3,400 p.s.f. (from fig. 5)

$E\left(\dfrac{t_B}{\ell}\right)^3 = 1.6$ psi (from fig. 5)

$$t_B = \left(\frac{1.6}{10^7}\right)^{1/3} \ell = 0.0054\ell$$

$t_B = 0.035$ inch

In this case there is neither sweep ($\Lambda = 0$) nor curvature ($N = 0$), and the panel is judged to be noncritical. Therefore the safety factor 1.30 from line 3 of table II is judged to be applicable and yields a design thickness

$$t_D = 1.30\,(0.035)$$
$$= 0.045\,\text{in}$$

(The flutter problem with this case was apparently solved by increasing the panel thickness from 0.032 to 0.050 in.)

(b) Second case, curved panel

Location—Upper fuselage, vicinity of cockpit
Symptom—Noise
Panel Length—11.25 in.
ℓ/w—0.55

Young's Modulus—10×10^6 psi
Skin thickness—0.03 inch
Flight condition at flutter—$M = 1.2$
$$h = 20\text{k ft.}$$
$\left[q/f(M)\right]_{cr} = 2000$ p.s.f.

$$E\left(\frac{t_B}{\ell}\right)^3 = 0.9$$

$$t_B = \left(\frac{0.9}{10^7}\right)^{1/3} \ell = 0.0045\ell = 0.05 \text{ in.}$$

Curvature $- N = \dfrac{h_o}{t_B} = 10.4$

$t_N/t_B = 0.98$ (fig. 6)
Safety factor—1.30 (noncritical panel)
$t_D = 0.98\,(1.30)\,0.05 = 0.064$ in.

(The "fix" in this case was made by adding a 0.03 in. doubler panel thus raising the total thickness to 0.06 in.)

The two cases cited above are based on very limited amounts of data and serve only to indicate how the criteria predictions compare with actual flutter experiences. The results show that the criteria give thicknesses that are in reasonable agreement with the actual thickness modifications that were made to alleviate the flutter problems. If the criteria had been available and applied in the manner indicated, the panels would presumably have been flutter-free.

References

1. Lemley, C.E.: Design Criteria for the Prediction and Prevention of Panel Flutter. Volume 2—Background and Review of State of the Art Final Report, AFFDL−TR−67−140−VOL−2, 1968. Available from the Air Force Flight Dynamics Laboratory.
2. Hess, Robert W.: Preliminary Results of an Experimental Study of the Effects of Compressive Stress on Panel Flutter. NASA LWP−177, 1966.
3. Minzner, R.A.; Champion, K.S.W.; and Pond, H.L.: The ARDC Model Atmosphere. AFCRC TN−59−267, Air Force Surveys in Geophysics, no. 115, 1959.
4. Kordes, Eldon E.; Tuovila, Weimer J.; and Guy, Lawrence D.: Flutter Research on Skin Panels. NASA TN−D−451, 1960.
5. Dugundji, J.: Theoretical Considerations of Panel Flutter at High Supersonic Mach Numbers. MIT ASRL−TR−134−1, 1965.
6. Olsen, J.J.: Local Aerodynamic Parameters for Supersonic and Hypersonic Flutter Analyses. AFFDL−TR−65−183, 1965.

Bibliography

Durvasula, S.: Flutter of Simply Supported Parallelogrammic, Flat Panels in Supersonic Flow. AIAA Paper 66−474, 1966.

Aeroelastic Model Theory[*]

Raymond L.Bisplinghoff, Holt Ashley, and Robert L. Halfman
Massachusetts Institute of Technology
Cambridge, Massachusetts 02139-4307

1.0 Introduction

Experimental investigations in the field of aeroelasticity have served two major purposes. They have been the guiding influence necessary to the development of useful theory and they have produced solutions to immediate practical problems in the large areas where existing theory is not yet dependable. Particularly in dealing with flutter, the testing of wind-tunnel models with properly scaled mass and stiffness properties has often been more rewarding than equivalent efforts using analytical techniques or even full-scale airplanes. In the course of this experimentation many new and valuable methods and techniques have been developed and have been transmitted only by word of mouth and by published paper. In order to provide a more adequate source of information, a presentation of the basic concepts of model theory is presented herein.

An intelligent approach to the design and use of models requires a thorough comprehension of model theory, which is the subject of this monograph. Appendix A describes the nomenclature, and appendix B discusses the dynamic equilibrium of the unrestrained elastic airplane. Appendix C discusses the twisting of a two-dimensional wing. The equations of equilibrium for a swept wing are presented in appendix D, followed by a presentation of classical two-degree-of-freedom flutter in appendix E.

2.0 Dimensional Concepts

Model theory, whether applied to airplanes or chemical processes, must be based on a clear understanding of the concept of dimensions and a familiarity with the principles of dimensional analysis. For this reason we shall start with a review of basic properties of scientific systems of measurement. Fundamentally, the need for a "dimension" arises when it is desired to measure some physical quantity. Thus the measurement of a distance requires the concept of length. Similarly, the measurement of velocity requires the concept of time as well as length. Of course, measurement of a distance requires an explicit rule by which numbers are associated with distances. A moment's reflection will reveal that the rule in common use states that the measure of a given distance is the number of times a unit length can be fitted into that distance. In a similar manner, the measure of a period of time requires the use of a unit time interval. As a consequence, the measure of a distance depends on the size of the unit length which is employed, in the manner that the measure is inversely proportional to unit size. This characteristic of the usual systems of measurement leads to the important result that the ratio of the measures of two distances is quite independent of the size of the length unit which is used to measure them. For instance, the aspect ratio of a lifting surface does not depend on whether inches or meters are used to measure the span and chord. All systems of measurement in scientific use have this characteristic, which is fundamental to the concepts of dimensional analysis.

In the process of measuring physical quantities it soon becomes evident that there are two types. The first and simplest type is made up of quantities each of which can easily be measured directly in units of its own kind. The second type is made up of quantities which are derived from quantities of the first type according to some rule of combination. In a problem involving a certain set of physical quantities all of the quantities can be derived from a small number of quantities of the first type, which are then called *primary* quantities. The remaining quantities are called *secondary* quantities. For example, in the problems of static structures all of the secondary quantities such as bending moment and modulus of elasticity can be derived from the primary quantities, force and length. In mechanics, mass, length, and time are conveniently chosen as the primary quantities, whereas in compressible aerodynamics and thermodynamics, temperature must often be added as a fourth primary quantity. It should be

---

[*]This material was taken from several sections of "Aeroelasticity" by Raymond L. Bisplinghoff, Holt Ashley, and Robert L. Halfman, Addison-Wesley, 1955 (ref. 1) and was arranged by the NASA Aeroelasticity Handbook editor as appears here. Used with permission.

noted that there is no fundamental reason why certain quantities must always be chosen as primary quantities, but rather it is the system of measurement which has been adopted which makes it convenient to call some quantities primary and others secondary.

An important restriction which must be embodied in the rules of combination for the derivation of secondary from primary quantities results from the previously mentioned characteristic of the usual scientific systems of measurement, that the ratio of the measures in two instances of a physical quantity, whether primary or secondary, is independent of the sizes of the units of the primary quantities. Thus the ratio of the measures of two velocities is the same whether the units are consistently miles and hours or feet and seconds. Bridgman (ref. 2) shows that this restriction limits the manner in which the measures of a secondary quantity can be derived from measures P_1, P_2, $\cdots$, P_m of the appropriate set of m primary quantities to the form

$$S = CP_1^{d_1} P_2^{d_2} P_3^{d_3} \cdots P_m^{d_m},$$ (1)

where C is a pure number. Thus every secondary quantity is expressible as a number multiplied by positive or negative powers of the measures of the primary quantities. The exponent d_k is called the "dimension" of the secondary quantity in the primary quantity P_k and is an integer for the usual sets of primary quantities.

To formulate some examples in the familiar field of mechanics, we arbitrarily (and customarily) choose mass, length, and time as the primary quantities and give their measures the symbols M, L, and T, respectively. Then the measure of a force is expressible as $CM^1L^1T^{-2}$. Similarly, the measure of a density is CM^1L^{-3}, of pressure is $CM^1L^{-1}T^{-2}$, and of velocity is CL^1T^{-1}. If the units in the force expression are pounds, slugs, feet, and seconds, or dynes, grams, centimeters, and seconds, the constant C has a value of unity. The other physical quantities of density, pressure, and velocity, unlike force, do not have special names for their commonly used units but use instead the names of other quantities. Thus the unit of density is written in terms of the primary quantities, slugs and feet, that is, slugs/feet^3. Pressure is usually written in terms of a secondary and a primary quantity, pounds/feet^2. In both cases the constant C has, of course, the value unity. In the case of velocity there is a less common unit, the knot, for which the constant C is not unity unless length is measured in nautical miles and time in hours.

It is important to realize that the form of the expression for the measure of a force,

$$F = CM^1L^1T^{-2},$$ (2)

is in general use primarily because of the practical importance of Newton's Second Law, which states that the mass of a body times its acceleration is proportional to the applied force. There is no fundamental reason why Newton's Law of Gravitation could not have determined the dimensions of force. This law states that the force of attraction between two masses is proportional to the product of the masses divided by the square of the distance between them. Thus the measure of the force could be written

$$F = CM^2L^{-2}.$$ (3)

Clearly, these two formulations of the secondary quantity, force, are incompatible and must not be used simultaneously. Consistent use of the first formulation requires that the Law of Gravitation be written as

$$F = \gamma \frac{m_1 m_2}{r^2},$$ (4)

where γ has the dimensional form $M^{-1}L^3T^{-2}$ and is the universal gravitational constant. A consistent (but less customary) use of the second formulation would require that the Second Law be written as

$$F = \beta m \frac{d^2 s}{dt^2},$$ (5)

where β might be called the "universal inertial constant" and would have the dimensional form $M^1 L^{-3} T^2$. In this text, the first and more usual formulation based on Newton's Second Law will be employed. Nevertheless, it is important to recognize the existence of dimensional constants, such as the gravitational constant, the speed of light, and the gas constant, and not to confuse them with the pure number C, which depends only on the unit sizes.

3.0 Equations of Motion

In order to describe a physical situation in terms of a mathematical equation, one or more physical principles must be applied. Typical of these principles in both mechanics and aerodynamics are Newton's Laws and the principle of conservation of matter. Application of appropriate principles to a given situation results in one or more equations containing the pertinent physical quantities as arguments, and these may be primary quantities, secondary quantities, or dimensional constants (which have the same form as secondary quantities). An equation derived in the foregoing manner, if it includes the necessary dimensional constants, will be essentially independent of changes in size of the units of the primary quantities. Such a change in primary unit size will simply change each term in the equation by the same factor because each term has the same dimensions. In other words, since the physical situation is not altered by changes in size of the primary units, an equation which completely describes the physical situation should likewise be independent of the primary unit size. Such an equation is called a "complete equation" and is the only kind considered in this book.

The only instance in which changing the size of a primary unit does not alter the coefficient of each term in a complete equation is when the terms are each dimensionless in that particular primary quantity. For example, the equation for the unaccelerated motion of a particle,

$$x = x_0 + v_0 t , \tag{6}$$

is not altered if the primary quantity, time, is measured in hours rather than seconds. In fact, dividing the equation by x_0 conveniently makes each term dimensionless in both primary quantities, time and length. Thus the dimensionless form,

$$\frac{x}{x_0} = 1 + \frac{v_0 t}{x_0} , \tag{7}$$

is completely independent of unit size. Furthermore, the apparent complexity of the equation is seen to be reduced in the dimensionless form in that only two dimensionless variables, (x/x_0) and $(v_0 t/x_0)$, need be considered, rather than the four original physical quantities x, x_0, v_0, and t.

This idea of writing complete equations in dimensionless form with fewer arguments has been generalized by Buckingham (ref. 3) and explicitly demonstrated by Bridgman (ref. 2). It is summarized in the "Π Theorem," which states that if a physical situation can be represented by means of a complete equation,

$$\psi(S_1, S_2, S_3, S_4, \cdots, S_n) = 0 \tag{8}$$

(where the n arguments include all the primary quantities, secondary quantities, and dimensional constants which must be considered in the problem), the equation can be written in the form

$$\phi(\Pi_1, \Pi_2, \Pi_3, \Pi_4, \cdots, \Pi_{n-m}) = 0 , \tag{9}$$

in which Π_1, Π_2, $\cdots$, Π_{n-m} are the ($n-m$) independent products of the arguments S_1, $\cdots$, S_n, which are dimensionless in the m primary quantities. The form of these dimensionless Π's can be found by a formal procedure (ref. 2) but can usually be constructed by inspection and the application of common sense. Typical Π's in general use are aspect ratio, reduced frequency, Mach number, and Reynolds number.

In model theory the advantages of using dimensionless variables are twofold. First, the problem is conveniently expressed in terms of the minimum number of variables. Secondly, since the dimensionless equation of motion is completely unaffected by scale effects (that is, changes in the size of the primary units) the values of the dimensionless variables must be the same for both the original problem and its model. This idea will be applied in detail in the following sections of this chapter.

4.0 Vibration Model Similarity Laws

As a first example of model theory, consider the problem of determining by the use of a conveniently small model the natural frequencies and mode shapes of a *cantilever tapered wing with a concentrated mass at its tip*. As shown in figure 1, the wing is of semispan l with tip weight M_T. It fits into the class of structures adequately described by simple beam theory and has a running mass $m(y)$, a varying area moment of inertia $I(y)$, and a deflection $w(y,t)$.

The problem of designing a suitable model of this wing will be attacked in the fashion suggested by the previous section. Thus, the governing equation of motion will be studied to ascertain the parameters which must enter the problem. These parameters will be formed into a suitable set of dimensionless parameters so that the equation of motion can be written in a dimensionless form involving the minimum number of variables. Since this equation is not affected in any way by changes in the size of the primary units, it applies equally well to the full-scale wing and to any model which is designed to simulate the full-scale wing. It shows directly the dimensionless parameters which must be built into the model so that the model will produce the same dimensionless answers as would be obtained from tests on the full-scale wing.

The actual scale factors to be used in the design of the model are found by considering the practical limitations imposed on the model. These may be allowable model size, methods of model fabrication, or perhaps available instrumentation and apparatus. If all of the dimensionless parameters appear independently in the equation of motion, the number of separate design limitations which can be imposed on the model is equal to the number of scale factors to be determined, that is, the number of primary quantities involved in the problem. In the simpler problems, one or more pairs of dimensionless parameters may appear only in a fixed combination. In these cases, additional design limitations may be imposed.

Following this plan of attack, then, the first step is to write the applicable equation of motion,

$$\left[EI(y)\, w''(y,t) \right]'' + m(y)\, \ddot{w}(y,t) = 0 \tag{10}$$

with appropriate boundary conditions at $y = 0$ and at $y = l$ to account for the cantilever root mounting and the effect of the concentrated tip mass M_T. This equation can be separated into two total differential equations,

$$\ddot{T} + \omega^2 T = 0 , \tag{11}$$

$$\left(EI(y)\, W''(y) \right)'' - \omega^2 m(y)\, W(y) = 0 \tag{12}$$

where the mode shapes $W(y)$ and frequencies ω which we seek are solutions of equation (12).
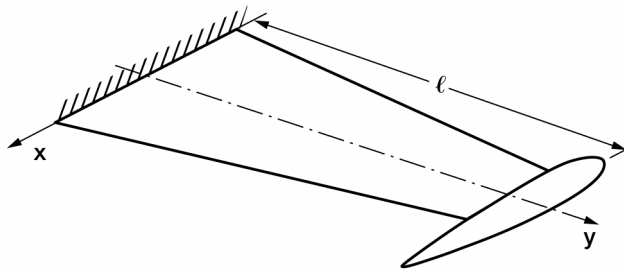
Figure 1.—Cantilever tapered wing with tip mass.

The dimensions of each of the parameters in this equation can be expressed in terms of the set of primary quantities mass, length, and time (M, L, and T). Before doing this, however, it should be noted that some of the parameters involve two concepts; they involve a variation with y as well as the idea of dimensional magnitude. The use of a notation which separates these concepts makes the coming steps more readily understandable and will be accomplished in the following manner. Let

$$m(y) = m_{root} m_N(y),$$ (13)

where m_{root} is the dimensional magnitude of the running mass at the root station and $m_N(y)$ is the variation of running mass along the wing normalized to have a value of unity at the root station. Thus $m_N(y)$ represents the mass distribution independent of the actual magnitude of the running mass at any station. It is, of course, a dimensionless quantity. Similarly, let

$$W(y) = W_{tip} \phi(y),$$ (14)

$$I(y) = I_{root} I_N(y).$$ (15)

The equation of motion now becomes

$$\left[EI_{root} \, I_N(y) \, \phi''(y) \right]'' - \omega^2 m_{root} \, m_N(y) \, \phi(y) = 0.$$ (16)

The dimensions of the parameters are

$$
\begin{aligned}
&y, l \sim L, \quad E \sim ML^{-1}T^{-2}, \quad I_{root} \sim L^4, \\
&\omega \sim T^{-1}, \quad m_{root} \sim ML^{-1}, \quad M_T \sim M, \\
&I_N(y), \quad \phi(y), \quad m_N(y) \sim \text{dimensionless}.
\end{aligned}
$$ (17)

These can be combined into the dimensionless set

$$\frac{y}{l}, \quad \frac{I_{root}}{l^4}, \quad \frac{M_T}{m_{root} l}, \quad \frac{\omega^2 m_{root}}{E}, \quad I_N(y), \quad \phi(y), \quad m_N(y).$$ (18)

As predicted by the Π Theorem, the dimensionless parameters (18) are three less in number than the dimensional parameters (17) and form a complete set because any other dimensionless parameters formed from the same dimensional set (17) can also be constructed from combinations of the dimensionless parameters in the complete set (18).

The dimensionless form of the equation of motion can be now written as

$$\left[I_N\!\left(\frac{y}{l}\right) \phi''\!\left(\frac{y}{l}\right) \right]'' - \left[\frac{l^4 \omega^2 m_{root}}{EI_{root}} \right] m_N\!\left(\frac{y}{l}\right) \phi\!\left(\frac{y}{l}\right) = 0$$ (19)

with appropriate boundary conditions at $y/l = 0$ and at $y/l = 1$ which involve M_T/m_{root} as well as parameters in the above equation. Here the primes denote differentiation with respect to y/l rather than y. It is apparent from the form of the equation that the parameters $\omega^2 m_{root}/E$ and I_{root}/l^4 do not appear independently in this problem but only in the combination $\omega^2 l^4 m_{root}/EI_{root}$.

The desired mode shapes and natural frequencies, in their dimensionless form $\phi(y/l)$ and $\omega^2 l^4 m_{root}/EI_{root}$ apparently can be obtained from any model with the correct area moment of inertia distribution $I_N(y/l)$, with the correct running mass distribution $m_N(y/l)$, and with the correct proportion of mass concentrated at the tip.

To obtain the dimensional properties to be designed into the model, the independent limitations which determine the three scale factors must be examined. Assuming that the model size is limited for practical and economic reasons to $\frac{1}{10}$ of the wing size, the length scale factor can be written

$$\frac{L_m}{L_w} = \frac{1}{10}. \tag{20}$$

Assuming also that the measuring equipment which is available is best suited to the frequency range above that expected of the wing vibrations (full-scale), the model should be designed to have frequencies perhaps three times those of the wing; that is,

$$\frac{T_m}{T_w} = \frac{1}{3}. \tag{21}$$

The third design limitation may be that the model must have a metal structure so that the internal damping is of the same order as for the full-scale wing. Thus the ratio of moduli of elasticity is determined by choice of material. If steel is used in the model, and aluminum alloy in the wing,

$$\frac{E_m}{E_w} = \frac{3}{1} = \frac{\left(ML^{-1}T^{-2}\right)_m}{\left(ML^{-1}T^{-2}\right)_w}. \tag{22}$$

Solving for the scale factor in the third primary quantity,

$$\frac{M_m}{M_w} = \frac{3}{1}\frac{L_m}{L_w}\left(\frac{T_m}{T_w}\right)^2 = \frac{1}{30}. \tag{23}$$

From these three scale factors in the primary quantities mass, length, and time, the model size of all the necessary dimensional quantities which appear in the equation of motion (19) can be determined. For instance, the tip weight on the model can be found from

$$\left(M_T\right)_m = \frac{1}{30}\left(M_T\right)_w, \tag{24}$$

and the reference value of the running mass becomes

$$\left(m_{root}\right)_m = \frac{1}{30}\left(\frac{1}{10}\right)^{-1}\left(m_{root}\right)_w = \frac{1}{3}\left(m_{root}\right)_w. \tag{25}$$

The area moment of inertia becomes

$$\left(I_{root}\right)_m = \frac{1}{10^4}\left(I_{root}\right)_w. \tag{26}$$

When the sizes of all these model properties have been computed they may be used to determine all other model properties which do not specifically appear in equation (19). It is not ordinarily correct to calculate these latter quantities by scaling them down according to the scale factors for mass, length, and time.

For example, we cannot conclude that the maximum stresses in the model for a scaled deflection in the first natural mode can be found by applying the appropriate scale factors to the full-scale stresses. The maximum stress at a given cross section depends not only on the local value of the bending moment and area moment of inertia but

also on the distance between the neutral axis and the outermost fiber. Although the first two quantities will be properly scaled, the last quantity depends, for instance, on the cross-sectional shape chosen for the model structure. There is no reason why this shape must be exactly the same as on the full-scale structure; the model cross section need only have the correct area moment of inertia to produce the desired frequencies and mode shapes. On most aeroelastic models the structural properties are actually obtained with the use of somewhat inefficient but easily fabricated structures which bear but slight resemblance to the full-scale structure.

Thus the model may be constructed of steel with $\frac{1}{10}$ the semispan, $\frac{1}{30}$ the total mass, and with the same distributions of mass and stiffness as the full-scale wing. The model frequencies will then be three times those of the wing in the corresponding modes of vibration, and the model mode shapes $\phi(y/l)$ will be identical with those of the wing. Of course, if the limitations on the model design were different from those assumed above, the scale factors would have been different.[1] The measured frequencies, when converted to full scale, would have been exactly the same.

As a second example of model theory, we shall consider a more generalized vibration problem written in terms of an integral equation rather than the differential equation used above. Suppose that we desire to build a vibration model of a *complete unrestrained airplane* in order to determine its many mode shapes and frequencies of vibration.

A complete equation describing the vibration of the airplane of figure 2 is derived in appendix B as

$$\omega^2 \iint_S G(x,y;\xi,\eta)\, W(\xi,\eta)\, \rho(\xi,\eta) d\xi\, d\eta = W(x,y), \tag{27}$$

where the $W(x,y)$ are the natural mode shapes, the ω's are the natural frequencies, $\rho(x,y)$ is the two-dimensional mass distribution, and

$$G(x,y;\xi,\eta) = C(x,y;\xi,\eta) - \iint_S C(r,s;\xi,\eta)\left[\frac{1}{M} + \frac{ys}{I_x} + \frac{xr}{I_y}\right]\rho(r,s) dr\, ds . \tag{28}$$
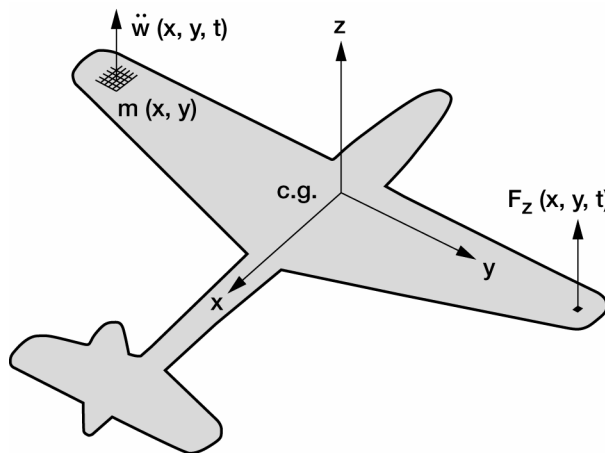
Figure 2.—Unrestrained elastic airplane.

---

[1]In this example, as mentioned earlier, the two dimensionless ratios I_{root}/l^4 and $\omega^2 m_{root}/E$ do not appear independently but only in the combination $\omega^2 l^4 m_{root}/EI_{root}$. As a result of this unusual situation, only the combined parameter must be simulated; a fourth independent limitation may be applied. For instance, if the scale factor for I_{root} is chosen different from 10^4, and if the scale factor for m_{root} differs in the same ratio from 3, the value of $\omega^2 l^4 m_{root}/EI_{root}$ will be unchanged. This modification also requires a change in the scale factor for M_T in order to leave unchanged $M_T/m_{root}l$.

In equation (28), $C(x,y;\xi,\eta)$ is the two-dimensional flexibility influence function and M, I_y, and I_x are the mass properties of the rigid airplane. The area of integration S can be characterized by the semispan l. As in the previous problem, some of the variables involve both the concept of a distribution over the plan of the airplane and a dimensional magnitude. To separate these concepts, let

$$\rho(x,y)=\rho_0\,\rho_N(x,y), \tag{29}$$

where $\rho_N(x,y)$ is normalized to have the value unity at the station $x=0$, $y=0$. Similarly, let

$$C(x,y;\xi,\eta)=C_{tip}C_N(x,y;\xi,\eta), \tag{30}$$

where C_{tip} is the value of C at $x=\xi=0$, $y=\eta=l$. The mode shape is expressed in terms of a normalized mode shape by

$$W(x,y)=W_{tip}\phi(x,y) \tag{31}$$

In order to cast the integral equation into dimensionless form, the dimensions of each parameter must first be written in terms of the three primary quantities mass, length, and time. Thus,

$$
\begin{aligned}
&\omega \sim T^{-1}, && \rho_0 \sim ML^{-2} && \left.\begin{matrix} x,y \\ \xi,\eta \\ r,s,b \end{matrix}\right\} \sim L, \\
&C_{tip} \sim M^{-1}T^2 && W_{tip} \sim L \\
&M \sim M && I_y, I_x \sim ML^2
\end{aligned}
$$
$$\rho_N(x,y),\quad C_N(x,y;\xi,\eta),\quad \phi(x,y) \sim \text{dimensionless} \tag{32}$$

A convenient set of dimensionless ratios can easily be constructed from these parameters. According to the Π Theorem, there should be three-less independent dimensionless ratios than there are parameters listed above, since there are three primary quantities in this problem. The dimensionless parameters are

$$\omega^2 MC_{tip}, \; \frac{\rho_0 l^2}{M}, \; \frac{I_x}{Ml^2}, \; \frac{I_y}{Ml^2}, \; \frac{W_{tip}}{l}, \; \frac{x}{l}, \; \frac{y}{l}, \; \frac{\xi}{l}, \; \frac{\eta}{l}, \; \frac{r}{l}, \; \frac{s}{l}, \; \rho_N, \; C_N, \; \phi. \tag{33}$$

The integral equation can be written in the form

$$\left(\omega^2 MC_{tip}\right)\left(\frac{\rho_0 l^2}{M}\right)\iint_S \frac{G\left(\dfrac{x}{l},\dfrac{y}{l},\dfrac{\xi}{l},\dfrac{\eta}{l}\right)}{C_{tip}}\phi\left(\frac{\xi}{l},\frac{\eta}{l}\right)\rho_N\left(\frac{\xi}{l},\frac{\eta}{l}\right)d\left(\frac{\xi}{l}\right)d\left(\frac{\eta}{l}\right)=\phi\left(\frac{x}{l},\frac{y}{l}\right) \tag{34}$$

where

$$
\frac{G\left(\dfrac{x}{l},\dfrac{y}{l},\dfrac{\xi}{l},\dfrac{\eta}{l}\right)}{C_{tip}} = C_N\left(\frac{x}{l},\frac{y}{l};\frac{\xi}{l},\frac{\eta}{l}\right) - \iint_S C_N\left(\frac{r}{l},\frac{s}{l};\frac{\xi}{l},\frac{\eta}{l}\right)
$$
$$
\times\left[1+\left(\frac{Ml^2}{I_x}\right)\frac{y}{l}\frac{s}{l}+\left(\frac{Ml^2}{I_y}\right)\frac{x}{l}\frac{r}{l}\right]\left(\frac{\rho_0 l^2}{M}\right)\rho_N\left(\frac{r}{l},\frac{s}{l}\right)d\left(\frac{r}{l}\right)d\left(\frac{s}{l}\right) \tag{35}
$$

Thus any model which has the same mass distribution ρ_N (and thus the same values of $\rho_0 l^2/M$, I_y/Ml^2, I_x/Ml^2) and the same flexibility distribution C_N over the same geometry (dimensionless area of integration) will produce the same mode shapes ϕ and dimensionless frequencies $\omega^2 MC_{tip}$ as the full-scale airplane. The three scale factors which determine for the model the dimensional magnitudes of the mass and flexibility distributions $(\rho_0)_m$ and $(C_{tip})_m$ as well as model size are determined, as in the previous problem, by three independent design limitations imposed on the model. They may be expressed, for example, as a restriction on model size, a desire to simulate the flexibility of various components using a single metal spar of reasonable dimensions, or in numerous other ways.

5.0 Similarity Laws for Systems Under Steady Airloads

As a further example of model theory, we consider the problem of studying by means of a model the static elastic deformations of a lifting surface under its airload in incompressible flow.

The angle of twist of a *two-dimensional elastically supported* wing in an airstream of velocity U is derived in appendix C as

$$\theta = \frac{C^{\theta\theta}\left[(\partial C_L/\partial\alpha)e\alpha^r + C_{MAC}\,c\right]qS}{1 - C^{\theta\theta}(\partial C_L/\partial\alpha)qSe} \tag{36}$$

Since this is a problem in statics, we have only two primary quantities which may be chosen as force (F) and length (L). It is evident that the dimensions of the quantities in equation (36) are

$$C^{\theta\theta} \sim F^{-1}L^{-1}, \quad S \sim L^2, \quad e \sim L, \quad q \sim FL^{-2}, \quad c \sim L,$$

$$\theta, \quad \alpha^r, \quad \frac{\partial C_L}{\partial\alpha}, \quad C_{MAC} \sim \text{dimensionless.} \tag{37}$$

The independent dimensionless ratios which can be formed from these quantities are, by inspection,

$$C^{\theta\theta}qSc, \quad \frac{e}{c}, \quad \frac{c^2}{S}, \quad \theta, \quad \alpha^r, \quad \frac{\partial C_L}{\partial\alpha}, \quad C_{MAC} \tag{38}$$

or two less in number, as predicted by the Π Theorem. In terms of dimensionless parameters, equation (36) becomes

$$\theta = \frac{\left[(\partial C_L/\partial\alpha)(e/c)\alpha^r + C_{MAC}\right]\left(C^{\theta\theta}qSc\right)}{1 - (\partial C_L/\partial\alpha)\left(C^{\theta\theta}qSc\right)(e/c)} \tag{39}$$

We can see from this dimensionless equation that any model of this semirigid wing must present the same airfoil shape to the airstream (C_{MAC} and $\partial C_L/\partial\alpha$),[2] must have the same dimensionless location of the elastic axis

---

[2] It should be mentioned that to obtain the same kinds of aerodynamic reactions on the model as on the wing the Reynolds number $\rho Uc/\mu$ should be the same. On a small model in air this would require a high airstream velocity which might be impractical. Since Reynolds number effects are often of secondary importance, this restriction is usually modified to restrict the Reynolds number from being less than a certain minimum value.

(e/c), the same initial angle of attack (α^r), and the same ratio of aerodynamic to elastic forces ($C^{\theta\theta}qSc$). Since the parameter c^2/S does not actually appear in equation (39), its simulation is not required for this problem. The two scale factors are determined by two independent design limitations.

Proceeding now from this relatively simple example to the case of the airload distribution on a *slender swept and tapered flexible lifting surface*, it is assumed that the airplane is in a maneuver which imposes a given steady acceleration on the lifting surface. The applicable integral equation derived in appendix D is

$$\mathcal{a}\left[cc_l^e\right] = q\int_0^l \overline{C}(y,\eta)cc_l^e\,d\eta + \bar{f}(y) \tag{40}$$

where

$$\bar{f}(y) = q\int_0^l \overline{C}(y,\eta)cc_l^r\,d\eta + q\int_0^l C^{\theta\theta}(y,\eta)c_{mAC}c^2\,d\eta$$
$$- g\int_0^l\left[C^{\theta z}(y,\eta) + \int_0^l C^{\theta\theta}(y,\eta)d(\eta)\right]m\,N\,d\eta, \tag{41}$$

$$\overline{C}(y,\eta) = C^{\theta z}(y,\eta) + e(\eta)\,C^{\theta\theta}(y,\eta). \tag{42}$$

The operator $\mathcal{a}$ is the functional relation between incidence distribution and lift distribution, and its form depends on the type of aerodynamic theory which is used. The product mNg represents the running weight multiplied by the load factor in g's. $d(y)$ defines the position of the center of gravity at any section.

In order to separate the concepts of distribution and dimensional magnitude, it is helpful to define

$$C^{\theta z}(y,\eta) = C_{tip}^{\theta z}C_N^{\theta z}(y,\eta),\ c(y) = c_{tip}c_N(y),$$
$$C^{\theta\theta}(y,\eta) = C_{tip}^{\theta\theta}C_N^{\theta\theta}(y,\eta),\ e(y) = e_{tip}e_N(y),$$
$$m(y) = m_{tip}m_N(y),\ d(y) = d_{tip}d_N(y). \tag{43}$$

The dimensions of the parameters appearing in equations (40) and (43) are

$$C_{tip}^{\theta z} \sim F^{-1},\quad C_{tip}^{\theta\theta} \sim F^{-1}L^{-1},\quad \left.\begin{matrix} l,c_{tip} \\ y,\eta \\ d_{tip},e_{tip} \end{matrix}\right\} \sim L,$$

$$q \sim FL^{-2},\quad \left(gm_{tip}\right) \sim FL^{-1},$$

$$\mathcal{a} \sim L^{-1},$$

$$\left.\begin{matrix} c_l^e,\ c_l^r,\ c_{mAC},\ N,\ C_N^{\theta z},\ c_N, \\ m_N,\ C_N^{\theta\theta},\ e_N,\ d_N \end{matrix}\right\} \sim \text{dimensionless}. \tag{44}$$

These can be combined into the dimensionless set:

$$
qc_{tip}lC_{tip}^{\theta z}, \quad \frac{c_{tip}C_{tip}^{\theta\theta}}{C_{tip}^{\theta z}}, \quad \frac{gm_{tip}}{qc_{tip}}, \quad \frac{d_{tip}}{c_{tip}},
$$
$$
\frac{e_{tip}}{c_{tip}}, \quad \alpha \, c_{tip}, \quad \frac{y}{l}, \quad \frac{\eta}{l}, \quad \frac{c_{tip}}{l}, \tag{45}
$$

to which must be added the dimensionless quantities already listed. The equation thus becomes

$$
c_{tip}\alpha \left[c_N c_l^e \right] = \left(qc_{tip}lC_{tip}^{\theta z} \right) \int_0^1 \frac{\overline{C}}{C_{tip}^{\theta z}} c_N c_l^e \, d\!\left(\frac{\eta}{l}\right) + \bar{f}, \tag{46a}
$$

where

$$
\bar{f} = \left(qc_{tip}lC_{tip}^{\theta z} \right) \left\{ \int_0^1 \frac{\overline{C}}{C_{tip}^{\theta z}} c_N c_l^r \, d\!\left(\frac{\eta}{l}\right) + \left(\frac{c_{tip}C_{tip}^{\theta\theta}}{C_{tip}^{\theta z}} \right) \int_0^1 C_N^{\theta\theta} c_{mAC}\, c_N{}^2 \, d\!\left(\frac{\eta}{l}\right) \right.
$$
$$
\left. - \left(\frac{gm_{tip}}{qc_{tip}} \right) N \int_0^1 \left[C_N^{\theta z} + \left(\frac{d_{tip}}{c_{tip}} \right)\!\left(\frac{c_{tip}C_{tip}^{\theta\theta}}{C_{tip}^{\theta z}} \right) C_N^{\theta\theta} d_N \right] m_N \, d\!\left(\frac{\eta}{l}\right) \right\}, \tag{46b}
$$

$$
\frac{\overline{C}}{C_{tip}^{\theta z}} = C_N^{\theta z} + \left(\frac{e_{tip}}{c_{tip}} \right)\!\left(\frac{c_{tip}C_{tip}^{\theta\theta}}{C_{tip}^{\theta z}} \right) C_N^{\theta\theta}\, e_N. \tag{46c}
$$

Since N always appears in a product with gm_{tip}/qc_{tip}, these two parameters are not independent in this problem and can be combined to form a single parameter Ngm_{tip}/qc_{tip}.

In order to find the load distribution $c_N c_l^e$ for the full-scale wing, it is necessary to construct a model which has:

a.) The same aerodynamic shape as the full-scale wing. That is, the planform, airfoil section, and initial "rigid" twist must be the same to produce the same aerodynamic center distribution, moment coefficient distribution, and aerodynamic operator $c_{tip}\alpha$ (of course, parameters such as Mach number and Reynolds number may also be important).

b.) The same ratio of aerodynamic to elastic stiffness $qc_{tip}\, l\, C_{tip}^{\theta z}$.

c.) The same elastic stiffness distributions $C_N^{\theta z}$, $C_N^{\theta\theta}$, and e_N.

d.) The same ratio of inertial forces to aerodynamic forces Ngm_{tip}/qc_{tip}.

e.) The same mass distribution m_N and d_N.

f.) The same ratio of bending to torsional stiffness $C_{tip}^{\theta\theta} / C_{tip}^{\theta z}$.

g.) The same location of elastic axis and center of gravity e_{tip}/c_{tip} and d_{tip}/c_{tip}.

This model will then have exactly the same load distribution as well as elastic deformation shape as the full-scale wing.

The scale factors of force and length are again determined by limitations on model design. Since the model is probably to be built for a particular wind tunnel, the model size and thus length scale are determined by the test section size. The dynamic pressure for the model is determined by the wind-tunnel capabilities or perhaps by the type of model construction. In any case, only two independent limitations can be imposed, since all of the dimensionless parameters are independent.

6.0 Flutter Model Similarity Laws

As a first example of flutter model theory, we shall consider a *uniform straight cantilever wing of moderate aspect ratio* whose behavior can be adequately described by Theodorsen's typical section equations (see appendix E). After the assumption of simple harmonic motion at the circular frequency ω in both vertical motion and pitching, the equations have the form

$$
-m\omega^2 h_0 + K_h h_0 - S_\alpha \omega^2 \alpha_0 e^{i\phi} + \pi\rho b^2 \left(iU\omega\alpha_0 e^{i\phi} - \omega^2 h_0 + ba\omega^2 \alpha_0 e^{i\phi} \right)
$$
$$
+ 2\pi\rho UbC(k)\left[U\alpha_0 e^{i\phi} + i\omega h_0 + ib\left(\frac{1}{2}-a\right)\omega\alpha_0 e^{i\phi} \right] = 0,
$$
(47a)

$$
-S_\alpha \omega^2 h_0 - I_\alpha \omega^2 \alpha_0 e^{i\phi} + K_\alpha \alpha_0 e^{i\phi}
$$
$$
+ \pi\rho b^3 \left[i\left(\frac{1}{2}-a\right)U\omega\alpha_0 e^{i\phi} - \omega^2 b\left(\frac{1}{8}+a^2\right)\alpha_0 e^{i\phi} + a\omega^2 h_0 \right]
$$
$$
- 2\pi\rho b^2 U\left(\frac{1}{2}+a\right)C(k)\left[U\alpha_0 e^{i\phi} + i\omega h_0 + ib\left(\frac{1}{2}-a\right)\omega\alpha_0 e^{i\phi} \right] = 0.
$$
(47b)

The parameters which appear in the two equations of motion number thirteen and, in terms of the primary quantities mass, length, and time, have the dimensions

$$
h_0, b \sim L, \quad K_h \sim ML^{-1}T^{-2}, \quad K_\alpha \sim MLT^{-2},
$$
$$
\omega \sim T^{-1}, \quad S_\alpha \sim M, \quad \rho \sim ML^{-3},
$$
$$
m \sim ML^{-1}, \quad I_\alpha \sim ML, \quad U \sim LT^{-1}
$$
$$
\alpha_0, \phi, a \sim \text{dimensionless.}
$$
(48)

The reduced frequency k is not listed because it can be formed from ω, b, and U. A convenient set of dimensionless parameters can be formed as

$$
\frac{h_0}{b}, \quad \frac{\omega b}{U}(=k), \quad \frac{m}{\rho b^2}, \quad \sqrt{\frac{K_h/m}{K_\alpha/I_\alpha}}\left(=\frac{\omega_h}{\omega_\alpha}\right), \quad \frac{\omega}{\sqrt{K_\alpha/I_\alpha}}\left(=\frac{\omega}{\omega_\alpha}\right),
$$
$$
\frac{S_\alpha}{mb}(= x_\alpha), \quad \sqrt{\frac{I_\alpha}{mb^2}}(= r_\alpha), \quad \alpha_0, \quad \phi, \quad a,
$$
(49)

and are ten in number, as predicted by the Π Theorem. Rewriting equations (47) in terms of these dimensionless parameters, we obtain

$$-\frac{h_0}{b} + \left(\frac{\omega_h}{\omega_\alpha}\right)^2 \left(\frac{\omega_\alpha}{\omega}\right)^2 \frac{h_0}{b} - x_\alpha \alpha_0 e^{i\phi} + \frac{\pi\rho b^2}{m}\left(\frac{i}{k}\alpha_0 e^{i\phi} - \frac{h_0}{b} + a\alpha_0 e^{i\phi}\right)$$

$$+\frac{2\pi\rho b^2}{m}\frac{1}{k}C(k)\left[\frac{1}{k}\alpha_0 e^{i\phi} + i\frac{h_0}{b} + i\left(\frac{1}{2}-a\right)\alpha_0 e^{i\phi}\right] = 0, \tag{50a}$$

$$-x_\alpha \frac{h_0}{b} - r_\alpha{}^2 \alpha_0 e^{i\phi} + r_\alpha{}^2\left(\frac{\omega_\alpha}{\omega}\right)^2 \alpha_0 e^{i\phi}$$

$$+\frac{\pi\rho b^2}{m}\left[\frac{i}{k}\left(\frac{1}{2}-a\right)\alpha_0 e^{i\phi} - \left(\frac{1}{8}-a^2\right)\alpha_0 e^{i\phi} + a\frac{h_0}{b}\right] \tag{50b}$$

$$-\frac{2\pi\rho b^2}{m}\frac{1}{k}\left(\frac{1}{2}+a\right)C(k)\left[\frac{1}{k}\alpha_0 e^{i\phi} + i\frac{h_0}{b} + i\left(\frac{1}{2}-a\right)\alpha_0 e^{i\phi}\right] = 0.$$

Since the equations are homogeneous in h_0/b and α_0, the number of dimensionless ratios can he further reduced to nine by dividing through by α_0 to form an amplitude-ratio parameter $h_0/b\alpha_0$. Of course, the effect of the viscosity μ of the air was not included in the equations, nor were the speed of sound a_∞ and the ratio of specific heats γ. If these had been included, the number of original variables becomes 16 and the number of dimensionless variables 13, where the additional ones are Reynolds number $\rho U b/\mu$, Mach number U/a_∞, and γ.

Now that the equations for the wing motion are in a form which is independent of primary unit size, all other wings which have the same dimensionless properties under the same dimensionless flight conditions will give the same dimensionless answers. Thus any one of these wings can be considered to be a flutter model of the original wing.

The incompressible case. First we shall consider the simpler case of a wind-tunnel model where compressibility (and thus Mach number and γ) is presumed to have no effect. The quantities we seek are $\omega_F b/U_F$, ω_F/ω_α, $h_0/b\alpha_0$, and ϕ, where the subscript F refers to values at flutter. To obtain these quantities, the model must have the correct frequency ratio ω_h/ω_α, mass coupling x_α, elastic axis location a, radius of gyration r_α, mass ratio $m/\rho b^2$, external shape, and Reynolds number.

The number of independent limitations to which the model can be designed cannot exceed three because all of the dimensionless parameters are independent and there are only three primary quantities in the problem whose scale can be changed. The length scale factor between model and wing, L_m/L_w, is usually determined by the ratio of the allowable model span in the wind tunnel to the actual span. This length scale factor, through the dimensionless parameters x_α, a, and r_α, determines the dimensional chordwise location in the model of the center of gravity and elastic axis, as well as determining the model radius of gyration. In the incompressible testing being considered, the operating speed range of the tunnel or perhaps the type of model construction sets an upper limit on the airspeed range in which flutter must occur. If, for instance, the desired model flutter speed is in the neighborhood of 70 mph and the estimated flutter speed of the actual wing is 350 mph, a velocity scale factor U_m/U_w of $\frac{1}{5}$ is required. From this velocity scale factor and the previously determined length scale factor the scale factor of a second primary quantity, time, can be determined:

$$\frac{T_m}{T_w} = \frac{U_w}{U_m}\frac{L_m}{L_w}. \tag{51}$$

The scale factor of the final primary quantity, mass, usually is set by consideration of the air density to be employed in the wind tunnel. Thus, since the mass ratio $m/\pi\rho b^2$ must be the same for both model and wing,

$$\frac{m_m}{m_w} = \frac{\left(\pi\rho b^2\right)_m}{\left(\pi\rho b^2\right)_w} = \frac{\rho_m b_m^2}{\rho_w b_w^2}.$$

(52)

Since m is defined as wing mass per foot of span, the mass scale factor can be written from equation (54) as

$$\frac{M_m}{M_w} = \left(\frac{L_m}{L_w}\right)^3 \frac{\rho_m}{\rho_w},$$

(53)

where the length scale factor and the air density ratio are known. The quantity ρ_m refers to the density of the air in the wind-tunnel test section, whereas ρ_w refers to the density of the air at the flight altitude of the wing.

It is important to note that the Reynolds number of the model test in the wind tunnel will usually be much lower than that of the wing at flight altitude and there is little that can be done about it. The three limitations already imposed on the model test, those of size, speed, and air density, together with the known viscosity of the air in the test section, completely determine the model Reynolds number. Fortunately, the effect of changes of Reynolds number on the oscillatory air forces is relatively small, provided the Reynolds number is above about 4×10^5, and the values, particularly of flutter speed and frequency, are relatively insensitive to Reynolds number variations. The test conditions are customarily chosen to make the Reynolds number as high as conveniently possible but the full-scale value is seldom approached.

When the three basic scale ratios have been obtained, it is possible to determine all of the dimensional properties of the model. For example, choose an airplane which weighs 10,000 lb, has a 50-ft span, and an estimated 500 mph flutter speed. If the maximum-span model which can be accommodated in the test section is 5 ft,

$$\frac{L_m}{L_w} = \frac{1}{10}.$$

(54)

If model design limits testing to speeds of 70 mph, an appropriate velocity ratio is

$$\frac{U_m}{U_w} = \frac{1}{8},$$

(55)

and from equation (51)

$$\frac{T_m}{T_w} = \frac{8}{10}.$$

(56)

Thus the time scale of the model is almost the same as that of the airplane, and the corresponding natural frequencies will be almost the same. If the wind-tunnel density has a sea-level value, whereas flight altitude, full scale, is such that

$$\frac{\rho_w}{\rho_m} = 0.5,$$

(57)

then equation (53) determines the third and final basic scale factor as

$$\frac{M_m}{M_w} = \frac{1}{500}.$$ (58)

The weight of the model (the gravitational constant g is not scaled) is then 10,000/500 or 20 lb. Similarly,

$$\frac{m_m}{m_w} = \frac{M_m}{M_w}\frac{L_w}{L_m} = \frac{1}{50},$$ (59)

$$\frac{I_{\alpha m}}{I_{\alpha w}} = \frac{M_m}{M_w}\frac{L_m}{L_w} = \frac{1}{5000}.$$ (60)

To find the bending stiffness on the model which will give the correct effective K_h at the typical section, remembering that the wing properties in this example do not vary along the span,

$$\frac{(EI)_m}{(EI)_w} = \frac{M_m}{M_w}\left(\frac{L_m}{L_w}\right)^3\left(\frac{T_w}{T_m}\right)^2 = \frac{1}{320{,}000}.$$ (61)

As was pointed out in section 4, other model properties which do not appear in the equations of motion should be computed from those that do rather than by direct application of the scale factors.

When the results of the flutter tests on the model are known, equations (55) and (56) can be used for converting to the dimensional full-scale flutter speed and frequency.

The compressible case. If the assumption cannot be made that the fluid is incompressible, that is, that the velocity of sound is very high compared with velocities over the wing, then the two additional parameters, Mach number and γ, must be considered. To make a true flutter model of a high-speed lifting surface, it is necessary that these dimensionless quantities as well as those of the incompressible case must have the same values in the model tests as in full-scale flight. To have γ the same implies that model tests must also be in ordinary air rather than some other gas such as Freon-12. (However, if it is simply desired to compare experimental flutter points with those predicted by calculation from a theoretical basis, there is no reason why tests cannot be run in gases such as Freon-12. The effect of changes in γ, such as from air to Freon-12, will be of secondary importance, as illustrated by the absence of γ from the linearized supersonic unsteady air forces.)

Just as in the incompressible case, no more than three independent limitations can be imposed on the model, since all of the dimensionless parameters are independent and there are only three scale factors to be determined, M, L, and T. Once again, the model size is definitely limited by the test equipment to be used, whether the testing method involves rockets, bomb drops, or wind tunnels. Thus the length scale factor is quickly established, at least within close limits. A second stringent limitation involves the attainment of the desired Mach number range, which usually also determines the model flight velocity and air density.

In rocket tests or bomb drops, flight velocity is directly related to Mach number as a function of altitude (or, more correctly, temperature, which is itself a function of altitude). Thus at any altitude a given desired Mach number fixes the model velocity, and from it and the previously determined length scale factor, the time scale factor can be found. The chosen altitude fixes the air density and thus the mass scale factor because the dimensionless parameter $m/\rho b^2$ must be kept constant (eq. (53)).

In wind-tunnel tests, tunnel design considerations usually determine the air velocity and density which go with a given desired Mach number. These relationships may vary considerably from one tunnel to another. For example, a blow-down intermittent tunnel will have a higher test-section density than a suck-down intermittent tunnel because the stagnation pressure is considerably higher. The test-section speed of sound and thus velocity for a given Mach number is a function of stagnation or stilling chamber temperature, which, of course, varies with different tunnels.

In the compressible case, it is usually impossible to obtain full-scale Reynolds numbers, and it is unfortunate that we do not yet know for unsteady compressible flow the Reynolds number range in which we can test with confidence.

7.0 The Unrestrained Flutter Model

As a second example of flutter model theory, we consider the difficult case of a flutter model of a complete airplane simulating unrestrained straight level-flight. This lack of restraint of the "rigid-body freedoms" is desirable in the many cases when the flutter modes involve considerable "rigid-body motion" and when the flutter and rigid airplane dynamic stability frequencies are close together.

The equations of motion of an airplane unrestrained in pitch, roll, and vertical translation are derived in terms of normal modes. If the axis directions coincide with the airplane's principal axes, these equations can be extended to include all six rigid-body freedoms as well as the normal modes of vibration. These equations are

$$
\begin{aligned}
& M_1 \ddot{\xi}_1 = \Xi_1 \\
& \qquad \vdots \\
& M_6 \ddot{\xi}_6 = \Xi_6 \\
& M_7 \ddot{\xi}_7 + M_7 {\omega_7}^2 \xi_7 = \Xi_7 \\
& \qquad \vdots \\
& M_\infty \ddot{\xi}_\infty + M_\infty {\omega_\infty}^2 \xi_\infty = \Xi_\infty
\end{aligned}
\tag{62}
$$

where $\xi_1, \ldots, \xi_6$ are the perturbation amplitudes for the rigid-body modes, $M_1, \ldots, M_6$ are the total mass and principal moments of inertia of the airplane, and the normalized deformation modes ϕ and frequencies ω are solutions to equation (C17).

M_j and Ξ_j are the generalized mass and generalized force respectively and are defined by

$$
M_j = \iint_S \phi_j^2 (x, y) \rho(x, y)\, dx\, dy
$$
$$
\hspace{4cm} \left(j = 7, 8, \ldots \infty \right) \tag{63}
$$
$$
\Xi_j = \iint_S F_z (x, y, t) \phi_j (x, y)\, dx\, dy
$$

where $F_z (x,y,t)$ is the applied dynamic force per unit area.

The coefficients of the left sides of equations (64) involve the magnitude and distribution parameters describing the mass, stiffness, and geometric properties of the airplane. These are analogous to the parameters m, S_α, I_α, K_h, K_α, b, and a in the previous example. The generalized forces Ξ on the right sides of equations (62) are calculated as indicated in equation (63) and involve the external aerodynamic, gravitational, and propulsive system loadings. The coupling between these equations is quite extensive, in that each generalized force contains terms in many of the coordinates. If the coordinates $\xi_7, \ldots, \xi_\infty$ are set equal to zero in the rigid-body equations, they reduce identically to the familiar rigid airplane dynamic stability equations except for the use of the unconventional axis system.

If we examine the parameters which appear as coefficients in the generalized forces, we find the ordinary dynamic stability coefficients such as C_L, C_D, $C_{L\alpha}$, $C_{M\alpha}$, C_{Mq}, etc., which are purely aerodynamic in origin and are functions of airplane shape and attitude. We also find unsteady aerodynamic terms similar to those in the previous problem which are functions of airplane geometry, vibration mode shape, and reduced frequency. If compressibility

is important, the coefficients will involve Mach number and they are always to some extent functions of Reynolds number.

If care is used in writing those equations which involve balances between equilibrium forces and moments, we will find terms involving the airplane weight which we can write in terms of the total mass and the gravitational constant g, and terms involving the equilibrium propulsive force as well as its variations with altitude, airspeed, etc. We will find a moment balance for longitudinal trim between wing, tail, and fuselage contributions. These equilibrium or steady-state balance relations should not be canceled out of the airplane equations unless they can be similarly canceled out of the model equations.

Consider, for example, the terms involving airplane weight. These terms are balanced by lift terms which are a function of airplane attitude. In fact, it is the airplane weight under given flight conditions which determines the equilibrium attitude. The model must have the same attitude in order to have the same C_L and the other coefficients which depend on it (e.g., roll due to sideslip, x force due to speed change). Thus, for the model to fly at the correct equilibrium attitude, the gravitational force terms must be scaled in the same manner as the aerodynamic, inertial, and elastic force terms. Let us see if this can be done when the scale factors are determined by typical model test restrictions.

As in the previous example, we are dealing with a problem in dynamics and will use the primary quantities mass, length, and time. Since all of the dimensionless parameters appear independently in the equations, only three independent model design limitations can be applied. As before, the length scale factor is determined by the ratio of allowable model size to airplane size. The time scale factor is determined by combining the length scale with the ratio of allowable test speed to estimated flutter speed in the incompressible case. For compressibility simulation, the test and full-scale Mach numbers must be the same. In conjunction with the temperatures, this condition determines the velocity and thus the time scale for the compressible case. In both cases the mass scale is determined by the condition that model and airplane density ratio be the same.

The dimensionless parameter involving weight will appear as a ratio of weight to aerodynamic force, $mbg/\rho U^2 b^2$, if the usual procedure is used. (If it appears as a ratio of weight to inertial force or elastic force, it can be reduced to a ratio of weight to aerodynamic force by proper multiplication by other parameters such as $m/\rho b^2$ and $\omega b/U$.) To see if the weight, or gravitational force, is correctly scaled, note that the ratio of gravitational to aerodynamic force can be written as

$$\frac{mbg}{\rho U^2 b^2} = \frac{m}{\rho b^2} \cdot \frac{g}{U^2/b}. \tag{64}$$

The mass ratio $m/\rho b^2$ is already the same on both model and airplane; however, the ratio[3] $g/(U^2/b)$ may be entirely different. The gravitational constant g must be the same, but U^2/b is generally not the same on the model and the full-scale airplane. That is, the acceleration scale factor is not normally unity for a flutter model. To illustrate the range over which it can vary, Table I has been prepared, in which typical scale factors have been assumed for a small high-speed fighter and a large jet transport for both low-speed and high-speed flutter models. The last column can also be interpreted as the ratio of model weight to model lift at the attitude which produced equilibrium on the full-scale airplane. It is apparent that the low-speed fighter model is probably incapable of supporting its own weight at any attitude, whereas the high-speed version flies at a very small value of the lift coefficient. It is fortunate and useful that the models of large transports and bombers fly at the correct attitudes at least in the case where compressibility effects are not simulated, because the flutter of these large flexible airplanes is usually inextricably related to freedom in the rigid-body motions.

---

[3]This ratio is the inverse square of the Froude number, so familiar to naval architects in their studies of wave drag.

TABLE I

	L_w/L_m	U_w/U_m	Acceleration$_w$ /Acceleration$_m$
Fighter— Low-speed model	10	10	10
High-speed model	10	1	$\frac{1}{10}$
Transport—Low-speed model	25	5	1
High-speed model	25	1	$\frac{1}{25}$

The fact that gravitational force is not properly scaled for most flutter models is one of the major difficulties in testing models with rigid-body freedom. Either we must accept results obtained with a model flying at lift coefficients which are too high or too low, or the model support must provide a suitable supplementary vertical force.

The disproportionately high weights characteristic of many low-speed flutter models give rise to another difficulty whether or not body freedoms are simulated. If the model is supported at the fuselage, the wings will exhibit an inordinate amount of droop unless the wing structure is initially designed with the correct amount of "negative droop."

8.0 The Dynamic Stability Model

Because of the increasing importance of the effect of structural flexibility on airplane dynamic stability and automatic control, we will look at the possibility of designing aeroelastic models to aid in the solution of this problem. The governing equations are equations (62) which we wrote down for the unrestrained flutter model. The difference is simply one of emphasis. In the flutter model we are interested in a neutral dynamic stability condition in which the elastic modes are dominant. In the dynamic stability model we are interested in a subcritical dynamic behavior which is dominated by the rigid-body modes of motion. In the flutter model we often accept the simplification of suppressing those rigid-body modes which are unimportant to flutter. Similarly, the dynamic stability model can have a reduced degree of simulation of the less important elastic deflection modes without compromising the subcritical behavior under investigation.

Nevertheless, the model design problem in both cases is basically the same. There are only three scale factors and these are fixed by considerations of model size, speed, and relative mass. It is necessary to build into the model the correct magnitudes and distributions of mass, stiffness, and shape. There is the redundant restriction on model attitude or weight which is difficult to meet for low-speed models and impossible when compressibility is simulated, unless the model support mechanism is capable of providing a supplementary vertical force.

The designer of the dynamic stability model cannot escape this redundancy even in the case where vibration frequencies are high compared with dynamic stability frequencies, because mass and stiffness simulation are required to obtain correct vibration frequencies. The correct mass distribution is also needed to simulate inertial loadings on the structure due to essentially rigid-body motions, and the correct stiffness distribution is needed to ensure proper deflection shapes under the air and inertial loadings arising from the rigid-body motions.

Even in the extreme case of designing a completely rigid dynamic stability model the four redundant restrictions must be satisfied. This is a result of the necessity of scaling the model so that the scale factor is the same for all four types of forces which are important-aerodynamic, elastic, inertial, and gravitational.

There is another more promising approach to the use of elastic models in the dynamic stability problem. Up to this point we have discussed the use of an entire unrestrained airplane model in an airstream as an analog computer which indicates over-all degree of stability. It solves the entire set of equations. The other approach uses the model to determine the effect of elasticity on the individual coefficients of the basic rigid-body motion equations. This procedure is primarily applicable to airplanes for which the stability and elastic frequencies are well separated and is somewhat analogous to the use of rigid sinusoidally-forced models to check the aerodynamic coefficients of the flutter equations.

For the "steady-state" stability coefficients such as lift, side force, pitching moment, and yawing moment due to the angular displacement rather than its time derivatives, the model design problem is essentially that of section 5. For the coefficients associated with time derivatives of angular displacements the model design problem is still that of section 5 or this section without the weight restriction. The major difficulties are usually related to model support and testing techniques.

References

1. Bisplinghoff, Raymond L.; Ashley, Holt; and Halfman, Robert L.: Aeroelasticity. Addison-Wesley Publishing Company, Inc., 1955.
2. Bridgeman, P.W.: Dimensional Analysis. Revised ed., Yale University Press, New Haven, CT, 1931.
3. Buckingham, E.: On Physically Similar Systems; Illustrations of the Use of Dimensional Equations. Phys. Rev., vol. 4, issue 4, 1914, pp. 345–376.

Appendix A
Nomenclature

a nondimensional elastic axis location (see fig. E1)

b half chord (see fig. E1)

c chord (see fig. C1)

c_1 local lift coefficient

c_l^e local lift coefficient distribution resulting from elastic twist, $\theta(y)$

c_l^r local lift coefficient distribution resulting from rigid twist, $\alpha^r(y)$

$c_N(y)$ chord at any wing section normalized to unit at the tip

c_{tip} chord at wing tip

C pure number constant

$C(k)$ Theodorsen's function

$C(x,y;\xi,\eta)$ two dimensional flexibility influence function describing the deflection at x,y due to a unit force at ξ,η

C_L wing lift coefficient

C_{mAC} local moment coefficient about aerodynamic center

C_{MAC} wing pitching moment coefficient about the aerodynamic center

C_N nondimensional flexibility influence function normalized to unity at $x = \xi = 0$, $y = \eta = l$.

C_{tip} magnitude of flexibility influence function at $x = \xi = 0$, $y = \eta = l$.

$C^{\theta\theta}$ flexibility influence coefficient of coiled spring, equations (36) through (39) (see fig. C1)

$C^{\theta\theta}(y,\eta)$ angular deflection in the θ direction at y due to a unit torque in the θ direction at η

$C^{\theta z}(y,\eta)$ angular deflection in the θ direction at y due to a unit force in the z direction at η

$d(y)$ position of c.g. at any wing section (see fig. D2)

$d_N(y)$ position of c.g. at any wing section, normalized to unity at the tip

d_k dimension of secondary quantity in the primary quantity P_k, usually an integer

d_{tip} position of c.g. at wing tip

e location of elastic axis (see fig. C1)

$e_N(y)$ location of elastic axis at any wing section normalized to unity at the tip

e_{tip} location of elastic axis at wing tip

E	modulus of elasticity
F	force, secondary quantity
F_z	applied dynamic force per unit area (see eq. (63))
$G(x,y;\xi,\eta)$	influence function of unrestrained airplane
h	plunging degree of freedom (see fig. E1)
h_0	amplitude of plunging degree-of-freedom
i	unit imaginary number
I	area moment of inertia
$I_N(y)$	dimensionless variation of running moment of inertia along the wing normalized to unity at the root station
I_{root}	area moment of inertia at root
I_x	mass moment of inertia of rigid airplane about x-axis
I_y	mass moment of inertia of rigid airplane about y-axis
I_a	mass moment of inertia per unit span about axis $x = ba$
l	wing semi span
k	reduced frequency, $k = \omega b/U$
K_h	stiffness of bending spring (see fig. E1)
K_α	stiffness of torsion spring (see fig. E1)
L	length, primary quantity. Lift per unit span (running lift) positive in the z direction
L_h	lift due to plunging motion
L_α	lift due to pitching or torsional motion
$m, m(y)$	mass per unit span (running mass)
m_N	dimensionless variation of running mass along the wing normalized to unity at the root station
m_{root}	magnitude of running mass at wing root
M	mass, primary quantity. Also, mass of rigid airplane
M_h	moment due to plunging motion
M_j	generalized mass (see eq. (63))
M_T	concentrated tip mass
M_y	moment per unit span (running moment) positive for positive rotation about the spanwise y-axis along $x = ba$

M_α	moment due to pitching or torsional motion
n	total number of primary quantities, secondary quantities and dimensional constants in a complete equation
N	load factor, g's
P_k	primary quantity
p_U	static pressure on upper surface of airfoil
p_L	static pressure on lower surface of airfoil
q	dynamic pressure
Q_h	generalized force in the h coordinate
Q_α	generalized force in the α coordinate
r	dummy variable in coordinate x
r_α	dimensionless radius of gyration, $\sqrt{I_\alpha/mb^2}$
s	dummy variable in coordinate y
S	area of integration. Also, wing area
S_α	static mass moment per unit span about $x = ba$, positive when the center of gravity is aft, $= mbx_\alpha$
t	time
T	time, primary quantity. Also temporal part of lateral deflection $w(y,t)$
U	free stream velocity
v_0	initial velocity (see eqs. (6) and (7))
$w(y,t)$	lateral deflection in z coordinate, $w(y,t) = W(y)T(t)$
$W(y), W(x,y)$	mode shapes, (see $w(y,t)$)
W_{tip}	deflection at wing tip station
x	chordwise coordinate (see fig. 2), also displacement of particle (see eq. (6))
x_0	initial displacement (see eqs. (6) and (7))
x_α	dimensionless static unbalance, S_α/mb
y	spanwise coordinate (see fig. 2)
z	transverse coordinate (see fig. 2)
α	angle of attack
α^r	initial angle of attack
α_0	amplitude of torsional degree-of-freedom

β	universal inertial constant
γ	universal gravitational constant
η	dummy variable in coordinate y
θ	angle of twist of two dimensional wing section
ξ	dummy variable in coordinate x
μ	viscosity
Ξ_j	generalized force (see eq. (63))
$\rho(x,y)$	two-dimensional mass distribution
$\rho_N(x,y)$	two-dimensional mass distribution normalized to unity at $x = 0$, $y = 0$
ρ_0	magnitude of two-dimensional mass at $x = 0$, $y = 0$
ϕ	argument of $\bar{\alpha}_0$, angle by which α leads h if the time origin is chosen so as to make $\bar{h}_0$ real (see eq. (E17))
$\phi(y)$	mode shape normalized to unity at the wing tip
ω	circular frequency
ω_h	uncoupled natural torsional frequency, $\sqrt{K_h/m}$
ω_α	uncoupled natural torsional frequency, $\sqrt{K_\alpha/I_\alpha}$

Subscripts

m	model
w	wing (full scale)
$(\ )'$	differentiation with respect to y or y/l
$(\ )''$	second derivative with respect to y or y/l
$\ddot{(\ )}$	second derivative with respect to t
$\bar{(\ )}$	complex quantity

Appendix B
Dynamic Equilibrium of the Unrestrained Elastic Airplane

Practical problems in aeroelasticity usually involve aircraft in flight. It is necessary, therefore, to use as a basis for such problems equations of motion of the unrestrained airplane. In the most general development of these equations it must, of course, be recognized that the airplane is a three-dimensional elastic object completely free to translate and rotate in space. In the present discussion, however, it will be assumed that the airplane is compressed into a flat elastic plate, as illustrated by figure 2, and that, in addition to its elastic degrees of freedom, it is permitted small displacements in vertical translation, pitch, and roll. The elastic plate is assumed rigid in its own plane. Although some loss of generality is incurred by these assumptions, they permit a concise development of the equations of motion. These equations are applicable to a majority of the practical aeroelastic problems involving aircraft in flight.

(a) *Integral equation of free vibration.* The deformation of the elastic airplane assumed here can be treated conveniently in terms of a two-dimensional influence function and its associated integral equation. Let us assume reference axes oriented with respect to the airplane, as illustrated by figure 2. The origin of the axis system is located such that it remains at the center of gravity of the deformed airplane. In addition, the *xyz*-axes always remain in coincidence with the principal inertial axes of the deformed airplane. Since the airplane is vibrating freely, the *xyz*-axes can be considered fixed in space. The deformation is described by a function $w(x,y,t)$ which represents the displacement of the weaving elastic surface with respect to the fixed *xy* p1ane.

Four equations of motion are required. For equilibrium of total forces along the *z*-axis, in the absence of external forces,

$$\iint_S \ddot{w}(x,y,t)\rho(x,y)\,dx\,dy = 0 \tag{B1}$$

where the integration is over the surface area of the airplane. For moment equilibrium of free vibration about the *y*-axis,

$$\iint_S \ddot{w}(x,y,t)x\rho(x,y)\,dx\,dy = 0 \tag{B2}$$

and for moment equilibrium about the *x*-axis,

$$\iint_S \ddot{w}(x,y,t)y\rho(x,y)\,dx\,dy = 0 \tag{B3}$$

A fourth equation of equilibrium relating elastic forces and inertial forces is

$$w(x,y,t) - w(0,0,t) - x\frac{\partial w(0,0,t)}{\partial x} - y\frac{\partial w(0,0,t)}{\partial y} = -\iint_S C(x,y;\xi,\eta)\rho\ddot{w}\,d\xi\,d\eta, \tag{B4}$$

where $C(x,y;\xi,\eta)$ is the two-dimensional influence function describing the deflection at x,y due to a force at ξ,η.

Where $w(0,0,t)$ is the deflection and $\partial w(0,0,t)/\partial x$ and $\partial w(0,0,t)/\partial y$ are the slopes of the elastic surface at the point pierced by the *z*-axis.

Introducing as a solution

$$w(x,y,t) = W(x,y)T(t), \tag{B5}$$

the equations of motion become

$$\iint_S W(x,y)\rho(x,y)dx\,dy = 0 \tag{B6}$$

$$\iint_S W(x,y)x\rho(x,y)dx\,dy = 0 \tag{B7}$$

$$\iint_S W(x,y)y\rho(x,y)dx\,dy = 0 \tag{B8}$$

$$T\left\{W(x,y) - W(0,0) - x\frac{\partial W(0,0)}{\partial x} - y\frac{\partial W(0,0)}{\partial y}\right\} = -\ddot{T}\iint_S C(x,y;\xi,\eta)\rho(\xi,\eta)W(\xi,\eta)d\xi\,d\eta. \tag{B9}$$

Equation (B9) is separable and reduces to two separate equations, as follows:

$$\omega^2\iint_S C(x,y;\xi,\eta)W(\xi,\eta)\rho(\xi,\eta)d\xi\,d\eta = W(x,y) - W(0,0) - x\frac{\partial W(0,0)}{\partial x} - y\frac{\partial W(0,0)}{\partial y}, \tag{B10}$$

$$\ddot{T} + \omega^2 T = 0, \tag{B11}$$

where ω^2 is a separation constant which represents physically the frequencies of the natural vibration modes.

Equations (B6), (B7), (B8), and (B10) can be combined into a single equation in which the amplitude $W(0,0)$, $\partial W(0,0)/\partial x$ and $\partial W(0,0)/\partial y$ are eliminated (ref. B1) Multiplying both sides of equation (B10) by $\rho(x,y)$ and integrating over the surface of the airplane, we obtain

$$\omega^2\iint_S \rho(x,y)\iint_S C(x,y;\xi,\eta)W(\xi,\eta)\rho(\xi,\eta)d\xi\,d\eta\,dx\,dy = \iint_S W(x,y)\rho(x,y)dx\,dy$$
$$- W(0,0)\iint_S \rho(x,y)dx\,dy - \frac{\partial W(0,0)}{\partial x}\iint_S x\rho(x,y)dx\,dy - \frac{\partial W(0,0)}{\partial y}\iint_S y\rho(x,y)dx\,dy. \tag{B12}$$

We observe that the first integral on the right side is zero, by virtue of equation (B6). The third and fourth integrals on the right side are zero, since the origin of coordinates is, by definition, at the center of gravity. The remaining terms may be solved for $W(0,0)$ as follows:

$$W(0,0) = -\frac{\omega^2}{M}\iint_S \rho(x,y)\iint_S C(x,y;\xi,\eta)W(\xi,\eta)\rho(\xi,\eta)d\xi\,d\eta\,dx\,dy. \tag{B13}$$

When equation (B10) is multiplied by $x\rho(x,y)$ and integrated over the surface, we obtain

$$\omega^2\iint_S x\rho(x,y)\iint_S C(x,y;\xi,\eta)W(\xi,\eta)\rho(\xi,\eta)d\xi\,d\eta\,dx\,dy$$
$$= \iint_S W(x,y)x\rho(x,y)dx\,dy - W(0,0)\iint_S x\rho(x,y)dx\,dy$$
$$- \frac{\partial W(0,0)}{\partial x}\iint_S x^2\rho(x,y)dx\,dy - \frac{\partial W(0,0)}{\partial y}\iint_S xy\,\rho(x,y)dx\,dy. \tag{B14}$$

The first integral on the right side of equation (B14) is zero, according to equation (B7). The second integral is zero, since the origin of coordinates is at the center of gravity. The fourth integral is zero since the xz-plane is a plane of symmetry. Thus, the remaining terms in equation (B14) can be solved for

$$\frac{\partial W(0,0)}{\partial x} = -\frac{\omega^2}{I_y}\iint_S x\rho(x,y)\iint_S C(x,y;\xi,\eta)W(\xi,\eta)\rho(\xi,\eta)d\xi\,d\eta\,dx\,dy \tag{B15}$$

where

$$I_y = \iint_S x^2\rho(x,y)dx\,dy.$$

Finally, when equation (B10) is multiplied by $y\rho(x,y)$ and integrated over the surface, the result can be reduced in a similar manner to

$$\frac{\partial W(0,0)}{\partial y} = -\frac{\omega^2}{I_x}\iint_S y\rho(x,y)\iint_S C(x,y;\xi,\eta)W(\xi,\eta)\rho(\xi,\eta)d\xi\,d\eta\,dx\,dy \tag{B16}$$

where

$$I_x = \iint_S y^2\rho(x,y)\,dx\,dy.$$

When equations (B13), (B15), and (B16) are substituted into equation (B10) we obtain a homogeneous linear integral equation in $W(x,y)$ as follows:

$$\omega^2\iint_S G(x,y;\xi,\eta)W(\xi,\eta)\rho(\xi,\eta)d\xi\,d\eta = W(x,y), \tag{B17}$$

where

$$G(x,y;\xi,\eta) = C(x,y;\xi,\eta) - \iint_S C(r,s;\xi,\eta)\left[\frac{1}{m} + \frac{ys}{I_x} + \frac{xr}{I_y}\right]\rho(r,s)dr\,ds. \tag{B18}$$

$G(x,y;\xi,\eta)$ is the influence function of the unrestrained airplane, and it can be computed from equation (B18) if the elastic and inertial properties are known. Equation (B17) is satisfied by an infinite number of pairs of deformation mode shapes $W_j(x,y)$ and frequencies ω_j.

Reference

B1. Levy, S.: Computation of Influence Coefficients for Aircraft Structures With Discontinuities and Sweepback. J. Aero. Sci., vol. 14, no. 10, 1947, pp. 547–560.

Appendix C
Twisting of Simple Two-Dimensional Wing

Static aeroelastic problems are characterized by several simplifying features. By definition, time does not appear as an independent variable and, as a result, vibratory inertial forces are eliminated from the equilibrium equations. Aerodynamics forces can be based upon well-known steady flow results rather than the more complex unsteady flow theories.

Consider the behavior of a rigid, elastically restrained wing segment in two-dimensional flow as shown in figure C1, which pictures a rigid segment of airfoil. The wing has constant chord c and area S. Its twisting is opposed by a linear coiled spring attached at the elastic axis, which is located at a distance e behind the aerodynamic center. All angular deflections of the wing are assumed small. The total angle of attack, measured from the zero-lift attitude, is taken as the sum of an initial angle α^r and an elastic twist θ:

$$\alpha = \alpha^r + \theta \tag{C1}$$

The elastic twist is proportional to the torque about the elastic axis,

$$\theta = C^{\theta\theta} T \tag{C2}$$

where $C^{\theta\theta}$ is the flexibility influence coefficient of the coiled spring.

The total aerodynamic torque about the elastic axis is

$$T = \left(C_L e + C_{MAC} c \right) qS \tag{C3}$$

where

C_L	=	wing lift coefficient,
C_{MAC}	=	wing pitching moment coefficient about the aerodynamic center,
q	=	dynamic pressure,
S	=	area of rigid wing segment.
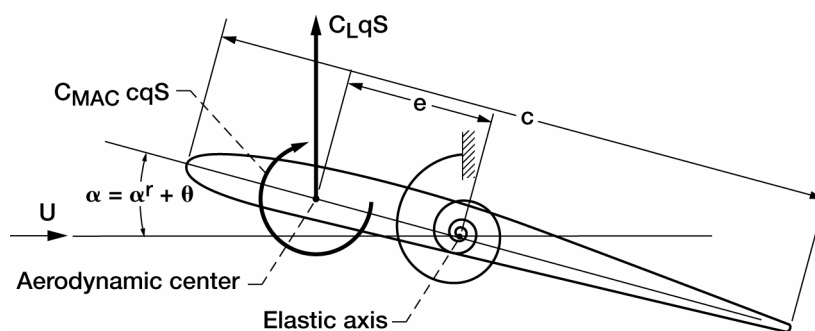
Figure C1.—Elastically supported rigid airfoil segment.

The total lift coefficient is related to the angle of attack measured from zero lift by

$$C_L = \frac{\partial C_L}{\partial \alpha}\left(\alpha^r + \theta\right) \tag{C4}$$

where $\partial C_L/\partial \alpha$ is the slope of the lift curve. The elastic twist of the wing can be computed by substituting eq. (C4) into eq. (C3) and combining the result with eq. (C2):

$$\theta = \frac{C^{\theta\theta}\left[(\partial C_L/\partial \alpha)e\alpha^r + C_{MAC}c\right]qS}{1 - C^{\theta\theta}(\partial C_L/\partial \alpha)qSe} \;. \tag{C5}$$

Appendix D
Integral Equation of Equilibrium of Swept Wing
of Arbitrary Planform and Stiffness

Consider the deformation of an elastic wing under the influence of a distributed normal load Z(x,y) as shown in figure D1. The deformation can be expressed by a single function w(x,y), defined by

$$w(x, y) = \iint_S C(x, y; \xi, \eta) Z(\xi, \eta) d\xi \, d\eta \tag{D1}$$

where C(x,y;ξ,η) is the two-dimensional influence function describing the deflection at x,y due to a unit force at ξ,η, and the integration is taken over the surface of the wing. In those cases where the wing is sufficiently slender so that chordwise segments of the wing parallel to the x-axis can be assumed rigid, the influence function can be written as follows:

$$C(x, y; \xi, \eta) = C^{zz}(y, \eta) - x C^{\theta z}(y, \eta) + \xi x C^{\theta\theta}(y, \eta) - \xi C^{z\theta}(y, \eta) \tag{D2}$$

where the influence functions are defined by C pq(y,η) = linear or angular deflection in the p-direction at y due to a unit force or torque in the q-direction at η.

The deflection can be expressed in the form
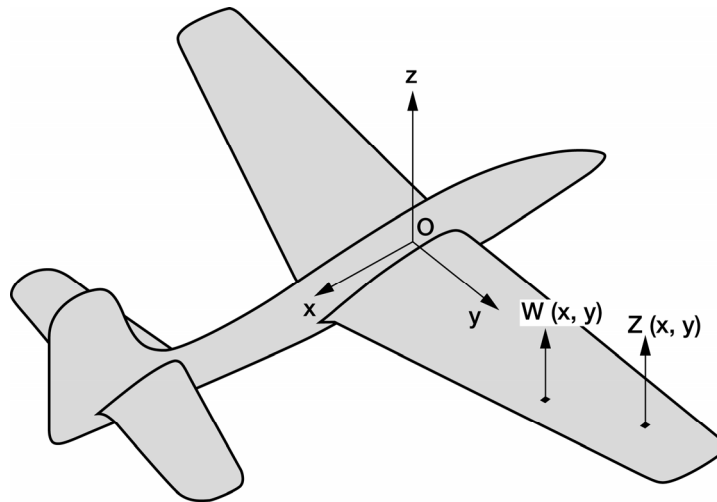
$$w(x, y) = w(y) - x \, \theta(y). \tag{D3}$$

Figure D1.—Airplane wing under distributed load, Z (x, y).

Substituting equations (D2) and (D3) into (D1), we obtain

$$w(y) = \int_0^1 C^{zz}(y,\eta)Z(\eta)d\eta + \int_0^1 C^{z\theta}(y,\eta)t(\eta)d\eta,$$ (D4)

$$\theta(y) = \int_0^1 C^{\theta z}(y,\eta)Z(\eta)d\eta + \int_0^1 C^{\theta\theta}(y,\eta)t(\eta)d\eta,$$ (D5)

where

$$Z(\eta) = \int_{chord} Z(\xi,\eta)d\xi,$$ (D6)

$$t(\eta) = -\int_{chord} \xi Z(\xi,\eta)d\xi.$$ (D7)

In deriving equations (D4) and (D5), the effects of chordwise drag loads on the wing have been neglected. Equations (D4) and (D5) apply in general to the case of unswept or swept wings with structural discontinuities. The principle elastic effects of sweep and structural discontinuities are to couple the bending and torsion actions. It should be observed that the assumption of rigidity along segments parallel to the x-axis becomes less valid with increasing angles of sweep. The error involved seems to be small for slender wings with angles of sweep up to about 45 degrees.

Consider again the integral equation of equilibrium, equation (D5), applying to a swept wing of arbitrary planform and stiffness, as illustrated by figure D2. We require the assumption that streamwise segments such as BC in figure D2 be essentially undeformable. Although this assumption implies a certain degree of slenderness, the wing may have any planform and stiffness properties consistent with it.

In applying equation (D5), the influence functions are defined such that the running torque $t(y)$ can be taken as the torque on each streamwise segment about an axis parallel to the y-axis. The reader may verify the location of the running torque $t(y)$ by referring to figure D2. Expressions for the running force $Z(y)$ and the running torque $t(y)$ which appear in equation (D5) are those given by

$$Z(y) = qc\,c_l - mNg$$ (D8)

and

$$t(y) = qec\,c_l + q\,c^2 c_{mAC} - mNgd$$ (D9)

respectively.

Substituting equations (D8) and (D9) into equation (D5) gives

$$\theta(y) = \int_0^1 C^{\theta z}(y,\eta)(qc\,c_l - mNg)d\eta + \int_0^1 C^{\theta\theta}(y,\eta)\left(qec\,c_l + q\,c^2 c_{mAC} - mNgd\right)d\eta.$$ (D10)

Substituting $c_l = c_l^r + c_l^e$ into equation (D10) and reducing yields

$$\theta(y) = q\int_0^1 \overline{C}(y,\eta)c\,c_l^e\,d\eta + \bar{f}(y),$$ (D11)
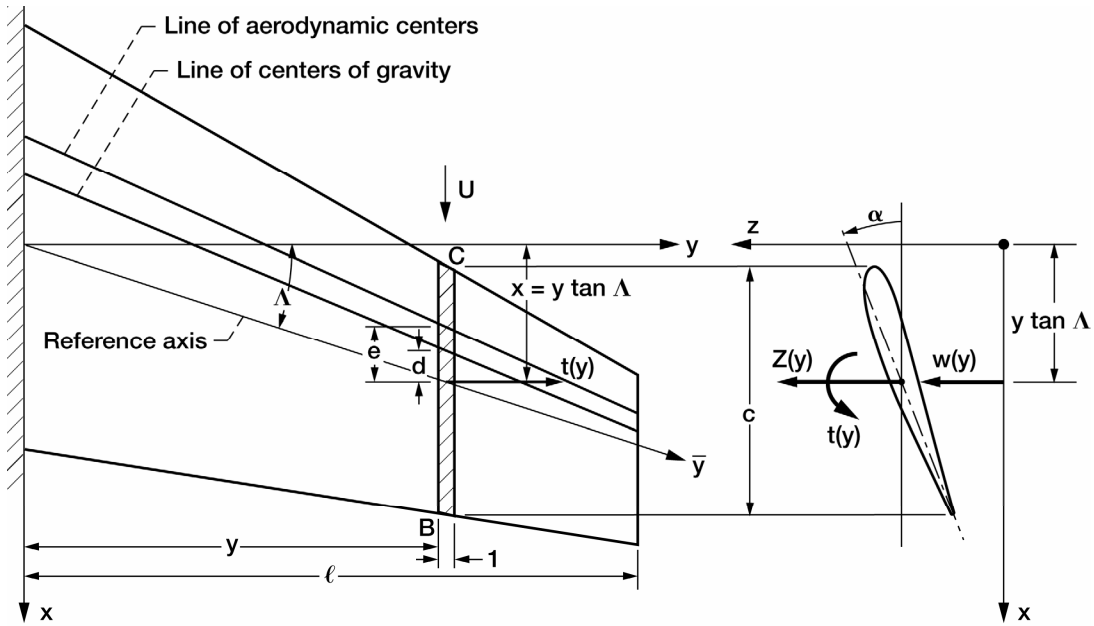
Figure D2.—Swept wing of arbitrary planform and stiffness.

where

$$\bar{f}(y) = q \int_0^1 \overline{C}(y,\eta) c\, c_l^r\, d\eta + q \int_0^1 C^{\theta\theta}(y,\eta) c_{mAC} c^2\, d\eta$$

$$- g \int_0^1 \left[C^{\theta z}(y,\eta) + C^{\theta\theta}(y,\eta) d(\eta) \right] mN\, d\eta, \tag{D12}$$

$$\overline{C}(y,\eta) = C^{\theta z}(y,\eta) + e(\eta) C^{\theta\theta}(y,\eta).$$

The quantities c_l^e and θ in equation (D11) are unknown, and all other quantities are regarded as known. The known quantities depend upon the physical properties of the wing and the type of maneuver under consideration. The nature of the influence functions $C^{\theta Z}(y,\eta)$ and $C^{\theta\theta}(y,\eta)$ depend upon the elastic properties of the particular wing under investigation.

When a functional relation between incidence distribution and lift distribution is introduced, equation (D11) can be used to compute the static aeroelastic behavior of a swept wing. This functional relation has the form

$$\theta(y) = \mathcal{a}\left[c\, c_l^e \right]. \tag{D13}$$

Appendix E
Flutter of a Simple System with Two Degrees of Freedom

Probably the most dangerous, although not the most frequently encountered, type of aircraft flutter results from coupling between the bending and torsional motions of a relatively large aspect-ratio wing and tail. A great deal of qualitative information can he obtained about the influence of various system parameters on this kind of flutter by studying the stability of the simple airfoil illustrated in figure E1, which shows the location of the coordinate system along with some quantities of primary aerodynamic interest. This airfoil is just the "representative section" of Theodorsen and Garrick (refs. E1 and E2), specialized for the bending and torsion degrees of freedom. These authors suggest, and subsequent experience has confirmed, that for purposes of flutter prediction it can be made to represent fairly well a straight wing of large span by giving it the geometric and inertial properties of the station three-quarters of the way from center line to wingtip.

Consider the system consisting of a spring supported rigid wing segment illustrated by figure E1. If the wing segment is permitted freedom to execute small vertical and angular displacements, the coordinates h and α shown by figure E1 are convenient generalized coordinates for describing the displacement configuration of the system. The wing displacement w, in terms of the generalized coordinates is

$$w = -h - x\alpha .$$

(E1)
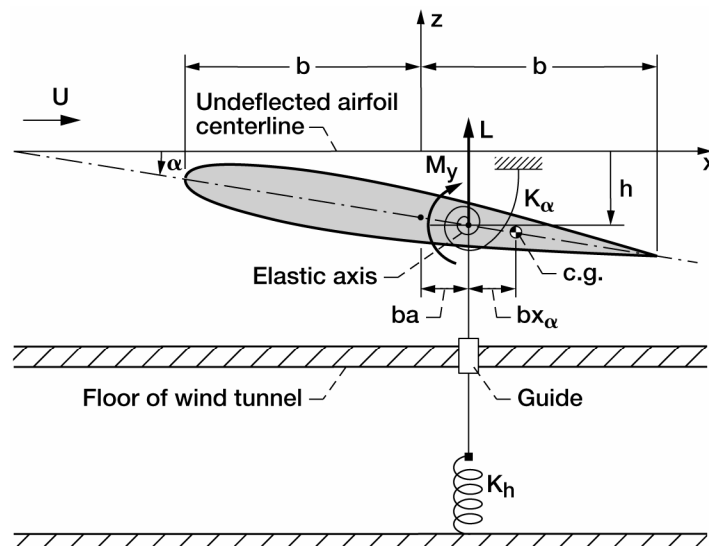

Figure E1.—Airfoil restrained from bending and torsional motion in an airstream by springs K_h and K_α, acting a distance ba aft of midchord. Also shown are lift L and pitching moment M_y about the axis of twist.

The kinetic energy of the wing segment is

$$T = \frac{1}{2} \int_{chord} \dot{w}^2 \, dm = \frac{1}{2} \int_{chord} \left(\dot{h} + x\dot{\alpha} \right)^2 dm \qquad \text{(E2)}$$

Integration of equation (E2) gives a quadratic function of the velocities $\dot{h}$ and $\dot{\alpha}$ as follows:

$$T = \frac{1}{2} m\dot{h}^2 + \frac{1}{2} I_\alpha \dot{\alpha}^2 + S_\alpha \dot{\alpha}\dot{h} \qquad \text{(E3)}$$

where

m = mass per unit span,
I_α = mass moment of inertia per unit span about the elastic axis ($x = ba$), and
S_α = $mb\,x_\alpha$ = static mass moment per unit span about the elastic axis ($x = ba$), positive when the center of gravity is aft.

If the stiffness of the bending and torsion springs are represented by K_h and K_α, respectively, the strain energy is given by

$$U = \frac{1}{2} K_h h^2 + \frac{1}{2} K_\alpha \alpha^2 \qquad \text{(E4)}$$

Lagrange's equations applied to this problem are

$$\frac{d}{dt}\left(\frac{\partial T}{\partial \dot{h}} \right) + \frac{\partial U}{\partial h} = 0, \quad \frac{d}{dt}\left(\frac{\partial T}{\partial \dot{\alpha}} \right) + \frac{\partial U}{\partial \alpha} = 0 \qquad \text{(E5)}$$

It should be observed that the terms $\partial T/\partial q_i$ do not appear in the above equations, since T is a function of the velocity terms only in the present example. Inserting equations (E3) and (E4) into equations (E5), the following equations of motion are obtained:

$$m\ddot{h} + S_\alpha \ddot{\alpha} + K_h h = 0, \quad S_\alpha \ddot{h} + I_\alpha \ddot{\alpha} + K_\alpha \alpha = 0 \qquad \text{(E6)}$$

It is sometimes convenient, particularly in flutter analysis, to write equations (E6) in terms of the frequencies of the uncoupled system. The system can be uncoupled by putting the inertial coupling terms, S_α, equal to zero. Thus,

$$m\ddot{h} + K_h h = 0, \quad I_\alpha \ddot{\alpha} + K_\alpha \alpha = 0 . \qquad \text{(E7)}$$

Inserting solutions

$$h = h_0 \sin(\omega_h t), \quad \alpha = \alpha_0 \sin(\omega_\alpha t), \qquad \text{(E8)}$$

we obtain the uncoupled natural frequencies in bending and torsion, ω_h and ω_α respectively:

$$\omega_h = \sqrt{\frac{K_h}{m}}, \quad \omega_\alpha = \sqrt{\frac{K_\alpha}{I_\alpha}} . \qquad \text{(E9)}$$

Solving equations (E9) for the spring constants in terms of the uncoupled natural frequencies and substituting the results into equations (E6), we obtain

$$m\ddot{h} + S_\alpha\ddot{\alpha} + m\omega_h^2 h = 0, \quad S_\alpha\ddot{h} + I_\alpha\ddot{\alpha} + I_\alpha\omega_\alpha^2\alpha = 0 . \tag{E10}$$

If the thin airfoil is subjected to a distribution of pressure difference $(p_U - p_L)$ because of the air flowing past, we must include generalized external forces in the equations of motion:

$$m\ddot{h} + S_\alpha\ddot{\alpha} + m\omega_h{}^2 h = Q_h, \tag{E11}$$

$$S_\alpha\ddot{h} + I_\alpha\ddot{\alpha} + I_\alpha\omega_\alpha{}^2\alpha = Q_\alpha. \tag{E12}$$

The work δW_e done by the air pressures during infinitesimal virtual displacements δh and $\delta\alpha$ yields expressions for Q_h and Q_α per unit span of the airfoil:

$$\begin{aligned}\delta W_e &= Q_h\delta h + Q_\alpha\delta\alpha \\ &= \int_{-b}^{b}\{(p_U - p_L)dx\,\delta h + (p_U - p_L)[x - ba]dx\,\delta\alpha\}.\end{aligned} \tag{E13}$$

From equation (E13) it follows that

$$Q_h = \int_{-b}^{b}(p_U - p_L)dx = -L \tag{E14}$$

and

$$Q_\alpha = \int_{-b}^{b}(p_U - p_L)[x - ba]dx = M_y, \tag{E15}$$

where L is the running lift (positive in the z-direction) and M_y is the running moment (positive for positive rotation about the spanwise y-axis along $x = ba$).[4] To use these directly, we agree that the section has unit length in the y-direction.

For the prediction of flutter, we are interested only in dynamic variations of h and α from whatever steady-state values they assume. The wing would probably be flying at some positive angle of attack, and there might also be contributions to L and M_y due to camber of the airfoil. For our purposes, however, we subtract the equilibrated system of steady-state forces and moments from equations (E11) and (E12) leaving only the time-dependent portions.

The standard scheme of flutter analysis resembles the one for free vibrations in that we specify simple harmonic motion in advance by setting

$$h = \bar{h}_0\,e^{i\omega t} , \tag{E16}$$

---

[4]The reader will, of course, have no difficulty in deriving equations (E1), (E2), (E4), and (E5) by direct application of Newton's Second Law of Motion to this simple system.

$$\alpha = \alpha_0 e^{i(\omega t + \phi)} = \overline{\alpha}_0 \; e^{i\omega t} . \tag{E17}$$

This complex representation is justified because the linearity of the equations of motion and the aerodynamic theories to be employed shows that all dependent variables in the problem contain time only as the factor $e^{i\omega t}$. We tacitly agree that the actual quantities are always found by taking the real parts of their complex counterparts, recognizing that the algebraic simplification achieved by complex notation outweighs any loss of physical clarity. Since phase shifts in the aerodynamic loads produce a phase difference between h and α, we allow for this by letting one or both of the amplitudes $\overline{h}_0$ and $\overline{\alpha}_0$ be complex numbers. If the time origin is chosen so as to make $\overline{h}_0$ real, the angle by which α leads h is defined in equation (E17) as ϕ, the argument of $\overline{\alpha}_0$.

The assumption of simple harmonic motion changes equations (E11) and (E12) into

$$-\omega^2 mh - \omega^2 S_\alpha \alpha + \omega_h{}^2 mh = -L , \tag{E18}$$

$$-\omega^2 S_\alpha h - \omega^2 I_\alpha \alpha + \omega_\alpha{}^2 I_\alpha \alpha = M_y . \tag{E19}$$

Our choice of particular aerodynamic expressions to replace L and M_y depends on the Mach-number range in which flutter is expected to occur. We simplify the discussion in the present section by assuming low-speed flow; this permits us to put L and M_y into the notation of ref. E3.

$$L = -\pi\rho b^3 \omega^2 \left\{ L_h \frac{h}{b} + \left[L_\alpha - L_h \left(\tfrac{1}{2} + a \right) \right] \alpha \right\} , \tag{E20}$$

$$M_y = \pi\rho b^4 \omega^2 \left\{ \left[M_h - L_h \left(\tfrac{1}{2} + a \right) \right] \frac{h}{b} + \left[M_\alpha - \left(L_\alpha + M_h \right)\left(\tfrac{1}{2} + a \right) + L_h \left(\tfrac{1}{2} + a \right)^2 \right] \alpha \right\} , \tag{E21}$$

where L_h, L_α, and M_α are elaborate functions of the reduced frequency k only, and M_h is just $\frac{1}{2}$ in the incompressible case. Substituting equations (E20) and (E21) into equations (E18) and (E19), and dividing by $\pi\rho b^3 \omega^2 e^{i\omega t}$ and $\pi\rho b^4 \omega^2 e^{i\omega t}$, we get the dimensionless flutter equations

$$\frac{\overline{h}_0}{b} \left\{ \frac{m}{\pi\rho b^2} \left[1 - \frac{\omega_h{}^2}{\omega^2} \right] + L_h \right\} + \overline{\alpha}_0 \left\{ x_\alpha \frac{m}{\pi\rho b^2} + \left[L_\alpha - L_h \left(\tfrac{1}{2} + a \right) \right] \right\} = 0 \tag{E22}$$

$$\frac{\overline{h}_0}{b} \left\{ x_\alpha \frac{m}{\pi\rho b^2} + \left[\tfrac{1}{2} - L_h \left(\tfrac{1}{2} + a \right) \right] \right\} + \overline{\alpha}_0 \left\{ r_\alpha^2 \frac{m}{\pi\rho b^2} \left[1 - \frac{\omega_\alpha{}^2}{\omega^2} \right] + M_\alpha - \left(L_\alpha + \tfrac{1}{2} \right)\left(\tfrac{1}{2} + a \right) + L_h \left(\tfrac{1}{2} + a \right)^2 \right\} = 0 . \tag{E23}$$

Since Equations (E22) and (E23) are homogeneous, they constitute an algebraic eigenvalue problem with finite solutions occurring at those combinations of speed and frequency for which the characteristic determinant vanishes.

References

E1. Theodorsen, Theodore; and Garrick, I.E.: Mechanism of Flutter—A Theoretical and Experimental Investigation of the Flutter Problem. NACA−TR−685, 1940.

E2. Theodorsen, Theodore: General Theory of Aerodynamic Instability and the Mechanism of Flutter. NACA−TR−496, 1949.

E3. Smilg, Benjamin; and Wasserman, Lee S.: Application of Three-Dimensional Flutter Theory to Aircraft Structures (With Corrections for the Effects of Control Surface Aerodynamic Balance and Geared Tabs). Air Corps TR−4798, 1942.

Some Remarks on the Use of Scale Models[*]

Raymond G. Kvaternik
National Aeronautics and Space Administration
Langley Research Center
Hampton, Virginia 23681

Aeroelastically-scaled wind-tunnel models have played an important role in the design, development, and verification process in diverse fields of engineering, including aerospace engineering (see, for example refs. 1 to 6). Their use is particularly prolific in the field of aeronautics wherein dynamic aeroelastic (i.e., flutter) models are extensively employed both to substantiate that an aircraft design is free of aeroelastic instabilities within its flight envelope, and to validate analyses. Analytical capabilities for addressing aeroelastic design issues of aircraft have improved significantly over the years. However, because aircraft have continued to increase in structural and aerodynamic complexity, the need to rely on wind-tunnel tests of subscale models to verify predicted behavior and performance before entering the flight test stage of a development program remains. Such models are also widely used in research investigations dealing with such issues as active control of aeroelastic stability and response, buffet load alleviation, and for the validation of analytical and computational methods used in design.

The importance of subscale models for helicopter research has been recognized as early as 1953 (refs. 7 and 8). Subscale models have also played a valuable, although perhaps less prominent, role in the design and development of helicopters, tiltrotors, and V/STOL aircraft (for example, see refs. 5, 6, 9, and 10). Both government and industry have acknowledged the significance and role of subscale models in rotorcraft research and development on many occasions. For example, references 11 and 12 emphasized the importance of a properly conducted wind-tunnel test program that includes both model-scale and full-scale testing to reduce the technical risk of a rotorcraft development program, and to lessen the chance for surprises in the flight test stage.

Model Scaling Considerations

Dynamic aeroelastic models may be classified into two general groups: (1) research models, and (2) prediction models. Research models do not represent any particular aircraft and are at most only broadly representative of full-scale designs. They are used primarily to gain insight into aeroelastic problems (e.g., identify the types of flutter which may be associated with a new or unusual configuration), to provide experimental data for comparison with analysis, and to provide general design information on flutter trends that occur with variations in system parameters. Prediction models are based on actual full-scale designs and are intended to predict the full-scale behavior of specific aircraft. These models are related to the full-scale designs that they represent by certain scaling relationships. It should be noted that prediction models can also be used effectively as research models.

A model will exhibit similitude or similarity to a full-scale structure provided certain dimensionless ratios have the same values for both. These dimensionless ratios may be determined by dimensional analysis of all the quantities involved in the problem or (if the structure is simple enough) from the differential equations which define the system. The objective of the theory of similitude (refs. 1, 2, 13 to 15) is to establish those relationships that must be maintained to permit reliable predictions to be made from measured model behavior. Usually, not all dimensionless

---

ratios can be maintained at full-scale values with reasonable choices of materials and scale factors in available test facilities. In such cases, complete similarity cannot be maintained and compromises must be made, based on experience and knowledge of the problem, by which the less important dimensionless ratios are allowed to deviate from full-scale values. Fortunately, a model is usually designed to study only a particular phenomenon (or class of phenomena), in which case only those dimensionless ratios important for the phenomena of interest need be maintained at their full-scale values.

The requirements for achieving dynamic and aeroelastic similitude of model and full-scale aircraft and helicopters are replete in the literature (see, for example, refs. 14 to 19) and will be reviewed here only briefly as they apply to rotorcraft. As mentioned above, the similarity requirements can be obtained either by applying dimensional analysis to the problem or by examining the appropriate governing equations written in nondimensional form. Application of such procedures results in the identification of the basic independent nondimensional parameters that must have a one-to-one correspondence between model and full scale to ensure adequate representation. For the study of dynamic aeroelasticity and unsteady aerodynamics phenomena, five basic similarity parameters are indicated: Mach number, advance ratio (reduced frequency), Lock number (mass ratio), Reynolds number, and Froude number. The other dependent ratios relating model quantities to full-scale quantities can be derived from these basic similarity parameters. The models must also be geometrically similar to their full-scale equivalents in external shape as well as in their distribution of mass and stiffness. In addition, any important body degrees-of-freedom must be included in the models.

The simultaneous satisfaction of the five similarity parameters noted above is not possible because of conflicting requirements that result for the design of a model. In conventional wind tunnels using atmospheric pressure air as the test medium, only three of the five parameters can be maintained at their full-scale values. For the simulation of flight conditions where compressibility effects are important, it is well established that the full-scale values of Mach number, advance ratio, and Lock number must be maintained in the model. This is true whether the model is to be tested in air or heavy gas. However, if the model is designed for testing in the heavy gas test medium of the Langley Transonic Dynamics Tunnel (TDT), Froude number may be maintained simultaneously with Mach number, advance ratio, and Lock number by selecting an appropriate length scale factor (about 0.20 to 0.29 depending on the simulated full-scale altitude). For simulation of flight conditions where compressibility effects are not important, models are usually designed to maintain full-scale values of advance ratio, Froude number, and Lock number when tested in air. However, for suitable length scale factors, these models can simultaneously obtain near full-scale values of Mach number when tested in heavy gas. It is generally not possible to simulate full-scale Reynolds number in either the air or heavy gas test mediums of the TDT. However, the use of heavy gas permits a nearly three-fold increase in Reynolds number over comparable conditions in air.

Some of the more important aeroelastic scale factors applicable to rotorcraft models in the TDT are summarized in table 1. Scale factors are tabulated for testing in air, R-12, and R-134a for the cases in which either Mach number or Froude number is maintained at its full-scale value in addition to Lock number and advance ratio.

TABLE 1.—AEROELASTIC SCALE FACTORS APPLICABLE TO ROTORCRAFT MODELS IN THE LANGLEY
TRANSONIC DYNAMICS TUNNEL FOR EQUAL LOCK NUMBERS (MASS-DENSITY RATIOS)
AND ADVANCE RATIOS (REDUCED FREQUENCIES)

Parameter	Mach Numbers Equal				Froude Numbers Equal			
	General	Air	Freon-12	R-134a	General	Air	Freon-12	R-134a
Length	L	L	L	L	L	L	L	L
Mass	$L^3\rho$	$L^3\rho$	$L^3\rho$	$L^3\rho$	$L^3\rho$	$L^3\rho$	$L^3\rho$	$L^3\rho$
Time	$L(\gamma RT)^{-1/2}$	$LT^{-1/2}$	$2.227\,LT^{-1/2}$	$2.066\,LT^{-1/2}$	$L^{1/2}g^{-1/2}$	$L^{1/2}$	$L^{1/2}$	$L^{1/2}$
Mach number	1	1	1	1	$(Lg)^{1/2}(\gamma RT)^{-1/2}$	$L^{1/2}T^{-1/2}$	$2.227\,L^{1/2}T^{-1/2}$	$2.066\,L^{1/2}T^{-1/2}$
Froude number	$(Lg)^{-1}(\gamma RT)$	$L^{-1}T$	$0.202\,L^{-1}T$	$0.234\,L^{-1}T$	1	1	1	1
Reynolds number	$L\rho\mu^{-1}(\gamma RT)^{1/2}$	$L\rho T^{-0.26}$	$0.449\,L\rho\mu^{-1}T^{1/2}$	$0.484\,\rho\mu^{-1}T^{1/2}$	$L^{3/2}\rho\mu^{-1}g^{1/2}$	$L^{3/2}\rho T^{-0.76}$	$L^{3/2}\rho\mu^{-1}$	$L^{3/2}\rho\mu^{-1}$
Force	$L^2\rho(\gamma RT)$	$L^2\rho T$	$0.202\,L^2\rho T$	$0.234\,L^2\rho T$	$L^3\rho g$	$L^3\rho$	$L^3\rho$	$L^3\rho$
Speed	$(\gamma RT)^{1/2}$	$T^{1/2}$	$0.449\,T^{1/2}$	$0.484\,T^{1/2}$	$L^{1/2}g^{1/2}$	$L^{1/2}$	$L^{1/2}$	$L^{1/2}$
Linear acceleration	$L^{-1}(\gamma RT)$	$L^{-1}T$	$0.202\,L^{-1}T$	$0.234\,L^{-1}T$	g	1	1	1
Frequency	$L^{-1}(\gamma RT)^{1/2}$	$L^{-1}T^{1/2}$	$0.449\,L^{-1}T^{1/2}$	$0.484\,L^{-1}T^{1/2}$	$L^{-1/2}g^{1/2}$	$L^{-1/2}$	$L^{-1/2}$	$L^{-1/2}$
Angular acceleration	$L^{-2}(\gamma RT)$	$L^{-2}T$	$0.202\,L^{-2}T$	$0.234\,L^{-2}T$	$L^{-1}g$	L^{-1}	L^{-1}	L^{-1}
Moment, Work	$L^3\rho(\gamma RT)$	$L^3\rho T$	$0.202\,L^3\rho T$	$0.234\,L^3\rho T$	$L^4\rho g$	$L^4\rho$	$L^4\rho$	$L^4\rho$
Power	$L^2\rho(\gamma RT)^{3/2}$	$L^2\rho T^{3/2}$	$0.091\,L^2\rho T^{3/2}$	$0.113\,L^2\rho T^{3/2}$	$L^{7/2}\rho g^{3/2}$	$L^{7/2}\rho$	$L^{7/2}\rho$	$L^{7/2}\rho$
Moment of inertia	$L^5\rho$	$L^5\rho$	$L^5\rho$	$L^5\rho$	$L^5\rho$	$L^5\rho$	$L^5\rho$	$L^5\rho$
Pressure, Stress	$\rho(\gamma RT)$	ρT	$0.202\,\rho T$	$0.234\,\rho T$	$L\rho g$	$L\rho$	$L\rho$	$L\rho$
Stiffness (EI,GJ)	$L^4\rho(\gamma RT)$	$L^4\rho T$	$0.202\,L^4\rho T$	$0.234\,L^4\rho T$	$L^5\rho g$	$L^5\rho$	$L^5\rho$	$L^5\rho$

Scale factors equal ratio of model to full-scale values [of the quantities indicated]; e.g., $L = L_M/L_F$, $\gamma RT = (\gamma RT)_M/(\gamma RT)_F$, etc., where T = absolute temperature, ρ = test medium density, R = gas constant, μ = viscosity, γ = specific heat ratio for gas, and g is the acceleration due to gravity.

Air constants based on $\gamma = 1.4$, $R = 1716$ ft^2/sec^2 $^{\circ}$R

Freon-12 constants based on $\gamma = 1.137$, $R = 427.3$ ft^2/sec^2 $^{\circ}$R, (95% Freon-12/air mixture)

R-134a constants based on $\gamma = 1.114$, $R = 505.3$ ft^2/sec^2 $^{\circ}$R, (95% R-134a/air mixture)

References

1. Murphy, Glenn: Similitude in Engineering. Ronald Press Co., New York, NY, 1950.
2. Baker, Wilfred E.; Westine, Peter S.; and Dodge, Franklin T.: Similarity Methods in Engineering Dynamics: Theory and Practice of Scale Modeling. Hayden Book Company, Rochelle Park, NJ, 1973.
3. Nielsen, William C., et al.: Proceedings of Symposium on Aeroelastic & Dynamic Modeling Technology. AFFDL Report RTD–TDR–63–4197, 1964.
4. Regier, A.A.: The Use of Scaled Dynamic Models in Several Aerospace Vehicle Studies. NASA TM X–50350, 1963.
5. Guyett, P.R.: The Use of Flexible Models in Aerospace Engineering. RAE–TR–66335, 1966.

6. Kuntz, W.H.; Wasserman, L.S.; and Alexander, H.R.: Dynamically Similar Model Tests of Rotary Wing and Propeller Types of VTOL Aircraft. Proceedings of the Air Force V/STOL Technology and Planning Conference, Las Vegas, NV, 1969.

7. Brooks, G.W.: The Application of Models to Helicopter Vibration and Flutter Research. Proceedings of the Ninth Annual Forum of the American Helicopter Society, Washington, DC, May 14–17, 1953.

8. Fradenburgh, E.A.; and Kiely, E.F.: Development of Dynamic Model Rotor Blades for High Speed Helicopter Research. J. Am. Helicopter Soc., vol. 9, 1964, pp. 3–20.

9. Albrecht, C.O.: Factors in the Design and Fabrication of Powered, Dynamically Similar V/STOL Wind Tunnel Models. Proceedings of the Mideast Region Symposium on the Status of Testing and Modeling Techniques for V/STOL Aircraft, Essington, PA, 1972.

10. Ormiston, R.A.: Helicopter Modeling/18th Henson and Stringfellow Lecture. Aeronaut. J., vol. 77, 1973, pp. 579–591.

11. Rabbott, J.P., Jr.: Model Versus Full Scale Rotor Testing (V/STOL Model Small Scale Tests Compared With Full Scale Tunnel or Flight Tests, Considering Normal Differences in Parameters and Rotor Instability). Proceedings of the CAL/AVLABS Symposium on Aerodynamics of Rotary Wing and V/STOL Aircraft, vol. II , Buffalo, NY, 1969.

12. Kelly, M.W.: The Role of Wind Tunnel Testing in the Development of Advanced Rotary-Wing Aircraft. Proceedings of the Mideast Region Symposium, Essington, PA, 1972.

13. Langhaar, Henry L.: Dimensional Analysis and Theory of Models. John Wiley & Sons, Inc., New York, NY, 1951.

14. Templeton, H.: Models for Aero-Elastic Investigations. Aeronautical Research Council CP–255, 1956.

15. Molyneux, W.G.: Aeroelastic Modelling (Requirements for Aeroelastic Similarity Between Aircraft and Model in Relation to Flow Regimes). RAE–TN–STRUCT–353, 1964.

16. Hunt, G.K.: Similarity Requirements for Aeroelastic Models of Helicopter Rotors. ARC–CP–1245, RAE–TR–72005, 1972.

17. Lee, C: Weight Considerations in Dynamically Similar Model Rotor Design. Presented at the 27th Annual Conference of the Society of Aeronautical Weight Engineers, SAWE Paper 659, 1968.

18. Hanson, P.W.: An Assessment of the Future Roles of the National Transonic Facility and the Langley Transonic Dynamics Tunnel in Aeroelastic and Unsteady Aerodynamic Testing. NASA TM–81839, 1980.

19. Singleton, Jeffrey D.; and Yeager, William T., Jr.: Important Scaling Parameters for Testing Model-Scale Helicopter Rotors. J. Aircraft (AIAA Paper 98–2881), vol. 37, no. 3, pp. 396–402.

REPORT DOCUMENTATION PAGE

Form Approved
OMB No. 0704-0188

Public reporting burden for this collection of information is estimated to average 1 hour per response, including the time for reviewing instructions, searching existing data sources, gathering and maintaining the data needed, and completing and reviewing the collection of information. Send comments regarding this burden estimate or any other aspect of this collection of information, including suggestions for reducing this burden, to Washington Headquarters Services, Directorate for Information Operations and Reports, 1215 Jefferson Davis Highway, Suite 1204, Arlington, VA 22202-4302, and to the Office of Management and Budget, Paperwork Reduction Project (0704-0188), Washington, DC 20503.

1. AGENCY USE ONLY (Leave blank)	2. REPORT DATE	3. REPORT TYPE AND DATES COVERED
	November 2006	Technical Paper

4. TITLE AND SUBTITLE

NASA Aeroelasticity Handbook
Volume 2: Design Guides
Part 2

5. FUNDING NUMBERS

WBS 561581.02.08.03.04.04

6. AUTHOR(S)

John K. Ramsey, editor

7. PERFORMING ORGANIZATION NAME(S) AND ADDRESS(ES)

National Aeronautics and Space Administration
John H. Glenn Research Center at Lewis Field
Cleveland, Ohio 44135–3191

8. PERFORMING ORGANIZATION REPORT NUMBER

E–14035

9. SPONSORING/MONITORING AGENCY NAME(S) AND ADDRESS(ES)

National Aeronautics and Space Administration
Washington, DC 20546–0001

10. SPONSORING/MONITORING AGENCY REPORT NUMBER

NASA TP—2006-212490-VOL2-PART2

11. SUPPLEMENTARY NOTES

Responsible person, John K. Ramsey, organization code DES, 216–433–6032.

12a. DISTRIBUTION/AVAILABILITY STATEMENT

Unclassified - Unlimited
Subject Categories: 05, 07, 08, 18, and 61

Available electronically at http://gltrs.grc.nasa.gov

This publication is available from the NASA Center for AeroSpace Information, 301–621–0390.

12b. DISTRIBUTION CODE

13. ABSTRACT (Maximum 200 words)

The NASA Aeroelasticity Handbook comprises a database (in three formats) of NACA and NASA aeroelasticity flutter data through 1998 and a collection of aeroelasticity design guides. The Microsoft Access format provides the capability to search for specific data, retrieve it, and present it in a tabular or graphical form unique to the application. The full-text NACA and NASA documents from which the data originated are provided in portable document format (PDF), and these are hyperlinked to their respective data records. This provides full access to all available information from the data source. Two other electronic formats, one delimited by commas and the other by spaces, are provided for use with other software capable of reading text files. To the best of the author's knowledge, this database represents the most extensive collection of NACA and NASA flutter data in electronic form compiled to date by NASA. Volume 2 of the handbook contains a convenient collection of aeroelastic design guides covering fixed wings, turbomachinery, propellers and rotors, panels, and model scaling. This handbook provides an interactive database and design guides for use in the preliminary aeroelastic design of aerospace systems and can also be used in validating or calibrating flutter-prediction software.

14. SUBJECT TERMS

Forced vibration; Self excitation; Wing oscillations; Self induced vibration; Buffeting; Transonic flutter; Supersonic flutter; Subsonic flutter; Panel flutter; Flutter; Airfoil oscillations; Aircraft structures; Aerothermoelasticity; Aeroservoelasticity; Aeroelasticity

15. NUMBER OF PAGES

569

16. PRICE CODE

17. SECURITY CLASSIFICATION OF REPORT	18. SECURITY CLASSIFICATION OF THIS PAGE	19. SECURITY CLASSIFICATION OF ABSTRACT	20. LIMITATION OF ABSTRACT
Unclassified	Unclassified	Unclassified	